«Saint Petersburg OPEN 2021»

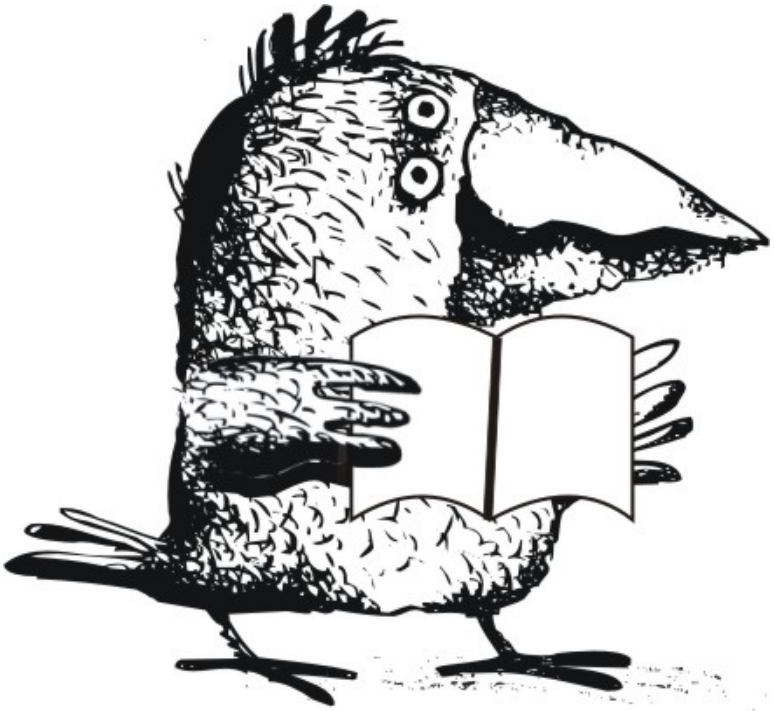

BOOK of ABSTRACTS

8th International School and Conference on Optoelectronics, Photonics, Engineering and Nanostructures

May 25-28, 2021 • Saint Petersburg, Russia

“Saint Petersburg OPEN 2021”

8th International School and Conference on Optoelectronics, Photonics, Engineering and Nanostructures

St. Petersburg, Russia, May 25 – 28, 2021

BOOK of ABSTRACTS

Academic University Publishing
St. Petersburg, 2021

NATIONAL RESEARCH UNIVERSITY

8th International School and Conference "Saint Petersburg OPEN 2021" on Optoelectronics, Photonics, Engineering and Nanostructures carries on the tradition of annual conferences and schools organized at St Petersburg Academic University for students, PhD students and young scientists.

More detailed information on the School and Conference is presented on *https://spb.hse.ru/spbopen/*

The Book of Abstracts includes abstracts of contributed works accepted for presentation at the Conference.

The volume was composed by HSE University - St. Petersburg from electronic files submitted by the authors. Only minor technical corrections were made by the composers.

Chief Editor: A. E. Zhukov

Published by
HSE University - St. Petersburg,
Soyuza Pechatnikov 16, 190121, St Petersburg,
Printed in Russian Federation

Organizers

NATIONAL RESEARCH UNIVERSITY

St Petersburg Academic University

Acknowledgements

RSF

SPIE. STUDENT CHAPTER
SAINT-PETERSBURG ACADEMIC UNIVERSITY RUSSIAN ACADEMY OF SCIENCES

IOP Institute of Physics

НАЦИОНАЛЬНЫЕ ПРОЕКТЫ РОССИИ

НАУЧНЫЙ ЦЕНТР МИРОВОГО УРОВНЯ
«ПЕРЕДОВЫЕ ЦИФРОВЫЕ ТЕХНОЛОГИИ»

ПОЛИТЕХ

Санкт-Петербургский политехнический университет Петра Великого (координатор консорциума)

Санкт-Петербургский государственный морской технический университет

Тюменский государственный университет

НИИ гриппа имени А.А. Смородинцева Минздрава России

Head of Program Committee

Alexey E. Zhukov

corr. member of the RAS, *HSE University, Russia*

Program Committee

Aleksandr V. Omelchenko (HSE University- St.Petersburg)

Andrey A. Lipovskii (Peter the Great St.Petersburg Polytechnic University, Russia)

George E. Cirlin (Alferov University, Russia)

Valentina V. Zhurikhina (Peter the Great St.Petersburg Polytechnic University, Russia)

Natalia V. Kryzhanovskaya (HSE University- St.Petersburg)

Anna Baldycheva (University of Exeter)

Kate Berseneva (University of Exeter)

Head of Organizing Committee

Alexey E. Zhukov (HSE University- St.Petersburg)

Organizing Committee

Mikhail V. Maximov (Ioffe Institute, Alferov University, Russia)

Andrey A. Lipovskii (Peter the Great St.Petersburg Polytechnic University, Russia)

Valentina V. Zhurikhina (Peter the Great St.Petersburg Polytechnic University, Russia)

Vladimir V. Korenev (Alferov University, Russia)

Eduard I. Moiseev (HSE University- St.Petersburg)

Anna S. Dragunova (Alferov University, Russia)

Svetlana A. Kadinskaya (Alferov University, Russia)

Yulia S. Balezina (Alferov University, Russia)

Elizaveta O. Kotko (HSE University- St.Petersburg)

Invited Speakers

Crystal growth and structural properties of semiconductor materials and nanostructures

Lasers, solar cells and other optoelectronic devices

Nanophotonics, Spectroscopy, Microcavities, Optics, Plasmonics

Nanobiotechnology, Biophysics and Biophotonics

Electric, Magnetic and Microwave Devices

Other Aspects of Nanotechnology

Will it be possible to make room temperature THz quantum cascade lasers?

R.A. Khabibullin[1], D.S. Ponomarev[1], D.V. Ushakov[2], A.A. Afonenko[2]

[1]V.G. Mokerov Institute of Ultra High Frequency Semiconductor Electronics, Russian Academy of Sciences, Moscow 117105, Russia
[2]Belarusian State University, Minsk 220030, Belarus

E-mail: khabibullin@isvch.ru

Abstract. Over the past two decades, the operation temperature of terahertz quantum cascade lasers (THz QCLs) has continuously increased from cryogenic level to the current record value of 250 K (about -23ºC) [1]. Here we review the state-of-the-art and future prospects of high-temperature THz QCL designs with three- and two-quantum wells in period based on conventional heterojunction GaAs/AlGaAs and alternative material system HgCdTe. We have analyzed the temperature dependence of the peak gain and predicted the maximum operation temperatures of the given designs. The growth issues of multi-layered structures for high-temperature THz QCL are also discussed.

The limiting factors for increasing the operation temperatures of THz QCLs are associated with strong optical phonon scattering, the presence of parasitic current channels and the formation of electric field domains as was shown in [2,3]. Recently, the mode loss spectra for THz QCLs with double metal waveguide (DMW) were demonstrated in [4]. It was shown the high level of propagation loss of THz radiation in DMW, which exceeds 30 cm^{-1} for room temperature. Thus, to improve the high-temperature performance of THz QCLs it is needed to develop new concepts of active region designs and to reduce losses in DMW.

To calculate the THz QCL characteristics we have used the balance equation method with "tight-binding" wave-function basis. This basis has been obtained as superposition of eigenstates of the Schrödinger equation for the entire active region of a THz QCL by minimization of the spatial extension of wave functions of tunnel-coupled states. The localized ("tight-binding") basis is more stable for dephasing impact, as degenerate basis states with $\Delta E \lesssim 3$ meV have a small overlap of wavefunctions and, correspondingly, a low self-scattering rate.

First, we have analyzed the 3-well design based on GaAs/$Al_xGa_{1-x}As$ and optimized the height of potential barriers with a high Al content (see Table 1). In Fig. 1 we demonstrate the operation principle of the given designs and the current flow through the energy levels. In Fig. 2, we compare the temperature dependence of the peak gain at 3.9 THz and show the ability to operate above 200 K for designs with Al content x>0.2. Second, we simulate THz QCLs on the basis of narrow-gap HgCdTe quantum wells and calculate its characteristics. The characteristics of a single period, including current through localized states, leakage currents to continuum states, gain spectra and losses, were found by solving a system of balanced equations. We have proposed the 3-well and 2-well HgCdTe designs with maximum operation temperatures of 170 K and 225 K, respectively [6].

Table 1. Parameters of optimized 3-well designs of THz QCL based on GaAs/$Al_xGa_{1-x}As$.

	x	Barrier height U_0, meV	Layer sequence in period - **potential barrier**/quantum well, nm
Bosco design [5]	0.25	212.5	**1.98**/16.37/**3.39**/7.91
Design A	0.2	178.5	**2.3**/16.4/**4.2**/7.3
Design B	0.25	212.5	**2.0**/17.2/**3.4**/7.9
Design C	0.3	244.5	**1.7**/17.0/**3.1**/7.9

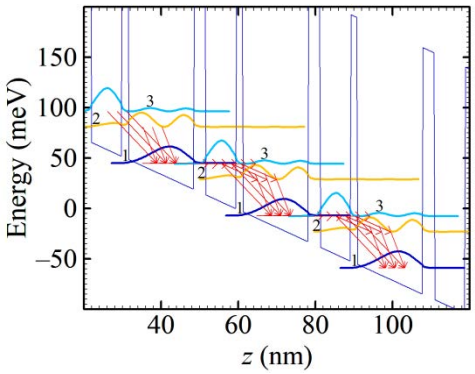

Fig. 1. Conduction band diagram and squared modules of wavefunctions for GaAs/Al0.3Ga0.7As design.

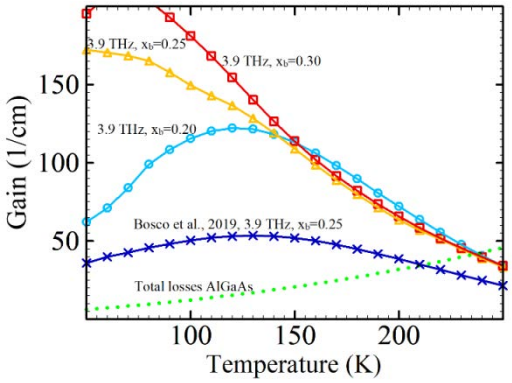

Fig.2. The temperature dependencies of peak gain are shown for GaAs/AlGaAs design with various Al content in barriers.

Acknowledgments
This work was supported by the Russian Science Foundation Grant No. 21-72-30020.

References

[1] Khalatpour A. et al. 2020 *Nat. Photonics*, https://doi.org/10.1038/s41566-020-00707-5.
[2] R.A. Khabibullin, N.V. Shchavruk et al *Opto-Electronics Review* **27** 329.
[3] Ushakov D.V., Afonenko A.A. et al. 2019 *Quantum Electronics* **49** 913.
[4] Ushakov D.V., Afonenko A.A. et al. 2018 *Quantum Electronics* **48** 1005.
[5] Bosco L. et al. *Appl. Phys. Lett.* 2019 **115** 010601.
[6] Ushakov D.V., Afonenko A.A. et al. 2020 *Opt. Express* **28** 25371.

Towards International Year of Glass: from Vessels to Photonics

A A Lipovskii
World-class Research Center: Advanced Digital Technologies, Peter the Great St. Petersburg Polytechnic University, St. Petersburg 195251, Russia

Abstract. Since glass is of great importance to humanity, the United Nations is currently considering an application to declare 2022 the International Year of Glass. Glass was first synthesized about 5000 years ago. By now, it has gone from the first glass vessels to modern technical glasses, for example, architectural, and to photonic glasses. A very incomplete list of the latter includes glasses designed for fiber optics, lasers and amplifiers, glass ceramics, gradient optics, nonlinear optics, integrated optics, and solar power. Despite the long history and well-developed glass science and technology, new discoveries in the field of glass appear regularly, and a number of questions remain unanswered.

1. Introduction

The number of Web of Science references for "semiconductor" and for "glass" is ~420,000 and ~540,000, and Google search returns ~180,000,000 and ~2,500,000,000 items, respectively. This reflects roughly the same amount of research in these two areas and the very high importance of glasses in everyday life. This is why the application to declare 2022 the International Year of Glass is being considered by the United Nations after 2020 has been declared the International Year of Light. The first evidence of glass synthesis found in Mesopotamia dates back to around 5000 BC, the earliest glass vessels date from around 1500 BC (Egypt), then the centers of glass production moved through Ancient Rome to Venice (~ 1000 AD), France (~ 17th century) and Germany (19th century). Today glass is produced worldwide. The emergence of a new branch of glass science, in addition to research and development of technical glasses (for vessels, windows, mirrors, for architectural applications) and optical glass (mainly for lenses and color filters), corresponds to the development of the first laser glass (1963) and glass for optical fibers (1968). This was the beginning of the photonic glass era. In addition to photonic applications, glass for textiles, fertilizers, battery electrodes (fast conductors), for medicine (bioglass), for ecology (nuclear waste disposal) and many others are under intensive development.

2. Briefly about the current state of photonic glasses

Modern photonics uses glasses and glass ceramics obtained via controlled crystallization of specially designed glasses. Both are in use for lasers, in which glass ceramics provides crystal-like surrounding of light emitting entities allowing for narrower emission spectrum and efficient pumping. Other, some of the many, uses of glass ceramics are in the manufacture of mechanically stable mirrors for large telescopes and electro-optical modulators. High purity silica optical fibers are capable of transmitting an optical signal over long distances with low loss, and this signal can be enhanced with fiber optical amplifiers. Optical fibers are also widely used in sensors and fiber lasers aimed for industry and research. Special attention is paid by glass scientists to glassy nanocomposites that are glasses embedded with metallic or semiconductor nanoparticles. Besides these media have been known since the Middle Ages

as stained-glass windows, later as color filters, recent studies of their nanostructure and properties have allowed have allowed to find new applications for such materials, in particular, in nonlinear optics. Photosensitive glasses capable of recording optical patterns with high spatial resolution also have been designed. It is worth mentioning glasses designed for ion exchange, that is, replacing cations from glass (for example, sodium ions) with cations from molten salt (e.g. silver ions) in which the glass is immersed. This processing allows the formation of a predetermined distribution of the refractive index of the glass and is the main technology of Graded Index (GRIN) Optics. The same method is widely used in integrated optics for the manufacture of optical waveguides and other elements. One more of numerous directions of glass science relates to so-called low-phonon glasses perspective for light amplification and extra low-loss optical fibers for mid-infrared communication. The latter has been predicted but not yet obtained, presumably due to technological difficulties.

3. Existing problems: the origin

To date, many glasses of different composition have been synthesized. However, target glass design still faces challenges due to the mainly semi-empirical approach used for glass design. This is because of extremely flexible structure of this material, in which only short-range order and partly mid-range order exist. A random network of glasses and a variety of compositions, including multiple choices of both glass formers and modifiers, provide plenty of room for glasses with different properties, which details can hardly be predicted accurately. In addition, the transport properties of glasses responsible for their crystallization, ion exchange and electrical conductivity (typical multicomponent glass is an ionic conductor) are still poorly understood although several models describing ion exchange and conductivity are in use, e.g. ion hopping model. Additional features of glasses are their easy absorption and dissolution impurities, including crucible materials and gases, in synthesis, and the dependence of their properties on thermal history, which is luckily weak. Despite these, glass science has accumulated a lot of knowledge that made it possible to single out the general directions of glass design for various purposes. Enumerated problems define the necessity of studies aimed at understanding regularities in glass properties and establishing relations in the chain composition-synthesis-properties of glasses.

4. An example of research

Discussed difficulties in understanding of glass behavior can be illustrated by the studies of thermal poling of glasses. Thermal poling, first considered about 30 years ago, consists in the application of DC voltage, several hundreds of volts, to heated glass plate and subsequent cooling of the plate under the voltage. Briefly, the displacement of glass cations under the voltage results in spatial electric charge which electric field compensates the field applied to the glass in poling. This field should stay in the cooled glass, for spatial charge of the displaced cations stays “frozen” after glass cooling because of kinetic restrictions. Besides, poled glass loses initial central symmetry and demonstrates Pockels electrooptical phenomenon and second order optical nonlinearity forbidden in isotropic media. The majority of researchers associate these phenomena with the effect of the frozen electric field. However, the physics of glass poling is much more complicated than the one described above. The depletion of the subsurface region of the glass with charge carriers (mobile cations) in the poling results in a redistribution of electric field in the glass, and, in the depleted region, it can be as high as parts of volt per nanometer. This magnitude is sufficient to restructure the glass in this region, and in some cases to crystallize it. By now, an adequate model of the poling process and spatial charge formation has not been designed, the relaxation of the spatial charge and electric field has not completely understood, and the properties of the modified subsurface layer, which is actually a different glass with unique properties and a different composition from the original, are still being studied. At the same time the usability of thermal poling of glasses in nonlinear optics and for the formation of given microrelief on the glass surface (because of the change in chemical durability of the poling-modified subsurface region of the glass) is already demonstrated. Accounting for the variety of glasses, optimal choice of a glass and the mode of its thermal poling to provide, e.g. highest optical nonlinearity remains a challenging task.

Termo induced functional material based on Mie-resonant silicon nanoparticles covered with polymer shell

Anna A. Nikitina[a] *, Valentin A. Milichko[a, b], Artem O. Larin[a], Mikhail V. Rybin[a], Yuri S. Kivshar[a], Ekaterina V. Skorb[a]

[a] ITMO University, 9 Lomonosova street, 191002, St. Petersburg, 191002, Russia
[b] Université de Lorraine, Institut Jean Lamour, UMR CNRS 7198, Nancy F-54011, Franceype

nikitina@itmo.ru

Abstract. Here we report on the design and realization of stimuli-responsive bio-integrated optical materials based on silicon nanoparticles covered by an ensemble of similarly charged polyelectrolytes (heparin and sodium polystyrene sulfonate). The nanostructures' dynamic tuning's visual response by light is due to light-induced heating of the nanoparticles and accompanying swelling of the polyelectrolyte shell. The resulting reversible hydrophilic/hydrophobic transitions lead to the significant change in the shell thickness and shift of scattering spectra up to 60 nm at mild conditions. Our findings have both fundamental importance and potential for *in vivo* application as "smart" nanomaterials.

1. Introduction

Dielectric photonic nanostructures, due to their abundant unique properties and high compatibility, are becoming a forward class of nanomaterials. Tuning of electronic and optical properties contributes a novelty platform for a productive and valuable system for a new generation of nanophotonic devices as smart sensors[1,2].

In the present study, novelty properties of the system of silicon nanoparticles were achieved by functionalization with polyelectrolytes. Amphiphilic behavior of charged macromolecules allowed the rearrangement mechanism on the surface nanoparticles by the heating[3]. The driving force for hydrophobic/hydrophilic exchange mechanism can be obtained with vast types of stimuli: chemical, physical or mechanical effect[4,5].

2. Results and discussion

The strategy of changing between swelled and shrinking state-enforced with temperature inducing. Polyelectrolyte shell was formed with heparin and polystyrene sulfonate (PSS). The opportunities of hydrophobic/hydrophilic interaction of the similarity-charged polyelectrolytes were investigated by density functional theory. The results were shown that self-assembly of heparin and PSS is thermodynamically favorable (by 7.9 kcal/mol in terms of Gibbs free energies). Switching was confirmed with transmission electron microscopy (TEM) and also with z-potential measuring. Z-potential of nanoparticles changed correlated with the temperature: with room temperature it

corresponds to -5 mV, meanwhile with 60°C z-potential dramatically decreased to -60 mV. The effect was repeated at least five times.

The light-induced heating of each nanoparticle was performed by coherent light with tunable wavelengths. Numerical modeling was also performed to analyze the polymer shell thickness's effect on the spectral position of Mie resonances. Full-wave numerical simulations of near fields were carried out using commercial software CST Microwave Studio employing Finite Integral Technique. To calculate optical modes, we considered the irradiation by an infinite plane wave and integration of all scattered power. The polymer shell was considered a homogeneous medium with a refractive index of 1.48 and an extinction coefficient of 3.

3. Conclusion

We have demonstrated a strategy of stimuli-responsive materials based on optical properties of silicon nanoparticles and amphiphilic structure of heparin and PSS. Our suggestion that similarity-charged polyelectrolytes assembly can form shell structure was proved with DFT calculations.

Dynamic tuning of optical scattering spectra was observed by light-heating forcing swelling of the polyelectrolyte shell. Therefore, we expect further research toward scalable production of multicomponent. This mechanism provides numerous opportunities for application, from real-life application to bio-integrated nanophotonics.

Acknowledgments

Authors acknowledge RSF grant no. 19-19-00508 for the support of PEs study for the formation of robust PE shell and RSF grant no. 17-19-01637 for the support of NP preparation. ITMO Fellowship and Professorship Program 08-08 is acknowledged for Infrastructural Support.

References

[1] Bahng J H, Jahani S, Montjoy D G, Yao T, Kotov N and Marandi A 2020 Mie Resonance Engineering in Meta-Shell Supraparticles for Nanoscale Nonlinear Optics *ACS Nano* **14** 17203–12

[2] Ha M, Kim J H, You M, Li Q, Fan C and Nam J M 2019 Multicomponent Plasmonic Nanoparticles: From Heterostructured Nanoparticles to Colloidal Composite Nanostructures *Chem. Rev.* **119** 12208–78

[3] Richardson J J, Tardy B L, Ejima H, Guo J, Cui J, Liang K, Choi G H, Yoo P J, De Geest B G and Caruso F 2016 Thermally Induced Charge Reversal of Layer-by-Layer Assembled Single-Component Polymer Films *ACS Appl. Mater. Interfaces* **8** 7449–55

[4] Parakhonskiy B V., Parak W J, Volodkin D and Skirtach A G 2019 Hybrids of Polymeric Capsules, Lipids, and Nanoparticles: Thermodynamics and Temperature Rise at the Nanoscale and Emerging Applications *Langmuir* **35** 8574–83

[5] Tsuruoka A, Takahashi A, Aoki D and Otsuka H 2020 Fusion of Different Crosslinked Polymers Based on Dynamic Disulfide Exchange *Angew. Chemie - Int. Ed.* **59** 4294–8

Study of the effect of plasma frequency on the parameters of vertically oriented CNT

N N Rudyk, O I Il'in, M V Il'ina, **O R Polyvyanova**, **A A Fedotov**
Southern Federal University, Institute of Nanotechnologies, Electronics and Equipment Engineering, Taganrog, 347922, Russia

Abstract. The effect of the frequency of a pulsed plasma generator on the growth of carbon nanotubes (CNTs) by the method of plasma chemical vapor deposition (PECVD) has been studied. A comparative study of the mode of direct and pulsed current for the height and diameter of the obtained CNTs has been carried out. It is shown that the use of the pulsed mode makes it possible to additionally control the height of synthesized CNTs.

1. Introduction

Carbon nanotubes is a unique material for creating new devices and elements of nanoelectronics. The growth of carbon nanotubes (CNT) by thermal chemical vapor deposition (TCVD) is most in demand, but the plasma-CVD (PECVD) method has a number of advantages: lower synthesis temperature, increased growth rate, and the ability to control the direction of CNT growth [1]. The most common method for generating plasma is a discharge between two parallel capacitively coupled electrodes. This method, in contrast to inductively coupled plasma, makes it possible to generate a stable and homogeneous plasma and to grow uniform CNT over a larger area [2]. Among the varieties of this method there are: direct current and pulsed current. In pulsed PECVD, in addition to voltage and current control, pulse repetition rate, duty cycle, rise time are added [3]. In addition, in the presence of a pulsed current, the composition of the gas mixture in the growth chamber changes, which leads to a redistribution of the contribution of various chemical compounds to the formation of CNTs and a change in their parameters [4]. In this work, an experimental study of the effect of the frequency of a pulsed plasma generator on the geometric parameters of the obtained CNT was carried out.

2. Experiments and methods

As experimental samples, we used Si (100) substrates, on which films of a TiN sublayer (100 nm) and a catalytic Ni layer (10 nm) were successively deposited by magnetron sputtering. CNT were grown by the pulsed PECVD method. As working gas we used: Ar, C2H2, NH3. The pulse frequency at the Advanced Energy Pinnacle PLUS + 5kW plasma source was set in the range of 0 - 350 kHz. In our case, the sample was grounded, and a pulsed voltage was applied to the upper electrode, which was a shower for supplying process gases. The heating temperature in the growth of CNT was 660 ºC. The study of the samples was carried out using scanning electron microscopy (SEM) on a Nova Nanolab 600.

3. Results and Discussion

The analysis of the obtained results showed that the frequency of the pulsed plasma generator makes it possible to control the geometric parameters of the CNT. The dependences of the height and diameter of CNT on the plasma frequency have been obtained (Fig. 1). It can be seen from the obtained dependences

that the average height of the obtained CNT arrays increases from 3.16 ± 0.32 μm to 5.2 ± 0.69 μm (Fig. 1, a) with an increase in the plasma generation frequency. The monotonic increase in altitude observed in the frequency range 140-350 kHz may be due to an increase in the efficiency of decomposition of C_2H_2 and NH_3 with an increase in the pulse power. An increase in the pulse frequency leads to a decrease in their duration, and, consequently, to a higher energy, and an increase in the concentration of active radicals in the discharge area. However, the composition of the plasma, the concentration of ions and free radicals in it require additional research. With increasing frequency, the spread of the CNT height also increases from 0.32 μm to 0.69 μm. The average diameter of CNTs practically does not change with increasing frequency and is in the range from 43 ± 18 nm to 58 ± 35 nm (Fig. 1, b). However, an increase in frequency relative to a constant current mode leads to an increase in the diameter dispersion. This may be due to a decrease in the uniformity of the sizes of catalytic centers during their intensive processing in a plasma of a higher pulse power.

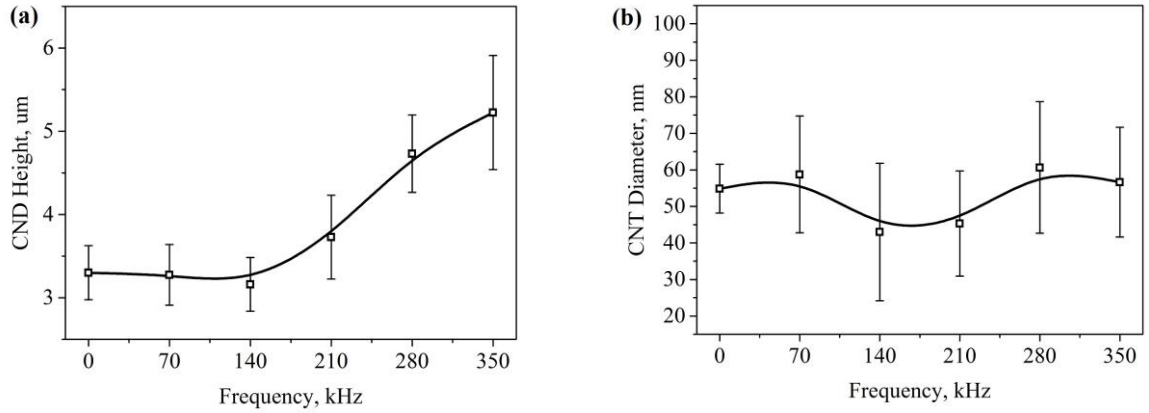

Figure 1(a,b). Dependence of the height **(a)** and diameter **(b)** of the CNTs on the pulse frequency.

The presented results show that the use of a pulsed plasma source is an additional source of control over the CNT parameters and makes it possible to increase the growth rate. However, a large dispersion in the diameter and analysis of the structural perfection of CNTs requires additional research. The obtained results can be used for creating elements and devices of micro- and nanoelectronics and nanopiezotronics.

4. Acknowledgments
This work was funded by the Russian Foundation for Basic Research according to the research project No. 20-37-70034.

References

[1] Ahmad M, Ravi S, Silva P 2020 Carbon **158** 24-44
[2] Baro M, Gogoi D, Ratan Pal A, Adhikary N, Bailung H, Chutia J 2014 Chemical Vapor Deposition **20** 1-9
[3] García-Céspedes J, Rubio-Roy M, Polo M C, Pascual E, Andújar L J, Bertran E 2007 Diamond & Related Materials **16** 1131-1135
[4] Wang H, Moore J 2010 Journal of Vacuum Science & Technology B **28** 1081-1085

Nanostructuring at oblique incidence deposition of cobalt

A A Akulov[1], O S Trushin[2], A A Popov[2], A N Pestova[2] and L A Mazaletsky[2]

[1] Department of Nanotechnology in Electronics, P.G. Demidov Yaroslavl State University, Sovetskaya Street 14, Yaroslavl, 150003, Russia
[2] Valiev institute of physics and technology of RAS, Yaroslavl Branch, Universitetskaya, 21, Yaroslavl, 150007, Russia

alekseyakulov@mail.ru, otrushin@gmail.com

Abstract. Nanocolumnar Co thin films growth by oblique angle deposition on Si substrate is experimentally studied. Formation of regular arrays of tilted Co nanocolumns has been observed at incidence angles more than 70 degrees. Such films might be perspective material for applications as a magnetic recording media for next generations of hard disks.

1. Introduction

The progress in the field of microelectronics is largely due to the improvement of the technology for producing thin films. A promising method for the formation of films with special properties is their nanostructuring during growth. One of the known technological methods allowing the growth of nanostructures is oblique angle deposition [1,2]. It is well known that by varying the angle of incidence one can change the direction of magnetic anisotropy. Magnetic thin films with easy axis tilted to the substrate surface are of considerable interest as a promising material for ultradense magnetic recording. Main goal of this work was to study the mechanisms of the growth of nanostructured Co thin films by oblique angle deposition and finding optimal conditions for the formation of perpendicular magnetic anisotropy (magnetization vector tilted to the film surface).

2. Experiment

Experiments on the deposition of Co films on an inclined substrate were carried out on an Oratoria-9 electron beam evaporation unit. The deposition conditions were as follows: base vacuum 4 10^{-6} Torr, electron beam voltage 8 kV, current 0.5 A. A standard single-crystal silicon wafer with a thermal oxide layer 300 nm thick was used as a substrate. The growth rate of the film was equal to 1 nm/s. The surface morphology of the obtained films was investigated by scanning electron microscopy (SEM) (Supra 40). Morphology of the film surface was studied using atomic force microscopy (AFM) (SMM-2000).

3. Results

Cross-section of the film deposited at incidence angle $\varphi=85^{o}$ is shown at figure 1(a). One can see that tilted fibrous microstructure is formed at this conditions. More complete information about the morphology of the film is obtained from the analysis of top view on its surface shown at figure 1(b). One can see that separate Co fibers have shape of narrow and thin strips with the width less than 40 nm and the thickness of several nanometers.

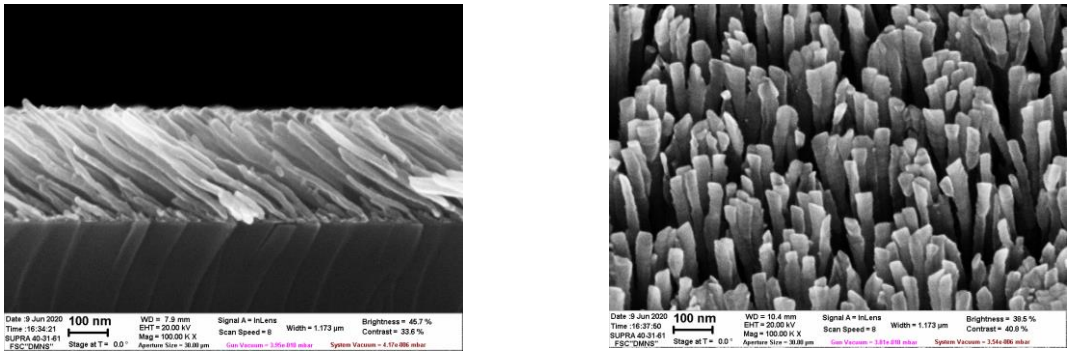

a b

Figure 1. Cross-section of the Co film (a) and top view on its surface (b). The images were obtained using electron scanning microscopy (SUPRA-40).

These observations are also confirmed by the results of atomic force microscopy, shown at figure 2.

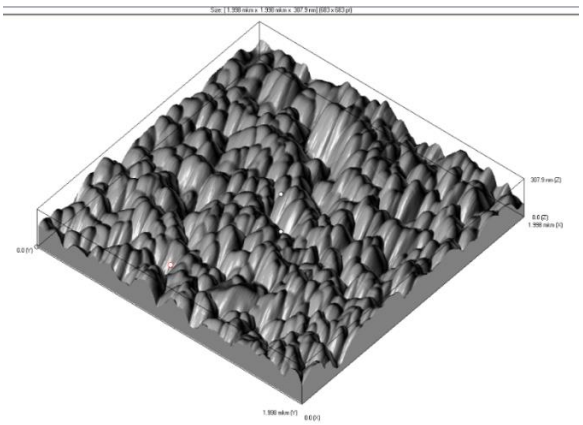

Figure 2. The morphology of Co film obtained using atomic force microscopy (SMM-2000).

4. Conclusion

In summary, as the results of experimental studies of the growth of Co thin films by oblique angle deposition it was found that optimal conditions for nanostructuring are achieved at the angle of 85º. Such films might be perspective for application in in high density magnetic recording.

Acknowledgments

This work was carried out on the equipment of the center for collective use of scientific equipment "Diagnostics of micro- and nanostructures" within the framework of the State assignment of the P.I. K.A. Valiev RAS Ministry of Education and Science of the Russian Federation on topic No. 0066-2019-0003 "Fundamental and applied research in the field of creating promising instrument nanostructures for storing information on new physical principles."

References

[1] Barranco A, Borras A, Gonzalez-Elipe A and Palmero A 2016 *Perspectives on oblique angle deposition of thin films: From fundamentals to devices* (*Progress in Materials Science* vol 76) pp 59–153

[2] Hawkeye M, Taschuk M and Brett M 2014 *Glancing Angle Deposition of Thin Films* (UK: John Wiley & Sons Ltd) pp 1-299

Synthesis of gold nanoparticles by the spark discharge method for ultraviolet plasmonics

V I Borisov[1], A A Lizunova[1], D Malo[1], A A Ramanenka[2] and V V Ivanov[1]

Moscow Institute of Physics and Technology, National Research University,
[1]Institutsky lane 9, Dolgoprudny, Moscow region, 141700, Russia
[2]National Academy of Sciences of Belarus, B.I. Stepanov Institute of Physics, Minsk, 220072, Belarus

Corresponding author's e-mail: borisov.vi@mipt.ru

Abstract. This work demonstrates synthesis of metal Au nanoparticles with a plasmon resonance in the visible optical region by the spark discharge method in atmosphere of argon of purity 6.0. Obtained particles were agglomerates with a median size from 270 to 90 nm, which consisted of primary nanoparticles with a crystalline structure with sizes in range from 5 to 120 nm. Synthesized nanoparticles ensembles had broad absorption peaks with maximum in the visible optical region with peak positions approximately at 490 nm. High temperature sintered particles had a spherical shape and an additional peak at approximately 640 nm.

1. Introduction

The plasmon enhancement effect is interest for purposes such as sunlight energy conversion, catalysis, chemical and biological sensors and Raman spectroscopy. In the last two decades Au nanoparticles characterized by plasmon resonance in a visible range became a subject of intense research, due to variety of optical properties related to surface plasmons, high chemical and physical stability and ease of surface functionalization with organic and biological molecules [1]. All of this makes the search for new methods of the Au nanoparticles synthesis urgent. Here, we presented a method of synthesis metal Au nanoparticles with a plasmon resonance in the visible region.

2. Methods and Materials

Custom-built spark discharge generator (SDG), the similar scheme of the setup was presented in [2], was used with the following conditions: capacitor 107 nF, discharge voltage 0.6 kV and pulse repetition rate 0.5 kHz. Nanoparticles synthesis was carried out in the discharge chamber that was made from glass (Duran glass, KF50, Millab) in which two hollow Au electrodes (mass fraction of gold is 0.9999) were opposite mounted. Gas path that was made of stainless steel vacuum fittings KF was pumped to a pressure of 0.4 torr before gas supplying. Further argon of purity 6.0 (oxygen volume fraction lesser than $3 \cdot 10^{-5}$) at a pressure of 1.5 bar and a flow rate of 1 L/min was fed to the discharge chamber through the hollow electrode, that ensured effective nanoparticles removing from the discharge gap. Synthesized nanoparticles has been passed for 2 seconds through a custom-built tube furnace at temperatures from 25 to 950 °C and were collected on TEM copper grid with a carbon film and cellulose filter.

The particle size distribution in the flow was measured by using a TSI SMPS 3936 Aerosol spectrometer. These measurements give an equivalent size of the primary nanoparticles agglomerates. The images of primary nanoparticles, their size and crystal structure was received by microscopy studies on transmission electron microscope (TEM) Jeol JEM 2100 (200 kV) with energy dispersive X-ray spectrometer X-MAXN OXFORD Instruments. The UV-vis-NIR spectra of nanoparticles on cellulose filter were obtained using JASCO V–770 spectrophotometer.

3. Results and Discussion

TEM and electron diffraction images show that the particles have crystalline structure, the average primary particle size in ten samples synthesized at 25, 100, 150, 180, 210, 350, 500, 650, 800 and 950 ºC varies from 5 to 120 nm. With an increase in sintering temperature (from 210 ºC) the median agglomerates diameter decreases more than twice, that means the sintering of nanoparticles occurs (Figure 1a). However, according to TEM images complete sintering with the formation of spherical particles occurs at temperatures above 950 ºC.

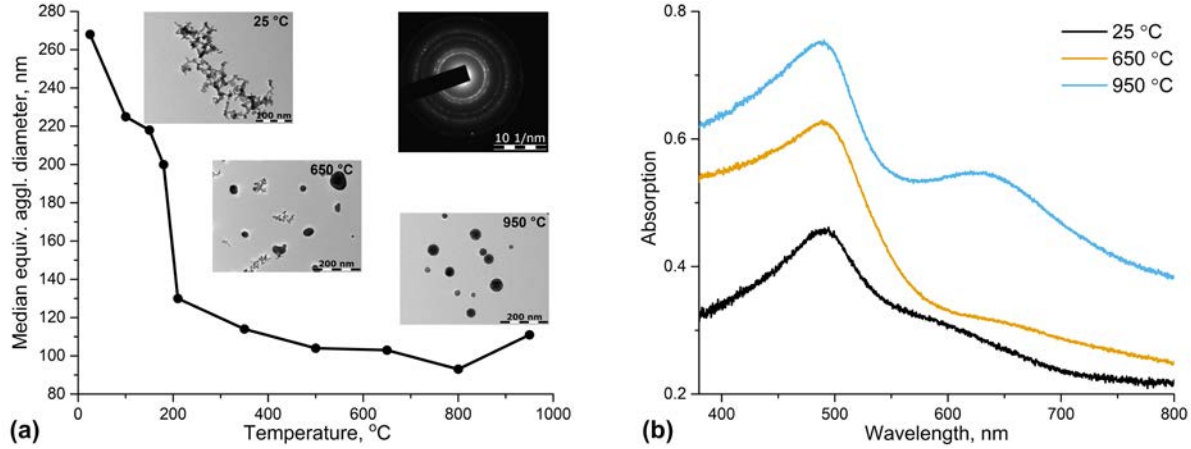

Figure 1. **(a)** Dependence of median particle diameter of the agglomerates on the sintering temperature; Insets: TEM image of typical particles at 25, 650 and 950 °C and the electron diffraction pattern, **(b)** Absorption spectra of synthesized particles sintered at 25, 650 and 950 °C.

The measurements of the Au nanoparticles absorption spectra showed the presence of wide absorption peaks in the visible optical region with peak positions approximately at 490 nm for all sintering temperatures and additional at 640 nm for particles sintereted at 950 °C (Figure 1b). In future experiments absorption peaks can be narrowed by extraction of monodisperse nanoparticles using a differential mobility separating column.

Thus, a simple synthesis of metal Au nanoparticles with plasmon resonance in the visible optical region by the spark discharge method has been shown. It is possible to focus particles on substrate or collect them for production nano-inks, that give capacity to use this method as a nanoparticles source in the aerosol jet printing.

Acknowledgments

The reported study was funded by RFBR and BRFBR, project number 20-53-00042.

References

[1] Amendola V, Pilot R, Frasconi M, Maragò O M and Iatì M A 2017 *J. Phys.: Condens. Matter* **29** 203002

[2] Efimov A A, Arsenov P V, Borisov V I, Buchnev A I, Lizunova A A, Kornyushin D V, Tikhonov S S, Musaev A G, Urazov M N, Shcherbakov M I, Spirin D V, Ivanov V V. 2021 *Nanomaterials* **11** 234

Growth of lithium niobate thin films by PLD on SiO_2/Si structures

Z Vakulov[1], D Khakhulin[2], A Geldash[3], V S Klimin[4], O A Ageev[3,4]
[1]Federal Research Centre The Southern Scientific Centre of the Russian Academy of Sciences (SSC RAS), Rostov-on-Don 344006, Russia
[2]Laboratory of Functional Nanomaterials Technology, Southern Federal University, 347922 Taganrog, Russia
[3]Research and Education Centre "Nanotechnology", Southern Federal University, Taganrog 347922, Russia
[4]Institute of Nanotechnologies, Electronics, and Equipment Engineering, Southern Federal University, 347922 Taganrog, Russia

zvakulov@sfedu.ru

Abstract. This paper shows the results of studying the effect of repetition rate during laser ablation on the parameters of $LiNbO_3$ films grown on SiO_2/Si structures. It was found that the dependence of surface roughness on the repetition rate has a minimum (3.53±0.18 nm) at 6 Hz. The subsequent increase in frequency to 10 Hz leading to an increasing in the roughness to 3.85±0.31 nm, which can be linked to the effect of "inheritance" of SiO_2 sub-layer morphological parameters. Obtained results make it possible to fabricate $LiNbO_3$ films, which can be used to developing promising lead-free energy converters for eco-friendly energy devices.

1. Introduction

Lithium niobate ($LiNbO_3$) is a promising ferroelectric material with a unique combination of electro-optical, nonlinear-optical, acousto-optical, piezoelectric and pyroelectric properties. The material is widely used in the manufacture of integrated optics devices, waveguide structures, phase modulators, piezoelectric transducers, and surface acoustic wave devices [1]. Recently, the emphasis on the development of micro-and nanoelectronics has shifted to the use of thin $LiNbO_3$ films and the development of a technology for their production, integrated with silicon semiconductor technology [2]. In addition, the combination of the "lithium niobate on an insulator" technology with using of silicon substrates makes it possible to expand $LiNbO_3$ films applications (MEMS, Si photonics, etc.). Therefore it is highly desirable to integrate $LiNbO_3$ films with a SiO_2 layer on the surface of the Si substrate [3]. Nowadays, one of the most effective technological methods for $LiNbO_3$ films growth are magnetron sputtering and pulsed laser deposition (PLD) [4, 5]. The latter differs significantly from other technological methods of deposition due to the very high kinetic energy of ablated particles falling on the substrate and the high deposition rate during each laser pulse [6]. However, the precise mechanisms of crystallization of complex oxides are still poorly understood [7]. Thus, this work aims to study the influence of repetition rate during PLD on the growth of $LiNbO_3$ films on SiO_2/Si structures.

2. Experiment

$LiNbO_3$ films were deposited by using the Pioneer 180 PLD module (Neocera Co., USA) of the NANOFAB NTK-9 nanotechnological complex (NT-MDT, Russia). The number of impulses was constant at 50 000. The repetition rate was varied from 4 Hz to 10 Hz. The films were obtained at a temperature of 600 ° C on SiO_2/Si structures. Figure 1 shows AFM images of $LiNbO_3$ films obtained at different repetition rates, as well as the dependencies of the roughness and grain diameter of the obtained films on repetition rate.

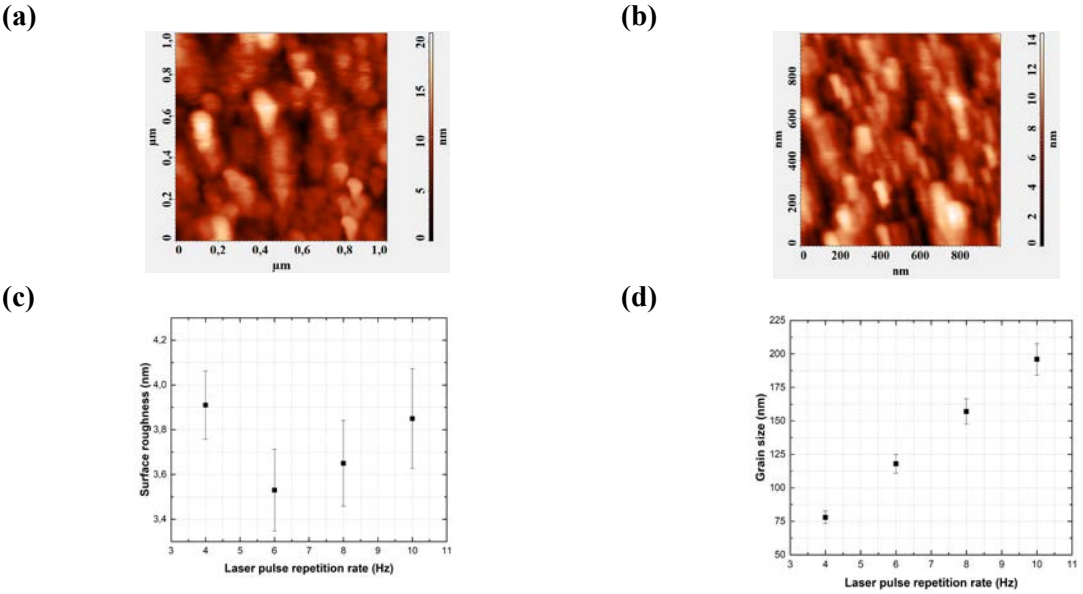

Figure 1 (a, b, c, d). AFM images of $LiNbO_3$ films obtained at different laser pulse repetition rates: 4 Hz **(a)** and 10 Hz **(b)**, dependences of the surface roughness **(c)** and grain size **(d)** on the repetition rate

Increasing repetition rate from 4 Hz to 10 Hz, $LiNbO_3$ films grain size increasing from 78±4.68 nm to 196±11.76 nm. The dependence of surface roughness on the repetition rate has a minimum (3.53±0.18 nm) at 6 Hz. A subsequent increase in frequency to 10 Hz leads to an increase in roughness to 3.85±0.31 nm, which may be associated with the effect of "inheritance" of the morphological parameters of SiO_2. Increasing repetition rate from 4 Hz to 8 Hz, the concentration of charge carriers in $LiNbO_3$ films increasing from $1 \cdot 10^{13}$ cm^{-3} to $4 \cdot 10^{13}$ cm^{-3} with decreasing the mobility of charge carriers decreases from 13 $cm^2/(V \cdot s)$ to 5 $cm^2/(V \cdot s)$. Obtained results allow fabricating $LiNbO_3$ films for developing promising lead-free energy converters and eco-friendly energy devices.

Acknowledgments

The reported study was funded by the Russian Foundation for Basic Research, projects numbers 19-38-60052 and 18-29-11019 mk. The results were obtained using the infrastructure of the scientific and educational center ”Nanotechnology” of the Southern Federal University.

References

[1] Irzaman H, Jenie R P 2018 *Ferroelectrics and Their Applications* (London: IntechOpen)
[2] Shih W C, Wang T L, Sun X Y and Wu M S 2008 *Jpn. J. Appl. Phys.* **47** 4056
[3] Takigawa R, Higurashi E and Asano T 2018 *Jpn. J. Appl. Phys.* **57** 06HJ12
[4] Ageev O A, Konoplev B G (ed.) 2019 *Nanotechnology in Microelectronics* (Moscow: Nauka) ISBN 978-5-02-040201-0
[5] Tomar M, Gupta V, Mansingh A and Sreenivas K 2001 *J. Phys. D: Appl. Phys.* **34** 2267
[6] Blank D H A, Dekkers M and Rijnders G 2013 *J. Phys. D: Appl. Phys.* **47** 034006
[7] Christen H M, Eres G 2008 *J. Phys. Condens. Matter* **20** 264005

Influence of magnetron sputtering modes on the parameters of ZnO:Ga films

A A Geldash[1, 2], E Yu Gusev[1], V N Dzhuplin[2], O A Ageev[1, 2]
[1]Department of Nanotechnology and Microsystems, Southern Federal University, Taganrog 347922, Russia
[2]REC «Nanotechnology» Southern Federal University

Abstract. The aim of this work is to study the influence of magnetron sputtering modes (pressure, heating temperature, and DC power) on the morphology and electrophysical parameters of ZnO:Ga films, which can be used as contact layers to the nanostructures of photovoltaic converters. It was found that with an increase in the heating temperature, the grain size and surface roughness of the films decrease, as well as the resistivity and mobility of charge carriers, while the concentration of charge carriers increases. With an increase in the power of the direct current source, the grain size and surface roughness of the films increase, while the resistivity and mobility of charge carriers increase, and the concentration of charge carriers decreases. With increasing pressure, the grain size on the surface of the ZnO:Ga films increases, as a result of which their roughness also increases. In this case, the resistivity and mobility of charge carriers increase, and the concentration of charge carriers decreases.

1. Introduction

The development of efficient photoconverters of energy is a topical direction in the development of alternative energy. The task is not only to find and study materials suitable for energy conversion, but also materials that play the role of upper contact layers [1]. One of the most common materials for contact layers in photovoltaic converters is conductive indium tin oxide (ITO) [2]. However, there is a need to find alternative materials in order to achieve better performance. Therefore, more and more attention is directed to the study of methods for the formation and post-processing of conductive oxide films. One of these materials can serve as a conductive oxide ZnO:Ga [3]. Zinc oxide is a direct-gap semiconductor with a wurtzite structure and a band gap of 3.36 eV [4]. At the same time, thin ZnO films have good optical quality, stability, and piezoelectric properties. therefore, they are used in various fields of micro- and nanoelectronics [5]. The aim of this work is to study the effect of magnetron sputtering modes (pressure, heating temperature, and power of a direct current source) on the morphology and electrophysical parameters of ZnO:Ga films, which can be used as contact layers to nanostructures of photovoltaic converters.

2. Materials and Methods

Before the formation of the samples, the ceramic glass substrates were chemically cleaned. The formation of thin ZnO:Ga films was carried out by DC magnetron sputtering using an Auto 500 (Boc Edwards) sputtering device. The source of the vaporized material was a ZnO:Ga target (GIRMET Ltd). The first series of experiments was aimed at investigating the effect of heating temperature on the morphology and electrophysical parameters of the films; four samples with ZnO:Ga films were formed in the temperature range 30-140 ºC. In this case, the pressure and power of the direct current source were constant and amounted to p = 0.135 Pa and W = 100 W, respectively. The second series

of experiments was aimed at investigating the effect of the power of a direct current source on the morphology and electrophysical parameters of the films; four samples were formed with ZnO:Ga films in the power range of 80-140 W. The pressure and temperature were constant and amounted to p = 0.135 Pa and t = 140 ºC, respectively. The third series of experiments was aimed at investigating the effect of pressure on the morphology and electrophysical parameters of the films; four samples were formed with ZnO:Ga films in the pressure range of 0.1-0.2 Pa. In this case, the temperature and power of the direct current source were constant and amounted to t = 140 ºC and W = 100 W, respectively. The thickness of the deposited films was monitored with a quartz thickness gauge. The study of the electrophysical parameters of the ZnO:Ga films was carried out by measuring the Hall EFM using an Ecopia HMS-3000 setup (Ecopia Co., Korea). The study of the surface morphology of the films was carried out by scanning electron microscopy (SEM) and atomic force microscopy (AFM) using a Nova Nanolab 600 scanning electron microscope (FEI.Co, Netherlands) and an Ntegra probe nanolaboratory (Company NT-MDT, Russia), respectively.

3. Results and discussion

As a result of the studies, it was found that with an increase in the heating temperature from 30 to 140 ºC, the size and height of grains on the surface of the ZnO:Ga film decreases, its surface is characterized by a uniform distribution of grains with sizes of the same order over the entire sample area (Figure 1, a). The film thickness on all samples was 300-340 nm (Figure 1, b). In this case, the mobility of charge carriers decreases from 5.86 to 3.42 $cm^2/(V \cdot s)$, the concentration increases $1.87 \cdot 10^{19}$ to $1.04 \cdot 10^{20}$ cm^{-3}, and the resistivity of the films decreases from $5.56 \cdot 10^{-2}$ to $9.133 \cdot 10^{-3}$ Ω·cm (Figure 1, c).

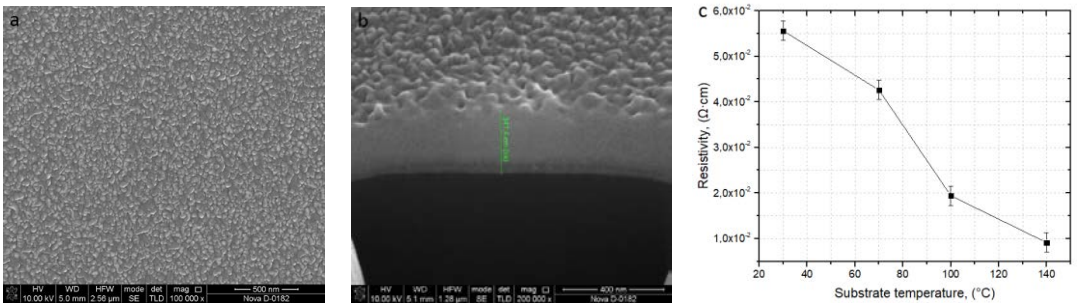

Figure 1. a) ZnO:Ga film surface, b) ZnO:Ga film thickness, c) dependence of the resistivity of ZnO:Ga films on the substrate temperature.

With an increase in the power of the direct current source from 80 to 140 W, the morphology of the ZnO:Ga films is characterized by an increase in the grain size and its surface roughness. The mobility of charge carriers increases from 2.95 to 4.07 $cm^2/(V \cdot s)$, the concentration decreases from $7.87 \cdot 10^{19}$ to $4.12 \cdot 10^{19}$ cm^{-3}, and the resistivity of the films increases from $1.11 \cdot 10^{-2}$ to $7.2 \cdot 10^{-2}$ Ω·cm. With an increase in pressure from 0.1 to 0.2 Pa, the grain size on the surface of the ZnO:Ga films increases, as a result of which its roughness also increases. The mobility of charge carriers increases from 1.84 to 4.07 $cm^2/(V \cdot s)$, the concentration decreases from $4.87 \cdot 10^{19}$ to $1.77 \cdot 10^{19}$ cm^{-3}, and the resistivity of the films increases from $3.13 \cdot 10^{-2}$ to $6.18 \cdot 10^{-2}$ Ω·cm.

4. Acknowledgments

The reported study was funded by RFBR, project number 19-31-27001. The work was done on the equipment of the Research and Education Centre «Nanotechnology» Southern Federal University.

References

[1] Meyer F, Savoy A, Juan J et al. 2021 *Solar Energy Materials and Solar Cells* **110815** 219
[2] Ahmed M, Bakry A, Qasem A, Dalir H 2021 *Optical Materials* **110866** 113
[3] Mondal P, Das D 2017 *Applied Surface Science* **411** 315
[4] Berger L I 1997 *Semiconductor Materials* (Boca Raton: CRC Press) p 496
[5] Ageev O A and Konoplev B G et al. 2019 *Nanotechnology in microelectronics* (Moscow: Nauka) p 511

Method for the modification of graphite to a solid mixture of single crystals of silicon carbide and graphite

A S Grashchenko, S A Kukushkin, A V Osipov and A V Redkov.
Institute of Problems of Mechanical Engineering, Russian Academy of Sciences, 199178, Saint Petersburg, Russia

E-mail: asgrashchenko@bk.ru

Abstract. Here we present a new method for formation of a thermal protective, chemically resistant coating based on a composite material of silicon carbide and graphite in subsurface area of a graphite plate. The composition and structure of both the composite material itself and the interface between the composite material and the carbon matrix were investigated using the methods of scanning electron microscopy and Raman spectroscopy. Studies have shown that the composite material obtained by this method has a branched fibrous structure consisting of small tubular layers of silicon carbide interspersed with large monocrystalline grains of silicon carbide of the cubic polytype, which leads to significant strengthening of the material.

1. Introduction

Composite materials are widely used in dentistry, aerospace, construction, automotive, shipbuilding and many other fields of industry. There are many methods for obtaining different composite materials. In this work, we present a new method for modifying the subsurface layer of graphite with a composite material consisting of small SiC particles having nano sizes interspersed with large single-crystal SiC particles of about 10 μm in size inside the graphite basement. Large single-crystal SiC particles act as reinforcing elements that provide the necessary mechanical characteristics of the material, and the graphite matrix acts as a binder. This technology can be used both to increase the chemical inertness and operating temperature of graphite products, and to obtain a single-crystal SiC powder. Thus, studying the processes occurring during modification and studying the physical characteristics of the resulting mixture of SiC and graphite is a relevant task.

2. Materials and methods

The graphite modification method [1] is based on the technology of synthesis of epitaxial SiC films inside a silicon (Si) matrix due to the replacement of Si atoms by carbon atoms [2-4]. The synthesis of SiC films occurs at a temperature of 1100-1300 ° C in an atmosphere of carbon monoxide (CO). It should be noted that the thickness of SiC films obtained by atomic substitution does not exceed 250 nanometers. Upon further heating to 1400-1450 ° C, the silicon base melts and if it is placed on a graphite surface, then graphite is being modified to a mixture of graphite and SiC crystals, and a silicon carbide film is formed on the surface. To study the structure obtained by this method, a graphite plate was taken, on which a piece of a silicon plate with an area of 1 cm^2 was put. The system was heated in a vacuum chamber to 1410 ° C in an atmosphere of CO 5 minutes. The pressure in the chamber during heating was constant 2 torr. The resulting structure was investigated using a scanning electron microscope (SEM). Studies of the surface and cross-section of the modified region were carried out. Also, the

resulting structure was investigated by Raman spectroscopy. The Raman spectra were recorded both in the region of a graphite plate over which Si was initially put and far from this region.

3. Results and discussion

The figure 1 shows the SEM-images of surface of the modified region of the graphite plate its cross-section. One can note from the image of the surface that it is covered with crystals of different sizes. The obtained crystals do not have a common crystallographic direction. Visually, the area of the graphite plate over which the fusion occurred in this case has a greenish tint. From the cross-section image, one can determine the depth to which graphite was modified, that is about 1 mm. A further magnification of the cross-section shows that the entire modified region consists of individual faceted crystals.

The figure 2 shows the Raman spectra taken from the surface of the graphite plate in the modified region and far from it. Far from the region in which the modifications took place, the Raman spectrum is typical for graphite [5], all its main bands are clearly visible (1351 cm^{-1}, 1571 cm^{-1} *и* 2692 cm^{-1}). In the case of the modified region, the spectrum radically differs from the typical graphite spectrum, the main bands of the spectrum becomes the SiC band of the cubic polytype (796 cm^{-1}) [6], and graphite bands disappear at all. The obtained result suggests that mainly cubic SiC crystals lie on the surface of the modified region.

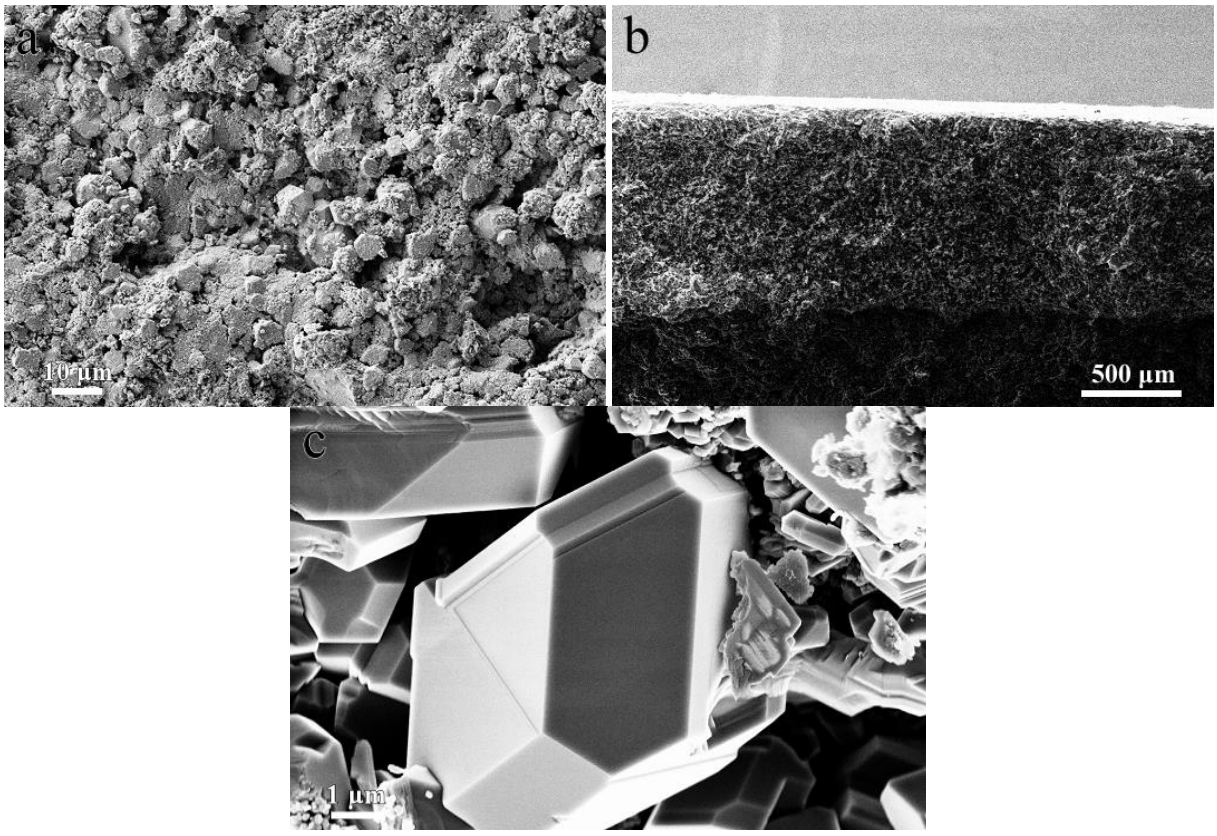

Figure 1. SEM image of a modified region of a — surface, b — cross-section, c — microcrystal SiC on the cross-section.

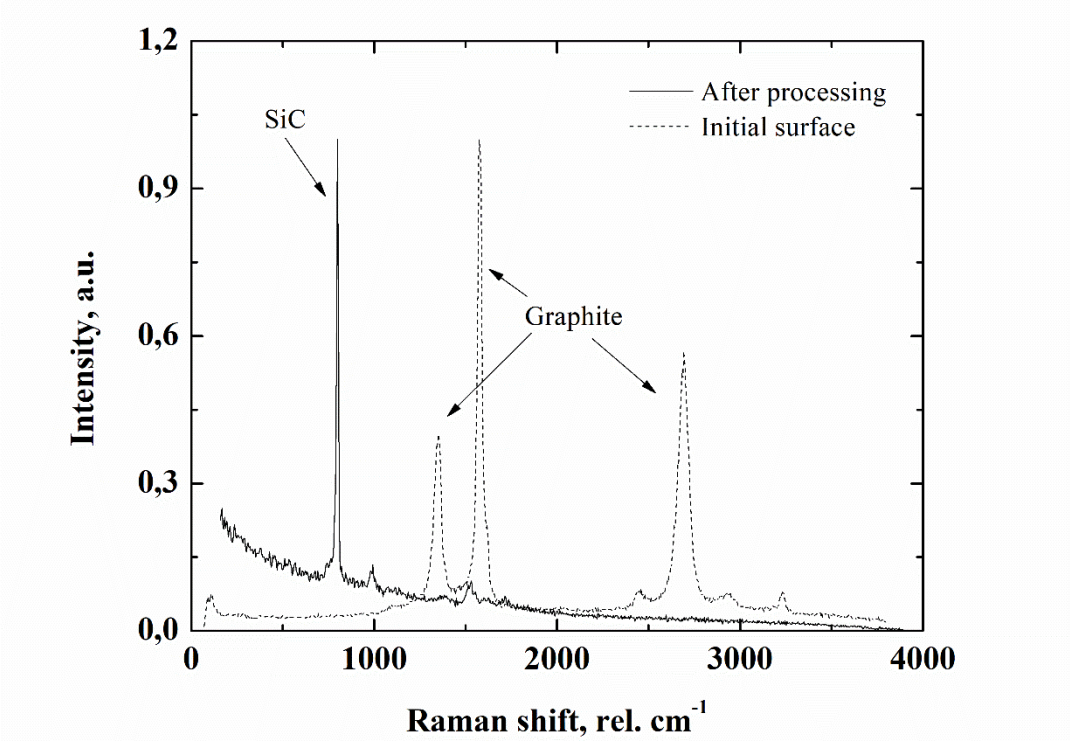

Figure 2. Micro-Raman spectrum of the initial surface of a graphite plate, and the surface of the modified region.

4. Conclusions

A method of graphite modification into crystalline SiC by melting Si substrates on the surface of the graphite plate in a CO atmosphere is presented. Structural studies of the modified region were carried out. It is shown that the modification occurs not only on the surface, but extends to the depths up to 1 mm. It was also found that the entire modified region consists of separate non-textured misoriented SiC crystals. Using the Raman technique, an analysis of the composition of the modified region was carried out. Analysis of the Raman spectra showed that the modified region consists mainly of cubic SiC with with a small proportion of a hexagonal one.

5. References

[1] Grashchenko A S,Kukushkin S A, Osipov A V, Redkov A V, Feoktistov N A 2008 Patent of invention № 2695423
[2] Kukushkin S A, Osipov A V 2008 Physics of the Solid State **7** 1238
[3] Kukushkin S A, Osipov A V 2013 Journal of Applied Physics **2** 024909
[4] Grashchenko A S,Kukushkin S A, Osipov A V 2014 Technical Physics Letters 40 1114
Kukushkin S A, Osipov A V 2013 Journal of Applied Physics **2** 024909
[5] Reich S, Thomsen C 2004 Mathematical, Physical and Engineering Sciences 362 2271
[6] Wasyluk, J, Perova T S, Kukushkin S A, Osipov A V, Feoktistov N A, Grudinkin S A 2010 In Materials Science Forum 645 359

The scalable production of high-quality nanographite by organic radical-assisted electrochemical exfoliation.

E Grushevski[1], D Savelev[1], L Mazaletski[1], N Savinski[2] and D Puhov[2].

1Department of Nanotechnology in Electronics, P.G. Demidov Yaroslavl State University, Sovetskaya Street 14, 150003, Yaroslavl, Russia.
2Valiev Institute of Physics and Technology of Russian Academy of Sciences, Yaroslavl Branch, 150007, Universitetskaya Street 21, Yaroslavl, Russia.

E-mail: yaregor@mail.ru

Abstract: Producing high-quality graphene on a large scale, at an affordable price, and in a reproducible manner is still a big challenge. Here we report a method based on the controlled electrochemical exfoliation of graphite in an aqueous ammonium sulfate electrolyte to produce graphene precursor (nanographite) in large quantities and with outstanding quality. Since the radicals (e.g., HO•) formed during the electrolysis of water are responsible for the formation of defects on graphene during electrochemical exfoliation, a number of reducing agents have been investigated as additives to eliminate these radicals and thus control the exfoliation process. Remarkably, DMSO-assisted exfoliation results in large graphene sheets (5−10 μm on average) and extremely high carbon to oxygen (C/ O) ratios (~69).

1. Introduction

The exceptional electronic, thermal, optical, and mechanical properties of graphene render it a remarkable candidate for the next generation of electronic and optoelectronic devices [1].

Techniques for the scalable production of high-quality, solution-processable graphene are needed. Among the numerous protocols employed to date, the exfoliation of bulk graphite is most common for harvesting graphene sheets on a large scale because of its low process complexity and costs.

Direct exfoliation in the solid state (e.g., scotch-tape cleavage, ball milling or in a liquid phase (e.g., liquid phase sonification, shear force exfoliation, also known as physical exfoliation)), provides feasible means for producing graphene with a low number of defects. In comparison, chemical exfoliation, which generally relies on Hummers' method, offers a wide range of flexibility for the production of graphene oxide (GO) and related materials because of the potential scalability, impressive conversion efficiency (100%), and superior processability. The unique physical properties of graphene are seriously compromised and cannot be sufficiently recovered, even upon reduction, because of the appreciable fraction of oxygen groups and defects that are left behind. These oxygen groups restrict its usage in fine applications.

Electrochemical exfoliation has recently emerged as a promising strategy for producing graphene on an industrial scale with high efficiency, at low cost, and in an environmentally friendly manner [2].

2. Electrochemical exfoliation.

Graphite exfoliation was conducted in a home-built setup that used graphite foils as working electrodes and platinum foils as counter electrodes. An aqueous solution containing ammonium sulfate

with a range of reducing agents was tested as an electrolyte. Anionic intercalation (primarily in aqueous electrolytes) is less time demanding and can take less than 1 h. The graphene produced is generally decorated with functional oxygen groups that occur due to the positive potentials used, especially with acidic electrolytes.

Nevertheless, the radicals (e.g., HO•) generated from water electrolysis will unavoidably disrupt the graphite structure during the exfoliation process [2]. In our previous study [3], we identified the products of electrochemical exfoliation of graphite as oxidized nanographite with 20-30 graphene layers. In this study, the electrochemical exfoliation of graphene is carried out in the presence of a series of antioxidants such as ascorbic acid, hydrazine, sodium borohydride, dimethyl sulfoxide (DMSO), (2,2,6,6-tetramethylpiperidin-1-yl)oxyl (TEMPO), 2,2,6,6-tetramethyl-4-one-piperidin-1-yl)oxyl (IPON), Dimer (2,2,6,6-tetramethylpiperidin-1-yl)oxyl-fulvalene (YARSIM-0215) in a neutral aqueous electrolyte (ammonium sulfate) to suppress the formation of radicals from water electrolysis. Remarkably, using DMSO, the electrochemically exfoliated graphene produced is of exceptionally high-quality, and the process gives high exfoliation efficiencies. The exfoliated graphene sheets were then transferred onto a Si/SiO2 substrate using the Langmuir−Blodgett method. Scanning electron microscopy (SEM) and energy-dispersive X-ray spectroscopy (EMF) by means electron microscopes SUPRA-40 and QUANTA were used to study the morphology of graphene flakes on the SiO2 surface, the size of hundreds of micrometers, and the carbon and oxygen content in the sample.

In general, the efficient intercalation of electrolyte into graphite interlayer and the subsequent gas eruption are the key factors governing graphite exfoliation. It is well-known that, in dilute or moderately concentrated salt solutions, water splitting takes place at a potential of 1.23 V, generating oxygen gas at the anode. Nevertheless, the high anodic overpotential (e.g., 10 V) discharges water into active intermediates, such as hydroxyl radicals, at the graphite interfaces.

In the meantime, hydroxyl radicals (HO•) start to corrode the graphite electrode at the edges which is necessary to open the boundaries such that the sulfate ions are able to intercalate. By using DMSO, the extent of damage in graphene lattice, which is possibly caused by radical attack, could in principle be very low. DMSO is oxidized by HO* to form the stable, nonradical compound, methane sulfinic acid, which can be easily measured spectrophotometrically.

3. Conclusion

We have developed a controllable electrochemical approach for graphite exfoliation with the assistance of antioxidants. Among them, DMSO was found to promote exfoliation, which led to nanographite exhibiting superior quality in high yield. The exfoliated graphite sheets are large in size, and they have and high carbon to oxygen (C/O) ratios (69). Given that all of the reagents employed in this exfoliation system are commercially available and inexpensive and that the process is extremely fast, compatible to scale-up, and free of polluting byproducts.

Acknowledgements

This research was financially supported within the framework of the state assignment of the Valiev Institute of Physics and Technology of the Russian Academy of Sciences Yaroslavl Branch of the Ministry of Education and Science of the Russian Federation No. 0066-2019-0003 and the state assignment of P.G. Demidov Yaroslavl State University No. 0856-2020-0006. Some experimental results were obtained on the equipment of the Center for Collective Use "Diagnostics of Micro-and nanostructures" with the support of the Ministry of Education and Science of the Russian Federation.

References

[1] Novoselov K S, Geim A K, Morozov S V, Jiang D, Zhang Y, Dubonos S V, Grigorieva I V and Firsov A A 2004 *J. Science* **306** 666

[2] Yang S, Brüller S, Shuai Wu Z, Liu Z, Parvez K, Dong R, Richard F, Samorì P, Feng X and Müllen K 2015 *J. Am. Chem. Soc.* **137** 13927−32

[3] Savinsky N G, Melesov N S, Parshin E O, Vasiliev S V, Bachurin V I and Churilov A B 2020 *Bulletin of the Russian Academy of Sciences: Physics* **84** N 6 732–735

Estimation of thermodynamic stability of isoperiodic epitaxial structures whith GaInSbAs and GaInAsP solid solutions

E M Danilina, A S Paschenko
[1]Federal research centre the Southern Scientific Centre RAS, 41, Chekhov st., Rostov-on-Don, 344006, Russia

Abstract. The work studied the thermodynamic stability of GaInSbAs, GaInAsP heterosystems on GaSb, InSb substrates. The isotherms of spinodal decomposition caused by chemical changes in the internal energy of the alloy and by elastic stresses at the layer-substrate interface are obtained with the model of quasiregular solutions. It has been found that elastic stresses lead to an expansion of the region of thermodynamic stability of isoperiodic solid solutions for GaSb substrates and a decrease in the critical temperature.

1. Introduction

The heterostructures with multicomponent semiconductor solid solutions A^{III} - B^{V} are currently being actively studied as promising materials for electronic and photonic devices [1]. This is due to the need to expand the spectral range and improve the structural perfection hetero-boundaries by matching of epitaxial layers with respect to the lattice period and thermal expansion coefficient.

However, the formation of unstable component phases can be observed in multicomponent alloys. This leads to their disintegration into coexisting liquid or, respectively, solid phases of different composition [2].

The experimental study of the process is very time-consuming and involves the use of high-precision phase analysis methods. At the same time, the information about the breaks in the solubility of components in the solid phase is extremely important. The immiscibility and instability of solid solutions significantly limit the range of compositions with desired properties for use in creating optoelectronic devices.

Therefore, the theoretical studies of equilibria between the liquid and solid phases in the epitaxy process are important.

2. Materials and Methods

In the state of thermodynamic equilibrium between the coexisting phases, the Helmholtz free energy should take on a minimum value [3]. In accordance with the approximation of a regular solution, a multicomponent solution can be represented as a set of binary compounds and the free energy are given by

$$F = F_0 + \Delta F_M^{Sid} + \Delta F_M^{Sex} + F_{st},$$

where

F_0 – the free energy of the mole fraction of binary components;

ΔF_M^{Sid} – the free mixing energy, the interaction energy between the components is negligible;

ΔF_M^{Sex} – the excess mixing energy, taking into account the interaction of binary components;

F_{st} – elastic stress energy.

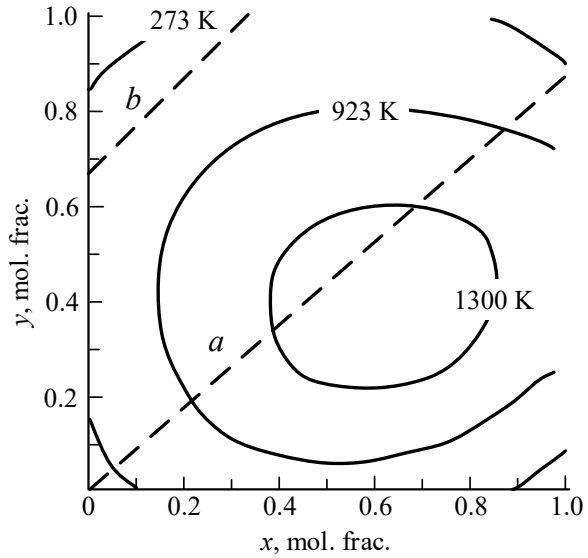

Figure 1. Isotherms of spinodal decomposition of $Ga_xIn_{1-x}Sb_yAs_{1-y}$ solution on GaSb substrate without elastic stresses,
$a - \Delta a = 0\%$ alloys lattice-matched to GaSb;
$b - \Delta a = 5\%$ to GaSb;

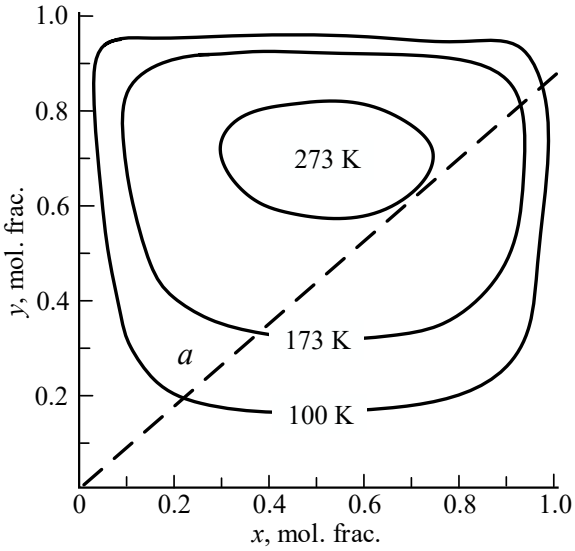

Figure 2. Isotherms of spinodal decomposition of $Ga_xIn_{1-x}Sb_yAs_{1-y}$ solution on GaSb substrate with elastic stresses,
$a - \Delta a = 0\%$ alloys lattice-matched to GaSb

3. Discussion and Conclusions

The regions of existence of solid solutions of four-component compounds on GaSb and InSb substrates are calculated. The model of quasiregular solid solutions was used for analysis of heterophase equilibria in Ga−In−Sb−As и Ga−In−As–P systems. The thermodynamic stability regions of solid solutions to spinodal decomposition are identified. The isotherms of spinodal decomposition caused by chemical changes in the internal energy of the alloy and by elastic stresses at the layer-substrate interface are obtained (fig. 1).

It has been shown that compositions with a mismatch between the crystal lattice parameters of the solid solution and the substrate for heterosystems on GaSb substrates can exist fig. 1 (a, b). It has been found that elastic stresses lead to an expansion of the region of thermodynamic stability of isoperiodic solid solutions for GaSb substrates and a decrease in the critical temperature fig 2. Among the considered four-component solid solutions, there aren't founded the isoperiodic compositions for InSb substrates at room temperature.

Comparisons between the analysis results for the Ga – In – Sb – As and Ga – In – As – P heterosystems and the experimental data showed good agreement. This allows us to speak about the correctness of the calculations, the adequacy of the model, and use the results of calculations to justify the technological modes of epitaxial growth.

4. Acknowledgments

This work was funded by as a part of a state order to the Southern Scientific Center of the Russian Academy of Sciences, projects nos. 01201354240. This work was carried out with financial support by the Russian Science Foundation grant 19-79-10024.

References

[1] Weih R., Bauer A., Kamp M., Höfling S. 2013. *J. Optical Materials Express.* **3 (2013**) 1624–1631
[2] Bychinskii V. A., Tupitsyn A. A., Chudnenko K. V., Mukhetdinova A. V., Fomichev S. V., Krenev V. A. 2013. *Russian Journal of Inorganic Chemistry.* **58 (2013)** 1197–1202
[3] V.A. Elyukhin, *Elsevier*, Amsterdam, **2016**.

Study of In/GaAs nanodroplet formation in conditions of non-stationary supersaturation during droplet epitaxy

D D Dukhan, S V Balakirev, N E Chernenko, M M Eremenko and M S Solodovnik

Institute of Nanotechnologies, Electronics and Equipment Engineering, Southern Federal University, Taganrog 347922, Russia

Email: duhan@sfedu.ru

Abstract. In this paper we present results of Monte Carlo investigation of In/GaAs growth by droplet epitaxy in conditions of non-stationary vapor supersaturation. These conditions allow achievement of the independent control of size and surface density of nanostructures. The material redistribution is realized on the surface when indium deposition is interrupted as compared with the continuous growth. At that, an average droplet size increases whereas the wetting layer becomes thinner. Additional nucleation is also observed during growth interruption which can be used to increase surface density of droplets.

1. Introduction

Independent control of size and surface density of quantum dots is one of the most challenging issues, especially in the field of quantum cryptography and computing where parameters of nanostructures and their mutual arrangement are both important. In this paper, we carry out Monte Carlo simulations to study the effect of non-stationary supersaturation of indium vapor on the parameter of In nanostructures formed by droplet epitaxy on the GaAs surfaces.

2. Method

Previously developed kinetic Monte Carlo model [1,2] was upgraded to take into account the droplet epitaxial growth in the conditions of non-stationary vapor supersaturation.

3. Results and discussion

The simulation results demonstrate that the material redistribution occurs on the surface during the growth interruption. Due to the fact that the probability of decay of a stable supercritical island is extremely small, atoms mainly migrate from the wetting layer into the droplet areas. As a result of the material redistribution, the average droplet size increases, while the thickness of the wetting layer decreases. This process has a more pronounced effect when the exposure time is increased from 1 to 3 seconds. Furthermore, the difference in droplet size increases with increase of substrate temperature. At a temperature of 150 °C, the average diameter of droplets deposited in a continuous mode and with a double interruption for a period of 3 seconds increases from 18 to 22 nm (by 18%), while at a temperature of 300 °C, a change is from 107 to 144 nm (by 26%).

It was also found that the non-stationary supersaturation has an influence on the intensity of island nucleation, which is caused by an increase in the intensity of surface diffusion of adatoms due to a

decrease in the deposition rate of indium atoms. As a result, the final surface density of droplets at a temperature of 300 °C decreases from $1.8 \cdot 10^8$ to $5.2 \cdot 10^7$ cm^{-2} with a twofold interruption of growth for 3 seconds as compared with continuous deposition. In this case, a twofold interruption of growth at intervals of 1 second did not lead to a significant change in the surface density of nanostructures.

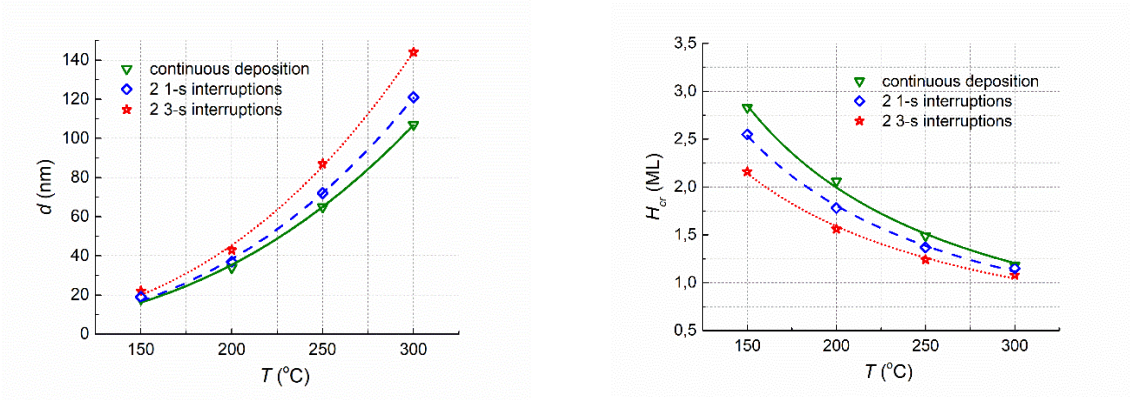

(a) *(b)*

Figure 1. Temperature dependences of the average droplet diameter and critical thickness of droplet formation after deposition of 3 ML of indium at various conditions of vapor supersaturation.

As in the case of the average size and critical thickness of droplet formation, the effect of interruption of deposition on the surface density of droplets becomes less significant with decreasing temperature. Thus, at a temperature of 150 °C, the surface density of droplets decreases by only 9% – from $2.2 \cdot 10^{10}$ to $2.0 \cdot 10^{10}$ cm^{-2}.

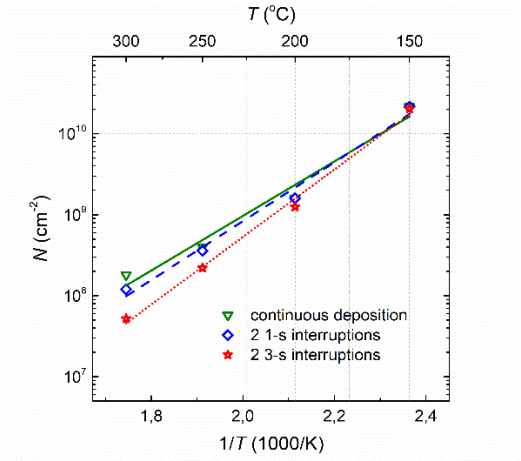

Figure 2. Temperature dependences of the surface density of droplets after deposition of 3 ML of indium at various conditions of vapor supersaturation.

Acknowledgments
This work was supported by the Russian Science Foundation Grant No. №19-79-10099.

References

[1] Balakirev S V, Solodovnik M S, Eremenko M M, Konoplev B G, Ageev O A 2019 *Nanotechnology* **30** 505601
[2] Balakirev S V, Solodovnik M S, Ageev O A 2018 *Phys. Status Solidi B* **255(4)** 1700360

Stress relaxation mechanisms in hybrid SiC/Si(111) substrates grown by the atomic substitution method

I.A. Eremeev[1,2], A.A. Koryakin[2] and S.A. Kukushkin[2]

[1] Alferov St. Petersburg Academic University, St.Petersburg 194021, Russia
[2] Institute for Problems of Mechanical Engineering, Russian Academy of Sciences, St. Petersburg 199178, Russia

Abstract. Stress relaxation mechanisms in hybrid SiC/Si substrates grown by the atomic substitution method are investigated. The elastic properties of the macroporous silicon layer at the SiC/Si interface are studied using the finite element method. The biaxial modulus of this layer is obtained as a function of porosity considering different shape of pores. Mechanical stresses in the 3C-SiC(111)/Si- porous/Si(111) are found. Stress relaxation due to the folding of SiC layer, the bending of SiC/Si substrate and due to the formation of dislocations at the SiC/Si interface are also considered.

1. Introduction

Epitaxial silicon carbide thin films synthesized on silicon substrates by the atomic substitution method [1] allow the growth of crack-free thick AlN, GaN and AlGaN layers for optoelectronic devices. Growth mechanism of AlGaN films is influenced by the residual mechanical stresses in the SiC/Si substrate containing a porous silicon layer. There have been relatively few works regarding the stress relaxation mechanism in the SiC/Si-porous/Si substrates. Telyatnik et al. [2] estimated the residual mechanical strain in the SiC layer (about 2×10^{-3} that corresponds to the stress about 0.5 GPa) using the dependence of the substrate curvature on temperature. Also, different mechanisms of stress relaxation in AlN/SiC/Si were investigated in [2]. However, the real structure of porous silicon was not considered. The elastic constants of porous silicon layer were estimated as a function of porosity using the model of spherical pores in [3]. This report continues the investigation of the porous silicon layer [3] considering the octahedral form of the pores and the presence of thin SiC layer on the surface of pores.

2. Dependence of biaxial modulus on porosity

The calculation of elasticity tensor of porous Si is performed by the finite element method (FEM). The three types of errors are minimized during computation: the finite size effects, discretization errors, and statistical fluctuations (see [3] for details). Model geometry of the systems contains spherical pores with a fixed radius in presence of the thin SiC boundary layer. The characteristic size of the system is more than 5 times larger than the size of the elementary pore R. To analyze the influence of the form of the pores, the regular octahedron inscribed to the sphere with radius R is considered. The latter is set to have boundaries in the (111) plane.

The calculation shows porous silicon to have cubic symmetry having 3 independent constants of the elastic tensor (C_{11}, C_{12}, C_{44}) in all cases. Dependence of biaxial modulus in the [111] direction M_{111} on the porosity of porous silicon layer is shown in figure 1. M_{111} obtained for the model with octahedral pores is slightly lower than that of the spherical form (filled circles and daggers

respectively [3]). Solid lines show the linear approximation of the result. The value of M_{111} increases with the thickness of SiC layer in the pores (tSiC). The results calculated with tSiC/R =0.04, 0.12 and 0.28 are shown by the circles.

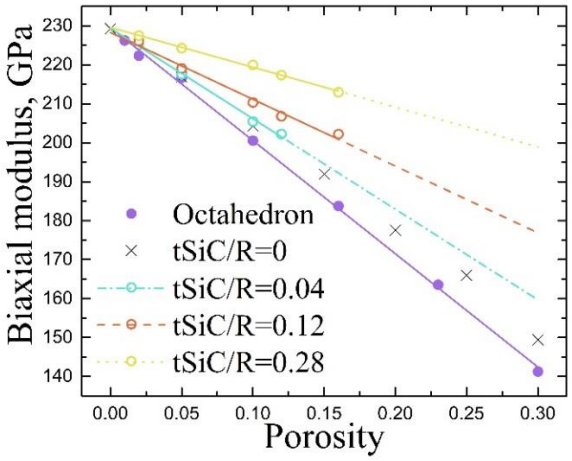

Figure 1. Dependence of M_{111} on the porosity of porous silicon. Filled circles depict the case of the octahedrons. Dashed lines show linear extrapolation of M_{111} to 30% of porosity for tSiC/R=0.04, 0.12 and 0.28. The data obtained in case of the spherical pores is shown by daggers [3].

3. Stress relaxation mechanisms

The following relaxation mechanisms are considered: the reduction of the elastic modulus of silicon layer due to the increase of porosity; the folding of SiC layer; the dislocation formation at the SiC/Si interface; the bending of the substrate.

The lateral component of the stress tensor in the SiC film is investigated using FEM with linear elastic theory approximation. The geometry of the model to be analyzed: silicon substrate of the thickness of 400 um, 2um of the Si-porous layer with M_{111}=229.3-258.9ϕ GPa with respect to the porosity (ϕ) and 100 nm of the SiC film [2]. During FEM calculation the curvature influence is considered. The resulting stress in the SiC film equals 50 GPa. The presence of the Si-porous layer decreases the stress by about 1%

The influence of the formation of folds on the mechanical stress is calculated using FEM. Decreasing of the contact surface of SiC/Si interface leads to the about one percent decrease of the stress in the SiC film.

Using density functional method, Kukushkin et al. [4] have shown that the 3C-SiC/Si(111) interface is the conjugation of 5 elementary cells of 3C-SiC(111) and 4 cells of Si(111). Such configuration corresponds to the minimum energy of the system. This feature of the structure grown by the atomic substitution method greatly decreases the lattice mismatch leading to a compressive strain of the SiC film. Therefore, the stress relaxation probably occurs due to the formation of the ordered set of dislocations at the SiC/Si interface (such as misfit dislocations).

Acknowledgments

This study was carried out within the framework of the Russian Science Foundation, project no. 20-12-00193.

References

[1] Kukushkin S A, Osipov A V and Feoktistov N A 2014 *Phys. Solid State* **56** 1507.
[2] Telyatnik R S, Osipov A V and Kukushkin S A 2015 *Phys. of the Solid State* **57** 162.
[3] Koryakin A A, Eremeev Yu A, Osipov A V and Kukushkin S A 2021 *Tech. Phys. Lett.* **47** 25.
[4] Kukushkin S A and Osipov A V 2020 *Tech. Phys. Lett.* **46** 1103.

Study of the initial stage of GaAs growth on FIB-modified silicon substrates

M M Eremenko[1], M S Solodovnik[1], S V Balakirev[1], N E Chernenko[1] and O A Ageev[1,2]

[1]Institute of Nanotechnologies, Electronics and Equipment Engineering, Southern Federal University, Taganrog 347922, Russia
[2]Research and Education Center "Nanotechnologies", Southern Federal University, Taganrog 347922, Russia

Email: eryomenko@sfedu.ru

Abstract. In this work, studies of the effect of the rate and dose of implantation on the morphology of the resulting nanostructures were carried out. It is shown that an increase in the growth rate at the initial stages of the growth process leads to the transition of the growth regime from layered-like to one-dimensional with the formation of nanowires. An increase in the implantation dose during processing with a focused ion beam led to disordering of the directions of the grown nanowires due to the absence of the influence of the substrate structure.

The formation of high-quality III/V light-emitting sources on silicon remains one of the important modern tasks of optoelectronics and nanophotonics [1]. The growth of the III/V polar semiconductor on a non-polar Si substrate leads to a decrease in the slope efficiency compared to native substrates. Despite the fact that a wide range of techniques is used to improve the structural and functional characteristics of the III/V optical components on Si, completely new approaches are required to reduce the defectiveness of the resulting structures. In this work, we investigated the effect of the implantation dose upon treatment with a focused ion beams and the growth rate on the morphology of the grown GaAs structures.

The epitaxial materials were fabricated using a SemiTEq STE 35 molecular beam epitaxy system with solid-state sources. The studies were carried out on on-axis Si(001) substrates with local modification areas. The surface modification was carried out by local implantation of Ga ions into the Si substrate by the method of focused ion beams. The implantation dose varied from 1 to 21 pC/μm^2 and the current was 1pA. The growth rate varied from 0.1 ML/s to 1 ML/s. The removal of native oxide from the Si surface was carried out at 900°C in vacuum for 30 minutes [2]. Then, a high temperature (600°C) GaAs buffer layer was deposited.

Studies have shown that an increase in the GaAs growth rate from 0.1 to 1.0 ML/s with a constant As_4 flux leads to an intensification of the nucleation and growth processes of GaAs nanowires, regardless of the implantation dose. This behavior is due to the local accumulation of uncompensated Ga, which is associated with the presence of an excess of Ga atoms in the modified areas of Si, which arises due to the introduction of ions into the substrate. It should also be noted that outside the modification areas, an increase in the GaAs growth rate leads to a sharp increase in the density and

size of GaAs crystallites, reducing the selectivity of nucleation and growth processes, which, nevertheless, does not lead to the formation of a continuous film.

It is important to note that with an increase in the implantation dose and, as a consequence, the degree of amorphization of the Si crystal lattice, the degree of influence of the crystal lattice of the substrate on the growth of GaAs nanocrystals decreases: from those oriented in accordance with the structure of the substrate in the directions [110], [1-10] , [-110] and [-1-10] (the case of actually inheriting the structure of the substrate) to randomly oriented - the case of the absence of the influence of the structure of the substrate.

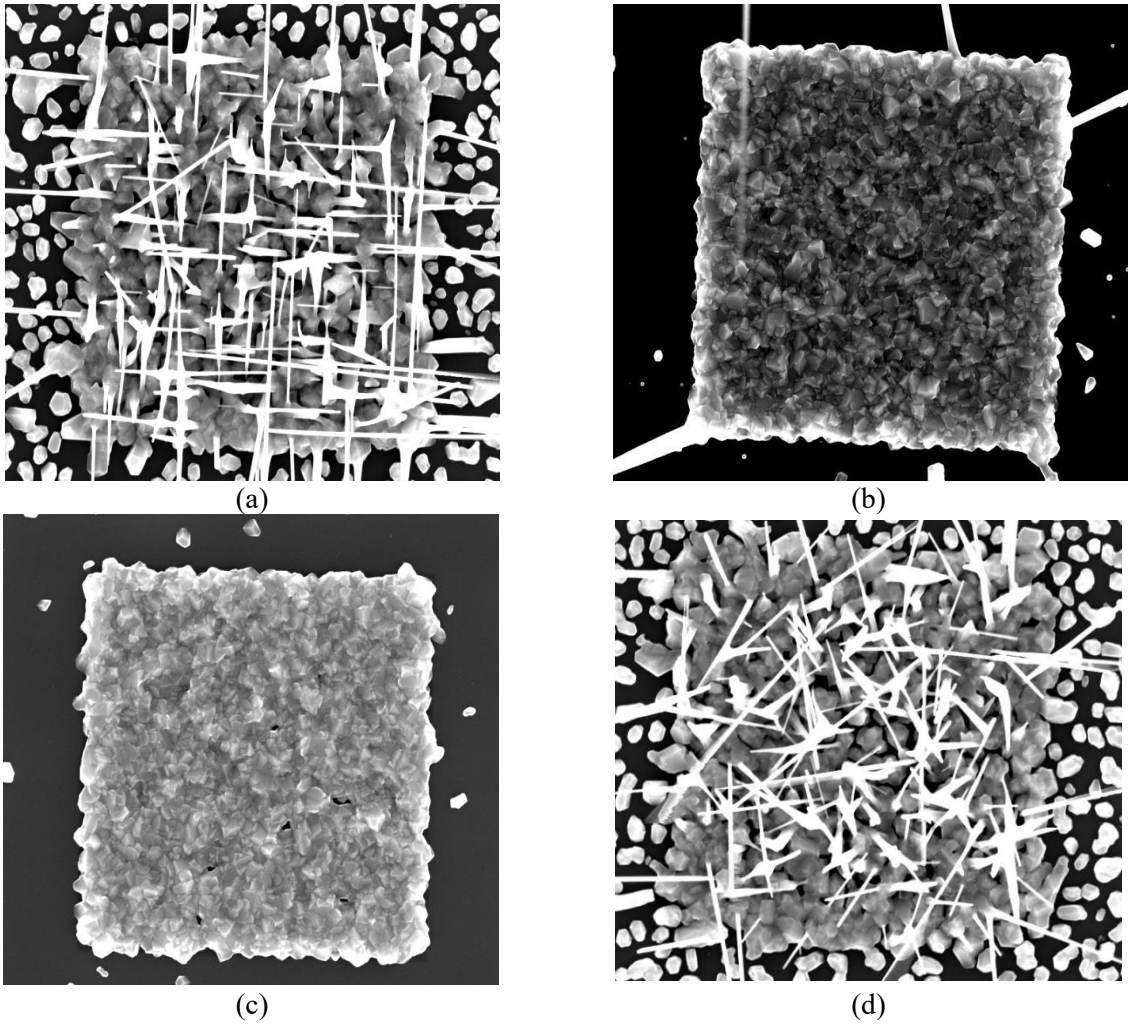

Figure 1. SEM images of modified Si regions after deposition of H = 200 nm GaAs at T = 600ºC with different deposition rates: (a), (d) v = 1 ML/s, (b) v = 0.25 ML/s, (c) v = 0.1 ML/s. The implantation dose and current were 7 pC/μm^2 and 1 pA for (a)-(c), and 21 pC/μm^2 and 1 pA for (d) respectively.

Acknowledgments

This work was supported by the Russian Science Foundation Grant No. 20-69-46076. The results were obtained using the equipment of the Research and Education Center "Nanotechnologies" of Southern Federal University.

References

[1] Wan Y, Li Q, Geng Y, Shi B, Lau K M 2015 *Appl. Phys. Lett.* B **107** 081106

[2] Eremenko M M, Solodovnik M S, Balakirev S V, Chernenko N E, Kots I N, Ageev O A 2020 *J. Phys.: Conf. Ser.* **1695** 012013

The Structure of a Multilayer Heterogeneous System $[(Co_{40}Fe_{40}B_{20})_{34}(SiO_2)_{66}/ZnO/SnO_2]_{33}$

O.V. Zhilova, S.Yu. Pankov, V.A. Makagonov, I.V. Babkina, D.N. Mosolov

Voronezh State Technical University, Voronezh, Russia

zhilova105@mail.ru

Abstract. Multilayer heterogeneous films $[(Co_{40}Fe_{40}B_{20})_{34}(SiO_2)_{66}/ZnO/SnO_2]_{33}$ were obtained by ion-beam sputtering. The thickness of each layer was several nanometers. The periodicity parameter calculated using the small angle X-ray diffraction method coincides with the interlayer thicknesses. This confirms the presence of a multilayer structure. During crystallization of the films (annealing temperature of ~ 550 °C), the multilayer structure is destroyed.

1. Introduction

Wide gap oxide semiconductors are the main functional materials used in transparent electronics. Therefore, when creating electronic devices, it is necessary to predict possible solid-state interaction reactions between semiconductor, dielectric and metal phases. The material for studying such processes can be a multilayer film with nanometer thicknesses of layers.

In this work, a thin-film multilayer structure $[(Co_{40}Fe_{40}B_{20})_{34}(SiO_2)_{66}/ZnO/SnO_2]_{33}$ was investigated.

2. Methods

Thin-film structure obtained by ion-beam sputtering [1]. For deposition of multilayer films, three targets were sputtered: a composite target $Co_{40}Fe_{40}B_{20}$ + SiO_2 and targets made of semiconductors ZnO and In_2O_3. To obtain films with different layer thicknesses, a V-shaped screen was installed between the target and the substrate holder. This made it possible to obtain a smooth change in the thickness of the layers in one technological cycle. The number of $(Co_{40}Fe_{40}B_{20})_{34}(SiO_2)_{66}/ZnO/SnO_2$ layers was 33.

The structure was investigated by X-ray diffraction (XRD) on a D2 PHASER diffractometer (BRUKER). To decipher the obtained diffraction patterns a licensed software was used. Transmission electron microscopy (TEM) images of the cross section and electron diffraction were obtained on a Hitachi HT7700 TEM [2].

3. Results and discussion

Small-angle X-ray diffraction results show the presence of periodic oscillations in all the samples under study. This confirms the presence of a layered structure. The thickness of the layers was calculated using the Wolfe-Bragg formula [3]. This value is close to the values calculated from the technological modes of spraying.

The second option for confirming the multilayer structure of the film in the original state was the study of the cross section of the sample by the method of transmission electron microscopy. (figure 1).

It can be seen from the figure that the film does indeed contain distinct layer boundaries. The total film thickness was 600 nm.

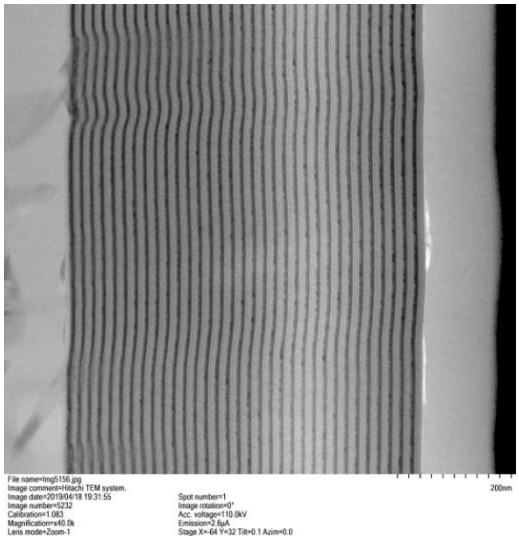

Figure 1. Cross-section of a multilayer structure $[(Co_{40}Fe_{40}B_{20})_{34}(SiO_2)_{66}/ZnO/SnO_2]_{33}$

The results of X-ray and electron microscopic studies are completely correlated with each other. They confirm the multilayer structure and are consistent with the technological modes of the deposition process.

We also measured diffraction curves in the region of small angles after heat treatment. Analysis showed that up to an annealing temperature of 550 °C, the films remain ordered. At a temperature of ~ 550 ° C, the destruction of the layers occurs, and an insignificant increase in the size of the crystallites is observed. An increase in the structural stability in the $[(Co_{40}Fe_{40}B_{20})_{34}(SiO_2)_{66}/ZnO/SnO_2]_{33}$ films with an increase in the thickness of the studied samples is not observed.

Study of the films at medium Bragg angles (2Θ= 10-60 °) showed an X-ray amorphous state of the structure, which is characterized by a wide halo. With an increase in the film thickness in the region 2Θ at about 35 °, an intense peak is observed, which corresponds to the (101) plane of SnO_2.

Acknowledgments

This work was supported by the Ministry of Education and Science within the framework of state assignment No. FZGM-2020-0007.

References

[1] Rylkov V.V., Nikolaev S.N., Chernoglazov K.Y., Demin V.A., Presnyakov M.Y., Vasiliev A.L., Tugushev V.V., Granovsky A.B., Sitnikov A.V., Kalinin Y.E., Perov N.S., Vedeneev A.S. 2017 *Phys. Rev. B*. **95** 144202

[2] Zhilova O.V., Makagonov V.A., Pankov S.Yu., Sitnikov A.V., Kalinin Yu.E., Babkina I.V. 2018 *AIP Conference Proceedings:PTI-2018* 020124.

[3] Andreev A.V. 1958 *Sov. Phys. Usp.* **28**(1) 70

Effect of the Young's modulus of polycrystalline silicon on the characteristics of MEMS accelerometer

J Y Jityaeva[1], E Yu Gusev[2]
[1]Southern Federal University, Laboratory of Functional Nanomaterials Technology, Taganrog 347922, Russia
[2]Southern Federal University, Institute of Nanotechnologies Electronics and Equipment Engineering, Taganrog 347922, Russia
zhityaeva@sfedu.ru

Abstract. The parametric model of the sensing element of the three-axis capacitive micromechanical accelerometer was refined considering the experimental values of Young's modulus of polysilicon. The influence of Young's modulus on the displacement and the first six eigenfrequencies of the micromechanical structure was determined by simulation. The thickness of the structural layer of polycrystalline silicon was ranged from 1 to 6 μm. The eigenfrequency increased by 29% when changing Young's modulus from 120 to 200 GPa. The displacements were 44-77 nm along the X(Y)-axes and 55-750 nm along the Z-axis.

1. Introduction

The development of micromechanical devices is a promising direction in the development of modern technology [1, 2]. The main task during their development is to improve functional characteristics and reduce overall dimensions. Polycrystalline silicon films are widely used in the technology of surface micromachining as structural layers due to their electrical and mechanical properties [3, 4]. Its mechanical properties vary depending on the crystalline structure which has a high sensitivity to the technical method, as well as to the deposition and post-processing conditions. As a result, the mechanical properties of the films, such as Young's modulus, microhardness, and mechanical stresses, can vary over a wide range. It needs to be considered when developing new designs. Thus, determining the influence of the mechanical properties of structural layer material on the functional characteristics of the sensitive elements of MEMS devices is an urgent problem.

The purpose of the work is a study of Young's modulus effect of polycrystalline silicon films on the deflection and eigenfrequencies of a sensitive element of a capacitive micromechanical accelerometer.

2. Experimental details

The parametric model of the accelerometer sensing element considering the experimentally obtained values of Young's modulus was developed for numerical modeling. The model based on the design of a 3-axis capacitive micromechanical accelerometer featuring up to ± 10 g presented in [5]. The sensitive element consists of a square proof mass, elastic suspensions from four sides and a capacitive transduction system.

The material of the sensitive element was polycrystalline silicon. Young's modulus was selected based on previously conducted experimental studies of Young's modulus of polycrystalline silicon films obtained by plasma-enhanced chemical vapor deposition [6].

3. Results

Numerical modeling of the eigenfrequency and displacement of the sensing element along 3-axes were carried out. The first six eigenfrequencies were determined for different values of Young's modulus and a structural layer thickness of 1 to 6 μm. Analysis all the simulation results showed that an increase in Young's modulus from 120 to 200 GPa leads to an increase in eigenfrequency by 29%, regardless of the thickness of the structural layer. The first six eigenfrequencies were in the range of 1 to 9 kHz.

A simulation of the displacement of the sensing element at an acceleration of 10 g was carried out. With increasing Young's modulus from 120 to 200 GPa, the displacement of the comb-finger decreases from 77 to 44 nm at acceleration along the X-axis (figure 1a). The dependence of the displacement at the Z-axis of the center of proof mass at the acceleration of 10 g to the Young's modulus for various thicknesses of polycrystalline silicon is shown in figure 1b. The obtained results could be useful to optimize the design and technology process conditions in developing MEMS accelerometer and other insertional devices.

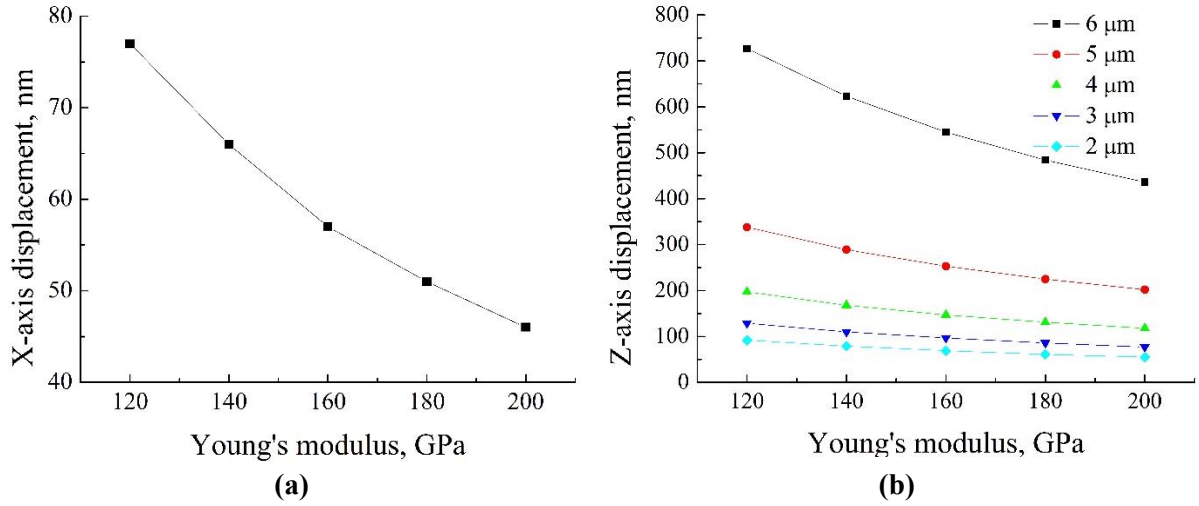

Figure 1. The displacement of microstructure at acceleration of 10 g along axis: (a) X and (b) Y

4. Conclusion

The values of the eigenfrequencies and displacements of the sensitive element were theoretically determined using the refined parametric model of the micromechanical accelerometer. The model considers the experimental values of Young's modulus. The regularities of the influence of the change in Young's modulus on the change of eigenfrequencies, deviations as well as the derivatives of the characteristics are determined.

Acknowledgments

This work was supported by the Ministry of Science and Higher Education of the Russian Federation; the state task in the field of scientific activity No. 0852-2020-0015. The equipment of the Research and Education Center "Nanotechnologies" of Southern Federal University was used for the study.

References

[1] Lim S, Souza C D 2020 International Journal of Industrial Ergonomics **76** 102937

[2] Ageev O A, Konoplev B G (ed.) 2019 Nanotechnology in microelectronics (Moscow: Nauka) 511

[3] French P J 2002 *Sensors and Actuators A: Physical* **99** 3-12

[4] Chun-Hyung C 2009 Current Applied Physics 9 538-545

[5] Ryndin E, Konoplev B, Lysenko I, Kulikova I, Popov A 2019 *Electronics (Switzerland)* **8(9)** 932

[6] Gusev E Yu, Jityaeva J Y, Ageev O A 2018 *Journal Materials Physics and Mechanics* **37(1)** 67-72

Development of epitaxial PbS layers obtaining method for photoelectric transducers

T O Zinchenko, E A Pecherskaya, A V Volik, O A Timohina, V S Alexandrov, V V Antipenko

[1] Penza State University, Krasnaya str., 40, 440026 Penza, Russia
e-mail: pea1@list.ru

Abstract. This paper describes obtained by the hotwall epitaxy method epitaxial PbS layers technology. Materials, methods, technological parameters of synthesis were selected and substantiated. A theoretical model of the p-n transition has been developed. The calculation of the main parameters has been done. The hotwall epitaxy method was chosen for the synthesis. BaF2 was chosen as the substrate.

1. Introduction

The semiconductor industry is actively developing in the modern world. One of the uses is photonics [1]. This article is devoted to the methods study and the techniques development for obtaining epitaxial layers of photovoltaic cells or photoelectric converters. At the present stage, converters based on GaAs and Si arsenide are actively used [2]. PbS was chosen because this material has high exponential photosensitivity.

2. Selection and justification of techniques, materials, technological parameters.

BaF_2 was chosen as the substrate, because in this case a smaller difference in the identity periods and the layer and the substrate thermal expansion coefficients is achieved. The hotwall epitaxy method was chosen because it offers all the advantages of vacuum deposition methods. It is necessary to calculate the deposition time in order to set the n- and p-conductivity layers. The deposition time determines the layer thickness. The kinetic regularities of obtaining layers on BaF_2 substrates (Fig. 1) and the dependence of the charge carriers concentration on pressure (Fig. 2) should be investigated to select the synthesis conditions [4].

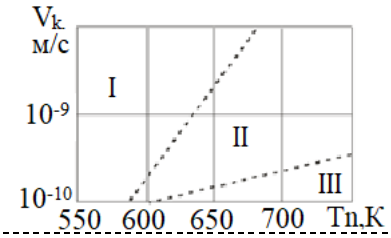

Figure 1. PbS kinetic regularities.

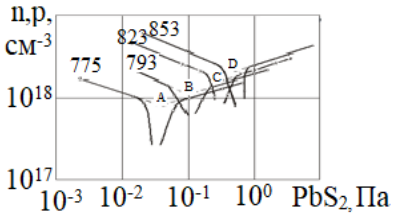

Figure 2. Dependence of the charge carrier's concentration on pressure.

As a result of the experimental data analysis, it was concluded that it is advisable to choose a condensation rate of $2.143 \cdot 10^{-9}$ m/s and a substrate temperature of 700 K. The evaporation temperature

will be 793 K. For 793 K, the pressure $P = 3 \cdot 10^{-2}$ Pa and $P = 2 \cdot 10^{-1}$ Pa, with impurity concentration $n = 2.6 \cdot 10^{18}$ cm^{-3} and $p = 10^{18}$ cm^{-3}.

3. Calculation of the parameters of the p-n transition.

The calculation of the intrinsic concentration of electrons and holes was made according to the following formulas:

$$n^i = p^i = \left(N^c \cdot N^v\right)^{\frac{1}{2}} \cdot \exp\left(-\frac{\Delta E}{2 \cdot k \cdot T}\right) = 5.938 \cdot 10^{19}\, см^{-3} \quad (1)$$

where Nc – effective number of states in the conduction band reduced to the band bottom, Nv – effective number of states in the valence band reduced to the band ceiling, k – Boltzmann's constant, T – temperature, ΔE – value of band gap, n^i,p^i – intrinsic concentration of electrons and holes [5].

The height of the potential barrier is determined as follows:

$$\varphi^0 = k \cdot T \cdot \ln\left(\frac{p \cdot n}{(n^i)^2}\right) = 3.603 \cdot 10^{-20}\, Дж \quad (2),$$

where n – electron concentration, p – hole concentration, φ^0 – potential barrier height.

The thickness of the space charge layer of the abrupt p-n transition is:

$$d = \left(\frac{2 \cdot \varepsilon \cdot \varepsilon_0 \cdot \varphi^0}{n \cdot q^2}\right)^{\frac{1}{2}} = 1.216 \cdot 10^{-5}\, см \quad (3)$$

where ε_0 – permittivity of vacuum, ε – dielectric constant, q – elementary charge.

Performed calculations showed that to obtain a p-n transition under the given conditions, the time t = 56.783 s is required. It is necessary to take into account the phenomenon of self-diffusionIt was found that the width of self-diffusion processes is about from 0.3 to 0.5 μm. The choice of thickness should be in the range from 1.5 to 3 μm (one layer). So, the thickness should be 2.25 μm.

Conclusion

The obtained indicators prove that the chosen hotwall epitaxy method is one of the most suitable for the use of such structures. Secondly, the selected substrate materials and layers for the p-n transition have the required characteristics for use in photovoltaic converters. Thirdly, the main indicators of the p-n transition are calculated, which make it possible to resolve the topology of the photocell.

Acknowledgments

The study was carried out with the financial support of the Russian Foundation for Basic Research within the framework of scientific project No. 20-38-90044.

References

[1] Timur Zinchenko, Ekaterina Pecherskaya and Dmitriy Artamonov 2019 The properties study of transparent conductive oxides (TCO) of tin dioxide (ATO) doped by antimony obtained by spray pyrolysis *AIMS Materials Science* vol. 6 (2) pp 276–287

[2] Edward M. Gaddy 1996 Cost trade between multijunction, gallium arsenide and silicon solar cells *Progress in photovoltaics: research and applications* vol 4 155-161

[3] Averin I A 2007 Controlled synthesis of heterogeneous systems: technology and properties *Dissertation for the degree of Doctor of Technical Sciences* (Penza State University, Penza), 2007 381 p

[4] Shur Michael, Singh Jasprit 1990 Physics of Semiconductor Devices *Phys. Today* 43(10) p 98

Optical and structural properties of the GaAs heterostructures grown using AlGaAs superlattice buffer layer on compliant Si(100) substrates with the preformed porous-Si (por-Si) layer.

Zolotukhin D,*[1], Seredin P[1], Lenshin A[1], Goloshchapov D [1], Khudyakov Y[1], Radam Ali O[1], Arsentyev I[2], Leiste H[3]

[1]Voronezh State University, Universitetskaya pl. 1, 394018, Voronezh, Russia

[2]Ioffe Institute, Politekhnicheskaya 26, 194021, St. Petersburg, Russia

[3]Karlsruhe Nano Micro Facility H.-von-Helmholtz-Platz 1, 76344 Eggenstein-Leopoldshafen, Germany

E-mail: seredin@phys.vsu.ru

Abstract. The 360 nm and 700 nm thick GaAs layers were grown by MO MOCVD growth technique directly on compliant Si (100) substrate and on supper-lattice (SL) AlGaAs buffer layer. The XRD study revealed better structural quality for the sample grown on SL / por-Si buffer as well as AFM study revealed a smoother sample surface with blocks of a more regular rectangular shape and larger size. Photoluminescence spectra of the samples revealed an energy shift of PL maximum intensity for both samples. Sample grew on SL buffer also showed higher PL intensity corresponding to better crystalline perfection.

1. Introduction

The integration of the III-V technology with the most established Si technology is the actual problem for state of art science. However, large lattice and thermal expansion coefficient (TEC) mismatch between Si and GaAs (~120.4% and ~4.1%, respectively) [1] leading to the generation of the high density of threading dislocations (TD). As shown in our previous work [2] the usage of por-Si layer helps to suppress stress generation and TD propagation. In this work we compare optical and structural properties of the GaAs layers grown by MO MOCVD technique on por-Si/Si(100) (sample **A**) and SL/por-Si/Si(100) (sample **B**) templates.

2. Experiment

The Por-Si was formed on the c-Si (100) substrate by electrochemical etching in the alcohol solution of the fluoric acid [3]. Growth procedures were performed on EMCORE GS3100 MO MOCVD setup with growth pressure of 77 Thor and substrate rotation speed of 1000 rpm. TMG ($(Al(CH_3)_3)$) and Arsine (AsH_3), were used as source gases and H_2 was used as a carrier gas. Both substrates were annealed at

20 min under AsH_3 flow and T_s=750 ˚C. After annealing the 10-nm-thick AlAs overlaid by 20-nm-think GaAs buffer layer was grown at the T_s=450 ˚C. The GaAs layer with a thickness of 390 nm was grown for sample **A** and the SL buffer layer with a thickness of 100 nm and overlaying 700-nm-thick GaAs layer was grown for sample **B** at the T_s=550 ˚C.

3. Results

The AFM study of both samples (Figure 1.**a** and **1.b**) revealed mosaic surface morphology, but for sample **B** the surface blocks have larger size and more rectangular shape corresponding to better crystalline quality. This fact also can be confirmed by HRD study of the samples (Figure **1.c**) where for sample **B** more intensive (400) peak can be observed. Also no other peaks except (200) and (400) been observed, corresponding to monocrystalline structure of both samples.

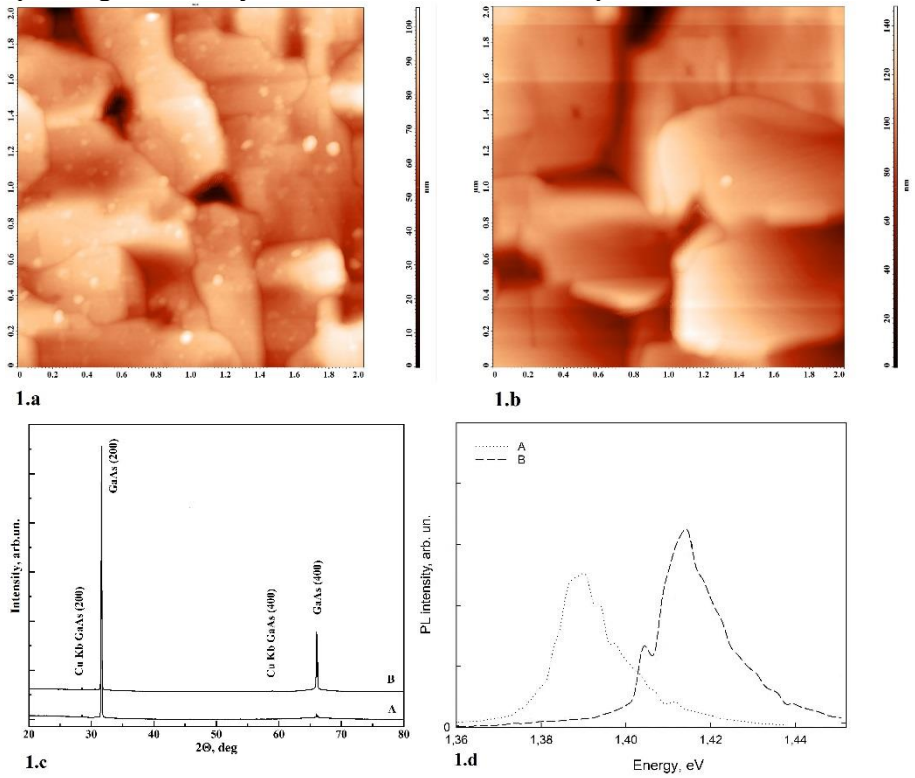

Figure 1 The AFM image (**1.a**, **1.b)** XRD spectra (**1.c**), and PL spectra **d**) of sample **A** and **B**

The PL spectra of the samples (Figure **1.d**) demonstrates bright emission at ~1.39 eV for sample **A** and 1.5 eV for sample **B** shifted from normal value for GaAs 1.42 eV to the low energy area. The nature of this redshift is under study.

Acknowledgments

The study was financially supported by the Russian Science Foundation (grant no. 19-72-10007).
P.V.S. carried out his part of the study with the support from the Ministry of Science and Higher Education of Russian Federation (grant no. FZGU-2020-0036) under the State assignment to higher school institutions.

References

[1] Kukushkin *et al.* Rev Adv Mater Sci n.d. **17**, 1 (2008)
[2] P.V. Seredin, *et al.*, Phys. E Low-Dimens. Syst. Nanostructures, **104**, 101 (2018)
[3] A.S. Lenshin, *et al.*, Mat. Sci. Semicond. Proc. **30**, 25 (2015)

Core-shell InGaN nanowires on Si substrates: MBE growth and physical properties

V O Gridchin[1], R R Reznik[1-3], K P Kotlyar[2], A S Dragunova[1], D A Kirilenko[3], N V Kryzhanovskaya[1], G E Cirlin[1-3]

[1]Alferov University, St. Petersburg 194021, Russia
[2]Saint Petersburg State University, St. Peterburg 198504, Russia
[3]Ioffe Institute, St. Petersburg 194021, Russia

e-mail: gridchinvo@yandex.ru

Abstract. InGaN nanostructures are among the most promising candidates for visible solid-state lighting and renewable energy sources. This work is devoted to the study of structural and optical properties of InGaN nanowires grown on Si substrates. It was obtained that the InGaN nanowires have a spontaneously formed core-shell structure with the In content about 40 % inside the core and about 4 % inside the shell. The grown nanostructures are promising for the RGB and phosphor-free white light emitting diodes.

1. Introduction

InGaN ternary compounds are paramount materials for applications in the solid-state lighting and renewable energy sources since it has a direct bandgap in the range from 0.7 to 3.43 eV achieved by tuning the alloy composition [1]. However, the enormous difference of the bond lengths between InN and GaN results in the miscibility gap in $In_xGa_{1-x}N$ layers with x_{In}=0.2-0.8 at the usual growth temperature. At the same time, the synthesis of high-quality InGaN epitaxial layers is difficult due to the lack of lattice-matched substrates and the different thermal expansion coefficients between InGaN and other materials. These problems can be solved via the synthesis of InGaN nanowires (NWs). Recently, it has been demonstrated that the InGaN with the whole chemical composition range can be obtained [2]. Another benefit of the elastic strain relaxation is the ability of the growth of almost defect-free NWs on substrates with another lattice constants and thermal expansion coefficients, in particular on Si [3].

Here, we study the growth of InGaN nanowires directly on Si substrates by plasma-assisted MBE. The influence of the growth temperature on structural properties of InGaN NWs is investigated.

2. Experiments

The InGaN nanostructures were grown using Riber Compact 12 MBE system equipped with In and Ga effusion cells and a nitrogen source. The growth was performed on unprepared Si substrates at equal each other In and Ga fluxes and under N-rich conditions. The structural properties of the samples were examined using a SUPRA 25 C. Zeiss scanning electron microscope (SEM) and high-angle annular dark-field scanning transmission electron microscopy (HAADF STEM, JeolJEM-2100FTEM) with

energy-dispersive X-ray (EDX) spectroscopy techniques (XFlash 6TI30, Bruker. The optical properties of the samples were studied using the photoluminescence (PL) method.

3. Results

It was obtained that at the narrow temperature range the structural properties of InGaN NWs can be sufficiently changed. The coalesced InGaN NWs at the substrate temperature about 665-670 C. The TEM study of this sample demonstrates that the NWs corresponding to the inhomogeneously distributed areas with different In and Ga content. At the lower substrate temperatures, the separated InGaN NWs are formed. The TEM study shows that the NWs consist of the spontaneously formed core-shell structure with high In content (30-40 %) inside the shell and low In content (below 4 %) inside the core. The PL study of the samples shows pronounced emission in the wavelength range from blue to red.

4. Conclusion

To conclude, we have studied the influence of the substrate temperature on the physical properties of InGaN NWs grown on Si and defined the conditions for the growth of separated InGaN NWs with pronounced core-shell structure with high In content inside the core and low In content inside the shell. The results are promising for creating highly efficient LEDs on Si substrates.

References

[1] Shubert E 2006 *Light-Emitting Diodes* (New York: Cambridge University Press)

[2] Roche E, André Y, Avit G, Bougerol C, Castelluci D, Réveret F, Gil E, Médard F, Leimarie J, Jean T, Dubrovski V G and Trassoudaine A 2018 *Nanotechnology* **29** 465602

[3] Dubrovskii V G, Cirlin G E and Ustinov V M 2009 *Semiconductors* **43** 1539

Effect of the ultra-low arsenic flux on characteristics of In(As) nanostructures formed during droplet epitaxy

D V Kirichenko, S V Balakirev, N E Chernenko, M M Eremenko and M S Solodovnik

Institute of Nanotechnologies, Electronics and Equipment Engineering, Southern Federal University, Taganrog 347922, Russia

Email: dankir@sfedu.ru

Abstract. In this paper, we present the results of an experimental study of the influence of the ultra-low arsenic flux on the parameters of In nanodroplets obtained by droplet epitaxy on the GaAs substrate. We demonstrate that the arsenic flux can be used to alter the size of droplets without changing their surface density. An increase in the arsenic flux leads to a saturation of the size of nanostructures (~30 nm) which ensures good reproducibility of the process.

1. Introduction

One of the most significant challenges in modern electronic and photonic devices is a possibility to control characteristics of single nanostructures. Applications of quantum communication and computing require operation with single quantum dots with defined parameters. Droplet epitaxy is a method of A3B5 nanostructure growth which allows two-stage formation of nanostructures, namely deposition of metal and its further crystallization in the group-V flux [1, 2]. In this paper, we carry out a study of the ultra-low arsenic flux effect on the characteristics of indium droplets formed on the GaAs(001) surface.

2. Experiment

For experimental study, we first prepared GaAs(001) epi-ready substrates by standard oxide removal and further 400-nm buffer layer growth. Then we closed the arsenic valve and cooled down the substrate to a deposition temperature of 300°C. After the background pressure reduced to a value below $1 \cdot 10^{-7}$ Pa, we formed droplet arrays on GaAs(001) substrates by deposition of 3.0 equivalent monolayers (ML) of indium. Then we exposed the samples to arsenic fluxes of various ultra-low values.

3. Results and discussion

As we observed previously [1, 2], deposition of 3.0 ML of indium on the GaAs(001) surface at a temperature of 300°C leads to the formation of arrays of droplets with an average diameter of about 150 nm and a surface density below $1 \cdot 10^{8}$ cm^{-2}. Exposure of In droplets to the arsenic flux is normally used to crystallize them into InAs nanostructures requiring further capping for the quantum dot formation. However, we used arsenic fluxes of ultra-low values in order to alter the droplet size without their transformation into InAs nanodots, nanorings or nanoholes.

We demonstrate that an increase in the As pressure ratios leads first to a simple decrease of the average droplet size (Figure 1*a,b*). At larger As fluxes the ring formation occurs along the droplet perimeter but the droplet still continues decreasing in size (Figure 1*c,d*). The fact that a droplet changes in parameters under the As flux is well-known and mostly used for the purpose of nanoring

and nanohole formation. However, we observe that the droplet size can be altered before the final crystallization into InAs nanostructure.

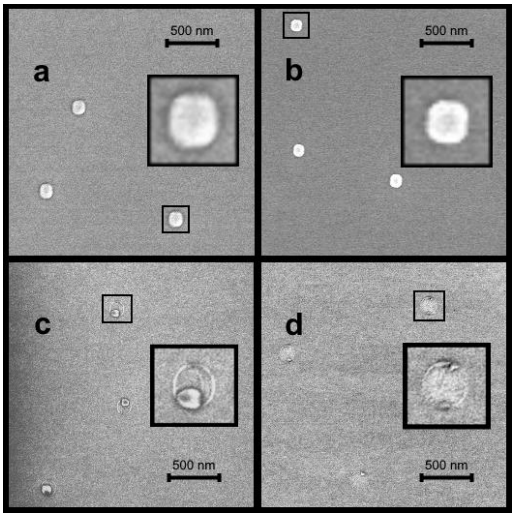

Figure 1. SEM images of nanostructures obtained after deposition of 3.0 ML of In and further exposure to the ultra-low As flux P/P_0: a) 1, b) 4, c) 6, d) 8.1. Insets: 250×250 nm^2.

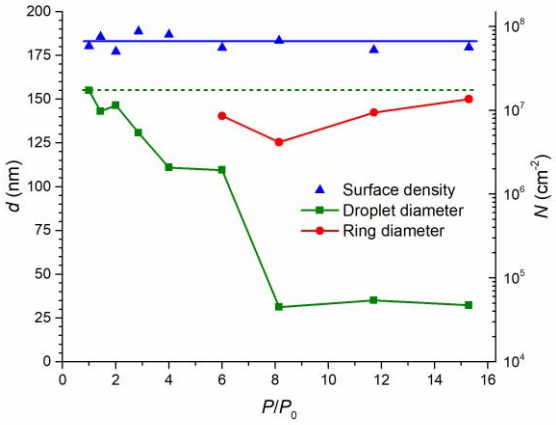

Figure 2. Arsenic pressure ratio dependences of the average size and surface density of droplets obtained after deposition of 3.0 ML of In and their further exposition to the ultra-low As fluxes.

Figure 2 demonstrates As flux dependences of the surface density and average diameter of droplets and rings after deposition of 3.0 ML of In. Droplets shrink under the As flux in a whole range of its increase. At $P/P_0 = 6$ a droplet transforms into the droplet-ring complex so that the ring diameter is approximately equal to the initial droplet size. The ring forms at the interface of three phases due to an increase in the As concentration and, hence, In to InAs crystallization intensity.

One of the most significant results we can observe in Figure 2 is the shrinkage of droplets without the ring formation around them. This phenomenon is realized below a certain critical value of the As pressure ($P/P_0 = 6$ in Figure 2) above which the rings start to form. One more important observation is a saturation of the droplet size to a value of about 30 nm in the range of As pressure ratios from 8 to 15.3. In this range, an increase in the As flux does not lead to a noticeable decrease in the droplet size or to its decay. The saturation phenomenon opens the way to a controlled decrease in the droplet size and good reproducibility of this process.

4. Conclusion

Thus, an independent control of the size of nanostructures can be achieved by using an exposure of droplets to the ultra-low As flux. In order to obtain droplets of a small size to further crystallize them into optically efficient InAs quantum dots, a minimum value of the ultra-low As flux and long exposure times should be used. Otherwise, the formation of rings and holes is possible which can in turn be useful for some specific applications.

Acknowledgments

This work was supported by the Russian Science Foundation Grant No. №19-79-10099.

References

[1] Balakirev S V, Solodovnik M S, Eremenko M M, Chernenko N E and Ageev O A 2020 *Nanotechnology* **31** 485604

[2] Balakirev S V, Solodovnik M S, Eremenko M M, Konoplev B G, Ageev O A 2019 *Nanotechnology* **30** 505601

Quantitative analysis of metastable wurtzite phase into the self-catalyzed GaP NWs

Koval O Yu[1], Fedorov V V[1,2], Eliseev I E[1], Bolshakov A D[1,3], Burkovsky R G[2], Mukhin I S[1,3]

1 Alferov University, Khlopina 8/3, 194021, St. Petersburg, Russia
[2] Peter the Great St.Petersburg Polytechnic University, Polytechnicheskaya 29, 195251, Saint Petersburg, Russia
[3] ITMO University, Kronverksky prospekt 49, 197101, Saint Petersburg, Russia

*Correspondence: o.yu.koval@gmail.com

Abstract. In this letter, we report the growth of the self-catalyzed GaP nanowires with a high concentration of wurtzite phase by molecular beam epitaxy. Formation of rotational twins and wurtzite polymorph in vertical nanowires was observed by the developed a complex approach based on the transmission electron microscopy and X-ray diffraction methods. We obtained wurtzite polytype segments with thicknesses lying in the range from several tens up to 500 nm. The results of the work open new perspectives for high phase purity phosphide NWs synthesis and its fast and reliable investigation with XRD techniques using an in-house X-Ray source.

1. Introduction

Nowadays, there are no reports on the formation of the wurtzite GaP phase in self-catalyzed nanowires by means of molecular beam epitaxy (MBE), only grown Au-catalyzed WZ GaP NW by CBE or MOVPE methods are reported [1], [2]. Self-catalyzed nanowires presented in this report are free from gold or carbon extrinsic impurities acting as deep trapping levels for charge carriers. Control and analysis of the crystal phase in semiconductor nanowires are of high importance owing to the high potential of the phase bandgap engineering [3].

The scientific soundness of the presented paper is based on the presentation of both novel material (wurtzite GaP) and original approach for quantitative characterization of this type of nanostructures. Commonly used crystal phase characterization techniques (i.e. transmission electron microscopy (TEM) or X-ray diffraction (HR-XRD)) are lacking both integral and microscopic data. Thus, the TEM studies reveal only microscopic data and do not allow to evaluate lattice parameters with high accuracy. Thus, the use of Rietveld refinement [4], [5] approach to HR-XRD data handling to perform crystal structure solution, as well as the estimation of volume fraction of the crystalline phases in epitaxial nanoheterostructures are suggested to be inaccurate.

2. GaP nanowires synthesis

GaP NW arrays were synthesized on vicinal silicon (111) substrates with a 4˚ miscut in $<11\overline{2}>$ direction, using Veeco GEN-III MBE machine equipped with Ga effusion cell and valved phosphorus cracker for P_2 molecular flux ($T_{cracker}$ = 900°C). To establish the influence of the growth temperature on NW crystal structure, three samples were grown at the substrate temperature of 590°C, 610°C and

620°C. In this work, a two-stage growth with a change of V/III element fluxes ratio, namely 12 and 18, was presented.

3. Result and discussion

3.1. TEM study

Crystal structure is studied with TEM using JEOL JEM–2100F field emission gun TEM (Tokyo, Japan) operating at 200 kV (with point-to-point resolution of 0.19 nm in TEM mode).

According TEM study (Figure 1a)) there is the existence of 2 crystal phases – cubic ZB and hexagonal WZ. Also, the average NW

According to X-ray diffraction reciprocal space mapping analysis, there are the existence of ZB twinning and absence of WZ twinning (not presented here).

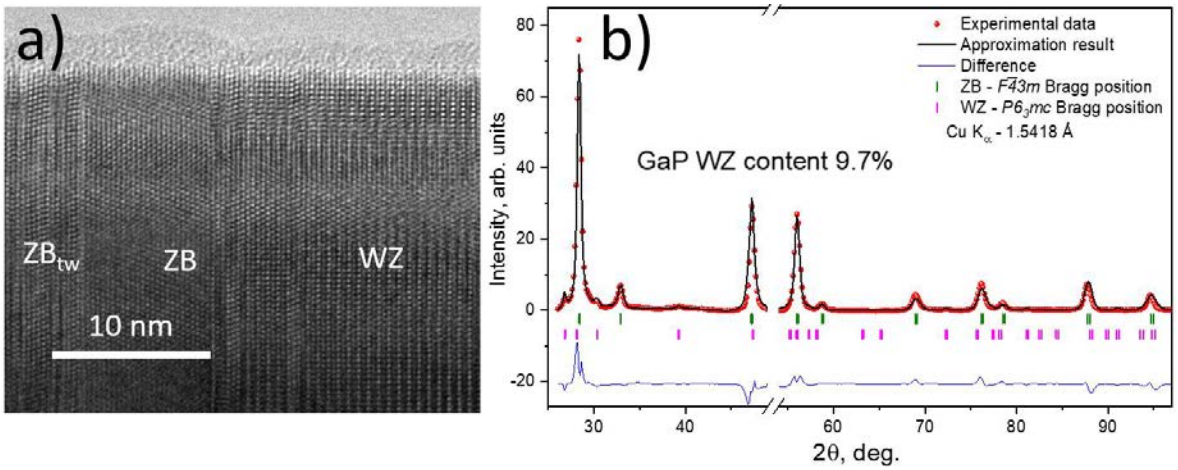

Figure 1. a) HRTEM image of individual studied GaP NW, b) Approximated XRD powder diffraction pattern obtained from disordered GaP NWs into the scotch glue, which was grown at 610˚ C

3.2. XRD study

The study is performed using SuperNova (Rigaku Oxford Diffraction, Japan) diffractometer, radiation generated by IμS microfocus X-ray tube with Cu Kα-radiation (λ = 1.5418 Å, ~8 keV). NW synthesis by the MBE method is always accompanied by the formation of a two-dimensional parasitic island. That is why, we detached the NW array from the substrate using "scotch-taping" technique for avoiding XRD signal from parasitically grown islands.

As clearly in Figure 1 b) there are many Bragg reflexes, the highest intensity corresponding to the cubic ZB GaP phase with $F\bar{4}3m$ space group (positions depicted with green sticks) [6] and reflexes with lower intensity can be attributed to WZ phase with P6$_3$mc space group (positions depicted with magenta sticks) [7]. Quantitative phase analysis and evaluate the WZ GaP phase lattice parameters we present a simple express Rietveld refinement [5]. The obtained data provide statistics across a large number of disordered NWs in one measurement which makes it more practically useful compared to TEM analysis.

Conclusions

We report on the controllable stabilization of the polymorphic wurtzite crystal phase in the MBE grown self-catalyzed GaP NWs and refine the crystal lattice parameters of metastable WZ GaP phase. We employ TEM that enables direct observations of the WZ phase stabilization up to 500 nm long GaP NW segment. The proposed approach can be used for a quantitative evaluation of the mean volume fraction of polytypic phase segments in heterostructured nanowires highly desirable for optimization of growth technologies.

Acknowledgments
The authors thank the Ministry of Science and Higher Education of the Russian Federation (FSRM-2020-0005). O. Yu. Koval thanked the Russian Foundation for Basic Research (RFBR project № 19-32-90232).

References
[1] J. K. Panda *et al.*, "Electronic band structure of wurtzite GaP nanowires via temperature dependent resonance Raman spectroscopy," *Appl. Phys. Lett.*, vol. 103, no. 2, p. 023108, 2013
[2] S. Assali *et al.*, "Direct Band Gap Wurtzite Gallium Phosphide Nanowires," *Nano Lett.*, vol. 13, no. 4, pp. 1559–1563, Apr. 2013
[3] X. Yang, H. Shu, P. Liang, D. Cao, and X. Chen, "Crystal Phase and Facet Effects on the Structural Stability and Electronic Properties of GaP Nanowires," *J. Phys. Chem. C*, vol. 119, no. 21, pp. 12030–12036, 2015
[4] N. Clavier *et al.*, "Purification of uranothorite solid solutions from polyphase systems," *J. Nucl. Mater.*, vol. 441, no. 1–3, pp. 73–83, 2013
[5] H.-R. Wenk, L. Lutterotti, P. Kaercher, W. Kanitpanyacharoen, L. Miyagi, and R. Vasin, "Rietveld texture analysis from synchrotron diffraction images. II. Complex multiphase materials and diamond anvil cell experiments," *Powder Diffr.*, vol. 29, no. 3, p. 220–232, 2014
[6] L. M. Foster, "A Lattice Parameter Criterion for Miscibility Gaps in the III–V and II–VI Pseudobinary Solid Solutions," *J. Electrochem. Soc.*, vol. 121, no. 12, p. 1662, 1974
[7] C. B. Maliakkal *et al.*, "Growth, structural and optical characterization of wurtzite GaP nanowires," *Nanotechnology*, vol. 30, no. 25, p. 254002, 2019

Laser sintering of oxidized copper nanoparticles deposited by dry aerosol printing

D V Kornyushin[1], A A Efimov[1], A I Buchnev[1], E I Kameneva[1] and V V Ivanov[1]

[1]Moscow Institute of Physics and Technology (National Research University), Dolgoprudny 141701, Russia

kornyushin.d@phystech.edu

Abstract. Sintering of oxidized copper nanoparticles arrays in the form of lines by the local treatment of laser radiation with wavelengths of 527 nm and 980 nm was studied. To form lines with a width of 40–150 μm and a thickness of 0.5–4 μm focused aerosol jets with average nanoparticle sizes of 110 and 65 nm were used. The production of semiconductor arrays from oxidized copper nanoparticles with a specific electrical resistance of 10^{-3} Ω·m using laser radiation with a wavelength of 980 nm was demonstrated.

1. Introduction

Nowadays, the field of printing technologies for the production of electronic devices (solar cells [1], gas sensors) is actively developing. New methods for the formation of functional microstructures are emerging, which are aimed at simplifying, reducing the cost and minimizing hazardous waste. One of these methods is aerosol printing, based on the selective deposition of aerodynamically focused beams of nanoparticles on substrates. Earlier, the authors of [2-3] demonstrated the possibility of forming arrays of nanoparticles using the dry aerosol printing method.

It is advisable to sinter arrays of nanoparticles formed on a substrate with laser radiation, since this method of energy transfer is local and does not damage the substrate material. Therefore, an urgent task is to find the optimal conditions for laser sintering, which depends on the shape and size of nanoparticles and the parameters of laser radiation. In the present work, we explore the optimal conditions for laser sintering of oxidized copper nanoparticles arrays formed using the method of dry aerosol printing.

2. Experimental

The experimental setup for the formation of nanoparticles arrays in the form of lines (schematically shown in figure 1a) includes the following key elements: a spark discharge generator of nanoparticles, a thermal nanoparticles optimizer for controlling the size and shape of nanoparticles, a coaxial micro-nozzle for focused deposition of nanoparticles on a substrate, a coordinate table with the ability to moving the substrate at a given speed relative to the micronozzle. The formation of nanoparticles arrays is carried out in dry form without the use of surfactants and solvents. The generation and deposition of nanoparticles obtained as a result of electrical erosion of copper electrodes are carried out in an atmosphere of gas mixture Ar + H_2 (5%). The processes of sintering by laser radiation were carried out using a fixed optical stand, in which the formed arrays were attached to the same coordinate table. The sintering of the arrays was studied using continuous laser radiation with wavelengths of 527 nm and

980 nm. In the experiments, the power of laser radiation and the speed of laser spot moving over the nanoparticles arrays were also varied.

The size, shape and elemental composition of nanoparticles are studied using a transmission electron microscope (TEM) and an aerosol spectrometer. The structural properties of nanoparticles arrays are studied using a scanning electron microscope and an optical profilometer. Nanoparticles arrays are formed in the form of lines with a width and thickness equal to 40–150 μm and 0.1–4 μm, respectively. The size and shape of the nanoparticles are controlled by varying the operating modes of the thermal nanoparticles optimizer.

It was experimentally established that the quality of sintering depends on the size and shape of nanoparticles, which are controlled by a thermal nanoparticles optimizer. At a heating plate temperature of 300 ° C, the resistivity of the arrays formed by the primary nanoparticles (PNPs) after sintering with laser radiation turned out to be 3-4 times higher than that of the arrays formed by thermally optimized nanoparticles (TNPs). According to the TEM images this difference in electrical resistivity correlates with the fact that arrays formed by PNPs have higher porosity than arrays formed by TNPs.

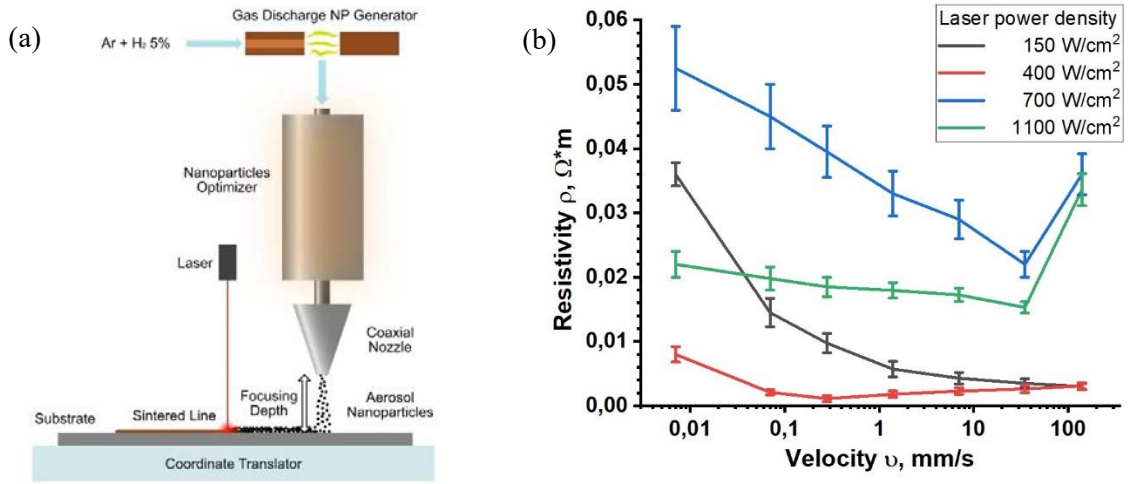

Figure 1(a, b). (a) The scheme of the experimental setup; **(b)** The dependency of electrical resistivity of sintered samples versus the speed of the laser spot moving over the nanoparticle array with different laser power densities for the wavelength of 980 nm.

Figure 1b shows an experimental dependence of the electrical resistivity of arrays formed by TNPs versus the speed of the laser spot moving over the nanoparticles array with different laser power densities. On the graph, the minimum resistivity is observed near the speed of 0.28 mm/s and equal to 10^{-3} Ω·m. The similar study was carried out for sintering by the usage of laser radiation with a wavelength of 527 nm.

3. Conclusion

The advantage of combining the method of dry aerosol printing and laser sintering was demonstrated by the example of sintering arrays of oxidized copper nanoparticles. It was found that with an increase in the scanning velocity of the laser spot, a monotonic decrease in the specific resistance of the printed lines occurs. The minimum resistivity at a heating plate temperature of 300 ° C was observed for arrays formed from TNPs and sintered by laser radiation with wavelength 980 nm near the speed of 0.28 mm/s and equal to 10^{-3} Ω·m.

Acknowledgments

This work was supported by the Russian Science Foundation (project # 19-79-00375).

References

[1] Yang C, Zhou E, Miyanishi S, Hashimoto K and Tajima K 2011 ACS Appl. Mater. Interfaces **3** 4053–58

[2] Khabarov K, Kornyushin D, Masnaviev B, Tuzhilin D, Saprykin D, Efimov A and Ivanov V 2020 *Appl. Sci.* **10(1)** 246

[3] Kornyushin D V, Efimov A A, Khabarov K M and Ivanov V V 2020 *J. Phys.: Conf. Ser.* **1695** 012032

Method for β-$FeSi_2$ thermoelectric films fabrication by pulsed laser deposition in vacuum

Yu M Kuznetsov[1,2], M V Dorokhin[2], A V Nezhdanov[1], D A Zdoroveyshchev[1,2] and V P Lesnikov[2]

[1]Lobachevsky state university, 603022, Russia, Nizhny Novgorod, Gagarin av. 23 b.3
[2]Scientific Research Institute of Physics and Technology of Lobachevsky State University, 603022, Russia, Nizhny Novgorod, Gagarin av. 23 b.3

Mail: yurakz94@list.ru

Abstract. The paper considers a method for the formation of the β-$FeSi_2$ phase films on silicon and sapphire substrates by pulsed laser deposition in vacuum. A series of structures with varying of iron concentration in the sputtered target was prepared. The phase composition of the films is analysed via the identification of peaks in the Raman spectra. The study of the magnetic properties of the samples was carried out by recording the magnetic field dependence of the Hall resistance. The formation of additional magnetic Fe_3Si and FeSi phases is shown upon the growth conditions that provide an increased incorporation of Fe atoms into the formed layer.

1. Introduction

The semiconducting β-$FeSi_2$ compound is a promising material for various applications. According to [1], the material exhibits photoluminescence at 1.54 μm, which makes it possible to consider β-$FeSi_2$ in optoelectronic applications. The magnetic properties of iron and silicon compounds, which can be revealed at room temperatures [2, 3], are of interest to research for use in spintronic devices.

2. Investigated structures

The structures were formed by pulsed laser deposition in vacuum (~ 10^{-6} Torr). In the process of deposition, a composite target including Si and Fe sectors was sputtered with a pulsed YAG:Nd laser. The substrate temperature was 500 °C. A series of structures was prepared in which the concentration of iron was varied. The composition was varied by changing the ratio of the Fe and Si components in the sputtered target (by changing the corresponding angle of the sector).

To analyze the effect of iron diffusion during growth on the properties of the films being formed, the following substrates were chosen: silicon <100> (Si) and sapphire <1102> (Al_2O_3) wafers.

3. Experimental technique

The phase analysis of the obtained structures was carried out by recording the Raman spectra using the NTEGRA SPECTRA facility . The study of the magnetic properties was carried out by recording the magnetic field dependence of the Hall resistance at room temperature in the magnetic field range of ± 2.8 T. The Hall voltage was recorded using a Keithley-2401 programmable voltage meter.

4. Experimental

In the course of the work, were recorded. The spectra of Raman light scattering of the structures under study are shown in Fig. 1(a) - 1(b). The composition of the films is indicated on the legend for the graphs. For comparison, the spectrum of Raman scattering from a silicon substrate is presented.

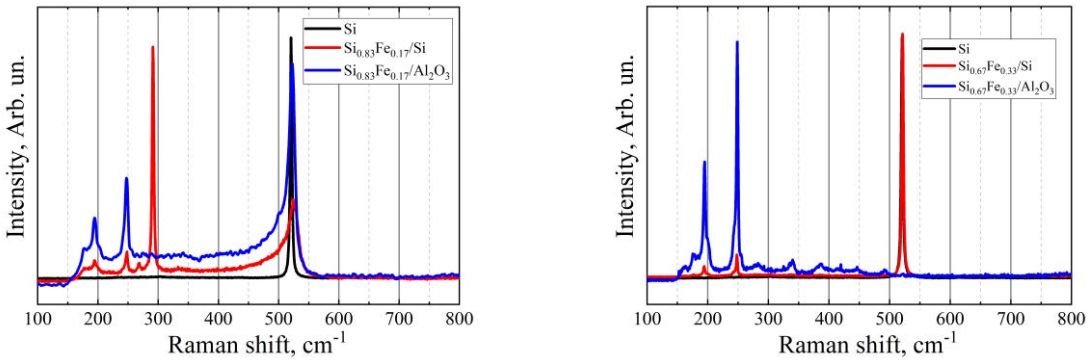

(a) (b)

Figure 1. The experimentally obtained dependence of the Raman spectra of the structures under study.

Peak identification is shown in Table 1 (peak position, phase and relationship).

	Peak position, cm^{-1}	Phase		Peak position, cm^{-1}	Phase
1	161	*FeSi (Fe-Fe)*	**7**	291	*Fe_3Si (Si-Fe)*
2	178	*β-$FeSi_2$ (Fe-Fe)*	**8**	340	*β-$FeSi_2$ (Si-Fe)*
3	194	*β-$FeSi_2$ (Fe-Fe)*	**9**	386	*β-$FeSi_2$ (Si-Si)*
4	221	*β-$FeSi_2$ (Fe-Fe)*	**10**	441	*β-$FeSi_2$ (Si-Fe)*
5	248	*β-$FeSi_2$ (Fe-Fe)*	**11**	525	*Si (Si-Si)*
6	268	*Fe_3Si (Si-Fe)*	**12**	615	*FeSi (Fe-Fe)*

It can be seen from the presented Raman spectra and following Table that the β-$FeSi_2$ phase is present in all of the films. In addition to this phase, almost all structures contain an amorphous silicon peak. Some structures exhibit the presence of side magnetic phases FeSi and Fe_3Si. The magnetic properties of these films were investigated by recording the magnetic field dependence of the Hall resistance.

5. Conclusion

The paper shows a method for the formation of the β-$FeSi_2$ phase by pulsed laser deposition in vacuum. When using the silicon and gallium arsenide substrates side ferromagnetic phases of iron silicide are formed, in addition to the β-$FeSi_2$ phase. The latter is associated with a change in the conditions for film formation due to the diffusion of iron atoms into the substrate during the growth of the structure. In dielectric plates used as substrates, the diffusion of iron is significantly slowed down, which makes it possible to obtain the β-$FeSi_2$ phase without the formation of additional phases of iron silicide.

Thus, the possibilities of the method of pulsed laser deposition in vacuum as a technology for the formation of the β-FeSi2 phase on both silicon and sapphire substrates were shown.

Acknowledgments

This work was supported by the RFBR grants (20-38-70063, 20-32-90032).

References

[1] Zhengxin L, Shinan W, Naotaka O, Yasuhito S, Masato O, Yasuhiro F, Teruhisa O, Yasuhiko N, Hisao T and Yunosuke M 2007 *J. Cryst. Growth* 307 82

[2] Wan Q, Wang T H and Lin C L 2003 *Appl. Phys. Lett.* 82 **19** 3224

[3] Han Y P, Wang X J, Hou Q R, Wang Q R and Wang J X 2012 *Mod. Phys. Lett. B* 26 **15** 1250097

The dispersion of flexural modes in the borophene lattice.

I.M. Kuimov[1], I.O. Raikov[1], D.A. Parshin[1]

[1]Alferov University, 199034 Saint-Petersburg, Russia

E-mail: 001meridian@mail.ru

Abstract. Vibration dynamics of crystalline borophene is considered in the framework of a simple scalar model. The vibrations perpendicular to the plane (flexural modes) are studied. The dispersion law of these vibrations is giving by the function ω on q, where q is the wave vector and ω is the frequency. In comparison with experiment it have a linear dispersion law. In contrast, flexural modes, as in graphene, have a quadratic dispersion law $\omega \sim q^2$.We're discuss the possible reason for this phenomena.

1. Introduction

One of the most interesting topics in the modern condensed matter physics is studying of crystalline graphene. As it is well known the crystalline graphene, due to the unusual geometry of the band structure, has exceptional mechanical [1,2], physical [3,4] and optical properties [5], which find applications [6] in various fields. Note here its record high thermal conductivity. For graphene, it was found, that it has unique properties of electrical conductivity and thermal conductivity, therefore, it is of great importance in microelectronics. The discovery of graphene sparked intense research activity. And later a whole class of new materials with no less unique properties appeared. One of these materials is borophene.

2. Borophene

The graphene lattice has a hexagonal honeycomb structure with 2 atoms in a unit cell. Unlike graphene, borophene has a triangular lattice with a single atom in the unit cell, but many elements of graphene symmetry are present in borophene. The study of the difference between the flexural modes in graphene and borophene is particularly relevant.

This is due to the fact that in this problem an important role is played by the second coordination sphere of interaction between the next nearest neighbors. In this paper, it was assumed that the elastic constants of the springs k_2 can be negative between not the nearest neighbors, but the neighbors through one. Therefore, it is necessary to check whether such a requirement is not met for borophene and whether borophene has a quadratic law of dispersion of flexural modes like graphene.

In the framework of a simple scalar model, we solved the problem of the vibrational spectrum of borophene.

Since borophene, unlike graphene, has only one atom in the unit cell, it has 3 acoustic modes like graphene, but no optical modes. Thus we have in borophene LA, TA and ZA modes.

It is shown that, under certain conditions, the phonon dispersion law for flexural modes turns out to be quadratic ($\omega \sim q^2$). In graphene, this is the condition that the speed of sound vanishes, and thus the condition for the occurrence of quadratic dispersion looks like this:

$$k_1 + 6k_2 + 4k_3 = 0 \quad (1)$$

For borofen, this condition is written a little differently:

$$k_1 + 3k_2 + 4k_3 = 0 \quad (2)$$

This is due to a different crystal lattice structure.

3. The dispersion law of the flexural mods

According to the second law of Newton the equation of motion of the flexural mods looks as the following [7,8]

$$m\frac{d^2U_{n,m}}{dt^2} = E(U_{n+1,m} + U_{n-1,m} + U_{n,m+1} + U_{n,m-1} + U_{n-1,m+1} + U_{n+1,m-1} - 6U_{n,m}) \quad (3)$$

where m is a mass, E is the Young's modulus and $U_{n,m}$ is the offset from the equilibrium position.

$$\omega^2 = 4\Omega_1^2\left(\sin^2\left(\frac{\vec{q}\cdot\vec{e}_1}{2}\right) + \sin^2\left(\frac{\vec{q}\cdot\vec{e}_2}{2}\right) + \sin^2\left(\frac{\vec{q}\cdot\vec{e}_3}{2}\right)\right) \quad (4)$$

where $\Omega_1^2 = \frac{\vec{q}}{m}$.

From the equation (4) it follows that ω depends on the direction of the wave vector $\vec{q}$. We will analyze this equation in the full version of the conference proceedings.

Acknowledgments

We are grateful very much to Andrey Ipatov and Yury Galperin for discussions of our results

References

[1] Wirtz L and Rubio A 2004 *Sol. State Comm*. **131** 141.
[2] Hobson J P and Nierenberg W A 1953 *Phys Rev* **89** 662.
[3] Maradudin A A, Montroll E W, Weiss G H and Ipatova I P 1971 *Theory of Lattice Dynamics in the Harmonic Approximation* (New York: Academic Press).
[4] Weige A, Wellein G, Alvermann A and Fehske H 2006 *Rev Mod Phys* **78** 275.
[5] Beltukov Y M, Kozub V I and Parshin D A 2013 *Phys. Rev*. B **87** 134203
[6] Beltukov Y M and Parshin D A 2016 *JETP Letters* **104** 552
[7] Falkovsky L A 2012 *JETP* **142** 560.
[8] I. O. Raikov *et al* 2020 *J. Phys.: Conf. Ser.* **1695** 012179

Electrically conductive CNT networks formed by laser

A V Kuksin[1], U E Kurilova[1] and A Yu Gerasimenko[1,2]

[1] Institute of biomedical systems, National Research University of Electronic Technology, Zelenograd, Moscow, Russia
[2] Institute for Bionic Technologies and Engineering, I.M. Sechenov First Moscow State Medical University, Moscow, Russia

nix007@mail.ru

Abstract. Materials containing conductive CNT networks were investigated in this work. Binding of CNTs to each other was carried out using laser radiation in scanning mode. As a result of experimental studies, radiation power density at which the effect of SWCNT binding occured was found – 0.061 J/cm^2. Mechanism by which formation of porous materials with SWCNTs in composition takes place has been established. Materials from CNTs and biopolymers with controllable pore sizes that make up more than 60% of nanocomposite volume have been made.

1. Introduction

Nowadays laser radiation is widely used for modification of nanomaterials made from metals, dielectrics, and semiconductors. It is known that laser radiation in pulsed and continuous modes can bind carbon nanoparticles (carbon nanotubes, graphene), with each other. This effect is achieved due to two main mechanisms: sublimation of the most defective nanotubes or graphene sheets under the influence of laser radiation and subsequent condensation of sublimation products at nanotubes and graphene junctions; and due to the formation of covalent bonds in defect regions of nanoparticles during laser heating. Defective areas of nanoparticles have the least thermal conductivity and they are the most chemically active.This leads to appearance of chemical bonds in defective areas. It is known that carbon nanoparticles have semiconducting and electrically conductive properties. When nanotubes and graphene are bonded to each other, electrically conductive nodes (percolation nodes) appear. It is necessary to create a complex of percolation nodes in a given area or in a given volume for fabrication of electrically conductive compounds for nanoelectronics or functional 3D materials in bioelectronics.

In this work, fabrication of such materials was carried out by depositing disordered system of single-walled carbon nanotubes (SWCNT) on a substrate. Forming of SWCNT network inside its structure helps to achieve high strength and electrical conductivity of material. This is of great relevance in the field of creating bioelectronic devices, for example, when creating electrically conductive implants. In this regard, we have developed a technology for creating electrically conductive biopolymer nanocomposites consisting of CNT network of in matrix of biopolymers: albumin, collagen and chitosan.

2. Materials and methods

First stage in preparation of samples was creation of homogeneous dispersion of SWCNT in solvent (dimethylformamide - 90% and methylethylkitone - 10%). The resulting dispersion was applied using a nitrogen sputtering system onto a polished silicon wafer for nano- and microelectronics located on a heating stage for solvent evaporation. The application was carried out in layers. After that, disordered system of SWCNT, consisting of 500 layers up to 2 nm thick each was treated with laser action in a scanning mode. Sample was uniformly coated with laser impulses with the same power density. Laser scanning was carried out using computer program along given trajectory.

Nanocomposites with biopolymers were created by the action of laser radiation on homogeneous dispersions of chitosan, collagen, and albumin with SWCNTs. Dispersions were deposited in layers on silicon substrate using the similar method, but they were irradiated with pulsed laser radiation immediately after each deposition.

All the obtained samples were examined in detail using a scanning electron microscope (SEM).

3. Results and discussion

An ordered network of connected SWCNT was shown with scanning electron microscopy. As a result of experimental studies, radiation power density at which SWCNTs bind to each other was established. This effect was achieved with power density 0.061 J/cm2. SWCNT network had high hardness and electrical conductivity. It is known from nonlinear optical studies of materials with carbon nanotubes that nonlinear absorption and nonlinear scattering of radiation occur in liquid dispersed medium exposed to pulsed laser radiation (with high pulse energy). In this case, the energy of laser pulse is absorbed by carbon nanotube and converted into heat. Further, gas bubbles appear around the carbon nanotubes because of heating. The resulting bubbles scatter the rest of the pulse and subsequent laser pulses. Nonlinear processes in dispersion with carbon nanotubes are triggered if laser pulse has the sufficient threshold energy density. At the same time, threshold energy density was established, at which formation of nanocomposites with a given structure (porosity) took place. By determining the threshold radiation energy density, it is possible to control pore size in solid composite. The energy density at which the porosity of biopolymer composites is more than 60% was determined in this work. Biopolymer composites of albumin, collagen, and chitosan with SWCNT had clearly visible porosity, the sizes of pores were 1-5 μm and 100-200 μm at the threshold energy densities of 0.057, 0.032, and 0.083 J/cm2, respectively. Large pores should promote cell adhesion and proliferation. Small pores are necessary for vascularization and innervation processes. Created nanocomposites can be used as electrically conductive interfaces for restoration of nerve and muscle tissues of the body.

Acknowledgments

This work was supported by the Ministry of Science and Higher Education of the Russian Federation No. 075-03-2020-216 from 27.12.2019.

Fabrication technique of 3D all solid-state thin film lithium-ion batteries

S V Kurbatov[1], A S Rudy[1], O V Morozov[2], A S Mironenko[1] and V V Naumov[1]

[1]Yaroslavl Demidov State University, Yaroslavl, Russia
[2]Valiev Institute of Physics and Technology of Russian Academy of Sciences, Yaroslavl Branch, Russia

Author's e-mail for corresponding: kurbatov-93@bk.ru

Abstract. The processes of manufacturing 3D solid-state lithium-ion batteries (3D SSLIBs) with $LiCoO_2$/LiPON/Si-O-AL electrochemical system is described. A microstructured substrate for 3D SSLIBs which constitutes truncated microcones array on silicon surface, was fabricated using a modified Bosch-process. Then, a battery stack was deposited on the microstructured substrate by RF magnetron sputtering. The galvanostatic cycling tests of a 3D SSLIB show a discharge specific capacity about 12.5 μAh/cm^2 at a current density of 35 μA/cm^2, indicating that is promising the described technology.

1. Introduce

The main disadvantage of all-solid-state lithium-ion batteries is their low specific capacity (<200 mAh/g) [1]. One of the promising approaches to increasing the specific capacity is the use of 3D architecture [2-3]. The third dimension (height) uses in this approach to increase the amount of the active material per surface unit without increasing the electrode film thickness. In this case, the capacity is scaled by increasing the surface area of the 3D substrate. However, only a few working samples of 3D SSLIBs were demonstrated due to the complexity fabrication process [4-7]. The purpose of our study is developing and optimization of the 3D SSLIBs fabrication process.

2. Methods and discussion

The microstructured substrate for 3D SSLIBs, which constitutes truncated microcones array on silicon surface, was fabricated by a modified Bosch-process using the resist with a spherical profile as mask [8]. In this method, the third stage of etching the photoresist mask in Ar/O_2 plasma was added to the established two-stages Bosch-process. The duration of the additional stage was set in such a way as to provide the same shift of the mask edge Δa in each etching cycle (see Figure 1). In this case, θ (in degrees) is calculated from a simple equation:

$$\theta = \frac{180}{\pi} arctg \frac{\Delta H}{\Delta a}$$

where ΔH is the depth of silicon etching per cycle.

The preparation of the mask was carried out in two stages: at the first stage, an array of circles with 10 μm diameter on a silicon substrate was patterned by photolithography using a Microposit S1813 photoresist; in the second stage, the wafer was hard baked in a drying furnace during 20 minutes at the

temperature of 145 °C. The mask profile becomes the spherical shape in these conditions of photoresist reflow [9].

Plasmalab System 100 (Oxford Instruments) with inductively coupled plasma source ICP 380 was applied for silicon etching using the modified Bosch-process and the prepared mask. After plasma-chemical etching of the silicon substrate it was oxidized at a temperature of 1080°C in a dry oxygen for 0.5 hours and in moist oxygen for 4 hours, until a 0.9 μm thick SiO_2 film was formed. This SiO_2 layer was used as an electrical insulator and ion blocking layer between the battery stack and the substrate.

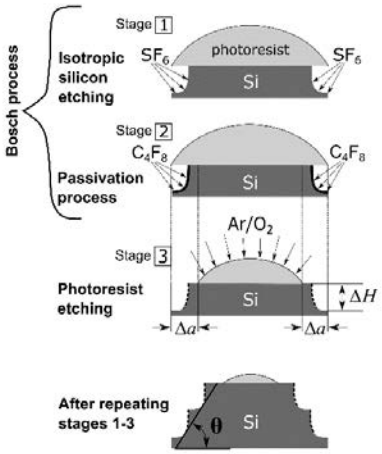

Figure.1. Scheme of silicon etching using a modified Bosch-process.

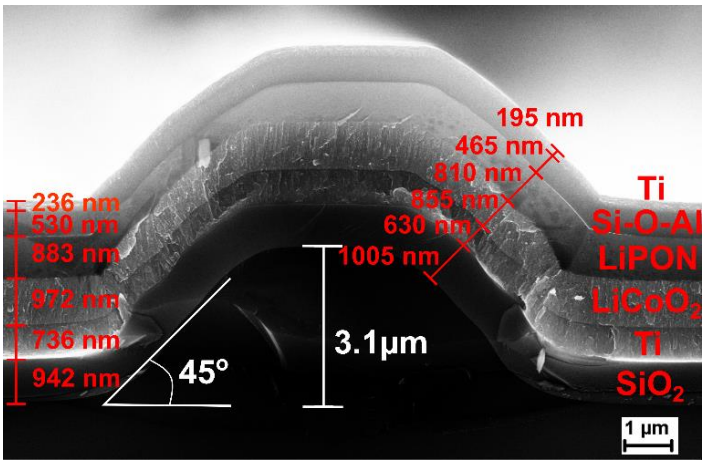

Figure.2. SEM cross-section image of the 3D SSLIB.

The functional layers were deposited on microstructured substrate using RF magnetron sputtering on a SCR 651 Tetra (Alcatel) system. The deposition scheme was as follows: Ti (lower current collector), $LiCoO_2$ (cathode), LiPON (solid electrolyte), Si-O-Al (anode) and Ti (upper current collector). Figure 2 shows a SEM cross-section image of the 3D SSLIB. The shape truncated microcones allows to deposit of continuous low-defect layers. However, the thicknesses of the films on the sidewalls of the microcones and in the valleys differ on average of 20%, which lead to nonuniform internal current density distribution [5].

The electrochemical testing of batteries was carried out by the method of galvanostatic cycling at a multichannel potentiostat-galvanostat P-20x8 (Electrochemical Instruments) with a subsequent increase in the discharge current from 5 μA in 1-5 cycles (potential window 0-2.5 V) to 70 μA in 33-35 cycles (potential window 2-4 V). The maximum specific capacity 12.5 μAh/cm^2 was reached at a discharge current of 35 μA (cycles 21 to 25), a further increase in the discharge current led to battery failure due to the Si-O-Al film lift-off. It was caused by volumetric changes of the film during the lithium ions intercalation/deintercalation process.

3. Conclusions

This work presents a technology for the manufacture of 3D SSLIBs using established technologies of microelectronics such as the plasma-chemical etching for fabrication of 3D microstructured substrate and RF magnetron sputtering for deposition of functional layers. We have fabricated a workable battery that demonstrated a specific capacity of up to 12.5 μAh/cm^2 at a discharge current density of 35 μA/cm^2. However, there are still unresolved problems associated with inequality deposition of thin films on microstructured substrate and behaviou of the anode/solid electrolyte interface during cycling. These challenges are the purposes of our further studies.

Acknowledgments

This work was carried out with financial support from the Ministry of Education and Science of the Russian Federation within the framework of the state assignment of P.G. Demidov Yaroslavl State University No. 0856-2020-0006.

References

[1] Sun C, Liu J, Gong Y, Wilkinson D P and Zhang J 2017 *Nano Energy* **33** 363–86.
[2] Long J W, Dunn B, Rolison D R, and White H. S 2004 *Chem. Rev.* **104** 4463-92
[3] Yue C, Li J and Lin L 2017 *Front. Mech. Eng.***12** 459–76
[4] Yim H, Kong W Y, Yoon S-J, Kim Y C and Choi J-W 2013 *J. Nanosci. Nanotechnol*. **13** 3459–63
[5] Talin A A, Ruzmetov D, Kolmakov A, McKelvey K, Ware N, Gabaly F E, Dunn B and White H S 2016 *ACS Appl. Mater. Interfaces* **8** 32385−91
[6] Notten P, Roozeboom F, Niessen R and Baggetto L 2007 *Adv. Mater.* **19** 4564–67
[7] Pearse A, Schmitt T, Sahadeo E, Stewart D M, Kozen A, Gerasopoulos K, Talin A A, Lee S B, Rubloff G W and Gregorczyk K E 2018 *ACS Nano* **12** 4286–94
[8] [Will be published] Rudy A C, Morozov O V, Kurbatov S V 2021 *Surf. Invest.: X-Ray, Synchrotron Neutron Tech.*
[9] O'Neilla F T, Sheridana J T 2002 *Optic* **113** 1-14

Near-surface layer dislocation density of lithium niobite single crystal wafers

Roman S. Ponomarev, Alexey V. Sosunov

Perm State University, 614990 Perm, Bukireva St. 15, Russia

rsponomarev@gmail.com

Abstract. Using chemical etching it was shown that the density of dislocation in lithium niobate (LN) single crystal wafers is higher near the surface in depth about 20 um than in the depth of crystal. It caused to change of diffusion coefficient during the waveguide formation with proton exchange (PE) method and can increase DC-drift of intensity optical modulators based on PE-waveguides.

1. Samples preparation and results

Electro-optical intensity and phase modulators based on lithium niobate single crystal are used in telecommunication systems with high data transmission rate, fiber-optic gyroscopes and optical vector analyzers [1]. Also, these devices have one big disadvantage – drift of waveguide refraction index during time and DC-voltage on electrodes called *DC-drift* [2].

We investigate the microstructure of break-surface of X-cut LN single crystal using chemical etching and electron microscopy of etch holes. We found that dislocation density is bigger near surface of crystal and have nonlinear change moving in depth of crystal. High-density layer thickness is about 20 um and change along the sample side. Also, this parameter is changing for samples manufactured by different vendors in spite of identical wafer datasheets.

Usually dislocation density is not controlled for LN wafers and wafer datasheet have no data about it. But if LN wafers are used for integrated optical device manufacturing only near-surface layer is working for waveguide formation. It seems that wafer datasheet not provide full data about crystal structure for PE-process in manufacturing of LN-devices.

Acknowledgments: The reported study was funded by RFBR and Perm Territory, project number 20-42-596001

References

[1] Morozov, O.; Nureev, I.; Sakhabutdinov, A.; Kuznetsov, A.; Morozov, G.; Il'in, G.; Papazyan, S.; Ivanov, A.; Ponomarev, R. Ultrahigh-Resolution Optical Vector Analyzers. Photonics 2020, 7, 14.

[2] Sosunov, A.V., Ponomarev, R.S., Yur'ev, V.A. et al. Effect of the structure and mechanical properties of the near-surface layer of lithium niobate single crystals on the manufacture of integrated optic circuits. Optoelectron.Instrument.Proc. 53, 82–87 (2017)

Study of nonlinear optical phenomena in silicon nanowires

Mastalieva V.A.[1], Neplokh V.[1,3], Morozov I.A.[1], Nikolaeva A.A[2], Gudovskikh A.S.[1], Mukhin I.S[1,2], Makarov S.V.[2]

[1] Saint Petersburg National Research Academic University, 8/3 Khlopina, St. Petersburg 194021, Russia
[2] ITMO University, 49 Kronverksky pr., St. Petersburg 197101, Russia
[3] Peter the Great St.Petersburg Polytechnic University, 29 Politekhnicheskaya, St. Petersburg 195251, Russia

E-mail: strindberg76@mail.ru

Abstract. This work studies generation of second and third harmonics in arrays of vertically oriented silicon nanowires (SiNWs) encapsulated into a silicone membrane and separated from the growth substrate. The structures were produced by plasma-chemical etching of silicon substrate resulting in a formation of homogeneous arrays of SiNWs. Such SiNW-based membranes demonstrated efficient infrared-to-visible light conversion by generation of second and third harmonic signals visible by a naked eye. This study contributes to the development of technology of optical devices based on silicon and presents a new route for visualization of infrared radiation.

1. Introduction

Converters of infrared (IR) radiation to the visible range are in demand for various optoelectronic devices [1, 2], visualizers of IR radiation, and other nonlinear optical applications. Commercial IR visualizers are based on ceramics which are very sensitive and do not require activation by light [3,4]. However, ceramic visualizers have limited optical transparency and mechanical flexibility and emit light at a fixed wavelength, making it impossible to distinguish between different wavelengths of incident IR radiation. A new alternative approach for visualization of IR radiation based on the generation of the second harmonic (SHG) in arrays of GaP nanowires (NWs) transferred into transparent silicone membrane was presented in our article [2].

The presented GaP NWs-based silicone membranes double the frequency of incident radiation allowing visualization of IR radiation in the range of 800-1400 nm [5]. However, the fabrication of such membranes requires expensive molecular beam epitaxy. In this work, we propose an approach similar to [2] based on SiNWs. Bulk silicon has an efficient third harmonic generation (THG), while only the silicon surface has SHG due to a crystal symmetry violation. Thus, SiNW arrays having large surface area and encapsulated into optically transparent silicone represent a promising object for studying nonlinear optical phenomena. Due to the developed surface of NWs, such membranes allow the study of SHG, while SiNW volume

provides a significant THG signal. SiNW membranes can be used for integrated with silicon electronics optical devices, including development of optical information transmission technologies [6].

2. Study of SHG and THG signal

2.1. Samples fabrication

The SHG and THG has been studied in arrays of vertically oriented SiNWs encapsulated into a silicone membrane and peeled from the growth substrate. NWs were produced by plasma-chemical etching of bulk silicon substrates resulting in arrays of vertical-oriented nanostructures. Dense monolayers of SiO_2 spheres served as masks for microsphere lithography. The length of obtained NWs was about 6 μm, while diameter was about 1.5 μm.

Further, the NW arrays were encapsulated into a polymer matrix and separated from the growth substrate. This technology enables not only reuse of growth substrates, but also combination of various material systems in order to create ultra-thin (up to several microns thickness) flexible transparent functional structures, and fabrication of large area (up to 50 sq. cm.) samples.

2.2. Measurements of SHG and THG

The SHG and THG signal was measured using a setup of IR femtosecond laser and spectrometer operating in the visible spectral range. The laser power before the objective was 30 mW, and 3 mW after the objective, the fluence was $12*10^{-3}$ mJ / cm^2. Under these excitation conditions the samples generated a THG signal visible by a naked eye in the range of 400-600 nm (1200-1800 nm of incident IR radiation, respectively). The measured spectra also registered a strong SHG response of two orders of magnitude weaker in comparison to the THG, this may be associated with less efficient processes on the NW surface and a relatively large ratio of the NW volume to its surface area.

3. Summary

In conclusion, we demonstrated efficient IR visualizers based on SiNW/silicone membranes having THG signal visible to a naked eye. The studied structures also demonstrated a strong SHG signal, which can be further enhanced by increasing the contribution of the NW surface (via NW diameter reducing) and surface treatment. This study contributes to the further development of the physics and technology of optical devices based on silicon

Acknowledgments

VN thanks the Russian Foundation for Basic Research (RFBR project № 19-32-60040) for PDMS/NW membrane fabrication.

References

[1] Morozov, I.A. Physico-technological foundations of microstructuring processes for the creation of vertically oriented photoconversion structures based on silicon [Text]: dis. Cand. tech. Sciences:05.27.06 / Morozov Ivan Alexandrovich. -St. Petersburg, 2020.-161 p.

[2] Cazzanelli, M., Bianco, F., Borga, E., Pucker, G., Ghulinyan, M., Degoli, E., ... & Pavesi, L. (2012). Second-harmonic generation in silicon waveguides strained by silicon nitride. Nature materials, *11*(2), 148-154.

[3] weblink:https://www.thorlabs.com/newgrouppage9.cfm?objectgroup_id=296,last accessed 16/02/2021

[4] weblink: https://www.alphalas.com/products/laser-diagnostic-tools/infrared-to-visible-converters-ir-laser-beam-visualizers-ir-detectors-ir-vis series.html?gclid=Cj0KCQiAgomBBhDXARIsAFNyUqPq76KpwEcZf99j8kRnwNFnr8VHRF3c-RL3YMIy_m36inblJXCKt0EaAsVpEALw_wcB, last accessed 16/02/2021

[5] Fedorov, V. V., Bolshakov, A., Sergaeva, O., Neplokh, V., Markina, D., Bruyere, S., ... & Mukhin, I. S. (2020). Gallium phosphide nanowires in a free-standing, flexible, and semitransparent membrane for large-scale infrared-to-visible light conversion. ACS nano, 14(8), 10624-10632

[6] Castellan, C., Trenti, A., Vecchi, C., Marchesini, A., Mancinelli, M., Ghulinyan, M., ... & Pavesi, L. (2019). On the origin of second harmonic generation in silicon waveguides with silicon nitride cladding. Scientific reports, 9(1), 1-12.

Nanostructured electrodes for supercapacitors

I O Yavtushenko[1], M Yu Makhmud-Akhunov[1], A A Adamovich[1]
[1]Ulyanovsk State University, Ulyanovsk 432017, Russia

Abstract. The paper presents the results of studies on the formation of planar capacitive systems based on nanoporous anodic oxide films and a conducting polymer. Based on voltammetric data, the capacity of the systems under study was determined. The structure of the porous layers was evaluated by impedance spectroscopy and electron microscopy.

1. Introduction

The design and creation of elements and systems with increased capacity is a relevant and actively developed area of modern electronics. Improvement of the electrical characteristics of such objects is achieved both through the use of various materials of electrodes and electrolytes, and through the formation of developed surfaces. From this point of view, metals and semiconductors nanostructured due to anodic treatment are promising [1-3]. The advantage of this technique lies in the simplicity of controlling the parameters of the structures being formed.

In this paper, supercapacitors based on nanoporous oxides of titanium and aluminum will be considered.

2. Experimental

Metal sheets based on titanium and aluminum with two types of surface oxide layers were used as capacitor plates: solid (thermal oxidation) and porous (anodizing). Layers of nanoporous titanium oxide films were produced by electrochemical anodic treatment of titanium foil in aqueous 0.6 wt. % HF solution at 20 V for 50 min [4]. The porous alumina was formed using a standard two-stage anodic treatment at 4 wt. % aqueous solution of $H_2C_2O_4$ at U = 40 V. Each electrode was covered with a layer of the emeraldine form of polyaniline (PANI). A solution of polyvinyl alcohol with 3.4 M orthophosphoric acid served as an interlayer between the electrodes. The parameters of the system under study were estimated by the method of cyclic voltammetry on a pulse potentiostat-galvanostat P-45X in the range from –0.5 to 0.5 V at a potential sweep rate of 20 and 100 mV/s.

3. Results and discussion

A typical view of voltammograms (VAG) for the structures under study is shown in Figure. 1. The results of processing showed a capacitance value of $5.6.10^{-3}$ F for a structure based on titanium oxide (sweep rate 20 mV/s), which is three orders of magnitude higher than that for a capacitor with electrodes based on porous alumina.

A specific feature of the formation of porous titanium oxide films in aqueous solutions is the limitation in thickness, which, as a rule, does not exceed 500–600 nm [5]. Also, anodic titanium oxides, in comparison with oxide films on aluminum, in some cases can have dielectric permittivity values by an order of magnitude higher. All this determines the best capacitive properties of the titanium oxide-based system. However, the deviation of the VAG in both cases from an ideally rectangular shape may indicate the influence of the sequential capacitive component of the electrolyte resistance, in this case,

polyvinyl alcohol with orthophosphoric acid, as well as Faraday processes proceeding in parallel due to the small thickness of the barrier layer in the pore covered with a thin layer of PANI.

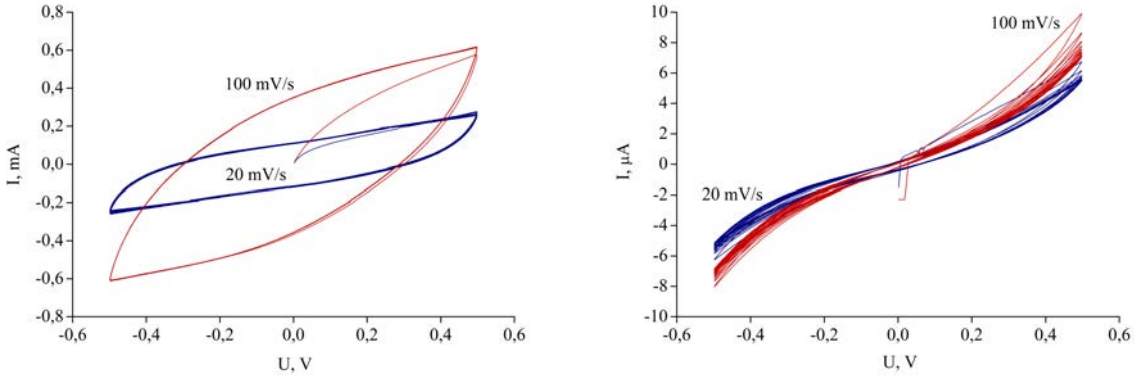

a b

Figure 1. Cyclic voltammograms of supercapacitors based on porous films and PANI: a – titanium oxide; b – aluminum oxide

The features of the structure of the functional layers of the formed multilayer capacitive systems were evaluated from the data of impedance spectroscopy. The dependences Im Z (Re Z) are typical for capacitors and have sections with a shape close to a semicircle, which, as noted above, characterizes a high value of the Faraday resistance. For the system with aluminum oxide, this parameter is three orders of magnitude higher in comparison with titanium oxide.

The use of electrodes with a developed surface (pore size ~ 80-100 nm) determines an almost linear increase in the low-frequency region of the impedance curve characterizing the surface roughness (element with a constant phase – CPE) [6], and this characteristic is observed only for systems based on titanium oxide with less resistance.

4. Conclusions

Thus, the paper considered the features of using nanostructured electrodes based on porous oxide films of titanium and aluminum to create capacitive systems with improved characteristics. The capacity of the system based on titanium oxide is three orders of magnitude higher in comparison with the structure of electrodes with aluminum oxide and amounted to $5.6.10^{-3}$ F. This character is due to the difference in the dielectric constant and the thickness of the formed porous films.

5. Acknowledgments

This work is supported by the Russian Science Foundation (project no. 19-71-10063).

References

[1] Rekha S, Subrata M, Shrestha K, Ariga K 2020 *Nanomaterials*. **10**. pp 3–27
[2] Sharma V, Singh I, Chandra A 2018 *Scientific Reports*. **8**. pp 1–12
[3] Cuihua A, Zhang Y, Guo H, Wang Y 2019 *Nanoscale Advances*. **1**. pp 4644–4658
[4] Peng Z, Ni J 2019 *Royal Society Open Science*. **6**. pp 1–15
[5] Macak J, Tsuchiya H, Ghicov A, Yasuda K, Hahn R, Bauer S, Schmuki P 2007 *Current Opinion in Solid State and Materials Science*. **11**. pp 3–8
[6] Sibatov R. T., Uchaikin V. V. 2019 *Appl. Eng. Life Soc. Sci*. **87**.

Study of annealing temperature effects on aluminum-induced crystallization of a-SiOx thin films

I E Merkulova[1], **N A Lunev**[1], **A O Zamchiy**[1], **E A Baranov**[1]
[1]Laboratory of rarefied gases, Kutateladze Institute of Thermophysics SB RAS, Novosibirsk 630090, Russia

Abstract. In present work, the kinetics of aluminium-induced crystallization (AIC) of amorphous silicon suboxide thin films with low stoichiometry (x = 0.23) at temperatures below the eutectic point was investigated. The samples with "a-$SiO_{0.23}$/SiO_2/Al" layer stack were annealed at temperatures 350-400 °C for 5 to 24 hours. Using optical micrographs of the film surface, cover fraction as a function of annealing time was obtained and reached a constant value of 54% for all annealing temperatures. Optical micrographs showed that the increase of annealing temperature is accompanied by growth of the nucleated Si grains density and decrease of the average lateral size of grains. It was suggested that a kinetics of growth is described with the model of diffusion-limited aggregation. The activation energy of AIC a-SiO_x, estimated by analysing an Arrhenius plot was 3.5 eV, what is higher than the activation energy of AIC of a-Si.

1. Introduction

Aluminum-induced crystallization (AIC) of amorphous silicon (a-Si) is a promising approach for obtaining thin films of polycrystalline silicon (poly-Si) on low-temperature substrates [1]. This method makes it possible to obtain poly-Si films at low temperatures (below the eutectic point of the “Al/Si” system - 577 °C) and short annealing times. The result of AIC of a-Si is a macroscopic layer exchange between Al and Si with the poly-Si film formation. The impurities in the a-Si film (for example, oxygen) affect the kinetics of the AIC process. Therefore, in present work, the kinetics of AIC of amorphous silicon suboxide (a-SiO_x) with low stoichiometry (x = 0.23) at temperatures below the eutectic point was studied. Previously, the authors have described the features of the AIC process for a-SiO_x thin films with high (x = 1.8) and low (x = 0.2) stoichiometry [2].

2. Experimental

The a-SiO_x thin films (x = 0.23) with 160 nm thickness were synthesized from a SiH_4-O_2 gas mixture by plasma-chemical deposition on quartz substrates. The films oxidation at the atmosphere led to the SiO_2 membrane layer formation. After that, 130 nm-thick poly-Al layers were sputtered on the structure. The as-deposited samples with "quartz/substrate/a-$SiO_{0.23}$/SiO_2/Al" layer stack were annealed in a vacuum furnace (10^{-5} Pa) at temperatures of 350-400 °C for 5 to 24 hours.

3. Results and discussion

Cover fraction (CF) as a function of annealing time was obtained for temperatures of 370, 385 and 400ºC using optical micrographs of the film surface. It is shown that the CF reaches a constant value of 54% for all annealing temperatures what implies the completion of the layer exchange process. This

value of CF was obtained for the ratio of a-$SiO_{0.23}$ and Al layers thicknesses equals to 1.23. As the temperature rises, time to complete the layer exchange process decreases significantly.

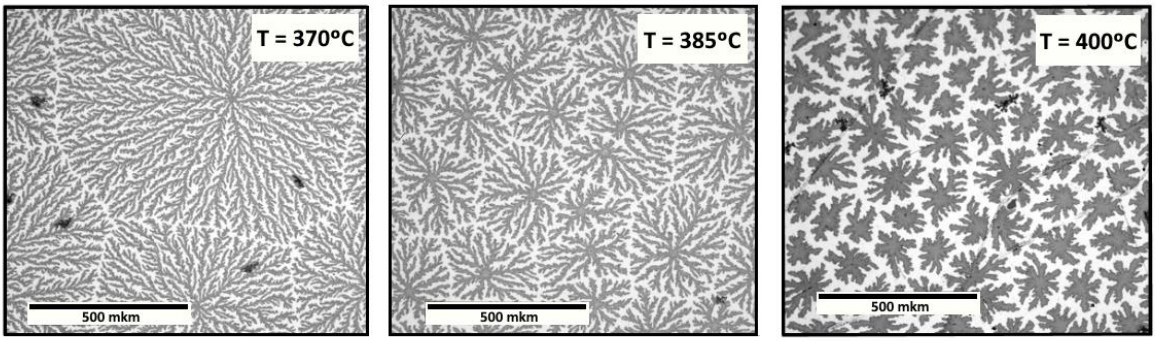

Figure 1. Optical micrographs of films surface morphology after annealing at 370, 385 and 400°C.

Figure 1 shows optical micrographs obtained for a CF = 54% at annealing temperatures of 370, 385 and 400°C. It is shown that with the annealing temperature increase, the density of nucleated Si grains also grows, which leads to a reduction of the average lateral size of crystalline structures. The surface morphology for low temperatures shows dendritic structures, which, probably, described with the diffusion-limited aggregation (DLA) mathematical model. The analysis of the Arrhenius plot [4] resulted the activation energy of AIC a-$SiO_{0.23}$ - 3.5 eV. This value is much higher than the activation energy of AIC a-Si – 1.3 eV [5].

References

[1] Nast O, Puzzer T, Koschier L M, Sproul A B and Wenham S R 1998 *Appl Phys Lett* **73(22)** 3214-3216
[2] Zamchiy A O, Baranov E A, Khmel S Y, Volodin V A, Vdovin V I and Gutakovskii A K 2018 *Appl Phys A* **124(9)** 1-4
[3] Lee D W, Bhopal M F and Lee S H *AIP Advances* **7(9)** 095207
[4] Meechan C J and Brinkman J A 1956 *Phys Rev* **103** 1193
[5] Nast O 2000 doctoral thesis, Marburg/Lahn, Germany 80

Laser-induced optical nonlinearity in a Li-rich glass

A Yu Moroz[1], E S Babich[2], V P Kaasik[3], A A Lipovskii[3], V G Melekhin[4], A V Redkov[5] D K Tagantsev[3]

[1]Department of Physics and Technology of Nanostructures, Alferov University, St. Petersburg 194021, Russia

[2]Institute of Physics, Nanotechnology and Telecommunications, Peter the Great St. Petersburg Polytechnic University, St. Petersburg 195251, Russia

[3]Sector of Optics of Heterogeneous Structures and Optical Materials, Alferov University, St. Petersburg 194021, Russia

[4]A. F. Ioffe Physical-Technical Institute, Polytechnicheskaja 26, 194021, Saint-Petersburg, Russia

[5]Laboratory of Phase Transitions, Institute of Problems of Mechanical Engineering, St. Petersburg 199178, Russia

Abstract. The selective crystallization of a photosensibilized lithium silicate glass after a light emitting diode (365 nm) and a nanosecond laser (355 nm) UV irradiation and subsequent heat treatment was studied. Using a focused beam of the laser allows successive drawing regions in which the formation of silver nanoparticles after 500 °C heat treatment of the glass co-doped with silver and cerium results takes place. It is shown that this treatment is a necessary step for the growth of sodium metasilicate crystals under the second thermal treatment of the glass at 600 °C, while these regions after preheating demonstrate second optical harmonic generation of falling 1064 nm nanosecond laser radiation.

1. Introduction

Foturan lithium-silicate glasses were designed for the formation of relief structures by means of hydrofluoric acid etching of UV-irradiated regions of these glasses after thermal processing [1]. These glasses are photosensitive due to their doping with Ag^+ and Ce^{3+} ions. Under UV irradiation the reaction $Ce^{3+} + h\nu + Ag^+ \rightarrow Ce^{4+} + Ag^0$ takes place, subsequent and thermal processing of the glass first results in silver atoms clustering and then in the growth of lithium metasilicate microcrystals (Li_2SiO_3), the silver clusters behaving as the crystallization nuclei. Being much less chemically durable than initial glass is, the crystallites can be dissolved in a diluted hydrofluoric acid. Selective etching of the UV-exposed regions allows applications of this glasses in micro-electro-mechanical-systems (MEMS), microfluidics, microoptics, etc. Here we present the studies of the crystallization of a synthesized Fituran-like glass and show that the local laser irradiation of the glass with allows "drawing" optically non-linear glass regions.

2. Experiments and results

In the experiments, we used synthesized glass which composition is presented in Table 1. 1 mm thick polished plates of the glass were irradiated either with light emitting diode (LED) at 365 nm wavelength or the 3rd harmonic of nanosecond laser at 355 nm wavelength. The irradiated samples were annealed at

the temperature of 500 ºC for 1 h and then at 600 ºC for 1 h. The rate of the heating was equal to 5 ºrc/min for both thermal processing's.

Table 1. Composition of the glass in weight % of oxides.

Component	SiO_2	Li_2O	Al_2O_3	K_2O	Na_2O	ZnO	Ag_2O	CeO_2	Sb_2O_3
Weight %	75.55	10.44	5.33	5.74	1.17	1.13	0.236	0.085	0.33

Initial and processed samples were characterized with optical absorption and microRaman spectroscopy, and the presence of the second harmonic of the radiation of a nanosecond laser radiating at 1064 nm wavelength was verified. Both LED and laser irradiation resulted in similar transformation of optical absorption spectra, which are presented in Figure 1.

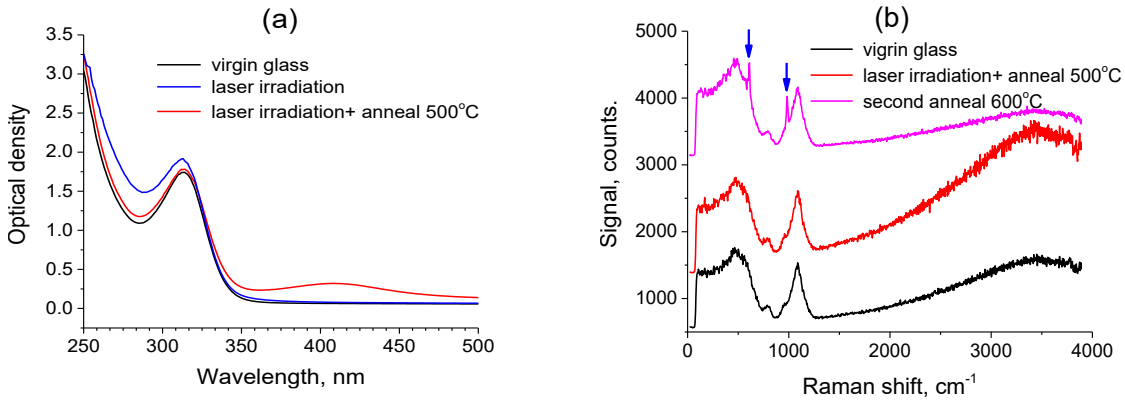

Figure 1(a)(b). Optical absorption (a) and Raman (b) spectra of the glass samples.

3. Discussion

The appearance of the left wing of optical absorption in the cerium peak at 280 nm after the irradiation indicates the formation of neutral silver atoms, and the surface plasmon resonance peak at 415 nm after the first anneal shows the formation of silver nanoparticles. The second anneal results in increased light scattering by grown crystallites. In the Raman spectrum of the UV-irradiated and annealed sample one can see the growth of the signal in the range 2700-3700 cm^{-1}, which can be attributed luminescence of numerous small silver clusters [2,3] formed, and a small peak at 962 cm^{-1}, possibly indicating the glass pre-crystallization. The second anneal results in the Raman lines corresponding to orthorhombic lithium metasilicate Li_2SiO_3 [4]. Its low symmetry permits the second optical harmonic generation (SHG), and the latter was observed in our experiments. We supposed that small Li_2SiO_3 prenuclei formed after the first anneal around silver clusters provided the SHG.

Acknowledgments

The study was supported by the Ministry of Science and Higher Education of Russian Federation, project FSRM-2020-001. E.B. thanks the Council for Grants of the President of the Russian Federation (project SP-1491.2021.4).

References

[1] Stookey S D 1953 *Ind. Eng. Chem.* 45 115–8

[2] Eichelbaum M, Rademann K, Hoell A, Tatchev D M, Weigel W, Stößer R and Pacchioni G 2008 *Nanotechnology* 19 135701

[3] Dubrovin V D, Ignatiev A I, Nikonorov N V., Sidorov A I, Shakhverdov T A and Agafonova D S 2014 *Opt. Mater. (Amst).* 36 753–9

[4] Brawer S A and White W B 1975 *J. Chem. Phys.* 63 2421–32

TiO_2-SnO_2 thin films prepared by new pyrolysis solid-phase method

M G Volkova[1], V Yu Storozhenko[1], V V Petrov[2], E M Bayan[1]

[1]Department of Chemistry, Southern Federal University, Rostov-on-Don, 344090, Russia,
[2]Research and Education Centre "Microsystem technics and multisensor monitoring systems", Southern Federal University, Taganrog, 347922, Russia

vstorozhenko@sfedu.ru

Abstract. Nanoscale TiO_2-SnO_2 films with the Ti:Sn ratio 1:99, 3:97 and 5:95 mol%, respectively, were obtained by solid-phase low-temperature pyrolysis method. It was shown that both with Ti^{4+} concentration and the calcination temperature increasing, the particle size also increases. The best crystallization was noted for material containing 1 mol% of Ti^{4+}.

1. Introduction

Nanomaterials based on tin dioxide, doped with different modifying agents, are common used for the production of optical coatings, gas-sensitive sensors, photocatalysts, etc. [1-2]. Composite materials based on mixed oxides exhibit better optical, electrophysical, and other properties than pure oxide materials. Thus, nanomaterials based on titanium dioxide doped with tin exhibit better properties than pure titanium dioxide [3]. Since the ionic radii of tin and titanium are close, it can be expected that titanium will be replaced by tin ions in the titanium dioxide crystal lattice. Obtaining promising results for titanium dioxide doped with tin ions allows us to assume a positive effect of titanium on the properties of tin dioxide-based materials.

The aim of this work was to synthesize thin tin dioxide films doped with titanium by solid-phase low-temperature pyrolysis method.

2. Experiment

To obtain thin film materials by solid-phase low-temperature pyrolysis method, $SnCl_4 \cdot 5H_2O$, $(C_4H_9O)_4Ti$, organic acid, and 1,4-dioxane as a solvent were used as precursors. The preparation of the intermediate product was carried out with the introduction of tin tetrachloride required amount (molar ratio Ti:Sn was 1:99, 3:97, 5:95 for materials 1, 2, 3, respectively) in the melt of organic acid and tetrabutoxytitane. The resulting product was dissolved in dioxane, and the obtained solution was applied to the pre-prepared substrates three times. Temperature treatment was carried out for two hours at a certain temperature in the muffle furnace, the heating rate was 10o/min. The phase composition of the obtained films was studied by X-ray diffraction (XRD) using an ARLX'TRA diffractometer, Thermo ARL (Switzerland) with CuKα X-rays. The morphology and thickness of the films were studied using a scanning electron microscope (SEM) on an EMXplus 10/12 Bruker device (Germany).

3. Results and discussion

The results of the XRD analysis showed that all synthesized materials are nanoscale and contain mainly cassiterite phases (Fig. 1). With an increasing of the modifying agents concentration the peaks intensity also increased. According to the calculations, for materials 1, 2, and 3 the crystallinity was 47, 45, and 43%, respectively. With increasing of the modifying agents concentration, an increase in the particle size calculated according to the Scherrer equation was also observed (19, 23 and 29 nm for materials 1, 2, 3, respectively). A similar regularity of the particle size increasing also was observed with the calcination temperature increasing.

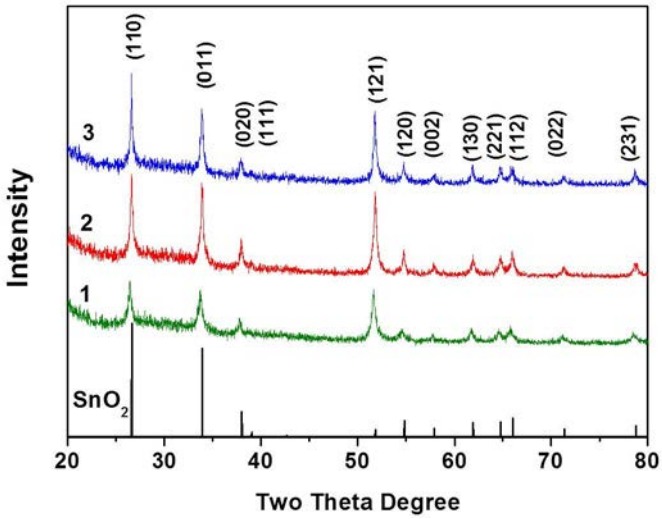

Figure 1. XRD patterns of SnO_2-TiO_2 materials calcined at 550 °C (explanations are presented in text)

According to SEM analysis, the obtained films are homogeneous, dense and have a thickness of about 45 nm for three-time application. The obtained data indicate a high-quality technology for the formation of composite thin films materials based on tin and titanium oxides of the controlled thickness.

4. Conclusion

Homogeneous and dense thin film nanomaterials TiO_2-SnO_2 were obtained by solid-phase low-temperature pyrolysis method. It was shown that the particle size increases with both increasing of the modifying agents concentration and the calcination temperature.

Acknowledgments

This work was financially supported by the RFBR, project 20-07-00653 A.

References

[1] V. V. Petrov, E. M. Bayan, S. A. Khubezhov, Y. N. Varzarev and M.G. Volkova, Investigation of Rapid Gas-Sensitive Properties Degradation of ZnO–SnO_2 Thin Films Grown on the Glass Substrate, *Chemosensors*, **8(2),** 40 (2020).

[2] Q. Liu, X. Wu, B. Wang, & Q Liu, Preparation and super-hydrophilic properties of TiO_2/SnO_2 composite thin films. *Materials Research Bulletin* **37(14),** 2255-2262 (2002).

[3] E.M. Bayan, T.G. Lupeiko, L.E. Pustovaya and M.G. Volkova. Synthesis and photocatalytic properties of Sn–TiO_2 nanomaterials. *Journal of Advanced Dielectrics,* **10 (1,2),** 2060018, (2020).

Investigation of the features of the porous morphology of anodic alumina films at the initial stage of anodization

K V Chernyakova[1], E N Muratova[2*], I A Vrublevsky[3] and N V Lushpa[3]

[1]State Scientific Institute Center for Physical Sciences and Technologies, Savanoriu Ave. 231, Vilnius, LT-02300, Lithuania
[2]Saint-Petersburg state electrotechnical university «LETI», 5 Prof. Popova Street, Saint Petersburg, 197376, Russia
[3]Belarusian State University of Informatics and Radioelectronics, 6 P.Brovki Street, Minsk, 220013, Belarus

[*]Corresponding author's e-mail: Sokolovaeknik@yandex.ru

Abstract. The work is devoted to the study of the porous structure formation of anodic alumina films at the initial stage of aluminium anodizing. SEM images of the surface morphology of the oxalic acid anodic films were analyzed. It was shown that at the initial stage, both major and minor pores are formed, the diameter ratio of which is about 1.16 and does not depend on the anodizing voltage. The results obtained indicate that the minor pores in the anodic films are located inside hexagonal cells composed of the major pores.

1. Introduction

One of the effective methods of forming a material with a controlled porous structure is the process of anodic oxidation of aluminum [1,2]. Films of porous anodic alumina (AOA) obtained as a result of this process are characterized by a regular porous structure with pore sizes proportional to the anodizing voltage. For the widespread use of AOA films as nanostructures in optics, sensors, and nanotechnologies [3], an important condition is the production of anodic films with high ordering and a given pore diameter. The key role in this is played by the initial stage of the formation of the porous structure of anodic films during anodizing of aluminum, which is poorly studied.

At present, the following mechanism has been adopted to explain the pore nucleation process. In the first stage of anodizing, the aluminum surface is covered with a layer of barrier aluminum oxide. In this case, in the depressions and defects of the oxide film, the electric field strength increases sharply. This leads to local dissolution of the oxide layer due to temperature rise and dissolution under the action of an electric field. Due to the competition of neighboring points for charge drain, some of the pores stop growing and, as a result, a uniform growth of the AOA film begins with a constant distance between the pore centers. At the same time, it can be assumed that the development of pores in the initial region of disordered growth has its own characteristics.

The aim of this work was to study the features of the formation of the porous morphology of AOA films at the initial stage of aluminum anodization.

2. Results

Figure 1 (a) shows an SEM image of the surface morphology of a porous alumina film on an aluminum substrate obtained in a potentiostatic mode at 40 V in oxalic acid. To determine the pore diameter, computer processing of the surface morphology of the anodic film was carried out using the ImageJ program. Then, according to the processing results, a graph of the pore diameter distribution was plotted (Fig. 1b). As can be clearly seen from the graph, the pore diameter distribution has two distinct peaks at 22.5 ± 0.2 and 26.4 ± 0.2 nm. The major pores have a larger diameter of 26.4 nm, and the minor pores in the AOA film have a diameter of 22.5 nm. This indicates that at the initial stage of aluminum anodization, the simultaneous development of both major pores and minor pores with similar diameters is observed. The results obtained indicate that the ratio of the diameters of such pores in the anodic films does not depend on the anodizing voltage and is equal to approximately 1.16. It should be noted that the number of minor pores is of the same order as the major pores. Therefore, it can be argued with high probability that the minor pores do not have a chaotic distribution in the anodic film, but are located inside hexagonal cells composed of the major pores. At the same time, at the initial stage of anodizing, the shape of such hexagonal cells is strongly distorted.

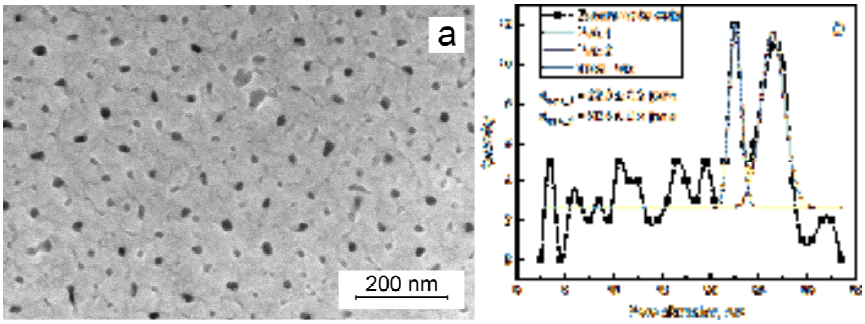

Figure 1. SEM image of the surface morphology (a) and pore diameter distribution (b) for a thin film of porous AOA formed on aluminum in oxalic acid at 40 V for 390 s

The results obtained indicating the presence of major pores and minor pores with similar diameters and the same density in the anodic film are in good agreement with the data presented in [4] for the pore size distribution determined by the method of capillary condensation of isopropanol vapors.

3. Conclusion

It was found that at the initial stage of aluminum anodization, the porous morphology of the anodic films is characterized by the simultaneous development of both major and minor pores of a certain diameter. The ratio of the sizes of the major and minor pores is about 1.16 and does not depend on the anodizing voltage in oxalic acid. The results obtained indicate that the minor pores do not have a chaotic distribution in the anodic film, but are located inside hexagonal cells composed of the major pores.

Acknowledgments

This work was supported by the grant of the President of the Russian Federation: MK-2268.2020.8: agreement No. 075-15-2020-520 dated 04/13/2020 and BRFFR project No. F19VTNG-001.

References

[1] Muratova E N, et.al. 2013 *Glass Phys. and Chem.* **39 (**3) p. 320-328

[2] Lushpa N V et.al. *New Materials: Preparation, Properties and Applications in the Aspect of Nanotechnology*, ed. by A G Syrkov and K L Levine (Nova Science), chapter 13 p. 125-132

[3] Moshnikov V A, Muratova E N and Spivak Y M 2017 *Altern. Ener.and Ecol.* **42** (34) 21817-21821.

[4] Casanova F, et.al. 2008 *Nanotech.* **19** (31) 315709

The influence of the surface density of oriented nickel networks on the conducting electrode's optical transparency

I R Nizameev[1,2], G R Nizameeva[3], M K Kadirov[1]

[1]Arbuzov Institute of Organic and Physical Chemistry, FRC Kazan Scientific Center, Russian Academy of Sciences, Kazan 420088, Russia
[2]Kazan National Research Technical University named after A.N. Tupolev - KAI, Kazan 420111, Russia
3Kazan National Research Technological University, Kazan 420015, Russia

E-mail: inizameyev@iopc.ru

Abstract. This study is part of the work on the creation of a transparent conductive electrode (TCE) based on oriented nanonetwork and submicron nickel fibres. It is devoted to finding the optimal values of electrical conductivity and optical transparency of the developed coating. In this work, we study the transmission spectra of oriented nickel networks on a glass substrate in the UV, visible and near-IR regions at different amounts of deposited metal.

1. Introduction

The use of conductive optically transparent coatings has expanded significantly thanks to the development of optoelectronic devices operating on transparent electrodes, such as touch displays and sensors, smart windows and solar panels. In this work, we present part of the work devoted to developing and improving an alternative to indium tin oxide (ITO). ITO is an electrically conductive coating on a glass surface. In [1], we developed a technique for creating a transparent electrode based on oriented nickel networks. The basis of the technique is precipitation from the liquid phase by chemical reduction of the nickel salt [2-3].

Within this study's framework, we investigate the effect of the amount of used nickel on the transmission spectra of the developed coating on a glass substrate in the UV, visible and near-IR regions. The surface density of the metal deposition (mass referred to the substrate's surface area) was taken as the value that determines the amount of nickel used.

2. Results and discussion

In this work, samples of the developed coating on glass with different amounts of metallic nickel were obtained: $0.6 \cdot 10^{-6}$ - $311 \cdot 10^{-6}$ g / cm^2. The smallest value in this range corresponds to a coating consisting only of nickel nanowires.

All obtained samples were examined on a spectrophotometer in the wavelength range of 290-1100 nm. The averaged transmission spectra for some deposition densities of nickel networks are shown in Figure 1. As expected, with an increase in the density of nickel deposition on the glass surface, a monotonic decrease in the transparency coefficient is observed over the entire optical range.

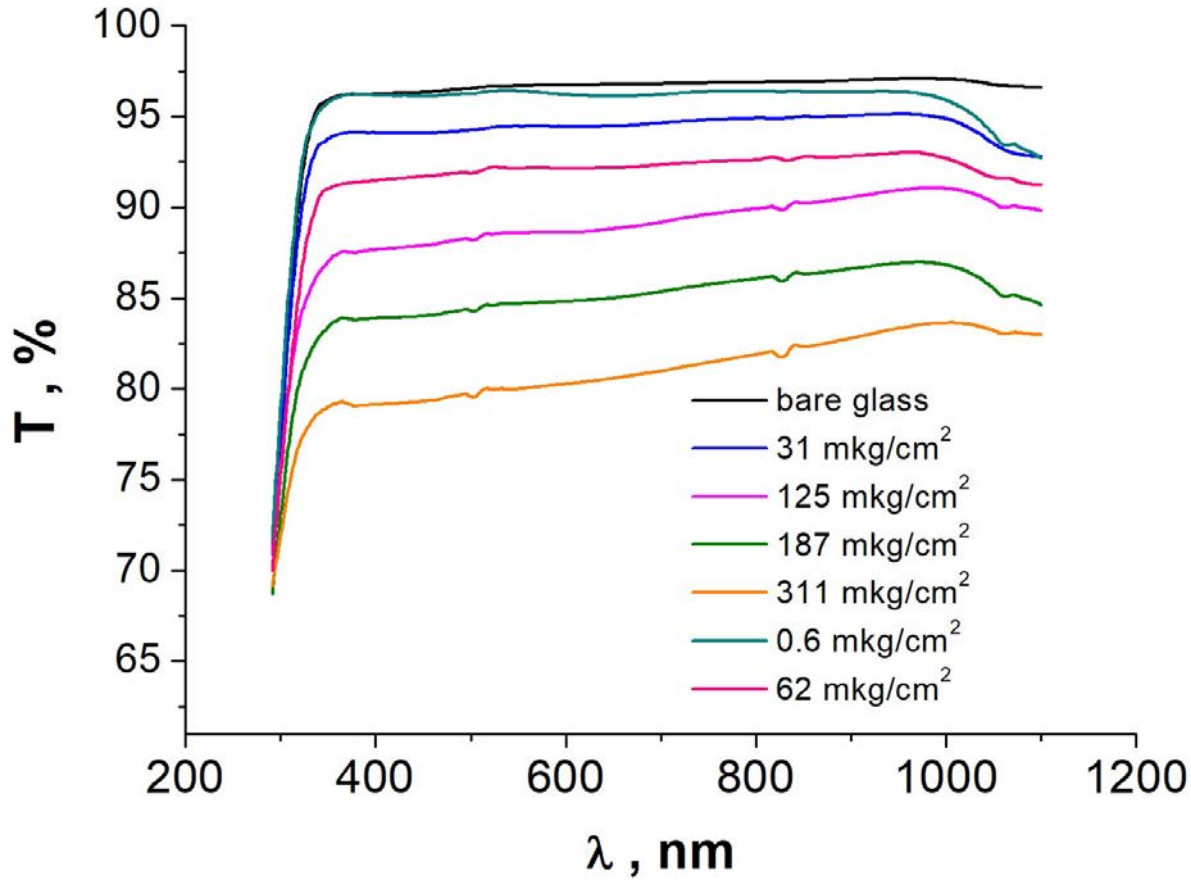

Figure 1. Transmission spectra of oriented nickel networks on a glass substrate in the UV, visible, and near-IR regions at different amounts of deposited metal

In the research, we discovered an interesting feature of the coating: in the range of 950 nm and above, there is a "bend" of the transmission spectrum downward. This bend (increased absorption of radiation in the near-IR region) is observed only in the presence of nickel nanonetwork and is not typical for a pure submicron network.

Acknowledgments
The reported study was funded by RFBR according to the research project № 19-03-00345.

References
[1] Nizameev I R et al. 2021 *ChemPhysChem* **22** 288.
[2] Nizameev I R, Nizameeva G R, Kadirov M K 2019 *ChemistrySelect* **4** 13564.
[3] Nizameev I R, Nizameeva G R, Kadirov M K 2019 *Journal of Physics: Conference Series* **1409** 012038.

Transmission spectra of transparent electrodes based on oriented platinum nanowires at various concentrations of the metal used

G R Nizameeva[1], I R Nizameev[1,2], E S Nefedev[1], M K Kadirov[2]

[1]Kazan National Research Technological University, Kazan 420015, Russia
[2]Arbuzov Institute of Organic and Physical Chemistry, FRC Kazan Scientific Center, Russian Academy of Sciences, Kazan 420088, Russia

E-mail: guliya.riv@gmail.com

Abstract. The paper investigates the optical transparency dependence of a coating based on an oriented network of platinum nanowires on the amount of metal used. Oriented platinum nanowires on a glass surface are produced by chemical deposition from an aqueous hexachloroplatinic acid solution. The topography of the deposited metal layer on glass is visualized using atomic force microscopy. Optical transparency was investigated with a spectrophotometer.

1. Introduction

Transparent electrodes have received significant attention due to their importance in electronics. They are an integral part of many optoelectronic devices such as touch displays and sensors, bright windows, solar panels, etc. Transparent oxides of some metals, films of carbon nanotubes [1], graphene [2], metal nanowires and nano-networks are used today as transparent electrodes. From a functional point of view, oriented metal nanowires are of greatest interest due to the combination of low surface resistance, high transparency [3], resistance to mechanical deformation and high operating temperatures.

In this work, a transparent electrode based on oriented platinum nanowires was obtained on a glass substrate's surface. Within this study's framework, we investigate the effect of the amount of platinum used on the transparency of the resulting coating on a glass substrate in the UV, visible and near-IR regions.

2. Results and discussion

In this work, samples of coating on glass with different amounts of platinum metal were synthesized. The change in the amount of platinum on the glass surface was carried out by adjusting hexachloroplatinic acid concentration ($H_2PtCl_6 \cdot 6H_2O$). The concentration of hydrochloric platinum acid in the aqueous solution varied in the range 0.01 - 5 mM.

All obtained samples were examined on a spectrophotometer in the wavelength range of 290-1100 nm. The averaged transmission spectra for some deposition densities of platinum nanowires are shown in Figure 1. As expected, with an increase in the density of platinum deposition on the glass surface, a monotonic decrease in the transparency coefficient is observed over the entire optical range.

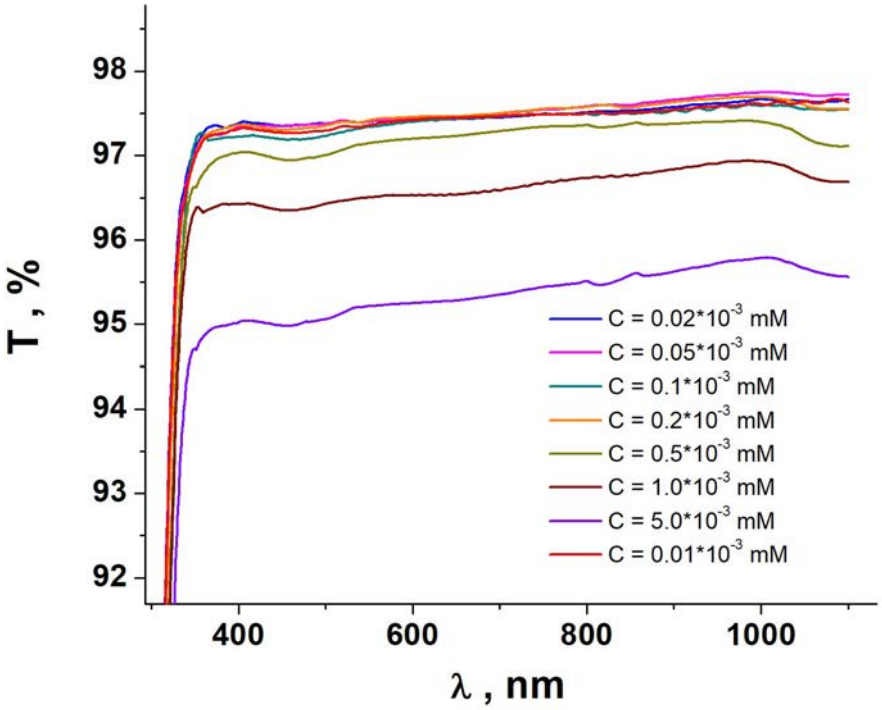

Figure 1. Transmission spectra of oriented platinum networks on a glass substrate in the UV, visible, and near-IR regions at different amounts of deposited metal

As a result of the studies carried out, the dependences of the coating's transparencyon the amount of platinum used were obtained. In almost the entire region of optical radiation, the transparency is approximately 98%. The absorption spectrum shows that the absorption coefficient increases sharply in the near UV region. This phenomenon is due to the properties of the glass substrate: it strongly absorbs UV radiation.

Acknowledgments
This work was supported by the President of Russian Federation grant for the governmental support of young Russian scientists [MK-2264.2019.3].

References
[1] Rathmell A R et al. 2012 *Nano letters* **12** 6.
[2] Kim K S et al. 2009 *Nature* **457** 7230.
[3] Guo C F, Ren Z 2015 *Materials Today* **18** 3.

Investigation of the effect of annealing on Si(001) substrate modified by Ga^+ focused ion beam

L S Nikitina[1], M M Eremenko[1], N A Shandyba[1], S V Balakirev[1], N E Chernenko[1], M S Solodovnik[1] and O A Ageev[1,2]

[1]Institute of Nanotechnologies, Electronics and Equipment Engineering, Southern Federal University, Taganrog 347922, Russia
[2]Research and Education Center "Nanotechnologies", Southern Federal University, Taganrog 347922, Russia

Email: larnikitina@sfedu.ru

Abstract. In this work, we studied the effect of annealing the silicon surface on the morphology of regions modified by a focused ion beam. It was found that an increase in the ion beam accelerating voltage during surface treatment significantly affects the morphology and the appearance of the implanted material on the surface or its absence/evaporation during annealing. It is shown that an increase in number of ion beam passes leads to the formation of holes on the surface of the modified areas, which is a sign that significant damage to the substrate material has occurred.

Recently, interest has increased in possible solutions for the integration of A3B5 structures on Si [1-3]. However, achieving the desired low-defect and, as a result, high-performance structures remains a difficult task. To date, a large number of techniques are used to reduce more defects during the monolithic integration of A3B5 on Si [2, 3]. However, studies of the initial stage are still crucially important for understanding the processes of formation of further grown layers, and will also make it possible to obtain regimes with the lowest density of defects, most of which are assumed to be localized in the lower layers.

In this work, we studied the effect of initial annealing on the modified areas of silicon. Silicon substrates were modified with a focused ion beam (Ga^+) at various accelerating voltages and beam passes. Accelerating voltages varied from 5kV to 30kV, and number of passes were 1, 5, 30 and 200. Annealing was carried out at temperature equal to 800°C.

A decrease in the accelerating voltage from 30kV to 5kV led to the disappearance of Ga droplets in almost all ranges of the considered modifications and temperatures, except for 200 beam passes at a temperature of 800°C. We believe that this is due to the intense evaporation of the material from the surface, which does not lie deeply, and this process is more advantageous when modifying the surface with beams with a low accelerating voltage and annealing at high temperatures. On the other hand, with an increase in the accelerating voltage on the surface of the modified areas, the implanted material emerges on the surface already from 5 beam passes. We explain its presence by the fact that at a high accelerating voltage, the depth of the material is high and the material gradually comes out to the surface and does not have time to completely desorb from the surface during annealing. However, it should be noted that during processing with an accelerating voltage of 30kV and 200 beam passes, holes were left

on the surface of the modified areas, without the presence of droplets of implanted Ga. The presence of such holes is apparently caused by a large deformation of the Si surface during processing by focused ion beams. In the future, it is planned to study these samples using Raman spectroscopy to confirm or disprove our theories.

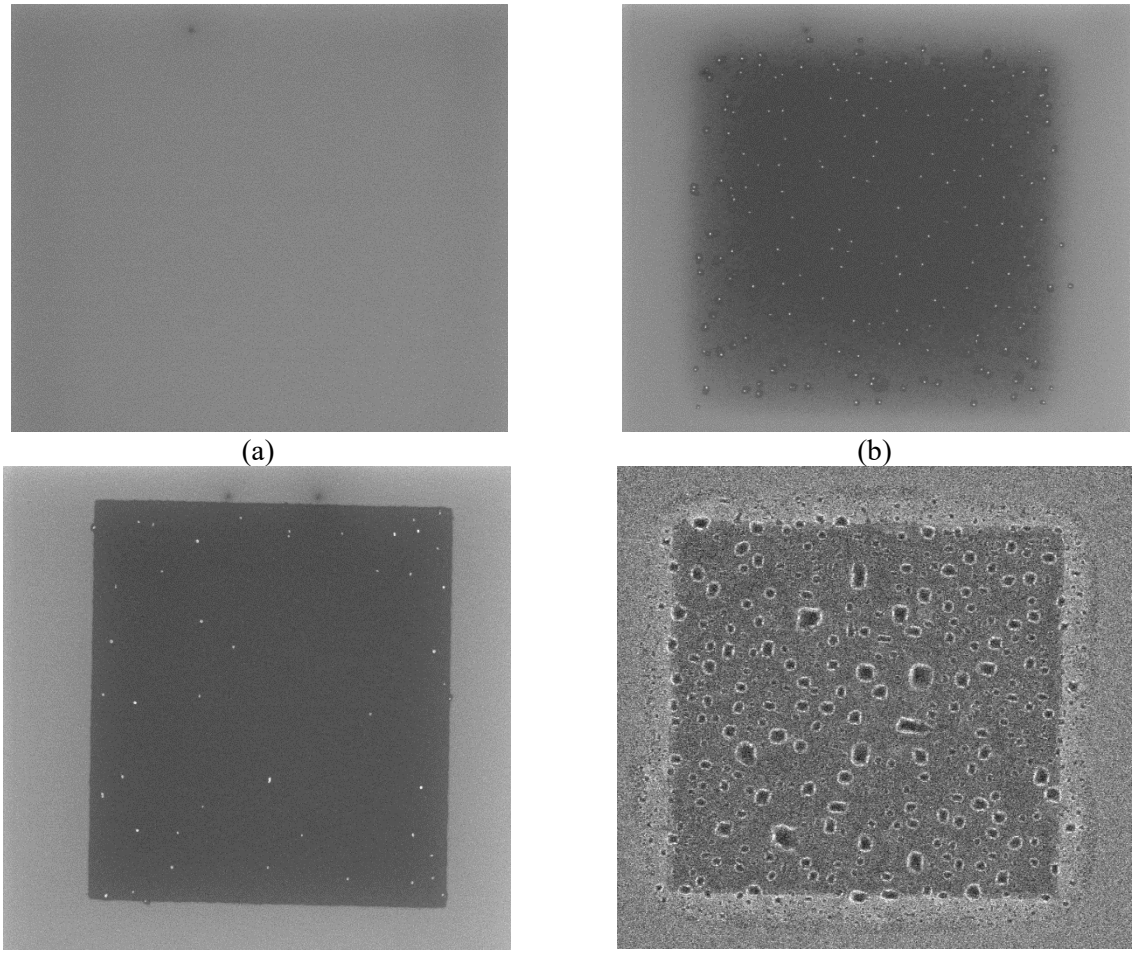

Figure 1. SEM images of modified Si areas after annealing at $T = 800^{o}$C and various accelerating voltages and beam passes, respectively: (a) 5kV and 5, (b) 5kV and 200, (c) 30kV and 5, (d) 30kV and 200.

Acknowledgments

This work was supported by the Russian Science Foundation Grant No. 20-69-46076. The results were obtained using the equipment of the Research and Education Center "Nanotechnologies" of Southern Federal University.

References

[1] Wang Z, Tian B, Paladugu M, Pantouvaki M, Le Thomas N, Merckling C, Guo W, Dekoster J, Van Campenhout J, Absil P and Van Thourhout D 2013 *Nano Lett.* **13** 5063–9

[2] Tang M, Park J-S, Wang Z, Chen S, Jurczak P, Seeds A and Liu H 2019 *Prog. Quant. Electron* **66** 1-18

[3] Grundmann M, Krost A and Bimberg D 1998 *J Vac Sci Technol B Microelectron Nanometer Struct* **9** 2158–66

Study of the 9R-Si hexagonal phase formation with variations in the synthesis conditions

A A Nikolskaya, D S Korolev, A N Mikhaylov, A I Belov, A A Konakov, D A Pavlov and D I Tetelbaum

Lobachevsky University, 23/3 Gagarin prospect, Nizhny Novgorod, 603022, Russia

email: nikolskaya@nifti.unn.ru

Abstract. Hexagonal modifications of silicon attract the attention of researchers in connection with the possibility of increasing the emission properties of silicon, which is the main material of electronics. Obtaining such polytypes is associated with extreme synthesis conditions, which are difficult to implement in large-scale production. In this work, we consider the hexagonal 9R-Si modification synthesized in a silicon substrate using ion implantation as the traditional method of microelectronics. This phase is formed in silicon substrate at the interface with SiO_2 oxide upon implantation of SiO_2 films with heavy ions followed by annealing. The resulting SiO_2/Si structures have photoluminescence at ~ 1235 nm. The influence of the initial substrates, parameters of ion implantation, and annealing on the formation and photoluminescent properties of the 9R-Si phase is analyzed and interpreted.

1. Introduction

Silicon, due to its unique properties and widespread availability, is the main material of modern electronics. However, its use in promising photonic devices for data processing and transmission is limited by the indirect bandgap in its energy structure and, accordingly, extremely low luminescence intensity. At the same time, the development of methods for obtaining single-crystalline silicon and technological processes for manufacturing Si-based devices determines the relevance of the problem of overcoming this fundamental obstacle. One of the new promising approaches is the use of hexagonal modifications of silicon, for which a significant improvement in emissivity has been demonstrated compared to the traditional cubic modification. However, for practical application, it is required to develop a technology that is fully compatible with modern silicon technology. We have recently demonstrated that inclusions of the 9R-Si hexagonal phase are formed in the substrate at the interface with the SiO_2 film under ion implantation of heavy ions into SiO_2/Si structures followed by annealing. For such structures, we found the luminescence line at a wavelength of ~ 1235 nm [1, 2]. In this work, we study the luminescence properties of SiO_2/Si structures in which inclusions of the 9R-Si phase are formed under various conditions of ion implantation, post-implantation annealing, and for different initial SiO_2/Si structures.

2. Experimental

The initial samples were SiO_2 thermal films with a thickness in the range of 50–300 nm on *n*- and *p*-type silicon substrates with orientations (100), (111), and (112). Then the samples were irradiated by krypton, silicon, arsenic ions with an energy of 85 keV and doses in the range of 10^{15}-10^{17} cm^{-2}. The

thicknesses of the films and the irradiation regimes were selected to ensure a different mutual arrangement of the profile of implanted atoms and the film-substrate interface. Post-implantation annealing was carried out in the temperature range of 600-900 °C for 30 minutes in a nitrogen gas atmosphere. The study of luminescent properties was carried out under excitation with a 405 nm laser and temperatures of 10-300 K.

3. Results and discussion

A line at ~ 1235 nm is present in photoluminescence (PL) spectra due to the formation of the 9R-Si hexagonal phase inclusions in the silicon substrate at the interface with the film as revealed by transmission electron microscopy [1, 2]. It is established that the intensity of PL line significantly depends on the implantation conditions: the type of ion, irradiation dose and annealing temperature, as well as on the initial parameters of the structure: substrate orientation, type of doping and oxide thickness. A regular change in PL intensity with an increase in the film thickness and an increase in the irradiation dose, as well as a dependence on the orientation of the initial substrate is found for different film thicknesses. Based on the experimental results, a hypothesis is proposed on the mechanism of the 9R-Si hexagonal phase formation in the considered structures. The roles of various factors in the mechanism are discussed: the chemical nature and mass of ions, mechanical stresses, crystal anisotropy, oxygen recoil atoms, defect formation, and structural conjugation of two phases.

Acknowledgments

The reported study was funded by Russian Foundation for Basic Research (project number 20-32-90204). D.K. acknowledges the support of the President of the Russian Federation grant (MK-4092.2021.1.2). A.N. acknowledges the support of the President of the Russian Federation fellowship (SP-1894.2021.5).

References

[1] Nikolskaya A A, Korolev D S, Mikhaylov A N, Belov A I, Sushkov A A, Krivulin N O, Muhamatchin K R, Elizarova A A, Marychev M O, Konakov A A, Tetelbaum D I and Pavlov D A 2018 *Appl. Phys. Lett.* **113** 182103

[2] Nikolskaya A A, Korolev D S, Mikhaylov A N, Konakov A A, Belov A I, Marychev M O, Murtazin R I, Pavlov D A and Tetelbaum D I 2020 *Surf. Coat. Technol.* **386** 125496

Application of graphene structures formed on silicon carbide substrates as elements of field emission devices

V V Niftalieva[1] , I O Kessler[1], J V Morozova[1], , A A Rezvan[1] and V S Klimin[12]

[1]Department of Nanotechnology and Microsystems, Southern Federal University, Taganrog 347922, Russia
[2]Research and Education Center "Nanotechnologies", Southern Federal University, Taganrog 347922, Russia
e-mail: Niftalieva@sfedu.ru

Abstract. This article describes the technology of obtaining graphene films on the SiC surface using the methods of focused ion beams and plasma-chemical etching in a fluorine-containing medium. Due to the fact that the method of thermal decomposition of silicon carbide is low cost, it is also possible to obtain homogeneous nanocarbon films of a large area on the basis of both conducting and semi-insulating substrates, it can be considered that it is superior over others.

1. Introduction

Currently, promising self-organizing materials are gaining increasing importance in micro- and nanoelectronics, one of such promising materials is graphene and its derivatives. The prospect of its use is due to a number of advantages, the main of which are high carrier mobility and resistance to ionizing effects [1].The main method for obtaining graphene films on the SiC surface is thermal decomposition (thermal destruction) of the SiC surface [2]. The advantage of the method of thermal decomposition of silicon carbide is its low cost and the possibility of obtaining homogeneous nanocarbon films of a large area on the basis of both conducting and semi-insulating substrates [3]. However, this method has a significant drawback - annealing is required at very high temperatures, which can lead to the formation of high mechanical stresses in the structure. In this regard, it is important to study the use of a combination of focused ionic and plasma-chemical etching to obtain graphene films on SiC [4].

2. Materials and methods

At the initial stage, experimental studies on the formation of nanoscale structures were carried out by the method of focused ion beams. For this purpose, a scanning electron microscope with an ion column NovaNanoLab 600 (FEI, Netherlands) was used. The built-in tools of the microscope control program formed templates for the subsequent etching of structures with a focused ion beam. The templates were formed in the form of a torus with an outer diameter of 2 microns and an inner diameter of 600 to 800 nm. These dimensions allow the performance of the resulting structure to be measured. The ion beam current was 30 pA. The accelerating voltage was 30 keV. The holding time at a point is 1 μs. The structures were then etched onto a silicon carbide substrate according to these figures.

3. Results

As a result of experimental studies, structures were obtained, the AFM image of which is shown in Figure 1.

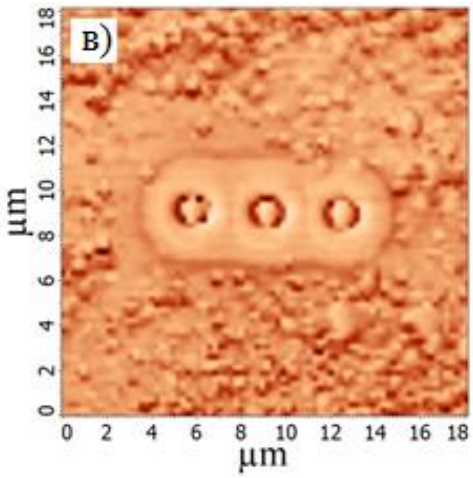

Figure 1 Experimental structures obtained in the course of studying the formation of field emission emitters

The resulting structures had a height of 280-600 nm. The samples obtained were examined for field emission characteristics. The current density of the investigated samples was 96.32. ± 8.81 A /cm2

4. Discussion and Conclusions

In this experiment, studies were carried out for the formation of carbon nanostructures on the surface of silicon carbide. Experiments on the production of graphene on the surface of silicon carbide by plasma etching with fluoride plasma have been carried out. The parameters of the emission cell were investigated; it has been proven that the use of carbon nanostructures as an active element of an emission cell is useful and cost-effective. This technology can be used for the formation of modern vacuum microelectronic devices, as well as for the development of pressure and gas sensors.

Acknowledgments

This work was supported by the Russian Foundation for Basic Research Project № 18-29-11019 mk. The results were obtained using the equipment of the Research and Education Center "Nanotechnologies" of Southern Federal University

References

[1] V S Klimin, A A Rezvan, O A Ageev Research of using plasma methods for formation field emitters based on carbon nanoscale structures // J. of Phys: C.S,2018. V.1124. – P. 071020.

[2] Li J, Yan X, Gou G, Wang Z, Chen J 2014 Phys. Chem. 161850

[3] Chen J, Li J, Yang J, Yan X, Tay B-K, Xue Q 2011 Appl. Phys. Lett.99173104

[4] Klimin V S, Solodovnik M S, Lisitsyn S A, Rezvan A A, Balakirev S V 2018 J. Phys.: Conf. Ser.1124041024

The structure and optical properties of the ZnO/SnO multilayered system

S Pankov, O Zhilova, M Kashirin, V Makagonov, M Kopytin, I Il'yashev

Voronezh State Technical University, Voronezh, 394026, Russia

srgpank@mail.ru

Abstract. In this work we studied multilayered ZnO/SnO_2 thin films were obtained by ion-beam sputtering. XRD analysis of the structure showed that ZnO and SnO_2 layers are amorphous. Thin films have high transparency (> 90 %) in the visible range and optical band gap value in a range of 3.3-3.6 eV, which depends of the bilayer thickness.

1. Introduction

Multilayered heterostructures consisting of oxide semiconductors layers attract significant and growing interest for electronics devices application. In most cases, such heterostructures exhibit improved or new physical properties and can combine the properties of two different materials. One of the most frequent examples of using multilayer heterostructures consisting of oxide semiconductor layers is TFT channels [1-2]. That makes it possible to obtain a TFT channel structure with high mobility and stability.

Obtaining such multilayered heterostructures is undoubtedly an important task, including controlling the thickness of the layers, which can vary from 1 to 10 nm. It is important to take into account the chemical interaction and diffusion between the layers. As a result, the most widely used methods for producing multilayer heterostructures of transparent oxide semiconductors are methods in which the processes of deposition of layers occur at rather low temperatures of the substrate surface (atomic layer deposition, pulsed laser ablation method and etc. [1,2]). In this case, the method of ion-beam sputtering used by us can be applied to obtain multilayer systems due to a slight (up to 40° C) heating of the substrate surface during the deposition process [3,4], which reduces the influence of surface chemical reactions and diffusion processes on the sample structures.

2. Experiment

Multilayered ZnO/SnO_2 thin films were observed by ion beam layer-by-layer sputtering of ZnO and SnO_2 targets according to the method described in [3,4]. Deposition was carried out in argon atmosphere (Ar purity of 99.998 %) at a pressure of 7×10^{-4} Torr on ceramic ST-50 (sitall), glass and silicon substrates. The $[ZnO/SnO_2]_{76}$ sample thickness (where 76 is the number of ZnO/SnO_2 bilayers) changed from 47 to 380 nm. The bilayer thickness h_{bl} changed from 0.6 to 5.0 nm.

The structure was investigated by X-ray diffraction methods (XRD) on a Bruker D2 Phaser diffractometer using DIFFRAC.EVA 3.0 software with the ICDD PDF Release 2012 database. Thickness of the samples was measured using the MII-4 optical interferometer.

The optical measurements of the $[ZnO/SnO_2]_{76}$ films were performed on an ECOVIEW UV-6100C dual-beam spectrophotometer in the spectral range of 300-1100 nm.

3. Result and discussion

XRD pattern of $[ZnO/SnO_2]_{76}$ thin film samples showed one broad peak in the angles range of $2\Theta = 28 - 32°$which does not depend on the bilayer thickness. Thus, $[ZnO/SnO_2]_{76}$ can be characterized as an X-ray amorphous structure. The analysis of XRD patterns at small Bragg angles ($2\Theta < 9°$) showed that a layered structure is formed, The period of the structure d was calculated by the Wulff-Bragg formula [3,4] completely corresponded to the results of optical interferometer measurements.

Figure shows the transmission spectra of multilayered $[ZnO/SnO]_{76}$ thin films deposited on glass substrates with different bilayer thickness. The samples obtained have a sufficiently high transparency in the wavelength range λ from 300 to 1100 nm. The transmittance increases with h_{bl} increase from 70% for structures with $h_{bl} = 0.6$ nm to 90% for structures with $h_{bl} = 4.8$ nm. The variation of absorption coefficient with photon energy for direct allowed transitions between bands should obey the relation [3]:

$$\alpha hv = A(hv - E_g)^{1/2}$$

Where α is the absorption coefficient, hv is photon energy, A is constant and E_g is energy band gap. The energy band gap of multilayered $[ZnO/SiO]_{25}$ thin films can be determined by extrapolating the linear part of the plot $(\alpha hv)^2$ vs. photon energy. As it seen on inset in the figure 1 the energy band gap values were decreased from 3,6 to 3,3 eV with increasing h_{bl} from 0,6 to 4,8 nm respectively. Increasing band gap for lower bilayer thickness can be explain by quantization in nanomaterials [4].

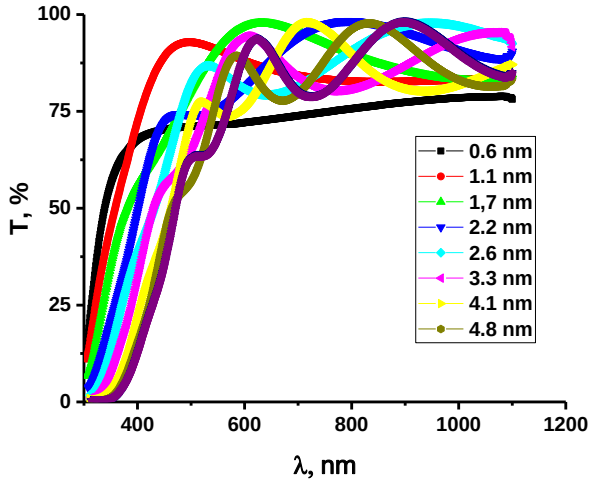

Figure 1. Dependence of the transmittance on the wavelength of multilayered $[ZnO/SnO]_{76}$ thin film samples with different bilayer thickness

Acknowledgments

This work was supported by the Ministry of Education and Science within the framework of state assignment No. FZGM-2020-0007.

References

[1] Lee S-J et.al. 2015 *Etri Journal* **37** 1135-1142

[2] Nam S et.al. *Journal of Materials Chemistry C* 2016 **4** 11298-11304

[3] Zhilova O V et al. 2019 *Materials research express* **6** 086330

[4] Zhilova O V et. al. 2019 *Journal of materials science-materials in electronics* **30** 11859

[5] Coleman V A , Jagadish C 2006 *Zinc oxide bulk, thin films and nanostructures: processing, properties and applications* (Elsevier science bv, Amsterdam)

Investigation of gallium oxide crystals depending on growth conditions

D.I. Panov[1], V.A. Spiridonov[1], D.A. Zakgeim[1], A.V. Kremleva [1], D.A. Bauman[1], A.E. Romanov[1], V.E. Bougrov[1]

[1]ITMO University, St. Petersburg, 197101, Russia

E-mail: Dmitriipnv@gmail.com

Abstract. The influence of growth atmosphere on the production of a bulk gallium oxide crystal by the Czochralski method is considered. The optical properties of the obtained gallium oxide crystal were studied. As-grown β-Ga2O3 crystals were characterized
by X-ray diffraction and optical transmission measurements.

1. Introduction

Currently, there is a great interest in the development of new semiconductor materials all over the world. One such promising material is gallium oxide (β-Ga2O3). Today, β-Ga2O3 is already successfully used in many applications, for example, in MOSFETs with a breakdown voltage above 1000 V [1], conducting transparent substrates for epitaxy of optoelectronic structures based on III-nitrides [2]. This is possible due to the unique physical properties of β-Ga2O3, such as a wide band gap (~4.8 eV), high breakdown voltage (>8 MV/cm), relatively high electron mobility (~150 cm2/Cm) [3,4], and transparency in the visible and UV spectral ranges [5-7]. An important advantage of gallium oxide over nitride semiconductors (GaN, AlN) is relatively simple technology of obtaining its volume single crystals. It is common practice to grow β-Ga2O3 crystals by the well-known methods of Stepanov (EFG) [8], Czochralski [5,7], and zone melting [9], among others.

However, the growth of bulk crystals of gallium oxide from the melt is complicated by the tendency of this material to chemical decomposition at the melting temperature. Depending on the external redox conditions, the Ga2O3 melt can decompose into divalent gallium oxide, monovalent oxide and, finally, metallic gallium (Ga2O3 → GaO → Ga2O → Ga and O2). As a result, metallic gallium can form intermetallic alloys (Ir-Ga) with elements of growth equipment (crucibles, shaper (EFG method).

2. Experiments and results

To obtain a crystal, a NIKA-3 growth unit with induction heating was used, which allows to grow crystals by the methods of Czochralski and Stepanov. Gallium oxide powder was used as the starting material. An iridium crucible was used to produce the melt. All samples were synthesized in a closed system with a constant atmosphere. The growth atmosphere consisted either of pure CO2 or a mixture of gaseous Ar and O2 at a pressure of 1 bar, with the O2 content varying within 0–10 vol %.

A plane-parallel sample 1 mm thick was obtained by cleaving a crystal and its optical properties were studied. Spectroscopic studies of the obtained sample showed that it is transparent in the near UV and visible range, the absorption band starts from 250 nm.. The band gap was estimated from the

experimental absorption spectrum, which was about 4.7 eV. According to the results obtained, it can be assumed that today the technology is not fully developed and defects are present in the crystal.

Structural properties were studied by X-ray diffraction. X-ray diffraction scan showed that crystal faces were formed by (200),(400),(600) family of crystallographic planes.

3. Conclusion

The paper considers the possibilities of practical application of the material. The influence of growth atmospheres on the possibility and quality of obtaining a gallium oxide crystal is investigated. The optical properties of the sample were studied and the band gap of the crystal was estimated at 4.7 eV. Based on the estimated band gap, it was concluded that at the moment the crystal has defects and structural damage.

Acknowledgements

This work was supported by the Russian Science Foundation, Project No. 19-19-00686.

References

[1] Hu, Z., Nomoto, K., Li, W., Tanen, N., Sasaki, K., Kuramata, A., Nakamura, T., Jena, D., Xing, H.G., 2018,*IEEE Electron Device Letters* **39**, 869–872

[2] Víllora, E.G., Arjoca, S., Shimamura, K., Inomata, D., Aoki, K., 2014. *Presented at the SPIE OPTO, San Francisco, California, United States*,. 89871

[3] Pearton, S.J., Yang, J., Cary, P.H., Ren, F., Kim, J., Tadjer, M.J., Mastro, M.A., 2018. *Applied Physics Reviews* **5**, 011301

[4] Stepanov, S.I., Nikolaev, V.I., Bougrov, V.E., Romanov, A.E., 2016 *Rev.Adv.Mater.Sci.* **44**, 63–86.

[5] Galazka, Z., 2018. *Semicond. Sci. Technol*. **33**, 113001

[6] Zakgeim D.A., Panov D.I., Spiridonov V.A., Kremleva A.V., Smirnov A.M., Bauman D.A., Romanov A.E., Odnoblyudov M.A., Bougrov V.E. 2020. *Technical Physics Letters*, **46**, 1144 -1146

[7] Panov D.I., Spiridonov V.A., Zakgeim D.A., Kremleva A.V., Bauman D.A., Romanov A.E., Bougrov V.E . 2020, *Journal of Physics: Conference Series*, **1695**, 012024

[8] Kuramata, A., Koshi, K., Watanabe, S., Yamaoka, Y., Masui, T., Yamakoshi, S., 2016, *Jpn. J. Appl. Phys*. **55,** 1202A2

[9] Hossain E., Kulkarni R., Mondal R., Guddolian S., Azizur Rahman A., Thamizhavel A., and Bhattacharya A. ECS 2019, *Journal of Solid State Science and Technology*. **8**. 3144-3148

Research of FIB local milling processes for creation of nanosized field emission structures

I V Panchenko[1], **N A Shandyba**[1], **A S Kolomiytsev**[1]

[1]Southern Federal University, Taganrog 347924, Russia

E-mail: ivpanchenko@sfedu.ru

Abstract. The paper presents the results of experimental studies of the influence of the main parameters of local FIB milling on the accuracy of transfer of the pattern to the substrate for the creation of nanoscale field emission structures. In this work, the optimal FIB current is determined, equal to 0.1 nA, at which the minimum amount of distortion is introduced into the formed structures and the most accurate transfer of the pattern to the surface is ensured. The results on the formation of nanoscale structures with sizes from 0.1 to 2 μm using the method of local ion-beam milling are presented. The regularities of the influence of the shape and size of FIB on the formed nanoscale structures are experimentally established and methods for increasing the accuracy of their formation are proposed.

1. Introduction

One of the urgent and important tasks in the development of modern electronics is the creation of miniature vacuum devices operating on the effect of field emission. The development and formation of vacuum field emission nanoelectronics structures allows achieving high performance, noise immunity and low power consumption in electronic devices. These properties can be achieved by reducing the overall parameters of the device elements down to nanometers. For example, a decrease in the interelectrode distance allows a sharp decrease in the threshold voltage of the beginning of emission, but this leads to many technological difficulties. Modern production processes based on the operation of optical lithography, liquid and plasma etching do not allow achieving sufficient accuracy and resolution in the formation of structures of field emission nanoelectronics. The application of the focused ion beam (FIB) method helps to overcome the main limitations of traditional methods and expand the ranges of parameters of the resulting structures. The FIB method allows performing technological operations of local milling and deposition of materials from the gas phase under high vacuum conditions without the need for resists, masks, and chemical etchants. The aim of this work is to experimentally study the main FIB parameters during surface profiling and to determine their optimal values for creating nanoscale field emission structures.

2. Experimental

One of the main parameters of FIB in ion-beam milling of a surface is the ion beam current. It determines the miling rate, the profile of the final structure, as well as the degree of deviation of the obtained object sizes from those specified in the template. In this work, we carried out experimental studies of the accuracy of transfer of the pattern pattern to the substrate during local ion-beam milling for several FIB currents. For this purpose, a template was generated for controlling the ion beam,

consisting of 20 circles with different diameters varying in the range from 0.1 μm to 2 μm with a step of 100 nm. The following main FIB parameters were used: accelerating voltage 30 kV, beam current 0.1–0.5 nA, beam dwell time (Dt) 1 μs and overlap 50%. SEM images of the resulting structures are shown in Figure 1, a.

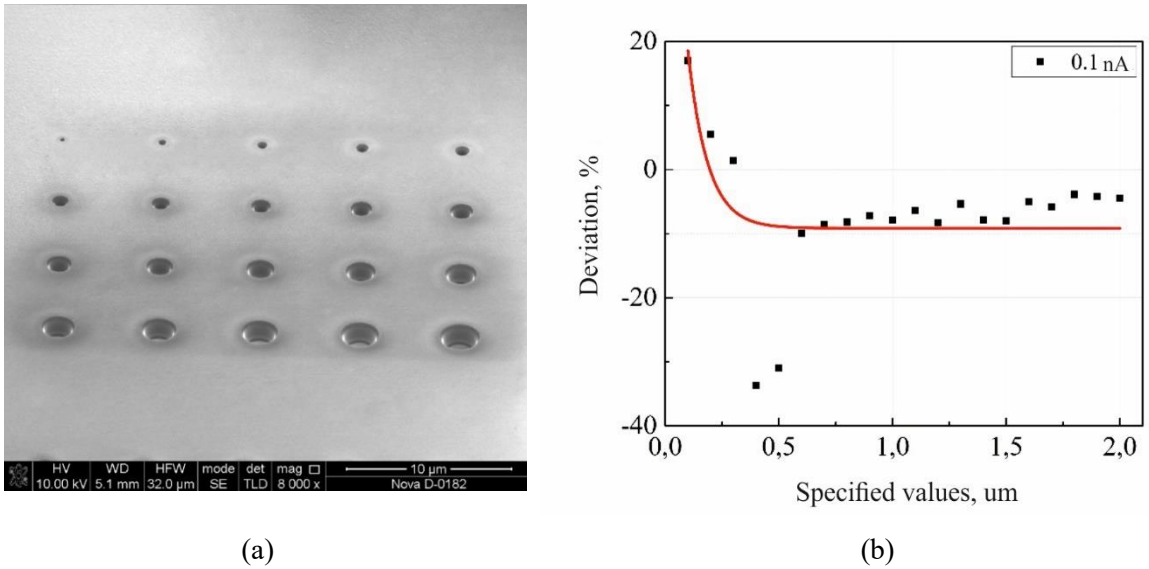

(a) (b)

Figure 1. SEM image of the formed structures (a) and the dependence of the deviation of the values of the diameters of the recesses from those specified in the milled pattern at a FIB current of 0.1 nA (b).

Analysis of SEM images showed that the experimentally obtained structures have a surface raster area near the circumference, and the angle between the side walls of the recesses and the substrate surface is different from 90 °. This is because the shape of the FIB beam is determined by the Gaussian function. In this regard, the milling profile of the substrate is very different from that specified in the template and has certain inaccuracies when transferring the pattern of the template to the substrate. Also, the diameters of the formed structures were measured and the dependences of their deviations from those specified in the template were plotted. The most optimal value of the FIB current is 0.1 nA, since it has the smallest deviation. The exponential deviation of the size of the structures in the range of values less than 500 nm is associated with the difficulty of obtaining the minimum diameter of the ion beam due to various physical effects.

3. Conclusions

Thus, from the results of experimental studies, the optimal FIB current was determined, equal to 0.1 nA, at which the minimum number of distortions is introduced into the formed structures and the most accurate transfer of the pattern pattern to the surface is ensured. The data obtained can be used in the formation of field-emission cells with a vertically oriented emitter, as well as other nanoscale field-electronic structures. To reduce the deviation in the range of values less than 500 nm, it is necessary to additionally investigate such FIB parameters as the time of exposure to the beam at a point and the degree of overlap.

4. Acknowledgments

The research was supported by the Ministry of Science and Higher Education of the Russian Federation: the state task in the field of scientific activity No. 0852-2020-0015.

Modelling electroforming process under constant bias conditions

O O Permyakova[1, 2], **A E Rogozhin**[1]
[1]Laboratory of Microstructuring and Submicron Devices, Valiev Institute of Physics and Technology RAS, Moscow 117218, Russia
[2]The School of Electronics, Photonics and Molecular Physics, Moscow Institute of Physics and Technology (State University), Dolgoprudny 141701, Russia

o.permyakova@phystech.edu

Abstract. In order to understand changing in defect concentration during the electroforming process we modelled electroforming process in Ta/HfO2/Pt under constant bias. For this purpose kinetic Monte-Carlo and finite elements methods was utilized. vacancy profiles were obtained for forming voltages from 3 V to 5 V, modelling of lower stresses is time consuming. It was found that with decreasing voltage, vacancies begin to accumulate near the inert electrode.

1. Introduction

The most promising type of non-volatile memory is resistive random access memory (RRAM) [1]. The main advantage of RRAM is low switching time of fewer than a 10 ns [2] and scalability less than a 10 nm [3]. Additionally, the RRAM element can be used for processing information [4]. The main problem of RRAM is low repeatability of characteristics between elements [1].

A ReRAM element usually has two possible states which differ in resistance value: low resistance state (LRS) and high resistance state (HRS). The transition from one state to another occurs when charge flows through the structure, this process is called resistive switching. Eventually, the most stable resistive switching indicated in RRAM elements based on transition metal oxides (TMOs) such as HfO_X [2, 3] and TaO_X [2].

Resistive switching in RRAM element based on TMOs mostly takes place due to reduction and disruption of conductive filament (CF). So, RRAM variability strongly depends on the shape and properties of CF [5]. The initial formation of a CF occurs during electroforming at the voltage values, significantly higher than the operating voltage, this process is called. Electroforming is a stochastic process, therefore, using the same electroforming process for various elements of the same structure, it is difficult to get similar CF. Structure which do not require electroforming process called forming-free structures, such structures have low variability [6].

In this work we present result of modelling electroforming process under different constant bias conditions for structures Ta/HfO2/Pt. Results of such model can be used in the development of the forming-free memristor technology.

2. Model description

To model electroforming process in oxide with thickness 5 nm we used kinetic Monte-Carlo and finite element methods. Monte-Carlo approach was used for simulation of the oxygen vacancy motion and

electric current passing through the structure. According to the model vacancies formation only takes place near the active electrode. After that vacancies diffuses to the inert electrode. Vacancy movements were simulated till full filament short-circuited the electrodes. A more detailed description of the model can be found in our previous work [7]. In this work the growth of CF was simulated under the constant-voltage conditions.

3. Result and Discussion

It was found that higher bias leads to larger concentration of vacancies near the inert electrode. Simulated vacancy concentration profiles are presented in the Figure 1. We believe that the vacancy concentration profile is determined by the ratio of the rates of vacancy motion and generation. The rate of vacancy generation decreases with stress bias as the rate of vacancy diffusion, but activation energies for vacancy generation (1.1 eV) is much lower than for diffusion (0.7 eV). Additionally, higher forming time can be explained by the accumulation of vacancies near the inert electrode.

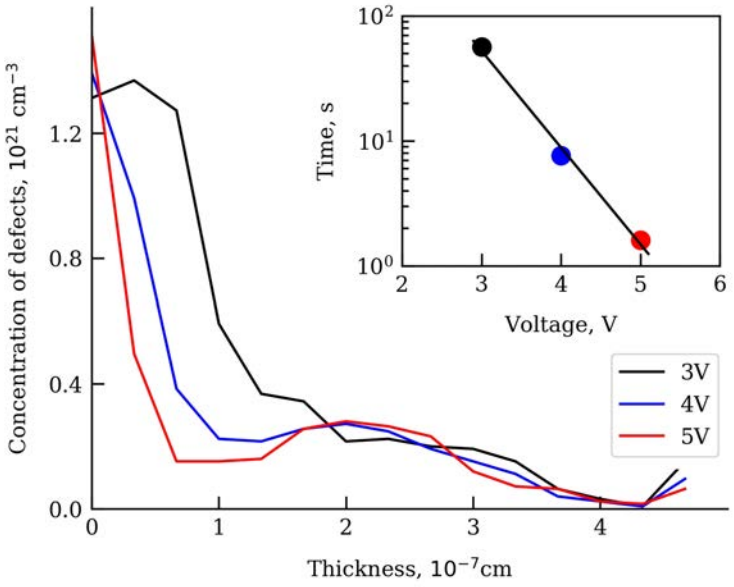

Figure 1. Simulated distribution of vacancy concentration along the oxide thickness, with active electrode in the right and inert electrode in the left. Inserted figure shows dependence of filament formation time on constant bias. Slope of the trend line is 0.77.

Acknowledgments

The investigation was supported by program №0066-2019-0004 of the Ministry of Science and Higher Education of Russia for Valiev Institute of Physics and Technology of RAS.

References

[1] Lanza M et al. 2019 *Adv. Electron. Mater.* **5** 1800143

[2] Wong H-S P, Lee H Y, Yu S, Chen Y S, Wu Y, Chen P S, Lee B, Chen F T and Tsai M J 2012 *Proc. IEEE* **100** 1951

[3] Govoreanu B et al. 2011 *IEEE Electron Device Lett.* **31** 6

[4] Zahoor F, Zulkifli T Z A and Khanday F A 2020 *Nanoscale Res Lett* **15** 90

[5] Gonzalez M B, Raf J M, Beldarrain O, Zabala M and Campabadal F 2014 *IEEE Transactions on Device and Materials Reliability* **14** 769

[6] Zhang H, Liu L, Gao B, Qiu Y, Liu X, Lu J, Han R, Kang J and Yu B 2011 *Appl. Phys. Lett* **98** 042105

[7] Permiakova O, Miakonkikh A, Rudenko K and Rogozhin A 2020 *Int. Conf. on Information Technology and Nanotechnology,* 26-29 May, Samara, Russia, (New York: IEEE) p 1

Plasma surface treatment of local modify Si plates

A A Rezvan[1], V S Klimin[1,2]

[1]Department of Nanotechnology and Microsystems, Southern Federal University, Taganrog 347922, Russia
[2]Research and Education Center "Nanotechnologies", Southern Federal University, Taganrog 347922, Russia

arezvan@sfedu.ru

Abstract. It is proposed to develop new techniques and processes for formation of nanoelectronic elements on silicon using combined techniques. Local modification of regions on surface of silicon substrates with a focused ion beam, followed by plasma treatment in a fluorine containing plasma at various process parameters was carried out. Analysis of obtained results shows that dependences of modes combination of focused ion beams and plasma chemical etching, two types of action can be realized: masking of the substrate surface and etching activation of substrate during plasma activation.

1. Introduction

Silicon electronics with approved standard manufacturing processes are reaching their limit for miniaturization of elements, maximum operating frequency and number of elements per wafer [1-7]. However, due to the high availability and distinctive parameters of the material, it is proposed to develop new methods and processes for the formation of nanoelectronic elements on silicon using combined techniques.

2. Experiment

On surface of silicon substrates, local modification of 5x5 μm regions was carried out with a focused Ga^+ ion beam at an accelerating voltage U_{ACC} = 30 keV and an ion beam current I_{IB} = 10 pA with a different number of beam passes (10 - 100) and different doses (2.5 - 25 pC/μm^2), respectively.

Plasma treatment of samples with modified regions was carried out in fluorine containing plasma with the following parameters: fluorine containing gas flow N_{SF6} = 15 cm^3/min, argon flow N_{Ar} = 100 cm^3/min, pressure in the reactor P = 2 Pa, power of the inductively coupled plasma source W_{ICP} = 200 W , the power of the capacitive plasma source W_{CPS} = 35 W, the bias voltage U_{BV} = 24 V, the processing time is 30 - 120 seconds.

Analysis of obtained results shows that dependences of modes combination of focused ion beams and plasma chemical etching, two types of action can be realized: masking of the substrate surface and etching activation of substrate during plasma activation.

Figure 1 shows a SEM image (fig. 1 a) and an AFM image (fig. 1 b) of surface samples with modified regions at 100 passes of focused ion beam and plasma chemical treatment for 120 seconds.

The analysis shows that with the specified combination of modes, locally modified region is characterized by a lower etching rate (V_{moSi} = 0.019 nm/sec), than the unmodified region of substrate surface (V_{Si} = 2.21 nm/sec). The masking effect can be explained by the formation of a layer saturated with embedded Ga^+ ions in the near surface, locally modified region of the silicon substrate, which are characterized by a greater inertness with respect to fluorine containing plasma ions than silicon atoms.

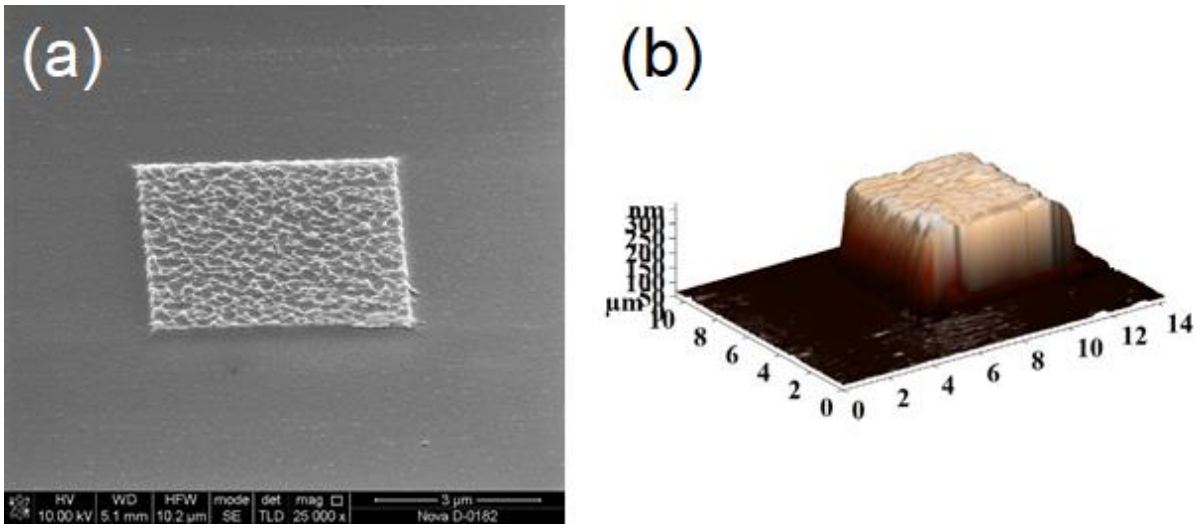

Figure 1 (a, b). The structure of silicon surface after local modification by focused ion beam method at 100 passes of ion beam and plasma chemical treatment in a fluorine containing plasma for 120 seconds: (a) SEM - image; (b) AFM - image

In fig. 1 (a, b) it can be seen that masking area has a more developed surface relief in relation to the surrounding area. This can be explained by predominance in this area of physical component of reactive ion sputtering.

Acknowledgments
This work was supported by the Grant of the Russian Science Foundation № 20-69-46076. The results were obtained using the equipment of the Research and Education Center "Nanotechnologies" of Southern Federal University.

References
[1] Tok E S, Neave J H, Zhang J, Joyce B A and Jones T S 1997 Surf. Sci. 374 397
[2] Shiraishi K and Ito T 1998 Phys. Rev. B 57 6301
[3] Kley A, Ruggerone P and Scheffler M 1997 Phys. Rev. Lett. 79 5278
[4] Huffaker D L, Park G, Zou Z, Shchekin O B and Deppe D G 1998 *Appl Phys. Lett.* **73** 2564
[5] Wong P S, Liang B and Huffaker D L 2010 *J. Nanosci. Nanotechnol.* **10** 1537–1550
[6] Grundmann M, Stier O and Bimberg D 1995 *Phys. Rev. B* **52** 11969
[7] Yamaguchi K, Yujobo K and Kaizu T 2000 *Jpn. J. Appl. Phys.* **39** L1245–L1248

MBE growth and properties of III-V nanowires with quantum dots

R R Reznik[1-5], K P Kotlyar[1,2], V O Gridchin[1,2], I V Ilkiv[1,2], A I Khrebtov[1], Yu B Samsonenko[1,4], I P Soshnikov[1,4,6], N V Kryzhanovskaya[1], L Lorenzo[7], N Akopian[7] and G E Cirlin[1-4]

[1]Alferov University, Khlopina 8/3, 194021, St-Petersburg, Russia
[2]St. Petersburg State University, 199034 St. Petersburg, Russia
[3]ITMO University, Kronverkskiy pr. 49, 197101, St. Petersburg, Russia.
[4]Institute for Analytical Instrumentation RAS, Rizhsky 26, 190103, St-Petersburg, Russia
[5]Innolume GmbH, 44263 Dortmund, Germany
[6]Ioffe Institute, 194021 St. Petersburg, Russia
[7]DTU Fotonik, 2800 Kongens Lyngby, Denmark

E-mail: moment92@mail.ru

Abstract. Semiconductor nanostructures based on III-V nanowires with quantum dots were synthesized by molecular-beam epitaxy technique on silicon substrates. Morphological, structural and optical properties of grown nanostructures were studied. Research results have shown that synthesized objects are promising for optoelectronic applications, in particular, sources of single photons.

1. Introduction

Combination of nanowires (NWs) with quantum dots (QDs) are promising building blocks for future optoelectronic devices, in particular, single-photon emitters. The most studied epitaxially grown QDs are self-assembled, i.e., grown by island nucleation in the Stranski-Krastanow growth mode. The size, shape, and density of self-assembled QDs can be controlled by changing of the growth parameters such as substrate temperature, growth rate and growth time, but in the end it is a self-organized strain induced process and controlling the properties of the array independently is a challenging task. QDs in nanowires have, in contrast, shown great potential as a highly controllable system. The diameter, height, and density of the QDs are defined by the NW diameter, the growth time, and the NW density, respectively, and can be chosen more predictable. Due to a very efficient strain relaxation on the free sidewalls, coherent growth can be much easier realized in the NW geometry, where a small footprint is dictated by a metal catalyst particle assisting the NW growth via the vapor-liquid-solid (VLS) mechanism [1]. Moreover, it has recently been shown that [111] grown nanowires, especially heterostructured, are ideal candidates for the generation of entangled photon pairs [2].

Experimentally, all the samples in the present work were grown by molecular beam epitaxy (MBE). For GaAs/AlGaAs and InAsP/InP material systems, different growth conditions were applied, but the strategy was the same: we have used Au-assisted growth of the NWs on Si(111) substrate,

firstly we grew the AlGaAs and InP base of the NW, secondarily, the GaAs or InAsP nanoinsertion with lower bandgap, or QD, was formed and we end the structure with the core with the same material as the base. In case of GaAs/AlGaAs NWs it was found that during the growth spontaneous, independently on the Al fraction, core-shell structures with lower aluminum content in the cores are formed. Optically, our growth method results in the formation of GaAs QD in a AlGaAs NW having very narrow spectral linewidth (< 10ueV), single-photon emission in the wavelength range 750 – 820 nm in dependence on the QD growth recipe. Moreover, the emission wavelengths al-lows one to design light emission devices in a red range by simply changing of the Al fraction in AlGaAs NWs. In case of InAsP/InP NWs it was found that using a special procedure of substrate preparation immediately before the growth made it possible to obtain a nanowire coherency with the substrate of nearly 100%. A high-intensity emission from nanostructures was observed at a wavelength of ~1.3 μm at room temperature. In addition, NWs with QDs based on other systems of materials were synthesized and their physical properties were studied.

References

[1] Wagner R S, Ellis W C 2011 *Appl. Phys. Lett*. **4** 89.
[2] Singh R, Bester G 2009 *Phys. Rev. Lett.* **103** 063601

Wafer fusion technique features for efficient and effective bonding of A3B5 materials

S S Rochas[1], I I Novikov[1], L Ya Karachinsky[1], S A Blokhin[2], S A Blokhin[2], V N Nevedomsky[2], K O Voropaev[3], A Yu Egorov[1]

[1]ITMO University, St. Petersburg, 197101 Russia
[2]Ioffe Institute, St. Petersburg, 194021 Russia
[3]OKB-Planeta PLC, Veliky Novgorod, 173004 Russia

E-mail: stanislav_rochas@itmo.ru

Abstract. We present the results of studies of the conditions for the formation of A3B5 semiconductor compounds heterointerfaces, which contain InP, InGaAsP and GaAs layers. Improvement of planarity and homogeneity over the thickness of heterointerface boundaries using optimized preliminary preparation of semiconductor wafer surfaces was demonstrated. No additional extended defects, such as dislocations, at the heterointerface were found.

1. Introduction

Nowadays, the technology of wafer bonding with inter-mediate layer includes many methods such as adhesive wafer bonding, thermo-compression wafer bonding, metal wafer bonding, transient liquid phase wafer bonding etc. All these methods are usable for a hybrid integration in silicon photonics [1] but they are not suitable for lasers based on A3B5 material systems in the near-infrared range due to the formation of huge losses inside the lasers cavity. Direct wafer bonding technology includes molecular wafer bonding (wafer fusion), suitable for bonding Si and A3B5materials, such as GaAs and InP. This method is based on high temperature annealing of plates at a certain orientation relative to each other under significant applied pressure. Wafer fusion of GaAs and InP heterostructures, operating parameters: pressure of 3 kPa – 3 MPa, temperatures of 550–650 °C, is carried out in a chemically active liquid medium or in an oxygen-free medium [2].

2. Experiment

We performed wafer fusion of GaAs and InP, GaAs and InGaAsP epitaxial layers grown on GaAs and InP substrates by molecular-beam epitaxy (MBE) in an oxygen-free medium. For a wafer fusion an EVG 510 fusion machine with a pneumatic press under high vacuum conditions was used. The pressure was 10^{-6} mbar, the temperature was 600 °C, the contact force was 7 kN for 30 min. The fused structures have been subjected to comprehensive studies, including transmission electron microscopy (TEM) study. We chose a slow cooling mode of the sample with a cooling rate not exceeding 10 °C/min to prevent the destruction of fused interfaces.

3. Results

Analysis of TEM images of the GaAs/InGaAsP fused interfaces indicated many pores in the amorphous layer at the fused interface both from the InGaAsP side and from the GaAs side. Due to the difference in lattice parameters, the fused interface should contain edge misfit dislocations [3],

however, in our case, the dislocations lie in an amorphous layer, which removes the elastic stress fields from dislocations. Subsequent optimization of the preliminary preparation of the plates' surfaces in oxygen plasma and etchants with an increase in the temperature of preliminary surface annealing of the plates to 200 °C made it possible to ensure high planarity of the boundaries and uniformity in the region of the fused interface thickness. TEM studies did not reveal any misorientation of the GaAs and InP lattices in the (110) cross-sectional plane. The thickness of the fused interfaces of the GaAs/InP (Figure 1) was 3-10 nm.

Analysis of TEM images of the fusion of GaAs/InGaAsP before optimization showed an increase in the thickness of the fused interface to 5-8 nm. Optimization of the surface cleaning in the etchant and annealing at 525 ° C made it possible to effectively remove oxides from the overgrown InGaAsP surface. In comparison with the fused interface GaAs/InP, the optimized fused interface GaAs/InGaAsP (Figure 2) had a smaller thickness (1–2 nm).

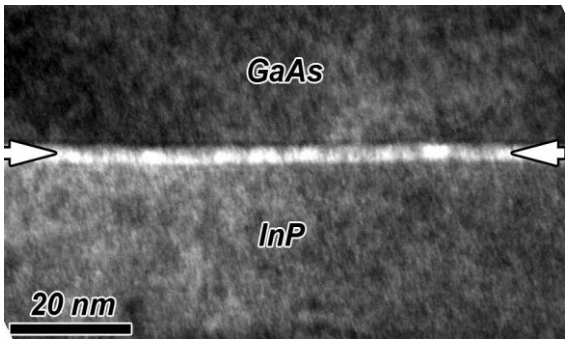

Figure 1. TEM image of the fused interfaces of the GaAs/InP

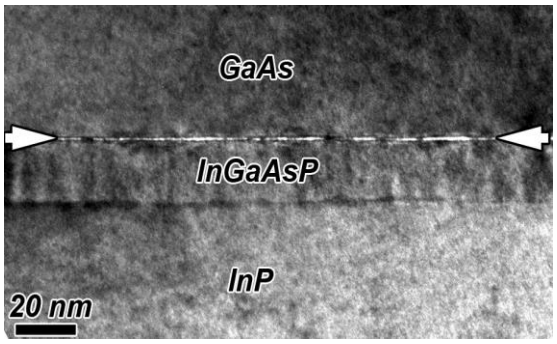

Figure 2. TEM image of the fused interfaces of the GaAs/InGaAsP

In conclusion we have demonstrated an improvement in planarity and uniformity over the thickness of the boundaries of heterointerfaces when using optimized preliminary preparation of surfaces of semiconductor wafers due to the removal of oxide films and adsorbed water molecules. TEM studies have shown that extended defects, such as dislocations, do not propagate into the bulk of the fused wafers. Optimized preliminary preparation before wafer fusion opens up the possibility of creating hybrid VCSELs using only the MBE technology and wafer fusion technique.

Acknowledgments
The reported study was funded by RFBR, project number 20-32-90198.

References
[1] Liang D. et al. 2010 *Materials* **3** 1782
[2] Black A. et al. 1997 *IEEE Journal of selected topics in quantum electronics* **3** 943
[3] Sirbu A. et al. 2010 *Semiconductor science and technology* **26** 014016

Influence of ultrasonic treatment on the change of monocrystalline silicon defective region

A A Solovyev[1], V V Rybin[1], A V Kulagin[1]

[1]Faculty of Physics and High Technology Engineering, Ulyanovsk State University, Ulyanovsk 432017, Russia

vlad_rib@mail.ru

Abstract. The article presents the results of an experimental study of ultrasonic action on monocrystalline silicon samples. The influence of the processing modes on the surface strength of the material under study was found.

1. Introduction

It is known that ultrasonic treatment of silicon crystals leads to a change in the dislocation movement speed at a constant mechanical load [1]. There are practically no data in the literature on the effect of ultrasound on the dislocations mobility in silicon single crystals in the internal stresses field. Therefore, this work is devoted to the study of the ultrasonic treatment effect of silicon single crystals on the defect region dynamics in the field of internal stresses.

2. Experimental technique

In this work, p-Si samples (ρ = 1 Ohm·cm, surface orientation (100)) with formed stress concentrators – scratches (load during scribing 0.5–2.0 N), being in distilled water, were subjected to ultrasonic processing with a signal from the ultrasonic generator at a frequency of 63.4 kHz. The processing time varied from 30 min to 5 hours, after which the samples were annealed at a temperature of T = 650 ° for t = 180 min. At a given annealing time, the introduced internal stresses completely relax and dislocation transport stops. To experimentally study the distribution of dislocations in crystals, we used the method of dislocations selective etching.

3. Results and discussion

The research results showed a decrease in dislocation paths from stress concentrators with processing time (Figure 1). In addition, a decrease in the number of etch pits in the selected slip lines is observed. In this case, a regular increase in the controlled parameters with the load on the indenter is clearly recorded when the crystal surface is scribed. The observed decrease in the length of dislocation runs after ultrasonic treatment indicates a decrease in the mobility of dislocations, i.e. the phenomenon of surface hardening is observed.

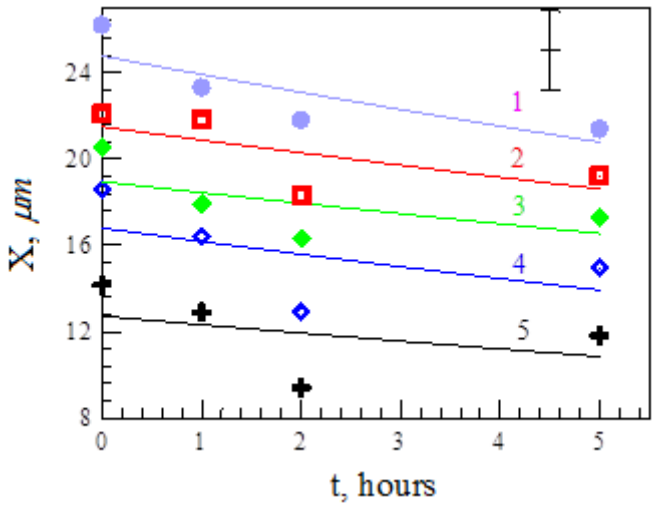

Figure 1. Change in the maximum path of dislocations in slip lines from the time of ultrasonic treatment at various scribing loads: 1 - 2 N; 2 - 1.75 N; 3 - 1.5 N; 4 - 1 H; 5 - 0.5 N. Annealing at T = 650 ° C, t = 3 h.

It is known that stimulated diffusion of vacancies and impurities occurs under the action of an ultrasonic wave [2]. Taking into account the fact that in our experiments the dislocation half-loop consists of short segments with their ends reaching the surface, as well as the fact that the surface and dislocations play the role of an almost infinite sink of point defects, it can be assumed that the observed effects are associated with an increase in the concentration of point defects under the influence of ultrasonic treatment.

4. Conclusion

To check the change in the surface hardness of single crystals under various modes of ultrasonic treatment, a series of experiments was carried out to measure the microhardness of the test samples. The research results recorded a regular increase in the surface microhardness with the time of ultrasonic treatment, which is consistent with the assumptions made on the strengthening of the silicon crystals.

References

[1] Ostrovskii I V, Korotchenkov O A, Goto T, Grimmeiss H G 1999 *Phys. Reports* **311(1)** 1-46

[2] Ermolovich I B, Milenin V V, Konakova R V, Primenko L N, Prokopenko I V, Gromashevskii V L 1997 *Semiconductors* **31(4)** 427–430

ZnO nanorods coating modified with $AgInS_2$ quantum dots

A A Ryabko*, O A Korepanov, A A Bobkov, V A Moshnikov

Saint-Petersburg state electrotechnical university «LETI», 5 Prof. Popova Street, Saint Petersburg, 197376, Russia

*Corresponding author's e-mail: a.a.ryabko93@yandex.ru

Abstract. This paper presents the effect on the visible light photoresponse caused by the modification of ZnO nanorod coating with colloidal $AgInS_2$ quantum dots. The modification of ZnO nanorods by immersion in colloidal solution results in the enhancement of visible absorption and photoresponse. Obtained results indicate the possibility of local heterojunctions between ZnO and $AgInS_2$.

1. Introduction

Zinc oxide (ZnO) is an n-type semiconductor with a direct bandgap (3.37 eV at room temperature). ZnO nanorods with colloidal quantum dots (QDs) could be applied in resistive gas sensors, photocatalysis, and photovoltaic cells (Dye-Sensitized Solar Cells, Colloidal Quantum Dot Solar Cells). The modification of ZnO nanorods with QDs shifts the photoactivation region of the gas sensing or photocatalysis process to the visible region. Ternary metal chalcogenides ($AgInS_2$ and $CuInS_2$) are less toxic materials in comparison with binary ones containing lead, cadmium, or tellurium [1]. The formation technology of heterogeneous nanostructured coatings based on ZnO nanorods with $AgInS_2$ QDs and their photoresponse are discussed in this article.

2. Experiment and results

The layer of ZnO nanorods was formed in two stages [2]. In the first stage, a seed layer of ZnO was deposited by ultrasonic spray pyrolysis of a zinc acetate aqueous solution. In the second stage, ZnO nanorods were grown-up in an aqueous solution of zinc nitrate and hexamethylenetetramine by a low-temperature hydrothermal method. After synthesis, the coating of ZnO nanorods was annealed at a temperature of 500°C for 5 minutes to remove organic molecules from the surface. $AgInS_2$ QDs stabilized by 3-mercaptopropionic acid were synthesized in aqueous medium by heating-up method [3]. The modification of ZnO nanorods with $AgInS_2$ QDs was performed by substrate immersion in the colloidal solution. Photoresponse was carried out on ceramic substrates with counter-pin gold electrodes.

The surface presence of QDs after immersion was controlled by absorption spectroscopy (Figure 1). To record the photoresponse (Figure 2), the sample was preheated at 150 °C for 10 minutes before and after the QDs modification to reduce the effect of adsorbed moisture.

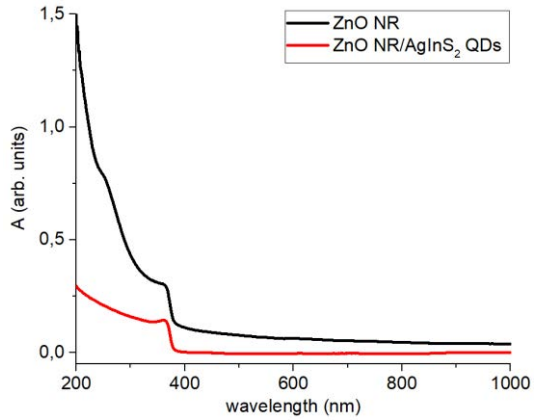

Figure 1. Absorption spectrum of ZnO nanorod array on quartz glass substrate before and after modification with $AgInS_2$ QDs

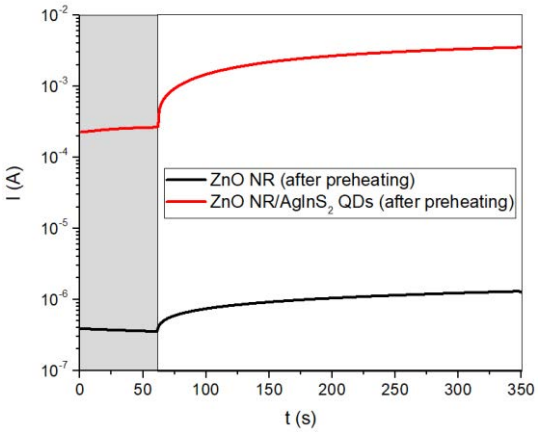

Figure 2. Photoresponse of an array of ZnO nanorods on a quartz glass substrate before and after $AgInS_2$ QDs modification. The radiation source is a blue LED (460 nm). The area without irradiation is highlighted in grey

The nanostructured coating enhances the absorption property in the visible region after ZnO nanorods were modified with $AgInS_2$ QDs (Figure 1). Nanorods without QDs modification show ~3.7 times conductivity change (I_{light}/I_{dark} ratio) under blue light irradiation (for ~5 min), which is due to the influence of intrinsic defects [4]. Modification of nanorods with $AgInS_2$ QDs leads to an increase in the photoresponse of the sample up to ~ 13.4 times (for ~ 5 minutes), which points to the formation of local heterojunctions between ZnO and $AgInS_2$.

3. Conclusion

Modification of ZnO nanorod array with $AgInS_2$ QDs leads to an increase in the photoresponse to visible light irradiation. This may indicate the formation of local ZnO/$AgInS_2$ heterojunctions. Short-term annealing at 150 °C does not destroy the colloidal nanocrystals, but allows partial removal of moisture from the surface of the nanostructured coating. Obtained results indicate the possibility to create gas sensors, photocatalysts, and photovoltaic structures based on the ZnO nanorods with $AgInS_2$ colloidal QDs.

Acknowledgments

The reported study was funded by RFBR, project number 19-38-90088

References

[1] Hong S P, Park h K, Oh J H, Yang H, Do Y R 2012 *Journal of Materials Chemistry*. **22** 18939

[2] Ryabko A A, Maximov A I, Verbitskii, et. al. 2020 *Semiconductors* **54** (11) 1257-1263

[3] Korepanov O A, Mazing D S, Aleksandrova O A, Moshnikov V A 2019 *Journal of Physics: Conference Series* **1410** (1) 012024

[4] Khokhra R, Bharti B, Lee H-N, Kumar R 2017 *Scientific Reports.* **7** 15032

Effects of plasma treatment parameters on the adsorption properties of tin dioxide-based nanomaterials

A P Sigaev[1], **I A Averin**[1], **A A Karmanov**[1], **I A Pronin**[1], **N D Yakushova**[1]

[1]Department of Nano- and Microelectronics, Penza State University, 440026, Penza, Russia

alexsigaev-94@yandex.ru

Abstract. We have studied the effect of nitrogen plasma exposure on the adsorption properties of SnO_2-based nanomaterials synthesized by the sol-gel method. We have established the correlation between the adsorption properties and plasma treatment parameters. The scanning electron microscopy has confirmed integrity violation of the original structure of nanomaterials and an increase in their specific surface area with high-power plasma source.

1. Introduction

The use of nanomaterials having a developed hierarchical structure with a fractal type of spatial organization is promising in the development of adsorption-type gas sensors. The problem of designing a simple and cheap technique to manufacture nanomaterials with relatively high selectivity is still urgent [1], despite numerous fundamental and applied studies [2, 3].

One of the possible ways to modify the adsorption properties of sensitive nanomaterials is plasma treatment [4-6]. In this work, we investigate the effect of various nitrogen plasma powers on the adsorption properties of SnO_2-based nanomaterials synthesized by the sol-gel method.

2. Experiment

The formation of SnO_2-based nanomaterials was carried out by the sol-gel method [7]. A film-forming sol was deposited onto glass substrates by centrifugation at 2,750 rpm. The final stage of the formation of nanomaterials is their thermal annealing at a temperature of 575°C for 50 minutes in air. The samples of nanomaterials were added to aluminum foil under the same modes for scanning electron microscopy.

Inductively coupled plasma processing of nanomaterials was performed under various modes of nitrogen plasma treatment: the power of inductively coupled plasma source P_1, which determines the energy and density of plasma, and the power of supplementary high-frequency source P_2, which characterizes the ion flow intensity and direction.

An analysis of adsorption site distribution on the surface of synthesized samples was carried out by the adsorption method of acid-base indicators in combination with spectrophotometry. Ten indicators having acid strength values *pKa* in the range from 0.8 to 11.1 were selected for the experiment.

3. Results and Discussion

To analyze the adsorption site concentration of a certain acid strength, three solutions were prepared for each sample and the selected indicator. Transmittances of the solutions were measured with a

spectrophotometer. Based on the obtained results, the concentration of adsorption sites was estimated for each *pKa* value (Figure 1) according to the following equation:

$$Q(pKa) = \frac{C_{ind} \cdot V_{ind}}{A_0} \cdot \left| \frac{|A_1 - A_0|}{S_1} \pm \frac{|A_2 - A_0|}{S_2} \right|, \quad (1)$$

where C_{ind} is the concentration of the indicator in the solution, V_{ind} is the volume of the indicator solution, S_1 and S_2 are the areas of the studied nanomaterials, A_0, A_1, A_2 are the corresponding absorption factors based on the calculated transmittances with a spectrophotometer.

The analysis of obtained histograms showed that Brönsted acidic sites prevail quantitatively on the surface of synthesized SnO_2-based nanomaterials (Figure 1, a). The total number of adsorption sites on the surface of nanomaterials decreased after plasma treatment due to the formation of defects, being a result of ionic bombardment, and due to thermal action (Figure 1, b).

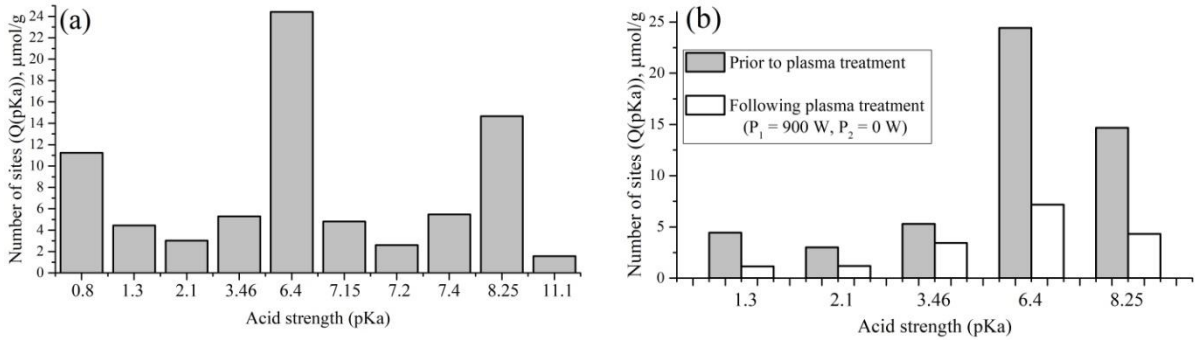

Figure 1 (a, b). Distribution of adsorption sites on the surface of SnO_2-based nanomaterials prior to (**a**) and following (**b**) nitrogen plasma treatment

Degradation in the structure of nanomaterials at high plasma power P_1 values is confirmed by the data of scanning electron microscopy (SEM) (Figure 2). These results are consistent with the dependences of the concentration of adsorption site, having acid strength (pKa = 6.4), on the parameters of plasma treatment (Figure 3, a).

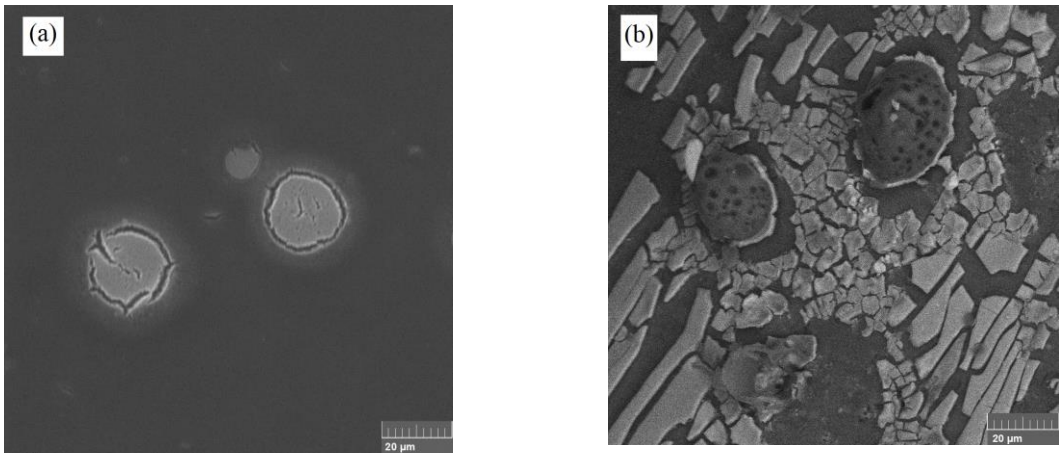

Figure 2 (a, b). SEM images of the surface of SnO_2-based nanomaterials prior to (**a**) and following (**b**) nitrogen plasma treatment

The analysis of the results in Figure 3, b showed that the simultaneous use of inductively coupled plasma source (P_1 > 600 W) and supplementary high-frequency source leads to a noticeable decrease in the number of adsorption sites, located on the surface of SnO2-based nanomaterials.

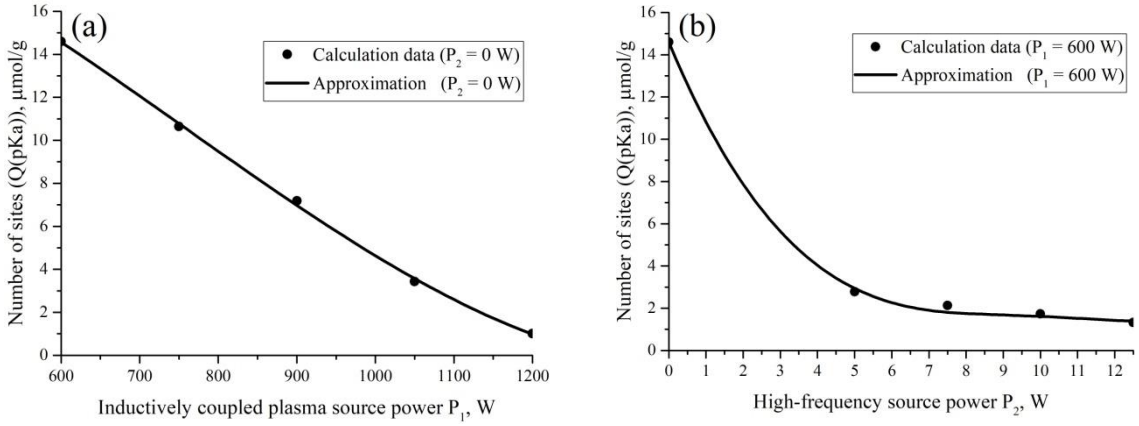

Figure 3 (a, b). Dependence of the concentration of adsorption site, having acid strength (*pKa* = 6.4), on the power of an inductively coupled plasma source (**a**), and on the power of a high-frequency source (**b**)

4. Conclusions

Nitrogen plasma treatment of SnO_2-based nanomaterials leads to modification of their surface properties due to partial destruction of quasi-spherical aggregates (Figure 2, a), typical for nucleophilic increase in sol-gel systems. This ensures the formation of supplementary macro-, meso-, and micropores in nanomaterials (Figure 2, b), increasing their specific surface area. With high-power plasma sources (P_1 > 600 W), the overall integrity of the structure of nanomaterials is violated due to the effect of high-energy ions.

Acknowledgments

The study was carried out with the financial support of the Russian Foundation for Basic Research (projects No. 20-38-90155 and No. 19-08-00924 A).

References

[1] Shikunov D A, Simakov V V, Sinev I V, Shcherbakova E A, Timoshenko D A 2019 *Physical and chemical aspects of the study of clusters, nanostructures and nanomaterials* **11** 665

[2] Sun G, Qi F, Zhang S, Li Y, Wang Y, Cao J, Bala H, Wang X, Jia T, Zhang Z 2014 *Journal of Alloys & Compounds* **617** 192

[3] Ellert O G, Tsodikov M V, Novotortsev V M 2010 *Russian Chemical Reviews* **79** 693

[4] Dao H T, Makino H 2019 *Materials Science in Semiconductor Processing* **96** 46

[5] Sigaev A P, Averin I A, Karmanov A A, Pronin I A, Yakushova N D 2020 *Physical and chemical aspects of the study of clusters, nanostructures and nanomaterials* **12** 162

[6] Danilova M N, Pylinina A I, Platonov E A, Yagodovskii V D 2015 *Russian Journal of Physical Chemistry* **89** 1339

[7] Pronin I A, Goryacheva M V 2013 *Surface and Coatings Technology* **235** 835

Growth of bulk $(Al_xGa_{1-x})_2O_3$ crystals from melts using the Czochralski method and study of their physical properties

V A Spiridonov[1], D I Panov[1], D A Zakgeim[1], A V Kremleva[1], D A Bauman[1], A E Romanov[1], V E Bougrov[1]

[1]ITMO University, St. Petersburg, 197101, Russia.

Abstract. The $(Al_xGa_{1-x})_2O_3$ crystals with different aluminum concentrations were obtained by the Czochralski method. The optical properties of the obtained crystals were investigated and the aluminum content in the initial melt and the obtained crystals was compared. It is shown that with increasing aluminum content in the crystal, the width of its bandgap zone increases.

1. Introduction

Numerous research groups around the world are currently developing new semiconductor materials. One of such promising materials is gallium oxide. β-Ga_2O_3 monocrystal is a wideband semiconductor with a bandgap of ~4.8 eV, high breakdown voltage (>8 MV/cm) and relatively high electron mobility (~150 cm2/Vs) [1-3]. The first mentions of successful fabrication of gallium oxide devices with record characteristics began to appear in the literature. For example, in [4] the authors report the creation of a MOSFET with a breakdown voltage above 1000V. However, monocrystals of solid solutions of gallium and aluminum oxides $(Al_xGa_{1-x})_2O_3$ are more promising materials for the component base of power electronics because of high breakdown voltage (up to 10 MV/cm depending on solid solution composition) and wider band gap zone (bandgap width of Al_2O_3 is ~8.8 eV) [5]. One way to create such a semiconductor is to add aluminum oxide to the initial β-Ga_2O_3 charge and form a ternary compound $(Al_xGa_{1-x})_2O_3$, that is, a solid solution of Al_2O_3 and Ga_2O_3. By adding aluminum to gallium oxide in different concentrations, it is possible to control the value of the bandgap of the crystal, without significant changes in the technology of its production.

2. Experiments and results

In this work, $(Al_xGa_{1-x})_2O_3$ crystals were obtained by the Czochralski method in the Nika-3 growth unit. Al_2O_3 and Ga_2O_3 powders of 5N purity were used as starting materials. An iridium crucible was used for melt. The samples were synthesized in a closed system with a constant atmosphere. The atmosphere was a mixture of 95% argon and 5% oxygen. As a seed, crystals $(Al_xGa_{1-x})_2O_3$ grown on sapphire seed were used.

Crystals were obtained from gallium oxide melts with the addition of varying amounts of aluminum oxide. Flat-parallel samples with a thickness of 1 mm were obtained by cleaving the crystals and their optical properties were studied. The composition of the samples was measured by energy-dispersive X-ray spectral microanalysis (EDS).

As a result of measurements, it was found that the samples are transparent in the middle UV, visible and near IR optical ranges. The bandgap width was 4.5 eV for pure β-Ga2O3, 4.7 eV for the sample containing 7.5% aluminum oxide in the melt, and 5 eV for the sample containing 15% aluminum

oxide in the melt. According to EDS data in the sample containing 7.5% aluminum oxide in the melt, the atomic ratio was as follows: O2 - 59.31%, Al - 4.63%, Ga - 36.06%. For a sample with 15% aluminum in the melt: O2 - 63.68 Al - 9.11 Ga - 27.22. For pure gallium oxide: O2 - 53.67, Ga - 46.33. Thus, it was shown that with increasing aluminum oxide content in the crystal the width of its bandgap increases.

Acknowledgments
This work was supported by the Russian Science Foundation, Project No. 19-19-00686.

References
[1] Galazka Z 2018 *Semicond. Sci. Technol.* **33** 113001
[2] Stepanov S I, Nikolaev V I, Bougrov V E and Romanov A E 2016 *Rev.Adv.Mater.Sci.* **44** 63–86
[3] Pearton S J, Yang J, Cary P H, Ren F, Kim J, Tadjer M J and Mastro M A 2018 *Applied Physics Reviews* **5** 011301
[4] Hu Z, Nomoto K, Li W, Tanen N, Sasaki K, Kuramata A, Nakamura T, Jena D and Xing H G 2018 *IEEE Electron Device Letters* **39** 869–72
[5] Santos R C R, Longhinotti E, Freire V N, Reimberg R B and Caetano E W S 2015 *Chemical Physics Letters* **637** 172–6

MBE growth of AlGaAs/Ge/AlGaAs core-shell nanowire

A N Terpitskiy[1], I V Ilkiv[1,2], K P Kotlyar[1,2], D A Kirilenko[3], G E Cirlin[1]

[1]Alferov University, St. Petersburg, 194021, Russia
[2]St. Petersburg State University, St. Petersburg, 199034, Russia
[3]Ioffe Institute, St. Petersburg 194021, Russia

E-mail: terpiczkij@mail.ru

Abstract. Ge nanostructures, such as quantum dots, wires and wells, formed in the hexagonal phase can be used as light emitters in the telecommunication wavelength region. In this work, AlGaAs/Ge/AlGaAs quantum well heterostructures were synthesized by molecular beam epitaxy using AlGaAs nanowires as templates. Structural characterization of the samples obtained showed the formation of core-shell AlGaAs/Ge/AlGaAs nanowires with ultrathin germanium layer having a hexagonal crystal structure. The hexagonal phase of Ge was also confirmed by Raman spectroscopy.

1. Introduction

Low-dimensional Ge-base nanostructures, such as quantum dots, wires and wells, are sustain great interest over the years due to the possible application in nano- an optoelectronics. For instance, tensile-strained Ge/SiGe layers [1] and GaAs/Ge/GaAs heterostructures with an essentially thin germanium layer (< 2 nm) [2] are promising candidates for creation of light emission devices. However, the synthesis of such structures still remains a difficult task [1, 2]. In turn, one promising approach may be based on the use of thin germanium layers synthesized in the hexagonal phase. Unlike cubic, hexagonal Ge has been predicted to have a direct band gap structure [3]. Meanwhile, a new promising approach to the growth of hexagonal Ge layers has recently been demonstrated using semiconductor nanowires as templates [4].

2. Experimental and results

In this study, we present the results on the formation of AlGaAs/Ge/AlGaAs core-multishell nanowires. The structures were synthesized by molecular-beam epitaxy using gold as catalysts. After the AlGaAs nanowire formation, Ge was deposited, after which the cover layer was formed. The morphological and structural properties of the obtained samples were studied by scanning and transmission electron microscopies, and also by Raman spectroscopy. The nanowires obtained were found to have pencil-like shape with a diameter of 70 nm. TEM studies of nanowires revealed that a 2-3 nm thick germanium layer was formed between AlGaAs-core and capping layer. It was shown that the Ge and the AlGaAs layers have a hexagonal crystal structure. In addition, the hexagonal Ge phase was also confirmed by Raman spectroscopy.

Acknowledgments

This work was financially supported by the Ministry of Science and Higher Education of the Russian Federation (0791-2020-0003).

References

[1] Gatti E, Isa F, Chrastina D, Müller Gubler E, Pezzoli F, Grilli E and Isella G 2014 *Journal of Applied Physics* **116** 043518

[2] Aleshkin V Ya, Dubinov A A, Kudryavtsev K E, Rumyantsev V V, Tonkikh A A, Zakharov N D and Zvonkov B N 2014 *Journal of Applied Physics* **115** 043512

[3] Rödl C, Furthmüller J, Suckert J R, Armuzza V, Bechstedt F and Botti S 2019 *Phys. Rev. Materials* **3** 034602

[4] Zeng H, Yu X, Fonseka A, Gott J, Tang M, Zhang Y, Boras G, Xu J, Sanchez A M and Liu H 2018 *Nano Lett.*, **18(10)** 6397-6403

Conformality of a-Si:H deposited by low temperature PECVD for solar cells application

A V Uvarov[1,2], A I Baranov[1,2], I A Morozov[1,2], D A Kudryashov[1,2], A A Maximova[1,2], E A Vyacheslavova[1,2], A S Gudovskikh[1,2]

[1]St. Petersburg Academic University, St. Petersburg 194021, Russia
[2]St. Petersburg Electrotechnical University "LETI", St. Petersburg 197376, Russia

lumenlight@mail.ru

Abstract. This article is devoted to the study of the preparation of amorphous silicon by plasma enhanced chemical vapour deposition at 250 °C on developed surfaces with a high aspect ratio. The resulting structures were investigated by scanning electron microscopy.

1. Introduction

Amorphous silicon is currently used in such areas of the semiconductor industry as the creation of solar cells, thin-film transistors and TFT displays. PECVD deposition method allow one to obtain best quality amorphous silicon.

This deposition method allows one to obtain thin layers of amorphous silicon at temperatures of 150-250 °C, which effectively passivates defects on the surface of silicon substrates. Most solar cells are manufactured using a-Si:H/c-Si heterojunction. However, to reduce the amount of reflected light from solar cells, a textured surface of the substrates is required. In this case, the larger the aspect ratio (height/width) in the texture, the less will be the reflection loss and the higher the resulting efficiency of the solar cell [1]. At the moment, it is of interest to study the formation of thin layers of amorphous silicon on textured silicon substrates with a high aspect ratio.

2. Experiment

In this work, test structures of a developed surface with different aspect ratios were formed by photolithography and plasma-chemical cryogenic etching. The process of plasma-chemical deposition of amorphous silicon was carried out at the temperature of 250 °C. The resulting structures were studied by scanning electron microscopy.

Acknowledgments

This work was supported by the RFBR project № 21-58-46001

References

[1] Repo, Päivikki, Antti Haarahiltunen, Lauri Sainiemi, Marko Yli-Koski, Heli Talvitie, Martin C. Schubert, and Hele Savin 2013 *IEEE Journal of Photovoltaics* **3** (1) 90–94.

Self-consistent modeling of MBE self-catalyzed GaAs nanowire growth

S V Fedina[1], A A Koryakin[2], V V Fedorov[1], G A Sapunov[1] and I S Mukhin[1]

[1] Nanotechnology Research and Education Centre of the Russian Academy of Sciences, Alferov University, Khlopina 8/3, 194021 St. Petersburg, Russia
[2] St. Petersburg State University, St.Petersburg 199034, Russia

e-mail: fedina.serg@yandex.ru

Abstract: Self-catalyzed GaAs nanowires are synthesized by molecular beam epitaxy at various arsenic fluxes and growth temperatures. The growth of GaAs nanowires is simulated taking into account the kinetics of material transport in the catalyst droplet. As a result, the re-evaporation coefficient of arsenic is estimated for the given growth conditions. Calculated nanowire growth rate is in satisfactory agreement with the experimental data.

1. Introduction

Epitaxial arrays of III-V semiconductor nanowires (NW) are a promising material for modern optoelectronics. When forming NW by the vapor-liquid-solid (VLS) mechanism, the most extensive possibilities for controlling the morphology of NW arrays are opened when using catalytic particles of foreign materials, usually an Au droplet, pre-deposited on the growth substrate. However, the catalyst material can be embedded into the lattice of a growing NW, resulting in deep-level defects that reduce the lifetime of charge carriers and increase the probability of non-radiative recombination. The NW formation by a self-catalytic mechanism, when using an element of the III-group of the NW itself as a catalyst (namely, Ga for GaAs) excludes contamination of III-V compounds, but imposes serious restrictions on the range of possible growth parameters and, as a result, the morphology of the formed NW's arrays [1].

2. Experiment and theory

Epitaxial GaAs NWs arrays were synthesized on the vicinal Si(111) substrate with a 4° miscut orientation in [11$\bar{2}$] direction using the PA-MBE Veeco GEN-III machine with Ga effusion cell and valved arsenide cracker for As_4 direct molecular flux. Before loading into the MBE chamber, the silicon substrates were cleaned using a modified Shiraki method. The morphology of synthesized GaAs NWs was studied with scanning-electron microscope (SEM) (Zeiss SUPRA 25-30-63).

For the theoretical assessment of the GaAs NW growth rate, the model proposed in [2] within the "As-only" approach [3] is used. In this model, the nucleation-limited growth rate which is given by the Zeldovich nucleation rate times the surface area of the top NW facet is considered. The growth rate of 2D islands on the NW top facet (see figure 1) limited by the diffusion flux of arsenic into the droplet is obtained as a function of droplet composition. Self-consistent modeling is achieved by considering the material balance equation for species in the droplet.

3. Results and discussion

The re-evaporation coefficient of arsenic that characterizes the arsenic evaporation flux from the substrate and the NW sidewalls used as the sole fitting parameter. The obtained value of this coefficient (3.0), as well as the value of the conversion factor (2.27×10^{24} m^{-2} s^{-1} $Torr^{-1}$) linking the beam equivalent pressure and the arsenic flux are consistent with the data obtained by Glas et al. [3]. The calculation is performed at the interphase energy of the GaAs island side facet (0.309 J m^{-2}) [2]. Also, the dependences of the growth rate on the group V fluxes and the growth temperature for epitaxial arrays of self-catalyzed GaAs NWs are calculated. As a result, the growth rate and the height of self-catalyzed GaAs NWs are predicted by the model.

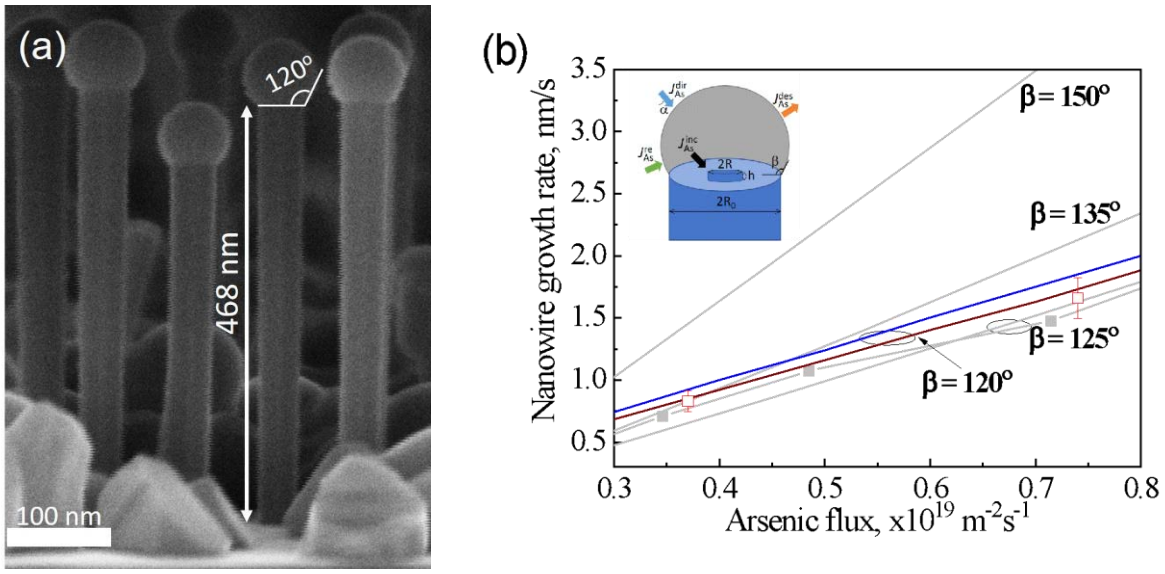

Figure 1. a) cross-sectional SEM image of GaAs NW array, b) calculated (lines) and experimental (dots) dependencies of NW growth rate on arsenic flux (red and blue lines are dependencies simulated at 873 K and 843 K; grey lines are dependencies obtained in [2,3] at 883 K); schematic representation of self-catalyzed VLS growth of GaAs NW is shown in the inset.

Sample	Calculated length, mm	Measured length, mm
S1	3.168	2.998±0.3
S2	0.552	0.502±0.04

Table 1. Nanowire length calculated with the model and measured in the experiment.

We found that the growth rate obtained in the model is consistent with the real growth rate of synthesized GaAs NWs with an accuracy of about 80-85 percent.

Acknowledgments

The nanowire samples were grown and characterized under the support of the Ministry of Science and Higher Education of the Russian Federation (project No. 0791-2020-0005). Nanowire growth modeling was performed under financial support of the Russian Science Foundation under grant 19–72–30004.

References

[1] Dubrovskii, V G, Cirlin, G E, Ustinov V M 2009 *Semiconductors*,**43**, 1539

[2] Koryakin A A, Kukushkin S A 2021 *Phys. Status Solidi B*, 2000604 (*in print*)

[3] Glas F, Ramdani,M R, Patriarche G, Harmand J C 2013 *Phys. Rev. B*, **88**, 195304

Effect of Yb^{3+}doping level on the structure and spectroscopic properties of ZnO optical ceramics

E Gorokhova[1], I Venevtsev[2], I Alekseeva[1], A Khubetsov[1,*], O Dymshits[1], L Basyrova[3], E Oreschenko[1], S Eron'ko[1], F Muktepavela[4], K. Kundzins[4] A Zhilin[1], and P Loiko[3]

[1]S.I. Vavilov State Optical Institute, 36 Babushkina St., 192171 St. Petersburg, Russia
[2]Peter the Great St. Petersburg Polytechnic University, 29 Polytechnic St., 195251, St. Petersburg, Russia
[3]Centre de Recherche sur les Ions, les Matériaux et la Photonique (CIMAP), UMR 6252 CEA-CNRS-ENSICAEN, Université de Caen Normandie, 6 Boulevard du Maréchal Juin, 14050 Caen Cedex 4, France
[4]Institute of Solid State Physics, University of Latvia, 8 Kengaraga St., LV1063, Riga, Latvia

*e-mail: khubezov@gmail.com

Abstract. Optical ceramics of zinc oxide (ZnO) with hexagonal structure doped with 0.6 –5.0 wt% Yb were fabricated by uniaxial hot pressing of commercial oxide powders at 1180 °C in vacuum. They were characterized by X-ray diffraction, SEM, EDX, X-ray and optical spectroscopy. Yb^{3+} ions are present in C-type Yb_2O_3 crystals and located at the ZnO grain boundaries as evidenced by X-ray diffraction, SEM, EDX and X-ray fluorescence studies.

1. Introduction

Zinc oxide (ZnO) is a direct wide band gap semiconductor with unique optical and luminescent properties coupled with high radiation tolerance. Ytterbium (Yb^{3+}) doped ZnO nanostructures and films demonstrate efficient energy transfer between the defect states in the ZnO structure and the doping Yb^{3+} ions [1], making them promising for application as down-conversion layers for enhanced solar cells [2]. In this work, the effect of Yb doping level on the structure, optical and spectral-luminescent properties of ZnO optical ceramics was studied for the first time.

2. Fabrication of ceramics

ZnO optical ceramics with Yb content of 0.6– 5.0wt% were fabricated from commercial reagent grade ZnO and Yb_2O_3 powders by hot pressing in vacuum at a temperature of 1180 °C. After polishing, ceramic disks with a slight grey coloration had a diameter of 25 mm and a thickness of about 0.5 mm.

3. Results and discussion

The XRD patterns of Yb:ZnO ceramics evidence crystallization of hexagonal (sp. gr. $P6_3mc$) phase of ZnO with wurtzite structure and Yb_2O_3 with a cubic (sp. gr. $Ia\bar{3}$) bixbyite structure, Fig. 1(a). The unit cell parameters of ZnO are a = 3.251 Å and c = 5.202 Å. They do not change with increasing the Yb content indicating that Yb^{3+} ions do not enter the ZnO structure. For Yb_2O_3 crystals, a = 10.441 Å and their size is ~70 nm. The volume fraction of Yb_2O_3in ceramics increases with the Yb content. The EDX mapping indicates that Yb^{3+} ions may also localize at the boundaries of the ZnO grains, Fig. 1(b-d).

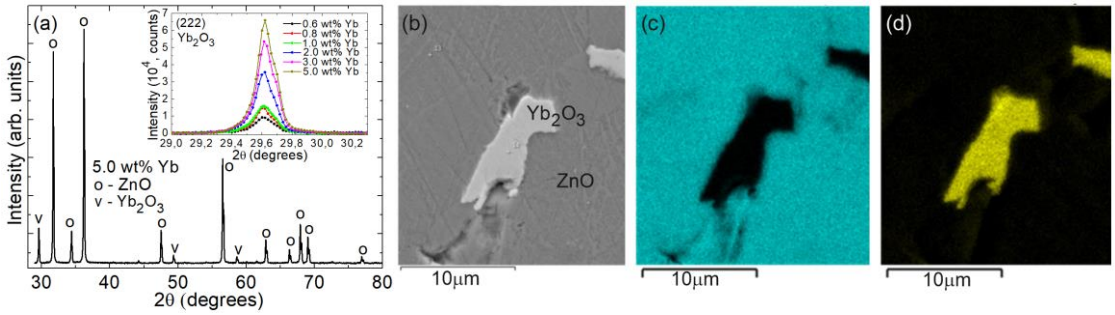

Figure 1(a-d).(a)XRD pattern of 5 wt% Yb:ZnO ceramic, *inset* – a close look at the range of diffraction angles $2\theta = 29.0 – 30.3°$; **(b)** SEM image of the polished and etched surface of the 2 wt% Yb:ZnO ceramic; **(c,d)** EDX element mapping of **(c)**Zn (Lα) and **(d)**Yb (Mα).

The transmission spectra of Yb:ZnO ceramics contain the characteristic Yb^{3+} absorption band due to the $^2F_{7/2} \rightarrow {}^2F_{5/2}$ transition, Fig. 2(a). The maximum value of total transmission in the visible decreases from ~55% to 35% with increasing the Yb content. The addition of Yb also results in the shifts of the UV and IR absorption edges of ceramics, from 0.38 to 0.39 μm and from 4.0 to 2.5-2.7 μm, respectively. The latter effect is assigned to increased concentration of free carriers in ZnO, from 3.1×10^{18} cm^{-3} to $7.4–8.0\times10^{18}$ cm^{-3}. The X-ray luminescence spectrum presents two intense emission bands, Fig. 2(b). The band at ~390 nm is due to the near-band-edge (NBE) transitions. The broad band centered at ~520 nm is the defect luminescence (DL). The intensity of DL for Yb:ZnO ceramics is by order of magnitude weaker than that of undoped ceramic. With increasing the Yb concentration, the NBE intensity increases and saturates for 5 wt% Yb doping. Yb doping accelerates the decay of ZnO luminescence, Fig. 2(c). The luminescence lifetimes of Yb^{3+} ions ($^2F_{5/2}$ state) are about 10 μs, Fig. 2(d).

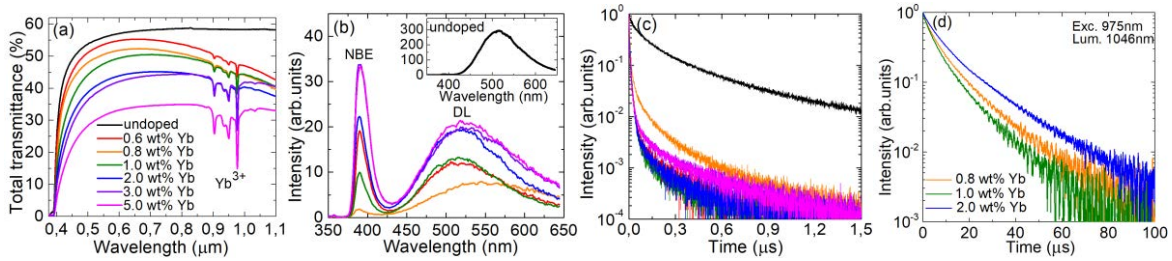

Figure 2(a-d). Spectroscopy of Yb:ZnO optical ceramic:**(a)** total transmission spectra, thickness: 0.5 mm; **(b)** X-ray luminescence spectra; **(c)** X-ray luminescence decay curves; **(d)** luminescence decay curves for Yb^{3+} ions, $\lambda_{exc} = 975$ nm, $\lambda_{lum} = 1046$ nm.

4. Conclusion

Yb:ZnO optical ceramics were fabricated for the first time. They exhibit attractive optical properties indicating ZnO ↔ Yb^{3+} energy-transfer. These ceramics are promising for optoelectronic applications.

Acknowledgment

This work was partly supported by the RFBR (Grant 19-03-00855).

References

[1] Shestakov M, Baranov A, Tikhomirov V, Zubavichus Y, Kuznetsov A, Veligzhanin A, Kharin A, Rösslhuber R, Timoshenko V, Moshchalkov V, 2012 *RSC Adv.* **2** 8783

[2] Balestrieri M, Ferblantier G, Colis S, Schmerber G, Ulhaq-Bouillet C, Muller D, Slaoui A, Dinia A, 2013 *Sol. Energy Mater. Sol. Cells* **117** 363

Hybrid molecules based on fullerene C_{60} and fulgimides - promising molecular switches

A A Khuzin[1], **A R Tuktarov**[1], **A R Tulyabaev**[1], **U M Dzhemilev**[1]
[1]Institute of Petrochemistry and Catalysis of RAS, Ufa 450075, RU

Abstract. The hybrid molecules based on C_{60} fullerene and fulgimides are synthesized for the first time. The experiments show that the resulting hybrid compounds possess photochromism.

Introduction

The main chemists' efforts are to functionalize new nanosized carbon structures to obtain promising materials since the discovery of fullerenes and the elucidation of their structure in subsequent years.
The dynamic and accelerated development of electronic devices leads to a constant increase in requirements for the efficiency of microelectronic components and their production technology. Currently, modern microelectronics is produced at the atomic level, when the typical sizes of transistors are several tens of atomic layers. Further decrease in size of conventional silicon transistors appears to be a great challenge, so that many companies develop actively the alternative technologies. One of the most promising areas is the production of molecular computers based on organic electronics, whose basic element is molecular switches.
The photochromic compounds (hetarylethenes, spiopyrans, spirooxazines, fulgides, and azabenzene) are considered as the most popular molecular switches. We showed previously[1–4] that the hybrid compounds based on a C_{60} fullerene and dithienyletenes (or spiropyrans) undergo reversible phototransformations depending on external factors.
We synthesized new hybrid molecules based on a C_{60} fullerene and fulgimides under the Prato reaction conditions to obtain nanomaterials with adjustable properties.

Results and Discussion

We found that the pyrrolidinofullerenes **1** and **2** are formed after the interaction of azomethine ylides generated in situ from the corresponding aldehydes in the presence of a sarcosine with C_{60} fullerene in 60 and 70% yields, respectively.

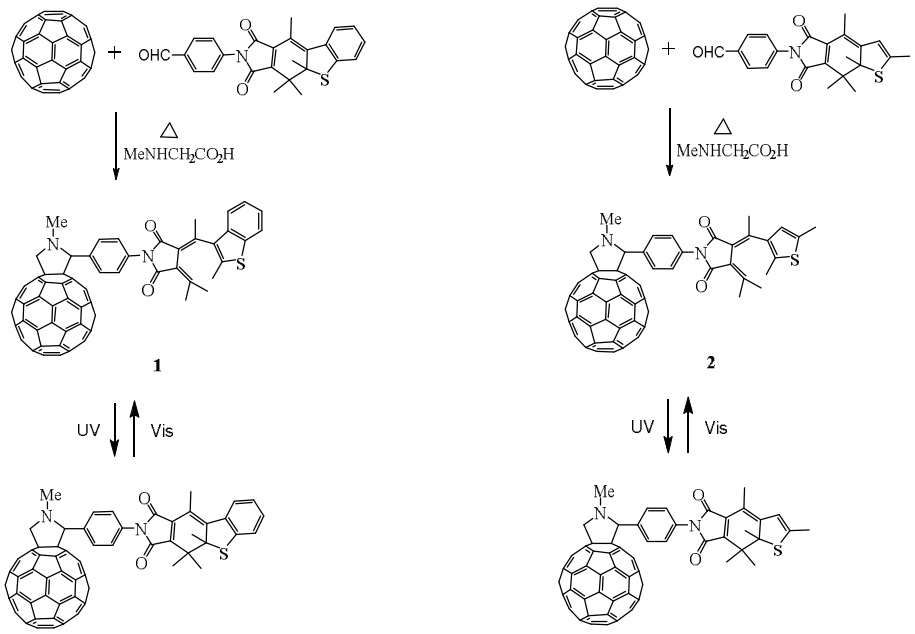

Scheme 1. Synthesis of fulgimides-containing photochromic pyrrolidinofullerenes **1** and **2**.

Preliminary physicochemical studies of the pyrrolidinofullerenes **1** and **2** showed that both hybrid compounds undergo reversible phototransformations.
The synthesized hybrid compounds have been sent to the Photochemistry Center (Russian Academy of Sciences) for a more detailed study of their spectral and kinetic properties.

Acknowledgments
This work was financial supported by the Russian Science Foundation (project no. 19-73-00082)

References

[1] Tuktarov A.R., Khuzin, A.A., Akhmetov A.R., Khalilov L.M., Tulyabaev A.R., Barachevskii V.A., Venediktova O.V., Dzhemilev U.M. *Mendeleev Communications*, 2016, 26, 2, 143-145

[2] Tuktarov A.R., Khuzin, A.A., Dzhemilev U.M. *Mendeleev Communications*, 2019, 29, 2, 229-231

[3] Galimov D.I., Tuktarov A.R., Sabirov D.S., Khuzin A.A., Dzhemilev U.M. *Journal of Photochemistry and Photobiology A: Chemistry*, 2019, 375, 64-70

[4] Khuzin A.A., Tuktarov A.R., Barachevsky V.A., Valova T.M., Tulyabaev A.R., Dzhemilev U.M. *RSC Advances*, 2020, 10, 27, 15888-15892

The influence of temperature and arsenic molecular form at crystallization stage on the InAs nanostructure growth during droplet epitaxy

N E Chernenko, S V Balakirev, M M Eremenko and M S Solodovnik

Institute of Nanotechnologies, Electronics and Equipment Engineering, Southern Federal University, Taganrog 347922, Russia

Email: nchernenko@sfedu.ru

Abstract. In this work, experimental studies of the influence of the arsenic molecular form (di- or tetramers) and substrate temperature on the crystallization of In/GaAs droplet nanostructures during droplet epitaxy have been carried out. We have shown the critical influence of the temperature and form of arsenic on the reproducibility of the characteristics of an array of self-organizing InAs nanostructures during crystallization. We also showed that a decrease in the initial In droplet size has a positive effect on the reproducibility of the parameters of the InAs nanostructures arrays.

1. Introduction

Droplet epitaxy is currently one of the most interesting methods of molecular beam epitaxy due to its capabilities in the formation of semiconductor and hybrid nanostructures. At the same time, despite a number of advantages, the use of this technology is still very limited due to its complexity and a huge number of control parameters [1] especially at the stage of crystallization, when nanodroplets transform into crystalline nanostructures. The goal of this work was experimental study the effect of the arsenic molecular form on the crystallization of indium nanodroplet structures and their transformation into InAs nanostructures during droplet epitaxy.

2. Experiment

For experimental study, we initially formed arrays of In nanodroplet arrays on GaAs(001) substrates using droplet epitaxy technique [1] at effective thicknesses of 1.5 and 3.0 ML and substrate temperature of 150°C and 300°C. Then we exposed obtained samples under identical conditions in equivalent arsenic fluxes at two different cracking zone temperatures of the valve source, providing arsenic supply in the form of dimers (As_2) or tetramers (As_4) and different substrate temperature during crystallization.

3. Results and discussion

Our experimental studies have shown that the crystallization temperature has a crucial effect on InAs nanostructure formation. As it can be seen from Figure 1, decreasing of temperature during crystallization stage from 500°C to 400°C leads to to suppression of separate InAs quantum dot synthesis and the stage-by-stage formation of the nanodots + ring + diffusion disk and diffusion disk (without any dots) systems at lowest sample temperature.

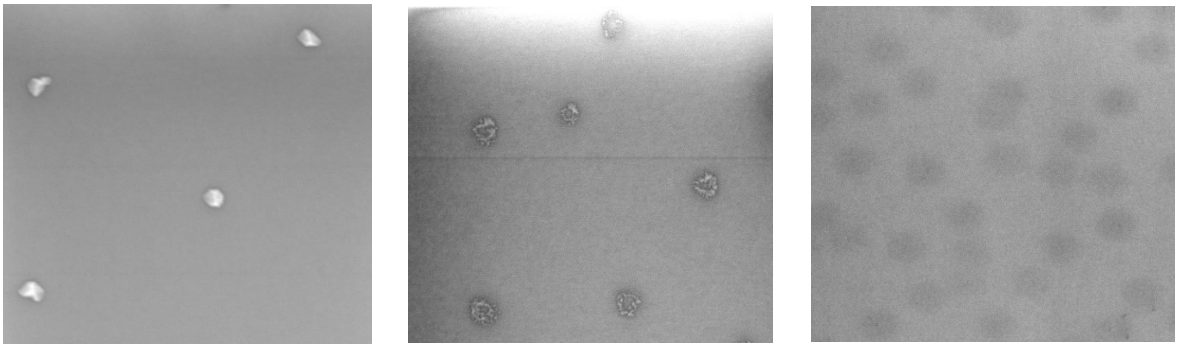

(a) *(b)* *(c)*

Figure 1. SEM images of InAs nanostructures, obtained during crystallization of In nanodroplets using As_4 flux at different temperatures: *(a)* 500°C, *(b)* 450°C, *(c)* 400°C.

The study of arsenic molecular form influence has shown that the use of tetramers (As_4) makes it possible to obtain crystal InAs nanostructures which correlate in their parameters (size, density) with their predecessors – an ensemble of In nanodroplets. This is true over the entire range of temperatures under consideration. It is important to note that with a decrease in the initial size of In droplet nanostructures, the degree of their correlation with the final size of InAs crystal nanostructures increases, and their morphology also improves (Figure 2*a*).

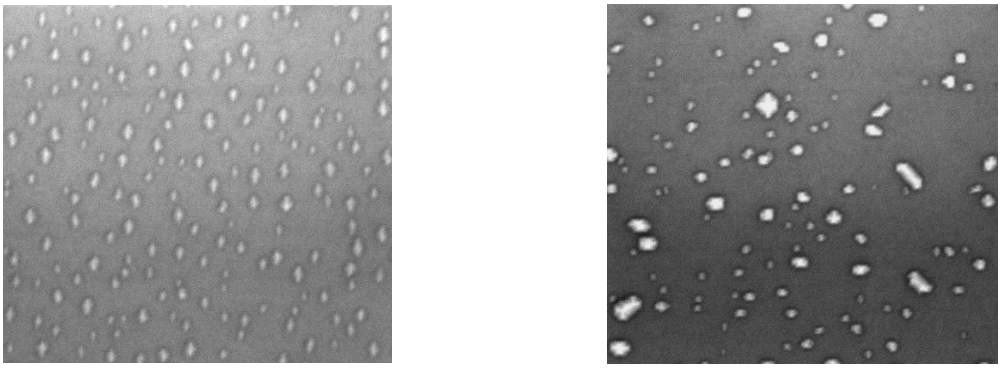

(a) *(b)*

Figure 2. SEM images of InAs nanostructures obtained by crystallization of In droplets in a fluxes of arsenic tetramers *(a)* and dimers *(b)*. Droplet growth mode: growth mode: temperature of 150°C, deposition thickness of 3.0 ML.

In the case of dimers, the situation is completely different. On the one hand, the use of a flux of arsenic dimers leads to the formation of structures with a diameter of 20 – 50 nm in the entire range of considered conditions (Figure 2*b*). At the same time, the correlation between the parameters of the ensemble of metal nanodroplets and the final crystal structures is practically not observed either in density or in size – regardless of the initial density and the initial size of the structures after crystallization, approximately the same picture is observed. The difference between InAs crystal structures obtained using different arsenic forms increases with increasing growth temperature.

Acknowledgments
This work was supported by the Russian Science Foundation Grant No. №19-79-10099.

References

[1] Balakirev S V, Solodovnik M S, Eremenko M M, Chernenko N E and Ageev O A 2020 *Nanotechnology* **31** 485604

Effect of wet chemical treatment on the properties of GaAs FIB-modified surface

N A Shandyba, N E Chernenko, J Y Zhityaeva, O I Osotova, M M Eremenko, S V Balakirev and M S Solodovnik

Institute of Nanotechnologies, Electronics and Equipment Engineering, Southern Federal University, Taganrog 347922, Russia

Email: shandyba@sfedu.ru

Abstract. We present the results of studies of the effect of wet chemical treatment on the properties of a GaAs surface modified by a gallium focused ion beam. Our studies based on results of AFM, KpAFM and Raman spectroscopy measurements have shown that, during wet chemical treatment, the damaged areas disappear completely in the case of low accelerating voltages and small doses of ions. At the same time, large accelerating voltages lead to the formation of extended damaged regions, the complete removal of which requires a longer treatment.

1. Introduction

Despite active research recently, the problem of positioning self-organizing nanostructures (quantum dots, nanowires, etc.) is still urgent. The complexity of solving this problem is largely due to the fact that the epitaxial synthesis of nanostructures is carried out on surfaces modified by various methods, which sharply increases the requirements for surface quality, especially in terms of defectiveness and the presence of impurities. This requires the development of methods for the pregrowth treatment of modified surfaces, which would improve their quality for subsequent epitaxial synthesis. This is very important for obtaining electrically and optically active nanostructures.

In this paper we present the results of studies of the effect of selective wet etching on the properties of GaAs (001) surfaces modified by the Ga^+ focused ion beams (FIB).

2. Experiment

For experimental studies we formed regular arrays of local pits on the GaAs (001) surface (epi-ready substrate) using by the FIB technique at various mode of modification. The accelerating voltage of the ion beam was varied from 10 to 30 keV, the beam current was varied in the range from 0.3 to 10 pA, the number of passes was varied in the range from 1 to 300. After that, the samples were treated in an HCl solution for 1, 2, and 3 min. Then all the samples, including the control sample (with only FIB modification), were examined by AFM, Kelvin probe AFM (KpAFM) and Raman spectroscopy.

3. Results and discussion

The results of the AFM study showed that an increase in the accelerating voltage does not lead to any significant changes in morphology (Figure 1) - the depth of the pits for the limiting modes is comparable (30 – 35 nm). However, after wet chemical etching, the character is different. At low voltages, the

surface surrounding the modification point is etched, which may be associated with more intense ion scattering in the near-surface region. At the same time, at 30 keV, an increase in the pit depth is observed, which may be associated with an increase in the penetration depth of Ga^+ ions into the GaAs substrate.

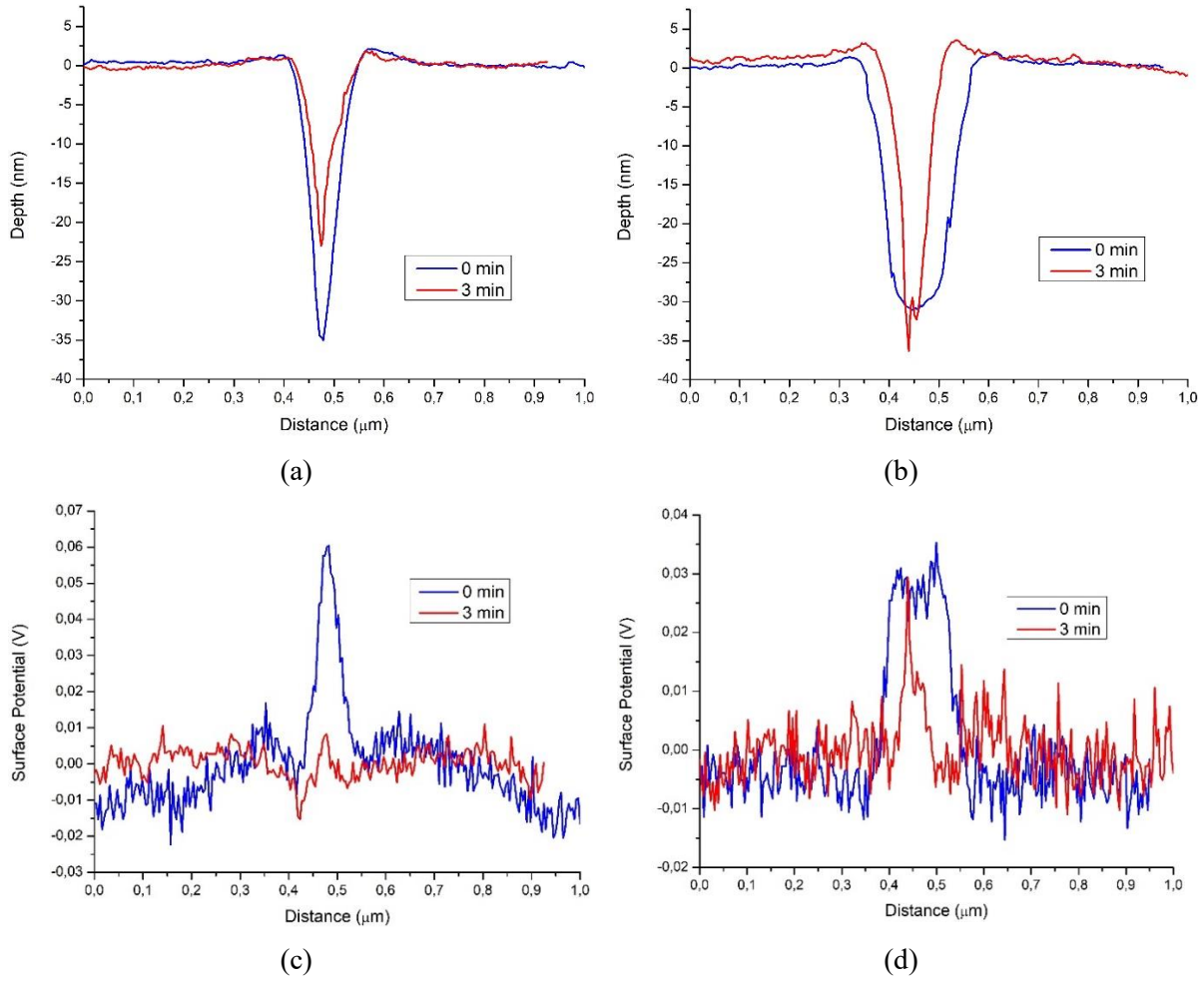

Figure 1. AFM profiles of GaAs surface morphology (a, b) and of potential distribution (c, d) for samples before (0 min) and after wet chemical treatment (3 min) obtained at different FIB-modes: 10 keV, 0.3 pA (a, c) and 30 keV, 10 pA (b, d).

Analysis of the surface potential distribution by the KpAFM showed that in the case of low accelerating voltages, the embedded Ga^+ ions are localized at the near surface layer, which leads to higher surface potential values (+0,06 V) in comparison with the points formed at higher voltages (+0,03 V), when ions are distributed over a larger volume of the substrate, but with a lower density (Figure 1, c, d). This leads to the fact that after wet chemical treatment in areas obtained at low accelerating voltages and implantation doses, potential peaks disappear, while at points with a high accelerating voltage, the potential value practically does not change. The KpAFM results are in good agreement with the Raman spectroscopic data.

Acknowledgments
This work was supported by the Russian Science Foundation Grant No. №19-79-10099 and by Ministry of Science and Higher Education of the Russian Federation; the state task in the field of scientific activity No. 0852-2020-0015.

Study of electrophysical and resistive switching parameters of nanocrystalline vanadium oxide films

I A Shikhovtsov[1], **I S Ugrumov**[1], **R V Tominov**[1], **V A Smirnov**[1]
[1]Institute of Nanotechnologies, Electronics and Electronic Equipment Engineering, Southern Federal University, Taganrog, 347922, Russia
shihovcov@sfedu.ru

Abstract. We have experimentally studied the oxygen pressure on the electrophysical parameters of vanadium oxide films made by pulsed laser deposition technique. It is shown that an increase in an oxygen pressure from 3×10^{-4} Torr to 3×10^{-2} Torr leads to a decrease in the electron concentration of vanadium oxide from $(1.96\pm0.24)\times10^{17}$ cm^{-3} to $(0.25\pm0.06)\times10^{17}$ cm^{-3} and an increase in the resistivity from 16.41±7.33 Ω·cm to 652.74±71.84 Ω·cm. Resistive switching from HRS to LRS was observed at +3.5±0.2 V, and from LRS to HRS at -1.2±0.1 V R_{HRS}/R_{LRS} ratio was about 311. The results can be useful for based on vanadium oxide films neuromorphic systems manufacturing.

1. Introduction

One of the promising directions in the development of science and technology is the creation of neuromorphic systems that are capable of performing complex cognitive tasks for recognizing patterns and predicting various events [1]. One of the methods for the physical implementation of neuromorphic systems is arrays of memristor elements manufactured using crossbar technology. There are several types of memristors, such as ferroelectric memory FeRAM, magnetoresistive memory MRAM, phase change memory PRAM, resistive ReRAM, among which the latter stands out for its low power consumption, as well as for the presence of the multibit property, which is essential when creating artificial intelligence devices. The ReRAM operation mechanism is based on the effect of resistive switching – a change in the electrical resistance of a thin oxide film between the high-resistance HRS and low-resistance LRS states under the influence of an external electric field. The effect of resistive switching is manifested by many metal oxides (TiO_2, ZnO, TaO_x, MnO_x), among which vanadium oxide (VO_x) produced by pulsed laser deposition (PLD) stands out [2]. However, the manufacture of ReRAM elements based on vanadium oxide films is currently limited by the lack of systematic results of studying the influence of the control parameters of the pulsed laser deposition method on their electrophysical parameters, as well as studying the effect of resistive switching, which is the purpose of this work.

2. Experiment details

VO_x films were fabricated using a Pioneer 180 pulsed laser deposition system (Neocera Co., USA) equipped with a KrF excimer laser with a wavelength of 248 nm and an energy of 200 mJ. Silicon wafers with (100) crystallographic orientation were used as substrates. Titanium nitride (TiN) 50.2±11.6 nm thick bottom electrodes were formed using PLD at the following conditions: substrate temperature 800 °C, number of pulses 12 000, frequency 10 Hz, argon pressure 1 Torr. To study the effect of oxygen pressure O_2 on the electrophysical parameters of VO_x, five samples were prepared on

TiN/Si under the following conditions: substrate temperature 700 °C, laser frequency 10 Hz, number of pulses: 10 000. The samples were made at different O_2 pressures from 3×10^{-4} Torr to 3×10^{-2} Torr. The electrophysical parameters of vanadium oxide films were studied using an Ecopia HMS-3000 Hall effect system (Ecopia Co., Anyang, Korea). Based on the obtained results, the dependences of electron concentration (n_e) and film resistivity (ρ) on oxygen pressure were established (figure 1a).
The resistive switching effect in VO_x films was studied using a Keithley 4200-SCS semiconductor parameter analyzer (Keithley Instruments, USA) and an EM-6070A submicron probe system (Planar, Republic of Belarus). TiN bottom electrode was grounded, W probe with diameter about 80 nm was used as the top electrode. The compliance current was set to 10 mA to avoid thermal breakdown of vanadium oxide films. As a result, current-voltage (I-V) curves were obtained for the sweep voltage amplitude from -1.5 V to 3.7 V. Read voltage was at 0.75 V.

3. Results and discussion

Figure 1 shows the results of experimental studies of O_2 pressure on the electrophysical properties of VO_x films. It was shown that an increase in the pressure from 3×10^{-4} Torr to 3×10^{-2} Torr leads to a decrease in the electron concentration of vanadium oxide from $(1.96\pm0.24)\times10^{17}$ cm^{-3} to $(0.25\pm0.06)\times10^{17}$ cm^{-3} and an increase in the resistivity from 16.41±7.33 Ω·cm to 652.74±71.84 Ω·cm (figure 1a). This result can be explained by the fact that the n_e in the VO_x is proportional to the concentration of vanadium atoms, which is inversely proportional to the oxygen pressure. The study of the I-V curves was carried out on a sample with a VO_x film with a minimum resistivity obtained in this experiment, which is justified by the search for modes of obtaining oxide films with a minimum power consumption. The results of experimental studies showed that resistive switching from HRS to LRS was observed at +3.5±0.2 V, and from LRS to HRS at -1.2±0.1 V (figure 1b). Wherein R_{HRS} was equaled 114.3±12.5 kΩ, R_{LRS} was equaled 0.4±0.1 kΩ. R_{HRS}/R_{LRS} ratio was about 311.

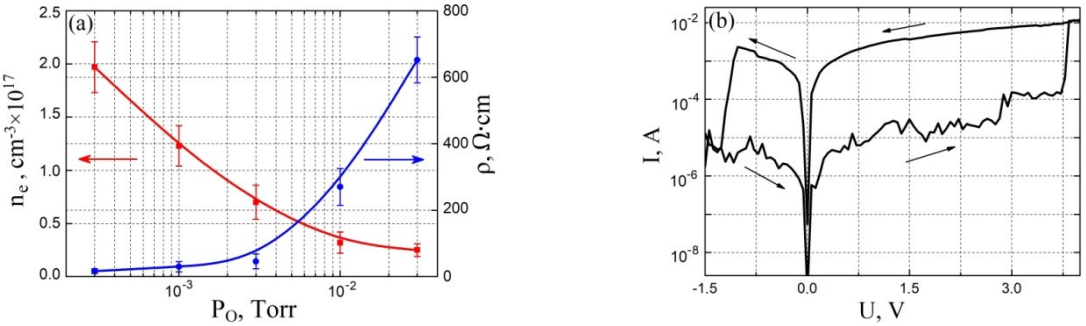

Figure 1(a, b). Study of electrophysics and resistive switching in vanadium oxide films: **(a)** electron concentration and film resistivity dependence on oxygen pressure **(b)** current-voltage characteristic

The results can be useful for based on vanadium oxide film neuromorphic systems manufacturing.

Acknowledgments

The reported study was funded by RFBR according to the research project № 19-29-03041_mk and by grant of the President of the Russian Federation № МК-6252.2021.4.

References

[1] Tominov R V, Vakulov Z E, Avilov V I, Khakhulin D A, Fedotov A A, Zamburg E G, Ageev O A 2020 *Nanomaterials* **10(5)** 1007

[2] Tominov R V, Vakulov Z E, Avilov V I, Khakhulin D A, Polupanov N V, Smirnov V A, Ageev O A 2021 *Molecules* **26(1)** 118

Separation of III-N layers from silicon substrates by KOH etching

K Yu Shubina[1], D V Mokhov, T N Berezovskaya and A M Mizerov

Nanoelectronics Lab, Alferov University, St. Petersburg 194021, Russia

[1] e-mail: rein.raus.2010@gmail.com

Abstract. The III-N/Si(111) epitaxial structures were synthesized by coalescence overgrowth of III-N nanocolumns using the plasma-assisted molecular beam epitaxy (PA-MBE) technique. Structural and electrical properties of these samples were studied. The process of separation of III-N layers from the substrate by wet chemical etching in KOH solution was investigated.

1. Introduction

Wide bandgap semiconductors, especially III-N compounds, are one of the most prospective materials for the development of modern electronics. III-nitrides have unique electrical, optical, mechanical, and other properties, which are important for optoelectronics, high-power and high frequency electronics [1]. Moreover, one of the main advantages of III-N materials is their extremely high thermal and chemical stability. Thus, nitrides can be a promising materials for microelectromechanical systems (MEMS) and devices, which can be used in harsh environments [2]. However, there is a well-known problem for further development of nitride technology associated with the lack of low-cost native substrates. For this reason, commercially viable III-N-on-Si epitaxial structures are attracting more and more attention.

At the same time, there are several fundamental challenges for heteroepitaxy of high quality III-N layers on silicon substrates due to the large lattice mismatch (16.9 % for GaN/Si(111)) and the large difference in their thermal expansion coefficients as well as growth peculiarities of polar III-N materials on non-polar Si(111) substrates [3]. Furthermore, there is a problem of Al, Ga and Si interdiffusion that leads to unintentional doping of III-N layers and silicon [4, 5]. One more problem limiting the direct growth of GaN on silicon substrates is meltback etching, which occurs due to the high solubility of silicon in gallium under growth conditions typical for molecular beam epitaxy (MBE) or metalorganic chemical vapor deposition (MOCVD) [6]. Thus, the crystalline quality of the GaN epilayers grown on silicon is not good enough, and their surface is quite rough. One of the promising approaches to improve the crystalline quality of GaN and AlN grown on Si(111) substrates can be the use of III-N layers, the morphology of which is changing from nanocolumnar to 2D during GaN growth.

In our previous work [7], it was shown that etching of such structures in a KOH solution can lead to the gradual separation of III-N layers from the substrate. At the same time, several damage of the sample surface was observed. In addition, a possibility of overetching of the III-N layer backside was found. This work is a continuation of research on the separation of III-N layers from the substrate by KOH etching.

2. Samples and experimental details

The III-N/Si(111) samples were obtained using a Veeco GEN200 MBE system equipped with a radio frequency (RF, 13.56 MHz) plasma source.

After growth, the samples were studied via scanning electron microscopy (SEM), profilometry, and Hall measurements. The crystallographic polarity of the samples, as well as the separation process of III-N layers from Si(111) substrates, were studied through experiments on KOH chemical etching. To avoid surface damage, the metal mask was formed on the sample surface by e-beam evaporation using BOC Edwards AUTO 500 system.

3. Results and discussion

As it can be seen in figure 1, coalescence of the AlN nanocolumns allows the transition to the growth of AlN layers. This approach can provide good quality AlN (0001) epilayers on silicon. The possibility of AlN separation from the substrate by etching Cr/AlN/NW AlN/Si (111) structures in KOH has been demonstrated (see figure 1, b). Cr film protects the AlN surface from defect-selective etching, helps to avoid cracking and breaking the layer off.

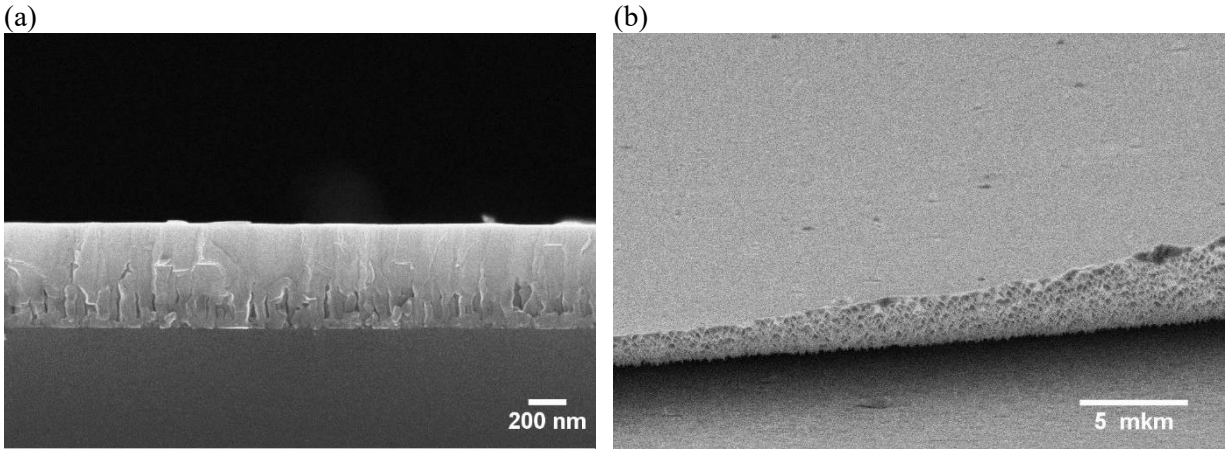

Figure 1. SEM images of (a) as-grown AlN/Si(111) epitaxial structure and (b) Cr/AlN/Si(111) structure after etching in 70 °C KOH solution for t = 5 min.

Acknowledgments

This work was supported by the the Ministry of Education and Science of the Russian Federation (grant № FSRM-2020-0008).

References

[1] Amano H et al 2018 *J. Phys. D: Appl. Phys.* **51** 163001

[2] Rais-Zadeh M, Gokhale V J, Ansari A, Faucher M, Théron D, Cordier Y and Buchaillot L 2014 *J. Microelectromech. Syst.* **23** 1252-71

[3] Lucci I et al 2018 *Phys. Rev. Mater.* **2** 060401(R)

[4] Zheng Y, Agrawal M, Dharmarasu N, Radhakrishnan K and Patwal S 2019 *Appl. Surf. Sci.* **481** 319-326

[5] Wei L et al 2020 *Appl. Phys. Lett.* **116** 232105

[6] Khoury M, Tottereau O, Feuillet G, Vennéguès P and Zúñiga-Pérez 2017 *J. Appl. Phys.* **122** 105108

[7] Shubina K Yu, Mokhov D V, Berezovskaya T N, Nikitina E V, Mizerov A M and Bouravleuv A D 2020 *J. Phys. Conf. Ser.* **1695** 012042

Investigation of Resistive Switching in Ag/Ge/Si(001) Stack by°Conductive Atomic Force Microscopy

V A Vorontsov*, D A Antonov, A V Kruglov, I N Antonov, M E Shenina, V E Kotomina, V G Shengurov, S A Denisov, V Yu Chalkov, D A Pavlov, D O Filatov and O N Gorshkov

Lobachevskii University of Nizhnii Novgorod, 603950 Nizhnii Novgorod, Russia

*vladislav.vorontsov1@gmail.com

Abstract. We report on an experimental study of resistive switching (RS) of individual dislocations in Ag/Ge/Si(001) stack by combined grazing incidence ion sputtering of the Ag electrodes and application of Conductive Atomic Force Microscopy to provide an electrical contact to individual Ag-filled dislocations in the Ge layer. Two types of RS were observed corresponding to two different RS mechanisms: (i) drift of Ag^+ ions inside the dislocation cores and (ii) redox reactions in residual native oxide GeO_x in the etch pits on the Ge surface.

1. Introduction

Recently, resistive switching (RS) attracted much attention due to potential application in application in non-volatile resistive random access memory (RRAM) [1]. RS is a bi-stable (multistable) reversible change in the resistance of a thin dielectric layer sandwiched between two conducting electrodes under a voltage applied to the ones. In most cases, RS mechanism is based on rapture/restoring of conductive filaments (CFs) shortcutting the electrodes. In conducting bridge (CB) RRAM, the CFs consist of metal atoms injected into the dielectric film [2]. Recently, a novel type of CB (Epitaxial RRAM or EpiRRAM) based on a relaxed SiGe/Si(001) epitaxial layers (ELs) was introduced [2]. The authors used dislocations in the SiGe ELs as templates for Ag CFs. This way, an improved stability of the RS parameters was achieved. However, many details of RS mechanism in EpiRRAM remain unclear.
In the present work, we applied Conductive Atomic Force Microscopy (CAFM) to study the RS in individual dislocations in an Ag/Ge/Si(001) EpiRRAM stack for the first time.

2. Experimental

The 190-nm thick Ge EL was grown on n^+-Si(001) by Hot Wire Chemical Vapor Deposition. Prior to deposition of the top 40-nm thick Ag electrodes, the Ge EL was etched to form the pits decorating the dislocations. The Ag-filled etch pits stimulated the drift of Ag^+ ions into the dislocation cores acting as the electric field concentrators [2]. More details on the growth of Ge/Si(001) ELs as well as on the structure and electrical properties of the Ag/Ge/Si(001) stacks can be found elsewhere [3–5].

The CAFM investigations were carried out using NT-MDT® Solver Pro™ insturment. The Ag electrodes were removed by small-angle (3°) grazing incidence low energy (2 keV) Ar^+ ion sputtering except small Ag droplets resident in the etch pits. This way, we measured the cyclic current-voltage (*I–V*) curves of the Ag CFs inside individual dislocations.

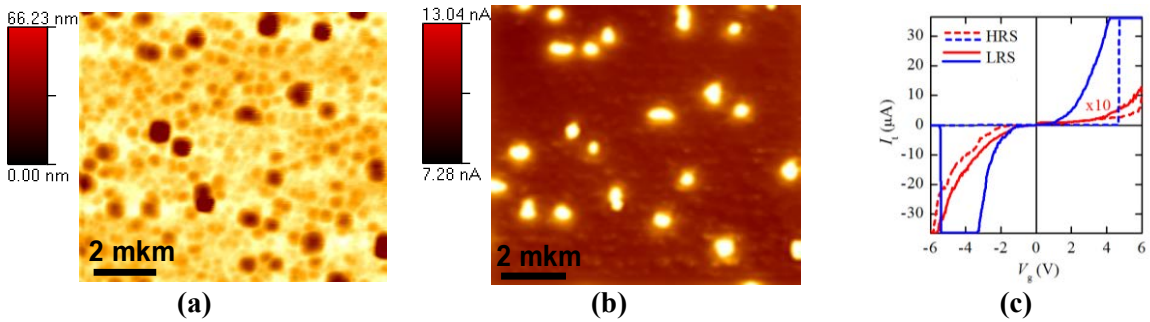

(a) **(b)** **(c)**

Figure 1(a, b, c). Morphology **(a)** and current image (V_g = –4 V) **(b)** of Ge/Si(001) surface after removing Ag; cyclic *I–V* curves of a contact of the CAFM probe to an Ag droplets inside the etch pits typical for two types of RS: for the CB RS (blue curve) and for redox one (red curve) **(c)**.

3. Results and Discussion

Figure 1a presents a topography of the Ge/Si(001) stack after removing the top Ag electrode. Numerous etch pits were observed on the Ge EL surface. Figure 1b presents a current image (a map of the current flowing through the CAFM probe I_t) recorded simultaneously with the topographic image in figure 1a at constant bias voltage V_g = –4 V applied to the CAFM probe relative to the sample. The areas of increased I_t matching the etch pits in figure 1a were associated with the Ag droplets resident inside the etch pits: every time the CAFM tip encounters an Ag droplet, I_t increases due to increased contact area of the Ag droplet to the inner etch pit surface (as compared to the one of the CAFM tip to the Ge EL surface). Note that $V_g < 0$ corresponds to a forward biased Schottky barrier of Ag to intentionally undoped (*p*-type) Ge EL.

Figure 1c shows typical cyclic *I–V* curves $I_t(V_g)$ recorded with the CAFM tip positioned onto the Ag droplets inside different etch pits. The cyclic *I–V* curves demonstrate pronounced hysteresis loops typical for bipolar RS. Two types of the *I–V* curves were observed that was attributed to different RS mechanisms. The wide hysteresis loops (see, for example, the blue curve in figure 1c) was associated with formation and destruction of the Ag CF in individual dislocation beneath the etch pit due to the drift of the Ag^+ ions inside the dislocation core (CB mechanism). The narrower nonlinear *I–V* curves (see, for example, the red curve in figure 1c) were attributed to the reduction/oxidation processes (redox RS mechanism) in the thin residual native oxide GeO_x layer between the Ag droplet and the inner etch pit surface. Similar *I–V* curves were observed when the CAFM probe was positioned onto the Ge EL surface (covered with the native oxide) between the etch pits.

4. Conclusion

The results of the present study demonstrate experimentally a possibility to study the RS in individual dislocations in EpiRRAM stacks combining the grazing incidence ion sputtering of the top metal electrodes and CAFM to provide an electrical contact to individual dislocations. Using this novel technique, we found two different RS mechanisms in an Ag/Ge/Si(001) EpiRRAM stack.

Acknowledgements

The present study was supported by Russian Foundation for Basic Research (19-29-03026).

References

[1] Zhang Y, Wang Z, Zhu J et al. 2020 Appl Phys Rev 7 011308
[2] Choi S, Tan S H, Li Z et. al. 2018 Nature Materials 17 335
[3] Gorshkov O N, Shengurov V G, Denisov S A et al. 2020 Tech Phys Lett 46 91
[4] Filatov D O, Shenina M E, Shengurov V G et al. 2020 Semicond 54 1833
[5] Gorshkov O, Filatov D, Koveshnikov S et al. 2020 J Phys Conference Series 1695 012158

Nanoobject mass measurement using the node displacement of the second harmonic of the nanomechanical resonator

N A Solomonov[1], K N Novikova[1], I V Nadoyan[1], A M Mozharov[1], V A Shkoldon[1,2], I S Mukhin[1,2]
[1] St. Petersburg Academic University, St. Petersburg 194021, Russia
[2] ITMO University, St. Petersburg 197101, Russia

ir.nadoyan@gmail.com

Abstract. Nanomechanical resonators based on amorphous carbon whiskers localized at the top of a tungsten tip have been fabricated and studied. The nanowhiskers were grown using a focused electron beam induced deposition in a scanning electron microscope. The mechanical properties of the nanoresonators based on single carbon nanowires on the tip of metal tips were investigated and the trajectory of their movement was visualized. The first and the second mechanical eigenmodes were used for mass measurements of single particles fixed at the ends of carbon resonators.

1. Introduction

The study of mechanical vibrations of single nanoobjects is of importance from both a fundamental point of view and the fabrication of various sensors [1]. In particular, nanoweights based on nanowhiskers (CNWs) can be used for the study of biological objects and other functional structures [2]. Resonators made of carbon CNWs are lightweight and have eigenmode frequencies in the MHz range, which provides high sensitivity for weighing of micro- and nanoobjects. The growth of NWs from the residual atmosphere of the scanning electron microscope (SEM) chamber was induced by focusing the electron beam of on the tips of tungsten needles. Thus, the use of such additive technology allows to obtain CNWs with tunable geometry.

The presented work is focused on technique for measuring the mass of a nanoobject localized at the end of a carbon nanooscillator of cantilever type by shifting either the first resonance frequency or the position of the node at the second resonance.

2. Sample and experimental setup

The studied sample was an amorphous carbon NWs with the length of 6.84 μm and the diameter of 120 nm, localized on the top of a sharp tungsten needle with the curve radius of about 500 nm (Fig. 1 a). The measured resonance frequencies of the first and second harmonics were 0,95 MHz and 4,5 MHz, respectively. Note, that the propriate CNW dimensions for excitation of two first mechanical eigenmodes are in the range of 5–10 μm in length and 70–300 nm in diameter.

The used resonant sensor of mass consisted of two main parts, namely a generator of mechanical oscillations and the working body of the nanoresonator, which, in our case, was a carbon NW localized at the tip of a sharp tungsten needle. A single carbon NW with predefined sizes was grown by focused electron beam deposition from the residual atmosphere of a FEI Quanta Inspect SEM. A tubular

piezoelectric transducer and a special form signal generator AKIP – 3413/3 were used as the generator of mechanical oscillations. To obtain the amplitude-frequency characteristic (AFC) of the studied resonator, we used the most simple-to-implement method, which was based on the SEM visualization of oscillations at the investigated frequency band. Figure 1 b shows the SEM image of the CNW at the first resonant frequency (950 kHz). At the first eigenmode the CNW movement has a fan-shaped blurred trajectory.

To study this CNW as a mass sensor the additional carbon mass was deposited at the very end of CNW. The insert of Fig. 1 b demonstrates the 118x650 nm object at the end of the studied NW. The localization of the extra mass at the end of the NW led to a shift of the first resonance frequency to a value of 800 kHz, which corresponds to the mass of $5.2 \cdot 10^{-17}$ kg. Note, this value is coincident with the theoretical value of $2.5 \cdot 10^{-17}$ kg calculated taking into account the density of carbon and the size of object. The difference in obtained value can be caused by the fact that the studied object was not the point mass.

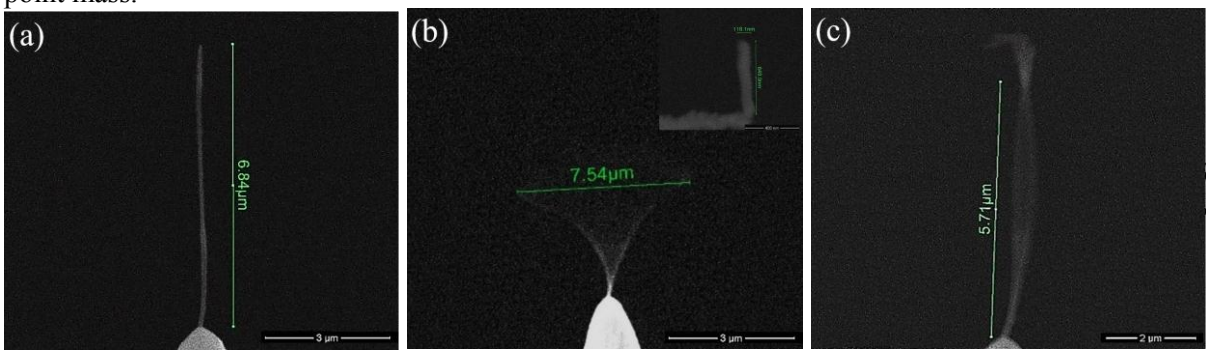

Figure 1 (a, b, c). (a) SEM image of a carbon nanowhisker; (b) SEM image of whisker oscillations in resonance at the first harmonic; (c) SEM image of whisker oscillations at resonance at the second harmonic and localized mass.

The recording of the AFC of the first resonance requires a long exposure of the sample, which leads to an uncontrolled increase in the NW mass and an unwanted shift of the resonant frequency. To overcome this problem an alternative approach of the nanoobject mass measurement should be developed. We propose to study the displacement of the node at the second resonance. Thus, the mass sensing is based on the shift of the position of the stationary point. In that case, it is necessary to apply a "package" of frequencies near the resonance, which greatly reduces the measurement time and, consequently, the value of mass from exposure. In addition, the position of the node depends only on the linear distribution of mass along the NW length [3], which allows to reduce the error associated with the inaccuracy of the NW size determining. It has been shown experimentally that adding the extra mass at the end of NW (see Fig. 3 c) led to a change in the node position of about 300 nm. This value can be easily detected in SEM.

3. Conclusion

High-precision mass sensors based on single carbon NWs, which allow measuring mass in the order of 10^{-17} kg, has been experimentally shown. The advantages of such detectors include high measurement sensitivity and the simplicity of use, as well as low fabrication cost in comparison with other sensors. The proposed method for mass measuring based on the node shift at the second resonance can significantly reduce the unwanted SEM exposure and increase the accuracy of measurements.

References

[1] Mukhin I S, Fadeev I V, Zhukov M V, Dubrovskii V G, Golubok A O 2015 *Ultramicroscopy* **148** 151–157

[2] Lukashenko S Y, Mukhin I S, Komissarenko F E, Gorbenko O M, Sapozhnikov I D, Felshtyn M L, Uskov A V, and Golubok A O 2018 *Phys. Status Solid* A **215** 1800046

[3] Tymoshenko S P, Kh, Y D & Weaver W 1985 **472** *Fluctuations in engineering. Mashinostroenie*

Local structural rearrangements in $Ge_2Sb_2Te_5$ thin films under thermal crystallization.

V Glukhenkaya, A Romashkin, A Yakubov, P Lazarenko, A Sherchenkov
National Research University of Electronic Technology, Zelenograd 124498, Russia

Abstract. Local structure rearrangements in $Ge_2Sb_2Te_5$ thin film during the thermal crystallization were investigated by "in-situ" measurements of the Raman spectra and resistivity temperature dependences. It was shown, that following crystallization amorphous→fcc occurs through the rearrangement of Ge/Sb atoms from tetrahedral and pyramidal coordination into a defective octahedral one, whereas the fcc→hcp transition take place mainly due to local rearrangements of Sb atoms.

1. Introduction

In the current elements of commercial multilevel nonvolatile optical phase change memory (Blu-Ray) and in the developing devices of nanophotonic and integrated optic have been successfully used the thin films of $Ge_2Sb_2Te_5$ (GST) as an active functional layer. It is possible due to the high-rate phase transformations (< 50 ns) from amorphous to crystalline states accompanied by the appearance of the large optical contrast between states [1]. However, the lack of a detailed understanding of the structural transformation mechanisms in GST thin films prevents further optimization and development of the multilevel PCM technology. So, the aim of this work is "in-situ" investigation of the local structural rearrangements in GST225 thin films during the thermal crystallization based on the simultaneous measurement of the temperature dependences of Raman scattering spectra and resistivity.

2. Methods and materials

The amorphous $Ge_2Sb_2Te_5$ thin films (30 nm thickness) were deposited by the magnetron sputtering on the SiO_2 substrates with a planar electrodes of TiN/W/TiN/Al (30/50/15/600 nm). The samples were heated by thermal stage (Linkam) in the temperature range from 25 to 350°C with precise time and heating rate control. Local structural transformations in amorphous GST films before, during and after heating were determined by Raman spectroscopy (Centaur U HR, λ = 532 нм). The temperature dependences of the Raman spectra and resistivity of the GST thin films were obtained during the simultaneously measurements in an Ar atmosphere. Structure analysis before and after thermal exposure was performed by X-ray diffraction method (XRD, Rigaku Smart Lab).

3. Results and discussion

The shape of the Raman spectrum of GST225 changes significantly with increasing temperature **(Fig. 1, a)**. The spectra with the most different shape at 25°C, 185°C and 350°C, corresponding to the amorphous, fcc- and hcp-phases, respectively, were decomposed on the 7 main peaks by the Gaussian fitting: A, C_1, C_2, and F correspond to the $v_1(A_1)$, $v_4(F_2)$, $v_2(E)$ and $v_3(F_2)$ vibrational modes of corner-sharing $GeTe_{4-n}Ge_n$ tetrahedra (n = 0, 1, 2, 3 and 4); D and E - E^2_g and A^2_{1g} vibrational modes of Sb-Te_3 pyramidal units; B - a mix of vibration of defect structural Ge, Sb, Te units, which cannot be separated **(Fig. 1, b-d)**. Heating leads to the peak position shiftings, peaks narrowing and changes of

their mutual intensity location, areas and FWHMs, which together indicates on the ongoing structural rearrangements.

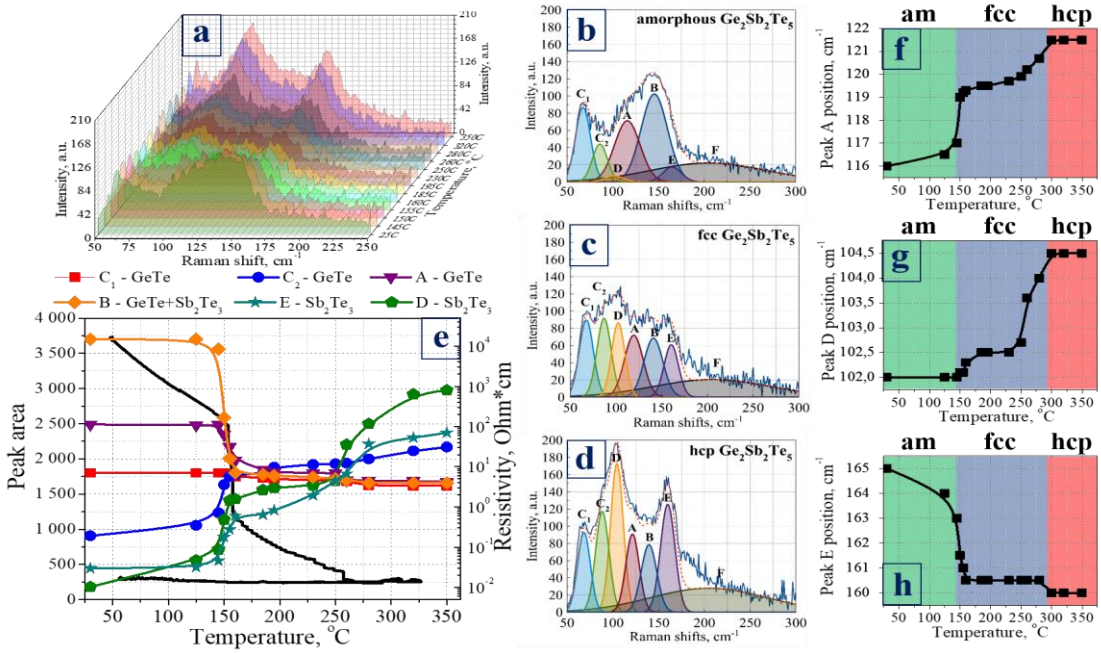

Figure 1 (a, b, c, d, e, f, g, h). (a) Raman spectra at 25÷350ºC; **(b-d)** Deconvolution of Raman spectra for amorphous (b), fcc (d) and hcp (c) structures; **(e)** Temperature dependences of peak areas and resistivity; **(f-h)** Shifts of the A, D and E peak positions.

Analysis of the temperature dependencies of the peak areas has shown, that the strongest changes have A, D and E peak areas **(Fig. 1, e)**. According to the resistivity curves, these changes occurs in the temperature ranges 145-160°C and 265-290°C corresponding to the transitions to fcc and hcp phases, respectively. It worth to be mentioned, that the area change rate of all deconvoluted peaks in the range of 145-160°C is identical, while in the region of the 2nd phase transition, only the D and E peaks areas continue to grow (Sb-Te_3 units), and the area of A peak (GeTe units) remains practically unchanged. In addition, the change rate of the A peak position in the range of 265-290°C is significantly lower than the change rates of D and E ones (**Fig. 1, f-h**). It confirms the dominant role of Sb-Te_3 units in the hcp phase transition. A quantitative analysis showed that the contribution of Sb_2Te_3 structural units to the formation of the hcp phase is more than GeTe (0.27 and 0.07 y.e.); calculations identified that in the region of the first phase transition the influence of GeTe and Sb_2Te_3 units on the fcc crystallization process (0.16 and 0.21 y.e.) is equal.

4. Conclusion

Local structural rearrangements of amorphous $Ge_2Sb_2Te_5$ thin films during the thermal crystallization were investigated. A quantitative and qualitative analysis of the temperature dependences of the Raman spectra showed that the crystallization of GST from the amorphous to the metastable fcc state equally take place through the rearrangement of Ge/Sb atoms from tetrahedral and pyramidal coordination into a defective octahedral one (for GeTe and Sb_2Te_3 compounds, respectively), whereas the fcc→hcp transition take place mainly due to the local rearrangements of Sb atoms caused by the elongation of the covalent bonds (from 2.91 to 3.07 Å).

5. Acknowledgements

This work was supported by Russian Science Foundation (project No. 20-79-10322).

References

[1] Wuttig M, 2017 J. Nat. Photonics. **11** 465–476.

Magnetron sputtered TiO_2 with metal NPs for plasmonic applications

D Konev[2], A Kazakin[1,2], A Vorobyev[1], Y Enns[1,2], A Kondrateva[1,2], M Mishin[1]

[1]Alferov University, St. Petersburg, Russia
[2]Peter the Great Saint-Petersburg Polytechnic University, St. Petersburg, Russia

Abstract. This work is aimed at finding the optimal technological modes for the deposition of TiO_2 films by reactive magnetron sputtering for use as a plasmonic material. The structural and optical parameters of the films obtained at different ratios of oxygen in a mixture of working gases were investigated. On the basis of the obtained results, a spectral characteristics numerical simulation of the TiO_2 with silver, aluminum, platinum and gold nanoparticles was carried out.

1. Introduction

Currently, much attention is paid to optoelectronic devices based on oxide semiconductors [1-4]. In particular, titanium dioxide (TiO_2) has excellent physical, chemical and optical properties and is widely used in applications such as UV photodetectors, gas sensors and photocatalysts [5-8]. TiO_2 is a well-studied metal oxide wide-gap n-type semiconductor (3.2 eV for anatase and 3.0 eV for rutile phases). Such wide band gap makes TiO_2 a suitable material for UV detection applications because it is insensitive to background visible and infrared light [6].

The electronic and optical properties of TiO_2 films are provided due to the formation of metal vacancies or interstitial O atoms [9]. Magnetron sputtering with an adjustable oxygen ratio and optimized annealing conditions can be used to improve the electrical and optical parameters of TiO_2 films [6]. In addition, compared with other methods used to obtain TiO_2 films [10–13], high-frequency magnetron sputtering has a number of advantages, such as high stoichiometry and significant film uniformity and density, possibility of using different substrates, and low growth temperatures [14, 15].

Plasmonic behavior of metal nanoparticles (NPs) is an effective way to improve the characteristics of optoelectronic devices and adjust their sensitivity range by changing the particle arrays geometric parameters [1-4]. Silver, aluminum, platinum, and gold are promising materials for distributed arrays of NPs [16]. Plasmonic effects in NPs of these materials lead to trapping of light in localized regions near metal nanoparticles, which leads to an increase in the electromagnetic field. However, NPs are also significantly influenced by the properties of the matrix material in which they are located.

This work is aimed at finding the optimal technological modes for the TiO_2 reactive magnetron sputtering. This paper presents a study of the oxygen content effect on structure and optical properties of formed thin films. The results obtained were used to numerically simulate plasmonic behavior with silver, aluminum, platinum, and gold NPs.

2. Results

In this work, TiO_2 films were obtained by reactive magnetron sputtering (DC) with a Ti target in an O/Ar gas mixture on amorphous quartz and Si substrates. The gas ratio varied in the range 0.2-1 at an

operating pressure of 1.8 mTorr. The thickness of the films was controlled by ellipsometry and stands at 43-70 nm. It is noted that an increase in the oxygen content leads to a decrease in the rate of film formation. Film structure was investigated using the Raman spectroscopy. The optical properties of the film were obtained from the transmission and reflection spectra. On the basis of obtained parameters, behavior of silver, aluminum, platinum and gold nanoparticles on the formed TiO_2 surface were simulated. For modeling, the technique described in [17] were used. The obtained simulation results are consistent with the published experimental data for particles with a diameter of 20 nm [18].

3. Acknowledgments
Authors wishing to acknowledge the Ministry of Education foundation for financial support assistance (№ FSRM-2020-0011).

References
[1] Shu J, Qiu Z L, Lv S Z, Zhang K Y, Tang D P 2018 *Anal. Chem.* **90** 2425-2429
[2] Wang H L, Zhang L S, Chen Z G, Hu J Q, Li S J, Wang Z H, Liu J S, Wang X C 2014 *Chem. Soc. Rev.* **43** 5234-5244
[3] Chen B, Zhang Z, Baek M, Kim S, Kim W, Yong K 2018 *Appl. Catal.* B **237** 763-771
[4] Yang R Y, Yan X X, Li Y M, Zhang X H, Chen J H 2017 *ACS Appl. Mater. Interfaces* **9** 42482-42491
[5] Lajvardi M M, Jahangiri M 2016 *IOP Conf. Series: Materials Science and Engineering* **108** 012031
[6] Huang H, Xie Y, Zhang Z, Zhang F, Xu Q, Wu Z 2014 *Appl. Surface Science* **293** 248-254
[7] Kumar S G, Devi L G 2011 *J. Phys. Chem.* A **115** 13211–13241.
[8] Shehzad N, Tahir M, Johari K, Murugesan T, Hussain M 2018 *J. CO2 Util.* **26** 98–122
[9] Liu Z 2015 *Sci. Rep.* **5** 14420
[10] Colgan M J, Djurfors B, Ivey D G, Brett M J 2004 *Thin Solid Films* **466** 92–96
[11] Modes T, Scheffel B, Metzner C, Zywitzki O, Reinhold E 2005 *Surf. Coat. Technol.* **200** 306
[12] Domaradzki J, Kaczmarek D, Prociow E L, Borkowska A, Schmeisser D, Beuckert G 2006 *Thin Solid Films* **513** 269–274
[13] Arconada N, Duran A, Suarez S, Portela R, Coronado J M, Sanchez B, Castro Y 2009 *Appl. Catal.* B **86** 1–7
[14] Heo C H, Lee S B, Boo J H 2005 *Thin Solid Films* **475** 183–188
[15] Kang S H, Kang M S, Kim H S, Kim J Y, Chung Y H, Smyrl W H, Sung Y E 2008 *J. Power Sources* **184** 331–335
[16] Goswami L, Aggarwal N, Shibin K, Singh M, Vashishtha P and Govind G 2020 *ACS Omega* **5** 14535−14542
[17] Enns Y, Kondrateva A, Mishin M 2020 *J. Phys. Conf. Series* **1695**(1) 012115
[18] Kondrateva A, Enns Y, Kazakin A, Morozov I, Karaseov P, Mishin M 2020 *Semiconductors* **54**(14) 1885–1888

Production of upconversion BaY_2F_8:Yb, Er nanoparticles by high-energy milling for photonic and biomedical applications

A V Koshelev[1,2], N A Arkharova[1], K V Khaydukov and D N Karimov[1]

[1] FSRC «Crystallography and Photonics» of Russian Academy of Sciences, 59, Leninskiy Prospekt, Moscow, Russia

e-mail address:koshelevsan4es@yandex.ru

Abstract. Upconversion nanoparticles are of practical interest for modern photonics and biotechnologies. The paper presents the study results of nanoparticles based on a low-symmetric crystal matrix rare earth doped BaY_2F_8. 10-20 nm sized nanoparticles BaY_2F_8 Yb, Er were obtained by high-energy milling of bulk single crystal, grown from melt by the Bridgman method. Size, morphological composition, and spectroscopic properties of the obtained samples are characterized. Comparative data of BaY_2F_8 Yb, Er nanoparticles and the most widely used β-$NaYF_4$ nanoparticles are presented.

1. Introduction

Upconversion nanocrystals (UCNPs) represent a separate class of new generation functional materials that provide a unified nanoplatform for solving problems in various fields of science and technology. The remarkable feature of these particles consists in the efficient conversion of exciting IR-radiation by rare-earth ions into higher-energy photons of the visible and UV-ranges (the phenomenon of upconversion). UCNPs based on inorganic fluorides attract special attention. The main advantages of fluoride upconversion nanoparticles in comparison with traditional phosphors (quantum dots and organic dyes) are the biological safety of IR radiation, resistance to photobleaching, non-toxicity and high chemical stability of fluorides, which leads to great prospects for the mass introduction of this class of phosphors in various areas of photonics: biomedicine, energy, photopolymerization etc. [1-3].

The choice of the optimal material for the crystal matrix in which REE ions are doped determines the efficiency of the upconversion process. In low-symmetric crystal matrices, in comparison with high-symmetric ones, the probability of electronic transitions in rare-earth ions is much higher due to the stronger influence of the crystal field of the matrix on their electron shell [2]. From this point of view, the BaY_2F_8 monoclinic crystal matrix (space group C2/m and C2 site symmetry for rare earth ions) can be considered promising object for a new type of upconversion nanocrystals with a superior luminescence efficiency. Previously, upconversion bulk crystals based on this material were studied as an active laser medium for UV and visible radiation generation [4, 5], but the methods for obtaining rare earth doped nanoscale BaY_2F_8 and their spectral properties are currently poorly investigated.

In this work, BaY_2F_8:Yb, Er nanoparticles were obtained by high-energy milling of a bulk single crystal in inert atmosphere and a complex characterization of the size, structural and spectral properties of these objects by X-ray diffraction, transmission electron microscopy and optical spectroscopy methods was performed.

2. Experimental details

The bulk single crystal of the composition $Ba(Y_{0.964}Yb_{0.03}Er_{0.006})_2F_8$ (fig. 1a), grown from the melt by vertical direction crystallization, had a monoclinic crystal structure (C2/m, a=0.698 nm, b=1.051 nm, c=0.426 nm, β=99°). The crystal was ground in a planetary ball mill PM-200 (Retsch, Germany). The resulted particles were dispersed in hexane (fig. 1b). According to the results of XRD analysis, the sample structure doesn't change during milling. Transmission electron microscopy results showed that the average size of the obtained particles was 10-20 nm. A qualitative and quantitative comparison of the luminescent characteristics of the obtained BaY_2F_8:Yb, Er particles and the most currently used $Na_{0.5}Y_{0.4}Yb_{0.09}Er_{0.01}F_2$ particles was performed. The BaY_2F_8:Yb, Er nanoparticles excited by 980 nm IR-radiation have an intense green luminescence in the 520-550 nm range (fig. 1c). The prospects of application the obtained particles in photonics and biotechnologies are discussed.

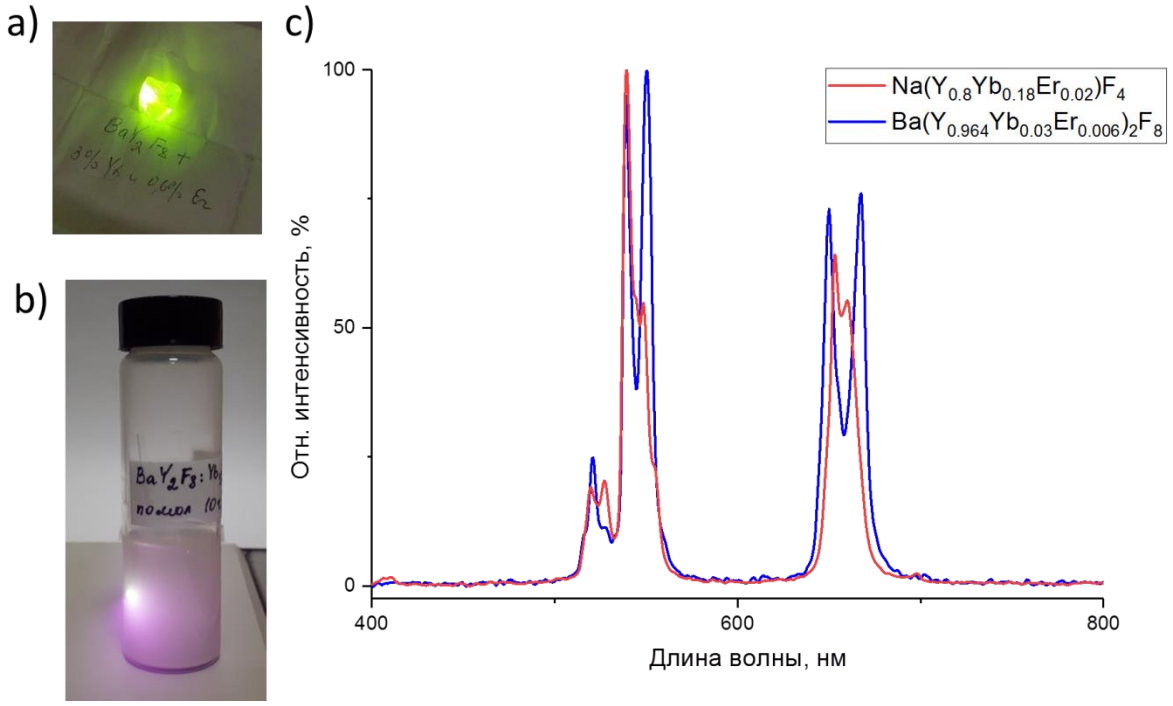

Fig. 1. a) single crystal, grown by the Bridgman method; b) image of $Ba(Y_{0.964}Yb_{0.03}Er_{0.006})_2F_8$ UCNPs, dispersed in hexane; c) comparative luminescence spectra of BaY_2F_8:Yb/Er and $NaYF_4$:Yb/Er nanoparticles, obtained by high-energy milling.

Acknowledgments

This work was supported by the RFBR research projects no. 19-02-00877 in the part of $UCNP_S$ synthesis, no. 20-32-70174 in the part of $UCNP_S$ structural characterization.

References

[1] Zhang Z, Han Q, Lau J W and Xing B 2020 *ACS Materials Letters* **2** 1516-1531

[2] Nadort A, Zhao J and Goldys E M 2016 *Nanoscale* **8** 13099-13130

[3] Karimov D N, Demina P A, Koshelev A V, Rocheva V V, Sokovikov A V, Generalova A N, Zubov V P, Khaydukov E V, Koval'chuk M V and Panchenko V Ya 2020 *Nanotechnologies in Russia* **15** 655–678

[4] A A Kaminskii 1990 *Laser Crystals: Their Physics and Properties* (Berlin: Springer-Verlag Berlin Heidelberg) p 407

[5] Uvarova T V, Pushkar A A and Uvarova A G 2011 *Physica status solidi (c)* **8** 2911-2914.

Catalytic growth of vertically aligned carbon nanotubes via chemical vapor deposition

N.V. Lyanguzov, D.V. Chalin

Department of Physics, Southern Federal University, Rostov-on-Don, 344006 Russia

n.lianguzov@mail.ru

Abstract. Arrays of vertically aligned carbon nanotubes were synthesized via catalytic chemical vapour deposition technique using an iron-(III) acetate as a catalyst precursor on Si substrates, covered by ultrathin (about 10-nm thick) Al_2O_3 sublayers. Rapid emplacement of the substrate into reaction media was proposed. The synthesis was carried out using very low pressure of carbon precursor gas (2 mbar). Growth rate of CNT reached up to 20 μm per minute. We have demonstrated that the amount of catalytic precursor directly influences morphology features of nanotubes arrays. Raman spectroscopy data shows the growth of carbon nanotubes with different chirality.

1. Introduction

Carbon nanotubes (CNT) due to its unique physical properties and various prospects of application have been actively studied over the last three decades. In terms of ordering, from full random orientation to ordered arrays, CNTs represent an active media for different electron devices [1-3]. Chemical vapor deposition is one of the most effective techniques to synthesize CNTs [4]. The chemical nature of carbon source and catalytic agent define the result of CNT synthesis in many ways, therefore an empirical search of necessary compounds and experimental approaches is still of great relevance [5-7]. In the present study a new catalytic precursor and a modified synthesis approach are proposed.

2. Experimental details

Arrays of the vertically aligned carbon nanotubes (VA CNTs) were synthesized on silicon substrates by catalytic chemical vapor deposition (CCVD) technique in horizontal tub quartz reactor placed in a resistive furnace. For the catalyst agent formation a 0.01 M solution of iron-(III) acetate (FeAc) in ethanol was used. First, 10-by-10 mm Si (111) substrates were covered by 10-nm thick alumina, after that they were covered by FeAC by drying out its solution on the surface of the substrate. The prepared substrate was placed in a reactor in a non-heated area on a quartz transport holder. Acetylene was used as a carbon source, hydrogen and argon as reduction and buffer gases respectively. Total flow was 1000 sccm. The CCVD reactor has been warmed up to 800 ^{o}C before the 3:1 mixture of argon and hydrogen was introduced. Then the substrate was transported from the unheated area to the heated reaction zone by moving the holder and was exposed to a mixture of argon and hydrogen gases in order to form catalytic nanoparticles from the FeAc layer. The process lasted for a few minutes. Thereafter, acetylene was added to the reaction medium in a flow of 2 sccm, and the VA CNTs growth

process continued for 10 minutes. Such a flow corresponds to a pressure of only 2 mbar in terms of carbon source partial pressure. Further, the substrate was removed from the heated reaction zone, and gas flow was stopped.

The morphology of prepared VA CNTs samples was examined by FE SEM on Zeiss SUPRA 25. Raman spectroscopy was performed to confirm the presence of CNTs and to determine the level of defectiveness. The spectra were obtained using 514 nm and 633 nm lasers and recorded with Renishaw inVia Reflex Raman spectrometer.

3. Results and discussion

A length of VA CNTs varies from 70 to 200 μm depending on a surface density of catalytic nanoparticles. CNT surface density varies from 2 to 7 10^3 tubes/μm. Increase in the thickness of the FeAc layer leads to an increase in Fe-NP surface density and hence to a tighter array of VA CNTs. In tighter arrays each single CNT is supported by neighboring ones and grows in a vertical direction. Several CNTs in array may occasionally clamp together into a vertical bundle. On the contrary, in sparse arrays single CNT tend to bend without the support from other tubes. Thus, denser VA CNTs consist of longer tubes due to a nice degree of vertical alignment. However, further increase in FeAc amount leads to the formation of sub-micron Fe droplets instead of Fe-NP and CNT growth does not happen.

Raman spectra of VA CNT shows an evident splitting of 1582cm^{-1} graphene-like mode into G^+ and G^- ones. The intensity of D-line is about three times less than the intensity of G^+ one and grows linearly when measured from the top of array to its bottom. This is most likely caused by an accumulation of amorphous carbon particles during the synthesis, and it is not due to formation of defects in CNTs. Low-frequency area contains singlet lines near 140, 180, 195, 220, 260 and 280 cm^{-1} with FWHM no more than 7 cm^{-1}, that appears to be depending on the excitation wavelength. This feature directly indicates the presence of the CNT with different chirality.

Acknowledgments

This study is supported by the Russian Foundation for Basic Research, project no. 18-29-19043-mk.

References

[1] R. H. Baughman, A. A. Zakhidov, and W. A. De Heer. Science 297 (5582), 787 (2002).

[2] M. F. L. De Volder, S. H. Tawfick, R. H. Baughman, and A. J. Hart. Science 339 (6119), 535 (2013).

[3] Y. Li. ACS Nano 11 (1), 1 (2017).

[4] V. Jourdain and C. Bichara. Carbon 58, 2 (2013).

[5] Yoku Inoue, Kazuyuki Kakihata, Yusaku Hirono, Toshinori Horie, Akihiro Ishida, and Hidenori Mimura. App. Phys. Lett. 92, 213113 (2008).

[6] Yongfeng Luo, XinjunмWang, Mengdong He, Xi Li, and Hong Chen. J. Nanomaterials, Article ID 542582 (2012).

[7] Md. Mahfuzur Rahmana, Hammad Younesa, George Nib, TieJun Zhanga, Amal Al Ghaferia.Mat. Res. Bulletin 77, 243–252 (2016).

Raman analysis of the crystallinity degree for the local regions in $Ge_2Sb_2Te_5$ films after laser exposure at different parameters

N M Tolkach[1, 2], N V Vishnyakov[2], A O Yakubov[1], A U Sudakova[2], E S Trofimov[2], A A Sherchenkov[1]

[1]National Research University of Electronic Technology, Zelenograd 124498, Russia
[2]Ryazan State Radio Engineering University, Ryazan 390005, Russia

Abstract. The evaluation of the crystallinity degree for the local regions in $Ge_2Sb_2Te_5$ (GST) thin films after phase state transformation by laser pulses at 405 nm was analyzed using the Raman spectroscopy. The modes of laser radiation for controlling the reflectivity and transmissivity at 1550 nm telecommunication wavelength of the local regions in the GST film were established.

1. Introduction

Electromagnetic waves cannot interact with each other, but they are capable to interact with matter. PCM (Phase Change Material) materials with phase state transformations are successful in this regard, in particular, chalcogenide glassy semiconductors, $Ge_2Sb_2Te_5$ material (GST). GST has a fast and low-energy phase transition. The sizes of the GST active regions are limited (~1 μm) by the wavelengths of the used laser radiation. Such active regions can be integrated into waveguide paths comparable to these sizes. This will allow good levels of integration, miniaturization, and performance in integrated optic and network-on-chip systems [1, 2]. In addition to the main phase states (amorphous and crystalline), there can be additional intermediate states due to the presence of partially crystalline and amorphous nanosized fractions of the material. Controlling the ratio of the fractional composition of GST opens wide possibilities in fine-tuning of its optical parameters, but at the same time, it requires studying the processes that occur when laser radiation is applied to the GST material. The ratio of amorphous and crystalline fractions in the bulk of the material is characterized by the crystallinity degree. The aim of this work is to study the crystallinity degree of the local regions of the GST film to select the optimal modes of laser exposure for the phase state transformations in the GST material.

2. Methods and materials

The GST thin film with the thickness of 24 nm were deposited by magnetron sputtering. The phase state of the local regions of the GST film (see figure 1a) was changed from crystalline to amorphous phase state by the pulsed laser with 405 nm wavelength, with the focused spot diameter of about 1 μm, pulse durations from 5 to 30 ns and energy exposure from 2 to 4 nJ/μm^2. The radiation of 405 nm wavelength was used due to its high absorption by the GST. The crystallinity degree was estimated from the Raman spectra (see figure 1c) in the same way as in the work [3]. Raman spectra were obtained using the Ntegra-Spectra probe nanolaboratory (NT-MDT SI, Russia). Photometry of the local regions was used to measure the reflectivity and transmissivity of the film at 1550 nm wavelength.

3. Results and discussion

The evaluation of crystallinity degree showed that amorphization of the crystalline GST film is observed when exposed to laser with a wavelength of 405 nm at pulse energy exposure of 3.26 nJ/μm^2 (see figure 1b), with pulse duration of 10 ns. The change of the spectra from 1 to 11 (see figure 1c) obtained after irradiation of local region in the crystalline film at 405 nm wavelength with radiant exposures from 2.92 to 3.26 nJ/μm^2 is due to the evolution of the crystallinity degree. Measurement of the reflectivity and transmissivity for 1550 nm radiation for the local regions of GST films with different crystallinity degree showed the change in these optical properties (see table 1), which allows multilevel amplitude modulation of an optical signal with a modulation depth of 45%.

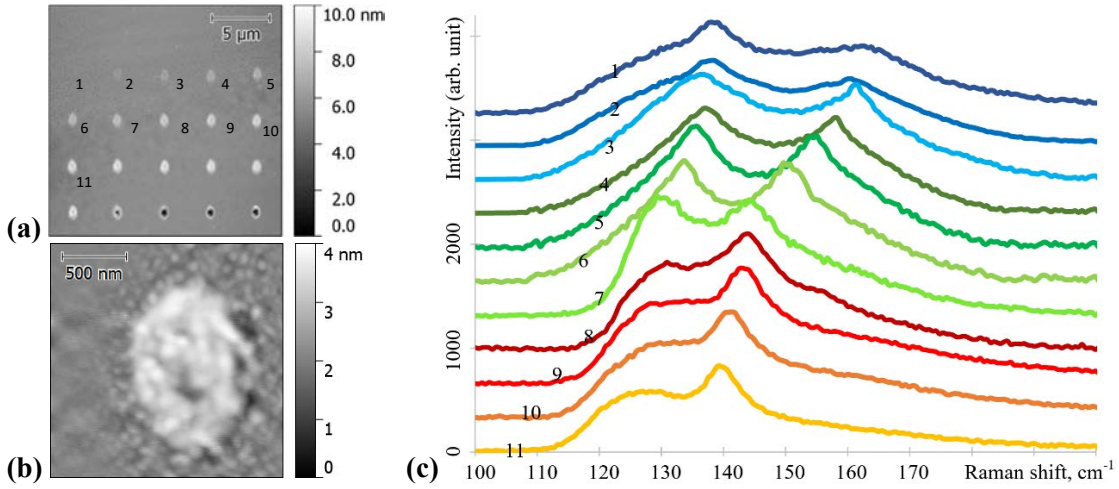

Figure 1(a, b, c). AFM image of the local regions in the GST film irradiated by laser with various energy exposure **(a)** energy exposure of 3.26 nJ/μm^2 **(b)**; Raman spectra local regions in the GST film between the crystalline (dark blue line No. 1) and amorphous (orange line No. 11) phase states **(c)**.

Table 1. Change of the properties of local GST regions after 1550 nm radiation

No. Raman spectra	1	2	3	4	5	6	7	8	9	10	11
Energy exposure, nJ/μm^2	2.92	2.95	2.99	3.02	3.06	3.09	3.13	3.16	3.19	3.23	3.26
Crystallinity degree	0.98	0.83	0.62	0.58	0.55	0.59	0.61	0.50	0.41	0.29	0.04
Reflectivity	0.57	0.55	0.54	0.51	0.48	0.46	0.41	0.35	0.32	0.27	0.23
Transmissivity	0.23	0.26	0.29	0.32	0.36	0.38	0.43	0.49	0.53	0.6	0.68

4. Conclusion

Thus, it was found that the change in the energy exposure of a laser pulse irradiation leads to the change of reflectivity, transmissivity, due to the evolution of the crystallinity degree. These results demonstrate the possibility of multilevel modulation of the optical signal at the 1550 nm wavelength and make it possible to establish the optimal modes of laser radiation at the 405 nm wavelength to initiate the phase state transformations of the GST material with necessary crystallinity degree.

Acknowledgments

The reported study was funded by RFBR according to the research project # 19-37-60023 used the equipment of Region Centre of probe microscopy of Ryazan State Radio Engineering University.

References

[1] Wen S, Meng Y, Jiang M, Wang J 2018 *Scientific Reports* **8** 4979

[2] Tolkach N M, Vishnyakov N V, Lazarenko P I *et al* 2020 *J Phys: Conf Ser* **1695** 012075

[3] Samuel A Z 2020 *Spectrochim Acta A Mol Biomol Spectrosc* **224** 117431

The properties of interface between a-Si:H and silicon nanowires formed by cryogenic dry etching

A I Baranov[1], D A Kudyashov[1], I A Morozov[1], A V Uvarov[1], A A Maximova[1,2], E A Vyacheslavova[1], A S Gudovskikh[1,2]

[1]Alferov University, 194021 St Petersburg, Russia.
[2]St Petersburg Electrotechnical University "LETI", 197376 St Petersburg, Russia.

baranov_art@spbau.ru

Abstract. Arrays of vertical aligned silicon nanowires with height of 6-10 μm and diameter 1.2–1.8 μm were fabricated by cryogenic dry etching. The post-processing technology was developed to fill arrays of NWs by SU-8 form Schottky diodes to different parts of SiNWs. It was shown that cryogenic dry etching does not lead to defect formation with concentration higher 10^{12} cm^{-3} in silicon. However, oxygen plasma used for etching of SU-8 and opening of top side of SiNWs leads to defects formation with Ea=0.35 and Ea=0.17 eV due to plasma treatment.

1. Introduction

Nowadays, modern types of semiconductor solar cells (SC) like silicon single-junction one and multi-junction ones based on the III-V compounds have almost reached their theoretical limit of efficiency, and their further optimization leads to complication and cost rise. Therefore, fabrication of SC based on low dimensional structures are considered as perspective concepts to increase its efficiency with using of standard processing methods, which can be transferred to industry in the future [1]. Recently, it was shown that usage of vertically aligned silicon nanowires (SiNWs) formed with nanosphere lithography allows one to enhance the absorption of solar radiation in active layers of a-Si:H based top subcell in full silicon a-Si:H/c-Si double-junction SC. In our previous work, cryogenic dry etching allows one to form arrays of vertical aligned nanowires with height of 4-5 μm and diameter of 400-700 nm with smooth side surface of NWs using latex sphere with 1 μm diameter. However, such diameter is not sufficient to fabricate SC due to fully depletion of NWs for silicon wafer with n=10^{15}-10^{16} cm^{-3}. Furthermore, using deep-level transient spectroscopy (DLTS) it was shown formation of defects in near-surface area due to plasma influence but it can be partially reduced after wet etching in KOH solution [2]. Here, we use latex sphere with higher diameter of 2 μm which enlarges diameter of SiNWs and can improve performance of SC device. Influence of cryogenic plasma etching will be studied, and also post-growth encapsulation of obtained SiNWs arrays by SU-8 will be studied.

2. Experiments and results

Silicon wafers (n=10^{16}-10^{18} cm^{-3}) were etched in ICP mode in gases flow of SF_6 and O_2 in Oxford Plasma Lab ICP 380 at -140 °C with mask of 2 μm latex spheres to form arrays of vertical aligned nanowires with height of 6-10 μm and diameter 1.2–1.8 μm. Optimal parameters of post-processing filling of SiNWs array by SU-8 and openning of top side of SiNWs was developed. In result, two type

of samples with Schottky barrier were fabricated: full area of SiNWs array was covered by gold and only top side of SiNWs was covered (Figure 1). Then, different capacitance methods (capacitance-voltage characterization, DLTS, admittance spectroscopy) were performed to explore defect properties of structure after post-growth operations. It was shown that cryogenic dry etching does not lead to defect formation with concentration higher 10^{12} cm^{-3} in depth of 100-300 nm and deeper in bulk silicon. However, oxygen plasma used for opening of top side of SiNWs leads to defects formation: (i) trap for electrons with Ea=0.35 eV which is divacancy arising due to oxygen plasma [3], and (ii) trap for holes with Ea=0.17 eV. Further, layers of (p)a-Si:H/(i)a-Si:H were deposited on array of SiNWs to fabricate a-Si:H/c-Si heterojunction. Admittance spectroscopy was used to study a-Si:H/ SiNWs interface properties, in particular, interface states and bulk defects were selected by variation of applied bias voltage. The correlation between defect and photoelectrical properties (I-V curves and quantum efficiency) will be presented in conference.

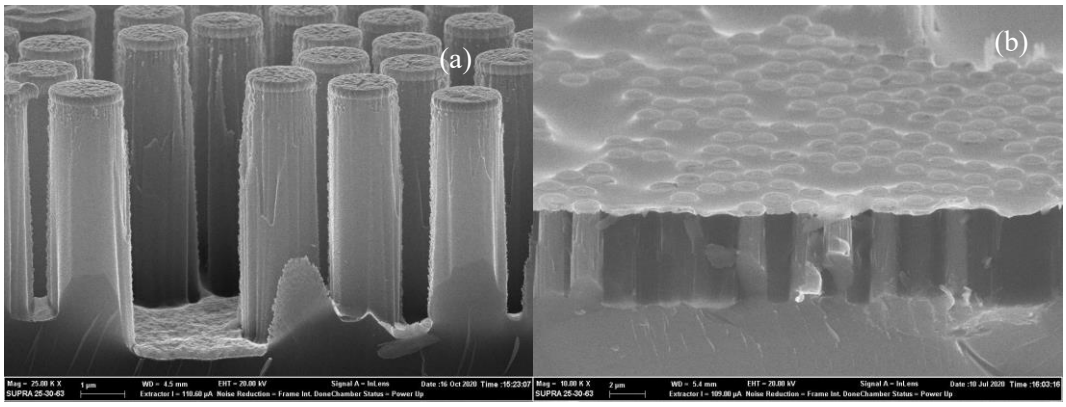

Figure 1. SEM image of structure covered by gold metallization: initial SiNWs (a) and filled by SU-8 and opened top side of SiNWs (b).

Acknowledgments
The work is supported by the Russian Scientific Foundation under Grant No. 19-79-00338.

References
[1] Al-Ghzaiwat M et al. 2018 *Scientific Reports* **8**, 1651
[2] Baranov A I et al 2020 *J. Phys.: Conf. Ser.* **1697**, 012060
[3] Xu I G et al. 1988 *Phys Rev B* **38** 3395

Feature of degradation of silicon-based solar photovoltavic cells

Linda Boudjemila[1, 2], V V Davydov[1, 3], V G Malyshkin[4] and V Y Rud[3, 4]

[1]Peter the Great St. Petersburg Polytechnic University, St. Petersburg 195251, Russia
[2]Department of Mechanical Engineering, University of science and technology Houari Boumedien Bab Ezzouar 16111, Algiers, Algeria
[3]All-Russian Research Institute of Phytopathology, Moscow Region 143050, Russia
[4]A.F. Ioffe Physicotechnical Institute, St. Petersburg, 195256, Russia

e-mail: Lariessai21@gmail.com

Abstract. This work intends to present a method for efficient analysis of the phenomenon of degradation in photovoltaic cells in Saint Petersburg (Russia) and Algiers (Algeria). The data used contained only weather parameters (T°, wind, solar radiation) in 10 years. The results of calculations of the rates of degradation of Si- photovoltaic cells were done. It was noted from the results of comparing various data that the main factor in the formation of the degradation process is the technology of manufacturing photovoltaic cells.

1. Introduction

The development of the technology in the last two centuries required more and more the use of the electrical energy. As it's known the production of the electricity from fossils resources has caused many problems of pollution, that's why scientists are interested to the alternative energies such as solar energy. Recently the solar cell of first generation has known a rapid development and a certain maturity which had led the price to get lower. Unlucky these cells are very delicate and many factors such as the shadow, humidity, the hot weather, the wind… can cause the degradation in a short time. One of the important elements of studies about the degradation is the modeling of the operation of a solar power plant, taking into account the climatic conditions of operation of photovoltaic converters, the processes of their degradation, etc.

2. Features of the degradation of solar photovoltaic cells

The data base used when simulating the operation of a solar power plant in Algiers and saint-Petersburg is the NASA data on climatic factors illumination of a horizontal surface in energy units per day, temperature and wind speed; these last two parameters are measured at 2 meters altitude. An analysis of the climatic conditions between the two cities shows large differences in illumination and temperature and little difference in wind speed. The first two factors have a significant impact on the power generated by a solar power plant throughout the year. Wind speed has a different effect on the rate of degradation of photovoltaic converters (warm or cold wind and humidity are of great importance). In Saint-Petersburg the low temperatures, strong winds and humidity are a determining stressor in the mechanisms of corrosion and delamination. In Algiers, the degradation process is affected by the high temperatures and humidity which caused the discoloration, hot spots and bubbles.

the inhomogeneities in solar panels have a more significant impact on the work process. This facts must be taken in consideration while the modeling degradation process.
The preferred method of degradation estimation is the annual (YOY) approach [1,2]. The algorithm includes: Normalizing the measured PV power, by site irradiance and temperature, Filtering the data (the most common filter is a low irradiance cutoff of about 200 W/m²), and Data Analysis step. There are actually two major categories of degradation calculation methods: with an independent measurement of solar irradiation and without it. Advances in algorithm processing [1, 3] allows to obtain sufficiently accurate value of the degradation rate even without independent irradiation measurements. Data availability is one of the major issues. In Figures 1 (a,b) show the results of calculations of the rate of distribution of the generated power ˙ ′ a solar power plant and the confidence interval for the degree of degradation of photovoltaic stations for Algeria and St. Petersburg.

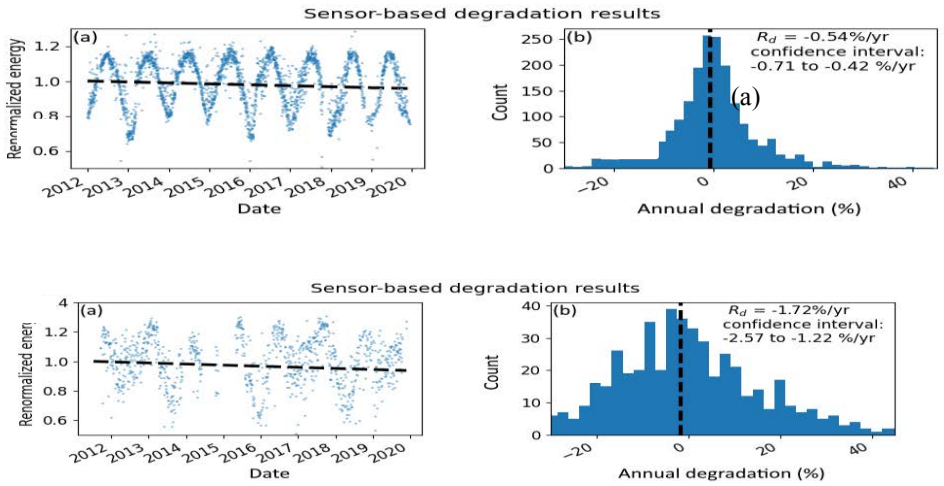

Figure 1. The results of research a work of solar power plants over the past 8 years: (upper) in Algeria; (lower) in Saint- Petersburg: (a) is calculations of the rate of distribution of the generated power by a solar power plant, (b) is confidence interval for the degree of degradation of photovoltaic stations.

The obtained results of modeling the operation of a solar power plant show that degradation process are more actively occurring at the solar power plant located in the region of St. Petersburg. For the research, data was taken on the operation of SES, in which photovoltaic converters of one company are used.

3. Conclusion

The modeling done in this work showed that the rate of degradation in solar cells is not very high. Degradation occurs over years of use. In other words, the efficiency of the solar panel is not affected. Harsh climatic conditions (severe frosts and high temperatures), leads to increase the rate of degradations visible to the naked eye. The results obtained shows that the location of the solar power plan is very important. The rate of degradation in Saint Petersburg (with the cold and windy weather) is much higher than in the city Algiers which is much warmer and humid. Another factor may be responsible is the different defects in solar cells during the fabrication.

References

[1] Jordan D, Deline C, Kurtz S, Kimball G and Anderson M 2018 *IEEE Journal of Photovoltaics* **8(2)** 525-531

[2] https://github.com/NREL/rdtools
[3] John J, Alnuaimi A, Elnosh A, Stefancich M and Banda P 2018 *In 2018 IEEE 7th World Conference on Photovoltaic Energy Conversion (WCPEC)* IEEE, pp. 712-714

Processing and characterization of GaP nanowires encapsulated into a PDMS large-scale membrane for flexible optoelectronics

S M Mukhangali[1], V Neplokh[1,2], F M Kochetkov[1], V V Fedorov[1], A G Nasibulin[3], S V Makarov[4], I S Mukhin[1,4]

[1] Saint Petersburg Academic University, 8/3 Khlopina, St. Petersburg 194021, Russia
[2] Peter the Great St. Petersburg Polytechnic University, 29 Politekhnicheskaya, St. Petersburg 195251, Russia
[3] Skolkovo Institute of Science and Technology, 30 Bolshoy Boulevard, bld. 1, Moscow 121205, Russia
[4] ITMO University, 49 Kronverksky pr., St. Petersburg 197101, Russia

E-mail: sungat15004@gmail.com

Abstract. This paper presents the methods of fabricating arrays of semiconductor III-V NWs transferred into a flexible polymer membrane made of polydimethylsiloxane. Molecular beam epitaxy was used to synthesize GaP NWs. The large-scale NW arrays on substrates were encapsulated into a silicone membrane by a big swinging-bucket centrifuge. After, the membranes were treated in a plasma mixture to open the NWs top parts, which enables the application of single-walled carbon nanotubes. Second method is more useful for optical experiments as two PDSM membranes are bonded by the additional plasma treatment. Finally, the membranes were separated from substrates utilizing a razor blade and the second carbon nanotubes contact was formed. The obtained membranes have a high practical potential in flexible optoelectronics.

1. Introduction

Nowadays, the demand for flexible optoelectronics is growing every year. Flexible optoelectronics benefits from conventional electronic devices due to the possibility of transferring to objects with a complex form. For example, paper-like displays, foldable touch screens, wearable biosensors, and antennas are widely spread [1,2]. Today, the most popular and developed flexible technology is based on organic materials [3]. For instance, organic light-emitting diodes (OLEDs) that are commonly used, have a low manufacturing price and a relatively good performance. However, OLEDs are still behind inorganic materials in terms of values of quantum efficiency (EQE) of 2-30% and brightness of 10^2-10^4 cd/m^2, and a limited lifespan [4,5]. Meanwhile, flexible devices based on inorganic thin films are challenged by a highly complicated transfer to flexible carriers, since it requires laborious operations of etching, structuring, and separation from the growth substrate. The use of nanowires (NWs) array embedded in a flexible polymer is one of the promising ways to solve this problem since it combines the efficiency of inorganic materials and the simplicity of manufacturing flexible devices [6].

2. Fabrication

Our work is aimed at the method of fabricating semiconductor III-V NWs arrays encapsulated into flexible polymer membranes made of polydimethylsiloxane (PDMS). Firstly, GaP NWs arrays were synthesized by molecular beam epitaxy on 3" large area Si wafers. Then arrays of NWs were encapsulated into a PDMS membrane by the G-coating method using a heavy-load swinging-bucket centrifuge. For the membrane material, the commercial PDMS Sylgard 184 was used. On the next stage, the membrane was etched in a RF plasma mixture of O_2 / CF_4 gases to open the NWs top parts, enabling the application of transparent conductive contact pads based on single-walled carbon nanotubes (SWCNT) synthesized by aerosol chemical method. The PDMS/NW membranes with SWCNT top contact pads were peeled from the substrate by a steel razor blade and SWCNT contact pads were applied to the NW bottom parts. To characterize the fabricated NW/PDMS membranes the I-V curves were measured.

It should be noted that such large-scale membranes with embedded III-V NWs could be used for optical applications such as second harmonic generators. To achieve this the encapsulated NW arrays on the substrate and additional PDMS film of 50-150 μm thickness (PDMS cap film) were etched in O_2 plasma to modify the surface of PDMS. Then the cap-film was put on the PDMS/NW membrane forming strong Si-O-Si bonds due to the O2 plasma surface modification and the whole structure was mechanically peeled off from the substrate.

In conclusion, this work demonstrated a functional large area flexible membrane based on vertically oriented GaP NWs in the silicon matrix that can be used for LEDs or IR-to-Vis light converters [7]. The developed method has a high potential for applications in flexible optoelectronics.

Acknowledgments

VN thanks the Russian Foundation for Basic Research (RFBR project № 19-32-60040) for PDMS/NW membrane fabrication.

References

[1] Li H, Cao Y, Wang Z and Feng X 2019 *Opt. Mater. Express* ***9***(10) 4023-4049

[2] Seo J H, Swinnich E, Zhang Y Y and Kim M 2020 *Mater. Res. Lett.* **8**(4) 123-144

[3] Huh B IHS Technology 2015 OLED Display Market Tracker https://cdn.ihs.com/www/pdf/1118/abstract-oled-displaymarket-tracker.pdf (Accessed 15 April 2021)

[4] Salehi A, Fu X, Shin D H and So F 2019 *Adv. Funct. Mater.* **29**(15) 1808803

[5] Dai X, Messanvi A, Zhang H, Durand C, Eymer J, Bougerol C, Julien H and Tchernycheva M 2015 *Nano Lett.* **15**(10) 6958-6964

[6] Neplokh V, Kochetkov F M, Deriabin K V, Fedorov V V, Bolshakov A D, Eliseev I E, Mikhailovskii V Y, Ilatovskii D A, Krsnikov D V, Tchernycheva M, Cirlin G E, Nasibulin A G, Mukhin I S and Islamova R M 2020 *J. Mater. Chem.* C **8**(11) 3764-3772

[7] Fedorov V V, Bolshakov A, Sergaeva O, Neplokh V, Markina D, Bruyere S, Saerens G, Petrov M I, Grange R, Timofeeva M, Makarov S V and Mukhin I S 2020 *ACS Nano* **14**(8) 10624-10632

Method development to secure the stability of the parameters of pulsed and continuous radiation in laser systems with semiconductor pumping

S R Abdurakhmanova[1, 2], G D Bukharov[1], Z S Gheisser[2], V V Davydov[1, 3] and V Yu Rud[3]

[1]Peter the Great Saint-Petersburg Polytechnic University, Saint Petersburg, Russia, 195251
[2]LLC FEDAL, Saint Petersburg, Russia, 197342
[3]All-Russian Research Institute of Phytopathology, Moscow Region 143050, Russia

Abstract. The necessity of increasing the stability of the parameters of pulsed and cw laser radiation when operating at peak powers is substantiated. Particular attention is paid to the parameters of pulsed laser radiation in systems with semiconductor pumping. The main requirement in this case is the repeatability of the parameters of the output pulses with high accuracy. This condition is ensured by the stability of the diode supply drivers, especially at peak powers, which are required for scientific research. It was found that even a short-term excess (about 1 ms) of the upper range of the permissible current leads to damage to the laser diode, which instantly degrades the parameters of laser radiation. The developed technique can significantly reduce the likelihood of these phenomena and increase the reliability of the laser.

1. Introduction

Nowadays diode-pumped CW and pulsed lasers are used in all the main directions of the development of nanophotonics and in many areas of optics [1, 2]. When carrying out many scientific research and practical work in industry, biology, medicine, chemistry, high power of laser radiation with a high degree of stability of its parameters is required, especially when operating in a pulsed mode. Any failure in the operation of laser systems at high powers is highly undesirable [2]. Taking into account the fact that constantly in order to solve new problems it is necessary to increase the peak power of laser radiation, the need to develop devices that will control, configure and maintain expensive laser equipment is extremely urgent [2]. In article presents a developed technique for monitoring the parameters of power supplies for diode drivers that pump a semiconductor laser and its practical implementation.

2. Experimental setup and research method

In laser systems currently in operation, the permissible wavelength shifts for laser diodes differ in ranges, for example, in IR for λ = 808 nm and higher, the shift to the long-wavelength side with increasing temperature is 0.2-0.3 nm per degree. This allows the stabilization system to control this process and restore the temperature regime if necessary. With large sharp temperature effects or an increase in current, which leads to heating, mode effects appear in laser radiation, pulse duration changes, fronts are distorted, etc. It becomes impractical to use such radiation. In figure 1 (a) shows an unstable signal at the output of the power driver.

a) b)

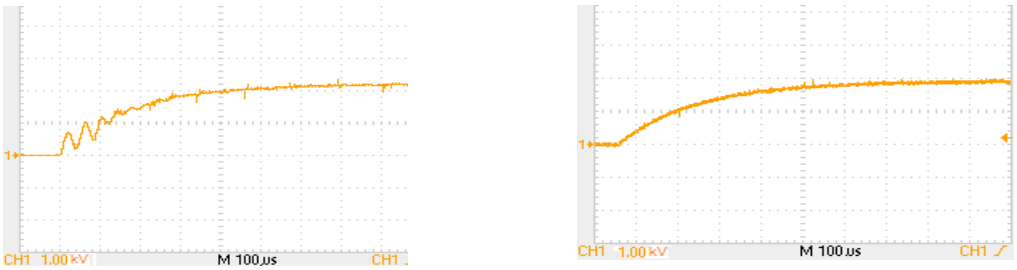

Figure 1. Power driver output signal: a) - unstable mode is present; b) - compensation of signal distortions

In the developed method to stabilize the parameters of laser radiation, it is proposed to use a modernized circuit for comparing currents. Calculations and experiments have shown that the use of the bridge method with a voltage difference of 10 V between the arms of the circuit allows you to work out a sharp increase in voltage and begin the stabilization process at the initial distortion section, in contrast to other circuits that work out the result of the completed process or at the stage of its completion. In fig. 1 (b) shows the result of the operation of this circuit (the output signal at the output of the power driver).

3. Result of experimental investigations

As an optical result, fig. 2 shows the directional diagram of laser radiation, where curve 1 was taken after stabilization of the power supply, curve 2 - before stabilization of the noise of the power supply at the initial stage.

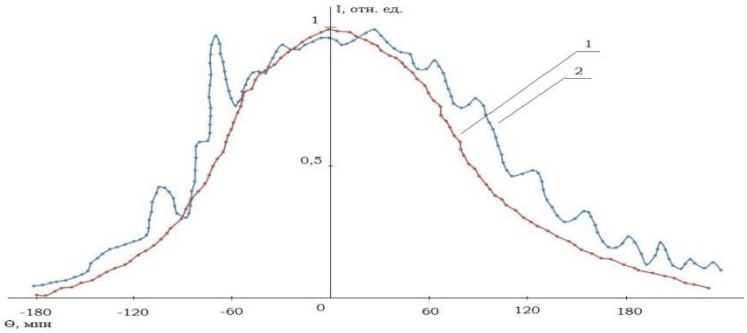

Figure 2. Laser radiation pattern

Analysis presented in fig. 2 of the measurement results shows that even with small noise in the power driver, distortions occur in the laser radiation pattern, which do not allow the use of this radiation for solving many practical and scientific problems.

4. Conclusion

The obtained experimental results of the operation of the stabilization scheme with the developed technique showed that most of the distortions in the fronts of laser pulses associated with the initial section of overheating of the laser diode becomes insignificant, even at its high steepness. There is also no mode distortion in laser radiation compared to the use for stabilization of other techniques.

References

[1] Davydov R V and Antonov V I 2018 *Journal of Physics: Conference Series* **1124(1)** 081037

[2] Davydov V V, Nikolaev D I, Bukharov G D and Pavlova Z S 2020 *Proceedings of the 2020 IEEE International Conference on Electrical Engineering and Photonics, EExPolytech 2020* (Saint-Petersburg) **9243948** p. 227-229

Surface reconstruction post-processing method for 3D-scanned objects

P D Badillo[1], **V A Parfenov**[1], **N L Shchegoleva**[1]

[1] Saint Petersburg Electrotechnical University (SPbETU "LETI"), 197376 St. Petersburg, Russia

pbadillo@gmail.com

Abstract. 3D scanning is widely used in multiple applications to obtain high precision / non-destructive documentation of real-life objects, which is especially important in Cultural Heritage (CH) preservation. However, some issues (in particular missing parts which are commonly known as "holes") affect the accuracy of the obtained 3D model after the scanning procedure and requires time-consuming post-processing procedures, which include manual editing by highly-trained personnel. In this article an automatic method to reconstruct the obtained surface of 3D models is proposed, improving previously obtained results for high-density point clouds.

1. Introduction

3D scanning is widely used in multiple applications thanks to its high-precision measurements of real-life objects. It has particular importance in Cultural Heritage (CH) preservation as a non-destructive documentation method for artworks, which has multiple uses like art conservation tracing and replication.

Although the 3D scanning procedure is getting faster and easier with the use of laser-based techniques, it still requires to be performed by highly qualified personnel to reduce acquisition-related problems (mainly connected with missing parts in the surface of the object seen as holes in the final created 3D model) and complex and time-consuming post-processing procedures (often requiring manually editing the surface) to improve the accuracy of the final result of the created model. All these factors affect the required quality of such procedures used for documentation of CH objects.

As was above mentioned, one of the most recurrent problems in the application of 3D scanning techniques is the appearance of "holes", due to the absence of measurement data of some parts of the scanned object during the acquisition process. This problem decreases the overall accuracy of the model created and its faithful representation, both problems of particular interest in the CH field.

In this work, a method to improve the accuracy of the computer digital 3D models is described. Its use will allow to increase the speed, reduce the computing costs and the time involved in the post-processing phase. The inverse distance method, developed and used to improve the reconstruction quality of the human face for biometry applications [1], showed good results in the reconstruction of 3D point clouds without the need of a previous mesh creation process [2]. The results are further improved in terms of accuracy and speed by subsampling the surface and applying the corrections in the areas where acquisition data is missing.

2. Method used

Most of the 3D-scanning techniques are based on the response of the object under study to a light source. In some cases, the reflected light is measured to determine the distance to the object (triangulation and time-of-flight techniques), in other cases the deformation of a well-known pattern is evaluated (structured light), in other cases photographs taken from different angles are used to obtain a 3D model using special software reconstruction tools (photogrammetry). The common problem that appears in more or less degree in the use of all these techniques is the presence of areas of the surface in which the sensor cannot measure, generating "holes" in the measurement. This problem could be caused by different factors, but mainly it can be seen when the reflected light is not able to reach the sensor of the device (due to occlusions caused by other parts of the object, highly reflective surfaces like glass or highly light-absorbing like black leather [3-5]). As the sensor is not able to obtain information about the object under study in this area, the device identifies this portion as a "hole" or an empty area in the obtained point cloud. This problem, of course, reduces the overall accuracy of the created digital model, which can compromise the goal of the whole procedure.

To correct these acquisition errors post-processing techniques are used [6]. These techniques include manual procedures, where highly trained personnel reconstruct the missing area trying to keep the shape as close as possible as the original object, and automatic procedures. Automatic procedures [7] use different techniques (from simply "connecting" the mesh using geometrical figures to more advanced techniques that follow the local curvature of the shape) but all have in common a high computing cost and that they are time-consuming processes.

The method of inverse distances was developed for the reconstruction of the 3D surface of a human face in biometry applications. The method uses a small number of points of an irregular grid of measurements to generate the missing points, creating a regular grid along the area. A more detailed description of the method could be found in [2]. In the cited article, it was proven the performance of the method in small areas (300 x 300 pixels), comparable with other more complex methods and requiring less computing power, being able to fix successfully surfaces with missing parts ranging from 3% to 30% of the total area. The method showed a lower performance with a larger number of points (15000 points or more).

To solve this issue, the proposed technique tested along this article detects the holes in the surface of the obtained scan as a first step, then selects an appropriate area around the hole to applies the method. Finally, the processed parts are added to the surface to obtain the final result.

This newly proposed technique shows all the advantages of the method of inverse distances applied to 3D-model correction and improves its performance in high-density point clouds, obtained by modern 3D scanning devices.

References

[1] Shchegoleva N 2012 *JTACS Journal of Theoretical and Applied Computer Science* **6(4)** 37-50.
[2] Shchegoleva N, Parfenov V, Smolina S 2020 *WSEAS Transactions on Computers* **19(4)** 26-30.
[3] Matusik W et al 2002 *Proceedings of the 13th Eurographics Workshop on Rendering* 267–278.
[4] Eren G. 2010 *Université de Bourgogne*.
[5] Zaimović-Uzunović N, Lemeš S 2010 *10th International Symposium on Measurement and Quality Control* 408–411
[6] Berger M et al 2014 *Eurographics*
[7] Pérez E. et al. 2016 *International Journal of Applied Mathematics and Computer Science* **26(4)** 885-903.

Magnetoresistive current driven light-emitting diode

M Ved, Yu Danilov, P Demina, M Dorokhin, A Kudrin, Yu Kuznetsov, A Zdoroveishchev, D Zdoroveishchev

Research Institute for Physics and Technology of UNN, Gagarina ave., 23/3, Nizhny Novgorod, 603950

mikhail28ved@gmail.com

Abstract. A magnetoresistive light-emitting diode operating by controlling the ratio of the currents of the majority and minority carriers in a diode structure with a Schottky barrier is considered. The device is a LED based on an InGaAs/GaAs quantum well heterostructure with an Al_2O_3/Au Schottky contact, which is connected in series with a spin valve consisting of $Cr/Co_{90}Fe_{10}/Cu/Co_{90}Fe_{10}$ layers. It is shown that even with a relatively small amplitude of modulation of the magnetoresistance (about 1.5%), a 100% change of intensity is possible when selecting the optimal operating mode of the diode.

1. Introduction

The creation of light-emitting devices with an ability to control the intensity of electroluminescence by applying an external magnetic field is an urgent problem in spintronics. One of the options for creating such a device is the constructive combination of a magnetoresistive element (spintronic device) and a light-emitting diode [1,2]. In such a device, the magnetoresistive element controls the current through the structure (by switching its state with an external magnetic field), and the current through the structure sets the intensity of the LED radiation. The maximum percentage of modulation of the luminescence intensity by a magnetic field in [1,2] was in the range of 10-60%.

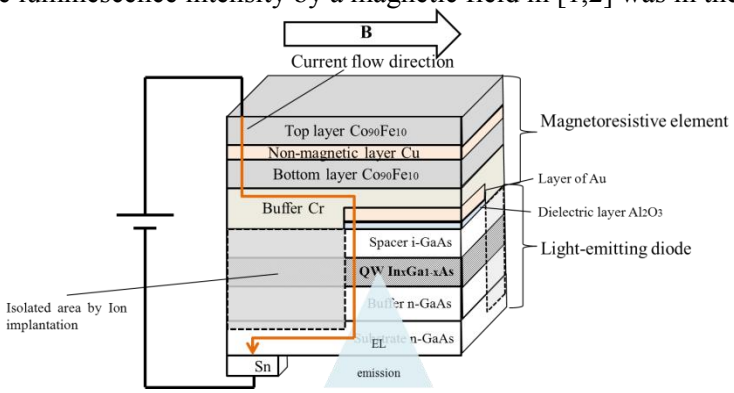

Figure 1. Combined device scheme.

2. Experimental technique

A magnetoresistive light-emitting diode was formed, which is a combination of an emitting part based on a heterostructure with an InGaAs/GaAs quantum well with an Al_2O_3/Au Schottky contact, connected in series with a spin valve consisting of $Cr/Co_{90}Fe_{10}/Cu/ Co_{90}Fe_{10}$ layers. The base

contact to the substrate was formed by sparking of Sn foil. The device was powered in the current source mode. Fig. 1 shows a scheme of a combined device. For the electrical insulation of the semiconductor structure around the mesa contacts, the parts of the structure, which do not covered by the contacts, were bombarded with He^{++} ions before applying magnetoresistive layers [3].

3. Results and discussion

Fig. 2 shows the magnetic field dependences of the resistance of the combined device. The resistance measurements were carried out at forward bias of the diode (3.5 V), which corresponds to the complete potential barrier straightening. The shape of the curves of the static magnetoresistance was similar to the magnetic field dependences of the resistance of an individual magnetoresistive element.

A change of the resistance for the magnetoresistive contact layer leads to modulation of the intensity of the electroluminescence. Fig. 3 shows the magnetic field dependence of the relative electroluminescence intensity of the device. It should be noted that at a current of 46 mA, the structure operates in the key mode: in a magnetic field of ± 30 mT, the relative intensity takes on maximum values; in zero magnetic field, as well as in a field above 100 mT it is zero.

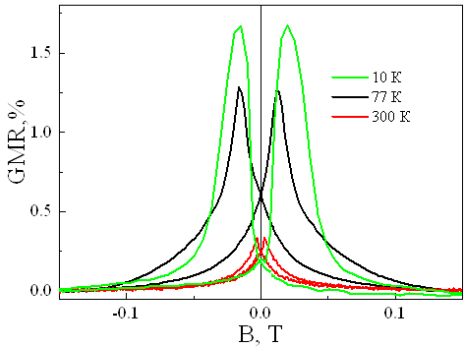

Figure 2. Magnetic field dependences of resistance for a combined device.

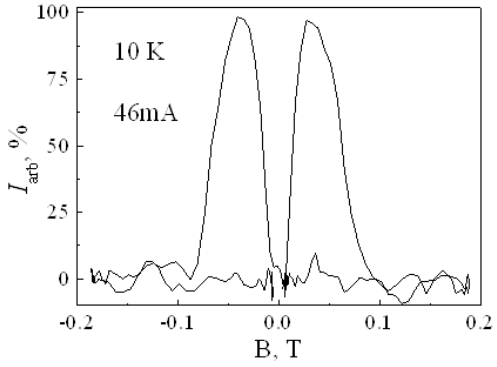

Figure 3. Magnetic field dependence of the relative emission intensity for a combined device.

When the LED is introduced into an external magnetic field, the resistance of the magnetoresistive contact layer increases and, hence, the overall resistance of the structure. The measurements of electroluminescence were carried out in the constant current mode, so an increase of the structure resistance leads to an increase of the voltage drop across it. The main fraction of this voltage falls on the magnetoresistive contact layer. This additional voltage leads to an increase of the electroluminescence intensity. A similar effect was considered earlier in [4]. In these studies, an increase of the minority carrier current was associated with a shift of the Fermi level in the metal toward the top of the valence band of the semiconductor. It lowers the barrier for minority carriers and increases the fraction of the minority carrier current in the total current through the structure.

Acknowledgments

This work was supported by the Russian Science Foundation (project no. 21-79-20186) and by the grant of the President of the Russian Federation (project no. MK-445.2020.2).

References

[1] Appelbaum I, Russel K, Monsma D, Narayanamurti V, Marcus C, Hanson M, Gossard A 2003 *Appl. Phys. Lett.* **83** 4571.

[2] Saha D, Basu D, Bhattacharya P 2008 *Appl.Phys.Lett.* **93** 194104.

[3] De Souza J, Danilov I, Boudinov H 1996 *Appl. Phys. Lett.* **68**(4) 535.

[4] Card H, Rhoderick E 1973 *Solid. State. Electr.* **16**(3) 365.

Development of visual display and data transmission system for patients with chronic disorders of consciousness

S A Degtiareva[1], D S Shiryaev[1], Y S Andreev[1], I S Polukhin[1], E A Kondratieva[2], I G Smirnova[1], V E Bougrov[1]

[1] Faculty of Laser Photonics and Optoelectronics, Saint-Petersburg, Russia
[2] Polenov Neurosurgical Institute, the Branch of Almazov National Medical Research Centre, Saint-Petersburg, Russia

E-mail: svetlanadegtiareva@itmo.ru

Abstract. The monitoring is essential to the daily care, as such vital physiological signs as heart rate, hemodynamic, temperature, saturation are the key to predict patient's recovering. They are collected from medical sensors to bedside monitors to detect unexpected life-threatening conditions or to record some changes continuously. It is commonly used for patients with chronic disorders, because monitoring of the critically ill patient requires prompt and accurate decisions so that life-saving therapy can be appropriately applied. However, taking into account the workload of doctors in the intensive care unit, there was a need to capture, display all physiological changes visually and collect them in a critical care setting. It will help to facilitate the monitoring process and predict the course of diseases. The aim of the work is to develop an optoelectronic system for visual monitoring and data transmission of patients in a coma by optical wireless communication.

1. Introduction

A coma is a deep state of prolonged unconsciousness as a result of traumatic brain injury, stroke, brain tumor, diabetes or an infection. But coma usually lasts for less than 2 to 4 weeks in itself, then a person may wake up into a vegetative state/unresponsive wakefulness state (VS/UWS) or minimally conscious state (MCS). It requires operative action to preserve life and brain function as well as visual controlling of basic physical cues such as heart rate, pulse, body temperature.

Imaging techniques, including functional magnetic resonance imaging, EEG and FDG positron emission tomography are proven to be useful in determining the diagnosis of VS/UWS and MSC [1-3]. However, diagnosis of the VS/UWS and MSC should be based on a patient's clinical history and on simple visual observations as well. Therefore, monitoring systems should be applied.

Diagnosis of chronic disorders of consciousness is a threat to the patient's life and requires a continuous monitor of the values on bedside monitors, even in the face of increased workload of medical personnel. Thus, there is a need to develop a system that helps to read vital physiological parameters, display their changes in real-time and indicate a deterioration or improvement of the patient's internal state. The development of a visual display object with established light-emitting

diodes allows to represent physiological changes by controlling parameters and send them by optical wireless communication immediately.

2. Methods

Sensors on the patient's body are the main part of the visual display and data transmission system. It is designed to collect the values of physiological parameters from sensors, display received data according to specified scenarios of changes in the color of LED radiation, and transmit data to a server or personal computer using optical wireless communication technology for viewing. The system will help to read the state of patients with chronically impaired consciousness, such as the vegetative state (such vital functions as heart activity and breathing are preserved), the state of minimal consciousness (pain stimuli, environmental eye-tracking persist) the syndrome of unresponsive wakefulness (cognitive functions are preserved). Under signs of these types of depression of consciousness, the most important indicators of the physiological state of patients as heart rate, arterial blood oxygen saturation, and body temperature were selected as measured signals.

Light-emitting diode strips are established in groups on a cotton substrate to visualize the physiological parameters of patients in several scenarios: the values of physiological parameters are normal, the values of physiological parameters are lower than normal values, the values of physiological parameters are higher than normal values. If the values are in the range of normal values, the scenario is implemented in the form of a pulsating green color. When the values go beyond the lower bound, the LEDs have a chromaticity in the range of cold colors. When the values go beyond the upper bound, the LEDs have a chromaticity in the range of warm colors.

A color scale of possible scenarios of light-emitting diodes for given parameters is bounded by a triangle on the CIE color space diagram. It has vertices in the chromaticity coordinates, reflecting a wide range of colors for specifying all necessary parameters: $x_r = 0.71, y_r = 0.29$; $x_g = 0.18, y_g = 0.72$; $x_b = 0.16, y_b = 0.03$.

3. Conclusion

Patients with chronic disorders of consciousness remain a challenge for clinical practice. A bedside monitor should be provided for monitoring of vital parameters, such as: heart rate; arterial blood oxygen saturation, and body temperature. However, after intensive care unit patients are admitted to the rehabilitation unit without any monitoring system, cause he or she is considered stable. Nevertheless, the need to monitor the physiological parameters remains. The use of visual display and data transmission system will allow medical staff to respond to some changes in time and prevent critical situations.

Acknowledgments

We thank Almazov Research Medical Centre for its great contribution and consulting support.
This work was supported by RFBR grant № 19-29-01066/2020

References

[1] Heiss W D 2011 Pet in Coma and in vegetative state *Europian J. of Neurology* **19**, pp 207-211

[2] Edlow B L, Giacino J and Wu O 2013 Functional MRI and Outcome in Traumatic Coma *Current Neurology and Neuroscience Reports*

[3] Bates D 2001 The Prognosis of Coma *J. of Neurology, Neurosurger and Psychiatry* **71** pp 20-23

[4] Martin M Monti and Walter G Sanita 2016 *Brain Function and Responsiveness in Disorders of Consciousness* (Switzerland: Springer International Publishing)

[5] Cruse D, Chennu S, Chatelle C, Bekinschtein T A, Fernández-Espejo D, Pickard J D, Laureys S and Owen A M 2011 Bedside detection of awareness in the vegetative state: a cohort study», *The Lancet*, **378**, pp. 2088-94

Optical properties of single crystals of $BaF_2 – SrF_2 – ErF_3$ solid solutions

V.Yu. Zhmykhov*, E.A. Dobretsova, V.B. Tsvetkov, V.A. Konyushkin, A.N. Nakladov, P.P. Fedorov, Yu.N. Pyrkov, S.V. Kuznetsov

Prokhorov General Physics Institute of the Russian Academy of Science, 38 Vavilova street, Moscow 119991, Russia

*****Corresponding author, e-mail: Vadimzhmykhov56@gmail.com

Abstract. Absorption spectra of single crystals of BaF_2 - SrF_2 - ErF_3 solid solutions containing Er^{3+} of 5-10 mol.% have been recorded in a wide spectral range at room temperature. Judd-Ofelt parameters have been calculated.

1. Introduction.

Rare-earth-doped MF_2 (*M* = Ca, Sr, Ba) single crystals are well known as active media for lasers [1]. To date, effective laser media with a lasing efficiency of more than 80% have been developed based on three-component disordered solid solutions with the fluorite structure. Special attention should be paid to materials capable of lasing in an infrared range of a spectrum, including those doped with thulium, erbium, and holmium ions [2].

2. Results and discussion.

This work presents spectral-kinetic studies of single crystals of BaF_2 - SrF_2 - ErF_3 solid solutions growing by the Bridgman technique. The absorption spectra of the single crystals with an Er^{3+} content of 5-10 mol% have been recorded in a wide spectral range at room temperature. Based on the experimental absorption spectra, the Judd-Ofelt parameters have been calculated. The comparative study of the samples performed suggests that the structure of the nearest environment of impurity Er^{3+} ions change at increasing the Er^{3+} content. The Ω_2 value is strongly affected by asymmetry of the crystal field around Er^{3+}. Decreasing Ω_2 with increasing the Er^{3+} content points to higher degree of local symmetry in the sample doped with Er^{3+} of 10 mol. %.

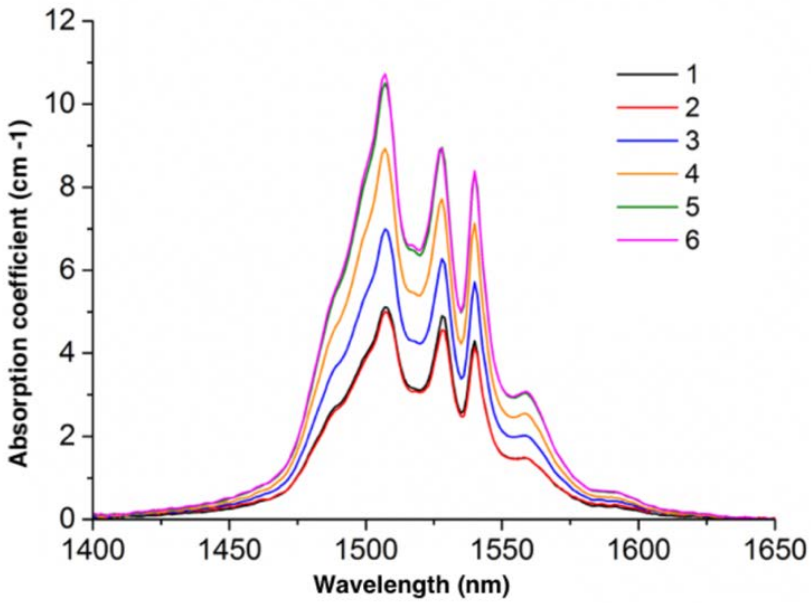

Fig.1 Absorption spectra of single crystals of BaF_2 - SrF_2 - ErF_3 solid solutionswith Er^{3+} content of: 5 mol.% (1), 6 mol.% (2), 7 mol.% (3), 8 mol.% (4), 9 mol.% (5), 10 mol.% (6).

References

[1] Kaminskii A A, 2013 *Laser crystals: their physics and properties*. (Springer)
[2] Sulc J, Nemec M, Jelinkova H , Doroshenko M E, Fedorov P P and Osiko V V. 2015 (SolidState Lasers XXIII: Technology and Devices, CA, USA) **34** 912-914

A comprehensive study of current-crowding effect in high power vertical AlInGaN LEDs under high pulsed current

A E Ivanov[1,2*], A V Aladov[1], A E Chernyakov[1,2] and A L Zakgeim[1]

[1] Submicron Heterostructures for Microelectronics Research and Engineering Center RAS, St Petersburg 194021, Russia
[2] Saint-Petersburg Electrotechnical University ETU "LETI", St. Petersburg 197376, Russia

*a-e-ivano-v@yandex.ru

Abstract. The goal of the reported study is examination of current-crowding effect in high power AlInGaN LEDs. This effect was experimental study by mapping of spectral and EL under high pulse current (~70 A). For this we used nitride LED chips of vertical design. The LEDs operating under high pulsed current density are interesting for different applications, such as pumping lasers, VLC & LiFi, accelerated process degradation process of LED.

1. Introduction

The scope of application of light-emitting diodes (LEDs) keeps expanding. The study of the operation of LEDs in pulsed mode to exclude self-heating at high excitation levels is of great interest for establishing the injection and recombination mechanisms and identifying the reasons that limit the energy capabilities of devices [1-4] In this work, we studied blue commercial LEDs of «vertical» design [5].

2. Experimental

Commercial non-casted Enhanced Vertical LED dice, EV-B40A (peak emission wavelength λp = 460 nm), produced by SemiLEDs with the emission area of 1100x1100 μm^2 were chosen for our study, having a simple contact geometry (inset Figure 1).

Current-voltage (I-V) and light-current characteristics of the LEDs were measured by the OL 770-LED Highspeed LED Test and Measurement System by Optronic Laboratories Inc. [6], using an integrating sphere.

The optical parameters of the devices under test were measured in pulsed regime. To ensure the predetermined pulse regime, an Agilent 8114A pulse generator was used with a PicoLAS LDP-V 80-100 V3.3 external amplifier. The pulse width and duty cycle were monitored with a Tektronix TDS3044B oscilloscope. Pulse repetition rate was chosen to avoid self-heating at f = 50 Hz.

Near-field distribution of electroluminescence (EL) intensity was monitored by using Mitutoyo optical microscope and Avantes AvaSpec-2048. The minimum and maximum field of view of the optical system was 536×357 μm^2 and 5362×3520 μm^2, respectively, with the best spatial resolution of 25 μm. The optical system collected the light within the 15° cone around the normal direction.

3. Results and discussion

The distribution map of intensity NF on the die surface at different operating currents was obtained By optical microscopy This graph shows the normalized intensity of the radiation at CC A. As we see at low operating current uniform distribution of blue emission takes place Light intensity distribution is directly proportional to the current density over the area of p-n junction. But at the current 2A and higher Near-field EL emission confirms considerable current crowding effect. The optical power depends on current nonlinearly.
The spectral analysis (Figure 2) in cross-section A (inset figure 1) showed only blue shift effect consequently our regime does not have self-heating.

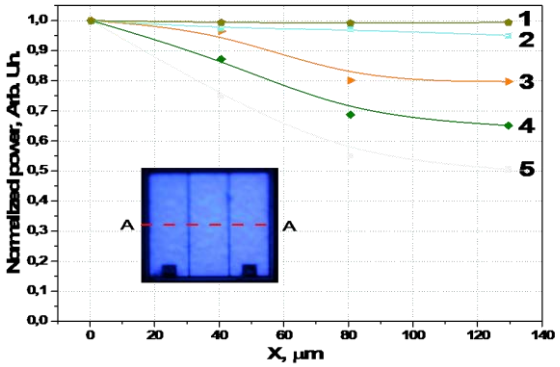

Figure 1. The distribution of relative power as a function of the coordinate on the chip. Current: 1 – 0.1A, 2 – 0.7A, 3 – 4A, 4 – 20A, 5 – 70A.

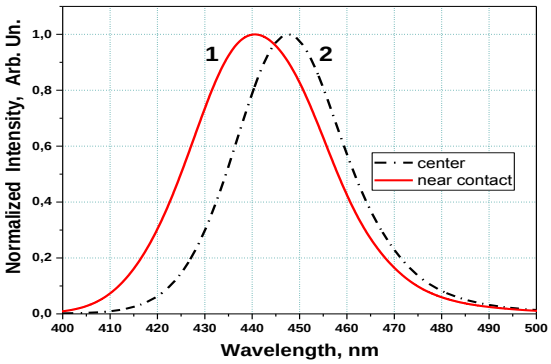

Figure 2. Normalized LED spectrum near the n-electrode (1) and in the center of the chip (2) at a current of 70A.

Thus, the pre calibration of the depending wavelength at the current are allow you to graph the current density distribution between the electrodes in the cross-section A.

4. Conclusion

The experimental EL near-field emission patterns obtained at current up to 70A for "vertical" chip show that EL intensity (respectively, the current density) increases near the edge of the n-electrode, due to the insufficient conductivity a semi-transparent contact to n-GaN and a thin n-GaN semiconductor layer.
The mapping of current density was built by analysis of spectral in each point of p-n junction area under the high current. Under the current more than 2 A, it is incorrect to use the average current density to display characteristics due to the effect current-crowding was shown.

Acknowledgments

This work was carried out at the Center of Multi-User Facilities «Element Base of Microwave Photonics and Nanoelectronics: Technology, Diagnostics, and Metrology».

References

[1] Yadaev A, at al. 2016 SPIE Proceedings 9768
[2] Karpov S, at al. 2014 IEEE J. Quantum Electron 50 911-20
[3] Aladov A, Ivanov A, at al. 2020 ICLO 1109
[4] Chernyakov A, at al. 2015 16th Int. Conf. on Thermal, Mechanical and Multi-Physics Simulation and Experiments in Microelectronics and Microsystems, pp. 1-5, doi: 10.1109/EuroSimE.2015.7103132
[5] LEDs datasheet blue https://www.semileds.com/system/files/EV-B45A.pdf
[6] Zakgeim A and Chernyakov A 2013 LIGHT & ENGINEERING 21 Iss. 4 64-70

Optimization of the profile and material of wire contacts for an IR photodetector

A V Kamarchuk [1*], **D A Bauman** [1], **A I Marchenko** [1]

[1] Saint-Petersburg National Research University of Information Technologies, Mechanics and Optics, Saint-Petersburg 197101, Russia

*Corresponding author, e-mail: annakamarchuck@itmo.ru

Abstract. The study is devoted to the influence of the choice of geometry and materials of wire contacts on the reflection coefficient and thermal characteristics of the photodetector and the quality of the device design. The process of diffusion of materials of wire contacts and contact pads on a photodetector crystal is investigated.

1. Introduction

One of the key components of radiophotonics is high-speed photodetectors.

Many radio-photonic systems today use PIN-type photodiodes. The desirable characteristics of photodetectors are high sensitivity, wide dynamic range and large bandwidth, but in practice these parameters cannot be achieved simultaneously due to the physical foundations of the photodiode operation and design solutions. It should be noted that in terms of designs and evolving technologies that allow compromise solutions to achieve high bandwidth and high operating power, there are a large number of solutions. Optimization of technologies for creating a photodetector design is one of the main solutions to ensure high technical characteristics of the device.

2. Description of the model

This section describes the construction of models of a photodetector device with different materials for forming wire contacts (Al, Au, Ag, Cu) and different geometries of contacts for solving a two-dimensional problem of heat conduction in a homogeneous medium.

Numerical modeling of various mechanisms of heat transfer makes it possible to analyze the thermal state of the structural elements of the photodetector, determine the temperature modes of its operation and the overall energy efficiency.

3. Results and discussion

Results of the analysis of thermal conductivity models in the design of the photodetector.

Influence of different geometry of the loop profile and materials (Al, Au, Ag, Cu) of the wire when creating a coordinated design of the photodetector (board and crystal) in a homogeneous medium (air). Analysis of the thermal distribution in the design of the photodetector at different currents and voltages and the effect on the deformation of the contact material Analysis of the strength quality of the photodetector structure, based on the analysis of the diffusion process of materials and methods of testing the structure for strength. The studies were carried out using a scanning electron microscope.

4. Conclusion

Thus, simulation of thermal processes in a photodetector, optimization of design solutions (formation of certain wire profiles and material selection), optimization of technological solutions in the process of mounting wire contacts made it possible to create a better design of a photodetector from a structural point of view (analysis of the diffusion process of materials, creation of a consistent design) and technical (achieving a reflection coefficient below -10 dB).

References

[1] Harman G Wire bonding in microelectronics. Third edition. McGraw Hill. 2010

[2] Kurushin A A Solution of multiphysics microwave problems using CAD COMSOL-M., One-Book, 2016. 376 pages.

Computer simulations of solar cells based on silicon/boron phosphide selective contacts

S Y Kiyanitsyn[1], **A S Gudovskih**[1,2]
[1]Department of Photonics, St. Petersburg Electrotechnical University ("LETI"), 197376 St. Petersburg, Russia
[2]St. Petersburg Academic University of RAS, 194021 St. Petersburg, Russia

E-mail:serg-kianitsyn@mail.ru

Abstract. The work is devoted to the calculation of the characteristics of silicon solar cells with selective contacts based on boron phosphide. Improving the efficiency of silicon solar cells is critical for the continued development of renewable energy sources. To understand how the defects in the near-surface layer and at the interface have been influenced the computer simulations were performed. As a result, calculations of the dependence of the characteristics of solar cells on parameters such as the density of interface states, the concentration of defects in the near-surface region, and its width were made.

1. Introduction

Currently, an intensive search is underway for ways to improve the efficiency of Si solar cells being the main material for solar energy. The theoretical limit of the conversion efficiency of Si solar cells is 29.1% [1], but the real efficiency of such solar cell is below 26%. One of the most promising ways to increase the efficiency is the use of selective contacts to Si, which should provide selective charge carriers transport, a low level of recombination at the interface, and have a high optical transparency for solar radiation. From this point of view, a completely new hole-selective contact based on boron phosphide Si/BP may be of great interest [2]. BP has tremendous potential because it is an indirect gap $E_g \sim 3$ eV and has a negative (-0.3 ± 0.1 eV) valence band offset ΔE_V at the BP/Si interface. In addition, this material can be formed at low temperatures using plasma deposition, which is attractive in terms of mass production. However, the use of plasma can potentially lead to the formation of defects both at the BP/Si interface and in the near-surface region of Si. In this work, computer simulation study of the dependence of the characteristics of solar cells on parameters such as the density of surface states, the concentration of defects in the near-surface region and its width was carried out.

2. Experiments and results

The AFORS-HET v2.5 software package was used to calculate the characteristics of solar cells based on the p-BP/n-Si heterojunction. At the first stage, we studied the effect of the density of interface states (D_{it}) at the BP/Si interface. The obtained dependences are shown in Fig. 1 (a). It can be seen that the open circuit voltage (Voc) is highly dependent on Dit, while the short-circuit current (Jsc) is practically independent of Dit. It should be noted that the sensitivity to surface states is significantly

affected by the valence band offset ΔE_V. As shown in Fig. 1 (b), an increase of ΔEv leads to weaker dependence of Voc on Dit, which is associated with an increasing band bending in Si. Thus, to predict the sensitivity of the characteristics of solar cells based on p-BP/n-Si to Dit, it is necessary to experimentally determine the value of ΔE_V.

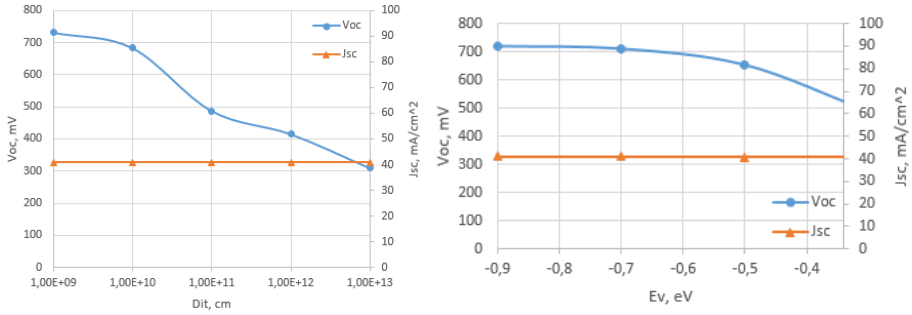

(a) (b)

Figure 1 (a, b). Dependences of Voc and Jsc on **(a)** the density of surface states (Dit) *at the BP / Si interface* **(b)** on the discontinuity of the valence bands ΔEv for $D_{it} = 10^{11}$ cm^{-2} eV^{-1}

At the second stage, we studied the effect of defects in the near-surface region of Si. Figure 2 shows the obtained dependences on the charge carriers lifetime in the defect layer (τ) and on its depth (d). It can be seen that the formation of a defect region near the BP/Si interface also significantly affects Voc. An increase in the concentration of defects, leading to a decrease in τ to 10^{-7} s and an increase in the defect region above 10 nm, leads to a decrease in Voc.

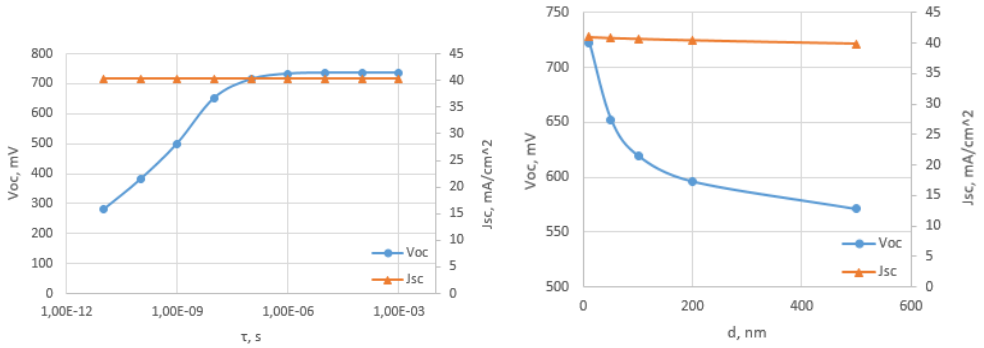

(a) *(b)*

Figure 2(a, b). *Dependences of Voc and Jsc on* **(a)** *he lifetime in the near-surface region at d = 100 nm* **(b)** *on the penetration depth of defects at* $\tau=10^{-8}$ s.

Acknowledgments

This work was supported by Ministry of Science and Higher Education of the Russian Federation (research project 0791-2020-0004).

References

[1] Yoshikawa K., Kawasaki H.,Yoshida W., Irie T., Konishi K., Nakano K., Uto T, Adachi D., Kanematsu M., Uzu H., Kenji *Article Nature Energy*

[2] Gudovskikh A.S., Kudryashov D.A. , Baranov A.I. , Uvarov A.V. , Morozov I.A. Formation of selective BP / Si contact using low-temperature plasma-chemical deposition// Technical Physics Letters, 2021, 47, pp. 96–98.

Stretchable transparent light-emitting diode membranes based on multiple quantum well InGaN microwires and carbon nanotubes

F M Kochetkov[1], V V Neplokh[2], V A Mastalieva[1], S Mukhangali[1], M S Mukhin[1] and I S Mukhin[1]

[1] Nanotechnology Research and Education Centre of the Russian Academy of Sciences, Alferov University, Khlopina 8/3, 194021 St. Petersburg, Russia
[2] St. Petersburg State Technical University, St.Petersburg 195251, Russia

e-mail: azemerat@rambler.ru

Abstract: We demonstrate both flexible and stretchable blue light-emitting diodes based on core/shell InGaN/GaN microwire/polydimethylsiloxane (MW/PDMS) membranes. GaN/InGaN core-shell microwires were grown by metal-organic vapour phase epitaxy, encapsulated into a PDMS film and then released from the growth substrate. The fabricated free-standing membrane LEDs with single wall carbon nanotubes-based contacts can stand up to 20% stretching while maintaining efficient operation.

1. Introduction

Stretchable and flexible optoelectronic structures are the envisioned base for next generation of smart wearable devices with enhanced functionality and usability. Stretchable optoelectronics is a focus of research for many companies specialized in numerical billboards and displays as a final phase of the evolution of flexible displays. The major advantage is their form factor adapting for various applications such as foldable screens, bio-integrated devices and wearable sensors Nowadays, the most developed and commercially successful flexible device technology is based on organic materials. The main advantage of the organic light-emitting diodes (OLED) is a relatively inexpensive and scalable fabrication with agreeable electroluminescence efficiency. However, organic devices are inferior to inorganic semiconductor materials in terms of long-term stability, luminance and external quantum efficiency, especially in the blue and red spectral ranges. Semiconductor microwires (MWs) have been investigated since the last 5 years as ideal candidates for flexible LEDs. Owing to their small footprint, MWs can be bent without structural damage. Applied to a polymer/MW membrane stretching and bending result in a negligible deformation of the MWs thus preserving the device function. Therefore, a composite polymer/MW membrane can stand high stretching thanks to the polymer elasticity [1].

2. Result and discussion

The light-emitting diode structure (LED) studied in this work is an array of filamentous GaN/InGaN microwires (MW) with a p-i-n doping profile grown by the method of deposition of organometallic compounds from the gas phase (MOCVD), which has a luminescence line in the blue spectral range (455 nm). This array was encapsulated in a polymer matrix of polydimethylsiloxane (PDMS) by the method of gravity winding [2]. Single-walled carbon nanotubes (SWCNTs) with a transparency of 80%

acted as an electrical transparent contact to this structure. Next, the MW/PDMS membrane were mechanically peeled from the growth substrate by a microtome blade.

Studies have shown that, despite the elasticity and strength of SWCNTs, when stretching the membrane with MW by 20%, there was a decrease in conductivity by 40%, which negatively affects the energy efficiency of the LED. The low conductivity remained in the relaxed state, and gradually increased with each subsequent stretching of the LED. Presumably, this effect is associated with a violation of percolation in the SWCNT array.

Experiments have shown that for such contacts to the membranes, when stretched by 20%, the drop in the SWCNT conductivity was only ~5% and remained constant in subsequent iterations, which made it possible to create effective stretchable light-emitting structures.

The LEDs based on PDMS membranes, InGaN MWs, and pre-stretched CNT contacts were studied by electroluminescence (EL), photoluminescence (PL), and cathodoluminescence (CL). The optical transparency of the stretchable flexible LED was also measured using an integrating sphere, which was 43%.

Acknowledgments

The authors thank the Ministry of Science and Higher Education of the Russian Federation (FSRM-2020-0005).

References

[1] Su Y, Ping X, Yu K 2016 *Advanced Materials*, **29(8)**, 1604989

[2] Neplokh V, Kochetkov F M, Deriabin K V 2020 *Journal of Materials Chemistry C*, **8(11)**, 3764-3772.

.

Optimization of p-aSi:H/p-Si ohmic contact for solar cells

D A Kudryashov[1], A I Baranov[1], A V Uvarov[1], I A Morozov[1], A O Monastyrenko, A S Gudovskikh[1,2]

[1]Alferov University, St. Petersburg 194021, Russia

[2]Department of Photonics, Saint Petersburg Electrotechnical University "LETI", St. Petersburg, 197376 Russia

E-mail: kudryashovda@spbau.ru

Abstract. Start your abstract here…

1. Introduction

Nowadays solar cells have become an important part of our life. We can find them everywhere ranging from portative charges to large solar farms collecting and transforming solar energy to electricity. It is all because of well developed technology and price of raw materials such as silicon. The highest efficiency for the most used solar cells of 26% was reached [1]. Further efficiency increase may be realized with an optimization of individual layers properties and contacts. For example, there are still lack of data related to effective p-aSi:H/p-Si ohmic contact used for solar cells fabrication by PECVD method. The point is that three trimethylboron (TMB) used as a doping component for p-type a-Si:H formation is a very sensitive material to process parameters that are individual for different deposition systems. Boron concentration in amorphous silicon depends on plasma power, substrate temperature, pressure and other parameters. This papers presents last results on process parameters optimizations for a p-aSi:H/p-Si ohmic contact formation.

2. Experimental detail

CZ p-type silicon wafers (100) with a resistivity of 1-5 Ohm cm were used as a substrate. Prior the deposition silicon wafer was immersed in HF:H_2O solution to remove native oxide. Amorphous silicon layers were deposited by Oxford plasmalab 100 PECVD system at a power of 5 W and a temperature of 250 °C. Silane, TMB and hydrogen were used as source gases. After the deposition silver contacts were formed by thermal deposition in TLM geometry. Current-voltage characteristics were measured with Keithley 240 source meter.

3. Results

Figure 1 shows current-voltage characteristics measured for the p-aSi:H/p-Si contact formed at a fixed silane flow (40 sccm) and different TMB flow. A non-linear behavior is observed with a maximum current value at a TMB flow of 50 sccm.

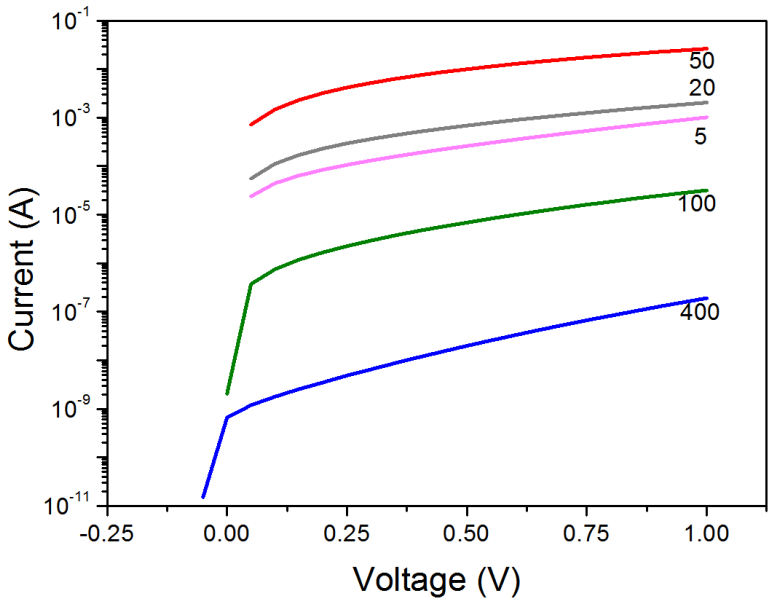

Figure 1. I-V characteristics of the p-aSi:H/p-Si contact formed at a fixed silane flow and different TMB flow.

Additional results and detailed discussion will be presented at the conference.

Acknowledgments

This work was supported by Ministry of Science and Higher Education of the Russian Federation (research project FSRM-2020-0004)

References

[1] Yoshikawa K., Kawasaki H., Yoshida W., Irie T., Konishi K., Nakano K., Uto T., Adachi D., Kanematsu M., Uzu H., Yamamoto K. // Nat. Energy. 2017. V. 2. P. 17032.

Three-component magnetic field monitoring system for autonomous space devices

S E Logunov[1, 2], V V Davydov[2, 3] and V Yu Rud[3, 4]
[1]Northwest Open Technical University, Saint Petersburg 195027, Russia
[2]Peter the Great Saint-Petersburg Polytechnic University, Saint Petersburg 195251, Russia
[3]All-Russian Research Institute of Phytopathology, Moscow Region 143050, Russia
[4]A.F. Ioffe Physicotechnical Institute, St. Petersburg, 195152, Russia

Abstract. The necessity of additional study of magnetic field variations in the magnetic transition layer, in the magnetopause, as well as in the plasma layer and in the tail of the magnetosphere in a wide range of distances from the Earth is substantiated . To obtain additional information in comparison with the studies that are being carried out in outer space at the present time, it is necessary to simultaneously monitor the magnetic field at various points in outer space. It is also necessary to register the dynamics of changes in the magnetic field in time in space by three components. To accomplish this task, a small-sized three-component quantum variometer with autonomous power supply has been developed for space devices, which can be lost in the course of short-term research. The results of the operation of the system when controlling the magnetic field are presented.

1. Introduction

The Earth's magnetosphere is the most important component of the ecological state of the planet. It protects all life on Earth from streams of ionizing radiation (solar wind). An important element of the Earth's magnetosphere is the boundary (magnetopause), at which the pressure from the Earth's magnetic field is equal to the pressure of the solar wind shock wave. There are regions in the magnetosphere that are geomagnetic traps that hold particles in a limited volume. This forms the Earth's radiation belts. All these areas of magnetic fields in order to predict various situations, both on Earth and in outer space in near-Earth orbits, must be investigated in the process of the evolution of the universe. Information from quantum magnetometers [1, 2] located on the Ulysses spacecraft is insufficient for spatial monitoring of various zones of the magnetosphere. Autonomous magnetic field sensors are needed, which will make it possible to carry out measurements for a long time in an autonomous flight.

2. Three-component quantum meter of magnetic field variations

In studies of variations in the magnetic field in the Earth's field from a moving object, a design of an autonomous sensor based on a ferrofluid cell with a magnetic fluid was proposed [3 , 4]. The variation of the magnetic field in the direction of the lines of force of the Earth (one component) was

measured, since the moving object creates the greatest distortions in this direction. In the event of exposure to the solar wind (the magnetic field of the Sun is 100 times greater than the magnetic field of the Earth - about 50 μT), three sensors are installed on an autonomous object (three modules with a common power supply from solar cells). The ferrofluid cell in each of these sensors is positioned in the controlled magnetic field of the solenoid. Laser radiation with λ = 632.8 nm arrives at the transparent walls of the cell perpendicular to the magnetic field. If the magnetic field is uniform, then the photodetector registers a symmetric diffraction pattern in the form of stripes from the laser radiation transmitted through the cell (Figure 1.a). The resolution of the resulting picture is determined by the number of pixels of the photodetector per 1 cm 2. So the resolution of the photodetector is 3840x2160, which corresponds to 8 MP. The size of one pixel is 1.4 microns. When the induction BW of the magnetic field of the solar wind is exceeded, the induction of the solenoid field is distorted (Figure 1.b). By adjusting the field of the solenoid, you can determine B_{sv} in a given direction. Build a spatial picture of the field at a point in space using three sensors.

.

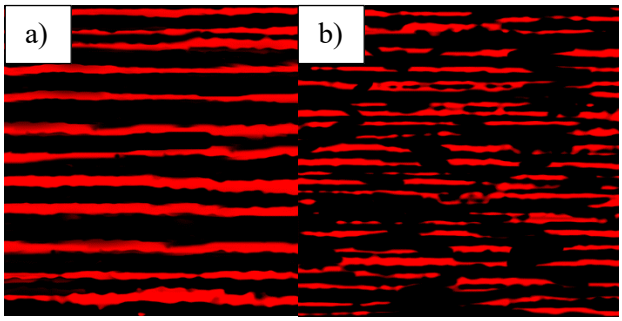

Figure 1. Diffraction pattern from laser radiation for the cases of placement of a ferrofluid cell: a) in a uniform magnetic field, b) - inhomogeneous.

An analysis of the results obtained (Figure 1) shows that by controlling the magnetic field of the solenoids, one can obtain information both on the magnitude of the three components of the magnetic field in outer space, and on the nature of their change (variations) in time. To do this, it is necessary to perform a preliminary calibration of the sensors and put in them various versions of the program for measuring the magnetic field.

3. Conclusion

Experimental studies have shown that the service life of such sensors with an autonomous power source is more than 1 year, with the use of solar cells it can significantly increase (until the protective layers of an autonomous object made of non-magnetic material are destroyed). Such a design of sensors allows them to be sent into outer space from a spacecraft at least several dozen.

References

[1] Vershovskii A K, Dmitriev S P and Pazgalev A S 2013 *Technical Physics Journal* **83** 879
[2] Aleksandrov E B and Vershovskii A K 2009 *Physics-Uspekhi* **52** 573-601
[3] Logunov S.E., Koshkin A.Yu., Davydov V.V., Petrov A.A. 2016 *Journal of Physics: Conference Series* **741(1)** 012092
[4] Logunov S E, Davydov V V, Vysoczky M G and Mazing M S 2018 *Journal of Physics: Conference Series* **1038(1)** 012093

Study of GaP/Si electron-selective contact deposited by plasma

Maksimova A.A. [1], Baranov A.I. [2], Uvarov A. V. [2], Gudovskikh A.S. [1,2], Kudryashov D.A. [2], Morozov I.A. [2]
[1]Department of Photonics, Saint Petersburg Electrotechnical University "LETI", St. Petersburg, 197376 Russia
[2]St. Petersburg Academic University, St. Petersburg 194021, Russia

E-mail: maksimova_alina@spbau.ru

Abstract. The article is based on an important characterization task to accurately evaluate the properties of the layers, their interfaces with c-Si, and to select the best candidates to integrate them into a c-Si-based solar cell. The work has shown that GaP could be doped with n-type doping, thus providing a selective contact for the electrons, and has a significant valence band offset with c-Si, making it an excellent candidate as a selective contact, without requiring an additional ITO layer.

1. Introduction

Crystalline silicon-based photovoltaics (c-Si) has experienced a new boom in recent years due to the novel concept of selective contacts. It was first opened with silicon heterojunction cells (HET-Si). These use a stack consisting of a very thin layer of hydrogenated amorphous silicon (a-Si:H) ensuring a good chemical passivation of the surface of the c-Si, and a layer of doped a-Si:H, n-type or p-type, for contact selectivity to extract electrons or holes, respectively. However, the conductivity of a-Si:H, even highly doped, is not sufficient to ensure good lateral flow of the charges, so HET-Si cells also require a layer of Indium Tin Oxide (ITO) to be applied. In addition, despite energy conversion efficiencies of more than 25% on large surface cells, this technology is struggling to make its way into the industrial sector, particularly because of the use of indium, which is a barrier given the limited long-term visibility of its availability and price.

Another recently proposed alternative uses a stack consisting of an ultra-thin layer of silicon oxide (SiO2), and highly doped polysilicon layer. The first has to provide the passivation of c-Si while allowing the charge carriers to pass through (either by tunnelling or through nano-holes), the second provides the carrier selectivity and it can be obtained by depositing amorphous silicon followed by high temperature crystallization annealing. Conversion efficiencies of more than 25% have been published on small cells, but industrialization of this process is not yet on the agenda, and it faces the number of additional steps to be implemented.

In the proposed thesis, a new path based on phosphide-type materials, which have attractive characteristics for this application, is studied. Thus, gallium (GaP) phosphide has a band gap significantly larger than c-Si and higher than a-Si:H, thus limiting the absorption of the solar spectrum in these layers, which augurs well for a gain on the short-circuit current compared to the use of a-Si:H. Preliminary work has shown that GaP can be highly doped with n-type doping, and has a significant

valence band offset with c-Si, making it an excellent candidate as a selective electron contact, without requiring an additional ITO layer [1].

2. Experiment details

The phosphide layers are grown by plasma technique using the Oxford Plasmalab 100 PECVD setup. This is a reliable, industry-relevant technique that allows one to grow electronic-quality films at low temperature on large areas. Recently was developed low-temperature (250-380 °C) plasma-chemical synthesis technology of thin GaP layers on Si [2], and the possibility of their donor doping [3], thus small (0.2–0.35 eV) conduction band gap (ΔE_C) for GaP/Si [4, 5] provides necessary selectivity based on the heterojunction band diagram.

Here, electrophysical properties of GaP/Si multilayer structures grown on n-Si wafers by PE-ALD are studied. The material and heterojunction properties are analyzed by capacitance techniques: capacitance vs voltage to address the doping and band offset issues, admittance spectroscopy (capacitance and conductance as a function of frequency and temperature) and DLTS (Deep Level Transient Spectroscopy) to study defects in the layers and at the interface.

The work has shown that GaP could be doped with n-type doping, thus providing a selective contact for the electrons, and has a significant valence band offset with c-Si, making it an excellent candidate as a selective electron contact, without requiring an additional ITO layer.

Acknowledgments

This work was supported by the Russian Scientific Foundation under Grant № 17-19-01482

References

[1] Wang, X.-L., Wakahara, A., & Sasaki, A. (1996). Si and Zn doping of GaP grown by OMVPE using tertiarybutylphosphine. Journal of Crystal Growth, 158(1-2), 49–52. doi:10.1016/0022-0248(95)00341-x

[2] Gudovskikh, A. S., Morozov, I. A., Uvarov, A. V., Kudryashov, D. A., Nikitina, E. V., Bukatin, A. S., … Kleider, J.-P. (2018). Low temperature plasma enhanced deposition of GaP films on Si substrate. Journal of Vacuum Science & Technology A: Vacuum, Surfaces, and Films, 36(2), 021302. doi:10.1116/1.4999409

[3] Gudovskikh, A. S., Uvarov, A. V., Morozov, I. A., Baranov, A. I., Kudryashov, D. A., Zelentsov, K. S., … Kleider, J.-P. (2018). Interface Properties of GaP/Si Heterojunction Fabricated by PE-ALD. Physica Status Solidi (a), 1800617. doi:10.1002/pssa.201800617

[4] Wagner, H., Ohrdes, T., Dastgheib-Shirazi, A., Puthen-Veettil, B., König, D., & Altermatt, P. P. (2014). A numerical simulation study of gallium-phosphide/silicon heterojunction passivated emitter and rear solar cells. Journal of Applied Physics, 115(4), 044508. doi:10.1063/1.4863464

[5] Sakata, I., & Kawanami, H. (2008). Band Discontinuities in Gallium Phosphide/Crystalline Silicon Heterojunctions Studied by Internal Photoemission. Applied Physics Express, 1, 091201. doi:10.1143/apex.1.091201

Polarization control algorithm for QKD systems

E E Mekhtiev[1,2,4], I S Gerasin[1,2,4], N V Rudavin[1,5], A V Duplinsky[1,3,4], Y V Kurochkin[1,2,3,4]

[1]QRate, Novaya av. 100, Moscow, Russia
[2]Moscow Institute of Physics and Technology, 9 Institutskiy per., Dolgoprudny, Moscow Region, 141701, Russian Federation
[3]NTI Center for Quantum Communications, National University of Science and Technology MISiS, Leninsky prospekt 4, Moscow 119049, Russia
[4]Russian Quantum Center, Bolshoy Boulevard 30, bld. 1, Skolkovo, Moscow 121205, Russia
[5]Federal State Budget Educational Institution of Higher Education, MIREA—Russian Technological University, 78, Vernadskogo avenye, 119454 Moscow, Russia

{e.mehtiev, i.gerasin, n.rudavin, a.duplinsky, yk}@goqrate.com

Abstract. The crucial task for polarization-encoding fiber QKD is to compensate polarization drift occurring in a quantum channel. To solve this problem, the receiver usually uses a polarization controller. For proper operation, this device must be efficiently managed in real-time. In this work, a gradient-descent-based algorithm is proposed to solve this problem. The algorithm was implemented and tested on a QRate commercial QKD fiber system, that utilizes BB84-protocol. Low and stable QBER has been obtained during 50 hours of continuous operation.

1. Introduction

Today commercial implementations of quantum key distribution (QKD) mostly use phase or polarization encoding. The polarisation encoding approach requires an active feedback system, that aims to compensate for polarization disturbance in the channel between sender (Alice) and receiver (Bob). The EPCs based on fiber-squeezers are common devices used in QKD systems profiting from their low insertion loss. These devices are usually driven by the number of applied voltages on its channels which are chosen to minimize polarisation misalignment (expressed in terms of QBER in a quantum case). It is to say that polarization disturbance is not constant and evolves with time. Mathematically this task can be considered as an optimization problem, namely finding the minimum of polarisation misalignment or QBER as a function of voltages applied to the polarization controller.

The standard approach to the task stated above is to use gradient-descent-like algorithms. In [1] authors use the Hill-Climbing-based minimization algorithm. In [2] authors calculate first-order approximations of derivatives to make gradient-descent steps on each channel. Unlike previous considerations, we take advantage of the target function structure to improve algorithm convergence.

2. Algorithm

We take advantage of the internal structure of QBER as function of voltages and use Newton's method with second-order derivative approximation to minimize it. Minimization is performed in turn for each EPC's channel. We limit the size of the step as the second derivative can be extremely small. In the general case, Newton's method finds extremum (maximum or minimum) and we should separate this situation. To do this we add half of the voltage period on the channel if the current point is around the maximum.

3. Numerical and experimental results

Firstly, we construct a model of the QKD fiber system in terms of John's matrices. The simulation shows that gradient-descent for each channel with the second-order first derivative approximation is more stable in the minimum than the first-order approximation for the first derivative but has the same convergence speed. Using Newton's method with a second-order approximation for the first derivative we achieve faster convergence compared to mentioned above algorithms preserving the stability of the gradient descent with the second-order first derivative approximation.

The proposed algorithm uses only one hyperparameter h - step for derivative estimation. To find an optimal value of this parameter we run the simulation with the numbers of parameters h and find the optimal. Lastly, we implement the proposed algorithm in the QRate commercial QKD scheme with 50 km of fiber and measure the stability of the QBER during 50 hours.

For real-time polarization compensation QKD schemes our approach allows us to maintain QBER at a low level. For QKD systems that work in generation and polarization setup regimes, the proposed algorithm allows to achieve fast and stable convergence.

Acknowledgments

This work was supported by The Russian Science Foundation (Grant No. 17-71-20146)

References

[1] This Almeida, Álvaro J., et al. "Continuous control of random polarization rotations for quantum communications." *Journal of Lightwave Technology* 34.16 (2016): 3914-3922.

[2] Chen, Hua, et al. "New scheme for finite-retardation limitations of linear retarders with fixed axes in polarization control." *Optics Communications* 358 (2016): 208-214.

Asymmetric barrier layers design for 980 nm diode laser

M E Muretova[1,*], F I Zubov[1,2], M V Maximov[1,2], A E Zhukov[2], L V Asryan[3]

[1] Alferov University, St Petersburg, 194021 Russia
[2] HSE University, St Petersburg, 190008 Russia
[3] Virginia Polytechnic Institute and State University, Blacksburg, Virginia 24061, USA
* e-mail: muretova.maria@gmail.com

Abstract. A search for optimal asymmetric barrier (AB) designs for 980 nm InGaAs QW laser with GaAs waveguide was conducted. 3 optimal designs for each type of AB, p-side and n-side, intended for blocking electrons and holes, consequently, have been founded. The residual parasitic recombination current for various pairs of optimal AB-designs was calculated.

1. Introduction

The parasitic recombination in waveguide layers is one of the most significant problem limiting the efficiency of diode lasers [1]. A concept of asymmetric barrier (AB) layers has been proposed to suppress the parasitic recombination [2]. The AB layers are placed on both sides of the active region and are supposed not to let carriers enter the waveguide layer beyond the active region (see figure 1). Previously, in [3] using an example of 980 nm QW InGaAs/GaAs laser we have found that for significant reduction of the waveguide recombination parasitic-flux suppression ratios of ABs should be at least 10^3. Here we study the possibility of creating such AB-layers using conventional materials.

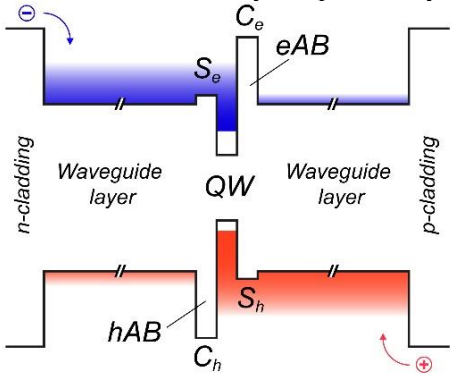

Figure 1. Schematic energy band diagram illustrating the concept of a laser with ABs.

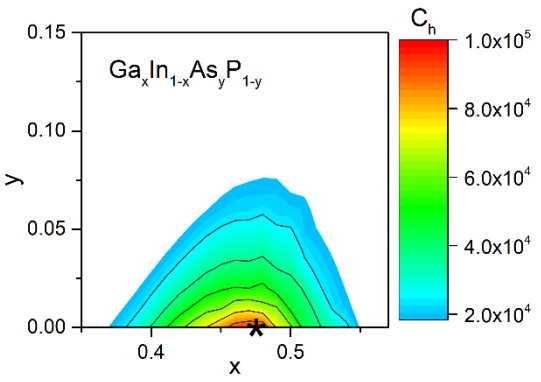

Figure 2. Contour plot for the parasitic hole flux suppression ratio C_h for ABs based on $Ga_xIn_{1-x}As_yP_{1-y}$.

2. Calculation details

Model laser structure had 800 nm wide GaAs waveguide cladded by $Al_{0.2}Ga_{0.8}As$ emitters. 7 nm $In_{0.18}Ga_{0.82}As$ QW placed in the center of the waveguide characterized by 41 and 116 meV electron and hole localization energies, correspondingly. Characteristics of the laser with ABs were calculated according to [2] under assumption of neutral active region.

The search for AB-designs was conducted among ternary and quaternary compositions formed from Al, Ga, In, As, P and Sb elements. We used the following limitations: AB-layer lattice mismatch ≤ 2%, AB-layer thickness is not higher than the critical thickness of dislocations formation or 15 nm (what is lower) and AB useful flux suppression ratios (S_e and S_h for electrons and holes, respectively) ≤ 100. The optimal ones were considered those AB-designs that provide the greatest parasitic-flux suppression ratios (C_e and C_h for electrons and holes, respectively).

3. Results and discussion

We have found 3 optimal designs for p-side AB for blocking electrons (eAB1-eAB3) and 3 optimal designs for n-side AB for blocking holes (hAB1-hAB3). Table 1 lists their compositions along with the main parameters. Also, as an example, we present the contour plot for C_h for n-side ABs based on GaInAsP (see figure 2), on which asterisk corresponds to the optimal composition hAB1.

Table 1. Founded materials for ABs.

	Composition	Optimal thickness, nm	Suppression ratio for undesirable flux	Suppression ratio for useful flux
eAB1	$Al_{0.37}Ga_{0.5}In_{0.13}As$	9.6	$C_e = 2.8 \cdot 10^4$	$S_h = 91$
eAB2	$Al_{0.31}Ga_{0.69}P_{0.61}Sb_{0.39}$	8.7	$C_e = 4.8 \cdot 10^6$	$S_h = 95$
eAB3	$Ga_{0.8}In_{0.2}P_{0.76}Sb_{0.24}$	15.0	$C_e = 2.0 \cdot 10^4$	$S_h = 96$
hAB1	$Ga_{0.48}In_{0.52}P$	5.4	$C_h = 9.6 \cdot 10^4$	$S_e = 97$
hAB2	$Ga\ P_{0.79}Sb_{0.21}$	6.0	$C_h = 1.1 \cdot 10^3$	$S_e = 93$
hAB3	$Al_{0.26}In_{0.74}P$	3.4	$C_h = 2.9 \cdot 10^3$	$S_e = 98$

Table 2 shows the residual parasitic current for various combinations of n- and p-side ABs with respect to the reference laser without AB-layers. It is seen that the unwanted recombination can be suppressed very significantly, e.g., for combination eAB2 and hAB1 the remaining parasitic current is only 0.2%.

Table 2. Residual parasitic current in laser with ABs with respect to reference laser without ABs, %.

		p-side AB for electrons blocking		
		eAB1	**eAB2**	**eAB3**
n-side AB for holes blocking	**hAB1**	7	0.2	7
	hAB2	19	13	19
	hAB3	12	5	12

4. Conclusions

Thus, we have shown that for 980 nm QW InGaAs/GaAs laser structure by using conventional materials it is possible to design AB-layers that provide very high parasitic flux suppression ratios (≈ 10^6 for electrons and ≈ 10^5 for holes), sufficient for almost complete suppression of the parasitic recombination in the waveguide.

References

[1] Frevert C, Crump P, Bugge F, Knigge S and Erbert G 2016 *Semicon. Sci. Technol.* **31** 025003
[2] Asryan L V and Luryi S 2003 *Solid-State Electron.* **47** 205
[3] Zubov F I, Muretova M E, Payusov A S, Maximov M V, Zhukov A E and Asryan L V 2020 *Semiconductors* **54** 366

Random bit generator on quantum dot micropillar lasers

A A Petrenko[1] **and A V Kovalev**[1]

[1] ITMO University, St. Petersburg, 197101, Russia

E-mail: aapetrenko@itmo.ru

Abstract. Results are presented on quantum dot micropillar lasers random bit generator physical characteristics modeling. A sample of three semiconductor micropillars total field intensity values with a 100 GSa/s frequency is implemented to obtain a bit sequence. Random bit sequences is shown successfully passed NIST statistical tests at a speed of 400 Gbit/s keeping 4 significant bits with sequence length at least 11142860.

1. Introduction

Currently random number generators utilization has been rapidly gaining popularity in various fields of science and technology, including communications, information technology, mathematical modeling, cryptography, and distributed computing. Random number generators are devices capable of creating independent elements bit sequences. In a random sequence of bits, the probability of 0 and 1 occurring is 0.5.

Since every subsequent bit in the sequence cannot be predicted, no matter how many bits have already been generated, reproducing such sequences is not possible, which, for example, greatly increases the safety of random number generators utilization to reproduce quantum keys.

In recent years few various random bit generators hardware implementations based on different principles have been presented: on vacuum fluctuations [1], on single-photon emission [2], homodyne [3] and heterodyne-based [4]. Semiconductor micropillar lasers with quantum dots utilization is of paramount interest since their dynamics is chaotic enough to obtain high-quality random sequences.

2. Model setup

An array of three conjugated semiconductor micropillar lasers is used as a chaotic signal source in the random bit generator model. At the initial stage the total field intensity values sampling frequency is set. The selected frequency is 100 GSa/s. The obtained values are normalized and sampled in accordance with the resolution of the 8-bit ADC. Sampled intensity values from the range 0 ... 255 are converted into bit representation. For each bit representation, the 4 least significant bits are selected. The resulting bit values are concatenated into the final sequence, the length of which was 11142860. At the final stage, the sequence randomness is checked using a NIST 800-22 statistical tests pack. The test is considered successful if the p-value is greater than 0.01. It is shown that with the parameters set, all tests are passed successfully, and the bit generation rate is 400 Gbit/s.

Table 1. Results of NIST SP 800-22 statistical tests. For "success" using 11142860 bit sequence the *p*-value should be larger than 0.01. For the tests which produce multiple *p*-values, the worst case is chosen.

Statistical test	Test *p*-value	Decision
Frequency Test (Monobit)	0.414	Success
Frequency Test within a Block	0.026	Success
Run Test	0.026	Success
Longest Run of Ones in Block	0.767	Success
Binary Matrix Rank Test	0.613	Success
Discrete Fourier Transform (Spectral) Test	0.435	Success
Non-Overlapping Template Matching Test	0.908	Success
Overlapping Template Matching Test	0.184	Success
Maurer`s Universal Statistical Test	0.453	Success
Linear Complexity Test	0.517	Success
Serial Test	0.991	Success
Approximate Entropy Test	0.260	Success
Cumulative Sums (Forward) Test	0.250	Success
Cumulative Sums (Reverse) Test	0.736	Success

3. Conclusion

It is shown that an array of three lasers based on semiconductor micropillars with quantum dots is capable of generating a random bit sequence with an equiprobable distribution of 0 and 1 with a performance of 400 Gbit/s. For each NIST 800-22 statistical test performed, the p-value was greater than 0.01. Developed model can be proposed for creating random bit generators with a high sequence generation speed.

Acknowledgements

This work was supported by the Ministry of Science and Higher Education of the Russian Federation, research project no. 2019-1442.

References

[1] Zheng Z, Zhang Y, Huang W, Yu S and Guo H 2019 *Rev. Sci. Inst.* **90** 043105.
[2] Luo Q, Cheng Z, Fan J, Tan L, Song H, Deng G, Wang Y and Zhou Q 2020 *Opt. Let.* **45** 4224-7.
[3] Huang L and Zhou H 2019 *JOSA* B **36** B130-6.
[4] Avesani M, Marangon D G, Vallone G and Villoresi P 2018 *Nat. Com.* **9** 1-7.

Numerical simulation of transients in $A^{III}B^{V}$ photodetector with controlled relocation

I V Pisarenko[1], **E A Ryndin**[2], **I D Isakov**[2]

[1]Southern Federal University, Institute of Nanotechnology, Electronics and Electronic Equipment Engineering, Department of Electronic Apparatus Design, 2 Shevchenko St., Taganrog 347922, Russia
[2]Saint Petersburg Electrotechnical University "LETI", Faculty of Electronics, Department of Micro- and Nanoelectronics, 5a Professor Popov St., Building 5, Saint Petersburg 197376, Russia

ivan123tgn@yandex.ru

Abstract. The development of $A^{III}B^{V}$ photodetectors with subpicosecond response time is an urgent problem in the field of modern nanoelectronics. Its solution is required, in particular, for the implementation of high-speed optical interconnections in ultra-large-scale integrated circuits. Previously, we proposed a photodetector with controlled relocation of carrier density peaks that applies the principle of mobility and lifetime modulation for the reduction of back-edge photocurrent lag in *p-i-n* heterojunction. In this paper, we perform the analysis of electron and hole transport in the aforementioned sensor based on the drift-diffusion approximation of the semiclassical approach to semiconductor device simulation. Numerical solution of the system that contains the two-dimensional continuity and Poisson equations allows us to evaluate key characteristics of the photodetector with controlled relocation and to modify its structure and photoreceiver circuit reasonably.

1. Introduction

In papers [1], [2], we demonstrated that it is possible to improve the response time of an $A^{III}B^{V}$ *p-i-n* photodiode through the formation of a transverse control heterostructure, whose electric field relocates photogenerated charge carriers from an absorbing region to special recombination layers with short lifetime and low carrier mobility during the back edge of an optical pulse. According to the results of quantum-mechanical numerical simulation, the high-to-low transient in a supply circuit of a photodetector with controlled relocation of carrier density peaks has the duration of about 0.1 ps. However, a quantum-mechanical model of the sensor does not take into account certain aspects of charge carrier transport in its structure, and the thorough analysis of transients in the photodetector with controlled relocation demands the implementation of a two-dimensional drift-diffusion model.

2. Drift-diffusion model and simulation technique

The time-domain drift-diffusion model of the photodetector with controlled relocation consists of the following fundamental equations [3]:

$$\frac{\partial n}{\partial t} = -\operatorname{div}\left\{\mu_{\mathrm{n}}\left[n \cdot \operatorname{grad}\left(\varphi + V_{\mathrm{n}}\right) - \varphi_{\mathrm{T}} \cdot \operatorname{grad}(n)\right]\right\} + G - R_{\mathrm{n}}; \quad (1)$$

$$\frac{\partial p}{\partial t} = \mathrm{div}\left\{\mu_\mathrm{p}\left[p \cdot \mathrm{grad}\left(\varphi - V_\mathrm{p}\right) + \varphi_\mathrm{T} \cdot \mathrm{grad}(p)\right]\right\} + G - R_\mathrm{p}, \quad (2)$$

$$\mathrm{div}\left[\varepsilon \cdot \mathrm{grad}(\varphi)\right] = -\frac{q}{\varepsilon_0} \cdot \left(p - n + N_\mathrm{d} - N_\mathrm{a}\right), \quad (3)$$

where n, p are the electron and hole concentrations; t is time; μ_n, μ_p are the electron and hole mobilities; φ is the electrostatic potential; V_n, V_p are the heterostructure potentials in conduction and valence bands; φ_T is the temperature potential; G is the generation rate of electron-hole pairs; R_n, R_p are the recombination rates of electrons and holes; ε is the dielectric permittivity of a semiconductor material; q is the electron charge; ε_0 is permittivity of vacuum; N_d, N_a are the concentrations of ionized donors and acceptors.

To solve differential equations (1)–(3) numerically, we designed the finite difference simulation technique that combines the mixed variable base, explicit and first-order upwind schemes, Newton and Gummel iterative methods. The considered technique was realized by the original software package written in the Octave programming language.

3. Simulation results

The analysis of the drift-diffusion simulation results enables to draw the following important conclusions:

- The mechanism of carrier mobility and lifetime modulation due to their controlled transverse relocation between thin semiconductor layers grown by molecular beam epitaxy at different temperatures ensures the decrease in photodetector response time to 0.1–0.5 ps when maintaining sufficiently high pulse sensitivity comparable to *p-i-n* photodiode with similar parameters.
- The fastest photoresponse of the sensor with controlled relocation is provided at certain optimal ratio between charge carrier mobilities in the absorbing and low-temperature-grown (LTG) regions. If mobility ratio is higher than the described one, the redistribution of charge carriers in the LTG regions is more durable, and response time gradually elongates. In contrast, if the ratio is lower, the mobility modulation is less efficient.
- The redistribution of electrostatic potential in the photodetector regions during the control voltage edges leads to the flowing of adverse capacitive current pulses through supply contacts. In the detection mode, these pulses are superimposed on the photocurrent, and it causes false activations of photoreceiver circuit. To deal with this problem, we propose to generate a measurement signal using two device structures connected with a high-speed differential amplifier. Both structures have the same constructive and technological parameters, supply and control voltages, but only one device is attached to an optical waveguide and acts as a photodetector. It means that the output signal of the differential amplifier contains only the useful photoresponse component, and displacement currents of similar photodetector structures approximately compensate each other.
- The control voltage shutdown before the recombination of the most part of non-equilibrium charge carriers in the LTG layers induces the photocurrent surges, those amplitude is comparable with the magnitude of photoresponse. The solution of this problem implies the adding of special carrier-holding LTG layers located between the control junctions and usual LTG layers and have the deepest quantum wells in the whole heterostructure.

References

[1] Pisarenko I and Ryndin E 2020 *Photonics* **7** 21
[2] Pisarenko I V and Ryndin E A 2020 *J. Phys. Conf. Ser.* **1482** 012037
[3] Palankovski V and Quay R 2004 *Analysis and Simulation of Heterostructure Devices* (Vienna: Springer)

Simulation of double-junction III-phosphides/silicon solar cells

A. A. Rakitina[1], **A. S. Gudovskikh**[1,2]

[1]St. Petersburg Electrotechnical University "LETI", 197376 St Petersburg, Russia.
[2]St. Petersburg Academic University of RAS, 194021 St Petersburg, Russia.

aarakitina@stud.etu.ru

Abstract. The characteristics of two-junction solar cells were calculated in this work, in which phosphides of group III are used as the top junction, and Si as the bottom junction. The following ternary phosphide compounds $Ga_{0.52}In_{0.48}P$ (1.85 eV), $GaPN_{0.02}$ (1.9 eV), and $GaPN_{0.04}$ (1.7 eV) were considered as the active material of the top junction. The use of $GaPN_{0.04}$ allowed one to reach the current matching with the bottom Si junction and an efficiency of 30% was achieved. In addition, the influence of the layer thickness, the lifetime of minority charge carriers and the electronic affinity on the efficiency of solar energy conversion were considered.

1. Introduction

The development of solar energy requires a further increase in conversion efficiency. However, silicon single-junction solar cells (SCs), which are the basis of terrestrial photovoltaics, have practically reached the efficiency limit [1]. A further increase in efficiency is possible with an increase in the number of junctions. One of the most promising ways to create two-junction SC based on Si is integration with III-V compounds. The formation of III-V layers on the silicon surface is a complex technological task that requires the use of expensive epitaxial methods, high growth temperatures, and also imposes restrictions on the choice of materials in terms of the crystal lattice parameter, which together is a significant obstacle to the development of this path. However, it has recently been shown that epitaxial and microcrystalline layers of III-phosphides can be obtained by plasma deposition at low temperatures [2]. The possibility of mass production of this technology is promising for photovoltaics. In this work, using computer simulation, an assessment was made of the potential possibility of using III-phosphides as the top junction of a double-junction SC with a bottom junction based on a Si substrate. The key feature of this simulation is that it was carried out taking into account the microcrystalline structure of phosphide layers, therefore the p-i-n structure was considered, and the effect of defects was also taken into account.

2. Experiments and results

Computer modeling was carried out using the AFORS-HET v2.5 program. The following phosphides were considered as active materials of the top junction: $Ga_{0.52}In_{0.48}P$ (1.85 eV), $GaPN_{0.02}$ (1.9 eV), and $GaPN_{0.04}$ (1.7 eV). Based on the calculation results, two structures providing the best current matching were selected being $Ga_{0.52}In_{0.48}P$ and $GaPN_{0.04}$ (1.7 eV). $Al_{0.53}In_{0.47}P$ and GaP layers were used as a wide-gap window and BSF. An n-GaP/p-Si heterojunction was used as the bottom junction. According

to the calculation results, it was found that the top junction based on $GaPN_{0.04}$ (1.7 eV) provides higher values of the open-circuit voltage (V_{OC}) and short-circuit current (J_{SC}) as compared to $Ga_{0.52}In_{0.48}P$. A schematic representation of a variant of the GaPN/Si design for which the efficiency reaches 30% and the I-V curve are shown in Figure 1 (a, b). The spectral dependences of the quantum efficiency of two-junction SCs based on GaPN/Si and GaInP/Si are shown in Fig. 1 (c). It also shows why the GaPN structure is preferred.

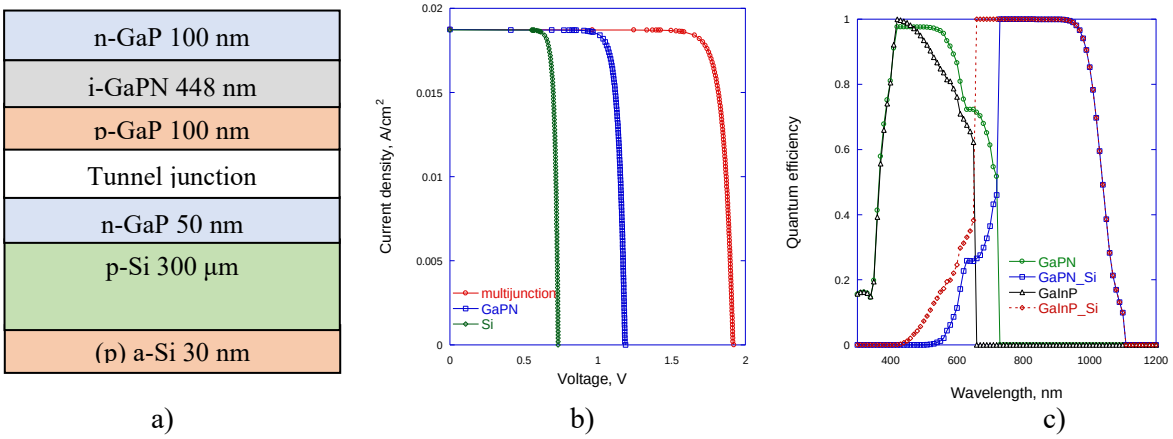

Figure 1 Schematic representation of the GaPN/Si design (a) and I-V curves (b) and quantum efficiency spectra of double-junction SC based on GaPN and GaInP (c)

It was also shown the influence of the lifetime of charge carriers and the electronic affinity on the fill factor of the I-V curve and the efficiency of the solar cell. The variation conducted for the lifetime showed that in order to achieve the best current matching, the values should reach at least 10^{-9} s. The growth of band discontinuities at the GaPN/GaP interface leads to the formation of potential barriers that prevent the transport of charge carriers and, as a consequence, to a significant decrease in the fill factor of the I–V curve.

Acknowledgments
This work was supported by RFBR research project #20-08-00870

References

[1] Yoshikawa K., Kawasaki H., Yoshida W., Irie T., Konishi K., Nakano K., Uto T., Adachi D., Kanematsu M., Uzu H., Yamamoto K. (2017). Silicon heterojunction solar cell with interdigitated back contacts for a photoconversion efficiency over 26%. Nature energy, 2(5), 1-8.

[2] Uvarov, A. V., Gudovskikh, A. S., Nevedomskiy, V. N., Baranov, A. I., Kudryashov, D. A., Morozov, I. A., & Kleider, J. P. (2020). Low temperature epitaxial growth of GaP on Si by atomic-layer deposition with plasma activation. Journal of Physics D: Applied Physics, 53(34), 345105.

Numerical modeling of non-planar GaN LED with CNT top contact

S A Raudik[1,3], D M Mitin[2,1], A A Vorobyev[1], A M Mozharov[1] and I S Mukhin[1]

[1]Saint Petersburg Academic University, 8/3 Khlopina, St. Petersburg 194021, Russia
[2]Peter the Great St. Petersburg Polytechnic University, 29 Politekhnicheskaya, St.Petersburg 195251, Russia3
[3]Skolkovo Institute of Science and Technology, 30 Bolshoy Boulevard, bld. 1, Moscow 121205,Russia

E-mail: raudik_sa@mail.ru

Abstract. GaN NWs are good candidates for the fabrication of stretchable and flexible LEDs operating in a visible light range. In this paper, the theoretical study of LED based on GaN NWs with CNTs contact has been presented. The main electrical and optical characteristics of LED have been numerically calculated.

1. Introduction

In the last decades, III-Nitrides attract attention as materials for optoelectronic devices due to their outstanding properties. AlN, GaN, and InN and their alloys have a direct bandgap varied from 0.7 eV to 6.2 eV [1]. It allows producing light emission diodes (LEDs) with a broad range of emitted wavelengths.

Recent progress in the development of wearable and bio-compatible devices faced a challenge to get stretchability and flexibility of electronics and, in particular, LEDs. These properties can be achieved with III-Nitrides by a transition from conventional planar geometry to 1D structures such as nanorods or nanowires (NWs)[2].

Using of NWs decides many inherent problems of thin-films LEDs. Firstly, dislocation density declines in GaN nanowires with a high surface-to-volume ratio. Also, the more intensive strain relaxation was observed in comparison with planar GaN, which led to decreasing internal electrical fields induced by lattice mismatch with traditional substrates such as sapphire and Si[3]. Secondly, such structure changes suppress the waveguide effect on interfaces GaN/air (n =2.4) and promote light extraction [4]. Moreover, such geometry gives additional advantages, the main of which is the ability to control a radiation pattern [5] and wavelength of emitted light[6] by changing the structure sizes and shape.

To take all advantages mentioned before, the contacts to a LED should be transparent and retain their properties upon deformation. One of the promising materials satisfying these conditions is carbon nanotubes (CNT). Low cost, unique optical and mechanical properties make it an appropriate option for use as stretchable and transparent contacts [7].

In this paper, the GaN NWs-based LED has been considered and numerically modelled to determine attainable characteristics

2. Modeling

The considered LED is an array of axial heterojunction GaN NWs with inserted InGaN quantum well. Array of NWs locates on the substrate. CNTs are on the top of NWs. In this system,current flows mostly vertically due to the geometrical restriction. Thus each NW separately could be modelled as a 1D structure instead of 3D or 2D with axial symmetry. In the area of InGaN insertion, the Schroedinger–Poisson equation has been solved to determine the density of states in the quantum well and calculate charge tunnelling through it. IV curves and emission spectra of a single NW have been obtained during the calculation. In the next step, an array of NWs has been modelled by integrating currents and light emission over the surface, taking into account the optical losses in the CNT layer. The Ohmic losses in the CNTs film and the substrate have been taken into consideration to calculate voltage drop with increasing distance from contacts.

3. Conclusion

The numerical model of GaN NWs-based LED with CNT contact has been implemented. Themain characteristics of LED have been obtained. In a 0.5×0.5 mm NWs array, the Ohmic lossesin CNTs were 2.7% with an operating current density of 250 A/cm2. This proves the possibilityof using CNTs as transparent contact

Acknowledgments

The reported study was funded by RFBR, project number 19-38-60008, the Ministry of Scienceand Higher Education of the Russian Federation (grant 0791-2020-0005).

References

[1] Adachi S 2009 *Properties of semiconductor alloys: group-IV, III-V and II-VI semiconductors* vol 28 (JohnWiley & Sons)

[2] Dai X, Messanvi A, Zhang H, Durand C, Eymery J, Bougerol C, Julien F H and Tchernycheva M 2015 *Nanoletters* **15** 6958–6964

[3] Bai J, Wang Q and Wang T 2012 *Journal of Applied Physics* **111** 113103

[4] Tsai Y L, Lai K Y, Lee M J, Liao Y K, Ooi B S, Kuo H C and He J H 2016 *Progress in Quantum Electronics* **49** 1–25

[5] Soshnikov B, Lysak V, Kotlyar K and Soshnikov I 2016 *Journal of Physics: Conference Series* vol 741 (IOP Publishing) p 012154

[6] Sekiguchi H, Kishino K and Kikuchi A 2010 *Applied physics letters* **96** 231104

[7] Neplokh V, Kochetkov F M, Deriabin K V, Fedorov V V, Bolshakov A D, Eliseev I E, Mikhailovskii V Y,Ilatovskii D A, Krasnikov D V, Tchernycheva M *et al.* 2020 *Journal of Materials Chemistry C* **8** 3764–3772

Photon counting statistics with imperfect detectors

Aleksei Reutov[5,6] and Denis Sych[1,2,3,4]

[1] P.N.Lebedev Physical Institute, Russian Academy of Sciences, Moscow, 119991, Russia
[2] Department of Physics, Moscow Pedagogical State University, 119992, Russia
[3] NTI Center for Quantum Communications, National University of Science and Technology MISiS, Leninsky prospekt 4, Moscow 119049, Russia
[4] Sirius University of Science and Technology, 1 Olympic Ave, 354340, Sochi, Russia
[5] Moscow Institute of Physics and Technology, Dolgoprudny 141700, Russia
[6] "Qrate" LLC, St. Novaya, d. 100, Moscow region, Odintsovo, Skolkovo village, 143026, Russia

e-mail: aleksey.reutov@phystech.edu

Abstract. Measurement of photon counting statistics is one of the tools for the verification of quantum properties of light. We analyze the simulated sub-Poissonian distribution with dead-time corrections. We derive functional dependence between the mean number of photons and the mean number of photon counts for the pulsed or continuous wave coherent light sources.

1. Introduction

Quantum properties of light play the key role in various research areas of modern quantum technologies, for example, in quantum communications. In order to verify applicability of theoretical concepts, such as single photon states or weak coherent states, to the real world applications, such as quantum key distribution, one has to certify the experimental sources of light. One of the simplest ways to do this task is the measurement of photon counting statistics. For the single photon states, it should lead to the well known anti-bunching effect, while for the coherent states we should observe Poissonian distribution of photo counts.

However, all the realistic measurements suffer from various imperfections which affect the photon counting statistics and modify the statistical distributions. In particular, detector's dead time and jitter lead to either sub-Poissonian or super-Poissonian distributions.

In this work we show how the detector's dead-time corrections affect the Poissonian distribution for the pulsed or continuous wave coherent light sources. We calculate mean value of photons, its variance, and high-order moments and determine a connection between the mean number of photons and the mean number of photon counts. Our statistical analysis allows to include the effects of a time-varying repetition rate of laser pulses, source intensity fluctuations and a photo detector jitter.

The results can be directly applied to the security enhancement of quantum key distribution protocols, as well as the development of novel protocols that rely on photon counting detectors.

2. Methods

We used the normalized cumulative distribution function, a convenient tool for the statistical analysis of photon count distribution [1]. It can be naturally generalized for arbitrary sequences of measurement time windows and arbitrary source of coherent light. There are used machine learning tools for determining a connection between the mean number of photons and the simulated mean number of photon counts.

3. Results and discussion

The simulated sub-Poissonian distribution is shown in Fig. 1. Calculated properties of distribution (mean value, variance, high-order moments) for different values of parameters (mean number of photons, dead-time) is used for machine learning analysis and calculation the mean number of photons and the dead time as functions of mean value and variance.

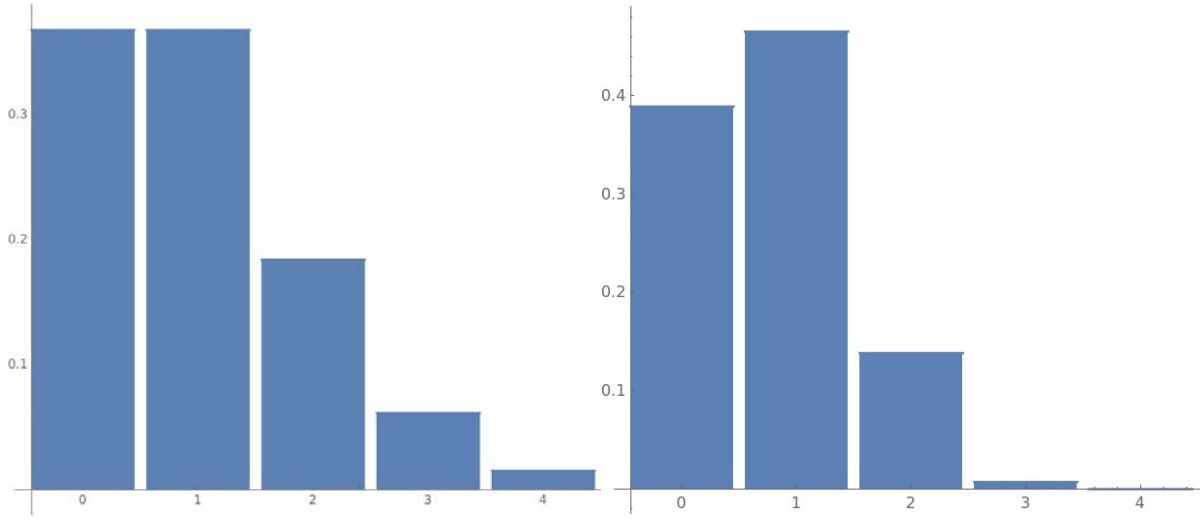

Figure 1. Probability function for Poissonian distribution (left) and sub-Poissonian distribution of photon counts (right). Mean number of photons is equal to 1. Dead time is equal to 0.3 time window of measurement.

Acknowledgments

The work is supported by Russian Foundation for Basic Research grant 20-32-51004.

References

[1] G Bédard 1967 Proc. Phys. Soc. **90** 131

Spray deposited thin uniform NiO/Spiro-OMeTAD composite hole transport layer with top carbon nanotube layer

A V Romashkin, Yu A Polikarpov, E V Alexandrov

National Research University of Electronic Technology, Moscow 124498, Russia
romaleval@gmail.com

Abstract. Thin Spiro-OMeTAD and NiO nanoparticles layers, as well as their composite layer was formed layer-by-layer spray deposition as hole-transport layer (HTL), with followed CNTs deposition to form Ti/TiO_2/HTL/CNT structures. Layers uniformity was estimated by Raman intensity maps, AFM and current-voltage characteristics (CVC) of the CNT layer and between CNT and Ti, and showed the possibility of spray deposition forming of thin ~ 150 nm pinhole-free uniform composite NiO/Spiro-OMeTAD layer, even with top CNT layer.

1. Introduction

Due to the insufficient time stability of solar cells based on organic materials in work at ambient conditions, new materials and principles for the hole-transport layers (HTL) formation are developing, which characterized by dopant-free conception, using composites based on oxide nanoparticles and low molecular weight organic compounds or polymers [1]. Although it is possible to achieve relatively acceptable quantum efficiency even using the dopant-free thin Spiro-OMeTAD layer formed by vacuum deposition, the best values are achieved only with dopant, however, it significantly decreases time stability at ambient conditions [2]. Time stability can be also increased by inorganic compounds adding to the HTL composition [3]. Thus, the development of thin composite HTL based on undoped Spiro-OMeTAD or other molecules with nanoparticles, formed by low temperature spray deposition is a relevant task, which is the subject of present work. An another important aspect of present work is the possibility of using carbon nanotubes (CNT) and its composites with polymers as the top conductive layer (possibly, also transparent), which allows to improve the perovskite cells stability [4].

2. Results and discussions

Spray deposition of undoped Spiro-OMeTAD (99 % (HPLC), Sigma Aldrich, USA) on a substrate does not provide a thin (< 150 nm) uniform layer, which was revealed both by AFM and Raman 1620 cm^{-1} region intensity map [2] (Figure 1a, where shaded areas is the Raman spectrometer background signal < 180 arb.un. with Spiro-OMeTAD absence, according to AFM). The substrate was heated to 120 °C during deposition, so Spiro-OMeTAD crystallinity enhanced, which was confirmed by Raman spectroscopy. The use of a uniformly deposited NiO nanoparticles (nNiO) sublayer (d <80 nm, but with presence of large conglomerates ~ 150 nm, 99.9 %, Simplex LLC, Russia), which have an energy levels similar to Spiro-OMeTAD and suitable for HTL formation, significantly improved the Spiro-OMeTAD uniformity in sequentially spray-deposited uniform nNiO/Spiro-OMeTAD composite layer (Figure 1b). The nonuniformity was determined by ratio of standard deviation to median value of Raman intensity [5], that was 0.8 for Spiro-OMeTAD in composite layer, which, although higher than for spray deposited CNTs (ratio is 0.3), but much lower than for pure Spiro-OMeTAD layer, only partially covered the surface (ratio is 3.3). Spiro-OMeTAD

uniformity significantly depends on the nNiO density on the substrate: low nanoparticles covering degree (<50 %) forms areas without Spiro-OMeTAD.

Four types of structures were formed to analyze the possibility of CNT layer forming (P3-SWNT, Carbon Solutions, USA; on a rectangular area 4x1.5 mm) on top of the proposed composite HTL (round area Ø 2 mm) by spray deposition using shadow masks, on substrates with Ti with a TiO_2 layer (~ 3-10 nm thick): A) CNT, B) nNiO/Spiro-OMeTAD/CNT, C) nNiO/CNT and D) Spiro-OMeTAD/CNT (Figure 2). CNT layer resistance was: A - 35.7 kΩ, B - 37.6 kΩ, C - 116.9 kΩ, D - 51.8 kΩ; while the CNT surface density differences were <10 % (control by Raman spectroscopy). According to the AFM data there is a smoother and denser CNT layer on top of composite nNiO/Spiro-OMeTAD with less roughness and a smaller amount of observed deepened areas in comparison with on nNiO sublayer. And finally CNTs wasn't observed on top of pure Spiro-OMeTAD (complete CNTs dipping into covered by pure Spiro-OMeTAD areas in sublayer is realized or mixing with it). But composite structure provides the absence of CNTs, deeply dipped into the HTL sublayer (in contrast to structure D), with nonlinear CVC between CNT and Ti and therefore the pinhole absence and shunting of HTL through formation of direct CNT-TiO_2/Ti contacts, in contrast to the CVC for structures C and D, which indicates better sublayer quality and continuous and uniformity HTL structure realizing by nNiO/Spiro-OMeTAD composite sublayer. That behavior also confirmed by similar CNT layer resistance for structure B in comparison with A, having smooth substrate, in contrast to the increased CNT layer resistance on nNiO sublayer of structure C, where some CNTs were dipped between nanoparticles (according to AFM there is lower CNTs density on the top of structure C than for A or B). Despite CNTs to Spiro-OMeTAD dipping in structure D, it weakly affects the uniformity of presumably thin and dense CNT layer (according to Raman map but couldn't detected under Spiro-OMeTAD by AFM), so CNT resistance insignificantly differs from structure A, despite alcohols used in the CNTs deposition, partially dissolve Spiro-OMeTAD, and lowest influence of that to CNT resistance in composite sublayer was obtained. And Spiro-OMeTAD uniformity over the composite layer at least didn't get worse, even after the top CNT layer deposition.

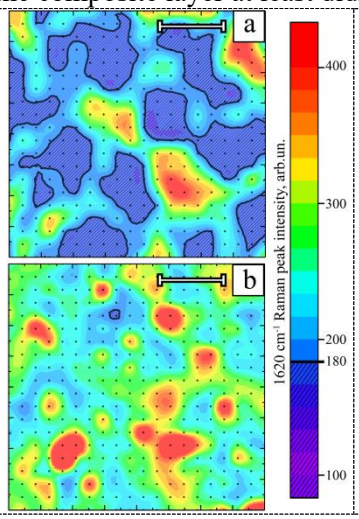

Figure 1. Raman map of:
a) Spiro-OMeTAD peak for pure Spiro-OMeTAD,
b) composite layer nNiO/Spiro-OMeTAD.
Scale bar is 10 um.

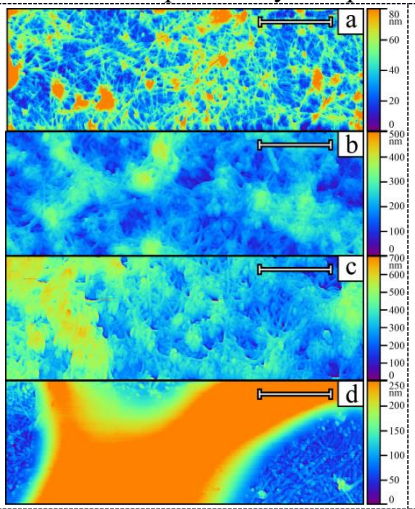

Figure 2. AFM data for structures:
a) CNT,
b) nNiO/Spiro-OMeTAD/CNT,
c) nNiO/CNT,
d) Spiro-OMeTAD/CNT.
Scale bar is 1 um.

Acknowledgments

This work was supported by grant of President of the Russian Federation (grant No MK-1024.2020.8).

References

[1] A Guo Y, Lei H, Xiong L, Li B, Fang G 2018 *J. Mater. Chem. A* **6** 2157
[2] Barranco A, Lopez-Santos M C, Idigoras J, et al 2020 *Adv. Energy Mater.* **10** 1901524
[3] Jin I S, Park S H, Kim K S, Jung J W 2020 *J. Alloys Compd.* **847** 156512
[4] Ahn N, Jeon I, Yoon J, et al 2018 *J. Mater. Chem. A* **6** 1382
[5] Polikarpov Y A, Romashkin A V, Struchkov N S, and Levin D D 2019 *IEEE Conf. of Russian Young Researchers in Electrical and Electronic Engineering (Moscow)* (IEEE) p 1980

QKD key generation control protocol

N V Rudavin[1,5], I S Gerasin[1,2,4], E E Mekhtiev[1,2,4], A V Duplinsky[1,3,4] and Y V Kurochkin[1,2,3,4]

[1]QRate, Novaya av. 100, Moscow, Russia
[2]Moscow Institute of Physics and Technology, 9 Institutskiy per., Dolgoprudny, Moscow Region, 141701, Russian Federation
[3]NTI Center for Quantum Communications, National University of Science and Technology MISiS, Leninsky prospekt 4, Moscow 119049, Russia
[4]Russian Quantum Center, Bolshoy Boulevard 30, bld. 1, Skolkovo, Moscow 121205, Russia
[5]Federal State Budget Educational Institution of Higher Education, MIREA—Russian Technological University, 78, Vernadskogo avenye, 119454 Moscow, Russia

{n.rudavin, i.gerasin, e.mehtiev, a.duplinsky, yk}@goqrate.com

Abstract. Polarization-encoding fiber QKD requires compensation of polarization distortion caused by birefringence in optical fiber. Solving this task inevitably requires losing some effectiveness in terms of the final key rate. In this work, a time-division multiplexing protocol for polarisation calibration is suggested. This protocol was implemented in a QRate commercial QKD fiber system on 50 km link, utilizing BB84-protocol. Parameters of the protocol were optimized to maximize the secret key rate.

1. Approaches to QKD key generation control

Quantum technologies evolve rapidly and now the quantum key distribution (QKD) fiber systems become more and more available. The fiber QKD systems have the advantage that they can be directly deployed on existing telecom optical fiber infrastructure. However, for polarization-encoding protocols polarization control is required since in single-mode optical fiber any given input polarization of light passing through optical fiber suffers time-dependent disturbance. To provide a high secure key-rate efficient polarization calibration protocol should be used.

There are two main approaches to organize polarisation calibration protocols: (i) interrupting scheme and (ii) real-time scheme. The first approach requires stopping the key generation process in order to send a sequence of calibration pulses (either quantum or classical) [1]. The second method implies utilizing WDM for calibration signals [2] or using some part of the secret key to estimate QBER [3]. WDM systems require some additional equipment to multiplex signals which leads to the cost increase. Interrupting schemes allow to send high-intensity calibration pulses that can gather statistics for error estimation faster than from the weak pulses used for secret key generation. In this work, we propose interrupting calibration protocol with flexible switch criteria.

2. Protocol description and implementation

During the calibration mode, key generation is impossible so one needs to decide when to switch into key generation and back. Consider the work of some iteration algorithm that minimizes QBER (e.g.

gradient descent). Usually, iteration algorithms do not have well-defined stop criteria. On the one hand, if protocol switches to the key-generation mode too early during the convergence, the final QBER value is not optimal and the maximum secure key-rate is not achieved. On the other hand, if protocol switches to the generation too late, the key-rate is maximized but key generation time is decreased. Thus, for interrupting protocol, a crucial thing is to choose switching criteria efficiently in terms of secret key length.

The whole process of QKD is divided into two parts: key-generation mode (GM) and calibration mode (CM). In calibration mode, on each iteration of the convergence algorithm, we measure M values of QBER (each point is measured during the same time interval τ). Then mean $\overline{QBER}$ and the standard deviation σ_{CM} is calculated for each iteration that lasts $M\tau$. During GM $\overline{QBER}$ is calculated from decoy-state clicks and σ_{GM} is estimated as the standard deviation of the ratio of two random values $N_{wrong\ clicks}$ / $N_{total\ clicks}$ with the Poissonian distribution. Generally, σ_{GM} can be chosen in other ways depending on QBER estimation technique during key generation. Switching criteria from CM to GM is based on QBER linear interpolation as a function of time via MSE (N last points are used) and comparison the slope with some threshold, which is dynamically calculated on each iteration of the convergence algorithm. Moving back to the CM is regulated with a certain threshold based on QBER statistics analysis.

The proposed protocol was implemented and tested on QRate commercial QKD fiber system with 50 km optical link. We run the key distribution process with the fixed parameters $(N, M) \subset \{4, 6, 8\} \otimes \{3, 5, 8\}$, measure the average secret key rate during 3 hours and find the optimal parameters of protocol.

Acknowledgments
This work was supported by The Russian Science Foundation (Grant No. 17-71-20146)

References

[1] Chen, Jie, et al. "Active polarization stabilization in optical fibers suitable for quantum key distribution." *Optics express* 15.26 (2007): 17928-17936.

[2] Xavier, G. B., et al. "Full polarization control for fiber optical quantum communication systems using polarization encoding." *Optics express* 16.3 (2008): 1867-1873.

[3] Ding, Yu-Yang, et al. "Polarization basis tracking scheme for quantum key distribution with revealed sifted key bits." *arXiv preprint arXiv:1608.00366* (2016).

Temperature dependence of the optoelectronic properties LED heterostructures with a staggered type II InAsSb/InAsSbP heterojunction

A A Semakova[1], V V Romanov[2], N L Bazhenov[2], K D Mynbaev[1,2] and K D Moiseev[2]

[1]ITMO University, St. Petersburg 197101, Russia
[2]Ioffe Institute, St. Petersburg 194021, Russia

E-mail: antonina.semakova@itmo.ru

Abstract. A study of the spectral and current-voltage characteristics of asymmetric InAs/InAs$_{1-x}$Sb$_x$/InAsSbP light-emitting diode heterostructures with a molar fraction of InSb in the ternary solid solution in the active region x_{InSb}=0.10, 0.15 and 0.16 in the temperature range 4.2–300 K is reported. It is found that a staggered type-II heterojunction is formed at the InAs$_{1-x}$Sb$_x$/InAsSbP heterointerface and affects the optical and electrical characteristics of structures. It is shown that interfacial radiative transitions at the type-II heterointerface make a dominant contribution in the temperature range of 4.2–180 K. This enables minimization of the temperature dependence of the operating wavelength of a light-emitting diode.

1. Introduction

At present, heterostructures are used to create almost all types of optoelectronic devices. Our research focuses on the optoelectronic properties of InAs(Sb)-based heterostructures, that are widely used in fabrication of light emitting diodes (LEDs) operating in middle wavelength infrared range. This spectral range (2–6 μm) is relevant for laser diode spectroscopy of gases and molecules, for systems for the detection of explosive substances, medical applications, and for environmental monitoring [1]. An integral property of semiconductor LEDs based on $A^{III}B^{V}$ materials is the temperature shift of the emission wavelength, which complicates their practical application. In this regard, it is relevant to optimize the design of the heterostructures with consideration of the features of the materials band structure, to improve the output characteristics of LEDs.

In this work, we performed variable-temperature (T=4.2–300 K) studies of spectral and electrical characteristics of LED n-InAs/n-InAs$_{1-x}$Sb$_x$/p-InAs$_{0.41}$Sb$_{0.28}$P$_{0.40}$ heterostructures with a molar fraction of indium antimonide in the active layer x_{InSb}=0.10–0.16. The heterostructures were fabricated by the metal-organic vapour-phase epitaxy (MOVPE), the details of the growth were presented in Ref. [2]. The LED chips were fabricated as 400×400 μm mesa structures. The chips were mounted on TO-18 holders.

2. Experimental results

The heterostructures under study demonstrated similar diode-type current-voltage (I-V) characteristics at temperatures close to 300 K. However, a significant difference in the electrical properties of the heterostructures was observed at low temperatures (from 4.2 to ~80 K). The I-V characteristics of the

$InAs/InAs_{0.90}Sb_{0.10}/InAs_{0.41}Sb_{0.28}P_{0.40}$ heterostructure had a region with negative differential conductivity and demonstrated an S-shaped kink. Raising the concentration of antimony atoms in the $InAs_{1-x}Sb_x$ solid solution led to the transformation of the *I-V* characteristics. For heterostructures with x_{InSb}=0.15 and 0.16 in $InAs_{1-x}Sb_x$ active layer, a specific break was observed in the forward branches of the *I-V* characteristics.

Variable-temperature (4.2–300 K) electroluminescence (EL) studies showed that at low temperatures (4.2–150 K), in the EL spectra of the heterostructures emission bands caused by radiative transitions of different origins were simultaneously observed. Besides the main emission band, intense electroluminescence was observed in the spectral range of 3.1–3.4 μm. In the heterostructures under study, the short-wavelength EL band is regarded as an additional radiative-recombination channel and is a factor whose analysis should make it possible to determine the nature of the leakage of injected carriers from the active region of the structure. The full width at half maxima of these EL bands was <15 meV, which is typical for materials with high crystalline perfection. Therefore, we examined the temperature dependence of the photoluminescence from the substrate InAs and EL from a single heterostructure *n*-InAs/*n*-$InAs_{0.32}Sb_{0.26}P_{0.42}$ produced by growing an InAsSbP epitaxial layer on the same substrate. Based on the obtain results it was concluded that short-wavelength bands were due to recombination involving donor-acceptor pairs formed by residual impurities and defects in the InAs substrate.

For the main emission band of the heterostructures, a weak temperature dependence of the spectral peak position of the emission band with increasing temperature was observed. With increasing temperature from 4.2 to 300 K, the spectral range of emission of the heterostructures with different compositions of the $InAs_{1-x}Sb_x$ ternary solid solution changed as follows: λ=4.2–4.5 μm (x_{InSb}=0.10); λ=4.4–4.9 μm (x_{InSb}=0.15); λ=4.7–5.1 μm (x_{InSb}=0.16). The specifics of the detected optical and electrical properties of the heterostructures can be related to the specific features of the InAsSb/InAsSbP heterojunction. It was found that a staggered type-II heterojunction was formed at the $InAs_{1-x}Sb_x$/InAsSbP heterointerface for the compositions studied. In this case, with an increase of x_{InSb} in $InAs_{1-x}Sb_x$, the energy-band offset in the valence band increases, which provides formation of potential wells at the $InAs_{1-x}Sb_x$/InAsSbP heterointerface. Thus, the effect of a change in the main channel of radiative recombination in this heterojunction was experimentally observed; it is shown that in the temperature range from 4.2 to ~180 K, EL is determined by interface radiative recombination, and with an increase in temperature to 300 K, radiative recombination transitions dominate in the bulk of the active region of $InAs_{1-x}Sb_x$. The localization of charge carriers at the $InAs_{1-x}Sb_x$/InAsSbP heterointerface led to the appearance of pronounced features of the *I-V* characteristics of heterostructures at low temperatures.

The study showed that the design of a mesa-LED based on the asymmetric heterostructures InAs/$InAs_{1-x}Sb_x$/$InAs_{0.41}Sb_{0.28}P_{0.40}$ with x_{InSb}=0.10, 0.15 and 0.16 makes it possible to minimize the effect of the temperature on the wavelength of the LED by changing the main channel of radiative recombination. These results are of interest for fabrication of thermostable emitters operating in the middle wavelength infrared range.

References

[1] Ting D, Soibel A, Khoshakhlagh A, Keo S, Rafol B, Fisher A, Pepper B, Luong E, Hill C, Guhapala S 2019 *Infr. Phys. Technol*. **97** 210

[2] Romanov V V, Moiseev K D and Ivanov E V 2019 *Phys. Sol. State* **61** 1699

Several processes participating in a decrease and the droop of external quantum efficiency in green InGaN/GaN MQW structures

N A Talnishnikh[1], E I Shabunina[2], N M Shmidt[2], A E Ivanov[1,3]

[1] Submicron Heterostructures for Microelectronics Research and Engineering Center RAS, St Petersburg 194021, Russia
[2] Ioffe Physical Technical Institute, St Petersburg 194021, Russia
[3] Saint-Petersburg Electrotechnical University ETU "LETI", St. Petersburg 197376, Russia

Nadya.fel@mail.ru

Abstract. The obtained experimental results allow us to clarify the processes due to the ionic nature of disordered InGaN alloy. These processes lead to a reduction in the external quantum efficiency (EQE) in green MQWs at $j \leq 10$ A/cm^2 and the EQE droop phenomena.

1. Introduction

InGaN/GaN MQW structures are the foundation for light-emitting diodes (LEDs) and lasers. Phenomena such as low values of the external quantum efficiency (EQE, η) at maximum and the EQE droop in green LEDs at $j > 10$A/cm^2 have been under intense discussions for the last decade and have yet to find a commonly accepted explanation [1-3]. Current-voltage (I-U) characteristics and EQE dependences on current in green LEDs are known to show more complex behaviors which could not be described by a popular ABC-model [2]. To clarify the processes resulting in low EQE values at maximum and the EQE droop in green MQWs we considered our experimental results in the framework of atomic [4], localization landscape [3], and trap-assisted tunnelling [5] models and took into account the tunneling radiative recombination at $j \leq 10$ A/cm^2 [6].

2. Experimental

We studied commercially available green LEDs based on MQW InGaN/GaN nanostructures having EQE in the range of 15-30% at 520-530 nm. We should note that η values ~ 30% at 530 nm in commercially available green LEDs can be considered reasonably high. All LEDs have 1 mm2 active area. We studied I-U characteristics, electroluminescence spectra (EL), η dependences on direct current (DC) and in pulse mode (PM) (100 ns pulse at 50 Hz) at 50-350 K and the distribution of both $\eta_{j,U}$ and full width at half maximum of EL (FWHM) over wavelengths.

3. Results and discussion

Our η(j) dependences at DC and in PM at 300 K in the green and blue LEDs shown in a semi-logarithmic plot demonstrate the η droop and a typical difference between η values in green and blue LEDs (Figure 1, a). Different shapes of regions I, II and III in η(j) dependences (Figure 1, a) reflect the presence of several mechanisms. The η(j) shape ~ $j^{1/2}$ of region I allows us to assume that the process

of radiative recombination of localized tunneling carriers in QWs situated at a depletion region of p-n junction observed in blue LEDs [7] also occurs in the green ones. The absence of a η increase at region II was found to correlate with the narrowing of FWHM values followed by a current increase (on the insert to Figure 1, b), the falling branches). Furthermore, the lower η values, the more prominent the effect.

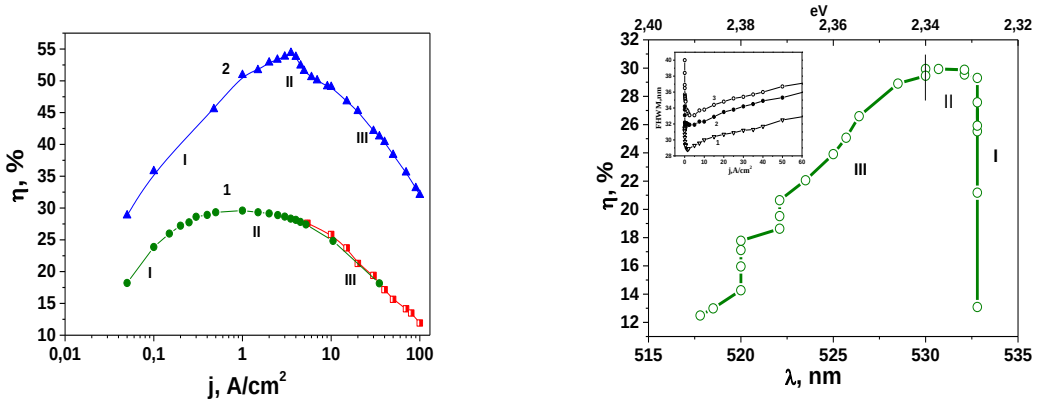

Figure 1. (a) EQE dependences on j in green (curve 1) and blue (curve 2) LEDs. The red curve shows EQE dependences in green LEDs in PM. (b) η distribution over wavelengths. On the insert: FWHM dependences on j in green LEDs with different η values: 28% (curve 1), 20% (curve 2), and 14% (curve 3).

We suggest that that the trapping of tunneling charge carriers by randomly distributed cations at local regions with disordered alloy alongside with non-radiative recombination at point defects can be the source of such an effect. As a result, these carriers do not participate in radiative recombination. This correlates with the atomic model [4] which takes into account the ionic nature of alloy disorder. The EQE droop begins at region III when $U > U_{th}$ (threshold voltage) and delocalized carriers start filling lateral random alloy fluctuations (LRAF). It seems that the distribution of EQE values over wavelengths (Fig. 1, b) at $2 < j < 30$ A/cm^2 visualizes this process as well as the others in regions I and II. LRAF values from Figure 1 (b) at region III is ~ 40 meV which is in good agreement with the data (40-50 meV) obtained for InGaN with 10-40% of In which was predicted by the landscape model [3]. Lateral migration of carriers in LRAF accompanied by the gradual filling of wells smooths out LRAF. The EQE droop at $j > 30$ A/cm^2 in a quite narrow range of wavelengths correlates with the occurrence of yellow defect band in GaN and can be caused by non-radiative recombination localized at extended defects and grain boundaries. All the processes are going to be discussed in detail during the presentation and in the paper.

Acknowledgments
Measurements of near-field EL intensity distribution were made at the Center of Multi-User Facilities "Element Base of Microwave Photonics and Nanoelectronics: Technology, Diagnostics, Metrology"

References

[1] Aurelien David, at al. ECS Journal of Solid State Science and Technology, 2020 9 016021
[2] Ilya E. Titkov at al. Materials 2017, 10, 1323; doi:10.3390/ma10111323
[3] Joachim Piprek at al. 2015 Applied Physics Letters 106 101101
[4] Marco Mandurrino at al. J. Comput.
[5] Chi-Kang Li, at PHYSICAL REVIEW B 95, 144206 (2017)
[6] P. Perlin at al., Appl. Phys. Lett., 69, 1680 (1996)
[7] N M Shmidt at al. Technical Physics Letters 46, 1253, 2020, doi:10.1134/S1063785020120275

Laser treatment of ITO thin films with Carbon Nanotubes for Liquid Crystal Devices

A S Toikka[1,3]**, N V Kamanina**[1,2,3]
[1]Department of Photonics, St. Petersburg Electrotechnical University ("LETI"), 197376 St. Petersburg, Russia
[2]Lab for Photophysics of media with nanoobjects, Vavilov State Optical Institute, 199053 St. Petersburg, Russia
[3]Advanced Development Division, Petersburg Nuclear Physics Institute, 188300 Gatchina, Russia

Abstract. In this paper, the influence of laser ablation on the refractive properties of indium tin oxides (ITO) thin films with deposited single-wall Carbon Nanotubes (CNTs) was considered. Sputtering of CNTs was preliminary based-on the laser oriented method with application of the external electric field. The laser ablation of ITO-CNTs coatings allows changing of the electric, optical and mechanical properties dramatically. Moreover, this technical operation permit to switch the topology of the surface, thus it leads to the conversion of the refractive index. The possibility of index-matching due to the laser treatment contributes to the expansion of the technical capabilities of LC devices.

1. Introduction

Liquid Crystals – is a mesophase that combines the optical anisotropy and properties of liquids. These molecules have no regularity of mass, however, their orientation can be controlled with external exposure (optical beam, electric and magnetic field, acoustic waves). These features allow to construct devices for the optical modulation issues such as electro-optical and spatial light modulators, optical switching elements, lenses with the variable focus point, etc. In common case, electro-optical LC devices require high optical transmittance in the operating spectra range and low electric consumption. The spectral properties of mesophase depend on the LC modifications and the materials of sensitizers. One of the most perspective ways for optical optimizing of LC is structuring with the nanoparticles, such as fullerenes, nanotubes, quantum dots and others [1-2]. Moreover, they are able to increase the local polarizability of media which correlated with the temporal characteristics of devices [3]. Another approach for tuning parameters is connected with the topology and composition of the adjacent layers to the LC phase in the construction of the device. In order to decrease the response time of LC molecules, variable approaches can be used. The deposition of single-wall nanotubes permits not to use of high-resistive orienting layers and increases the laser strength [4]. It should be noticed, that these nanoparticles can realize anti-reflection functions that depend on the deposition parameters, such as density, penetration depth and tilt angle.

In the current research, we processed via the CO_2 laser the surface of ITO with the deposited CNTs. It influences the topology of films, thus refractive properties can be modified under irradiation. In this paper, we compare the refractive indices of two groups of samples — with the laser ablation and without the laser ablation.

2. Materials and methods

For deposition of the CNTs on the ITO surface, we used a laser-oriented deposition (LOD) method based on a CO_2 laser (λ = 10.6 μm, P= 30 W, d= 5 mm and speed of treatment v was 1-3 cm×s^{-1}). The supply grid with the electric field 100 V×cm^{-1} was in LOD scheme as well. The laser ablation was performed with the laser marker (λ = 10.6 μm, P= 5 W, d= 100 μm, f= 1 kHz, v=3 cm×s^{-1}, the distance between laser grooves was 500 μm). The refractive index of structures was measured with the ellipsometry method (J.A. Woollam M-2000RCE) in 26 points for each sample per aperture 20 mm. The thickness of ITO was approximately 100 nm.

3. Results

The focused incident beam influences the surface with the two mechanisms. The first one is connected with the direct laser ablation. In this case, the width of the grooves is near the beam diameter of 100 μm. However, the initial beam can induce a surface electromagnetic wave (SEW) which propagates along the surface with a period is multiple of 10.6 μm. This type of laser interaction is more precise due to the less width of grooves (1 nm and less) and the less penetration depth. In figure 1 is shown the influence of SEW on the refractive properties of conducting ITO coating with CNTs.

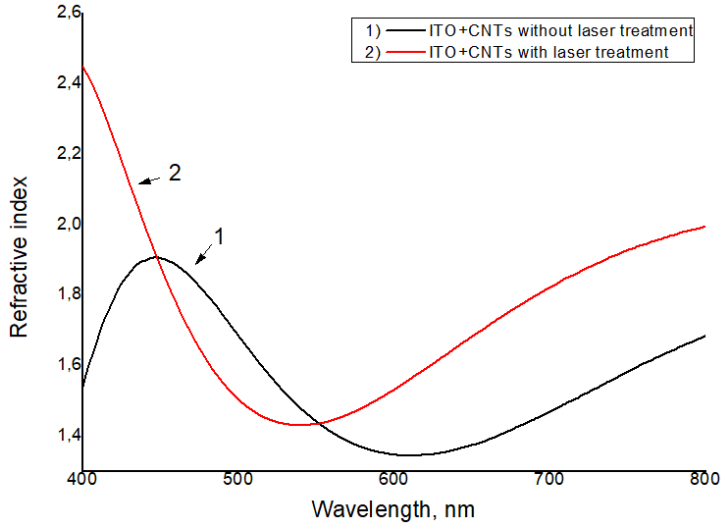

Figure 1. Spectral dependence of refractive index for ITO with CNTs before and after laser treatment

Induced SEW changes the relief of the surface and leads to the variation of the refractive index. Thus this mechanism permits to switch of the optical properties of ITO structures with high precision and in the width spectra range. These advantages give us the possibility to create ITO layers that will be index-matched with the LC mesophase. It means, that optical transmittance of LC devices after laser ablation with the SEW can be increased for the required spectra range. Moreover, in order to create the optimal deposition parameters of CNTs, this technique can be applied before their sputtering.

4. Acknowledgments

The authors would like to thank A.V. Kandakov (Institute of Problems of Mechanical Engineering RAS, St. Petersburg).

References

[1] Chausov D N, Kurilov A D, Kazak A V, Smirnova A I, Velichko V K, Gevorkyan E V, Rozhkova N N and Usol'tseva N V. *Liquid Crystals.* 2019. **46(9)** 1345-1352
[2] Petrescu E and Cirtoaje C. *Beilstein J. Nanotechnol.* 2018. **9** 233-241
[3] Kamanina N V, Zubtsova Yu A, Toikka A S, Likhomanova S V, Zak A and Tenne R. *Liq. Cryst. and their Appl.* 2020. **20(1)** 34–40
[4] Kamanina N, Toikka A and Gladysheva I. *Nano Express.* 2021. **2** 1-7

Investigation of the dynamic parameters of electroluminescence in different parts of the spectrum in local regions of the light-emitting heterostructure

I V Frolov[1,2]**, O A Radaev**[1]**, V A Sergeev**[1,2]
[1]Ulyanovsk Branch of Kotel'nikov Institute of Radio-Engineering and Electronics of Russian Academy of Sciences, Ulyanovsk 432071, Russia
[2]Ulyanovsk State Technical University, Ulyanovsk 432027, Russia

e-mail: ilya-frolov88@mail.ru

Abstract. A method for measuring the distribution of the differential charge carriers lifetime over energy levels in the local region of a light-emitting heterostructure is presented. The method has been tested on commercial green InGaN-based LEDs. It is shown that the relative inhomogeneity of the distribution of the charge carriers lifetimes in local regions of the chip in the long-wavelength part of the electroluminescence spectrum is higher than in the short-wavelength part of the spectrum.

1. Introduction

The spatial inhomogeneity of the distribution of electroluminescence parameters over the area of the active region of InGaN-based light-emitting heterostructures is due to the inhomogeneous distribution of nonradiative recombination centers and local clusters of indium atoms [1-3]. According to the model of inhomogeneous distribution of indium concentration in the heterostructure [4], the short-wavelength part of the emission spectrum is formed by the emission of local regions with a low concentration of indium, and the long-wavelength part is formed by the emission of local regions with a high concentration of indium. It was shown in [5] that the differential lifetime of charge carriers occupying low energy levels in the quantum well is longer than the differential lifetime of charge carriers occupying high energy levels. This means that the process of radiative recombination in the regions of the heterostructure with a low indium concentration proceeds more intensively, which is the reason for the increase in the current density in this region. Existing measurement methods make it possible to determine the distribution of the differential charge carriers lifetime over energy levels, averaged over the entire area of the structure. The report presents a method for measuring the distribution of the differential charge carriers lifetime over energy levels in local regions of a light-emitting heterostructure.

2. Results and discussion

The method consists in sequentially measuring the 3dB frequencies $f_{3\mathrm{dB}}$ distribution profiles of the electroluminescence over the LED chip area by the method described in [6, 7], when LED emission is passed through optical filters with different central wavelengths of the transmission spectrum λ_{max} and with a bandwidth several times smaller than the width of emission spectrum. The differential carriers lifetime τ is defined as the reciprocal of the 3dB frequency [8]: $\tau = \sqrt{3}/(2\pi f_{3dB})$. The energy level is determined by the formula: $E[eV] = 1240/\lambda_{\max}[nm]$.

The measurement method was tested on the example of Oasistek green commercial InGaN-based LEDs with a chip size of 200 × 130 μm and a center wavelength of the emission spectrum of 535 nm (Fig. 1). The distribution profiles of the 3dB frequencies of electroluminescence were measured in turn by passing the LED emission through optical filters with the central wavelengths of the transmission spectrum of 505 nm, 535 nm, and 565 nm and the transmission spectrum width of 8 nm. Based on the results of measurements of the 3dB frequencies distribution profiles, the charge carriers lifetimes distribution profiles over the area of the chip were calculated. Then, the chip area was conventionally divided into local regions 10 × 10 μm in size. For each optical filter, the average lifetime τ in local regions was calculated. Figure 2 shows the dependences of the differential charge carriers lifetime in two local regions of the LED chip on the energy level.

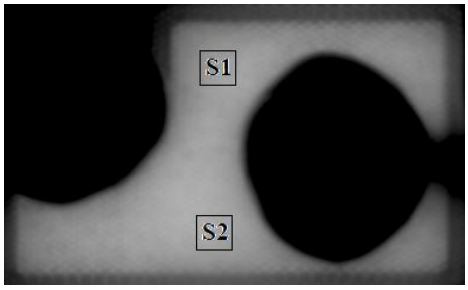

Figure 1. The LED chip image

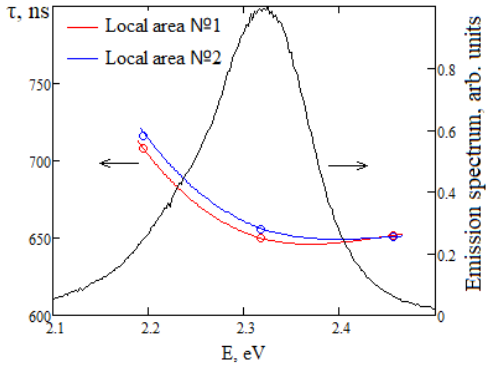

Figure 2. Dependences of the differential charge carriers lifetime on the energy level in two local regions of the LED chip

It has been determined that with an increase in the energy level, the charge carriers lifetime decreases. In the energy range 2.3 – 2.5 eV (short-wavelength part of the emission spectrum), the $\tau(E)$ dependence is weakly expressed. The relative inhomogeneity of the distribution of the τ over the LED chip, defined as the ratio of the standard deviation to the mean value, is about 0.5%. In the energy range 2.2 – 2.3 eV (long-wavelength part of the emission spectrum), the dependence $\tau(E)$ is significantly pronounced, and the relative inhomogeneity of the distribution of the τ over the LED chip is about 2%.

3. Conclusions

The obtained results indicate that, in the investigated structure, the degree of inhomogeneity of the local regions distribution with a high concentration of indium is higher than the degree of inhomogeneity of the local regions distribution with a low concentration of indium. The presented measurement method can be used as a tool for the lateral homogeneity diagnostic of the composition of light-emitting heterostructures.

Acknowledgments

The work was supported by the Russian Foundation for Basic Research, the project No. 19-07-00562 A.

References

[1] Tian P, Edwards P R, Wallace M J et al 2017 *Journal of Physics D: Applied Physics* **50** 075101
[2] Gelžinytė K, Ivanov R, Marcinkevičius S, Zhao Y, Becerra D L, Nakamura S, DenBaars S P, Speck J S 2015 Journal of Applied Physics 117 023111More references
[3] Peng Z, Lu Y, Gao Y, Chen G, Zheng J, Guo Z, Lin Y, Chen Z 2018 IEEE Photonics Journal 10 8201908
[4] Manyakhin F I 2018 Physics of Semiconductor Devices 52 359
[5] Frolov I V, Radaev O A, Sergeev V A 2020 Journal of Physics: Conference Series 1695 012076
[6] Frolov I V, Radaev O A, Sergeev V A 2019 Journal of Physics: Conference Series 1410 012092
[7] Sergeev V A, Frolov I V 2020 Patent Russia 2725613
[8] Schubert E F 2006 Light Emitting Diodes (Cambridge University Press)

Photovoltaic characteristics of structures with porous silicon obtained by various technological plans

D A Shishkina[1,2], **N A Poluektova**[1], **I A Shishkin**[2]
[1]Faculty of Electronics and Instrument Engineering, Samara National Research University, Samara, 443086, Russia
[2]Department of Physics, Samara National Research University, Samara, 443086, Russia

Abstract. In this paper, the influence of technological parameters on the current-voltage characteristics of solar cells with porous silicon was studied. It is shown that for structures with a developed surface, the selection of optimal technological plans is required.

1. Introduction

The conversion of solar energy into electrical energy is an important scientific and technical problem related to the promising direction of future energy. It is shown in [1] that the use of porous silicon as a working layer can improve the efficiency of solar cells. However, the different order of technological processes can negatively affect the characteristics of structures, and as a result, their efficiency.

2. Materials and methods

Samples of photosensitive structures with a porous layer were divided into two groups. In one group, the first stage was the creation of a p-n junction by diffusion of alloying components into a p-type silicon wafer, and the second stage was the creation of a porous layer by electrochemical etching in a horizontal cell [2] or metal-stimulated chemical etching [3]. The other group had the reverse order of technological plans.

3. Results and discussions

Figure 1 shows the results of measurements of the current-voltage characteristics of porous structures made by various methods before diffusion (purple curve) and after diffusion (green curve).

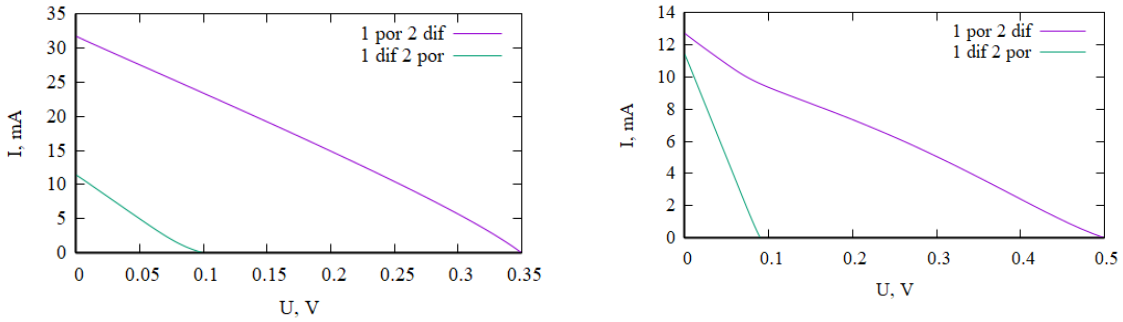

Figure 1 (a, b). Current-voltage characteristic of photosensitive structures with a porous layer made (a) by electrochemical etching in a horizontal type cell (b) MACE, before diffusion (purple line), after diffusion (green line).

The analysis of the graphs shows that for both methods of manufacturing porous layers, the route in which the porous layer is first made, and then diffusion is carried out, is more effective. If the diffusion is carried out before vaporization, then as a result of etching, there is an active leaching of the n-type from the substrate, which negatively affects the main parameters of the solar cell: short-circuit current and no-load voltage.

It was also observed that the method of creating a porous layer affects the characteristics of the solar cell (Figure 2).

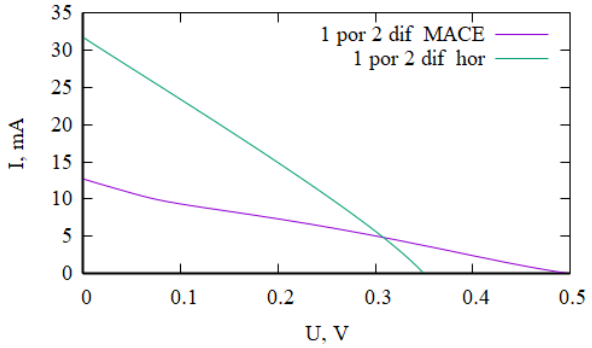

Figure 2. Comparison of the current-voltage characteristics of structures with porous silicon produced by horizontal etching (green line) and MACE (purple line)

This is primarily due to the characteristics of the resulting porous layer on the textured surface (Figure 3). With MACE, a porous layer is formed over the entire surface of the pyramid, forming a better light capture, which affects the higher no-load voltage. However, in horizontal etching, where the porous layer runs only along the bases of the pyramids, the short-circuit current is higher than in MACE. The lower short-circuit current in MACE-manufactured structures is associated with current losses caused by poor contact.

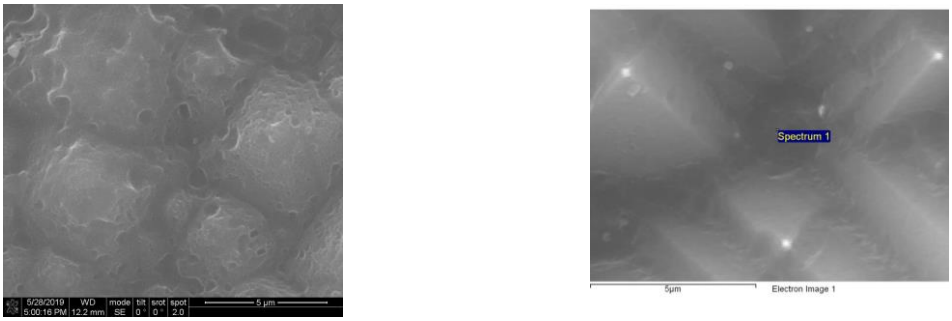

Figure 1 (a, b). SEM images of a porous layer manufactured by (a) MACE (b) horizontal electrochemical etching

4. Conclusion

Thus, the conducted studies have shown that the optimal technological route is pore formation and subsequent diffusion. However, this technological route requires further refinement, namely, the selection of the optimal mode of diffusion and the reduction of recombination losses.

References

[1] Kirsanov N Y Latukhina N V Lizunkova D A Rogozhina G A Stepikhova M V Semiconductors 2017 **51** 3

[2] Sze S M and Kwok K Ng 2006 *Physics of Semiconductor Devices*.

[3] Bandarenka H V, Girel K V, Niauzorau S A, Gonchar K A, Timoshenko V U 2016 *Doklady BGUIR* **2** 74

Simulation of nanowires structures optical properties.

I A Shishkin[1], D A Lizunkova[1], N V Latukhina[1]

[1]Samara National Research University, Samara 443086, Russia

Abstract. In this study, three-dimensional fragments of nanowires structures were simulated in which the thread cross sections had a square, triangular and round shape. The theoretical data were compared with the experimental results, described in detail in [1]. The influence of the shape of the filaments on the theoretical course of the reflection curve is also shown.

1. Introduction

Silicon nanowires are a modern and promising nanomaterial of great interest for various fields. Due to the complex surface, silicon nanowires have unique properties that allow them to be used as an anti-reflective coating for solar cells. Simulation of the spectral characteristics of nanostructures was carried. At the moment, there are few models that can plausibly describe the real course of the reflection curve for nanostructured materials, including silicon nanowires. This work shows that the theoretical reflection coefficient depends on the shape of the wires (square, triangular, pyramidal), and one of the simulated structures coincides with the experimental results described in the article [1].

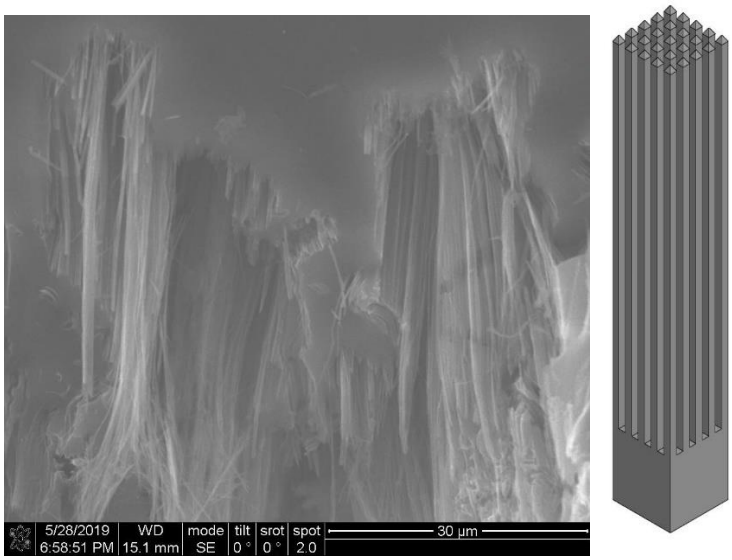

Figure 1. SEM image of the real structure of nanowires and one of the structures that is used in the Comsol Multiphysics software package.

2. Results and discussion

The description of the passage of electromagnetic waves in a nanowires structure consisting of 25 nanowires with a thickness of 0.2 microns was carried out in the Comsol Multiphysics software package [2]. To solve this problem, a system was chosen in which a part of the silicon substrate is located in an air medium, so a wave equation was taken based on the variable electric field for two media. The boundary conditions in which the condition n×E=0 is satisfied in this system are the side faces of the bounded air medium. The upper plane of this scheme is the plane of the energy flux density of the incident radiation, which is described by the incoming mode of the electric field.

Figure 2 presented the results of the modeled dependence of the light reflection coefficient on the incident wavelength. Electromagnetic radiation passed through a structure with nanowires, in which the distance between each element of the nanowires system was 0.2 microns. The analysis shows that in the wavelength range from 300 to 800 nm, the minimum reflection coefficient for theoretical models is in different values, but it is the triangular-shaped nanowires that are as close as possible to the practical values obtained in [1].

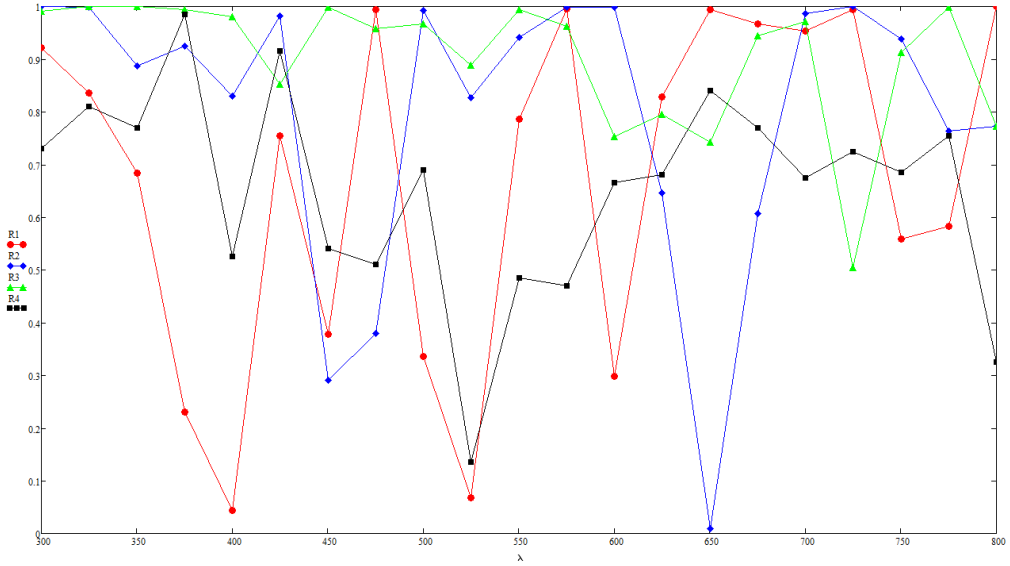

Figure 2. Graphs of the dependence of the reflection coefficient on the wavelength obtained in various theoretical models (square, triangular, pyramidal) and practical data: red line - triangular nanowires, blue line - square nanowires, green line - pyramidal nanowires, black line - practical data.

Acknowledgments

This work was supported by the Foundation for Assistance to Small Innovative Enterprises, grant № 12980GU/2018.

References

[1] Yilbas B S et al. 2016 *Scientific Reports.* **6.1** 1-13

[2] Hochbaum A I 2005 *Nano Letters.* **5** 457.

Determination of hole diffusion length in n-GaN

D S Arteev[1], A V Sakharov[1], A E Nikolaev[1], E E Zavarin[1], W V Lundin[1], A F Tsatsulnikov[2]

[1]Ioffe Institute, 26 Politekhnicheskaya, 194021, St. Petersburg, Russia
[2] Submicon Heterostructures for Microelectronics, Research & Engineering Center, RAS, 26 Politekhnicheskaya, 194021, St. Petersburg, Russia

e-mail: ArteevDS@mail.ioffe.ru

Abstract. The paper presents the results of a study of hole diffusion length in n-GaN by means of photoluminescence. The estimated hole diffusion lengths are 100 nm and 200 nm in the case of low and high excitation, respectively, which could be explained by saturation of non-radiative recombination centers in GaN with photoexcited carriers.

1. Introduction

III-nitride optoelectronic devices, like light-emitting diodes and lasers or photodetectors, are of great interest due to their high efficiency. Carrier transport in such structures is an important issue. Minority carrier diffusion length (usually holes, as even unintentionally doped GaN is n-type with electron concentration of 10^{16}-10^{17} cm^{-3}) is one of the key parameters that can directly affects the device performance. In this work, hole diffusion length along the c-direction in n-type GaN were studied by means of photoluminescence at different excitation levels.

2. Experimental details

A set of GaN/InGaN/GaN single quantum well (QW) structures with different capping layer thickness (i.e. different distance from QW to the surface) was grown by metalorganic chemical vapour deposition on c-face sapphire substrates in our in-house Dragon-125 epitaxial system with a horizontal reactor using conventional precursors. The growth conditions were exactly the same for all the samples. In order to mitigate the effect of internal spontaneous and piezoelectric field, GaN layers were doped with [Si]~10^{18} cm^{-3}. Photoluminescence studies were performed using a continuous wave He-Cd laser (325 nm, 10 mW) in low and high excitation regimes by changing focused spot diameter from ~5 mm to ~0.5 mm. An AvaSpec-2048 Fiber Optic Spectrometer was used for the spectra measurements.

3. Results

Change in GaN cap layer thickness influences only PL intensity; position and shape of spectra from QW were unchanged. Symbols in figure 1 show the dependence of integrated PL intensity on the cap layer thickness, normalized to the intensity of the samples with 10 nm GaN cap. Since absorption coefficient of GaN at 325 nm is relatively high ($\alpha=1.2\cdot10^5 cm^{-1}$ [1]), most of the carriers are generated in thin near-surface region. Therefore, the thicker the cap layer, the fewer holes can reach the QW via

diffusion to recombine radiatively, being in line with [2]. However, the relative decrease in PL intensity of the samples with thicker cap layer is lower in the case of high excitation, which may indicate larger diffusion length. Similar effect was reported for iron-, carbon- [3] and magnesium-doped [4] bulk GaN under long-term electron beam irradiation. In order to estimate the diffusion lengths, a simple model was used (figure 2). Photogenerated carriers profile is:

$$G(x) \sim e^{-\alpha x} \tag{1}$$

where α is the absorption coefficient in GaN. Carrier collection probability depends on diffusion length and can be expressed as:

$$P(x) = e^{-\frac{|x-x_{QW}|}{L}} \tag{2}$$

where L is hole diffusion length, x_{QW} is position of QW. Then, neglecting carriers drift and considering that recombination constants are the same for all the samples at a given excitation density, integrated PL intensity is:

$$I = \int_0^{\infty} G(x)P(x)dx \tag{3}$$

The calculation results are shown in figure 1 as solid lines. The estimated hole diffusion lengths are 100 nm and 200 nm in the case of low and high excitation, respectively. Such increase in diffusion length could be attributed to saturation of non-radiative recombination centers in GaN with photoexcited carriers.

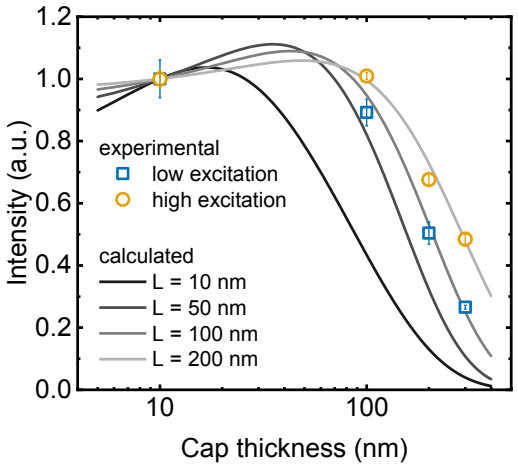

Figure 1. PL intensity vs. cap layer thickness in low and high excitation regimes. Symbols are experimental data. Lines are calculation results for different values of hole diffusion length *L*.

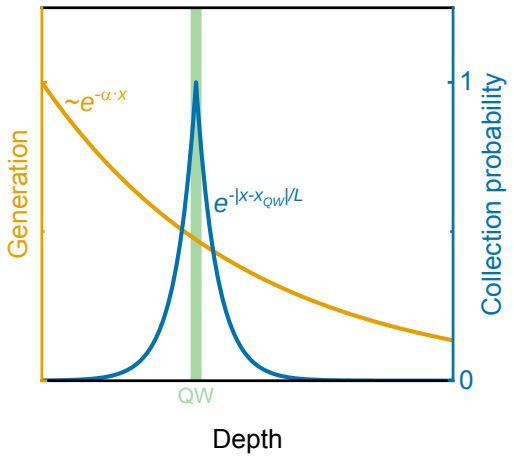

Figure 2. Schematic profiles of photogenerated carriers and collection probability. Pale shaded area indicates position of the quantum well.

References

[1] Muth J F, Lee J H, Shmagin I K, Kolbas R M, Casey H C, Keller B P, Mishra U K and DenBaars S P 1997 *Appl. Phys. Lett.***71** 2572–4

[2] Hafiz S, Zhang F, Monavarian M, Avrutin V, Morkoç H, Özgür Ü, Metzner S, Bertram F, Christen J and Gil B 2015 *J. Appl. Phys.***117** 013106

[3] Lopatiuk O, Osinsky A, Dabiran A, Gartsman K, Feldman I and Chernyak L 2005 Electron trapping effects in C- and Fe-doped GaN and AlGaN *Solid-State Electron.***49** 1662–8

[4] Chernyak L, Burdett W, Klimov M and Osinsky A 2003 Cathodoluminescence studies of the electron injection-induced effects in GaN *Appl. Phys. Lett.***82** 3680–2

Numerical simulation of effective light transmission through a photonic memory cell

M E Makarov [1,2], A A Sapegin [1,3] and R T Minnullin [1,3]
[1]JSC Molecular Electronics Research Institute, Moscow 124460, Russia
[2]Institute of Microelectronics Technology and High-Purity Materials of Russian Academy of Sciences, Chernogolovka 142432, Russia
[3]Moscow Institute of Physics and Technology, Dolgoprudny 141701, Russia

Abstract. This paper is devoted to numerical simulation of a non-volatile photonic memory cell based on phase-change material $Ge_2Sb_2Te_5$ (GST). The parameters of a light propagation are presented for both crystalline and amorphous GST phases. The cell structure is optimized for single TE-mode regime that is suitable for short- and long-distance communication lines.

1. Introduction

Nowadays, the upward trend in data volume is accelerating along with the spreading of high-speed mobile networks, IoT devices and artificial intelligence applications. In these conditions, the requirements for processing, transmission and storage devices are increasing [1]. It becomes more difficult for microelectronic technologies to go beyond the device capabilities. However, the use of silicon photonics offers several promising solutions [2, 3, 4].

This paper presents numerical simulation of light propagation through a non-volatile photonic memory cell. The cell consists of Si strip waveguide with 10 nm thick GST layer on its top. The logical state depends on the phase state of GST and can be read by passing low energy light pulse through the waveguide. Different transmission levels occur because the amorphous GST phase has lower absorption index than the crystalline one. Recording and erasing are also performed by passing light pulses through the waveguide, but their power must be sufficient to switch the GST phase state.

The goal of present work is to find the best ratio of the waveguide dimensions to provide the larger difference between the transmission levels of the photonic memory cell.

2. Device simulation and discussion

To reach the goal, two stages of numerical calculations were performed. In the first stage, 2D numerical simulations were carried out. The simulated structure had finite size in the XY plane. The thickness of the SiO_2 substrate was selected 2 μm to ensure low losses due to the proximity of the substrate. The distance from the side walls of the waveguide to the boundaries of the simulated area was set to 3 μm; the distance from the GST layer to the top boundary of the simulated area was 2 μm. As a result, mode distributions of the photonic storage element were obtained for both GST phase states and different waveguide geometry. Figure 1a shows how the mode distribution changes with the waveguide dimensions. It is possible to notice that the mode distributions corresponding to amorphous and crystalline GST phases are different. This fact allowed us to find the certain range of the waveguide widths and heights, in which single TE-mode regime was insensitive (“immune”) to switching GST phase state. However, light generally enters the photonic memory cell through a Si strip waveguide and its mode distribution should also be taken into account. The overlap between the “immune” regime and single TE-mode regime of the Si strip waveguide guarantees single TE-mode regime in the entire photonic memory cell (Figure 1b).

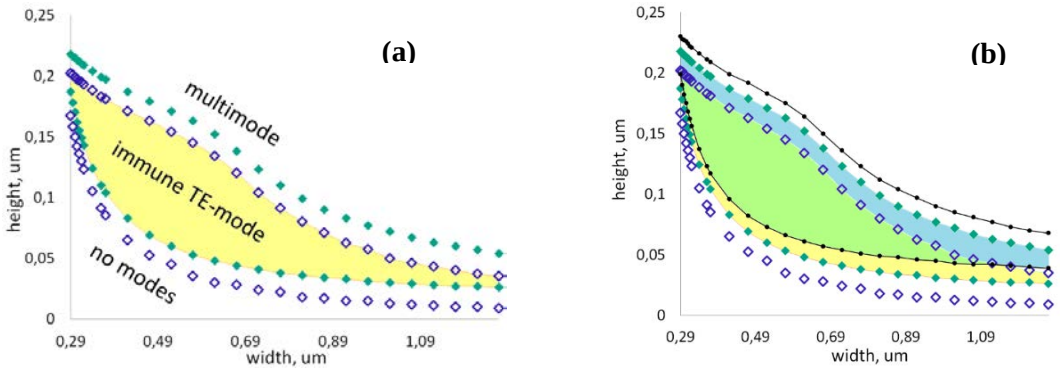

Figure 1. (a) Optical mode regime of the photonic storage element. Green and hollow dots correspond to amorphous and crystalline phase states. Yellow area corresponds to the "immune" regime. **(b)** The overlap between mode distributions of the photonic storage element and Si strip waveguide (area inside the black outline). Light green area provides single TE-mode regime and blue one corresponds to both TE and TM modes.

Single TE-mode regime was selected for several reasons. It should be noted that both- short and long-distance transmission lines generally use signals of one polarization to reduce losses. Usually it is TE polarization [5]. Bragg gratings are used to connect fiber transmission lines and silicon photonics devices. Bragg condition for a given wavelength and the angle of incidence can only be applied for a single polarization. As a rule, TE polarization is selected because it corresponds to the fundamental waveguide mode when the width of the waveguide is greater than its height [6]. The possibility of creating Bragg grating for TM polarization was shown, but its efficiency factor was 20% lower than for TE polarization [6, 7].

In the second stage of numerical calculations, transmission characteristics of the photonic memory cell were analyzed. It was determined at what waveguide dimensions the maximum difference between transmission levels is reached. For this purpose, 2D and 3D numerical calculations were carried out. The length of the GST layer was 1 μm and all the other dimensions were the same as in the first stage. Both 2D and 3D calculation provided fairly similar results. The difference between transmission levels decreases with the waveguide height. The largest difference between the transmission levels of the photonic memory cell may be achieved on the bottom border of the overlap between "immune" zone of the photonic memory cell and single TE-mode regime of the Si strip waveguide (bottom black line on figure 1b). It reaches about 80 percentage points in the center of the overlap.

3. Conclusion

In conclusion, the optimal geometry of the photonic memory cell suitable for long- and short- distance communication was determined. Furthermore, the approach of designing single TE-mode devices with a switching refractive index, which may be useful for creating silicon photonics devices or photonic integrated circuits, was shown.

Acknowledgments

This study was supported by the Russian Foundation for Basic Research, project 19-29-03040.

References

[1] G. Y. Krasnikov, N. A. Zaytsev *et al.* 2015 *Journal of nano- and microsystem technique* **4** 63
[2] V. Stojanović, Rajeev J. Ram, Milos Popović, Sen Lin *et al*. 2018 *Optics Express* **10** 13106
[3] J. Feldmann, N. Youngblood, M. Karpov, H. Gehring, X. Li *et al*. 2021 *Nature* **589** 52
[4] J. Feldmann, N. Youngblood, C. D. Wright *et al.* 2019 *Nature* **569** 208
[5] Dan-Xia Xu, G. T. Reed 2014 *IEEE Journal of Selected Topics in Quantum Electronics* **20** 189
[6] W. Bogaerts *et al* 2013 *Handbook of Silicon Photonics* ed L. Vivien and L. Pavesi (US: Boca Raton, Florida) p 121
[7] D. Vermeulen *et al.* 2010 *Proc. European Conf. on Integrated Optics* (Cambridge University)

1.3 μm vertical-cavity surface-emitting lasers based on InGaAs/InGaAlAs superlattice

S S Rochas[1], L Ya Karachinsky[1], A V Babichev[1], I I Novikov[1], A G Gladyshev[1], P E Kopytov[1], E S Kolodeznyi[1], S A Blokhin[2], A Yu Egorov[1]

[1]ITMO University, St. Petersburg, 197101 Russia
[2]Ioffe Institute, St. Petersburg, 194021 Russia

E-mail: stanislav_rochas@itmo.ru

Abstract. Vertical-cavity surface-emitting lasers of 1.3 μm spectral range with the active region based on InGaAs/InGaAlAs superlattice were studied. Upper and lower distributed Bragg reflector and active region were fabricated by molecular-beam epitaxy and fused by double wafer-fusion technique. VCSELs demonstrated a stable operation at speed of 10 Gbit/s at 20 °C and bias current of 10 mA,

1. Introduction

Vertical-cavity surface-emitting lasers (VCSELs) of 1.3 μm spectral range are promising light sources for telecommunication systems, various hybrid optical interconnections and silicon photonics. Optimization of the active region, which is responsible for the amplification of light, has always been the basis of progress in the development of semiconductor lasers. We have recently shown that using of InGaAs/InGaAlAs superlattice as a VCSEL's active region can substitute active regions of VCSELs based on heterostructures with highly strained quantum wells and increase the gain of the device [1]. VCSELs based on InGaAsP/InP grown in one epitaxial process have several disadvantages [2]. The use of wafer fusion technique [3,4] makes it possible to combine the advantages of an active region based on InP and distributed Bragg reflector (DBR) with a high reflection coefficient based on AlGaAs/GaAs materials. In this paper, we present the results of study of 1.3 μm VCSEL with the active region based on an InGaAs / InGaAlAs superlattice.

2. Heterostructure

The VCSEL heterostructures was fabricated by double wafer fusion of AlGaAs/GaAs upper and lower DBR grown on GaAs substrates with an InAlGaAs/InP optical microcavity grown on an InP substrate. Molecular beam epitaxy was used as epitaxial method. The upper DBR consisted of 21.5 layer pairs, the lower DBR consisted of 35.5 layer pairs. The active region was based on a 24-period InGaAs/InGaAlAs superlattice with layer thicknesses of 0.8 nm/2 nm, respectively. The wavelength of the photoluminescence peak of the active region emission was about 1280 nm at 20°C. The buried tunnel junction (BTJ) with an etching depth of 25 nm was made of layers n^{++}-InGaAs/p^{++}-InGaAs/p^{++}-InGaAlAs. To reduce optical absorption loss BTJ layers were placed at the node of the electromagnetic field intensity of the optical cavity mode. The total thickness of optical microcavity was 3λ.

3. Results

The use of a BTJ with an etching depth of 25 nm made it possible to provide the threshold current of the VCSEL at a level of 1.25 mA with a current aperture diameter of 5 μm. Due to relatively low internal losses, the differential quantum efficiency of lasers reached 70%. In combination with a low series resistance, a maximum output optical power of more than 6 mW (at a current of 15 mA) was achieved. Small-signal frequency analysis made it possible to estimate the maximum speed of the developed VCSEL at the 6 GHz level. In the mode of amplitude modulation with a large signal VCSELs demonstrate stable operation at a speed of 10 Gbit/s at 20 °C and bias current of 10 mA. Further increase in the data transfer rate led to a sharp decrease in the eye diagram, however, the eye diagrams were still open up to 15-16 Gbit/s.

Acknowledgments

This work was supported by the Ministry of Science and Higher Education of Russian Federation, research project no. 2019-1442.

References

[1] Karachinsky L. Y. et al. 2019 *Optics and Spectroscopy* **127** 1053
[2] Park M. R. et al. 2006 *IEEE photonics technology letters* **18** 1717
[3] Blokhin S. A. et al. 2020 *Technical Physics Letters* **46** 854
[4] Syrbu A. et al. 2004 *IEEE Photonics Technology Letters* **16** 1230

Photosensitive heterostructure for wavelength up to 1.3 μm with digital metamorphic buffer on GaAs

I.V. Samartsev[1*], S.M. Nekorkin[1], B.N. Zvonkov[1], K.E. Kudryavtsev[2], A.V. Zdoroveyshchev[1], S.M. Plankina[1], A.V. Rykov[1]

[1] Research Institute of Physics and Thechnology, Nizhny Novgorod State University, Nizhniy Novgorod 603950, Russia
[2] Institute for Physics of Microstructures RAS, Afonino 603087, Russia

woterbox@mail.ru

Abstract. The photosensitive heterostructure with digital metamorphic buffer layer has been grown by the method of MOCVD on GaAs substrate. Investigation of the stimulated emission spectra and Raman scattering have been carried out. Photodiodes produced from this structure were used to study the photocurrent spectra and current-voltage characteristics. It is shown that this method of forming metamorphic buffer layer makes it possible to obtain an $In_{0.3}Ga_{0.7}As$ photodiode on GaAs substrate for the photosensitive range 0.7–1.3 μm with defect density of about 10^6 cm^{-2}.

1. Introduction

Photodiodes operating in the short infrared range (up to 3 μm) grown on GaAs substrates are interest as a replacement for devices currently used for this range grown on InP substrates. One of the directions of creating such photodiodes is the use of metamorphic buffers (MB) [1]. The practical implementation of metamorphic heterostructures on GaAs, the characteristics which would not be low to those of heterostructures on InP, is hindered by incomplete suppression of the intergrowth of dislocations into active layers of the structure and the appearance of surface microrelief. Thus, it is current task to search for and optimize the MB design in order to improve the crystal quality of the obtained heterostructures. In this work, we present the results of the study of photosensitive GaAs heterostructures and photodiodes based on them, obtained by MOCVD on GaAs (100) substrates using digital MB.

2. Experimental samples

The investigated heterostructure was obtained by MOCVD method at atmospheric pressure. The 180 nm thickness n-GaAs buffer layer doped with silicon (10^{18} cm^{-3}) was grown on n-GaAs substrate. Then digital MB with total thickness of 1300 nm (doped with Si up to 10^{18} cm^{-3}) and p-i-n structure consisting of layers: n-$In_{0.3}Ga_{0.7}As$ with thickness of 360 nm (doped Si up to 10^{18} cm^{-3}), i-$In_{0.3}Ga_{0.7}As$ with thickness of 1420 nm and p-$In_{0.3}Ga_{0.7}As$ with thickness of 360 nm (doped with Zn up to 7×10^{17} cm^{-3}). The formation of digital MB layer is changing thicknesses of variable materials GaAs and InGaAs in opposite directions as the buffer layer grows, while the composition remains the same. Thus, at the initial stage of growth, the thicknesses of GaAs and $In_{0.3}Ga_{0.7}As$ were 62 nm and 3 nm, respectively. With the growth of the buffer layer, the GaAs thickness decreased and the $In_{0.3}Ga_{0.7}As$

thickness increased. At the final stage of MB growth, the GaAs layer thickness was 3 nm, the $In_{0.3}Ga_{0.7}As$ thickness was 62 nm. The total number of variable layers was 38. Thus, discrete MB consists of many GaAs/$In_{0.3}Ga_{0.7}As$ periods of various thicknesses, in which the propagation of dislocations at heterointerfaces is blocked.

On the structure side, AuGe ohmic contacts were deposited by the method of thermal evaporation in vacuum, then, 0.56 mm diameter meze was etched. On the substrate side, ohmic contacts were applied by the method of spark-ignition Sn. The surface of the samples was subjected to reactive ion etching in an oxygen atmosphere and subsequent thermal oxidation to minimize the surface dark current.

3. Results and discussion

The surface roughness was studied using atomic force microscopy. The root mean square deviation (RMS) was 20 nm. The dislocation density can be estimated from the density of etching pits, which was calculated using optical microscopy and amounted to 10^6 cm^{-2}. Under conditions of pulsed laser pumping at threshold power of 250 kW /cm^2, narrow ($\Delta\lambda$ <12nm) intense emission line appears in the radiation spectrum of the sample at wavelength of 1183 nm. In order to investigate the composition of the photosensitive region and the crystalline quality of the MB, we studied the Raman spectra from the cross section (110 plane) of the structure at room temperature using 473 nm laser. The approximation of the Raman spectra by the Lorentz function reveals the modes allowed in this geometry, corresponding to transverse optical phonons (TO) of the solid solution: low-intensity InAs-like mode and closely spaced GaAs-like and comparable in intensity DATO mode (disorder activated transverse optical mode [2]). In the lightly doped part of the photosensitive region, the frequency of the phonon modes of InGaAs changes small and is 230 and 260 cm^{-1} for InAs and GaAs-like TO modes, respectively. Such frequency values correspond to indium content in InGaAs of about 30%. In the MB region, there is increase in the frequency of all modes of the solid solution (compared to the lightly doped InGaAs region) and a decrease in the frequency of the GaAs TO mode from 268 cm^{-1} in the substrate to 262 cm^{-1} at the interface with the p-i-n InGaAs layer. This change in frequency corresponds to tensile stresses in the GaAs layers, and compressive stresses in the InGaAs layers.

Thus, the MB is in tense state. The spectral dependence of the photocurrent of photodiodes based on the obtained structures has maximum at wavelength of 1160 nm, where the photosensitivity range 700 - 1300 nm at 10% of maximum level at room temperature. The dark current with reverse bias voltage of 4 V was 5×10^{-6} A. Thus, the proposed design of digital MB layer is promising for the formation of photosensitive structures in the wavelength range of 0.7 - 1.3 μm grown on GaAs substrate by MOCVD.

References

[1] I. V. Samartsev, S. M. NekorkinB. N. Zvonkov, Semiconductors, 52 (12), 1564 (2018).
[2] J. Groenen, R. Carles, G. Landa. Phys. Rev. B., 58 (16), 10452 (1998).

Focused ion beam milling of ridge waveguides of edge-emitting semiconductor lasers

G O Kornyshov[1], A S Payusov[2], M I Mitrofanov[2,3], G V Voznyuk[2], A A Serin[2], M M Kulagina[2], V P Evtikhiev[2], N Yu Gordeev[2] and M V Maximov[1]

[1]Alferov University, 8/3 Khlopina, St Petersburg 194021, Russia
[2]Ioffe Institute, 26 Polytechnicheskaya st., St Petersburg 194021, Russia
[3]Submicron Heterostructures for Microelectronics, Research & Engineering Center, RAS 26, Politekhnicheskaya st., Saint-Petersburg, 194021, Russia

supergrigoir@gmail.com

Abstract. Since focused ion beam (FIB) instruments have become commercially available, it allows post-processing of ridge waveguide lasers. Our experiments show that one can remove as much as 50 μm of the 4 μm wide ridge of the 1,5 mm edge-emitting laser without fatal degradation of the main laser parameters. The approach could be used for the formation of the passive section of conventional mode-locked or microring lasers.

1. Introduction

FIB milling is widely used in today semiconductor industry for the fabrication and modification of integrated circuits, microelectromechanical systems, sample preparation for a transmission electron microscope and many more [1]. It brings such advantages as nanoscale resolution, maskless process, capabilities of the ion implantation of selected areas, removing and depositing metals or isolators. Since FIB instruments have become commercially available, all these advantages are used during prototyping various optoelectronic devices. In particular, distributed Bragg reflector and distributed feedback lasers [2,3], edge-emitting lasers with modified mirrors [4] with FIB processing have been successfully demonstrated. At the same time, there are only few studies on FIB milling of the ridge waveguides of edge-emitting lasers [5]. This potentially would allow introducing modifications and creation of passive sections in the ridge waveguide of devices after the fabrication process, and vary their parameters as many times as needed. In this work, we present a study on the milling of ridge waveguides of InGaAs/GaAs edge-emitting diodes and its effect on device characteristics.

2. Experiment details

For our experiments we have chosen the 4 μm ridge lasers with the cavity length of 1.5 mm based on InGaAs quantum well-dots similar to devices studied in [6]. The devices were mounted p-side up onto copper heat-sinks using In solder. Figure 1a shows the scanning electron microscope (SEM) image of the laser facet. Arrows and extension lines denote heights with respect to the metal surface in between ridges which we took as the base plane for further measurements with an atomic force microscope (AFM).

The FIB milling was performed in ultra-high vacuum using a custom-designed 35 keV Ga^+ FIB lithography system after devices were processed, tested and mounted. Ultra-high vacuum prevents

unwanted oxidation during the process. The ion dose for AlGaAs cladding layer was in the range of $(1..3)\cdot 10^{17}$ cm^{-2} depending on the sample. The ion beam current was 500 pA.

AFM measurements were carried out with NT-MDT Smena-A instrument in tapping mode. Figure 1b shows the heights profile of the sample L2. White rectangles denote areas where mean milling depth (h_e) and maximum/minimum (h_{max},h_{min}) heights were determined. Measurements of laser characteristics were repeated after the milling process.

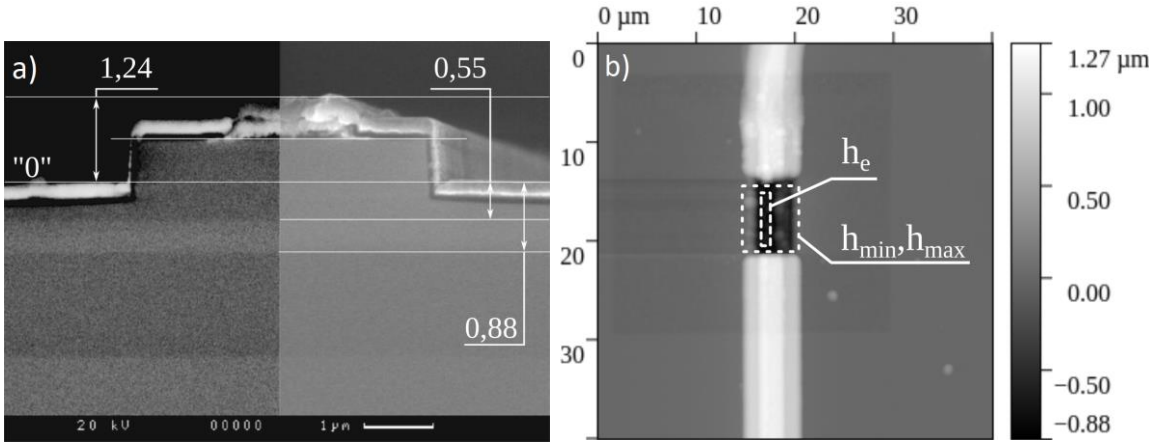

Figure 1. SEM image of the laser facet (a) and AFM image of the L2 sample (b).

3. Results and discussion

The results of our experiment are summarized in table 1. Deterioration of the device parameters correlates well with the minimum height. Samples L2 and L3 also demonstrate a blue-shift in lasing spectra by 10-13 nm indicating increased internal optical loss due to FIB induced defects. Similar results were obtained in [5]. However, the milling area for our devices is 40 times larger for samples L1-L3 and 200 times for L4 and L5. Obtained results indicate that optimization of the flatness of the milled area will allow cutting ridge waveguides in order to create passive sections in conventional edge-emitters as well as microring devices.

Table 1. Relative to the waveguide (h_{WG}=-0,55µm) heights and lasers characteristics of milled samples. L_{fib} denotes the length of the milled section.

Sample	L_{fib}, µm	(h_e-h_{WG}), µm	(h_{min}-h_{WG}), µm	$I_{th\ fib}/I_{th}$	$\eta_D/\eta_{D\ fib}$
L1	10	+1.4	+0.84	1	1
L2	10	+0.08	-0.43	1.53	2.55
L3	10	-0.17	-0.33	1.42	3.57
L4	50	+0.71	+0.08	1	2.07
L5	50	+0.66	+0.21	1	1.55

Acknowledgments

The research was supported by the Ministry of Science and Higher Education of the Russian Federation (project 0791-2020-0002).

References

[1] Langford R M *et. al.* 2002 *Mater. Sci. Technol.* **18** 743–8

[2] Steckl A J 1995 *J. Vac. Sci. Technol. B Microelectron. Nanom. Struct.* **13** 2570

[3] Reithmaier J P 2003 *AIP Conference Proceedings* **680** 584
[4] Payusov A S *et. al.* 2017 *J. of Phys.: Conf. Ser.* **917** 052035
[5] Musil C R *et. al.* 1997 *Nucl. Instr. Meth. Phys. Res. B* **127**–**128** 428–32
[6] Kornyshov G O *et. al.* 2020 *J. of Phys.: Conf. Ser.* **1697** 12177

Selectively excited photoluminescence spectroscopy of InAs/InGaAs/GaAs quantum dot arrays in 20-200 °K temperature range

D A Rybalko[a], A M Nadtochiy[a,b], M V Maximov[a,b]

[a] St Petersburg Academic University, 8/3 Khlopina Str, St Petersburg, 194021, Russia

[b] National Research University Higher School of Economics, Soyuza Pechatnikov, 16, St. Petersburg, 190008, Russia

dimarybalko91@gmail.com

Abstract. A detailed study of self-organized InAs/InGaAs/GaAs quantum dots by selectively excited photoluminescence in the 20-200°K temperature range is presented. We that found along with the ground state emission there is intense luminescence from the optical region of the second excited state of quantum dots, which previously was never reported. An improved interpretation of the 3-LO phonons' replicas in the photoluminescence spectrum is developed.

1. Introduction

Heterostructures with arrays of self-organized quantum dots (QDs) are the basis of a many devices in modern semiconductor physics. In particular, such structures are promising for a wide class of applications – lasers, solar cells, single-photon emitters, quantum informatics hardware devices [1-7]. The main specific and advantages of QDs are the discrete energy spectrum and correspondent features in lateral transport and relaxation processes. Besides, the desirable properties of QDs are strongly depending on the intended application. For example, light-emitting devices require the active medium with effective and fast relaxation of charge carriers from excited states to the ground one. In turn, quantum informatics is expecting an active area with the longest possible time of relaxation of charge carriers, since nonresonant relaxation leads to the loss of quantum coherence [7].

The relaxation of charge carriers in QDs has been studied for more than 20 years, however, the question of detailed relaxation mechanics in QDs is still disputable in the scientific community. In particular, theoretically predicted phonon bottleneck is not observed experimentally, and the role and the relationship of various relaxation mechanisms in QDs (scattering by LO and LA phonons, Auger recombination, etc.) are the subjects of the research still.

2. Results and discussion

In this work, we analyze energy spectrum and relaxation mechanisms of two structures with arrays of InAs/InGaAs/GaAs self-organized QDs using selectively excited photoluminescence (SEPL) spectroscopy in the 20-200 K temperature range. The excitation laser wavelength was varied in the range of 990-1075 nm with the 1-nm step. A relatively small excitation energy step variation allowed

us to represent the PL data as a surface of PL intensity depending on detection energy (E_{det}) and energy difference of excitation and detection (E_{pump}-E_{det}). Such a way of data representation allowed us to compare them with the results of prior photoluminescence excitation spectroscopy (PLE) studies. Moreover, the surface-like data representation allowed us to use various surface analysis methods, in particular, the gradient analysis method, local contrast, filtering, and so on. The results obtained are in good agreement with the previously presented PLE ones for the same structures [8].

The studies of InAs QD arrays with PLE spectroscopy, as well as its detailed analysis on the basis of PL-surface (E_{det}, E_{pump}-E_{det}) were carried out previously by many groups (see, for example, [9]). Also, there are several works on the investigation of similar QDs by selectively excited photoluminescence spectroscopy (see, for example, [10]). Our results confirm, in general, the interpretations proposed in these papers [9, 10]. However, we emphasize several discrepancies. In particular, the SEPL spectra in our experiment exhibit intense luminescence in the region close to the QDs' second excited state (ES2), while the radiation from the first excited state (ES1) is not observed. In [10], the SEPL spectra corresponding to our range of excitation and detection energies did not show any emission from the regions of both QDs' first and second excited states. We assume that intense radiation from ES2 state may indicate slow relaxation of charge carriers from this state (i.e. LO-bottleneck). In turn, relaxation processes from the first excited state are clearly faster. Variation in dynamics of charge carriers can be a consequence of interlevel energy spacing variations in a particular QD array.

In [10], a double 3LO-phonon replica, shifted from the excitation line by ~ 85 and ~ 105 meV was observed in the background of the ground state emission in SEPL spectra. However, our data allow us to identify the ~ 85 meV-shifted line as the first excited state. This follows from a comparison of obtained SEPL spectra and PLE spectra from our previous work [8].

The behavior of LO-phonon replicas with temperature increasing partially confirms the interpretations proposed in [10, 11]. The presence of LO-phonon replicas in the background of the ground-state emission in SEPL spectra at low temperatures generally corresponds to the idea of selective excitation of QDs [9]. LO-phonons provide a fast relaxation mechanism resulting in an effective population of the ground state of QDs certain size, which ground state transition energy is spaced away from the energy of laser line by multiple LO-phonon energy. An increase in temperature leads to emerging of inter-QDs' carrier transport (equilibrium carrier distribution) and consequent gradual weakening of the selection of QDs by size. Therefore at a temperature of ~ 140-160 °K LO-replicas' intensity decreases dramatically.

Concluding, the detailed study of heterostructures with InAs/InGaAs/GaAs self-organized QD arrays using SEPL spectroscopy is presented. The results obtained partially agree with previously published ones. Certain correction of previously suggested interpretations was proposed. Further studies will allow a better understanding of the nature of the energy spectrum of QDs and relaxation mechanisms, which are important both for studying the fundamental properties of InAs/InGaAs/GaAs QD arrays and for the realization of advanced QD-based devices.

Acknowledgments

References

[1] Asryan L V and Suris R A 2004 Semiconductors 38, 1

[2] Bimberg D, Grundmann M, Ledentsov N N 1999 Quantum Dot Heterostructures (Wiley, London)

[3] Blokhin S A, Sakharov A V, Nadtochy A M, Pauysov A S, Maximov M V, Ledentsov N N, Kovsh A R, Mikhrin S S, Lantratov V M, Mintairov S A, Kaluzhniy N A and M. Z. Shvarts 2009 Semiconductors 43, 514

[4] Luque A and Marti A 1997 Phys. Rev. Lett. 78, 5014

[5] Zrenner A, Beham E, Stufler S, Findeis F, Bichler M and Abstreiter G 2002 Nature 418, 612

[6] Ustinov V M, Maleev N A, Zhukov A E, Kovsh A R, Egorov A Yu, Lunev A V, Volovik B V,

Krestnikov I L, Musikhin Yu G, Bert N A, Kop'ev P S and Alferov Zh I 1999 Appl. Phys. Lett. 74, 2815
[7] Bryant G W, Solomon G S 2005 Optics of Quantum Dots and Wires, Artech House (Boston, London, UK)
[8] Rybalko D A, Nadtochiy A M, Maximov M V and Zhukov A E 2020 Optics and Spectroscopy 128, 1
[9] Heitz R, Stier O, Mukhametzhanov I, Madhukar A and Bimberg D 2000 PHYSICAL REVIEW B 62, 16
[10] Steer M J, Mowbray D J, Tribe W R, Skolnick M S and Sturge M D 1996 PHYSICAL REVIEW B, 54, 24
[11] Kryzhanovskaya N V, Gladyshev A G, Blokhin S A, Maksimov M V, Semenova E S,
Vasil'ev A P, Zhukov A E, Ledentsov N N, Ustinov V M and Bimberg D 2005 Semiconductors, 39, 10, 2005

Optical properties of plasmonic metal nanoparticles on GaN surface

P Alay[1], Y Enns[1,2], A Mizerov[1], A Kondrateva[1,2], M Mishin[1]

[1]Alferov University, St. Petersburg, Russia
[2]Peter the Great Saint-Petersburg Polytechnic University, St. Petersburg, Russia

Abstract. This paper presents the results of studying the plasmon effect in metal nanoparticles formed on the GaN surface. Silver and gold nanoparticles are formed by solid-state dewetting methods on epitaxial GaN grown by molecular beam epitaxy (MBE). Theoretical and experimental optical characteristics show the appearance of the surface plasmon resonance effect. The results of the work show the possibility of increasing the efficiency of GaN-based optoelectronic devices.

1. Introduction

Gallium nitride (GaN) is widely applied in innovative electronics such as light-emitting diodes (LED), lasers, photodetectors and other power and high-frequency electronics devices [1,2]. Attention to this material is due to the combination of its physical properties such as wide and direct bandgap, high values of disruptive voltage and high mobility of charge carriers good thermal conductivity and chemical inertness [3]. Photodetectors based on GaN are considered promising devices for detecting UV radiation (wavelength λ <365 nm). The high value of the bandgap allows to provide high selective photosensitivity to UV which make to avoid the necessity of using additional films to filter optical and infrared radiation. Recently, attention has been to improve the performance of optoelectronic devices due to the plasmonic behaviour of metal nanoparticles (NPs) [4-6]. Such structures are capable of exhibiting the effect of localized surface plasmon resonance (LSPR). It`s widely used for tuning optoelectronic processes in photovoltaics [7], photocatalysis [8], and photodetectors [9] due to improved optical absorption and / or charge transfer [10]. At the same time, the most common among the materials of nanoparticles are NPs of silver [11], aluminium [4], platinum [5] and gold [6] because of their high optical activity.
In this study, the plasmon effect leading to the capture of photons in the process of localized scattering is studied in detail, which increases the time of interaction of light and material. The efficiency of the electro-optical conversion can be increased by enhanced interaction stimulating by scattering.

2. Results

The synthesis of GaN layers by PA MBE on virtual substrates GaN /Al_2O_3 obtained by gas-phase epitaxy from organometallic compounds was carried out on a Veeco Gen 200 industrial-type setup. Before the start of the MBE PA synthesis of GaN layers the surfaces of virtual substrates had been cleaned according to the method developed by us described in detail in [12]. After the end of the pre-epitaxial cleaning of the surfaces of virtual substrates silicon-doped GaN layers with a thickness of ~ 300 nm were grown on it with PA MBE method at constant values of the substrate temperature T_s = 700 °C, a gallium flux F Ga ~ 0.25 μm/h, and an activated nitrogen flux F N ~ 0.05 μm/h. Silicon flux used in the experiments made it possible to reach an electron concentration in the GaN layers of ~3.7×10^{18} см$^{-2}$

The morphology and electrical parameters of the films were researched. NPs of gold and silver were formed on the GaN surface from pre-deposited metal films 3 nm thick using the method described in [13] at annealing temperatures of 500 °C. The measurement of optical reflectance spectra showed appearing of the LSPR effect. Based on the obtained data virtual math simulation of the plasmonic reaction of NPs of gold, silver, platinum, and aluminum on the GaN surface was carried out. The simulation was carried out using the solution of the full-wave equation based on the method described in [14]. The simulation results obtained are consistent with published experimental data.

3. Acknowledgments
The work was done as a part of the state assignment (№FSRM-2020-0008) of the Ministry of Education.

References
[1] Wasisto H S, Prades J D, Gülink J, Waag A 2019 *Appl. Phys. Rev.* **6**.
[2] Ueda T 2019 *J. Appl. Phys.* **58**.
[3] Fu N, Li E, Cui Z, Ma D, Wang W, Zhang Y, Song S, Lin J, 2014 *J. Alloys Compd.* **596** 92-97.
[4] Chang S, Chang M, Yang Y 2017 *J. Phot.* **9 1−7**.
[5] Zhang X, Liu Q, Liu B, Yang W, Li J, Niu P, Jiang X 2017 *J. Mater. Chem*. C **5** 4319.
[6] Shetty A, Sundar K J, Roul B, Mukundan S, Chandan G, Mohan L, Ghosh A, Vinoy K J, Krupanidhi S B 2014 *IEEE 2nd International Conference*.
[7] Hwang J D, Chan Y D & Chou T C 2015 *Nanotechnol* **26** 465202-1–465202-6.
[8] Ewa, K, Orlando O P M, Ryu A. & Bunsho O 2010 *Chem. Phys.* **12** 2344–2355
[9] Narendar G, Arun K S, Sumita S, Santanu M & Samit K R 2014 *Sci. Rep.* **4** 6483-1–6483-9.
[10] Mark L B, Naomi J H & Peter 2015 *Nat. Nanotechnol.* **10** 25–34.
[11] Li D, Sun X, Song H, Li Z, Chen Y, Jiang H *Adv. Mater.* 2012 **24** 845−849.
[12] Mizerov A M et al //2019 *Semiconductors* 53 8 1120–1130.
[13] Kondrateva A, Enns Y, Kazakin A, Morozov I, Karaseev P, Mishin M 2020 *Semiconductors* **54**(14) стр. 1885–1888
[14] Enns Y, Kondrateva A, Mishin M // *Journal of Physics: Conference Series* 2020 **1695**(1) 012115

Fiber Optic Attenuator

D P Andreev[1]
[1]Institute of Physics, Nanotechnology and Telecommunications, Peter the Great St. Petersburg Polytechnic University, St. Petersburg 194064, Russian Federation

Abstract. A study of a bending-type fiber-optic attenuator has been carried out. It is shown that the use of G.655 - optical fiber provides the largest dynamic range of the attenuator. The spectral dependence of the bending losses was measured in a wide range of wavelengths: from 1270 to 1610 nm.

1. Introduction

At times in a fiber optic network the need arises to reduce or balance the power of the light transmitted from one device to another device. A fiber optic attenuator is used in such cases. Fiber optic attenuator are used for reducing the power of the light in the fiber optic network [1-2]. Attenuators allow tuning the transmitting and receiving equipment without the danger of overloading the signal registration system, measuring optical power and loss level etc. The most used attenuators are adaptor type. They are simple in design and use, but this also has its disadvantages: such attenuators introduce large return losses, which can adversely affect the operation of the transmitting equipment. The lowest level of back reflections is provided by attenuators, made in the form of a fiber-optic connecting cord (patchcord) with a macrobend. They can be fixed or variable. For practical use, such characteristics of the device as the achieved dynamic range, linearity of regulation, and a low level of return loss are important.

To study the effect of bending of an optical fiber on its characteristics, a stand was assembled, the block diagram of which is shown in Figure 1.

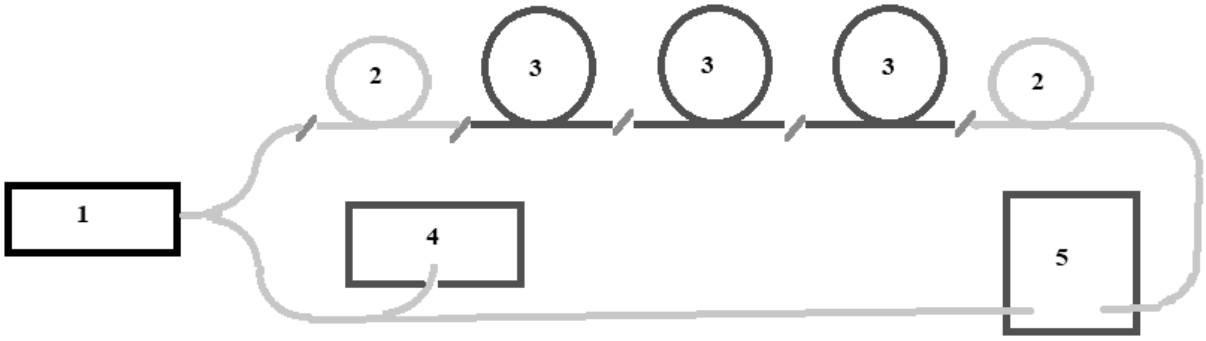

Figure 1. Block diagram of the measuring setup: 1 - optical source, 2 - measuring optical fiber, 3 - tested optical fibers, 4 - optical spectrum analyzer, 5 - optical power meter.

An experimental of the bending losses was carried out by the differential method [3]. For optical fibers of the G.652, G.655, and G.657, the spectral dependence of the bending losses was measured in a wide range of wavelengths: from 1270 to 1610 nm. CWDM SFP modules (Small Form-Factor Pluggable) were used as optical sources. The optical signal registration was carried out by the differential method with the spectral sensitivity photodetector correction [3]. Optical power measurements were carried out using a Rubin-300 stationary optical power meter. The source parameters were monitored using a Yokogawa AQ6370C optical spectrum analyzer. The measurement results are shown in Figure 2.

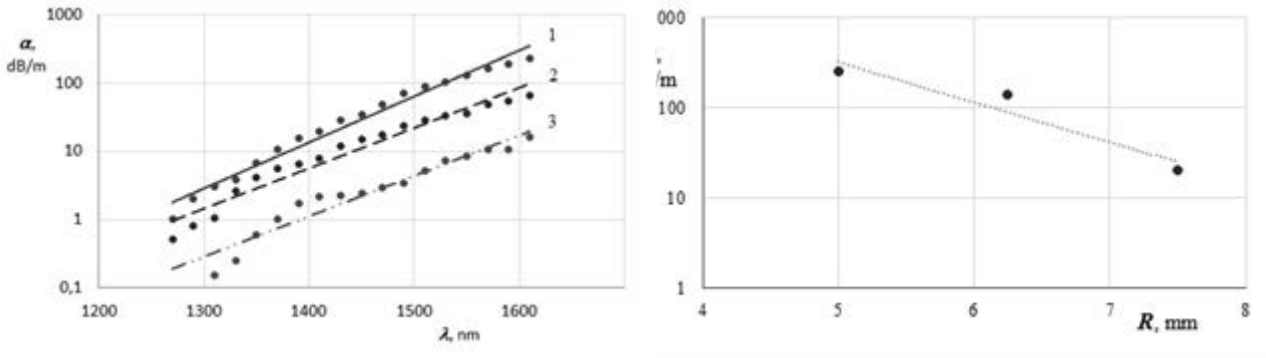

Figure 2(a, b). Bending loss α for optical fibers: 1 - G.655, 2 - G.652, 3 - G.657 with a bend radius R = 6.25 mm **(a)**, and $\alpha(R)$ for λ= 1550 nm **(b)**.

Conclusion

A study of a bending-type fiber-optic attenuator has been carried out. The effect of macrobending on the attenuation of the optical signal in the fiber has been studied experimentally. The values of bending losses for optical fibers of various standards are presented: G.652, G.655 and G.657. It is shown that the use of G.655 - optical fiber provides the largest dynamic range for a fixed optical fiber length in the device. Measurement of the spectral dependence of losses in the range of 1270… 1610 nm. It is shown that in the 1550 nm wavelength region the attenuator provides an attenuation of the transmitted signal by more than 100 dB/m, is easy to use.

References

[1] Fiber optic technology: current state and prospects Collection of articles, ed. Dmitrieva S A and Slepova N N 2010 p 608
[2] Zenevich A O 2019 No. 3, 2019. p 55-59
[3] Andreev D P, Andreeva E I, Sergeev A N, Sumkin V R 2020 ICAIT Proc. vol 1 p 57

Influence of low temperatures and thermal annealing on the optical properties of InGaPAs quantum dots

V V Andryushkin[1], A S Dragunova[2], S D Komarov[2,3], A M Nadtochiy[2], A G Gladyshev[1], A V Babichev[1], A V Uvarov[2], I I Novikov[1], E S Kolodeznyi[1], L Ya Karachinsky[1], N V Kryzhanovskaya[1], A Yu Egorov[4] and V E Bugrov[1]

[1]ITMO University, St. Petersburg 197101, Russia

[2]Alferov University, St. Petersburg 194021, Russia

[3]Saint Petersburg State Electrotechnical University "LETI", St. Petersburg 197376, Russia

[4]Connector Optics LLC, St. Petersburg 194292, Russia

Abstract. This paper describes optical properties of InGaPAs quantum dots formed by substituting phosphorus for arsenic in the InGaP layer deposited on GaAs directly during epitaxial growth. The influence of low temperatures and thermal annealing on the optical properties of InGaPAs quantum dots was studied.

1. Introduction

There is a great interest in the creation of single photon sources and arrays of micro-emitters based on them due to the development of modern quantum cryptographic communication systems. The most promising types of heterostructures for such applications are heterostructures with an active region based on quantum dots (QDs) placed in a microcavity. However, in contrast to typical laser applications where QD arrays must have a high surface density, the opposite requirement is imposed on QD arrays in the above applications — low QD density (less than $1 * 10^{10}$ cm^{-2}) [1]. It was shown earlier [2,3] that in heterostructures grown by molecular beam epitaxy, when arsenic is replaced by phosphorus in a thin layer of InGaP during growth, InGaPAs QDs are formed, with an estimated density of $1.3*10^{10}$ cm^{-2} (based on the analysis of transmission electron microscopy data). Such QDs emit in the spectral range of 952-978 nm at room temperature. The shift of the photoluminescence (PL) peak spectral position associated with traditional InGaAs QDs in this range is due to changes in the InGaP layer thickness, substrate temperature, and exposure time of the arsenic flow during the epitaxial growth [2,3].

2. Experiment

Additional studies of the (PL) efficiency in the temperature range 78-300 K were done. The samples were also studied by PL excitation spectroscopy at a temperature of 10 K. To study the effect of thermal annealing on the optical properties of heterostructures, the samples were rapidly annealed (2 min.) at temperature of 600°C.

3. Results

It was shown that PL spectra of all studied samples with InGaPAs QDs demonstrate the drop in the integral PL intensity (I) with an increase of temperature (T) and a long-wavelength shift in the position of the PL peak associated with InGaPAs QDs. The smallest drop in the integral PL intensity of QDs

with an increase in temperature (by a factor of 400) was obtained for the structure with the longest - wavelength (InGaP layer thickness = 2 nm, substrate temperature = 535°C, exposure time in the arsenic flow = 5 min.). At the same time, in the initial part of the curve I(T) (78-120 K), intensity changes slightly, and at temperatures above ~ 120 K, a monotonous drop of intensity is observed with increasing temperature. The dependence of the half-width at half-height (FWHM) of the PL was measured depending on temperature also has two characteristic sections associated with the temperature redistribution of charge carriers within the array of InGaPAs QDs with different localization depths. In the temperature range of 78-120 K, a decrease in FWHM is observed due to the escape of the carriers from weakly localized states in small QDs and their recapture to the deeper levels in large QDs. A further increase in temperature leads to the thermal escape of carriers into QDs with a lower localization potential or into the matrix material (GaAs). This process leads to a broadening of the PL line associated with InGaPAs QDs and decreasing of the PL intensity due to nonradiative recombination on structural defects in matrix. The temperature where the minimum value of FWHM is observed depends on the type of structure and the depth of localization of carriers in QDs.

Two absorption lines are observed on the photoluminescence excitation spectra. The spectral position of the maxima of the absorption lines does not depend on the detection wavelength. The first line ~ 818 nm corresponds to the absorption in GaAs, the second line with a maximum near 838 nm, can be associated with the absorption in the residual two-dimensional InGaPAs layer. These absorption lines coincide for the all studied samples.

Performed a rapid thermal annealing of the samples led to a slight blue shift in the position of the PL peak associated with InGaPAs QDs, an increase in the intensity of the PL peak associated with InGaPAs QDs (about 3 times), and a significant increase in the intensity of the PL associated with the luminescence of the GaAs matrix. In addition, for all structures after annealing, a decrease in FWHM was observed in the studied temperature range (78-300 K), which indicates the formation of a more homogeneous array of QDs.

Acknowledgments

The work was supported by the Ministry of Science and Higher Education of the Russian Federation (research project No. 2019-1442).

References

[1] Michler P 2009 *Single semiconductor quantum dots* vol 231 (Berlin: Springer)

[2] Andryushkin V V, Gladyshev A G, Babichev A V, Kolodeznyi E S, Novikov I I, Karachinsky L Ya, Nevedomskii V N and Egorov A Yu 2020 *J. Phys.: Conf. Ser.* **1697** 012106

[3] Gladyshev A G, Babichev A V, Andryushkin V V, Denisov D V, Nevedomskii V N, Kolodeznyi E S, Novikov I I, Karachinsky L Ya and Egorov A Yu 2020 *Tech. Phys.* **65** 2047–50

The origin of PL decay in QDs-rGO system

A A Babaev[1*], A V Fedorov[1], A V Baranov[1], A P Litvin[1]

1. Center of Information optical technology, ITMO University, St. Petersburg 197101, Russia

*Corresponding author, e-mail: a.a.babaev1@gmail.com

Abstract. The PL intensity quenching and PL lifetime reduction of fluorophore in the system where charge and energy transfer is possible generally explained by quenching due to these processes. Analysing the rGO/PbS QDs systems average PL lifetime to components ratio dependence we surprisingly found that it cannot be interpreted by these two processes only. We suppose the model based on the auger-recombination of the exactions in QDs on the excess holes left after the charge transfer process. As a solid validation of the supposed model, we provide the experiment with an additional hole utilization channel for QDs. We have also provided the simulation of the system average PL lifetime to components ratio dependence based on the supposed model and it perfectly fits the experimental data.

1. Introduction

Time-resolved spectroscopy is one of the most ubiquitous methods for analyzing various luminescent nanosystems [1]. One can determine the efficiency of the charge transfer or the energy transfer in numerous systems like sensors[2], solar cells[3], and so on. The quenching of PL intensity and PL lifetime usually indicates one of these processes but the appearance of another nonradiative exciton relaxation pathway can also quench PL intensity and shorter PL lifetime. In this paper, we have studied an rGO - PbS nanosystem and found one of charge and energy transfer independent quenching process, which together with interdot energy transfer totally dominate PL kinetics of the system.

2. Results

We have studied covalently bounded reduced graphene oxide rGO - PbS quantum dots (QDs) system in order to determine the factors that affect the charge transfer process and surprisingly found, that the systems average PL lifetime depends on the rGO to QDs ratio while measured in colloidal solution. Since the QDs is 0D material, rGO is 2D material, QDs is bounded to rGO with organic linker and rGO is the only quencher of the QDs in the solution, the observed dependence indicates the charge carrier transfer-independent quenching of the QDs PL. Analyzing other QD-rGO system-related papers we assume that the careful charge carrier balance in the system is required for the correct PL interpretation. Adding the external hole utilization channel into the rGO-QDs system colloidal solution we have observed a great increase in PL lifetimes and PL intensity, which is opposite to the behavior of the QDs in the same conditions. Knowing, that the excess holes are the source of the PL quenching, we suggest a model, in which the well-known from the QDs blinking theory excess hole induced nonradiative auger-recombination is the main source of the PL quenching.

The supposed model was applied for numerical simulation. The simulation details revealed that the nonradiative energy transfer between QDs is another key for the system PL lifetime to rGO/QDs ratio

dependence understanding. Due to energy transfer between QDs and excess charge induced PL redshift, even small amounts of quenched QDs can significantly reduce system average PL lifetime. Assuming model and energy transfer we obtain the simulated curve, that fits experimental data as one can see from Figure 1.

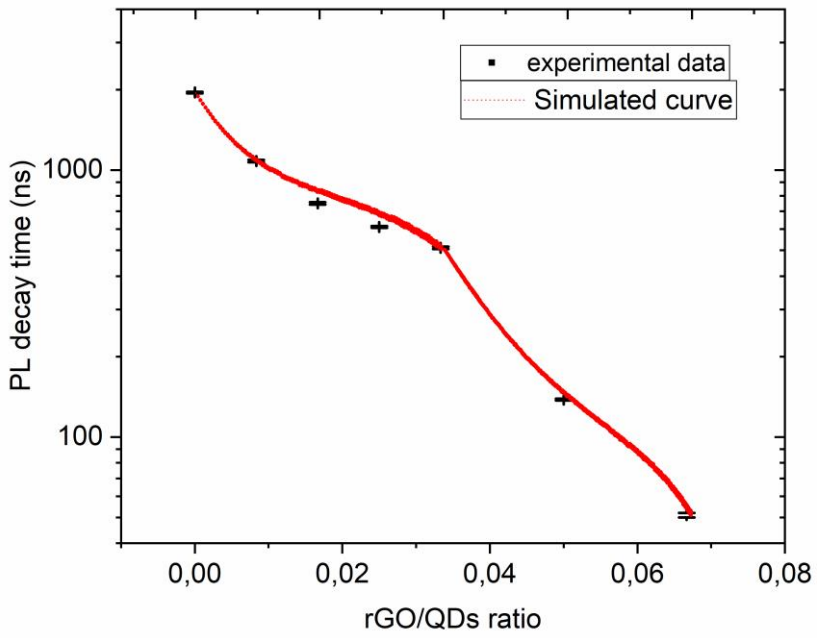

Figure 1. The simulated plot of average PL lifetime to rGO/QDs ratio with experimental points.

Acknowledgments

This work was supported by the Russian Science Foundation (19-13-00332).

References

[1] Millar D 1996 *Curr. Opin. Struct. Biol.* **6** 637–642.
[2] Szmacinski H and Lakowicz J 1995 *Sensors Actuators B. Chem.* **29** 16–24
[3] Yamada Y, Yamada T, Shimazaki A, Wakamiya, A, Kanemitsu Y 2016 *J. Phys. Chem. Lett.* **7** 1972–1977

Mn^{4+} concentration effect on spectral properties of lithium-germanate glass-ceramics

A N Babkina, M S Kovova, E V Kulpina, A S Pavlyuk, K S Zyryanova, A I Bukhvostov

Research Institute of Nano-Photonics and Optical Information Technology, ITMO University, Saint Petersburg 199034, Russia

e-mail: babkina.anastasya@bk.ru

Abstract. A series of lithium-germanate glasses with different manganese concentration is synthesized. Luminescent glass-ceramics are obtained from initial glasses by standard volume crystallization method. The glass-ceramics possess intense emission near 660-670 nm under UV/blue excitation. The glass-ceramics obtained can be used as sources of deep-red radiation.

1. Introduction

A narrow-band red emission has been major requirement in solid-state lighting technologies in terms of a white-light- emitting diode (w-LED) with an InGaN UV/blue LED chip [1]. Currently, there are two primary strategies to fabricate the w-LED. One is employing the blue LED with yellow- emitting phosphor $Y_3Al_5O_{12}$:Ce (YAG:Ce) and nitride red phosphor [2], the other is combining UV LED chips with tri-color (blue, green, and red) phosphors. Between these two methods, the red-emitting phosphor is the indispensable component to obtain the vivid and warm white light illumination.

There have been mainly reported two different ions, namely, Mn^{4+} and Eu^{2+}, doped as the red-emitting activator ions in various hosts [3]. The general performances of Mn^{4+} (Eu^{2+}) as an activator ion are peak emission at 600–650 nm, excitation peak edge of 450-500 nm, photoluminescence decay lifetime of a few milliseconds (a few microseconds or less), and quantum yield of 80–90%. With this regard and from an economic point of view, it seems that non-rare-earth Mn^{4+} is superior than Eu^{2+}.

Herein, we successfully synthesized novel lithium-germanate glass-ceramics doped with Mn^{4+} with red emission under UV/blue excitation and studied its properties under the influence of manganese concentration.

2. Material and methods

The initial glasses were synthesized with the following composition: $xMnO_2$-$10Li_2O$-(90-x) GeO_2 (where x=0.005; 0.05; 0.1; 0.25; 0.5; 1; 2). In brackets the concentrations are given in mol. %. The synthesis was carried out in air atmosphere at a temperature of 1250°C using corundum crucibles. For the synthesis of glass-ceramics based on germanate glass the samples were subjected to the heat treatment at 560°C in programmable muffle furnaces (Nabertherm).

The glass optical density spectra were measured by a Lambda 650 spectrophotometer (Perkin Elmer) in the spectral range of 200–900 nm with a step of 1 nm at room temperature. For the luminescence and excitation spectra recording, we used the LS-55 spectrofluorimeter (Perkin Elmer).

The luminescence spectra were corrected considering the spectral sensitivity of the spectrofluorimeter photodetector. For the excitation spectra, no correction was conducted.

3. Experimental results

The luminescence and excitation spectra of the obtained glass-ceramics are shown in Figure 1. A band with a maximum at 667 nm prevails in the luminescence spectra regardless of the excitation. The excitation spectrum possesses two bands at 336 and 460 nm.

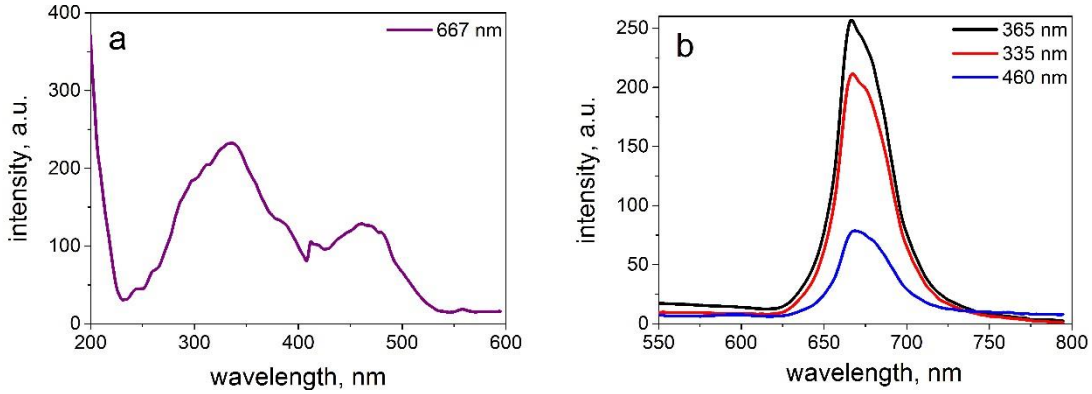

Figure 1. The excitation (a) and luminescence (b) spectra of the obtained glass-ceramics. Numbers above the graphs show the luminescence (a) and excitation (b) wavelengths.

It is known [1,3] that Mn^{2+} ions have a broad luminescence in the region of 500-750 nm with a maximum of about 620 nm. So, the specific location and shape of the luminescence band indicates that the manganese ions in this matrix have an oxidation state of 4+. Due to this, lithium-germanate glass-ceramics with manganese are a promising material for the development of deep red radiation sources.

Acknowledgments

Research was funded by Russian Science Foundation (Agreement #19-72-10036).

References

[1] Adachi S 2018 *J. Lumin.* **202** 263–81

[2] Li K, Zhu D and Van Deun R 2017 *Dye. Pigment.* **142** 69–76

[3] Chen D, Zhou Y and Zhong J 2016 *RSC Adv.* **6** 86285–96

Unambiguous state discrimination and joint measurement attacks on passive side channel of the light source in BB84 decoy-state protocol

D Babukhin[1,2,3], **D Sych**[2,3,4,5]
[1]QRate LLC, Moscow 121353, Russia
[2]National University of Science and Technology MISiS, 119049, Moscow, Russia
[3]Sirius University of Science and Technology, 1 Olympic Ave, 354340, Sochi, Russia
[4]Department of Physics, Moscow Pedagogical State University, 119992, Russia
[5]P.N.Lebedev Physical Institute, Russian Academy of Sciences, Moscow, 119991, Russia

Abstract. Quantum communication has a promise of unconditionally secure distribution of a secret key between two legitimate parties (Alice and Bob). This promise is based on the laws of quantum physics. However, the real-world implementation of quantum key distribution (QKD) in hardware has loopholes, which compromise their security. Here we investigate two attacks on the passive side channel of the light source along with the individual unitary attack on the BB84 decoy-state protocol. We calculate an upper bound for the secret key rate for these situations and demonstrate, that the joint measurement of the signal and the side-channels degrees of freedom is more effective to the adversary (Eve).

1. Introduction

The promise of quantum communication is an unconditionally secure distribution of the secret key between two parties due to the impossibility to perfectly clone a quantum state of the carrier photon (the "no-cloning theorem" of quantum theory). When QKD protocol is realized in the hardware, different loopholes and side channels arise, leading to additional information leakage to an eavesdropped. This leakage does not lead to an increase of communication errors on receiving side, making impossible to correct these errors during security amplification. As a consequence, the security of the theoretical QKD protocol is compromised. For example, a light source, may be composed of several lasers, which generate photons with slightly varying spatial, spectral, and temporal modes. These discrepancies allow the adversary to distinguish photons more effectively than just attacking the signal degree of freedom, which carries a secret bit.

In this work, we investigate two attacks, which the adversary can use to get additional information about the secret bit from the passive side channels of the light source. We give an estimate for this information by using the Hong-Ou-Mandel (HOM) interference [1] for an explicitly-implemented individual unitary attack on the BB84 protocol with decoy states. We calculate an upper bound for the secret key rate and demonstrate, that the joint measurement of the signal and the side-channels degree of freedom is more effective to the adversary.

2. Methods

We use an additional quantum state, augmented to phase-randomized weak coherent states of light in BB84 decoy-state protocol, as a model of the passive side channels. The distinguishability of quantum states is estimated from the HOM interference visibility. We calculate secret key rates under the unambiguous state discrimination (USD) and joint measurement attacks on the side channel along with the individual unitary attack on the BB84 protocol for different values of the HOM visibility.

3. Results and discussion

The calculated secret key rate for several values of HOM interference visibility (0.3,0.4,0.5) is shown in figure 1. We see, that the joint measurement of the signal degree of freedom after phase-covariant cloner attack and the side channel degree of freedom allows Eve to gain more information about the secret bit, than using the USD attack on the side channel alone and then proceeding with the attack on the signal degree of freedom if the USD attack fails. For HOM visibility values in the range from 0.4 to 0.5 (which correspond to the state-of-the-art values of contemporary light sources), we see only a slight decrease in the secret key generation rate. We conclude, that the presence of a physical mismatch between carrier photon properties of contemporary light sources does not compromise the security of the BB84 protocol with decoy states.

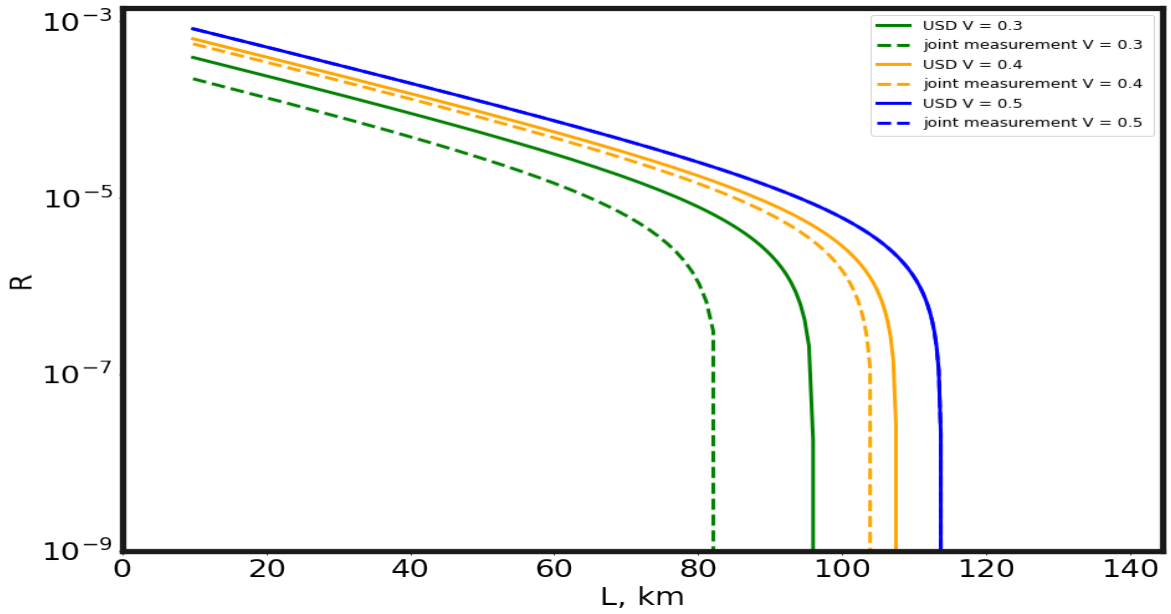

Figure 1. Secret key rate R as a function of fiber-optic communication distance L for different values of HOM interference visibility V, under the individual unitary attack on the BB84 decoy-state protocol for two attacks on the side channel degree of freedom (USD attack and joint measurement attack). We assume the standard single-mode optical fiber loss of 0.2 dB/km.

Acknowledgements

Denis Sych acknowledges support from Russian Foundation for Basic Research grant 20-32-51004, and Danila Babukhin acknowledges support from FASIE.

References

[1] Duplinskiy A and Sych D V Preprint arXiv:1908.04703 [quant-ph]

Encapsulation of Recrystallized Inorganic Perovskite Quantum Dots in Nonwoven Fluoropolymer Fibers

M Baeva[1], V Neplokh[1], D I Markina[2], A M Pavlov[3], D A Kirilenko[4], I S Mukhin[1], A P Pushkarev[2], S V Makarov[2] and A A Serdobintsev[3]

[1]Department of Physics, Alferov University, Khlopina 8/3, 194021 St. Petersburg, Russia;
[2]Department of Physics and Engineering, ITMO University, Lomonosova 9, 197101 St. Petersburg, Russia;
[3]Education and Research Institute of Nanostructures and Biosystems, Saratov State University, Astrakhanskaya 83, 410012 Saratov, Russia;
[4]Ioffe Institute, Politekhnicheskaya 29, 194021 St. Petersburg, Russia;

* Correspondence: baeva@spbau.ru

Abstract. Since emerging Metal Halide Perovskites were attracting elevated attention from scientific and industrial communities. Although, we still yet to see commercial products based on perovskite materials a significant body of work has been already done. Here we present our own method of Metal Halide Perovskites integration into possible industrial applications. Our way of Perovskite Quantum Dots encapsulation in polymer fibers provides exceptional water and ambient stability as well as optimal photoluminescence.

1. Introduction

The promising photoactive materials with a general stoichiometry of ABX3, where A = Cs, MA, FA; B = Pb, Sn; X = Cl, Br, I, - Metal Halide Perovskites (MHPs) - captivate the attention of the international industrial and scientific community due to their excellent optical and electrophysical properties. For instance, Inorganic Metal Halide Perovskite (IMHP) Quantum Dots (QDs), CsPbBr3 QDs in particular, were reported to possess not only the tunable with the QDs size photoluminescence (PL) spectra but also the 95% efficient PL quantum yield[1]. Therefore, a significant body of work has already been done to apply CsPbBr3 QDs in photovoltaic (solar cells) or/and optoelectronic devices (LEDs, LASERs, LASER beam detectors, etc.)[2-6] Nevertheless, to introduce any flexible device into the civil use market it is of crucial importance to encapsulate CsPbBr3 QDs to improve their stability and user safety (Pb toxicity concerns).

In this work, we present the synthesis of fluoropolymer nonwoven mats with CsPbBr3 QDs encapsulated in their fibers, where during the polymer fiber electrospinning, we observe the self-organized IMPH QDs recrystallization.

2. Results and Discussion

Recrystallized QDs (mean QD size 10,5 nm) in fibers demonstrate a slightly wider QDs size distribution as well as a PL signal red-shift when compared to the as-synthesized CSPbBr3 QDs (mean QD size 9,5 nm) in colloid solution. It was experimentally shown that the CsPbBr3 QDs nonwoven mats demonstrate a visible luminesce coming from the two-photon nonlinear absorption phenomenon, which is essential

for the IR LASER light detection. Additionally, we conducted water stability tests of our recrystallized QDs: IMHP QDs in nonwoven mats show only a 40% PL signal intensity drop after a 9-hour immersion test, whereas as-synthesized QDs in colloid solution dissolve immediately when placed into water.

Acknowledgments
This work was supported by State assignment of the Russian Ministry of Science and Higher Education № 0791-2020-0005.

References
[1] Sutherland, B.R.; Sargent, E.H. *Nat. Photonics* 2016, 10, 295
[2] Green, M.A.; Ho-Baillie, A.; Snaith, H.J. *Nat. Photonics,* 2014, 8, 506–514
[3] Lu, M.; Zhang, Y.; Wang, S.; Guo, J.; Yu, W.W. *Adv. Funct. Mater.* 2019, 29, 1902008
[4] Polushkin, A.S.; Tiguntseva, E.Y.; Pushkarev, A.P. *Nanophotonics* 2020, 9, 599–610
[5] Luo, W.; Yan, L.; Liu, R.; Zou, T. *Semicond. Sci. Technol*. 2019, 34, 074004.
[6] Soranyel, G.C.; Galian, R.E.; Pérez-Prieto, J. *J. Mater. Chem. A* 2015, 3, 39187–39193

Microwave transport in a single-photon detector based on an array of Josephson cells

M.V. Bastrakova*, D.S. Pashin

Lobachevsky State University of Nizhny Novgorod, Nizhny Novgorod 603022, Russia

*bastrakova@phys.unn.ru

Abstract. We consider the detection process of the array Josephson cells on the microwave transport of photons, propagating in an open one-dimensional waveguide. Within the framework of the formalism of a non-Hermitian Hamiltonian we obtained the expressions for the transmission and reflection coefficients for array Josephson cells.

1. Introduction

Quantum electrodynamics of superconducting circuits and quantum computing are among the rapidly and intensively developing areas of modern physics [1]. At the same time, one of the most important tasks is the development of systems for manipulating single-photon pulses of the microwave field with the states of qubits, as well as the development of methods for detecting single microwave photons for qubit tomography.

We have proposed a model of a sensitive sensor based on an array of N Josephson cells, each of which is a superconducting qubit connected to a Josephson bifurcation amplifier (JBA) [2]. In this case, the states of the qubits in the cells are controlled due to their capacitive coupling with a one-dimensional waveguide. We have analytically investigated the transport of a microwave signal in a waveguide with an array of Josephson cells. We also consider the effects of the reverse effect on the microwave transport by the amplifier.

2. Discussion of the results

In our work, we have calculated the expressions for the transmission and reflection coefficient, as well as the probability of qubit excitations are calculated based on the non-Hermitian Hamiltonian [3], taking into account the single-photon approximation. In this case, it is believed that the photon can be in the waveguide provided that that all qubits are in the ground state, either one of the qubits must be excited, and there is no photon in the waveguide. For two sensor cells, the amplitudes of the probability of excitation and transmission of the microwave field were found depending on their different coupling strength with the waveguide line (strong / weak mode).

It is shown that for a single qubit, the resonant frequency of the photon, at which the probability of excitation of the qubit or reflection of the photon is maximal, shifts with the increase in the level number of the initial state of the JBA. This effect is significant, since the qubit measurement occurs with a small dissipation of the amplifier [4]. To solve the problem of scattering on an array of bistable sensor cells, a method was proposed that takes into account multiple re-reflections of a photon from qubits.

3. Conclusion

Our calculations show that the Josephson sensor cell system can act as a highly sensitive single-photon sensor of microwave photons. At the same time, using the technique of non-destructive reading of the states of qubits by a bifurcation amplifier, it is possible to determine by the shift of the resonant frequency which qubit from the array emitted or absorbed a photon into the waveguide line.

Acknowledgments

The work was supported by the grant of the President's program no.MK-2740.2021.1.2.

References

[1] Gu X, Kockum A F, Miranowicz A, Yu-xi L and Nori F 2017 *Physics Reports* **718** 1
[2] Siddiqi I, Vijay R, Metcalfe M, *et.al*. 2006 *Phys.Rev. B* **73** 054510
[3] Greenberg Ya S and Shtygashev A A 2015 *Phys. Rev. A* **92** 063835
[4] Pashin D S and Bastrakova M V 2020 Int. J. Quantum Inf. **18** 1941014.

Exciton-polaritons in planar dielectric waveguides integrated with WSe_2 monolayer.

F. A. Benimetskiy[1], A. Mikhin[1], A. Yulin[1], V. Kravtsov[1], E. Khestanova[1], A. K. Samusev[1] and I. V. Iorsh[1]

[1]Department of Physics and Engineering, ITMO University, St. Petersburg, 197101, Russia

E-mail: fedor.benimetskiy@metalab.ifmo.ru

Abstract. We experimentally study strong light–matter coupling between waveguide photons and excitons in a photonic system based on slab dielectric waveguides with embedded 2D materials of transition metal dichalcogenides.

1. Introduction

Over the last decades, the field of photonics and optoelectronics has seen rapid progress. This was made possible by the huge progress in the development of miniature passive (waveguides, beam splitters, microcavities, etc) and active photonic devices (lasers). Step by step scientific community is getting closer to the realization devices on-chip for quantum and ultrafast classical optical information processing. Despite current progress in this area, the list of active basic elements in compact photonics is not complete. In this regard, there is a need to continue the development of on-chip active photonic devices, where light can be controlled by light of very weak intensity.

One of the solutions to achieve efficient photon-photon interactions at low intensities could be the strong photon-exciton coupling, resulting in the emergence of new quasiparticles, so-called exciton-polaritons. Along with the study of polaritonic systems where materials III – V are used as an active media, two-dimensional semiconductors attract the attention of the scientific community due to the fact that excitons in transition metal dichalcogenides (TMDs) are defined by large oscillator strength and binding energies, which makes them an excellent active medium for new polariton systems, including room temperature [1].

In this work we have demonstrated strong light–matter coupling between waveguide photons and excitons in a photonic system based on slab dielectric waveguides with embedded 2D materials of transition metal dichalcogenides as highly nonlinear optically active media.

2. Results and discussion

To realize a polaritonic system, we choose an unpatterned Ta_2O_5 waveguide on a SiO_2 sublayer. Light is coupled in/out through the grating couplers. After preliminary characterization of the waveguide transmission, the WSe_2 monolayer, which was fabricated by mechanical exfoliation from a commercial bulk crystal from HQ Graphene, was transferred onto the waveguide surface between grating couplers (Fig.1a).

In order to characterize the transmission of the fabricated hybrid structure, we used the setup for Fourier plane imaging combined with a closed-cycle helium cryostat. We used a halogen lamp as a

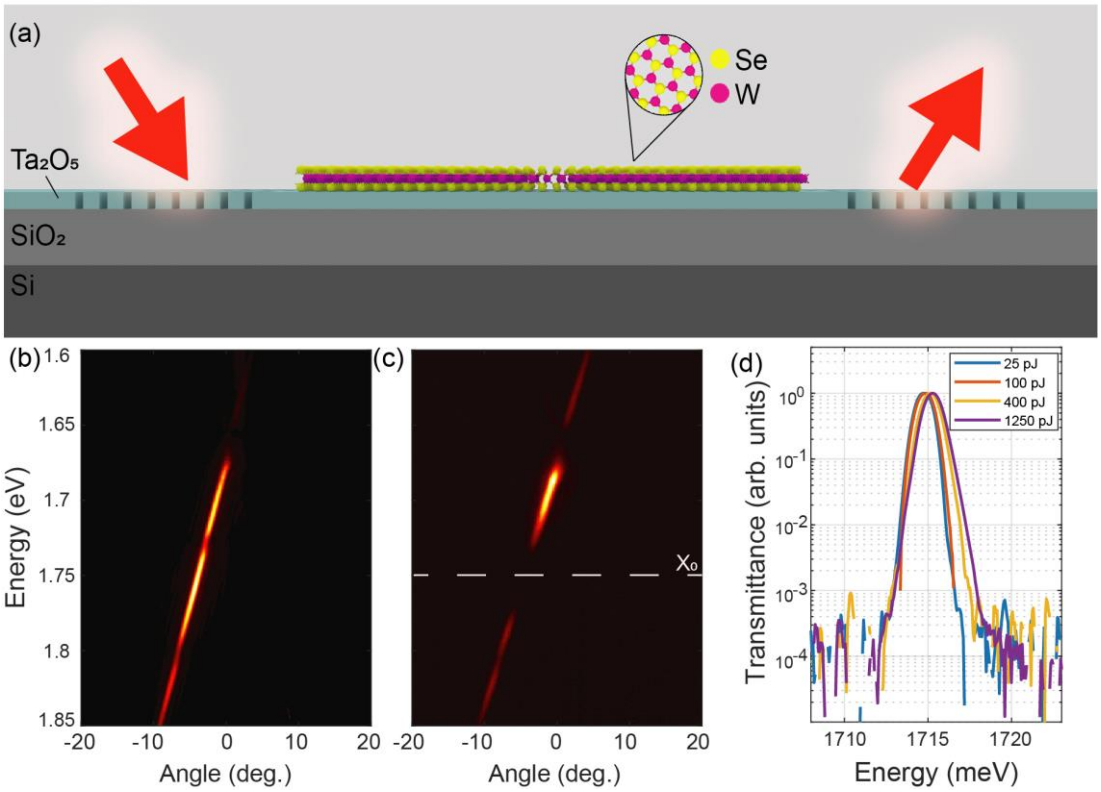

Figure 1. (a) Schematic diagram of waveguide integrated with WSe_2 monolayer. Angle- and wavelength-resolved transmittance maps (b) before and (c) after transfer of a monolayer. For the transmission measurements, a halogen lamp was used as a white light source. The exciton position highlighted by a white dashed line. (d) The evolution of the transmission spectra of the ps pulses with increasing pulse energy.

white light source for the transmission measurements. Figures 1b, c show the measured angle-resolved transmission map before and after a TMD monolayer transfer (the temperature is 7 K). We observed a dip in the transmission spectrum at the wavelength corresponding to the neutral exciton in the WSe_2 monolayer. We measured the evolution of the transmission spectra of the ps laser pulses (OPA Light Conversion Ltd + pulse shaper) with increasing pulse energy in order to verify the realization of the strong coupling of light and matter in the hybrid structure (Fig.1d). The detuning of the laser spectrum from the exciton resonance is approximately -36 meV, despite this, in the experiment, we observed a blue shift of the laser spectrum. Such behavior is typical for polariton systems and related to nonlinear exciton-exciton interaction [2].

Conclusions

To summarize, we have experimentally observed strong light–matter coupling between waveguide photons and excitons in a hybrid photonic system based on slab dielectric waveguides integrated with two-dimensional semiconductors.

Acknowledgments

The reported study was funded by RFBR, project number 19-32-9026.

References

[1] Schneider, Christian, et al. "Two-dimensional semiconductors in the regime of strong light-matter coupling." Nature communications 9.1 (2018): 1-9.

[2] Kravtsov, Vasily, et al. "Nonlinear polaritons in a monolayer semiconductor coupled to optical bound states in the continuum." Light: Science & Applications 9.1 (2020): 1-8.

SYNTHESIS AND STUDYING PROPERTIES OF THE GNPs@FexOy STRUCTURE

Bespalova P.G.[1,2], Vorobyev A.A.[2], Speshilova A.B.[1], Studzinsky V.M.[1], Karasev P.A.[1], Mishin M.V.[2]

[1] Peter the Great St. Petersburg Polytechnic University, St. Petersburg 195251, Russia
[2] Saint Petersburg Academic University, St. Petersburg 194021, Russia

polinlin0508@mail.ru

Abstract. An article presents a study of the regularities of the formation of gold up to 8 nm thick, deposited by vacuum thermal deposition on silicon wafers with a natural oxide, its annealing and subsequent deposition of iron oxide by chemical vapor deposition. The stages were accompanied by SEM analysis of the sample surface, as well as fixation of the optical spectra and I–V characteristics of the obtained structures.

1. Introductiom

Iron oxide is a widespread compound, interest in which is justified by the presence of various phases with significantly different properties. It is obtained in the form of particles and films by chemical vapor deposition, plasma-chemical methods, magnetron sputtering, etc [1]. The selected method allows to obtain a phase with desired properties. At the same time, the subsequent modification of such a material can lead to a significant change in certain properties. Therefore, the study of laws of formation and basic properties (optical and electrical) is quite urgent.

In turn, the patterns of gold formation are of great interest in connection with the manifestation of LSPR, and the combination of surface plasmon resonance and oxide matrices is relevant for a variety of sensors - gas sensors, IR reflectors, SERS, etc [2,3].

In work, gold of various thicknesses was deposited on n-Si silicon substrates by vacuum thermal sputtering. Then, by chemical deposition from the gas phase, iron oxide (Fe2o3) was applied (the process is described in more detail here [4] at a temperature of 250 °C. At the same time, gold was annealed with different thicknesses. The thickness of the gold was determined by the RBS method. Gold-oxide coatings were studied by scanning electron spectroscopy, spectrophotometry, IR spectroscopy. An I–V characteristics were also measured using two probe method.

2. Results

The thickness of the coatings was measured by Rutherford backscattering spectroscopy. The gold thicknesses were 1, 1.5, 2.5, 3, and 6 nm.

The study of the formation patterns showed that on the natural oxide, gold of a smaller thickness forms particles, and with an increase in the thickness of the structure forms "golden islands".

With the simultaneous folding of gold and the application of iron oxide on thin films, particles of two sizes were formed, the structures of the "golden islands" type were simply covered, while maintaining the topology as in simple annealing. The type of crystals is most characteristic of alpha-iron oxide.

The optical reflection spectra are presented for gold and gold with iron oxide in the range of 200-1600 nm. It can be seen that for both groups of spectra, the maximum reflection is in the region of 800 nm, while for samples without iron oxide, a maximum is observed in the region of 300 nm, which is typical for silicon. 6 nm gold with iron oxide also has a minimum reflection (10%) in the region of 500 nm.

IR spectra show a decrease in the transmission intensity of gold, while the 6 nm film almost completely absorbs IR radiation. Films of smaller thickness have peaks characteristic of silicon and its oxide and a lower transmission intensity.

The I-V measurements of the obtained samples was fixed at a longitudinal displacement. As the thickness of the initial gold film increased, an extreme value of the photoinduced current was observed. As the film thickness increases, the ohmic nature of the dependence begins to prevail on the barrier character. Presumably, this is due to the thickness of the final coating after the deposition of iron oxide, namely, the efficiency of light capture and separation of charge carriers.

Acknowledgments

The reported study was partially supported by Ministry of Science and Higher Education of the Russian Federation (research project FSRM-2020-0011). Metal contacts' fabrication and I−V-investigations was funded by RFBR, project number 20-38-90243. Research group thanks Ioffe Institute Ferroics Physics Laboratory for the provided equipment (Shimadzu UV-3600 Plus spectrophotometer).

References

[1] Vorobyev, A., Sedov, Y., Bespalova, P., Shakhmin, A., Kondrateva, A., Gabdullin, P., ... & Mishin, M. (2020). Controlled formation of iron oxide nanoparticles by pulse-modulated RF discharge at atmospheric pressure. Materials Today: Proceedings, 30, 417-421.

[2] Kondrateva, A., Enns, Y., Kazakin, A., Kleimanov, R., Morozov, I., Karaseov, P., & Mishin, M. (2020). Electrooptical Properties of TiO 2 Doped with Gold Nanoparticles. Semiconductors, 54(14), 1885-1888.

[3] Kondrateva, A., Enns, Y., Komarevtsev, I., Kudryashov, D., & Mishin, M. (2020, December). Au Nanoparticle Sub-Monolayers Buried between Magnetron Oxide Thin Layers. In Journal of Physics: Conference Series (Vol. 1695, No. 1, p. 012002). IOP Publishing.

[4] Bespalova, P., Enns, Y., Kunkel, T., Balanov, V., Speshilova, A., Vorobyev, A., ... & Karaseov, P. (2020). Gold Nanoparticle Array Formation by Low-Temperature Annealing. In International Youth Conference on Electronics, Telecommunications and Information Technologies (pp. 255-262). Springer, Cham.

Tunable laser induced periodic surface structures in Ge2Sb2Te5 thin films

Irina G. Bessonova[1], Pavel I. Trofimov[1], Petr I. Lazarenko[2], Demid A. Kirilenko[3], Nikolay A. Bert[3], Sergey A. Kozyukhin[4], Ivan S. Sinev[1]

[1]Department of Physics and Engineering, ITMO University, St. Petersburg, Russia
[2]National Research University of Electronic Technology, Zelenograd, Moscow, Russia, [3]Ioffe Institute, St. Petersburg, Russia, [4]Kurnakov Institute of General and Inorganic Chemistry of the Russian Academy of Sciences, Moscow, Russia

irina.bessonova@metalab.ifmo.ru

Abstract. Planar photonic structures, such as gratings and metasurfaces, are routinely used for beam steering, waveguide coupling, and light localization. However, conventional fabrication techniques that involve lithography are demanding in terms of time and cost. Much cheaper and simpler methods for surface patterning and formation of periodic surface structures are enabled by direct laser processing. Here, we demonstrate low-cost rapid fabrication of high-quality phase gratings based on the formation of laser induced periodic surface structures (LIPSS or ripples) in $Ge_2Sb_2Te_5$ (GST) thin films. Due to unique phase change properties of GST, the structures demonstrate strong modulation of refractive index with period controlled by the wavelength of laser irradiation. We study the formation of phase change LIPSS in a broad range of excitation wavelengths and observe transition between regimes with different orientations of generated ripples with respect to laser polarization.

1.Introduction

Chalcogenide phase change materials (PCM) is a unique family of optical materials that can maintain two different phase states at normal conditions – amorphous and crystalline – with large contrast of optical and electrical properties. PCM can be rapidly switched between these two states when exposed to optical, or electrical pulses of nanosecond duration [1]. On the other hand, an important effect that frequently accompanies the action of pulsed laser radiation on the surface of solid material is the formation of laser-induced periodic surface structures (LIPSS or ripples). This direct non-contact surface patterning method is already a viable alternative to lithography and can be used for various applications [2]. The mechanism of the formation of LIPSS is still under discussion and depends on the material of the exposed substrate and the regimes of laser irradiation [3]. Generally, two types of laser-induced periodic surface structures can be observed: high (HSFL) and low (LSFL) spatial frequency LIPSS. In both cases these surface structures reproduce the interference pattern of the incident and scattered light which is imprinted in the sample material through absorption usually followed by ablation of the overheated material.

However, this is not the case for the LIPSS formed in the PCM thin films there the absorption leads to a phase transition accompanied with a change in density and a significant change in the optical properties, in particular, the refractive index. Thus, LIPSS formation in PCM films leads to appearance

of both periodic surface relief (due to the material volume change during phase transition) and spatial modulation of the optical properties [4]. Moreover, in line with the majority of phase transitions in PCM, this process is potentially reversible, allowing formation of rewritable gratings with variable period and direction depending on the laser irradiation regimes.

In this work we study the fabrication of LIPSS-based GST phase change gratings using fs-laser pulses. We scale the gratings using line-by-line scanning of the laser beam over the PCM film surface and study different regimes of grating formation with varying period and direction with respect to laser polarization.

2.Results and discussion

To create 2D phase gratings in 100 nm thick GST films on sapphire substrates we focus a laser beam with tunable wavelength (Light Conversion Pharos + Orpheus optical parametric amplifier, 1MHz repetition rate, 300 fs pulse duration) at the film surface from the substrate side. We then scan the beam waist across the film surface using a piezoscanner to irradiate 50x50 um^2 areas (Figure 1a). Making use of the wide tuning range of the laser system, we studied the spectral dependence of LIPSS period and direction of periodic pattern in a wide spectral range from 600 to 2000 nm. To determine the period of the formed LIPSS-based gratings we perform atomic force microscope (AFM) scanning of the laser-imprinted area. Examples of the obtained AFM images are shown in Figure 1 c, d. The crystallized regions of the film are suppressed below the surface of the initial amorphous film by several nanometers due to a decrease in material volume during the crystallization.

The dependence of LIPSS period on the laser wavelength for 100 nm GST film extracted from the AFM data is shown in figure 1b. For the wavelengths from 1200 to 2000 nm, periodic surface structures are formed parallel to laser polarization, which can be attributed to the “dielectric” type of LIPSS formation [5]. In contrast, for the wavelengths lower than 800 nm the regime of the LIPSS formation is changed. In this wavelength region for GST film of 50 nm the LIPSS perpendicular to the polarization of the laser beam are formed, which in turn can be attributed to the “metallic” regime [6].

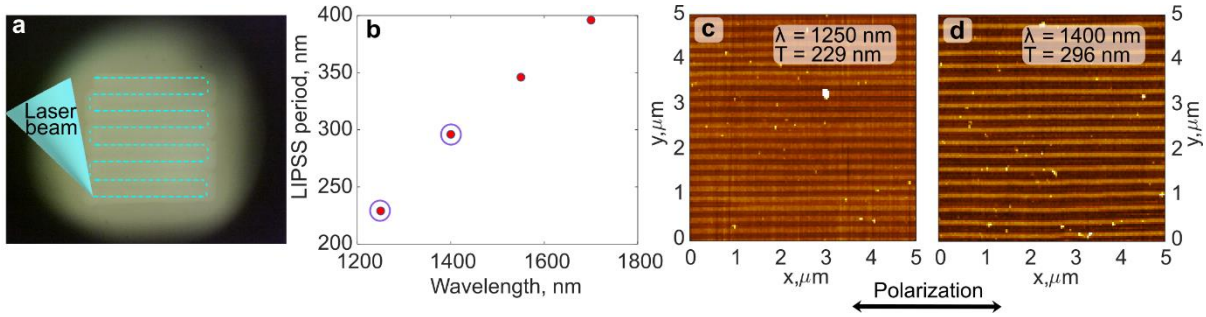

Figure 1. (a) Scheme of phase grating fabrication in GST thin film using femtosecond laser writing. (b) Dependence of the LIPSS period on the wavelength for 100 nm GST film on sapphire. (c, d) AFM images of the obtained gratings in 100 nm GST film at different wavelengths. Data denoted with blue circles in (b) are extracted from AFM images (c, d).

In conclusion, we showed the formation of laser-induced phase change gratings in thin $Ge_2Sb_2Te_5$ films on sapphire. We demonstrate the possibility of producing high-quality phase change gratings flexible in terms of period and direction with respect to laser polarization, are fast and easy to fabricate and are potentially re-writable. These qualities make them strong candidates for realization of rewritable on-chip couplers and beam steering devices.

Acknowledgments

The reported study was funded by RFBR according to the research project № 20-32-90220

References

[1] Wuttig M, Bhaskaran H and Taubner T Phase-change materials for non-volatile photonic applications. *Nature Photonics* 2017, **11**, 465-476.

[2] Fuentes-Edfuf Y, Garcia-Lechuga M, Puerto D, Florian C, Garcia-Leis A, Sanchez-Cortes S, Solis J, Siegel J Coherent scatter-controlled phase-change grating structures in silicon using femtosecond laser pulses. *Scientific Reports* 2017, **7**.

[3] Bonse J, Graf S Maxwell Meets Marangoni — A Review of Theories on Laser-Induced Periodic Surface Structures. *Laser & Photonics Reviews* 2020, 2000215.

[4] Kozyukhin S, Smayev M, Sigaev V, Vorobyov Y, Zaytseva Y, Sherchenkov A, Lazarenko P Specific Features of Formation of Laser-Induced Periodic Surface Structures on Ge2Sb2Te5 Amorphous Thin Films under Illumination by Femtosecond Laser Pulses. *Phys. Status Solidi (B) Basic Research* 2020, 257, 1900617.

[5] Bonse J, Hohm S, Kirner S V, Rosenfeld A, Kruger J Laser-induced periodic surface structures — A scientific evergreen. *IEEE Journal of selected topics in quantum electronics* 2016, 23.

[6] Fuentes-Edfuf Y, S´anchez-Gil J A, Florian C, Giannini V, Solis J, Siegel J Surface Plasmon Polaritons on Rough Metal Surfaces: Role in the Formation of Laser-Induced Periodic Surface Structures. *ACS Omega* 2019, 4, 6939–6946.

Identification of pigments of Russian icons by means of X-ray fluorescence spectroscopy

A V Vasilieva [1,2], **V A Parfenov** [1] and **N S Sosnova** [1]

[1] Photonics Department, Saint Petersburg Electrotechnical University "LETI", 5 Professora Popova str., 197376 St. Petersburg, Russian Federation
[2] Corresponding e-mail: anastasiastru@mail.ru

Abstract. In this work the analysis of paint layers of Russian icons of the 16th-19th centuries and painting of the 19th century from a private collection was carried out by means of X-ray fluorescence spectroscopy. The data obtained on the elemental composition of pigments made it possible to identify them. The results of the research will be used to create a database of XRF-spectra of pigments, which were used by Russian icon painters of certain schools and time periods. XRF-data from the paint layer of a private painting in conjunction with computer analysis of its images allowed to conclude that this painting is forgery.

1. Introduction

This work is devoted to use of the method of X-ray fluorescence analysis (XRF) in the field of conservation and restoration. Before starting the restoration process of an art object, it is necessary to conduct studies, which mainly rely on experience of restorers and art historians, according to the current practice in Russia, where instrumental methods of artwork analysis started to be used in recent years only. Meanwhile, non-destructive optoelectronic diagnostic methods are actively developed and widely used in museum work all over the world, due to the fact that they are non-invasive and do not require sampling [1]. Currently, one of the most frequently used methods for studying Cultural Heritage objects is the XRF method. It is based on the detection of X-ray fluorescence emission from inorganic substance atoms, which occurs when X-ray radiation interacts with a substance. As a result, obtained XRF-spectra give information about the elemental composition of analyzed substances. XRF analysis of artworks provides information about the time of its origin, modifications that could occur to it, and about the authenticity of objects [2–4].

2. Investigation of the paint layer from Russian icons

In the experiments, NitonXL3tGold+ spectrometer (Thermo Fisher Scientific, USA) was used. Icons for investigation were provided by the Department of Easel Painting Restoration of the St.Petersburg State Academic Institute of Painting, Sculpture and Architecture named after I.E. Repin. Figure 1 shows XRF-spectrum registered at the analysis the icon "Five-figure half-length Deisus" (Vologda State Historical-Architectural and Art Museum-Reserve, 18th century). The measurements were carried out according to a set of reference points, which correspond to the main colors of paints and were chosen by the restorers.

Our studies allowed to identify most typical red and green pigments, which were used in Russian icons created by artists of Russian cities Pskov and Novgorod. Obtained XRF-spectra will be used for

systematization of information about specific pigments of different time periods and icon painting schools. It allows creating a database of XRF-spectra of Russian icons of that period, which will become an important information resource for restorers and art historians.

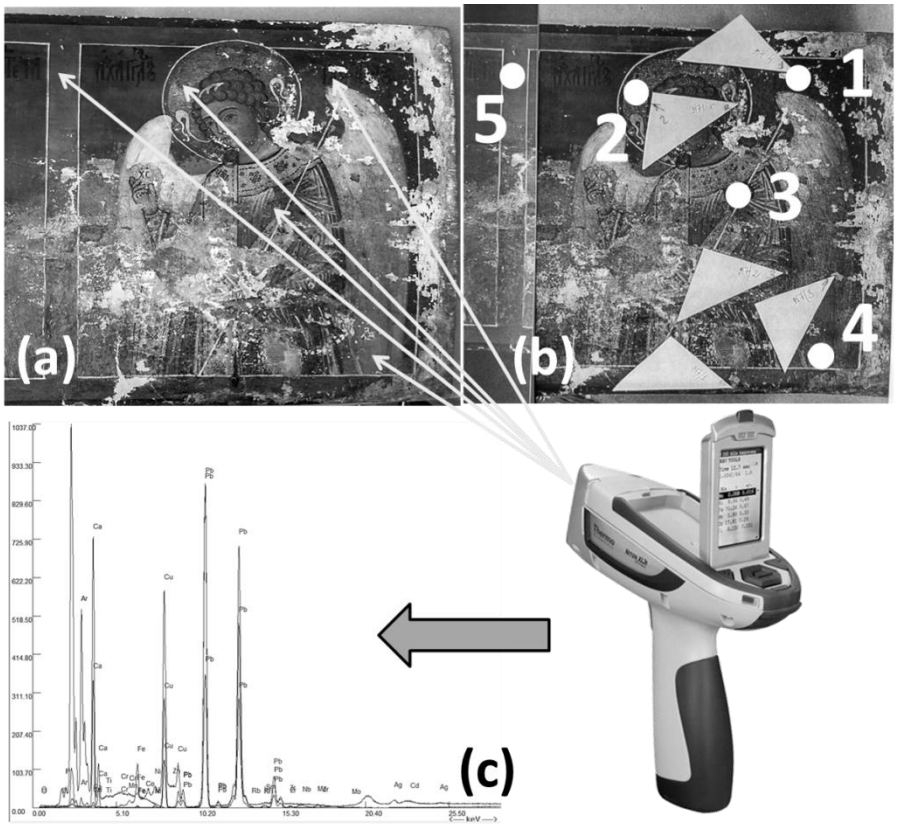

Figure 1. Measurement of XRF-spectra: general view of the icon (a), the same photo with set of reference points (b), example of XRF-spectrum (c).

It should be noted that in the experiments it was revealed that some groups of pigments could not be identified with XRF analysis, for example, pigments imitating gilding, or ocher. These pigments require additional study by means of alternative diagnostic methods to identify impurities in them, including organic ones, which may provide more complete information about their origin and properties.

3. Investigation of a 19th century painting from a private collection

Using a complex technique based on XRF and computer analysis of digital optical images, a painting from a private collection which was supposedly created by Russian artist Alexei Bogolyubov (1824 - 1896) was examined. As a result, it turned out that the painting does not belong to the hand of the artist in question, and, therefore, is a forgery.

References

[1] Janssens K et.al. 2016 *Top Curr Chem (Z)* 374:81
[2] Gao N and Janssens K 2004 *XRay Spectrometry: Recent Technological Advances* (Chichester: Wiley & Sons)
[3] Moran Th, Kaye A, Rao A and Bueno F 2016 *Journal of Forensic Radiology and Imaging* **5** 38–46
[4] Revenko A and Revenko V 2007 *Methods and Objects of chemical analysis* **2 Issue 1** 4–29

Performance of microheaters for tunable on-chip interferometer

I O Venediktov[1], M S Elezov[1,2,3], A I Prokhodtsov[1,4,5], V V Kovalyuk[1,5] , P P An[1,5], A D Golikov[1], M L Shcherbatenko[1,2,3], D V Sych[1,2,3,6], G N Goltsman[1,4]
[1]Department of Physics, Moscow State Pedagogical University, 119992, Russia
[2]National University of Science and Technology MISiS, Moscow, 119049, Russia
[3]Sirius University of Science and Technology, 1 Olympic Ave, 354340, Sochi, Russia
[4]National Research University Higher School of Economics, Moscow, 101000, Russia
[5]Institute of Applied Physics of the Russian Academy of Sciences, Nizhny Novgorod, 603950, Russia
[6]P.N.Lebedev Physical Institute, Russian Academy of Sciences, Moscow, 119991, Russia

e-mail: ilia1999ven@gmail.com

Abstract. In this work we study microheaters of tunable on-chip interferometer on silicon nitride (Si_3N_4) platform for telecomm wavelength (1550 nm) consisting of several Mach-Zehnder interferometers (MZIs). MZI are needed for experimental realization of displacement-based quantum receivers that can discriminate weak coherent states of light with low error rate. Microheaters on one of the arms of MZI provide the change of the refractive index of the material with temperature due to thermo-optical effect, which gives phase shift. We demonstrate frequency response curve and bandwidth of microheaters.

1. Introduction

Photonic integrated circuits have many advantages over fiber and free space realizations because of small footprint of device itself, less susceptibility to heat and phase fluctuations and higher stability. Microheaters are one of elements which are used in the integrated optics to phase shift of light. Microheaters operate by the thermo-optical effect, i.e. the refractive index of waveguides material is changing due to temperature changes. Those microheaters can be used as phase modulators for experimental realization of displacement-based [1] receivers that can discriminate weak coherent states of light [2]. Such a receivers were already demonstrated in optical fiber [3]. Microheaters have specific cooling and heating time, therefore it's important to measure their bandwidth to operate it.

2. Device and experimental results

The tunable on-chip interferometer on silicon nitride consisting of 3 Mach-Zehnder interferometers (MZI) shown in figure 1(a). As waveguide material, we used Si_3N_4 due to its low absorption in infrared (IR) and good mechanical properties [4]. 5 golden microheaters are used to operate interferometer, 4 of them used as phase modulators (PM) and one of them (PM4) used to operate a beam splitter to split optical power between two output ports (output 2 and 3). To measure the bandwidth we apply to microheaters sinusoidal voltage using lock-in amplifier and measure optical power on output port 1. Optical power was measured by semiconducting detector, which output voltage was measured by lock-in amplifier. Frequency response curve (fig. 2b) was obtained and fitted.

By the fitting parameters it was observed that bandwidth of microheaters is 30 kHz.

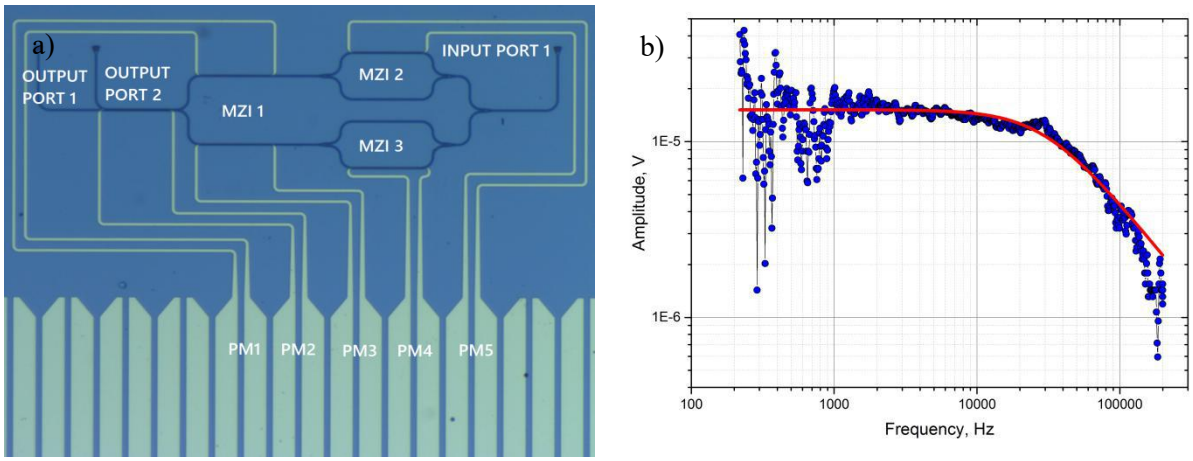

Figure 1. (a) optical micrograph of interferometer, (b) Frequency response curve

3. Conclusion

The output frequency response curve was obtained and fitted. After fitting bandwidth value 30kHz was obtained. These results have potential for using this tunable on-chip interferometer as a part of quantum receiver of weak coherent signals.

Acknowledgments

Denis Sych, Mikhail Elezov and Mikhail Scherbatenko acknowledge Russian Foundation for Basic Research grant 20-32-51004. Iliia Venediktov acknowledges FASIE.

References

[1] Denis Sych and Gerd Leuchs 2016 *Phys. Rev. Lett.* **117**, 200501

[2] Shcherbatenko M L, Elezov M S, Goltsman G N and Sych D V 2020 *Physical Review* A **101** (3), 032306

[3] Elezov M S, Scherbatenko M L, Sych D V and Goltsman G N 2019 *EPJ Web of Conferences* **220**, 03011

[4] Ramelow S, Farsi A, Clemmen S, Orquiza D, Luke K, Lipson M, and Gaeta A L 2015 ArXiv:1508.04358v1

Photoionization of polarized xenon atoms

E.A.Viktorov[1], A.A.Pastor[1], P.Yu.Serdobintsev[1], N.N.Bezuglov[1]
[1] Department of Optics, Faculty of Physics, St. Petersburg State University, 198504, Russia
*e-mail: eaviktorov@yandex.com

Abstract. We studied the ionization of a coherently two-photon excited superposition of 4f states of Xe atom by probe femtosecond pulse laser in a supersonic beam. The revealed oscillational structure in the photoionization signals is associated with the coherent superposition of two these states. Our results demonstrate the high efficiency of proposed scheme for registering quantum beats. Our scheme is based not on the analysis of results of fluorescence oscillations, but on the observation of oscillations in the photoelectron current.

1. Introduction

Analyzing of fluorescence signals after exciting atomic states by polarized light is an important brunch of modern spectroscopy. Observation of magnetic resonances in polarized gas media is the basis of construction and realization of sensitive magnetometers. Diverse types of oscillating structures in detected signals in the presence magnetic fields allow making precision measures of atomic state parameters beyond limitations due to Doppler broadening. Traditional methods of spectroscopy are associated mainly with bound-bound optical transitions [1]. In the present report, we demonstrate, a possibility to examine photocurrent oscillations which occurs due to the interference between excited atomic states.

2. Experiment

In this work, the supersonic beam of Xe atoms crosses a focused laser beam in the presence of a magnetic field, it is necessary to draw the electrons from the ionization region (Fig.1). We use a "pump-probe" experiment with two-photon excitation of Xe atoms to nearby states $5p^5(^2P_{3/2})4f[^3/_2]_2$ and $5p^5(^2P_{3/2})4f[^5/_2]_2$ using a "pump" pulse. Excitation is performed by a horizontally polarized femtosecond laser pulse at a wavelength of about 220nm. Photoionization of the excited atoms in the J=2 states is performed by a “probe” pulse of a horizontally polarized Ti: sapphire femtosecond laser at a wavelength of 795nm, the spectral width of the ionization pulse is greater than the distance between these 4f levels.

An electron spectrometer of the “magnetic bottle” type was used to record the electron energy spectra. Analysis of the energy spectra of electrons, obtained in different delay times of the probe pulse relative to the pump pulse, made it possible to obtain data on quantum beats. The energy spectra provide information on the levels from which ionization took place and on the intensity of ionization from these levels.

The Ti-Sapphire femtosecond laser PULSAR 10 (Amplitude Technologies, France) has the following characteristics: main wavelength - 790nm, pulse energy - 5mJ, pulse duration - 50fs, repetition rate - 10Hz. The outcoming pulse was divided into two parts: (i) 70% of the pulse power pumped parametric amplifier TOPAS and was converted to UV radiation for twophoton excitation of atomic

states. (ii) The rest 30% of the power was used as probe radiation in the form of the first harmonic for ionization of pump-excited atoms.

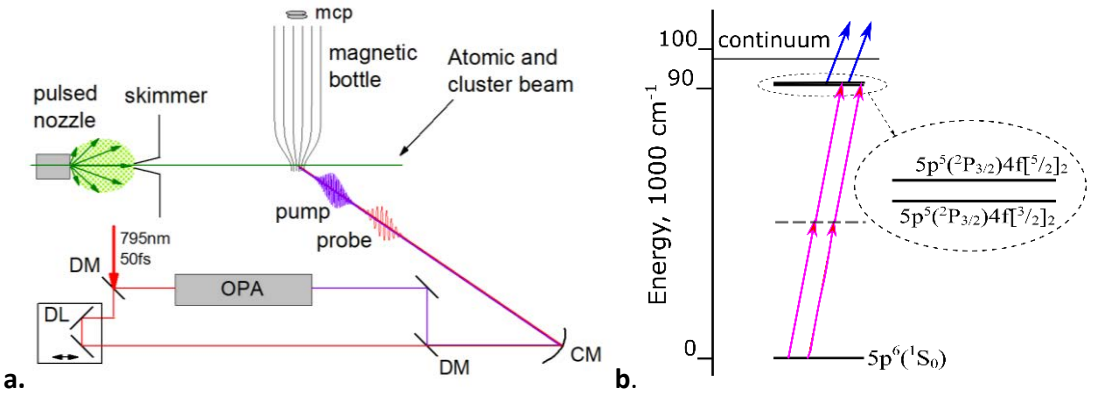

Figure 1. a. Experimental setup: OPA – optical parametric amplifier; DL – delay line; DM – dichroic mirrors; CM – concave mirror. **b.** Researched Xe levels

An optical system was used to control the delay time between pulses. The delay time between laser pulses was varied from 0 to 24ps. With a change in the delay time t, periodic oscillations of the intensity of the photoelectron current appear at the difference frequency of the levels $\Delta\omega$ (Fig. 2). Which equal to the frequency distance between levels $\Delta\omega=\omega_{5/2}-\omega_{3/2}$. From the experimental data shown in Figure 2, we have a beat period of 0.549ps. This is in good agreement with the energy gap between these xenon levels (Xcm-1), which corresponds to a beat period of 0.55ps.

3. Conclusion

Two excited nearby levels $5p^5(^2P_{3/2})4f[^3/_2]_2$ and $5p^5(^2P_{3/2})4f[^5/_2]_2$ differ in the quantum number K. For them, $K=J_1=3/2$ and $K=J_1+l=5/2$, respectively, where J_1 is the principal quantum number of the core, l is the orbital angular momentum of the 4f electron. In this case, the value of the principal quantum number $J=2$ $(J=K\pm{}^1/_2)$ is the same for both nearby levels. The matrix elements of the density matrix for coherent superposition of these levels oscillate at the difference frequency $\Delta\omega=\omega_{5/2}-\omega_{3/2}$ [2]. The photoionization cross section is expressed in terms of these matrix elements.

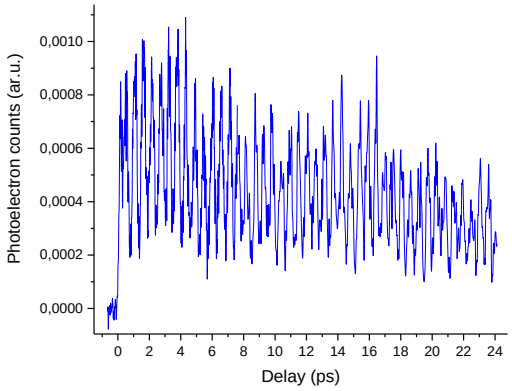

Figure 2. Temporal dependence of the photocurrent I.

We observed the effect of quantum beats, i.e. interference of coherent quantum states, in the form of oscillations in the integral photocurrent.

References

[1] M. Auzinsh, D. Budker, and S. Rochester, Optically Polarized Atoms. Understanding light-atom interactions (Oxford University press, 2010).
[2] E.B. Alexandrov, M.P. Chaika, G.I. Khvostenko, Interference of Atomic States. Springer Series on Atoms and Plasmas, vol. 7 (Springer, Berlin, 1993)

Polarized spectroscopy of electric and magnetic dipole transitions of Europium (III) ions in C_2 sites

A Volokitina[1,2,*], P Loiko[3], E Dunina[4], A Kornienko[4], J M Serres[2], M Aguiló[2], F Díaz[2], A Pavlyuk[5], and X Mateos[2]

[1]ITMO University, 49 Kronverkskiy Pr., 197101 St. Petersburg, Russia
[2]Universitat Rovira i Virgili, Física i Cristal·lografia de Materials i Nanomaterials (FiCMA-FiCNA)-EMaS, Marcel.li Domingo 1, 43007 Tarragona, Spain
[3]Centre de Recherche sur les Ions, les Matériaux et la Photonique (CIMAP), UMR 6252 CEA-CNRS-ENSICAEN, Université de Caen Normandie, 6 Boulevard du Maréchal Juin, 14050 Caen Cedex 4, France
[4]Vitebsk State Technological University, 72 Moskovskiy Pr., 210035 Vitebsk, Belarus
[5]A.V. Nikolaev Institute of Inorganic Chemistry, Siberian Branch of Russian Academy of Sciences, 3 Lavrentyev Ave., 630090 Novosibirsk, Russia

*e-mail: anna.itmo@gmail.com

Abstract. Polarization anisotropy of luminescent properties of europium (III) ions in low-symmetry C_2 sites is studied using monoclinic (sp. gr. *C*2/*c*) tungstate crystal $KY(WO_4)_2$. The $^5D_0 \rightarrow {}^7F_6$ (where J = 0...6) transitions are characterized for the principal light polarizations. Polarization selection rules for the magnetic dipole $^5D_0 \rightarrow {}^7F_1$ transition are presented. The crystal-field splitting for Eu^{3+} ions is also determined.

1. Introduction

Trivalent europium ions (Eu^{3+}) having an electronic configuration of $[Xe]4f^6$ are well-known for their emissions in the visible owing to the $^5D_0 \rightarrow {}^7F_J$ (J = 0...6) transitions. Among them, the electric dipole (ED) transition to the $^7F_2$ state falling in the red (~610 nm) typically dominates in the spectrum. This determines the applications of Eu^{3+}-doped materials as red phosphors with high colour purity [1]. This ED transition is a hypersensitive one: its intensity depends significantly on the site symmetry and its distortion. The adjacent transition to the $^7F_1$ state is of purely magnetic dipole (MD) nature and it is weakly dependent on the host matrix. Because of this, Eu^{3+} ions are also used as structural probes.

Recently, low-symmetry tungstate and molybdate crystals doped with Eu^{3+} ions located in C_2 sites attracted a lot of attention for solid-state lighting and laser applications [2]. In the present work, we have studied the polarization anisotropy of ED and MD transition of Eu^{3+} ions in C_2 sites.

2. Results and discussion

As a host matrix, we have used monoclinic (sp. gr. *C*2/*c*) double tungstate crystal, $KY(WO_4)_2$, doped with Eu^{3+} ions (2 at.%). The dopant cations (Eu^{3+}) replace for the host-forming ones (Y^{3+}) in a single type of sites (C_2 symmetry) with an VIII-fold coordination by O^{2-}. $KY(WO_4)_2$ is optically biaxial and its principal optical directions (optical indicatrix axes) are denoted as (N_p, N_m and N_g).

An overview luminescence spectrum of Eu^{3+} ions in this crystal (for unpolarised light) is shown in Fig. 1(a). The emissions are due to the transitions from the metastable state ($^5D_0$) to the lower-lying

states ^7F_J (J = 0...6), $^7F_0$ is the ground-state. The luminescence lifetime of the $^5D_0$ state is 430 μs. The dominant $^5D_0 \rightarrow {}^7F_2$ transition determines the red emission colour of high purity (p > 98%). At first, we focused on the ED transitions terminating at the $^7F_2$ and $^7F_4$ levels. The luminescence spectra were measured for the principal light polarizations and the stimulated-emission cross-sections σ_{SE} were calculated, Fig. 1(b,c). Note the difference of the spectra for light polarized along the C_2 symmetry axis (|| N_p) and orthogonal to it (|| N_m, N_g), and strong polarization anisotropy of emission properties.

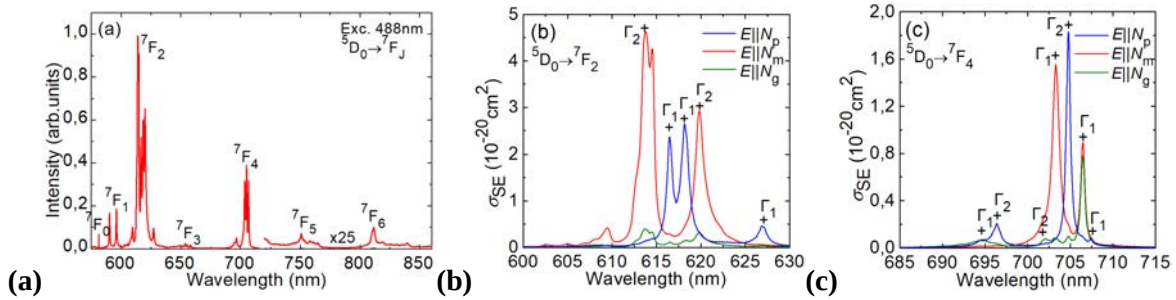

Figure 1. Luminescence of Eu^{3+} ion in C_2 sites in the monoclinic $KY(WO_4)_2$ crystal: **(a)** unpolarized spectrum showing $^5D_0 \rightarrow {}^7F_J$ (J = 0...6) emission bands, λ_{exc} = 488 nm; **(b,c)** polarized stimulated-emission cross-section spectra for electric-dipole (ED) transitions (**b**) $^5D_0 \rightarrow {}^7F_2$ and (**c**) $^5D_0 \rightarrow {}^7F_4$.

For the MD $^5D_0 \rightarrow {}^7F_1$ transition, the number of emission peaks and their relative intensity depend both on the light polarization and the propagation direction, see Fig. 2(a) where the Porto's notations from the Raman spectroscopy are used. The MD transition is caused by an interaction of the active ion with the magnetic field component of the light through the magnetic dipole ***M***. Thus, the orientation of the magnetic field vector ***H*** with respect to ***M*** is relevant. Polarization selection rules for the $^5D_0 \rightarrow {}^7F_1$ transition of Eu^{3+} ions in C_2 sites are presented explaining well the observed emission behavior.

The crystal-field splitting for Eu^{3+} ions in $KY(WO_4)_2$ was also determined, cf. Fig. 2(b).

The obtained information is important for the development of complex tungstate and molybdate red phosphors and laser materials.

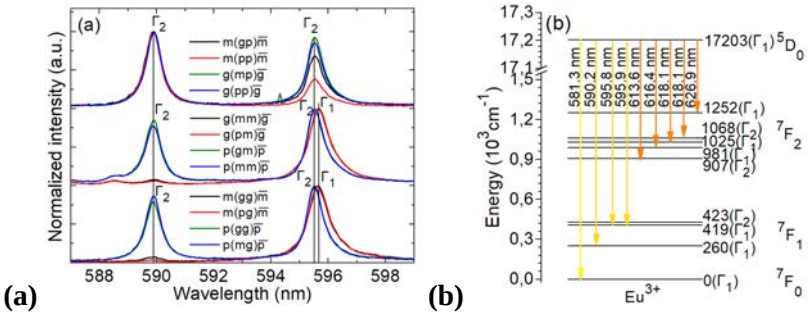

Figure 2. (a) Anisotropy of emission corresponding to the magnetic dipole (MD) transition $^5D_0 \rightarrow {}^7F_1$ of Eu^{3+} ions in C_2 sites in the monoclinic $KY(WO_4)_2$ crystal, Porto's notations are used; **(b)** Crystal-field splitting of the $^5D_0$ and $^7F_{0\text{-}2}$ Eu^{3+} multiplets, *arrows* indicate the transitions in emission.

Acknowledgments

The reported study was funded by RFBR, project number 19-32-90199.

References

[1] Huang X, Guo H, Li B 2017 *J. Alloys Compd.* **720** 29

[2] Volokitina A, Loiko P, Vilejshikova E, Mateos X, Dunina E, Kornienko A, Kuleshov N, Pavlyuk A 2018 *J. Alloys Compd.* **762** 786

Crystallization of bi-layers bi-substituted iron films

T V Mikhailova[1], Yu E Vysokikh[2], A N Shaposhnikov[1], V N Berzhansky[1], S Yu Krasnoborodko[2], A S Lutovinov[2].

[1]V.I. Vernadsky Crimean Federal University, Simferopol, 295007, Russia
[2]Scientific and Technological Centre of Unique Instrumentation of the RAS, Moscow, 117342, Russia
visokihy@gmail.com

Abstract. Magneto optical structures are widely used for different application in the fields of magnetoplasmonics, magnetooptics, photinics e.t.c. Bi-layers Bi-substituted iron garnet films is high-performance MO material. Integration of Bi:YIG films to silicon semiconductor technology gives new opportunities to create nanoscale hight performance magneto optical devices. Vacuum sputtering deposition allows to fabricate Bi:YIG structures on different substrate types. Authors investigate crystallization process of Bi:YIG films in a different process parameter (different layers composition and its thickness, temperature and time of annealing) using gadolinium gallium garnet and SIO2 substrates to determine dependences which impact on crystallization.

1. Introduction

Magneto optical devices gives opportunities to create high performance isolators, modulators and switches, nanophotonic devices, plasmonic circuit elements [1,2]. The bi-layers films given successful results in magnetophotonic crystals and Tamm structures design [3, 6−9]. Crystallization process in one of most important factors which determine films' quality. Integration of YIG films to silicon semiconductor process is important due possibility of fabricating new nanoscale and high-performance devices.

2. Experimental

YIG films were fabricated by reactive ion beam sputtering method (RIBS). The films were deposited from ceramic target on gadolinium gallium garnet (GGG) and fused quartz SiO2 substrates [3, 4−6]. Different composition of Bi:YIG with thicknesses in the range of 60 nm – 200 nm were used for bi-layers structure synthesis on each substrates. The garnet phase was formed by crystallization annealing at the temperature range from 650^0C to 710^0C. Annealing time was varied from 20 min to 60 min.

Surface structure of bi-layers reveals crystallization features which depends on process parameters (type of substrate, thickness of layers, temperature and time of annealing). Atomic force microscopy was used to investigate the films' surfaces. Average roughness of each film was measured to determine the regime which allows to minimize this parameter.

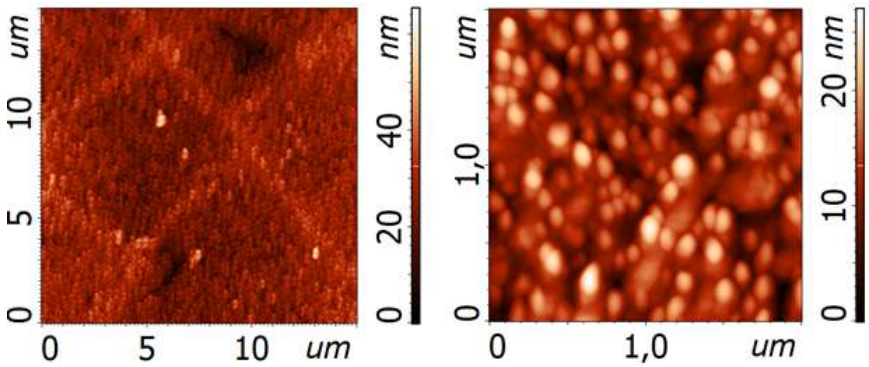

Fig. 1 The example of poly-crystalline grain structure of bi-layers Bi-substituted iron garnet films in SIO2 substrate.

Acknowledgments

The authors from V.I. Vernadsky Crimean Federal University TVM, ANSh, VNB acknowledge support by the Russian Ministry of Education and Science (Megagrant project N 075-15-2019-1934) for the synthesis of film samples with optimized magnetic parameters and the Russian Science Foundation (project no. 19-72-20154) for laser polarization investigations of films.

The authors from Scientific and Technological Centre of Unique Instrumentation of the RAS YuEV, SYuK, MFB, DVCh acknowledge support by the Ministry of Science and Higher Education of the Russian Federation under the State contract No. 0069-2019-0009 for the development of high-resolution magneto-optical microscopy and films measurements. This work was performed using the equipment of the Shared Research Facilities of the STC UI RAS.

References

[1] Inoue M, Baryshev A V, Goto T, Baek S M, Mito S, Takagi H and Lim P B 2013 Magnetophotonic Crystals: Experimental Realization and Applications *Magnetophotonics* eds. Inoue M, Levy M, Baryshev A V (Springer-Verlag Berlin Heidelberg) chapter 7 p. 163

[2] Armelles G, Cebollada A, García-Martín A and González M U 2013 *Adv. Optical Mater* **1** 10

[3] Berzhansky V N, Karavainikov A V, Mikhailova T V, Prokopov A R, Shaposhnikov A N, Shumilov A G, Lugovskoy N V, Semuk E Y, Kharchenko M F, Lukienko I M, Kharchenko Yu M, Belotelov V I 2017 *JMMM* **440** 175

[4] Berzhansky V, Mikhailova T, Shaposhnikov A, Prokopov A, Karavainikov A, Kotov V, Balabanov D, and Burkov V 2013 *Appl. Opt.* **52** 6599-6606

[5] Berzhansky V N, Karavainikov A V, Milyukova E T, Mikhailova T V, Prokopov A R, Shaposhnikov A N *Functional materials* 2010 **17 (1)** 120-126

[6] Berzhansky V N, Shaposhnikov A N, Prokopov A R, Karavainikov A V, Mikhailova T V, Lukienko I N, Kharchenko Yu N, Golub V O, Salyuk O Yu, Belotelov V I 2016 *Journal of Experimental and Theoretical Physics* **123** 744-751

[7] Mikhailova T V, Berzhansky V N, Shaposhnikov A N, Karavainikov A V, Prokopov A R, Kharchenko Yu M, Lukienko I M, Miloslavskaya O V, Kharchenko M F 2018 *Opt. Mater.* **78** 521

[8] Mikhailova T, Shaposhnikov A, Prokopov A, Karavainikov A, Tomilin S, Lyashko S and Berzhansky V 2018 *EPJ Web of Conferences* **185** 02016

[9] Mikhailova T V, Lyashko S D, Tomilin S V, Karavainikov A V, Prokopov A R, Shaposhnikov A N, Berzhansky V N 2017 *J. Phys. : Conf. Ser.* **917** 062053

Passive decoy-state quantum key distribution with imperfect source

A Gavrilovich[1,2,3], D Sych[4,5,6,7], Y Kurochkin[1,2,6]

[1] QRate, Moscow, 121353, Russia
[2] Russian Quantum Center, Moscow, 143026, Russia
[3] Moscow Institute of Physics and Technology, Dolgoprudny, 141700, Russia
[4] P.N.Lebedev Physical Institute, Russian Academy of Sciences, Moscow, 119991, Russia
[5] Department of Physics, Moscow State Pedagogical University, 119992, Russia
[6] NTI Center for Quantum Communications, National University of Science and Technology MISiS, Leninsky prospekt 4, Moscow 119049, Russia
[7] Sirius University of Science and Technology, 1 Olympic Ave, 354340, Sochi, Russia

gavrilovich.aa@phystech.edu

Abstract. Passive decoy-state quantum key distribution (QKD) is an elegant solution to utilise an internal source of quantum randomness of the transmitter's scheme. It can be profitable, for example, in setups running at high transmission rates. However, original analysis of passive protocol does not allow for real-life source imperfections, thus potentially compromises the security of the system. Here we develop a general method of passive decoy-state estimation for an arbitrary intensity distribution and show that the refined bound on the secret key rate stays similar to the one of an active scheme, thus proving passive generation to be a practical means of constructing QKD systems.

1. Introduction

QKD is a procedure enabling two distant parties to generate an identical sequence of random bits, a so-called secret key, in the presence of an eavesdropper. The prevailing number of experimental realisations of QKD is based on BB84 decoy-state protocol [1, 2], which can provide high secret key rate in the case of using phase-randomised weak coherent source and transmitting via lossy channel. The conventional approach to state preparation is to use an active modulation controlled by an external quantum random number generator (QRNG). In some scenarios, for example, when the transmission rate is high, it is preferable to exploit the internal source of quantum randomness which is the difference in phases of the emitted laser pulses. By interfering them one can get pulses of random intensity with a known probability distribution function (PDF). This method of passive generation was introduced in [3]. However, the recent research [4] shows a significant dependence between probabilistic properties of such interference and different real-life effects such as chirp and jitter, therefore revealing the gap between theoretical model used in [3] and a real device. This mismatch can

lead to inaccurate estimation of secret key rate, thus potentially compromising the security of the protocol.

In this work we develop a general technique of decoy-state estimation for passive BB84 scheme with an arbitrary PDF of intensity, demonstrate our method by calculating secret key rate for the source with a linear chirp and evaluate the execution of an adjusted passive system model.

2. Methods

We extend H. F. Chau's analysis for decoy-state estimation [5] to passive BB84 protocol by introducing a modified Vandermode's matrix and deriving its inverse. Then we simulate PDF of pulse interference in accordance with [4] and numerically calculate secret key rate to compare the refined bound on the performance of passive protocol with that of an active one.

3. Results and discussion

The calculated secret key rate for passive and active setups is shown in Fig. 1. From the results of the simulation one can see that both schemes provide similar secret key rates. Therefore, we demonstrate that the refined analysis confirms the practicability of passive generation.

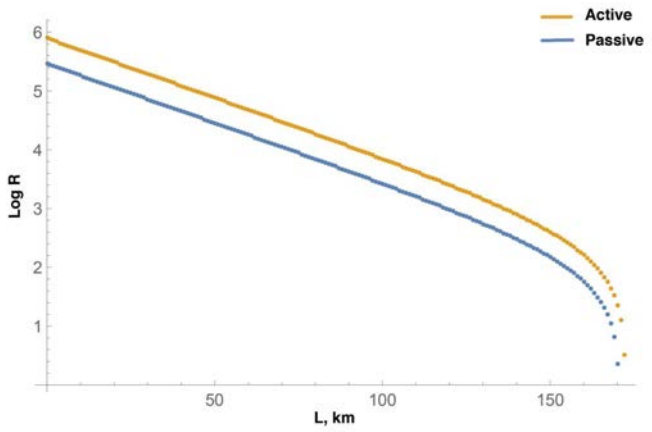

Figure 1. Secret key rate R as a function of distance L for active and passive BB84 decoy-state protocols.

Acknowledgments

Denis Sych acknowledges support from Russian Foundation for Basic Research grant 20-32-51004, and Arina Gavrilovich acknowledges support from FASIE.

References

[1] Bennett C. H., Brassard G, Proceedings of the IEEE International Conference on Computers, Systems and Signal Processing, 175-179, 1984

[2] Xiongfeng Ma, Bing Qi, Yi Zhao, and Hoi-Kwong Lo, Physical Review A 72, 012326, 2005

[3] Marcos Curty, Xiongfeng Ma, Bing Qi, and Tobias Moroder, Physical Review A 81, 022310, 2010

[4] Roman Shakhovoy, Denis Sych, Violetta Sharoglazova, Alexander Udaltsov, Aleksey Fedorov, and Yury Kurochkin, Optics Express 28(5), 6209-6224, 2020

[5] H. F. Chau, Physical Review A 97, 04030, 2018

Quantum error correction for quantum image transmission algorithm

S. S. Ivanov[1], **I Yu Popov**[1], **P. A. Gilev**[1]
[1]Faculty of Control Systems and Robotics, ITMO University, St. Petersburg, 197101, Russia

E-mail: GrandArchTemplar@gmail.com

Abstract. Quantum imaging is a simple algorithm for data transmission so there are quantum image transmission computer models. Taking two unpaired qubits and their entanglement leads to transmission not only of classical but quantum information. Quantum image transmission via optical interference between entangled qubits could be improved via applying Shor's code to the main qubit. Auxiliary qubits with current algorithms could be taken with relatively low correctness rate.

1. Introduction

There are some quantum information transmissions methods. Some of them are well studied (e. g. quantum channels [2]), some of them not (e. g. quantum imaging [1]). So we will research quantum imaging as a way for information transmission. In classical systems there are two qubits with maybe different nature (except both of them admit application of optical interference to them). After entangling one of them interacts with an information source when the other is transmitted and both of them interfere as optical waves. With that interference picture we can determine which information was transmitted. This algorithm has an essential disadvantage: relatively small correctness rate. A method to improve accuracy is applying Shor's algorithm [3].

2. Theoretical Model

Main object is a qubit — a pair of two real or complex numbers. Qubit as a vector can be tensor-produced with another qubit for a two-qubit system. Many-qubit systems can be obtained by sequentially tensor-producing. Quantum algorithm is a unitary operator which is applied to the qubit system.

Shor's algorithm is the way to correct sign-flip(one or two components of qubit change sign to opposite) or rotate-flip(change order of numbers). This error in quantum imaging can be found in qubit which transfers information. So we added to main qubit Shor's code to improve the correctness rate.

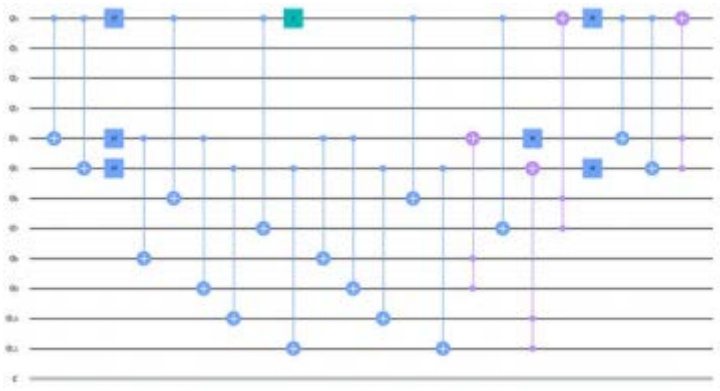

Figure 1. This scheme was modeled with the computer and quantum computer modeling python library "Qiskit".

3. Numerical results

There are several experiments with 2048 series numbers and some variations of accuracy for main, sub main and auxiliary qubits. Main trivial observations are strongly independent in wide spectre (error rate for auxiliary qubit changed from 0.1 to 0.35) between main qubit correctness rate and auxiliary qubit error rate. This allows us to use this improvement method with not very good prepared auxiliary qubits and set focus only for main and sub main qubit.

Acknowledgments

This work was partially financially supported by the Government of the Russian Federation (grant 08-08), by grant 16-11-10330 of Russian Science Foundation

References

[1] Pittman T.B., Shih Y.H., Strekalov D.V., Sergienko A.V. Optical imaging by means of two-photon quantum entanglement. Phys. Rev. A. 1995, **52** (5). P. R3429–R3432.

[2] John A. Holbrook, David W. Kribs, and Raymond Laflamme. "Noiseless Subsystems and the Structure of the Commutant in Quantum Error Correction." *Quantum Information Processing*. Volume 2, Number 5, p. 381-419. Oct 2003.

[3] Peres, Asher (1985). "Reversible Logic and Quantum Computers". *Physical Review A*. **32** (6): 3266–3276. doi:10.1103/PhysRevA.32.3266

Investigation of a single-photon hybrid emitting system based on nanodiamonds with NV-centers integrated with GaP NWs

A S Goltaev[1], A M Mozharov[1], V V Yaroshenko[2], D A Zuev[2] and I S Mukhin[1]

[1] Alferov University, Khlopina 8/3, 194021 St. Petersburg, Russia
[2] ITMO University, St. Petersburg, 197101 Russia

e-mail: akbapnym@yandex.ru

Abstract: Arrays of GaP nanowires were synthesized as a waveguide for nanodiamonds with color centers. The optical characteristics of deposited nanodiamonds on nanowires are analyzed. The influence of a dielectric waveguide on the photon lifetimes is investigated using the TCSPC method.

1. Introduction

Nanoscale quantum optical emitters are main elements of quantum optics and sensing. Nanodiamonds (NDs) with optically active point defects in the crystal lattice can be used as such sources. One of the most studied and useful defects is a nitrogen-substituted vacancy or NV-center. The spins of electrons in NV-centers can be adjusted at room temperature using a magnetic field, electric field, or optical radiation [1]. The main problem that limits application of NV-centers in quantum nanophotonic systems is related to the low brightness of zero-phonon line (ZPL) at room temperature due to broad phonon side-band [2]. A conventional approach to the problem of increasing the NV-center ZPL emission rate as well as efficient collection of emissioned photons assumes integrating the radiant nanodiamonds with optical cavities or waveguides. Gallium phosphide (GaP) nanowires (NWs) can be used as optical resonance systems, since NWs GaP has a narrow band gap and is transparent to the visible range, ideal for NV-centers. Another advantage is the refractive index, which about ~ 3.2 across the visible range, which is higher than most optical materials, for example, the refractive index of diamond is 2.4.

2. Experiment

Epitaxial GaP NWs arrays were synthesized on the Si (111) substrate using the PA-MBE Veeco GEN-III machine. The morphology of synthesized GaP NWs was studied with scanning-electron microscope (SEM) (Zeiss SUPRA 25-30-63). Microspectroscopic studies of the PL response and light Raman scattering (RS) of individual NWs and an ensemble of NDs were performed at 300 K to study the chemical composition and PL modulation by the resonator eigenmodes (see figure 1). The lifetimes of photons were obtained using the TCSPC method.

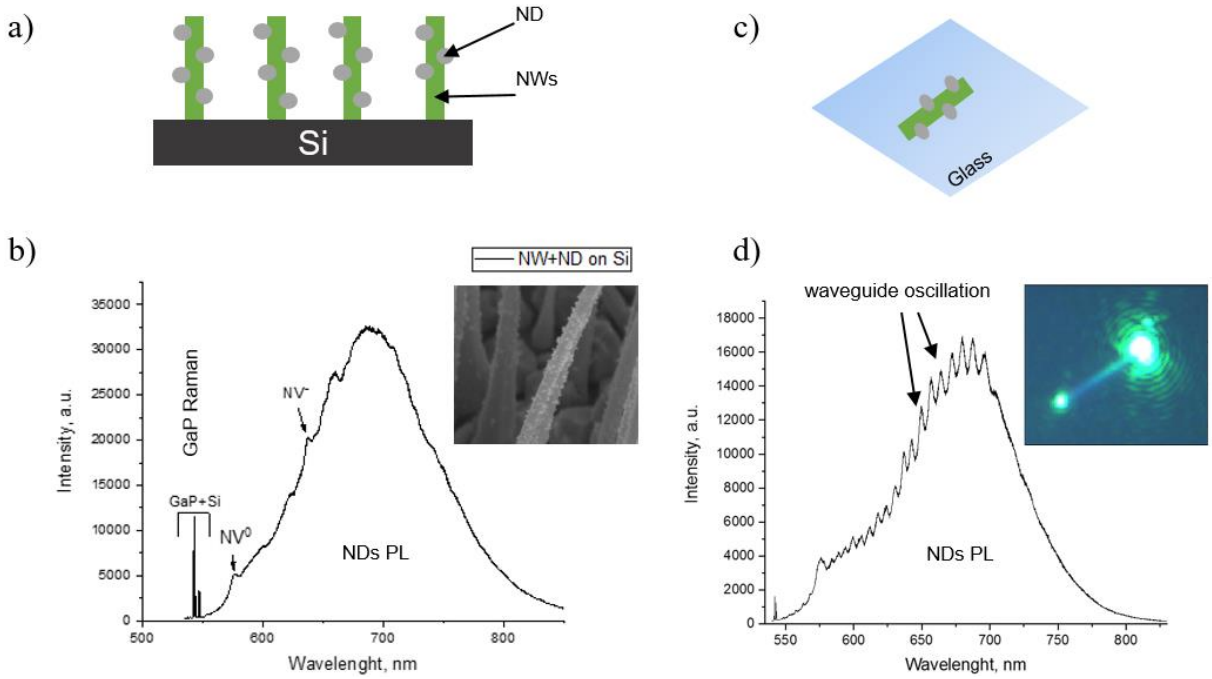

Figure 1. a) Scheme of vertical GaP nanowire structure with deposited nanodiamonds, b) PL spectrum of NW array with NDs; inset SEM image of the structure, c) scheme of a single NW with NDs on a glass substrate, d) PL spectrum of a single NW with ND; inset shows an optical image of a single nanowire under the laser exposure.

3. Conclusion

In this work the technological process for the integration of single-photon radiating sources into a resonant system of gallium phosphide nanowires was worked out. The optical properties of the fabricated structure were analyzed and the PL and RS spectra were obtained. The dependence of the spontaneous emission rate was investigated for both systems: reference ND layer on glass substrate as well as coupled NDs with single GaP NWs. The data showed an increase in the spontaneous emission rate upon the integrating the nanodiamonds with GaP NWs cavity.

References

[1] Maurer P C et al 2010 Far-field optical imaging and manipulation of individual spins with nanoscale resolution *Nature Phys.* **6-11** 912-918

[2] Aharonovich I, Castelletto S, Simpson D A, Su C H, Greentree A D and Prawer S 2011 Diamond-based single-photon emitters *Rep. Prog. Phys.* **74-7** 076501

[3] Verardo D, Lindberg F W, Anttu N, Niman C S, Lard M, Dabkowska A P and Linke H 2018 Nanowires for biosensing: lightguiding of fluorescence as a function of diameter and wavelength *Nano Lett.* **18-8** 4796-4802

Application of the evolutionary algorithm for fluorescence decay analysis

D P Golyshev[1], I A Gorbunova[2], M E Sasin[2], M K Krasnopevtseva[2] and O S Vasyutinskii[2]

[1] Peter the Great St. Petersburg Polytechnic University, 29 Polytechnicheskaya, St. Petersburg, 195251 Russia
[2] Ioffe Institute, 26 Polytekhnicheskaya, St. Petersburg, 194021 Russia

Abstract. Polarized fluorescence decay in biological coenzyme FAD molecule in water-MeOH solutions under excitation at 355 nm was studied by analysis of the fluorescence signals. Differential Evolution algorithm was used for non-linear least-squares problem for global proceeding fluorescence decay curves.

1. Introduction

Fluorescence lifetime imaging microscopy (FLIM) was actively developed during latest decades. Nowadays this approach plays a significant role in diagnostic of cell metabolism, cancer cell differentiation, etc. For making precise analysis of experimental data, multiexponential regression models are widely used [1]. However, the use of the models lead to additional difficulties in determination of the fluorescence decay parameters.

Major difficulties occur due to specific features of the least-squares method for fluorescence decay parameters estimation because of the problem of finding the global minimum of highly non-linear functions. This problem cannot be resolved analytically or by a simple brute force method. Thus, simultaneously accurate and fast iterative algorithms for finding the global minimum are required.

Since traditional gradient optimization algorithms, such as Levenberg-Marquardt, Gauss-Newton methods etc. have some disadvantages [2], a stochastic differential evolution (DE) algorithm becomes preferable. The aim of this paper is the use of DE algorithm for multiexponential fluorescence decay analysis.

2. Experimental data proceeding

Time-correlated single photon counting (TCSPC) technique was used for recording the fluorescence decay curves with high temporal resolution. Within this method, the decay of polarized fluorescence in biological cofactor FAD excited at 355 nm in water-methanol (MeOH) solutions was recorded in nanosecond and sub-nanosecond time domains and then processed by a time-correlated photon counting system.

In general, two orthogonally polarized fluorescence components $I_{\perp}$ and $I_{\parallel}$ are multiexponential functions with many parameters that can be presented in the form [1]:

$$I_{\parallel}(t,\theta)=\left(\alpha_1 e^{-\frac{t-t_0}{\tau_1}}+\alpha_2 e^{-\frac{t-t_0}{\tau_2}}\right)\left(1+2r_0 e^{-\frac{t-t_0}{\tau_{\text{rot}}}}\right),$$
$$I_{\perp}(t,\theta)=\left(\alpha_1 e^{-\frac{t-t_0}{\tau_1}}+\alpha_2 e^{-\frac{t-t_0}{\tau_2}}\right)\left(1-r_0 e^{-\frac{t-t_0}{\tau_{\text{rot}}}}\right), \quad (1)$$

where t_0 is an excitation time, τ_i are fluorescence decay times, α_i are weighting coefficients, r_0 is a fluorescence anisotropy, τ_{rot} is a rotational diffusion time, and $\theta=(\alpha_1,\alpha_2,\tau_1,\tau_2,r_0,\tau_{\text{rot}},t_0)$ is a set of parameters to be determined.

In many cases eqs. (1) should be convolved with the instrumental response function $IRF(t)$:

$$f(t,\theta)=I(t,\theta)*IRF(t), \quad (2)$$

where * is the convolution operator. The convolution was proceeded by the discrete Fourier transform.

For determination of the set θ the least-squares method was used:

$$\theta=\operatorname{argmin}\sum_i\left(y_i-f(x_i,\theta)\right)^2, \quad (3)$$

where (x_i, y_i) is a set of experimental data.

The problem (3) is a highly non-linear one. The DE algorithm [3] was used for global minimum determination. A set of vectors (generation) was randomly generated at each iteration step within specified limits and then each vector in generation changed under mutation and crossover operations. The best vector from each generation converged to the global minimum after further iterations.

3. Results and analysis

The results obtained are presented in Table 1. As can be seen from the Table the decay times τ_1, τ_2, anisotropy r_0 are independent from MeOH concentration within error bars. At the same time the rotational diffusion time τ_{rot} behaves non-monotonically that can be due to the change of viscosity in water-MeOH solution. The ratio of weighting coefficients α_2 / α_1 in Table 1 increases dramatically with MeOH concentration reflecting significant change in the FAD conformations distribution.

Table 1. Proceeding results

MeOH, conc. %	α_2 / α_1	τ_1, ns	τ_2, ns	r_0	τ_{rot}, ns
0	0.44 ± 0.05	2.2 ± 0.1	4.5 ± 0.1	0.24 ±0.02	0.15 ± 0.03
20	0.63 ± 0.08	2.3 ± 0.1	4.0 ± 0.1	0.22 ±0.03	0.24 ± 0.44
40	1.56 ± 0.41	2.2 ± 0.2	3.9 ± 0.2	0.23 ±0.01	0.30 ± 0.50
60	2.29 ± 0.33	2.2 ± 0.2	4.0 ± 0.1	0.21 ±0.02	0.33 ± 0.31
80	2.16 ± 0.16	2.2 ± 0.1	4.0 ± 0.1	0.24 ±0.01	0.25 ± 0.33

Acknowledgments

The authors Acknowledge support from Russian Foundation for Basic Research, grant № 18-53-34001.

References

[1] D H Vishwasrao, A A Heikal, K A Kasischke and W W Webb 2005 *Journal of Biological Chemistry,* 280(26) p 25119–25126.

[2] P J G Teunissen 1989 *Manuscripta geodaetica* 15 p 137–150

[3] Qin A K, Huang V L and Suganthan P N 2009 *IEEE Transactions on evolutionary computations* 13(2) p 398–417

On the possibility of using the optical method for express quality control of fruits

E M Gryaznova[1], V V Davydov[1, 2] and V Y Rud[2, 3]
[1]Peter the Great Saint-Petersburg Polytechnic University, Saint Petersburg, Russia, 195251
[2]All-Russian Research Institute of Phytopathology, Moscow Region, Russia, 143050
[3]A.F. Ioffe Physicotechnical Institute, St. Petersburg, 195152, Russia

e-mail: katya.gryaznova@mail.ru

Abstract. The express-method of fruit quality control using laser radiation is presented. The dependence of the degree of spatial coherence on the defects of the fruit surfaces has been investigated. The results of checks of defects, hardness, degree of maturation using the optical method are presented.

1. Introduction

Quality control of fruits is an integral part of their production and storage. With an increase in production rates and a desire to reduce costs, agricultural producers may neglect this procedure or use destructive methods based on visualization of anatomical features using microscopes [1] or analysis of acoustic, electrophysical, mechanical properties of integumentary and parenchymal tissues [2]. These methods are quite laborious and destructive in nature. Optical non-invasive methods based on color, spectrozonal or luminescent characteristics are ineffective if structural changes are not accompanied by significant and unambiguous biochemical processes. Another disadvantage of these methods is the duration of the measurements (long time).

In our work, we consider the possibility of using the correlation parameters of laser light scattering to register structural rearrangements of fruit tissues without a significant effect on the vital activity of the fruit and capable of being carried out in an express mode.

2. Quality determination method

The implementation of the method is based on obtaining the contrast of the interference pattern, which, when the intensities of the interfering beams are equal, is equal to the degree of spatial coherence (DSC). In Figure 1 shows a diagram of the setup for obtaining the DSC.

Various fruits with the most typical defects were examined. The DSC of the investigated fruits is significantly reduced in defective fruits, and the method does not depend on the biochemical state of the defect and the color of the fruit.

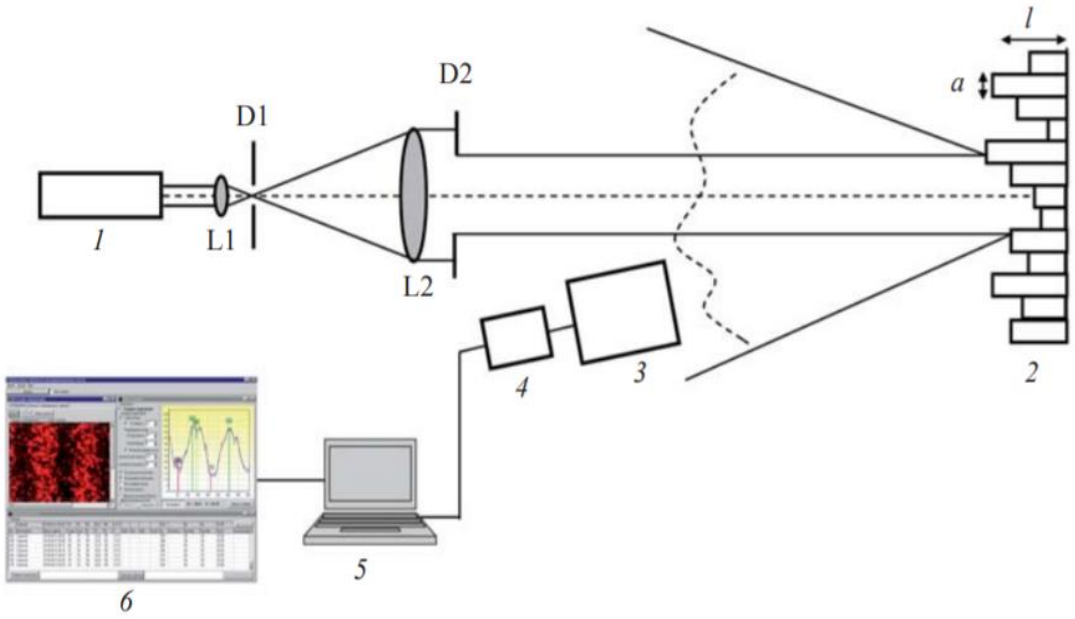

Figure 1. Installation diagram: 1 – helium-neon laser; 2 – biological object; 3 – polarization interferometer; 4 – CCD camera; 5 – PC; 6 – results processing software; L1, L2 – collimator lens; D1– Fourier filter, D2 – aperture diaphragm.

This method also tested the ripeness of the fruit, since the structure of the skin and pulp changes during the ripening process, which leads to a change in the DSC. For each type of fruit, the data on the hardness of the pulp obtained using a penetrometer coincide with the results of the considered optical method with a correlation coefficient of at least 0.95.

The method also makes it possible to determine the dynamics of fruit ripening, which is useful for predicting keeping quality or managing storage duration. For this, the degree of spatial coherence of light scattering in the process of accelerated ripening was recorded using the example of pear fruits. The correlation coefficient between the DSC and the hardness of the fruit with the skin is practically equal to the correlation coefficient between the DSC and the hardness of the pulp, which indicates a fairly close relationship between the phase parameters of light scattering and general physiological and physicomechanical changes occurring during ripening in all tissues of the fruit.

3. Conclusion

The data obtained confirm the possibility of using the considered method for quality control of fruit in express mode. The use of the DSC as an assessment of the characteristics of the state of the fruit has a sufficiently high accuracy, and the non-invasiveness and simplicity of the method make it attractive for use. The method allows you to assess not only the defects of fruits and the degree of their ripeness, but also to predict the dynamics of ripening.

References

[1] Zagoryan E M 1985 *Biological and chemical sciences* **6** 68-70
[2] Golev I M 2013 Storage and processing agricultural raw materials **12** 28-31

The development of an optical system for lighting various rooms with sunlight

I M Gureeva[1], V V Davydov[1, 2] and V Yu Rud[2, 3]
[1]Peter the Great Saint-Petersburg Polytechnic University, Saint Petersburg, Russia, 195251
[2]All-Russian Research Institute of Phytopathology, Moscow Region 143050, Russia
[3]A.F. Ioffe Physicotechnical Institute, St. Petersburg, 195152, Russia

Abstract. The necessity of using light in the room, the spectral composition of which corresponds to the spectrum of the sun for a comfortable state of a person, is justified. A passive system that does not consume energy is proposed. An energy-efficient natural light system has been developed, creating a comfortable environment for the eyes, well-being and mood of a person. An experimental study of the system operation was carried out. The dependence of the light intensity on the angle of incidence in the light guide is obtained.

1. Introduction

The efficiency of a person, his well-being, attention, mood, as well as interest in scientific and other activities depends on many factors. One of them is the level of illumination and the quality of the light wave. Numerous studies of scientists [1, 2] have shown that the most favorable effect on vision and the psyche is provided by sunlight. Therefore, it is not surprising that the developers of various light sources strive to reproduce the spectrum of sunlight in the light stream. The task of reproducing the spectrum of sunlight in lamps is difficult due to the fact that it is necessary to maintain a balance between energy consumption with a lamp lifetime and the fullness of the spectrum relative to the spectrum of the sun. Our research has shown that almost all currently produced LED lamps have a truncated spectrum of sunlight, especially with a long service life. Therefore, the search for solutions related to the possibility of using sunlight, especially in living rooms, is extremely relevant at the present time.

2. Optical system and research methodology

In this work, one of the possible solutions is considered – the design of a system containing a set of optical elements that concentrate daylight, transmit it through a system of quartz light guides and disperse it in the indoor areas of the building. The system shown in Figure 1 includes collecting and scattering lenses, a rotating prism, quartz light guides and a transparent protective panel. The transparent panel is placed on the roof of the house. This system will function throughout the daylight hours. The introduction of such a system has a positive impact on the health of people with continuous exposure to the visible spectrum of natural light. Other benefits include a reduction in energy losses and energy inputs from buildings, as well as a positive impact on the planet's ecology by reducing conditional CO2 emissions into the atmosphere. The use of quartz light guides ensures the operation of the system in any weather due to their resistance to low and high temperatures. The presence of a rotating prism eliminates additional light losses due to reflections on the bends and walls of the light guide when transmitting it from the collecting lens to the vertical light guide.

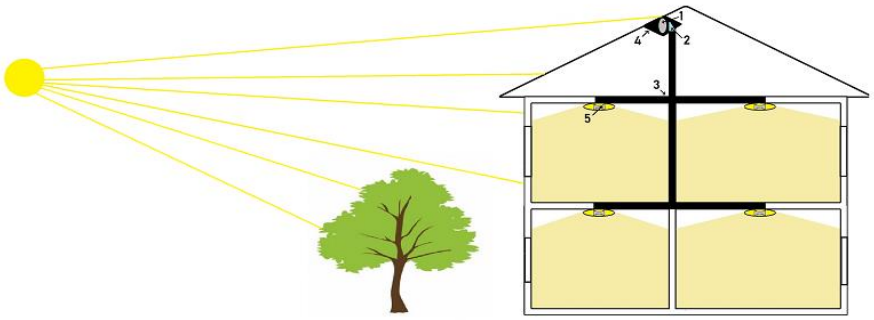

Figure 1. Operation of the optical system for transmitting sunlight: 1-collecting lens; 2-rotating prism; 3-quartz light guide system with couplers; 4-transparent protective panel; 5-scattering lens.

3. Result of experimental investigations

During an experimental study of light transmission through light guides, it was found that the transmitted spectrum is not distorted. As an additional study, the dependence of the intensity of light entering the premises on the angle at which the light stream enters the light guide was obtained. Dependence is shown in Figure 2.

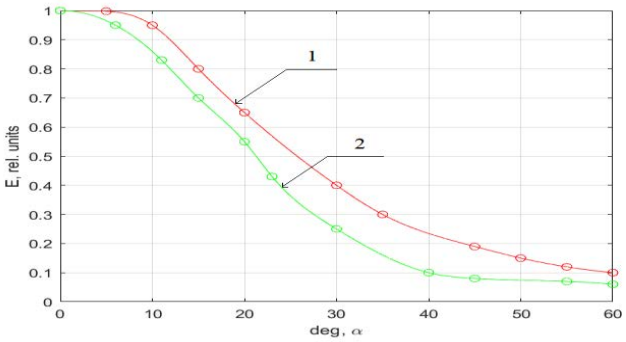

Figure 2. The dependence of the change in light intensity on the angle α at which light enters the light guide for two types of light guides, graph 1 – a single light guide, graph 2-a light guide with two branches.

4. Conclusion

Conducted studies have shown that when implementing the system, it is important to take into account the geometry of the roof and the angle at which the optical axis of the focusing lens will be located. The focus of the lens should be located on the outer surface of the light guide, the optical axis of the focusing lens should be perpendicular to the surface of the light guide on which the radiation falls. For each indoor lighting project, it is necessary to calculate the system and simulate its operation in order to determine the optimal configuration for the maximum intensity of light entering the premises.

Thanks to its properties, the developed optical lighting system creates an atmosphere of comfort in the premises, and significantly reduces the energy costs for lighting, heating and air conditioning of the buildings in which it is installed.

References

[1] Münch M, Wirz-Justice A, Brown S, Kantermann T, Martiny K, Stefan O, Vetter C, Wright K, K. Wulff K and Skene D 2020 *Clocks & Sleep* **2(1)** 61-85

[2] McCloughan C L B, Aspinall P A and Webb R S 1999 *International Journal of Lighting Research and Technology* **31(3)** 81-88

On necessity for analytical solution of the Bloch equations for nuclear magnetic resonance signals at condition express control of liquid medium

M N Davydov[1], V V Davydov[1, 2] and V Yu Rud[2, 3]

[1]Peter the Great Saint Petersburg Polytechnical University, St. Petersburg, 195251, Russia
[2]All Russian Research Institute of Phytopathology, Moscow Region, 143050, Russia
[3]A.F. Ioffe Physicotechnical Institute, St. Petersburg, 195152, Russia

e-mail: mdavydov2010@mail.ru

Abstract: The necessity of using express analysis methods to control medium condition is substantiated. It has been shown that the method of express control based on the phenomenon of nuclear magnetic resonance is one of the most preferable. It was found that to increase the information about the medium condition state obtained from the recorded NMR signal, it is necessary to use a mathematical model (based on analytical solutions of the Bloch equations). Two approaches are considered that are used to describe the NMR signal in a liquid medium. It is determined that in the classical approach in the system of Bloch equations it is possible to take into account the peculiarities of using radiotechnical methods of signal registration. The direction of the analytical solution of the Bloch equation is proposed. The experimental data are compared with the numerical solution.

1. Introduction

Nuclear magnetic resonance (NMR) is one of the promising methods of express control of liquid media right at the site of sampling [1, 2]. Measuring devices, applying the phenomenon of NMR, do not introduce irreversible changes in the composition and structure of the medium under study [1, 2]. Defining of the shape of the recorded NMR signal, received with use of the modulation technique, using exact analytical solutions to the system of Bloch equations will expand functionality of express control methods.

2. System of Bloch equations for the case of recording an NMR signal using a modulation technique

The system of Bloch equations in a rotating coordinate system is represented in the following form [3]:

$$\begin{cases} \dot{u} + \frac{u}{T^*_2} + \Delta\omega v = 0 \\ \dot{v} + \frac{v}{T^*_2} - \Delta\omega u = -|\gamma| H_1 M_z \\ \dot{M}_z + \frac{M_z}{T_1} - |\gamma| v H_1 = \frac{M}{T_1} \end{cases} \quad (1)$$

$$\begin{cases} \text{Ↄ} = v + ju \\ \frac{d\text{Ↄ}}{dt} + \left(\frac{1}{T^*_2} + j\Delta\omega\right)\text{Ↄ} = -|\gamma| H_1 M_z \\ \frac{dM_z}{d\tau} + \alpha M_z - v = \alpha M \end{cases} \quad (2)$$

By introducing new functions, system (1) is simplified (2). The general solution is found by the method of variation of arbitrary constants. After mathematical transformations, we obtain the Voltaire integral equation of the second kind for M_z

$$M_z = \frac{1}{T_1}\int_{-\infty}^{t} M(t')e^{-\frac{t-t'}{T_1}}dt' - \gamma^2 {H_1}^2 \int_{-\infty}^{t} M_z(t')K(t,t')dt' \quad (3)$$

This integral equation (3) is solved by the method of successive approximations [3]. The constructed solution can be interpolated. Interpolation of the response waveform by various orthogonal systems of functions and analysis of interpolation errors will be performed.

If a modulation technique is used to register an NMR signal, for example, a flowing environment or express medium state control (weak magnetic field) in the classical method, in the Bloch equations, the term containing Δω is transformed into the following form:

$$\Delta\omega = \gamma H_0 + \gamma H_m \sin(\omega_m t) - \omega_{nmr}, \quad (4)$$

where H_0 is the constant magnetic field, H_m is the modulation coil field, ω_m is the modulation frequency.

The NMR signal is recorded under conditions of rapid adiabatic passage through resonance. In addition, time dependency needs to be considered. In this case, the recorded NMR signal has the form:

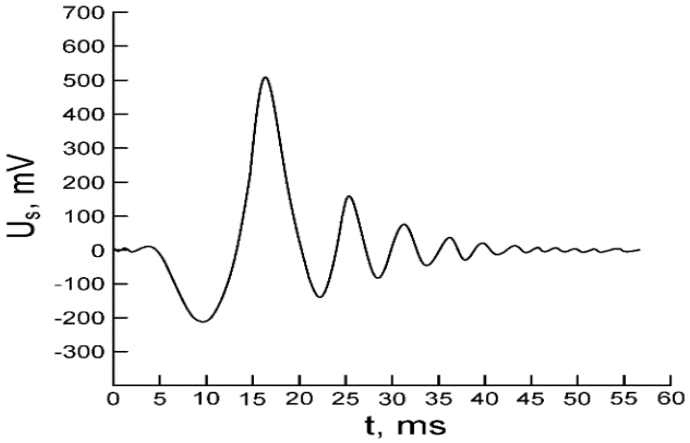

Figure 1. NMR waveform from tap water.

This can be taken into account only when obtaining an analytical solution to the Bloch equations. Therefore, the paper proposes to consider a method for obtaining an analytical solution of the Bloch equations using the Matlab software package used for technical computing problems.

3. Conclusion

The preliminary results obtained showed that the direction we have chosen to expand the functionality of using express control using an NMR signal is promising. The analytical solution of the Bloch equations will take into account the phase of the NMR signal and delineate long-term studies of media using the modulation technique.

References

[1] Myazin N S, Yushkova V V, Davydova T I and V Yu Rud' 2017 *Journal of Physics: Conference Series* **917** 042017

[2] Karseev A Yu, Cheremiskina A V, Davydov V V, Velichko E N 2014 *Journal of Physics: Conference Series* **541(1)** 012006

[3] Leshe A *Nuclear induction* 1963 (Veb Deustscher Verlag Der Wissenschaften, Berlin)

Four-spin chiral interactions in D_{3h} magnet

G R Rakhmanova, I V Iorsh

ITMO University, Saint Petersburg 197101, Russia

gulnaz.rahmanova@metalab.ifmo.ru

Abstract. We demonstrate that four-spin interaction causes a phase transition from a collinear ferromagnetic state to a non-collinear magnetic ground state in crystals with D3h point group symmetry that is rather common among two dimensional magnets. The corresponding non-collinear ground state may also be additionally stabilized by an external magnetic field. Taking into account possible four-spin chiral exchange interactions is important for understanding noncollinear magnetic order in these systems.

1. Introduction

Electron-mediated indirect asymmetric exchange between a pair of localized spins is commonly referred to as the Dzyaloshinsky-Moriya interaction (DMI) [1]. The DMI leads to a variety of magnetic structures from the collinear state to complex, non-collinear spin textures [2]. The presence of linear-in-gradient terms in micromagnetic energy may make a collinear (ferromagnetic or anti-ferromagnetic) order unstable and create cone, helix, vertex or skyrmion crystals. Such structures are indeed observed in many conducting magnets or magnetic multilayers with broken inversion symmetry such as MnSi, FeGe, Ir/Co/Pt or Pt/CoFeB/MgO [3]. But chiral structures in these substances exist in a rather narrow range of temperatures and external magnetic fields, that makes them practically inapplicable for practical purposes. That is why the interest of this work is associated with three specific point groups for crystals with broken inversion symmetry: Td, D_{3h} and C_{3h}, for which all LI terms in micromagnetic functional are forbidden, while multi-spin chiral exchange interactions are allowed by symmetry [4]. The tetrahedral group Td can only be realized in three-dimensional cubic crystals, while D_{3h} and C_{3h} are natural for 2D magnets with honeycomb magnetic lattices. A cubic tetrahedral magnet has been recently studied in [5], where it was demonstrated that a four-spin chiral exchange interaction causes a phase transition from a collinear state to a non-collinear cone ground state. We consider two-dimensional structures with the symmetry group D_{3h}. It is such crystals as CrI_3, Fe_3GeTe_2, $NiPS_3$, and many others. We propose a four-spin chiral exchange interaction in such magnet that leads to instability with respect to the formation of the helical ground state.

2. Free energy

Free energy functional of D_{3h} ferromagnet, that depends on a dimensionless magnetization vector field $m(r)$ of the unit length, is given by formula:

$$F[m] = \int d^2r[\omega(r) - \boldsymbol{Hm}], \quad (1)$$

where H stands for external magnetic field measured in energy units, $\omega(r)$ is the energy density of the magnet that reads:

$$\omega(r) = A\sum_{\alpha}(\nabla m_{\alpha})^2 + 8Bm_y\left(m_y^2 - 3m_x^2\right)[\nabla \times m]_z + Km_z^2\,, \qquad (2)$$

where $A > 0$, K – anisotropy constants. The first term represents usual symmetric exchange, the second term describes four-spin chiral interaction – independent fourth order invariant with respect to the magnetization field $m(r)$.

We describe a three-dimensional lattice of spins, which interact only with their nearest neighbors. A non-collinear ansatz for local magnetization field $m(r)$, that has the biggest chance to become a ground state, can be written in a form:

$$\boldsymbol{m(r)} = \boldsymbol{n}\cos\alpha + [\boldsymbol{m_1}\cos(\boldsymbol{kr}) + \boldsymbol{m_2}\sin(\boldsymbol{kr})]\sin\alpha, \qquad (3)$$

where $\boldsymbol{n}$, $\boldsymbol{m_1}$ and $\boldsymbol{m_2}$ are mutually perpendicular unit vectors. The angle $\alpha = 0$ corresponds to a collinear state, $\alpha = \pi/2$ – to a pure helix state.

Substituting (2) and (3) into (1) and considering external magnetic field parallel to the plane (H_z=H_y=0) we minimize equation (1) with respect to k_x, k_y and get the free energy as a function of three variables θ, ϕ, α:

$$\frac{F[m]A}{VB^2} = -\frac{9}{64}(\sin\alpha + 5\sin 3\alpha)^2\sin^4\theta\cos^2\theta + \frac{KA}{B^2}\cos^2\theta\cos^2\alpha + \frac{KA}{2B^2}\sin^2\theta\sin^2\alpha - \frac{H_xA}{B^2}\cos\phi\sin\theta\,. \qquad (4)$$

The result of numerical energy minimization of equation (4) with respect to θ, ϕ, α is illustrated in Figure 1 by plotting the dependence α (an angle describing a transfer from collinear to helix state) on both KA/B^2 and HA/B^2 at the absolute energy minimum. The graph shows a phase transition from a collinear state ($\alpha = 0$) to non-collinear state ($\alpha \neq 0$) and back with K increasing. In addition, the angle α smoothly decreases from $\pi/6$ to almost 0 with H increase. The corresponding jumps are also seen in the left panels.

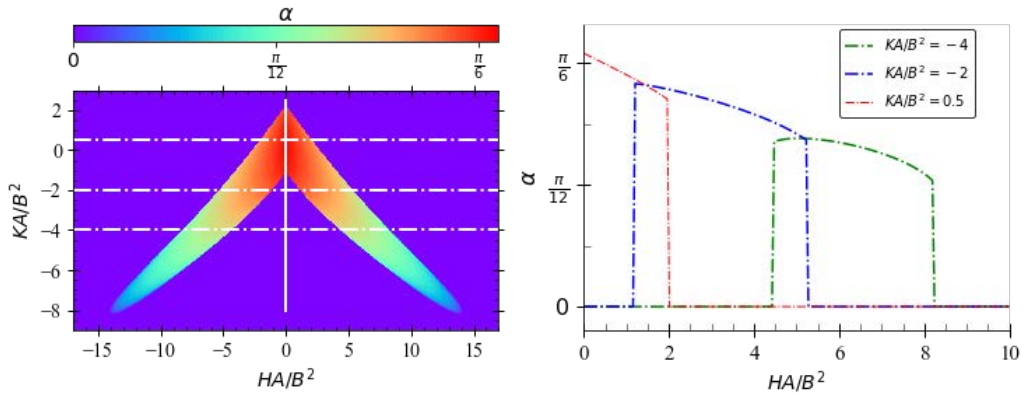

Figure 1. The color plot obtained by numerical minimization of the function (4) that represents the value of α at the global minimum with external magnetic field directed parallel to the plane. The left panel shows three vertical crosssections for K = - 4, - 2 and 0,5.

In conclusion, we demonstrate that the DMI on a lattice with D3h point group symmetry (common among two dimensional magnets) does not contribute to the energy functional and cannot cause an instability of the collinear order, while the existence of the four-spin indirect magnetic interaction may be responsible for the appearance of a non-collinear magnetic order.

References

[1] Dzyaloshinsky I 1958 J. Phys. Chem. Solids 4 241
[2] Ishikawa Y, Tajima K, Bloch D and Roth M 1976 Sol. Stat. Comm. 19, 525
[3] Muhlbauer S, Binz, B, Jonietz F, Pfleiderer C, Rosch A,Neubauer A and Georgii R 2009
[4] Ado I, Qaiumzadeh A, Brataas A and Titov M 2020 Phys.Rev. B 101, 161403
[5] Ado I, Tchernyshyov O and Titov M 2020 arXiv:2012.07666v1

Fiber-optic sensor for remote monitoring the γ-radiation of various powers

D S Dmitrieva[1], V V Davydov[2,3] and V Y Rud[3,4]

[1]The Bonch-Bruevich Saint Petersburg State University of Telecommunications, Saint-Petersburg, Russia, 193232
[2]Peter the Great Saint Petersburg Polytechnic University, Saint Petersburg, Russia, 195251
[3]All-Russian Research Institute of Phytopathology, Moscow region, Russia, 14305
[4] The Ioffe Institute, Saint Petersburg, Russia, 194021

e-mail: emilylitov@gmail.com

Abstract. The necessity of improving the metrological characteristics and functional capabilities of the fiber-optic sensor for measurements at the large distances (more than 10 km) is substantiated. The new method for constructing a communication line with the fiber-optic sensor for controlling exposure dose in a large range of its variation (several orders of magnitude) in a remote mode is proposed. The functional capabilities of the sensor are determined; its connection setup and measurement limits are developed. The experimental results are presented.

1. Introduction

The development of scientific and technical progress led to the appearance of large number of facilities, both scientific and technical, which work with using radioactive materials. [1,2]. The number of cases of leakage of radioactive materials (it is entry into the water and the soil, into the atmosphere, etc.), and also release of radiation (mainly γ - radiation) outside the protective zone (through protective screens and overlapping) has increased. [2]. So, this is the reason, why it is important to constant control the radiological situation in the atmosphere and on the territory of various facilities [2].

One of the most actual tasks is remote control of radiological situation (at the distance of 10 km and more) in the automatic mode in a case, when the exposure dose D_R can change by several orders of magnitude in a short period of time. After the exposure dose is terminated, device after some time takes measurements in the normal mode. One of the perspective directions for such measurements is the use of the fiber-optic sensors. Nowadays the developed fiber-optic sensors based on the measurements of the change in the polarization of laser radiation under the influence of γ-radiation can register rather weak D_R changes, which cause decrease in the laser radiation power by 0.05 dB. If D_R has high value, the laser radiation in them is completely damped and the sensor stops working for a long time. The relaxation processes without interventions can take 10^6 s and more, even in the case of small exposure doses of radiation. [3]. So, this is the reason, why the development of new models of the fiber-optic sensors is actual.

2. Remote fiber-optic sensor

Our previously researches of the trunk FOCL [3] allowed to develop the new method of the fiber optic communication lines recovery under γ-radiation influence during its long-term operation. Therefore, it is proposed to connect an optical sensor to the FOCL with a core of pure quartz (the optical fiber 100 m long with a SiO_2 – GeO_2 core with various alloying). The results of measurement of the radiation-induced losses level in sensor when exposure dose of radiation will change are showed at the fig.1 as an example.

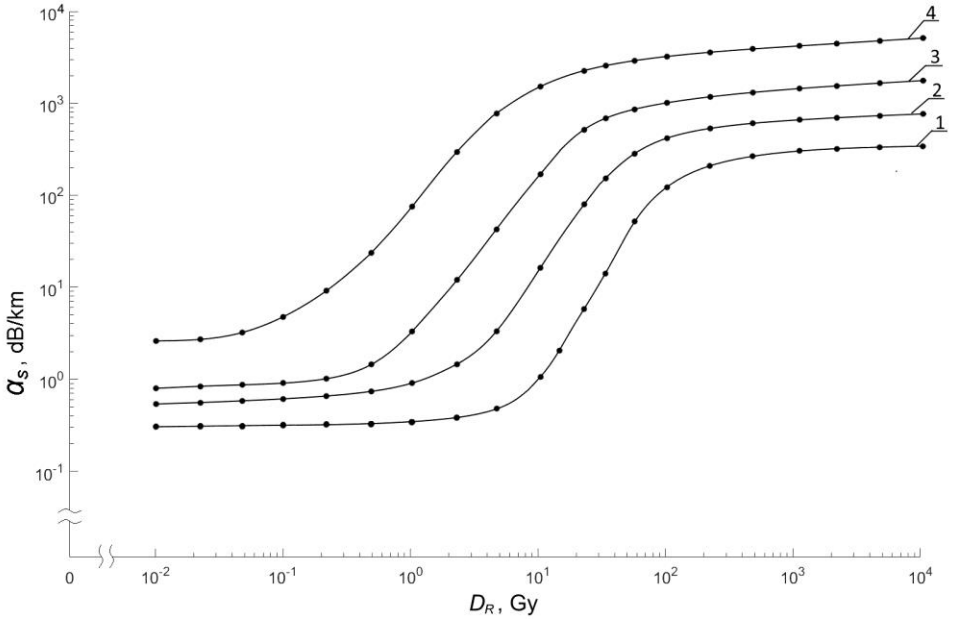

Figure 1. Dependence of the radiation-induced losses α_s with exposure dose D_R at a wavelength λ=1550 nm for a single-mode fiber with a SiO_2 – GeO_2 core at a T = 294.2 K. Charts 1, 2, 3 and 4 are corresponding to different alloying in %: 1.5; 4.0; 10.0 and 20.0.

Analysis of the results shows that the increase of the alloying percent increases the sensitivity of the optical fiber to the exposure dose. It allows to register changes in small D_R values, which decrease the laser radiation power at the FOCL output by 0.2 dB.

3. Conclusion

Obtained experimental results showed the reliable operation of the developed sensor for monitoring the exposure dose from 0.1 to 1000 G in the remote mode with the possibility of operation mode recover with using the additional laser radiation with a wavelength λ=1310 nm, as in the previously developed trunk FOCL [3]. In the optical sensors with measurements, based on the polarization, it is difficult to apply our developed method, because there is high possibility of failure of the photodetectors with increased sensitivity used in them.

References

[1] Davydov R, Antonov V, Makeev S, Batov Y, Dudkin V and Myazin N 2019 *E3S Web of Conferences* **140** 02001

[2] Davydov R, Antonov V and Angelina M 2019 *In Proceedings of the 2019 IEEE International Conference on Electrical Engineering and Photonics, EExPolytech 2019*, vol. **8906791**, pp. 42–45

[3] Dmitrieva D, Pilipova V, Andreeva E, Dudkin V and Davydov V 2020 In Proceedings of ITNT 2020 - 6th IEEE International Conference on Information Technology and Nanotechnology, vol. **9253348**, pp. 34-39

Growth and Optical Properties of The Bixbyite-type Thulium-doped Yttrium Scandate

E Dobretsova*, O Alimov, V Kashin, S Kutovoy, S Rusanov, V Tsvetkov

Prokhorov General Physics Institute of the Russian Academy of Science, 38 Vavilova street, Moscow 119991, Russia

*elenadobretsova89@gmail.com; eadobr@kapella.gpi.ru

Abstract. A crystal fiber of thulium-doped yttrium scandate has been synthesized through laser-heated pedestal growth for the first time. Fluorescence excitation measurements show two complex local positions of Tm^{3+} in the crystal structure.

1. Introduction.

Yttrium scandate, $YScO_3$, has polymorphic nature. The high-temperature modification belongs to the bixbyite-type cubic structure (space group *Ia*3) [1] like yttria (Y_2O_3) [2] and scandia (Sc_2O_3) [3]. In the bixbyite-type structure there are one position for the oxygen atom and two symmetrically independent positions for cations: 8*b* site (C_{3i} symmetry) and 24*d* site (C_2 symmetry). The unit cell contains three cations in the C_2 site and one in the C_{3i} site. Two types of 6-vertex polyhedra share corners and edges to form a chessboard packing, derived from the fluorite structure type [4, 5]. There are additional free cavities of octahedral shape in the structure that may serve as a reservoir for the insertion of Tm atoms.

Nd lasers have been already realized successfully in the $YScO_3$ [6] and isostructural $(Lu_{1-x}Sc_x)_2O_3$ seqioxide [7]. Moreover, due to broadened luminescence lines disordered active media have promising applications in ultrafast lasers and their further chirped pulse amplification [8, 9].

2. Results and discussion.

Here we report the characterization of the Tm^{3+}-doped $YScO_3$ crystal fiber obtained through the laser-heated pedestal growth (LHPG) [5, 10, 11]. The method is characterized with the high temperature of heating and following quick cooling. The spectral-kinetic characteristics of the Tm^{3+}: $YScO_3$ crystal fibers were measured under selective laser excitation and luminescence determination. Figure 1 shows the luminescence excitation spectra for two neighboring fluorescence lines for the crystal fiber at low temperature (T = 77 K). However, the electric dipole−dipole transitions are forbidden for rare-earth ions placed in C_{3i} sites due to inversion symmetry, and the luminescence from these centers must be absent. Well-resolved fluorescence from two types of Tm^{3+} local centers observed with comparable intensities might be responsible for decreasing of local symmetry due to the substitution of Y^{3+} for Tm^{3+} ions in the C_{3i} site, or inclusion of the Tm^{3+} ions in the octahedral voids between the basic polyhedra.

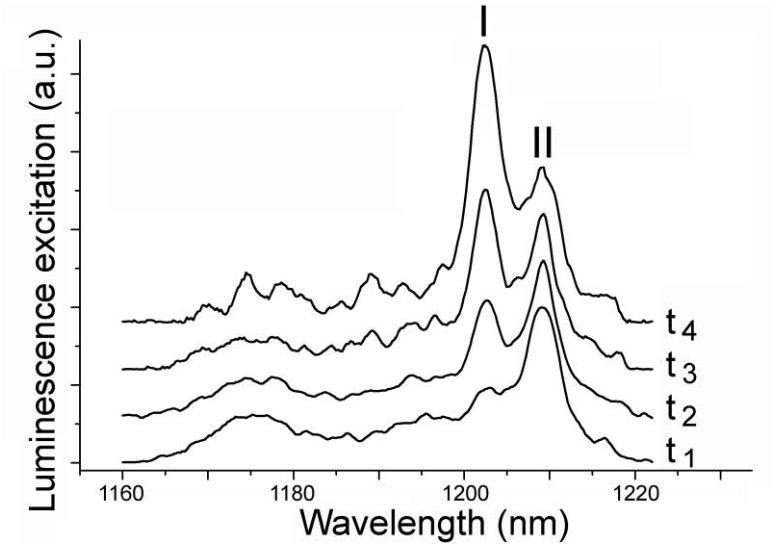

Figure 1. Luminescence excitation spectra of Tm: $YScO_3$ (decay times: t_1 = 0.6 ms, t_2 = 6 ms, t_3 = 10 ms, t_4 = 12 ms).

References

[1] Clark J, Richter P and Du Toit L 1978 *J. Solid State Chem.* **23** 129

[2] Hanic F, Hartmanová M, Knab G, Urusovskaya A and Bagdasarov K S 1984 *Acta Crystallogr.B* **40** 76

[3] Geller S, Romo P and Remeika J 1967 *Z. Kristallogr. Cryst. Mater.* **124** 136

[4] Moore P and Araki T 1976 *Am. Mineral.* **61** 1226

[5] Alimov O, Dobretsova E, Guryev D, Kashin V, Kiriukhina G, Kutovoi S, Rusanov S, Simonov S, Tsvetkov V, Vlasov V, Voronov V and Yakubovich O 2020 *Cryst. Growth Des.* **20** 4593

[6] Bagdasarov K, Kaminskii A, Kevorkov A, Li L, Prokhorov A, Tevosian T and Sarkisov S 1975 *Dokl. Akad. Nauk SSSR* **224** 798

[7] Reichert F, Fechner M, Koopmann P, Brandt C, Petermann K and Huber G 2012 *Appl. Phys. B* **108** 475

[8] Liu W, Lu D, Pan S, Xu M, Hang Y, Yu H, Zhang H and Wang J 2019 *Cryst. Growth Des.***19** 3704

[9] Liu W, Lu D, Guo R, Wu K, Pan S, Hang Y, Sun D, Yu H, Zhang H and Wang J 2020 *Cryst. Growth Des.* **20** 4678

[10] Bufetova G, Kashin V, Nikolaev D, Rusanov S, Seregin V, Tsvetkov V, Shcherbakov I and Yakovlev A 2006 *Quantum Electron.* **36** 616

[11] Feigelson R S 1986 *J. Cryst. Growth* **79** 669

Electrical resistivity, magnetotransport and optical properties of WTe_2 single crystal before and after quenching

A N Domozhirova[1], S V Naumov[1], A A Makhnev[1], E I Shreder[1], S M Podgornykh[1], E B Marchenkova[1], V V Chistyakov[1], J C A Huang[2], and V V Marchenkov[1,3]

[1]M.N. Mikheev Institute of Metal Physics, UB RAS, 620108 Ekaterinburg, Russia
[2]National Cheng Kung University, 70101 Tainan, Taiwan
[3]Ural Federal University, 620002 Ekaterinburg, Russia

Abstract. The electrical resistivity, magnetoresistivity, and Hall effect of tungsten ditelluride before and after quenching were investigated in the temperature range from 2 K to 300 K and in magnetic fields of up to 9 T; the optical properties were studied at room temperature. Relatively small changes were revealed in the transport properties of the quenched sample, in particular, in the electrical resistivity value, which is associated with an increase in the number of defects of the sample after heat treatment. At the same time, it is assumed that no changes in the electronic structure occur.

1. Introduction

Quasi-two-dimensional transition metal dichalcogenides (TMDs) are currently of great interest, since they can exhibit novel physical properties and are promising materials for optoelectronics, nanoelectronics and spintronics.TMDs represent a family of compounds with the chemical formula MX_2 where M is a transition metal, X is a chalcogen. Some of which, such as tungsten and molybdenum ditellurides, exhibit the properties of topological Weyl semimetal (TWS). These materials possess unique quasiparticles, chiral massless Weyl fermions, which always appear in pairs and are topologically protected. The electronic band structure is characterized by linear dispersion along three momentum directions near Weyl points. And special surface states, Fermi arcs, connect the projections of Weyl points with opposite chirality on the surface Brillouin zone. Topologically non-trivial materials can exhibit remarkable electronic properties such as non-saturated large magnetoresistance, ultrahigh mobility of charge carriers, spin-polarized transport, superconductivity, etc. Therefore, they attract great attention of researchers in the field of physics and materials science.

In addition, there are TMDs, which can crystallize in various structures, exhibiting drastically different properties. For example, $MoTe_2$ exists in $2H$ (hexagonal), $1T'$ (monoclinic), and T_d (orthorhombic) structures, where $2H$ phase is semiconductor, whereas $1T'$ and T_d phases are semimetal. In order for the semiconductor-semimetal transition in $MoTe_2$ to occur, quenching from a temperature of ~ 900°C must be performed. Finally, the transition from the $1T'$ to T_d phase takes place when semimetallic $MoTe_2$ is cooling below 250 K. Orthorhombic $MoTe_2$ is known to exhibit TWS properties as well as its isomorphic analogue WTe_2. Therefore, it is interesting to trace how heat treatment affects the structure and properties of tungsten ditelluride. In this work, we investigated the electrical resistivity, magnetoresistivity, Hall effect and optical properties of WTe_2 before and after quenching.

2. Experimental

Tungsten ditelluride single crystals were grown by the chemical vapour transport method [1]. XRD analysis revealed that WTe_2 have an orthorhombic structure with the space group $Pmn2_1$ and lattice parameters a = 3.435(8) Å, b = 6.312(7) Å, and c = 14.070(4) Å. Grown single crystals were quenched from 900°C in water. XRD analysis showed no significant changes in the crystal structure of WTe_2 after quenching. The chemical composition of the samples and microstructure of their surface were investigated using a FEI Inspect F SEM equipped with an EDAX attachment.

Electrical resistivity, magnetoresistivity and Hall effect were measured by the four-probe technique in the temperature range from 1.8 K to 300 K in magnetic fields of up to 9 T using a PPMS-9 system (Quantum Design) in the Collaborative Access Center "Testing Center of Nanotechnology and Advanced Materials", IMP UB RAS. An electric current flowed in the *(00l)* plane of the sample and a magnetic field was directed perpendicular to it. The optical properties were measured using the Beattie method with one reflection from the *(00l)* plane in the spectral range of 0.2–5.0 eV at room temperature.

3. Results and Discussion

SEM studies of the surface microstructure showed that WTe_2 has a layered structure both before and after quenching; however, additional heat treatment leads to an increase in the number of defects in the sample. It is assumed that this can affect the transport properties of the single crystal.

The temperature dependence of the electrical resistivity $\rho(T)$ of WTe_2 shows a “metallic” behaviour with ρ increasing monotonically with temperature from 20 to 860 μOhm·cm according to a quadratic law at low temperatures (T < 60 K). A similar T^2-dependence has been observed in the related compound T_d-$MoTe_2$ in [2]. Quenching does not cause large changes in resistivity behaviour; only a relatively small increase in its value (<65%) is observed, which is associated with the scattering of current carriers by defects arising after heat treatment. Whereas in $MoTe_2$, strong changes in the behaviour and value of the resistivity were detected (8 orders of magnitude at low temperatures) [3]. When a magnetic field is turned on, a “metal-insulator” transition is observed inWTe_2, a temperature of which increases in higher magnetic fields. The magnetoresistivity reaches 1750% (T = 2 K, B = 9 T). The data on the Hall effect allowed us to conclude that the majority charge carriers are electrons with the concentration ~ 10^{19} cm^{-3} and the mobility 7500 $cm^2/V \cdot s$ at T = 2 K. Optical studies showed that, the optical conductivity spectrum $\sigma(E)$ is one broad band centered at 3.4 eV, formed by interband transitions. In the infrared region of the spectrum, low values of the imaginary part ε_2 and positive values of the real part ε_1 of the complex permittivity indicate the absence of the contribution from free carriers in the investigated spectral region. No considerable differences in the optical properties of the sample before and after quenching indicates the absence of changes in the electronic structure.

Thus, relatively small changes were revealed in the transport properties of WTe_2 before and after quenching, in particular, in the resistivity value, which is associated with an increase in the number of defects after heat treatment. At the same time, there are no changes of the electronic structure.

Acknowledgments

The research was carried out within the state assignment of the Ministry of Education and Science of the Russian Federation (theme “Spin”, No. AAAA-A18-118020290104-2 and theme “Electron”, No. AAAA-A18-118020190098-5), supported in part by RFBR (project No. 20-32-90069) and the Government of Russian Federation (Decree No. 211, Contract No. 02.A03.21.0006).

References

[1] Domozhirova A N, Naumov S V, Podgornykh S M, Marchenkova E B, Chistyakov V V, Semiannikova A A, Huang J C A, and Marchenkov V V 2021 *J. Phys.: Conf. Ser.* to be published

[2] Zandt T, Dwelk H, Janowitz C, and Manzke R 2007 *Journal of Alloys and Compounds* **442** 216

[3] Marchenkov V V *et al.* 2020 *J. Phys.: Conf. Ser.* **1695** 012144

Star calibration of the single-photon receiver for satellite-to-ground QKD

A V Khmelev[1,2], A V Duplinsky[1,5], V L Kurochkin[1,3,4], and Y V Kurochkin[1,2,3,4]

[1]QRate, Novaya av. 100, Moscow, Russia
[2]Moscow Institute of Physics and Technology, 9 Institutskiy per., Dolgoprudny, Moscow Region, 141701, Russian Federation
[3]NTI Center for Quantum Communications, National University of Science and Technology MISiS, Leninsky prospekt 4, Moscow 119049, Russia
[4]Russian Quantum Center, Bolshoy Boulevard 30, bld. 1, Skolkovo, Moscow 121205, Russia
[5]Bauman Moscow State Technical University, Moscow, Baumanskaya 2-ya, 5/1, 105005, Russian Federation

{a.khmelev, al.duplinsky, v.kurochkin, yk}@goqrate.com

Abstract. Currently, the challenge is to deploy large-scale quantum communication networks with a communication range of thousands kilometres. It is convenient to use single photons as carriers of quantum states, and to encode information in the phase, time interval or polarization of a particle. The most common types of such systems use optical fiber, which imposes restrictions on the range of operation, as well as narrows the potential range of consumers. Another way is to use free-space optical technologies which expand the capabilities of traditional fiber systems.

1. Implementation of satellite QKD

Quantum key distribution (QKD), the technology that allows secure communication immune against future advances in computational power, is now being deployed on a large geographic scale. The transfer of photon states is possible either through optical fiber[1,2] or through open space.

Distribution of secret keys over optical fiber causes the losses of quantum states that increase exponentially with the distance that significantly limits the speed and range of secure key distribution over long distances. At the same time, experiments in open space are carried out both along the earth's surface using telescopes[3], drones[4], and between an artificial satellite and ground stations[5]. Thus, satellite quantum key distribution as a new method to share secret information for extra long distances can be the realization of an alternative way to the fiber optic distribution.

2. Star calibration and free-space QKD receiver

Here, we report the ground receiver for downlink quantum key distribution with satellite. An optical part of this system including an active tracking loop is mounted on a 600-mm Ritchey-Chretien telescope and permits to distinguish polarization states in two mutually unbiased bases and to perform QKD between ground and satellite. Moreover, a procedure of calibration the receiver using stars with known

brightness is presented. It is crucial to have the highest possible level of useful signal during the entire communication session with the satellite. Consequently, we measure the photon count rate of bright stars in the spectral range of 845nm ~ 855nm and compare it with an estimate.

Thus, our ground station demonstrates the optical efficiency in accordance with the expectation. So, the value is equal to 6-9% depending on the weather conditions, and the results take into account factors as an obstruction of the secondary mirror, atmosphere transmission, and quantum efficiency of detectors.

Acknowledgments
This work was supported by The Russian Science Foundation (Grant No. 17-71-20146)

References
[1] Chen, J.-P. et al. Sending-or-not-sending with independent lasers: secure twin-field quantum key distribution over 509 km. Phys. Rev. Lett. 124, 070501 (2020).
[2] Chen, YA., Zhang, Q., Chen, TY. et al. An integrated space-to-ground quantum communication network over 4,600 kilometres. Nature 589, 214–219 (2021).
[3] Christopher J Pugh et al 2017 Quantum Sci. Technol. 2 024009
[4] Hua-Ying Liu et al. Drone-based entanglement distribution towards mobile quantum networks, National Science Review, Volume 7, Issue 5, May 2020, Pages 921–928,
[5] Liao, S.-K. et al. Satellite-to-ground quantum key distribution. Nature 549, 43–47 (2017).

Characterization of telecom focusing grating couplers in the first and second diffraction order

A Elmanova[1], I Elmanov[1], P An[1,2], V Kovalyuk[1,2], A Kuzin[1,4], A Golikov[3], G Goltsman[1,2,3]

[1]Department of Physics, Moscow Pedagogical State University, 119992, Russia
[2]FRC Institute of Applied Physics RAS, 603950 Nizhny Novgorod, Russia
[3]National Research University Higher School of Economics, Moscow 101000, Russia
[4]Skolkovo Institute of Science and Technology, 121205, Russia

Abstract. In this work we have studied how the focusing grating couplers, designed for infrared spectral range, can be used in visible range. We have compared our experimental results with numerical modeling. The work is important for different photonic applications.

1. Introduction

Focusing grating couplers (FGCs) have found their wide application for input/output of radiation due to the well-developed CMOS processing together with waveguides, as well as flexible footprint in any place of the nanophotonic chip. Such couplers have efficient filtering of light in the selected spectral range, usually corresponding to the first order of interference. However, for a number of quantum applications, for example, quantum key distribution or linear optical quantum computing, in order to reduce parasitic illumination the coupler efficiency in higher diffraction orders should be known. In this work, the spectra of FGCs, developed for telecom operation 1550 nm, in the first and second diffraction order was studied.

2. Device design and fabrication

For device fabrication we used commercially available silicon substrates with SiO_2=2.6 μm and Si_3N_4=450 nm layers atop. From the one step of e-beam lithography (Crestec, CABL-9050C) followed by half etching with reactive ion etching (RIE) in CHF_3 atmosphere for device finalizing. General view of the device is shown in Fig.1a and the microphotograph one of the FGC is given at Fig.1b. The device consists of two FGCs with period 1.086 μm and filling factor 0.7, connected via silicon nitride waveguide

3. Experimental setup and results

In this work, we used two experimental setups for measuring the transmission spectra of nanophotonic devices. The firs setup for measurements at telecom wavelengths consists of a tunable laser (NewFocus TLB-6600 with tune range 1510-1620 nm), a polarization controller, 3D stage with piezo motors, a fast photodetector, as well as a fast analog-to-digital converter.

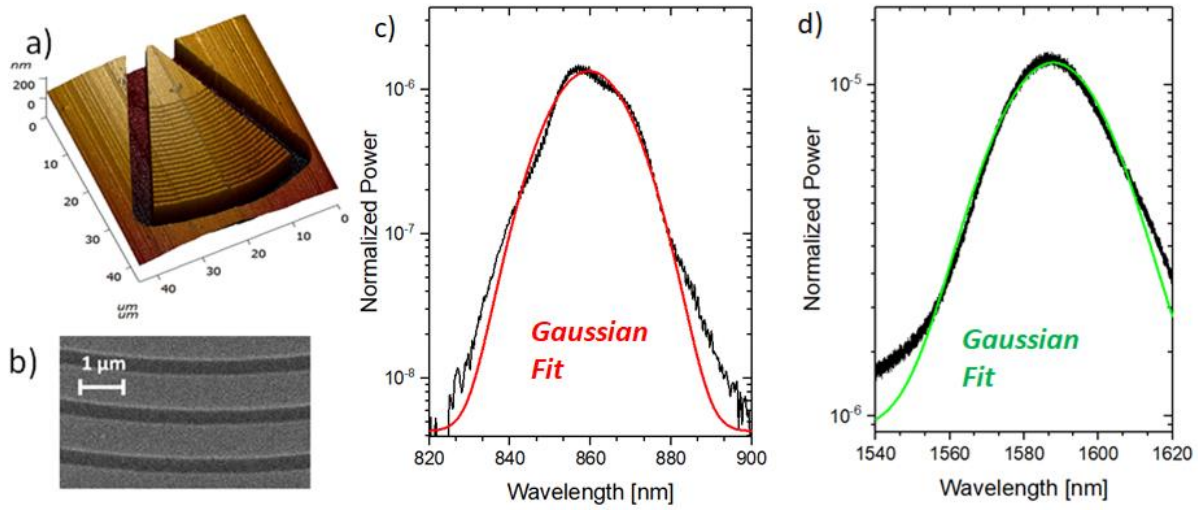

Fig.1. (a) Atomic force microscope scan of one studied FGC. **(b)** Scanning electron microscope image of one FGC. **(c)** Normalized transmission of the coupler near 850 nm wavelength. **(d)** Normalized transmission of the coupler in telecom wavelength range.

The second setup consisted of the broadband fiber-coupled super continuum source (Leucos Rock 400 4) and the spectrum analyzer (Maya 2000 Pro). The experimental results obtained by set up for telecom wavelength (1.55 µm) and is shown in Fig. 1. The results obtained were approximated using Gaussian Amplitude Fit, the full width half maximum (FWHM) values were calculated from the approximation parameters using the formula

$$FWHM = 2w\,(\ln 4)^{1/2}. \quad (1)$$

Here w is an approximation parameter. Therefore, for infrared range we got FWHM = 35.428 nm and for visible FWHM = 20.193 nm.

4. Conclusions

We have studied the performance of FGCs designed for telecommunications wavelengths in the visible range. This work is of significant importance for research and work with quantum emitters, for using pumping at a wavelength of shorter than radiation, thus filtering pumping from radiation, and studying the emission spectra of nanophotonics devices in two different wavelength ranges.

Acknowledgements

The research was performed by support of Ministry of the Russian Science Foundation grant No. 19-72-10156 experimental study.

References

[1] Quaranta G, et al 2018 *Laser Photonics Rev.* **12** 1800017

[2] Cheng L, et al 2020 *Micromachines* **11** 666

Structure and spectral properties of Fe:$ZnAl_2O_4$ transparent glass-ceramic and ceramic

K Eremeev[1,*], L Basyrova[2], O Dymshits[3], S Balabanov[4], A. Belyaev[4], I Alekseeva[3], A Khubetsov[3], M Tsenter[3], A. Zhilin[3], V Popkov[5], P Loiko[2]

[1]Saint-Petersburg State Institute of Technology, 26 Moscovsky Pr., 190013 St. Petersburg, Russia
[2]Centre de Recherche sur les Ions, les Matériaux et la Photonique (CIMAP), UMR 6252 CEA-CNRS-ENSICAEN, Université de Caen Normandie, 6 Boulevard du Maréchal Juin, 14050 Caen Cedex 4, France
[3]S.I. Vavilov State Optical Institute, 36 Babushkina St., 192171 St. Petersburg Russia
[4]G.G. Devyatykh Institute of Chemistry of High-Purity Substances of the Russian Academy of Sciences, 49 Tropinin St., 603950 Nizhny Novgorod Russia
[5]Ioffe Institute, 26 Politekhnicheskaya St., 194021 St Petersburg, Russia

E-mail: kirilleremeev42@gmail.com

Abstract. Transparent glass-ceramics based on iron-doped $ZnAl_2O_4$ (gahnite) nanocrystals were prepared by melt-quenching (at 1580 °C) with subsequent heat-treatments (at 720 – 1050 °C). Polycrystalline transparent Fe:$ZnAl_2O_4$ ceramic was synthesized by hot pressing of powders (at 1600 °C, 50 MPa) using the sintering additive, ZnF_2. A comparative study of the structure, Raman spectra and absorption properties of these materials was performed.

1. Introduction

Gahnite ($ZnAl_2O_4$) is a promising optical material belonging to the family of spinels, AB_2O_4. It is very suitable for doping with transitions metal ions [1]. Divalent iron ions (Fe^{2+}) are of interest because of their broadband absorption extending into the mid-infrared [2]. The growth of gahnite crystals is rather complex. Thus, it is relevant to develop other $ZnAl_2O_4$-based transparent materials, such as transparent nanophase glass-ceramics (GCs) and ceramics. In the present work, we report on the fabrication of such materials doped with iron ions, as well as their structure and optical properties.

2. Results and discussion

The glass of the ZnO-Al_2O_3-SiO_2 system nucleated by TiO_2 was doped with 1.0 mol% FeO and melted at 1580 °C. Transparent gahnite-based GC was prepared from the glass by a two-stage heat-treatment at 720 °C and at 1050 °C (duration of each stage is 6 h). Transparent $ZnAl_2O_4$ ceramic doped with 1.0 at.% Fe was fabricated by hot pressing of powders at a temperature of 1600 °C and a pressure of 50 MPa using ZnF_2 as a sintering additive.

Scanning electron microscopy (SEM) revealed a close-packed microstructure of ceramic, Fig. 1(a). Intense peaks in the XRD pattern of the ceramic, Fig. 1(b), belong to gahnite, $ZnAl_2O_4$, with a cubic structure (sp. gr. $Fd\bar{3}m$). The unit cell parameter of gahnite ceramic a is 8.12 Å. The increased a value as compared with that for undoped $ZnAl_2O_4$ (a = 8.088 Å) indicates a certain degree of inversion. A comparison of the XRD patterns of the GC and ceramic revealed that they differ in phase composition,

size and fraction of gahnite crystals. The XRD pattern of the GC shows broad peaks of gahnite, broad peaks of low intensity due to rutile, TiO_2, and a weak halo due to the residual highly siliceous glass phase. The mean size of gahnite nanocrystals in the GC is 18 nm and their unit cell parameter **a** is 8.098 Å, also manifesting a certain degree of inversion. The average size of rutile crystals is 39 nm. The volume fraction of gahnite in the GC is about 40%. The complex phase composition of the GC is also revealed in its Raman spectrum, see Fig. 1(c).

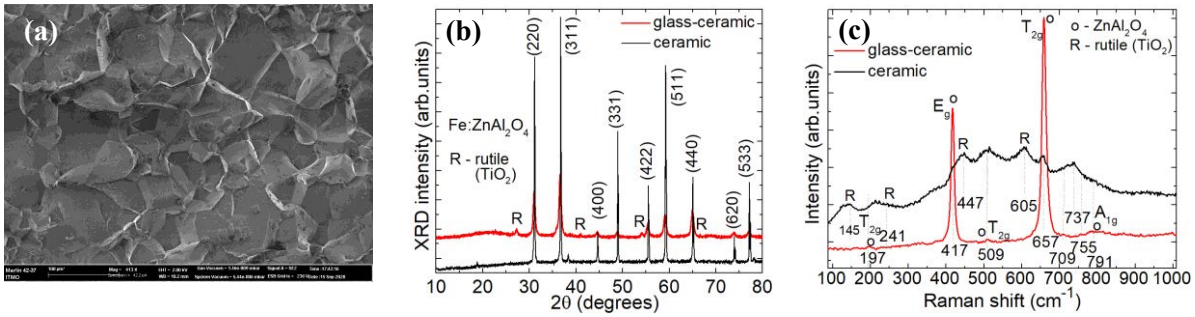

Figure 1(a-c). Structural characteristics of Fe:$ZnAl_2O_4$-based transparent GC and Fe:$ZnAl_2O_4$ ceramic: **(a)** SEM image of the fracture surface of ceramic; **(b)** XRD patterns, **numbers** denote the Miller's indices (**hkl**); **(c)** Raman spectra, λ_{exc} = 514 nm.

The absorption spectra of both the GC and ceramic demonstrate absorption of Fe^{2+} ions in tetrahedral (T_d) sites in gahnite crystals due to the $^5E \rightarrow {}^5T_2(^5D)$ transition, Fig. 2. The inversion of Fe:$ZnAl_2O_4$ is confirmed by absorption of Fe^{2+} ions in octahedral (O_h) sites (the$^5T_2(^5D) \rightarrow {}^5E$ transition). The profound red-shift of the UV absorption edge for the GC as compared with that of the ceramic is due to intervalent and charge-transfer transitions in multiphase GC.

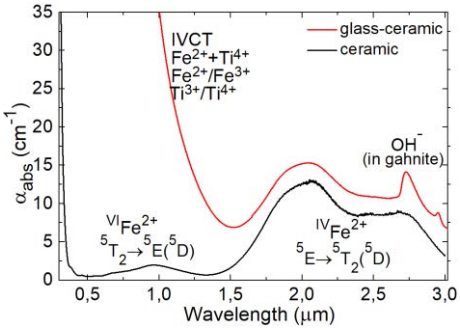

Figure 2. Absorption spectra of Fe:$ZnAl_2O_4$-based transparent GC and Fe:$ZnAl_2O_4$ ceramic.

3. Conclusion

Transparent materials based on iron-doped gahnite (a glass-ceramic and a ceramic) were prepared. Their structure and spectral properties were evaluated and compared. A broad absorption band at 1.5-3 μm due to the $^5E \rightarrow {}^5T_2(^5D)$ transition of Fe^{2+} ions in T_d sites in gahnite crystals makes these materials promising for saturable absorbers of lasers emitting in the short-wave infrared spectral range.

Acknowledgment

This work was partly supported by the RFBR (Grant 19-03-00855).

References

[1] Loiko P, Belyaev A, Dymshits O, Evdokimov I, Vitkin V., Volkova K, Tsenter M, Volokitina A., Baranov M, Vilejshikova E, Baranov A, Zhilin A 2017 **J. Alloys Compd. 725** 998

[2] Mirov S, Fedorov V, Moskalev I, Martyshkin D, Kim C 2010 **Laser Photon Rev. 4** 21

Features of the fiber-optics data system using optical solitons

A A Ermolaev[1], **M A Shevchenko**[1], **E I Andreeva**[1]

[1]The Bonch-Bruevich Saint-Petersburg State University of Telecommunications, St.Petersburg 193232, Russia

e-mail: artur_ermolaev1999@mail.ru

Abstract: The analysis of the parameters of a high-speed information data system using dispersion-managed solitons is carried out. It is shown that the quality of information transmission can be increased by choosing the input-output point of the symbol sequence on the dispersion map.

1. Introduction

Soliton information transmission systems are distinguished by high reliability of information transmission [1-5]. Various variants of the soliton-like regime are used depending on the specific problem. The classical regime of the fundamental soliton provides a high speed in the transmission channel but requires a relatively high peak power of symbol pulses. The use of wavelength division multiplexing is hindered by the effect of the interaction of solitons. Pass-average solitons suitable for long hop systems but has symbol width limitations. For high-speed WDM systems, it is advisable to use the dispersion-managed soliton mode. The distinguishing feature of this mode is the low threshold level forming soliton in an optical fiber, which ensures a low level of inter-channel interference. To implement this mode, the topology of a dispersion map (Figure 1b) with alternating segments with a dispersion β_2 of opposite signs is used. Along the segment length, the parameters of the soliton pulse, such as the pulse duration $T(z)$, the frequency chirp $C(z)$, experience periodic changes, keeping their values T_o and C_o at the segment boundary (Figure 1a).

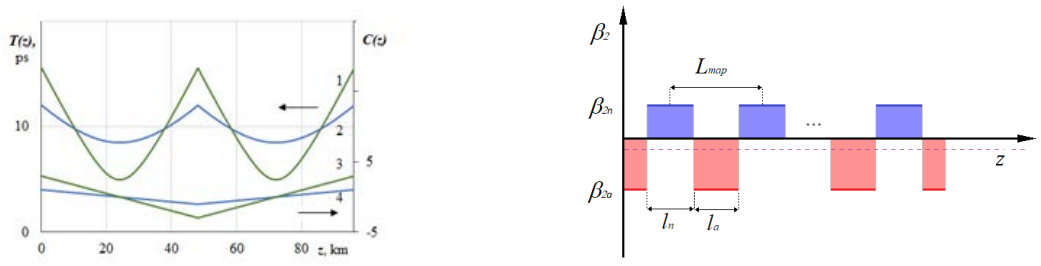

a) *b)*

Figure 1(a, b). Spatial dynamics of changes in the pulse width $T(z)$ (1 - 2) of a soliton and a chirp $C(z)$ (3 - 4) at $C_o = 1$ (1, 3) and $C_o = 3$ (2, 4) (a) on the period of the dispersion map $l_a = l_n = 48$ km, $|\beta_2| \cong 3$ ps^2/km (b).

The dispersion map parameters largely determine the bit rate. However, with the given parameters of the dispersion map, it is possible to select the parameters of the symbol pulse (Figure 2), providing a higher bit rate and higher SN-ratio in the system. For this, a differential dispersion map is used, which makes it possible to input / output data at the midpoint of the segment, the so-called point of zero chirp, where the pulse width takes on a minimum value.

As shown by computer simulation with the OptiSystem-program, with an initial value of C_o = 1 and entering the middle of a segment with anomalous dispersion, the value of the Q - parameter increases by 3 times. An increase in the initial energy E_o of the pulse and, accordingly, an increase in C_o = 3 additionally increases the Q - parameter. However, a further increase in these values C_o already leads to a decrease in the value of the Q - parameter since the pulse duration at the segment boundary and the interaction of solitons significantly increase.

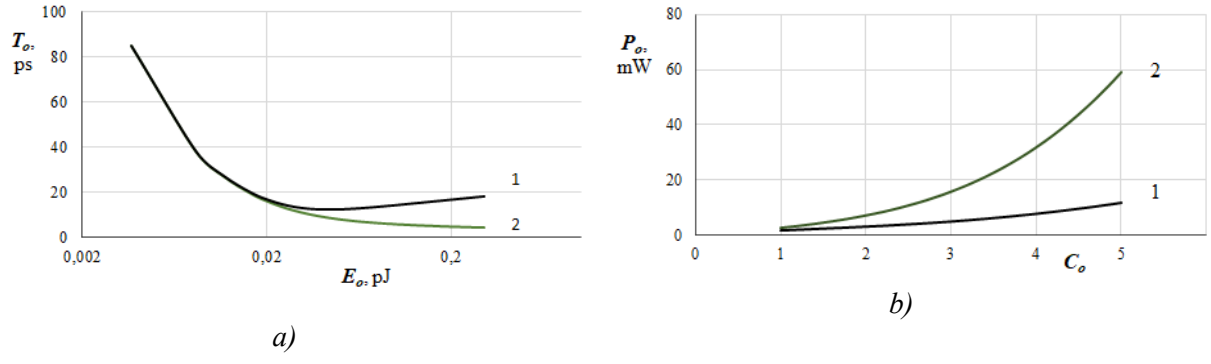

Figure 2. a) Dependence of the pulse width T_o at the boundary of segments with different dispersion (1) and the width T_{min} (2) in the middle of the segment on the initial energy E_o of the soliton pulse, **b)** symbol pulse power P_o at the initial value of the chirp C_o.

2. Conclusion

The computer simulation of the fiber-optic data transmission system using optical solitons has been carried out. It is shown that when constructing the system with a dispersion map, which assumes input-output of spectrally limited pulses, the quality of data transmission increases. The optimal parameters of such a system can be chosen.

References

[1] Andreeva E I, Bylina M S, Glagolev S F, Chaimardanov P A 2018 *Proceedings of Telecommunication Universities* V 1 P 5–12

[2] Shcherbakov A S, Andreeva E I 1996 *Performance data of lengthy-span soliton transmission system Optical Fiber Technology* V 2 P 127-133

[3] Agrawal G 2013 San Diego USA *Nonlinear Fiber Optics* 5th Academic Press

[4] Kivshar Y, Agrawal G 2003 New York USA *Optical solitons. From Fibers to Photonic Crystals* The Institute of Optics University of Rochester

[5] Andreeva E I, Bylina M S, Glagolev S F, Chaimardanov P A 2018 *Proceedings of Telecommunication Universities* V 2 P 26–35

Simulation of the photonic nanojet effect for Raman scattering enhancement in the diagnostics of oxide films

A I Ivanina[1], D S Agafonova[1]
[1] Saint Petersburg Electrotechnical University «LETI», Department of Photonics, Saint Petersburg 197376, Russia

aiivanina@stud.etu.ru, dsagafonova@gmail.com

Abstract. Raman light scattering is a powerful and highly selective tool that allows you to identify the chemical composition and determine the features of materials. The effect of photonic nanojets can significantly enhance the effects of Raman spectroscopy, which in turn is of great interest for practical developments in a wide range of fields, including for the diagnosis of metal oxide films. The aim of this work is to study the effect of microspheres on the enhancement of Raman scattering on films ZnO and PZT. The optimal wavelengths for amplification of the electromagnetic field were found.

1. Introduction

Raman spectroscopy is a method of molecular spectroscopy based on the interaction of light with matter. It can be used to obtain information about the chemical composition and phase transition of the material under study. [1]. Several mechanisms are used to improve the Raman signal, in this work we will consider amplified Raman signal using the photonic nanojet effect. Individual microparticles and arrays of microparticles can enhance the intensity of the light incident on them, working as a focusing lens. When the particles are irradiated with light, a local amplification of the electromagnetic field is formed behind the shadow surface of the particle. In [2], the enhancement of Raman scattering due to the use of nanojet on silicon dioxide particles is demonstrated, and it is shown that the most effective enhancement occurs when the particle diameter is equal to the size of the incident radiation spot. In [3], the amplified Raman scattering of light using individual polystyrene microspheres was investigated, and it was found that the maximum amplification occurred when the sphere was approximately equal to the size of the incident beam.

2. Aims and Methods.

In this work, the possibility of amplifying Raman scattering using microspheres for the diagnosis of thin metal oxide films is investigated. The following materials were selected for the manufacture of microspheres: silicon dioxide and barium titanate. Zinc oxide and lead zirconate-titanate (PZT) were taken as metal oxide films. Zinc oxide films are of interest as conducting transparent and barrier layers in optoelectronics, in particular, in solar energy, the conductive and optical properties of which are modified by doping and special surface treatment [4]. Films of PZT are characterized by a wide

variability of properties depending on the composition and can crystallize in different phases [5], which differ in refractive indices.

The study of the possibilities of amplifying Raman scattering using microspheres was carried out by numerical simulation in the COMSOL Multiphysics software. A Gaussian beam was modelled, the beam width of which corresponds to the dimeter of the spheres. The diameter of the spheres ranged from 1 μm to 40 μm. Simulation in a wide range of wavelengths to show the results, three values of the most common laser sources were selected: $\lambda_1 = 422\,nm, \lambda_2 = 532\,nm,\ \lambda_3 = 632\,nm$. The effect of photonic nanojet was achieved by focusing a Gaussian beam through microspheres. The materials used for the microspheres were chosen from easily available materials on the market with a low cost. Materials with different refractive indices were selected: silicon dioxide ($n_1 = 1.5$) and barium titanate ($n_2 = 1.9$). In the simulation, medium host – air ($n_0 = 1$). Investigated sample: ZnO and PZT films in the pyrovskite and pyrochlore phases. The thickness of the films varied from 0.2 microns to 1 micron.

3. Results

As a result of the simulation, a picture of the field distribution was obtained ($E_0 = 1$ В/м). One of the results of numerical field amplification for particles with a diameter of 10 microns is given. For a barium titanate (BaTiO3) microsphere with a sample ZnO $\lambda_1 = 422\,nm, \mathrm{E} = 5.38\,\mathrm{V/m}$; $\lambda_2 = 532\,nm, \mathrm{E} = 4.9\,\mathrm{V/m}$; $\lambda_3 = 632\,nm, \mathrm{E} = 4.4\,\mathrm{V/m}$. BaTiO3 with sample PZT (pyrochlore): $\lambda_1 = 422\,nm, \mathrm{E} = 6.22\,\mathrm{V/m}$; $\lambda_2 = 532\,nm, \mathrm{E} = 4.96\,\mathrm{V/m}$; $\lambda_3 = 632\,nm, \mathrm{E} = 4.84\,\mathrm{V/m}$. For a silicon dioxide (SiO2) microsphere with a sample ZnO: $\lambda_1 = 422\,nm, \mathrm{E} = 4.72\,\mathrm{V/m}$; $\lambda_2 = 532\,nm, \mathrm{E} = 3.98\,\mathrm{V/m}$; $\lambda_3 = 632\,nm, \mathrm{E} = 4.2\,\mathrm{V/m}$. SiO2 with a sample PZT (pyrochlore): $\lambda_1 = 422\,nm, \mathrm{E} = 3.97\,\mathrm{V/m}$; $\lambda_2 = 532\,nm, \mathrm{E} = 4.01\,\mathrm{V/m}$; $\lambda_3 = 632\,nm, \mathrm{E} = 3.42\,\mathrm{V/m}$.

In each variant of the simulation (particle – sample), an increase in the electromagnetic field was observed. The highest intensity is achieved when the particle is illuminated by light with wavelengths in the UV region of the spectrum. The study on particles with different refractive indices showed that the greatest gain can be achieved if the difference between the refractive index of the particle and the refractive index of the sample is minimal.

4. Conclusions

In this paper, it was demonstrated using numerical simulations that it is possible to achieve Raman scattering amplification using microspheres for the diagnosis of metal oxide films. The formation of Gaussian beams and photonic nanostructures in air is studied at various parameters of radiation, the refractive index of the microsphere, the diameter of the microsphere, and the refractive index of the film under study. With the correct selection of the radiation wavelength, the refractive index of the microsphere and the refractive index of the film, it is possible The method of using the photonic nanostructure effect is simple, economical, and can provide field amplification for registering Raman scattering.

References

[1] A Darafsheh. Photonic nanojets and their applications, *J. Phys. Photonics 3* (2021).

[2] K J Yi, H Wang, H Lu, Y.F Yang, Enhanced Raman scattering by self-assembled silica spherical microparticles. *Appl. Phys*. (2007).

[3] C L Du, J Kasim, Y M You, D N Shi, Z X. Shen, Enhancement of Raman scattering by individual dielectric microspheres *J. Raman Spectrosc*. Vol 42, p145-146. (2011)

[4] V P Afanasjev, N V Mukhin, D N Redka Surface Modification of ZnO by Plasma and Laser Treatment *Ferroelectrics.* 2017. V. 508, No 1. P. 124–129.

[5] N. V Mukhin Investigation of the formation kinetics of grain boundary inclusions of lead oxide in lead zirconate-titonate films *Glass Physics and Chemistry.* 2016. V. 42, No 1. P. 64–69.

Polarization-sensitive terahertz spectroscopy of graphene nanostructures

A Kvitsinskiy[1], M Rybin[2], A Zaitsev[1], K Bogdanov[1], D Zykov[1], and E Obraztsova[2,3]

[1] ITMO University, 49 Kronverkskiy Prospekt, Building A, Saint Petersburg, 197101, Russian Federation
[2] Prokhorov General Physics Institute of the Russian Academy of Sciences, 38 Vavilova Street, Moscow, 119991, Russian Federation
[3] Moscow Institute of Physics and Technology, 4 Nauchny Pereulok, Dolgoprudny, Moscow Region, 141701, Russian Federation

E-mail: anatolykvitsinskiy@gmail.com

Abstract. Efficient devices for control temporal and spatial properties of electromagnetic waves are essential for the development of terahertz (THz) technologies. In this regard, one of the most important tasks of photonics is a study of advanced materials, on a basis of which it is possible to create devices with characteristics that exceed all existing analogues. But despite the great progress achieved in a study of graphene, the influence of the number of graphene layers on its optical and electrical properties in the THz frequency range has not yet been sufficiently studied. In this work, we experimentally studied optical and electrical properties of multilayer graphene (MLG) thin films in the frequency range 0.2–0.8 THz (corresponding to a wavelength range ~1.50–0.37 mm), at a controlled room temperature of 291 K, and a relative humidity of 40%. Using our custom-made THz time-domain spectroscopic polarimetry system, we obtained spectra of the complex relative permittivity and the electrical conductance of the chemical vapor deposition graphene with ~14, ~40, and ~76 layers of graphene on borosilicate glass substrates. Our results show that by using MLG it is possible to create tunable devices that can be used in the advanced areas of THz photonics.

1. Introduction

In recent years, there has been a strong improvement in technologies that are aimed at developing methods for generating, detecting, and modulating electromagnetic (EM) waves in the terahertz (THz) frequency range. THz radiation is widely used to solve fundamental and applied problems of physics, astronomy, chemistry, and medicine. In this regard, one of the most important tasks of modern THz photonics is a study of advanced materials, on a basis of which it is possible to create devices with characteristics that exceed all existing analogues [1]. A promising solution to the foregoing problem is a study of low-dimensional nanostructures for use as a functional medium in THz wave modulators. But despite the great progress achieved in a study of graphene-based nanostructures, the influence of the number of graphene layers on its optical and electrical properties in the THz frequency range has not yet been sufficiently studied.

The goal of our work was an experimental study of multilayer graphene (MLG)-based films with different graphene layer numbers using the THz time-domain spectroscopic polarimetry (TDSP) method in a frequency range 0.2–0.8 THz (corresponding to a wavelength range ~1.50–0.37 mm).

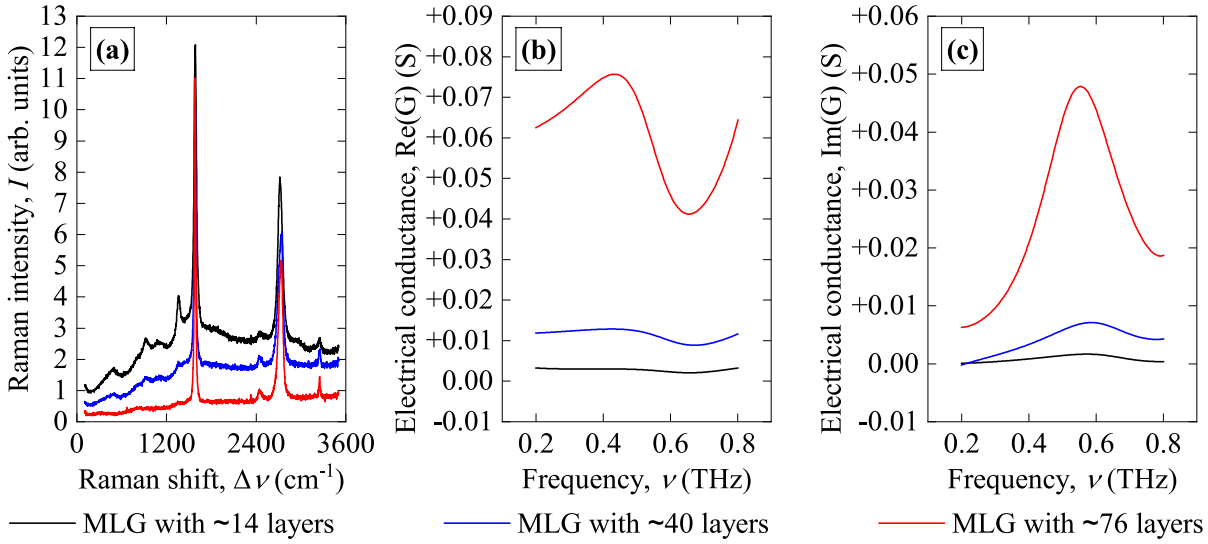

Figure 1. (a) Raman spectra, **(b)** the real, and **(c)** the imaginary parts of the electrical conductance of the MLG thin films with different number of the graphene layers.

2. Materials and methods

For our study, we selected three samples of MLG thin films with different number of graphene layers. The films were synthesized by the modified chemical vapor deposition (CVD) method on the nickel foil as described in Ref. [2]. Then the films were transferred onto the borosilicate glass substrates with a thickness of ~150 μm. To study the structural properties of the samples, we performed the Raman spectroscopy using an excitation wavelength of 488 nm (see Fig. 1 (a)). To study the electrical properties of the samples using the THz-TDSP method [3], a system based on a THz time-domain spectrometer and three wire grid polarizers was used. All measurements were done under a controlled room temperature of 291 K, and a relative humidity of 40%.

3. Results and conclusions

The obtained results of the Raman spectroscopy clearly show that with an increase in the number of graphene layers, an enhancement of the G-band and suppression of the 2D-band occur, which indicates a transformation from two-dimensional carbon-based structures to quasi-bulk ones. For the analysis of the obtained waveforms of the THz waves transmitted through the samples we used the basic Tinkham thin-film calculations and modernized data processing techniques [4]. Thus, we managed to obtain the complex relative permittivity and the electrical conductance of the MLG thin films based on THz polarimetric measurements (see Fig. 1 (b–c)). The results show that the real part of the graphene conductance nonlinearly depends on the number of layers and reaches values of 0.06 S for ~76 layers. These results show that by using MLG it is possible to create tunable devices that can be used in the advanced areas of THz science and technology.

Acknowledgments

The reported study was funded by the Russian Foundation for Basic Research (RFBR), project No. 20-32-90203.

References

[1] Han P *et al.* 2020 *Adv. Opt. Mater.* **8**(3) 1900533
[2] Rybin M G *et al.* 2018 *Phys. Status Solidi B* **255**(1) 1700414
[3] Kvitsinskiy A *et al.* 2019 *SN Appl. Sci.* **1**(12) 1714
[4] Zaitsev A D *et al.* 2020 *Appl. Sci.* **10**(8) 2724

Thermo-optical properties of nanophotonic devices with carbon nanotube films

S Komrakova[1], P An[2], V Kovalyuk[2], A Golikov[2,3] Y Gladush[4], A Mkrtchan[4], A Nasibulin[4] and G Goltsman[1,2,5]

[1]National Research University Higher School of Economics, 101000, Moscow, Russia
[2]Department of Physics, Moscow Pedagogical State University, 119992, Russia
[3]Moscow Institute of Physics and Technology (State University), 141700, Russia
[4]Skolkovo Institute of Science and Technology, Nobel Street 3, 43026 Moscow, Russia
[5]FRC Institute of Applied Physics RAS, 46 Ulyanov Str., 603950 Nizhny Novgorod, Russia

Abstract. Here, thermo-optical properties of hybrid nanophotonic circuits SWCNT/SiN were investigated. After experimental and theoretical study we found the thermo-optical coefficient of SWCNT film is equal to 2.02 10^{-6} RIU/^{0}C. The results obtained are promissing for further design and fabrication of fully integrated nanophotonic ciurcuts.

1. Introduction

Silicon nitride (SiN) based photonic integrated circuits are promising for creating of fully functional optical microcircuits on a chip [1]. Due to their weak nonlinearity, the creation of active elements should be performed based on additional nonlinear materials. A promising candidate is single-walled carbon nanotube (SWCNT) film because its unique electrical [2], mechanical [2] and optical [3] properties. The development of photonic devices based on SWNT requires knowledge of the thermo-optical properties of films on a nanophotonic waveguide. Since the expected value of the thermo-optical coefficient is small, it cannot be measured by direct methods. Therefore, we made the SiN O-ring resonators (ORRs) with SWCNT film cells atop. The shifts of resonances in the transmission spectrum ORR due to a change of SiN/SWCNT structure refractive index was found. Since the silicon nitride thermo-optical coefficient is also small, such a measuring device is highly sensitive to the study of the thermo-optical properties of SWCNT film.

2. Device design and fabrication

For device fabrication, we used commercially available 540 μm thickness silicon wafers with 2.6 μm thermally oxidized and low-pressure chemical vapor deposited (LPCVD) 450 nm layer of Si_3N_4 atop. The ORRs were formed by direct e-beam lithography and etching of 225 nm SiN in a CHF_3 plasma atmosphere. The resonator waveguide width of 1.6 μm, the ring length of 400.417 μm, and the 1.4 μm gap between the ring and bus waveguide of were chosen, supporting a free spectral range (FSR) of about 3 nm. Then, the films of SWNTs were deposited on the nanophotonic chips. The films were made by the aerosol (floating catalyst) chemical vapor deposition method. Further, the nanotube film was transferred to our device by dry transfer. The nanotubes were grown, so that the diameter corresponded to the S_{11} optical transition in the region of 1550 nm. The thickness of the film was measured as 22±4

nm. The AFM image of the SWCNT film is shown in Figure 1 (a). In the end, the rectangular cells of SWCNT films using laser lithography and O_2 plasma etching were finalized (Fig. 1 b).

3. Experimental results

The transmission spectra of ORR with films of different thicknesses and without film at different stage temperatures were measured. Heating the sample led to a shift of resonance peaks in the transmission spectrum of the ORRs. Compared to ORR without nanotubes, the shift of the resonance wavelength occurs faster, which indicates that such a scheme is sufficiently sensitive to measuring the thermo-optical coefficient of the SWCNT film. The wavelength shift without SWCNT is equal to 1.922×10^{-2} nm·K^{-1}, as well as the wavelength shift with SWCNT is equal to 1.942×10^{-2} nm·K^{-1}.

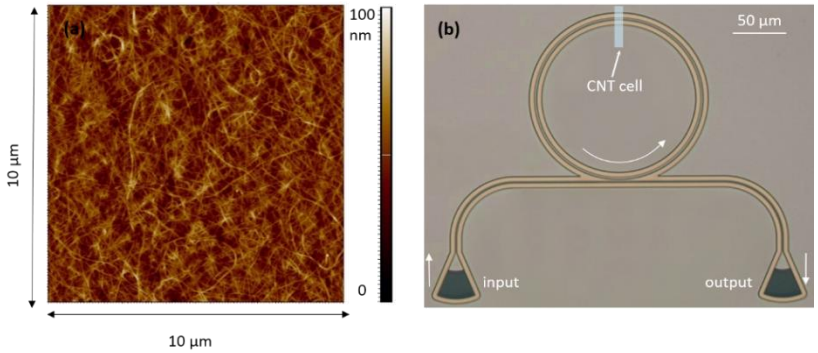

Figure 1. (a) The optical image of the fabricated ring resonator; **(b)** AFM image of SWCNT film

First, using the formula: $\Delta n_{eff} = \Delta\lambda_c(T)/2\pi Rm$, connected the order of interference m, waveguide parameters and resonance peak wavelength, we extracted the effective refractive index of the ORRs. The average value of dn_{eff}/dT extracted from the linear fit was found as 1.6616 10^{-5} RIU/^{0}C. Then, using the literature data for $(dn/dT)_{Si3N4}$ =2.51×10^{-5}, $(dn/dT)_{SiO2}$=0.96×10^{-6} [5] and numerical simulation in COMSOL Multiphysics, we found the values of $(dn/dT)_{SWCNT}$ in a good agree with the experimental data. The obtained value of $(dn/dT)_{SWCNT}$ = 2.02×10^{-6} RIU/^{0}C for the temperature range from 25 ^{0}C to 70 ^{0}C was found.

4. Conclusion

Using experimental and theoretical study, we found the thermo-optical coefficient of SWCNT film equals to 2.02×10^{-6} RIU/^{0}C. The results obtained are promissing for further design and fabrication of fully integrated nanophotonic ciurcuts. The proposed method can also be used to study other materials with a weak dependence of the refractive index on temperature

Acknowledgments

We acknowledge support of the Russian Science Foundation, grant No. 19-72-10156 (experimental study), as well as the Russian Foundation for Basic Research, grants No. 18-29-27031 (waveguide fabrication).

References

[1] Blumenthal D, Heideman R, Geuzebroek D, Leinse A, Roeloffzen C 2018 *Proceedings of the IEEE*, 1–23

[2] Sankar J, Udhaya K 2011 *European Journal of Scientific Research* 3 342-358

[3] Pei S, Ma L, Cheng H 2014 *Advance Materials* 26 1958−1991.

[4] Elshaari A, Zadeh I, Jöns K , Zwiller V 2016 *IEEE Photonics Journal* 3 1943-0655

Traffic interception in fiber optical video-systems

Krivenko Yu.E.[1], Kalashnikov A.S.[1], Andreeva E.I.[1],
[1]The Bonch-Bruevich Saint-Petersburg State University of Telecommunications, St.Petersburg, 193232, Russian Federation

Abstract. In fiber-optic video systems, as well as in optical communication systems, standard single mode optical fibers (SSMF, standard G 652) are usually used. One of the advantages of these fibers is the ability to use CWDM in a wide spectrum. At the same time, more optimal near the wave-length of 1550 nm are provided by non-zero dispersion fiber (NZDSF, standard G 655) fibers. However, as studies have shown, these optical fibers have an increased sensitivity to bending. This fact can be used to traffic interception. It is shown that fiber-optics systems with SSMF have more protection from traffic interception than systems with NZDSF. To transmit a high-confidentiality video signal, special techniques, such as frequency modulation, can be used, or additional noise signals can be added.

1. Introduction

The use of the optical cable in the communication systems provides such advantages as information capacity, reliability, durability and protection. To achieve these advantages, different types and standards of fibers are used [1-3]. However, this does not exclude the interception of the transmitted information.

Often the optimization some system parameter is associated with difficulties in maintaining the proper level of other system parameters. One of the key issues in the design of a video surveillance system is the choice of the type of optical fiber as a direct signal transmission medium. The characteristics of the optical fiber must ensure the maximum of the transmission distance on the one hand, and the protection from the interception of the transmitted information on the other. To provide the transmission a high-quality video signal, it is necessary to transmit a wide- spectrum optical signal. Therefore, to transmit the such optical signal over a long distance, fibers with a low losses and low dispersion can be used, such as NZDSF – nonzero dispersion shifted fibers (standard G.655). In fiber-optic video surveillance systems, as well as in optical communication lines, standard optical fibers (SSMF, Standard Single Mode Fiber, standard G.652) are most often used. One of the advantages of these fibers is the ability to use the CWDM wavelength division multiplexing in a wide spectrum range (from 1270 to 1610 nm). At the same time, the optimal parameters for losses and dispersion in the third transparency window (near the wavelength of 1550 nm) are provided by NZDSF fibers. However, as studies have shown, these fibers have an increased sensitivity to bending. This can lead to additional losses when laying optical cables and an increased risk of unauthorized access. To mitigate these risks, the Bending Loss Insensitive Fiber (BLIF – fibers, standard G.657) can be used.

Experimental investigation of the bend sensitivity of the different fibers is presented in figure 1.

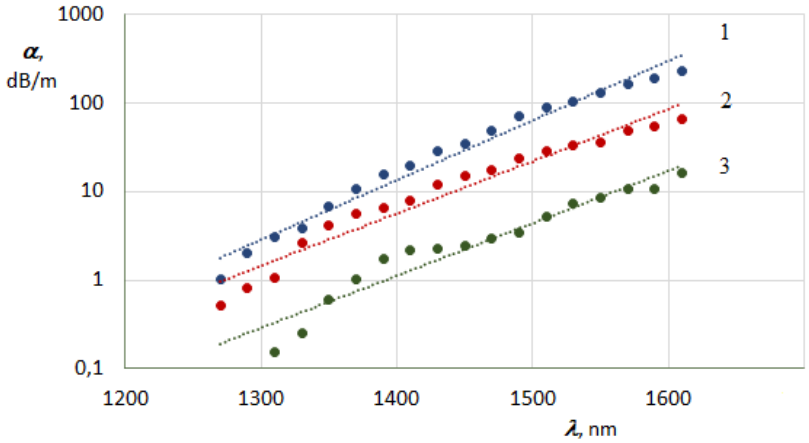

Figure 1. The bend loss α in dependence from wavelength λ. for NZDSF (standard G.655) (1), for SSMF (standard G.652) (2) and BLIF (standard G.657A2) (3) is presented. (The bend diameter is 12.5 mm.)

In WDM systems, part of the transmitted signal can fall into the adjacent spectral channel due to FWM (Four Wave Mixing). The simulation was carried out in the OptiSystem program. The optical signal was fed into the spectral channels of the CWDM grid: 1470 and 1490, 1530 and 1550nm. After passing the effective loss manifestation length L_{eff}=20km, signals due to the original ones were observed in the neighboring spectral channels. The level of these signals is 53 ... 55 dB lower than that transmitted in NZDSF and 55 ... 60 dB lower than that transmitted in SSMF. This fact reflects the difference in the nonlinearity coefficient of these optical fibers. Standard optical fibers are characterized by greater protection from unauthorized access then NZDS fibers.

2. Conclussion

It is experimentally confirmed that NZDS-fibers (with low dispersion) of the G.655-standard are characterized by increased sensitivity to bending, as result of which they require greater security to avoid interception of the transmitted signal traffic. NZDSFs provide more long-distance transmission of video signal. At that time SSMFs provide greater protection against traffic interception.
To transmit a high-privacy video signal, special modulation methods, such as frequency modulation, can be used, or additional noise signals can be added.

References

[1] Andreev D, Andreeva E, Sergeev A, Sumkin V 2020 *APINO Proc*. **1** p 57–61
[2] Andreeva E, Valyukhov V, Kuptsov V 2019 *APINO Proc.* **1** p 56–60
[3] Andreeva E, Valyukhov V, Kuptsov V 2018 *APINO Proc.* **1** p 57–61

MOF-based non-linear optical composite

Nikita K. Kulachenkov[a], Yulia Kenzhebayeva[a], Yuri A. Mezenov[a], Valentin A. Milichko[a,b]

[a] ITMO University, St. Petersburg 197101, Russia

[b] Institut Jean Lamour, Université de Lorraine, Nancy F-54011, France

Nikita.kulachenkov@metalab.ifmo.ru

Abstract. Here we report second harmonic generation signal from ZIF-8 metal-organic framework incorporated in PMMA upon extremal near-infrared laser irradiation. The SHG intensity signal was compared to commercial inorganic crystal such as potassium dihydrogen phosphate (KDP).

1. Introduction

Metal-organic frameworks is a class of crystallinity porous material consisting the formation of coordination bonds between metal ions as nodes and organic linkers [1]. As a result, optically responsive MOF to demonstrate non-linear effects associated with structural crystallographic lattice, such as second harmonic generation. Moreover, various MOF can be incorporated into thermoplastic polymer matrices for instance polymethylmethacrylate (PMMA). The zeolitic imidazolate framework ZIF-8 is thermally and chemically stable compound and demonstrates SHG signal due to its non-centrosymmetric cubic I-43m space group symmetry and ideally useful for creating membraned and polymer matrices [2-4]. Here we report composite material based on metal-organic frameworks ZIF-8 incorporated into PMMA matrix. The assemble demonstrates second harmonic generation signal that we compared with KDP single crystal.

2. Result and Discussion

For synthesis polymer matrix (Figure 1, left) we utilized the commercial compound ZIF-8 (Sigma-Aldrich) and solution based on methyl methacrylate (Sigma-Aldrich) as the main monomer, ethylene glycol dimethacrylate (Sigma-Aldrich) as a stitch reagent to create the 3D structure of polymethylmethacrylate, and 2-hydroxy-2-methylpropiophenone (Sigma-Aldrich) as a photoinitiator for UV polymerization.

For the optical experiments, the ZIF-8–PMMA composite and KDP crystal were placed on a glass substrate. The SHG spectra measurements have been performed using a home-made confocal microscope setup. The excitation by Yb3+ laser (1047 nm, 80 MHz, 150 fs laser pulse duration) has implemented via 10x0.26NA objective. The integral power of the laser varied from 0 to 500 mW (80 MHz) which cause damage to inorganic materials, such as gold and silicon[]. The SHG signal was collected by 50x0.65NA objective and then analysed by a confocal spectrometer, HORIBA Labram with

a water-cooling Andor DU 420A-OE 325 CCD camera and 150-g/mm diffraction grating. The SHG visualisation has been realized using commercial camera (Figure 1, centre)

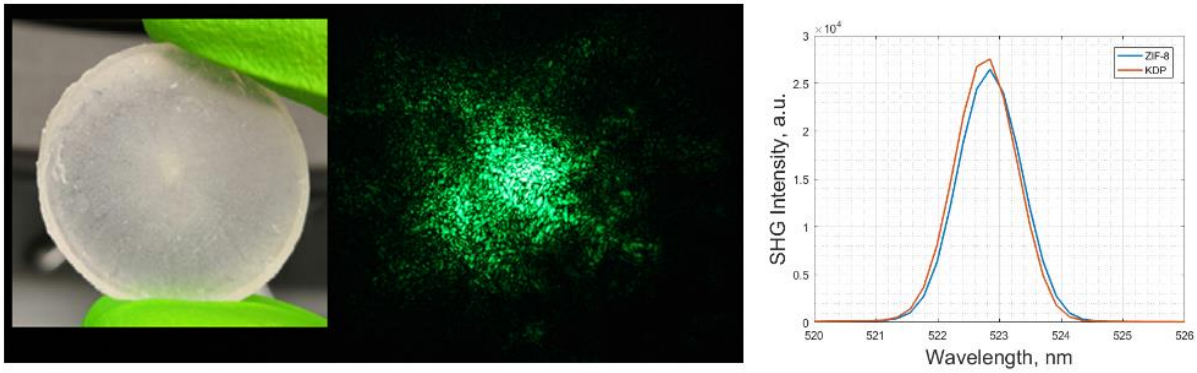

Figure 1. The ZIF-8 in PMMA composite (left), SHG visualization (centre), and SHG comparison.

The ZIF-8–PMMA composite has demonstrated stable SHG signal upon extremal laser irradiation conditions. Moreover, the intensity of SHG signal is comparable (Figure 1, right) with XDP crystal expand opportunity to apply the current materials as an element of optical generators and visualization systems.

References

[1] Mezenov, Y. A., Krasilin, A. A., Dzyuba, V. P., Nominé, A., Milichko, V. A., Metal–Organic Frameworks in Modern Physics: Highlights and Perspectives. Adv. Sci. 2019, 6, 1900506.

[2] Park, K.S.; Ni, Z.; Côté, A.P.; Choi, J.Y.; Huang, R.; Uribe-Romo, F.J.; Chae, H.K.; O'Keeffe, M.; Yaghi, O.M. Exceptional chemical and thermal stability of zeolitic imidazolate frameworks. Proc. Nat. Acad. Sci. USA 2006, 103, 10186–10191

[3] Cleuvenbergen, S.V.; Stassen, I.; Gobechiya, E.; Zhang, Y.; Markey, K.; De Vos, D.E.; Kirschhock, C.; Champagne, B.; Verbiest, T.; van der Veen, M.A. ZIF-8 as nonlinear optical material: Influence of structure and synthesis. Chem. Mater. 2016, 28, 3203–3209

[4] Yin, H.; Kim, H.; Choi, J.; Yip, A.C.K. Thermal stability of ZIF-8 under oxidative and inert environments: A practical perspectives on using ZIF-8 as a catalytic support. Chem. Engineer. J. 2015, 278, 293–300.

[5] Makarov, S.V.; Milichko, V.A.; Mukhin, I.S.; Shishkin, I.I.; Zuev, D.A.; Mozharov, A.M.; Krasnok, A.E.; Belov, P.A. Controllable femtosecond laser-induced dewetting for plasmonic applications. Laser. Photon. Rev. 2016, 10, 91–99.

Peculiarities of ion-exchange in poled glasses

E A Lubyankina[1,2], D V Raskhodchikov[1,2], E S Babich[1,2], V.P. Kaasik[1,2], A A Lipovskii[1,2]

[1]Department of Physics and Technology of Nanostructures, Alferov University, St. Petersburg 194021, Russia

[2]Institute of Physics, Nanotechnology and Telecommunications, Peter the Great St. Petersburg Polytechnic University, St. Petersburg 195251, Russia

Abstract. We demonstrate for the first time that the results of ion-exchange processing of thermally poled glasses essentially depend on the poling conditions. In particular, processing of vacuum-poled soda-lime glasses in silver-sodium nitrate melt results in the reduction of silver ions and clustering silver nanoparticles in the subsurface layer of the glass, while air-poling completely prevents silver ions diffusion in glass. Depending on anodic electrode configuration (closed or opened) and voltage using in vacuum-poling, silver precipitation can be increased or suppressed. The origin of this behavior is considered.

1. Introduction

Study of processes taking place in thermal poling (TP) of glasses is of interest due to the possibility to use thermally poled regions of glasses as dielectric masks in thermal ion exchange-based formation of structures for integrated optics [1]. TP of multicomponent glasses modifies their subanodic regions, the modification being dependent on the TP mode. In the case of closed anode TP, when penetration of atmospheric species in subanodic region of glass is prevented, about 1 μm-thick subanodic layer of the glass becomes depleted with both alkali and alkaline earth ions [2]. If open anode TP configuration is used, the subanodic glass layer becomes enriched with H^+/H_3O^+ ions diffused from atmospheric water vapors [3]. These ions take positions of alkali ions, while alkaline earth ions keep their position [4]. In this case, the thickness of the modified glass layer falls in several microns range. Because of this difference in open anode and closed anode TP, the modified glass layers differently behave in ion-exchange processing. Below we present and discuss the peculiarities of silver-to-sodium ion-exchange processing of differently poled glasses. For the first time, the ion-exchange processing of glass poled in vacuum is demonstrated.

2. Experiments and results

We used 1 mm thick soda-lime glass slides which composition is presented in Table 1.

Table 1. Composition of the glass in wt. % of oxides.

SiO_2	Al_2O_3	Na_2O	K_2O	MgO	CaO	others
72.2	1.2	14.3	1.2	4.3	6.4	0.33

The slides were thermally poled in vacuum and air using either pressed glassy carbon electrodes (as anode) or 55 nm-thick gold films deposited onto both surfaces of the slides. The TP was performed at the temperature of 300 °C under 500 and 800 V applied. The poled glasses were ion-exchanged in the

melt of $Ag_{0.05}Na_{0.95}NO_3$ (in wt.%) for 20 min at 325 ºC. It has been found that vacuum poling with pressed electrodes leads to the reduction of silver ions within the glass during the ion-exchange. Optical absorption spectrum (Fig. 1a) of 500V-poled glass evidences that neutral silver is mostly in the form of Ag_6-Ag_9 clusters which absorption peak is at 370 nm [5]. The absorption in 430-700 nm range indicates the formation of a polydisperse ensemble of silver nanoparticles. The increase in applied voltage up to 800 V results in the formation of predominantly silver nanoparticles (Fig.1a). The number of nanoparticles essentially increases.

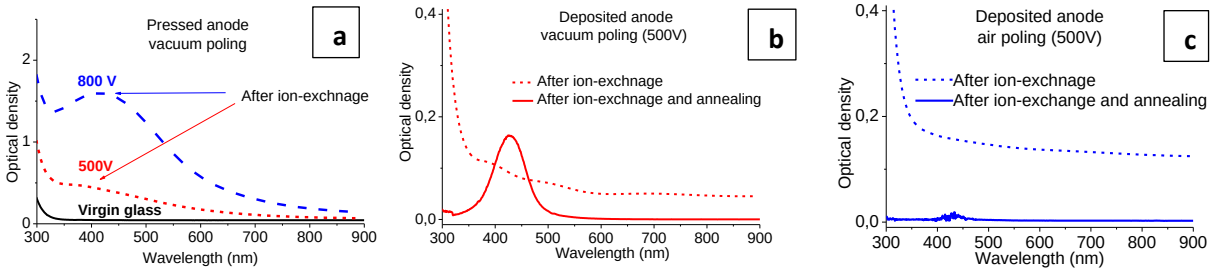

Figure 1. Absorption spectra of glass poled in vacuum with (a) pressed and (b) deposited anodes and (c) glass poled in air with deposited anode after ion-exchange and annealing in air.

Vacuum TP with deposited gold electrodes suppresses the formation of silver clusters in the glass during subsequent ion-exchange (Fig. 1b) contrary to the case of pressed electrodes. However, annealing in air atmosphere (600 °C, 1 h) leads to the formation of numerous nanoparticles on anode surface of the glass (Fig. 1b). Contrary to vacuum-poling, air-poling completely prevents silver ions diffusion in glass. There is no resonant peak corresponding to silver clusters/nanoparticles in absorption spectrum of air-poled glass either after ion-exchange or ion-exchange followed by annealing (Fig. 1c).
Thus, one can control silver ions diffusion and precipitation in glass during ion-exchange using different poling conditions.

Acknowledgments
The study was supported by the Ministry of Science and Higher Education of Russian Federation, project FSRM-2020-001.

References

[1] Ikutame N, Kawaguchi K, Ikeda H, Sakai D, Harada K, Funatsu S and Nishii J 2013 *J. Appl. Phys*. **114** 083514
[2] Redkov A, Melehin V, Raskhodchikov D, Reshetov I, Tagantsev D, Zhurikhina V and Lipovskii A 2019 *J. Non-Cryst. Solids* **503** 279-283
[3] Doremus R 2005 *Appl. Phys. Lett.* **87** 232904
[4] Lepienski C, Giacometti J, Leal Ferreira G, Freire F Jr and Achete C 1993 *J. Non-Cryst. Solids* **159** 204-212
[5] Harb M, Rabilloud F, Simon D, Rydlo A, Lecoultre S, Conus F and Félix C 2008 *J. Chem. Phys*. **129** 194108

Computation of optical waveguide interaction for quantum gates implementation

A A Lytaev[1], I Yu Popov[1]
[1]Faculty of Control Systems and Robotics, ITMO University, St. Petersburg, 197101, Russia

e-mail: a.lytaev30@gmail.com

Abstract. The system of two coupled optical dual-mode waveguides is considered. The coupling of the system is studied with the aim to be used as a principle for building a control switch for two qubit gates. The classical coupled mode theory is applied and the exact expressions for coupling coefficients are derived. The parameters of the system to perform the desired operations are numerically computed and analysed.

1. Introduction

The physical implementation of quantum computer is a problem of vital importance. One of the main obstacles on the way to build a multiple qubit quantum computer is a quickness of the system decoherence. The optical quantum computing is an approach that allows to reduce the effect of decoherence due to the low effectiveness of photon-photon and photon-environment interaction. However, the existing models of linear optical two-qubit gates are probabilistic with 1/9 probability of success, that can be increased only with a large number of ancilla qubits, thus, making them unscalable for building a complex computational scheme. One of the possible solutions was suggested in [1]. Different order optical waveguide modes were suggested to be used as a qubit encoding, with nonlinearities at MZI arms being used to perform qubit operations. This work was devoted to the development of this approach by studying the system of two similar two-mode waveguide that can be used as a control switch for nonlinear CNOT gate.

2. Coupled mode theory analysis

Consider a symmetrical system of two parallel optical slab waveguides. The classical coupled mode theory can be used to describe the interaction between the modes of the waveguides [2]. The resulting field in the system can be approximated as a sum of separate waveguide fields with amplitude coefficients. Using the Maxwell equations one can derive a system of differential equation for the amplitude coefficients in the symmetrical case in assumption of weakness of interaction between different order modes.

$$\frac{\partial A_1}{\partial z} = \mathrm{i}c_1 A_2 \tag{1}$$

$$\frac{\partial A_2}{\partial z} = \mathrm{i}c_2 A_1 \tag{2}$$

The exact solution for the system can be derived analytically.

$$A_1^j(z) = A_1^j(0)\cos(c^j z) + iA_2^j(0)\sin(c^j z)$$
$$A_2^j(z) = iA_1^j(0)\sin(c^j z) + A_2^j(0)\cos(c^j z) \quad (3)$$

The analytical solution (3) is valid for both orders of waveguide modes, while the coupling coefficient c^j changes with order of the mode j. This allows the system to be used as a mode separate-combine switcher transferring TE_1 to MZI arm and back, while keeping TE_0 in the control switcher. The paraxial approximation of the quantum ray theory approach to describe waveguide as a potential well given in [3] allows one to directly call the TE_0 and TE_1 amplitude coefficients the ψ_0 and ψ_1 qubit state vector coordinates.

The necessary condition for the system to perform this operation is to satisfy

$$\frac{4v_1+1}{4v_0} = \frac{c^1}{c^0}, \qquad v_0,\ v_1 \in \mathrm{N} \quad (4)$$

The analytical expressions for c^j were obtained by directly evaluating the integral expressions with TE mode fields given in [2].

$$c^0 = 4\pi^2\left(n_{wg}^2 - n_{env}^2\right)\cos(\chi_0 d)\exp\left[-\gamma_0(R-d)\right]\beta_0^{-1}(\lambda n_{env})^{-2}\left(\gamma_0^2+\chi_0^2\right)^{-1}$$
$$* \left[\gamma_0\cos(\chi_0 d)\mathrm{sh}(\gamma_0 d) + \chi_0\sin(\chi_0 d)\,\mathrm{ch}(\gamma_0 d)\right]\left[d + \frac{\sin(2\chi_0 d)}{2\chi_0} + \frac{\cos^2(\chi_0 d)}{\gamma_0}\right]^{-1} \quad (5)$$

$$c^1 = 4\pi^2\left(n_{wg}^2 - n_{env}^2\right)\sin(\chi_1 d)\exp[-\gamma_1(R-d)]\mathrm{ch}(\gamma_1 d)\beta_1^{-1}(\lambda n_{env})^{-2}\left(\gamma_1^2+\chi_1^2\right)^{-1}$$
$$* \left[\chi_1\cos(\chi_1 d) - \gamma_1\sin(\chi_1 d)\right]\left[d - \frac{\sin(2\chi_1 d)}{2\chi_1} + \frac{\sin^2(\chi_1 d)}{\gamma_1}\right]^{-1} \quad (6)$$

Hence, the ratio (4) can be satisfied by adjusting the coupling distance R to match almost any given pair of v_1 and v_2. However, R can not be taken arbitrarily small due to the waveguide manufacturing technological limitations.

The coupling length L, that makes the system to perform the desired control operation can be expressed as

$$L = \left(2c^1\right)^{-1}(4v_1+1) \quad (7)$$

3. Results

The numerical evaluation of the coupling coefficients and various propagation constants as a solution of transcendental equation was implemented for a symmetrical system of coupled waveguides. The system parameters are the light wavelength λ, the waveguide width $2d$ and the refractive indices n_{wg} and n_{env} of the core and cladding layers respectively. The modern waveguide manufacturing techniques allow to produce waveguides with scales of micrometres. The numerical analysis conducted shows that for $R = 1$ μm the coupling coefficients ratio c^1/c^0 is more than 1, the further increase of R makes it exponentially grow. Therefore, the power exchange between TE_0 modes can be said to proceed at slower pace than that for TE_1 modes, thus making the value of L obtained in (7) to perform the desired power transfer for TE_0 modes with high stability to any computational error. However, the fast power exchange for TE_1 modes is less stable to errors, thus any inconsistencies between the model and the real system could possibly hinder, so consideration of losses and higher order interaction might be required.

References

[1] Fu J and Tang S 2003 *Chinese Phys. Lett.* **20** 1426

[2] Marcuse D 1982 *Light Transmission Optics* ed S Mitra (New York: van Nostrand Reinhold) chapter 10 pp 519–531

[3] Gloge D and Marcuse D 1969 *J. Opt. Soc. Am.* **59** 1629

Features of spectral analysis of nuclear magnetic resonance signal for express-control of hydrocarbon media

S S Makeev[1], V V Davydov[1, 2] and V Yu Rud[2]

[1]Peter the Great St. Petersburg Polytechnic University, Saint Petersburg 195251, Russia
[2]All-Russian Research Institute of Phytopathology, Moscow Region 143050, Russia

e-mail: st_makeev@mail.ru

Abstract. The article substantiates the need to study the structure of the nuclear magnetic resonance signal recorded during the express-control of hydrocarbon media. The features of recording of the nuclear magnetic resonance signal using the modulation technique have been determined. A mathematical model has been developed for the representation of the NMR signal in the form of a spectrum, taking into account the features of its recording during the express-control of hydrocarbon media. The results of experimental studies are presented.

1. Introduction

Devices based on the nuclear magnetic resonance phenomenon are now used extensively in the express-control of hydrocarbon media. Unlike other hydrocarbon media research methods, NMR measurements do not introduce irreversible changes in the physical structure and chemical composition of the studied media [1, 2]. Other types of devices can only insure this condition when working with a certain class of media. Therefore, the current direction is to expand the possibilities of studying hydrocarbon media during express-control using an NMR signal.

In modern NMR spectrometers, which are used for express monitoring of hydrocarbon media, the NMR signal is recorded by an autodyne detector using a modulation technique. When carrying out experimental studies [1-3], we found that the developed methods for determining the composition of media using the NMR signal have a number of disadvantages affecting the accuracy and time of measurement. Therefore, we have developed a new method for processing the recorded NMR signal during express-control of hydrocarbon media.

2. Features of constructing the nuclear magnetic resonance signal spectra for express-control of hydrocarbon media

Our analysis showed that the NMR signal (fig. 1) cannot be described using periodic functions, which does not allow obtaining additional information on the composition of the medium [3]. Spectral analysis can solve this problem. It is most appropriate to use the discrete Fourier transform (DFT) to construct the spectrum of the recorded NMR signal using the modulation technique.

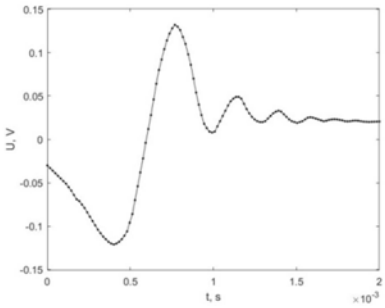

Figure 1. The NMR signals from the engine oil using the modulation technique.

Relaxation constants T_1 and T_2 are measured using the recorded NMR signal to calculate absorption and dispersion signals using Bloch's equations. Amplitude and phase spectra are plotted for these signals (fig. 2).

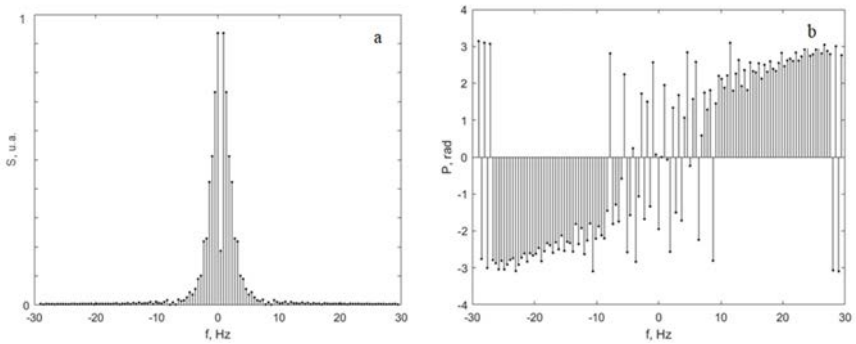

Figure 2. The spectra from the calculated NMR signal: a) amplitude, b) phase.

The amplitude and phase spectra of the experimental signal are also plotted. By choosing the weighting coefficients in the spectra, it is possible to obtain harmonics coincidence between experiment and theory. The numerical estimates were carried out to confirm this. The result shows the validity of the method.

3. Conclusion

As a result of the experiments, it was found that the developed spectral research method has no restrictions on its use. It is important that the NMR signal from the medium can be recorded. In the case of a mixture, the composition of the matter is determined by the selections of the coefficients and values of T_1 and T_2 in the solutions of the Bloch equations, according to which the composition of the mixture is determined. The concentration is determined by the weight factors of the resulting ratios when the spectra are compared.

Acknowledgments

This research work was supported by the Academic Excellence Project 5-100 proposed by Peter the Great St. Petersburg Polytechnic University.

References

[1] Myazin N S, Davydov V V, Yushkova V V, Davydova T I and V Yu Rud' 2017 *Journal of Physics: Conference Series* **917** 042017
[2] Karseev A Yu, Cheremiskina A V, Davydov V V, Velichko E N 2014 *Journal of Physics: Conference Series* **541(1)** 012006
[3] Myazin N S and Davydov V V 2018 *Journal of Physics: Conference Series* **1124(1)** 031004

Organic phosphor based fiber-optic sensor for detection of UV radiation

A S Matrosova[1,2,3], V A Ananyev[2], G A Pchelkin[1,3,4], D N Shurupov[1,4], S K Evstropiev[1,2,3,5], V M Volynkin[1], V V Demidov[1,3] and N V Nikonorov[2]

[1] R&P Association Vavilov State Optical Institute, St. Petersburg 192171, Russia
[2] ITMO University, St. Petersburg 197101, Russia
[3] Bauman Moscow State Technical University, Moscow 105005, Russia
[4] Peter the Great St. Petersburg Polytechnic University, St. Petersburg 195251, Russia
[5] Saint-Petersburg State Institute of Technology, St. Petersburg 190013, Russia

Abstract. The paper presents a simple and low-cost fiber-optic sensor for detection of UV radiation. A sensor construction consists of a silica capillary with a photoactive composition based on organic phosphor, organic solvent and epoxyacrylate inside and a multimode optical fiber in contact with each other. By adjusting the proportion of components in a photoactive composition, it is possible to obtain a pronounced optical signal at wavelength 440 nm which is the luminescence emission wavelength of the chosen organic phosphor. The perspective of using the construction as a UV sensor is confirmed by the linear dependence of the optical signal amplitude at the fiber output on the optical power supplied to the fiber input.

1. Introduction

Generally, there are three types of ultraviolet (UV) radiation which are UV-A, UV-B, and UV-C ranges bringing risks to human health including eye diseases, cancer, DNA damages [1]. Hence, it is significant to monitor UV radiation in real time. On the other hand, UV radiation can be used for medical purposes (phototherapy of tissues, production of vitamin D, control of maximum valid sun irradiation dose, etc), control of technological processes, and calibration of UV radiation emitters [2].

Fiber-optic sensors have many advantages over other types of sensors [3]. They are compact, light, and electrically safe and can provide distributed or localized measurements along the whole length. Nowadays, more attention is paid to luminescent fiber-optic sensors which benefits are fast response and high sensitivity [4].

The paper discusses construction and performance issues of a simple and low-cost fiber-optic sensor for detection of UV radiation based on a photoactive composition with luminescing centers emitting at wavelength 440 nm.

2. Materials and methods

To synthesize a photoactive composition, 1 g of the organic phosphor 1,3,5-triphenyl-2-pyrazoline and 10 g of the organic solvent dimethylformamide were thoroughly mixed in normal conditions until a homogeneous non-viscous substance was received. Then this substance was mixed with 10 g of UV-curable epoxyacrylate under the same conditions providing high viscosity. The final substance was put inside a silica capillary of 1 mm in diameter and 50 mm in length close to the capillary end. A piece of low-OH multimode optical fiber 100 mm length with a core of 200 μm in diameter and numerical aperture 0.22 was passed through the capillary from the other end to contact with the photoactive

composition. Finally, the whole construction was irradiated with a UV lamp for 10 seconds resulting in obtaining a solid optical element (figure 1).

To investigate photoluminescence (PL) properties of the photoactive composition, another sample in the form of a thin film on the surface of a silica plate was prepared and measured using the method in [5]. Spectral properties of the fiber-optic sensor were evaluated according to the technique in [5].

Figure 1. Basic sensor design (left) and the fabricated fiber-optic sensor under UV radiation (right)

3. Results and discussions

Experimentally studied luminescence properties of the photoactive composition revealed the existence of PL excitation at wavelength 365 nm and PL emission at wavelength 440 nm. To check the presence of a pronounced optical signal at the fiber output after focusing precisely radiation at the fiber input, the transmission was measured (figure 2, left). With a view to excluding the influence of optical signal at the PL excitation wavelength, a light filter made of SZS-7 glass was placed in front of the detector.

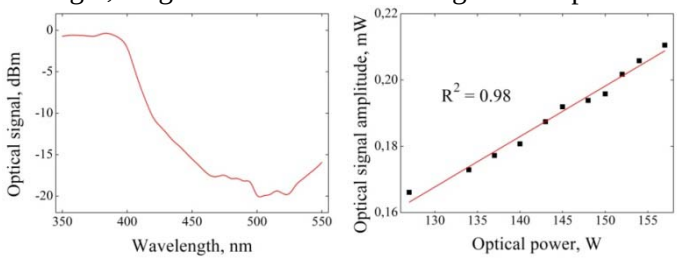

Figure 2. Transmission spectrum (left) and dependence of the optical signal amplitude on the optical power of radiation from the light source (right) of the fabricated fiber-optic sensor

The linear dependence of the optical signal amplitude on the optical power injected from the light source after passing both the photoactive composition and multimode optical fiber (figure 2, right) indicates the possibility to apply the produced fiber-optic sensor for detection of UV radiation.

4. Conclusions

A construction of luminescent fiber-optic sensor for UV radiation detection was developed. The sensor consisted of a capillary with a photoactive composition based on organic phosphor, organic solvent and epoxyacrylate inside and a multimode optical fiber in contact with each other. The linear dependence of the optical signal amplitude at the fiber output on the optical power supplied to the fiber input indicated that the produced sensor is a promising instrument to measure UV radiation.

Acknowledgements

This research is supported by the Russian Science Foundation (Project No. 19-19-00596).

References

[1] Joza A V, Bajic J S, Stupar D Z, Slankamenac M P, Jelic M and Zivanov M B 2012 *Telfor Journal* **4** 133

[2] Agafonova D S, Kolobkova E V, Ignatiev A I, Nikonorov N V, Shakhverdov T A, Shirshnev P S, Sidorov A I and Vasiliev V N 2015 *Opt. Eng.* **54** 117107

[3] Grattan K T V and Sun T 2000 *Sens. Act. A: Phys.* **82** 40

[4] Jackson R G 2004 *Novel sensors and sensing* (London: CRC Press)

[5] Kuzmenko N K, Evstropiev S K, Aseev V A, Danilovich D P, Nikonorov N V, Ignatiev A I, Matrosova A S, Demidov V V, Emerson A V and Sevastyanova I M 2020 *J. Phys.: Conf. Ser.* **1695** 012184

Tuning of weak plasmon mode radiation damping in graphene structure with asymmetric unit cell

K. V. Mashinsky [1], **D. V. Fateev** [1,2], **V. V. Popov** [1]
[1] Kotelnikov Institute of Radio Engineering and Electronics of the Russian Academy of Sciences (Saratov Branch), 410019 Saratov, Russia
[2] National Research Saratov State University, 410012 Saratov, Russia

Abstract. Terahertz lasing on resonance plasmon modes in structure based on graphene screened by metal dual grating gate with asymmetric unit cell is considered. The changing of the radiation damping of a weak ("nonradiative") plasmon mode upon reaching the lasing regime as a function of the gate electrode width was investigated theoretically. Weak plasmon mode radiation damping can be changed by tuning of structure unit cell asymmetry.

1. Introduction

Graphene is a perspective material for creating terahertz THz devices. The most important features of this material are zero band gap [1], high carriers mobility reaches around 100000 $cm^2/(Vs)$ [2] and its momentum relaxation time reaches 2 ps [3] at room temperatures. Graphene can be used for amplification and generation of THz radiation [4]. Strong plasmon electric fields localization in graphene allows electromagnetic radiation efficiently interact with inverted charge carriers.

The THz radiation lasing on resonant plasmon modes in a structure based on spatially homogeneous graphene, screened by a metal dual grating gate (DGG) with asymmetric unit cell (Fig. 1, a) is studied theoretically in this paper. Graphene is placed on a SiC substrate with a dielectric constant ε=9 and separated from DGG by SiC barrier layer. DGG consists of two subgratings laterally shifted in respect to each other to introduce an asymmetry into the structure unit cell. Inverted distribution of charge carriers created in graphene [5] allows for reaching radiative recombination in the THz range [6].

The THz wave normally incident on DGG structure and excites plasmon modes amplified in inverted graphene. In spatially asymmetric structure excitation of both strong ("radiative") and weak ("non-radiative") plasmon modes is possible [7]. Widths of gates are w_1=150 nm and w_2=220 nm, sum of gaps between gates are s_1+s_2=578 nm, the thickness of the barrier layer is d=15 nm and charge carrier momentum relaxation time is τ=1 ps.

2. Results and discussion

The changing of the radiation damping of a weak plasmon mode upon reaching the lasing regime as a function of the gap width s_1 (the subgrating under which the weak plasmon mode is excited) (Fig. 1, b-e) was investigated theoretically. Since the wave vector of plasmons is defined by the geometric parameters of the subgrating as $\pi p/s_{1,2}$ it is possible to choose and adjust the required frequency for laser generation on weak plasmon modes. Radiation damping frequency of weak mode decreases by an order of magnitude (to values of 0.0005 THz) due to the separation of the excitation frequencies of the weak and strong (excited under the gate s_2) plasmon modes.

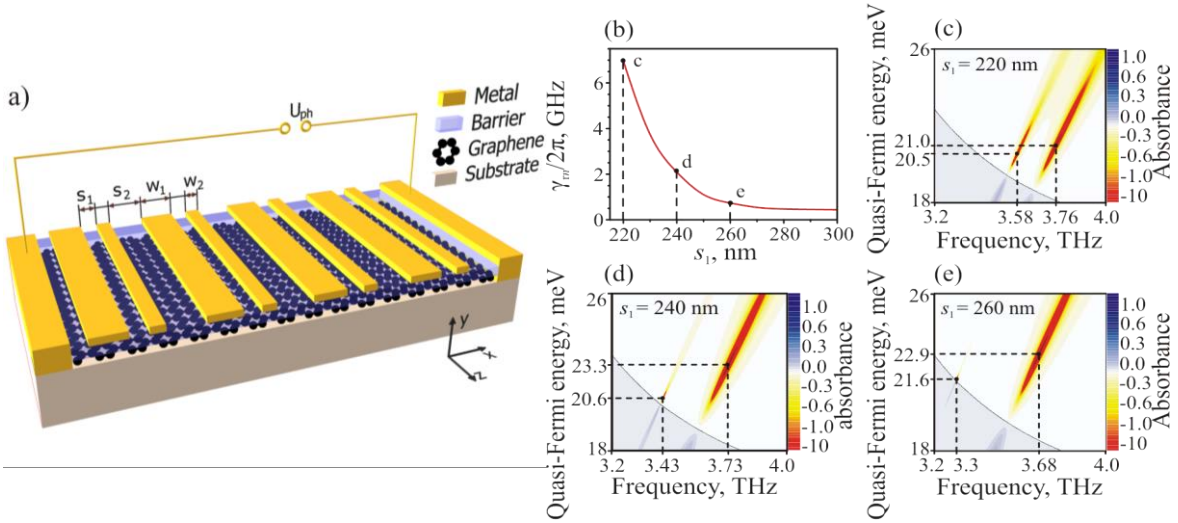

Figure 1. (a) Schematic view of graphene structure screened by DGG with asymmetric unit cell. **(b)** Dependence of radiation damping frequency on the gate width s_1 in lasing regime on weak mode. **(c-e)** Dependence of absorption on quasi-Fermi energy and plasmon frequency for different gate widths s_1. Each of graphs shows weak (at lower frequency) and strong (at higher frequency) modes.

Radiation damping of strong and weak modes differs by two orders of magnitude, what makes possible reducing required pump power for reaching lasing regime in DGG graphene structure. It can be reduced almost to level of dissipative damping compensation. The frequency of weak plasmon modes radiation damping is about 0.0005 THz, while the damping of strong ones is about 0.08 THz, which comparable to dissipative damping of plasmons is 0.079 THz for momentum relaxation time τ=1 ps. Laser regime of plasmon amplification requires not only compensation of dissipative losses, but also radiation losses. Thus, decrease of weak modes radiation damping can significantly lower the lasing threshold.

The studied DGG structure is open for electromagnetic waves, as result of which excited or amplified plasmons are re-emitted into outgoing electromagnetic waves. Magnitude of plasmon mode radiative dumping determines level of re-emitted electromagnetic waves and Q-factor of plasmon resonance. Narrow frequency spectrum of weak plasmon modes amplification makes possible using of single-mode laser regime for plasmon modes with low radiative damping. At the same time, laser regime for strong plasmon modes with a large radiative damping is characterized by wider frequency range, which leads to a multimode lasing regime.

In this work we calculate radiative damping of plasmon modes and found that the radiative damping of weak modes can be changed by changing asymmetry of the structure unit cell. In spatially symmetric system weak modes are not excited and their radiative damping is equal to zero. Lasing at low radiative dumping modes characterized by narrower laser peak, which corresponds to single-frequency coherent radiation from the structure.

3. Acknowledgement

The work was carried out within the framework of a state task.

[1] K.S. Novoselov et al., Nature 490, 192 (2012).
[2] A. S. Mayorov et al., Nano Lett. 11, 2396 (2011).
[3] D. Svintsov et al., J. Appl. Phys. 111, 083715 (2012).
[4] A.N. Grigorenko et al., Nat. Nanotechnol. 9, 780 (2014).
[5] V. Ryzhii et al., J. Appl. Phys. 101, 083114 (2007).
[6] D. Yadav et al., J. Nanophoton. 7(4), 741 (2018).
[7] D. V.Fateev et al., Phys. Rev. Appl. 11(6), 064002 (2019).

Magneto-Optical Spectra of Magnetic Photonic Crystal with Composite (SiO_2-Au) Layer

T V Mikhailova*, S V Osmanov

V.I. Vernadsky Crimean Federal University, Simferopol 295007, Russia

*taciamikh@gmail.com

Abstract. The resonant enhancement of magneto-optical effects due to structure modes arising at the boundary of magnetic photonic crystal $[TiO_2 / SiO_2]^m$ / iron garnet / SiO_2 / (SiO_2-Au), in which the upper layer (SiO_2-Au) is a composite layer of SiO_2 with metallic Au nanoscale inclusions and iron garnet is a bi-layer of composition $Bi_{1.0}Lu_{0.5}Gd_{1.5}Fe_{4.2}Al_{0.8}O_{12}$ / $Bi_{2.3}Dy_{0.7}Fe_{4.2}Ga_{0.8}O_{12}$, has been considered by modelling of 4×4 transfer matrix method.

1. Introduction and motivation

The synthesis and investigation of magnetic photonic crystals (MPC) with one-dimensional (1D), two-dimensional (2D) and three-dimensional (3D) structuring attract the attention of researchers due to the implementation of new effects associated with the propagation of light waves inside such structures [1]. Structuring opens up the possibility of localizing and amplifying the electromagnetic field of a light wave inside magnetic layers of 1D structures or magnetic elements of various shapes of 2D and 3D structures, creating resonance features in optical and magneto-optical (MO) spectra. The use of metal and composite metal-dielectric components allows transformation of properties due to the excitation of propagating surface plasmon-polaritons, localized plasmons and optical Tamm states (OTS). It should be noted, that the properties of MPCs based on composites have not been considered previously. The authors present the modelled optical and MO spectra of a similar structure – MPC with a composite layer (SiO_2-Au).

2. Results

The structure under consideration can be represented by the general formula

No.1 – $[TiO_2 / SiO_2]^m$ / G1 / G2 / SiO_2 / (SiO_2-Au).

There, $[TiO_2 / SiO_2]^m$ is Bragg mirror made of silicon and titanium dioxide layers with repetition number m; G1 is bismuth-substituted garnet layer $Bi_{1.0}Lu_{0.5}Gd_{1.5}Fe_{4.2}Al_{0.8}O_{12}$; G2 is bismuth-substituted garnet layer $Bi_{2.3}Dy_{0.7}Fe_{4.2}Ga_{0.8}O_{12}$; SiO_2 is a buffer layer of silicon dioxide and (SiO_2-Au) is a composite layer with nanoparticles Au.

As a comparison, we also present the MO spectra of MPC with an upper continuous layer of Au:

No.2 – $[TiO_2 / SiO_2]^m$ / G1 / G2 / SiO_2 / Au.

In order to simulate the optical and MO properties of MPC and numerically solve Maxwell's equations, a software algorithm was implemented using the transfer matrix method 4×4. The software algorithm takes into account the angle of incidence of light on the structure θ, incident light wave polarization state Ψ, anisotropy and gyration of structure layers [2]. The dielectric constant of composite

(SiO_2-Au) layer was calculated based on the Maxwell-Garnett model. The sizes of nanoparticles in the matrix should be much less than the wavelength, that is, should not exceed 30 nm. For such structures, the optical Tamm state exists only in a certain area – in the area, where the composite is similar to metal [3]. In general, the properties of the composite will depend on the volume fraction *f* and the geometry of nanoparticles affecting the depolarization parameters $L_{\perp}$ and $L_{\parallel}$.

Figure 1 shows the spectral dependences of Faraday Effect for structural modes – the OTS (No. 1 and No. 2) and resonant mode (No. 1).

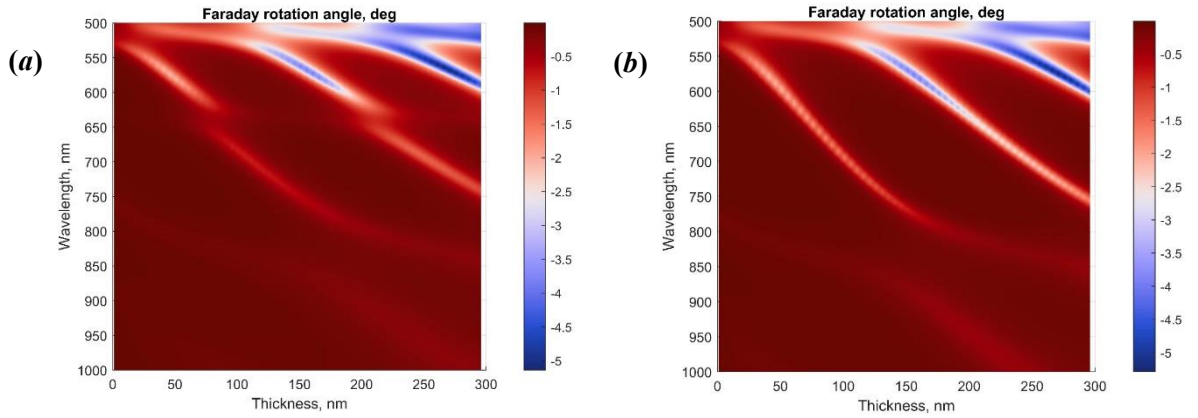

Figure 1 (a, b). Faraday rotation spectra of MPCs No. 1 **(a)** and No. 2 **(b)** at normal incidence $\theta = 0$ deg depending on the thickness of a layer G2. m = 4. The parameters of structures: the thicknesses of Bragg mirror layers TiO_2 and SiO_2 are 71 nm and 105 nm, respectively; the thickness of G1 is 80 nm; the thickness of G2 is varied from 0 nm to 300 nm; the thickness of top SiO_2 layer is fixed at 30 nm. The Au layer in No. 2 **(b)** and composite (SiO_2-Au) in No. 1 **(a)** have the thicknesses of 30 nm and 60 nm, respectively. $f = 0.45$; $L_{\perp} = L_{\parallel} = 1/3$.

It is demonstrated that, depending on the parameters of composite layer, the excitation of OTS and resonance defect modes is possible. The structure parameters were optimized in order to achieve the highest MO quality factor. It should be noted that one of the useful properties of such composites is that as a result of imperfect particles, the composite can work as a polarizer. Longitudinal and transverse components of electromagnetic waves will interact with the structure in different ways.

Acknowledgments
This work was supported by Russian Science Foundation (project No.19-72-20154).

References

[1] *Magnetophotonics* 2013 (Springer-Verlag Berlin Heidel-berg; eds. M. Inoue et al.).
[2] Passler N C, Paarmann A 2017 Generalized 4 × 4 matrix formalism for light propagation in anisotropic stratified media: study of surface phonon polaritons in polar dielectric heterostructures *Journal of the Optical Society of America B* 34 (10) 2128
[3] Vetrov S Ya, Bikbaev R G, Timofeev I V 2013 Optical Tamm states at the interface between a photonic crystal and a nanocomposite with resonance dispersion *JETP* 117 (6) 988

Neural networks application to determine the types and magnitude of aberrations from the pattern of the point spread function out of the focal plane

P A Khorin[1*], A P Dzyuba[3], P G Serafimovich[1,2] and S N Khonina[1,2]

[1]Samara National Research University, 34, Moskovskoye Shosse, 443086, Samara, Russia
[2]IPSI RAS - branch of the FSRC «Crystallography and Photonics» RAS, 151 Molodogvardejskaya street, 443001, Samara, Russia
[3]Saint-Petersburg National Research University of Information Technologies, Mechanics and Optics, 49, Kronverksky Prospekt, 197101, Saint Petersburg, Russia

*Corresponding author, e-mail: paul.95.de@gmail.com

Abstract. Recognition of the types of aberrations corresponding to individual Zernike functions were carried out from the pattern of the intensity of the point spread function (PSF) outside the focal plane using convolutional neural networks. The PSF intensity patterns outside the focal plane are more informative in comparison with the focal plane even for small values/magnitudes of aberrations. The mean prediction errors of the neural network for each type of aberration were obtained for a set of 8 Zernike functions from a dataset of 2 thousand pictures of out-of-focal PSFs. As a result of training, for the considered types of aberrations, the obtained averaged absolute errors do not exceed 0.0053, which corresponds to an almost threefold decrease in the error in comparison with the same result for focal PSFs.

1. Introduction

Recently, to solve the problem of recognition and compensation of optical system aberrations from the PSF intensity pattern in a certain plane, the means of intellectual analysis and machine learning are increasingly being used [1-5]. Some works [4, 5] showed the problems of using focal PSF at low levels of aberrations, when the intensity pattern is almost indistinguishable from the focal spot.

The purpose of this work is to investigate the possibility to improve the results of using neural networks to solve the problem of recognizing the type and magnitude of wavefront aberration from the PSF pattern outside the focal plane. The architecture of the neural network corresponded to the Xception [6] adapted for the regression problem.

A numerical experiment showed that, trained on 8 separate types of aberrations, matched with the Zernike functions, the neural network confidently copes with the classification task, i.e. detection in a superposition of two different types of aberrations of their presence. The obtained averaged absolute errors do not exceed 0.0053, which corresponds to an almost threefold decrease in the error as compared to the analogous result for focal PSFs.

2. Results and discussion

Wavefront aberrations are usually described in terms of Zernike functions $Z_{nm}(r,\varphi)$:

$$W(r,\varphi)=\exp\lfloor i\psi(r,\varphi)\rfloor, \tag{1}$$

where $\psi(r,\varphi)=2\pi\alpha\sum_{n=0}^{n_{\max}}\sum_{m=0}^{n}C_{nm}Z_{nm}(r,\varphi)$. (2)

The PSF outside the focal plane z can be calculated using the Fourier transform with the addition of the defocusing function to the wavefront (1):

$$G(u,v,z)=\int_{-\infty}^{\infty}\int_{-\infty}^{\infty}W(x,y)\exp\left[\pi i/\lambda z(x^2+y^2)\right]\exp\left[-2\pi i(ux+vy)\right]dxdy\cdot \tag{3}$$

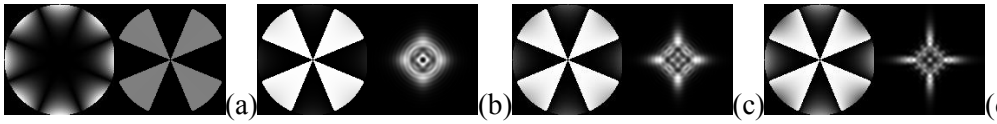

Figure 1. Fragment of dataset for z=500 mm, λ=540 nm: (a) – amplitude and phase Z_{44}, (b)-(d) – wavefront phase $W(r,\varphi)$ and PSF intensity at α equal to 0.1, 0.25, and 0.5, respectively

A dataset with 2 thousand images of out-of-focal PSFs (Fig. 1) was used to train the neural network. It was divided in a 4:1 ratio into training and validation sets. The neural network architecture corresponded to the Xception neural network adapted for the regression problem. Adam was chosen as the optimization algorithm, the initial learning factor was 0.0001, and the number of epochs equal was 250. The loss function was the mean absolute error, which was obtained in the range from 0.0041 to 0.0053.

3. Conclusion

Within the framework of this work, PSF patterns were simulated outside the focal plane for a coherent case, and a neural network training process was carried out to recognize the type and magnitude in a superposition of two different types of aberrations. The use of out-of-focal PSFs made it possible to almost 3 times reduce the recognition error in comparison with the same result for focal PSFs.

Acknowledgments

This work was supported by the Russian Foundation for Basic Research (grants 20-37-90129, 19-29-09054).

References

[1] Guo H, Korablinova N, Ren Q, Bille J 2006 Wavefront reconstruction with artificial neural networks *Opt Express* **14** 6456-6462 DOI: 10.1364/OE.14.006456.

[2] Paine SW, Fienup JR 2018 Machine learning for improved image-based wavefront sensing *Opt Lett* **43** 1235-1238 DOI: 10.1364/OL.43.001235.

[3] Dzyuba AP 2019 Optical phase retrieval with the image of intensity in the focal plane based on the convolutional neural networks *J Phys Conf Ser* **1368** 022055 DOI: 10.1088/1742-6596/1368/2/022055.

[4] Nishizaki Y, Valdivia M, Horisaki R, Kitaguchi K, Saito M, Tanida J, Vera E 2019 Deep learning wavefront sensing *Opt Express* **27** 240-251 DOI: 10.1364/OE.27.000240.

[5] Rodin IA, Khonina SN, Serafimovich PG, Popov SB 2020 Recognition of wavefront aberrations types corresponding to single Zernike functions from the pattern of the point spread function in the focal plane using neural networks *Computer Optics* **44** 923-930 DOI: 10.18287/2412-6179-CO-810.

[6] Chollet F 2017 Xception: Deep learning with depthwise separable convolutions *Proc IEEE Conf on Comp Vis Pattern Recogn* 1251-1258 DOI: 10.1109/CVPR.2017.195.

The study of molecular composition in biomimetic interface of biocomposite/dentin

D Goloshchapov[1], V Kashkarov[1], K Nikitkov[1] I Ippolitov[2], Yu Ippolitov[2], J Vongsvivut[3] and P Seredin[1]

[1]Department of Solid State Physics and Nanostructures, Voronezh State University, Voronezh, Russia
[2]Department of Pediatric Dentistry with Orthodontia, Voronezh State Medical University, Voronezh, Russia
[3] Australian Synchrotron (Synchrotron Light Source Australia Pty LTD), 800 Blackburn Rd Clayton, VIC 3168, Australia
e-mail: goloshchapov@phys.vsu.ru

Abstract. The aim of the study is the problem of formation of the biomimetic interface between the dental product and dentin of the human tooth as well as the investigations of molecular-chemical features in biointerface with the use of molecular multi-dimensional IR-visualization. The data on synchrotron IR-mapping made it possible ensured to differentiate the regions of sound dentin tissue and biomimetic transition layer and also to determine molecular groups responsible for the process of integration.

1. Introduction

Biomimetic remodeling of enamel and dentin of teeth demonstrates that in order to improve integration of dental products with the hard dental tissue it is required to form nano-filled biomimetic buffer layers and their composition should involve nanocrystalline hydroxyapatite (n-HAP) and amino acid matrix [1]. Engineering of biomimetic interface between the dental composite and natural dentin as well the study of organic-mineral interaction appearing in biointerface with the use of molecular IR-visualization technique was the aim of our study.

2. Materials and methods

The study was performed on tooth samples removed from patients aged 20-40 according to the orthodontic criteria. With the use of Er:YAG laser hard dental tissue was prepared up to dentin. Next, dentin conditioner, bio-primer and universal adhesive were deposited layer by layer on the prepared surface of dentin in the conditions of alkaline environment with pH > 11 for the formation of the buffer hybrid layer [2]. To promote formation of the bond with the apatite of dentin polar amino acids – L-lysine hydrochloride and L-arginine hydrochloride were additionally introduced in the composition of bio-primer. Nanocrystalline carbonate-substituted hydroxyapatite (n-CHAP) was introduced as a filler in the universal adhesive [3].

In accordance with the requirements of the microspectroscopic research techniques for the geometry of the samples, we prepared plane-parallel segments of the teeth. Molecular composition of the interface samples was studied with the use of synchrotron ATR FTIR-microspectroscopy [4].

3. Results

Applying the proposed technique of molecular analysis mapping of biointerface was performed for the region between biomimetic apatite layer and dentin tissue of the human tooth (60×30 μm) (figs. 1,2) with a spatial resolution of 1 μm. Basing on the color coding one-dimensional IR-maps were designed that demonstrate the distribution of molecular group of ether –$COOCH_3$ (1762-1701 cm^{-1}) associated with compomer (Fig. 1) and vibrations of molecular groups CH_2, CH_3, the bands of Amid III and collagen which are present in dentin (Fig. 2).

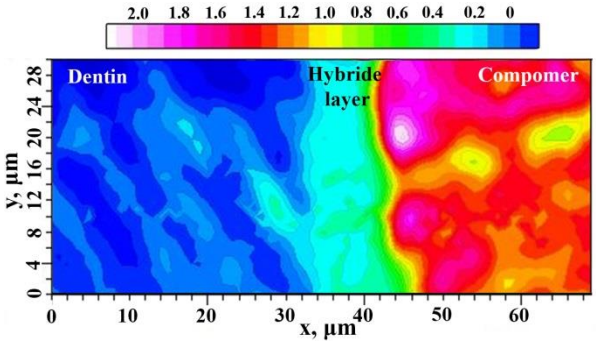

Figure 1. The FTIR map of dentin\composite interface calculated on the basis of color coding of the absorption band 1762-1701 cm^{-1} intensity.

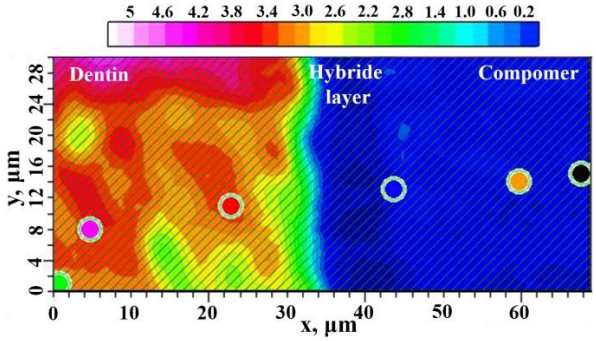

Figure 2. The FTIR map of dentin\composite interface calculated on the basis of color coding of the absorption band 1485-1376 cm^{-1} intensity.

The following hierarchical cluster analysis of the spectral data [5] demonstrated that the interaction between dental product and the natural hard tissue of dentin is realized by the biomimetic buffer layer that is bound with partially demineralized dentin matrix (Fig. 1) and organic-mineral interaction occurs within the 10 μm region.

4. Conclusion

Applying synchrotron IR-mapping it was shown that our elaborated biomimetic buffer layer involving n-CHAP and the complex of the main polar amino acids which are characteristic for the natural dental tissue can produce the functional bond as with the dental compomer as with natural dentin. The use of biomimetic buffer layers makes it possible to achieve an excellent biocompatibility during repair of dental structure and it can form the basis for the new therapeutic approach in dentistry.

Acknowledgments

This work was supported by the grant of Russian Science Foundation, grant number 21-15-00026. The part of this research was undertaken with The Infrared Microspectroscopy (IRM) beamline at the Australian Synchrotron.

References

[1] Comeau P and Willett T 2018 *Sci. Rep.* **8** 12700
[2] Seredin P V, Goloshchapov D L, Prutskij T and Ippolitov Yu A 2017 *Results Phys.* **7** 1086–94
[3] Goloshchapov D L, Lenshin A S, Savchenko D V and Seredin P V 2019 *Results Phys.* **13** 102158
[4] Seredin P, Goloshchapov D, Ippolitov Y and Vongsvivut J 2020 *Sci. Rep.* **10** 20891
[5] Savić D, Joković N and Topisirović L 2008 *Dairy Sci. Technol.* **88** 273–90

Analogue of the Kerker effect for spontaneous parametric down-conversion process in dielectric nanoparticle

A A Nikolaeva[1], K S Frizyuk[1], N A Olekhno[1], A S Solntsev[2], M I Petrov[1]

[1] ITMO University, St. Petersburg 197101, Russia
[2] University of Technology Sydney, 15 Broadway, Ultimo NSW 2007, Australia

e-mail: anna.nikolaeva@metalab.ifmo.ru

Abstract: A study of generation and propagation of entangled photon pairs is one of the key topics in contemporary quantum optics. In the present paper, we theoretically describe a generation of such photon pairs in the process of spontaneous parametric down-conversion of light by a resonant spherical nanoparticle made of dielectric material with a $\chi^{(2)}$ nonlinearity. We assume that the size of a nanoparticle satisfies the condition of resonant eigenmodes existence that can be described by Mie theory. We study the correlation between generated photons and show nonlinear Kerker effect at the collinear photon emission.

1. Introduction

Creation of correlated photon pairs is one of the key topics in contemporary quantum optics [1]. Here, we theoretically describe the generation of photon pairs in the process of spontaneous parametric down-conversion (SPDC) in a resonant spherical nanoparticle made of a dielectric material with bulk $\chi^{(2)}$ nonlinearity. During this nonlinear process one pump photon at frequency ω_{pump} is absorbed and two photons, the idler and the signal, are generated at frequencies ω_i and ω_s respectively so that $\omega_i + \omega_s = \omega_{pump}$ [2]. Nowadays, considerable attention in areas of nonlinear and quantum optics is attracted to this optical phenomenon at the nanoscale. Resonant interaction of light with nanostructures is of particular interest. For example, the Mie resonant nanostructures have already been suggested to enhance spontaneous photon emission processes such as Raman scattering [3, 4], photoluminescence emission [5, 6] as well as SPDC process [7]. We reveal that highly directional photon-pair generation can be observed utilizing the nonlinear Kerker-type effect, and that this regime provides useful polarization correlations.

2. Results

We obtain that to observe this nonlinear Kerker effect, as well as for linear one, we need decay into two crossed dipole modes and also to the two same dipoles [8]. For example, to observe the directivity along z-axis: first decay - magnetic with respect to x-axis and electric with respect to *y*-axis; second one - two electric dipoles with respect to *y*-axis. Also, according to the selection rules [9] to observe directional radiation, a certain type of tensor $\chi^{(2)}$ is required. For example, to observe the directivity along z-axis, the green components of the tensor (figure 1d) must be non-zero, in particular, this corresponds to the BaTiO3 lying along *x*-axis. The figure 1e shows the prevalence of forward scattering for such a configuration (figure 1b) at the collinear photon emission $\boldsymbol{r}_i = \boldsymbol{r}_s = \boldsymbol{r}$.

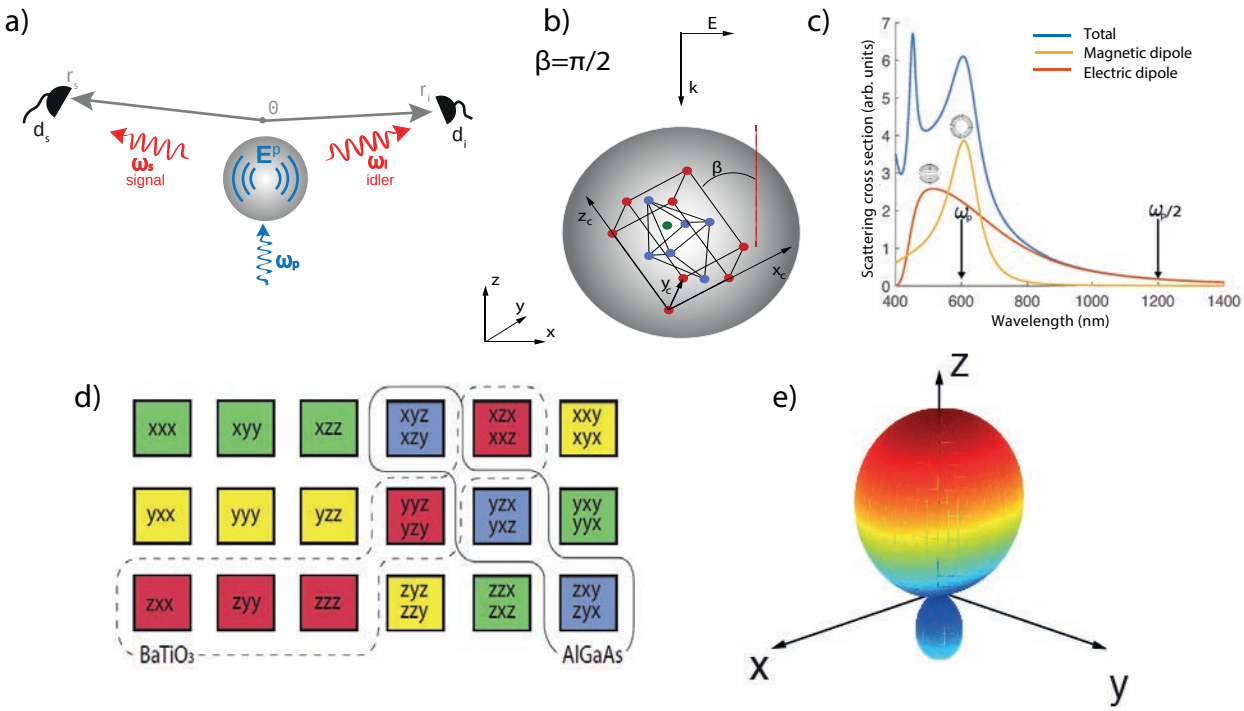

Figure 1. a) schematic of SPDC process: signal and idler photons are being detected at the point in the far-field region. The process is degenerate; therefore, the frequencies of the signal and idler photons are equal $\omega_s = \omega_i = \omega_{pump}/2$; b) $BaTiO_3$ lying along x-axis ($\beta = \pi/2$); c) scattering cross-section of $BaTiO_3$ nanoparticle of 240 nm diameter, blue line - total, yellow line - magnetic dipole (MD), red line - electric dipole (ED); d) nonlinear susceptibility tensor $\chi^{(2)}$; e) directionality diagram of collinear two-photon detection $|T(\boldsymbol{r}_f; \boldsymbol{r}_i)|^2$ for $BaTiO_3$.

Acknowledgments

A. A. N. acknowledges support by the Quantum Technology Centre, Faculty of Physics, Lomonosov Moscow State University.

References

[1] Horodecki R, Horodecki P, Horodecki M, and Horodecki K 2009 *Rev. Mod. Phys.* **81**
[2] Klyshko D, Penin A, and Polkovnikov B 1970 *JETP Lett.* **11**
[3] Frizyuk K, Hasan M, Krasnok A, Al´u A, and Petrov M 2018 *Phys. Rev. B* **97** 085414
[4] Dmitriev P, et. al. 2016 *Nanoscale* **8** 9721
[5] Zambrana-puyalto X and Bonod N 2015 *Physical Review B* **91** 195422
[6] Rocco D, et. al. 2020 *Journal of the Optical Society of America B* **37** 2738
[7] Poddubny A and Smirnova D 2018 *arXiv*:1808.04811
[8] Nikolaeva A, Frizyuk K, Olekhno N, Solntsev A, Petrov M 2021 *Phys. Rev. A* **103** 043703
[9] Frizyuk K, Volkovskaya I, Smirnova D, Poddubny A and Petrov M 2019 *Phys. Rev. B* **99**

Mass spectrometry analysis of C-dots produced by femtosecond laser irradiation of L-lysine film.

A A Astafiev[1], A A Gulin[1], A A Vasin[1], A M Shakhov[1], A D Zalessky[1], A A Osychenko[1] and V A Nadtochenko[1]

[1]N.N. Semenov Federal Research Center of Chemical Physics, Russian Academy of Sciences, Kosygina 4, Moscow, Russia

*e-mail: alina.chemphys@gmail.com

Abstract. The production of carbon dots (C-dots) by femtosecond lasers within living cells and tissues is a novel approach, which has a great potency for intracellular bioimaging. An exact mechanism of fluorescent particles production as well as their composition still remains unknown. In this work we use L-lysine film as a model system to study the mechanism and the composition of C-dots produced by femtosecond laser irradiation investigated by time-of-flight secondary ion mass spectrometry (ToF-SIMS).

1. Introduction

Fluorescent bioimaging is the key method of living cell structure and functioning investigation. Usually bioimaging requires exogenous fluorophore delivery or insertion of genes, coding special fluorescent proteins. A novel approach for bioimaging has been proposed recently [1-3], which is based on the generation of fluorescent carbon dots (C-dots) within a cell or a tissue from its material by femtosecond laser. But chemical-physical processes, leading to C-dots formation, are poorly described and debatable.

Complexity and heterogeneity of the chemical composition of cells and tissues make it difficult to analyse the laser synthesis processes of fluorescent products. In this work we used a film made of L-lysine amino acid as a model system to investigate laser synthesis of C-dots. Being subjected to intensive femtosecond laser radiation, L-lysine is known to be an effective precursor of fluorescent species synthesis. L-lysine film, exposed to 80 MHz and 50 kHz 800 nm femtosecond laser, was then analysed by ToF-SIMS.

2. Methods

2.1. L-lysine film preparation

10 μl of L-lysine solution (0,5 g/l) was placed at the cover glass (24*24 mm, Heinz Herenz), previously subjected to UV lamp (185 and 254 nm), and then covered with another cover glass, which was not subjected to UV. This "sandwich" was dried for 24 hours at 40°. Then the upper cover glass was deleted, and the smooth L-lysine film remained at the lower glass.

2.2. Laser parameters

The detailed scheme of C-dots formation is described here [1]. In these experiments we used following parameters for the irradiation of different areas of L-lysine film: (1) λ = 790 nm, υ = 50 kHz, pulse

energy 6 nJ, the area has been irradiated 10 times; (2) the same as (1), but the area has been irradiated only once (single irradiation); (3) λ = 790 nm, υ = 80 MHz, pulse energy 1,9 nJ, single irradiation; (4) λ = 390 nm, υ = 80 MHz, pulse energy 1,3 nJ, single irradiation; (5) λ = 390 nm, υ = 80 MHz, pulse energy 0,17 nJ, single irradiation.

2.2. Mass spectrometry imaging by ToF-SIMS

L-lysine film was analyzed by mass spectrometer ToF-SIMS 5 (ION-TOF, Germany). Bi_3^+ cluster ions were used as primary ions. Primary ions dose density was 4 x 10^{11} ions/cm^2. Scanning area was 400 x 400 μm with pixels size ~0.8 μm. Chemical maps were obtained for both positive and negative secondary ions.

3. Results.

Figure 1 represents chemical maps of irradiated areas for different secondary ions. Lysine ($C_6H_{15}N_2O_2^+$) signal (d) alters for each irradiated area. The lowest signal was observed in the area 1, which corresponds to the highest irradiation dose. NH_3^+ yield (b) dropped in the area 1 as well, which is likely caused by nitrogen splitting off. Lysine and NH_3^+ redistribution was clearly observed in the areas 3 and 4 and could evidence lysine diffusion under laser irradiation. Interestingly sodium signal increased in the area 1. One may suggest that sodium diffused into the film from the surface of substrate (cover glass). However silicon signal was not detected hence the film in the area 1 was not evaporated completely. Ion with m/z = 177 also showed increase yield in the area 1. This ion may be attributed to $C_{12}H_{17}O^+$ - the product of lysine dimerization. On the contrary ion with m/z = 171 (possibly $C_8H_{17}N_3O^+$, $C_9H_{17}NO_2^+$ or $C_9H_{19}N_2O^+$) showed increase intensity in areas 2, 4 and 5.

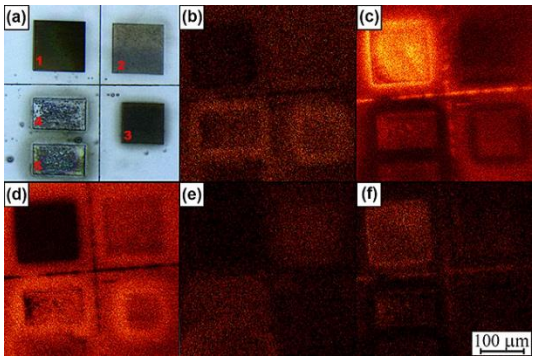

Figure 1. Mass spectrometry imaging of L-lysine film irradiated by femtosecond laser. Numbers indicate areas with different parameters of laser irradiation. (a) optical image; (b) NH_3^+ distribution, (c) Na^+ distribution, (d) – lysine molecular ion ($C_6H_{15}N_2O_2^+$) distribution, (e) distribution of ion with m/z = 171, (e) distribution of ion with m/z = 177.

Acknowledgments

The work has financial support from the Russian Foundation for Basic Research grant 19-53-52007 in the part of ToF-SIMS analysis. Laser synthesis of C-dots was supported by the Russian Scientific Foundation grant No.21-72-20169. The work was performed on facilities of ACBS Center of the Collective Equipment (no. 506694, FRCCP RAS).

References

[1] Sun Q, Qin Z, Wu W, Lin Y, Chen C, He S, Li X, Wu Z, Luo Y and Qu J 2018 *Biomed. Opt. Express* **9** 581-90

[2] Astafiev A A, Shakhov A M, Osychenko A A, Syrchina M S, Karmenyan A V, Tochilo U A and Nadtochenko V A 2020 *ACS OMEGA* **5** 21 12527-38

[3] Osychenko A, Zalessky A, Astafiev A, Shakhov A, Kostrov A, Krivokharchenko A and Nadtochenko V 2020 *Exp. Cell Res.* 111887

Absorption properties of bromide photo-thermo-refractive glasses doped with Ytterbium

V Pesnyakov[1], R Kharisova[1], A Ignatiev[1]
[1] Department of Photonics, ITMO University, St. Petersburg 197101, Russia

Abstract. In this work bromide photo-thermo-refractive glasses with different Ytterbium concentration were explored. It is shown that UV irradiation and subsequent heat treatment cause significant red-shift absorption line from 410 nm with temperature lower than T_g to 517 nm with temperature T_g +60 °C.

1. Introduction

Photo-thermo-refractive (PTR) glass is a very promising material which is widely used for photonic applications such as recording the volume Bragg gratings [1], waveguide structures [2] and lasers structuring [3]. The main processes in PTR glasses which lead to the formation of Ag nanoparticles and subsequent growth of the AgBr-NaBr shell are the following [4,5,6]. On the first stage samples are exposed under UV irradiation into the Ce^{3+} absorption band (310 nm) which causes the formation of neutral silver molecular clusters. The subsequent heat treatment near the glass transition temperature (T_g) leads to the silver nanoparticle formation. With subsequent thermal treatment higher than T_g causes in growth of AgBr-NaBr shell on formed Ag nanoparticles.

2. Experiment and results

In this research bromide PTR glasses with Na_2O-ZnO-Al_2O_3-SiO_2 matrix doped with photosensitizers such as CeO_2 (0,007 mol.%), Sb_2O_3 (0,04 mol.%), Ag_2O (0,064 mol.%) and with variable Yb_2O_3 concentration (2 and 1 mol.%) were studied. To find the value of glass transition temperature the scanning calorimeter STA 449 F1 Jupiter (Netzsch) was used. The obtained T_g for Yb 2 mol.% is 590 °C and for 1 mol.% is 550 °C.

Studied temperatures were chosen according to the following rule: -40, 0, +20, +40, +60 °C from T_g. Hence samples with Yb 2 mol.% were thermally treated with temperatures 550, 590, 610, 630, 650 °C and for samples with Yb 1 mol.% temperatures 510, 550, 570, 590, 610 °C were chosen. First, samples were UV irradiated with mercury lamp and then were thermally treated with described temperatures for 1, 3 and 10 hours. Absorption spectrum was recorded on each step and for each temperature. Obtained results for 10 hours thermally treated glasses are shown in figure 1. For comparison absorption spectra for sample without UV irradiation (VIR) and after UV irradiation but without any thermal treatment (UV) are also shown. With increase of thermal treatment, the absorption peak line corresponding to the plasmon resonance also shifts to the red part of spectra. Also, it can be noticed the equal absorption line on 517 nm appears in both samples Yb 2 mol.% and Yb 1 mol.% after the same heat +60 °C from T_g treatment.

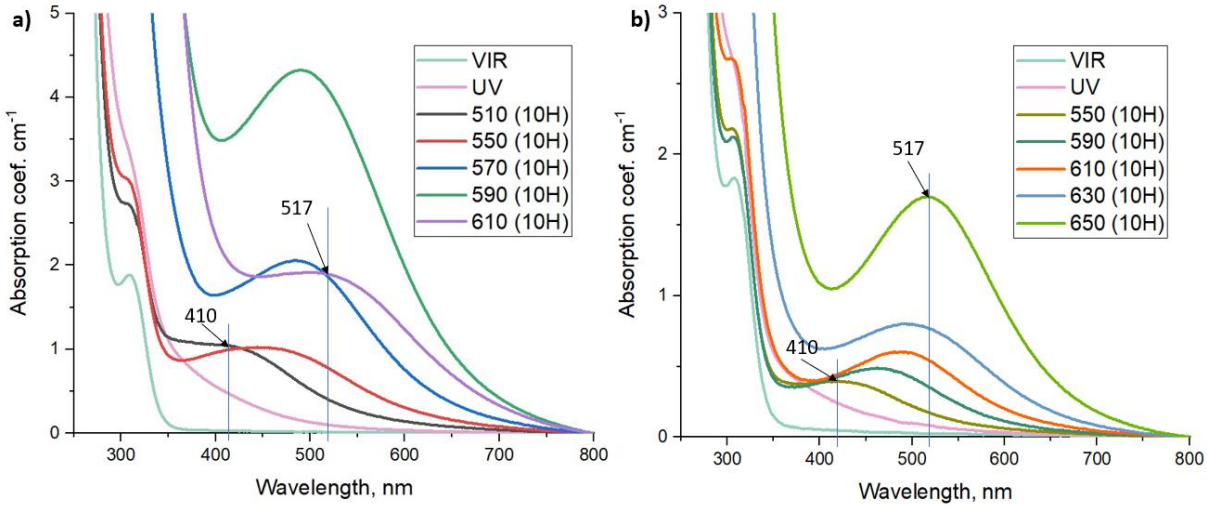

Figure 1(a,b). **(a)** Absorption coefficient spectra for samples with Yb 1 mol.% thermally treated for 10 hors; **(b)** absorption coefficient spectra for samples with Yb 2 mol.% thermally treated for 10 hours.

3. Conclusion

In conclusion, bromide PTR glasses doped with Ytterbium were studied. Absorption spectra for glasses with 1 and 2 mol.% Yb were obtained after UV irradiation and subsequent heat-treatment with different temperatures. It was shown that with increase of heat-treatment temperature absorption line shifts to the higher wavelengths: from 410 nm to 517 nm.

References

[1] Glebov, Alexei L., et al. Volume Bragg gratings as ultra-narrow and multiband optical filters. *Micro-Optics* 2012. **8428**. International Society for Optics and Photonics, 2012.

[2] Sgibnev, Yevgeniy M., et al. Optical gradient waveguides in photo-thermo-refractive glass formed by ion exchange method. *Journal of Lightwave Technology* 33.17 (2015): 3730–35.

[3] Ivanov, S. A., and V. A. Aseev. "Resonator free Er-Yb laser based on photo-thermo-refractive (PTR) glass." *Solid State Lasers XXIII: Technology and Devices*. **8959**. International Society for Optics and Photonics, 2014.

[4] Nikonorov, N. V., et al. Effect of a dielectric shell of a silver nanoparticle on the spectral position of the plasmon resonance of the nanoparticle in photochromic glass. *Optics and spectroscopy* **107.5** (2009): 705–7.

[5] Dubrovin, Victor, Nikolay Nikonorov, and Alexander Ignatiev. Bromide photo-thermo-refractive glass for volume Bragg gratings and waveguide structure recording. *Optical Materials Express* **7.7** (2017): 2280–92.

[6] N. Nikonorov, A. Sidorov, Silver nanoparticles in silicate glasses: synthesis, modification and destruction. *METAL NANOPARTICLES* (2018): 61.

Development of a fiber-optic system for testing instruments for monitoring nuclear power plants

V M Pilipova[1], V V Davydov[2, 3] and V Yu Rud[3, 4]

[1]Bonch-Bruevich Saint Petersburg State University of Telecommunications, Saint Petersburg 193232, Russia
[2]Peter the Great Saint Petersburg Polytechnic University, Saint Petersburg 195251, Russia
[3]All-Russian Research Institute of Phytopathology, Moscow Region 143050, Russia
[4]A.F. Ioffe Physicotechnical Institute, St. Petersburg, Russia

Abstract. The necessity of testing the equipment for monitoring the operation of nuclear power plants is justified. It is proposed to use optical fiber and pulsed laser radiation for these purposes. It is established that optical fiber is more resistant to radiation than other communication systems. The design of a fiber-optic emergency simulator is developed. The calculation of its characteristics is carried out. Their experimental research was carried out. It was found that with an optical signal delay of 98.6 microseconds, the loss is – 26 dB with an uneven frequency response of ± 2 dB. This makes it possible to test the entire set of equipment that uses optical signals used to control a nuclear power plant.

1. Introduction

New nuclear reactor designs are being developed for mobile maritime facilities (ships, floating nuclear power plants, etc.) and existing ones are being upgraded [1, 2]. The verification of nuclear power plants (NPP) requires reliable equipment. One of the main conditions for the safe operation of nuclear power plants is the smooth operation of cooling systems. For cooling the sea-based nuclear power plant uses «heavy» water whose flow rate and parameters are controlled by the nuclear magnetic resonance (NMR) of flow-type meters [2].

In the event of an emergency situation in the nuclear reactor, the level of ionizing radiation acting on «heavy» water of the reactor cooling system is increased dramatically. It has been experimentally established that in this case there is a time shift in the occurrence of the NMR signal in the recording system and a change in its appearance. This shift will be one-time. By measuring this one-time shift (time interval) between the recorded NMR signals and comparing it with that previously determined, and by using the previously received data on such events, a decision can be made much more quickly in the current emergency situation.

In order to keep the time interval measurement system operational, regular testing and testing are required. Considering that a fiber-optic communication link is used in the nuclear power plant control systems to transmit nuclear magnetic resonance signals, it is more logical to develop a device based on optical fiber and laser radiation in order to simulate a nuclear power plant emergency.

2. Experimental results

In this work, a fiber -optic simulator is designed on the basis of a passive fiber -optic delay line which is incorporated into the structure at the entrance of the optical insulator in order to exclude backfired signals [1]. To simulate an emergency, three simulators were developed for different delay times τ3 (49, 75 and 98.6 μs) of the optical signal. The optical signal attenuation was calculated for them (the maximum value was 26 dB, taking into account the system attenuation reserve at the regeneration site of 2 dB. Figure 1 presents as an example the measured delay time τ3 of one simulator. The top signal is not switched on, the bottom signal is with a simulator.

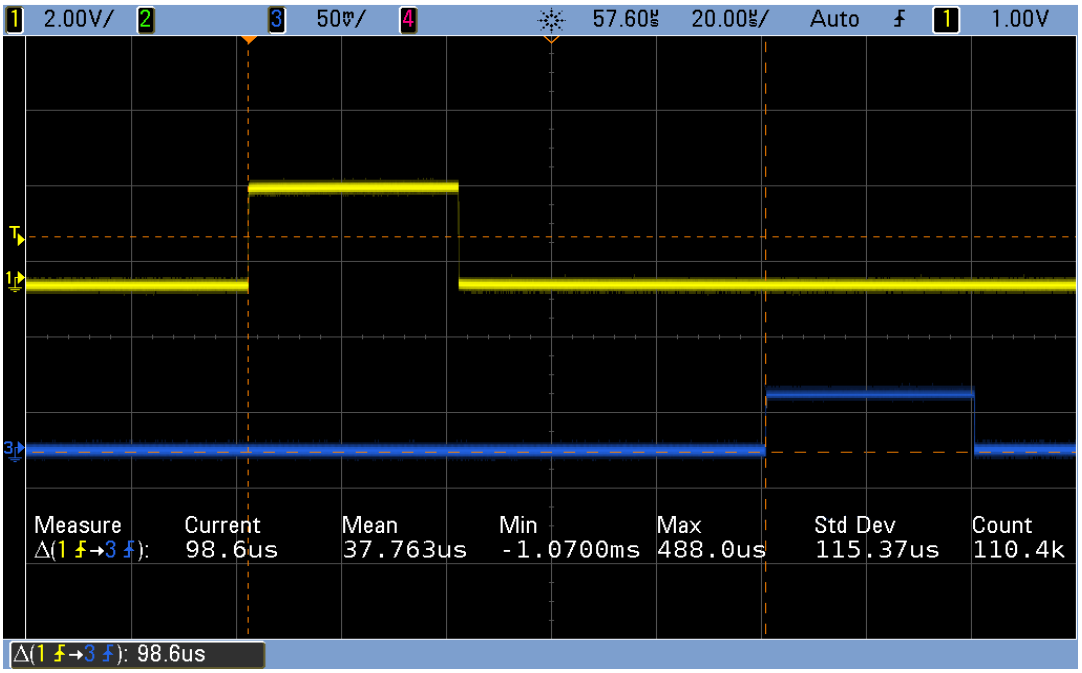

Figure 1. Signal transitions by 98.6 μs. Horizontal division cost 20 μs

Analysis of the signals received shows a reduction in power. Therefore, if a fiber -optic simulator is incorporated into a fiber -optic NMR signal transmission system for testing nuclear power plant control systems, the transmitted signals will need to be amplified, to ensure the necessary accuracy of measurements during testing. The measured dynamics of fiber -optic simulators showed that three instrument designs have a dynamic range of at least 56 dB. Therefore, this reinforcement is relatively simple to implement.

3. Conclusion

The fiber -optic simulator studies have shown that they can also be successfully applied to radar equipment testing, as the noise factor of the developed simulator in the frequency range from 2 to 18 GHz varies by 7 dB (maximum value 27 dB). This shows the wide functionality of the device.

References

[1] Lenets V A, Tarasenko M Yu, Davydov V V, Rodugina N S and Moroz A V 2018 *Journal of Physics: Conference Series* **1038(1)** 012037

[2] Ledbetter M P, Pustelny S, Budker D, Blanchard J W and Pines A 2012 *Physical Review Letter* **108(24)** 243001

Numerical simulation of optical coupling between a microring resonator and a directly connected straight waveguide

V V Pirogov[1], S A Scherbak[1,2]

[1]Department of Physics and Technology of Nanoheterostructures, St. Petersburg Academic University RAS, St. Petersburg 194021, Russia
[2]International Laboratory of Quantum Optoelectronics, Higher School of Economics, St. Petersburg 194100, Russia

e-mail: vladimirpirogovspb@gmail.com

Abstract. We studied numerically optical coupling of whispering gallery modes of a microring resonator with modes of a straight waveguide directly connected to the microring. Optical outcoupling from the resonator through the waveguide was calculated for different widths of the latter. The output was maximized under conditions when the width fits an odd integer number of half-wavelengths of light inside the microring.

1. Introduction

Semiconductor microdisk (MD) and microring (MR) lasers support optical whispering gallery modes (WGMs) which have extremely high Q-factor. This determines interest in them, particularly, for optical communications and integrated optics. However, the problem of directional output of their radiation is actual. A promising way to achieve this is to couple a laser with an optical waveguide (OW), either nearly located [1] or directly connected one [2,3]. The former requires fine tuning and provides relatively low output. The latter can ensure more efficient coupling, however modeling of this phenomenon has not been conducted for now. In this study, we numerically model outcoupling from a MR resonator through a straight optical waveguide (2D structure) directly connected to it in radial direction.

2. Modeling

To simulate optical coupling between a MR resonator and an OW, we used COMSOL Multiphysics software. Via finite element method, we calculated eigenfrequencies of WGMs, corresponding electromagnetic field distributions in the structure and power flow in the OW. We considered eigenfrequencies in a near infrared region (around wavelength 1.3 μm). The MR inner/outer radii were 2.6/3.0 μm and its index n_{in}=3.4 (close to GaAs); index of the OW was chosen n_{ow}=1.5 (close to some glasses or polymers); width of the OW, d, was varied in calculations. The microring shape of the resonator was chosen because WGMs of interest are of low radial order (1st or 2nd), and higher radial modes are absent in a ring and do not interfere with calculations.

3. Results and discussion

We simulated a WGM of the 1st radial and the 42nd azimuthal order, TE-polarized (E-field of the mode is out-of-plane), designated as TE(1,42). Properties of TM-polarized modes would be qualitatively the

same. The wavelength of this mode is λ=1344.2 nm. The isolated MR possesses axial symmetry, therefore, WGMs orientation regarding azimuthal angle is arbitrary. However, the OW connected to the MR breaks axial symmetry, and TE(1,42) mode (as well as others) splits into two modes: symmetric (S) and asymmetric (A) one relatively to the symmetry axis (see figure 1). Wavelengths of S and A modes slightly differ from each other and from initial wavelength 1344.2 nm, but the difference does not exceed a few angstroms that indicates a weak influence of the OW on the MR.

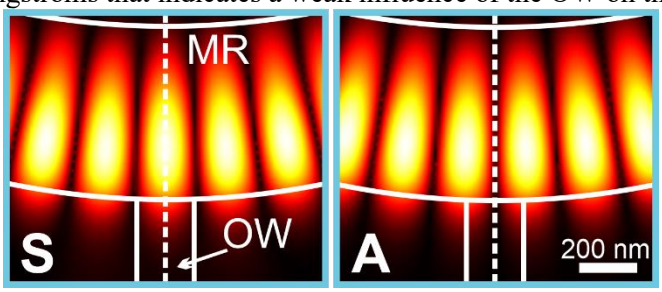

Figure 1. Images of |E|-field of symmetrical (S) and asymmetrical (A) modes. Regions of the microring (MR) and the optical waveguide (OW) are designated. Dashed line is a symmetry axis.

In figure 2 we demonstrate dependence of the relative coupling coefficient (normalized by maximal outcoupling) of the S-mode on the OW width. The coupling coefficient is maximized at certain OW widths: 270, 690, 1170, 1620 nm, etc. Apparently, periodicity of these maxima (approximately 440 nm) correlates with wavelength of light inside the MR, which is $\lambda/n_{in}\approx$400 nm. Also, |E|-field distributions in figure 2 show that the coupling peaks approximately correspond to a condition when the OW width fits an odd integer number of half-wavelengths inside the MR. The distributions also demonstrate through which kind of the OW mode outcoupling occurs. Peaks 1 and 2 correspond to excitation of the fundamental (1st) mode of the OW, since the OWs of the given widths do not support higher odd modes (3rd, 5th, etc.). However, OWs of widths corresponding peaks 3 and 4 do support 3rd mode, and in the insets 3 and 4 one can observe superposition of 1st and 3rd OW modes. These reasonings are also valid for the A-mode, though in this case even OW modes (2nd, 4th, etc.) would be under discussion.

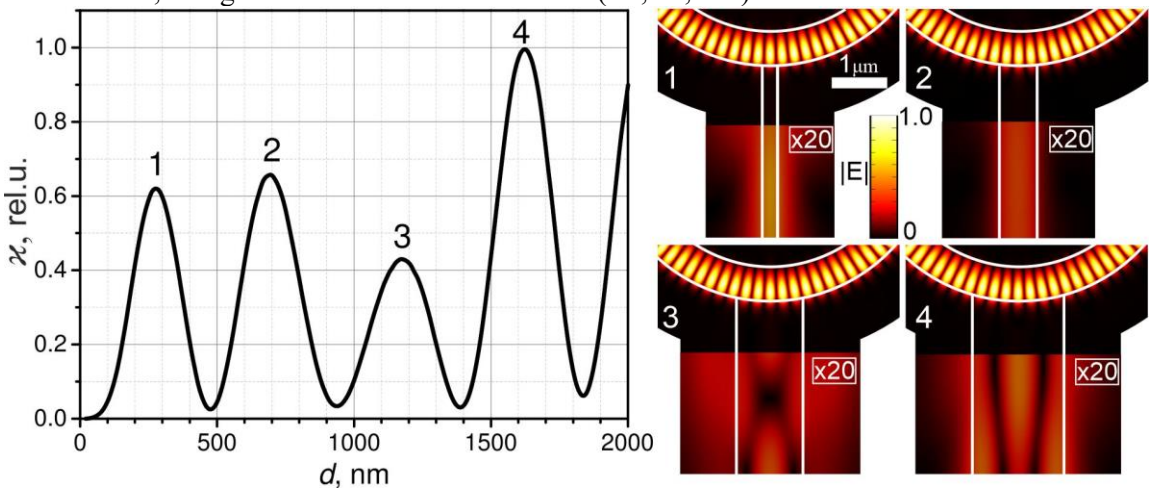

Figure 2. Dependence of the relative coupling coefficient on the OW width. Insets 1-4: |E|-field distributions for maxima of the output (d = 270, 690, 1170, 1620 nm, respectively); |E|-field in the OW and its vicinity is 20-fold artificially enhanced for better visualization.

Acknowledgements

The research leading to these results has received funding from the Basic Research Program at the National Research University Higher School of Economics.

References

[1] Cai D P, Lu J H, Chen C C, Lee C C, Lin C E and Yen T J 2015 *Sci. Rep.* **5** 10078
[2] Liu S, Sun W, Wang Y, Yu X, Xu K, Huang Y, Xiao S and Song Q 2018 *Optica* **5** 612
[3] Ma X-W, Lv X-M, Huang Y-Z, Yang Y-D, Xiao J-L and Du Y 2014 *J. Opt. Soc. Am.* B **31** 2773

Features of the construction of photonic integrated circuits for communication systems

N I Popovskiy[1], V V Davydov[2, 3] and V Yu Rud[3, 4]
[1]The Bonch-Bruevich Saint-Petersburg State University of Telecommunication, Saint Petersburg 195251, Russia
[2]Peter the Great Saint Petersburg Polytechnic University, Saint Petersburg 195251, Russia
[3]All-Russian Research Institute of Phytopathology, Moscow Region 143050, Russia
[4]A.F. Ioffe Physicotechnical Institute, St. Petersburg, 195152, Russia

nikitanikita24@mail.ru

Abstract. The article discusses the main methods of signal processing in a coherent optical transport network based on a photonic integrated circuit to increase the speed and the onset of the terabit era in optical transport networks, cloud and high-performance computing systems. The properties and operational characteristics of the main material platforms of photonic integrated circuits and their future technological units are considered.

1. Introduction

The development of optical transport network technology is stimulated by the emerging services such as data center cloud interconnection services, ultra-bandwidth video services, and 5G mobile network services will drive future optical communications industry development and architecture transformation. Service providers have driven higher speed Ethernet solutions for decades. Router connections, client side optics for optical transport networks (OTN) equipment, and wireless backhaul have continually pushed Ethernet to higher rates and distances to meet the demands for wireless connectivity. And with global demand by consumers for video, this shows no signs of changing.

2. Optical Communication Systems

In connection with the increase in video traffic on the Internet and with an increase in the transmission speed over fiber-optic data transmission systems up to 100 Gbps, and in the future up to 400 Gbps per channel, there is a problem of packet processing on switches and routers of the aggregation and core levels telecom operators, since the speed there is limited by electronic components, where the maximum frequency is 50 GHz. Photonic integrated circuits can meet this growing demand. Super channels allow you to increase the DWDM bandwidth in terabits in one cycle without any loss in terms of spectral efficiency and with the same optical range as the current generation of coherent transponders.

All major optical functions on all 10 100G line cards are bundled into one PIC pair - one for transmit and one for receive. All 10 carriers can now be brought into service in a single duty cycle, consuming much less power than 10 discrete transponders, and the result is significantly improved

service reliability. PICs bring the same engineering usability to super channels that electronic integration brings to multi-core processors or graphics engines.

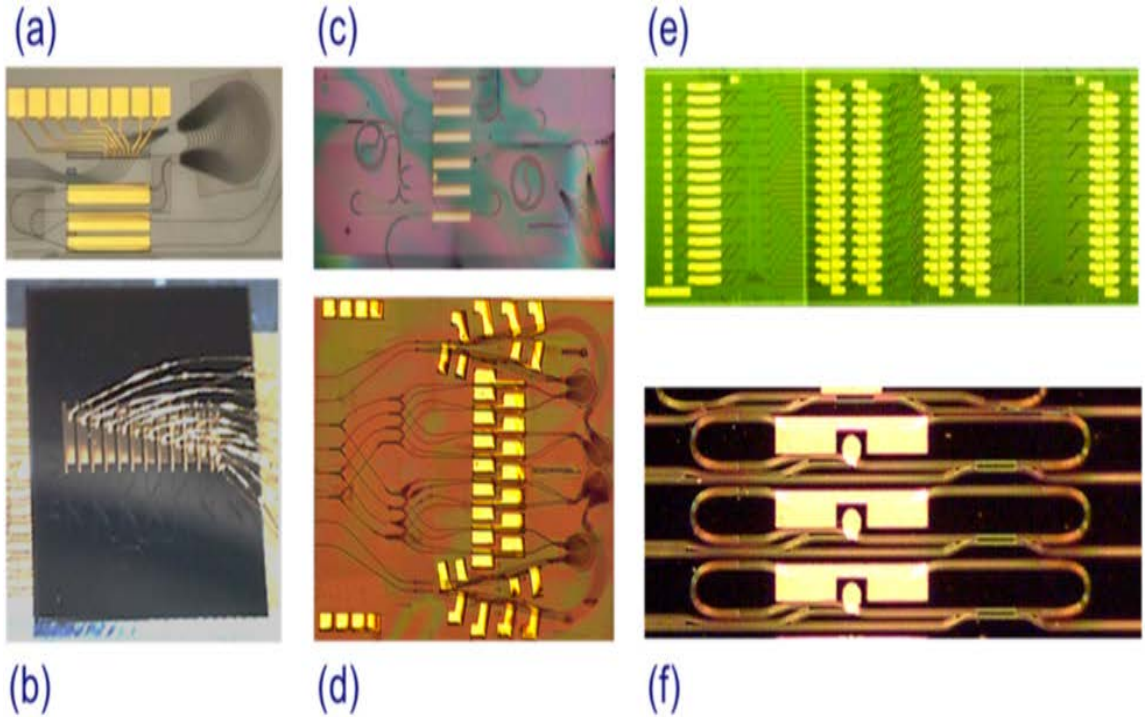

Figure 1. Examples of PICs realized on the generic COBRA platform. (a) AWG-based discretely tuneable laser with nanosecond switching speed (1.5 × 3.5 mm^2); (b) 320 Gb/s monolithic multistage SOA switching circuit, (c) multifunctional delay interferometer (4 × 2 mm^2); (d) 4 × 4 space and wavelength selective cross-connect (4.2 × 3.6 mm^2); (e) monolithic 16 × 16 photonic switch for broadband photonic packet-routing (4.0 × 13.2 mm^2); (f) broad frequency comb laser (0.3 × 2.2 mm^2).

Within reasonable limits, the more carriers there are in the superchannel, the simpler the electronics and the better the optical performance. PICs remove the complexity limitation of optical components and allow you to choose the right engineering balance. As PIC technology advances, new circuits will emerge that will either allow new applications to reliably combine different technologies or continue to scale the component density for photonic VLSI systems.

3. Conclusion

The paper reviews the main application for increasing the demand on internet traffic and for coming the terabit era in optical transport network, in cloud and in high performance computing systems. The new technologies and signal processing in coherent optical transport network based on photonic integrated circuit are described. The properties and performance of the three main material platform of photonic integrated circuit and their future technology nodes are reviewed.

References

[1] Popovskiy N I and Davydov V V and Valiullin L R 2020 Journal of Physics: Conference Series **1695(1))** 012120

[2] Karanov B and Chagnon M 2018 *J. Lightwave Technol* **36 (20)** 4843-4855

Thermo-optical properties of silicon nitride Mach-Zehnder interferometer for the on-chip quantum random number generator

A Prokhodtsov[1,2,3], V Kovalyuk[2,3], P An[2,3], A Golikov[2,4], Y Konyshev[1,2], R Shakhovoy[5,6], V Sharoglazova[5], A Udaltsov[5], Y Kurochkin[5,6,7], G Goltsman[1,2,3]

[1]National Research University Higher School of Economics, Moscow, 101000, Russia
[2]Department of Physics, Moscow State Pedagogical University, 119992, Russia
[3]Institute of Applied Physics of the Russian Academy of Sciences, 603950, Russia
[4]Moscow Institute of Physics and Technology (State University), 141700, Russia
[5]QRate, 100 Novaya str., Skolkovo, Russia
[6]NTI Center for Quantum Communications, National University of Science and Technology MISiS, 4 Leninsky prospekt, Moscow, Russia
[7]Russian Quantum Center, 45 Skolkovskoye shosse, Moscow, Russia

Abstract. We demonstrate the thermo-optical properties of an on-chip silicon nitride Mach-Zehnder interferometer (MZI). The spectral shift of the MZI is associated with a change in the chip temperature. This can be explained by a change in the division ratio of directional couplers, as well as a significant change in phase difference between arms. We experimentally found a phase shift of 2π when heated by 0.8 degrees, theoretically obtained a formula for an arbitrary division ratio of directional couplers in an interferometer, and determined the temperature stability required to the device operation inside a quantum cryptography system.

1. Introduction

High thermo-optical (TO) stability of photonic integrated circuits (PICs) is required in most modern applications, such as quantum key distribution and quantum random number generators, where passive elements, such as Mach-Zehnder interferometers (MZIs), are used to transfer phase-encoded signals into amplitude modulation. In fact, MZIs generally require accurate resonant wavelengths; therefore, the temperature dependence of the effective refractive index n must be taken into account. Inasmuch as the temperature coefficient of the refractive index in silicon nitride, Si_3N_4, (2.45×10^{-5} K^{-1} [2]) is much smaller than that in silicon on an insulator (1.8×10^{-4} K^{-1} [3]), the former is less sensitive to temperature fluctuations. However, due to the large difference between the arms in our Si_3N_4 interferometers [4], even a small change in temperature can significantly affect the operation of the device due to the shift in the optical spectrum. Here, we study the temperature dependence of the optical spectrum, extinction ratio, resonant wavelengths and the phase shift in the MZI.

2. Experimental setup and results

First, we characterized the transmission of MZI in the wavelength range 1510-1620 nm and the extinction ratio (ER) at a wavelength of 1552.85 nm. The change in the temperature of the stage in the range 25 - 30 °C occurred due to the Joule heating of the resistor, which in turn heated the stage on which the sample was located. The stage temperature was controlled using a PID-controller. After the

temperature normalization, the transmission spectrum of the MZI was measured. Figure 1 (a) shows the measured normalized transmission spectra of the MZI without coupling loses for two different temperatures (T), equal to 25 ºC and 30 ºC degrees. ER was calculated as the ratio of the maximum (P_{max}) to the minimum at a wavelength of 1552.82 nm (P_T) optical transmission (Fig. 1b) and is changing from 0.3 to 13 dB in the temperature range of 26.3-26.9 ºC.

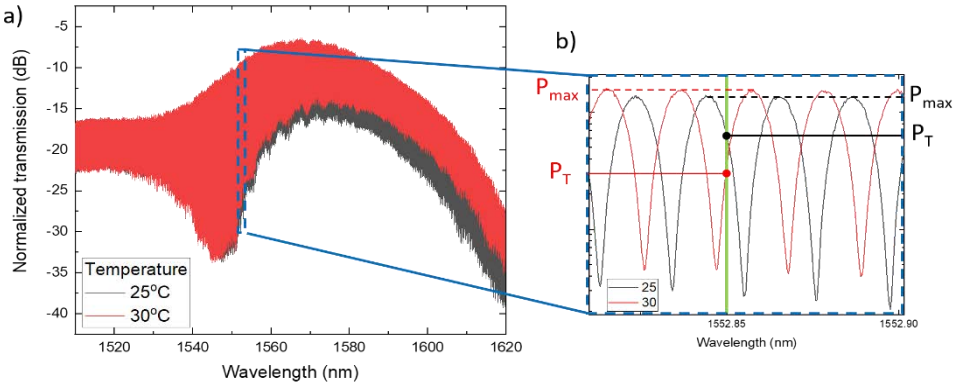

Figure 1. (a, b). (a) The measured normalized transmission spectra of MZI without coupling loses for different temperatures. **(b)** Zoomed transmission spectra of MZI.

Based on the measurement data, we found changes in resonant wavelengths at different temperatures ($d\lambda/dT$) equal 15.5 pm/ºC as well as a phase shift by 2π with a change in the substrate temperature by 0.8-degrees. We also theoretically obtained a formula for an arbitrary division ratio of directional couplers in an interferometer, and determined the temperature stability required to operate inside a quantum cryptography system.

3. Conclusion

We have demonstrated a change in resonance wavelengths by 15.5 pm/ºC, as well as the phase shift by 2π with a change in the substrate temperature by 0.8-degrees, and showed the change in the extinction ratio at a temperature of 26.3-26.9 ºC is changing from 0.3 to 13 dB.

Acknowledgments

We acknowledge support of the Russian Science Foundation grant No. 19-72-10156 (waveguide fabrication), grant No. 17-71-20146 (theoretical and numerical calculations).

References

[1] Stegmaier, M, Ríos, C, Bhaskaran, H, & Pernice W. H, 2016, *Acs Photonics 3*(5), 828-835.

[2] Arbabi A, & Goddard L. L, 2013, *Optics letters 38*(19), 3878-3881.

[3] Komma J, Schwarz C, Hofmann G, Heinert, D, & Nawrodt R, 2012, *Applied Physics Letters 101*(4), 041905.

[4] Prokhodtsov, A., Kovalyuk V, An P, Golikov A, Shakhovoy R, Sharoglazova V, Udaltsov A, Kurochkin Y, and Goltsman G, 2020, *Journal of Physics: Conference Series* 1695, 012118

Control of the mode composition of optical radiation in a microstructured fiber

G A Pchelkin[1, 2], V B Fadeenko[1, 3], V V Davydov[1, 4] and V Yu Rud[4]

[1]Peter the Great St. Petersburg Polytechnic University, Polytechnicheskaya street, 29, Saint-Petersburg, Russia, 195251
[2]Joint Stock Company «Scientific and Production Association S. I. Vavilov State Optical Institute», Babushkina street, 36, bldg.1, Saint-Petersburg, Russia, 192171
[3]Joint Stock Company «Concern «Granit-Electron», Gospitalnaya street, 3, Saint-Petersburg, Russia, 191014
[4]All-Russian Research Institute of Phytopathology, Institutsky pr., 5, Moscow region, Russia, 143050

e-mail: beegrig@mail.ru

Abstract. The construction structure of microstructured fibers is considered. A research scheme of the mode composition and defects control in optical fibers is developed. A microstructured fiber for studying optical vortex fields has been developed and manufactured. The results of studies of the same fiber structure and the distribution of optical radiation depending on the parameters of the technological cycle of its production are presented.

1. Introduction

The volume of transmitted information increase contributes to the rapid scientific and technological progress development [1]. The greatest advantages of communication networks are currently possessed by fiber-optic communication lines (FOCL) [2]. However, modern researchers face the main problem-limiting the volume and speed of data transmitted over a single-mode fiber when developing and modernizing fiber optic communication systems. This problem is faced both on the main communication lines and on the local ones. Technologies based on spectral densification in communication channels have reached their limit. The introduction of even more compaction leads to a sharp and rapid increase in signal attenuation during transmission and loss of information [1].

One of the modern problem solutions associated with constraints is the introduction of a microstructured fiber with a given mode distribution into the fiber optic system. Such fibers, as well as single-mode ones, are resistant to a large temperature range and mechanical influences from outside. With the optimal choice of some fiber parameters, it is possible to ensure that it has only three modes (LP_{01}, LP_{11}, LP_{21}), which are necessary for stable transmission of large amounts of information and low losses. The parameters for the technological production of such fibers are selected at the first stage of development – using modeling. However, the main stage is an experimental study. This is due to the fact that the modeling may not take into account all the factors that affect the microstructured fiber being developed. The paper presents one of the options for solving this problem based on the conducted research.

2. Control of the mode composition of optical radiation and defects in the fiber

Figure 1, as an example, shows the topologies of chiral microstructured fibers., Studies were carried out for them and the distributions of optical radiation at their output were obtained for manufacturing cases with different twisting frequency ω_c and other parameters of the technological cycle.

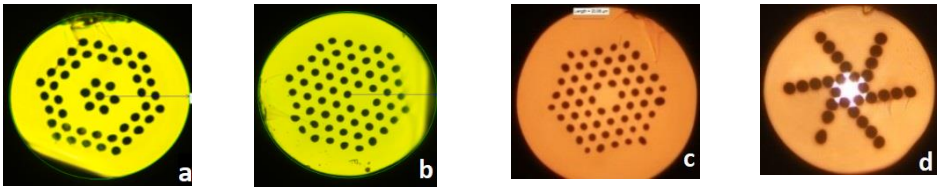

Figure 1. Images of the cross-section of the studied objects microstructured fibers

Figure 2, as an example, shows the distribution of optical radiation at the output of a microstructured fiber, the topology of which is shown in Figure 1 (d), at different speeds of rotation of the workpiece on the stand per meter of fiber length.

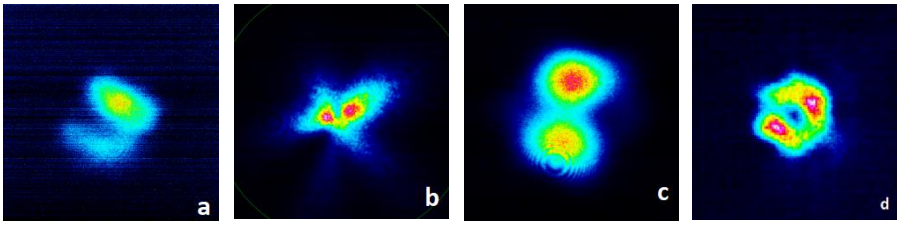

Figure 2. Images of the cross-section of microstructured fibers at different speeds of rotation on the stand. The rotational speeds are respectively equal in Hz: a) 10; b) 20; c) 65; d) 200.

Experimental studies have shown that the fiber mode composition significantly depends on the rotation speed of the workpiece during technological research. And were also calculated using the developed mathematical model of the mode distribution in the cross-section of some types of microstructured fibers. The use of spatial modes LP_{01}, LP_{11}, LP_{21} significantly affects the stability of the resulting signal due to the similar geometry of the intensity distribution.

3. Conclusion

Experimental results confirm that the mode composition in various microstructured fibers depends on the rotation speed of the workpiece and the temperature during its manufacture. The obtained data allow us to improve the technological process of fiber manufacturing to obtain clear three modes necessary to reduce losses in the fiber and increase the information content of the channels.

References

[1] Grebenikova N, Moroz A, Bylina M and Kuzmin M 2019 *IOP Conference Series: Materials Science and Engineering* **497(1)** 012109

[2] Burdin V A, Dashkov M V, Demidov V V, Zhukov A E and Bourdine A V 2020 *Fibers* **8(3)** 18

Features of using a shutter-type modulator in fiber-optic systems

S A Rodin[1], B K Reznikov[1], V V Davydov[2,3] and V Yu Rud[3,4]

[1]The Bonch-Bruevich Saint-Petersburg State University of Telecommunications, Saint-Petersburg 191186, Russia
[2]Peter the Great Saint-Petersburg Polytechnic University, Saint-Petersburg 195251, Russia
[3]All-Russian Research Institute of Phytopathology, Moscow Region 143050, Russia
[4]A.F. Ioffe Physicotechnical Institute, Saint-Petersburg 194021, Russia

E-mail: psnp.174.sut@gmail.com

Abstract. In this work we justify the necessity of using shutter-type modulators to create laser radiation with the required parameters in fiber-optic systems.This is necessary to detect the fact of making changes in the optical system (unauthorized connection with the restoration of the function of communication channels). We have developed a shutter-type optical radiation modulator design. This modulator design has no fundamental limitations on the power of laser radiation, which is used to solve various problems. The results of the modulator to transform the laser light at different frequencies are presented.

1. Introduction

The development of scientific and technological progress has affected various areas of information transmission and control systems for the parameters of various signals [1]. A special place among communication systems is occupied by fiber-optic communication lines and various sensors and systems for converting and monitoring the parameters of optical radiation [2]. The main advantage of using optical systems is passivity to electromagnetic radiation, which is growing every year. In addition, the power of electromagnetic interference increases, which leads to malfunctions in different systems. One of the problems that arise during the maintenance of fiber-optic communication lines is unauthorized access to the system. Such connections are used to solve various tasks. They must be installed promptly. Various methods and techniques have been developed to detect such intrusions into the optical system. One of them is associated with the modulation of laser radiation at different frequencies.

In communication systems, electro-optical modulators (EOM) are used to modulate laser radiation. This is an expensive technology. And its use for the previously described tasks is irrational, because the cost of the system with, for example, 20 channels will increase very significantly. In addition, in some cases, for space control systems, it is necessary to use high-power laser radiation, which is not always combined with the basic design of the EOM, which is being developed for fiber-optic communication lines, in which the laser radiation power is of the order of 10-20 μW. It is also not always advisable to use a laser transmitting module with internal modulation, since the basic designs of these devices have power limitations and their service life during long-term operation is much less than that of standard laser systems. Therefore, the development of simple and reliable designs of

optical radiation modulators, which do not have fundamental limitations when operating in terms of laser radiation power and can operate in a wide frequency range, is an urgent task.

2. Shutter-type modulator design features and the results of its work

In this work we propose a shutter-type modulator design. By the principle of its construction, this is a universal type modulator. Figure 1 shows one of the versions for its design.

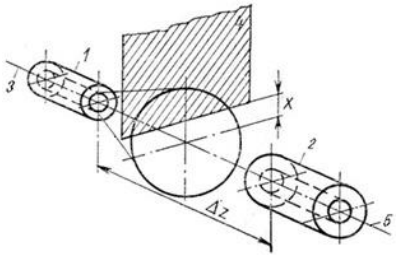

Figure 1. Design of a shutter-type optical radiation modulator: 1 and 2 – optical fibers; 3 – input laser radiation; 4 – movable shutter, fixed on a piezoceramic plate; 5 – modulated laser radiation

There is a gap between a pair of optical fibers - "input" - 1 and "output" - 2. With the use of a membrane placed in this gap - a shutter, modulation of the laser radiation from the “input” fiber to the “output” is performed. The shutter is fixed on a piezoceramic plate connected to a signal generator, the frequency of which can change up to tens of MHz. The modulation process was monitored using an oscilloscope, the input of which was supplied with voltage from the photodetector module. For a more complete representation of the operation of the modulator, standard laser radiation was supplied to the input fiber. The results of the modulation are shown in figure 2.

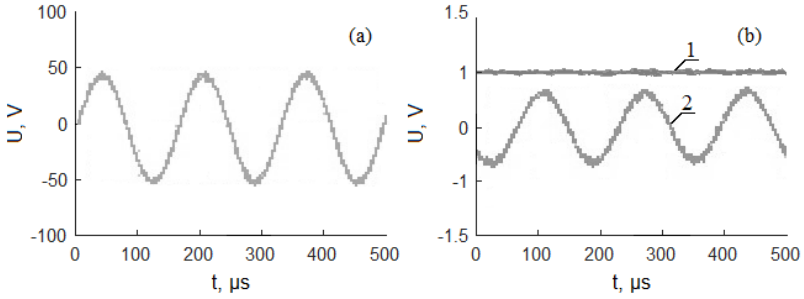

Figure 2. Oscillograms of voltages: (a) – signal from the generator arriving at the piezoceramic plate, (b) – signal from the photodetector: graph 1 –without modulation, graph 2 – after modulation.

The results obtained show that a part of the optical flux that fell on the photodetector is modulated with the same frequency with which the piezoceramic plate vibrates.

3. Conclusions

As a result of the experiment, it was found that the shutter-type modulator developed by us does not distort the signal. This allows to control the change in phase shift in case of unauthorized connection to the system.

References

[1] Makolkina M, Pham V D, Kirichek R, Gogol A and Koucheryavy A 2018 Lecture Notes in Computer Science **11118 LNCS** 547–559

[2] Grebenikova N M, Moroz A V, Bylina M S and Kuzmin M S 2019 IOP *Conference Series: Materials Science and Engineering* **497** 012109

Two-particle topological states induced by quantum statistics and their electric circuit emulation

A D Rozenblit[1], N A Olekhno[1] A A Dmitriev[1], P S Seregin[1], and M A Gorlach[1]
1ITMO University, 197101 Saint Petersburg, Russia

E-mail: alina.rozenblit@metalab.ifmo.ru

Abstract. Features of the topological edge states of particles with fractional quantum statistics (anyons) offer great opportunities for robust quantum computations. In the present work, we demonstrate that a one-dimensional array of cavities can possess statistics-induced topological states of two interacting anyons. As an experimental realization of cavity chains is challenging, we develop a way of emulation of such a system with a classical electrical circuit.

1. Introduction

Anyons are quantum particles characterized by fractional statistics in-between bosons and fermions and described by the statistical angle θ, which is 0 for bosons and π for fermions. They represent great interest for fundamental physics as well as for the practical implementations of quantum computers [1]. Such particles have been observed directly in the fractional quantum Hall effect [1]. Since their direct realizations are challenging, various ways for emulating anyons with alternative platforms are being developed [2, 3]. In the present work, we study the formation of topological edge state of two anyons, and demonstrate that the location of such states depends on the type of quantum statistics. We also develop an electrical circuit emulating a one-dimensional array of coupled cavities.

2. Theoretical model and electrical circuit emulation

We consider a one-dimensional (1D) array of cavities with tunneling couplings, as shown in figure 1(a). This two-particle problem can be reduced to the two-dimensional (2D) tight-binding model, depicted in figure 1(b). Thus, we can represent wavefunctions as two-dimensional maps of coefficients β_{mn} with coordinates (m,n) corresponding to spatial positions of one anyon at the m-th cavity and another one in the n-th cavity. Mode profiles for the system of 9 cavities with tunneling links J = 1, P = –0.75, and the energy of on-site interaction between two anyons U = 1.5 are shown in figure 1(c,d). It is seen that topological edge states of bosonic and fermionic pairs, corresponding to the limiting cases of quantum statistics, localize at the opposite edges of the array.

Tight-binding equations for the considered system can be mapped to the Kirchhoff's rules for the electrical circuit in figure 1(e), allowing to emulate topological edge states of interacting anyons with an electrical circuit. In such a circuit, tunneling links J and P correspond to the capacitors C_J and C_P, respectively. In the limiting cases of statistical angle θ = 0 and θ = π, the element Z(θ) represents positive C_J or negative $-C_J$ capacitor, respectively. The results of circuit simulations confirm the presence of topological edge states of two anyons. The corresponding isolated resonances appear at sites (1,1) and (9,9) for θ = 0 and θ = π, as shown in figure 1(f). Impedance maps of the respective states demonstrate excellent agreement with mode profiles obtained theoretically, figure 1(g,h).

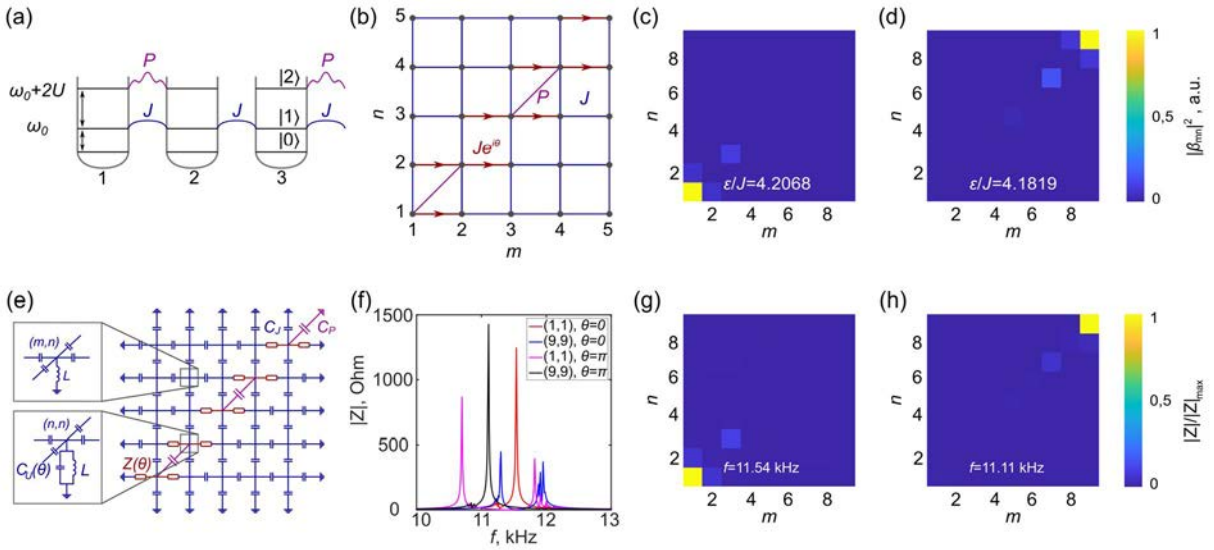

Figure 1. (a) Energy diagram of the considered system. A 1D array of cavities coupled via links J describing the tunneling of one anyon to the neighboring cavity, and tunneling links P corresponding to the simultaneous tunneling of two particles. The energy of one anyon is ω_0 and the energy of on-site interaction between two anyons is 2U. (b) Equivalent 2D tight-binding model with the statistical exchange angle θ. (c,d) Amplitude maps of two-particle wave functions for the array consisting of 9 cavities in the case of the topological edge state of two bosons θ = 0 (c) and two fermions θ = π (d) with state energies indicated in the respective panels. (e) Electrical circuit schematic. Capacitors C_J and C_P, and variable impedances Z(θ) corresponding to the tunneling couplings J, P and $Je^{i\theta}$ are shown in blue, purple and red, respectively. Diagonal nodes are grounded by the LC circuits with capacitors $C_U(\theta)$ and inductors L, while others are grounded just by inductors L. (f) Simulated spectra of the absolute value of impedance at the sites (1,1) and (9,9) for two bosons (red and blue solid lines) and two fermions (purple and black solid lines). (g,h) Maps of the absolute value of impedance for the frequencies corresponding to the topological edge states of two bosons (g) and two fermions (h).

3. Conclusion

We have demonstrated that topological edge states of anyons localize at the opposite edges of the cavity array in the limiting cases of bosons and fermions, facilitating the emergence of statistics-induced topological states. The electrical circuit emulating such states is developed and analyzed.

References

[1] Nayak C, Simon S H, Stern Ady, Freedman M, and Das Sarma S 2008 Rev. Mod. Phys. 80, 1083–1159
[2] Longhi S, and Della Valle G 2012 Opt. Lett. 37, 2160–2162
[3] Todorić M, Jukić D, Radić D, Soljăić M, and Buljan H 2018 Phys. Rev. Lett. 120, 267201

Interlayer Exciton-Polaron in Atom-thin Bilayers

Z A Iakovlev[1], M M Glazov[1,2]

[1] Ioffe Institute, St. Petersburg, Russia
[2] National Research University Higher School of Economics, St. Petersburg, Russia

e-mail: iakovlev.zakhar@gmail.com

Abstract. The interaction between the flexural phonons in bilayers based on two-dimensional semiconductors and interlayer excitons is analyzed. A novel type of exciton-phonon bound state is studied. The energy and effective mass of the polaron are calculated and analyzed. The role of tension, which makes phonons more rigid, is explored and we address the effects of the phonon energy renormalization due to the anharmonicity and their manifestations in the polaron properties. Possible manifestations of these effects in transport and optical properties are discussed.

1. Introduction

Coupling between lattice vibrations and excitons in solids is a key interaction controlling optical properties and kinetics of quasiparticles in two-dimensional (2D) semiconductors. One of key features of 2D crystals is the presence of soft, flexural phonons with $\omega \propto q^2$ dispersion, where q is the in-plane wavevector. These vibrations are accompanied with the out-of-plane atomic displacements which cost almost no energy. Flexural vibrations give rise to the rippling and crumpling of 2D layers and affect their elastic and thermodynamic properties [1].

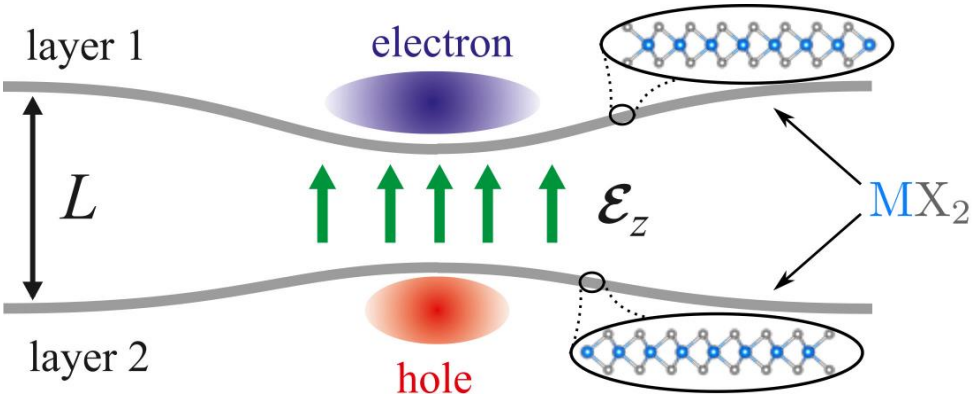

Figure 1. Schematic illustration of the bilayer exciton-polaron. Here the space between the monolayers is not filled by any material. The attraction between electron and hole described by the electric field $\mathcal{E}_z$ leads to deformation of the monolayers and formation of a nanosize polaron state.

2. Results and discussion

Here we study a novel type of exciton-phonon bound state – interlayer polaron – in a double-layer 2D semiconductor with transition metal dichalcogenides as an example, figure 1, predicted in [2]. We show that the interaction of the interlayer exciton with the soft modes of out-of-plane vibrations caused by van der Waals forces and flexural rigidity gives rise to a bound quasiparticle.

We focus here on the role of tension in the system which makes dispersion of the long-wavelength phonons linear $\omega \propto q$ and also the effects of anharmonicity. The dependencies of the polaron energy and mass are calculated analytically in the weak coupling regime by means of the second-order perturbation theory. Regimes of high and low tension are distinguished and analyzed, as illustrated in figure 2.

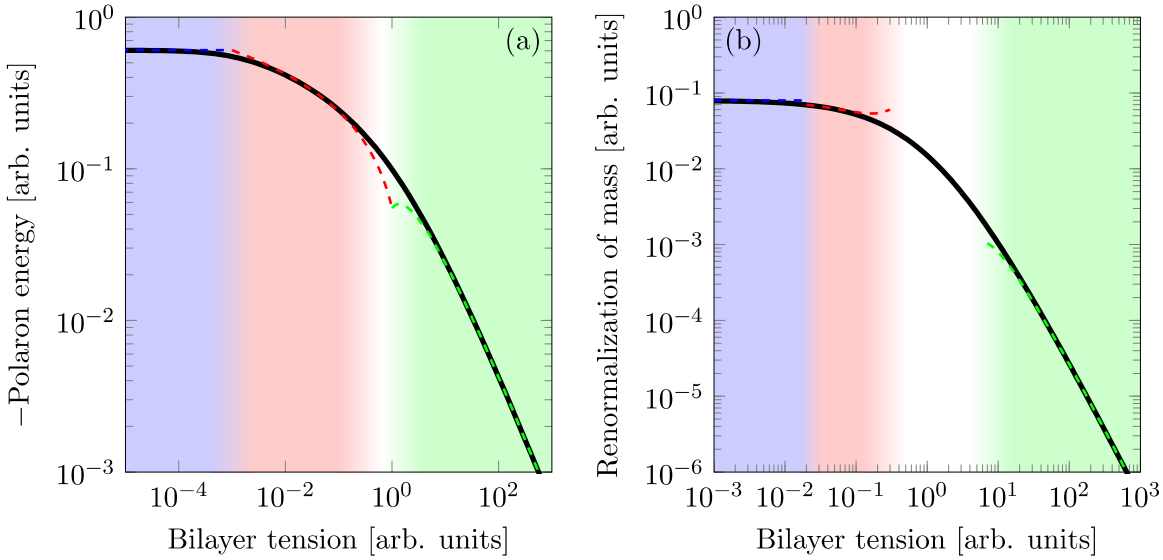

Figure 2. Absolute value of the a) polaron energy and b) renormalization of mass as function of the bilayer tension. Solid black lines show the full dependencies. Color dashed lines shows extreme cases. Blue line corresponds to a negligible tension, red line corresponds to a low tension and green line corresponds to a high tension. These regions are highlighted for clarity.

We also study the effects of anharmonicity in the system. The latter results in the coupling between the flexural and in-plane vibrations giving rise to critical behavior and non-analytical phonon dispersion $\omega \propto q^{2-\eta}$ with $\eta < 1$. The polaron corrections are calculated in this case as well.

Acknowledgments

The work is supported by the Russian Science Foundation project 19-12-00051.

References

[1] M. I. Katsnelson, *The Physics of Graphene* (2020, Cambridge University Press).

[2] M. A. Semina, M. M. Glazov, E. Sherman, *Ann. Phys.* (Berlin), 2000339 (2020).

The investigation of the features optical vortices focusing by ring gratings with the variable height using high-performance computer systems

D A Savelyev[1,2]

[1]Samara National Research University, Moskovskoye Shosse 34, Samara, Russia
[2]Image Processing Systems Institute - Branch of the Federal Scientific Research Centre "Crystallography and Photonics" of Russian Academy of Sciences, Molodogvardeyskaya str. 151, Samara, Russia

dmitrey.savelyev@yandex.ru

Abstract. The diffraction of vortex laser beams with circular polarization by ring gratings with the variable height was investigated in this paper. Modelling of near zone diffraction is numerically investigated by the finite difference time domain (FDTD) method. The change in the length size of the light needle is shown depending on the type of the ring grating.

1. Introduction

The interesting properties of singular beams make it possible to use them for optical manipulations with micro- and nanoparticles [1], material processing [2] and in microscopy [3]. In addition, the optical vortices are used in wireless communication systems [4], for transmitting information over fiber [5] and in quantum informatics [6]. Such beams can be obtained using spiral and twisted axicons [7], spiral phase plates [8], multi-order diffractive optical elements [9].

The introduction of a vortex phase singularity into the input beam makes it possible to enhance the longitudinal component of uniformly polarized laser beams on the optical axis in the focal region [10]. So, it is makes it possible to change the diffraction pattern due to the redistribution of energy between the components of the electromagnetic field [11].

The diffractive axicon (ring grating) as the conical axicon forms an extended light needle along the optical axis [12]. It is also possible to obtain dynamic focus by complementing the optical system with an adjustable lens or axicon [13]. The change in the substrate thickness has a significant effect on the diffraction pattern of a limited plane wave by diffraction axicons with different numerical apertures (NA). This action was shown earlier to change the substrate thickness from 0.2λ to 0.3λ [10].

The features of focusing optical vortices on ring gratings with the variable relief height h are studied in this paper. Numerical calculations (3D) of laser radiation propagation were performed using the finite difference time domain (FDTD) method using high-performance computer systems [14].

2. The investigation of focusing by ring gratings with variable height

Modeling parameters: wavelength $\lambda = 0.532$ μm, computational cell size x, y, z $\in [-5.6\lambda; 5.6\lambda]$. The thickness of the absorbing layer PML ~ 1.1λ, the sampling step in space is λ/16, the time step is λ/(32c), where c is the light speed. The refractive index of the considered optical elements and the substrate n was equal to 1.5. The height h was varied as follows: at the center h = 3λ, then the height

decreased with each subsequent grating ring with a step of 0.25λ up to h = 1.75λ to the edge of the element (the direct ring grating). The opposite case is also considered: in the center there is a minimum, h = 1.75λ and the height increases to 3λ from the center to the grating edge (the inverse ring grating). The diffractive axicon (h = 3λ) with NA = 0.95 was also considered for comparison. The period of all considered ring gratings was 1.05λ. The Laguerre-SuperGauss modes (1,0) of degree 6 with circular polarization (polarization is opposite in sign of the introduced vortex phase singularity) are considered as the input laser radiation. The research results are shown in Figure 1.

The size of the focal spot on the optical axis was estimated from the full width at half maximum (FWHM) of the intensity, and the length of the light needle was also estimated from the depth of focus (DOF), also at half maximum. It should be noted that the most compact focal spot was obtained for the case of the direct ring grating (FWHM = 0.54λ), and the longest light needle was obtained for the case of the inverse ring grating (DOF = 4.81λ).

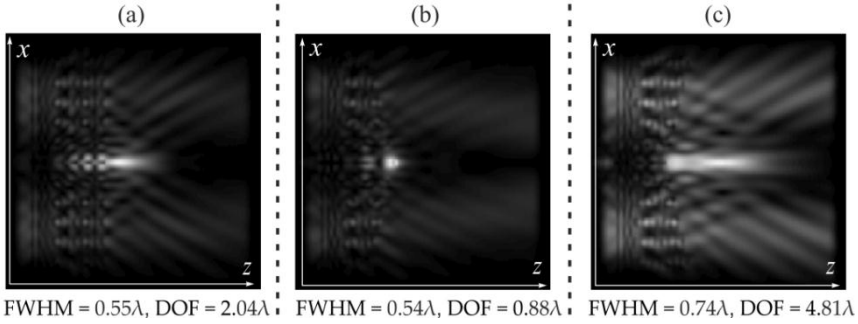

Figure 1. The longitudinal cross section (xz) of propagation laser radiation, propagation through: (a) the diffractive axicon, (b) the direct ring grating, (c) the inverse ring grating.

3. Conclusion

The formation of the Laguerre-superGauss modes (1,0) with circular polarization by ring gratings with the variable height were investigated. It should be noted that a significant increase in the length of the light needle is observed with an increase in the height of the grating rings from the center to the edges in comparison with the standard diffractive axicon.

Acknowledgments

This research was funded by the Russian Science Foundation (project No. 20-72-00051) in the parts «The investigation of focusing by ring gratings with variable height», «Conclusion»; and was performed under the «ERA.Net RUS plus» program and funded by RFBR, project number 20-52-76021 in the parts «Introduction».

References

[1] Dennis M R, O'Holleran K and Padgett M J 2009 *Progress in Optics* **53** 293
[2] Nivas J J et. al. 2017 *Appl. Surf. Sci.* **418** 565
[3] Khonina S N and Golub I 2012 *JOSA A* **29** 2242
[4] Li S et. al. 2020 *Advanced Optical Materials* **8** 1901666
[5] Pryamikov A, Alagashev G, Falkovich G and Turitsyn S 2020 *Scientific Reports* **10** 1
[6] Li S, Pan X, Ren Y, Liu H, Yu S and Jing J 2020 *Physical Review Letters* 124 083605
[7] Supp S and Jahns J 2018 *J. Eur. Opt. Soc.-Rapid Publ.* **14** 18
[8] Kotlyar V V et. al. 2007 *J. Opt. Technol.* **74** 686
[9] Khonina S N and Ustinov A V 2019 *Applied Optics* **58** 8227
[10] Khonina S N and Savelyev D A 2013 *Journal of Experimental and Theoretical Physics* **117** 623
[11] Savelyev D A, Khonina S N 2015 *Computer Optics* **39** 654
[12] Khonina S N et. al. 2012 *Journal of Optical Technology* **79** 626
[13] Khonina S N, Ustinov A V and Porfirev A P 2019 *JOSA A* **36** 1039
[14] Khonina S and Savelyev D 2015 *Radiophysics & Quantum Electronics* **57** 650

Development of a light control system using an optical aerial information transmission system

D D Savin[1], V V Davydov[1, 2] and V Yu Rud[2, 3]

[1]Peter the Great Saint Petersburg Polytechnic University, 29 Politechnicheskaya str., Saint Petersburg, Russia, 195251
[2]All-Russian Research Institute of Phytopathology, 5 Institutsky Ave., P. B. Vyazemy, Moscow Region, Russia, 143050
[3]A.F. Ioffe Physicotechnical Institute, St. Petersburg, 195152, Russia

e-mail: savin.dd@edu.spbstu.ru

Abstract. The inefficiency of the use of electric energy for indoor lighting is shown. The necessity of modernization of lighting control systems in the workplace area is justified. The method of automatic control and adjustment of illumination of workplaces and zones where it is necessary is offered. A control system has been developed that is integrated into the aerial optical information transmission system (Internet). The simulation of the system operation is carried out, its parameters are calculated. The main characteristics are measured.

1. Introduction

An increase in the volume of electricity production caused by an increase in the volume of its consumption adversely affects the ecological state of the planet [1]. Every year, the volume of electricity consumption is growing and over the past decade has reached huge values. Therefore, solving the problems of efficient use of generated electricity is a very urgent task for humanity, which affects several areas.

One of the ways to reduce electricity consumption is to reduce its lighting costs, especially in office and educational premises with windows. This problem is still very relevant, despite the large number of technical solutions. The main disadvantage of these systems is that they are aimed at controlling the illumination from artificial lighting in some points of the room with automatic adjustment of the power of lighting devices.

2. Automatic light control system with optical communication channel.

In Figure 1 shows a block diagram of the automatic lighting control system of workplaces integrated into the optical air information transmission system (Internet).

The information from the light sensors is sent to the information processing unit developed by us. An important device in this case is a device for switching channels through which information is transmitted to the electro-optical modulator in the receiving and transmitting module of the optical channel. After that, the information gets to the server, which gives commands to the lighting control system.

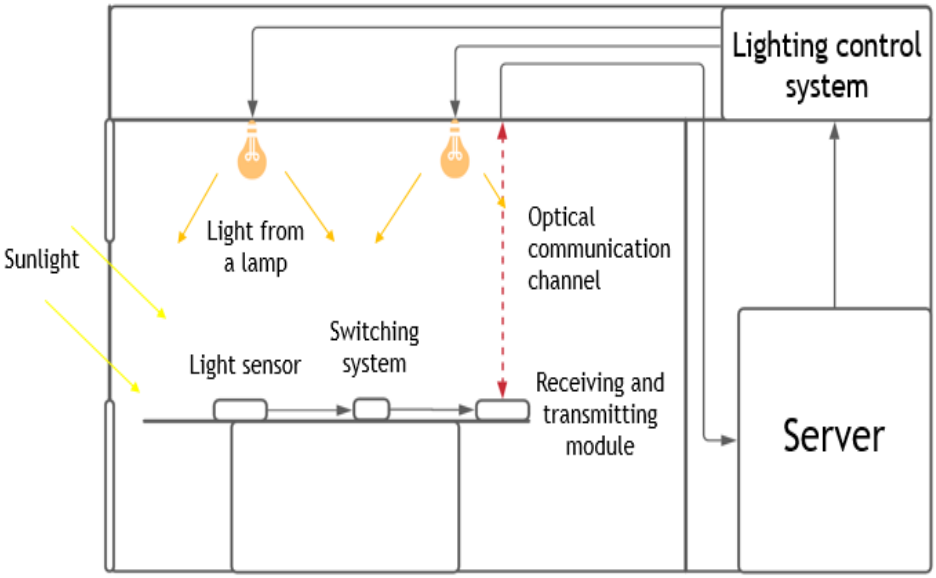

Figure 1. Scheme of an automatic illumination monitoring system using an optical aerial information transmission system.

This system adjusts the voltage on each lamp according to the received data.

3. Result of simulation of the system operation

The conducted simulation of the operation of the lighting control system showed that the Internet speed does not decrease significantly. The additional energy of the electrical voltage, which is necessary for the stable operation of the system, is not more than 5 % of the electrical energy consumed for the operation of the optical communication channel.

4. Conclusion

The simulation of the developed light control system and the calculation of its parameters showed that this system does not introduce significant distortions in the transmitted information over the optical channel for Internet users. For different seasons of the year, preliminary estimates have shown that the use of this system allows you to reduce the electricity consumption for indoor lighting from 10 to 20 %.

References

[1] Alekseev P N, Gagarinskiy A U and Kalugin M A 2019 *Atomic Energy* **126(4)** 183-187
[2] Sazonov D and Kirichek R 2019 *Communications in Computer and Information Science* **1141 CCIS** 597–611

Use of differential refractometer for condition control of flowing liquid

V I Sviatkina[1], V V Davydov[1, 2] and V Yu Rud[2, 3]
[1]Peter the Great Saint-Petersburg Polytechnic University, Saint Petersburg 195251, Russia
[2]All-Russian Research Institute of Phytopathology, Moscow Region 143050, Russia
[3]A.F. Ioffe Physicotechnical Institute, St. Petersburg, 195152, Russia

Abstract. A new design of flowing refractometer of differential type for flowing liquid condition control both in laminar and turbulent flow regimes is considered. A new method of measuring the refractive index n in new developed design of refractometer is implemented. The technique allowing to reduce the influence of change of the optical density of the flowing liquid on the measurement error of refractive index n is proposed. The results of experimental investigations for different liquids are presented.

1. Introduction

Presently there is an increasing number of tasks related to scientific research in automated mode, cooling system monitoring, etc. are required. [1]. This requires the development of new or upgraded condition control of flowing liquid systems [2]. At present, non-contact measurement methods based on the phenomenon of refraction are preferred [2, 3]. These methods meet high requirements for accuracy and reliability and do not change the physical and chemical properties of the medium. In addition, the use of refractometers makes it possible to monitor both the current and stationary state of the medium with a single measuring instrument. Among refractometers, two types are most commonly used: differential refractometers and refractometers based on the total internal reflection (TIR) phenomenon of laser radiation from two fluids [3]. A number of problems arise in refractometers with PBOs. As the temperature changes, the refractive indices of the flowing liquid and prism change, requiring a quick automatic adjustment of the optical part of the instrument. With fast liquid flows, the error in measuring the refractive index is affected by the Huss-Haenkhen optical beam shift phenomenon, which complicates the operation of the instrument and limits the measuring range n.

Therefore, the development of new designs of differential flow refractometers and techniques for measuring the refractive index n with an error of less than 10^{-4} is an urgent task.

2. Results of experimental research carried out with the developed refractometer design

The investigation of the influence of changes in optical density on the measurement error of the flowing fluid index allowed a new design of a flow refractometer of the differential type (Fig. 1) to be developed. In this design of refractometer, the differential method is used for registration of laser light. Therefore, the refractometer can be considered a differential refractometer.

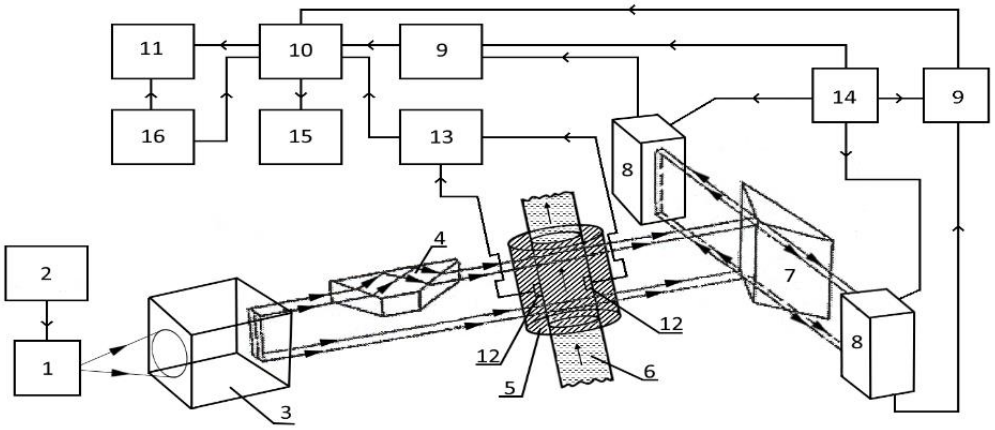

Figure 1. The Block diagram of a laboratory model of a differential refractometer: 1 - semiconductor laser; 2 - power source; 3 - optical system; 4 - prism Dove; 5 - closed cuvette; 6- flowing cuvette; 7 - dividing prism; 8 - photodiode array; 9 - ADC; 10 - processing device; 11 - indicating device; 12 - temperature sensor; 13 - device for processing information with a temperature sensor; 14 - specialized power supply ADC and photodiode arrays; 15 - laptop; 16 - power supply unit for processing and indication devices.

The validity of measurements n using the developed refractometer design was tested on several liquids at different temperatures T. Figure 2 shows the dependencies of n(T) for several flowing liquids.

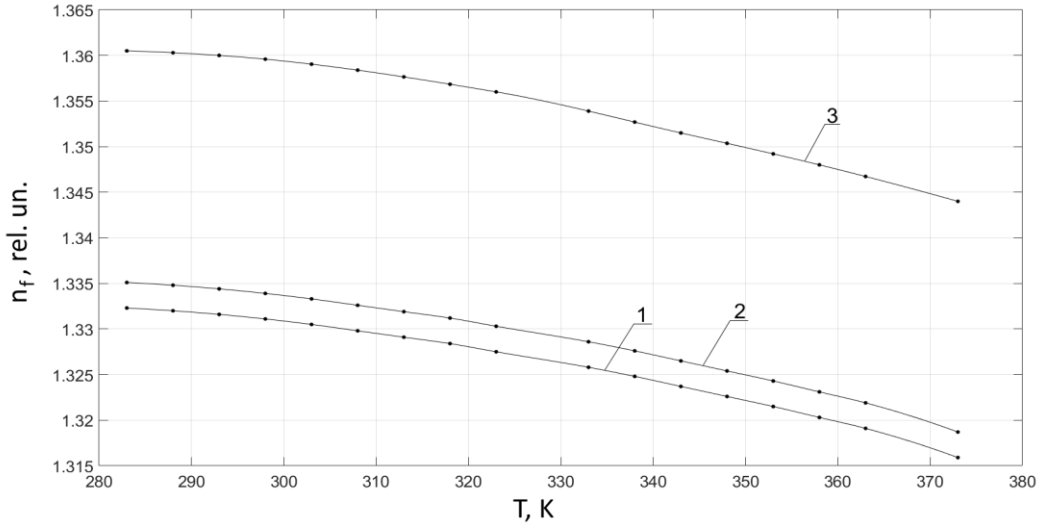

Figure. 2. The dependence of the refractive index n from the temperature T. Charts 1, 2, 3 correspond to the following environments: distilled water, tap water, ethyl alcohol.

3. Conclusion

The experimental results confirmed the possibility of using our developed refractometer design to investigate changes in the optical density of flowing liquids.

References

[1] Velt I D and Mikhailova Yu V 2013 *Measurement Techniques* **56(3)** 283
[2] Davydov V V, Grebenikova N M and Smirnov K J 2019 *Measurement Techniques* **62(6)** 519
[3] Karabegov M A 2012 *Measurement Techniques* **55(11)** 1104

Discrete optical Zeno effect for polarization of light

K O Sedykh[1,2], **D V Sych**[1,2,3,4]
[1]Moscow State Pedagogical University, Moscow 119992, Russia
[2]National University of Science and Technology MISiS, Moscow 119049, Russia
[3]Sirius University of Science and Technology, 1 Olympic Ave, 354340, Sochi, Russia
[4]P. N. Lebedev Physical Institute, Moscow 119991, Russia

e-mail: kseniaolegovna98@gmail.com

Abstract. Quantum Zeno effect concerns deterministic dynamics of a quantum system, induced by a series of projective quantum measurements. Applying this effect in optics, one can achieve an arbitrary lossless transformation of linear polarization of light with help of linear polarizers. However, to demonstrate this effect in practice, we have to take into account unavoidable losses in each polarizer that limits probability of successful transformations. In this work, we theoretically study a realistic quantum Zeno effect with an optimal discrete set of polarizers and find the maximum success probability.

1. Introduction

There is no motion according to Zeno's arrow paradox [1]. Since a flying arrow is at rest at every moment of time in a certain point in space, this means that it is at rest all the time. In other words, it is motionless. The quantum Zeno effect is the inhibition of the evolution of the state of a quantum system by method of repeated measurements [2]. If there is a particle which tends to abandon its initial quantum state and we try to observe how it changes its quantum state, the probability of the change tends to zero. With quite frequent observation rate, we can keep the state of the particle, and the probability for this tends to unity.

The relevance of the research topic is due to the development of the direction of quantum control and quantum interaction-free measurements research, and finds applications in quantum communication. Quantum Zeno effect can be applied in the counterfactual communication in which information is transferred by the phase part of wave function [3].

In our work, we investigate discrete version of the quantum Zeno effect and want to make an arbitrary deterministic transformation of the quantum state with help of only projective measurements.

2. Ideal and real cases of Zeno effect

Consider a case, when we put horizontally (H) and vertically (V) oriented polarizer one after another. Apparently, there is no light passes through such system of polarizers. However, if we add a diagonally oriented polarizer between them, we can observed a part of light that passes through the system. The more polarizers added to the system, the greater part of light passes through it, if we pay attention how to put these devices to the optical scheme. There is a special relation between the number of added polarizers and correct angle of their polarization angle. There is a rotation by $\frac{\pi}{2N}$, so the initially polarized light is orthogonally polarized at the end.

Find the probability of light passing through the set of polarizers and understand the connection between the probability and number of additional polarizers. Calculating the limit of probability for infinite number of polarizers, we can verify the validity of the obtained result. The more polarizers are added to the optical system, the more light we can obtain. This is the ideal case of the optical Zeno effect.

For the real case, we take into account the transmittance (or unavoidable losses) of the polarizers, which affects the result. Calculate the probability of light passing through a set of polarizers, with respect to the different transmittance coefficients versus the number of added devices. According to the achieved values, the maximum light passing through the system can be obtain using four additional polarizers with 0.9 transmittance. Calculating the limit of probability for infinite number of polarizers with respect to non-ideality of devices, we can verify the validity of the obtained result. Due to losses on each device, instead of 100% light transmission, only a small part (~35%) remains for the case of 10% loss on each polarizer.

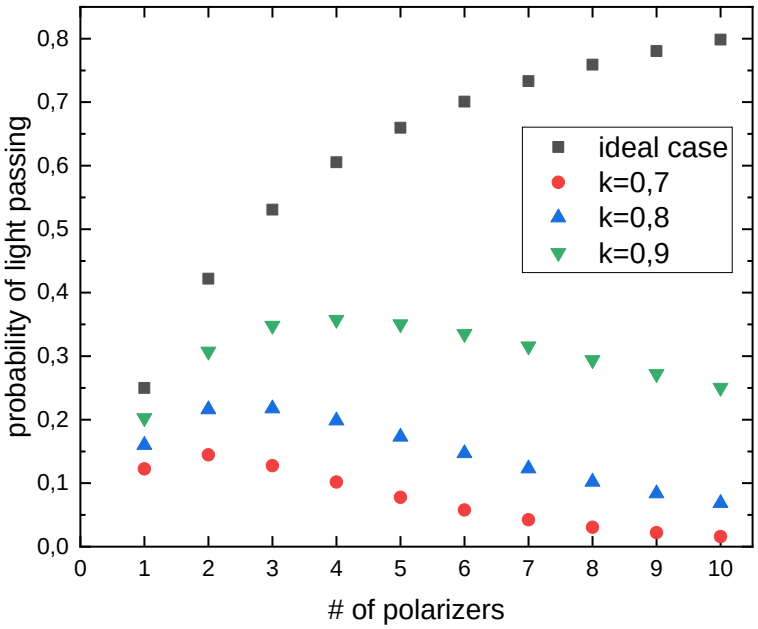

Figure 1. Zeno effect for ideal case and for the case with different transmittance coefficients (k).

3. Conclusion

In this work, we consider a realistic version of the quantum Zeno effect on the example of changes of polarization of light with a set of polarizers. In the ideal case, the more polarizers we put to the system, the more light we can obtain. In the real case, we have to take into account unavoidable losses in each polarizer, and obtained the optimal number of polarizers for which the maximum light transmittance can be achieve.

Acknowledgments

The work is supported by Russian Foundation for Basic Research grant 20-32-51004.

References

[1] Aristotle *Physics*, **VI** 9 239b10

[2] Misra B and Sudarshan E C G 1979 *J. Math. Phys*. **18** 756

[3] Yuan Cao *et al.* 2017 *Proc. Natl. Acad. Sci*. **114** (19) 4920-24

Temperature-dependent near-IR photoluminescence of lead selenide nanoplatelets

I D Skurlov[1], A V Sokolova[1], T Galle[2], S A Cherevkov[1], E V Ushakova[1], A V Baranov[1], V Lesnyak[2], A V Fedorov[1] and A P Litvin[1]

[1]Center of Information Optical Technology, The Laboratory "Optics of Quantum Nanostructures", ITMO University, 49 Kronverksky Pr., St. Petersburg 197101, Russia
[2]Physical Chemistry, TU Dresden, Zellescher Weg 19, 01069 Dresden, Germany

sky_id@itmo.ru

Abstract. Semiconductor colloidal nanoplatelets (NPLs) are a promising new class of nanostructures that can bring much impact on lightning technologies, light-emitting diodes (LED), and laser fabrication. To date, state-of-the-art near-infrared (NIR)-emitting NPLs are significantly inferior to their visible-range counterparts. In this study, we report a comprehensive analysis of steady-state and time-dependent photoluminescence (PL) properties of four monolayered PbSe NPLs. We show that multiple emissive states, both band-edge and trap-related, are responsible for the formation of the NPLs' PL band. Additionally, we demonstrate that the widening of the PL band is caused by the inhomogeneous broadening rather than homogeneous one, and analyze the possible contributions to PL broadening.

1. Introduction

Colloidal nanoplatelets (NPLs) are a new type of semiconductor nanomaterials with superior light-emitting properties which are highly demanded for displays and light-emitting diodes (LED) [1,2]. Due to their thickness-dependent optical properties and the possibility of synthesis of NPLs of strictly specified thickness, extremely narrow photoluminescence (PL) bandwidths are observed for such nanostructures. In order to understand the prospects of using semiconductor colloidal NPLs in the NIR to build LEDs with broadly tunable emission wavelengths, it is necessary to understand the mechanisms leading to the broadening of spectral lines in such nanoplatelets. Pb chalcogenide-based NPLs make an ideal model system for that study. The study of temperature dependencies of PL parameters is a versatile tool to understand the energy structure of nanomaterials and mechanisms of radiative and non-radiative recombination. Although great efforts were made to study the PL behavior of CdSe NPLs, there is a lack of such investigations for other types of semiconductor NPLs. Carrying out such studies for lead chalcogenide-based NIR-emitting NPLs is especially important for understanding the mechanisms of radiative recombination and assessing the nature of the broadening of their PL bands.

2. Results and discussion

PbSe nanoplatelets were synthesised using cation exchange from parent 4 monolayer CdSe nanoplatelets. The intense NIR PL band of four-monolayer PbSe nanoplatelets is centered at 0.93 eV (1330 nm) with full width at half maximum (FWHM) of 116 meV. Steady-state and kinetic PL

measurements were performed in a temperature range of 78–300 K. Due to the effect of giant oscillator strength transition we observe the growth of PL intensity and PL decay time shortening with lowering temperature.

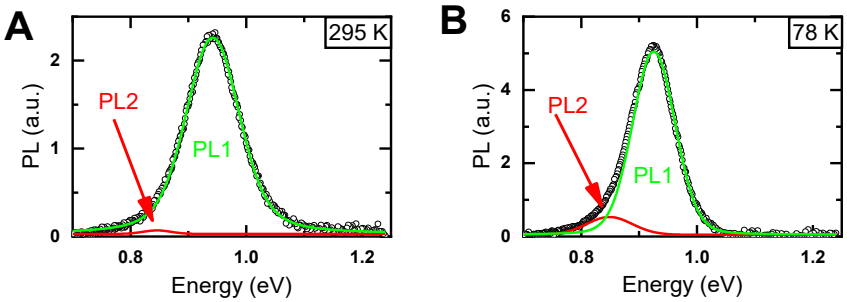

Figure 1. PbSe nanoplatelets PL spectra at 295 K (a) and 78 K (b).

PL spectrum at 78 K demonstrates noticeable asymmetry and can be described by a sum of two peak functions as shown in the Figure 1. Tthe high-energy peak (PL1) is described by a Voight function and we attribute it to the band-edge emission. The low-energy peak (PL2) can be well fitted by a Gaussian function and attributed to the surface trap related emission.

Detailed study of the Voight-shaped PL1 band reveals information about homogeneous and inhomogeous PL linewidth. Voight function is a convolution of the Gaussian and Lorentz peak functions. The Gauss component is usually ascribed to inhomogeneous broadening, while the Lorentz one describes the homogeneous broadening. The Gaussian linewidth does not depend on temperature, and the medium value is 82 ± 4 meV. The Lorentz component narrows from ~40 to ~10 meV with decreasing temperature. This behavior is similar to that demonstrated by the parent CdSe NPLs. Thus, widening of the PbSe PL spectrum is not associated with the internal mechanisms of emission but is associated with an increase in width due to inhomogeneous broadening.

Increase in the inhomogeneous broadening can be induced by a several factors:

1. Variance in the size, shape, and geometry of the nanoparticles. Presence of 0D-confined nanocrystals in the ensemble.
2. Quality of the nanoplatelet's crystal lattice can have an impact on its PL linewidth. The structural disorder or internal lattice defects in PbSe NPLs can arise from atoms rearrangement during the cation exchange reaction.
3. Presence of surface defect induced trap states: shallow traps can form a continuum of sublevels that will contribute to the emission and lead to its broadening.

3. Conclusions

We present a comprehensive PL study of four ML PbSe NPLs prepared by the cation exchange method. We have demonstrated that besides the band-edge related emission from the lowest excitonic state, NPLs possess additional red-shifted emission band. We showed that this emission is also temperature-dependent and more pronounced for air-processed NPLs, which proves its surface-trap related nature. We have revealed that wide FWHM of the band-edge NPLs' PL is attributed to the inhomogeneous broadening. In addition, we present the discussion about possible mechanisms of inhomogeneous PL broadening.

Acknowledgments

This work was supported by the Russian Science Foundation (19-13-00332).

References

[1] Nasilowski, M.; Mahler, B.; Lhuillier, E.; Ithurria, S.; Dubertret, B. Two-Dimensional Colloidal Nanocrystals. *Chem. Rev.* **2016**, *116* (18), 10934–10982.

[2] Xiao, P.; Huang, J.; Yan, D.; Luo, D.; Yuan, J.; Liu, B.; Liang, D. *Emergence of Nanoplatelet Light-Emitting Diodes*; MDPI AG, 2018; Vol. 11, p 1376.

Investigation of laser and thermal sintering processes of silver nanoparticles agglomerates synthesized by spark discharge

S S Tikhonov[1], M Nouraldeen[1], K M Khabarov[1], A A Efimov[1] and V V Ivanov[1]

[1]Moscow Institute of Physics and Technology (National Research University), Dolgoprudny 141701, Russia

sergei.s.tikhonov@phystech.edu

Abstract. Changes in the shape and size of silver nanoparticles (NPs) during their laser and thermal sintering have been studied experimentally and theoretically. Aerosol silver NPs forming chain agglomerates 180 nm in size were synthesized by spark discharge and exposed to laser radiation and high temperatures up to 750 °C. The shape and size of the NPs were investigated depending on the power of the laser radiation and the temperature of the gas. It is estimated that at a power density of green laser radiation of the order of 10^2-10^3 W / cm^2, complete sintering of NPs is achieved with the formation of spherical NPs with an average size of 140 nm, similar to NPs subjected to thermal heating in gas at 750 °C for 6 s.

1. Introduction

Currently, nanoparticles (NPs) remain an essentially interesting object of study, due to their high demand in many technological industries. With their help, point delivery of drugs, detection of hazardous substances, change in the optical and electronic properties of materials is carried out [1]. There are many ways to obtain NPs: lithographic, colloidal, laser ablation, etc. [2]. However, one of the most effective ways to obtain NPs is their synthesis in a gas discharge. This method makes it possible to control the delivery, composition and morphology of NPs and their agglomerates directly in the aerosol flow using external influences [3]. In this work, we investigate the effect of laser radiation and high temperatures on aerosol silver NPs synthesized in a spark discharge in order to obtain non-agglomerated particles. The obtained spherical silver NPs are promising as "building blocks" of elements of electronic and optical devices, antimicrobial agents and catalysts.

2. Experiment and discussion

Silver NPs obtained by spark discharge were investigated using the aerosol spectrometer and the transmission electron microscope (TEM). Agglomerates of NPs were subjected to two types of exposure: thermal, in a heated section of the gas path, and laser, in a quartz cell, in which the aerosol flow was combined with laser radiation with wavelengths of 527 and 980 nm.

Thermal modification of NP agglomerates was carried out in a heated section of the gas path 40 cm long at a temperature of 750 °C. Analysis of the data obtained using an analyzer of aerosol nanoparticles and the TEM showed that at a gas flow of 200 ml / min, agglomerates of NPs significantly change their shape, turning into spheres with an average diameter of 140 nm, determined from TEM images (figure 1 (c)).

It was experimentally found that at an output laser power of about 1.2 W for two wavelengths, an infrared laser has practically no effect on NPs, while a green laser causes a slight change in the size of

agglomerates of silver NPs at threshold powers. This effect is achieved due to the fact that agglomerates of NPs are modified by absorbing radiation, while the absorption peak for silver NPs is in the blue region of the spectrum, which is much closer to 527 nm than to 980 nm.

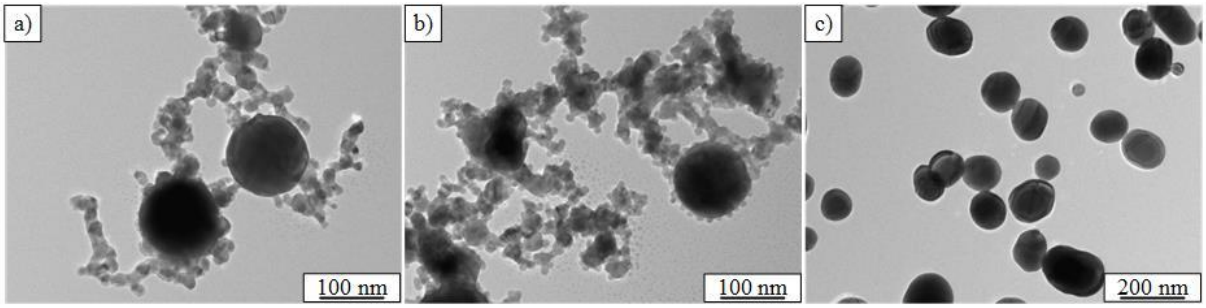

Figure 1. TEM images of silver NPs: primary (a), passed through a quartz cell with laser radiation of 527 nm at a power of 1.2 W (b) and optimized in a heated section of the gas path at a temperature of 750 °C (c).

Analysis of the power of laser radiation at the entrance and exit of the quartz cell showed that NPs more efficiently absorb laser radiation with a wavelength of 527 nm, starting from 1 W of laser power. In this case, the absorption efficiency of laser radiation with a wavelength of 980 nm did not depend on the radiation power injected into the cell.

TEM images of NPs (figure 1) confirm that thermal sintering of agglomerates of NPs at a temperature of 750 °C is more efficient than sintering with laser radiation, in which the agglomerates of NPs do not undergo significant changes. However, it can be seen that the agglomerates exposed to laser radiation are the structures of individual NPs with more resolvable boundaries, in comparison with agglomerates of primary NPs.

Theoretical calculations show that to improve the efficiency of modification of NPs in a gas cell, the radiation power or radiation absorption efficiency should be an order of magnitude higher for a green laser and two orders of magnitude for an infrared one.

3. Conclusion

As a result of a comparison of two types of exposure (thermal and laser), it was found that for sintering agglomerates of NPs to comparable shapes and sizes, it is necessary to increase the radiation power or radiation absorption efficiency by an order of magnitude for a wavelength of 527 nm and by two orders of magnitude for 980 nm. This feature allows us to conclude that at high laser radiation powers, or at radiation wavelengths closer to the plasmon absorption peak of the NPs under study, it is possible to achieve results comparable to those obtained by modifying particles in the heated section of the gas path.

Acknowledgments

The reported study was funded by RFBR and BRFBR, project number 20-53-00042 in part of the investigation of thermal sintering of nanoparticles and by the Russian Science Foundation, project number 19-79-00375 in part of the investigation of laser sintering of nanoparticles.

References

[1] Kuznetsov A I, Miroshnichenko A E, Brongersma M L, Kiyshar Y S and Luk'yanchuk B Optically resonant dielectric nanostructures 2016 *Science* **354**
[2] Ealia S A M and Saravanakumar M P 2017 *IOP Conf. Ser.: Mater. Sci. Eng.* **263** 032019
[3] Lizunova A, Mazharenko A, Masnaviev B, Khramov E, Efimov A, Ramanenka A, Shuklov I and Ivanov V 2020 *Materials* **13** 4431

Phase Detection of Surface Plasmon Resonance

S V Tomilin, V N Berzhansky and O A Tomilina

Institute of Physics and Technology, V.I. Vernadsky Crimean Federal University, Crimea, Simferopol, 295007, Russian Federation

tomilin_znu@mail.ru

Abstract. In paper the research results of possibility of sensitivity increasing for plasmonic sensors by detection the phase displacement between p- and s-components of reflected beam at prism excitation of surface plasmon-polariton resonance are representative. It was shown that when the plasmonic waves are excite by prism using Kretschmann configuration the width of resonance line at phase detection is less than the width of resonance peak at half height at detection the intensity of reflected beam in 4.2 times, and it is less than the width of resonance line on the curve of Fresnel coefficient derivative for p-component in 2.1 times.

1. Introduction

The operation principle of sensors on surface plasmon-polariton resonances (SPPR) is based on a physical effect of changing the resonant frequency of surface plasmon-polariton waves depending on the dielectric constant of the environment which adjacent to a sensitive metal (plasmon) layer [1]. At the prism excitation of surface (propagative) plasmon waves (Kretschmann scheme [2]) the resonance condition is determined by phase synchronism when the projection of wave vector of exciting (incidence) electromagnetic wave is equal to wave vector of plasmon wave.

The interaction of electromagnetic and plasmonic waves leads to phase displacement of the p-component comparatively to the s-component. This phase displacement can be determined using ellipsometry investigation in the SPPR area. The phase displacement of the p-component comparatively to the s-component is according to ellipsometric Δ parameter. In this work we study the phase displacement of electromagnetic wave during her interaction with plasmonic wave.

2. Simulation technique and results

The model of Kretschmann configuration (figure 1,a) has been proposed for investigation the SPPR influence on phase displacement of electromagnetic wave. In this model the optical triangular glass prism with flat apex angle of 120 deg is used ($\varepsilon_{prism} = 2.28$, we disregard by imaginary part). The thin film of gold is deposited on the bottom plane of prism with thickness of 50 nm ($\varepsilon_{Au} = -11.647 + 1.263i$). The permittivity of environment ε_{env} can be variable for modeling the sensory properties of plasmonic structure. The laser beam with wavelength $\lambda = 632.8$ nm is used as exciting wave. The beam has right circular polarization, i.e. the phase difference between p- and s-components has the initial value $\Delta = 90$ deg.

In figure 1,b the resonance curves are presented in the form of angular dependence of Fresnel coefficient Rp for p-component and ellipsometric parameter Δ. It can be seen, that the resonance condition is conforming to incidence angle of exciting beam of 51.44 deg. In this case the minimum of function $R\text{p}(\theta)$ is observed, and the function $\Delta(\theta) = 90$ deg. When the beam is deviate from resonance

location the p-component obtain the phase change (positive or negative) but s-component has no change so the Δ parameter become different from 90 deg.

In figure 1,c the comparison of SPPR resonance lines width when it detected as Fresnel coefficient $R_p(\theta)$ and ellipsometric parameter $\Delta(\theta)$ is shown. It can be seen, that the width of resonance line on curve $\Delta(\theta)$ is less than the width of resonance on half height of peak on curve $R_p(\theta)$ in 4.2 times.

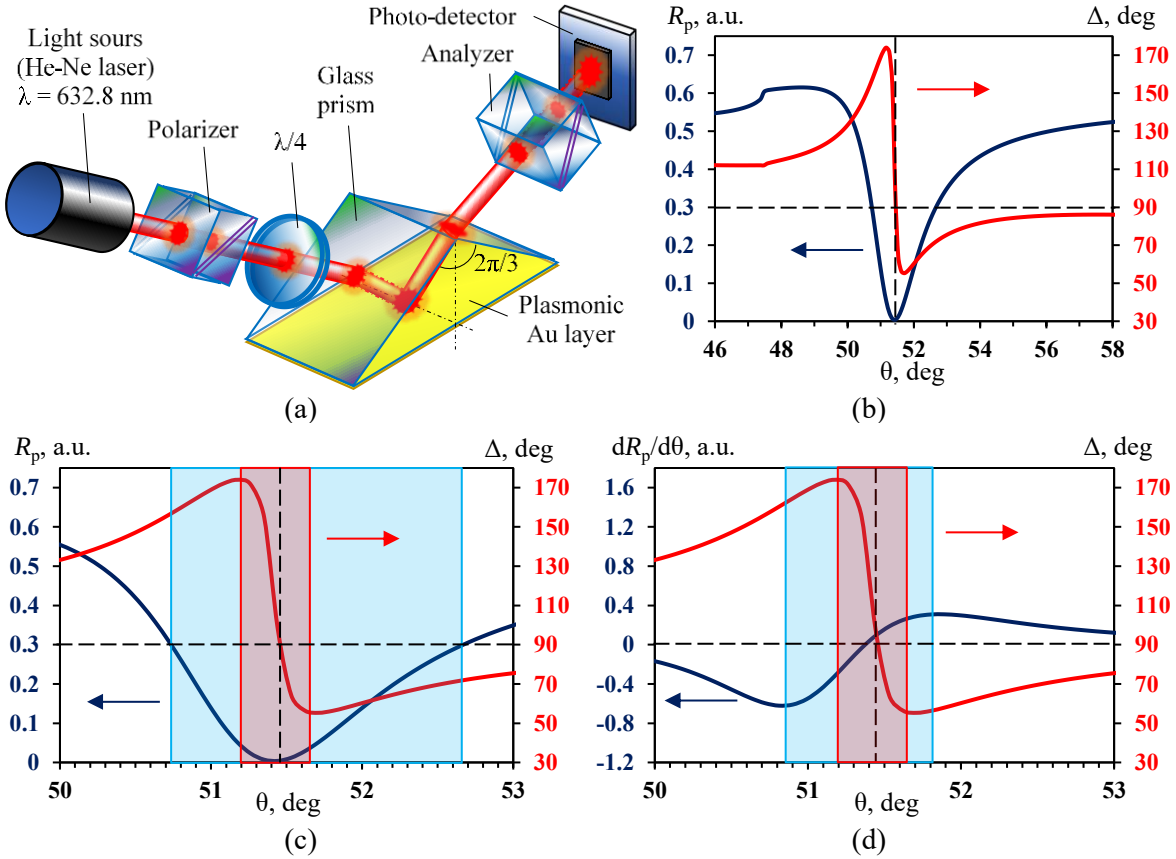

Figure 1. The simulation of different methods of SPPR registration: (a) – the scheme of investigated model; (b) – angular dependence of the Fresnel coefficient R_p for p-component and the ellipsometric parameter Δ; (c) – the comparison of SPPR resonance lines width in the curves $R_p(\theta)$ and $\Delta(\theta)$; (d) – the comparison of SPPR resonance lines width in the curves $dR_p(\theta)/d\theta$ and $\Delta(\theta)$

In figure 1,d the results of the comparison of SPPR resonance lines width when the resonance detected as the derivative of Fresnel coefficient $dR_p(\theta)/d\theta$ and the ellipsometric parameter Δ are presented. In this case the width of resonance line on curve $\Delta(\theta)$ is less than the width of resonance line on curve $dR_p(\theta)/d\theta$ in 2.1 times.

Acknowledgments

This work was financially supported by the Russian Ministry of Education and Science, Megagrant project N 075-15-2019-1934

References

[1] S A Maier 2007 *Plasmonics: Fundamentals and Applications* (Springer)

[2] E Kretschmann and H Raether 1968 *Z. Naturforsch.* A **23(12)** 2135

Ellipsometry of plasmonic nanostructures

O A Tomilina, V N Berzhansky, S V Tomilin

Institute of Physics and Technology, V.I. Vernadsky Crimean Federal University, Crimea, Simferopol, 295007, Russian Federation

olga_tomilina@mail.ru

Abstract. This paper presents the results of a study of the optical and ellipsometric properties of plasmonic nanostructures in the form of layers containing ensembles of self-assembled gold nanoparticles. It is shown that in the synthesis of self-assembled nanoparticles using the method of thermally activated granulation of thin films, the initial thickness of the granulated coating has a significant effect. In the optical transmittance spectra of self-assembled nanoparticles, minima are revealed that correspond to the excitation of localized plasmon resonance. In this case, only excitation of the plasmon resonance dipole mode is observed for the "thin" part of the sample, and for the "thick" one – the dipole and quadrupole modes. Analysis of the ellipsometric properties showed that the dielectric properties of ensembles of self-assembled plasmonic nanoparticles can be described in the framework of approximation by a homogeneous isotropic layer with an equivalent layer thickness and effective dielectric constant.

1. Introduction

Self-assembled metal nanoparticles and structures based on them are a very common material for creating plasmonic nanocomposites and nanostructures. Such ensembles of self-assembled nanoparticles are often obtained by dispersing of macromaterials, in particular, by thermal granulation of ultrathin films, which deposited on a support-substrate [1].

When designing and modeling photonic devices containing layers of such self-assembled plasmonic nanoparticles, one of the important parameters is the effective dielectric constant ε of these layers. When the size of plasmonic nanoparticles is much smaller than the wavelength of electromagnetic radiation, one can use the effective medium approximation (EMA) model [2], but such estimates give only approximate values of ε. More correct real values of effective ε can be obtained by direct optical measurements, for example, by ellipsometry.

2. Experimental technique and results

The system of self-assembled gold nanoparticles $Au_{(NP)}$ on a single-crystal gadolinium-gallium garnet (GGG) substrate was obtained by thermally activated granulation of a gold film in air at 800°C during 120 min. The Au/GGG film was obtained by thermal vacuum deposition at a residual gas pressure of no more than $6 \cdot 10^{-4}$ Pa. At the Au deposition, a coating technique with a gradient of effective thickness along the selected direction was used [3]. This technique makes it possible to obtain nanoparticles with different sizes in different areas of the sample.

The optical characteristics of the obtained sample was studied by transmission spectrophotometry in the spectral range of 400 – 1000 nm. In fig. 1 the transmittance spectra of a system of self-

assembled nanoparticles in the “thin” part (solid line) and in the “thick” part of the sample (dashed line) are shown. The inset show the spectra of the first derivative of the transmittance dT/dλ. The minimum points in the transmittance spectrum (the points of intersection with the abscissa in the dT/dλ spectrum, marked by circles) correspond to the excitation of various modes of localized plasmon resonance (LPR) in nanoparticles. It can be seen that in the “thin” area of the sample, only the dipole plasmon mode is excited at a wavelength of λ = 620 nm. In the “thick” part of the sample, there are two types of plasmon modes are excited: a dipole mode at a wavelength of λ = 750 nm and a quadrupole mode at λ = 536 nm.

Ellipsometric measurements were carried out using an LEF-3M-1 null-ellipsometer. A He-Ne laser with a wavelength of λ = 632.8 nm was used as an optical source. The analysis of the ellipsometric model of the effective environment was carried out using the WinSpall software package. In fig. 2,b,c the results of ellipsometric investigation of the $Au_{(NP)}$/GGG structure are shown. Fig. 2,b corresponds to the results of ellipsometry in the “thin” part of the film, and Fig. 2,c – in the "thick" one.

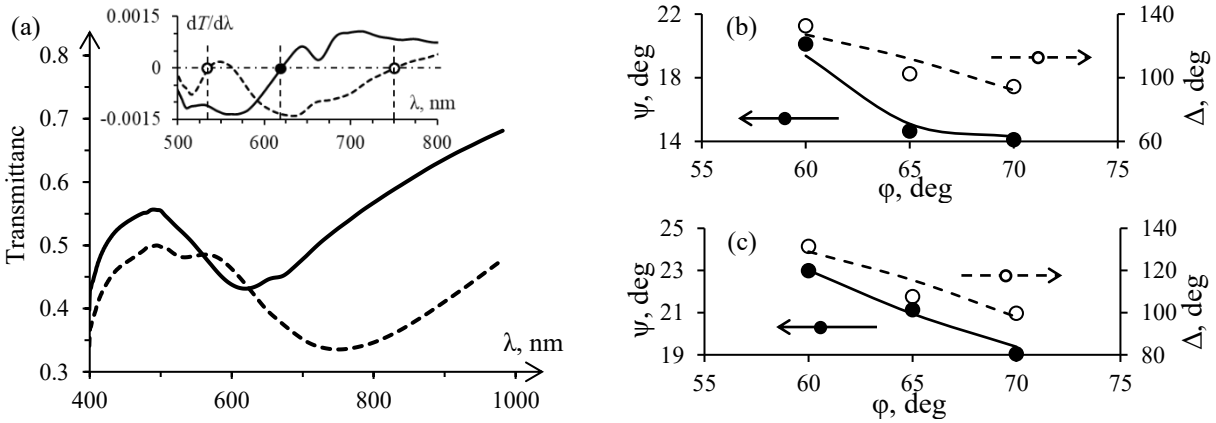

Figure 1. Optical properties of the $Au_{(NP)}$/GGG structure: a) transmittance spectra in the “thin” part (solid line) and in the “thick” part of the sample (dashed line), the inset show the spectra of the derivative of the transmittance dT/dλ; b) the results of ellipsometry investigation in the "thin" part; c) the results of ellipsometry investigation in the "thick" part (circles – experimental results, lines – simulation analysis).

A simulation analysis of the ellipsometry results showed that the studied systems of self-assembled plasmonic nanoparticles with a high degree of reliability can be considered as layers with a certain thickness and with the corresponding effective dielectric constant ε. In particular, for the “thin” part of the sample, the values of the thickness h = 39 nm and the effective dielectric constant ε = -2.36 + 5i were obtained. For the “thick” part of the sample, respectively, h = 87 nm, and ε = -3.5 + 7.1i.

Acknowledgments
This work was financially supported by the Russian Ministry of Education and Science, Megagrant project N 075-15-2019-1934

References
[1] Tomilin S V, Berzhansky V N, at. All. 2020 *Physics of the Solid State* **62(1)** 144
[2] Stroud D 1998 *Superlattices and Microstructures* **23(3/4)** 567
[3] Tomilina O A, Berzhansky V N, Tomilin S V, Milyukova E T 2019 *Journal of Physics: Conference Series* **1410** 012008

Characterization of In(Ga,Al)As/GaAs metamorphic heterostructures for mid-IR emitters by FTIR photoreflectance spectroscopy

D D Firsov[1], **M Yu Chernov**[2], **V A Solov'ev** [2] **and O S Komkov**[1]
[1] Micro- and nanoelectronics department, St. Petersburg Electrotechnical University "LETI", Professora Popova 5, Saint Petersburg 197376, Russia
[2]Ioffe Institute, Politekhnicheskaya 26, Saint Petersburg 194021, Russia

Abstract. Infrared photoreflectance (PR) spectra of In(Ga,Al)As/GaAs metamorphic heterostructures have been obtained using a novel photomodulation FTIR spectroscopy technique. The critical point energies corresponding to the direct interband transitions in various regions of the In(Ga,Al)As heterostructure were obtained from the features of PR spectra. Observation of Franz-Keldysh oscillations originating from the InAlAs virtual substrate and a thick InGaAs layer has enabled contactless determination of the built-in electric field intensity within the heterostructure.

1. Introduction

In(Ga,Al)As/GaAs metamorphic heterostructures have been recently shown to be very promising for high-efficiency semiconductor lasers and light-emitting diodes operating in the 3–5 μm mid-infrared (mid-IR) spectral range [1]. The key element of such structures is a convex-graded $In_xAl_{1-x}As$ metamorphic buffer layer (MBL) [2], which enables fabrication of low-defect-density active region on strongly lattice mismatched but well-developed GaAs substrates.

This work is devoted to applying a novel photomodulation spectroscopy technique based on a Fourier-transform infrared (FTIR) spectrometer [3] for studying the properties of In(Ga,Al)As/GaAs metamorphic structures, which are playing the role of "virtual substrate" for the active region of mid-IR emitters.

2. Experimental setup

The studied In(Ga,Al)As metamorphic structures were grown by molecular-beam epitaxy (MBE) in a RIBER 32P setup on semi-insulating (SI) GaAs (001) substrates via convex-graded $In_xAl_{1-x}As$ (x=0.05–0.82) MBL [2]. The composition profile of the MBL is described by a dependence $x(z) = x_i + (x_{max} - x_i)(z/L)^{0.5}$, where x_i and x_{max} are the In contents at the bottom and the top of MBL, and L – its total thickness [4]. Virtual substrate (VS) representing the layer of constant composition $In_{0.75}Al_{0.25}As$ was grown atop the MBL. Some of the studied structures also included a thick InGaAs layer within an InAlAs VS (see inset of the Fig.1), which is a prototype of a waveguide where an emitting quantum well is to be located.

The optical setup for photomodulation measurements was based upon a VERTEX 80 FTIR spectrometer equipped with InSb and CdHgTe detectors, enabling spectra measurements in the 0.9 - 16 μm range [5]. During the photoreflectance (PR) measurements, the samples were excited by a 405 nm or an 809 nm laser diode (P_{las} up to 100 mW), which was modulated at 3.5 kHz. The PR

component of the signal was amplified by a SR-830 lock-in amplifier tuned to the frequency of modulation, then digitized by the spectrometer's internal ADC, and processed using an algorithm described elsewhere [6]. Additionally, photoluminescence (PL) spectra of the studied samples were measured with the same spectrometer, excitation laser, and a closed-cycle helium cryostat (Janis CCS-150) as described earlier [7]

3. Results and discussion

The photoreflectance spectrum ΔR/R of a typical In(Ga,Al)As/GaAs metamorphic heterostructure is presented in Figure 1. The PR spectra exhibit characteristic derivative-like features attributed to the interband critical points of the band structure [8].

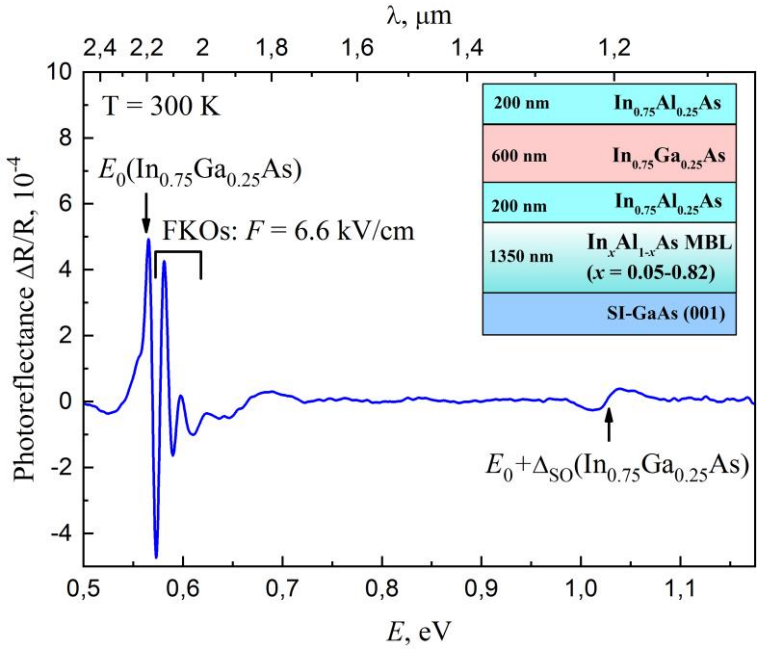

Figure 1. Photoreflectance spectrum of a metamorphic structure with an InGaAs waveguide layer. The arrows mark the transition energies obtained using the technique from Ref. [9]. The bracket shows the spectral region containing Franz-Keldysh oscillations in InGaAs. The inset shows the sketch of the layers within the heterostructure.

The critical point energies (marked by arrows on Figure 1) were determined from the PR spectra using a technique described in Ref. [9]. The signal E_0 at 0.568 eV can be attributed to the direct band gap of $In_{0.75}Ga_{0.25}As$, which was also confirmed by observation of a PL peak at the same energy. The higher-energy transition (at 1.028 eV) is significantly above the band gap of bulk $In_{0.75}Al_{0.25}As$ at 300 K (0.890 eV according to [10]). However, a 0.46 eV difference between this signal and the E_0 peak is close to the expected spin-orbit splitting value for an In-rich alloy (Δ_{SO} = 0.39 eV for InAs [10]), and thus the 1.028 eV peak can likely be interpreted as a E_0+Δ_{SO} transition in $In_{0.75}Ga_{0.25}As$.

The periodic oscillating structure in the PR spectrum (0.57-0.62 eV range) corresponds to Franz-Keldysh oscillations (FKOs) within the InGaAs layer. The period of FKOs enables determination of the intensity F of the internal electric field, using a technique described in Ref. [8]. The obtained field value for the sample from Fig. 1 is F = 6.6±0.3 kV/cm. Since the $In_{0.75}Ga_{0.25}As$ layer is capped with 200 nm of $In_{0.75}Al_{0.25}As$, the observed electric field is not related to the surface states, but rather to a heterointerface within the metamorphic structure. Therefore, an active region grown within the $In_{0.75}Ga_{0.25}As$ waveguide will be placed into a strong built-in electric field, which will undoubtedly affect the efficiency of future mid-IR emitters.

4. Acknowledgments

D D Firsov acknowledges the support of the Grants Council of the President of Russian Federation, project # SP-4626.2021.3.

The authors would like to deeply thank Prof. S V Ivanov for the original concept of the studied metamorphic heterostructures, and his prolonged guidance of their research.

5. References

[1] Ivanov S V, Chernov M Yu, Solov'ev V A, Brunkov P N, Firsov D D, and Komkov O S 2019 *Progress in Crystal Growth and Characterization of Materials* **65** 20
[2] Chernov M Yu, Komkov O S, Firsov D D, Meltser B Y, Semenov A N, Terent'ev Y V and Solov'ev V A 2017 *Journal of Crystal Growth* **477** 97
[3] Komkov O S, Firsov D D, Lvova T V, Sedova I V, Semenov A N, Solov'ev V A and Ivanov S V 2016 *Physics of the Solid State* **58** 2394
[4] Pobat D B, Solov'ev V A, Chernov M Y and Ivanov S V 2021 *Physics of the Solid State* **63** 84
[5] Firsov D D, Komkov O S, Solov'ev V A, Semenov A N and Ivanov S V 2017 *Journal of Physics: Conference Series* **917** 062025
[6] Firsov D D, Komkov O S 2013 *Technical Physics Letters* **39** 1071
[7] Firsov D D, Komkov O S, Solov'ev V A, Kop'ev P S, and Ivanov S V 2016 *Journal of Physics D: Applied Physics* **49** 285108
[8] Pikhtin A N, Komkov O S and Bazarov K V 2006 *Semiconductors* **40** 592
[9] Hosea T J C 1995 *Physica status solidi b* **189** 531
[10] Vurgaftman I, Meyer J R and Ram-Mohan L R 2001 *Journal of Applied Physics* **89** 5815

Formation of planar plasmon microstructures by dry aerosol printing

K M Khabarov[1], A A Lizunova[1], M N Urazov[1] and V V Ivanov[1]
[1]Moscow Institute of Physics and Technology (National Research University), Dolgoprudny 141701, Russia

kirill.khabarov@phystech.edu

Abstract. Optical properties and microstructure of samples formed by dry aerosol printing are studied. Silver nanoparticle flat layers of two types were formed on substrates surfaces and were investigated by a spectrophotometer, a scanning electron microscope, and a transmission electron microscope. It is shown that all microstructures maintain a plasmon resonance on individual nanoparticles with the Q factor depending both on the width of the nanoparticles size distribution in the aerosol and on their tendency to agglomeration and aggregation.

1. Introduction

The optical properties of nanoparticle planar arrays significantly depend on the material and morphology of the particles, as well as on their level of ordering in the sample. For instance, periodic lattices of gold spherical nanoparticles simultaneously exhibit several resonances in the visible spectral range associated with the excitation of plasmon oscillations [1]. Currently, the task of manufacturing such structures is massively solved by lithography and vacuum deposition methods [2]. At the same time, aerosol dry printing allows to synthesize and precipitate chemically pure nanoparticles in real time for similar tasks of manufacturing planar microstructures [3] with resonant features on optical spectra.

2. Experiment

The studied silver nanoparticle microstructures were deposited by dry aerosol printing on the surface of glass and silicon substrates in the form of a square 3x3 mm^2. Two sample types were presented in the work, differing in the average diameter of spherical nanoparticles. For all cases, the thickness of the manufactured samples did not exceed 1 μm. Nanoparticle morphology, microstructure, and optical spectra of the samples were studied by the transmission electron microscopy (TEM), the scanning electron microscopy (SEM), and the spectrophotometry, respectively (Figure 1). In this case, the size distribution of nanoparticle agglomerates was studied directly in the aerosol flow by the electrodiffusion method.

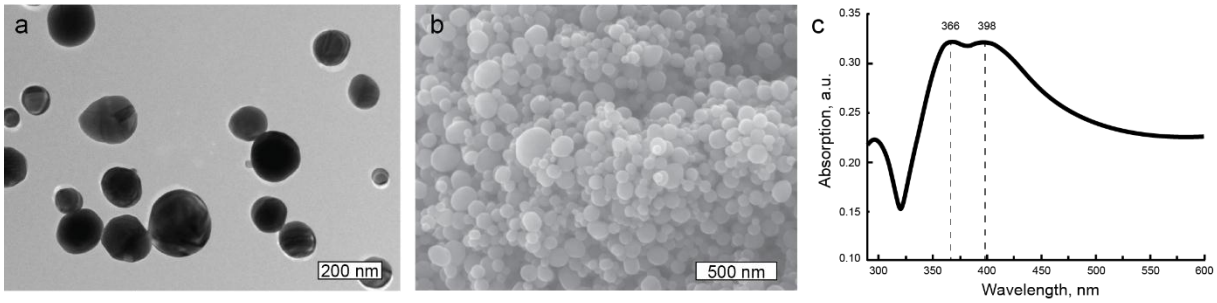

Figure 1. For the arrays of nanoparticles with an average diameter 140 nm, not forming agglomerates: the TEM image (a), the SEM image of the surface microstructure (b), and the absorption spectrum (c).

The analysis of TEM and SEM images and agglomerate sizes showed that the first type of microstructures consisted of nanoparticles with an average diameter 10 nm, forming agglomerates with an average size 160 nm, and the second type of microstructures consisted of nanoparticles with an average diameter 140 nm, mainly not forming agglomerates.

We observed resonant features on the samples optical spectra, which were associated with plasmon oscillations on individual particles. However, the Q factor of the resonances was small both for the arrays of nanoparticles with an average diameter 10 nm, and for the arrays of nanoparticles with an average diameter 140 nm. This effect may be a consequence of a wide range of the particle size distribution, and also be caused by agglomeration and aggregation of those particles. In this case, the nanoparticles in agglomerates and aggregates work as a whole, exhibiting properties of the extended dendrite-like plasmon nanoantennas [4].

3. Conclusion

Spherical silver nanoparticle arrays formed by dry aerosol printing support plasmon oscillations, appearing as wide shape resonances on optical absorption spectra. The Q factor of these resonances is small both for the arrays of nanoparticles with an average diameter 10 nm, forming agglomerates with an average size 160 nm, and for the arrays of nanoparticles with an average diameter 140 nm, mainly not forming agglomerates. This effect may be a result of a wide range of the particle size distribution, and also be caused by agglomeration and aggregation of those particles. On the contrary, a greater Q-factor may be achieved by reducing a width of the nanoparticle size distribution and preventing their agglomeration.

Acknowledgments

This research was funded by the Ministry of Science and Higher Education of the Russian Federation (state contract no. 075-03-2021-095, project identifier 0714-2021-0007, project title: “Development of functional materials with controlled electrical, chemoresistive and catalytic properties for manufacturing sensor microsystems by using methods of printed electronics”)

References

[1] A. N. Shaimanov, K. M. Khabarov, A. M. Merzlikin, I. V. Bykov, and A. V. Baryshev, “Plasmon resonances in a two-dimensional lattice of metal particles in a dielectric layer: Structural and polarization properties,” *J. Exp. Theor. Phys.*, vol. 124, no. 4, pp. 584–591, Apr. 2017, doi: 10.1134/S1063776117030165.

[2] K. Seshan, *Handbook of Thin Film Deposition*. William Andrew, 2001.

[3] A. A. Efimov, G. N. Potapov, A. V. Nisan, and V. V. Ivanov, “Controlled focusing of silver nanoparticles beam to form the microstructures on substrates,” *Results in Physics*, vol. 7, pp. 440–443, 2017, doi: 10.1016/j.rinp.2016.12.052.

[4] K. D. Sattler, *Handbook of Nanophysics: Nanoparticles and Quantum Dots*. CRC Press, 2016.

Bimodality in the electroluminescence spectra of "quantum well-dots" InGaAs nanostructures

A.A. Kharchenko[a], A.M. Nadtochiy[b], M.V. Maximov[a]

[a] Nanophotonics Lab., Alferov University, 8/3 Khlopina, 194021 St Petersburg, Russia
[b] National Research University Higher School of Economics, Soyuza Pechatnikov, 16, St. Petersburg, 190008, Russia

antoshkerrr@gmail.com

Abstract. The electroluminescence spectra of waveguiding structures based on quantum well-dots were investigated with polarization resolution in the temperature range of 20-300 K. It is found that the ground state emission consists of two peaks with different degrees of TE-polarization and these peaks are getting closer with temperature decrease. The data obtained associated with the existence of two different nanoobjects in the active region: the quantum well-dots, which have partially TE-polarized emission, and quantum dots emitting almost fully TE-polarized light.

1. Introduction

Heterostructures based on InGaAs quantum wells (QWs) and InAs quantum dots (QDs) grown on GaAs substrates are currently used in many fields of science and technology, in particular, in semiconductor photoelectric converters and light-emitting devices.[1].

In this paper, we focus on recently developed structures which are referred to as quantum well-dots (QWDs) [2]. QWDs can be described as InGaAs/GaAs quantum well with pronounced modulations in indium composition and thickness emitting in the 1050-1100 nm range. Alternatively, QWDs can be described as a super-dense array of shallow InGaAs QDs. It was shown that this new type of heterostructures has some advantages over both QWs and QDs while retaining their key features. For instance, it is possible to grow more than 15 dislocation-free QWD layers, which is hardly achievable in case of InGaAs/GaAs QWs without using any special strain compensation techniques. Also, QWDs are found to have a much higher gain (absorption) compared to InAs/GaAs QDs. Due to these features of QWDs, a number of efficient optoelectronic devices were successfully created, such as a micro optocoupler based on a microdisk laser and a photodetector with QWD active region [3], and GaAs-based photovoltaic converters which demonstrated a record-high increase of photocurrent[4].

Due to relative novelty and the great complexity of detailed computer modeling of QWDs electronic structure, they are little studied yet, so the study of their properties and features is relevant.

2. Experiment, results and discussion

In this work, we experimentally study planar waveguide *p-i-n*-structures with $In_{0.4}Ga_{0.6}As$ QWD active region. We measured polarization-resolved electroluminescence (EL) spectra in the 20-300 K temperature range. Radiation from the sample edge mounted in closed-cycle He cryostat was detected

with cooled germanium diode using lock-in technique. A Glan-Taylor prism was utilized as a polarization analyzer. We used low injection-current conditions to avoid significant stimulated emission in the spectra. The data obtained showed that the ground state emission of QWDs clearly breaks up into two peaks with different degrees of TE-polarization (DoP). Next, we represented EL spectra as the 3D surface plot as the function of the polarization angle and the EL wavelength. Approximation of the surface by an analytical expression based on the sum of two partially-polarized Gaussian functions allowed us to robustly identify peaks' positions and their DoPs. Temperature dependencies of the peaks' positions showed, that peaks are getting closer with temperature decrease.

Earlier it was shown that the photoluminescence (PL) spectra exhibit two overlapped peaks due to the presence in the QWD array additional objects of bigger size (quantum dots) emitting at longer wavelengths [5]. The data obtained were confirmed by TEM images that actually demonstrated two different objects in the structure. The temperature dependencies of the two PL peaks caused by bimodality showed very similar behavior to the EL one. However, such a bimodality of the QWD array was hardly observable in the emission spectra of planar waveguide structures without polarization resolution.

Thus, we suppose that these two peaks in the EL spectrum are of the same nature as those in the PL spectrum and associated with the existence of two different nanoobjects in the active region. The fact that QWDs' peak is partially TE-polarized, whereas QDs' peak is almost fully TE-polarized is essential for understanding fundamental properties of QWD electronic structure and should be taken into account in case of QWD device applications.

3. Conclusions

On the basis of the polarization-resolved EL of QWD-based waveguiding structures, it is found that the ground state emission of QWDs consists of two peaks with different degrees of TE-polarization and these peaks are getting closer with temperature decrease. Comparing the data obtained with the previously measured photoluminescence spectra and TEM images allowed us to associate the peaks with the bimodality of QWD array.

Acknowledgments

N.A.M. acknowledges the support of the Basic Research Program of the National Research University Higher School of Economics.

References

[1] Maximov M V., Nadtochiy A M, *et al.*, 2020 Light emitting devices based on quantum well dots *Appl. Sci.* **10**

[2] Mintairov S A, Kalyuzhnyy N A, *et al.*,2015 GaAs quantum well-dots solar cells with spectral response extended to 1100 nm *Electron. Lett.* **51** 1602–4

[3] Kryzhanovskaya N V., Moiseev E I, *et al.*, 2020 A Micro Optocoupler Based on a Microdisk Laser and a Photodetector with an Active Region Based on Quantum Well-Dots *Tech. Phys. Lett.* **46** 629–32

[4] Mintairov S A, Kalyuzhnyy N A, *et al.*, 2018 Multilayer Quantum Well–Dot InGaAs Heterostructures in GaAs-based Photovoltaic Converters *Semiconductors* **52** 1249–54

[5] Nadtochiy A M, Mintairov S A, *et al.*, 2015 Effect of the bimodality of a QD array on the optical properties and threshold characteristics of QD lasers *Semiconductors* **49** 1090–4

Simple representation of the quantum entanglement of coupled harmonic oscillators in terms of the reflection coefficient

Yu V Tsykareva and D N Makarov

Northern Arctic Federal University named after M V Lomonosov, Arkhangelsk 163002, Russia

E-mail: aisonoka@gmail.com

Abstract. Simple expressions for the quantum entanglement of coupled harmonic oscillators, expressed in terms of the reflection coefficient R, were found. It is shown that the derivation of the expression can have applications in quantum optics, in particular in quantum metrology.

1. Introduction

Studying the properties of coupled harmonic oscillators is a relevant area of modern physics. The interest towards it stems primarily from the fact that models of such systems can be encountered in many applications of quantum and non-linear physics, molecular chemistry and biophysics [1-2]. In quantum physics this interest generally originates from quantum entanglement for such a system. In particular, quantum communication protocols such as quantum cryptography, quantum dense coding, quantum calculation algorythms and teleportation of quantum states can be explained using entangled states. On the other hand, physical models of coupled harmonic oscillators are used in biophysics to explain the issue of phontosynthesis [3] which is still considered an unsolved puzzle.

2. Results and discussion

Through the solution of the time-dependent Schrödinger equation for Hamiltonian (1)

$$\widehat{H} = \frac{1}{2}\left(\frac{1}{m_1}\hat{p}_1^2 + \frac{1}{m_2}\hat{p}_2^2 + Ax_1^2 + Bx_2^2 + Cx_1x_2\right), \quad (1)$$

work [4] shows that quantum entanglement of two coupled harmonic oscillators can be characterized by a single parameter that accounts for all other factors – reflectance R. Reflectance itself is determined by parameters set by original oscillators. Nevertheless, there is no simple analytical dependence of quantum entanglement on reflectance R. Here we obtain this dependence for various initial states of oscillators. It is demonstrated that the obtained expressions can be applied in quantum optics, particularly, in quantum metrology.

Acknowledgments

The work was supported by Russian Science Foundation grant № 20-72-10151.

References

[1] Fetter A L and Walecka J D 1971 *Quantum Theory of Many Particle Systems* (New York:

McGraw-Hill)
[2] Makarov D N 2018 *Scientific Reports* **8** 8204
[3] Romero E, Augulis R, Novoderezhkin V I, Ferretti M, Thieme J, Zigmantas D and van Grondelle R 2014 *Nature Physics* **10** 676–682
[4] Makarov D N 2020 *Phys. Rev.* E **102** 052213

Coherent tunable difractional pulse shaping and generation of the 0π-pulse in Rb vapor

S N Bagayev[1], V A Averchenko[2], I A Chekhonin[2], M A Chekhonin[2], I M Balmaev[2] and I B Mekhov[2]

[1]Institute of Laser Physics, Novosibirsk 630090, Russia
[2]St. Petersburg State University, St. Petersburg 199034, Russia

E-mail: chekhonin@mail.ru

Abstract. We have experimentally studied for the first time a new operation principle of the coherent difractional pulse shaper (Rabi shaper). In the experiment, we observed an effect of tunable pulse shaping of nanosecond semiconductor laser pulse during the resonant pumping of the D_2 line (780.24 nm) of ^{87}Rb vapor in the range of self-difraction angles $\varphi = \pm 4^o$. We observed the synthesis of nanosecond 0π-pulses at the small length of the nonlinear interaction 0.1...1 mm. We propose to use the Rabi shaper as an energy efficient tunable shaper of classical and single-photon wave packets. We analyze a possibility of the Rabi shaper operation in quantum systems with feedback.

1. Introduction

As known, laser pulses with the shaped amplitude, frequency, phase, and wave vector $\boldsymbol{K}$ excite atoms and molecules more efficiently, which can be applied for the problems of all-optical signal processing and quantum technology.

A problem of the angular deflection of laser radiation is the most difficult problem of the laser radiation control [1]. In [2-3], we proposed a new principle of the angular deflection of radiation wave vector during the laser pulse diffraction from the atomic resonant diffraction grating with the spatial pitch, which is time dependent – the Rabi deflector or Rabi pulse shaper.

In this report, we present the study of transformation of the shape and pulse area during the increase of the pulse self-diffraction angle φ in the resonant medium: positive pulse → 0π-pulse → negative pulse.

2. Experimental

The description of experimental setup and the signal processing method are presented in [3]. A cell with ^{87}Rb vapor was pumped by a pulsed tunable laser diode with the duration of 5.15 ns at the wavelength of transition D_2 (780.24 nm). The density of ^{87}Rb atoms was $N_o = 2.78 \cdot 10^{12}$ cm^{-3}. The cell was filled by buffer gas Ar at the pressure of 1 Torr. Laser pulse power did not exceed 10 mW. The transverse spatial distribution of the pump filed $E_{in}(t,x) = E_{in}(t) \cdot G(x)$ had a Gaussian shape: $G(x) = \exp[-(x/\sigma)^2]$, $\sigma = 0.017$ mm. The full pulse area was $\theta_{in} = 3\pi$.

In the experiment, we analyzed the form and pulse area of the diffraction pulse scattered from the resonant cell at different diffraction angles φ. The pulse form was registered by the single-photon counting method using Single Photon Avalanche Diode with the time resolution of 27 ps. After

treating the temporal histogram of detected photons, one can obtain the radiation pulse $E_p(t)$ of the resonant polarization of a medium in the form of a signal $S1(t) - S2(t) \approx 2E_{in}(t) \cdot E_p(t)$ [3].

We performed the calculation, which models the operation of a Rabi shaper prototype. We solved numerically semiclassical Bloch equations in the model of a two-level medium for a transition with the homogeneous line broadening and given spatial profile of the pump field $E_{in}(t,x)$ (cf. Figure 1). The shape of an experimentally synthesized 0π-pulse is shown in Figure 2.

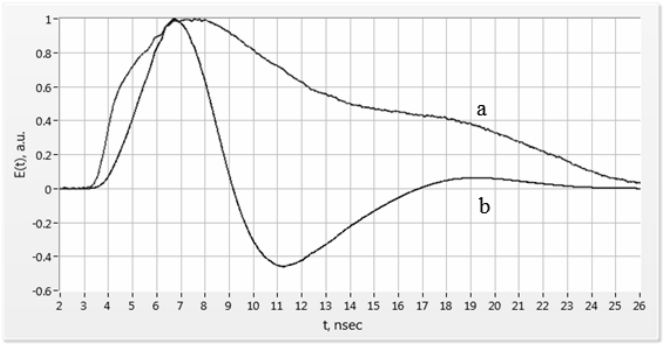

Figure. 1. (a) a realistic pump pulse $E_{in}(t)$; $E_{in}(t) \sim (N_{ph/channel})^{1/2}$.
(b) calculated normalized quantity $2E_{in}(t) \cdot E_p(t)$ at the diffraction angle of $\varphi = 1.82^o$.

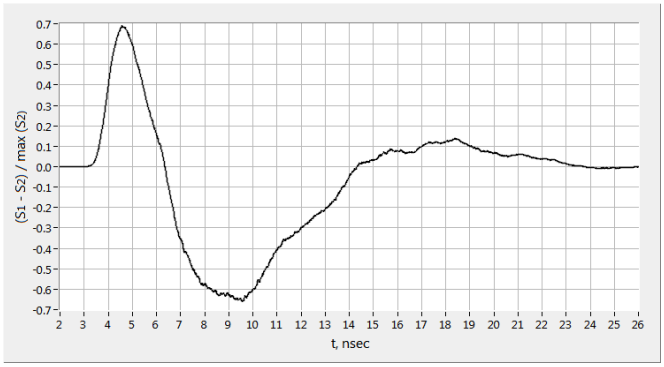

Figure. 2. The measured value of $2E_{in}(t) \cdot E_p(t)$ at the diffraction angle of $\varphi = 1.82^o$.

3. Conclusion

In this report, we analyze a possibility to use the tunable Rabi shaper of classical and single-photon wave packets. Note that the studied Rabi shaper can perform shaping of nanosecond pulses at the small distances of nonlinear interactions of 0.1 ... 1 mm.

The coherent tunable Rabi shaper can be used as a prototype of perspective quantum systems with a feedback loop [4].

Acknowledgements

This work was supported by Russian Science Foundation (project № 17-19-01097-P).

References

[1] Sarantos C H, Heebner J E 2010 *Opt. Lett.* **35** (9) 1389-1391

[2] Arkhipov R M, Arkhipov M V, Egorov V S, Chekhonin I A, Chekhonin M A and Bagayev S N 2015 *J. Phys.: Conf. Ser.* **643** 012029

[3] Bagayev S N, Averchenko V A, Chekhonin I A, Chekhonin M A, Balmaev I M and Mekhov I B 2020 *J. Phys.: Conf. Ser.* **1695** 012129

[4] Ivanov D A, Ivanova T Yu, Caballero-Benitez S F and Mekhov I B 2020 *Phys. Rev. Lett.* **124**, 010603

Simulating the spectral characteristics of reflection in planar porous structures with antireflection coatings ZnS/DyF_3

D A Shishkina[1,2], **I A Shishkin**[1], **P D Tishin**[,2]
[1]Department of Physics, Samara National Research University, Samara, 443086, Russia
[2]Faculty of Electronics and Instrument Engineering, Samara National Research University, Samara, 443086, Russia

Abstract. This paper presents the results of modeling a planar multilayer structure with layers of porous silicon, ZnS and DyF3 coatings by the optical matrix method. It was shown that the optical matrix method, taking into account the model of porous silicon with a variable band gap, which takes into account the porosity gradient, allows us to approximate the course of the curve of the real experiment.

1. Introduction

Porous silicon is a material of particular interest for solar energy, due to its large absorbing surface area. Due to the porous nature (Figure 1), the effective refractive index of porous silicon is lower than that of bulk material.

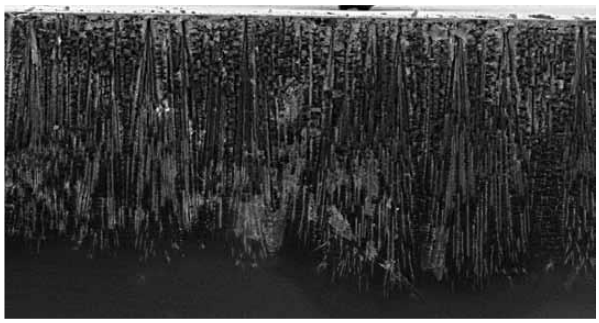

Figure 1. Поперечный слой пористой структуры [1].

Simulating the reflective properties of a multilayer structure allows us to identify the optimal parameters of the layers, which lead to a decrease in the reflection coefficient in the entire spectral range under study. In this paper, the reflective properties of a multilayer structure with a porous layer were modeled using the optical matrix method. This approach was used by the authors of [2,3] for structures with a single-layer antireflection coating of porous silicon and showed good agreement with the experiment.

2. Experiment

The porous layer was obtained by electrochemical etching on a silicon substrate in alcoholic solutions of hydrofluoric acid. The thickness of the porous layer of the resulting structure was 10 microns. The

ZnS and DyF_3 coatings were applied by thermal evaporation in vacuum. The spectral characteristics of the reflection coefficient were studied using a Shimadzu UV-2450 spectrophotometer. The reflection spectrum of the experimental sample is shown in Figure 2 (purple curve). Метод оптических матриц, используемый для данной модели, подробно описан в работе [2]. Основные параметры моделирования приведены в таблице 1.

Table 1. Simulation parameters

	Si	por –Si	ZnS	DyF_3
n	3.42	3	2.2	1.6
D, μm	270	10	0.056	0.13

Taking into account the porosity gradient of the structure (Figure 1), several modifications of the model were considered: 3 porous layers, 6 porous layers, 8 porous layers. The control graph was the graph of the real experiment. The simulation results are shown in Figure 2.

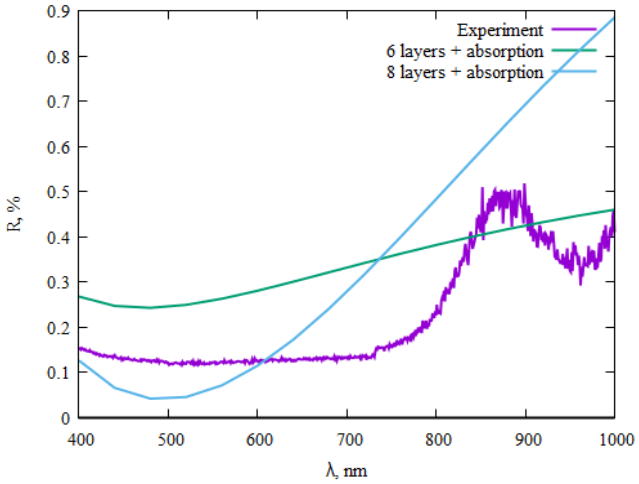

Figure 2. Results of simulating a multilayer structure with optical coatings and a porous layer: green-6 layers, blue-8 layers, violet - experiment.

From the analysis of the obtained graphs, it can be seen that the representation of porous silicon in the form of 8 layers of the same thickness with a refractive index varying from silicon to air allows us to approximate the course of the curve of the real experiment. However, the discrepancy between the theory and the experiment can be explained by the features of absorption in real porous structures, which were not taken into account sufficiently fully in this model.

3. Conclusion

Thus, the resulting model allows us to determine the optimal parameters of the photosensitive structure without the use of complex mathematical calculations, which will further simplify the technological process of creating multilayer solar cells with a low reflection index.

References

[1] Latukhina N, Chepurnov V, Pisarenko G 2013. *ELECTRONICS science technology business* **4** 00126
[2] Aroutiounian V M, Maroutyan K R, Zatikyan A L, Touryan K J 2002 *Thin Solid Films*
[3] Adamian Z N, Hakhoyan A P, Aroutiounian V M, Barseghian R S, Touryan K 2000 *Solar Energy Materials & Solar Cells* **64**

STM Light Emission and I(V) study of single gold nanoantenna at ultra hight vacuum

V A Shkoldin[1,2], D V Levedev[1,3,4], A M Mozharov[1], D V Permyakov[2], L N Dvoretckaia[1], A K Samusev[2], A O Golubok[4], I S Mukhin[1,2]

1 Alferov University, 8/3 Khlopina str., St. Petersburg, 194021 Russia
2 ITMO University, 9 Kronverksky pr., St. Petersburg, 197101 Russia
3 Saint Petersburg State University, 7/9 Universitetskaya nab., St. Petersburg, 199034 Russia,
4 Institute for analytical instrumentation RAS, 26 Rizhskii pr., St. Petersburg, 190103 Russia
E-mail: shkoldin@spbau.ru

Abstract. Hight-speed optical nanoemitters are of importance for on-chip optical data processing. A tunnel junction can be a base of such light emitters; however such structures suffer from low quantum efficiency. One of the ways to enhance efficiency is the increase of the local density of optical states by using of optical nanoantennas. In this work, we study optoelectronic properties of single gold nanodisc with high spatial resolution. We show nonuniform distribution of electromagnetic near-fields, which is consistent with nanoantenna's optical modes. And we show direct correlation between nanoantenna optical states and features on current-voltage characteristics.

1. Introduction

The optical communication transfer enormous amount of information and this volume grows every year at 20-30% [1]. Optical transmission systems are the best way to transfer information on long distance. At the same time metal wires are commonly used for data transfer within the parts of integrated circuit. Optical signal processing has many advantages, including the absence of ohmic losses and big speed of signal propagation. In present, the size mismatch between nanophotonic components, CMOS-components and optical sources is a technological bottle neck. Available today light emitting sources, such as Fabry-Perot lasers or microring and microdiscs lasers, have resonators with minimal sizes significantly exceeding their emission wavelength. One of ways to overcome this threshold is based on the use of inelastic electron tunneling process causing light emission. This phenomenon makes it possible to create subwavelength light sources.

A process of light emission in the metal-insulator-metal (MIM) structures was discovered by the first time by Lambe and McCarthy in 1976 [2]. However, quantum efficiency (QE) of this process is very low (10e-6 – 10e-4 photon/electron). In the resent years, many articles were focusing on the improvement of light emission from a tunnel junction [3,4]. It was showed that QE can be enhanced with increasing of the local density of optical states (LDOS) in the tunnel junction. Theoretically, the value of QE may reach 10% [5,6] due to a large LDOS enabled by plasmonic confinement. Using of nanoantennas is a promising way to increase LDOS in the tunnel junction.

2. Experiment

In this article, we used ultrahigh vacuum scanning tunnel microscope (STM) combined with optical setup to study the LDOS distribution of single gold nanodisc by a Pt/Ir STM probe (Bruker). The array of nanodiscs was made on thin gold film on mica substrate with low roughness. The nanodiscs produced by e-beam lithography have 50 nm height and 180 nm diameter. We modified used STM VT650, Omicron by connecting a single photon counter in order to collect light emission from tunnel contact. It makes possible to acquire STM topography and obtain light emission map simultaneously.

We experimentally observed the increase of light emission on edges of the nanodiscs. We investigated the current-voltage (I-V) characteristics at points on the line crossing the disk (Figure 1 a). Figure 1 b) demonstrates I-V curves acquired at the edge of nanodisk. One can see the features on I-V dependence near 1.6 V and 2.2 V. The fingerprint map presented in Figure 1 c) shows d^2I/d^2V. The features associated with inelastic tunneling and consequent light emission process [4] appears in the form of puddles on the color map. This map allows to estimate the area of nanodisc with enhanced LDOS. Also, we did simulation of the field distribution of the electric dipole mode exited in a plasmonic nanodisc by a plane optical wave or an point optical dipole. Experimental results well correlate with it and show the enhanced LDOS at the edge of nanoantennas.

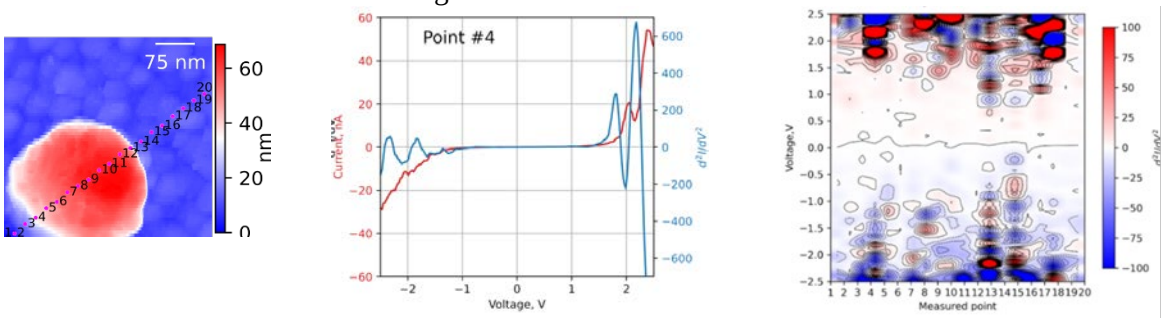

(a) (b) (c)

Figure 1. (a) STM topography image of a nanodisc (I_{SP} =0.08 nA; V_{bias}=1.0 V) with the markers enumerating the points of I(V) study. (b) Typical single I-V, d^2I/d^2V dependences measured at the edge of the disc. (c) d^2I/dV^2 "fingerprint" map of the gold disc.

3. Results

The I-V studies of the tunnel contact may simplify the development of nanostructures for local optical sources based on inelastic electron tunneling phenomenon. This technique is essential for the development of electrically-driven plasmonic optical sources for on-chip optical data processing.

Acknowledgments

This work was done with the financial support of the Russian Federation President Council (MK-2428.2020.2) and the Russian Foundation for Basic Research (project 19-32-90028).

References

[1] "Cisco Annual Internet Report (2018–2023) White Paper" https://www.cisco.com/c/en/us/solutions/collateral/executive-perspectives/annual-internet-report/white-paper-c11-741490.html (access data: 01.03.2021)

[2] Lambe J and McCarthy S L 1976 *Physical Review Letters* ***37***(14) 923–925.

[3] Shalem G, Erez-Cohen O, Mahalu D and Bar-Joseph I 2021 *Nano Letters* ***21***(3), 1282–1287.

[4] Lebedev D V, Mozharov A M, Bolshakov A D, Shkoldin V A, Permyakov D V, Golubok A O, Samusev A K and Mukhin I S 2020 *Physica Status Solidi - Rapid Research Letters* ***14***(3).

[5] Doderer M, Parzefall M, Joerg A, Chelladurai D, Dordevic N, Fedoryshyn Y, Agrawal A, Lezec H J, Novotny L, Leuthold J and Haffner C 2019 *2019 Conference on Lasers and Electro-Optics, CLEO 2019 - Proceedings*, 3–4.

[6] Parzefall M and Novotny L 2019 *Reports on Progress in Physics* ***82***(11), 112401.

Effect of the FWM and SRS on the fiber optics wavelength multiplexing system parameters

N V Yakovlev[1], A V Bykov[1] and E I Andreeva[1]

[1] The Bonch-Bruevich Saint-Petersburg State University of Telecommunications, St.Petersburg, 193232, Russian Federation

yakovlev.nv_spbopen@mail.ru

Abstract. Results of the computer simulation nonlinear effects in fiber optics data systems with WDM are presented. Comparison of systems using standard single mode fiber (SSMF) and non-zero dispersion shifted fiber (NZDSF) with different number spectral channel has been made. In a dispersion-shifted fiber (with a low chromatic dispersion value), the effect of stimulated Raman scattering (SRS) is less, since in these fibers the evolution of symbol pulses is significantly affected by the effect of four wave mixing (FWM). Effect of FWM was studied also. To reduce the FPM effect influence on the system parameters passive spectral channel can be used. In fibers with a high chromatic dispersion, the SRS effect is less pronounced than at low dispersion values. The SRS effect influence on the system parameters depends on the total number of spectral channels in the WDM-system. With increasing number of spectral channels with fixed spectral - width on total power product result of SRS-effect become smaller.

1. Introduction

Stimulated Raman scattering (SRS) describes the parametric interaction of light with molecular vibrations [1-5]. Longer wavelength channels will be amplified by short wavelength channels in the WDM system. For WDM system with N channels spaced apart by the frequency interval Δf with peak power P_o per channel, effect of SRS on the system parameters will be provided by the factor [1]

$$NP_0(N-1)\Delta f \tag{1}$$

where NP_o – is the total optical power in system, and $(N\text{-}1)\Delta f$ – total optical bandwidth. However, it is necessary to take into account the loss of α and the dispersion D. The effect of loss is shown on the effective length of the fiber $L_{eff} = (1 - \exp(-\alpha L))/\alpha$.

In standard single mode fiber (SSMF) L_{eff} = 20 km (α = 0.2 dB/km).

2. Simulation

We considered 2 cases with similar values of the product of the bandwidth by the total power introduced in the optical fiber. In the first case, the number of spectral channels N = 14, spectrum band $(N\text{-}1)\Delta f$ = 12 THz ($\Delta\lambda$=8nm) with a power P_o = 20 mW in the cannel: $NP_0(N-1)\Delta f = 3360$ GHz W.

Exceeding the threshold value is selected with on-off ratio q = 5. Also it is necessary to take into account such nonlinear effects as FWM and the dispersion D. In the second case, we considered 2 spectral channels with a power P_o = 100 mW, spaced across the spectrum by an amount corresponding

to the maximum gain: N=2, (N-1)Δf = 12 THz ($\Delta\lambda$ = 100nm). The product of the spectral band width by the full power was: $NP_0(N-1)\Delta f = 2400$ GHz W, which, in accordance with (1), means that the threshold level of the SRS of the spectral band is exceeded at full power.

In the first case for optical fibers with a large chromatic dispersion (such as SSMF), the SRS effect is weaker than for optical NZDS fibers (small dispersion value). This is due to the "run-up" effect of the symbol pulses. At the same time the increasing the number N of spectral channels further reduces this effect.

In the multichannel system with NZDSF the effect of SRS is less, since in these fibers, the evolution of symbolic pulses is significantly influenced by the FWM- effect. As a result of this effect, the power in the working channels is reduced, and, as a result, the effect of SRS is weakened. The maximal difference between the output cannel power was nearly 8% in computer simulation.

In optical fibers with a large value of chromatic dispersion, such as SSMF, with a large number of the spectral channels N, the maximal difference between the output cannel power was nearly 4%.

The FWM-effect and the fiber dispersion are studied by the computer simulation with OptiSystem program. To reduce the negative effect of FWM, the passive spectral band method can be used.

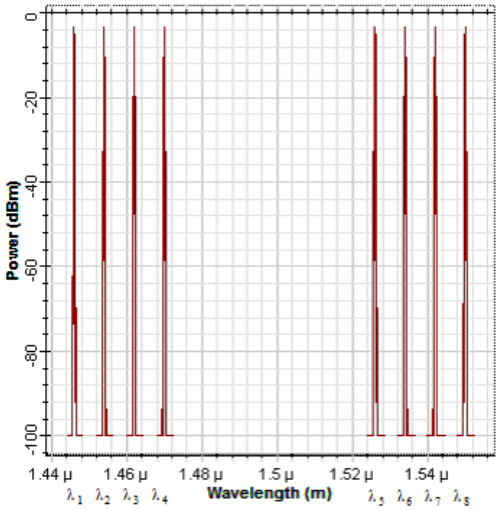

Figure 1. Input signal spectrum.

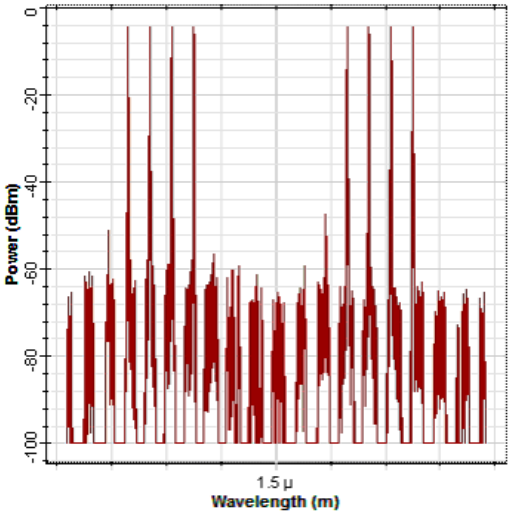

Figure 2. Output signal spectrum

Figure 1 and 2 show the spectrum of the input signal and the output signal with a set of combination frequencies – FWM- products. As can be seen from Figure 2, the power of these components decreases rapidly and does not fall into the adjacent operating spectral range.

3. Conclusion

The effect of SRS significantly depends on not only the factor (1) and on the fiber dispersion D.

To reduce the FPM effect influence on the system parameters passive spectral channel can be used.

References

[1] Chaplyvy A R 1990 *J. of Lightwave Techn.* **8** 1548-57

[2] Agrawal G 2013 *Nonlinear Fiber Optics* (San Diego: 5th Academic Press)

[3] Kivshar Y and Agrawal G 2003 *Optical solitons. From Fibers to Photonic Crystals* (New York: The Institute of Optics University of Rochester)

[4] Shcherbakov A S and Andreeva E I 1996 *Performance data of lengthy-span soliton transmission system* (*Optical Fiber Technology* vol 2) pp 127-13

[5] Andreeva E I, Bylina M S, Glagolev S F and Chaimardanov P A 2018 *Proceedings of Telecommunication Universities* vol 4 chapter 6 pp 5-12

Raman spectroscopy and optical microscopy of medical infusion solutions for parenteral nutrition

E V Pimakhina[1*], A A Pimakhin[1], N V Vishnykov[2], N M Tolkach[2], S B Arsentiev[3]

[1]Ryazan State Medical University, Ryazan 390026, Russian Federation
[2]Ryazan State Radio Engineering University, Ryazan 390005, Russian Federation
[3]Regional Clinical Hospital, Ryazan 390039, Russian Federation

*E-Mail: elenapim@yandex.ru

Abstract. Usage of Raman spectroscopy, optical microscopy, and retaining track membranes to find 20% SMOFlipid microparticles with a diameter of 5 to 10 μm and to prevent complications that arise during parenteral nutrition.

1. Introduction

Parenteral nutrition methods are widely used in intensive care and intensive care units. Solutions and emulsions for parenteral nutrition are composed of nutritional support ingredients which are administered intravenously. [1] Optical microscopy and Raman spectroscopy in a 20% SMOFlipid solution revealed homogeneous microparticles with sizes from 1 μm to 50 μm (average size ~ 10 μm), an average concentration of 10,000 particles / ml, and a volume fraction of 6.4×10^{-3}. Filters of standard medical droppers with a pore diameter of 150 microns do not retain the above-described microparticles. The circulation of microparticles through the bloodstream for 60 minutes was experimentally established when the centrifuged plasma of women aged 19 to 42 was added (10 to 1 by volume) to each of the AB0 / rhesus combinations. The average size of microparticles at 36.6 ° C did not change within 60 minutes, which is due to the specifics of the enzymatic activity of plasma albumin, liver and kidney enzymes and the properties of cell receptors. The Doppler method was used to calculate the transit time of the injected solution through the subclavian vein of full-term newborns - 0.07 s, which is incomparable with the period of lipolysis activation 60 minutes. When microparticles enter the pulmonary and cerebral bloodstream, they cause microembolism, which leads to a pathological decrease in ventilation-perfusion relations.

2. Experiment and methods

It is proposed to filter microparticles through track membranes with a pore diameter of 3 μm, which retain microparticles with a diameter of 5 to 10 μm, which is confirmed by the homogeneous composition of the filtered microparticles and their absence in the solution during repeated filtration. The presence of microparticles and their absence on the surfaces of the track membranes used for filtration were established by optical microscopy. The homogeneity of the microparticles was established by Raman spectroscopy.

The filtration efficiency was confirmed by testing on laboratory rats - microscopy of lung sections revealed a smaller number of neutrophils in the airspace and a smaller proportion of the airspace

containing hyaline membranes, in comparison with sections of the lungs of intact rats. It is caused by a reduction in capillary stasis and a decrease in the intensity of perifocal inflammation. With parenteral nutrition of full-term newborns with 20% SMOFlipid, the use of additional medical filters of the Octopus brand with a pore diameter of 3 μm did not reveal complications associated with impaired hemostasis, while when using filters of standard medical droppers, increased bleeding was revealed, which is manifested by point intradermal hemorrhages in the area of catheter placement, short-term bleeding from the umbilical wound against the background of normal values of fibrinogen, antithrombin, 8 coagulation factor.

3. Results and discussion

Complications that arise during parenteral nutrition using standard medical dropper filters can be explained by the manifestation of hypercoagulation against the background of latent fibrinolysis. The penetration of a large number of microparticles of the infusion emulsion into the peripheral, and then into the pulmonary and cerebral blood flow causes a deviation of hemostasis parameters and activation of the fibrinolytic link. To determine the state of hemostasis accurately, it is necessary to conduct thromboelastometry followed by analysis of the thromboelastogram.

Thus, microparticles in a 20% SMOFlipid solution cause symptoms of hemorrhagic disease of newborns. The introduction of the solution must be carried out with the obligatory use of a filter with a micropore size of up to 5 microns. The infusion rate should correspond to the rate of activation of plasma enzymes and should not exceed the rate recommended in the drug's instructions.

Acknowledgments

The work was performed on the equipment Regional Center of probe microscopy collective use Ryazan State Radio Engineering University named after V.F. Utkin.

References

[1] Pardeshi N N, Qi W, Dahl K *et al* 2017 *Journal of pharmaceutical sciences* **106 (2)** 511

Photonic topological states controlled by hybrid dipole resonances

Daniel Bobylev and Maxim Gorlach

Department of Physics and Engineering, ITMO University, Russia

E-mail: daniil.bobylev@metalab.ifmo.ru

Abstract. Photonic topological states have brought an assortment of promising tools for back-scattering immune routing and robust localization of light at stable frequency. To date, topological states engineering is focused mainly on proper lattice geometry adjustment, which results in the non-trivial band topology and the emergence of topological edge states. However, this recipe restricts topological states performance and tunability. Here, we propose a novel strategy to tailor photonic topological states based on meta-atoms with hybrid magneto-electric dipole resonances. The key feature of such meta-atoms is that their interaction strongly depends on their mutual orientation, allowing to reduce the topological properties control from lattice symmetry orchestration to a single particle optimization. We demonstrate photonic topological states and phase transitions in 1D array of particles with hybrid resonances (split-ring resonators) in full-wave numerical simulations. The proposed approach opens an alternative route of photonic topological states engineering which potentially can be generalized to higher dimensions and higher-order topological states both in microwave and optical domains.

1. Introduction

The emergence of topological photonics uncovered a multitude of remarkable engineering solutions such as topological waveguides, lasers and resonators, which operate with extremely high requirements to their stability [1]. Current progress and experience allows to gradually integrate topological concepts into classical as well as quantum photonic devices, thereby fostering a general trend of substitution of electronics with photonics.

However, there are still many challenges in photonic topological states performance related to poor localization, low protection and lack of tunability. Here, we perform a strategy to realize and tune photonic topological states via alternating hybrid dipole response of the constituting resonators (Fig. 1a). Since hybridization arises due to the spatial inversion symmetry breaking, the effective coupling between two resonators can be easily tuned by angles of their rotation (Fig. 1c) characterizing their mutual orientation. Unlike the conventional strategy to tune the coupling via interparticle distance, such approach provides an easy access to tune the magnitude of coupling dynamically.

Being an alternative implementation of symmetry-protected topological states, they inherit all their advantages related to independence on external fields or modulations, but do not suffer from the sensitivity to the lattice geometry.

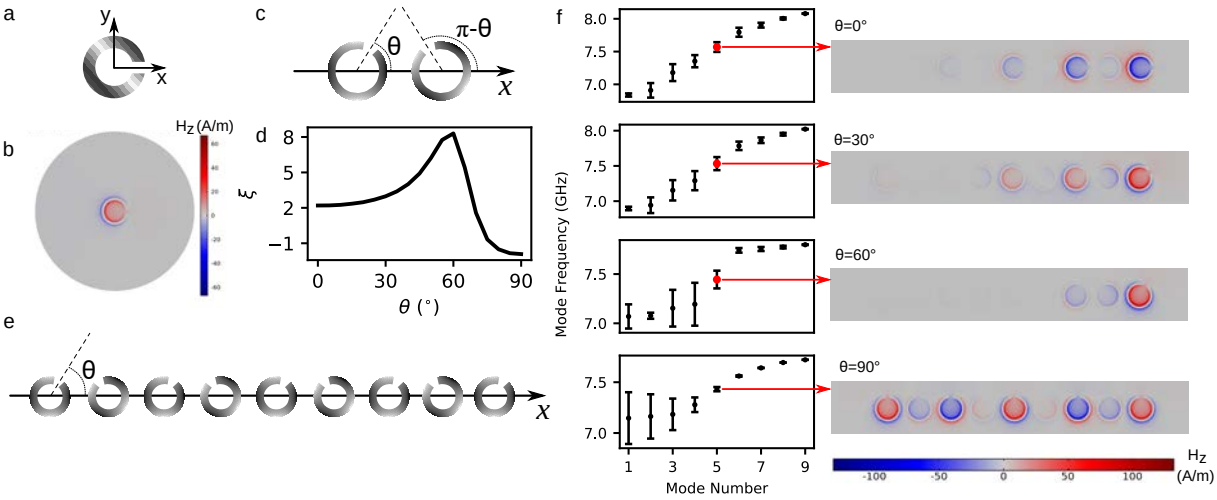

Figure 1. The utilized platform for the electromagnetic topological states engineering via alternating bianisotropy. (a) Specific realization of bianisotropic meta-atom based on a split-ring resonator (SRR); mean radius $R = 3$ mm, thickness $t = 0.75$ mm, gap width $g = 0.75$ mm. (b) Result of full-wave numerical simulation of a single SRR eigenmodes. The eigenfrequency $f = 7.49 - 0.14i$ GHz, dipole moments are $|p_y| \cdot c = 2.89$ A $\cdot$ m^2, $arg(p_y) = 150.5°$ and $|m_z| = 2.23$ A $\cdot$ m^2, $arg(m_z) = 61.5°$. (c) Dimer geometry. The distance between SRRs is $a = 8$ mm. (d) Full-wave numerical simulation results of the dimer eigenmode splittings. $\xi = \Delta(\theta)/\Delta(\pi - \theta)$, where $\Delta(\theta)$ is the eigenfrequency splitting for a specific tuning angle, quantifies dimerization. (e) Geometry of a one-dimensional array of SRRs. Angle θ is responsible for photonic band topology tuning. (f) Full-wave numerical simulation results of a 1D array eigenmodes depending on the tuning angle θ. Black dots correspond to the bulk modes, the errorbar lengths are equal to the imaginary part of the corresponding eigenfrequencies and red dots correspond to edge localized modes; for $\theta = 90°$ dimerization is absent and the topological state disappears.

2. Results

Based on the recently studied design of photonic topological states induced by staggered bianisotropy [2], we take a step forward and focus on the topological properties depending on the mutual orientation of bianisotropic meta-atoms (Fig. 1c). Since bianisotropy is manifested in meta-atoms with broken inversion symmetry, their angles of rotation may significantly contribute to the eigenfrequency splitting $\Delta(\theta)$, quantifying the effective coupling ratio $\xi = \Delta(\theta)/\Delta(\pi - \theta)$, which corresponds to dimerization in tight-binding model. It appears that dimerization exhibits strong dependence on tuning angle manifesting a characteristic peak at $\theta \approx 60°$ (Fig. 1d). In this case we expect that topological state in the corresponding one-dimensional array will be well-localized and the topological band gap will have the maximal width. For $\theta = 90°$ $\Delta(\theta) = \Delta(\pi - \theta)$, so $\xi = 1$, which should break topological properties.

Finally, we simulated a one-dimensional array of SRRs and found the eigenmodes (Fig. 1f). The localization and very existence of topological edge states depends on the value of tuning angle defining dimerization. For instance, the most localized state corresponds to $\theta = 60°$, which corresponds to the largest ξ. Thus, one can easily tune the edge state.

3. Conclusion

To sum up, we have demonstrated the possibility of electromagnetic topological states tuning by bianisotropy. The dependence of coupling between two bianisotropic metaatoms was shown which allows to reconfigure the coupling between the particles constituting the topological structure. We have verified these predictions numerically on the example of a one-dimensional array of metallic split-ring resonators. Furthermore, the proposed approach is also applicable for designing topological structures of higher dimensionality as well as higher-order topological states [3, 4].

References

[1] T. Ozawa et al., *Rev. Mod. Phys.* **91**, 015006, 2019

[2] D.A. Bobylev, D.A. Smirnova and M.A. Gorlach, *Laser Photonics Rev.* **15**, 1900392, 2021.

[3] S. Mittal, V. Orre, G. Zhu et al., *Nat. Photonics* **13**, 692–696, 2019.

[4] M. Li, D. Zhirihin, M.Gorlach et al., *Nat. Photonics* **14**, 89–94, 2020.

On need to control of the upper edge prism state in a flow refractometer for measurements with error a less than 10^{-4}

F A Isakov[1], V V Davydov[1, 2] and V Yu Rud[2]
[1]Peter the Great Saint Petersburg Polytechnic University, Saint Petersburg 195251, Russia
[2]All-Russian Research Institute of Phytopathology, Moscow Region 143050, Russia

Abstract. The article substantiates the need to use a flow-through refractometer to control the state of a flowing liquid during scientific research, when automating a technological process, etc. The main negative factors that affect an increase in the measurement error of the refractive index n of a flowing liquid are determined. It was found that one of these factors is the formation of a thin film (plaque) on the upper face of the prism, which is in contact with the medium under study. The study of the influence of this film on the measurement error has been carried out. A method has been developed to eliminate plaque from the upper face of the prism during the operation of the refractometer. The results of experimental studies are presented.

1. Introduction

The development of scientific and technological progress has posed a number of difficult tasks for scientists. One of which is monitoring the state of the current environment in real time [1, 2]. Especially great difficulties arise if the medium flows through the pipeline at high pressure and temperature. The measurements should not change the flow pattern and the head loss of the system. For most liquid media, measurements should not also change the physical structure and chemical composition of the controlled environment [2, 3]. This is especially important when conducting experiments, in control systems in the food and pharmaceutical industries, and others. At present, only nuclear magnetic flowmeters-relaxometers and flow-through refractometers meet these requirements [1-3]. The latter, in contrast to nuclear magnetic flowmeters-relaxometers, can monitor the state of the liquid in the pipeline both in the current state and in the stationary state. And they have a number of other advantages [1-3].

In contrast to the operation of stationary or portable refractometers, a number of problems arise during the operation of a flow-through refractometer. One of them is the formation, during the operation of the device, of a thin film deposit on the surface of the prism, which interacts with the sample under study. The formation of this plaque does not depend on the studied environment. Even water that stagnates during the maintenance of the entire pipeline can form a deposit on the prism. In stationary refractometers, after each measurement, the prism is cleaned and this problem is not.

2. Experimental setup and research results

Studies have shown that with a coating layer thickness of about 0.3 mm, changes in the refractive index n in the current medium due to the ingress of impurities and other factors will not affect the readings of the refractometer. It will measure the refractive index of the plaque formed. Control over the state of the current environment will be completely lost. In fig. 1 shows the design of a refractometer with an ultrasonic transducer, developed by us, for studying the process of formation and elimination of plaque.

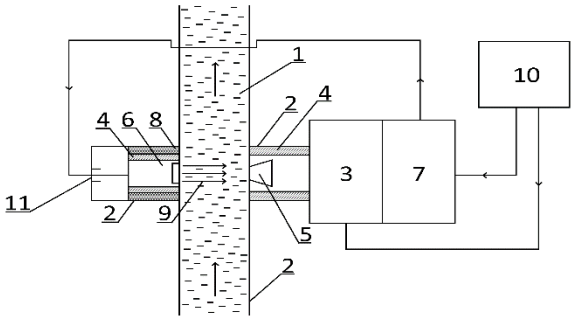

Figure 1. Refractometer design with a pipeline section: 1-flowing medium, 2 - pipeline wall, 3-refractometer, 4 - sealing gaskets, 5- prism, ultrasonic transducer, 7 - device for monitoring the state of the prism surface, 8-inserts in the pipeline, 9-ultrasonic wave , 10-multifunctional power supply, 11-plug with hydraulic conduit for cable.

In fig. 2 shows the results of studying the influence of plaque on the control of the state of drinking water and the result of the work of the developed method for cleaning the upper edge of the prism.

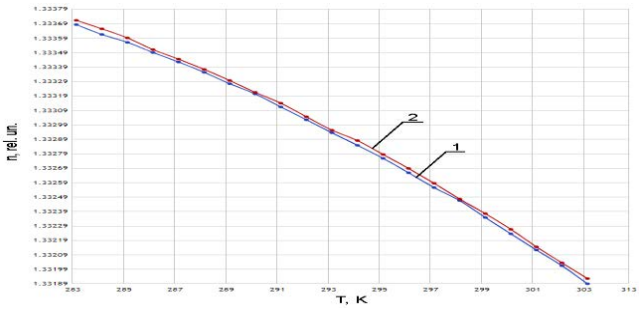

Figure 2. The dependence of the change in the refractive index n of drinking water on the temperature T. The graphs correspond to the state of the prism edge: 1 - no plaque, 2 - plaque is formed.

Comparison of the obtained results of the study of the state of water with the data in [1, 3] showed that the measurement error and the value of n when using an ultrasonic prism cleaner in the refractometer design correspond to the standard. In the presence of plaque, the measurement error n is very high, monitoring the state of the environment is difficult.

3. Conclusion

The conducted studies have shown that the use of the developed design for placing a refractometer with an ultrasonic cleaner and placing it on the vertical section of the pipeline completely eliminates the influence of plaque formation on the measurement error n.

References

[1] Karabegov M A 2013 *Measurement Techniques* **55(11)** 1301–1310
[2] Myazin N S., Yushkova V V, Taranda N I and Rud V Yu 2019 *Journal of Physics: Conference Series* **1410(1)** 012130
[3] Davydov V V, Grebenikova N M and Smirnov K Y 2019 *Measurement Techniques* **62(6)** 519–526

High-detailed electro- and optical investigation of the cell/toxin interaction

A A Abelit,[1] **D D Stupin**[1]

[1] Alferov University, Khlopina 8/3, 194021 St. Petersburg, Russia
E-mail: anna.abelit@gmail.com, Stu87@ya.ru

Abstract. In this study, we provide a detailed investigation of the living HeLa cell's interaction with the Triton x114 toxin. To achieve this goal, we used a Petri dish with a transparent indium tin oxide (ITO) electrode at the bottom, which makes it possible to study the viability of HeLa cells using both high-resolution impedance spectroscopy and laser-pumped confocal fluorescence microscopy. As a result, we have demonstrated that the combination of these two methods allows us to simultaneously study cell morphology and variations in the structure of cell membranes in the presence of a toxin in the cellular environment, which paves the way for high-detailed investigation of the cells/bio-active compound interaction.

1. Introduction

Nowadays progress of biotechnology largely determined by the symbiosis of the physical and biological experimental methods. One of the powerful tools for living cell investigation – laser-pumped confocal fluorescence microscopy [1] – has now become a conventional technique for cell visualization. However, this method provides information mainly about lateral (in xy-plane) cell morphology. Contrary, another promising tool for investigating cells – impedance spectroscopy (IS) [2] – could provide information not only about cell membrane properties and cell morphology [3] in z-direction but also about the cellular environment and cell-carrying electrode [2]. For this reason, several scientific groups propose the combination of the optical and impedance-based cell diagnostics [4]. In this paper, we have proposed and approbated the improved by high-resolution IS [5] opto-electrical sensor which leads us to extract meaningful biological data from the experiment.

2. Results and discussion

The results are presented in Fig. 1, particularly, from Fig. 1(a-c) follows that toxin drastically distorts cells membrane. At the same time in Fig. 1(d) we have observed two regions in the impedance evolution: the 20-s constant-like region and the exponential-like region with the time constant equal to 20 s. As follows from the comparison between optical and impedance data, the second region corresponds to membrane distortion with bubbles formation. Finally, the high-resolution data depicted in Fig. 1(e) indicate that toxin addition does not destruct electrodes, because their impedance before and after toxin addition has pseudo-capacitance behavior (the minima on spectra is due to ammeter non-ideality), and thus the obtained two-region picture in the Fig. 1(d) corresponds to pure biological phenomena in living cells. So, the obtained data allow us to conclude that toxin at beginning interact with the membrane during 20 s, after which it completely destroy the membrane in a time 3×20 s=1 minute. Summarising the study, we can also conclude that by merging the optical and electrical characterization methods it possible to study cells in real-time with achieving rich and informative data sets, which could be used for high-detailed investigation of the biological processes in cells and for a deeper understanding of the

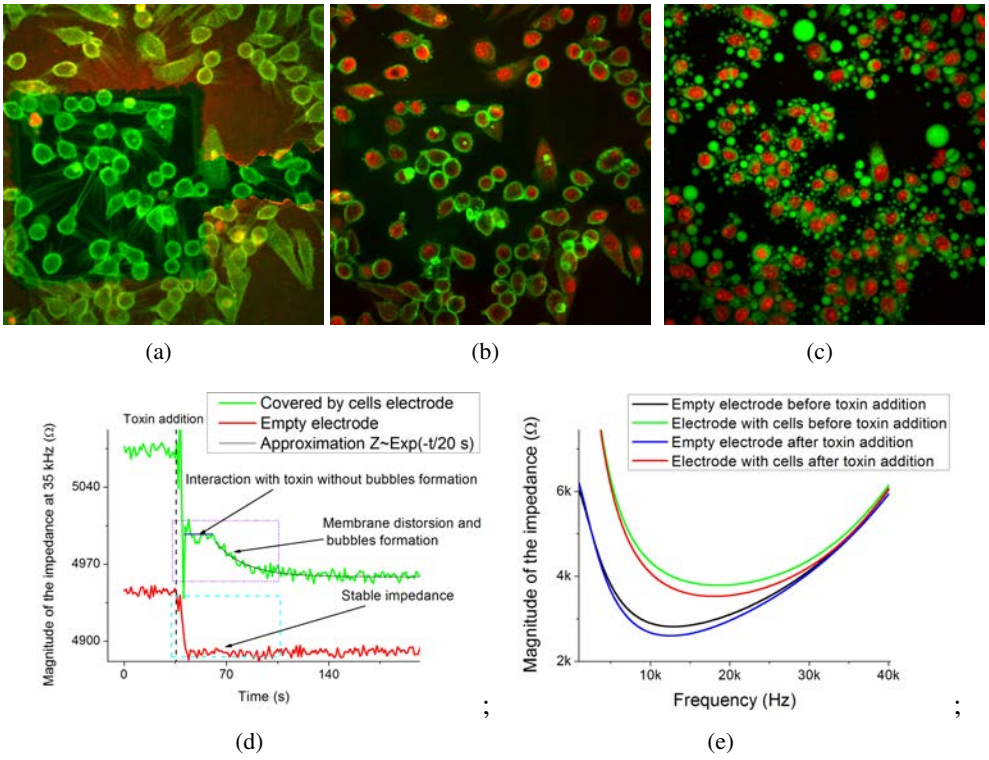

Figure 1. The electro-optical investigation of the HeLa cells in the presence of toxin Triton x114 in cells medium. (a), (b), and (c) are obtained on Zeiss Observer.Z1 microscope confocal images of the HeLa cells on the ITO electrode (200×200 μm^2) at time moments 0 s, 50 s and 150 s respectively. The green color corresponds to Deep Red Cell Mask dye fluorescence and the red color corresponds to propidium iodide fluorescence of the nuclei of the dead cells. (d) The evolution of the impedance spectra of the empty and covered by HeLa cells ITO electrodes during toxin addition. (e) Impedance spectra of the empty and covered by cell electrodes before and after toxin addition.

mechanisms of cell functioning. We believe that proposed in this study high-detailed electro-optical approach will bring to a new level nowadays biosensors for science and healthcare application.

Acknowledgements

The authors acknowledge M.I. Blinova, N.A. Knyazev, A.A. Kornev, and M.V. Dubina for comprehensive assistance and support. The study was supported by the Ministry of Education and Science of the Russian Federation (Project FSRM-2020-0006).

References

[1] Brian Matsumoto 2002 *Cell Biological Applications of Confocal Microscopy* 2nd ed Methods in Cell Biology 70

[2] Stupin D D, Kuzina E A, Abelit A A, Koniakhin S V, Emelyanov A E, Nikolaev D M, Ryazantsev M N and Dubina M V 2020 *ACS Biomaterials science and engineering*

[3] Wegener J, Keese C R and Giaever I 2000 *Experimental cell research* **259** 158–166

[4] Choi C K, Margraves C H, Jun S I, English A E, Rack P D and Kihm K D 2008 *Sensors* **8** 3257–3270

[5] Stupin D D, Koniakhin S V, Verlov N A and Dubina M V 2017 *Phys. Rev. Applied* **7**(5) 054024

Influence of applied power on tissue impedance for carrying out radiofrequency ablation of biological tissue and determination the transmurality effect achieving moment

V V Antipenko[1], E A Pecherskaya[1], S A Antipenko[2], O A Timokhina[1], D V Artamonov[1], A I Levin[1]

[1]Department of Information and measuring equipment and metrology, Penza State University, Penza 440026, Russia
[2]JSC PO Elektropribor, Penza 440011, Russia

v.antipenko7@yandex.ru

Abstract. Radiofrequency ablation (RFA) is used to treat both congenital and acquired heart diseases, including arrhythmias of various types. In this work, experimental studies are carried out on biological tissues under the influence of the applied power on the tissue. Based on the experiments carried out, it was concluded that the effectiveness of the effect on biological tissue and the quality of the result obtained clearly depend on the correct choice of power applied to the treated tissue.

1. Introduction

The RFA method is currently used in the treatment of congenital and acquired heart defects, ischemic heart disease complicated by arrhythmias, as well as in isolated forms of arrhythmia.

The purpose of the method is to destroy the areas of the myocardium through which pathological impulse activity is conducted. Destruction is carried out by applying radiofrequency energy to specific areas of the myocardium from the apparatus using a consumable instrument containing electrical contacts. After the destruction process, the abnormal impulses propagation that excite the myocardium stops, which allows maintaining the correct heart rhythm.

The currently used equipment and consumable tools have significant drawbacks. The main disadvantage is inaccurate determination of the achieving transmural lesion effect in the exposure process. This indicates the relevance of improving the hardware, methods of exposure and determining the achievement of the transmurality effect, to which this study is devoted).

2. The biological tissue impedance measurement while applied power exposed to tissue

This method is based on the biological tissue impedance measuring when the power is applied to the tissue. The graph of the impedance change on time dependence (Figure 1) while applied power exposed to tissue consists of three main sections [1]:

1. Impedance decrease.
2. The impedance level has reached a minimum value, possibly constant for some time, or changes insignificantly.
3. Impedance increase.

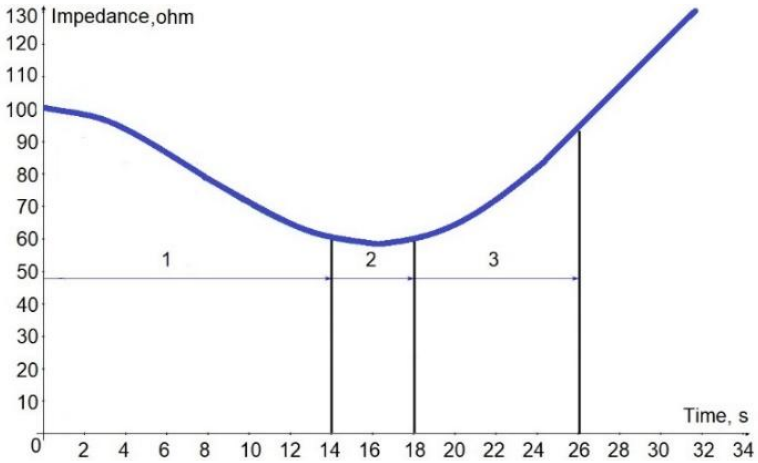

Figure 1. A graph of the change in impedance on time dependence

Based on the data on the tissue impedance and the "operating point" position on the graph of the impedance change on time dependence, it is necessary to investigate and draw conclusions about the course of the ablation process and the achievement of transmural damage to the myocardial tissue.

The task of obtaining a transmural zone of myocardial damage is the need for the shortest possible period of time to heat the required area of the myocardium.

When analyzing a number of scientific studies [2 - 4], it was found that after passing the flat section of the graph and reaching the section of impedance growth, there is a certain impedance threshold, the achievement of which may indicate the achievement of transmurality. The impedance threshold is individual in nature and for each specific situation it is different. Experimental studies carried out by the authors on biological tissues have shown that after passing the point on the graph of the impedance change on time dependence, corresponding to the minimum tissue impedance, there is a rapid, often avalanche-like increase in the tissue impedance.

The impedance change rate depends on a number of parameters: thickness of myocardial tissue; the state of myocardial tissue; power applied to the tissue, the area (or line length) of the instrument's contact with the tissue, etc. When high power is applied to the biological tissue, excessive heating of the tissue surface layers and insufficient heating of the inner layers occur. The impedance of the tissue region will be the sum of the impedances of the surface layers and the inner layers.

Conclusion

In the course of experimental studies, it was proved that the effectiveness of the effect on biological tissue and the quality of the result obtained clearly depend on the correct choice of power applied to the treated tissue, which was used in the development of a software and hardware complex that implements the RFA method and achieves the effect of transmurality.

References

[1] Artyukhina E A, Taymasova I A and Revishvili A S 2020 Catheter ablation of atrial arrhythmias in patients after thoracoscopic ablation of persistent atrial fibrillation, *Russian Journal of Cardiology*, 25(7), 3655

[2] Antipenko V V, Pecherskaya E A, Zinchenko T O, Artamonov D V, Spitsina K Yu and Pecherskiy A V 2020 Development of an automated bioimpendance analyzer for monitoring the clinical condition and diagnosis of human body diseases *J. Phys. Conf. Ser*. 1515 (5) 052075

[3] Golubkov P E, Pecherskaya E A, Karpanin O V, Kraynova K Y, Artamonov D V and Shepeleva Y V 2018 Automated system for bioimpedance measuring *19th International Conference of Young Specialists on Micro/Nanotechnologies and Electron Devices* (*EDM*) pp 641 – 644

[4] Starchenko E I. 2009 Low-Voltage Precision Analogue Multiplier with wide Frequency Range, *2nd IEEE International Conference on Circuits and Systems for Communications* p 156

BrUSLEE and his shadow: two cryogenically stable emissive states within a GFP variant

E.G. Maksimov[1], T. Sen[2], A.V. Mamontova[3], K.A. Lukyanov[3], A.I. Krylov[2] & A.M. Bogdanov[3#]

[1]Faculty of Biology, Lomonosov Moscow State University, 119992, Moscow, Russia;
[2]Department of Chemistry, University of Southern California, Los Angeles, CA 90089, USA;
[3]Shemyakin-Ovchinnikov Institute of Bioorganic Chemistry, Moscow 117997, Russia;

[#]Correspondence: bogdanoff@ibch.ru

Abstract. The BrUSLEE – a recently described variant of the enhanced green fluorescent protein (EGFP) – demonstrates non-typical combination of high fluorescence brightness at a short fluorescence lifetime. Peculiarities of its photobehavior call studying the fine determinants of the fluorescence lifetime in connection with the brightness as well as the limitations of their tuning in the proteins with the GFP-like chromophore. In this contribution, we have analyzed the BrUSLEE time-resolved fluorescence behavior at a high resolution and found its 2 discrete subpopulations existing stably within a wide temperature range (4-300 K). We show that these emissive states both change their fluorescence lifetimes over a temperature dramatically, and display "cryogenic lifetimes" vastly different from each other and from that of the parental EGFP.

1. Introduction

Fluorescent proteins (FPs) from diverse marine animals possess a unique ability to form a fluorophore group autocatalytically using their endogenous amino acid residues, and are therefore widely applied as the genetically encoded fluorescence probes in biomedical imaging [1].

Fluorescence lifetime (FL), which represents an intrinsic characteristic of any fluorophore, acts as an important albeit secondary parameter in FPs engineering. In most cases, FL value is considered to be rigidly tied to the fluorescence quantum yield (FQY). It is thus expected that a bright (high FQY) FP would have longer FL than its dimmer counterpart, and vice versa, a short FL would predict mediocre brightness. With that, a general question of the lifetime determination within a given FP type, or the limits of its tuning at a given FQY value remain largely unanswered.

Recently, we described bright ultimately short lifetime enhanced emitter (BrUSLEE) – a close homolog of the EGFP, a green fluorescent protein conventionally utilized in biological imaging. The BrUSLEE displayed unusual combination of subnanosecond FL with rather high FQY of 0.3 and an overall brightness comparable to that of EGFP [2]. Of note, FPs having similar lifetimes are usually characterized by the extremely low FQYs (<0.1) [e.g., 3]. Thus, the BrUSLEE could represent a perspective model object to study the molecular determinants of FL/FQY tuning within the GFP family. Earlier we revealed a crucial role of Thr65Gly mutation (which is among 3 substitutions discriminating BrUSLEE from the parental EGFP), providing 2-fold shortening of the average FL and

causing a biphasic fluorescence decay character probably by altering hydrogen bond network within the chromophore region [4,5]. In this contribution, we show our current progress in deciphering peculiar phenomenology of the BrUSLEE fluorescence.

2. Results and discussion

To understand the relationships between radiative and radiationless excited-state processes in the BrUSLEE photobehavior and to evaluate possible differences in its radiative rate constant from that of the parental EGFP, we have monitored the fates of the emissive states described earlier [5] within a wide temperature range by high resolution picosecond fluorescence spectroscopy.

2.1. Time-resolved fluorescence spectroscopy within the 4-300 K temperature range

In contrast to monoexponential decay of EGFP at low temperatures, biphasic decay was characteristic to the BrUSLEE in a wide range of temperatures. We have detected and monitored 2 fluorescent subpopulations of the BrUSLEE: the major "short-lived" one (~500 ps, 85%, at room temperature) and the minor “long-lived” one (1.4 ns, 15%, at room temperature). Time-resolved spectroscopy carried out on a cryostatic setup, have shown that as the temperature decreases from 300 to 4 K (i.e., where it is expected to reduce the efficiency of nonradiative processes in an excited state), the lifetime of the major component increases from 500 ps to 2.2 ns and the minor one – from 1.4 to 5.5 ns. Thus, we were unable to unambiguously determine an intrinsic fluorescence lifetime (tau 0) of the BrUSLEE, and thus to estimate the fluorescence rate constant. Even at temperatures of <10 K, the emission of this protein is characterized by two components, which apparently correspond to two alternative chromophore configurations. Importantly, both low-temperature lifetimes differ drastically from the corresponding EGFP lifetime (~3.2 ns).

2.2. Atomistic calculations to interpret fluorescence data

Atomistic calculations (QM/MM/MD) based on the BrUSLEE preliminary X-ray structure, to our surprise, have not revealed heterogeneity in both ground and excited states of the BrUSLEE. However, several intriguing points were understood.

Thus, in the ground state, the average number of H-bonds between the chromophore and the surrounding amino acid residues in BrUSLEE is 0.5 less than in EGFP (2.4 versus 2.97). At the same time, the substitution Phe165Tyr promotes an increase in the average number of hydrogen bonds, which explains the increase in the quantum yield of BrUSLEE fluorescence compared to other Thr65Gly mutants.

Calculations for the excited state of the chromophore (more than 100 trajectories for each protein, allowing to observe the evolution of torsion angles in a time window of 3 ns) show that in the EGFP about 80% of the molecule population retains the planar chromophore’s conformation, while for the BrUSLEE, a rapid twisting of the chromophore is characteristic. It is noteworthy that the kinetics of this twisting (t = 0.85 ns) correlates well with the experimentally measured average fluorescence lifetime.

The fact that at high temperature (>100 K) different populations do not interconvert and lead to different lifetimes is probably explainable by the longer timescales for interconversion as compared to fluorescence. For example, if we have millisecond rate of interconversion between different conformations in the ground state, it means they all will be sampled and populated with Boltzmann weights in the course of ground-state dynamics. But then in the excited states there will be no time to interconvert (on the nanosecond scale), so one would see distinct populations.

Acknowledgments
This project was supported by the Russian Foundation for Basic Research grant 19-04-00845 (acquired by A.M.B.)

References
[1] Chudakov D M, Matz M V, Lukyanov S, Lukyanov K A 2010 *Physiol Rev*. **90** 1103-63
[2] Mamontova A V, Solovyev I D, Savitsky A P, Shakhov A M, Lukyanov K A, Bogdanov A M 2018 *Sci Rep.* **8** 13224
[3] Matela G, Gao P, Guigas G, Eckert A F, Nienhaus K, Nienhaus G U 2017 *Chem Commun* **53** 979-982
[4] Sen T, Mamontova A V, Titelmayer A V, Shakhov A M, Astafiev A A, Acharya A, Lukyanov K A, Krylov A I, Bogdanov A M 2019 *Int J Mol Sci.* **20** 5229
[5] Mamontova A V, Shakhov A M, Lukyanov K A, Bogdanov A M 2020 *Biomolecules*. **10** 1547

Investigation of the cytotoxicity of silver nitrate and silver-cysteine nanocomplexes

Bogdanov A.A.[1,2,3,4], Shmakov S.V.[5],Verlov N.A.[1,2,4], Klimenko V.V.[1,2], Knyazev N.A.[1,2], Terterov I.N.[1,2], Bogdanov A.A.[1,2]

[1] Saint-Petersburg clinical scientific and practical center for specialised types of medical care (oncological)», St. Petersburg, Russian Federation
[2] State Research Institute of Highly Pure Biopreparations, St Petersburg, Russian Federation
[3] Institute for Analytical Instrumentation of the Russian Academy of Sciences, St Petersburg, Russian Federation
[4] Petersburg Nuclear Physics Institute NRC Kurchatov Institute, Gatchina, Russian Federation
[5] St Petersburg Academic University, St Petersburg, Russian Federation

E-mail: vip.nasa@bk.ru

Abstract: Currently, a large number of studies are devoted to the investigation of the antitumor activity of silver nanoparticles and compounds, one of which is silver nitrate. However, silver nitrate has systemic and local toxic effects. In this work, a method was proposed for the synthesis of non-metallic complexes that do not contain toxic nitrate ions, and the cytotoxicity of silver nitrate and silver-amino acid nanocomplexes was investigated.

1. Introduction

The study of the antitumor activity of silver nanoparticles and compounds in vitro and in vivo, as well as the study of the mechanisms underlying these effects, is relevant today. There is a theory that the main active agent is not the nanoparticles themselves, but silver ions Ag +, dissociating from the surface [1-4]. However, the molecular mechanisms underlying the antitumor activity of silver ions and the molecular triggers responsible for the activation of these mechanisms have not yet been identified [5]. In addition, there are no studies in which the in vivo effect of silver is studied in, presumably, the most active, ionic form, where the most soluble salt, silver nitrate, acts as an ion donor. This can be explained by the high general and local toxicity of silver nitrate when administered into the bloodstream, in particular, due to the formation of nitric acid during the interaction of silver ions with sulfide groups of proteins and amino acids, toxicity of nitrate ion, as well as the formation of insoluble particles of silver chloride during the interaction of Ag + with Cl- ions present in the blood. One of the problems of silver nanoparticles that prevent their systemic administration is the presence of a metal core that prevents their biodegradation and excretion from the body.

The aim of this work is to study the toxicity of silver nitrate and silver-cysteine nanocomplexes, as well as to develop a method for the synthesis of these nanocomplexes.

2. Materials and methods

Flow cytometry and colorimetric MTS test were used for determination of cytotoxicity of silver nitrate and silver cysteine nanocomplexes. Chemical method was developed to synthetize new silver-cysteine nanocomplexes. The physical properties of silver-cysteine nanocomplexes were studied using dynamic light scattering method.

3. Results

Earlier in the study of the cytotoxic and antitumor activity of silver nitrate, we showed that silver nitrate has a cytotoxic effect, as a result of the study, an IC50 value for the HeLa and K-562 tumor lines was obtained, which is 20 times higher than the IC50 for normal human MNCs. .It has also been shown that silver nitrate has an antitumor effect against Ehrlich's solid tumor, but the compound also has systemic and local toxic effects [6]. Presumably, one of the mechanisms of local toxicity is the release of nitric acid during the interaction of silver ions with sulfide-containing compounds, such as cysteine, the concentration in the blood of which is normally 166.6-249.9 μM, which, with the introduction of silver nitrate (excluding buffer capacity of blood), can cause a local decrease in blood pH to 4 at a normal value of 7.5. The nitrate ion, in turn, is also a toxic compound. A possible way to reduce the systemic and local toxicity observed with the introduction of pure silver nitrate is the synthesis of non-metallic complexes that do not contain toxic nitrate ions. The simplest, most accessible and physiological complexing substance can be the amino acid cysteine, which can effectively bind Ag + ions. In the course of the work, the development of a general synthesis scheme and the selection of the optimal conditions for the synthesis and purification of such complexes were carried out.

When an aqueous solution of cysteine interacts with silver nitrate at various ratios R = Cys/Ag, nanoscale complexes are formed. The hydrodynamic diameter of these complexes for different R was measured by the method of dynamic light scattering, and the values of the electrokinetic potential of the obtained complexes were also determined. The complexes under study have a characteristic size of several tens of nanometers up to the ratio R = 1/2; with an increase in the mole fraction of silver nitrate in the initial mixture to 2.5, the hydrodynamic diameter increases to ~ 100 nm, and upon reaching at R = 1/4 a micron size. The electrokinetic potential of the investigated particles increases uniformly with an increase in R, when the ratio R= 1/1, its value is 35 ± 3.78 mV, with an increase in R to 1/4, the value of the electrokinetic potential increases to 52 ± 4.4 mV. When measuring the spectra of ultraviolet and optical absorption of the obtained complexes, it was shown that the absorption values increase with an increase in the ratio R over the entire investigated wavelength interval. The absence of a broad plasmon resonance peak at □ = 410 nm, characteristic of metallic silver nanoparticles, confirms the nonmetallic nature of the synthesized complexes. The measured pH value of the solution after the formation of AgCys nanocomplexes was 1.5, which makes the crude complexes unsuitable for both in vivo and in vitro studies. After the obtained nanocomplexes were purified from nitric acid as well as the residues of unreacted starting compounds, the pH value of the resulting solution was 7, which indicates the absence of nitric acid and the potential applicability of the complexes for in vitro and in vivo studies. Based on the results of the synthesis and purification of silver-cysteine complexes, we investigated the antitumor activity of these complexes in vitro on various tumor and normal, human and mouse cell cultures. IC50 for AgCys nanocomplexes were obtained for various cell cultures: K-562 - IC50 = 22.2 ± 1.61 μg / ml; HeLa - IC50 = 22.2 ± 1.61 μg / ml; 3T3b - IC50 = 22.2 ± 1.61 μg / ml; CT-26 - IC50 = 9 ± 2.17 μg / ml, no toxicity for MNCs of human peripheral blood was observed in the range of the studied concentrations, which could be the evidence of the selective action in relation to tumor cells.

4. Conclusion

As a result of this work, the method for the synthesis of silver-cysteine nonmetallic nanocomplexes was proposed, and the optimal conditions and concentrations were investigated and selected. The antitumor activity of silver-cysteine nanocomplexes was shown in various normal and tumor cell cultures of humans and mice.

References

[1] Kim, S., Choi, J. E., Choi, J. 2009 *Toxicology in vitro*. **23(6**) 1076-1084
[2] Jannathul F.M., Lalitha P 2015 *Prog Biomater*. **4(2-4**) 113-121
[3] Jeyaraj M., Rajesh M., Arun R. 2013 *Colloids Surf B Biointerfaces*. **102(1)** 708–717
[4] Rutberg F.G., Dubina M.V., Kolikov V.A. 2008 Dokl Biochem Biophys..421 191
[5] Gurunathan S., Lee K.J., Kalishwaralal K., 2009 Biomaterials. **30(31)** 6341–6350
[6] Bogdanov A.A., Verlov N.A., Shmakov S.V. 2020 Collection of scientific papers on materials XII International Scientific Conference. 4-10

Identification of new silk-like protein from *B.magister* and development of functional materials based on it

A A Vronskaia[1], A D Mikushina[1] and I E Eliseev[1]

[1]Alferov University, St. Petersburg 194021, Russia
vrons.ann@gmail.com

Abstract. Tandem repeat proteins are in high demand today due to their composite structure and unique properties, which allow them to be used in multiple fields, such as soft photonics, drug delivery and textile industry. Recently discovered squid ring teeth (SRT) proteins have turned out to belong to this group and have complemented the existing range of repetitive polypeptides. We have chosen previously unexplored squid — *B. magister* for our research, have developed methods for both DNA extraction and further sequencing and have also established techniques to purify isolated SRT and fabricate various materials from them.

1. Introduction

Conventional hard materials, including synthetic polymers, are typical for manufacturing photonic devices [1], however, the common requirements of biodegradability and biocompatibility to work with live systems cannot generally be fulfilled for them. On the other hand, natural proteins can be optimized to provide various materials with diverse functionalities and complex structure [2].

Squid ring teeth are located inside suction cups on tentacles of squid and serve to grip tightly on a diverse array of objects [3]. These teeth are built of native protein complex, which has been studied to be a novel silk-like fibrillar protein with tandem repeat structure [1] that allows its use in the polymer industry [4] and other multiple fields [1]. Although it has been shown that SRT proteins meet the requirements of biodegradability and remarkable physical properties [4], nevertheless, the knowledge of clear structure-property relationships remains elusive [1]. This fact together with such unique properties of SRT proteins demands further research in order to design materials with desired characteristics for building devices with novel functionalities, which are difficult to achieve or previously unattainable [2].

2. Results and discussion

For our research we have chosen another cephalopod — a squid *B. magister.* New SRT proteins have been isolated and purified with acetic acid and organic solvents. SRT protein solutions were evaporated on PDMS at different temperatures to get films. We also obtained particles that were formed by adding the protein solution to the NaCl solution. An example of the SRT film and SRT particles is presented in figure 1. To isolate main fraction of SRT proteins we used salt-induced precipitation and various types of chromatography. After initial analysis with gel electrophoresis we identified a single peptide, using trypsin digestion before mass-spectrometry. Using BLAST tool and gene databases of closely related species, we designed primers for PCR amplification of the sequence that encodes the protein of interest. Standard methods using chloroform and phenol were used to purify extracted genomic DNA. After a successful sequencing result, it is planned to continue work on production of recombinant proteins and fabrication other materials.

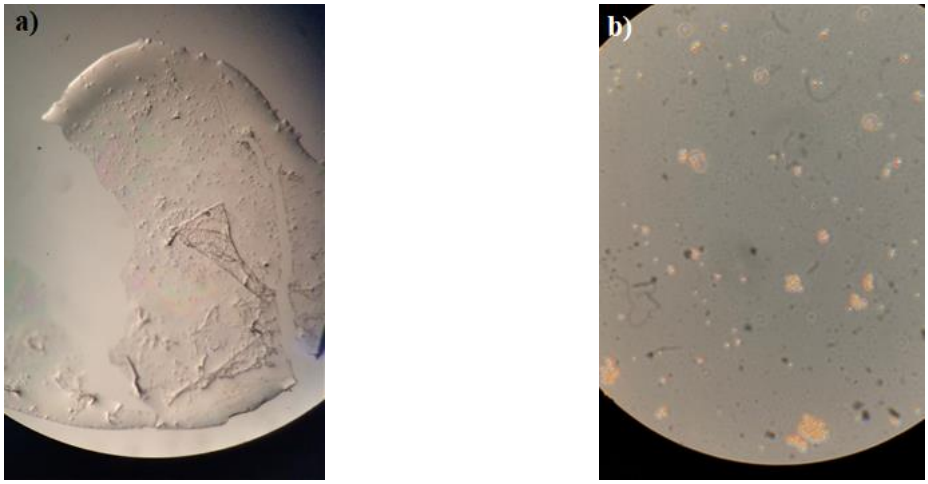

Figure 1. (a) SRT film, 5x magnification. The film is transparent, quite fragile, but elastic. The bubbles were caused as the solution was evaporating at low humidity. **(b)** SRT particles, 40x magnification. The obtained particles were observed using phase-contrast microscopy.

References

[1] Pena-Francesch A and Demirel M C 2019 *Front. Chem.* **7** 69
[2] Yılmaz H, Pena-Francesch A, Shreiner R, Jung H, Belay Z, Demirel M C, Özdemir S K and Yang L 2017 *ACS Photonics* **4** 2179-86
[3] Jung H, Pena-Francesch A, Saadat A, Sebastian A, Kim D H, Hamilton R F, Albert I, Allen B D and Demirel M C 2016 *PNAS* **113** 6478-83
[4] Pena-Francesch A, Florez S, Jung H, Sebastian A, Albert I, Curtis W and Demirel M C 2014 *Adv. Funct. Mater.* **24** 7401-09

The effect of optogenetic activation of astrocytes on the hippocampal neurons activity

E. I. Gerasimov[1], A. I. Erofeev[1], S. A. Pushkareva[1], A. V. Bol'shakova[1], A. A. Borodinova[3], P. M. Balaban[3], I. B. Bezprozvanny[1,2], O. L. Vlasova[1]

[1]Laboratory of molecular neurodegeneration, Peter the Great St. Petersburg polytechnic university, Saint-Petersburg, 195251, Russia
[2]Department of Physiology, University of Texas Southwestern Medical Center, Dallas, TX, USA
[3]Cellular Neurobiology of Learning Lab, Institute of Higher Nervous Activity and Neurophysiology of the Russian Academy of Science, Moscow 117485, Russia

e-mail: evgeniigerasimov1997@gmail.com, olvlasova@yandex.ru

Abstract. The method of optogenetics has spread widely in neurobiology over the past 10 years and has found extensive application in various fields of this sciences. It allows to control and regulate cellular activity with high spatial and temporal resolution. In this study, optogenetic activation was applied to astrocytes expressing ChR2. Optogenetic stimulation parameters were determined, in which the frequency of spontaneous currents of hippocampal pyramidal neurons significantly changed. In the future, it is planned to use the obtained data on the modes of optogenetic stimulation of astrocytes to normalize the functions of the hippocampus in mice-models of Alzheimer's disease.

1. Introduction

Astrocytes play an integral role in the maintenance and regulation of neural networks in the brain. They are able to influence neuronal activity by regulating the extracellular concentration of potassium ions, as well as neurotransmitters, due to the expression on their membrane of a large number of transporters of electrogenic mediators (glutamate [1], gamma-aminobutyric acid [2], glycine [3]). By releasing gliotransmitters, astrocytes act on neuronal receptors, modulating neuronal excitability, synaptic transmission, and plasticity. Astrocytes do not generate an action potential in response to a stimulus, but respond with intracellular calcium waves [Ca^{2+}] [4]. When this wave propagates, serine, cytokines, and lactate are released, which modulate the activity of neurons [5]. The ability of astrocytes to release glutamate allows to regulate the function of NMDA receptors, thereby controlling the excitation in the network of neurons [6]. Astrocytes are closely related to the pathogenesis and pathological processes of neurodegenerative diseases [7], so the ability to control their activity becomes an urgent and necessary task in the treatment of neurodegenerative diseases. As the main method for the activation of astrocytes, the method of optogenetics is used in this work, which allows selectively, with physiological space-time resolution, to regulate the activity of hippocampal astrocytes.

2. Results

The results of the studies showed an increase in the activity of hippocampal pyramidal neurons in response to optical stimulation of astroglial cells containing the AAV5 pZac2.1

GfaABC1D_ChR2(H134R)-mCherry virus and allowed us to determine the mode of light stimulation of astroglia. At the pulse mode t = 100 ms, T = 1c and continuous mode t = 5 s, a significant change in the EPSC frequency relative to the base level value was observed (figure 1).

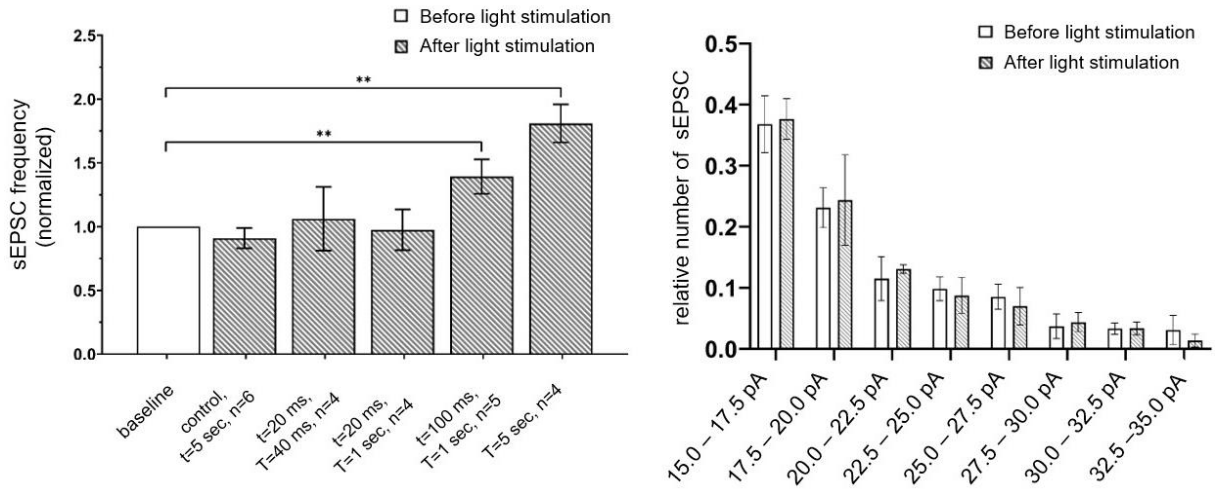

Figure 1. Values of the normalized EPSC frequency of hippocampal neurons in the CA1 region after light activation (t = 20 ms, T = 20 ms; t = 20 ms, T = 1c; t = 100 ms, T = 1c; continuously t = 5 s) of astrocytes. The data are presented as an average of ± SEM, **: p <0.01, the confidence is calculated by the Mann-Whitney test.

3. Conclusions

In this work, duration and frequency of light excitation of astroglia were determined. At these parameters of optogenetic stimulation (pulse mode t=100 ms T=1 sec and continuous excitation t=5 sec) significant change in activity of pyramidal neurons in acute hippocampal slices was observed. In the future, it is planned to use the obtained data on the modes of optogenetic stimulation of astrocytes for their excitation and registration of fEPSP in mice-models of Alzheimer's disease, long-term potentiation and conduct behavioral tests.

Acknowledgments

The work was supported by the grant of the Russian Science Foundation 20-65-46004 (OLV).

References

[1] Huang Y et al. 2004 *Curr. Opin. Neurobiol.* **14** 346–52
[2] Schousboe A 2000 *Neurochem. Res.* **25** 1241–4
[3] Jursky F et al. 1996 *J. Neurochem.* **67** 336–44
[4] Kuga N et al. 2011 *Neurosci.* **31** 2607–14
[5] Salmina A et al. 2021 *Rev. Neurosci.*
[6] Halassa M et al. 2009 *Annu. Rev. Physiol.* **72** 335–55
[7] Toniolo S et al. 2020 *Int. J. Mol. Sci.* **21** 1–37
[8] Osten P et al. 2007 *Nat. Protoc.* **1** 3166–73
[9] Ting J et al. 2018 *J. Vis. Exp.* 1–13

Chemical composition of extracellular vesicles of mesenchymal stromal cells: TOF-SIMS and BCARS approach

A A Gulin[1], A V Aybush[1], A A Kuzoiatova[2], M V Gubina[1], F E Gostev[1], A S Ermakov[2,3], E A Sazonova[2], E A Suprunenko[2]

[1]N.N. Semenov Federal Research Center for Chemical Physics RAS, Kosygina str., 4, Moscow 119991, Russia

[2]Lomonosov Moscow State University, Faculty of Biology, Department of Embryology, 1, b. 12 Lenin Hills, Moscow, 119991, Russia

[3]Koltsov Institute of Developmental Biology, Russian Academy of Sciences, Vavilova str., 26, Moscow, 119334 Russia

Abstract. Paracrine functions of mesenchymal stem (stromal) cells (MSCs) rely, at least partly, on membrane-bound extracellular vesicles (EVs) with rich composition of lipids, nucleic acids and signaling proteins. Elucidation the underlying chemistry could potentially lead to MSCs-free therapy. However, the EVs' composition is non-static and, in turn, depends on many other factors including surrounding cells and medium. Thus, the research techniques must be able to provide not only bulk but microscopy-scale data in a reasonable time. Two of these label-free techniques are subject of this work toward the question of chemical composition of the EVs.

1. Introduction

Exosomes and microvesicles derived from MSCs have recently become known as promising agents for tissue regeneration and immunomodulation [1]. These lipid containers differ in size (by convention, exosomes < 100 nm < microvesicles) and cellular origin, but both are extracellular membrane-bound vesicles and involved in cell-to-cell communication though the membrane substances and cargo of the EVs. In view of importance of potential applications, various techniques were already employed for EVs characterization, including DLS, TEM, AFM, SEM, different modalities of mass and vibrational spectroscopy [2]. In this work we study constituents of EVs using two modern rapid label-free chemical imaging techniques based on secondary ions mass spectrometry and broadband nonlinear Raman microspectroscopy.

2. Methods and materials

Adipose tissue-derived MSCs (d122, kindly provided by Koltsov Institute of Developmental Biology, Moscow, Russia) were prepared using a standard methodology. Culturing continued until ~90-95% confluence density was reached, followed by serum-free cultivation for 2 days. MSC-derived EVs were extracted from cells using Total Exosome Isolation Reagent (Invitrogen, ca # 4478359) after multi-stage centrifugation to obtain debris-free media. The pellet containing exosomes was re-suspended in DPBS (Gibco, ca #14190144). Secondary ion mass spectra were collected with a TOF-SIMS 5 mass spectrometer (ION-TOF, Germany) [3]. Broadband coherent anti-Stokes Raman scattering (BCARS) microspectrometer implemented as a part of femtosecond laser complex representing two pulses collinear scheme for CARS generation with simultaneous frequency coverage ~1000 1/cm [4].

Measured spectra of organic samples were related to ones of sapphire glass to eliminate non-resonant components of CARS.

3. Results and discussion

Bright-field microscopy with appropriate microscopic objectives (Mitutoyo HR, 100x, NA = 0.7) and illumination at 450 nm shows EVs as small as 300 nm (Fig.1a). Nanometer-sized EVs are supposed to be distributed across sample and contribute to average of TOS-SIMS spectrum over the scan area of 300x300 μm. In addition to mass peaks of phosphatidylcholine (PC) and other membrane lipids (PE, SM) observed in positive ions, the negative ion spectra show clear features of myristic (C14:0), palmitoleic (C16:1), palmitic (C16:0), linolenic (C18:3), linoleic (C18:2), oleic (C18:1), stearic (C18:0) acids (Fig.1b). Moreover, the following phosphate ion peaks (H4PO4+, PO3-, PO2-), as well as many fragments of carbohydrate ions (CH3O+, C2H5O+, C3H5O+, C5H5O+, C5H7O+, C5H9O3+) can also be an evidence of nucleic acid (NA) content of EVs [5].

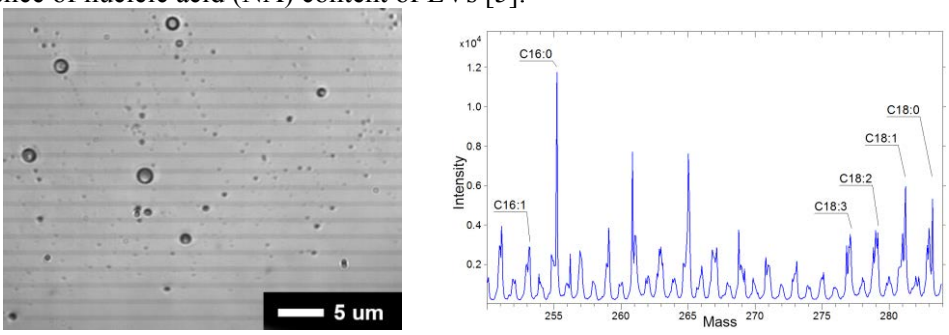

Figure 1. Bright-field microscopy (a) and TOF-SIMS negative ions average spectrum (b) of EV of MSC.

Submicron/micron sized EVs (Fig. 1a) are suitable for analysis in BCARS due to its high performance per single point allowing to collect hundreds of spectra for averaging of the EVs' vibration bands. The result spectrum (Fig.2) demonstrates many features of lipids (~1740, ~1650, ~1440, ~1300, ~1260, ~1180, ~1130, 970, 920), including unique fingerprints of PC (~720 1/см), cholesterol (~703, ~1178 1/см) and regions of high variance originating from combinations of lipid, NA and proteins bands.

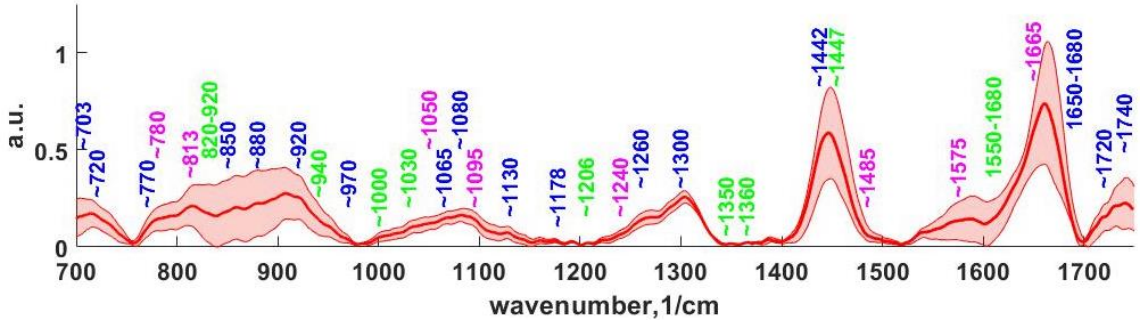

Figure 2. Averaged BCARS spectra (transformed to Raman bands) for MSC EVs with one standard deviation shown. The characteristic bands assigned to lipids (blue markers), NA (magenta) and proteins (green) are shown.

4. Acknowledgments

This work was supported by RFBR (Project No. 19-29-04136 mk).

References

[1] Phinney, D G, Pittenger, M F, 2017 *Stem Cells* **35**, 851–858
[2] Smith Z et al, 2015, *J Extracell Vesicles*, **7(4)**, 28533
[3] Gulin A A, Shakhov A M, Nadtochenko V A et al, 2019, *Applied Surface Science,* **481** 144
[4] Aybush A V, Gulin A A, Nadtochenko V A et al, 2020 *J. Phys.: Conf. Ser.* **1695** 012063
[5] May C J, Canavan H E, Castner D G, 2004 *Anal. Chem*. **76** 1114-1122

Blood vessels of inflammation visualization *in vivo* via colominic acid decorated upconversion nanoparticles

P.A. Demina[1,2*], N.V. Sholina[2], R.A. Akasov[2], A.N. Generalova[1,2], E.V. Khaydukov[2,1,3]

[1]Shemyakin-Ovchinnikov Institute of Bioorganic Chemistry of RAS, 117997, Moscow, Russia

[2]FSRC "Crystallography and Photonics" of RAS, 119333, Moscow, Russia

[3] I.M. Sechenov First Moscow State Medical University, Moscow, 119991, Russia

*Corresponding author, e-mail: polidemina1207@yandex.ru

Abstract. Inflammation accompanies various human diseases, including cancer, so it is important to detect it on the early stage. However, there is still no universal approach of sensitive visualization of inflammation site and solid tumors. In this work, we used upconversion nanoparticles modified with colomic acid, for solid tumors and blood vessels in inflammation site visualization.

1. Introduction

Visualization of pathological changes in living organism, such as inflammation and solid tumors formation in the early stages is an outstanding issue in biomedicine. Inflammation is associated with huge number of pathological changes, for example, arthritis, myocarditis, enteric and skin disease and is also often associated with the cancer development. Existing imaging techniques such as MRI, PET, and CT are not sensitive enough to monitor the inflammation development *in vivo*. *In vivo* visualization of solid tumors using different labels is often complicated by the limited choice of label-exciting radiation.

2. Results and discussion

The nanoreagents based on upconversion nanoparticles (UCNP) are powerful tool for highly sensitive inflammation and cancer tissue visualization. UCNPs represent an inorganic host matrix $NaYF_4$ doped with rare earth elements ions (Yb^{3+} as a sensitizer and Tm^{3+} as an activator) [1]. UCNP excitation is carried out by near-IR light (975 nm), which falls into the biological tissue "transparency window", and as a result, due to multistage nonlinear optical processes, UCNPs generate photons with higher energy in the UV, visible and near-IR spectral ranges. Nanoreagents on the platform of UCNPs allow deeper visualization with minimal scattering and absorption, have photostability, photosensitivity and high spatial resolution.

The successful UCNPs application for solving nanobiotechnology problems consist in the surface functionalization in order to obtain biocompatible non-immunogenic nanoreagents. We developed UCNP surface modification method based on endogenous polysaccharide, colominic acid [2]. The obtained collodal-stable nanoreagents retain their fluorescent properties, are non-toxic, do not induce

an immune response and have long circulation time, which leads to effective accumulation in the acute inflammation site and in solid tumors. The UCNPs accumulation in the inflammation site is associated with the features of the inflammatory tissue determined by the growth of new vessels and increased permeability of already existing vessels, which leads to the UCNPs accumulation by a mechanism similar to the EPR effect, which is characteristic of solid tumors [3]. The current approach make it possible to visualize large and small blood vessels in the area of inflammation, which is especially important for efficient high-resolution diagnostics and prediction of possible biodistribution of nanoreagents based on UCNPs.

Acknowledgments
The reported study was funded by RFBR, project number 18-29-01021.

References
[1] Generalova A N, Chichkov B N, Khaydukov E V 2017 *Adv. Colloid Interface Sci.* **245** 1
[2] Demina P A, Sholina N V, Akasov R A, Khochenkov D N, Arkharova N A, , Nechaev A V, Khaydukov E V, Generalova A N 2020 *Biomaterials science* **8** 4570
[3] Демина П А, Шолина Н В, Акасов Р А, Хоченков Д А, Нечаев А В, Балалаева И В, Хайдуков Е В, Генералова А Н, Деев С М 2021 *Доклады Российской академии наук. Науки о жизни* **497** 61

Diagnostic optical complex for non-invasive analysis of the oxygen status of human tissues

A.V. Egorova[1], M.S. Mazing[1,2], A.Yu. Zaitceva[2]

[1] Peter the Great Saint Petersburg Polytechnic University, Saint Petersburg

[2] Institute for Analytical Instrumentation of the Russian Academy of Sciences

e-mail: anna@da-24.ru

Abstract. An optical non-invasive system for diagnosing the oxygen status of human tissues has been created and investigated. The method is shown to be promising for studying the compensatory and adaptive capabilities of the human body.

1. Introduction

The oxygen status of tissues is currently considered as one of the key factors that determine the prognosis of the disease and the effectiveness of therapeutic effects. The currently known methods for determining the degree of tissue oxygenation have significant limitations. Immunohistochemical study allows you to get an accurate picture of the distribution of oxygenated and hypoxic zones, but it can only be carried out ex vivo and is not suitable for dynamic observation. Polarographic measurement of pO2, which is the "gold standard" for determining the oxygen status of tissues, is invasive and its use in the clinic is extremely limited. Magnetic resonance imaging, positron emission tomography and computed tomography with the emission of single photons with contrasting agents are inaccessible for widespread use due to their high cost. Thus, to date, there is no accessible and non-invasive method that allows obtaining information about the oxygen status of tissues before starting treatment, and subsequently conducting dynamic studies of its changes [1].

2. Materials and methods.

To determine the oxygen status of human tissues, an optoelectronic unit was used as a non-invasive measuring device, which records absorption and backscattered radiation in tissues. The system includes a multichannel optical spectrum analyzer and an optical radiation source. The spectrum analyzer microcircuit is designed to work with the visible part of the light. Working wavelengths 450/500/550/570 / 600/650 nm [2]. The radiation source is 2 white light LEDs integrated into the microcircuit. The method is based on the ability of oxyhemoglobin and deoxyhemoglobin to absorb different wavelengths.

3. Experimental study

Experimental studies were conducted with the participation of seven female subjects. To reduce the percentage of oxygen in the blood and to deteriorate the supply of oxygen to the tissues, the subjects were offered a functional load, which is holding the breath while taking a deep breath for the maximum possible time. The sensor was applied to the wrist of the left hand. The readings were taken

during rest for 60 seconds, holding the breath and recovering for 240 seconds. The respiratory functional load presented to the test subjects traditionally causes significant changes in the physiological functions of the body and reflects the body's resistance in conditions of a low oxygen content in the blood, tissues and organs (hypoxic state), reveals the adaptive reactions and compensatory capabilities of the human cardiovascular system during the period of hypoxic exposure, and also characterizes the functional state of the whole organism as a whole.

4. Results and discussion

Figure 1 shows a typical pattern of the standardized readings of six sensors over time.

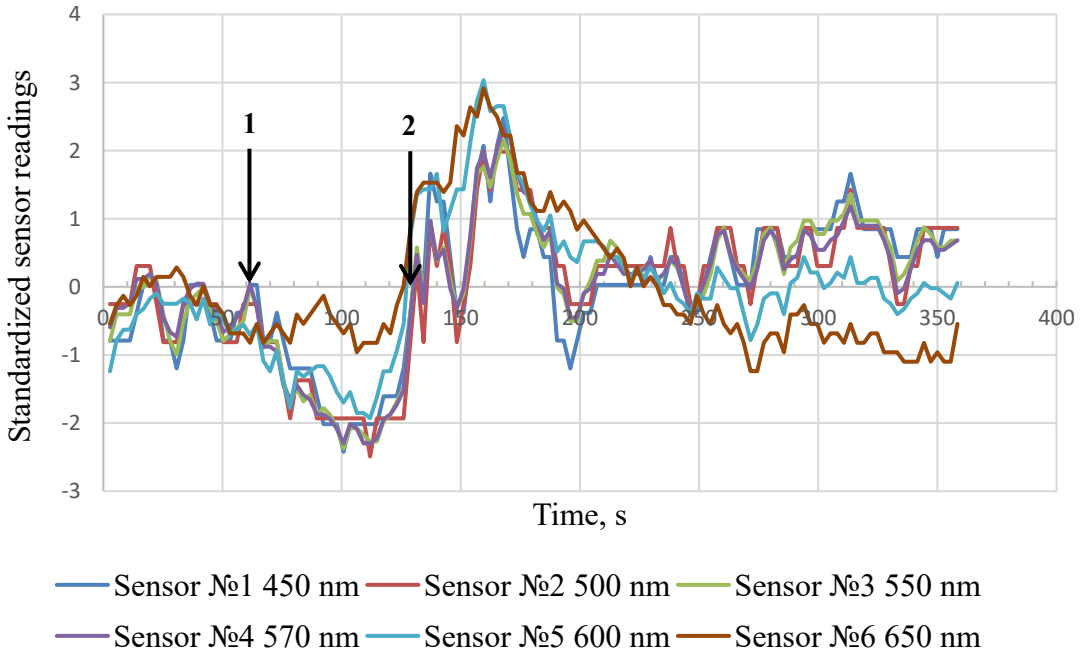

Fig. 1. Typical dependence of changes in standardized readings of 6 sensors over time. The horizontal axis is the time axis, the vertical axis is the axis of standardized sensor readings. State 1 is the beginning of air retention. State 2 - end of breath holding.

After 40 seconds from the beginning of the breath hold, there is a sharp drop in the readings of all sensors, except for the sixth one, which corresponds to a wavelength of 650 nm, and the peak of the graph falls on recovery within 30 seconds. After 240 seconds from the moment of expiration after the delay, the readings of the sixth sensor decrease compared to the resting state, and the readings of the remaining sensors increase.

The studies carried out show that the "images" of the oxygen status of the tissues of the subjects have general and individual characteristics. According to the recorded indicators, they are divided into two groups of different compensatory-adaptive responses to functional load.

The results obtained indicate the efficiency of the created complex and the prospects of its use for assessing the oxygen status of tissues of the human body.

Acknowledgments

The study was carried out within the framework of State Assignment No. 075-01073-20-00 SU NIR 0074-2019-0010

References

[1] NON-INVASIVE OPTICAL METHOD FOR EVALUATING THE OXYGEN STATUS IN BREAST NEOPLASMS A.V. Maslennikova, G.Yu. Golubyatnikov , A.G. Orlova, V.I. Plekhanov , A.A. Artifeksova, N.M. Shakhova, V.A. Kamensky , I.V. Turchin. Mammology.

Onkoginekologiya, 2010, 1, стр. 5-10.
[2] Kislyakov Y. Y. et al. Analytical Multisensory Trainable System for Diagnosing Vocational Aptitude of Military Medical Specialists by Ion Content in the Expired Breath Condensate //Journal of Computational and Theoretical Nanoscience. – 2019. – Т. 16. – №. 11. – P. 4502-4507.

Microfluidic chips for real-time PCR

A Zubik[1], G Rudnitskaya[1], A Bulyanitsa[1], T Lukashenko[1] and A Evstrapov[1]

[1] Laboratory of Bio-& Chemosensors microsystems, Institute for Analytical instrumentation RAS, Saint Petersburg 190103, Russia

Abstract. The results of real-time PCR in single-chamber microfluidic chips made of silicon-glass materials and optically transparent polymethyl methacrylate are presented. Conditions for efficient thermal cycling in microchip devices with several reaction chambers are discussed.

1. Introduction

The development of micro-fabrication technologies, the improvement of bioanalytical methods have led to the emergence of various instruments and devices for studying biological samples at the "point-of-care" [1, 2], in particular, for the detection of nucleic acids by amplification methods (polymerase chain reaction (PCR), loop mediated isothermal amplification, etc.). At present, the relatively high cost of microchip devices in comparison with traditional test tubes or plates is a significant obstacle to their widespread use. The cost of microchip devices depends on the cost of the material and components, the manufacturing and sealing technologies used, in some cases – on the cost and laboriousness of additional technological operations (surface modification, integration of elements, lyophilization of components, etc.), serial production. For effective PCR, it is required to ensure high accuracy of the set temperatures during thermal cycling, both overheating and insufficient heating lead to a decrease in the PCR efficiency [3]. The high thermal conductivity of silicon (160 $W\cdot(m^2\cdot°C)^{-1}$) is an advantage for PCR chips, but this material requires additional surface modification in the reaction chamber. The use of polymers makes it possible to reduce the cost of the material for the chip; many available technologies for the formation of microstructures have been developed for them. However, polymers have a low thermal conductivity (0.1-0.3 $W\cdot(m^2\cdot°C)^{-1}$), therefore, they require more careful control of heating during PCR. This paper presents the results of real-time PCR obtained in microchip prototypes made of silicon-glass materials and polymethyl methacrylate (PMMA), with the same topology.

2. Materials and reagents

Polymer microchips consisted of two PMMA plates glued together. The top plate (with inlet / outlet holes) was 1 mm thick; the bottom plate (with the reaction chamber) was 1 mm or 0.8 mm thick. Reaction chambers with a depth of 300 μm and a volume of about 30 μL were engraved by laser ablation. Silicon-glass microchips with reaction chambers 250 μm deep and about 25 μl in volume were manufactured by "Svetlana-Electronpribor" JSC (St. Petersburg, Russia). The duration required for heating the liquid in the reaction chamber was determined using a test solution with fluorescent probes (the technique is presented in [4]). For real-time PCR, a kit of reagents was used to detect the DNA of the pathogen of potato ring rot (Cat. No. RN-001, "Syntol" LLC, Russia). Bovine serum albumin was added to the reaction mixture for these microchips to prevent the sorption of the DNA polymerase enzyme on the silicon surface. Real-time PCR was performed on devices developed at the IAI RAS: in test tubes – on ANK-32 and in microchips – the prototype device for microchips.

3. Results and discussion

The results of real-time PCR on microchips with a single chamber are shown in figure 1. An increasing or decreasing background signal on the graphs can be corrected using mathematical processing. The thermal cycling mode for all microchips was the same: denaturation at 94 °C – 20 s, annealing and elongation at 65 °C – 70 s. The curve for a polymer microchip (with a 1 mm bottom plate) is comparable to that obtained in conventional/traditional test tubes. The curve for a silicon glass microchip has a steeper slope and an earlier plateau. This is probably due to better heat transfer through the silicon bottom plate and, as a consequence, an increase in the reaction efficiency.

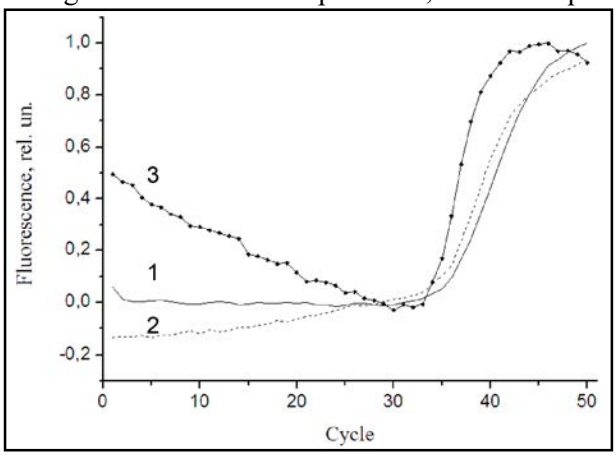

Figure 1. Amplification curves of real-time PCR: 1 – in test tubes on ANK32 (solid line); 2 – in a PMMA chip with a single chamber on the prototype device for microchips (dotted line); 3 – in a chip made of silicon-glass materials with a single chamber on the prototype device for microchips (line with dot).

The initial concentration of the target DNA was $5 \cdot 10^4$ copies / µl.

For the transition from single-chamber microchips to multichamber chips, the heating conditions were studied in more detail. The rate of temperature change in the reaction chamber of the microchip, in addition to the characteristics of the heater, is influenced by the following factors: the thermal conductivity and the thickness of the bottom of the microchip, the mass of heated objects, and the thermal contact between the surface of heater and microchip. The latter depends on the design of the clamping device and the materials of the contacting surfaces. After PCR in the PMMA microchips that were pressed against the heater, we observed an imprint of the heater on the lower surface of the microchip, which indicates a tight fit of the microchip to the heater. A fragile multichamber silicon-glass chip with significant clamping force can break if random hard irregularities (or microparticles) are found on the contacting surfaces. The absence of a clamp can lead to insufficiently tight contact with the heater; therefore, earlier [5] we used a thin (0.2 mm) elastic substrate that provides contact with surfaces and is suitable for repeated use. The thermal conductivity of the substrate is lower than that of silicon, which significantly reduces the heating / cooling rate of such a chip.

Using the test solution with fluorescent probes, the heating performance of the multichamber chips was determined. The results obtained allow us to draw conclusions: 1) a change in the thickness of the bottom polymer plate from 1 mm to 0.8 mm leads to an increase in the heating / cooling rate by 3 times; 2) the heating / cooling rate of a thin polymer chip without a substrate is only 2 times lower than that of a silicon-glass chip with a substrate (3 °C·c^{-1} versus 5.6 °C·c^{-1}) with a comparable weight.

Acknowledgments

The research was carried out within the state assignment of Ministry of Science and Higher Education of the Russian Federation (theme No. 075-00280-21-00).

References

[1] Zhu H, Fohlerova Z, Pekarek J, Basova E and Neuzil P 2020 *Biosens. Bioelectron.* **153** 112041
[2] Zhang L, Ding B, Chen Q, Feng Q, Lin L and Sun J 2017 *TrAC* **94** 106–16
[3] Grunenwald H Optimization of polymerase chain reactions 2003 *Methods Mol Biol* **226** 89–100
[4] Sochivko D, Varlamov D, Fedorov A and Kurochkin V 2016 *Tech. Phys. Lett.* **42** (4) 362–4
[5] Afonicheva P, Zubik A, Bulyanitsa A, Rudnitskaya G and Evstrapov A 2020 *JPCS* **1695** 012060

Combination of photodynamic therapy with radachlorin and cytostatic chemotherapy with cisplatin or doxorubicin reduced resistance of K562 and Hela human cell lines

Klimenko V.V.[1,2] Shmakov S.V.[3], Knyazev N.A.[1,2], Verlov N.A.[1,2,4], Bogdanov A.A.[1,2,4], Terterov I.N.[1], Bogdanov A.A.[1,2]

[1] Saint-Petersburg clinical scientific and practical center for specialised types of medical care (oncological)», 197758, St Petersburg, Russia
[2] State Research Institute of Highly Pure Biopreparations, 197110, St Petersburg, Russia
[3] St Petersburg Academic University, 194021, St Petersburg, Russia
[4] Petersburg Nuclear Physics Institute NRC Kurchatov Institute, 188300, Gatchina, Russia

E-mail: klimenko.vova@gmail.com

Abstract. In this work were study combined effect of photodynamic therapy and cisplatin/doxorubicin on the proliferation activity of leukemia K562 cells and cervical cancer Hela cells. A decrease in cell viability and an increase the fraction of apoptotic cells for combination therapy compared with single therapy were found. It has been shown that the G2 / M phase of cell cycle decreases compared with cisplatin alone, which demonstrates an increase in the anti-proliferative effect. The combination index of the Radachlorin-photodynamic therapy and cisplatin or doxorubicin was calculated and indicates a synergistic effect.

1. Introduction

Photodynamic therapy (PDT) is an actively developing method for the treatment of oncological diseases of various localization. However, in clinical practice PDT is rarely used as a monotherapy and is usually used in combination with chemotherapy as an additional antitumor effect. Currently, there are no unambiguous protocols for the combined use of cytostatic drugs and PDT. However, in a number of works [1, 2, 3], the effectiveness of the combined use of various chemotherapeutic drugs and PDT with the photosensitizer Photofrin in vitro was shown and a synergistic effect of the combination effect was revealed. Chlorin photosensitizers (Radachlorin, Photoditazin) have less toxicity than Photofrin and widely used in clinical practice in Russian Federation. The aim of this study was to study the combined effect of photodynamic therapy with Radachlorin and the cytostatic agent cisplatin or doxorubicin on leukemia (K562) and cervical cancer (Hela) cell lines. The work evaluates the cytotoxic and cytostatic effect in combination with the identification of the cell death mechanisms and the cell cycle changes.

2. Materials and methods

The K562 chronic myelogenous leukemia and Hela human cervical cancer cell lines were obtained from the cell culture bank of the Institute of Cytology Russian Academy of Sciences. The cells were cultured in RPMI/DMEM medium (HyClone, USA) supplemented with 10% FBS (HyClone, USA) in the presence of the antibiotic gentamicin in an atmosphere of 5% CO2. To assess survival and study the cell cycle, a Beckman Coulter Epics XL flow cytometer (Beckman Coulter, USA) was used. For photodynamic therapy was used a photosensitizer Radachlorin (RadaPharma, Russia) and a medical semiconductor laser 662 nm Lakhta-MILON (Milon, Russia). Kemoplat (Germany) and Doxorubicin-Teva (India) were used as a chemotherapy drugs for cisplatin and doxorubicin.

3. Results

In this work, at the first stage, the effect of the cytostatic agent cisplatin on the survival of K562 cells was investigated. Were obtained curves of the survival of K562 cells from the concentration of cisplatin for two time intervals of incubation: 24 and 48 hours. Were determined the concentration of cisplatin, leading to a decrease in the number of living cells to 50% of the control, they were 75 μM for 24 hours and 40 μM for 48 hours of incubation, respectively. To assess the cytostatic effect, a study of the cell cycle was carried out. Were obtained concentration dependences of the distribution of the phases of the cell cycle of K562 cells. The greatest changes in the cell cycle are observed in the range of cisplatin concentrations from 0 to 15 μM, in which there is a pronounced accumulation of cells in the S-phase - up to 90% of the population, while no cytotoxic effect is observed. With a further increase in the concentration of cisplatin (more than 30 μm), blocking of cells in the G0 / G1-phase is observed up to 50%, the S-phase decreases to 40%. This effect of cisplatin practically stops cell division and causes an increase in the sub-G1 region (apoptotic cells) up to 40 %, which correlates well with the data on survival. The presence of the G2 / M phase at high concentrations (60 and 80 μM) may be associated with the rapid action of the cytostatic and blocking the cell cycle at the time of addition of the drug. It is also worth noting that at low concentrations, up to 7 μM, there is an increase in the cell population up to 40 % in the G2 / M phase, followed by a decrease to 0% with increasing concentrations.

To study individual PDT for cell survival, K562 cells were scattered in 12 well plates in the amount of 10^5 cells per well. After 48 hours of incubation, a photosensitizer at a concentration of 2 μM was added to the cells. After 3 hours of incubation, the cells were exposed to laser radiation with radiation doses ranging from 0.125 to 5 J/cm^2. To study the effect of cisplatin and PDT on cell survival, we chose cisplatin 15 μM, which does not cause a toxic effect on the cell division cycle K562. The experiment was carried out according to the following scheme: cells were scattered into a 12-well plate in the amount of 10^5 cells per well; after 24 hours, 15 μM cisplatin was added; PDT was performed 48 hours later; after 72 hours, cell and cell cycle survival is achieved.

Flow cytometry data were obtained on the survival of K562 cells depending on the radiation dose under individual exposure to PDT and combined exposure to cisplatin and PDT. The radiation doses were determined, leading to a decrease in cell survival by up to 50% in relation to the control. For PDT, the dose is $IC50_{PDT}$ = 1.1 J/cm^2, for the combination exposure $IC50_{comb}$ = 0.2 J/cm^2. In this work, the values of cell survival and the magnitude of apoptosis under individual and combined exposure to cisplatin and PDT were studied. It has been shown that the combined effect of cisplatin at a concentration of 15 μM and PDT with a radiation dose of 0.5 J/cm^2 leads to a decrease in cell survival to 30 % and the initiation of cell apoptosis to values greater than 35 %, which significantly exceeds the values obtained for each of the effects separately, which indicates the presence of a synergistic effect.

The distributions of the phases of the cell cycle were obtained under the combined action of cisplatin and PDT. As noted above, the effect of cisplatin on K562 cells at a concentration of 15 μM leads to blocking of the cell cycle in the S-phase. PDT does not lead to strong changes in the cell cycle, however, an increase in the proliferative index and G2 / M phase is noted for surviving cells. The combined effect leads to the accumulation of cells in the S-phase of the cell cycle up to 98 % and a strong decrease in the G2 / M-phase to 1%. The values of the fraction of cells in the sub-G1 phase

correlate well with the values of the percentage of apoptotic cells obtained by flow cytometry using the Annexin V-FITC / PI test.

4. Conclusion

The data obtained demonstrate the presence of a significant synergistic effect in the combination of cisplatin and photodynamic therapy on K562 cells. It can be assumed that the demonstrated effect may be associated with a photodynamic effect on the mitochondria of cells [4], leading to membrane disruption, release of cytochrome C into the cytoplasm, followed by activation of caspase-3, which triggers the apoptosis cycle on the one hand, and on the other, with an increase in expression of the Fas/Fas ligand, which also activates the apoptosis mechanism, when exposed to cisplatin [5].

Acknowledgments

References

[1] Nonaka M, Ikeda H, Inokuchi T 2002 *Cancer Lett.* **184** 171-178
[2] Compagnin C, Mognato M, Celotti L, Canti G, Palumbo G, Reddi E 2010 *Cell Prolif.* **43** 262-274
[3] Yi X, Dai J, Han Y et al. 2018 *Commun Biol* **1**, 202
[4] Kessel D, Luo Y, Deng Y, Chang C K 1997 *Photochem. Photobiol.* **65** (3) 422–426
[5] Micheau O, Solary E, Hammann A, Martin F, Dimanche-Boitrel M T 1997 *J. Natl. Cancer Inst.* **89** 783–789

In vitro model of structural and functional recovery of brain injury in microfluidic chip

V N Kolpakov[1], Y I Pigareva[1], A A Gladkov[1, 3], A S Bukatin[4], I V Mukhina[2, 3], V B Kazantsev[2] and A S Pimashkin[1, 2]

[1] Lobachevsky State University of Nizhny Novgorod, Neuroengineering laboratory, Institute of Neuroscience, Nizhny Novgorod, 603950, Russia

[2] Lobachevsky State University of Nizhny Novgorod, Department of Neurotechnology, Institute of Biology and Biomedicine, Nizhny Novgorod, 603950, Russia

[3] Privolzhsky Research Medical University, Central Research Laboratory, Cell Technology Department, Nizhny Novgorod, 603005, Russia

[4] Alferov Saint-Petersburg National Research Academic University of the Russian Academy of Sciences, Saint-Petersburg, 194021, Russia

*corresponding author. Email: pimashkin@neuro.nnov.ru

Abstract. Development of new methods CNS injury treatment today is one of the main tasks in Medicine. In this study we modeled a brain injury by growing two weakly coupled neuronal networks in a three-chamber microfluidic chip and recovered it by plating new dissociated cells. Direction of connections were formed by asymmetric design of the chip and synaptic strength were modulated by electrical stimulation using synaptic plasticity mechanisms. Such technology can be used to develop a new type of scaffold to recover heterogeneous architecture of neural network and neurointerface to monitor and modify functional structure.

1. Introduction

Currently, no effective therapy is available to promote functional recovery following brain injury. Many studies were addressed to develop implants (scaffolds) of various biocompatible and biodegradable materials that carry neuronal cells to restore lost functions of damaged areas [1]. The microfluidic methods combined with microelectrode arrays allow to develop the in vitro model of brain injury and investigate the recovery of functional connections of the neural networks [2, 3]. We developed the microfluidic chip with three chambers connected by microchannels with asymmetric design. In this study we modified a previously proposed three chamber chip [4] to model a brain injury which causes weak connectivity. We showed that it can be recovered by integration of cells and then modified by electrical stimulation.

2. Materials and methods

To prepare the chips, we used PDMS silicone polymer (polydimethylsiloxane). Liquid PDMS was poured onto a master mold and cured in an oven at 70°C at least for two hours. Two assessable wells for loading the cells were cutted out by a 2 mm puncher in each chamber of the chip.

The chip consisted of three chambers: a source (1), an implant (2), and a target (3). The source chamber and the implant chamber were connected by 16 microchannels, each of which was 400 μm long and consisted of two triangular sections. The implant chamber and the target chamber were connected by 16 asymmetric microchannels 600 μm in length, each consisted of three sections. The second and third sections contained two 'traps' that prevent axons from growing in the 'target-implant' direction. Mouse hippocampal cells (E18) were planted in the 1st and 3rd chambers of the chip, the 2nd chamber remained empty, thereby modeling the damage of the nervous system. On day 7, the new hippocampal cells were plated into the implant chamber and it was modeling the implantation into the damage.

To record the electrophysiological activity, the cultures were combined with microelectrode arrays (MEA) so that 60 electrodes were located both in the chambers and along the microchannels. The recording of the bioelectrical activity was carried out using the multichannel registration of Multichannel Systems (Germany). Electrical stimulation consisted of bi-phasic pulses of ±800 mV voltage and 260 μs duration. It involved low-frequency control stimulation to evoke and evaluate the network responses and high-frequency tetanic stimulation to induce synaptic plasticity. Control stimulation was applied to four electrodes synchronously in the adjacent four microchannels and consisted of 60 stimuli with a 3-second interval between stimuli. Tetanic stimulation was introduced in the same way as control stimulation. The protocol consisted of 20 trains of 10 stimuli with a 50-ms interval between pulses and a 5-second interval between the trains.

3. Results and Conclusions

Axons of cells from the source chamber grew into the implant chamber at a distance of 400-600 μm by the third day *in vitro* (DIV 3). These axons formed the basis for directed synaptic connections with the implanted cells. Axons of cells from the target chamber grew only 200 μm into the wide section of the microchannels by the DIV 3. The length of the microchannels between the source and the implant chambers was 400 μm, that did not allow cell dendrites from the source chamber to grow into the implant chamber. It was done to reduce the effect of the integrated cells on cells in the source chamber. At 4-6 DIV, a small part of axon branches of cells from the source chamber grew into the middle section of microchannels between the implant chamber and the target chamber, where they met the processes from the target chamber. A weak unidirectional connection could be formed between the source and the target cultures before new cells were transplanted into the implant chamber.

On the 31 day after 'implantation' 19% of spontaneous bursts propagated from the Source to the Implant with mean delay 29 ms, 22% of bursts propagated from the Implant to the Target with mean delay 25 ms. On the 27th day after cell integration, low-frequency electrical stimulation of the electrodes in the source chamber caused synaptically mediated responses in the implant chamber and the target chamber with a 50% probability. Preliminary results showed that high-frequency stimulation resulted in a change of spike rate in the target chamber and in the implant chamber in response to test low-frequency stimuli in the microchannels between the source and the implant chambers.

We modified a previously developed experimental 3 chamber chip to fit standard 60 electrodes MEA in order to study spiking activity changes after integration of cells into weakly coupled and isolated neural networks. We showed that new cells formed a synaptic connectivity in a form of 'bridge' to transfer spontaneous and stimulus evoked spikes. Moreover, the connections can be changed by high-frequency electrical stimulation which induces synaptic plasticity.

Acknowledgments

This research was supported by Russian Science Foundation (project №19-75-00095).

References

[1] Chen Y, Harn H and Chiou T 2018 *Cell Transplantation* **27**(3) 407–422

[2] Shrirao AB, Kung FH, Omelchenko A, Schloss R, Boustany N, Zahn J, Yarmush M and Firestein B 2018 *Biotechnol Bioeng* **115**(4) 815–830
[3] Shimba K, Chang CH, Asahina T, Moriya F, Kotani K, Jimbo Y, Gladkov A, Antipova O, Yana Pigareva, Kolpakov V, Mukhina I, Kazantsev V and Pimashkin A 2019 *Front. Neurosci.* **13** 890
[4] Antipova O, Pigareva Y, Kolpakov V, Gladkov A, Bukatin A, Mukhina I, Kazantsev V and Pimashkin A 2018 *Journal of Physics: Conf. Series* **1124** 031022

Studying of the supramolecularly ordered layered structure of chitosan gel films

A.A.Konduktorova, V.A.Kurochkina, T.S.Babicheva, S.L.Shmakov, and A.B.Shipovskaya

Educational and Research Institute of Nanostructures and Biosystems, Saratov State University 83 Astrakhanskaya St., Saratov 410012, Russian Federation

e-mail: konduktorova.anastasiya@gmail.com

Abstract. Structural and morphological features of chitosan gel films with a radial periodic structure, obtained by neutralizing the polymer's salt form with sodium hydroxide or triethanolamine, were visualized by scanning electron microscopy. It was found that the formation of such supramolecularly ordered layered structures obeyed diffusion kinetics and the regularities of Liesegang periodic precipitation. The revealed dependence of the morphostructure of chitosan gel films on the nature of the neutralizing reagent used is due to differences in the diffusion rates of the inorganic and organic substance, as well as some spatio-temporal features of the mass transfer process.

1. Introduction

Currently, an urgent solution to the problem of the short duration of a drug substance in the biological environment, the uncontrolled release of a biologically active compound in the human body is the use of systems with targeted drug delivery to the desired localization zone [1]. At the same time, the targeted prolonged drug release from a polymer system makes it possible to effectively carry out therapy, simultaneously eliminating the negative effect of the drug on the gastrointestinal tract and other side effects. To solve this problem, systems (capsules, plates and films) with a multilayered structure are designed, for studying of which the methods of electron microscopy are promising. Knowledge of the physicochemical laws of mass transfer during the formation of supramolecularly ordered structures will make it possible to control the process of layered ordering and obtain materials with desired properties. In our recent work [2], multilayered chitosan-containing gel films promising for targeted drug delivery were obtained. The method for their preparation is based on the interphase reaction of polymer-analogous transformation chitosan salt → base. Strong alkali (NaOH) was used as a neutralizing reagent. However, to increase the variety of layered structures and, at the same time, increase the environmental friendliness of the process of their preparation, it is advisable to use an organic alkaline reagent (e..g. triethanolamine). In this work, we performed a comparative analysis of the morphostructure of chitosan gel films obtained with both an organic and inorganic base.

2. Experimental methods

Gel films obtained from chitosan solutions in glycolic acid were selected as the objects of our study. NaOH and triethanolamine were compared as neutralizing agents. The effect of the neutralizing agent nature on the morphostructure of the samples was evaluated by scanning electron microscopy on a MIRA \\ LMU microscope at a voltage of 15 kV and a conducting current of 400 pkA. The sample

was prepared as follows: a glass mold with removable rims was filled with a chitosan solution, a NaOH or triethanolamine solution was applied to the center until the salt groups were completely neutralized, the gel film sample was then removed from the mold, washed with distilled water until neutral pH, and dried in air. Before microscopic studies, a 5 nm thick layer of gold was deposited on each sample using a K450X Carbon Coater.

3. Results

The obtained chitosan-containing gel films are formed as supramolecularly ordered radial periodic structures with bulky annular zones. Our study of the longitudinal section of such a gel film showed that the formation of annular zones occurred not only on the surface, but throughout the entire volume of the sample. An increase in the initial polymer concentration increases the number of annular zones, but insignificantly affects the width of the rings with a common serial number. With distance from the boundary of the onset of the reaction to the periphery, the width of the rings increases. For both reagents, the formation of the chitosan base layer obeys diffusion kinetics and the regularities of Liesegang periodic precipitation [3-6]. The formation of rhythmic structures (n^{th} rings or bands at a distance X_n from the reaction onset boundary) was observed when diffusion processes lagged behind the precipitation process and obeyed the relationship $X_n \sim \sqrt{t_n}$, where t_n is the formation time of the n^{th} zone. The width ΔX_n of the supramolecular formations with X_n obeys a geometric progression with a denominator close to unity and increases with increasing n, and the ratio of the positions of any neighboring zones remains constant: $X_{n+1}/X_n = const$.

Features in the supramolecular morphology of our gel film interface were revealed depending on the neutralizing reagent nature. The use of triethanolamine in the preparation of gel films from a chitosan solution with a concentration of 4 wt% leads to a significant increase in the number of radial periodic structures. This may be due to an increase in the time of the polymer-analogous reaction chitosan salt → base.

Thus, the use of triethanolamine made it possible to obtain chitosan-containing gel films with a supramolecularly ordered radial periodic structure, containing a large array of concentric zones in comparison with NaOH. It is possible that the discovered effect will significantly expand the physicochemical and engineering capabilities of designing systems with targeted drug delivery.

References

[1] Sarode A., Annapragada A., Guo J. 2020. Biomaterials. **242**, 119929.

[2] Babicheva T.S., Konduktorova A.A., Shmakov S.L., Shipovskaya A.B. 2020 J. Phys. Chem. **124** *41* 9255–9266.

[3] Rajurkar N., Ambekar, B. 2015. J. of Molec. Liquids. **204**, 205–209.

[4] Molnaīr Jr F., Izsaīkbc F., Lagzi I. 2008. Phys. Chem. Chem. Phys. **10**, 2368–2373.

[5] Droz M. 2000. Journal of Statistical Physics. **101**, *1–2*, 509–519.

[6] George J., Varghese G. 2002. Colloid and Polymer Science., **280**, *12*, 1131–1136.

Time-resolved polarized fluorescence decay in FAD in water-methanol solutions

M K Krasnopevtceva[1], M E Sasin[1], I A Gorbunova[1], D P Golishev[1], V P Belik[1] and O S Vasyutinskii[1]
[1]Ioffe Institute, 26 Polytechnicheskaya, St. Petersburg, Russia

e-mail: marina.krasnopevtceva@gmail.com

Abstract: Anisotropies, lifetimes, and rotational diffusion times of FAD in water-methanol solutions of various methanol concentrations (0%, 20%, 40%, 60% and 80% MeOH) have been determined from experiment through analysis of the polarized fluorescence decay. The fluorescence excitation by picosecond laser pulses at 355 nm and 450 nm was used. The fluorescence decay parameters determined within each of the excitation channels have been analyzed.

Introduction

Flavine adenine dinucleotide (FAD) in its oxidized (FAD^+) and reduced ($FADH_2$) forms is an intracellular coenzyme involved in redox reactions in living cells. As known, FAD in the oxidized form fluoresces under excitation and does not fluoresce in the reduced form. This important feature allows to use FAD as a fluorescent probe for studying biochemical processes in living cells [1]. Detailed investigation of fluorescence decay dynamics of FAD in various solutions and the analysis of the fluorescence polarization allows to determine local solution viscosity and polarity [2] and to obtain important information on the molecular excited state dynamics and on the rotational mobility of molecules in various microenvironments [3]. Recently, time resolved fluorescence spectroscopy of FAD has demonstrated high potential as a method of cell diagnostics [4].

In this paper anisotropies, lifetimes, and rotational diffusion times of FAD in water-methanol solutions of various methanol concentrations (0%, 20%, 40%, 60% and 80% MeOH) have been determined from experiment through analysis of the polarized fluorescence decay. The fluorescence excitation by picosecond laser pulses at 355 nm and 450 nm was used for excitation within two lowest FAD absorption bands [2]. The fluorescence decay parameters determined within each of the excitation channels have been analyzed.

Experimental arrangement

A quartz cuvette (10x10 mm, 3.5 mL) containing FAD solution (FAD disodium salt at 98% purity) at the concentration of 60 μM was irradiated by a pulsed picosecond laser. Two laser sources were used in experiment: a semiconductor laser with output at 450 nm, a pulse duration of 30 ps, repetition rate of 2 MHz, and energy of 23 pJ/pulse and a Nd:YAG microchip laser with output at 355 nm, pulse duration of 400 ps, repetition rate of 4 KHz, and energy of 1.5 μJ/pulse. The fluorescence was detected at the right angle to the laser beam and focused on the entrance slit of a monochromator MDR-12. In all experiments the fluorescence was detected at 530 nm, close to the fluorescence intensity maximum of FAD in all solutions used. The experimental setup used was similar to that described in our

previous studies. Obtained experimental data were processed using the global fit procedure implemented in Python3 as described in our previous publications [6, 7].

Results

Tables 1 and 2 present the fluorescence decay times τ_1 and τ_2, weighting coefficients ratio a_1/a_2, fluorescence anisotropy r_0, and rotational diffusion time τ_{rot} determined from experiment as a function of MeOH concentration. In aqueous solution all fluorescence parameters in Table 2 are in good agreement within the experimental error bars with those reported earlier by Sengupta et al [3]. All the other data was obtained for the first time.

Conc.,	τ_1, ns	τ_2, ns	a_1/a_2	τ_{rot}, ps	r_0
0	4.46±0.12	2.17±0.11	0.44±0.05	149±28	0.24±0.02
20	4.08±0.09	2.30±0.06	0.64±0.08	238±44	0.23±0.03
40	3.94±0.17	2.19±0.16	1.57±0.41	295±50	0.23±0.01
60	4.00±0.13	2.22±0.19	2.30±0.33	329±32	0.21±0.02
80	4.05±0.08	2.22±0.07	2.17±0.17	251±33	0.24±0.02

Table 1. Fluorescence Decay Parameters under excitation at 355 nm

Conc.,	τ_1, ns	τ_2, ns	a_1/a_2	τ_{rot}, ps	r_0
0	4.52±0.21	2.40±0.12	0.43±0.06	260±10	0.33±0.01
20	4.36±0.12	2.69±0.07	0.43±0.07	308±14	0.37±0.01
40	4.46±0.06	3.03±0.05	0.44±0.03	369±14	0.36±0.01
60	4.50±0.08	3.20±0.05	0.55±0.05	403±17	0.35±0.01
80	4.58±0.15	3.23±0.10	0.59±0.05	366±11	0.34±0.01

Table 2. Fluorescence Decay Parameters under excitation at 450 nm

Acknowledgments

Financial support from Russian Foundation for Basic Research under the grant #18-53-34001 is gratefully acknowledged.

References

[1] Galbán, J., Sanz-Vicente, I., Navarro, J., de Marcos, S. (2016). The Intrinsic Fluorescence of FAD and its Application in Analytical Chemistry: a Review. *Methods Appl. Fluoresc.,* 4(4), 042005.

[2] Nakabayashi, T., Md. Islam, S., Ohta, N. (2010). Fluorescence Decay Dynamics of Flavin Adenine Dinucleotide in a Mixture of Alcohol and Water in the Femtosecond and Nanosecond Time Range. *J. Phys. Chem. B*, 114(46), 15254–15260.

[3] Sengupta, A., Khade, R.V., Hazra, P. (2011). pH Dependent Dynamic Behavior of Flavine Mononucleotide (FMN) and Flavine Adenine Dinucleotide (FAD) in Femtosecond to Nanosecond Timescale. *J. Photochem. Photobiol. A*., 221(1), 105–112.

[4] Chorvat, D., Chorvatova, A. (2006). Spectrally Resolved Time-Correlated Single Photon Counting: a Novel Approach for Characterization of Endogenous Fluorescence in Isolated Cardiac Myocytes. *Eur. Biophys. J.* 36(1), 73–83.

[5] Sasin M. E., Smolin A. G., Gericke K.-H., Tokunaga E., and Vasyutinskii O.S. (2018). Fluorescence anisotropy in indole under two-photon excitation in the spectral range 385–510 nm. *PCCP*, 20(30), 19922-19931.

[6] Krasnopevtseva M.K, Belik V.P., Semenova I.V., Smolin A.G., Bogdanov A.A. and Vasyutinskii O.S. (2020). Decay Times and Anisotropy in Polarized Fluorescence of Flavin Adenine Dinucleotide Determined with Subnanosecond Resolution. *Tech. Phys. Lett.*, 46(6), 614-616.

Application of an automated complex resistance and phase difference measuring method for rheographic studies in the diagnosis of human cardiovascular system diseases

A I Levin , E A Pecherskaya, Yu A Varenik, V V Antipenko, O A Timokhina

Department of Information and measuring equipment and metrology, Penza State University, Penza 440026, Russia

levin.alescha2013@yandex.ru

Abstract. The structure of an automated system for measuring the complex resistance of the human body and the phase difference is proposed. It is used in the rheographic method for diagnosing human cardiovascular system diseases using a multilevel microcontroller structure. The metrological analysis of the automated system made it possible to achieve an increase in the measurement accuracy both by reducing the methodological and instrumental components of measurement errors. The relative basic measurement error does not exceed ± 0.5%.

1. Introduction

Currently, a number of methods and instruments are known for non-invasive measurement of the parameters of the cardiovascular system (CVS). One of these methods is rheography. This method allows to measure the following parameters: blood volume (OS) for the registered areas; cardiac contractile function (SPS), determined by the amplitude of the systolic wave on the thoracic differential rheogram; stroke volume of the heart (VOS); a reduction in heart rate (HR), which is determined by processing rheograms (beats per minute); minute blood volume (MCV); index of blood volume or blood volume (TC) of the region and several dozen CCC parameters. Such an informative method of medical research confirms the relevance of creating rheographic automated information and measuring systems with high reliability of measurements.

2. The structure of the rheographic information and measuring system

The authors proposed the structure of a rheographic information-measuring system, which is based on measuring the complex resistance and phase difference with subsequent processing of the measurement results to study the parameters of the human cardiovascular system (Figure 1). The central node is the microcontroller, which controls the slave microcontrollers via the I^2C interface [1]. Slave microcontrollers (of which there can be up to 127 units in the system) generate a digital signal of various frequencies, which is fed to a digital-to-analog converter (DAC), where it is converted into an analog signal of a given frequency and amplitude. The signal frequency can be adjusted by the user from 1 to 100 kHz. From sources and medical practice at the moment it is known that the rheography method works only at frequencies up to 100 kHz, since the reactive component of the complex impedance weakens at frequencies above 10 kHz, and already at frequencies above 100 kHz its effect has no effect [2]. The received analog signal is fed to the

stage of operational amplifiers (OA) and amplified through the electrodes passes through the human body, where at the receiving electrode the weakened signal is fed to the receiving amplifying stage OA. Then, the amplified signal passes through a low-pass filter (LPF) and enters the input of a digital-to-analog converter (DAC), from where the value of the difference between the input and output voltage of a signal of different frequencies is formed in the slave microcontroller registers. Data is transmitted over the I^2C interface to the master microcontroller from each slave microcontroller. The host microcontroller processes the received packets and transmits them via the USB interface to a computer (PC) for displaying the obtained values of the complex resistance and phase difference in the dialog menu.

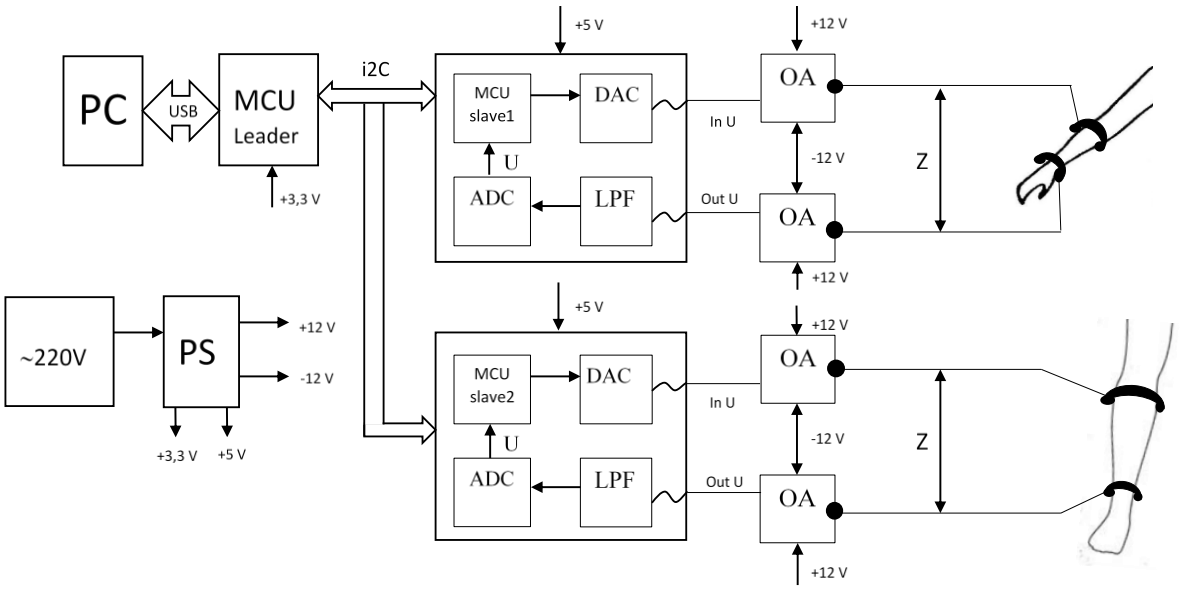

Figure 1 - The structure of the proposed rheographic IMS.

The use of several same types of measuring channels, the control of which is based on the I^2C data bus, makes it possible to provide a multichannel mode of simultaneous measurements in a miniature device [3-5].

3. Functioning of the measuring complex.

The control of the rheographic IMS and the processing of the measurement results are carried out according to the method, which is implemented in software using a computer (PC), master and slave microcontrollers[2, 6]. The master microcontroller contains a control program that controls the slave microcontrollers, sends control signals to each of them, and receives the obtained values. Then it transmits them to the PC, generates voltage signals with different frequencies to measure the complex impedance of a part of the human body. In this case, the microcontroller transmits the obtained results of the complex resistance calculation to the program dialog box on the computer. The slave microcontrollers generate voltage signals at different frequencies to measure the complex impedance and process the measured values of the voltage passing through the human body to calculate the complex resistance and phase difference. An integrated transducer of the spectral composition of the impedance operates in a wide frequency range based on a slave microcontroller, in which the active (R) and reactive (X) components of the impedance Z are calculated for each frequency, from which the impedance modulus is then calculated:

$$|Z| = \sqrt{R^2 + X^2}$$

and the phase is calculated:

$$\varphi = arctg\left(\frac{X}{R}\right),$$

and packets of the received data on the value of the complex resistance and the difference of the headlamp are formed for transmission to the master microcontroller.

4. Conclusion

The structure of an automated information-measuring system for measuring the complex resistance of the human body and the phase difference, which are used in the rheographic method for diagnosing human cardiovascular system diseases with a basic relative error of no more than ± 0.5%, is proposed. The obtained measurement results through subsequent calculations will allow modeling such parameters as the stroke volume of the heart, the amount of blood circulating through the vessels, etc. The measurement results can be displayed in graphical and tabular form, stored in a database for further research in dynamics. An increase in the measurement accuracy and reliability is also achieved by improving the hardware implementation and the method of multifrequency measurement of the conductivity of the human body with the subsequent calculation of the capacitive parasitic component of the measured signal.

References

[1] Tsai B, Birgersson E, Birgersson U 2018 Mechanistic multilayer model for non-invasive bioimpedance of intact skin *Journal of Electrical Bioimpedance* vol 9 pp 31-38

[2] Kawala A, Khoma V, Zmarły Y D, Sovyn Y 2008 Use of Wavelet Transform for Qualification of Rheograms Characteristic Points *Journal Plezegland Elektrotechniczy* vol 84 (3) pp 132-133

[3] Leonov S D, Obrazcov S A, Troickiy Y V 2011 A Bioimpedance Meter Measuring both Active and Reactive Components *Journal Biomedical Engineering* vol 45 (4) pp 128-131

[4] Malakhov A I, Tikhomirov A N, Shchukin S I, Kobelev I A, Kobelev AV, Belenkov Yu N, Shakaryants G A, Kozhevnikova M V, Kaplunova V Yu 2016 Electroimpedance Methods of Investigation of Cardiac Activity *Journal Cardiology* vol 56 (12), pp 33-39

[5] Podyacheva E , Zemlyanukhina T, Shadrin L, Baranova T 2020 Features of Hemodynamics of Pulmonary Circulation During the Diving Reflex *Journal Biological Communications* vol 65 (3) pp 244-251

[6] Righetti X, Thalmann D 2010 Proposition of modular I2C-Based wearable Architecture *15th IEEE Mediterranean Electrotechnical Conference "MELECON"* pp 802-805

Medical applications of porous silicon

E M Loginova[1], **D A Shishkina**[1]

[1]Department of Electronics and Instrument Engineering, Samara University, Samara 443086, Russia

Abstract. Porous silicon has good biocompatibility, which makes this material interesting for medical applications. One of the promising objects for the development of nanostructured systems is the delivery of porous silicon. The samples were obtained using electrochemical horizontal and vertical etching. The thickness was examined using a photomicroscope and spectra were taken using a spectrophotometer.

1. Introduction

Silicon is a component of all cells of the human body, its average daily consumption is about 20-50 mg. Depending on the degree of porosity, silicon particles can be biologically active, bioinert or biodegradable [1]. Mesoporous silicon in the human body is destroyed to monomeric silicic acids. Currently, the possibility of using porous silicon powders as materials for nanocontainers for transporting drugs is being actively studied. It is possible to regulate the rate of release of the drug and the rate of resorption of the container in the body by controlling the development of the surface and porosity [2]. Also of high interest is the absorption capacity of porous silicon, which allows it to be used for the treatment of cancer [3].

2. Experiment

Pretreatment of samples of silicon substrates was carried out in order to clean them from organic contaminants to ensure the uniformity of the etching process. For this, a solution of ammonium-ammonia peroxide was prepared in following proportions H_2O_2:NH_4OH:H_2O 1:1:4. Samples were immersed in a boiling solution for 7 minutes, then dipped in three waters.

Conducted vertical and horizontal electrochemical etching of the samples in a solution of water H_2O and concentrated hydrofluoric acid HF (1:1). Etched for 15 minutes with j=15 mA/m^2 and V=300 V. After etching, the samples were washed in distilled water and dried on filter paper.

3. Results

To evaluate the obtained nanostructures, some of the samples were examined with a NEOPHOT 21 photomicroscope. Pieces were cut off with a scalpel and their cleavage was examined to determine the thickness to tell if it corresponded to the average thickness of the nanostructured substrates. The thickness of the under study samples was about 3.7 microns.

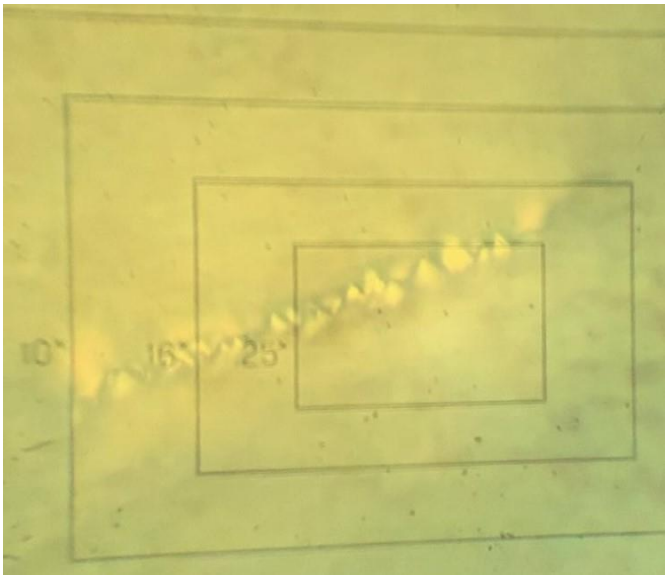

Figure 1. Image of the cleavage obtained with photomicroscope

The spectral characteristics of the reflection coefficient were studied using spectrophotometer ShimazuUV 2450.

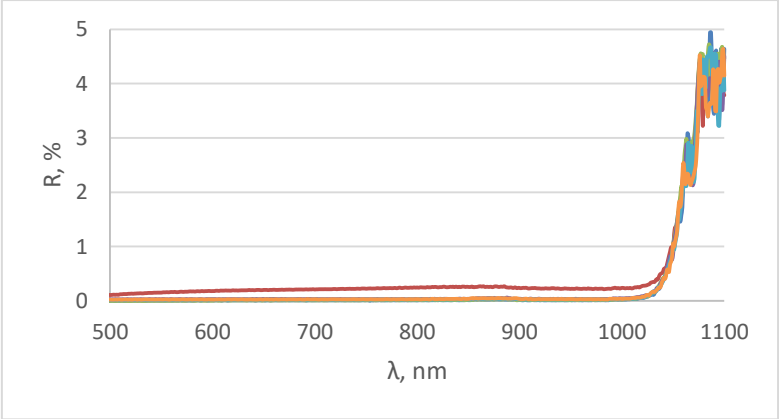

Figure 1. Reflection spectra of the obtained samples

The graph of the spectral characteristics of the reflection shows that the resulting structure has a low reflection index (less than 1%). This surface absorbs almost the entire visible and near-IR range, which makes these structures suitable for medical applications.

4. Conclusion

In the course of this work, samples of porous silicon were prepared using electrochemical etching and their absorption and reflection spectra were studied. In the future, it is planned to separate the porous layer from the substrate and fill it with drug, as well as to study the biodegradability of the samples.

References

[1] Canham L 2014 *Handbook of Porous Silicon* p 1017
[2] Anglin E J, Cheng L Y, Freeman W R and Sailor M J 2008 *Adv. Drug Delivery Rev.* **60** 1266-77
[3] Chen S *et al.* 2020 *Materials Today Adv.* **6** 100066

Application of the Kohonen neural network for monitoring tissue oxygen supply under hypoxic conditions

M S Mazing[1,2], A Y Zaitceva[1], R V Davydov[2]
[1]Institute for Analytical Instrumentation, Russian Academy of Sciences, 190103, St. Petersburg, Russia
[2]Peter the Great St.Petersburg Polytechnic University, Saint Petersburg 195251, Russia

Mazmari@mail.ru

Abstract. The article presents the results of using the Kohonen artificial neural network (KANN) in assessing the oxygen status of human tissues, as well as for studying the adaptive-compensatory response of the body to functional load. In the experiment, the registered digital oxygen images of the tissue of 31 subjects were distributed into three classes using the KANN. Each group is characterised by different resistance of the organism to hypoxia. The research results have shown the effectiveness of using an artificial neural network structure and the possibility of its implementation for recognising the functional state of a person.

1. Introduction

In the modern world, the global automation process has touched almost all spheres of human activity, including the medical industry. When monitoring biomedical indicators, doctors receive a large amount of data, which often requires automated processing. In addition to this, the task of developing devices for express diagnostics of the state of human health, as well as systems for supporting medical decisions, remains urgent. One of the possible options for solving this problem is the use of mathematical algorithms for cluster analysis and artificial neural networks [1]. Currently, most known diseases are directly or indirectly associated with oxygen deficiency in the body's organs and tissues. In this regard, the study of hypoxic conditions as well as the assessment of the oxygen supply of tissues, are of great importance in the therapy of critical conditions.

In this work we describe the application of an artificial neural network based on self-organising Kohonen maps (SOM) for analysis multidimensional data containing information about the oxygen status of human tissues with the purpose of projecting the data into a space of a lower dimension, identification the cluster structure and classification.

2. Method

A developed non-invasive optical diagnostic system based on a 6-channel analyser of optical spectra of the visible range was used to register oxygen digital images of human tissue [2]. The method is based on the ability of tissue chromophores (oxyhemoglobin and deoxyhemoglobin) to absorb diffusely scattered light of a certain wavelength. Each digital tissue oxygen image represents the readings of the sensors of a multichannel spectrum analyser recorded at different points in time during the functional load. Further, the obtained measurement results are analysed using the SOM. When working with a Kohonen network, unsupervised learning is used, which needs only input parameters.

3. Results

As a result of the study with the participation of 31 subjects, oxygen digital images of subjects obtained under functional load using a SOM were divided into 3 clusters. The result of grouping the nodes of the Kohonen map is shown in figure 1 (a). Also, the created cluster solution coincided with the result of clustering by the method of hierarchical complete-linkage clustering (figure 1 (b)), which indicates the statistical significance and stability of the cluster solution.

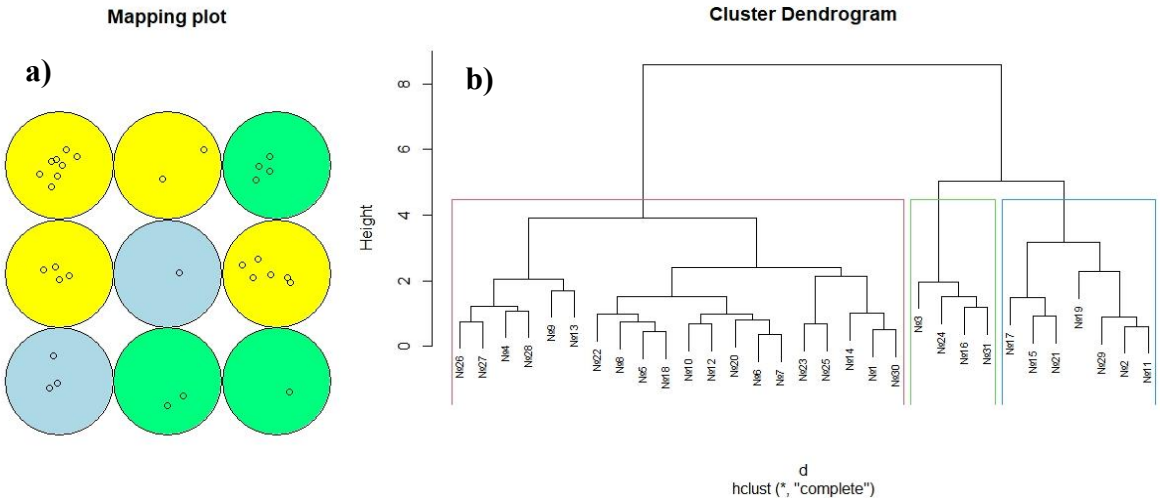

Figure 1. Cluster nodes of the Kohonen map with the distribution of subjects by nodes (a); the result of cluster analysis using the complete-linkage clustering with splitting the tree into three groups (b).

Cluster nodes are highlighted in different colours: yellow, green and blue. Each node contains a different number of objects (test subjects). Each cluster is characterised by both a different level of the body's resistance to hypoxia and a different general functional state of the subjects. The results are confirmed by independent biomedical research.

4. Conclusion

The proposed approach to assessing the oxygen status of human tissues and recognition of the general functional state of a person has shown prognostic ability. It can be used to create an intelligent information system for express diagnostics.

Acknowledgements

The study was carried out within the framework of State Assignment No. 075-01073-20-00 SU NIR 0074-2019-0010.

References

[1] Tuckova J 2013 *IEEE 11th International Workshop of Electronics, Control, Measurement, Signals and their application to Mechatronics* 1-6

[2] Mazing M, Zaitceva A and Kislyakov Y 2021 *International Youth Conference on Electronics, Telecommunications and Information Technologies* 233-239.

Influence of the nature of a polysaccharide on the surface-morphological and physical-mechanical properties of sol-gel plates

O N Malinkina, A B Shipovskaya

Department of High Molecular Compounds, Saratov State University, Saratov 410012, Russia

Olga-Malinkina@yandex.ru

Abstract. Thin-film sol-gel plates based on chitosan and glucomannan polysaccharides in a wide range of compositions were obtained. The effect of the polysaccharide component on the SEM surface morphology and physic-mechanical properties was evaluated. It was found that the introduction of the polysaccharide glucomannan into the composition of chitosan sol-gel plates increased the elastoplastic characteristics of the samples and had a significant effect on the surface relief of their solid phase.

1. Introduction

The use of biopolymers, e.g. natural polysaccharides, makes it possible to form photonic materials in the form of thin-film coatings and plates for use as selectively sensitive biosensors in functional nanomaterials [1]. In addition, the polysaccharide matrix contributes to the provision of an active biointerface of bionanocomposites with body tissues.

2. Results and discussion

In the present study, the effect of the nature of the polysaccharide (cationic chitosan or neutral glucomannan) on the surface-morphological and physic-mechanical properties of the sol-gel plates was studied. Silicon tetraglycerolate, a biologically active sol-gel precursor with the inorganic ≡Si–O–Si≡ network, was used to form thin-film structures [2–3]. Our studies have shown a significant effect of the polysaccharide's nature on the morphological and elastoplastic properties of the sol-gel plates. According to SEM, the resulting material belongs to nanocomposites, and glucomannan acts as a structure-forming component.

The obtained structures can be used for the design of bioadhesive sensor coatings with a high therapeutic effect, which is an urgent area for theranostics and regenerative medicine.

References

[1] Momtaz M and Chen J 2020 *ACS Appl. Mater. Interfaces* **12** 54104
[2] Shipovskaya A B, Zhuravleva Yu Yu, Tat'yana G K, Malinkina O N and Gegel N O 2019 *J. Sol-Gel Sci. Technol.* **92** 349
[3] Zhuravleva Yu Yu, Malinkina O N, Zudina I V and Shipovskaya A B 2020 *IOP Conf. Ser.: J. Phys.* **1695** 012099

Thermostability of lysozyme amyloid fibrils

N M Melnikova[1, 2], M I Sulatsky[3], Yu D Diordienko[1, 2] and A I Sulatskaya[1]

[1]Laboratory of Structural Dynamics, Stability and Folding of Proteins, Institute of Cytology, Russian Academy of Sciences, 4 Tikhoretsky avenue, 194064 Saint Petersburg, Russia
[2]Department of Molecular Biotechnology, State Institute of Technology, 26 Moskovsky avenue, 190013 Saint Petersburg, Russia
[3]Laboratory of Cell Morphology, Russian Academy of Sciences, 4 Tikhoretsky avenue, 194064 Saint Petersburg, Russia

Email: melnikova07nm@gmail.com

Abstract. Ordered protein aggregates, amyloid fibrils, are a marker of many serious diseases, such as Alzheimer's, Parkinson's, prion diseases, etc. At present, special attention is paid to the study of external influences that can affect the structure and stability of mature amyloid fibrils, which may be in demand in the development of approaches to the therapy of amyloidosis, as well as in the creation of new high-strength materials on the basis of these protein aggregates. An external factor, the influence of which on fibrils was studied in this work, was temperature denaturation. It was shown that heating amyloid fibrils to 60 °C does not lead to their degradation, but leads to a reversible increase in the intramolecular mobility of amyloid-forming proteins. At the same time, boiling of amyloids leads to their partial irreversible degradation, and amyloids forming larger clusters are more resistant to high temperatures. New data about the factors that increase the stability of amyloids can be applied in biotechnology for creating new high-strength nanomaterials on their basis.

1. Introduction

Highly ordered protein aggregates, amyloid fibrils are a marker of many serious diseases, such as Alzheimer's, Parkinson's, prion diseases, and others [1]. At the same time, physiological amyloid fibrils in bacteria, unicellular eukaryotes, fungi, plants, insects and mammals were found, which are necessary for the normal functioning of cells and tissues, which emphasizes the biological significance of amyloid formation [2, 3]. Due to the widespread occurrence of amyloid fibrils, as well as the variety of their functions (mechanical protection and modification of the cell surface; biotic or abiotic surface adhesion; internalization of cells; ensuring resistance to various external influences; biosynthesis of pigments, control of homeostasis, storage and the release of hormones, signal transduction, etc.), the study of amyloids is a very urgent task. The relevance of studying amyloid fibrils is also due to their unique mechanical properties, such as high strength and extensibility, which makes them an attractive object for the creation of new nanostructures and nanomaterials. The aim of this work was to analyze the resistance of amyloid fibrils to high temperatures. The object of the study was amyloid fibrils formed from the model globular protein lysozyme with different morphology.

2. Experimental techniques

Fibrillogenesis of lysozyme was carried out using two different protocols, making it possible to obtain aggregates with different morphologies [4]. According to one of the protocols, lysozyme was incubated in 20% acetic acid in the presence of 100 mM NaCl (pH 2) at 37 °C. According to the second protocol, the protein was incubated in 0.05 M KH_2PO_4-NaOH buffer in the presence of 3M GdnHCl (pH 7) at 57 °C. Both samples were incubated with constant stirring for 2 days. Then the fibrils were transferred to distilled water. The obtained amyloid fibrils was studied using absorption and fluorescence spectroscopy, the method of circular dichroism and electron microscopy. In addition, using a specially developed approach based on the samples preparation by equilibrium microdialysis [5], the interaction with amyloids of a specific fluorescent probe thioflavin T (ThT) was studied.

3. Results

According to electron microscopy data, amyloid fibrils obtained at pH 2 predominantly are thin fibers that practically do not interact with each other. At the same time, in the buffer solution with pH 7 fibrils with a significantly higher degree of clustering are formed. It was shown that heating lysozyme amyloid fibrils with different morphology up to 60 °C does not lead to their degradation. In this case, there is a reversible increase in the intramolecular mobility of amyloid-forming proteins and a decrease in the fluorescence intensity of the bound to fibrils fluorescent probe thioflavin T, which is due to the molecular rotar nature of the dye. It turned out that boiling lysozyme amyloid fibrils, obtained at pH 2, leads to partial degradation, as well as declusterization of not numerous fibrils clots into the separate thin filaments. The boiling of lysozyme amyloid fibrils obtained at pH 7 also leads to degradation of amyloid fibrils, which, however, manifests in a change in the secondary structure of amyloid-forming proteins, but practically does not lead to declusterization of fibrillar clots. Based on the obtained results, it was concluded that the degradation of lysozyme amyloid fibrils occurs at least 5 days after their boiling and is irreversible.

4. Conclusion

The heating lysozyme amyloid fibrils with different morphology up to 60 °C does not lead to their degradation, but causes a reversible increase in the intramolecular mobility of amyloid-forming proteins. At the same time, boiling of amyloids leads to their partial irreversible degradation, and amyloids with a higher initial degree of clustering are more resistant to high temperatures. New data about the factors that increase the stability of amyloids can be applied in biotechnology for creating new high-strength nanomaterials on their basis.

Acknowledgments

This work was supported by the Russian Science Foundation (project № 18-74-10100).

References

[1] Iadanza M G, Jackson M P, Hewitt E W, Ranson N A and Radford S E 2018 *Nat. Rev. Mol. Cell. Biol.* **19** 755-73
[2] Chiti F and Dobson C M 2006 *Annual Rev. Biochem.* **75** 333-66
[3] Fersht A 1998 *Structure and Mechanism in Protein Science: A Guide to Enzyme Catalysis and Protein Folding* vol 42, ed W H Freeman and Company (New York: W H Freeman) p 631
[4] Sulatskaya A I, Rodina N P, Povarova O I, Kuznetsova I M and Turoverov K K 2017 *Journ. Of Mol. Struct.***1140** 52-8
[5] Kuznetsova I M, Sulatskaya A I, Uversky V N and Turoverov K K 2012 *Mol. Neurobiol.* **45** 488-49

Study of pressure and finger actuated multilayer microfluidic devices, made by lithographic and 3d printed molds.

E I Naumov[1], **V V Grigorev**[1], **N A Filatov**[2], **A S Bukatin**[2]
[1]Peter the Great St. Petersburg Polytechnic University, St. Petersburg 195251, Russia
[2]Alferov Saint Petersburg National Research Academic University of the RAS, St. Petersburg 194021, Russia

Abstract. Microfluidic devices can manipulate fluids at a microscale level to conduct chemical reactions for point of care testing (POCT). In this study we investigated the operating principle and characteristics of finger and pressure actuated valves and pumps, integrated into microfluidic devices. The three-layered structure of the device allows to make user friendly microchip operating system.

1. Introduction

Point-of-care testing (POCT) is the concept of modern medicine where the medical tests necessary for illness treatment are taken and analysed directly near the patient to increase the speed of diagnostics and simplify its process. The simple examples are blood glucose monitors and pregnancy tests. Microfluidic microchips are the devices which can manipulate fluids at microscale and extract information from them. Such properties can be effectively applied in point of care testing. There are also recent advances in microfluidics for viral detection [1]. However, the most of such devices require a special qualification and technical skills to use them. Therefore, it is important to create devices, which can be operated with minimal qualification. They should have operating protocol with simple instructions to follow. A multi-layered pressure or finger actuated microchips has advantages suitable to overcome these challenges. The main working principle behind finger actuated microchips is using air pressure created by finger pushing the special button and creating and controlling liquid flows to perform necessary chemical reaction. As a result, such microchip has a user-friendly interface consisting of several simple buttons. There are operating devices which uses that principle to extract nucleic acids for Hepatitis B detection[2].

2. Experimental detail

In this study, we investigated the operating principle of microfluidic chips with finger actuated pumps and valves made from polydimethilsilixane (PDMS) by soft lithography using photolithographic and 3d printed molds. Two separate microchip designs were implemented to illustrate working of valves and pumps. Three valves on one chip were produced to investigate the pressure actuated fluid control with 30μm and 500μm thickness membrane and a system containing a pump, valves and a button was made to study the complex pressure actuated system. The process of silanization was used to generate a non-sticking membrane surface [3]. The samples fabricated with photolithography were able to control the liquid flow by closing and opening the valves using pressure. For 3d printing on a FormLab 2 SLA printer the width of microchannels was doubled due to the fabricating method characteristics [4].
After the printing, the mold was drown in isopropyl alcohol for 40 minutes, exposed to ultraviolet for 20 minutes and the cooled for 24 hours before fabrication of samples.

3. Results

We studied multi-layered finger actuated microfluidic microchips properties and fabrication methods. The devices were produced using photolithographic and 3d printed molds and tested with different membrane thickness. Opening and closing pressures, the speed and volume of passing liquids were measured. The devises produced with photolithography and 3d printing were also compared.

Acknowledgments

The work was supported by the Ministry of Education and Science of the Russian Federation (Project No 0791-2020-0006)

References

[1] Berkenbrock JA, Grecco-Machado R, Achenbach S 2020 *Proceedings of the Royal Society A,* **476.2243**, 20200398.

[2] Park J, Park JK 2019, *Lab on a Chip*, **19.18**, 2973-2977.

[3] Hu W 2021, *Advanced Materials Interfaces*, 2100038

[4] KaramZadeh V 2018, *Proceedings of the 5th International Conference of Fluid Flow, Heat and Mass Transfer,* **172**

Using of «bubble sensors» to control the quality of sequencing by the Illumina / Solexa method

Vladislav S. Reznik[1], Vladislav A. Kruglov[1], Shen' Ynudze[2], Van Din[3]

[1]Institute of Analytical Instrumentation of the Russian Academy of Sciences, St. Petersburg,
190103, Russia
[2]China University of Mining and Technology, Beijing 100029, China
3Xinjiang University, Urumqi, 720018, China

vlreznik97@gmail.com

Abstract. In the modern world, sequencing is an integral part of medicine, biology and other scientific fields. The Illimina / Solexa method is a new generation method and relates to methods of mass parallel sequencing. One of the features of using this method is the sequential pumping of various chemicals through the flow cell in which the reaction occurs. For uniformity and high quality of DNA sequencing, it is necessary that the amount of gas in liquids be minimized. Because many it can adversely affect both during chemical reactions and at the stage of recording reaction results. This article will examine the sequencing system using the Illumina\Solexa method using bubble sensors. An algorithm was developed that periodically receives information from bubble sensors in a microfluidic tube. The information received is processed and allows at certain stages to report deviations from the normal conditions for sequencing. The experimental results are presented.

1. Introduction

Currently, sequencing of the sequence of nucleotides that enter DNA and RNA has become a familiar and necessary phenomenon in various fields.

One of the widely used methods for carrying out this process is the use of the Illumina / Solexa method. The result of sequencing is data on the sequence of nucleotides that make up the sample. One of the important features of the implementation of this sequencing method is the use of an optical system during detection [1-3].

Illumina / Solexa sequencing uses many different chemicals. For ease of implementation, these reagents are placed in test tubes, and then through the flow channels enter the reaction cell.

In this connection, the problem of getting into the system of bubbles of gas dissolved in reagents arises. In addition, air can enter the system at the junction of the flow channel with the reaction cell.

The ingress of gas bubbles into the reaction cell at the stage of carrying out amplification can lead to a decrease in the number of clusters, which in turn will negatively affect the quality of further analysis [4].

On the other hand, the ingress of gas bubbles at the detection stage leads to a decrease in the total number of clusters in the field of view of the detection system [2, 4]. The used of other industrial devices for determining bubbles is excluded.

To solve this problem, it was proposed to use the so-called “bubble sensor”, which allows counting the number of gas bubbles passing through the reaction cell at all stages of sequencing.

2. Working process of bubble counting system

To count the number of bubbles, it is advisable to use an optical sensor as a sensitive element. This fact is justified primarily by the fact that flow tubes, due to their transparency, transmit light. The radiation intensity will be highly dependent on the medium. Accordingly, if a gas bubble passes through the flow channels, the value of the radiation intensity will change its value.

Therefore, it is necessary to use a combination of a radiation source and a photodetector. The obvious solution in this case will be the use of optocouplers.

To solve this problem, it was decided to use two optocouplers located perpendicular to each other. The block diagram of the total operation of the bubble detection system is shown in Figure 1.

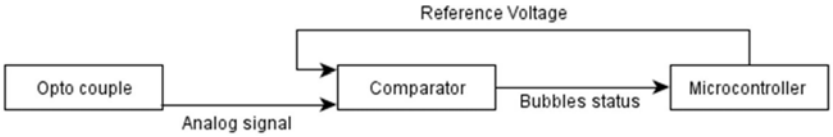

Figure 1. Block-diagram of signals in using of «bubble sensors»

The converted electrical signal is fed to the input of the comparator, the second input of which receives the reference signal. The level of this signal corresponds to the minimum level of radiation arising from the passage of a bubble. This signal is generated at the output of the digital-to-analog microcontroller converter. As a result of this, the level of this signal can be adjusted to different types of reagents and bubble sizes and is usually determined experimentally.

If the signal level from the optocoupler exceeds the value of the reference signal, a voltage is generated at the output of the comparator, which corresponds to the level of a logical unit, which in turn is interpreted by the microcontroller as the presence of a bubble.

Similarly, the processing of signals from the second optocoupler occurs.

3. Conclusion

Thus, the developed system for analyzing the number of gas bubbles passing through the reaction cell during mass parallel sequencing using the Illumina / Solexa method can significantly improve the quality of the output data of the analysis.

References

[1] Davydov, V.V., Myazin, N.S., Fadeenko, V.B., Logunov, S.E.: Formation of the Structure of NMR Signal from Condensed Medium in a Weak Magnetic Field. Technical Physics Letters 44(2), 153-156 (2018).

[2] Davydov, V.V., Myazin, N.S., Logunov, S.E., Fadeenko, V.B.: A Contactless Method for Testing Inner Walls of Pipelines. Russian Journal of Nondestructive Testing 54(3), 213-221 (2018).

[3] Myazin, N.S., Davydov, V.V., Yushkova, V.V., Rud, V.Yu.: On the possibility of recording absorption spectra in weak magnetic fields by the method of nuclear magnetic resonance. Journal of Physics: Conference Series1038(1), 012088 (2018).

[4] Davydov, R.V., Mazing, M.S., Yushkova, V.V., Stirmanov, A.V., Rud, V.Yu.; A new method for monitoring the health condition based on nondestructive signals of laser radiation absorption and scattering. Journal of Physics: Conference Series 1410(1), 012067 (2019).

Tunable modification of water-soluble semiconductor QDs for bioconjugation

B Ranishenka[1*], E Ulashchik[1], A Kruhlik[1], A Radchanka[2]

[1] Institute of Physical Organic Chemistry, National Academy of Sciences of Belarus, Minsk 220072, Belarus
[2] Research Institute for Physical Chemical Problems of the Belarusian State University, Leningradskaya str. 14, Minsk 220006, Belarus

*E-mail: ranishenka@gmail.com

Abstract. One-stage carbodiimide condensation procedure has been proposed for azide-functionalization of water-soluble semiconductor QDs. Controlled variation in surface functional group density and zeta-potential was demonstrated by functionalization of anionic (carboxylic) and analogous zwitter-ionic polymer-capped core-shell CdSe/ZnS QDs. QDs reactivity towards strain-promoted azide-alkyne cycloaddition (SPAAC) has been found to be nearly proportional to the relative surface azide groups density, and QDs zeta-potential correlates with the modifiers ratio. We demonstrated that QDs surface azido groups can be easily converted into primary amino groups under mild conditions using tris(2-carboxyethyl)phosphine (TCEP) as a reducing agent. Applicability of surface-functionalized QDs for bioconjugation was demonstrated by their conjugation with dye-labeled bovine serum albumin (BSA).

1. Introduction

Semiconductor QDs nanomaterial is promising for practical applications due to the unique optical properties (strong luminescence, high quantum yield, narrow photoluminescence (PL) band, high photostability and others). One of the most important steps for QDs application is their conjugation with biomolecules. QDs bioconjugation can be performed by several general approaches depending on QDs surface chemistry. Covalent bioconjugation via bioorthogonal chemical reactions is the most popular and perspective way [1,2]. On the other hand, polymer-encapsulated water-soluble QDs suitable for surface chemical modification have become widely commercially available during last decade. Carbodiimide condensation is a common way for conjugation of biomolecules. Widely used water soluble 1-Ethyl-3-(3-dimethylaminopropyl)carbodiimide (EDC) can lead to colloidal destabilization of negatively charged polymer-capped QDs because of its cationic nature [3]. We have demonstrated that fine tuning of the reaction conditions allowed EDC-mediated functionalization of carboxylic polymer-capped QDs without aggregation. Low stability of EDC and its intermediate in water makes SPAAC more popular for QDs bioconjugation through the last years [4,5]. Commonly used strained cycles like bicyclononyne (BCN) or dibenzocyclooctyne (DBCO) are hydrophobic and can potentially lower colloidal stability of the nanoparticles (NPs). Modification of QDs with azido groups, thus, is more preferable and allows potentially high functional group density due to small size and hydrophilicity. Functionalization of NPs can be performed at the stage of capping polymer

synthesis or QDs solubilization [7]. However, mentioned approaches are complex and expensive. On the other hand, carbodiimide condensation allows controlled introduction of desired functional groups and their combinations under homogeneous conditions. Due to difficulties in QDs functional group quantification a new approach based on QDs reactivity characterization was applied to demonstrate the capabilities of the method. Azido groups are known as widely used intermediate functionality for amino groups introduction. QDs surface azido groups reduction using sodium borohydride has been reported. In this report we have demonstrated azido groups reduction with TCEP on the QDs surface in aqueous solution followed by dye conjugation.

2. Materials and methods

Two types of QDs where used for the experiments: anionic (carboxylic) and zwitter-ionic ones. Both types have similar surface structure (fig. 1) with variable quantity of quaternary amino groups.

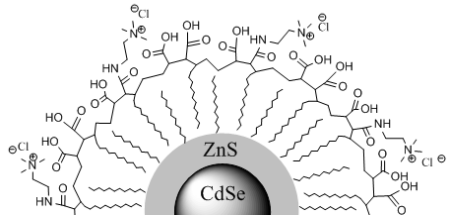

Figure 1. Surface structure of polymer-capped QDs (quaternary amines quantity is variable).

Ethanolamine-O-sulfate (EOS), aminotetraethylene glycol (H_2N-[TEG]-OH) and aminotetraethylene glycol azide (H_2N-[TEG]-N_3) were utilized as modifiers. Functionalization was investigated by studying the kinetics of organic dye JOE conjugation with QDs using SPAAC reaction and QDs zeta-potential measurements.

3. Results and discussion

Carbodiimide condensation using EDC under optimal reaction conditions is a covenient way for water-soluble polymer-encapsulated QDs functionalization. Functional groups surface density determines the QDs reactivity and can be controllably varied by adjusting the ratio of modifier amines. Surface zeta-potential is being changed during QDs functionalization and can be controllably tuned by using charged and uncharged amines and their combinations. QDs reactivity towards SPAAC has been found to be nearly proportional to the relative surface azide groups density, and QDs zeta-potential correlates with the modifiers ratio. Azido groups on the QDs surface can be redused by TCEP under mild conditions with sutisfactory yields. TCEP is not recommended for use as a reducing agent or a catalyst if the azido groups are present, its interaction with azides should be taken into account. Azido-functionalized QDs obtained by carbodiimide modification are capable for conjugation with proteins by SPAAC. Conjugation degree can be controlled by tuning the reagents concentrations. As QDs colloidal properties are mostly determined by the polymer coating and since polymer encapsulation was reported to be a general way for different NPs solubilization, the observations done are potentially applicable for other types of polymer-encapsulated NPs.

References

[1] Hildebrandt N, Spillmann C, Algar W, Pons T, Stewart M, Oh E, Kimihiro S, Díaz S, Delehanty J, Medintz I 2017 *Chem. Rev.* **117** 536
[2] Banerjee A, Pons T, Lequeux N, Dubertret B 2016 *Interface Focus* **6** 1
[3] Snee P T 2018 *Acc. Chem. Res.* **51** 2949
[4] Zhang H, Feng G, Guo Y, Zhou D 2013 *Nanoscale* **5** 10307
[5] Zavoiura O, Resch-Genger U, Seitz O 2018 *Bioconjugate Chem.* **29** 1690
[6] Schieber C, Bestetti A, Lim J P, Ryan A, Nguyen T-L, Eldridge R, White A, Gleeson P, Donnelly P, Williams S, Mulvaney 2012 *Angew. Chem. Int. Ed.* **51** 1

Vinyl group content as a tool to govern the properties of modified hyaluronic acid for scaffold fabrication via photoinduced crosslinking

A.V. Sochilina[1,2,*], A.G. Savelyev[2,3], V.P. Zubov[1], E.V. Khaydukov[1,2,3], A.N. Generalova[1]

[1] Shemyakin-Ovchinnikov Institute of bioorganic chemistry RAS, Moscow 117197, Russia

[2] Federal Scientific Research Centre 'Crystallography and Photonics' RAS, Moscow 119333, Russia

[3] I.M. Sechenov First Moscow State Medical University, Moscow, 119991, Russia

*Corresponding author, e-mail: ddraig@yandex.ru

Abstract. In this work, parameters of modification reaction of hyaluronic acid with glycidyl methacrylate were studied. The degree of substitution by vinyl groups in hyaluronic acid is considered as a tool to guide the physical-chemical properties of scaffolds based on modified hyaluronic acid. These scaffolds were fabricated exploiting 3D-printing attributed with the laser photocuring.

1. Introduction

Tissue engineering is an upcoming research field focused on development of biological substitutes that are able to support and reconstruct damaged or missing tissues and organs. Production of biological substitutes requires formation of 3-dimensional structures (scaffolds) based on special biomaterials. In order to be used in tissue engineering, biomaterials must meet certain requirements: biocompatibility, biodegradability, promotion of cell adhesion, optimal porosity and mechanical properties similar to substituted tissue.

Development of biomaterials that meet all the aforementioned requirements is a crucial task of tissue engineering. One of the most attractive materials is natural polysaccharide hyaluronic acid (HA). HA is *a priori* biocompatible and biodegradable due to endogenous origin but lacks mechanical stability due to water solubility. Photoinduced crosslinking is the most desirable way to improve physical-chemical properties of HA as it gives access to production of water-insoluble scaffolds with tunable properties by different methods using lasers *e.g.*, extrusion 3D-printing, micromolding and *in vivo* photocuring. Modification of HA with reagents containing vinyl groups, such as glycidyl methacrylate (GMA), is necessary to enable photoinduced crosslinking. Degree of substitution (DS) of polysaccharide backbone with GMA residues is a characteristic that significantly affects properties of modified HA and scaffolds based on it. Thus, it is particular of interest to assess the relationships between the DS and conditions of the modification reaction, as well as the use of DS variation to tune the physical-chemical properties of scaffolds based on modified HA.

2. Methods

Modification of HA was carried out as conjugation reaction of GMA with carboxyl and hydroxyl moieties of HA (0.5 wt%) in aqueous-organic solution (water:dimethylformamide = 64:41). DS was measured using quantitative method based on colorimetric reaction of potassium permanganate with vinyl groups reported in our previous work [1]. The product, HA modified with GMA (HA-GMA), can be crosslinked under the laser irradiation (450 nm) in the presence of endogenous photoinitiator flavin mononucleotide. Compositions for photocuring were prepared by dissolving 20 wt% of HA-GMA and 0.001 wt% of flavin mononucleotide in deionized water similar to [2]. Crosslinked hydrogels for properties evaluation were made using special silicone mold. Scaffolds were formed using extrusion 3D-printing equipment.

3. Results

3.1 DS dependence on the reaction parameters

The study of different reaction parameters demonstrated that initial conditions: neutral pH (6.4), 18 ml of GMA per 1 g of HA at 25°C for 4 days, made it possible to obtain DS 40%. Alkaline pH (12) decreased DS to 21% whereas acidic pH (4,5) did not significantly change DS. DS gradually increased with time: 15% at 1st day, 20% at 2nd day, 32% at 3rd day and 39-40% at 4th day. Temperature rising from 25°C to 40°C led to the DS increase to 64%. Increase of GMA concentration expectedly enabled the DS changing from 27% at 6 ml of GMA per 1 g of HA to 40% at 18 ml of GMA per 1 g of HA. Following increase did not significantly affect DS.

3.2 The effect of DS on physical-chemical properties of scaffolds

We found that increase in DS from 0% to 64% induced sharp viscosity drop in both HA-GMA solutions (0.5 wt%) and photocurable compositions with flattening of the curve above 35-40% DS. Compositions based on HA-GMA with 35-40% DS possessed optimal viscosity for extrusion methods, while higher DS may be more beneficial for micromolding. The same regularity was observed for degree of enzymatic degradation of hydrogels in hyaluronidase solution. Note the compression modulus of hydrogels raised from 0.5 to 2 MPa with increasing DS.

4. Conclusions

In this work, we demonstrated the influence of different reaction parameters on DS in HA-GMA and showed how to tune the diverse properties of hydrogels based on HA-GMA employing DS. This data is essential for rational design of scaffolds, selection of appropriate scaffold production methods and further research of this biomaterial.

Acknowledgments

The reported study was funded by RFBR, project number 19-33-90285.

References

[1] Sochilina A V, Savelyev A G, Demina P A, Sizova S V, Zubov V P, Khaydukov E V, Generalova A N 2019 *Meas. Sci. Technol.* **30** 075102.

[2] Savelyev A G, Sochilina A V, Akasov R A, Mironov A V, Semchishen V A, Generalova A N, Khaydukov E V, Popov V K 2018 *Sovrem. Tehnol. Med.* **10** 88

Femtosecond laser synthesis and comparative analysis of fluorescent carbon dots from L-lysine aqueous solution.

A A Astafiev[1], A M Shakhov[1], A A Gulin[1], A A Vasin[1], M V Gubina[1], M S Syrchina[1] and V A Nadtochenko[1]

[1]N.N. Semenov Federal Research Center of Chemical Physics, Russian Academy of Sciences, Kosygina 4, Moscow, Russia

Abstract. Laser synthesis of fluorescent species from biomolecules in living cells and tissues offers unique capabilities for fluorescent bioimaging, yet little is known about its mechanisms and characteristics of products. We examine synthesis of fluorescent products from water solution of L-lysine upon irradiation by trains of femtosecond laser pulses with varying parameters. We demonstrate that irradiation products contain nanoscale carbon-bases fluorescent particles (carbon dots) with multi-colour and excitation-dependent emission. Morphology, chemical composition and fluorescent characteristics of irradiation products strongly depend on laser pulses parameters.

1. Introduction

Production of fluorescents species in living cells and tissues by femtosecond laser irradiation is a novel approach to fluorescent bioimaging which offers a unique advantage of non-invasive, rapid, highly-localized and targeted fluorescent labelling [1-2]. Exact mechanisms of laser synthesis and chemical nature of fluorescent products remain debatable [2-3] and their analysis is complicated by heterogeneity of cells and tissues and difficulty of isolating irradiation products. A possible role of synthesis of fluorescent carbon dots (CDs) in laser production of fluorescent species was highlighted recently [2,4].

In order to clarify synthesis mechanisms and characteristics of products we examined femtosecond laser production of fluorescent species from a model biological molecule. A common proteinogenic amino acid L-lysine, which is also highly effective as precursor for hydrothermal or microwave synthesis of CDs, was chosen as a model compound. In order to understand the role of various physico-chemical effects of nonlinear absorption and the influence of laser parameters the water solution of l-lysine was irradiated with femtosecond laser pulses in three different regimes: one corresponding to laser breakdown in aqueous media and two sub-breakdown regimes with different laser wavelength, and comparative analysis of irradiation products was performed.

2. Methods

2.1. Laser synthesis and isolation of products

Water solution of L-lysine (0.5 g/mL) in a quartz cuvette was irradiated with trains of femtosecond laser pulses focused by a spherical lens (f=8 mm, 0.5NA) in three regimes: 800 nm wavelength, 1 kHz repetition rate, 50 fs pulse duration, 1.4 mJ pulse energy (sample 1); 20 h irradiation time; 740 nm, 80 MHz, 50 fs, 20 nJ, 70h (sample 2); 370 nm, 80 MHz, 100 fs, 4 nJ, 70h (sample 3). After irradiation samples were dialyzed for 72 hours in 2,000 MWCO dialysis units.

2.2. Samples characterization

Absorption of photoluminescence spectra of samples 1-3 in water were recorded with Shimadzu spectrophotometer (UV-3600) and spectrofluorometer (RF-5031 PC). Luminescence quantum yield (356 nm excitation) was estimated with the slope method using ethanol solution of anthracene as a standard. Samples diluted in ethanol and dried on a cover slip were analyzed with an atomic-force microscopy unit (SMENA-B, NT MDT). Mass spectroscopy analysis of dried samples in positive and negative ions was performed with TOF.SIMS 5 mass spectrometer (ION-TOF). Elemental analysis with energy-dispersive X-ray spectroscopy was performed using a Prisma-E electron microscope (Thermo-Fisher).

3. Results

All samples exhibited absorption in the UV region attributed to $\pi \rightarrow \pi^*$ and $n \rightarrow \pi^*$ electronic transitions and multiple and excitation-dependent photoluminescence (Fig.1). Sample 1 had the strongest visible emission and the highest quantum yield of blue luminescence (~0.06). Irradiation products included nanoscale luminescent particles (CDs), their size and content was the largest in the sample 1. Mass-spectra measurements demonstrate that laser irradiation resulted in decreased signal from lysine molecular ions ($C_6H_{15}N_2O_2^+$) as well as NH^-, CO_2^-, NH_4^+ functional groups ions, whereas a strong signal from CN^- and CNO^- ions appeared. Clear difference between chemical composition of the samples 1-3 was revealed by principal component analysis of mass spectrometry data, the sample 1 had also a higher content of carbon according to the elemental analysis. Chemical characterization suggests that laser irradiation results in polymerization of lysine molecules via peptide bond and formation of polymer nanoparticles incorporating luminescent chromophores, and further irradiation can induce carbonization of nanoparticles. Our findings demonstrate that luminescent CDs can be effectively produced by femtosecond laser irradiation from amino acids in cells and tissues and their characteristics can be tailored by laser parameters.

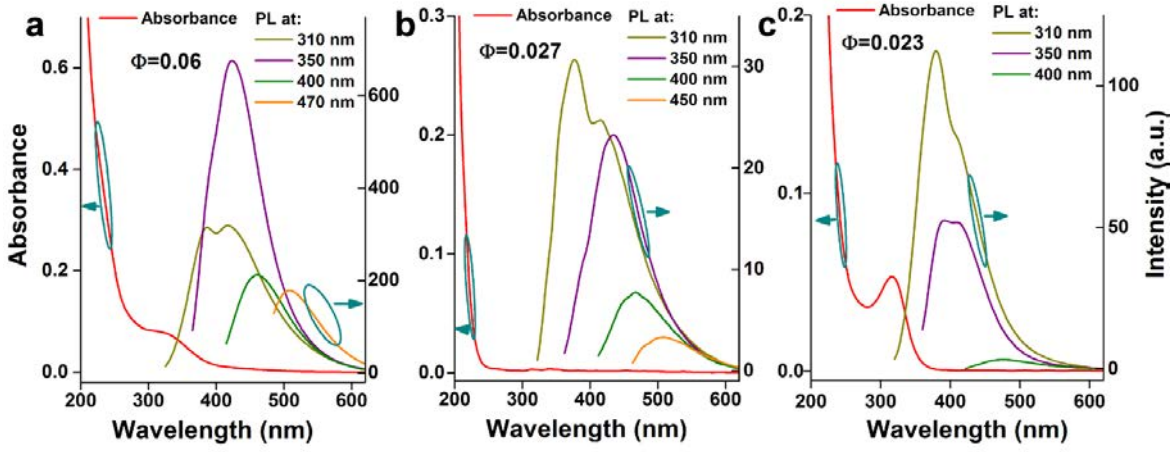

Figure 1. Absorbance and photoluminescence (PL) spectra of samples 1 (a), 2 (b) and 3 (c) in water.

Acknowledgments

The work has financial support from the Russian Scientific Foundation grant No.21-72-20169. The work was performed on facilities of ACBS Center of the Collective Equipment (no. 506694, FRCCP RAS).

References

[1] Sun Q, Qin Z, Wu W, Lin Y, Chen C, He S, Li X, Wu Z, Luo Y and Qu J 2018 *Biomed. Opt. Express* **9** 581-90

[2] Astafiev A A, Shakhov A M, Osychenko A A, Syrchina M S, Karmenyan A V, Tochilo U A and Nadtochenko V A 2020 *ACS OMEGA* **5** 21 12527-38

[3] Qin Z, Sun Q, Lin Y, He S, Li X, Chen C, Wu W, Luo Y and Qu J 2018 *Biomed. Opt. Express* **9** 3373-3390

[4] Astafiev A A, Shakhov A M, Kritchenkov A S, Khrustalev V. N. Shepel D V, Nadtochenko V A and Tskhovrebov A. G 2021 *Dyes and Pigments* **188** 109176

Computational modeling of schedule-specific chemotherapy outcomes in mouse tumor models

I.N. Terterov, V. A. Chubenko, N.A. Knyazev, V.V. Klimenko, A.A. Bogdanov, V.M. Moiseyenko, A.A. Bogdanov

Saint-Petersburg Clinical Scientific and Practical Center of Specialized Types of Medical Care (Oncological), Leningradskaya str, 68A., Pesochny, St. Petersburg 197758, Russia

ivan.terterov@gmail.com

Abstract. Despite the rapid development of new innovative strategies in cancer treatment like immunotherapy, chemotherapy still remains a common choice in many cases. Standard protocols of chemotherapeutic administration rely on a maximal tolerated dose paradigm, however there is a growing evidence that this approach is not always optimal. Alternative scheduling, like metronomic - low dose continuous drug administration - were recently proved their efficacy. The space of available variants of drug administration protocols is prohibitively large to be explored empirically, and there is an urgent need of predictive mathematical models for rational chemotherapeutic scheduling design. In this work we tested the ability of the pharmacokinetic-pharmacodynamics model to describe schedule-specific tumor volume time evolution in different mouse tumor models.

1. Purpose

In the standard maximal tolerated dose (MTD) protocol, chemotherapeutics are administered in high doses with the aim to affect the maximal number of cancer cells, however in some cases this does not lead to tumor eradication and the drug-resistance emerges. Alternative approaches were recently proposed, like metronomic chemotherapy (MC), which consists in low dose continuous drug administration [1]. MC is characterized with lower side effects while demonstrating promising efficacy. Tumor growth deceleration during MC therapy is attributed to anti-angiogenic, immunostimulation and cytostatic effects, which all take a minor role compared to direct toxicity in high dose MTD [1,2]. This diversity of biological mechanisms involved complicates the rational design of the optimal chemotherapeutic administration protocol in MC.

To date several predictive computational models were developed to assist schedule optimization of MC protocol, because the huge number of possible variants makes empirical search impractical. Many of these rely on pharmacokinetic-pharmacodynamics (PK/PD) modeling approach, which computationally links drug concentration in the body with its therapeutic action [2,3]. Such models were successfully applied in some cases [2,3], however they often contain a large number of adjustable parameters, and uncertainties in their estimation limits the model performance. Previously we

developed the PK/PD Minimal model that is defined by a small set of parameters, which is sufficient to capture schedule-specific outcomes. In this work we test transferability of the Minimal model results between data for mice bearing different tumor types.

2. Methods

The Minimal model comprises only three adjustable parameters and describes anti-tumor action of a chemotherapeutic drug with two major terms - direct cytotoxicity and anti-angiogenic effect. Previously we have shown that this model is able to efficiently describe tumor volume evolution in mouse tumors during MTD and MC applications of gemcitabine - a well known chemotherapeutic that is effective in MC setting [4]. In this work we compare the Minimal model descriptive and predictive power on the data from various gemcitabine therapy scheduling in two different tumor types, namly Earlich ascites carcinoma model in SHR mice and the model of colon cancer - CT26 in Balb/C mice.

3. Results and discussion

The model successfully describes mean tumor volume evolution in animal groups treated with MTD and MC gemcitabine for both mouse tumor models. While the same set of parameters is capable of describing data from both MTD and MC groups, data from the group treated with combined therapy (MTD+MC) was described only partially. The transition region observed in this group during the course of the therapy was not captured well in case of data from both mouse tumor models. The Minimal model parameters from fit to data for Earlich carcinoma and CT26 models differ slightly. This may be explained by the different forms of tumor evolution curve in the control groups observed for these two mouse tumor models. To further improve transferability of the Minimal model parameters for the same drug applied in treatment of different tumor types, detailed investigation of relations between unperturbed tumor growth kinetics and the response to application of chemotherapeutics is needed.

References

[1] Pasquier, E., Kavallaris, M., & Andre, N. Metronomic chemotherapy: new rationale for new directions. Nat. Rev. Clin. Oncol. 7(8), 455 (2010).

[2] Benzekry, S., Pasquier, E., Barbolosi, D., Lacarelle, B., Barlesi, F., Andre, N., Ciccolini, J. Metronomic reloaded: Theoretical models bringing chemotherapy into the era of precision medicine. Semin. Cancer Biol. 35, 53-61 (2015).

[3] Barbolosi, D., Ciccolini, J., Lacarelle, B., Barlési, F., Andre, N. Computational oncology—mathematical modelling of drug regimens for precision medicine. Nat. Rev. Clin. Oncol., 13(4), 242. (2016).

[4] Cham, K., Baker, J., Takhar, K., Flexman, J., Wong, M., Owen, D., Yung, A., Kozlowski, P., Reinsberg, S., Chu, E., et al.: Metronomic gemcitabine suppresses tumour growth, improves perfusion, and reduces hypoxia in human pancreatic ductal adenocarcinoma. Br. J. Cancer 103(1), 52–60 (2010).

Investigation of the polymerization rate of hydrogel microparticles in microfluidic device

A A Tushkevich[1,2], N A Filatov[1], A S Bukatin[1]

[1] Alferov Saint Petersburg National Research Academic University of the RAS, St. Petersburg 194021, Russia
[2] Peter the Great St. Petersburg Polytechnic University, St. Petersburg 195251, Russia

andre.tushkevich@gmail.com

Abstract. Fabrication of colloids and granules prepared from a suspension that undergoes polymerization requires many conditions for obtaining. One of them is the production of monodisperse emulsions, which can be achieved using droplet microfluidics. But the choice of optimal polymerization parameters is still remaining an open question. In this research we investigate the method of defining degree of polymerization based on emulsion flow dynamics, which can be used for the optimization of the parameters and choice of microfluidic chip's geometry.

1. Introduction

Monodisperse emulsions are a promising tool for creation of a variety of artificial materials. They are used for the production of polymer microparticles with complex internal structure such as Janus particles [1], which can find numerous applications in sensors, device displays and biological analyzers. Core-shell technology, the production of multilayers emulsion or double-emulsion droplets, may be used for making containers for target drug delivery [2]. One of the relatively new applications of monodisperse particles is bioprinting technologies, in which they are used as cell-based bioinks for scaffold-free printing and cell-encapsulating materials to construct cell-laden scaffolds [3]. These technologies are sensitive to emulsion characteristics and require their high monodispersity. Droplet microfluidics is a technology that allows the production of the monodispersed "water-in-oil" droplets in a highly efficient, controllable, and scalable manner. After the polymerization step such droplets transform into monodispersed microparticles. The successful production of such particles with acceptable characteristics in microfluidics device depends on full control of the degree of the polymerization during the process.

2. Experiment

In this work we investigated how flow dynamics of monodispersed emulsion was changing during the polymerization of the polyacrylamide gel inside the droplets. To make this study we used a microfluidic chip with a flow-focusing droplet generator and lengthened outlet channel that was created using standard soft lithography technique from PDMS Sylgard 184 (Dow Corning) [4]. The basic principle of generation's run is that supplied from the side channels continuous phase meets dispersed phase at the channels crossing, where the dispersed phase is compressed by the continuous

phase and separate into droplets [5]. Obtaining certain macroemulsion droplets size can be achieved by modifying the flow rates of the liquids. In this study we used droplets 45 - 55 μm in diameter. Experiments were conducted for two polymers: acrylamide and PEGDA. The continuous phase for the PEGDA particles consists of Mineral light oil (cat. N. 330779 SigmaAldrich) with 3.5% ABIL EM 180 surfactant (Evonik Industries). For the acrylamide continuous phase, we had all the same ingredients with added tetramethylethylenediamine, a polymerization catalyst, at a concentration of 1%. As a dispersed phase used to form PEGDA particles, we took a solution of Sigma-Aldrich 455008 PEGDA with the concentration 50%, to which Sigma-Aldrich 410896 Igracure 2959 photoinitiator with a concentration of 1% was added. Acrylamide dispersed phase consisted a water solution of acrylamide/bis-acrylamide (Bio-Rad) taken in concentration 30% with addition of ammonium peroxydisulfate (Bio-Rad) polymerization initiator (a concentration 0.3%). The polymerization for PEGDA particles appeared due to the influence of UV radiation from LED at a wavelength of 365 nm. The chip was also heated to a temperature of 45 °C in order to catalyze acrylamide polymerization process. For supplying continuous and dispersed phases into the microfluidic chip we used a custom pressure controller based on ITV001 electro-pneumatic regulators (SMC, Japan). The chip was set on an optical microscope Leica DM4000 B LED (Leica Microsystems) and after the generator stabilization, the droplets movement was recorded using a speed camera (USB 3.1 Gen1 cameras with Sony CMOS - xiC) at 100 fps on every section of channel with 1,8 mm gap. Python 3.9 with including libraries was used for data processing, which included recognition and tracking of droplets with defining of each droplet velocity.

During the experiments we observed changing of the velocity profile of moving droplets in a microfluidic channel after the droplet generator. This was because of the gel polymerization, which occurred while the droplets moved in the outlet channel. Such changes were quantitatively analyzed and could be explained by differences in hydrodynamic interactions between solid particles and liquid droplets with each other. These changes can be used as a marker of the polymerization degree and allowed us to calculate the duration of this process.

Acknowledgments

This work was financially supported by the Russian Science Foundation (project №20-74-10117).

References

[1] Nie Z, Li W, Seo M, Xu S, Kumacheva E. *Janus and ternary particles generated by microfluidic synthesis: Design, synthesis, and self-assembly* G. J Am Chem Soc. 2006;128(29):9408–12

[2] Choi A, Seo KD, Kim DW, Kim BC, Kim DS. *Recent advances in engineering microparticles and their nascent utilization in biomedical delivery and diagnostic applications*. Lab Chip,. 2017;17(4):591–613

[3] Guvendiren M. 2019 *3D Bioprinting in Medicine Murat* Guvendiren © Springer Nature Switzerland AG 2019 vol 1

[4] Bukatin AS, Mukhin IS, Malyshev EI, Kukhtevich I V., Evstrapov AA, Dubina M V. *Fabrication of high-aspect-ratio microstructures in polymer microfluid chips for in vitro single-cell analysis*. Tech Phys. 2016;61(10):1566–71

[5] Kukhtevich I V, Posmitnaya Y S, Belousov K I, Bukatin A S, Evstrapov A A 2015 *NAUCHNOE PRIBOROSTROENIE* Vol 25 No 3 pp 65–85

Synthesis of Calcium Carbonate Particles with Different Geometries

L.I. Fatkhutdinova[1], H. Bahrom[2], A.A. Goncharenko[3], O. Peltek[1], A. Muslimov[4,5], A. Manchev[2], I. Shishkin[1], R.E. Noskov[2], A. S. Timin[3,6], P. Ginzburg[2], M.V. Zyuzin[1]

[1] ITMO University, Saint Petersburg, Russian Federation
[2] Tel-Aviv University, Tel-Aviv, Israel
[3] Peter the Great St. Petersburg Polytechnic University, Saint Petersburg, Russian Federation
[4] St. Petersburg Academic University, Saint Petersburg, Russian Federation
[5] I.P. Pavlov State Medical University, Saint Petersburg, Russian Federation
[6] National Research Tomsk Polytechnic University, Tomsk, Russian Federation

E-mail: landysh.fatkhutdinova@gmail.com

Abstract. Nano- and microparticles are extensively used in different fields of science. In modern pharmacology and nanomedicine, nanoparticles can be applied for drug delivery due to their unique physicochemical properties. Particles of nano- and micrometric sizes with required properties such as biocompatibility, non-toxicity and high loading capacity are of great interest and can be utilized as carriers of bioactive compounds.[1] Porous calcium carbonate ($CaCO_3$) particles require all above mentioned properties and are widely used due to their simple and low-cost synthesis, biocompatibility, and bioavailability.[2] Here, we study the formation of $CaCO_3$ particles, as well as the possibility of using them for biomedical applications.[3]

1. Formation of calcium carbonate particles

The formation of $CaCO_3$ particles occurred in precipitation reaction of calcium chloride and sodium carbonate. The conditions of the formation of three existing polymorphic phases of $CaCO_3$ (calcite, vaterite, aragonite) were investigated. To obtain different geometries (spheroids, ellipsoids, toroids) of $CaCO_3$ particles, ratios of salts and organic additives in co-precipitation reaction were varied. The loading capacity and the internalization efficiency of the obtained particles was tested on the model of C6 glioma cells. Schematic illustration of the synthesis of $CaCO_3$ particles with different geometries is depicted in figure 1.

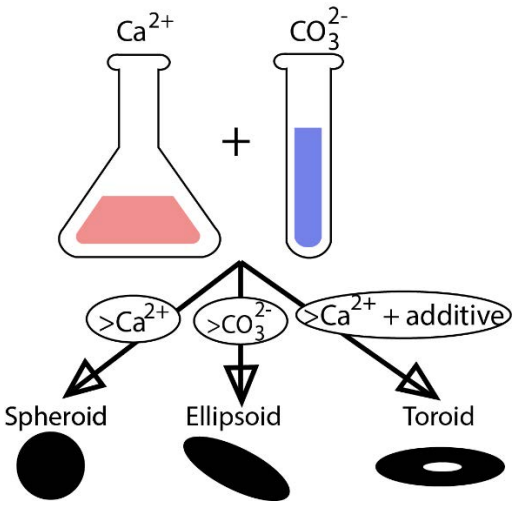

Figure 1. Schematic illustration of synthesis of $CaCO_3$ particles with different geometries.

2. Results and discussion

According to the obtained data, it was found that the polymorphic modification of $CaCO_3$ depends on the concentration of salts used for the synthesis. Also, all samples demonstrated good biocompatibility and non-toxicity. In particular, toroidal $CaCO_3$ particles showed the highest loading capacity of bioactive molecules, whereas the ellipsoidal particles demonstrated the highest internalization rate into C6 glioma cells. Therefore, nano- and micrometric $CaCO_3$ particles of different geometries can be considered as good candidates for the delivery bioactive compounds into cells.

Acknowledgments

This work was supported by Russian Science Foundation, Grant N 19-75-00039 (MVZ).

References

[1] K. Kantner, J. Rejman, K. Kraft, M. G. Soliman, M. V. Zyuzin, A. Escudero, P. del Pino, W. J. Parak. Laterally and Temporally Controlled Intracellular Staining by Light-Triggered Release of Encapsulated Fluorescent Markers, Chem. Eur. J. 24 (9), 2098–2102 (2018).

[2] B. Parakhonskiy, M. V. Zyuzin, A. Yashchenok, S. Carregal-Romero, J. Rejman, H. Möhwald, W. J. Parak, A. G. Skirtach. The Influence of the Size and Aspect Ratio of Anisotropic, Porous CaCO3 Particles on Their Uptake by Cells, J Nanobiotechnol. 13 (1), 53 (2015).

[3] H. Bahrom, A. A. Goncharenko, L. I. Fatkhutdinova, O. O. Peltek, A. R. Muslimov, O. Y. Koval, I. E. Eliseev, A. Manchev, D. Gorin, I. I. Shishkin, R. E. Noskov, A. S. Timin, P. Ginzburg, M. V. Zyuzin. Controllable Synthesis of Calcium Carbonate with Different Geometry: Comprehensive Analysis of Particle Formation, Cellular Uptake, and Biocompatibility, ACS Sustainable Chem. Eng. 7(23), 19142-19156 (2019).

Analysis of the limiting behavior of a biological neurons system with delay

E G Fedorov[1], I Yu Popov[1]

[1] Faculty of Control Systems and Robotics, ITMO University, St. Petersburg, 197101, Russia

fedevg95@gmail.com

Abstract. In this work an analytical and numerical analysis of the limiting behaviors of a system consisting of a pair of biological neurons was carried out. In this case connection between neurons will occur with a delay. As a neuron model, the FitzHugh-Nagumo model was chosen as a model that can reproduce many dynamic behaviors of a real neuron and, at the same time, is not very complex computationally.

1. Introduction

For different neurons and in different external conditions, the time for impulse transmission can differ significantly. In this case the behavior of the entire network as a whole can significantly depend on the strength of the connection and the delay time during the transmission of the impulse. These parameters correspond to the properties of the synapse and the speed of excitation propagation along the axon (see, e.g., [1]). By identifying dynamic behavior and controlling the dynamic behavior of the network, it is possible to identify and predict unwanted behaviors, as well as to restore the normal rhythms of the network's functioning.

To describe a biological neuron, one of the most complete models at the moment is the Hodgkin-Huxley model [2]. Later many other models were proposed to simplify the Hodgkin-Huxley model. One of these models was the FitzHugh-Nagumo model [3, 4], which retains the basic types of neuron behavior, but is much simpler from a computational point of view. In this work this model is used to describe a neuron and an analysis of possible types of behavior of a network of two connected neurons is carried out, depending on the main parameters of the model.

2. Model description

We will consider two neurons connected to each other through a sigmoidal connection (independent of the potential of the postsynaptic neuron) with a delay. Each neuron is described by the FitzHugh-Nagumo model. Then we can write down the final model of the considered system of neurons [5]:

$$\begin{cases} \dot{u}_1 = -a\,u_1 + (a+1)\,u_1^2 - u_1^3 - v_1 + c\tanh(u_2^\tau) \\ \dot{v}_1 = b\,u_1 - \gamma\,v_1 \\ \dot{u}_2 = -a\,u_2 + (a+1)\,u_2^2 - u_2^3 - v_2 + c\tanh(u_1^\tau)' \\ \dot{v}_2 = b\,u_2 - \gamma\,v_2 \end{cases}$$

where $i = 1,2$, functions $u_i = u_i(t)$ and $v_i = v_i(t)$ describe the state of the corresponding neuron at time t, a, b, γ are positive parameters, $u_i^\tau = u_i(t - \tau)$, c -- a positive parameter that corresponds to

the strength of the connection between neurons, τ -- time delay in the transmission of an impulse between two neurons.

3. Analytical results

Equilibrium points are analyzed for the described system. As a result, the number (from 1 to 9) of equilibrium points was determined depending on the parameter values. Also stability areas are determined for the found equilibrium points.

Further, the analysis of local bifurcations in the system is carried out. As a result, many transitions were found from stable equilibrium points to stable periodic synchronous and asynchronous oscillations.

4. Numerical result

All analytical results are confirmed numerically. The global bifurcations in the system are also numerically researched. As a result, for this system of a pair of neurons without external influences, such areas of parameter values have been found for which global stability, periodic oscillations, multistability, simultaneous synchronous and asynchronous stable oscillations, and chaotic oscillations are observed in the system.

5. Conclusion

A model of a pair of neurons was built based on the FitzHugh-Nagumo model. Analytical and numerical studies have been carried out for this model. This made it possible to identify the main types of dynamic behavior, as well as criteria for determining the types.

The main controllable parameters in such systems are the strength of the connection and the transmission rate of the impulse or the delay in transmission between neurons. Thus, based on the results obtained, undesirable behaviors in the system can be diagnosed, and then, by influencing the strength of the connection and the delay in transmission, the system can be brought to the desired state.

Acknowledgments

The reported study was funded by RFBR, project number 20-31-90036

References

[1] Fedorov E G, Popov A I and Popov I Y 2019 Metric graph version of the FitzHugh-Nagumo model *Nanosystems: Physics, Chemistry, Mathematics* **10** (6) pp 623–626

[2] Hodgkin A L and Huxley A F 1952 A quantitative description of membrane current and its application to conduction and excitation in nerve *The Journal of physiology* **117** (4) pp 500-544

[3] FitzHugh R 1961 Impulses and physiological states in theoretical models of nerve membrane *Biophysical journal* **1** (6) pp 445-466

[4] Nagumo J, Arimoto S and Yoshizawa S 1962 An active pulse transmission line simulating nerve axon *Proceedings of the IRE* **50** (10) pp 2061-2070

[5] Burić N, Grozdanović I and Vasović N 2005 Type I vs. type II excitable systems with delayed coupling *Chaos, Solitons & Fractals* **23** (4) pp 1221-1233

A split flavin binding fluorescent reporter to detect protein-protein interactions

A N Yudenko, A Smolentseva, I Maslov, O Semenov, I Kaiumov, A A Remeeva, and I Gushchin

Research Center for Molecular Mechanisms of Aging and Age-Related Diseases, Moscow Institute of Physics and Technology, Dolgoprudny 141701, Russia

yudenkoan@gmail.com

Abstract. Fluorescent proteins are important instruments for modern biological microscopy. One promising class of fluorescent reporters is flavin-binding fluorescent proteins (FbFPs). This class is derived from Light Oxygen Voltage (LOV) domains. We developed split-CagFbFP, a bimolecular fluorescence complementation system for detection of protein-protein interaction and for subsequent development of molecular sensors.

1. Introduction

Recently, we described FbFP from thermophilic bacteria *Chloroflexus aggregans* [1]. CagFbFP has one of the shortest amino acid sequences among LOV-domains described to date. A remarkable feature of this protein is stability in a wide range of pH and concentrations of solvent components such as NaCl or denaturants such as urea. High solubility and stability, due to the rigid structure, are good preconditions for engineering a bimolecular fluorescence complementation reporter from CagFbFP. The reporter can be used to detect protein-protein interactions.

2. Result and discussion

2.1. Rational design of split protein variants

To find the most favorable split sites, we performed bioinformatic analysis of the variability of loop lengths in the known LOV domains. To do this, we performed multiple sequence alignment of currently known amino acid sequences of the LOV domains (>6000) [2]. The analysis showed the most variation in the length of the three loops. We also analyzed the available atomic structures of LOV-domains. 3D alignment also showed the most difference in the thee loops. The three identified locations were used to split this fluorescent protein [3].

2.2. Application of Split-CagFbFP

2.2.1 Application of Split-CagFbFP in Bacteria and Mammalian cells

As protein-protein interaction model, we used a couple of antiparallel short zippers (NZ and CZ) [4]. N- and C-terminal parts of CagFbFP were fused to NZ and CZ, respectively, and cloned into different vectors. We expressed three pairs of polypeptides in bacteria: LOV48−58-NZ and CZ-LOV59-153, LOV48−91-NZ and CZ-LOV92-153, LOV48−137-NZ and CZ-LOV138-153. As negative control to model lack of interaction we made constructions without NZ.

All variants showed a fluorescent signal, while the negative control samples had a signal comparable to autofluorescence. We have also shown that split-CagFbFP can be used in mammalian cells. We transfected human-derived neuroblastoma cells SH-SY5Y with pairs of the genetic constructs. These constructs made it possible to visualize protein-protein interactions in the mitochondria of transfected cells.

2.2.2 Split-CagFbFP- based Calcium Sensor

Recently, an improved new generation calcium sensor FGCaMP7 was developed by Barykina *et al.* [5]. This sensor uses the ability of calmodulin to bind to the M13 peptide in the presence of calcium. We fused the CagFbFP parts to calmodulin and the M13 peptide to generate FbFP-based calcium sensor. We expressed the constructs in bacteria and observed calcium-dependent fluorescence changes.

Acknowledgements

The study was supported by the Russian Foundation for Basic Research (project No 18- 34-00742).

References

[1] Nazarenko, V. V., Remeeva, A., Yudenko, A., Kovalev, K., Dubenko, A., Goncharov, I. M., ...& Gushchin, I. 2019 A thermostable flavin-based fluorescent protein from Chloroflexus aggregans: a framework for ultra-high resolution structural studies. *Photochemical & photobiological sciences*, **18** (7), 1793-1805.

[2] Glantz, S. T., Carpenter, E. J., Melkonian, M., Gardner, K. H., Boyden, E. S., Wong, G. K.-S., and Chow, B. Y. 2016 Functional and Topological Diversity of LOV Domain Photoreceptors. *Proc. Natl. Acad. Sci. U. S. A.* **113** (11), E1442–E1451

[3] Yudenko, A., Smolentseva, A., Maslov, I., Semenov, O., Goncharov, I. M., Nazarenko, V. V., ... & Gushchin, I. 2021. Rational Design of a Split Flavin-Based Fluorescent Reporter. *ACS Synthetic Biology* **10** (1), 72–83

[4] Ghosh, I., Hamilton, A. D., and Regan, L. 2000 Antiparallel Leucine Zipper-Directed Protein Reassembly: Application to the Green Fluorescent Protein. *J. Am. Chem. Soc.* **122** (23), 5658–5659

[5] Barykina, N. V., Sotskov, V. P., Gruzdeva, A. M., Wu, Y. K., Portugues, R., Subach, O. M., ... & Subach, F. V. 2020 FGCaMP7, an Improved Version of Fungi-Based Ratiometric Calcium Indicator for In Vivo Visualization of Neuronal Activity. *International journal of molecular sciences*, **21** (8), 3012.

Comparison of the effectiveness of blood transfusion and reinfusion

E V Pimakhina[1*], A A Pimakhin[1], N V Vishnykov[2], N M Tolkach[2], S B Arsentiev[3]

[1]Ryazan State Medical University, Ryazan, 390026, Russian Federation
[2]Ryazan State Radio Engineering University, Ryazan, 390005, Russian Federation
[3]Regional Clinical Hospital, Ryazan, 390039, Russian Federation

*E-Mail: elenapim@yandex.ru

Abstract. Studies by atomic force and scanning electron microscopy have shown that erythrocytes of foreign blood have morphological defects. The sequestration of foreign erythrocytes makes it difficult for the erythron to self-repair.The actual solution to this problem is the application of the blood reinfusion technique using the Cell Saver apparatus. Transfusion of autoerythra suspension, harvested using the Cell Saver apparatus during the operation, stabilizes red blood counts in the early post-transfusion period in patients and reduces the manifestation of massive hemotransfusion syndrome. Hardware reinfusion of erythrocytes is effective and safe for massive blood loss in obstetrics. Reinfusion dictates the need for parallel correction of all blood parameters. Application of the principles of patient blood management can reduce the transfusion load, improve the quality of medical care.

1. Introduction

Donor blood transfusion in obstetric practice is characterized by large volumes. Transfused erythrocytes, especially those of long shelf life, are rapidly destroyed in the recipient's bloodstream, which contributes to the development of postoperative anemia.

2. Experiment and methods

To explain the complications from the transfusion of large doses of donor erythrocytes, we studied the structure of normal and donor erythrocytes membranes using atomic force microscopy (AFM, surface topography and morphometry) with large scanning fields on the equipment of the Regional Center of Probe Microscopy of Collective Use of the Ryazan State Radio Engineering University named after V.F. Utkin at the probe laboratory "Ntegra-Aura" (NT-MDT SI, Russia). AFM processing was performed using built-in software. Various forms of erythrocytes have been analyzed.

Studies by atomic force microscopy showed that erythrocytes of foreign blood have morphological defects. Similar results are found in the works of other authors. [1] The sequestration of foreign erythrocytes makes it difficult for the erythron to self-repair. The actual solution to this problem is the application of the blood reinfusion technique using the Cell Saver apparatus.

Comparative analysis of the effectiveness of reinfusion in comparison with blood transfusion was carried out using the example of typical cases.

3. Results and discussion

Blood transfusion with the Cell Saver apparatus for blood loss of 2700 ml. Blood counts before transfusion: Hb = 54 g / l (liters), erythrocytes = 1.65 * 10^{12} /l, Ht = 14.9%, leukocytes = 16.0 * 10^{9} /l, thrombocytes = 70.6 * 10^{9} /l. Transfusion: FFP = 1780 ml, erythrocyte suspension = 870 ml. Blood parameters after transfusion: Hb = 84 g / l, erythrocytes = 2.7 * 10^{12} /l, Ht = 23.6%, leukocytes = 14.7 * 10^{9} /l. Blood parameters values for different groups are presented in table 1.

Table 1. Dynamics of blood parameters during blood transfusion.

Group	Before transfusion	Immediately after transfusion	18 hours after transfusion	24 hours after transfusion	34 hours after transfusion
Hemoglobin g/l	54	84	80	58	50
Erythrocytes 10^{12} /l	1.65	2.72	2.5	1.8	1.62
Leukocytes10^{9} /l	14.9	14.7	18.1	11.1	11
Thrombocytes10^{9} /l	70.6	90	86	62	63

Blood transfusion with blood loss 4000 ml. Blood parameters before transfusion: Hb = 39 g / l, erythrocytes = 1.3 * 10^{12} /l, Ht = 11.5%. Transfusion: FFP = 2980 ml, erythrocyte suspension = 1825 ml, reinfusion of washed erythrocytes using the Haemonetics Cell Saver-5 apparatus was 982 ml. Blood counts after transfusion: Hb = 186 g / l, erythrocytes = 5.2 * 10^{12} /l, Ht = 55.5%, leukocytes = 20.1 * 10^{9} /l, thrombocytes = 258 * 10^{9} /l. Blood parameters values for different groups are presented in table 2.

Table 2. Dynamics of blood parameters during reinfusion.

Group	Before reinfusion	Reinfusion	7 hours after reinfusion	10 hours after reinfusion	24 hours after reinfusion	34 hours after reinfusion
Hemoglobin g/l	39	186	95	84	74	71
Erythrocytes 10^{12} /l	1.3	5.2	3.2	2.8	2.53	2.18
Leukocytes 10^{9} /l	20.1	11.5	11.5	9.6	4.9	-
Thrombocytes 10^{9} /l	258	154	159	103	100	-

Reinfusion is characterized by a decrease in hemoglobin (by 9 g / l, 10 g / l and 3 g / l), smooth and slow, in contrast to the methods of introducing donor erythrocyte mass (by 22 g / l, 8 g / l). 72 hours after the transfusion of blood products, a significant decrease in hemoglobin, erythrocytes, leukocytes and thrombocytes was noted. However, with reinfusion, the decrease was smoother and did not reach the initial low values.

Reinfusion of donor erythrocytes is cost-effective as well. So 1 dose of fresh frozen plasma costs 18,752 rubles, 1 dose of erythromass - 15,337 rubles, 1 dose of autoerythrocytes corresponds to 2-3 doses of donor hermass.

Transfusion of autoerythra suspension, harvested using the Cell Saver apparatus, stabilizes red blood counts in the early post-transfusion period and reduces the manifestation of massive blood transfusion syndrome. Hardware reinfusion of erythrocytes is effective and safe for massive blood loss in obstetrics. Reinfusion dictates the need for parallel correction of all blood parameters. Application of the principles of patient blood management can reduce the transfusion load, improve the quality of medical care.

Acknowledgments

The work was performed on the equipment Regional center of probe microscopy collective use Ryazan State Radio Engineering University named after V.F. Utkin.

References

[1] Yang Yu *et al* 2013 *Journal of experimental and therapeutic medicine* **5** 1466-1470

Double slot aerosol jet printed antenna for X-band applications

P V Arsenov, A S Sobolev, A A Efimov and V V Ivanov

Moscow Institute of Physics and Technology (National Research University), Dolgoprudny 141701, Russia

arsenov@phystech.edu

Abstract. A double slot antenna for X-band applications was designed and aerosol jet printing technology was used to fabricate the prototype with silver nano-ink on a flexible polyimide substrate. We investigated the microwave losses of printed antennas in the range from 100 kHz to 27 GHz, obtained at sintering temperatures of 200 °C and 250 °C. Double slot X-band antennas have been calculated and measured, which have an operating bandwidth of 10% in the region of the central frequency of 10.5 GHz.

1. Introduction

The currently developing printed electronics is attractive not only for the low cost of printing and simplicity of prototyping, but also for the possibility of creating flexible electronic circuits and devices [1]. Among the existing printing methods, aerosol jet printing is the most promising technology, since it allows the formation of functional elements with a minimum lateral size of up to 10 microns on different types of substrates [2]. The aerosol jet printing method is in demand for various fields of application, including the manufacture of transistors, sensors, solar cells, microheaters, microwave structures and interconnections [3].

Flexible planar microwave structures are in demand for creating conformal low-profile antennas that can be placed on curved aerodynamic surfaces of ground vehicles and aircraft. Double slot antennas are based on high impedance transmission lines and, unlike other antenna types, have high antenna efficiency. Single flexible antennas can be combined into conformal antenna arrays that cover large surface areas and have a high combined gain. In this paper, we optimized the printing parameters of silver nano-ink on flexible polyimide substrates and formed several samples of the X-band double slot antennas. This range can be used not only for high-speed communication channels, but also for airborne radars and proximity sensors.

2. Experimental

A double slot antenna in the form of a silver film of a given geometry was fabricated by focused deposition of aerosol microdroplets from silver nano-ink onto a polyamide substrate by pneumatic method using an AJ 15XE aerosol jet printer (Neotech AMT GmbH). The film material in the experiments was a mixture of silver nano-ink PG-007 (Paru Co. Ltd.) based on solvents 1-methoxy-2-propanol (MOP) and ethylene glycol (EG) in a volume ratio of 3:1, respectively. A nozzle with an outlet diameter of 300 μm was used to form the antenna. The antenna was formed at the values of aerosol and sheath flow rates, and printing speed equal to 50 sccm, 80 sccm, and 500 mm/min,

respectively. After deposition, a silver film was sintered at temperatures of 200 °C and 250 °C for 60 min to form a conductive structure.

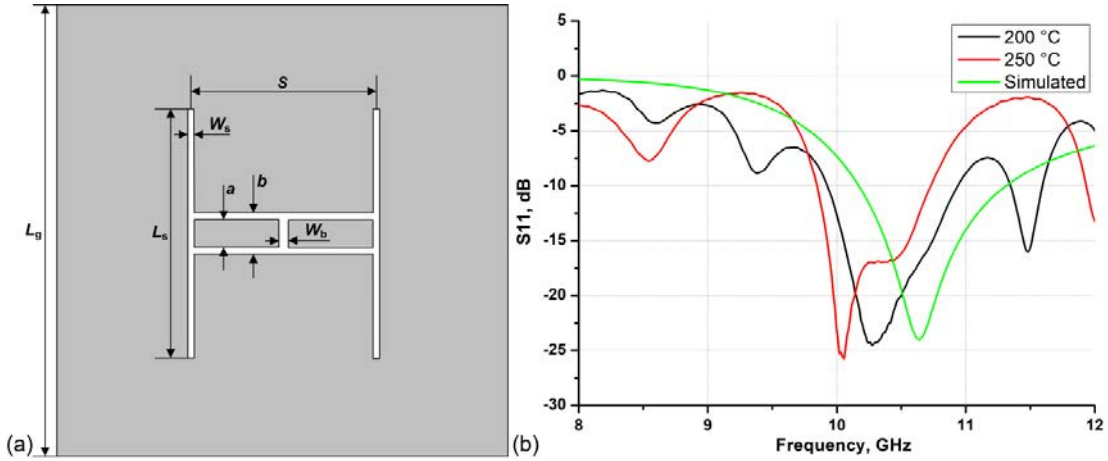

Figure 1. (a) The design of the double slot antenna (L_g = 20 mm, L_s = 11 mm, W_s = 0.1 mm, W_b = 0.4 mm, S = 8.4 mm, a = 1.2 mm, b = 1.8 mm) and **(b)** measured dependence of the return loss, S11-parameter, of the aerosol jet printed antennas.

The design of the double slot antenna is shown in Figure 1a. Antenna geometry is designed and optimized for 10.5 GHz using high frequency simulation software (HFSS). The antenna is designed on a flexible polyimide dielectric substrate 100 μm thick and dielectric constant 3.5. The antenna was a silver film 20x20 mm^2 in size and has thickness about 4 μm. Two narrow 0.1 mm holes in the form of rectangular slots were made in the silver film. Functionally, the antenna consisted of two magnetic dipoles formed by half-wave λ/2 resonators based on a slot line. The dipoles are also located at a distance of λ/2 and are interconnected by a coplanar line.

The vector analyzer (Keysight N5242A-200) was used to measure the return loss, S11-parameter, of antennas sintered at 200 °C and 250 °C, see Figure 1b. Also Figure 1b shows the results of an FDTD simulation of an antenna made of a Perfect electric conductor (PEC).

3. Conclusion

The agreement between the FDTD simulation and experiment is observed (see Figure 1b), taking into account the parasitic interaction of the antenna with the measuring cable. The measured bandwidth of the antennas is more than 1 GHz at a level of −10 dB, which corresponds to 10% of the center frequency. Thus, the possibility of forming antennas on flexible polymer substrates with high functional characteristics by aerosol jet printing method has been demonstrated.

Acknowledgments

The reported study was funded by RFBR, project number 20-31-70001.

References

[1] Ćatić N, Wells L, Al Nahas K, Smith M, Jing Q, Keyser U F, Cama J and Kar-Narayan S 2020 Aerosol-jet printing facilitates the rapid prototyping of microfluidic devices with versatile geometries and precise channel functionalization *Applied Materials Today* **19** 100618

[2] Arsenov P V, Efimov A A and Ivanov V V 2021 Optimizing Aerosol Jet Printing Process of Platinum Ink for High-Resolution Conductive Microstructures on Ceramic and Polymer Substrates *Polymers* **13** 918

[3] Borghetti M, Serpelloni M and Sardini E 2019 Printed Strain Gauge on 3D and Low-Melting Point Plastic Surface by Aerosol Jet Printing and Photonic Curing *Sensors* **19** 4220

Terahertz Detector Utilizing a SiO_2/Graphene/SiO_2 Sandwich Suspended at the Feed of a Planar Antenna

I Belikov[1], M Rybin[2], A Prikhodko[1,3], D Mikhailov[1,3], I Gayduchenko[1], A Shurakov[1], G Goltsman[1,3]

[1]Moscow Pedagogical State University, Moscow 119435, Russia
[2]Prokhorov General Physics Institute, RAS, Moscow 119991, Russia
[3]National Research University Higher School of Economics, Moscow 101000, Russia

nknki@mail.ru

Abstract. We report on the fabrication of a terahertz detector utilizing a SiO_2/graphene/SiO_2 sandwich suspended at the planar antenna feed. This design of the detector aims to enhance its sensitivity via weakening of the heat sink between graphene's phonons and those of the substrate. We achieve complete suspension of the sandwich only in case of a low fill-factor of the antenna feed area. Evaluated DC parameters of the samples are consistent with those reported in the literature. The fabrication process developed is suitable for implementing the detector proposed for signal frequencies up to several terahertz.

1. Introduction

Terahertz frequency range is gradually mastered, and terahertz receivers are currently in demand in numerous applications. Despite worse sensitivity compared to that of superconducting competitors, terahertz detectors utilizing graphene produced by the means of chemical vapor deposition (CVD) have certain advantages. Namely, a) they are naturally compliant with integrated circuits making use of various semiconductor platforms, b) recent advances in their development suggest the performance competitive with that of planar Schottky diodes (PSD) [1], c) this performance can be achieved at less technological expenses. For that to happen, however, certain technical issues have to be resolved.

In this paper we report on the fabrication of a terahertz detector utilizing a SiO_2/graphene/SiO_2 sandwich suspended at the feed of a planar antenna. Such a design of the detector is meant to enhance its sensitivity by enlarging the time constant through weakening of the heat sink between graphene's phonons [2] and a phonon reservoir presented by bulk SI-GaAs under the sandwich.

2. Fabrication and evaluation of detectors under study

To produce the samples, we relied on a 450 μm thick SI-GaAs wafer to make the fabrication process partially compliant with that of the PSD with a Γ-shaped anode suspended bridge earlier developed by us [3]. Pretreatment of the wafer surface by O_2 plasma was followed by the consecutive fabrication of Ti/Au (5/200 nm) alignment marks, a 50 nm thick SiO_2 sublayer and the outer part of a Ti/Au (5/200 nm) planar spiral antenna. Footprint of the SiO_2 sublayer was similar to that of the antenna inner part with a spatially-spanned load at its feed. Once a CVD graphene was transferred to the wafer, V/Au (10/50 nm) contacts to it were fabricated with the aid of a glancing angle deposition. Prior to the fabrication of the antenna inner part, we processed the wafer by O_2 plasma to etch the graphene within

its footprint and, consequently, to exclude possible AC shunting of the antenna metallization during operation of the detector. Further fabrication of a 75 nm thick SiO_2 cover overlapping the antenna feed area was followed by the removal of unprotected graphene regions. Both the SiO_2 sublayer and SiO_2 cover acted as etch-stoppers during the implementation of a SiO_2/graphene/SiO_2 sandwich suspended at the antenna feed. The local removal of the SI-GaAs underneath the sandwich was maintained through a dual sided opening (on both sides of the line connecting the antenna feed points) in the positive e-beam resist intended for the access of wet etchant.

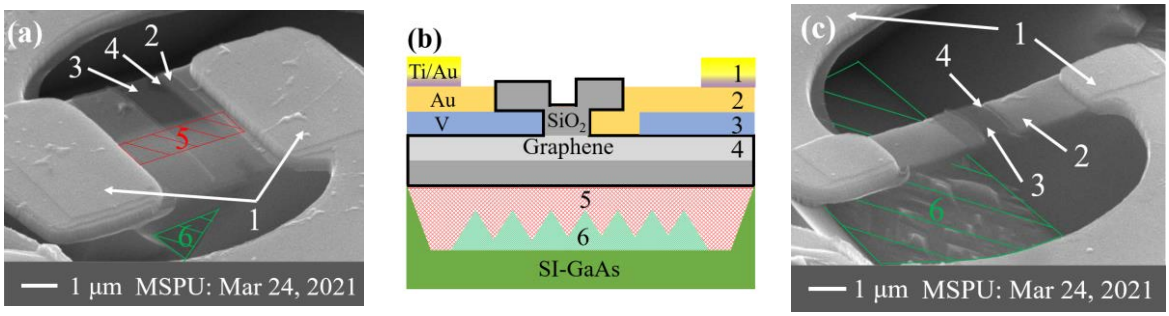

Figure 1(a, b, c). (a) SEM image of sample #1; **(b)** Samples' layered structure across the antenna feed; **(c)** SEM image of sample #2.

The fabrication process described hereinabove was employed to produce a set of terahertz detectors utilizing the suspended SiO_2/graphene/SiO_2 sandwich. Figures 1(a, c) provide images from a scanning electron microscope (SEM) for the detectors with different areas of graphene microbridge, the labels are denoted in figure 1(b). As one can clearly see, sample #1 (with a 0.6×6 μm^2 area of the microbridge) does not utilize a fully suspended SiO_2/graphene/SiO_2 sandwich, whose central part contacts the SI-GaAs substrate noticeably. The total contact area is 1.3×4 μm^2, whereas the contact of SI-GaAs to the region underneath graphene microbridge has significantly smaller area of 1.3×0.6 μm^2. We achieved the complete suspension of a SiO_2/graphene/SiO_2 sandwich only in case of a low fill-factor of the antenna feed area (sample #2), i.e. for graphene microbridge of 0.2×2 μm^2. Indeed, this geometry enables bigger opening in the e-beam resist which enhances access of wet etchant to the SI-GaAs being removed. Evaluated DC parameters of the samples produced are consistent with those reported in the literature: graphene's sheet resistance of 728±38 Ω/square and the contact resistivity of a V/graphene junction of 77±9 μΩ·cm^2 were obtained. We observed no drastic impact of the finishing removal of the SI-GaAs under SiO_2/graphene/SiO_2 on the samples' DC transport properties.

It is known that the deviation of the spiral antenna inner part from a self-complementary structure leads to the decrease of antenna efficiency at the upper edge of its input frequency range [4]. The minimum dimension, at which this deviation can still be tolerated, is ultimately limited by the resolution requirements imposed on the fabrication of graphene microbridge (equipped with an ohmic contact) with 50-100 Ω impedance. Therefore, we suggest that the proposed design within the fabrication process developed is suitable for the implementation of a graphene-based detector effective at signal frequencies up to several terahertz.

Acknowledgments
We acknowledge support of the Russian Science Foundation grant No. 19-72-10156.

References
[1] S. Castilla et al. 2019 *Nano letters* 19(5) 2765-2773
[2] J. Tong et al. 2018 *Nano letters* 18(6) 3516-3522
[3] A. Shurakov et al. 2020 *Journal of Physics: Conference Series* 1695(1) 012154
[4] A. Shurakov et al. 2012 *IEEE Transactions on Terahertz Science and Technology* 2(4) 400-405

The use of digital data processing to improve the metrological characteristics of the rubidium frequency standard

A P Valov[1], K G Arinushkina[2], V V Davydov[2, 3], V Yu Rud[3]
[1]The Bonch-Bruevich Saint - Petersburg State University of Telecommunications (Russia, St. Petersburg, 193232, 22 Bolshevikov)
[2]Peter the Great Saint Petersburg Polytechnical University (Russia, St. Petersburg, 195251, 29 Polytechniheskya str)
[3]All Russian Research Institute of Phytopathology (Russia, Moscow Region, 143050, B.Vyazyomy, Institute str., ownership 5)

Abstract. The necessity of improving the metrological characteristics of a quantum frequency standard when determining the coordinates of an object on the Earth's surface or long-term transmission of large amounts of data in satellite communication systems is substantiated. A new algorithm for digital processing of optical signals in the frequency standard is proposed. The results of experimental studies of the metrological characteristics of a quantum frequency standard based on rubidium atoms - 87 are presented

1. Introduction

A special place among devices for determining the frequency and time is occupied by frequency standards (FS) [1, 2]. The main advantage of the FS over other devices is the use of laser radiation frequency stabilization systems and optical elements in it for stable operation. A slight deviation of the frequency from the nominal value leads to large errors, especially when transmitting large data streams and determining the coordinates of an object. One of the main problems of the satellite system is the mutual synchronization of the time scales of satellites down to nanoseconds or less. For example, an error in navigation signals emitted by different satellites with a time mismatch of 10 ns causes an additional error in determining the location of an object of 10-15 meters. The solution of new problems in the transmission of information and determination of coordinates requires constant modernization of satellite navigation systems, including quantum frequency standards. In this paper, we consider one of the options for upgrading the rubidium frequency standard (RFS) to improve its metrological characteristics.

2. Principle of operation of the rubidium frequency standard

The operation of the RFS is based on the principle of tuning the less stable frequency of the voltage-controlled crystal oscillator (VCXO) to the highly stable frequency of the quantum transition of rubidium – 87 atoms. A microwave excitation signal is generated in the frequency multiplier block. The interaction of the microwave field with rubidium – 87 atoms causes their transitions to the corresponding unpopulated level. The signal-to-noise ratio (S/N) of the recorded resonant signal from the emitted photons at the photodetector in this case will be maximum. The received signal is used to generate a highly stable frequency which equal to 6834.7 MHz [1 - 3]. This frequency is corrected for effects that lead to frequency shifts of the central resonance. The main contribution to the frequency shift of the central resonance is made by the parameters of the microwave excitation signal. Therefore,

the process of generating a microwave signal, which is fed into the interaction zone of rubidium-87 atoms with the field along the waveguide path, needs to be given increased attention when upgrading the design of the FS.

3. Experimental studies

During long-term operation of the FS, especially in space, there is an imbalance in the parameters of its operation. To adjust them, it is necessary to calculate the values of the error signal. This signal is greatly influenced by various noises that are present in optical signals. Using median filtering of data from optical signals can reduce the effects of random noise in the error signal, thus reducing phase noise. When using optical light signals for recording resonance conditions on photodetectors, an important characteristic is the power spectral density Sφ. The optical signal arriving at the photodiode is digitized and fed to a control device based on a microcontroller. The data received by the control device are filtered and on their basis the control signal of the crystal oscillator is calculated to adjust to a more highly stable frequency of the rubidium junction. Figure 1 shows as an example the spectral density of noise in the frequency range of tuning the resonant frequency of a quantum transition.

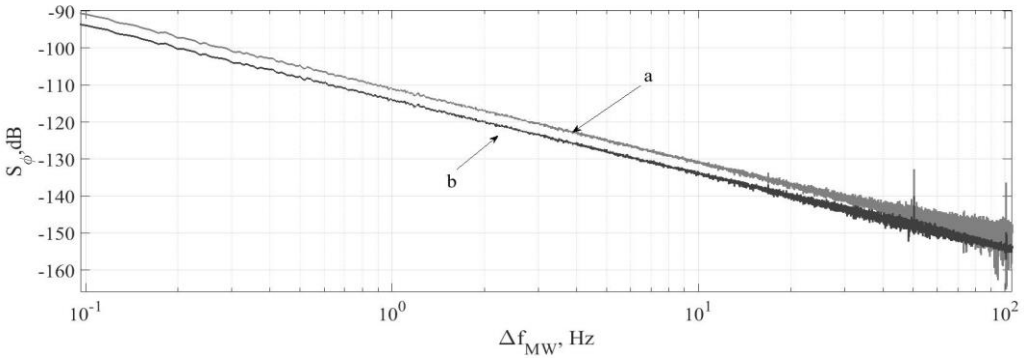

Figure 1(a, b). The phase noise spectral power density of error signal: a - the previous version of the software; b - the new version.

The analysis of the results of experimental studies obtained in Figure 1 showed that the use of median filtering and a microcontroller for control in the FS allows to reduce the power of phase noise in the output signal spectrum. The use of median data filtering in the automatic frequency control ring of the microwave excitation signal allows one to reduce one of the most important disturbing factors affecting the short-term frequency stability - the spectral noise density.

4. Conclusion

Experimental studies of the metrological characteristics of RFS have shown an improvement in the long-term frequency stability by 5%. The obtained improvements in the short-term and long-term frequency stability make it possible to increase the degree of reliability of the operation of satellite systems for transmitting large amounts of information and determining coordinates.

References

[1] V.M. Polyakov, E.A. Viktorov, A.V. Kovalev, and O.A. Orlov, International Conference Laser Optics, LO 2014, Saint Petersburg,.6886216, pp. 123

[2] A.V. Kovalev, V.M. Polyakov, and A.A. Mak, International Conference Laser Optics, LO 2016, Saint Petersburg, 6886216, pp. 201

[3] A. P. Valov, V. V. Davydov, V. Yu. Rud, Journal of Physics: Conference Series. – 2019. - Vol. 1410(1), - P. 012246.

Method for reducing phase fluctuations of a precision frequency response meter for microwave quantum generators

M A Vodopyanov[1], K A Menzorov[1], V V Davydov[1, 2] and V Yu Rud[2]

[1]Peter the Great Saint Petersburg Polytechnic University, St. Petersburg, 195251, Russia
[2]All Russian Research Institute of Phytopathology, Moscow Region, 143050, Russia

Abstract: The principle of operation of the device for measuring frequency characteristics is considered. Block diagram of a device for measuring the frequency characteristics of a digital frequency comparator with correlation quadrature processing and description of their components is illustrated. The block diagram of the frequency multiplier is given. The accuracy characteristics of the developed meter design are evaluated. They are compared with the characteristics of previously used devices. The Improve accuracy characteristics and increased stability of operation were found.

1. Introduction

The frequency response measurement device is designed to measure the frequency characteristics of quartz oscillator signals, frequency and time standards, and frequency synthesizer signals [1, 2]. An integral part of the operation of this device is the formation of a time discredit signal synchronized with one of the input matched signals, and the conversion of the input signal voltages into digital codes of quadrature components, storing these codes in the receiving computing device [2, 3]. As well as the power supply device of the board converts the AC voltage (220±22)V 50 Hz into a DC reference voltage power supply plus 24 V.

The reliable stability of the master generator is 10^{-15}, therefore, the precision meter must be at least 3 times more accurate to detect problems [2, 3].

2. The principle of operation of the frequency response measurement device

Figure 1 shows a block diagram of the frequency response measurement device for the quartz oscillators and frequency standards.

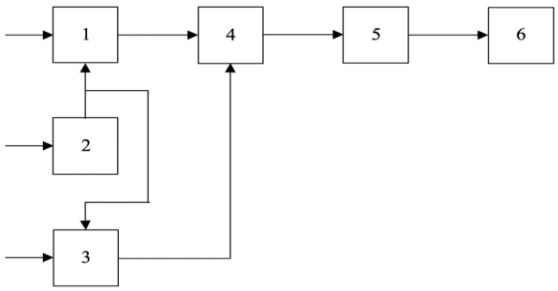

Figure 1. Block diagram of frequency response measurement device of a digital frequency comparator with correlation quadrature processing, where 1 and 3 are an ADC, 2 – frequency multiplier by 4, 4 –

digital signal processor (DSP), 5 – field-programmable gate array (FPGA), 6 - Micro Controller Unit (MCU).

The PLL circuit is designed for coherent synthesis of the generator output signal with the sinusoidal signal of the measuring channel. Switching scheme – for controlling the modes of operation of the frequency response measurement device. ADC of the reference channel – for converting the voltage of a reference sinusoidal signal with the clock frequency of a quartz oscillator coherent with the measured signal into a hexadecimal bit code. ADC of the measuring channel - for continuous conversion of the voltage of the measured sinusoidal signal with the clock frequency of a quartz oscillator coherent with the measured signal into a hexadecimal bit code. FPGA – for managing the modes of operation of the frequency response measurement device.

The frequency of one of the matched signals is multiplied by four and the signal from the output of the frequency multiplier is used to take digital samples of the harmonic input signals. The digital signal processor receives digital codes of voltage samples of the measured signal, averages them and filters them to form a code proportional to the phase difference and frequency of the compared signals. A time sampling signal with a nominal frequency of 20 MHz allows you to calculate phase samples of the measured signal every 50 ns. at the same time it forms the quadrature components of the compared signals. Therefore, at the data inputs of the digital signal processing processor (DSP), there are four types of samples: ai; bi; ci; di, following with a nominal period of 0.2 microseconds in each channel. Depending on the processor speed, the DSP processes the codes of these samples, for example, after a time interval of 1 microsecond, it depends on the processor speed.

S_a, 1 мкс = { a_1, a_2,... a_N)

S_b, 1 мкс = { b_1, b_2,... b_N)

S_c, 1 мкс = { c_1, c_2,... c_N)

S_d, 1 мкс = { d_1, d_2,... d_N)

The DSP processor converts the sample data into a phase difference and a frequency difference.

3. Conclusion

As a result of the research, it was found that in the previously developed precision meters, when exposed to noise and pulsation of power sources, spurious signals at the input, noise on the reactive circuits of frequency multipliers, there were fluctuations in the signal phase. These fluctuations affect the frequency measurement error of quartz oscillators, especially in long-term studies of physical processes or phenomena. In the new generation of precision meters, the presence of two ADC channels eliminates the phase fluctuations introduced by the frequency multiplier.

References

[1] Petrov A A and Davydov V V 2015 *Lecture Notes in Computer Science (including subseries Lecture Notes in Artificial Intelligence and Lecture Notes in Bioinformatics)* **9247** 739-744

[2] Valov A P, Davydov R V, Rud V Yu and Grevtseva A S 2019 *Journal of Physics: Conference Series* **1326(1)** 012040

[3] Grevtseva A S, Davydov R V, Dudkin V I and Rud' V Yu 2019 *Journal of Physics: Conference Series* **1326(1)** 012043

Improving the accuracy of the method for measuring the electrophysical parameters of soft magnetic materials

A V Volik, E A Pecherskaya, Yu A Varenik, T O Zinchenko, D V Artamonov, O A Timohina
Department of Information and measuring equipment and metrology, Penza State University, Penza 440026, Russia

@list.ru

Abstract. The structure of an automated system for measuring magnetic-hysteresis loops, normal magnetization curve, magnetic permeability with an error of no more than ± 1% is proposed. The measuring principle is based on the inferential measurements of the magnetic induction and the coercive force by integrating the secondary voltage and the excitation current. As a result of metrological analysis, an increase in the measurements accuracy is achieved both by improving the hardware implementation and calibrating the measuring channels, by introducing a correction for the systematic component of the error.

1. Introduction

The relevance of the study of the electrophysical parameters of magnetic materials is due to their wide application in power electronics devices, in motors, generators [1], as well as in micromechanical systems [2]. Experimental studies of the dependences of the parameters of magnetic materials make it possible to discover new directions for their use. For example, in [3], the results of measurements of hysteresis loops of a high-temperature magnetocaloric alloy are presented, which confirm the appearance of an additional phase transition near a temperature of 315 K. The analysis of the listed and other known instruments for measuring the electrophysical parameters of magnetic materials confirms the relevance of improving the principles and methods of measurements in order to increase their accuracy by performing metrological analysis.

2. The structure of the system for the magnetic materials parameters measuring

The authors have developed an automated information and measurement system (IMS) for studying the parameters of magnetic materials (Fig. 1), based on inferential measurements of the magnetic induction and the coercive force by integrating the secondary voltage and the excitation current, respectively. A toroid core is made of the investigated soft-magnetic material. The measuring unit generates the excitation currentin the winding I and converts the EMF of the winding II into a code proportional to the magnetic induction in the investigated soft-magnetic material.

3. Magnetic induction transfer function

Installation control and processing of measurement results is carried out according to unique methods, which are implemented in software using a computer (PC). In particular, both the Preisach model and the modeling methods previously tested by the authors on the hysteresis loops of ferroelectric materials were used to simulate magnetic-hysteresis loops [6, 7].

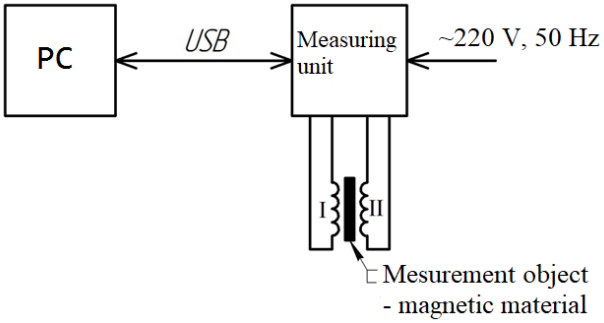

Figure 1. Block diagram of IMS for studying the soft-magnetic materials parameters

The value of the desired magnetic induction B is determined according to the following expression:

$$B = \frac{\int \varepsilon(t)dt}{S \cdot n_{II}}$$

where B – magnetic flux; S – the core cross-sectional area; n_{II} – number of magnetizing coil rings; ε- EMF of the measuring winding, which is converted into a digital code by means of an analog-to-digital converter (ADC).

As a result of the metrological analysis of the developed IMS, it was found that the main instrumental error in the magnetic induction measuring is due to the errors of the integrator based on the operational amplifier, the error in measuring the cross-sectional area S, and the metrological characteristics of the ADC. In order to minimize the integration error, it is proposed to use an integrator, in which the capacitor discharge is realized with a voltage that is formed by a discharge stage on an operational amplifier at the integrator output.

4. Conclusion

The proposed automated IMS performs automated measurements of magnetic-hysteresis loops, normal magnetization curve, magnetic permeability with an error of no more than ± 1%, as well as processing and displaying the results obtained on the monitor screen in graphical and tabular form, saving them in a database for further research. An increase in the measurement accuracy is achieved both by improving the hardware implementation and by calibrating the measuring channels by introducing a correction for the error systematic component.

References

[1] Josefina M Silveyra, Enzo Ferrara, Dale L Huber 2018 Todd C. Monson. Soft magnetic materials for a sustainable and electrified world *Science* vol. 362 (6413) eaao0195

[2] Mikhailin N Y, Romanov S.G., Kumzerov Y.A. et al. 2018 Superconducting Properties of Indium Nanostructured in Pores of Thin Films of SiO2 Microspheres *Phys. Solid State* 60 pp1942–1947

[3] Gozdur Roman, Najgebauer Mariusz 2019 Scaling analysis of phase transitions in magnetocaloric alloys *Journal of Magnetism and Magnetic Materials* vol 499 p 166239.

[4] Skresanov V N and Shubnyj A I 2006 Autogenerator Spectral Method for Testing of Electrophysical Properties of Materials in Millimeter-Wave Band *16th International Crimean Microwave and Telecommunication Technology* (Sevastopol, Ukraine) 2006 pp 741-742

[5] Gorst A, Zavyalova K, Shipilov S, Yakubov V, Mironchev A 2020 Microwave Method for Measuring Electrical Properties of the Materials *Appl. Sci*. vol 10 pp 8936

[6] Artamonov D V, Baranov V A, Pecherskaya E A, Pushkareva A V, Tsypin B V, Fimin A V 2019 Application of a Hyper-Complex Impedance Model for Indirect Measurements of Materials Parameters of Functional Electronics *International Conference of Young Specialists on Micro/Nanotechnologies and Electron Devices*, pp 760-764

[7] Golubkov P E, Pecherskaya E A, Golovyashkin A N, Golovyashkin A A, Pecherskiy A V, Shepeleva Y V 2018 Analysis of the technological parameters influence on the reproducibility of the active dielectrics properties *International Conference of Young Specialists on Micro/Nanotechnologies and Electron Devices*, pp 57-61

Graphene FET detector as THz mixer

A. Gazaliev[1,2], M. Moskotin[3], V. Belosevich[1,4], M. Rybin[5], I. Gayduchenko[1*] and G. Goltsman[1,4]

[1]Moscow Pedagogical State University, Moscow, 119435, Russia; [2]NRC «Kurchatov Institute», Moscow, 123182, Russia; [3]Moscow Institute of Physics and Technology (National Research University), Dolgoprudny, 141700, Russia; [4]National Research University Higher School of Economics, Moscow, 101000, Russia; [5]Prokhorov General Physics Institute, RAS, Moscow, 119991, Russia

[*]igorandg@gmail.com

Abstract. We report on our recent efforts toward development of a heterodyne THz detector based on a single layer graphene two-terminal device integrated with a bowtie antenna on a sapphire substrate. The heterodyne detection is achieved by quasi-optical coupling of signals from two sub-THz radiation sources to the same detector. The measured IF bandwidth was 5.8 GHz.

1. Introduction

The unprecedented increase in wireless data traffic has led to the need to expand of the carrier frequency range in order to increase the bandwidth of communication channels. One of the promising approaches for creating high-performance (over 100 Gb / s) wireless data transmission channels is the use of the terahertz frequency range (0.1-10 THz) [1]. For the practical implementation of such systems, it is necessary to develop an element base based on fast, cheap and energy-efficient THz detectors and photo-mixers.

Due to the gapless band structure and high mobility graphene is considered as a promising material for creating ultrafast photodetectors in a wide spectral range: from visible to terahertz [2]. A weak electron-phonon coupling, together with a small specific heat capacity of graphene, leads to a strong heating of its electronic subsystem under the incident electromagnetic radiation and, as a result, to a thermo-emf signal. The photo-thermoelectric effect in graphene allows you to potentially achieve high volt-watt sensitivity and speed up to picoseconds even at room temperature [3]. In this work we demonstrate a mixer based photo-thermoelectric graphene THz detector.

2. Measurements

Our devices are made in a two-terminal configuration, in which graphene synthesized by chemical vapor deposition is in contact with two electrodes made of metals with different work functions [4]. The electrodes are made in the form of bow-tie antenna to couple THz radiation to sensing element. In such a system, a thermo-EMF signal is generated under the incident THz radiation [5].

The measurement technique used in this study is based on the mixing of both low intensity LO and RF and described in ref. [6]. The setup includes two backward-wave oscillators (BWO), one as a fixed signal source. The second BWO was used as tunable LO source which corresponds to IF up to 13 GHz. The power of both BWOs controlled by means of an RF thermistor power meter. Two signals from the specified sources are coupled to Si lens on which graphene device are located. The IF signal

is amplified with wideband amplifier that is connected to FSV 9 kHz – 13.5 GHz Rohde & Schwarz spectrum analyzer.

3. Results

The heterodyne measurements for IF band ranging from 0.1 – 13 GHz are presented in Fig. 1. The measured IF gain data was fitted with function:

$$G = G_0 - 20\log(1 + \omega^2\tau^2)$$

, where G_0 is IF gain at low frequency, w is the angular frequency and t is the response time. The -3 dB bandwidth of the graphene based mixer is 5.8 GHz that might be limited by a bonding wires.

4. Conclusion

The graphene based mixers have a potential for high frequency room temperature detectors based on a photo-thermal effect. Further research on optimization and identification of physical mechanisms limiting the characteristics of graphene THz detectors may lead to the creation of fast mixers for next generation wireless networks.

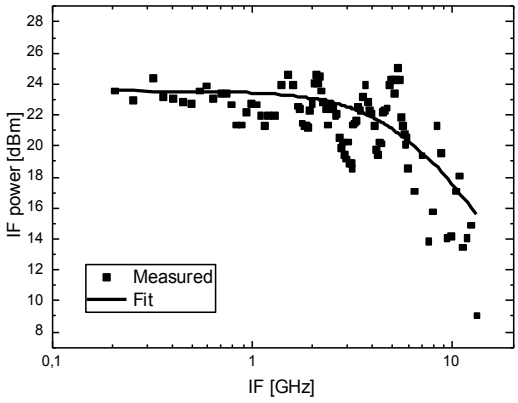

Fig. 1 IF bandwidth of the graphene based heterodyne detector

Acknowledgments

The reported study was funded by RFBR and DFG, project number 21-52-12041(DFG project number 449506295).

References

[1] Elayan, Hadeel, et al. "Terahertz communication: The opportunities of wireless technology beyond 5G." 2018 International Conference on Advanced Communication Technologies and Networking (CommNet). IEEE, 2018.

[2] Koppens, F. H. L., et al. "Photodetectors based on graphene, other two-dimensional materials and hybrid systems." Nature nanotechnology 9.10 (2014): 780-793.

[3] Sun, Dong, et al. "Ultrafast hot-carrier-dominated photocurrent in graphene." Nature nanotechnology 7.2 (2012): 114-118.

[4] Gayduchenko, I. A., et al. "Manifestation of plasmonic response in the detection of sub-terahertz radiation by graphene-based devices." Nanotechnology 29.24 (2018): 245204.

[5] Cai, Xinghan, et al. "Sensitive room-temperature terahertz detection via the photothermoelectric effect in graphene." Nature nanotechnology 9.10 (2014): 814.

[6] Krause, Sascha, et al. "Reduction of phonon escape time for NbN hot electron bolometers by using GaN buffer layers." IEEE Transactions on Terahertz Science and Technology 7.1 (2016): 53-59.

Features of the formation of the frequency of the microwave excitation signal in the quantum frequency standard on rubidium atoms - 87

A S Grevtseva[1], V V Davydov[1, 2] and V Yu Rud[2, 3]
[1]Peter the Great Saint Petersburg Polytechnical University, Russia, St. Petersburg, 195251
[2]All-Russian Research Institute of Phytopathology, Moscow Region 143050, Russia
[3]A.F. Ioffe Physicotechnical Institute, St. Petersburg, 195152, Russia

Abstract. The article discusses the main disadvantages of the current design of a quantum frequency standard based on rubidium-87 atoms. A solution is proposed to improve the design of the rubidium standard. A forecast for improving its metrological characteristics is presented. The results of experimental investigations are presented.

1. Introduction

In modern navigation, one of the important tasks is to determine the exact time and frequency. To solve this problem, global navigation satellite constellations such as the Russian GLONASS and the US Global Positioning Systems (GPS) are actively using quantum frequency standards (QFS). Among quantum standards in satellite communication systems, rubidium QFS are most widely used due to their small size and low cost in comparison with other types of standards [1, 2].

At present, with the development of electronic equipment, the requirements for the accuracy of satellite navigation systems are constantly increasing, which makes the task of their modernization especially urgent [2]. The modernization of frequency standards is no exception, this process includes changes in the dimensions and weight of the structure, as well as the improvement of metrological characteristics. It should be noted that for QFS, modernization can be carried out not for its entire structure, but only for individual units [1, 2]. This paper discusses one of the possible solutions for modernizing the design of a quantum frequency standard based on rubidium-87 atoms.

2. Modernization of the design of the rubidium frequency standard

In domestic and foreign models of QFS based on rubidium-87 atoms, the basic principles of operation remain unchanged. The principle is based on automatic tuning of the quartz generator (QG) frequency to the value of the quantum transition frequency in optically oriented Rb-87 atoms. To implement the tuning of the QG frequency, the optical cell of the atomic discriminator (AD) is irradiated with a microwave signal, the frequency of which corresponds to the frequency of the quantum transition of excited rubidium-87 atoms. There is a significant drawback in the currently used microwave generation methods. The spectrum of the output signal with a frequency of 5.313 MHz contains side amplitude components. The presence of lateral components creates additional optical signals, which can lead to an error in establishing the value of the frequency of the output signal of the rubidium standard.

The new design of the standard microwave signal with a frequency of 6834.7 MHz is proposed to be synthesized using a system of two circular phase-locked loop (PLL). The synthesis scheme is shown in Fig.1.

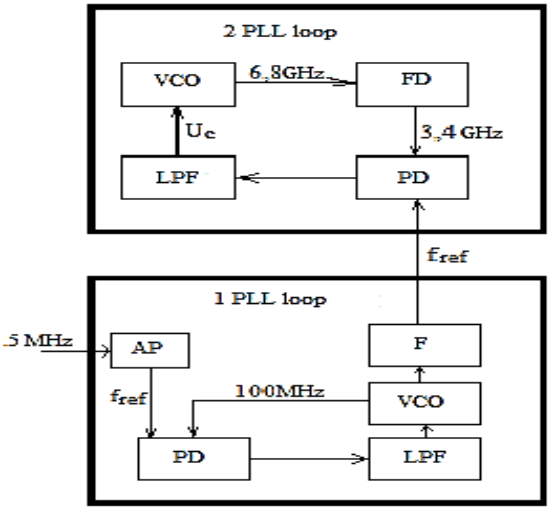

Figure.1. Block diagram of two PLL loop systems: VCO – voltage controlled generator; FD – frequency divider; PD – phase detector; LPF – low-pass filter; AP – analog part; F – filter.

The main elements of the PLL system are a phase detector (PD), one of the inputs of which is fed with a signal from a voltage-controlled oscillator (VCO). Another PD input is connected to a reference signal source with a frequency f_{ref}. A phase detector compares the signals at both inputs and generates an error signal, which, after filtering and amplifying (if necessary), adjusts the VCO frequency. As part of the PLL system, a low-pass filter (LPF) is also used, which is connected between the output of the PD and the input of the VCO and largely determines its frequency properties. The microwave signal is synthesized in two stages. In the first PLL ring, the VCO is adjusted with an output frequency of 100 MHz; for this, the division factors of the reference and input frequencies are selected in the PD chip according to formula (1).

$$f_{out} = \frac{f_{ref} * K}{K_{ref}}, \quad (1)$$

where f_{ref} = 5 MHz is the frequency of the reference signal, K is the division factor of the input frequency, K_{ref} is the division factor of the reference frequency, f_{out} is the output frequency of the VCO.

The second PLL loop similarly adjusts the VCO with an output frequency of 6.8 GHz. To create an accurate value for the frequency of the quantum transition, in the final stage, the fractional component is mixed into the output signal of the PLL. In this case, the required signal 6, 8347 GHz is immediately fed to the input of the AD, the microwave diode is excluded from the new circuit.

3. Conclusion

The developed design of the QFS unit has a number of main advantages: first, a cleaner spectrum of the output optical signal arriving at the photodetector. Second, the possibility of direct control of the microwave signal, and, consequently, its precise tuning to the resonant frequency of rubidium atoms. This makes it possible to reduce the error in establishing the actual value of the frequency of the output signal of the rubidium QFS, which improves the stability of the device.

References

[1] Grevtseva A S, Davydov V V and Rud V Yu 2020 *CEUR Workshop Proceedings* **2667** 15–18
[2] Valov A.P 2019 *Journal of Physics: Conference Series* **1410(1)** 012246.

Scanning ion-conductance microscope with modulation of the sample position along the Z-coordinate and separate Z-axial and lateral (X, Y) scanning

M V Zhukov, S Yu Lukashenko, I D Sapozhnikov, M L Felshtyn, O M Gorbenko, A O Golubok

Laboratory of scanning probe microscopy and spectroscopy, Institute for Analytical Instrumentation RAS, St. Petersburg 198095, Russia

E-mail: cloudjyk@yandex.ru

Abstract. Scanning ion-conductance microscope with independent piezoscanners in the lateral scanning plane XY and Z axis was designed and tested. For precise, fast and safe approach of the nanopipette to the sample surface, a coarse approach system based on a piezoinertial mover was used. Measurements of test periodic polymer structures were carried out using nanopipettes with an inner pipette diameter of about 100-150 nm. The optimal geometric parameters of the nanopipette were found and the resolution of the method was estimated. To increase the stability and reproducibility of SICM images, the Z-modulation of the position of the substrate with the sample was realized using a bimorph piezomembrane.

1. Introduction

The interest of measuring ion channels in cell membranes and studying of the mechanisms of cell functioning gradually led to the creation of a scanning ion-conductance microscope (SICM), which allows mapping the surface by monitoring of ion currents using micropipettes with an electrode as a probe [1]. However, this approach, as it turned out, have instability due to potential drift on the electrodes and external electrical interference, as well as instability when scanning soft objects of complex geometry, which led to probe breakdowns and artifacts [2]. In [3] the AC (alternating ionic current) SICM method with vibrating probe was developed that more stable for study of soft objects with complex geometry and has better space resolution. Another actual approach to improving the SICM quality is to increase the speed of the pipette in the Z-direction by improving the mechanical properties of the piezoelectric mover [4], as well as using high-frequency piezoelectric drives [5].

In this paper, we have explored the design of the scanning ion-conductance microscope by introducing separate scanning scheme in the XY plane, using piezo-membranes, and in the Z coordinate, using a rigid piezo-package, as well as independent Z-modulation of the sample using a piezo-membrane.

2. Experimental setup

In figure 1a shows a schematic diagram of a scanning ion-conductance microscope. The stacked multilayer piezoelectric element (2) is attached to the fixed base (1) on one side. A titanium guide rod (4) is attached to the opposite side of the piezoelectric element. The titanium carriage (3) is pressed against the surface of the titanium guide rod (4) by a spring. The stacked multilayer piezoelectric element provides both a precision stepwise approach (removal) of a fragile borosilicate nanopipette

(NP) to a sample in the range of ~ 5 mm, which protects the NP from destruction, and smooth displacement along the Z coordinate in the range of ~ 7 μm. The NP (6) fixed on an inertial Z-piezoscanner by a spring clamp (5) and a Petri dish (7) was filled with a 1% NaCl solution and had AgCl electrodes inside. The ionic current I_i at the AgCl electrodes in (6, 7) was converted into an electronic current I_e, which was converted into an electric voltage through converter (8). In our case, R = (0.1-1) GΩ. This electric voltage U is compared on a differential amplifier (9) with a reference voltage U_0 and fed to the input of the integrator (10) and then to high-voltage amplifier (11) connected to the Z-piezoscanner (5). In order to increase the stability of scanning, a mechanical Z-modulation of the substrate with the sample located opposite the vertical axis of the sample was added through a bimorph piezoelectric membrane.

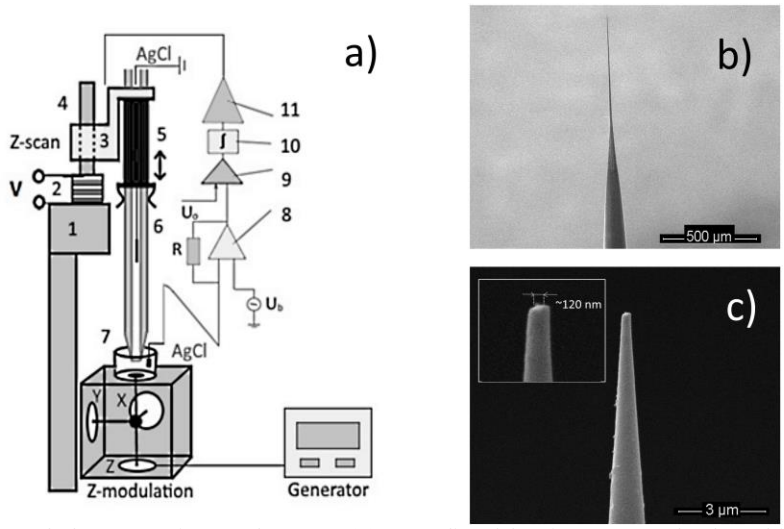

Figure 1. Scheme of the experimental setup (a): 1 - fixed basis, 2 - stacked multilayer piezoelectric element (approach and scanning), 3 - titanium carriage, 4 - titanium guide rod, 5 - NP clamp, 6 - NP with AgCl electrode, 7 - Petri dish with AgCl electrode, 8 - ion current-to-voltage converter, 9 - differential amplifier, 10 - integrator, 11 - high-voltage amplifier, U_b - bios voltage applied to the nanocontact, U_0 - set point voltage signal. SEM image with overview of NP shape (b) and magnification area (c) with approximate diameter of the NP tip is about 100-150 nm.

3. Results and Discussions

A sharp I-Z dependence for a small-diameter pipette about 100-150 nm located near the surface with modulation of Z coordinate of the sample was found. To control the characteristics of the pipette and estimate the radius of the pipette, the current-voltage characteristics (CVC) were measured. The geometric parameters of the NP were estimated in a scanning electron microscope (SEM) (figure 1b, c) before and after measurements. The SICM images of a test sample in the form of polymer replica of a rectangular periodic grid with and without the Z-modulation mode were received. On the standard SICM image one can see the slip lines and Z-scanner jumps at the boundaries of objects. The modulation mode makes it possible to increase the scanning stability. However, a small noise in feedback system was spotted at the imaging due to oscillations. In our case, the sensitivity of the piezomembrane was about 200 nm/V and swing amplitude along the Z axis was about 50 nm. The SICM image of a polymer replica at lower swing amplitude of about 20 nm was obtained, at which noise reduction was found. It is makes possible to distinguish typical small-sized objects on the grid surface, which amounted to a minimum lateral size of about 200 nm and a height of about 40 nm. Thus, it is possible to estimate the resolution of the SICM when using borosilicate probe blanks as double diameter of NP aperture in the lateral direction (X, Y) and double amplitude of Z-modulation in the vertical direction.

References

[1] Hansma P K, Drake B, Marti O, Gould S A C, and Prater C B 1989 *Science* **243** 641-643.
[2] Edwards M A, Williams C G, Whitworth A L, and Unwin P R 2009 *Anal. Chem.* **81** 4482–4492.
[3] David Pastre, Hideki Iwamoto, Jie Liu, et al. 2001 Ultramicroscopy **90** 13–19.
[4] Gesper A, Hagemann P, and Happel P 2017 *Nanoscale* **9** 14172–14183.
[5] Watanabe S and Ando T 2017 *Appl. Phys. Lett.* **111** 113106.

The influence of the lower electrode materials of aligned carbon nanotubes on their piezoelectric response

M V Il'ina[1], **O I Il'in**[1], **O I Osotova**[1], **N N Rudyk**[1] **and O A Ageev**[2]
[1]Southern Federal University, Institute of Nanotechnologies, Electronics and Electronic Equipment Engineering, Taganrog, 347922, Russia
[2]Southern Federal University, REC "Nanotechnologies", 347922, Taganrog, Russia

Abstract. The results of experimental studies of the effect of the lower electrode material on the piezoelectric response of aligned carbon nanotubes (CNTs) are presented. It is shown that the highest piezoelectric response (136 nA at a pressing force of 4 μN) is demonstrated by CNTs grown on a W electrode. This dependence is probably due to the geometric parameters of CNTs and the structure of the CNT array as a whole. The results obtained can be used to develop energy-efficient nanogenerators based on CNT arrays.

1. Introduction

Recent studies show that carbon nanostructures are capable of exhibiting anomalous piezoelectric properties as a result of violation of their centrosymmetric structure through the introduction of defects or the formation of uneven deformations [1-4]. Particular attention is attracted by vertically aligned carbon nanotubes (CNTs) due to the ability to transform nanoscale deformations into a surface potential, which leads to the generation of an electric current [4, 5]. This makes vertically aligned CNTs one of the most attractive materials for creating energy efficient nanogenerators [6]. However, work in this direction is at an early stage and requires comprehensive research. The purpose of this work is to study the effect of the material of the lower electrode, on which aligned CNTs are grown, on their piezoelectric response.

2. Experimental studies

To establish this dependence, a series of 4 arrays of vertically aligned CNTs was grown by the plasma enhanced chemical vapor deposition method. Ti, W, TiN and Cr were used as the material of the lower electrode. The growth temperature was 645 ° C. The thickness of the catalytic nickel layer was 5 nm. The average heights of CNTs ranged from 6.6 to 12.9 μm. The average diameters of CNT ranged from 35 to 72 nm. The density of CNTs in the array varied from 1 to 26 μm^{-2}. Scanning electron microscopy (SEM) images are shown in Figure 1. Experimental studies of the piezoelectric response of CNT arrays were performed by atomic force microscopy (AFM) using a previously developed technique [5]. As a piezoelectric response, we detected the current arising as a result of the formation of the surface potential of CNTs during their deformation upon pressing the AFM probe with a force of 4 μN. The top electrode was a commercial platinum-coated NSG10/Pt probe.

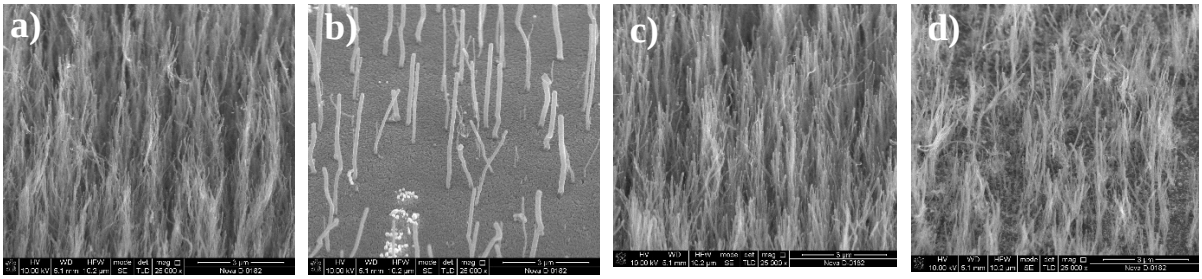

Figure 1. SEM images (magnification ×25000) of the CNT arrays grown on a Ti (a), W (b), TiN (c) and Cr (d) lower electrodes.

3. Results and discussion

An analysis of the results obtained showed that the magnitude of the piezoelectric response increased from 2 to 39 nA with an increase in the clamping force of the AFM probe from 0 to 4 μN to the surface of the CNT array grown on the Ti electrode. For an array of CNTs grown on a W electrode, the magnitude of the piezoelectric response increased from 40 to 136 nA under the same influences. For the CNT array grown on a TiN electrode, on the contrary, an insignificant decrease in the piezoelectric response from 18 to 13 nA was observed. An array of CNTs grown on a Cr electrode showed the smallest piezoelectric response (10 ± 2 nA), which weakly depends on the clamping force of the AFM probe. These dependences are probably due to the influence of the geometric parameters of CNTs and the structure of the CNT array as a whole. Thus, a decrease in the piezoelectric response of a CNT array grown on a TiN electrode is due to a high aspect ratio of the CNT length to diameter (~360), which led to large deviations of the CNT from its axis and the formation of bundles during the measurement. The formation of CNT bundles, in turn, caused a decrease in the total piezoelectric potential due to the compensation of positive and negative charges with each other. A similar situation was observed for a CNT array grown on a Cr electrode, which was initially combined into CNT bundles (Figure 1d). A gradual increase in the piezoelectric response for CNT arrays grown on Ti and W electrodes is due to an increase in the CNT deformation. In this case, a greater value of the response for CNTs on a W electrode is associated with a lower value of the aspect ratio (~92) compared to CNTs on a Ti electrode (~223), which led to a greater relative deformation of the CNTs at a given clamping force. It should be noted that the work function of electrons from Ti, Cr, and W is similar (4.5 - 4.6 eV) and could not have a decisive influence on the results obtained.

Thus, it has been shown that vertically aligned carbon nanotubes grown on the W lower electrode exhibit the maximum piezoelectric response. However, further research is required to establish the optimal geometric parameters of CNTs to their piezoelectric response. The results obtained can be used to develop energy efficient nanogenerators based on vertically aligned CNTs.

Acknowledgments

This work was supported by the Russian Science Foundation (project No. 20-79-00284)

[1] El-Kelany K. E., Carbonnière P., Erba A., Sotiropoulos J. M. and Rérat M. P. 2016 *J. Phys. Chem. C*, **120** (14)

[2] Ong M.T. and Reed E.J. 2012 *ACS Nano* **6** (2), 1387–1394

[3] Kundalwal S. I., Meguid S. A. and Weng G. J. 2017 *Carbon* **117**, 462–472

[4] Il'ina M.V, Il'in O.I., Blinov Yu.F., Smirnov V.A., Kolomiytsev A.S., Fedotov A.A., Konoplev B.G. and Ageev O.A. 2017 *Carbon* **123**, 514–524

[5] Il'ina M.V, Il'in O.I., Blinov Yu.F., Konshin. A.A., Konoplev B.G. and Ageev O.A. 2018 *Materials* **11**, 638

[6] Il'ina M.V, Konshin. A.A., Solomin E.G. 2018 *IOP Conf. Series: Journal of Physics: Conf. Series* **1124**, 071010

Research and calculation of dynamic characteristics of a microelectromechanical device

I E Lysenko[1], N F Kidyaev[1], O A Ezhova[2] D Y Sevostyanov[1],
[1] Southern Federal University, Taganrog 347900, Russia
[2] LLC «MEMS design», Iniciativnaya str., 60, Taganrog, Russia, 347936

Abstract. This paper presents a model of a three-axis micromechanical gyroscope-accelerometer. The stiffness of the suspension of a micromechanical gyroscope-accelerometer is calculated and the dependence of the change in the frequency of vibration of the micromechanical mass on the change in the thickness of the beams of the cruciform suspension element is obtained.

1. Introduction

In the modern electronics market, micromechanical devices (MEMS) have a growing demand. For a greater pace of development of MEMS devices, it is necessary to develop more advanced sensor models or work on improving existing ones [1, 2]. The work on the model of a three-axis micromechanical gyroscope-accelerometer presented in this article will improve its characteristics, and, consequently, increase the demand for Russian microelectronic products on the world market [3, 4].

2. Design and calculation

The developed model of a micromechanical gyroscope-accelerometer with three axis of sensitivity is shown in Figure 1 [5].

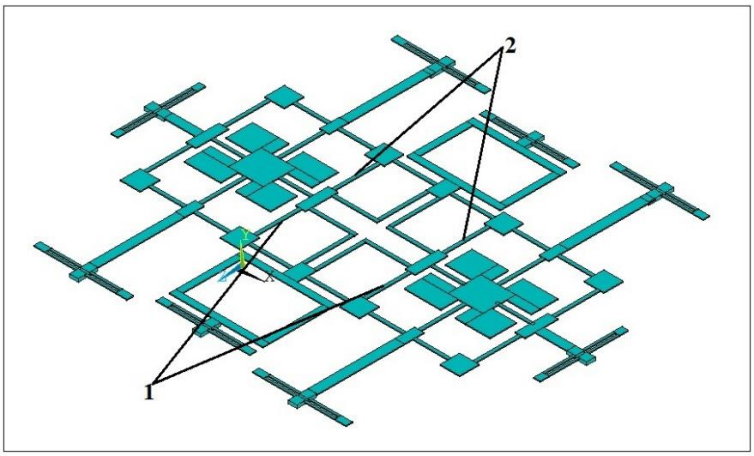

Figure 1. Design of the developed micromechanical gyroscope-accelerometer

This device allows you to measure linear accelerations along three axis and angular velocity along the X and Z axis located parallel to the substrate plane. A distinctive feature of this device is the presence of a cross-shaped element of rigidity, which is in the center of the structure. It allows the electrostatic actuators to simultaneously interact with the inertial masses of the gyroscope-accelerometer.
To understand the influence of the cross-shaped element design on the change in the frequency of inertial mass oscillations, the reduced design was calculated in the MATLAB system environment. The calculation is made for the design of a micromechanical gyroscope-accelerometer with different widths of elastic beams 1, 2 in the cruciform suspension element. The dependence of the frequency of natural oscillations of the inertial masses on the X-axis is shown in Figure 2.

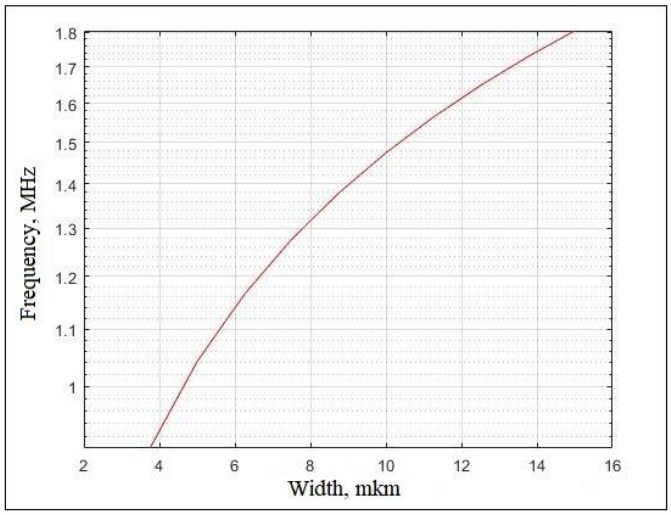

Figure 2. The dependence of the frequency of natural oscillations of the inertial masses along the X-axis

3. Conclusion

This paper presents a model of a three-axis micromechanical gyroscope-accelerometer. The results of calculations of the dynamic characteristics of the presented model, carried out using the MATLAB software, showed a linear dependence of the frequency of natural oscillations of the inertial masses on the change in the width of the elastic beams of the cruciform stiffener of the rake.

4. Acknowledgments

This work was financially supported by the grant of President of Russian Federation (project number MK-4577.2021.4).

References

[1] Raspopov V Ja 2007 *Micromechanical devices* (Tula: Tul'skijgosudarstvennyjuniversitet)
[2] Lysenko I E, Naumenko D V and Ezhova O A 2020 Design and simulation high aspect ratio torsion suspension of MEMS z-axis accelerometer Book of Abstracts of 7th International School and Conference «Saint Petersburg OPEN 2020» on Optoelectronics, Photonics, Engineering and Nanostructures (St. Petersburg: St. Petersburg Academic University) pp 478-479
[3] Lysenko I E Ezhova O A Tkachenko A V Naumenko D V Guha K Rao K S 2019 The results of modelling of a micromechanical accelerometer Journal of Physics: Conference Series. – IOP Publishing
[4] Lysenko I E 2019 The results of modelling of a micromechanical accelerometer *Journal of Physics: Conference Series* 1410 012226 DOI:10.1088/1742-6596/1410/1/012226
[5] Lysenko I E Konoplev B G Kidyaev N F Shafrostova S I Patent for invention No. 2683810 " "Integrated micro-mechanical gyroscope-accelerometer".

Study of characteristics of n-p-n type bipolar power transistor in small-sized metalpolymeric package type SOT-89

D A Knyaginin, E A Kulchenkov, S B Rybalka, A A Demidov
Bryansk State Technical University, Bryansk, 50 let Oktyabrya 7, Russia

Abstract. In this study the input and output characteristics of silicon n-p-n type medium power bipolar junction transistors KT242A91 made by the "GROUP KREMNY EL" in small-sized metalpolymeric package (SOT-89) have been obtained. It is shown that established characteristics for KT242A91 transistor correspond to similar transistor's characteristics.

1. Introduction

Widely known that the bipolar power junction transistors are key component of power semiconductor electronics devices that is primarily used as a switch [1]. It should be noted that at present the modern electronics industry produces a wide range of bipolar transistors of various ratings and in various packages type [2]. Moreover, modern production tends to miniaturize the component base without losing its power characteristics and therefore power electronic industry comes down to use of small type of metalpolymeric package such as SOT (Small Outline Transistor), QFN (Quad Flat No-leads) and others [2]. However, in Russia at this time moment there is no serial production of bipolar junction transistors in small type of metalpolymeric package (SOT-89, SOT-23 etc.). Therefore, recently by electronic company the «GROUP KREMNY EL» (Bryansk, Russia) the production of for power electronics components (SiC Schottky diodes, bipolar junction transistors etc.) in small type of metalpolymeric packages type began within the framework of import substitution program. For instance, in our previous studies it is established that some characteristics of the SiC Schottky type diodes made in small type of metalpolymeric packages [3] are comparable with the same similar types. In presented study the main goal is establish characteristics of n-p-n type bipolar junction transistor in small-sized (SOT-89) type of metalpolymeric package made by «GROUP KREMNY EL».

2. Materials and methods

In experiments was tested the following silicon medium power n-p-n type bipolar junction transistor KT242A91 (JSC «GRUPPA KREMNY EL», Bryansk, Russia) in small-sized SOT package type (SOT-89) which is analogous to a similar transistor BCX56 (Nexperia, Netherlands [4]). For measuring the characteristics were used a programmable source AKIP 1144-160-40, Tektronix MDO3102 two-channel oscillograph (bandwidth 1 GHz, refresh rate 5 GS/s) and Fluke 8845A digital multimeter.

3. Results and discussion

In Figure 1 is shown the output characteristic for silicon medium power n-p-n type bipolar junction transistor KT242A91 in small-sized (SOT-89) type package obtained at temperature of 20^{o}C. As can be seen from Figure 1 the produced transistor KT242A91 operates with collector current up to 1 A that corresponds to a similar transistor BCX56 (1 A [4]). In Figure 1 for comparison also presented data for original medium power n-p-n type bipolar junction transistor BCX56 (Nexperia [4]) for analogous

base currents (I_B=10 mA and I_B=20 mA). Estimation of current gain for transistor KT242A91 give us values from 40 to 180, which corresponds to a same transistor BCX56 (40-250 [4]). In Figure 2 presents the input characteristic of n-p-n type bipolar junction transistor KT242A91.

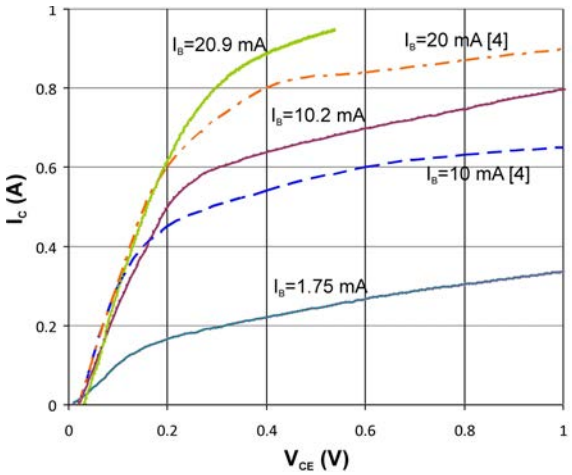

Figure 1. Output characteristics of n-p-n type bipolar junction transistor KT242A91 in small-sized SOT-89 type package.

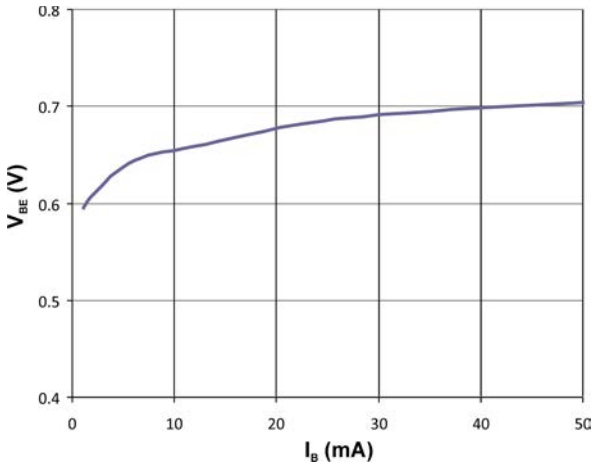

Figure 2. Input characteristics of n-p-n type bipolar junction transistor KT242A91 in small-sized SOT-89 type package (V_{CE}=0 V).

Thus, analysis of experimental results for silicon medium power n-p-n type bipolar junction transistor KT242A91 made by «GROUP KREMNY EL» shows that obtained characteristics corresponds to data for similar BCX56 (Nexperia) transistor.

4. Conclusions

The input and output characteristics of silicon medium power n-p-n type bipolar junction transistor KT242A91 made by «GROUP KREMNY EL» in small-sized (SOT-89) type package have been obtained. It has been established that the studied characteristics correspond to the Nexperia's analogue.

Acknowledgements

This work was carried out with financial support of the Russian Ministry of Science and High Education within the framework of complex project by creation of highly technological industry «Creation of highly technological industry of silicon and silicon carbide microelectronic technics products in small-sized metal-polymeric packages of the SOT, SO and QFN types» (agreement of 29 November No. 075-11-2019-035) at the organization of the leading performer of RDDTE (Research and Development Design and Technological Engineering) the Bryansk State Technical University.

References

[1] Baliga B J 2019 *Fundamentals of power semiconductor devices* (Berlin: Springer International Publishing AG)

[2] Lu D, Wong C P 2017 *Materials for advanced packaging* (Cham: Springer International Publishing)

[3] D A Knyaginin, Rybalka S B, Kulchenkov E A, Demidov A A, Zhemoedov N A, Drakin A Yu 2020 *J. Phys.: Conf. Ser*. **1695** 012160

[4] BCP56; BCX56; BC56PA 80 V, 1 A NPN medium power transistors, Rev. 9, 25 October 2011. https://www.nxp.com/docs/en/data-sheet/BCP56_BCX56_BC56PA.pdf

GaN power IC normally-on and normally-off transistors technology and simulation

V A Bespalov[1], V I Egorkin[1], O B Kukhtyaeva[1], V E Zemlyakov[1], V V Kapaev[1,2], A A Zaitsev[1]

[1]National Research University of Electronic Technology, Moscow, Russia, 124498

[2]P.N. Lebedev Physical Institute of the Russian Academy of Sciences, Moscow, Russia, 119991

Abstract. GaN technology has been waiting to be widely adopted because of its specific technical requirements. Integration of transistor and driver in a single die will enable to overcome problems with gate driving, high cost of circuit and low device reliability. This paper demonstrates technology of GaN-on-Si normally-on and normally-off transistor with different p-GaN cap-layer thickness as well as simulation of these devices. The simulation data confirm experimental results. P-GaN cap-layer thickness affects the current channel density: the more p-GaN thickness, the less channel density. The fabricated transistors have a maximum drain current in open state of about 800 mA/mm.

Introduction

Gallium nitride (GaN) is excellent material for high switching speed and high-power semiconductor device applications due to its properties namely maximum electric field strength, wide band gap and high saturation electron drift velocity. Present GaN-on-Si technology allows to fabricate improved integral E-mode GaN transistors with high breakdown voltages. Due to the modern level of integration many active and passive devices can be manufactured on the same die as in a planar IC process. These microcircuits have applications as AC/DC and DC/DC converters, switching power supplies etc. Monolithically driver integration solves problem with parasitic inductance in the gate driver loop. The parasitic inductance results in negative and positive gate spikes that can compromise the power FET reliability over time. Thus a monolithically integrated driver is so far the best solution.

Experiment and simulation

For the experiment 40 nm p-GaN/1nm AlN/12nm AlGaN/1nm AlN/GaN/Si heterostructures were grown by MOCVD. P-GaN layer provides normally-off behavior of the device. The technological route includes formation of alignment marks and isolation, then selective etching of p-GaN to form ohmic contacts and source and drain formation, gate metal deposition and then selective etching of p-GaN, passivation and first level metallisation. To fabricate p-GaN gate ICP-RIE etching process has been worked out. Also we have managed to learn to control of etched p-GaN thickness. Transistors with 1 um gate length, 1.5 um gate-to-source length, 3.5 um gate-to-drain length and different p-GaN thicknesses (40 nm, 20nm and 0nm) were created and simulated. Simulation has been done with Sentaurus Technology Computer Aided Design (TCAD). It has been noticed p-GaN cap-layer thickness influences on the current channel density.

Results

According to the simulation and experiment it has been established the more p-GaN thickness, the less channel density (Figure 1). Respectively p-GaN thickness affects the drain current at 0 V gate voltage (Figure 2). The fabricateded transistors are normally-on and have a maximum drain current 800 mA/mm in open state, different threshold voltages (from -3 to -2 V) and different drain currents in open state at 0V gate voltage (Figure 3). The experimental data confirm simulation ones. Therefore we have simulated the heterostructure with other parameters of layers to manufacture normally-off transistor. Thus we have developed technology of monolithically integrated driver (normally-on transistor) and normally-off transistor fabrication on a single die.

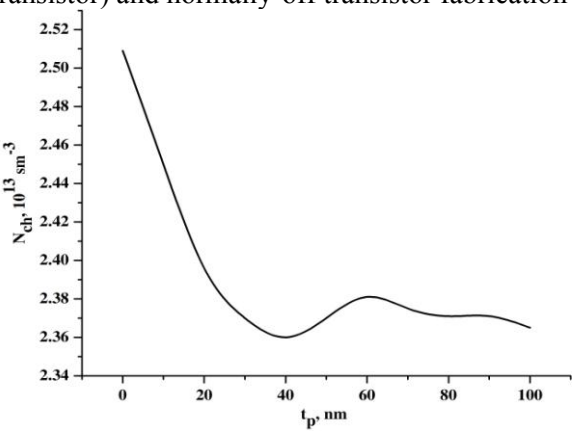

Figure 1. Dependence of channel carrier density (N_{ch}) on p-GaN layer thickness (t_p).

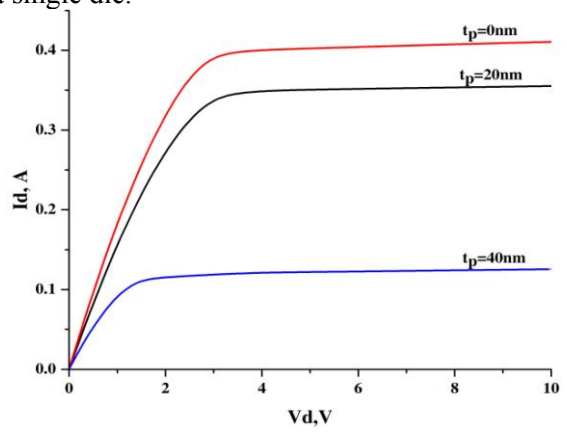

Figure 2. Current-voltage characteristics of HEMTs with different p-GaN layer thicknesses at gate voltage of 0 V.

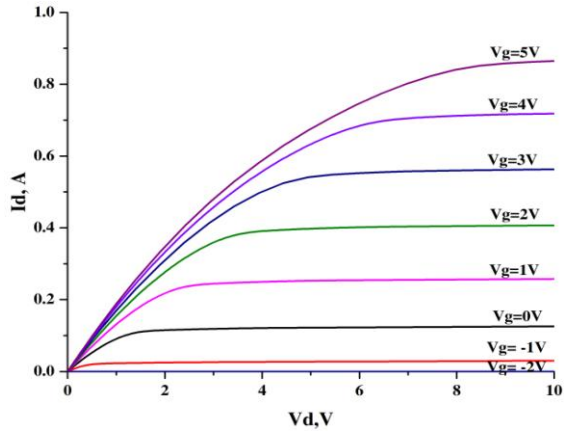

Figure 3. TCAD current-voltage characteristics of the HEMT.

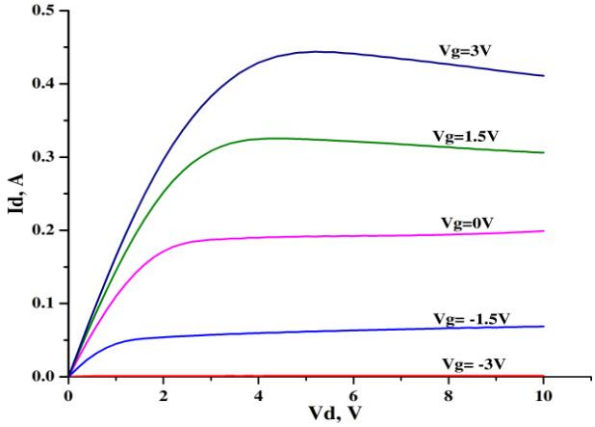

Figure 4. Experimental current-voltage characteristics of the HEMT.

Acknowledgments

This work was supported by the Ministry of education and science of the Russian Federation ("Technology development and technological preparation to manufacture transistor crystals based on gallium nitride heterostructures on a silicon substrate with diameter of 150 mm for power converter modules", grant agreement № 075-11-2019-068 from November 26, 2019).

References

[1] Chen K J, Haberlen O, Lidow A, Tsai Ch,Ueda T, Uemoto Y and Wu Y 2017 *IEEE Trans. Electron Devices* **64** 779

[2] You S, Li X *et al* 2019 ESSDERC *2019 - 49th European Solid-State Device Research Conf. (ESSDERC)* (Cracow, Poland) pp 158-161

Information and measuring system for monitoring the parameters of overhead power lines

V A Listyuhin, E A Pecherskaya, O A Timokhina

Department of Information and measuring equipment and metrology, Penza State University, Penza 440026, Russia

Abstract. The analysis of disturbances (accidents) on overhead power transmission lines and methods and means of the overhead power transmission lines parameters monitoring was carried out. It is shown that the most promising direction for ensuring the required indicators of the reliability of power supply is the development and implementation of information and measurement systems at the facilities of the power supply network complex. The structure of an intelligent information-measuring system for measuring parameters characterizing the state of wires, external factors influencing the state of power lines is proposed. The proposed decision support system will make it possible to promptly identify defective sections of overhead lines, increase the level of technological management of electrical networks.

1. Introduction

Nowadays, the overhead power lines (OHL) parameters monitoring is the most important task to ensure the reliability of power supply, which is implemented through the development and implementation of information and measurement systems (IMS). For example, in [1], it was proposed to introduce an all-optical information and measurement control system for overhead lines based on acousto-optic switching of fiber-optic cables; in [2], it was proposed to use a "smart" electromechanical system (EMS) to solve problems of operational recognition of the emergency mode of a line. Some studies are aimed at using IMS together with high-speed digital protection of transformers against short circuits in the network [3-4]. The authors have developed a version of IMS for measuring and monitoring the overhead lines state, combined with a neuro-fuzzy block of information processing (decision support), which will allow to identify defective sections of overhead lines quickly and increase the level of electrical networks technological control.

2. Requirements for the developed IMS

In order to reduce accidents on overhead lines, as well as to ensure timely maintenance and repair of power grid facilities according to the actual technical level state, it is necessary to develop an overhead lines operational parameters IMS, which makes it possible to identify defects at the stage of formation and predict pre-emergency modes under extreme weather conditions (mainly wind and ice loads).

The following requirements are imposed on the developed IMS: non-contact measurement method (the sensor is powered by a "parasitic" method due to the electromagnetic wire field); the ability to measure wind speed and ambient temperature as an input device (integrated hot-wire anemometer into the device under development); measurement results analysis using a neuro-fuzzy controller (information support for decision support); durability to the impact of external natural phenomena.

3. The operating principle and the main parts of the IMS

The operating principle of this device is realized by measuring the distance from the wire to the ground with a laser distance sensor (rangefinder). In parallel, the wind speed and ambient temperature are measured. The measurement results in real time (online) through the module built into the GSM measuring device are transmitted to the control room, where the data is processed in the neuro-fuzzy controller. Based on the measurement results, the decision support system analyzes the data and displays the following messages on the personnel PC, characterizing the state of the controlled object:

- normal mode (horizontal wire position and the wire position, taking into account the deviation from the horizontal position when exposed to non-critical wind loads);
- the initial stage of wire misalignment (non-critical sag of the wire relative to the normal position);
- pre-emergency mode (critical sag of the wire due to possible collision with other wires and the ground);
- emergency mode (wire snagging with other wires or contact of a wire with the ground).

Figure 1 shows a block diagram of the developed IMS.

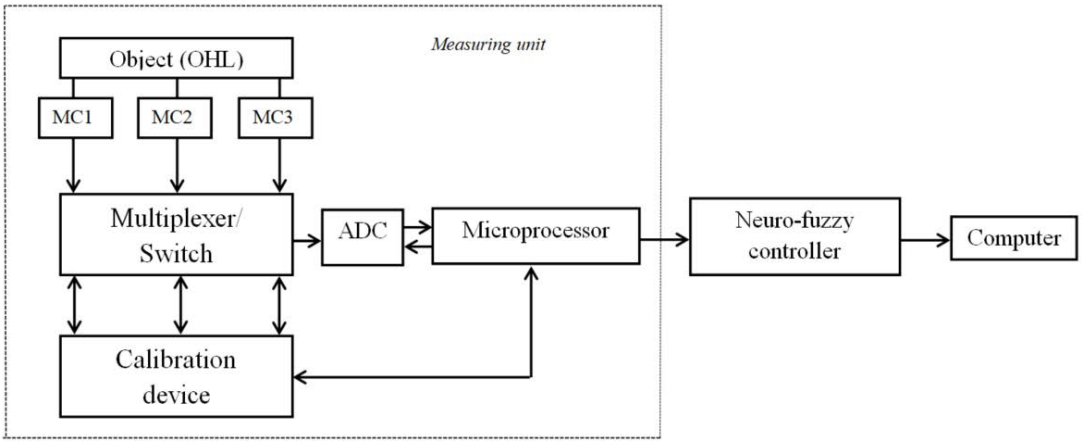

Figure 1. Block diagram of the developed IMS: MC1, MC2, MC3 - respectively, the measuring channels of the distances from the wire to the ground, wind speed, temperature; ADC - voltage-to-digital converter.

Implementation of the proposed IMS will allow: timely identification of defective areas by detecting the initial defect formation stage; to raise the level of technological management of power grid complex distribution networks; repair and maintain overhead lines according to their technical condition.

References

[1] Aydar A Mukhamadiev, I I Shaikhutdinov and Vasikh K Yasoveev 2020 Optical System for Monitoring Power Lines *2020 International Conference on Electrotechnical Complexes and Systems* (Ufa, Russia) pp 1-4

[2] Shilin A N, Shilin A A, Dementiev S S 2019 Smart Electromechanical Systems in Electric Power Engineering: Concept, Technical Realization, Prospects. In: Gorodetskiy A., Tarasova I. (eds) Smart Electromechanical Systems. *Studies in Systems, Decision and Control*, vol 174 (Springer, Cham)

[3] Khrennikov A Y 2016 Diagnostics of electrical equipment faults and power overhead transmission line condition by monitoring systems (Smart Grid): Short-circuit testing of power transformers (Nova Science Publishers)

[4] Khrennikov A Y 2012 New Intellectual Networks (Smart Grid) For Detecting Electrical Equipment Faults, Defects And Weaknesses *Smart Grid And Renewable Energy* vol 3 (1) pp 159-164

Modified quantum frequency standard on Hg-199 ions

N A Lukashev[1], V V Davydov[2, 3], V Y Rud[3]

[1]The Bonch-Bruevich Saint-Petersburg State University of Telecommunications, Saint Petersburg 195251, Russia
[2]Peter the Great Saint-Petersburg Polytechnic University, Saint Petersburg, Russia, 195251
[3]Department of Ecology, Russian Research Institute for Phytopathology, 143050, Moscow Region, Odintsovo district, B.Vyazyomy, Russia

n-lukash@list.ru

Abstract. The world around us depends on devices capable of producing or maintaining a signal with an extreme precision. Quantum frequency standards are the answer to this problem. This article presents a modified version of newly developed quantum frequency standard based on trapping Hg-199 ions by magnetic field. The new prototype was developed a while ago and now it was modified due to algorithm improvements and renewed digital hardware, analog and digital circuitry being reordered. Results for Allan deviation show 3 % improvement for long-term frequency stability and more than 5 % for short-term stability

1. Introduction

The Carrying out various scientific studies, transmitting information, determining the coordinates of an object strictly requires the use of time synchronization devices [1]. These devices have different principles of physical work, especially when applied at moving objects [2]. In some cases, instruments based on highly stable quartz are enough to ensure the operation of on-board navigation systems, radio monitoring and radar stations. In the case of operation of these devices for a long time in difficult conditions, a number of problems arise [3], especially in case of large congestion. The accuracy of determining the position of the object is reduced. The use of optical fibers and optical information processing methods [4] do not solve this problem.

The modernization process of standards' construction is not a trivial task, since the work of various blocks is related to each other. Therefore, the task of modernizing the frequency standard must be solved in a complex manner. By reducing the size and weight of the main units, the introduction of new algorithms for the automatic control system of the magnetic field and the photon registration system, the development of a system for automatic tuning of the resonant frequency, this task was realized within the framework of this work before the commissioning of the existing prototype).

2. Supplying scheme

The trap is the power consumer and the main operating unit of the Standard. For a new small-sized design of the trap and driver, a switching circuit was developed.

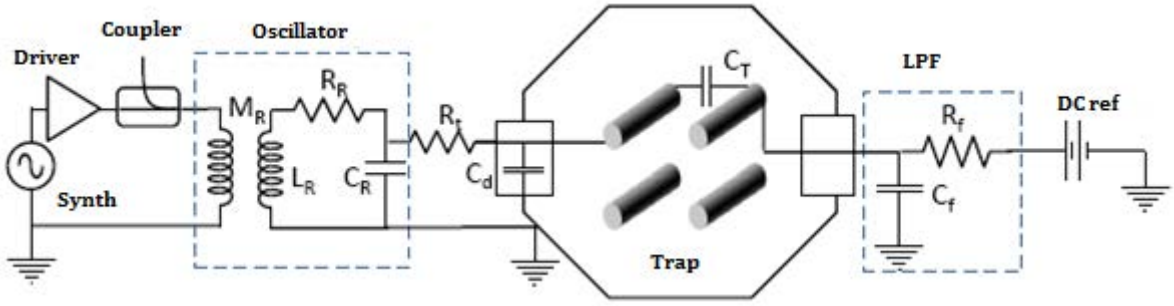

Figure 1. New supplying scheme.

To generate a signal of a certain type and control a power stage with a transformer, we have designed a miniature version of the driver. The signal is pre-amplified and sent through 2 single-shot channels to the key circuit, which accumulates energy in the primary winding of the transformer, feeding the trap electrodes. High response speed and good temperature parameters provide stable control over the RF signal.

The signals of the modulation frequency, clock frequency, as well as the input data received from the microcontroller are received at the counter input. The purpose of the counter is to generate a signal with variable count and pause windows, as well as to count photon pulses over the corresponding time interval. The counting of pulses is carried out with a positive or negative sign, depending on the half-period of the signal of the frequency synthesizer in which the photons were recorded. The resulting counting result characterizes the frequency detuning of the crystal oscillator, on the basis of which the microcontroller generates a control voltage that changes the frequency of the crystal oscillator.

After the assembly, experimental studies of the characteristics of the new prototype, as well as separately designed parts, were carried out. The signal from the driver was tested on a breadboard, which showed that there was no influence of parasitic components on the output signal spectrum. A review of residual oscillations after switching off the device was also carried out, which indicated a good tuning of the output circuit due to the absence of parasitic oscillations and dependences other than ~ exp (-t). The software was pre-tested in the ModelSim environment and then incorporated into the Standard.

3. Conclusion

The use of newly developed blocks and the use of new algorithms for automatic tuning made it possible, while reducing the size of the structure of the standard on mercury ions - 199 by three times and the weight by more than 65% compared to the previously operated ground sample and surpassing the accuracy characteristics of the standard applied on rubidium atoms: short-term (from 100 to 10,000 seconds) by 5%, and at long intervals (1 day) by 3% in comparison with previously used designs.

References

[1] Amelis Detti, Marco De Pas, Lucia Duca, Elia Perego, Carlo Sias, «A compact radiofrequency drive based on interdependent resonant circuits for precise control of ion traps», Physics.Atom-ph, 2018

[2] Davydov, V.V., Dudkin, V.I., Karseev, A.Y. «A two-channel nutation nuclear-magnetic magnetometer for remote control of the magnetic-field induction» Instruments and Experimental Techniques, 58(6), c. 787-793

[3] Jacques Vanier, Cipriana Tomescu, "The Quantum Physics of Atomic Frequency Standards: Recent Developments", T. 2, Taylor & Francis, 2015, p.468

[4] Norman F. Ramsey, "Molecular Beams", Oxford press, 1990, p. 490

Development of a fiber-optic microwave signal transmission system for an X-band receiving module with dual frequency conversion

A V Moroz[1, 2], V V Davydov[1, 3], D V Gubareva[2, 4] and V Yu Rud'[3]

[1]Peter the Great Saint Petersburg Polytechnic University, Saint Petersburg, 195251, Russia
[2]NTC JSC "Zaslon", Saint Petersburg 196084, Russia
[3]All Russian Research Institute of Phytopathology, Moscow Region 143050, Russia
[4]The Bonch-Bruevich St. Petersburg State University of Telecommunications, Saint Petersburg 193232, Russia

moroz.com3844@gmail.com

Abstract. The article discusses the use of double frequency conversion in the receiving module of the radar. To solve the resulting interference in the feeder paths, it is proposed to use a fiber-optic transmission system. The results of experimental investigations are presented.

1. Introduction

Modern radar stations with active phased antenna arrays (APAA) are used to solve an extremely wide range of problems in the field of science and technology [1, 2]. The design and study of receiving modules is an important cycle in the development of devices for radar operation. These modules are part of the receiving / receiving unit, which receives a signal from the APAA transducer, generates a probing signal and amplifies it to the level required for the APAA operation.

The development and improvement of the design of receiving modules is an urgent problem. Over the decades of work, various modernized versions of the receiver have been developed, which, in turn, require refinement and optimization [2, 3].

The receiving module is a superheterodyne radio receiver - one of the types of radio receivers based on the principle of converting the received signal into a signal of a fixed intermediate frequency (IF) with its subsequent amplification. The main advantage of a superheterodyne over a direct-amplified radio receiver is that the parts of the receiving path that are most critical for the reception quality (narrow-band filter, IF amplifier and demodulator) should not be tuned to different frequencies, which allows them to be performed with significantly better characteristics.

2. Superheterodyne radio receiver with double frequency conversion and FOTS

The main disadvantage of a direct gain receiver is the complexity of tuning from one frequency to another. It is almost impossible to make a filter with stable parameters when it is tuned in the frequency range.

In order to solve this problem, they began to divide the task into two stages - tuning in the frequency range, and ensuring selectivity in the adjacent channel. For tuning in the frequency range, they began to use the spectrum transfer to a certain (usually rather low) intermediate frequency.

Using the mixer, you can easily move the spectrum of the input signal in frequency by changing the frequency of the local oscillator [1].

Unfortunately, the superheterodyne receiver can receive both working and mirror channels. Therefore, when implementing a superheterodyne high frequency radio receiver, a contradiction arises between the requirement to reduce the intermediate frequency to facilitate cancellation of the adjacent channel in the intermediate frequency path and the requirement to increase the intermediate frequency to facilitate cancellation of the image channel. In this case, double frequency conversion is used.

One of the most vulnerable spots in APAA for interference are the feed paths from the reference signal generator and the local oscillator, since they have high requirements for frequency stability, signal-to-noise ratio and phase noise. One of our proposed solutions to this problem is the replacement of feeder paths transmitting these signals with fiber-optic transmission system, since optical fiber is not affected by high-frequency interference and has good noise characteristics when transmitting high-frequency signals, has high flexibility and low weight. Figure 1 shows a diagram of a superheterodyne receiver with a fiber-optic transmission system.

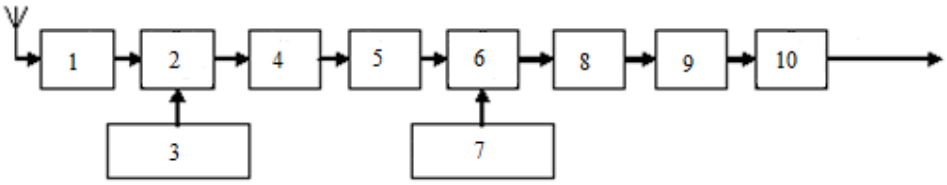

Figure 1. Block diagram of a superheterodyne radio receiver with double frequency conversion and FOTS, where 1 is an amplifier, 2 is a mixer, 3 is a local oscillator, 4 is a fiber-optic transmission system, 5 is an amplifier, 6 is a mixer, 7 is a local oscillator, 8 is a filter, 9 is an amplifier, 10 is a demodulator.

The use of the developed design allows to reduce the number of feeder paths. Provide complete isolation between receiving devices and signal processing systems.

3. Conclusion

As a result of testing the laboratory model of the FOTS developed by us, it was found that the effect of the phase incursion, which is associated with the stretching and compression of the optical fiber under the influence of temperature, on the frequency and amplitude characteristics of the transmitted optical signal is insignificant. Even with temperature fluctuations from - 30 to 50 ºC, since the distance over which the optical signal is transmitted in the APAA is less than 20 m.

References

[1] Lenets V A, Tarasenko M Yu, Davydov V V, Rodugina N S and Moroz A V 2018 *Journal of Physics: Conference Series* **1038(1)** 012037

[2] Petrov A A, Davydov V V and Myazin N S 2017 *Lecture Notes in Computer Science (including subseries Lecture Notes in Artificial Intelligence and Lecture Notes in Bioinformatics)* **10531 LNCS** 561-568

[3] Petrov A A, Grebenikova N M, Lukashev N A, Davydov V V, Ivanova N V, Rodugina N S and Moroz A V 2018 *Journal of Physics: Conference Series* **1038(1)** 012032

New nuclear magnetic resonance magnetometer design for studying variations of the mid-field magnetic strength

N S Myazin[1], **V V Davydov**[1]
[1]Peter the Great St. Petersburg Polytechnic University, St. Petersburg 195251, Russia

e-mail: myazin.n@list.ru

Abstract. The necessity to develop a magnetometer for variations research in the mid-fields magnetic strength with a relative error of 10^{-6} is justified. A new design of nuclear magnetometer with using to maser with flowing liquid is proposed. The block diagram of the magnetometer is presented, and the principle of its operation is described. The results of experimental investigations of various variations of magnetic fields are presented.

1. Introduction

In the modern world, data on the magnetic field characteristics are in demand in many areas of science and technology [1]. In most cases, it is necessary to control of magnetic field parameters with high accuracy. These problems are successfully solved using the quantum magnetometers based on nuclear magnetic resonance (NMR), which are highly accurate in time measuring of magnetic field variations [2]. There are several types of quantum NMR magnetometers. The most widely used magnetometers are based on a nuclear resonance filter [1] with a phase or frequency self-tuning of the external generator frequency to the frequency of the passive NMR line and the spin generator [2]. The first one has high requirements for the tracking system due to the very narrow NMR line. This creates several measurement problems. For example, significant dynamic errors occur in the case of temperature variations. Existing solutions of this problem significantly complicate the magnetometer design. Therefore, the upper limit of magnetic field induction measurement in most models of industrial quantum NMR magnetometers is 100 μT. To solve special tasks, laboratory versions of quantum NMR magnetometers with an upper measurement limit of up to 200 μT have been developed. These values of magnetic field induction B refer to low magnetic fields. The commissioning of new particle accelerators and tokamaks for research, the development of magnetic starting mechanisms for high-speed objects, new tasks for determining the coordinates of an underwater object at a depth with a remanent magnetization of 12 mT and much more have determined the need to control the magnetic field parameters in the range from 0.2 to 200 mT with a relative measurement error no worse than 10^{-6}.

2. Experiment and theory

Currently, the Hall effect magnetometers are used to measure mid-field magnetic strength ($0.2\ \text{mT} < B < 1000\ \text{mT}$). One of the best magnetic induction meters DX-180 has a relative measurement error of $5\cdot(10^{-5}\div10^{-4})$ in the measurement range from 10^{-5} to 0.3 T with a resolution of $10\div100$ nT. Therefore, the development of a new design of a magnetometer for measuring variations with a relative error no worse than 10^{-6} is extremely urgent.

Figure 1 shows the block diagram of the developed magnetometer. In its development, the data on the Benoit maser [3] were used. A solution of filtered tap water with alcohol is used as a liquid.

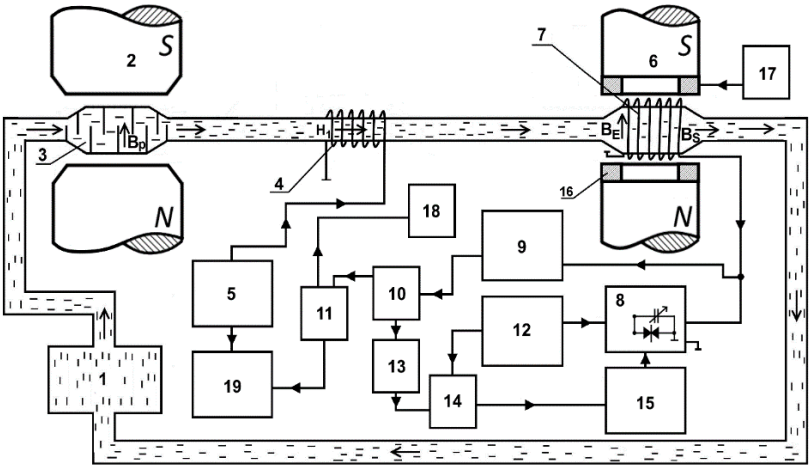

Figure 1. Block diagram of a nuclear magnetic magnetometer. Magnetometer consists of a centrifugal pump (1), polarizer magnet (2), polarizer vessel (3), pulse coil of water proton magnetization inversion (4), radiofrequency generator (5), electromagnet (6), measuring sensor (7), receiving circuit (8), regenerator (9), resonance amplifier (10), registration device (11), low-frequency generator (12), low-frequency amplifier (13), synchronous detector (14), control circuit (15), excitation coils (16), pulse radiofrequency generator (17), oscilloscope (18) and frequency meter (19).

In our nuclear magnetometer design, the transverse relaxation time T_2 is determined in two ways:

1. Using the decay time of the free induction signal when the spin system is excited by a π/2 pulse;
2. Using the decay time of the NMR signal recorded during the modulation of the magnetic field when switching the regenerator to self-excitation mode and disconnecting generator 5 from nutation coils 4 (Figure 1)

Using the relaxation time value, it is possible to evaluate variations of the magnetic field strength:

$$\Delta\omega_{\max} = 1/\left(T_2\sqrt{Q_c/Q_0 - 1}\right)$$

where Q_0 is the threshold quality factor at zero detuning, Q_c is the quality factor of the receiving circuit.

3. Results and discussion

The experiments results show that there is a wide range of variation of the expenditure q, in which the signal-to-noise ratio of the recorded NMR signal is high (more than 20). Specifically, this range is from $q_1 = 1.59 \pm 0.02$ ml/s to $q_2 = 4.74 \pm 0.05$ ml/s. In this case, a change in expenditure q (even by 10 %) will not have a significant impact on the error of measurement of physical quantities a during operating in the center of this range q.

The transverse relaxation time T_2 was determined in two ways for fluid flow $q = 3.06 \pm 0.03$ ml/s. Using free induction decay, $T_2 = 23.21 \pm 0.18$ ms was measured. Using magnetic field modulation, $T_2 = 23.04 \pm 0.23$ ms was measured. Measurements for both cases were repeated 10 times to average the data and estimate the measurement error according to standard methods.

In addition, the same solution at T = 295.3 K was studied on a Minispec mq 20M stationary NMR relaxometer (made by BRUKER company). The measured value is $T_2 = 23.198 \pm 0.065$ ms. All obtained values of T_2 coincided within the measurement error.

References

[1] Ledbetter M P, Pustelny S, Budker D, Blanchard J W and Pines A 2012 *Phys. Rev. Lett.* **108(24)** 243001
[2] Xu S, Crawford C W, Rochester S, Budker D and Pines A 2008 *Phys. Rev.* A **78(1)** 013404
[3] Benoit H, Friver P and Guibe L 1958 *Comptus Rendus* **246** 3608-14

Four-point probe stand for magnetoresistance measurement of unpatterned wafers

A N Pestova[1], O S Trushin[1]

[1]Valiev Institute of Physics and Technology of RAS, Yaroslavl Branch, 150007, Russia, Yaroslavl, Universitetskaya, 21

yablokowa-anastasia@yandex.ru, otrushin@gmail.com

Abstract. In this article a four-probe measuring stand is described. This stand is suitable for measurement magnetoresistance of unpatterned wafers with multilayer thin film structures.

1. Introduction

In the modern world, spin structures are becoming more common: spin gates, spin tunnel junctions [1]. The latter is used in the creation of memory cells. Quality control of spin tunnel structures is a very laborious and not always effective exercise.

Typically, to control the magnetoresistive effect, the spin tunnel structure is prepared by providing contact pads to the lower conductive bus and the upper layer. This preparation may be unsuccessful, as a result, the two conductive layers close together. In that case the magnetoresistive effect will not be observed. But there is another possible reason for the lack of effect: a poorly prepared multilayer structure. As a result of the above-mentioned control method, it will be impossible to determine the reason for absence of magnetoresistive effect [2]. Possible solution to that problem has been proposed in the paper [3] and called current-in-plane tunneling (CIPT) method. It is currently widely used in modern MRAM production.

This article describes a non-destructive quality control method for a multilayer spin tunnel structure capable of weeding out rejected wafers prior to production. This method is also suitable for controlling spin-valve structures, measuring AMR, etc.

2. Measuring stand

Magnetoresistive effects represents a change in the resistance of a structure in an alternating magnetic field. The resistance of such structures depends on the mutual magnetization of the magnetic layers. The measuring stand includes a 4-point probe being in a contact to the sample surface placed in an alternating magnetic field. A current is applied to two outer contacts, and the voltage is measured on the two middle contacts [3].

At this stage of development, three variants of probe heads with contact distances of 2.5 mm, 2 mm, 1.6 mm have been prepared. Work is underway to switch to submillimeter sizes. The processing of the input signal takes place on the computer. For this, a program was written in the development environment LabVIEW.

The figure 1 shows a diagram of the current flow through the sample and the equivalent circuit. The depth of current flow depends on the distance between the contacts. The signal increases as the probes approach each other. The effect of tunneling magnetoresistance is a change the resistance of the vertical resistors in the circuit.

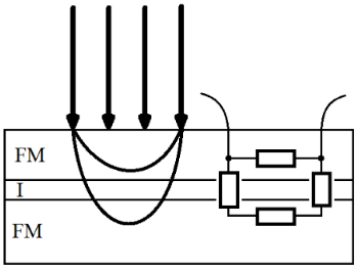

Figure 1. Diagram of the current flow through the sample and the equivalent circuit

3. Results

Measurements to control the magnetoresistive effects were carried out using probes with different distances between the contacts. The samples for measurements were spin-valve and spin tunnel structures. The figure 2 shows typical hysteresis loop for a spin tunnel structure.

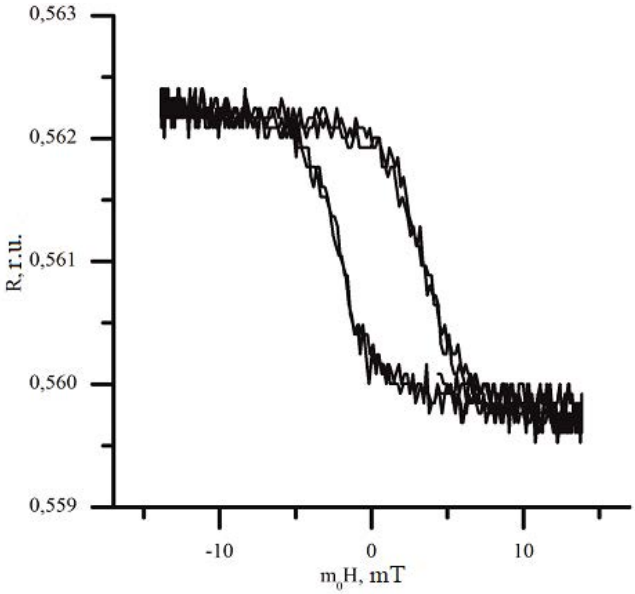

Figure 2. Hysteresis loops for probes with contact spacing 2.5 mm

4. Conclusion

This stand has shown its efficiency. Thanks to it, it is possible to carry out express diagnostics of structures for the presence of magnetoresistive effects. However, there are a number of imperfections that need to be addressed. Therefore, work on its improvement and debugging is still underway.

Acknowledgments

This work was carried out on the equipment of the center for collective use of scientific equipment "Diagnostics of micro- and nanostructures" within the framework of the State assignment of the P.I. K.A. Valiev RAS Ministry of Education and Science of the Russian Federation on topic No. 0066-2019-0003 "Fundamental and applied research in the field of creating promising instrument nanostructures for storing information on new physical principles."

References

[1] Fert A 2008 *UFN* **178** 12, 1336
[2] Trushin O S, Simakin S G, Vasiliev S V, Smirnov E A 2018 *Russian Microelectronics* **47** 6, 381
[3] Worledge D and Trouilloud D L 2003 *J. App. Phys. Lett.* **83** 84

Towards Multipixel THz Schottky Diode Detector with a Single RF Output Line

A Prikhodko[1,2], **I Belikov**[1], **D Mikhailov**[1,2], **A Shurakov**[1], **G Goltsman**[1,2]

[1]Moscow Pedagogical State University, Moscow 119435, Russia
[2]National Research University Higher School of Economics, Moscow 101000, Russia

anatprikh1995@yandex.ru

Abstract. We propose the design of a dual-pixel array of Schottky diodes. Each diode is fixed between the bow-tie antenna arms on top of a SI-GaAs membrane acting as a waveguide backshort for efficient coupling of the antenna to the feedline of high-directivity horn. The detector utilizes a single RF output line: microwave reflectometer is used for the readout. The pixels are equipped with dual-mode resonator filters to eliminate the cross-talk. We evaluate the design proposed via numerical simulation and performance tests of the array subunits: *NEP* of 300 pW/Hz$^{0.5}$ and dynamic range of 24 dB are demonstrated at 137.5 GHz.

1. Introduction

Terahertz coherent and direct detectors are in demand in numerous applications nowadays. The advantages of GaAs planar Schottky diode (PSD) direct detector are mainly related to a) its implementation-dependent time constant, which is determined only by the diode intrinsic RC-circuitry and output lines RF losses; b) decent sensitivity at room temperature; c) the ease of integration with complex RF circuits ensured by the strict control and reproducibility of the diode parameters. PSD detector also possesses a wide dynamic range beneficial in both the terahertz data transfer and medical imaging applications. However, it is difficult to combine high barrier diodes in array due to the need of DC biasing. This issue is traditionally solved via the use of Mott diodes providing low barriers resulting in high sensitivities if operated with zero-bias at room temperature. Alternatively, it is possible to use a microwave frequency comb to readout an array of Schottky diodes [1].

In this paper we report on the evaluated performance of a multipixel terahertz Schottky diode detector with a single RF output line.

2. Detector design and performance tests

In accordance with the design proposed, a dual-pixel array of Schottky diodes is arranged as follows. Each diode is fixed between the bow-tie antenna arms on top of a SI-GaAs membrane acting as a waveguide backshort for efficient coupling of the antenna to the feedline of high-directivity horn. There is only one RF output line intended for the injection of a probing microwave dual-frequency comb to readout the pixels [1] electrically connected by the Wilkinson power combiner (WPC). The pixels are equipped with miniaturized dual-mode resonator filters to eliminate the cross-talk. We evaluate the design proposed via numerical simulation and performance tests of the array subunits.

The footprint of the miniaturized band-pass filters developed for GaAs substrate is within 1.36×1.36 mm^2, which corresponds to a nearly quarter-wave linear dimension given their central

frequencies of 18.5 and 20.3 GHz; the fractional bandwidths of ~6 % ensure the pixels isolation of 19.6 dB. The insertion losses introduced by WPC are within 2.2-2.3 dB for each frequency channel, and the return losses are in the range of 15.7-19.8 dB.

The detector design adopts planar diodes with a Schottky contact diameter of 3 μm and series resistance of <30 Ω (our fabrication process is described elsewhere [2]) as sensors. It is known that Schottky diode features non-quadratic rectification characteristics at certain operating conditions [3]. Since the probing microwave power can be set for each pixel individually to tune the performance, we experimentally investigated the impact of various bias conditions (BC) of the diode on input dynamic range (*IDR*) and optical noise equivalent power (*NEP*) of the detector.

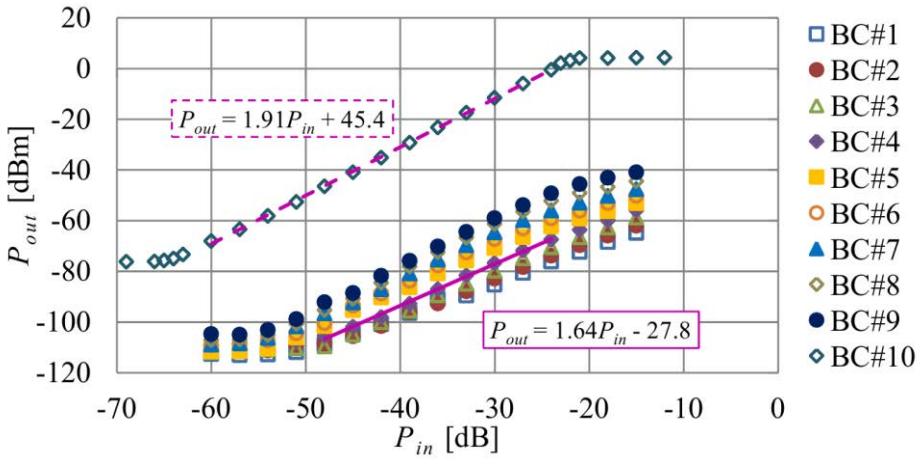

Figure 1. Linearity curves measured for a Schottky diode at different bias conditions.

In our experiments, Schottky diode is simultaneously biased by a source-meter and microwave frequency synthesizer. The latter also acts as a source of probing signal to readout the diode response to a sub-THz incident power. The output/input power ratio (P_{out}/P_{in}) is measured with the aid of a spectrum analyzer and a sub-THz CW source equipped with precision waveguide attenuator. Referring to figure 1, the slope of a "linear-response" region gradually grows from 1.34 to 1.88 along with a BC set's serial number. This corresponds to the gradual increase of the percentage of AC component (δI_{mw}) induced by the probing signal of 1.4 GHz in the diode bias current (I_b) from 1.25 % for BC#1 to 217.5 % for BC#9. We fix the DC current component (I_{dc}) to 200 μA in all the measurements and observed that $\Delta P_{out}/\Delta P_{in}$ reaches its maximum of 1.91 for BC#10, when the diode is biased by direct current solely and conventional readout scheme is employed. *IDR* > 30 dB can be achieved in both of the above readout options. The current components are related as $I_b = I_{dc}\,(1 + \delta I_{mw})$.

As a sweet-spot of the detector's linearity and sensitivity, we measured $\Delta P_{out}/\Delta P_{in}$ = 1.64, *IDR* = 24 dB and *NEP* = 300 pW/Hz$^{0.5}$ at signal frequency of 137.5 GHz for the diode biased by I_{dc} = 200 μA with δI_{mw} = 10 %. Given the capabilities of the microwave distribution network developed, it seems feasible to expand the design of a dual-pixel array of Schottky diodes to that of the linear array with a noticeably bigger number of elements.

Acknowledgments

We acknowledge support of the Russian Science Foundation grant No. 19-72-10156.

References

[1] A. Shurakov et al. 2020 *Journal of Physics: Conference Series* 1695(1) 012156
[2] A. Shurakov et al. 2018 *Microelectron. Eng.* 195 26-31
[3] T. Harter et al. 2019 *arXiv preprint arXiv*:1907.03630

The scalable production of high-quality nanographite by organic radical-assisted electrochemical exfoliation

D Savelev[1], E Grushevski[1], N Savinski[2], M Soloviev, V Turov[1] and V Krenev[1]
[1]Department of Nanotechnology in Electronics, P.G. Demidov Yaroslavl State University, Sovetskaya Street 14, Yaroslavl, 150003, Russia
[2]Valievinstitute of physics and technology of RAS, Yaroslavl Branch, Universitetskaya 21, Yaroslavl, 150007, Russia

dmitriy.savelev9@mail.ru

Abstract. The rapid increase in electromagnetic interference has received a serious attention from researchers who responded by producing a variety of radar absorbing materials especially at high gigahertz frequencies. Ongoing investigation is being carried out in order to find the best absorbing materials which can fulfill the requirements for smart absorbing materials which are lightweight, broad bandwidth absorption, stronger absorption etc. Therefore, this article introduces the electromagnetic wave absorption mechanisms and then reveals and reviews those parameters that enhance the absorption performance.

1. Introduction

With the development of electromagnetic technology, the problem of electromagnetic hazard is becoming more and more serious. So, the roles of electromagnetic absorption are attracting more attention in the military and civilian. Electromagnetic wave absorption coating, as an important means of radar wave absorption material, has a wide range of application. Because few materials in nature can respond to THz frequency, and because there is a lack of effective THz sources and detectors, it still remains a big challenge to effectively manipulate THz waves. Recently, graphene has been demonstrated as a viable alternative in realizing THz absorbers because of its high THz absorption and tunability of surface conductivity. The absorption of electromagnetic energy (EME) is due to dielectric, magnetic and conductivity losses, which are trying to maximize to achieve the maximum efficiency of shielding. Composite materials appear to provide the most attractive and promising solution to demands for lightweight, high-performance structures. Since composite materials have high specific strength and stiffness compared with bulk materials, the range of their applications is rapidly expanding from aerospace and military use to commercial activities.

2. Factors influence the electromagnetic wave absorption

Ferrites are considered to be the best magnetic material for electromagnetic wave absorbers due to their excellent magnetic and dielectric properties, but they are expensive and heavy. On the other hand, the use of polymers to protect the electronic devices from EME is popular due to the light weight, flexibility and cost-effectiveness. Here we report a method based on generation of materials with a wide range of adjustable electrical and magnetic properties: conductive polymers (polyanilines), flaky nanographite, nano - structured granular composites. A portable radar was used to study the absorption properties of electromagnetic radiation. The radar signal was processed using the

consistent filtering method. The consistent filtering assumes finding the filter response in the form of convolution of the radar input signal x(t) and the pulse characteristic of the filter $h(t_0-t)$, consistent with the probe radar signal. With this processing in the output signal of the matched filter (SF) z(t), the maximum signal-to-noise ratio is achieved by the accumulation of the useful signal energy and suppression of out-of-band noise. Additional measures may be used to suppress possible interference [1]. The test sample (target) was located to be in the Fraunhofer zone (far field) at a distance from two pairs of broadband radar antennas with a circular aperture of 5 cm and a beam half-width of 20°. The reflection measurements were carried out at incidence angles of 0°, 60°, 120° to the normal. For each sample, values were averaged over 100 parallel signals; the obtained data were averaged over 32 more polarizations and over 3 angles of incidence. The received data were normalized by the average reflection value of the sample of a fiberglass substrate without an absorbing coating.

As a target we used fiberglass in the form of an isosceles triangle with an edge 300 mm long, 0.8 mm thick, 390 cm^2 in area, weighing 33g. The cover was applied by pouring and with a flat brush, in the form of several layers with sequential drying at 80°C. As a binder was used a 30% (dry solids) water solution of polyvinyl acetate emulsion DF 50/5N. The dispersion of solids in the emulsion was carried by using a laboratory mechanical dispersant for 20 minutes. The thickness of the target coveris 50-170μ.

Table 1. Types of polymer matrix, filler, filler's particle size and its absorbing properties.

№ sample	Structure	Filler's particle size	Coating density (g/cm^2 10^{-2})	Reflection loss (dB) at 10 GHz
1	$BaFe_{12}O_{19}$ (Ferrite in the form of small balls, 3 mm in one layer (magnetized balls))	Barium ferrite3 mm.	94.0	-14.3
2	$BaFe_{12}O_{19}$ (1: 1 by mass to mass of 30% emulsion)	Barium ferrite 30μ	10.0	-11.2
3	Nanographite:1: 1 by mass to mass of 30% emulsion , 0.1% Syntanol-10,	Nano graphite 10-100μ	4.7	-14.4
4	Aluminum Powder PAP2 1: 1 by mass to mass of 30% emulsion ,	Aluminum powder 20-30μ	4.6	-11.8
5	PANI (Emeraldine salt, sulfonic acids)	Polyaniline	3.7	-13.3
6	Ultra-wide flexible radar absorbing material based on nanostructured ferromagnetic microwire [2].	JSC «CDB RPM» МРПК-1Л	10.0	-17.0

3. Conclusion

As a result, the nanographite coating has a power reflection coefficient of -14.4 dB. This value is close to the material МРПК-1Л (- 17 dB) [2]. But the advantage of nano-structured granular composites, particularly, nanographite is that coating thickness and weight less than competitors with the same degree of reflection and absorption of an electromagnetic waves.

Acknowledgments

This This research was financially supported within the framework of the state assignment of the Valiev Institute of Physics and Technology of the Russian Academy of Sciences Yaroslavl Branch of the Ministry of Education and Science of the Russian Federation on the topic No. 0066-2019-0003. Some experimental results were obtained on the equipment of the Center for Collective Use "Diagnostics of Micro-and nanostructures" with the support of the Ministry of Education and Science of the Russian Federation. We would like to thank A. Dubov an application ferrite of JSC «Ferros» Yaroslavl.

References

[1] Turov V E 2011 *Radar warfare. Construction and noise protection of basic correlation systems of passive location: Monograph.-M* (*Vuzovskaya kniga*) pp 205

[2] Available at:http://www.ckbrm.ru *electromagnetic wave absorber* Patent RU 2322735 C1.

Research Of Dynamic Characteristics Of A Three-axis Micromechanical Gyroscope-Accelerometer

I E Lysenko[1], D Y Sevostyanov[1], N F Kidyaev[1], A V Kovalev[1]
[1] Southern Federal University, Taganrog 347900, Russia

Abstract. In this paper, an original design of a micromechanical gyroscope-accelerometer is proposed. A parametrizable geometric and finite element model of a micromechanical device is presented. The dynamic characteristics of the structure are studied and the dependences of the natural oscillation frequencies on the geometric parameters of the gyroscope-accelerometer are obtained.

1. Introduction

The market of modern electronics puts developers before the need to improve the weight and size characteristics, increase energy efficiency and reduce the cost of the developed devices. Microelectromechanical devices (MEMS) are actively used in many systems, such as virtual reality devices, medical equipment and aerospace navigation systems [1, 2]. Therefore, the development of a micromechanical gyroscope-accelerometer with three axis of sensitivity, which allows measuring linear velocity and angular acceleration, and is a single device made on a single substrate in a single technological cycle, is an urgent task [3, 4].

2. Design and simulation

The developed original design of a micromechanical gyroscope-accelerometer with three axis of sensitivity is shown in Figure 1 [5, 6].

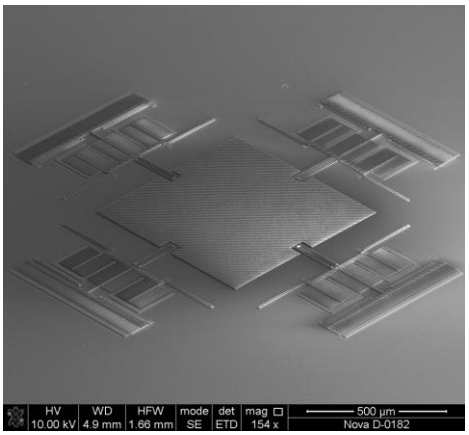

Figure 1. Design of the developed micromechanical gyroscope-accelerometer

This device has the ability to measure the values of angular velocities and linear acceleration along the X- and Y- axis located mutually perpendicular in the plane of the substrate, and the Z-axis directed perpendicular to the plane of the substrate. A special feature of the design is two inertial masses located one inside the other. It is assumed that this will improve the accuracy of recording linear acceleration along the Z-axis and reduce the values of the natural frequencies of oscillations along the X- and Y-axis.

The ANSYS program system was used for the research. In particular, the Mechanical APDL module was used to analyze the dynamic characteristics of the developed gyroscope-accelerometer. The result of the modal analysis of the developed design along the X- and Z-axis is shown in Figure 2.

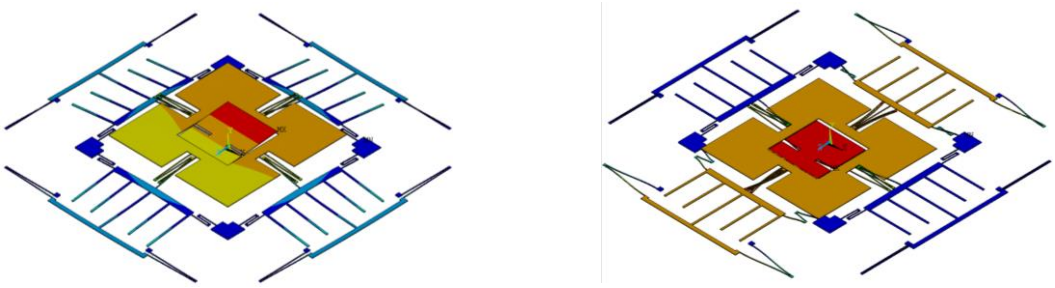

a b

Figure 2. The result of the modal analysis of the developed design along Z-axis **a** and X-axis **b**

3. Conclusion

In this paper, the design of a micromechanical sensor for linear accelerations and angular velocities was proposed, and the dynamic characteristics of a gyroscope-accelerometer were modeled. The simulation results revealed the dependence of the natural frequencies of vibrations on the geometric parameters of the micromechanical device.

4. Acknowledgments

The work was carried out at the expense of funds, task No. FENW-2020-0022 for the implementation of scientific research carrying out scientific research at the expense of the federal budget, in terms of scientific activities on the topic "Development and research of methods and means of monitoring, diagnostics and forecasting state of engineering objects based on artificial intelligence".

References

[1] Raspopov V Ja 2007 *Micromechanical devices* (Tula: Tul'skijgosudarstvennyjuniversitet)

[2] Lysenko I E Ezhova O A Tkachenko A V Naumenko D V 2020 Analysis of the micromechanical three-axis accelerometer *Book of Abstracts of 7th International School and Conference «Saint Petersburg OPEN 2020» on Optoelectronics, Photonics, Engineering and Nanostructures* (St. Petersburg: St. Petersburg Academic University) pp 449-450.

[3] Lysenko I E, Naumenko D V and Ezhova O A 2020 Design and simulation high aspect ratio torsion suspension of MEMS z-axis accelerometer *Book of Abstracts of 7th International School and Conference «Saint Petersburg OPEN 2020» on Optoelectronics, Photonics, Engineering and Nanostructures* (St. Petersburg: St. Petersburg Academic University) pp 478-479

[4] Lysenko I E 2019 The results of modelling of a micromechanical accelerometer *Journal of Physics: Conference Series* 1410 012226 DOI:10.1088/1742-6596/1410/1/012226

[5] Lysenko I E Yezhova O A Sevostyanov D Yu Konoplev B G Patent for invention No. 2716869 "Integral micromechanical gyroscope–accelerometer".

[6] Nanotechnology in microelectronics / Edited by Ageev O A and Konoplev B G – M.: NAUKA 2019 – 511p ISBN 978-5-02-040201-0

Silicon carbide of 4H-SiC type Schottky diode current-voltage characteristics in small-sized type metal-polymeric package SOT-89

S V Sedykh, S B Rybalka, A A Demidov, E A Kulchenkov
Bryansk State Technical University, Bryansk, 50 let Oktyabrya 7, Russia

Abstract. The forward and reverse current–voltage characteristics of Ti/4H-SiC Schottky diode in small-sized (SOT-89) type metal-polymeric package have been obtained. On the base of analysis it is shown that Schottky diode corresponds to the "ideal" diode with ideality factor $n \approx 1.012$ and effective Schottky barrier height $\varphi_B = 1.23$ eV.

1. Introduction

It is known that the silicon carbide (SiC) Schottky diodes are key component of power semiconductor electronics devices for high-temperature device applications because of its high breakdown voltage, low series resistance and stability under high temperature conditions [1]. Now modern power electronic industry comes down to use of small type of metalpolymeric package such as SOT (Small Outline Transistor), QFN (Quad Flat No-leads) and others [2], but in Russia manufacture of the main electronic components earlier was produced in standard large-sized package (DIP (Dual In-line Package), TO (Transistor Outline) and others) type. Therefore, recently by electronic company the «GROUP KREMNY EL» (Bryansk, Russia) the production of SiC Schottky diodes for power electronics began within the framework of import substitution program. In our previous studies were investigated some characteristics of the SiC Schottky type diodes made in small type of metalpolymeric packages [3]. In this study the main goal is establish current-voltage characteristics of Ti/4H-SiC Schottky diode made in small-sized (SOT-89) type of metalpolymeric package.

2. Materials and methods

In experiments was tested the following Ti/4H-SiC type Schottky diode DDSH411A91 (JSC «GRUPPA KREMNY EL», Bryansk, Russia) in small-sized SOT package type (SOT-89, package dimensions – 4.6×2.6 mm). The parameters of Ti/4H-SiC type Schottky diode were the following: the concentration of donors (nitrogen) in the substrate equals 10^{18} cm^{-3} (thickness of substrate is 300 μm), concentration of donors in the *n*-type epitaxial layer (nitrogen) equals 4.75×10^{15} cm^{-3}, concentration of p+ donors in the guard rings (boron, depth of guard about 2 μm) regions 10^{18} cm^{-3}, the guard p+ rings consist from one of big guard ring with width of 30 μm and five small guard rings with width of 5 μm (the distance between guard rings was 5 μm), JTE (Junction Terminate Extension) layer formed by boron implantation with p+ concentration 4.75×10^{17} cm^{-3} (extending 30 μm beyond the edge of the last p+ guard ring), anode material is Ti (titanium), the thickness of the epitaxial layer (4H-SiC) was 14 μm, the radius of the diode equals r=680 μm. For measuring the direct and reverse current-voltage characteristic were used a programmable source AKIP 1144-160-40, Tektronix MDO3102 two-channel oscillograph (bandwidth 1 GHz, refresh rate 5 GS/s) and Fluke 8845A digital multimeter.

3. Results and discussion

In Figure 1 is shown the forward current-voltage characteristic for DDSH411A91 Schottky diode in small-sized SOT-89 type package obtained at temperature of 25°C. Further, in Figure 2 presents the reverse current-voltage characteristics for DDSH411A91 Schottky diode (25°C). As follows from current-voltage characteristic the fabricated DDSH411A91 Schottky diode in small-sized package operate with forward current up to 2 A and breakdown voltage 1200 V in reverse direction mode.

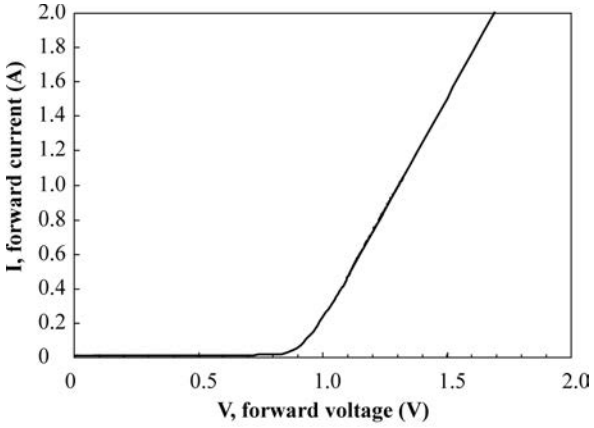

Figure 1. Ti/4H-SiC Schottky diode DDSH411A91 in small-sized SOT-89 type package forward current-voltage characteristic.

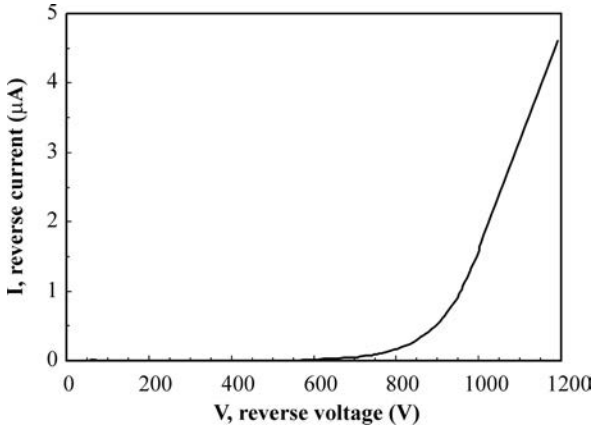

Figure 2. Ti/4H-SiC Schottky diode DDSH411A91 in small-sized SOT-89 type package reverse current-voltage characteristics.

Analysis of experimental results in framework of classical diode theory [1,4] shows that ideality factor of DDSH411A91 diode equal 1.012 and effective Schottky barrier height φ_B=1.23 eV.

4. Conclusions.

Forward and reverse current-voltage characteristic for DDSH411A91 (Ti/4H-SiC) Schottky type diode in small-sized SOT-89 metalpolymeric package were obtained. It is shown that fabricated Ti/4H-SiC Schottky diode demonstrate current up to 2 A in forward direction and breakdown voltage 1200 V. It is established that ideality factor of diode is 1.012 and effective Schottky barrier height φ_B=1.23 eV.

Acknowledgements

This work was carried out with financial support of the Russian Ministry of Science and High Education within the framework of complex project by creation of highly technological industry «Creation of highly technological industry of silicon and silicon carbide microelectronic technics products in small-sized metal-polymeric packages of the SOT, SO and QFN types» (agreement of 29 November No. 075-11-2019-035) at the organization of the leading performer of RDDTE (Research and Development Design and Technological Engineering) the Bryansk State Technical University.

References

[1] Baliga B J 2019 *Wide Bandgap Semiconductor Power Devices: Materials, Physics, Design, and Applications* (Cambridge: Woodhead Publishing–Elsevier)

[2] Lu D, Wong C P 2017 *Materials for advanced packaging* (Cham: Springer International Publishing)

[3] Rybalka S B, Kulchenkov E A, Demidov A A, Zhemoedov N A, Drakin A Yu, Zotin V F, Shishkina O A 2020 *J. Phys.: Conf. Ser.* **1679** 022045

[4] Ivanov P A, Grekhov I V, Il'inskaya N D, Kon'kov O I, Potapov A S, Samsonova T P, Serebrennikova O U 2011 *Semiconductors* **45**(5) 668

Structural, magnetic and electrical properties of the Co_2MnZ (Z = Al, Si, Ga, Ge) Heusler compounds – promising magnetic materials for spintronics

A A Semiannikova[1], Yu A Perevozchikova[1], E B Marchenkova[1] and V V Marchenkov[1,2]

[1]M.N. Mikheev Institute of Metal Physics, UB RAS, S. Kovalevskaya str., 18, 620108, Ekaterinburg, Russia
[2]Ural Federal University, Mira St., 19, 620002, Ekaterinburg, Russia

e-mail: semiannikova@imp.uran.ru

Abstract. Heusler compounds are promising materials for spintronics because of a high degree of the charge carriers spin polarization. Such compounds can be used as injectors of spin-polarized carriers in nanostructures. States of a half-metallic ferromagnet and a spin gapless semiconductor can be realized in the Co_2MnZ (Z = Al, Si, Ga, Ge) system of compounds. The structural, magnetic, and electronic transport properties of the Co_2MnZ (Z = Al, Si, Ga, Ge) Heusler compounds, the regularities of their behaviour, and the possible relationship with the degree of the current carriers spin polarization were studied. The magnetization and electrical resistivity were measured in the temperature range from 4.2 to 300 K in magnetic fields up to 30 kOe.

1. Introduction

In half-metallic ferromagnets (HMFs) and spin gapless semiconductors (SGSs) based on Heusler compounds, close to 100% spin polarization of charge carriers can be realized. Consequently, these new materials are promising for use in spintronic devices [1]: they can be used in nanostructures as injectors of spin-polarized carriers. At the Fermi level, HMF and SGS for electronic states with spin "down" have a wide ($\Delta E \sim 1$ eV) gap, while for the opposite spin projection in the HMF there is no gap, and in SGS there is a zero energy gap [2, 3].

States close to HMF and / or SGS are observed in the Co_2YSi (Y = Ti, V, Cr, Mn, Fe, Co, Ni) Heusler compounds (see, for example, [4]). Apparently, such states can also appear in other Co-based Heusler compounds, in particular, in the Co_2MnZ system (Z = Al, Si, Ga, Ge) upon varying the Z-component, which should inevitably manifest itself in their electronic transport and magnetic properties. Thus, the purpose of this work is to study the structure, magnetic and electrical properties of the system of compounds Co_2MnZ (Z = Al, Si, Ga, Ge), to establish the regularities of their behavior and the possible relationship with the degree of spin polarization of current carriers.

2. Experimental

The Co_2MnZ (Z = Al, Si, Ga, Ge) Heusler compounds were prepared by arc melting methods in a purified argon atmosphere and annealed at 800K during 48h. The atomic content of elements in the

polycrystalline alloy was monitored using an FEI Company Quanta 200 scanning electron microscope equipped with an EDAX X-ray microanalysis unit. All samples were formed in $L2_1$ structure.

3. Results and discussion

As a result of the studies carried out, it was found that with a change in the *Z*-component, the residual resistivity ρ_0, the saturation magnetization M_s, change significantly, and there is a correlation between them as well and the spin polarization coefficients known from the literature. The normal and anomalous coefficients of the Hall effect, type and mobility of charge carriers were found. Based on the results obtained, it was suggested that the Co_2MnSi compound can be used as an injector for spin-polarized electrons in spintronic devices.

Acknowledgments

The work was carried out within the framework of the state assignment of Ministry of Science and Higher Education of the Russian Federation (theme "Spin" No. AAAA-A18-118020290104-2), with partial support from the RFBR grant (project No. 20-32-90065) and the Government of the Russian Federation (Resolution No. 211, contract No. 02.A03.21.0006).

References

[1] Viglin N A et al. 2017 *Phys. Rev. B* **96** 235303
[2] Katsnelson M I et al. 2008 *Rev. Mod. Phys.* **80** 315
[3] Wang X L 2008 *Phys. Rev. Lett.* **100** 156404
[4] Perevozchikova Yu A et al. 2019 *Low Temp. Phys.* **45** 789

Electrophysical properties of SnO_2-ZnO thin films prepared by sol-gel method

V Yu Storozhenko[1], M G Volkova[1], A P Starnikova[2], V V Petrov[2], E M Bayan[1]

[1]Department of Chemistry, Southern Federal University, Rostov-on-Don, 344090, Russia,
[2]Research and Education Centre "Microsystem technics and multisensor monitoring systems", Southern Federal University, Taganrog, 347922, Russia

vstorozhenko@sfedu.ru

Abstract. Electrophysical properties of SnO2-ZnO thin films prepared by sol-gel method have been studied. Thin films have a temperature hysteresis of resistance, which is more distinct for films with the Sn: Zn molar ratios of 0.5: 99.5 and 1:99.The films resistance decreases up to two times when the temperature reaches 210-300 °C and returns to its initial value when cooling down to 90-30 °C.

1. Introduction

Thin films of semiconductor oxide materials are widely used in microelectromechanical systems, electronic devices, etc. One of the most used is a composite material based on mixed oxides of Zn(II) and Sn(IV) due to the combination of their high chemical stability, non-toxicity, and unique electrophysical properties [1]. The sol-gel method is the simplest method for producing films of complex composition [2]. The aim of this work was to synthesize SnO2-ZnO thin films with a Sn:Zn molar ratio from 0.5:99.5 to 5:95 by the sol-gel method and study their properties

2. Experiment

To obtain thin film materials by the sol-gel method, $SnCl_4 \cdot 5H_2O$, $Zn(NO_3)_2 \cdot 6H_2O$ and isopropanol were used. The Sn (IV):Zn (II) ratio in solutions was 0:100, 0.5:99.5, 1:99, 5:95 by mole. Calcination was carried out for 2 hours at 550 ºC. The phase composition of the obtained films was studied by the X-ray diffraction (XRD) using a diffractometer ARLX'TRA, Thermo ARL (Switzerland) with CuKα X-rays. The morphology and thickness of the films studied by scanning electron microscope (SEM) on an EMXplus 10/12 Bruker (Germany). The study of the electrophysical properties of the film samples was carried out according to the previously described method [3].

3. Results and discussion

According to XRD data, all the obtained materials are nanosized, insufficiently crystallized, and contain cassiterite and wurtzite phases. SEM data show that the surface and thickness of the films are inhomogeneous. The cross section shows that nanoscale films have a porous structure and an average thickness of about 120-130 nm. The thickness reaches 400-500 nm in some places, which

is typical for films formed by the sol-gel technology [2]. Temperature dependences of the resistance (R) measurements showed that the resistance of pure ZnO is 20% higher than that for films 0.5SnO2:99.5 ZnO and 1SnO_2:99ZnO, and 30% higher than that for material 5SnO_2:95ZnO (Fig. 1), which correspond with the another research works [3].

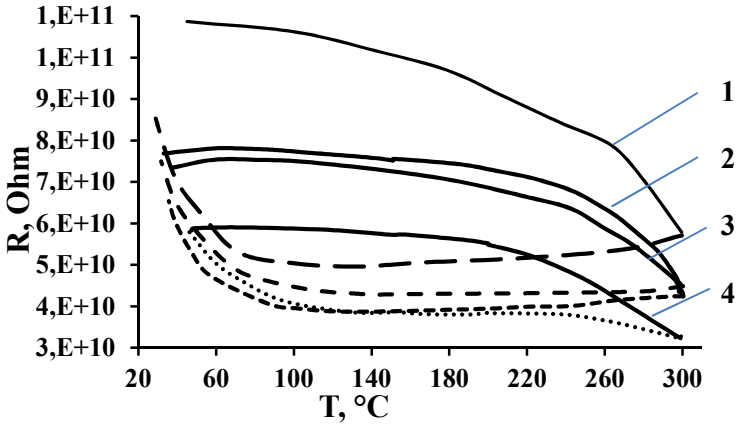

Figure 1. Temperature dependence of the resistance for films materials ZnO (1); 1SnO_2:99ZnO (2); 0,5SnO_2:99,5ZnO (3); 5SnO_2:95ZnO (4) obtained by sol-gel method

Changing the temperature dependence of the resistance showed that the temperature hysteresis of the resistance is observed in SnO_2-ZnO films, which is most distinct for films with the molar ratio Sn:Zn equal to 0.5:99.5 and 1:99. When the temperature increases from 30 to 210-240 °C, the resistance of the films changes insignificantly. With further heating up to 300 °C, resistance decreases almost twice. When the temperature decreases from 300 °C to 100-90 °C, the resistance reaches the minimum value (and even slightly decreases), and when cooling down to 30°C, increases to the initial value.

This phenomenon can be explained by the existence of several electrical conductivity mechanisms – temperature generation of charge carriers, adsorption-desorption processes of oxygen and water molecules on the films surface, and a possible reversible mechanism of electric current flow through different phases existing in the films.

4. Conclusion

Thin SnO_2-ZnO films have a temperature resistance hysteresis, which is most distinct for films with a molar ratio of Sn:Zn equal to 0.5:99.5 and 1:99. The films resistance decreases up to two times when the temperature reaches 210-300 °C and returns to its initial value when cooling down to 90-30 °C.

Acknowledgments

The present study was performed with financial support of RFBR, project number 20-07-00653 A.

References

[1] L. Schmidt-Mende, J.L. MacManus-Driscoll, ZnO–nanostructures, defects, and devices, *Materials today*, **10(5),** 40-48 (2007).

[2] V.V.Petrov, N.K.Plugotarenco, T.N.Nazarova, A.N. Korolev Preparation of Sols from Water–Alcohol Solutions of Tetraethyl Orthosilicate and $SnCl_4$ and the Effect of Sol Composition on the Surface Morphology of Sol–Gel Films *Inorganic Materials*, **43**, 9, 1010–1014 (2007),

[3] V.V. Petrov, E. M. Bayan, S. A. Khubezhov, Y. N. Varzarev and M.G. Volkova, Investigation of Rapid Gas-Sensitive Properties Degradation of ZnO–SnO_2 Thin Films Grown on the Glass Substrate, *Chemosensors*, **8(2),** 40 (2020).

Monolithic transistor switch for microwave radiometry

V G Tikhomirov[1], Y V Solov'ev[2], A G Gudkov[3,4,5], M K Popov[1], S V Chizhikov[3]

[1] Saint-Petersburg State Electrotechnical University "LETI", St. Petersburg 197376, Russia
[2] Closed Joint Stock Company "Svetlana-Electronpribor", St. Petersburg 194156, Russia
[3] Bauman Moscow State Technical University, Moscow 105005, Russia
[4] Peoples' Friendship University of Russia, Moscow 117198, Russia
[5] "Microwave radiometry global excellence" ltd., Moscow 115201, Russia

Abstract. Modern medical microwave diagnostic equipment requires the application of solutions related to the compactness of the developed devices and high performance. Ensuring these requirements is possible by using a modern semiconductor component base based on A^3B^5 compounds. One of the promising materials for this purpose is gallium nitride. The paper presents the design and manufacturing technology of one of the main control elements of the microwave signal in microwave radiothermometer - monolithic AlGaN/GaN/SiC HEMT SPDT transistor switch.

1. Introduction

Recently, the method of microwave radiometry, which has a number of advantages over traditional diagnostic methods, has been rapidly developing for the use in various fields of human activity. Today, a promising method for measuring soil moisture, based on the use of microwave radiometric sensors of various wavelength ranges, is in the process of implementation into commercial operation. In addition, microwave radiothermometry is actively developing for the functional study of human tissues and organs, which allows non-invasive detecting thermal heterogeneities in them, performing early diagnosis of cancer and correcting the treatment process by changing the parameters of electromagnetic radiation of tissues and organs [1-2].

2. Results

A domestic epitaxial HEMT structure grown by gas-phase epitaxy on a semi-insulating silicon carbide substrate with a diameter of 76.2 mm produced by Closed Joint Stock Company "Svetlana-Electronpribor" was used when developing the manufacturing technology of the transistor switch.

In the framework of this project, numerical modeling and experimental optimization of heterostructures design of high-electron-mobility transistors (HEMT) were carried out on the basis of the developed models and calibrations for AlGaN/GaN material systems.

The design of the monolithic switch was determined by the scope of developed radiometer application. The main requirements for switches are miniaturization and ensuring low insertion loss values and high decoupling values over a wide frequency range. The most sensitive to the response of the

microwave signal from the biological research object radiometers operate in the frequency range of 0.5-3 GHz. Another essential requirement for the developed element base is to ensure the radiometer ability to receive a signal and calibrate by "hot" and "cold" temperature load. Based on these requirements, the design of the SPDT type transistor switch (one input-two outputs of the microwave signal) with a minimum topological size of 0.4 microns was selected to ensure reliable operation in the specified frequency range (Fig. 1).

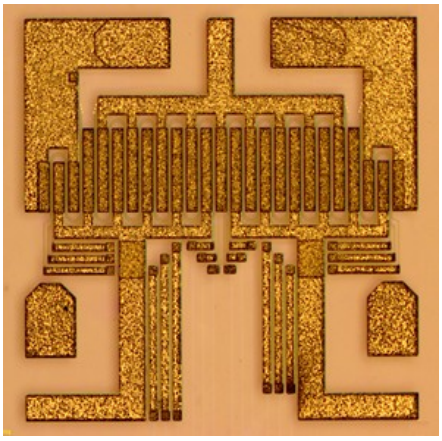

Figure 1. Fragment of the crystal HEMT AlGaN / GaN SPDT switch on the plate.

3. Conclusion

Thus, the design and manufacturing technology of the HEMT AlGaN/GaN SPDT switch on a domestic heterostructure on a semi-insulating silicon carbide substrate are presented. The measurements of the microwave parameters of the developed switch show the possibility of using this element component base as part of microwave radiometers, which will allow combining the principles of multi-channel, multi-frequency and miniaturization in one radiometric complex and will lead to the expansion of its functionality and a significant reduction in size.

The research is carried out to the research project No. 19-19-00349 on the theme: “Development of a methodology and a multichannel multifrequency microwave radiothermograph on the basis of monolithic integrated circuits for finding the 3D distribution and dynamics of brightness temperature in the depths of the human body” (Russian Science foundation).

References

[1] Gulyaev Yu.V., Leushin V.Yu., Gudkov A.G., Schukin S.I., Vesnin S.G., Kublanov V.S., Porohov I.O., Sedankin M.K., Sidorov I.A. Pribory dlya diagnostiki patologicheskih izmeneniy v organizme cheloveka metodami mikrovolnovoy radiometrii. Nanotekhnologii: rzrabotka, primenenie – XXI vek. 2017. T.9. № 2. S. 27-45 (In Russian)

[2] I. Sidorov, A. Gudkov, E. Novichikhin, A. Taradin, R. Haarbrink and C. Sergey, "The specific of 3D passive radars sensing alive and non-alive objects," *2019 International Conference on Engineering and Telecommunication (EnT)*, Dolgoprudny, Russia, 2019, pp. 1-4.

Design and analysis of the inline RF MEMS switch for application in 5G mobile networks

A V Tkachenko[1], I E Lysenko[1], A V Kovalev[1], D V Vertyanov[2]
[1]Southern Federal University, Rostov-on-Don region, Taganrog, 347922, Russia
[2]National Research University of Electronic Technology, Zelenograd, Moscow, 124498, Russia

Abstract. This article presents the results of the design and analysis of a radio-frequency switch made using microelectromechanical systems technology. The device is the capacitive shunt switch with a hybrid type of contact, in which the movable electrode of the structure – the membrane is part of the microwave transmission line of the coplanar waveguide and the shunt connection with the ground line of the coplanar waveguide is applied directly to the surface of the dielectric substrate. In addition, the switch design is characterized by a high capacitance ratio, obtained by using an additional fixed metal-insulator-metal capacitor. As the material of the insulation layer, a material with a high dielectric constant – titanium oxide is used. To reduce the value of the actuation voltage and increase the speed of the switch, the zig-zag elastic suspension is used. According to the results of the finite element analysis, the value of the actuation voltage is 2 V with a short switching time to the close state – no more than 7 us. The closure during the movement of the membrane occurs when a mechanical force of 0.33 uN is applied. Based on the results of the analysis of the scattering parameters, it follows that the central resonant frequency of the switch is a frequency of 3.8 GHz. In this case, in the open state, the value of the insertion loss is not more than -0.2 dB and the isolation value in the close state is not less than -55 dB. The effective frequency range is the S-band, as well as the C-, X-, and Ku-band, in which the isolation value is at least -30 dB. The presented inline RF MEMS switch is suitable for use in various types of ground and satellite communications, in particular for devices and systems of 5G mobile networks.

1. Introduction

In the last decade, devices manufactured using microelectromechanical systems (MEMS) technology have undergone tremendous development in various fields of information and communication technologies. One of the most promising areas of application of MEMS technology is associated with circuits and devices of ultra-high frequency (microwave) and radio-frequency (RF) communication. In recent years, the introduction and dissemination of new wireless communication standards, in particular the fifth generation of mobile radio communication – 5G, has set new challenges in the development of hardware for transceivers. Key RF subsystems in 5G RF transceivers include antennas, tunable filters, power amplifiers and MIMO (multiple-input multiple-output). At the same time, it can be noted that in all these RF systems or 5G subsystems, from a hardware point of view, the RF switch is one of the most fundamental and important components that is used to route signals along RF transmission paths with a high degree of efficiency; its RF characteristics, switching time, RF signal power and their reliability can directly affect the corresponding properties and performance of 5G applications. RF MEMS switches can effectively replace the currently used active semiconductor analogs based on PIN-diodes and FET-transistors at frequencies up to 10 GHz and compete with coaxial switches in the range up to 40 GHz or more.

Currently, capacitive shunt RF MEMS switches with metal-dielectric-metal contact are the most common in RF MEMS devices [1, 2]. The main reason for this type of RF MEMS switches is the imperfect roughness of the contacting layers, which leads to a decrease in the capacitance ratio of this type of RF MEMS switches. A decrease in the capacitance ratio, in turn, leads to a shift in the resonant frequency from the required one and a decrease in the isolation value in the close state of the RF MEMS switch.

To overcome the described disadvantages, an additional fixed metal–insulator–metal (MIM) capacitor on the substrate is developed and a switch is used to turn it on or off from the circuit [3, 4]. This results in a capacitance ratio that is independent of the roughness of the down electrode, and is therefore ideal for dielectrics with high permittivity and roughness. This method is also applicable to the design of RF MEMS switches with large capacitances in the close state based on nitride dielectrics. The disadvantage of this method of increasing the capacitance ratio is the high geometric dimensions of the movable switch electrode, as well as the additional contact resistance between the metal of the movable membrane electrode and the upper metal layer of the MIM capacitor.

The object of this work is to develop a design and analysis of an RF MEMS switch with a high value of the capacitance ratio, a small value of the air gap using a combined approach. This approach of increasing the value of the capacitance ratio consists in using the design of a floating metal movable electrode without restrictions of the minimum thickness of the dielectric layer and the minimum size of the air gap, as well as using the material of the dielectric layer with a high permittivity. To reduce the value of the actuation voltage and increase the speed of the switch in the presented design of the RF MEMS switch the zig-zag elastic suspension is used. In addition, the developed design of the RF MEMS switch should be characterized by a small form factor for use in RF devices and systems of 5G mobile networks.

2. Design and analysis

The 3D topology of the proposed inline RF MEMS switch is shown in Figure 1. The device is the capacitive shunt RF MEMS switch with a hybrid contact type. The membrane is part of the microwave transmission line (t-line) of the coplanar waveguide (CPW) and the shunt connection with the ground line of the CPW is applied directly to the surface of the dielectric substrate. The choice of materials is made on the basis of the results of the work [5-7].

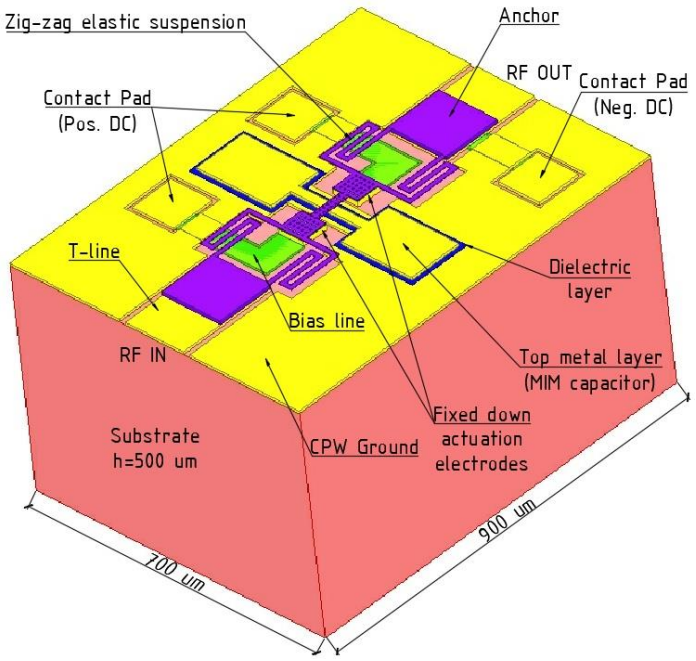

Figure 1. 3D topology of the proposed inline RF MEMS switch.

Figure 2 shows the results of the finite element analysis of the electromechanical and electromagnetic parameters of the developed inline RF MEMS switch design.

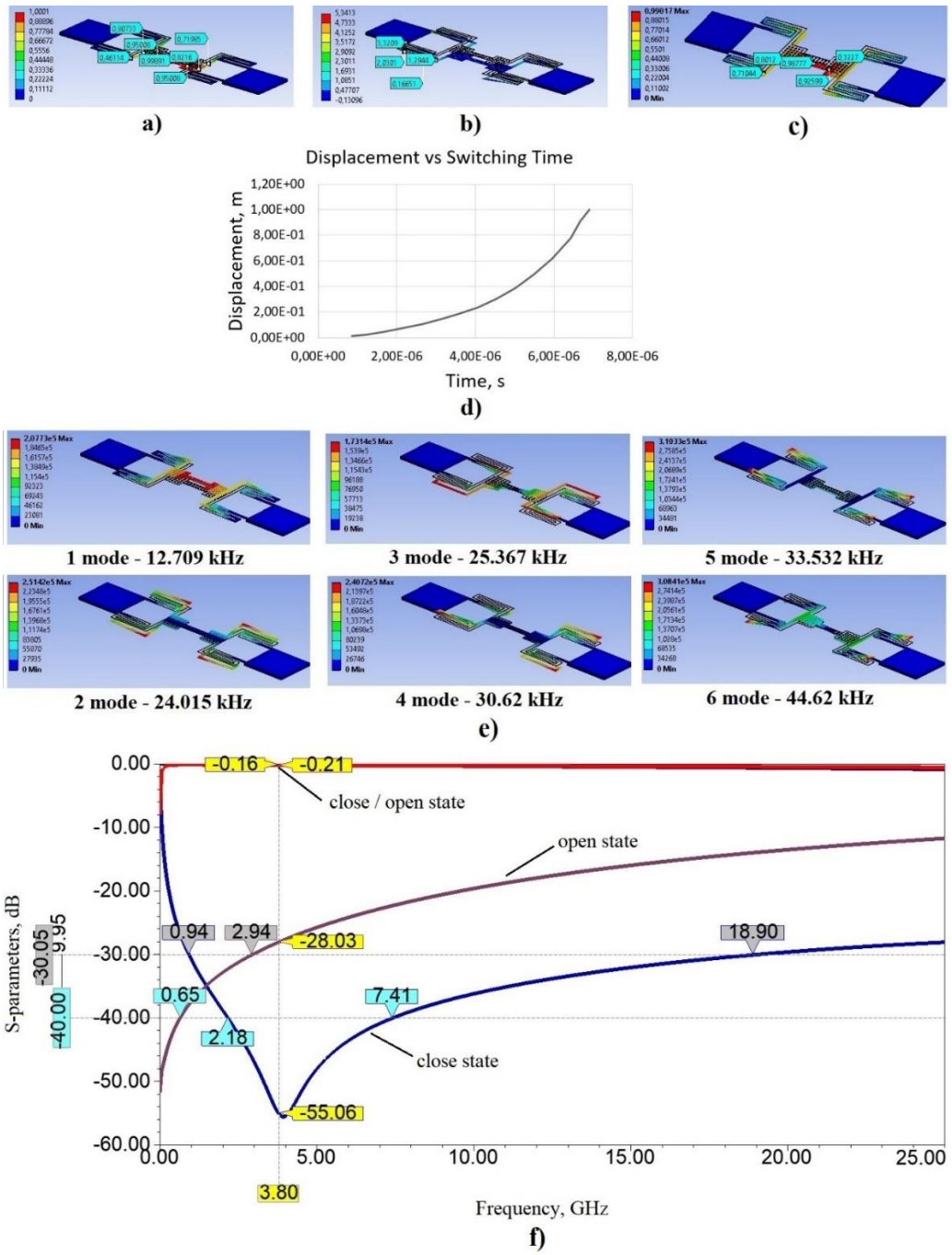

Figure 2. Finite element analysis of the developed inline RF MEMS switch design: a) displacement during electrostatic activation (V_p =2 V); b) mechanical stresses of the membrane structure and zig-zag elastic suspensions under electrostatic activation; c) displacement during the action of mechanical force 0.33 uN; d) switching time during electrostatic activation (V_s =5 V); e) modal analysis and main 6 modes of natural mechanical oscillation; f) simulation of S-parameters in open and close states.

3. Conclusion

This article presents the results of the design of the inline RF MEMS switch with a hybrid contact type. The device is the capacitive shunt switch with a hybrid type of contact, in which the movable electrode

of the structure – the membrane is part of the microwave transmission line of the CPW and the shunt connection with the ground line of the CPW is applied directly to the surface of the dielectric substrate. In addition, the switch design is characterized by a high capacitance ratio, obtained by using an additional fixed MIM capacitor. As the material of the insulation layer, a material with a high dielectric constant – titanium oxide is used. Changing the size of the titanium oxide ensures that the wave resistance ($50\,\Omega$) is matched between the RF input of the CPW transmission line and the connected load. The upper metal layer of the fixed MIM capacitor and the relatively narrow transmission line of the CPW are located under the membrane of the switch in order to obtain a low capacitance value in the upper position. To reduce the value of the actuation voltage and increase the speed of the switch the zig-zag elastic suspension is used.

According to the results of the finite element analysis, the value of the actuation voltage is 2 V with a short switching time to the close state – no more than 7 us. The closure during the movement of the membrane occurs when a mechanical force of 0.33 uN is applied. Based on the results of the analysis of the scattering parameters, it follows that the central resonant frequency of the switch is a frequency of 3.8 GHz. In this case, in the open state, the value of the insertion loss is not more than -0.2 dB and the isolation value in the close state is not less than -55 dB. The effective frequency range is the S-band, as well as the C-, X-, and Ku-band, in which the isolation value is at least -30 dB. The presented inline RF MEMS switch is suitable for use in various types of ground and satellite communications, in particular for devices and systems of 5G mobile networks.

The results obtained can be used as a foundation for the design of complex RF MEMS networks, such as multi-position attenuators (for example, 5-8 bits), the development of which would also reduce hardware redundancy in radio-frequency interface modules (RFFE) designed for mobile 5G networks. More signal shaping functions, such as attenuation and phase shift, can be combined in the same RF MEMS device, which makes such a technical solution even more attractive for 5G applications. In general, the development and development of an element component base using passive RF MEMS elements, such as antenna switches, intermediate frequency filters, LC filters and resonators, will lead to the replacement of traditional semiconductor analogues, while increasing the performance of mobile 5G networks, while causing a reconsideration of the architecture of transceivers.

Acknowledgments

The work was carried out at the expense of funds, task No. FENW-2020-0022 for the implementation of scientific research carrying out scientific research at the expense of the Federal budget, in terms of scientific activities on the topic "Development and research of methods and means of monitoring, diagnostics and forecasting state of engineering objects based on artificial intelligence".

References

[1]. Karthick R., Babu S. P. K. Review on Radio Frequency Micro Electro Mechanical Systems (RF-MEMS) Switch. International Conference on Communication, Computing and Electronics Systems – 2020. – p. 437 – 453.

[2]. Tongtong C., Tengjiang H., Yulong Z. Research Status and Development Trend of MEMS Switches: A Review. Micromachines – 2020. – 11(7). – p. 438 – 453.

[3]. Rizk J., Rebeiz G. M. Digital-type RF MEMS switched capacitors, in IEEE MTT-S International Microwave Symposium Digest. – 2002. – p. 1217 – 1220.

[4]. Puli A. K., Karumuri S. R., Sravani G. Design and Simulation of a MIM Capacitor Type RF MEMS Switch for Surface Radar Application. Lecture Notes on Electrical Engineering. – 2019. – p. 443 – 452.

[5]. Lysenko I. E., Tkachenko A. V., Ezhova O. A. Research of the microelectromechanical switch with different materials of metal membrane. Proc. of SPIE. – 2019. – 10226. – p. 1 – 12.

[6]. Lysenko I. E., Tkachenko A. V., Ezhova O. A., Konoplev B. G., Ryndin E. A., Sherova E. V. The Mechanical Effects Influencing on the Design of RF MEMS Switches. Electronics. – 2020. – 9(2). – p. 1 – 26.

[7]. Lysenko I. E., Tkachenko A. V., Sherova E. V., Nikitin A. V. Analytical Approach in the Development of RF MEMS Switches Electronics. – 2018. – 7(12). – p. 1 – 23.

A seesaw-type MEMS switch with enhanced contact force: the first results

I V Uvarov[1], **N V Marukhin**[2]
[1]Valiev Institute of Physics and Technology of Russian Academy of Sciences, Yaroslavl Branch, Universitetskaya 21, 150007 Yaroslavl, Russia
[2]P.G. Demidov Yaroslavl State University, Sovetskaya 14, 150003 Yaroslavl, Russia

Abstract. Microelectromechanical systems (MEMS) switches have a wide range of possible applications due to their promising working characteristics. However, low reliability limits their commercial success. Due to the small size, MEMS switch develops a low contact force, which results in unstable and high contact resistance. This paper reports the design, simulation and fabrication of the switch that develops 3.5 times higher contact force in comparison with the previously used device. The enhancement is achieved by the modified shape of the beam and electrodes without increasing the footprint and actuation voltage. The switch is equipped by the active contact breaking mechanism, which protects it from stiction.

1. Introduction

Wireless communication and radar systems develop rapidly in recent years, which is achieved through the use of advanced electronic components, including switches for routing and processing of radio frequency and microwave signals. However, the progress in electromechanical and semiconductor relays has almost reached its limit, and new approaches are required. The switches fabricated by MEMS technology are considered as an alternative to conventionally used components. They provide superior radio frequency characteristics, small size, low power consumption and high integration capability [1]. An important parameter of the switch is the contact resistance that strongly depends on the contact force. In contrast with the macroscopic counterparts, MEMS switches develop a rather weak force ~10 μN. This results in high and unstable contact resistance due to a small contact spot and inability to break thin contamination films. For reliable operation, the contact force has to be increased. Here we describe the optimized switch, which provides several times higher force in comparison with the previously demonstrated device [2]. The force is increased without enlargement of the size and actuation voltage. The finite element simulation of the performance and the fabrication route for the switch are reported. The samples ready for the test are fabricated and analyzed.

2. Design of the switch

The proposed switch is shown in figure 1. The movable electrode (source) is a 100 μm long beam attached to the anchors by torsion hinges. The beam has contact bumps on the bottom side. Gate and drain electrodes are located under the each arm of the beam, so the switch has the single-pole double-throw configuration. The beam and electrodes are separated by the air gap of 1.5 μm. The electrodes and bumps are made of Au or Pt, while the beam is fabricated from Al. When the driving voltage is applied to the gate, the beam tilts under the electrostatic force and touches the drain, turning the switch on. When the voltage is removed, the beam returns to the initial state under the elastic force of the hinges. In case of stiction, the voltage is applied to the opposite gate, thereby creating an additional

force that breaks the contact. Thus, the switch has the built-in protection from stiction. The previously demonstrated switch [2] provided the pull-in voltage of 30 V and the contact force of 15 μN at the driving voltage of 60 V. The present switch ensures 3.5 times higher force and 2 times lower pull-in voltage. The enhancement is achieved by the optimized design, which enlarges the overlap area of the beam and gate without increasing the footprint. Detailed description and comparison with the previous design can be found in our previous work [3]. The increase of the force will reduce the contact resistance and prolong the lifecycle of the switch.

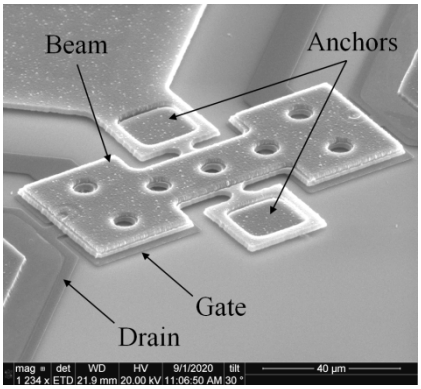

Figure 1. SEM image of the switch.

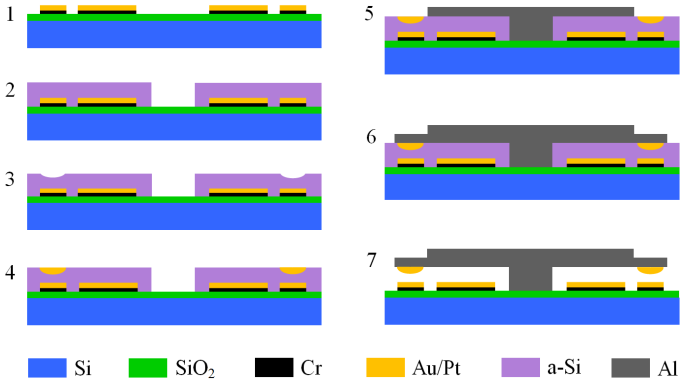

Figure 2. Fabrication procedure.

3. Fabrication

The switch is fabricated by surface micromachining on a 460 μm thick silicon wafer. The procedure is illustrated in figure 2. At the first step, a 0.9 μm thick SiO_2 layer is grown on the wafer by oxidation in wet oxygen, and the Au and Pt gate and drain electrodes with Cr adhesive layer are patterned by the lift-off technique. Futher, a 1.5 μm thick sacrificial layer of amorphous silicon (a-Si) is deposited. The openings for the anchors and low resistance signal lines are etched isotropically by SF_6 plasma through the photoresistive mask. After that, the dimples with a depth of 0.5 μm are made in the sacrificial layer by plasma etching and filled with a 100 nm thick Au or Pt layer. Then the first aluminum layer with a thickness of 1 μm is deposited and patterned by wet etching in an acid solution to form a reinforcing structure of the beam. Further, the second Al layer with a thickness of 1 μm is applied, which is followed by the patterning of the beam, hinges and anchors. The final step is the removal of the a-Si sacrificial layer from under the beam by isotropic etching in SF_6 plasma. The advantage of dry release is the absence of the fabrication-induced stiction under the capillary forces. The use of amorphous silicon as a sacrificial material reduces contamination of contacts with organic residues, which is typically observed for the sacrificial photoresist layers. Thus, the fabrication route is rather simple and ensures high yield. Further, we plan to measure the resonant frequency and pull-in voltage of the fabricated samples and to compare them with the theoretical predictions.

4. Acknowledgments

This work is supported by the grant of President of the Russian Federation № MK-945.2021.4 and the program No. 0066-2019-0002 of the Ministry of Science and Higher Education of Russia for Valiev Institute of Physics and Technology of RAS. The study is performed using the equipment of Facilities Sharing Centre “Diagnostics of Micro- and Nanostructures”.

References

[1] Rebeiz G M 2003 *RF MEMS: Theory, Design, and Technology* (Hoboken, New Jersey: John Wiley & Sons)
[2] Uvarov I V and Kupriyanov A N 2019 *Microsyst. Technol.* **25** 3243
[3] Marukhin N V and Uvarov I V 2020 *J. Phys.: Conf. Ser.* **1695** 012157

Design and simulation of the compact MEMS energy harvester based on aluminium nitride

P S Shlepakov[1,2], **I V Uvarov**[1]
[1]Valiev Institute of Physics and Technology RAS, Yaroslavl Branch,
Universitetskaya 21, 150007 Yaroslavl, Russia
[2]P.G. Demidov Yaroslavl State University, Sovetskaya 14, 150003 Yaroslavl, Russia

Abstract. A device for converting the energy of mechanical vibrations to electricity by the piezoelectric effect is presented. A main part of the transducer is a multilayer cantilever with the inertial mass at the tip. A piezoelectric layer is made of 0.5 μm thick aluminum nitride. A feature of the device is the compact lateral size of about 1 mm, which is 10 times smaller in comparison with conventional transducers. The design of the device is compatible with microelectromechanical systems (MEMS) technology. The cantilever has the natural frequency in range of 43 to 146 Hz, depending on the size and mass, and the bandwidth of 5 Hz. The transducer provides the output voltage of 0.56 V, which is high enough for rectifying by the diode bridge. The output power of 10 nW is relatively low due to the small size of the device. However, the figure of merit is comparable to conventional AlN-based energy harvesters.

1. Introduction

Power consumption of modern portable devices can be as low as several tens of microwatts. Typically, they are powered by a battery, which requires periodic replacement or charging. For particular devices, e.g. GPS trackers or strain gauges in buildings, these operations are inconvenient or impossible. Instead of the battery, the energy of environmental sources can be used, e.g. sunlight or wind. A promising energy source is mechanical vibrations. Oscillations of household appliances or human body can be converted to electricity by the harvester. This is a miniature device fabricated by MEMS technology. Among several harvesting principles [1], the piezoelectric transduction is the most popular one. The piezoelectric harvester has a simple design compatible with microtechology, and demonstrates the highest efficiency [2]. It consists of a resonator with a piezo-material sandwiched between two electrodes. The commonly used material for today is lead zirconate titanate (PZT). However, lead and its derivatives are toxic and globally considered as hazardous materials. Their usage is expected to be limited in the future, and PZT will be replaced by the lead-free material like aluminium nitride [3]. In recent decades, a lot of research are focused at the AlN-based transducers. These devices have a footprint of about 1 cm^2 and output power up to 64 μW. Their disadvantage is the narrow bandwidth, which limits the application of the harvester by a specific vibrating item. The bandwidth can be expanded by combining several resonators at the single chip, but the price is the significant increase of the harvester size. In this work, we propose a compact piezoelectric transducer of about 1 mm in size. Performance of the device is estimated by the finite element simulation.

2. Methods

A key part of the harvester is a multilayer cantilever illustrated in figure 1. The basic layer is a 0.9 μm thick thermally grown SiO_2. A piezoelectric AlN film has a thickness of 0.5 μm. It is located at the top

surface of the dielectric layer between two 0.1 μm thick chromium electrodes. The length and width of the cantilever are in the range of 500-1000 μm and 200-1000 μm, respectively. The cantilever is equipped by the inertial mass, which is made of 500 μm thick silicon. The harvester is attached to the energy source. When it moves with the acceleration, the cantilever deflects from its initial position. Mechanical stress polarizes AlN, which results in the potential difference between the electrodes and the current in the external circuit. Two operating regimes are considered. In the static regime, the acceleration is constant and equals to $g = 9.8$ m/s^2. The tip deflection, output voltage and natural frequency are of interest. In the oscillating regime, the acceleration changes with time t as $a = g \cdot sin(2\pi ft)$, where f is the frequency of external vibrations. An ideal resistor is connected to the electrodes. The resonant frequency, deflection and voltage amplitude, and the generated power are investigated.

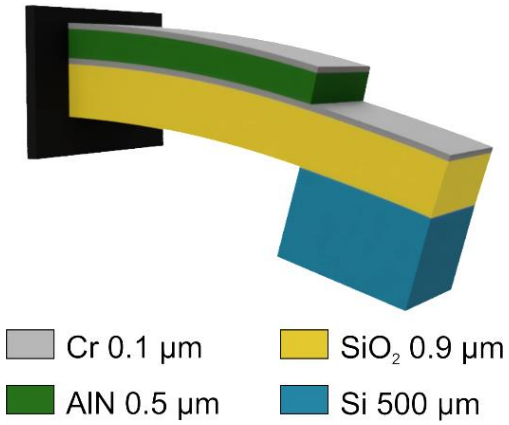

Figure 1. Design of the harvester.

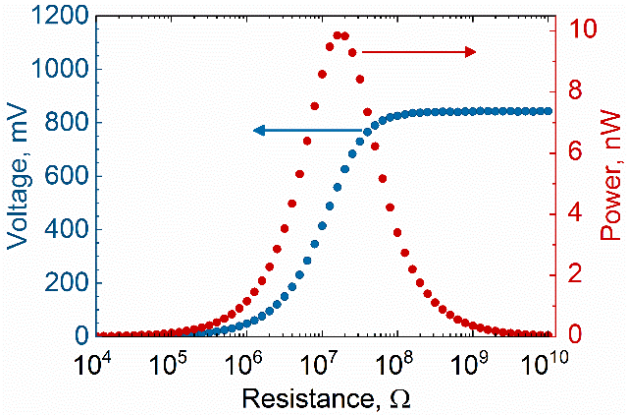

Figure 2. Dependence of the output voltage and power on the resistance at the resonant frequency.

3. Results and discussion

The longer cantilever develops the larger stress in AlN and the higher output voltage. The width doesn't affect the deflection, but it determines the electrode area and, therefore, the accumulated charge and current. Thus, the larger cantilever provides the better performance of the harvester. The addition of the inertial mass to the cantilever reduces the natural frequency for about 10 times and increases the output voltage for three orders of magnitude. The frequency varies from 43 to 146 Hz, while the static output voltage of 115 mV is achieved. In the oscillating regime, the device demonstrates the bandwidth of 5 Hz. The output voltage amplitude reaches 0.8 V in resonance. The highest power of 10 nW is generated at the optimal resistance $R \approx 16$MΩ, as shown in figure 2. In these conditions the voltage amplitude is 0.56 V, which is high enough for rectifying by the diode bridge. Although the power is rather low, the figure of merit $\xi = 3.9$ μW/(g^2·cm^2) is higher than that of many conventional transducers. Further, we plan to optimize the design in order to increase the performance.

Acknowledgments

This work is supported by Program no. 0066-2019-0002 of the Ministry of Science and Higher Education of Russia for Valiev Institute of Physics and Technology of RAS.

References

[1] Beeby S.P., Tudor M.J., White N.M. 2006. *Meas. Sci. Technol.* **17** R175.

[2] Roundy S., Wright P.K. 2004. *Smart Mater. Struct*. **13** 1131.

[3] Zhang Y., Kim H., Wang Q., Jo W., Kingon A., Kim, S., Jeong C.K. 2020. *Nanoscale Adv.* **2** 3131.

Single GaN nanowires for high current commutation devices

K Yu Shugurov[1], A M Mozharov[1], V V Fedorov[1], G A Sapunov[1] and I S Mukhin[1,2]

[1] Alferov University (former St. Petersburg Academic university), 8/3 Khlopina st., St. Petersburg 194021, Russian Federation

[2] ITMO University, 49 Kronverksky pr., St. Petersburg 197101, Russian Federation

E-mail: shugurov17@mail.ru

Abstract. GaN nanowires (NWs) are synthesized on Si substrate by molecular beam epitaxy and then transferred to auxiliary wafer with insulating layer. Electrical measurements at room temperature of single nanowires demonstrate that current density reaches an extremely high level of 2 MA cm^{-2} without NW damage.

1. Introduction

Silicon electronics today in terms of power and microwave devices have practically reached its operational limitations determined by the physical properties of the material in use [1], which has motivated the active search of new material systems. GaN is one of the promising materials for power and microwave electronics owing to its unique properties such as wide direct bandgap, breakdown voltage, thermal and radiation stability.

Simultaneously with the development of new materials, quasi-one-dimensional structures with high length to diameter ratio such as nanowires (NWs) have attracted attention in this field. This is motivated by their geometric features associated with high surface to volume ratio, which enable device miniaturization and development of gate-all-around architectures, extending the range of operating frequencies and increasing the device efficiency [2,3]. Taking into consideration the unique properties of GaN with the advantages of the nanostructures, GaN NWs can pave the ways for the development of a new generation of high power/high frequency transistors [4]. This has motivated an intense research in this field in the last few years [5,6]. However, due to the complexity of the 3D nanoscale architecture sensitive to surface charge effects, the quantification of the current density in NWs is not trivial. Quantitative evaluation of the current density and analysis of the operation stability of ultra-thin GaN NWs are lacking in the literature. This work is devoted to study the stability of GaN NWs under extremely high current loads.

2. Experiment

The undoped GaN NWs were synthesized on Si(111) substrates via plasma-assisted molecular beam epitaxy (PA-MBE) technique. Then, GaN NWs were separated from the growth substrate and were dropped on a Si wafer with a 50 nm SiN_x insulating layer. As a result, GaN NWs were horizontally placed on the auxiliary substrate. To perform electrical measurements Ti (20 nm)/Au (300 nm) contacts were fabricated to the edges of NWs.

For measurements of electrical properties, voltage pulses were applied to the single NWs connected in series with the SR 570 low-noise current preamplifier. A Keithley 2400 precise source-meter and

pulse-generator were used to form an output signal of a given amplitude. The electric field applied to the single NWs exceeds 10 V μm^{-1}. A current preamplifier was used to precisely define the current flow through GaN NWs. A digital multi-channel oscilloscope was used to obtain a voltage-time oscillogram. These data were in-situ converted to the NW current-voltage characteristic. All measurements were carried out at room temperature.

3. Summary

In this work, GaN NWs grown by molecular beam epitaxy were transferred to auxiliary Si wafer with SiN_x insulating layer. Ti/Au contacts were then formed to the ends of single NWs for electrical analysis. The extremely high current density of 2 MA cm^{-2} was measured and no damage of the GaN NWs was observed during 30 minutes operational period. Taking into account the depletion area of NWs we can estimate the effective maximum density of current as 3 MA cm^{-2}. The observe high current density and good stability can create new opportunities for the development of power and microwave electronics based on GaN NWs.

References

[1] Alves L F S, Gomes R C M, Lefranc P, De A. Pegado R, Jeannin P-O, Luciano B A and Rocha F V. 2017 SIC power devices in power electronics: An overview *2017 Brazilian Power Electronics Conference (COBEP)* vol 2018-Janua (IEEE) pp 1–8

[2] Feng X L, He R, Yang P and Roukes M L 2007 Very High Frequency Silicon Nanowire Electromechanical Resonators *Nano Lett.* **7** 1953–9

[3] Liu X, Long Y-Z, Liao L, Duan X and Fan Z 2012 Large-Scale Integration of Semiconductor Nanowires for High-Performance Flexible Electronics *ACS Nano* **6** 1888–900

[4] Fatahilah M F, Yu F, Strempel K, Römer F, Maradan D, Meneghini M, Bakin A, Hohls F, Schumacher H W, Witzigmann B, Waag A and Wasisto H S 2019 Top-down GaN nanowire transistors with nearly zero gate hysteresis for parallel vertical electronics *Sci. Rep.* **9** 10301

[5] Yu F, Yao S, Römer F, Witzigmann B, Schimpke T, Strassburg M, Bakin A, Schumacher H W, Peiner E, Wasisto H S and Waag A 2017 GaN nanowire arrays with nonpolar sidewalls for vertically integrated field-effect transistors *Nanotechnology* **28** 095206

[6] Hartensveld M and Zhang J 2019 Monolithic Integration of GaN Nanowire Light-Emitting Diode with Field Effect Transistor *IEEE Electron Device Lett.* **40** 427–30

Supercapacitor with electrodes based on high-purity single-walled carbon nanotubes

A Shumilin[1], N Gorshkov[1], A Aman[2], A Fomin[1], S Palis[2]

[1]Yuri Gagarin State Technical University of Saratov, Saratov 410054, Russia
[2] Otto von Guericke University, Magdeburg 39106, Universitaetsplatz, 2, Germany

E-mail: Shumilinai@yandex.ru

Abstract. We studied a supercapacitor with high purity carbon paper electrodes with a specific gravity of 20 g/m^2.The specific capacitance of the electrode during assembly in a coin cell housing with an aqueous 6M KOH electrolyte, at a scan rate of 1 mV/s, is 52 F/g. The specific power is 195.42 W/kg and the specific energy is 0.19 W·h/kg at a scan rate of 100 mV/s, which is included in the region of supercapacitors in the Ragone plot.

1. Introduction

Modern technologies involve significant waste of electrical energy and place high demands on storage elements. One type of device that allows you to accumulate and save electrical energy are capacitors, including supercapacitors [1,2,3].

A promising direction for improving supercapacitors is the use of porous carbon materials as electrodes, in which charges accumulate in the form of a double electric layer on a developed porous surface of carbon structures [4]. The issue of increasing the specific capacitance of supercapacitors remains relevant at present. New materials for electrodes and their combinations, alloying, surface modification, selection of the composition of electrolytes - these are the main directions for improving the characteristics of supercapacitors [4,5].

Therefore, it is important to study any, even already well-known material, if it has distinctive features. In this work, a preliminary study of the electrodes for a supercapacitor of single-walled carbon nanotubes with a high degree of purification was carried out.

2. Methodology

Technologies were developed: laser cutting (model LRS-50m) of electrodes, assembly of an coin cell CR2025 with an aqueous 6M KOH electrolyte. Cyclic voltammograms (CV) of samples were obtained according to a two-electrode circuit using a P-50 PRO potentiostat-galvanostat (LLC Elins, Russia) in the scan rate 1–100 mV/s, with a potential window of ± 500 mV, to determine the specific electric capacitance of the electrode material. A feature was the use of carbon paper from single-walled nanotubes with a high degree of purity of 99.9 % [6].

3. Results

Preliminary measurements of the assembled coin cell on the potentiostat showed the promise of research on the use of electrodes from high-purity buckypaper as plates of capacitors of increased capacity. In fig. Figure 1A, 1B shows cyclic voltammograms (CV) for carbon paper of various specific gravity at a scan rate of 100 mV/s.

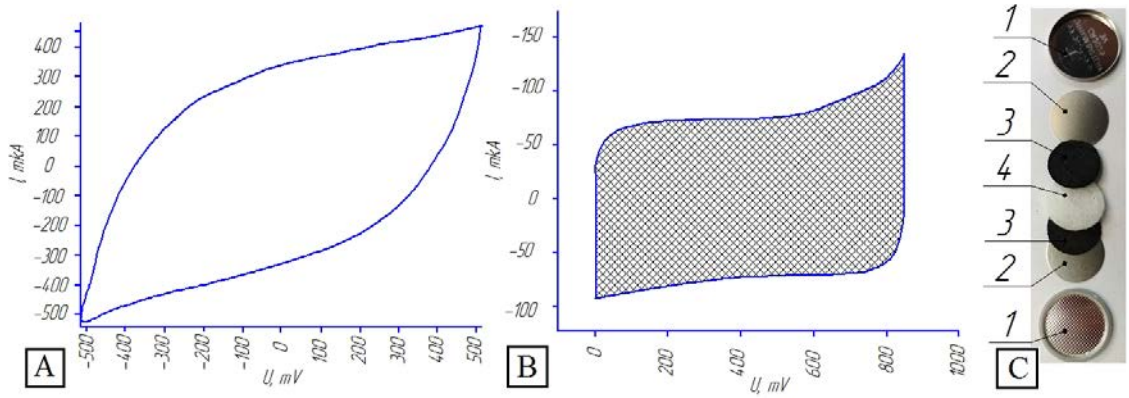

Figure 1. CV plot of the supercapacitor based of electrode with density 20 g/m^2, A – scan rate of 100 mV/s; B – 1 mV/s; C – Elements for assembling a coin cell CR2025: 1 – two parts of the outer case made of stainless steel, 2 – metal electrodes-collectors, 3 – electrodes from high-purity SWN-buckypaper, 4 – separator

The area of the figure in a limited graph corresponds to the capacitor power for one charge – discharge cycle. For a sample with a specific gravity of the electrode of 3 g/m^2 and 20 g/m^2, the calculated specific capacities were 1.7 F/g and 3.2 F/g, respectively. For a sample with a large specific gravity of the electrode, the calculated specific capacitance is almost twice as large. Graph 1B has a shape close to rectangular, which is typical for reversible processes of charge and discharge of a double electric layer [5]. In fig. 1B shows CV for the assembled capacitor at voltages U = ± 450 mV, the charge – discharge current reaches 70 μA. The stored energy in the capacitor under these conditions is of the order of 220 mJ per cycle. Given the mass of carbon fiber electrodes m_1 = 9.37 mg, m_2 = 9.09 mg, the specific capacity of this material was calculated 52 F/g.

4. Conclusion

Specific power and energy at a scan rate of 100 mV/s reach 195.42 W/kg and 0.19 W·h/kg, respectively, these values are in the region of supercapacitors in the Ragone plot [3]. However, this is not a high enough indicator for carbon materials and additional experiments with different types of separators and coin cell sizes are needed to ensure better electrical contact and greater mobility of electrolyte ions.

Acknowledgments

The research was supported by the Michael Lomonosov Programm - Linie B, 2021. Project executor Shumilin A.

References

[1] Zhang Y, Feng H and Zhang L 2009 *Int. J. Hydrogen Energy* **34** 4889
[2] Vivekchand S, Chandra S and Rao C 2008 *J. Chem. Sci.* **120** 9
[3] Béguin F, Raymundo-Piñeiro E and Frackowiak E *Handbook* 2008
[4] Gryzlov L, Rychagov A, Skundin A and Kulova T *Elec. Energ.* **15**(4) 160
[5] Frakowiak E and Beguin F 2001 *Carbon.* **39**(6) 937
[6] https://nanofract.com

Analysis of the possibility of creating an acoustic velocity sensor using GaN epitaxial films

Y. Enns[1,2], A. Kazakin[1,2], A Mizerov[1], R Kleimanov[2]

[1]Alferov University, St. Petersburg, Russia
[2]Peter the Great Saint-Petersburg Polytechnic University, St. Petersburg, Russia

Abstract. This paper results in results of analyzing the possibility of creating an acoustic velocity sensor using epitaxial GaN films. Technology for the fabrication of a microelectromechanical acoustic velocity sensor was developed and a prototype of the sensor was produced. The simulation of the characteristics of the obtained acoustic velocity sensors was carried out on the basis of the measured electrical characteristics, where the sensitivity and the directional pattern were determined.

1. Introduction

Vibration control is of high importance for the diagnosis of industrial equipment, marine, aerospace and nuclear industries. The high number and density of equipment requires the creation of a distributed system of vibration sensors. The overwhelming majority of dangerous vibrations have frequencies in the audio range, therefore, acoustic velocity sensors have received great prospects for vibration diagnostics [1]. The sensors comprise a microelectromechanical system (MEMS) of two short, thin and closely spaced platinum beams that are heated to about 300 ° C [2]. The resistance of the beams depends on the temperature. The action of the acoustic flow instantly changes the temperature distribution, forming a difference in resistance across the sensor beams. This difference in resistance is measured with a bridge circuit that provides a signal proportional to the acoustic flux. Despite the fact that these sensors are proven, their applying in harsh environments is very limited. Therefore, it is necessary to search for new materials that are stable during operation conditions of high temperatures and corrosive gases.

Due to its high chemical, temperature and radiation resistance, GaN is a promising material for electronics and sensors for harsh environments [3]. GaN sensitive elements can be used in miniature gas sensors, temperature and pressure sensors, thermal flow sensors and other MEMS. This work is aimed at creating a design and production technology for acoustic velocity sensors based on GaN epitaxial films.

2. Experimental results

Epitaxial n-GaN films were grown on silicon substrates by the method of molecular by plasma-assisted molecular beam epitaxy [4]. Contacting to the GaN layer was carried out using non-alloyed Ti-Al ohmic contacts, deposited by magnetron sputtering with preliminary ionic treatment of the GaN surface. The topology of GaN beam heaters was formed using the methods of plasma-chemical etching in chlorine plasma. The release of micromechanical structures was carried out by isotropic etching of silicon to a depth of 50 μm using plasma-chemical etching of silicon. The length of the formed beam heaters was 500 μm with 0.5 μm thickness and 10 μm width. The measured resistance

under normal conditions was ~ 60 kΩ. The dependence of the resistance of the beam heaters on the temperature change was measured. The characteristics of the obtained acoustic velocity sensors were simulated on the basis of the obtained data, where the sensitivity and the directional pattern were determined.

Acknowledgments
The work was done as a part of the state assignment (№FSRM-2020-0008) of the Ministry of Education.

References
[1] Guiot M, Comesaña D F, Pousa G C, 2015, Proc. Inter-Noise, 1-8
[2] Bree H-E, Leussink P, Korthorst T, Jansen H, Lammerink T S J, Elwenspoek M,
1996, Sensors and Actuators, 54, 552
[3] Rais-Zadeh M, Gokhale V J, Ansari A, Faucher M, Cordier Y, Buchaillot L, 2014 J. Microelectromech. Syst. 23 1252-71
[4] Timoshnev S.N., et al., 2018, Semiconductors, 52, 5, 660–663.

LK-5 glass surface modification by glass blowing method based on microsystem technology

A Dzhinikashvili[1], Y Enns[1,2], R Kleimanov[1,2] and A Kazakin[1,2]

[1]Peter the Great Saint-Petersburg Polytechnic University, St. Petersburg, Russia
[2]St. Petersburg Academic University, St. Petersburg, Russia

E-mail: wwwDgsa@gmail.com

Abstract. This paper considers the possibility of modifying the surface LK-5 glass by glass blowing methods to solve the problems of creating an atomic clock and ensuring a controlled distribution of metal nanoparticles on its surface. The evolution of the formation of a spherical profile of a glass surface on a hermetically welded cavity in a glass-silicon system was studied experimentally and theoretically. Also, the possibility of modifying the spatial parameters of arrays of nanoparticles distributed on the glass surface has been demonstrated. The obtained experimental and theoretical data demonstrate sufficient convergence.

1. Introduction

The applying of glass substrates as a structural material has become widespread in various sensor applications used in biomedicine, optics, photonics, plasmonics, and microelectromechanical systems (MEMS) [1]. Various technological methods have been developed for the integral fabrication of microfluidic channels, photonic waveguides, and microlenses, such as laser ablation [2], abrasive-jet blasting [3], reactive ion etching (RIE) [4], and femtosecond laser irradiation and chemical etching (FLICE) [5]. Recent studies in the field of creating integral cells of atomic clocks have shown the possibility of using glass blowing methods to produce spherical cells at the wafer level [6]. This technology is based on the formation of glass spheres under the influence of excessive pressure at glass softening temperatures. Excess pressure is formed when the gas is heated in a hermetically sealed cavity. It is a cylindrical hole etched in silicon using deep plasma-chemical etching, sealed with a glass substrate (Pyrex) using an anodic bonding. This paper considers the possibility of modifying the surface LK-5 glass by glass blowing methods to solve the problems of the produced atomic clock and ensuring a controlled distribution of metal nanoparticles on its surface.

2. Experimental results

The structures of the sealed cavities were fabricated on standard silicon substrates 350 μm thick and LK-5 glass 485 μm thick. Cylindrical cavities in a silicon substrate were formed by deep plasma-chemical etching. The etching depth was 200 μm with a variation in the cavity diameters in the range of 500-1500 μm. The anodic bonding of the plates was carried out at a temperature of 400 ˚C in the air. To study the formation of a spherical glass surface, the plate was divided into 1x1 cm chips by a circular saw. The study was carried out during high-temperature annealing in a muffle oven in the temperature range of 850-950 ˚C and the time range from 5 to 60 minutes. The samples cooled at the end of annealing at room temperature. The tendency of deformation of glass with a thickness of 100 μm was also investigated. The glass was thinned by wet etching methods. To investigate the possibility of ensuring

a controlled distribution of metal nanoparticles, an Au film 3 nm thick was deposited on the glass surface before annealing. The profile of the formed structures was studied using the AmbiosXP-1 profilometer. Upon completion of annealing, the formation of a spherical glass surface over the cavity was observed on the samples. The elevation of the glass surface was 19.1- 70.9 μm, and there was a tendency to increase the deformation of the glass with increasing temperature. The study of the evolution of the deformation over the annealing time showed a small effect, which indicates the onset of stationary equilibrium. However, upon prolonged annealing, the formation of a bead was observed along the perimeter of the chip, which makes further anodic connection impossible. In addition, at temperatures of 950 ˚C and prolonged annealing, the formation of a sitallized film on the glass surface was observed. The formation of nanoparticles was studied using SEM on samples with an Au film deposited, where the formation of NPs was observed. The study of the evolution of glass deformation was also simulated based on the viscoelastic model of glass. The results of the preliminary calculations showed a good agreement with the experimental data for the LK-5 glass. The study shows the possibility of modifying the surface of LK-5 glass by glass blowing methods to solve the problems of manufacturing atomic clock and ensuring a controlled distribution of metal nanoparticles on its surface. It should be noted that the obtained results of glass deformation are significantly lower than the similar work using Pyrex glass [6]. An increase in deformation can be achieved by optimizing the modes of the anodic bonding to provide a greater residual pressure in the sealed cavity. Thus, the results of the work provide a broad basis for further research.

Acknowledgments

This work was carried out in Peter the Great St.Petersburg Polytechnic University and was supported by a grant of Russian Science Foundation (project № 20-19-00146) and part of the work on the creation of nanoparticles was done with the support of the Ministry of Education (№FSRM-2020-0011).

References

[1] Asadian M H, Noor R M and Shkel A M 2019 *Proc. 2019 IEEE SENSORS* 1-4
[2] Niino H, Kawaguchi Y, Sato T, Narazaki A, Gumpenberger T and Kurosaki R 2006 *Applied surface science* **252** (13) 4387–91
[3] Belloy E, Sayah A and Gijs M 2000 *Sensors and Actuators A: Physical* **86** (3) 231–237
[4] Li X, Abe T, Liu Y and Esashi M 2002 *J. JMEMS* **11**(6) 625–630
[5] Bellouard Y, Said A, Dugan M and Bado P 2004, *J. Optics express* **12**(10) 2120–29
[6] Eklund E J, Shkel A M, Knappe S, Donley E and Kitching J 2008 *J. Sensors and Actuators A: Physical* **143** (1) pp. 175–180

Study of thermal relaxation in thin NbN films by noise thermometry

M D Soldatenkova[1], E M Baeva[1,2], A D Triznova[1], P I Zolotov[1,2], A I Lomakin[1,2], A I Kardakova[1,2], G N Goltsman[1,2]
[1]Moscow State Pedagogical University, Moscow 119435, Russia
[2]National Research University Higher School of Economics, Moscow 101000, Russia

Abstract
Here we report on study of thermal transport of normal NbN metal films on crystalline substrates (Al_2O_3, Si, and GaN) by noise thermometry in the temperature range of 15 to 50 K. We observe that the measured heat flow rate in the samples differs from the expected electron-phonon and interface cooling rates. Our findings can be applied for various electronic devices operating at low temperatures.

1. Introduction

Understanding of the thermal transport mechanism is necessary for optimization of various detectors and devices at low temperatures [1]. Heat transport experiments at these temperatures are usually described by various models [2-4] which include only electron-phonon coupling in metals and interface Kapitza resistance. However, some experiments on the thermal properties of various low-temperature devices poses further challenges. For instance, the observed phonon escape time in substrate, which restricts the response of superconducting single photon detectors [5-7], is observed to be much longer than the ballistic phonon time of flight [8,9]. Recently, several studies [9-11] explained the effect by considering of additional heat restriction mechanisms. It was shown in ref. [11] that the additional heat bottleneck can appears due to the low phonon mean free path l_{ph} in substrate. Nevertheless, the thermal property of devices on crystalline substrate with large l_{ph} is still intriguing question. In this letter we report on research of thermal transport in NbN thin films of different thickness on Al_2O_3, Si, and GaN substrates by noise thermometry above the critical superconducting transition temperature.

2. Details of sample fabrication and experimental setup.

Thin NbN films of thicknesses from 5 nm to 200 nm were deposed by DC magnetron sputtering onto Al_2O_3, Si, and GaN substrates. The NbN films were patterned to form micron-size bridges with width of 0.5-1 μm. To study the electron temperature T_e in the samples we use the Johnson-Nyquist noise thermometry. The experimental setup for measurement of sample noise is described in [3]. Above the critical temperature of NbN films, the samples are biased by direct current and spectral density of current noise S_I is measured. The noise temperature which is equivalent to T_e can be found according to the Johnson-Nyquist formula $T_N=S_I R_{diff}/4k_B$, where R_{diff} is a differential resistance of the sample. Here, it is instructive to estimate the approximate size of electron-phonon length l_{eph} in NbN and l_{ph} in crystalline substrates. Here we took the estimate of l_{eph}=12 nm in NbN at 15 K from ref [11]. In the dominant phonon regime, the thermal conductance of crystalline solids can be defined as $\kappa=l_{ph}v_s c_{ph}/3$, where v_s

and c_{ph} sound velocity and specific heat capacity of phonons. This yields estimations of l_{ph}≈1000-4000 μm for Si substrate, l_{ph}≈10^3-10^4 μm for Al_2O_3 substrate, and l_{ph}≈6-60 μm for GaN substrate at 15-40 K.

3. Results and Discussion

Figure 1(a) demonstrates the dependences of T_e on joule power of NbN films of different thicknesses on the Al_2O_3 substrate. The experimental data can be fitted by power dependence:

$$P_{3D} = \Sigma(T_e^n - T_b^n), \quad (1)$$

where P_{3D} is joule power normalized to the volume of NbN film, T_b is a bath temperature, Σ and n are cooling rate and exponent. The experimental data is fitted by eq.(1) with Σ=5·10^{10} $WK^{-3}m^{-3}$ and Σ=10^{10} $WK^{-3}m^{-3}$ for 200 nm film at n≈3 for both samples (dashed black lines). It is known that for disorder films electron-phonon cooling is modified and n can differ from 5 [12], however, here we observe, that the heat relaxation of 50 nm film is more efficient that the heat relaxation of 200 nm film, and this observation cannot be explained by electron-phonon cooling. Figure 1(b) demonstrates the power n for different film thicknesses d. The observed power n≈2-3 and its dependence on substrate also are quite unexpected in frame of Kapitza resistance. The power n≈2 (dash dotted line) has been observed in [11] due to substrate effect, which does not take place here, since large l_{ph} in substrate.

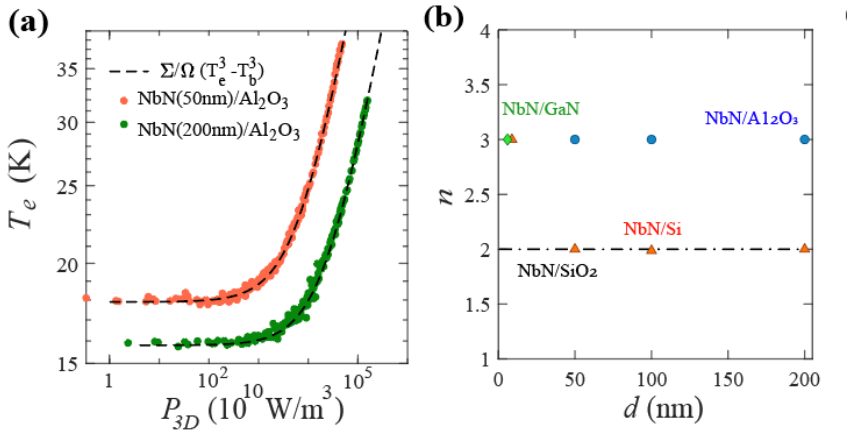

Figure 1. (a) The measured T_e is presented as function of P_{3D} for NbN samples on Al_2O_3 substrate. **(b)** The film thickness dependence of the exponents n observed in experiment for NbN on Al_2O_3, Si and GaN substrates.

Acknowledgments

Authors wishing to acknowledge the RSF project 19-72-10101 for the noise measurements.

References

[1] Giazotto F, Heikkila T, Luukanen A, Savin A M, Pekola J P 2006 *Rev. of Modern Physics* **78** 217
[2] Krause S, Mityashkin V, Antipov S et al. 2016 IEEE *Trans. on Ter. Sci. Technol*. **7** 1 53-59
[3] Baghdadi et al 2020 *Phys. Rev. Applied* **14** 054011
[4] Nozdrin Yu N, Levichev M Yu, Okomel'kov A V et al. 2020 *J. Phys. D: Appl. Phys.* **53** 395301
[5] Annunziata A J, et al. 2010 *Journal of Applied Physics* **108** 084507
[6] Marsili F, Najafi F, Herder C and Berggren K K 2011 *Appl. Phys. Lett.* **98** 093507
[7] Zhang L et. all. 2019 *Appl. Phys. Lett.* **115** 132602
[8] Sidorova M et al 2020 *Phys. Rev. B* **102** 054501
[9] Sidorova M et al 2018 *Phys. Rev. B* **97** 184512
[10] Baeva E M et al 2020 *JETP Letters* **111** 2 104-108
[11] Baeva E M et al 2021 arXiv/3563012
[12] Sergeev A and Mitin V 2000 *Phys. Rev. B* **61** 6041

Materials absorbing electromagnetic radiation with resistive coating $(Co_{40}Fe_{40}B_{20})_X(SIO_2)_{100-X}$

Tarasova Oksana Sergeevna[1], **Sitnikov Alexandr Viktorovich**[1], **Klapanov Anton Viktorovich**[1]

[1)] Voronezh State Technical University

E-mail: oksanchik2603@mail.ru

Abstract. In the frequency range from 270 MHz to 10 GHz, the frequency dependences of the complex magnetic permeability of structures absorbing electromagnetic radiation based on frequency selective gratings were studied, where the composite (Co40Fe40B20) X (SiO2) 100-X was used as a resistive material.

1. Introduction

Composite materials containing ferromagnetic or superparamagnetic particles in a dielectric matrix have a combination of magnetic, electrical, optical, and mechanical properties that are promising for applications.

2. Experiment

In this work, new structures were obtained that absorb electromagnetic radiation, based on resistive frequency-selective gratings, where the composite (Co40Fe40B20) X (SiO2) 100-X obtained by ion-beam sputtering was used as a resistive material [1].

To determine the optimal parameters affecting the functional properties of coatings absorbing electromagnetic radiation, in this work, six systems of samples with different contents of the dielectric and metal phases were obtained; the deposition was carried out in two stages. Sample parameters are shown in the table.

The frequency dependences of the real and imaginary parts of the complex magnetic permeability were obtained by comparing the resonance characteristics of a half-wave coaxial resonator without a sample and with a sample placed in the antinode of the magnetic field of a standing wave. The range of measured frequencies was 0.3 ÷ 10 GHz. The values of the real and imaginary parts of the complex magnetic permeability, for sample No. 2, showed the maximum of the imaginary part μ "of the complex magnetic permeability, corresponding to the frequency of natural ferromagnetic resonance and is 1.5 GHz. The values of μ" are significantly higher than zero in the entire measurement range (0.3 -10 GHz). In the frequency range of the order of 0.3-3 GHz, μ 'experiences a significant decrease. The frequency of natural ferromagnetic resonance, for samples No. 1, No. 3, No. 4, No. 5, No. 6, has a fairly wide peak and lies in the frequency range 0.7 - 2.75 GHz, The real part of the complex magnetic permeability μ 'undergoes a significant change at the maximum value of μ ". The behavior of the μ 'value is similar for all samples.

Table. Sample parameters.

№	Structure	h, μm	ρ, Ohm * m	ρ, Ohm / □	Natural ferromagnetic resonance frequency, GHz
1	$(Co_{40}Fe_{40}B_{20})_{72.4}(SiO_2)_{27.6}$	1.72	$1.9 \cdot 10^{-5}$	11.18	≈2.75
2	$(Co_{40}Fe_{40}B_{20})_{66.1}(SiO_2)_{33.9}$	1.44	$7.93 \cdot 10^{-5}$	114.64	≈1.5
3	$(Co_{40}Fe_{40}B_{20})_{66.1}(SiO_2)_{33.96}$	1.41	$3.34 \cdot 10^{-5}$	23.72	≈1.24-1.9
4	$(Co_{40}Fe_{40}B_{20})_{58.5}(SiO_2)_{41.5}$	1.4	$6.1 \cdot 10^{-5}$	40.69	≈1.26
5	$(Co_{40}Fe_{40}B_{20})_{53.1}(SiO_2)_{46.9}$	1.39	$2.1 \cdot 10^{-4}$	149.89	≈0.88-1.54
6	$(Co_{40}Fe_{40}B_{20})_{47.6}(SiO_2)_{52.4}$	1.4	$4.06 \cdot 10^{-3}$	2896.64	≈0.7-2

3. Conclusion

The results of the study of the frequency dependences of the complex magnetic permeability revealed excellent high-frequency properties of functional thin-film coatings with natural ferromagnetic resonance frequencies in the range of 0.7 - 2.75 GHz. All the samples under study are characterized by a wide maximum of the imaginary part of the complex magnetic permeability.

Acknowledgments

This work was supported by the RFBR grant No. 19-42-363011 r_mol_a

References

[1] Tarasova O.S., Sitnikov A.V., Kalinin Yu.E., Pasternak Yu.G., Mishin A.D., Rozanov K.N., Granovsky A.B., Chuguevsky V.I. 2019 *Inorganic Materials: Applied Research*. **10**(4) 812-817.

Prospective directions for the development of microwave frequency standards for satellite navigation systems

Ding Wang[1, 2], V V Davydov[1, 3] and V Yu Rud[3, 4]

[1]Peter the Great Saint-Petersburg Polytechnic University, Saint Petersburg, Russia, 195251
[2]Jiangsu Normal University, Xuzhou, China, 221116
[3]All-Russian Research Institute of Phytopathology, Moscow Region 143050, Russia
[4]A.F. Ioffe Physicotechnical Institute, St. Petersburg, 195152, Russia

e-mail: jssdwang06@mail.ru

Abstract. The state of essential various quantum standards of GNSS frequencies for today are collected and presented, the results of analysis in the direction of modernization of time synchronization systems in global navigation satellite systems are presented. The most perspective directions of modernization of global navigation satellite systems are mentioned – the development of new atomic clocks on the mercury ions -199. The data on experimental satellite gives encouraging results.

1. Introduction

Currently, global navigation satellite systems (GNSS) are constantly being developed and modernized [1-9]. The modernization process is determined by the structure of GNSS construction and by the tasks solved by it [8-14]. Four satellite constellations are currently deployed in outer space: the American system - GPS, the Russian system - Glonass, the European system - Galileo and the Chinese system - BDS [13-16].

The most important function of GNSS is to determine the location of an object and provide users with three-dimensional information about its coordinates. For positioning an object using the GNSS system, the time and coordinate system are of critical importance [5-8, 10, 17-22]. Any deviation in the value of time between satellites can have a huge impact on the accuracy of positioning [16, 23].

The coordinate system in GNSS is a reference system. It consists of the origin O, the X-axis, the Y-axis and the Z-axis, in the usual case, the origin O is in the center of mass of the Earth, the X-axis and the Z-axis are directed in different directions, the Y-axis makes a rectangular coordinate system with the X-axis and the Z-axis. For proper operation of the positioning system, while there is no single system, they can replace each other with complex mathematical calculations, this is not very convenient for everyone. This often creates problems. Therefore, it is important to determine the promising directions for the development of GNSS in order to reduce these problems to a minimum in the future.

In addition, the orbits of many satellite navigation systems are filled with space debris (decommissioned satellites). There are more and more of them every year. These satellites create problems both in the operation of guidance systems and in the placement of new satellites in orbits [29, 30, 38-40]. This must also be taken into account when determining the promising directions for the development of satellite navigation systems. The increase in the service life of the satellite, which is

now determined by the life of the quantum frequency standard, is a reduction in the rate at which the orbits are filled with "space" debris. This will gain time before an effective system for clearing orbits from "space" debris appears in space. The number of failures in the GNSS work every year due to the "space" garbage increases.

2. Analysis of characteristics of satellite space constellations for navigation systems

All navigation satellites GPS, Glonass, Galileo operate in Medium Earth Orbits (MEO), but each system has a different number of satellites in orbit and a different period of satellite rotation, BDS-3 uses a constellation of 3 orbits: Inclined Geosynchronous Orbits (IGSO), Geostationary Earth Orbits (GEO), and Medium Earth Orbits (MEO), the number of satellites and the rotation period of satellites in each orbit is also different [15, 16, 24-28]. In table 1 shows the data on the different systems.

Table 1. Data on the different system.

System	Orbit altitude (km)	Satellite orbit	Orbit inclination	Satellite rotation period
GPS	20200	MEO	55^0	11 h. 58 m.
Glonass	19100	MEO	64.8^0	11 h. 51 m.
Galileo	23222	MEO	56^0	14 h. 4 m. 45 s.
BSD-3	21528/35768/35768	MEO/GEO/IGSO	$55^0/0^0/55^0$	12 h. 53 m./ 24 h./ 24 h.

Each navigation system uses a different time system: GPS - GPST, Glonass - Glonass-ST, Galileo - GST, BDS - BDT. These time systems are linked together by Coordinated Universal Time (UTC). The UTC time system is based on international atomic time (TAI). There is no extra second in GPST, GST, and BDT after time starts, and there is an extra second in Glonass-ST. Each navigation system has its own coordinate system: GPS coordinate system (WGS-84), Glonass coordinate system (PZ-90), Galileo coordinate system (GTRF), BDS coordinate system (BDCS).

To transmit navigation signals, GPS, Galileo and BDS use code division multiple access (CDMA) technology, while traditional Glonass uses frequency division multiple access (FDMA), currently Glonass supports CDMA. Each system operates in different bands and has different carrier frequencies, in table 2 shows the carrier frequency data of different systems.

From the analysis of the data in table 2, it follows that GPS (L1), Galileo (E1), BDS-3 (B1) have the same carrier frequency 1575.42MHz, GPS (L5) and Galileo (E5a) have the same carrier frequency 1176.45MHz. This shows that the systems can easily be integrated with each other in case of a merger. This is one of the possible directions of modernization of the entire GNSS.

Table 2. Formatting sections, subsections and subsubsections.

System	Range	Carrier frequency (MHz)
GPS	L1, L2, L5	1572.42/1227.60/1176.45
Glonass	G1, G2, G3	1600.995/1248.06/1202.025
Galileo	E1, E5a, E5b, E6	1575.42/1176.45/1207.14/1278.65
BSD-3	B1, B2, B3	1575.42/1191.259/1268.52

The time system in GNSS is linked to the atomic clock of the satellite, which can also be called the heart of the whole satellite system. The GPS satellites use atomic clocks with rubidium (Rb-87) and passive hydrogen maser (PHM), the Glonass satellites use atomic clocks with cesium (Cs-133). The Galileo and BDS satellites (BDS-3) use two types of atomic clocks: passive hydrogen maser (PHM) and rubidium atomic frequency standard (RAFS). There is an experimental satellite with a mercury ion atomic clock (Hg-199) in space. In Figure 1 shows a diagram of the change in the number of

atomic clocks in orbit over 40 years. The total number of atomic clocks on active satellites is shown in parentheses.

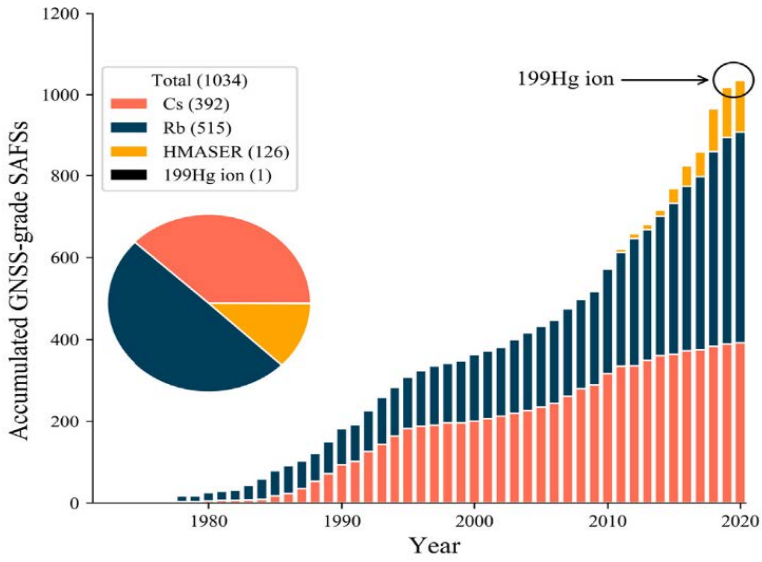

Figure 1. The estimated number of GNSS-grade or better SAFSs sent in space as of 2 March 2021.

Operational data have shown that the atomic clock PHM (Galileo) has the greatest long-term stability of the output characteristics (it does not require constant adjustment of the scale during a communication session with the Earth) [23, 29-33].

3. Analysis of metrological characteristics of quantum standard frequencies

Frequency stability is an important metrological characteristic for quantum standard frequencies, usually described using Allan deviation, Figure 2 and Figure 3 shows 2020 data on Allan deviation for various models of atomic clocks placed on satellites, including new designs of passive hydrogen masers and atomic clocks on mercury ions -199.

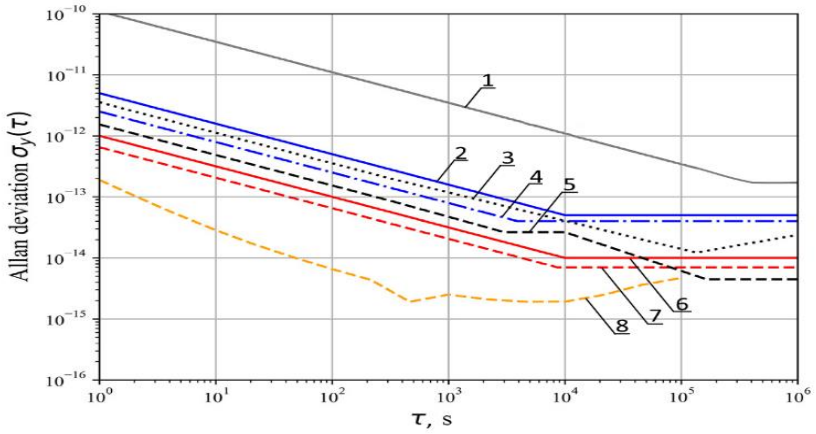

Figure 2. The Allan deviations of different current space atomic clocks**.** Graphs 1, 2, 3, 4, 5, 6, 7 and 8 correspond to the following atomic clock: Cs-133 – GPS; RAFS spec. – Galileo; RAFS – BDS; RAFS – Galileo; PHM–BDS; Cs-133 – Glonass; PHM – Galileo; Radioastron H-maser – GPS and Galileo.

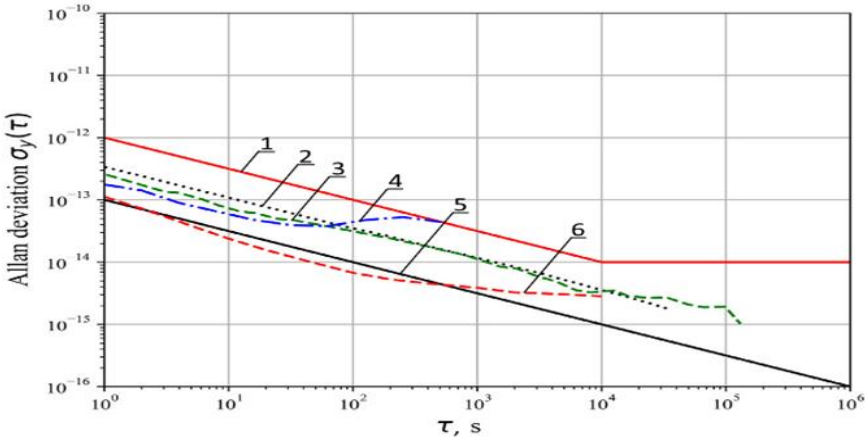

Figure 3. The Allan deviations of different current space atomic clocks and station communication on Earth. Graphs 1, 2, 3, 4, 5, and 6 correspond to the following atomic clock: Cs-133 – Glonass; PHM and RAFS – GPS; JPL 199Hg ion – GPS experimental – USA; Leonardo RAFS – Galileo; PHM – ship communication station; PHM – communication station on Earth.

Analysis of Allan deviation data for different models of atomic clocks (Figure 2), shows that PHM have the best values than other models of atomic clocks. Their disadvantages are limited operating life, high requirements for temperature stabilization and large size compared to atomic clocks on rubidium atoms.

The most prospective direction in the modernization of GNSS is the development of atomic clocks on mercury ions -199 [34-37]. These standards do not have the disadvantages of PHM noted above. The only problem is to work out the design of the Pauli trap while reducing its size and weight for the satellite system. Data on the experimental satellite give encouraging results.

4. Conclusion

The analysis of all the data obtained shows that the two directions of GNSS modernization are the most promising. Creation of a single GNSS system on Glonass orbit using two satellite orbits of the Chinese BDS system. This will solve many of the problems discussed in this article. Especially with the removal of space debris from orbit. The Glonass orbit is the lowest. Forced removal (currently implemented technology on the space robot Ullius) from this orbit of spent satellites will not create problems for other satellite navigation systems.

Or the replacement of all the satellites by new ones with atomic clocks on mercury ions -199. This will reduce the number of satellites in orbit, since the atomic clocks on mercury ions -199 needs almost no adjustment from Earth. The resource of the optical system of this clock is very long (longer than the electronics of the satellite). It is necessary to note that orbits are very cluttered with satellites, taken out of operation and there is less and less place on them. It will also reduce the rate at which space debris fill up orbits.

From this point of view, and taking into account the control of satellite constellation compared to global satellite navigation systems the Chinese system - BDS is the most reliable.

References

[1] Batori E, Almat N, Affolderbach C and Mileti G 2020 *Advances in Space Research (New York: Wiley–Interscience)*

[2] Semenov V V, Nikiforov N F and Ermak S V 1991 *Soviet journal of Communications Technology and Electronics* **36(4)** 59 – 63

[3] Petrov A, Vologdin A and Zalyotov V 2015 *Journal of Physics: Conference Series* **643(1)** 012087

[4] Petrov A A 2017 *Journal of Communications Technology and Electronics* **62(3)** 289–293

[5] Petrov A A 2016 *Journal of Physics: Conference Series* **769(1)** 012065
[6] Hagimoto K 2009 *IEEE Trans. Instrum. Meas.* **48** 496–499
[7] Petrov A 2017 *Lecture Notes in Computer Science (including subseries Lecture Notes in Artificial Intelligence and Lecture Notes in Bioinformatics)* **10531 LNCS** 561-568
[8] Petrov A A, Zalyotov D V, Shabanov V E and Shapovalov D V 2018 *Journal of Physics: Conference Series* **1124(4)** 041004
[9] Lukashev N A, Petrov A A, Grebenikova N M and Valov A P *2018 Proceedings of 18th International conference of Laser Optics ICLO-2018 (Saint-Petersburg),* vol. 8435889 (IEEE), p. 271
[10] Hudson A and Camparo J 2020 *Physical Review Applied* **13(6)** 064007
[11] Chan Y, Johnson W, Karuza S, Young A and Camparo J 2010 *IEEE Transactions on Instrumentation and Measurement* **59(2)** 330–334
[12] Valov A P 2019 *Journal of Physics: Conference Series* **1410(1)** 012246
[13] Petrov A A and Grebenikova N M 2018 *Lecture Notes in Computer Science (including subseries Lecture Notes in Artificial Intelligence and Lecture Notes in Bioinformatics)* **11118 LNCS** 641-648
[14] Petrov A A, Grebenikova N M, Lukashev N A, Ivanova N V, Rodygina N S and Moroz A V 2018 *Journal of Physics: Conference Series* **1038 (1)** 012032
[15] Hegarty C J and Chatre E 2008 In.: Proceedings of the IEEE, vol. 96(12), p. 1902-1917
[16] Hein G W 2020 Satell Navig **1** 22
[17] Petrov A A and Grebennikova N M 2018 *Journal of Communications Technology and Electronics* **63(11)** 1281–1285
[18] Petrov A A, Shabanov V E, Zalyotov D V, Bulyanitsa A L and Shapovalov D V 2018 *International Conference on Electrical Engineering and Photonics EExPolytech 2018 (Saint-Petersburg)*, vol. 8564389 (IEEE), p. 52-55
[19] Formichella V, Camparo J and Tavella P 2017 *Applied Physics Letters* **110(4)** 043506
[20] Martinez F 2014 *Performance of new GNSS satellite clocks* (Scientific Publishing, Karlsruher Institut fur Technologie)
[21] Petrov A and Shapovalov D 2019 *Journal of Physics: Conference Series* **1400(4)** 044008
[22] Lukashev N A, Davydov R V and Glinushkin A P 2019 *Journal of Physics: Conference Series* **1326(1)** 012046
[23] Tavella P and Petit G 2020 *Satell Navig* **1** 10
[24] Jaduszliwer B and Camparo J 2021 *GPS Solut* **25** 27
[25] Hofmann-Wellenhof B 2008 *GNSS - Global navigation satellite systems. GPS, GLONASS, GALILEO and more* (Springer Wien, N. Y.)
[26] Vannicola F 2010 *Proceeding of the 42th Ann. Precise Time and Time Interval Meeting*, p.181–195
[27] Cash P, Krzewick W, MacHado P, et al. 2018 In: 2018 European Frequency and Time Forum, EFTF 2018 (Institute of Electrical and Electronics Engineers Inc.), p. 65–71
[28] Valov A 2020 *CEUR Workshop Proceedings* **2667** 102–105
[29] Cao Y, Huang G, Xie W, et al. 2021 *Acta Geod Geophys* **3** 112
[30] Yang Y, Gao W, Guo S, Mao Yand Yang Y 2019 *NAVIGATION* **66** 7– 18
[31] Grevtseva A S, Davydov R V, Dudkin V I and Rud' V Y 2019 *Journal of Physics: Conference Series* **1326(1)** 012043
[32] Grevtseva A, Davydov V and Rud V 2020 *CEUR Workshop Proceedings* **2667** 15–18
[33] Micalizio S, Calosso C E, Levi F, et al. 2019 *In.: Proc. 2019 IEEE Int. Work. Metrol. AeroSpace, Metroaerosp.*, p. 682–686
[34] Lukashev N A and Moroz A V 2019 *Journal of Physics: Conference Series* **1236(1)** 012068
[35] Lukashev N A 2019 *Journal of Physics: Conference Series* **1400(2)** 022050
[36] Lukashev N A 2020 *Journal of Physics: Conference Series* **1695(1)** 012168
[37] Kuster J 1999 *Joint Meeting of the European Frequency and Time Forum and the IEEE International Frequency control Symposium*, vol. 87(5), p.156 – 168
[38] Petrov A A, Zaletov D V, Davydov V V and Shapovalov D V 2021 *Journal of Communications*

Technology and Electronics **66(3)** 295–299
[39] Batori E, Almat N, Affolderbach C, Gruet F and Mileti G 2020 Proceedings of European Navigation Conference, ENC 2020, (Dresden, Germany, Institute of Electrical and Electronics Engineers Inc), 9317388
[40] Logunov S E, Rud V Y, Davydov R V, Moroz A V and Smirnov K J 2019 *Journal of Physics: Conference Series* **1326(1)** 012024

Structure and characteristics of a thin-layer "aluminum-carbon nanotubes" sandwich structure

A Fomin[1], V Koshuro[1], A Aman[1,2], S Palis[3]
[1] Yuri Gagarin State Technical University of Saratov, Saratov 410054, Russia
[2] Otto Vollmann GmbH & Co. KG, Gevelsberg, Germany, 58285
[3] Otto-von-Guericke-Universität Magdeburg, Universitätsplatz 2, Magdeburg, Germany 39106

Abstract. The study describes a way to produce thin-layer sandwich structures containing layers of aluminum foil and an interlayer filler of carbon nanotubes (CNTs). To obtain a homogeneous structure of the composite, induction heat treatment was used combined with a device providing primary compression of the assembly. To determine the functional characteristics of sandwich structures, the homogeneity of their microstructure and surface conductivity were studied. It was found that the use of CNTs allowed increasing the surface conductivity by a factor of 8.3–9.5 compared to the sandwich structure without a filler.

1. Introduction

It is known that carbon nanotubes (CNTs) are a promising and available material that has a unique combination of strength and the ability to control physical properties such as electrical conductivity. This type of filler is widely used in the manufacture of composites. For example, CNTs are used to improve the strength of aluminum; however the limited ductility of high-strength aluminum matrix composites still remains a critical issue [1]. The elongation of Al/CNT composite (with small volume fraction 1.3 %) sintered at 900 K is enhanced 82 % comparing with that sintered at 800 K, while an increment of 18 % in yield strength (from 127 MPa to 150 MPa) is achieved, as well as 14 % in ultimate tensile strength (from 186 MPa to 212 MPa).

To obtain layers containing CNTs, various types of solvents are used, *e.g.* the *m*-cresol (3-methylphenol, $CH_3C_6H_4(OH)$) weak organic acid [2]. Composites with CNTs have higher mechanical properties and the ability to pre-form compared to the initial material [3]. An important fact is that the amount of filler providing a noticeable strengthening effect is at a low level – not more than 0.5–5 wt%.

2. Methodology

The samples were pressed and thermally treated layers of aluminum foil (thickness 12.9–13.0 μm, Fe impurity – 0.5–1 wt%). The sandwich structure had from 16 to 64 layers, which was associated with the peculiarities of the formation of test samples. The interlayer filler was applied by staining with a colloidal solution containing carbon nanotubes (5 mg CNTs in 100 ml *m*-cresol). Homogenization of the solution was carried out using ultrasonic treatment.

The induction treatment of sandwich structures was conducted using a special device that provided primary compression of the assembly. The treatment temperature of the layered assemblies lied in the range of $(0.9–0.95)\times T_m$ with a process duration within 0.5–1 min.

Surface electrical resistance was measured by a probes method using a picoammeter ("Keithley 6485", Textronix, US) and a DC voltage source ("Agilet 6614C", US). Surface resistance tests were performed in accordance with ASTM D4496–87 standard.

3. Results

During induction treatment of the formed assembly, there was a thermal effect on the system containing a special clamping device (Figure 1,*a*). As the temperature grew, the plasticity of the heated material increased as well, and in a number of cases, partial melting was observed. The pressure in the system decreased and a homogeneous structure was formed; however, during mechanical tests (bending), defects appeared, in particular delamination occurred (Figure 1,*b*).

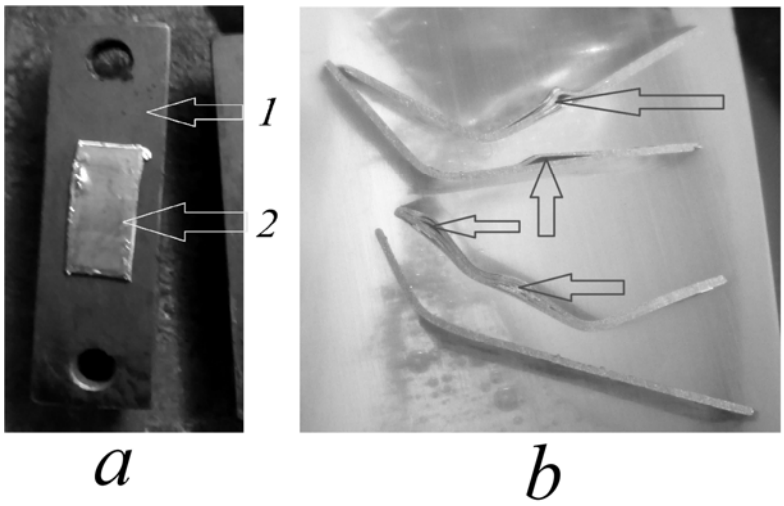

Figure 1(a,b). Sandwich structure *1* on the surface of mold half *2* (**b**); cross-section of "Al - CNTs" sandwich structures obtained with different parameters of induction treatment (**b**).

When studying the functional characteristics of the resulting samples, it was also found that the use of CNTs allowed increasing the surface conductivity by a factor of 8.3–9.5 compared to the sandwich structure without a filler. This may be due to the influence of CNTs on the integral value of the conductivity of a thin-layer system containing a strengthened aluminum alloy (Fe content of 0.5–1 wt%).

4. Conclusions

The possibility of creating a homogeneous "Al – CNTs" sandwich structure with increased strength was shown in the study. The use of CNTs filler allowed increasing the surface conductivity by a factor of not less than 8, which can find application in the creation of electromechanical systems.

Acknowledgments

The research was supported by the Ministry of Education and Science of the Russian Federation and German Academic Exchange Service (DAAD) in the framework of the program "Mikhail Lomonosov" (Project Executor Prof. Fomin A.A.).

References

[1] Chen B, Kondoh K, Imai H, Umeda J and Takahashi M 2016 *Scr Mater* **113** 158.
[2] Chiou K, Byun S, Kim J and Huang J 2018 *PNAS* **115** (22) 5703.
[3] Du J-H, Bai J and Cheng H-M 2007 *EXPRESS Polym Lett* **1** 5 253.

Investigation of the thermal properties of In-doped $Ge_2Sb_2Te_5$ materials for phase change memory application

A Bozhedomova[1], A Babich[1], A Yakubov[1], E Krivogina[2], I Voloschuk[1], A Sherchenkov[1]

[1]National Research University of Electronic Technology, Moscow, Russia
[2]Kurnakov Institute of General and Inorganic Chemistry of the Russian Academy of Sciences, Moscow, Russia

E-mail: nastya.bozhedomova@list.ru

Abstract. Thermal properties, in particular, the melting process of $Ge_2Sb_2Te_5$ materials with various In concentrations were investigated. The results obtained can be further used for the development and creation of the electrical phase change memory cells on the basis of Ge-Sb-Te system materials.

1. Introduction

Today, one of the most promising types of non-volatile memory is phase change memory (PCM), the working principle of which is based on the ability of chalcogenide materials reversibly transform from crystalline to amorphous state, and vice a versa. The most widespread and promising materials for use in phase change memory devices are chalcogenide alloys of the Ge-Sb-Te ternary system [1]. To improve the properties of materials and improve the technology of phase change memory, it is advisable to use doping [2]. In this work, indium was the alloying element. It is assumed that indium will not introduce significant deformations into the material matrix, since it is close in atomic radius to Ge. So, the aim of this work was to investigate the effect of indium (concentration from 0.1 to 5 at.%) on the structure and thermal properties of the $Ge_2Sb_2Te_5$ phase change memory material.

2. Methods and materials

The investigated materials with different indium concentrations were obtained by direct fusion of semiconductor purity materials in sealed quartz ampoules. The composition of the synthesized materials was studied by energy dispersive X-ray spectroscopy (EDX). Structural features were determined using X-ray diffraction (XRD). The analysis of the obtained data was carried out by registering the change in the intensity and position of the peak maxima. Thermal properties were investigated by differential scanning calorimetry (DSC). The measurements of synthesized materials were carried out in aluminum crucibles at a heating rate of 10 deg/min in a nitrogen flow on a DSC-50 calorimeter. The measurement temperature range was from room temperature to 630 °C. The weight of each sample for measurement was 10-15 mg. Empty Al pans were used as references.

3. Results

An analysis of the XRD data allowed to establish that the samples of all compositions are polycrystalline and correspond to the trigonal modification of the $Ge_2Sb_2Te_5$ material **(Fig. 1, a)**. The melting temperatures of the synthesized materials determined by DSC were above 600 °C **(Fig. 1, b)**. The melting heats were estimated by processing DSC curves with melting peaks. It was shown that the increase of the indium concentration leads to the increase of the melting temperature **(Fig. 1, c)**.

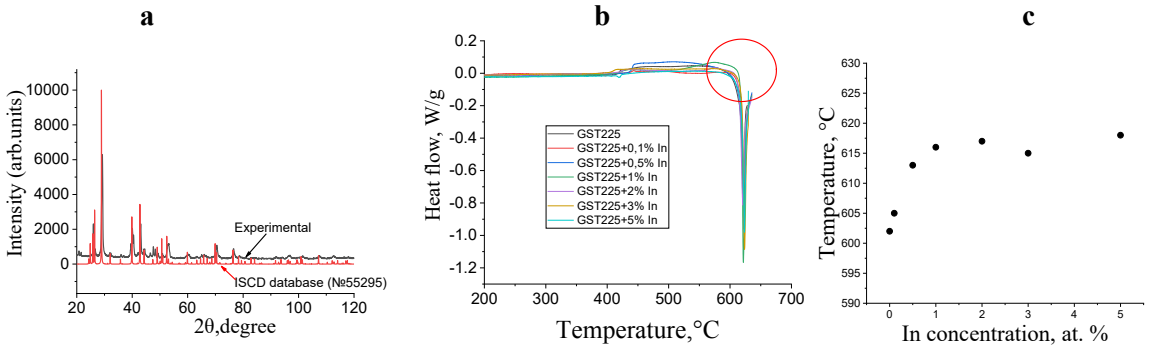

Figure 1. Results of studies of the GST225 + In materials: (a) Comparison of the diffraction pattern of the synthesized material $Ge_2Sb_2Te_5$ with the data from the ICSD database (No. 55295); **(b)** DSC curves of the first measurements of all materials in the temperature range from 450 to 700 °C; **(c)** Dependence of the melting temperature on the In concentration.

An endothermic peak appeared in the temperature range of 400-425 °C after the first and second measurements of the sample, which is due to the melting of the eutectic in the Ge-Te system. The $Ge_2Sb_2Te_5$ materials with an indium concentration of up to 2 at% can be noted as the promising materials for phase change memory devices. As a result, it can be concluded that indium is a promising impurity for controlling the properties of chalcogenide compounds, because it allows changing the melting point of the material, which in turn affects the speed of the phase change memory cell.

4. Acknowledgments

This work was supported by Russian Foundation for Basis Research (project No. 20-07-01092).

References

[1] Ting-Ting Jiang, et.al., 2019 J.APL materials, **7(8)**, 081121.
[2] Sherchenkov A, Sergey Kozyukhin, et.al., 2016 J. Solid State Phenomena, **247**, 30-38.

Varieties of carbon nanostructures in a flame

O V Vasilyeva[1], S I Ksenofontov[2] and A N Lepaev[3]

[1]Chuvash State University named after I.N. Ulyanov, Cheboksary 428015, Russia
[2]Chuvash State Pedagogical University named after I.Y. Yakovlev, Cheboksary 428000, Russia
[3]Cheboksary Institute (branch) of the Moscow Polytechnic University, Cheboksary 428000, Russia

E-mail: dprostokvashino@mail.ru

Abstract. In high temperature flame hollow tubes are formed from a liquid mass of diphenyl. The size of the tubes reaches several millimeters in length and 40 μm in diameter. The surface of the tube is a sieve that consists of carbon nanotubes. The cells of the sieve is less than 0.15 μm.

1. Introduction

The size of the primary particles of carbon formed in the flame of hydrocarbon fuel is not more than 5 nm. Particles of highly dispersed soot are formed as a result of agglomeration and growth of particles from the gas phase [1]. Particles of pyrolytic carbon are formed in the central zones of the flame (figure 1a, b), the size of the globules is 130 - 320 nm [2].

(a) (b)

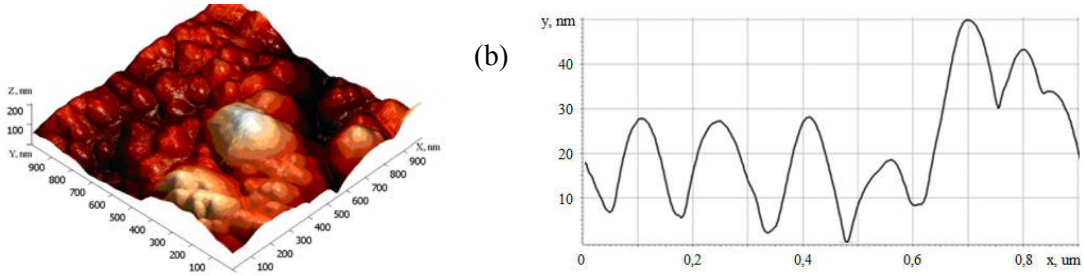

Figure 1. (a) 3D-topogram of pyrolytic carbon film; (b) plot of irregularities height along the OX axis. Scanning coordinate y = 900 nm.

Fullerenes can form in a flame when the pressure of the medium decreases. Carbon nanotubes grow out of the gas phase in the presence of catalysts. The time of nucleation and growth of nanotubes is measured in minutes [3].

2. Results and discussion

The paper presents a new method for obtaining carbon nanostructures, when the building material is supplied from the condensed phase. The time of nucleation and growth of nanostructures is tens of milliseconds. Diphenyl was used as a building material, as the most effective flame soot agent among aromatic compounds (figure 2a, b).

In a pyrotechnic flame, liquid diphenyl envelops the reacting particles. Diphenyl is a strong combustion phlegmatizer, and the maximum flame temperature is not more than 2200 K. In this limiting case, the vapor-phase mode of magnesium combustion is excluded.

(a) 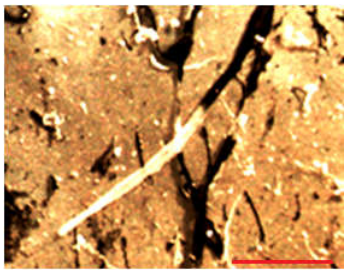 (b) 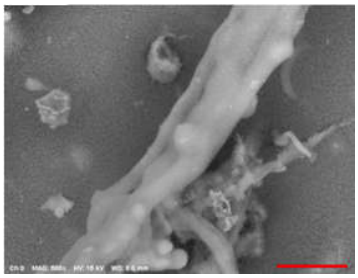

Figure 2. Magnesium oxide particles in a carbon grid. The length of the frame (a) 1 mm; (b) 100 μm.

The gaseous components of decomposition and combustion of NO_2, N_2, O_2, H_2O inflate the diphenyl shell from the inside into a tube. The transverse dimensions of the tube are commensurate with the dimensions of the original particles. The tube forms an almost cylindrical pipeline. The walls of the pipeline are a non-woven grid of nanotubes (figure 3). The direction of the tube is determined by the movement of two-phase flows of gasification products and condensed particles.

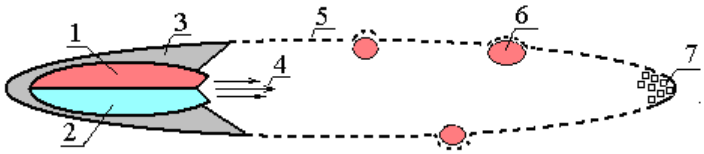

Figure 3. Model of the formation of a carbon tube: 1 – metal, 2 – oxidizer, 3 – diphenyl shell, 4 – two-phase flow of combustion products, 5 – tube, 6, 7 – dispersed particles

Fragments of the starting material several tens of microns in size are transported inside the tube, deforming the "smooth" walls of the tube in bulges. The gas component and dispersed particles of submicron size can leave the tube. Larger micron-sized particles settle inside the tube, blocking the cells. In this case, the packing of particles, for example, magnesium oxide, in the tube corresponds to the bulk density. When the cells are blocked, the hydrodynamic resistance of the tube increases, which leads to the growth of the tube. The length of the tubes reaches a millimeter or more.

Under certain conditions of magnesium combustion on the surface of the same reacting particle, several tubes may form. The tubes are oriented in different directions. A decrease in the percentage of diphenyl leads to a decrease in the number of tubes.

The existence of carbon tubes is limited in time and space. Burnout of the carbon grid occurs at the expense of oxygen, which is released during the decomposition of potassium nitrate. The external size of the burnt-out tube is retained due to the settled particles of magnesium oxide, but its mechanical properties change (figure 2a).

Tubes taken from the flame were subjected to thermal afterburning in air at a temperature of 1000 K. In this case, the carbon grid burns out completely, leaving a white skeleton of magnesium oxide particles. The shape and relative position of the tube elements change greatly during afterburning.

The effective size of dispersed particles deposited on the tube wall is 0.15 μm. The tube is a sieve with cells, the size of which is less than 0.15 μm.

References

[1] Tesner P A 1979 *Combustion, Explosion, and Shock Waves* vol 15 **2** 3

[2] Vasilyeva O V, Ksenofontov S I, Krasnova A G and Kokshina A V 2015 *International Scientific Journal for Alternative Energy and Ecology* **19** 105

[3] Romanenko A V 2007 *Industrial catalysis in lectures* (Moscow: Kalvis) p 128

Enhancing the physical and mechanical properties of tantalum by induction chemical thermal treatment

A V Voyko[1], A M Gerasimov[1], M A Fomina[1], and V A Koshuro[1]

[1] Yuri Gagarin State Technical University of Saratov, Saratov 410054, Russia

e-mail: voyko.leha@mail.ru

Abstract: The results of the chemical thermal treatment (CTT) of tantalum in a solid carbon-containing medium in the temperature range from 1000 to 1300 °C were presented. CTT consisted in heating a workpiece with a working medium in a container made of a refractory material. The induction heating method was used for heating. After strengthening treatment, tantalum samples were characterized by increased hardness, which grew from 140 to 1100 $HV_{0.02}$.

1. Introduction

Tantalum interacts with non-metallic elements that form interstitial solid solutions (H, C, N, O) [1]. For example, the absorption of hydrogen is slow under normal conditions, but at a temperature of about 500 °C, the absorption rate is maximal. As a result of this interaction, not only absorption occurs, but also the formation of chemical compounds – TaH hydrides. Tantalum absorbs nitrogen at a temperature of 600 °C, and at a higher temperature, TaN nitride is formed. Oxidation with atmospheric oxygen begins at a temperature of 200–300 °C, whereas above 500 °C intense oxidation occurs with the formation of the higher oxide Ta_2O_5. Simultaneous saturation with oxygen and nitrogen leads to the formation of a film with high mechanical strength compared to other coatings of tantalum oxide [2]. Carbon-containing gases (CH_4, CO) at the temperature of 1200–1400 °C react with metal, which results in the formation of hard and refractory carbides, e.g. TaC [3].

A method of chemical-thermal treatment (CTT) allows the production of the necessary compounds on the surface of metals and their alloys. One of the effective ways of CTT of tantalum is carburization in a solid carburizer such as graphite. The use of eddy currents arising during induction heating is effective as a heating source [4].

2. Methodology

For CTT, the prepared disk sample was placed in a heat-resistant container, and then graphite powder was poured from all sides. The container with the samples was subjected to induction heating. The change in the consumed electric power corresponded to different values of the inductor current (the main electrotechnological factor) and the heating temperature of the container from 1000 to 1300 ºC (step of temperature change 100 ºC) with a fixed exposure time of 4 min. After CTT, the chemical composition, surface morphology and microhardness of the resulting coating were investigated.

3. Results and discussion

The chemical composition of the surface of tantalum samples after CTT was represented by tantalum,

carbon and oxygen. The amount of tantalum in the samples in the entire temperature range varied within 23–31 at.%, carbon – 39–61 at.%, oxygen – 11–31 at.%. The surface morphology after CTT had significant changes, namely, the coatings with nanosized grains were formed on the surface. The grain size grew with an increase in the process temperature from 20 nm to 100 nm at 1000 °C and 1300 °C, respectively (Figure 1).

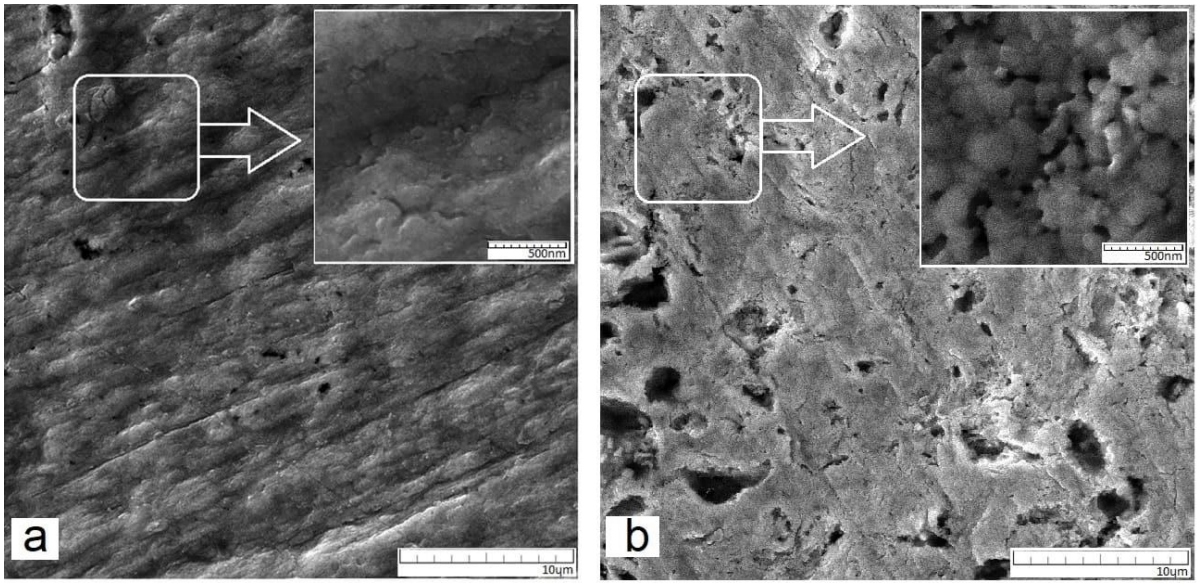

Figure 1. Surface morphology of tantalum samples after CTT at treatment temperatures of 1000 °C (a) and 1300 °C (b).

The hardness of the untreated samples was 140±10 $HV_{0.1}$. At the minimum temperature (T = 1000 ºC), the hardness of the coating and substrate was 610±65 $HV_{0.02}$ and 570±60 $HV_{0.1}$, respectively. At the highest CTT temperature (T = 1300 ºC), coatings with a high hardness of 1100±60 $HV_{0.02}$ were formed. The hardness of the tantalum substrate also increased significantly up to 740±55 $HV_{0.1}$.

4. Conclusions

Thus, in the course of the work, it was found that as a result of CTT, three-component coatings were formed consisting of tantalum, carbon and oxygen. The structure of the resulting coatings contained nanograins, the size of which grew with an increase in the temperature of the CTT process. The hardness of the coatings had the highest value at the maximum temperature T = 1300 ºC.

Acknowledgments

The research was supported by the Russian Science Foundation (project No. 18-79-10040).

References

[1] Puhr-Westerheide J, Elssner G 1970 *J Less Common Met* **20(4)** 371-374
[2] Hirpara Jignesh G, Chawla V, Chandra R 2020 *Mater Today Commun* **23** 101113
[3] Zhou H, Hu Y, Zhu K, Li F, Long Z, LuoW 2018 *J Vac Sci Technol* **38(1)** 48-52
[4] Fomin A, Voyko A, Fomina M, Mokrousov S, Koshuro V, 2020 *Compos Struct* **245** 112393

Investigation of the effect of temperature on the energy spectrum of indium antimonide quantum dots

M V Gavrikov[1], V F Kabanov[1]

[1]Department of Nano and Biomedical Technologies, Saratov State University, Saratov 410012, Russia

maks.gavrikov.96@gmail.com

Abstract. In this paper we have analyzed the broadening of the levels of the energy spectrum of indium antimonide quantum dots with a change of samples temperature. The position of the levels was determined by processing normalized differential tunneling current-voltage characteristics of a quantum dots. It is concluded that with a decrease in the quantum dots size and, accordingly, an increase in the energy gap $\varepsilon_{c1} - \varepsilon_{v1}$, the broadening in percentage will decrease, which should lead to an increase in the temperature stability of the electrophysical parameters.

1. Introduction

The possibility of using semiconductor quantum dots (QDs) as an active enviroment for heterostructure lasers is largely determined by the carrier relaxation rate. Among the main factors influencing relaxation are the spectrum of energy states of quantum dots, electron-hole interaction (exciton effect), spectrum of phonon states, electron-phonon interaction, the presence of excess carriers in quantum dots, as well as experimental conditions, in particular, the temperature of the sample.

In this regard, the purpose of this work was to study the effect of the temperature of macroscopic samples with indium antimonide quantum dots on their electronic energy spectrum.

2. Research methods

In this paper we investigated monolayers of quantum dots that were formed on the surface of an aqueous subphase, using the Langmuir-Blodgett technology, and transferred onto solid substrates with a conducting layer of indium tin oxide (ITO). The obtained samples were investigated by scanning tunneling microscopy (STM) using a SOLVER Nano scanning probe microscope.

3. Results and discussions

In this work, a group of indium antimonide quantum dots with characteristic sizes 8–10 nm were studied. The value of the first level of the QD energy spectrum ε1 was estimated in the range 0.20–1.4 eV.

Localized energy levels ε_i associated with the properties of a QD appear in normalized differential tunneling current-voltage characteristics (CVCs) as individual peaks. To analyze the experimental tunneling CVCs, similarly to the approaches described in [1, 2], we used the dependence of

(dI/dV)/(I/V) on the voltage *V*, since the method of normalized differential CVCs is more informative for experimental results processing.

A change in the system energy, for example, upon sample heating, should affect the broadening $\Delta\varepsilon_i$ and lead to changes in the energy spectrum of QDs. Typical experimental results of normalized differential CVCs are shown in figure 1.

As we can see the position of the peak, that corresponds to the local energy levels of QDs, is shifted by 3–6%.

This paper presents the calculated values of the broadening of the 1st energy level of InSb QDs upon heating to 95°C. For the calculations, we chose the energy intervals 2kT relative to εi. Estimation shows that in the considered energy range corresponding to the characteristic size of the QD, the broadening of the first level is in the range of 2.5–5.5%, depending on the level energy.

It should be noted that the in this work considered broadening of the QD energy levels associated only with a change in the electron energy, and other factors, for example, the spectrum of phonon states, electron-phonon interaction, and a number of others, were not taken into account.

Thus, we analyzed the effect of temperature change on the energy spectrum of InSb quantum dots taking into account the broadening of the energy spectrum levels. The obtained results can be used for investigation of optical and electronic characteristics changes of devices using semiconductor quantum dots.

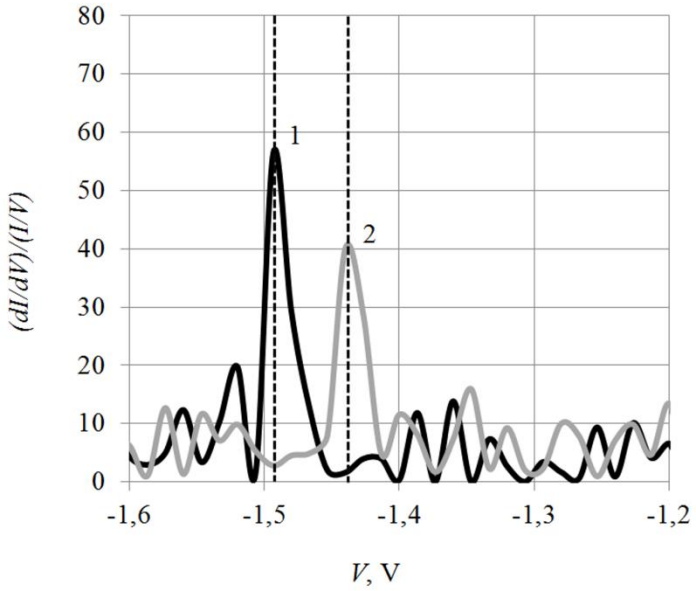

Figure 1. Typical normalized differential tunneling CVCs of InSb QDs at two temperatures: 1 – 23°C, 2 – 95°C.

Acknowledgments

This work was supported by grants from the Russian Foundation for Basic Research No. 19-07-00087 and 19-07-00086.

References

[1] Mikhailov A I, Kabanov V F, Gorbachev I A, Glukhovsky E G 2018 *Физика и техника полупроводников* **52**(6) 603

[2] Mikhailov A I, Kabanov V F, Glukhovskoy E G, Shishkin M I, Gavrikov M V 2018 *Nanosystems: Physics, Chemistry, Mathematics* **9** 464

Solid-state phase transition in n-alkanes of different parity

S A Gureva[1,2], A K Borisov[1,2], V A Marikhin[1], V M Egorov[1]
[1]Strength Physics Lab, Ioffe Institute RAS, St. Petersburg 194021, Russia
[2]Peter the Great St. Petersburg Polytechnic University, St. Petersburg, 195251, Russia

Abstract. The kinetics of the first-order solid-state structural transition in monodisperse n alkanes samples of tricosane $C_{23}H_{48}$ and tetracosane $C_{24}H_{50}$ was studied by DSC and FTIR spectroscopy. The initial nuclei location of the new phase was revealed. The process of crystal structure rearrangement is initiated in the interlayers between neighboring lamellar for odd tricosane, while the nanonuclei in even tetracosane arise in the crystalline lamellas cores. Thus, the influence of the number evenness of carbon atoms in the n-alkanes chains on the first-order structural phase transition has been proved.

1. Introduction

The purpose of this work was a fundamental study of temperature phase transitions (PTs) in long-chain molecular crystals (LCMC), using the example of normal alkanes with the general formula $CH_3(CH_2)_{n-2}CH_3$, by differential scanning calorimetry (DSC) and IR Fourier spectroscopy.

N-alkanes are model systems for studying the regularities of phase PTs in LCMC and polymers, and also have important practical applications as PCM (phase change materials). The objects of research are monodisperse samples of n-alkanes tricosane $C_{23}H_{48}$ and tetracosane $C_{24}H_{50}$ with a very high purity ~ 99.9%. During crystallization of n-alkanes, thin lamellar crystals are formed, in which depending on the number parity of methylene CH_2 groups molecules stacked in triclinic or orthorhombic sub-cell for even and odd n-alkanes, respectively.

2. Experiments and results

FTIR spectroscopic analysis reveals the kinetics of a first-order solid-state phase transition (PT-1) [1] by the smallest displacements in the molecular vibration spectra, which are due to changes in the symmetry of sub-cells in the crystalline cores of elementary lamellas.

Taking into account the lamellar structure of LCMC, it is possible to consider the development of PT-1 in two quasi-independent structural components: in the lamellas cores containing methylene sequences and in interlamellar layers formed by the van der Waals contact of adjacent lamellas. The study of the temperature transformations in the crystalline lamellas cores was carried out on the basis of the temperature dependences analysis of the frequencies and intensities of various vibration modes of CH_2 groups in methylene trans-sequences [2, 3]. It was shown that in the cores PT-1 develops to a heterogeneous mechanism in a temperature range $\Delta T = 40.3 – 41.7°C$ for tricosane and $\Delta T = 45.5 – 47.6°C$ for tetracosane in accordance with the diffuse phase transitions theory [4]. It was found that in the PT-1 temperature range a hexagonal phase nuclei appear in the volume of the initial triclinic or orthorhombic phase, and the amount of the new phase gradual increase occurs due to the disappearance of the former one.

In this work, we investigated the features of the rearrangement in the interlamellar space on the basis of the temperature dependences of various modes of the C-H bond stretching vibrations in the

terminal methyl CH_3 groups, where radical changes in the PT-1 range were also found. It was established that for tricosane PT-1 begins with a change of the stretching vibrations in the terminal CH_3 groups and in the CH_2 groups closest to them at $\Delta T = 39.5 – 41.0°C$. The rearrangement of the tetracosane crystal structure manifests in changes of vibrations in the terminal groups at more higher temperatures 46.2 – 47.8°C as compared to the vibrations inside the lamellas. It can be concluded that for even n-alkane $C_{24}H_{50}$ the initial nuclei of a new phase arise precisely in the lamellas cores and only then gradually extend over the entire volume. It is assumed that in this case before a complete transition to the hexagonal symmetry it is energetically more favorable for molecules inclined relative to the base plane of the lamellae to occupy a vertical position, and only after that to change the molecules packing, i.e. to change the contact of the terminal groups.

DSC researches were carried out to confirm and refine the results obtained. The dependences of heat capacity on temperature were received for tricosane and tetracosane samples. Methodological errors were eliminated by extrapolation to zero scanning speed [1]. The temperature dependences of heat capacity in the PT-1 range are shown on Figure 1. It can be seen that the transition covers the interval $\Delta T = 40.6 – 41.3°C$ for $C_{23}H_{48}$ and $\Delta T = 47.2 – 48.4°C$ for $C_{24}H_{50}$, that is consistent with IR data on the complete transition to the hexagonal phase.

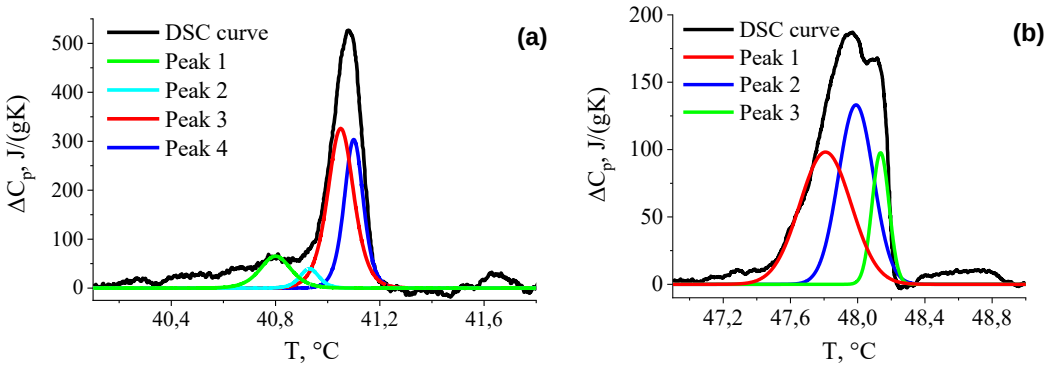

Figure 1. DSC PT-1 curve for tricosane (a) and tetracosane (b).

As can be seen from Figure 1, the shape of the curve is asymmetric in both cases; therefore, according to the theory of a self-consistent field [4], the separation into symmetric Λ-shaped peaks was performed. According to [1], the main peak is divided into two Λ-shape peaks (peaks 3 and 4 for tricosane and peaks 1 and 2 for tetracosane). Also, on the tricosane curve it was possible to distinguish additional peaks preceding the main one (peaks 1 and 2), and for tetracosane – peak after the main one (peak 3). The enthalpies for the main and secondary peaks are compared with the calculated values of the transition energies in the lamellas cores $\Delta H_{(n-4)CH2}=(n-4)\cdot 3.84 J/g$ and in the interlamellar space $\Delta H_{2CH3+2CH2}=16 J/g$ [5]. The experimental values of enthalpies for $C_{23}H_{48}$: $\Delta H_{exp1}+\Delta H_{exp2}=14 J/g$, $\Delta H_{exp3}+\Delta H_{exp4}=72.4 J/g$; and for $C_{24}H_{50}$: $\Delta H_{exp1}+\Delta H_{exp2}=71.9 J/g$, $\Delta H_{exp3}=12.6 J/g$ agree with theoretical ones.

In conclusion, FTIR spectroscopy and DSC have demonstrated the parity effect of n-alkanes depending on the chain length. It was shown that PT-1 begins in the interlamellar space in odd n-alkanes and in the lamellas cores in even n-alkanes.

References

[1] Egorov V M, Marikhin V A 2017 *Physics of the solid state* **59** 2044

[2] Marikhin V A, Gur'eva S A, Myasnikova L P, Volchek B Z, Medvedeva D A 2019 *Physics of the solid state* **61** 1785

[3] Gureva S A, Marikhin V A, Myasnikova L P, Volchek B Z, Medvedeva D A 2019 *J. Phys.: Conf. Ser.* **1400** 055040

[4] Malygin G A 2001 *Physics-Uspekhi* **171** 187

[5] Gureva S A, Borisov A K, Marikhin V A, Egorov V M 2020 *J. Phys.: Conf. Ser.* **1695** 012180

Design of the Two-Axis Micromachined Gyroscope

I E Lysenko[1], M A Denisenko[1], A S Isaeva[1]

[1]Southern Federal University, Taganrog, 347922, Russia

dema@sfedu.ru

Abstract. Micromechanical inertia sensors - accelerometers, gyroscopes, multisensor modules and systems based on them - are widely used in navigation, for compensation of other instruments (accelerometers, inclinometers) or stabilization (gyroscopes). The paper presents the designed construction of a MEMS angular rate sensor with two sensitivity axes, topology of gyroscope is presented; modal and static analysis is performed using ANSYS CAD; simulation results of micromechanical gyroscope operation under the action of angular velocities using VHDL-AMS are presented.

1. Introduction

In many segments of commercial MEMS s market inertial and pressure sensors dominate. In part, this is due to the existing problems. Inertia sensors - accelerometers, gyroscopes, multisensor modules and systems based on them - are widely used in navigation, for compensation of other instruments (accelerometers, inclinometers) or stabilization (gyroscopes). Inertial Measurement Units (IMU) are one of the main applications of inertial sensors in a MEMS design [1-3].

Recently known micromechanical sensors provide possibility to measure linear accelerations and angular velocities by single or double axes. These devices are manufactured in the form of hybrid or integrated microsystems [2, 3].

2. Design and simulation

In this work its authors investigated LL-type inertial micromechanical sensor, which structure is presented at figure 1 [4].

In such a way, developed micromechanical device represents integrated micromechanical gyroscope, providing opportunity to measure values of angular velocity along X axis, located in substrate plane, and Z axis, directed normally to substrate plane of the device.

The main feature of the developed angular velocities and linear accelerations sensor is that elastic suspensions, inertia mass, mobile and stationary comb electrodes of electrostatic drives, stationary electrodes of capacitive displacement transducers are all made in a single structural layer. Using two suspensions allows to exclude mutual influence of primary and secondary oscillations of MMG sensors.

Within this investigation geometrical and finite-elements models of a single sensor of proposed gyroscope with two sensitive axes were developed. In accordance with proposed simulation method, calculations of natural modes and oscillation frequencies of gyroscope sensor were performed.

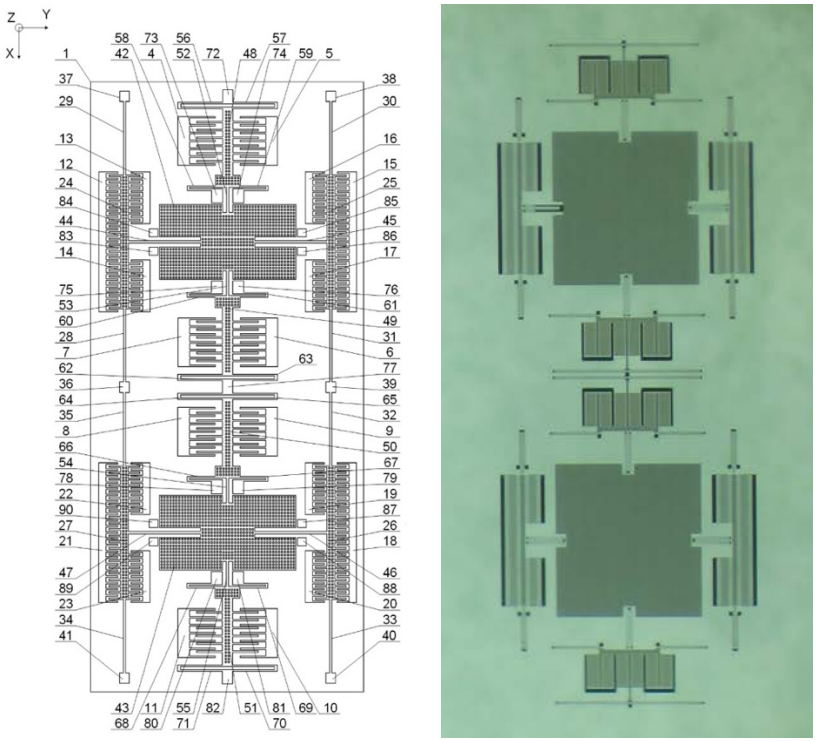

a) b)

Figure 1. Topology of the integrated micromechanical gyroscope with two sensitive axes

Geometrical and numerical models, modal analysis of micromechanical gyroscope sensor along axis of motion and statical analysis of micromechanical device under the action angular velocities along sensitivity axes also were carried out in ANSYS CAD.

3. Conclusion

From the results of performed investigations anyone can seen, that proposed construction of elastic suspensions of sensitive element of angular velocities micromechanical sensor in the mode of sensitivity along X and Z axes and in the mode of motion along Y axis with sensitivity and capacitance indicators, does not accede to analogues.

Acknowledgments

This work was financially supported by the grant of President of Russian Federation (project number MK-2130.2020.8).

References

[1] Raspopov V Ya 2007 Micromechanicheskie pribory: uchebnoye posobie (Tula: Tulskiy gos. Universitet) p 400

[2] Lysenko I E Ezhova O A Tkachenko A V Naumenko D V 2020 Analysis of the micromechanican three-axis accelerometer Book of Abstracts of 7th International School and Conference «Saint-Petersburg OPEN 2020» on Optoelectronics, Photonics, Engineering and Nanostructures (St.Petersburg: St. Petersburg Academic University) pp 449-450.

[3] Lysenko I E 2019 The results of modelling of a micromechanical accelerometer Journal of Physics: Conference Series 1410 012226 DOI:10.1088/1742-6596/1410/1/012226

[4] Lysenko I E 2013 Modeling of the micromachined angular rate and linear acceleration sensors LL-type with redirect of drive and sense axis (World Applied Sciences Journal vol 27) P 759-762

Determination of measurement fidelity for a superconducting photon-number resolving detector with micron-wide strips

M Dryazgov[1, 2], N Simonov[2], Yu. Korneeva[2], A Korneev[1, 2]
[1]Higher School of Economics - National Research University, 101000, Russia
[2]Department of Physics, Moscow State Pedagogical University, 119992, Russia

e-mail: mdryazgov@hse.ru

Abstract. We report a study of multiphoton detection fidelity for sequential photon-number resolving detectors based on micron-wide superconducting strips. It was found that an increase in the width of the superconducting strips by a factor of 5 leads to an improvement in the measurement accuracy by more than a factor of 10

1. Introduction

Photon-number resolving detectors (PNR detectors) [1, 2] based on superconducting strips have found applications in the areas where it is necessary not only to validation the fact of detecting a photon, but to find out the number of photons: quantum computers [3] and quantum cryptography [4].

The standard architecture of a PNR detector consists of several superconducting single-photon detectors (SSPD) [5] connected either in series with parallel resistors or in parallel with series resistors. Distinguishing the number of photons occurs using spatial multiplexing, when several sections are triggered simultaneously by several photons, and the voltage pulses from the sections are summed up resulting in the amplitude proportional to the number of photons. Here we address the issue of fidelity (or accuracy) of the photon number identification: due to electric noise the resulting amplitude may be smaller or larger, thus giving the wrong measurement result.

We consider the described detection fidelity as the probability, when i sections are triggered, to detect i photons, when the internal quantum efficiency of the detector is 100%.

2. Measurement procedure

Voltage pulses are obtained for a serial PNR detector with a strip width of 0.5 micrometer, 7 sections, the length of one section is 240 micrometers, and the total area is 35x30 μm^2. The pulses pass through 2 Mini-Circuits ZFL-1000LN amplifiers and are measured using a Rohde & Schwarz RTO1012 digital oscilloscope (fig. 1).

We obtain a histogram of the frequencies of the noise track, corresponding to the normal distribution (fig. 1 (in the inset)). Using the normal distribution formula for relative frequencies, the probability function of detecting noise with amplitude U_{noise} is obtained:

$$P(U_{noise}) = \frac{1}{\sigma\sqrt{2\pi}} \exp \frac{-U_{noise}^2}{2\sigma^2}$$

The $P(U_{noise})$ values were also plotted with a solid line (Fig. 1 (in the inset)).

To detect the $i-th$ pulse with the amplitude U_{imp}^i, the trigger value is $U_{tr}^i = (U_{imp}^i - U_{imp}^{i-1})/2$. This means that if the noise value is $U_{noise} \leq U_{tr}^i - U_{imp}^i$, the equipment will fix $i-1$ photon. Similarly, if $U_{noise} \geq U_{tr}^{i+1} - U_{imp}^i$, the equipment will capture $i + 1$ photons.

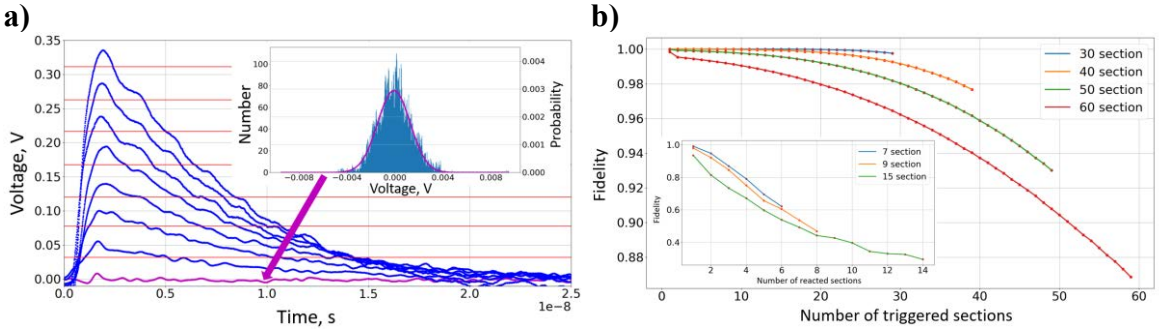

Figure 1. a) Experimentally obtained voltage pulses for a PNR detector with a 7 series connection of sections, the width of the superconducting strips is 0.5 μm. The noise track is highlighted in purple. Red lines are trigger levels. The inset shows a histogram of the voltage probability distribution of the noise track, the purple curve is the normal distribution of relative frequencies. b) Dependence of fidelity on the number of triggered sections for a PNR detector with a series connection of sections with a width of superconducting strips of 0.5 μm. Inset for 100 nanometer stripes.

Then we define fidelity as the probability of detecting exactly i pulses, taking into account thermal noise:

$$F = P\left(U_{tr}^{i} - U_{imp}^{i} < U_{noise} < U_{tr}^{i+1} - U_{imp}^{i}\right) = \int_{U_{tr}^{i}-U_{imp}^{i}}^{U_{tr}^{i+1}-U_{imp}^{i}} \frac{1}{\sigma\sqrt{2\pi}} \exp\frac{-U_{noise}^{2}}{2\sigma^{2}}\, dU_{noise}$$

With an increase in the number of sections, the difference in heights of neighboring pulses decreases, as well as with a decrease in the width of the superconducting strips. To assess this effect, the classical electro-thermal model [7], written for an SSPD with micron-wide superconducting strips, was adopted for a PNR-detector with a series connection of sections.

3. Results

Figure 1b shows the dependence of the calculated fidelity on the number of triggered sections for a PNR detector with a total number of sections in range 1 - 60. As can be seen from the graphs, with the total number of sections less than or equal to 30, the noise does not affect the probability of detecting i photons when i sections are triggered. The inset in fig 1b shows similar plots for a PNR detector with a series connection of sections with a superconducting strip width of 100 nanometers.

4. Conclusion

We demonstrate a method for determining the fidelity of detection of i-photon pulses of the PNR-detector for different widths of superconducting strips and different total number of sections. The use of micron-wide superconducting strips makes it possible to improve the fidelity of detecting voltage pulses for a PNR-detector with a series connection of sections due to a high critical current. This fact and low kinetic inductance give an advantage to micron-wide superconducting strips.

5. Acknowledgments

This work was supported by the Russian Science Foundation (RSF) Grant No. 20-12-00287.

References

[1] Mattioli F *at al* 2015 *Superconductor Science and Technology* **28**, 104001
[2] Divochiy A *at al* 2008 *Nature Photonics* **2**, 302–306
[3] You L 2020 *Nanophotonics* **9**, 2673–2692
[4] Cattaneo M *et al* 2018 *Phys. Rev. A* **98**, 012333
[5] Gol'tsman G *at al* 2001 *Applied Physics Letters* **78**, 705–707
[6] Zou K *at al* 2020 *Physical Review Applied* **14**, 044029
[7] Dryazgov M *et al* 2020 *Journal of Physics: Conference Series* **1695**, 012195

Study of the welded joint of VT1-0 titanium with 1.3343 steel

I Egorov[1], **A Fomin**[1]
[1]Yuri Gagarin State Technical University of Saratov, Saratov 410054, Russia

Abstract. The work describes a method for obtaining a composite structure of small plates. The resulting plates are a layered structure consisting of a substrate (1.3343 steel) and a titanium coating (VT1-0). A method of resistance welding in the open air was applied to form a layered structure. The resulting titanium-steel compound was tensile tested. The maximum force at break of the welded joint varied in the range from 1.05 to 2.17 kN.

1. Introduction

Production of composite materials largely involves the use of combined methods [1-3]. In many cases, these methods differ a lot from each other. The materials used can be dissimilar in their purpose and mechanical properties as well. In the case of various welding methods in the obtained joints between dissimilar materials, chemical non-homogeneity and intermetallic phases may arise, which lead to a decrease in physical and mechanical properties. The use of titanium-coated steel products has great practical interest. Steel products are used in almost all industries [1,2]. They are covered with various coatings and films in order to increase their service life.

Resistance welding conducted under certain conditions provides a strong and reliable connection between dissimilar materials [4,5]. In this work, a titanium coating (cp-Ti VT1-0) was applied on a substrate of 1.3343 tool steel (analogous to R6M5). A method of spot resistance welding was used for coating deposition.

2. Methodology

The materials used were 1.3343 steel with a square cross-section with a side of 13 mm, a height of 3.5 mm and a central hole of 4.2 mm, and VT1–0 titanium in the form of a 70×20 mm plate with a thickness of 0.5 mm.

Before welding, the contact surfaces of the samples were processed with abrasive paper to remove the oxide layer and impart the required roughness parameters. Further the surfaces were degreased in 96% ethanol.

The welded joint of steel with titanium was formed using "Telwin Digital Modular 230" resistance spot welding setup. The constant parameter of resistance welding was the compression force of the electrodes of about 600 N (±10 %) and the operating voltage of 2.5 V. The power and the consumed current were the output characteristics and varied in the following ranges: P = 3.6–8.2 kW (power consumption), I = 17–39 A (consumed current), and pulse duration t = 0.1–1.2 s.

Static tensile tests were carried out in "Impuls IR5282-100" software-controlled tensile testing machine. The stretching rate was chosen equal to 10 mm/s. When stretching, the maximum force was recorded. After the test, the fracture site was examined using "MBS-10" optical microscope.

3. Results

According to the results of the static tensile test, it was revealed that titanium was reliably fixed on the steel surface under almost all modes. At a current I = 39 A and a pulse duration of t = 0.4 s, the surface

of the titanium coating samples had macrodefects in the form of dents and metal splashes (Figure 1). This sample was destroyed before the tensile test when clamped.

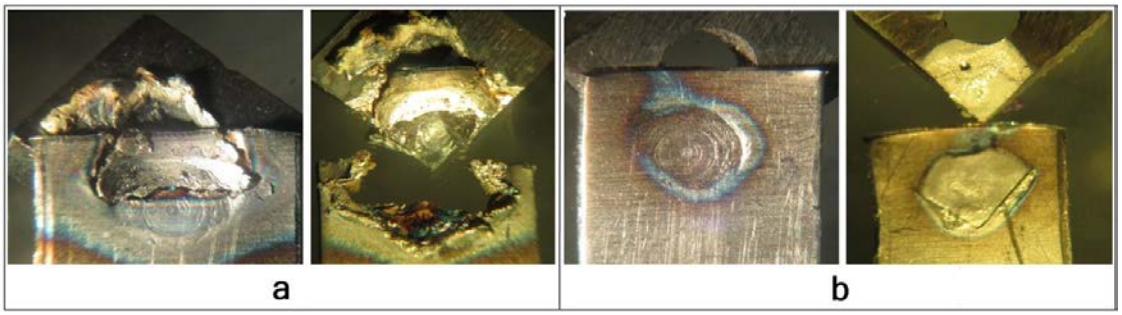

Figure 1(a, b). Samples after resistance welding and tensile tests obtained at various modes: I = 39 A, t = 0.4 s (**a**); I = 27 A, t = 0.4 s (**b**)

The sample obtained at an average current I = 27 A and t = 0.4 s, like the rest of the samples, was destroyed along the metal interface. The ultimate tensile strength during the test was 2.17 kN, and the minimum value was 1.05 kN.

4. Conclusions

Thus, the application of the resistance spot welding method for the formation of a welded joint between 1.3343 steel and commercially pure titanium was considered. According to the results of the study, it was determined that a pulse with a current strength of about 39 A led to the destruction of the samples. For the duration of 0.4–0.9 s and the current of about 27 A, overheating of the steel substrate and its embrittlement occurred. With other welding parameters, the steel retained its strength, and the resulting welded joint withstood forces from 1.05 to 2.17 kN.

Acknowledgments

The research was supported by the scholarship from the President of the Russian Federation (SP-571.2019.1). Part of the work (optical analysis of the surface morphology of the welded joint) was carried out within the framework of the "U.M.N.I.K." program (project 15686GU/2020).

References

[1] Kuz'min E V, Korolev M P, Lysak V I, Kuz'min S V, Zarubin M S and L'vov V. A 2020 *Izvestia VSTU* **246** 19-23
[2] Ren D, Jiang Y, Hu X, Zhang X, Xiang X and Ling H 2021 *Intermetallics* **132** 107115
[3] Li J, Vivek A and Daehn G 2021 *J Mater Sci Technol* **79** 191-204
[4] Egorov I, Shchelkunov A, Fomin A and Rodionov I 2018 *J Phys Conf Ser* **1124** 081015
[5] Fomin A, Egorov I, Shchelkunov A, Fomina M, Koshuro V and Rodionov I 2018 *Compos Struct* **206** 467

Entanglement of two dipole-coupled qubits induced by a thermal field of one-mode lossless cavity with Kerr medium

R K Zakharov[1] and E K Bashkirov[1]

[1]Samara University, 34, Moskovskoye shosse, Samara, 443086, Russia

rodionzhakharov@yandex.ru

Abstract. We studied the dynamics of two dipole-coupled qubits interacting with one-mode thermal quantum electromagnetic field of microwave cavity with Kerr medium. Using the exact solution for considered model we derived the qubit-qubit negativity for sepsrsble initial qubits states. We showed that Kerr medium and dipole-dipole interaction can greatly enhance the degree of qubits entanglement.on qubit-qubit entanglement is examined. We showed that Kerr medium can greatly enhance the amount of qubit-qubit entanglement.

1. Introductionr

Coupling distant qubits is an important goal for quantum information and for its potential applications. This kind of coupling needs the study of interaction between qubits and photons, which has been widely studied in a cavity quantum electrodynamics (CQED) [1]. Resent years a lot of schemes are proposed for generating, controlling and protecting the atomic entanglement in CQED systems such as trapped and cooled ions or neutral atoms, superconducting circuits, spins in solids, quantum dots interacting with quantum fields of cavities. The theoretical investigations of such schemes are based on a Jaynes-Cummings model (JCM) and its generalizations [2]. Particularly, a lot of authors studied the dynamics of atom interacting with field of one-mode cavity with a Kerr-like medium in a framework of nonlinear JCM (see Refs in [3]). The Kerr effect is a widely used phenomenon in nonlinear quantum optics, and has been successfully used to generate quadrature and amplitude squeezed states, parametrically convert frequencies etc. In practice, Kerr nonlinearities in atomic systems are, however, often small in comparison to photon loss rate, making the observation of these non-classical states of light difficult. As an alternative approach, strong photon-photon interaction can readily be realized in superconducting quantum circuits, demonstrated experimentally [4]. Note, that in the field of quantum optics with microwave circuits, the direct analogue of the Kerr effect is naturally created by the nonlinear inductance of the Josephson junctions.

Resent years we explored the influence of dipole-dipole interaction on atomic entanglement for qubits interacting with thermal cavity field [5].. It is of interest to expand our researches to more complicated CQED system with strong photon-photon interaction. In this paper, we study the influence of Kerr nonlinearity on atomic entanglement for system consisting of two identical dipole-coupled qubits interacting with one-mode thermal cavity field.

2. Model and its exact solution

We consider two identical dipole-coupled qubits resonantly interacting with cavity mode. We suppose that qubit-field coupling constants are equal. The suppose also that there is an additional Kerr medium in the cavity. The interaction Hamiltonian for the system under rotating wave approximation can be written as

$$H = \sum_{i=1}^{2} \hbar\gamma(\sigma_i^+ a + a^+ \sigma_i^-) + \chi a^{+2} a^2 + \hbar J(\sigma_1^+ \sigma_2^- + \sigma_2^+ \sigma_1^-),$$

where $\sigma_i^+ = |+\rangle_{ii}\langle -|$, and $\sigma_i^- = |-\rangle_{ii}\langle +|$ are the transition operators between the excited $|+\rangle_i$ and the ground states in the i th qubit ($i = 1,2$), a^+ and a are the creation and the annihilation operators of photons of the cavity mode, γ is the coupling constant between qubits and the cavity mode, χ is the dispersive part of the third- order nonlinearity of Kerr medium in the cavity and J is dipole-dipole couplin constant. The initial qubits state is assumed to be separable such as

$$|\Psi(0)\rangle_A = |+,-\rangle \text{ or } |\Psi(0)\rangle_A = |+,+\rangle.$$

The initial cavity mode state is assumed to be thermal one-mode state

$$\rho_{Field}(0) = \sum_k p_k |k\rangle\langle k|,$$

where $p_k = \bar{k}^k / \left(1+\bar{k}\right)^{k+1}$. The average photon number is $\bar{k} = \left(\exp\left[\hbar\omega / k_B T\right] - 1\right)^{-1}$, where T is the resonator temperature.

3. Results and discussion

We obtain**ed** the exact solution of the Liouville equation for whole system density matrix $\rho(t)$ with using the so-called "dressed" states representation. Taking a trace over the field variables we derived the reduced atomic density operator $\rho_A(t) = Tr_{Field}\rho(t)$ and calculated the two-qubit negativity. $\varepsilon = -2\sum \mu_i^-$, where μ_i^- is the negative eigenvalues of the partial transpose of a reduced atomic density matrix $(\rho_A^{T_1})$. The results of negativity computer simulation for the initial state of qubits $|+,-\rangle$ showed that in the absence of Kerr nonlinearity, the dipole-dipole interaction leads to a significant increase in the degree of qubits entanglement, while for a cavity with a Kerr medium, the dipole-dipole interaction only leads to a decrease in the envelope period of negativity Rabi oscillations. It is also shown that for initial qubits state $|+,+\rangle$ the qubit-qubit entanglement induced by the thermal cavity field arises only in the presence of Kerr nonlinearity. In this case, the strength intensity of the dipole-dipole interaction practically does not affect the maximum degree of entanglement of qubits. The results obtained can be useful in choosing the optimal modes of functioning of quantum devices, such as quantum computers and quantum networks.

References

[1] Georgescu I M, Ashhab S and Nori F 2014 *Rev. Mod. Phys.* **88** 153
[2] Shore BW and Knight P L 1992 *J. Mod. Opt.* **40** 1195
[3] Alqannas H S and ·Khalil E M 2021 *Optical and Quantum Electronic* **53(**34) 1
[4] Kirchmair G et al. 2013 *Nature* **495** 205
[5] Evseev M M and Bashkirov E K 2020 Proc. ITNT 2020 - 6th IEEE Int. Conf. Inform. Tech. Nanotech. 9253347

Electrophoresis of CNT-RuO_2 composite for planar supercapacitor

E P Kitsyuk[1], Yu P Shaman[1], E A Lebedev[2], Yu I Kakovkina[2], D A Kuzmin[2]

[1] SMC "Technological Centre", Moscow, 124498, Russia

[2] MIET, Moscow, 124498, Russia

e-mail: Kitsyuk.e@gmail.com

Abstract. The method of formation planar supercapacitor by combined electrophoresis of CNT and RuO_2 is demonstrated. The alcohol-acetone suspension was stable and consisted of oxidative treated CNTs, ruthenium oxide, cellulose and iodine. Influence of different solvents and components ratio on the morphology and the electrophysical characteristics of the electrodes was investigated. It was demonstrated the possibility of creating high-capacity and powerful compact supercapacitors for a wide range of applications in microelectronics.

1. Introduction

The advance of miniaturized electronics and Internet of Things (IoT) has a great impact on the development of energy storage miniaturized devices. Supercapacitors are considered as a perspective devices in this area, thanks to their compact device structure and high specific power. Great efforts have been made to maximize their performance with new carbon nanomaterials and increase their specific capacity and energy density by utilization of transition metal oxides such as RuO_2, MnO_2, NiO, Co_3O_4, SnO_2, ZnO, TiO_2, CuO, $Fe2O_3$, WO_3[1]. In this regard, we developed an electrophoresis deposition of electrodes from combined CNT-RuO_2 suspension for the development of planar supercapacitors.

2. Experimental detail

To fabricate the electrodes few walls carbon nanotubes (FWCNTs) synthesized by CVD method was used. The deposition of electrode material was carried out in the electrophoretic cell, consisted of two electrodes - a cathode (nickel foil) and an anode (gold electrode) in a container for suspension, and a current source. To limit the deposition area, the sample surface was partially masked using a rigid ceramic mask. Initial suspension was prepared in a 50 ml test-tube. Preliminary CNTs were underwent oxidative treatment in HCl and H_2O_2, that was necessary for their stability in suspension. All components (FCNT, RuO_2 * xH_2O, cellulose and iodine) with variations in the amount of ruthenium hydroxide were mixed in a test tube with a mixture of acetone and ethyl or isopropyl alcohol in a 1: 1 ratio. Dispersion of the resulting solution was carried out by submersible ultrasonic dispersant.

The layers received by electrophoretic deposition from ethyl (figure 1) and isopropyl (figure 2) alcohol suspensions were investigated by SEM and EDX methods and generally they have a very similar island structure.

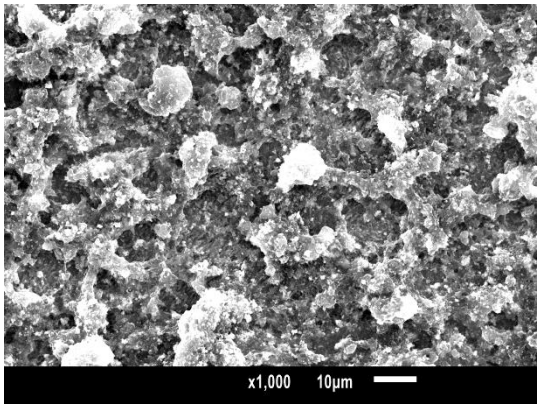

Figure 1. Layer of FWCNT-RuO_2composite deposited from ethanol-based suspension.

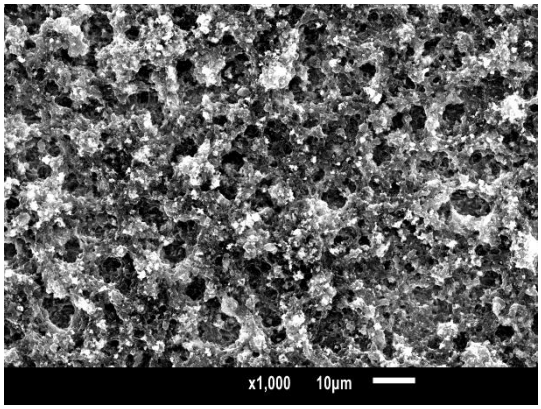

Figure 2. Layer of FWCNT-RuO_2 composite deposited from isopropyl-based suspension.

FWCNTs are uniformly distributed over the composite material and electrically and mechanically bind individual particles of ruthenium oxide (figure 3).

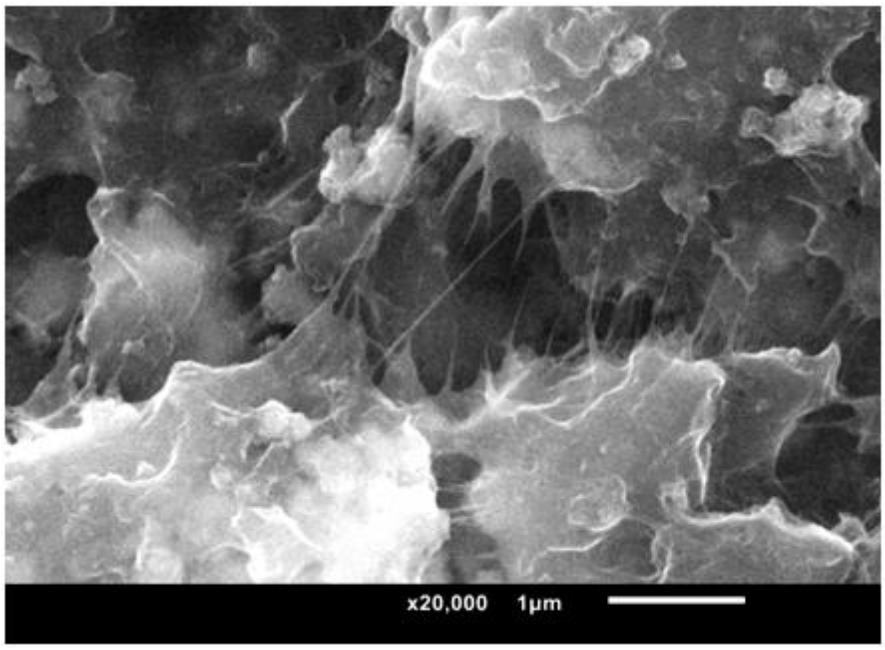

Figure 3. SEM of FWCNT between RuO_2 particles in electrode layer from ethanol-based suspension.

To study the electrophysical characteristics of supercapacitors, sandwich structures of two electrodes on nickel foil, separated by a separator impregnated with aqueous 1M KOH electrolyte was assembled. Commercially available porous polypropylene membranes were used as a separator. The sandwich structure was placed in a plastic envelope for lamination. Cyclic voltammetry (CV), galvanostatic charge–discharge (GCD) and electrochemical impedance spectroscopy (EIS) were performed to characterize the performance of the devices.

References

[1] Cuihua An, Yan Zhang, Huinan Guoa and Yijing Wang 2019 *Nanoscale Adv*. **12** 4644-58.

Lithium aluminosilicate glass-ceramics for low-temperature anodic sealing of MEMS sensors

R Kleimanov[1,2], I Komarevtsev[1,2], Y Enns[1,2], Y Akulshin[2], A Kazakin[1,2]

[1]Alferov University, St Petersburg 194021, Russia.
[2]Peter the Great St Petersburg Polytechnic University, St Petersburg 195251, Russia.

Annotation. The results of a study of the optical and electrical parameters of glass-ceramics based on lithium aluminosilicates which are promising as structural materials for various MEMS sensors are presented. A comparison of the transmission spectra in the optical range of these materials and classical for the MEMS industry glasses is carried out. The glass-ceramics electrical conductivity has been measured over a wide temperature range. The procedure of hermetic sealing of glass-ceramics by the method of anodic bonding at temperatures of the order of 150-200 °C has been worked out.

1. Introduction

For the correct operation of various modern sensor systems, an inert atmosphere or vacuum on the chip level is often required, as well as the optical transparency of the substrate. Such devices include microfluidic devices, quantum magnetometers and atomic clocks, pressure sensors, micromechanical resonators, gyroscopes and accelerometers, bolometers and other MEMS devices. For hermetic sealing of such devices on a wafer level, various bonding technologies are used, the most widespread of which is the high-temperature anodic bonding of the wafers [1]. Materials for the anodic bonding are special borosilicate glasses (in the case of silicon technologies, Borofloat 33, Pyrex 7740, Hoya SD-2, etc.). These glasses have high ionic conductivity at anodic bonding temperatures (about 300 - 500 ^{o}C), optical transparency, thermomechanical compatibility with other sensor materials [2]. At the same time, high voltages and temperatures required for high-quality anodic bonding of commercial borosilicate glasses, fixed coefficient of thermal expansion (CTE) and a number of other factors limit the application of this technology for some MEMS.

Transparent glass-ceramics which have a number of advantages over glass - high softening temperature, low gas permeability, low fragility, high strength, resistance to mechanical processing, ability to vary the CTE within wide limits due to the composition or temperature and duration of partial crystallization [3], can become alternative materials for anodic sealing of MEMS [4].

This article presents the results of the work carried out to assess the prospects for use of optically transparent glass-ceramics based on lithium aluminosilicates in MEMS industry.

2. Experiments and results

The objects of study were polished wafers with a thickness of 0.5 to 3 mm, made of glass-ceramics synthesized on the basis of lithium aluminosilicates and containing a crystalline phase of the spodumene and eucryptite types: commercial glass-ceramic material (optical sitall) SO-33M having a zero CTE and laboratory samples with an average CTE in the range from 3 - 4 · 10^{-6} 1/K. Temperature

dependence of the samples CTE were measured by comparative dilatometry method (reference samples were fused quartz and monocrystalline silicon).

We measured the transmission spectra of glass-ceramic samples in the wavelength range from 300 nm to 1000 nm and the transmission spectra of classical borosilicate glasses used in the production of MEMS sensors. Their comparative analysis showed a slight decrease in the transparency of these glass-ceramics in comparison with glasses, which is at the level of a few percent and depends on the degree of partial crystallization. For example, glass-ceramic material SO-33M transmits light 2% worse than Borofloat 33 glass in the entire measured range.

The study of the electrical conductivity of glass-ceramics was carried out on a laboratory equipment designed for anodic bonding of silicon and glass. The wafers were preliminarily divided into square samples with an area of 1 cm^2, and blocking electrodes made of an 0.5 μm thick aluminum film were deposited on both sample sides by magnetron sputtering. The obtained time dependences of the current density showed a purely ionic character of conductivity. The magnitude of the initial current peak at the moment of switching on the voltage was used to estimate the specific electrical conductivity of glass-ceramics at a given temperature. The measured values of specific electrical conductivity were 1 to 2 orders of magnitude higher than this value for Borofloat 33 glass in the temperature range of 200 - 300 °C.

This case made it possible to successfully carry out a hermetic anodic bonding of some samples of glass-ceramics with monocrystalline silicon already at a temperature of 150 °C and a voltage of 300 V. Samples of glass-ceramic SO-33M were successfully bonded to each other at a temperature of 120 °C. To perform this process a 100 nm thick polysilicon film was previously deposited on the one of samples. The obtained result can be applied in the technology of alkali vapor cells with anti-relaxation organic coatings on the walls for MEMS atomic clock.

A similar method can also be applied to seal Sitall SO-33M with fused quartz due to the equality of their CTE. This technology may be promising for low-cost manufacturing of microfluidic sensors for UV diagnostics of various biomaterials.

3. Acknowledgments

This work was carried out in Peter the Great St.Petersburg Polytechnic University and was supported by a grant of Russian Science Foundation (project № 20-19-00146).

References

[1] Dziuban J A 2006 Bonding in microsystem technology *Advanced Microelectronics* vol 24, ed K Itoh, T Lee, T Sakurai, W M C Sansen and D Schmitt-Landsiedel (Netherlands: Springer) p 331
[2] Sinev L S, Ryabov V T 2017 *J. Micro/Nanolith. MEMS MOEMS* **16**(1) 015003
[3] O Dymshits, M Shepilov, A Zhilin 2017 *MRS Bulletin* **42** 200–205
[4] H Li, Y Du, J Cheng , T Wang 2008 *Key Engineering Materials* **368-372** 1436-1438

Dependence of field-effect biosensor sensitivity on photo-induced processes in Si and its conductivity type

A V Kozlowski* **and S V Stetsyura**

Institute of Physics, Saratov State University, Saratov 410012, Russia

*kozlowsky@bk.ru

Abstract. The effect of photoelectron processes in *n*-Si and *p*-Si on the glucose sensitivity of a capacity field-effect biosensor based on electrolyte/oxide/semiconductor structure was investigated. We obtained that illumination of *n*-Si/SiO_2/polyethylenimine structure during the glucose oxidase (GOx) adsorption increases the glucose sensitivity by three times compare to GOx adsorption in the dark. In contrast, *p*-Si illumination during the GOx adsorption led to a decrease in sensor sensitivity from 2.9 mV/mM to 2.2 mV/mM. The result is explained by a change in the density of immobilized GOx molecules induced by photoelectron processes in Si substrate during enzyme adsorption.

1. Introduction

Electrolyte/oxide/semiconductor (EOS) structures are widely used to detect nano- and bio-objects ionized in solution. Also, EOS-structures are used to recognize enzymatic reactions [1], viruses [2], RNA/DNA sequencing. The parameters of enzyme biosensor based on EOS-structures can be improved by increasing the concentration of enzyme molecules adsorbed onto a semiconductor transducer surface. Ionic strength or pH of solution are commonly used to modulate the electrostatic interactions between enzyme molecules and semiconductor surface. However, variation of pH or ionic strength leads to a nonmonotonic and unpredictable change in the surface density of enzyme molecules.

Previously [3], we report on the influence of the white-light illumination of Si substrate during glucose oxidase (GOx) adsorption on the surface concentration of immobilized GOx molecules. This method is called photo-stimulated adsorption (PSA). The PSA efficiency of charged nano- and bio-objects significantly depends both on a Si conductivity type and on a buffer polyethyleneimine (PEI) layer on Si surface [4]. However, studies on the effect of PSA of enzyme molecules onto a semiconductor transducer surface on the sensitivity of a capacitive field-effect biosensor have not existed before. In this work, we studied the effect of photo-stimulated layer-by-layer adsorption of GOx on the glucose sensitivity of field-effect-based capacitive EOS-sensors.

2. Experimental section

The EOS-structures were fabricated using single-crystal (100) Si wafers (400±10 μm thickness) of *n*-type (ρ = 8-10 Ω cm) and *p*-type (ρ = 9-15 Ω cm). Initially, the wafers were boiled in a peroxide–ammonia solution and rinsed in deionized water. Afterwards, wafers were cut into substrates of 10×10 mm^2.

The glucose oxidase (GOx) form *Aspergillus niger* were used as enzyme molecules. Branched polyethyleneimine (PEI) with a molecular weight of 25 kDa was used as cationic polyelectrolyte to increase the adsorption of negatively charged GOx onto Si substrates. The organic molecules were

adsorbed onto Si substrates from the aqueous solutions during 10 min followed by rinsing in deionized water (ρ ~ 18.2 MΩ cm) during 10 min and drying in nitrogen flow. As working buffer, a 0.2 mM potassium phosphate buffer solution (pH = 7.3) containing 150 mM NaCl as an ionic strength adjuster was used. The photo-stimulated layer-by-layer adsorption technique suggested in [4] was used to adsorb GOx from aqueous solution onto Si substrates covered with PEI. The Si substrate was either in the dark or under illumination during the GOx adsorption, other things being equal. The glucose sensitivity of EOS-biosensors was studied by means of capacitance-voltage (C–V) measurements using a probe station (Cascade Microtech) controlled by a semiconductor device analyzer (Agilent B1500A).

3. Results and Discussion

Figure 1 shows exemplarily a typical C–V curves of the EOS-biosensor. With increasing glucose concentration in the solution, the C–V curves are shifted along the voltage axis in the direction to more negative voltage values. This is due to an increase in the H^+ concentration of on the EOS-sensor surface due to the enzymatic reaction. It was found that for EOS-sensor, where the GOx molecules were deposited in the dark, the sensitivity to glucose is 1.90 and 2.87 mV/mM for *n*-Si and *p*-Si, respectively. In the case of PSA - 5.8 and 2.23 mV/mM for *n*-Si and *p*-Si, respectively.

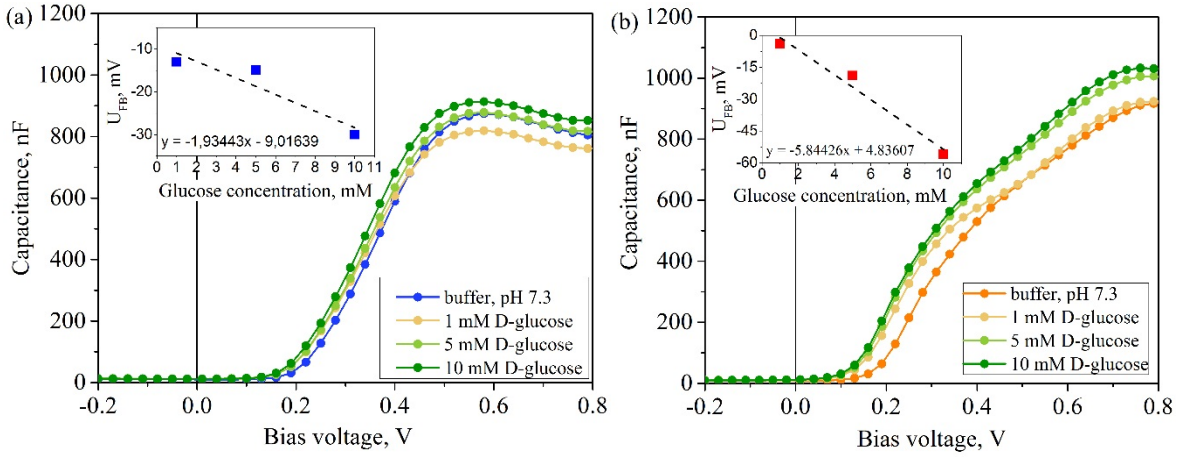

Figure 1(a, b). Typical C–V curves of the EOS-sensors measured in potassium phosphate buffer and in glucose solutions of different concentrations from 1 to 10 mM; **(a)** – GOx adsorbed in the dark, **(b)** – GOx adsorbed under illumination. Inset: calibration curves

4. Conclusion

Thus, it was shown that the white-light illumination of Si/SiO_2/PEI substrate during adsorption of GOx molecules from the aqueous solution increases or decreases the glucose sensitivity of EOS-biosensor depending on the Si conductivity type. The result is explained by a change in the density of immobilized GOx molecules induced by photoelectron processes in Si substrate during enzyme adsorption.

5. Acknowledgments

The work was supported by the German-Russian Interdisciplinary Science Center (G-RISC), Project no. P-2018a-10.

References

[1] Poghossian A, Schöning M 2020 *Sensors* **20** 5639
[2] Poghossian A et al. 2020 *Front. Plant Sci.* **11** 598103
[3] Maslennikova A, Kozlowski A, Santer S and Stetsyura S 2019 *Journal of Physics: Conference Series* **1400** 077052
[4] Malyar I, Gorin D, Santer S and Stetsyura S 2017 *Appl. Phys. Lett.* **110** 133104

Single-step alkaline etching of deep silicon cavities for chip-scale atomic clock technology

I Komarevtsev[1,2], Y Enns[1,2], A Kazakin[1,2]

[1]Alferov University, St Petersburg 194021, Russia.
[2]Peter the Great St Petersburg Polytechnic University, St Petersburg 195251, Russia.

Annotation. This paper presents the results of experiments on the development of the technology of MEMS alkali vapor cell for a miniature quantum frequency standard. The classical design of a two-chamber silicon cell containing an optical chamber, shallow connection channels and a technical container for a solid-state alkali source was implemented in a single-step process of wet anisotropic silicon etching. To prevent the destruction of the connection channels during etching of the through silicon cavities, the shapes of the compensating elements at the convex corners of the silicon nitride mask were calculated and the composition of the silicon etchant was experimentally found. The results of the experiments were used in the manufacture of chip-scale atomic clock cells containing vapors of ^{87}Rb or ^{133}Cs isotopes in the neon atmosphere.

1. Introduction

Miniature absorption cells containing alkali metal vapors are key elements of quantum magnetometers, atomic clocks, and other quantum devices that are used in spectroscopy, telecommunications, and navigation systems [1]. For the industrial production of chip-scale quantum devices, MEMS technologies (deep etching of silicon, anodic sealing of silicon and glass) and two-chamber cell designs are used [2,3]. Such cells consist of two sealed cavities with a volume of several cubic millimeters, connected by narrow filtration channels (Figure 1). One of the cavities is used to fill the cell with a solid-state source of alkali vapors. The other cavity contains only pure alkali metal vapors and an inert gas and provides optical absorption at a wavelength corresponding to the atomic line D1 of ^{133}Cs, ^{85}Rb or ^{87}Rb. Connection channels provides, due to a small cross-section, a transfer of alkali atoms into the optical cavity without byproducts formed during laser activation of the solid-state source. Usually, plasma chemical etching of silicon substrate is used to simultaneously form through-wafer cavities and connection channels [3]. Anisotropic alkaline etching of silicon is a cheaper process, but it is not used for the industrial manufacture of two-chamber cells. Due to excessive undercutting of convex corners, during alkaline etching to a depth of more than 500 microns, the channels completely disappear and the two cavities are transformed into one large cavity (Figure 2). But it is possible to compensate for the undercutting of convex corners by a suitable mask design.

The aim of this work is to develop a method of single-step alkaline etching for the manufacture of a gas cell containing two volume cavities of 3 x 1.5 x 0.6 mm connected by rectangular channels with a width of 200 microns.

2. Experiments and results

The objects of the study were polished silicon wafers with (100) orientation and a diameter of 76 mm. The wafers thickness was varied from 400 to 600 microns. Before etching, a 0.2 microns thick layer of

silicon nitride was deposited on both sides of the wafer, and a mask pattern was formed on one side by direct photolithography. Then, through etching of the cavities was carried out in aqueous solutions of KOH at 80 ^{o}C for a time of about 6-10 hours.

The pattern of the nitride mask corresponded to the basic topology of two-chamber alkali vapor cell. To preserve the filtration channels during long wet etching, various compensating elements on the convex corners of the nitride mask pattern were used. The shape and size of these elements were previously calculated on the basis of computer simulations of the silicon etching in alkaline etchants of various concentrations and compositions.

The best results were obtained when using an etchant consisting of one volume part of thirty percent potassium hydroxide and one volume part of isopropyl alcohol. After 8 hours of etching, the optical cavities were etched through, the compensation elements were completely etched, leaving the channels open and not over-etched. Figure 3 shows photo of the chip after the final stages of vapor cell manufacturing - filling with a source of rubidium (caesium) and anodic sealing with glass in a neon atmosphere [2].

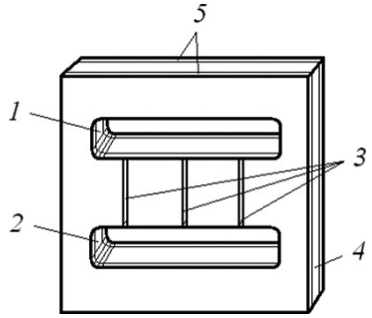

Figure 1. Cell scheme [2]: *1*, *2* – working and additional cavity, respectively, *3* – connecting channels, *4*, *5* – silicon and glass plates, respectively.

Figure 2. Degradation of the original cell topology after deep silicon etching during 6 hours in 30% KOH

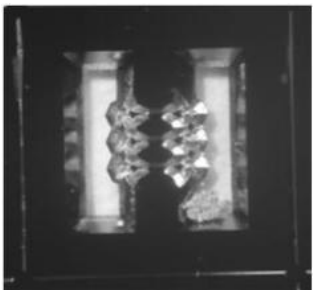

Figure 3. Manufactured vapor cell with a solid-state source of ^{87}Rb isotope.

3. Conclusion

In the course of the work, a method of single-step alkaline etching for manufacturing of two-chamber MEMS cells containing vapor of rubidium-87 or caesium-133 isotopes in a neon atmosphere was developed. The suitability of cells manufactured using this technology for chip-scale atomic clocks was confirmed by appropriate tests [2,4].

4. Acknowledgments

This work was carried out in Peter the Great St.Petersburg Polytechnic University and was supported by a grant of Russian Science Foundation (project № 20-19-00146).

References

[1] Kitching J 2018 *Appl. Phys. Rev.* **5** 031302
[2] Ermak S V, Semenov V V, Piatyshev E N, Kazakin A N, Komarevtsev I M, Velichko E N, Davydov V V, Petrenko M V 2015 *St. Petersb. Polytech. Univ. J. Phys. Math.* **1** 37–41
[3] Hasegawa M., Chutani R K, Gorecki C, Boudot R, Dziuban P, Giordano V, Clatot S, Mauri L 2011 *Sensors and Actuators A* **167** 594–601
[4] Bobrov M A, Blokhin S A, Maleev N A, Blokhin A A, Vasyl'ev A P, Kuzmenkov A G, Gladyshev A G, Novikov I I, Petrenko M V, Ospennikov A M, Ermak S V, Ustinov V M 2019 *J. Phys.: Conf. Ser.* **1400** 077014

III–V nanowires for ammonia detection

V. M. Kondratev[1], V. V. Fedorov[1], V. O. Gridchin[1], A. S. Kuznetsov[1], G. E. Cirlin[1], S. S. Nalimova[2], V. A. Moshnikov[2] and A. D. Bolshakov[1]

[1]Alferov University, St. Petersburg 194021, Russia
[2]Saint Petersburg Electrotechnical University "LETI", St.Petersburg, 197376, Russia

Abstract. Ammonia is an inorganic agent found both in nature and in the human body, which is of great interest for modern sensory applications. Ammonia in concentrations of the order of 1 ppm is produced by human and is a biological marker of pathological changes in human body, but concentrations of the order of 100 ppm, ammonia is toxic and hazardous. This work is aimed at fabrication and study of precise, technological and relatively cheap ammonia sensors compatible with a liquid medium, and motivated by the possibility of using this type of adsorption sensors in medical, environmental equipment and biological purposes.

1. Introduction

Among modern methods for detection of small concentrations of inorganic agents in liquids, indicator analysis and voltammetry methods are mostly often used. Adsorption sensors based on classical metal oxides, which have proven themselves in gas sensing, are widely presented. Despite the high ratio of the surface area compared to volume of nanowires (NWs) and the pronounced conductivity features of 1D structures compared to bulk materials, the adsorption properties of III–V NWs and their correlation with electrical characteristics are still very poorly studied. Classical works do not allow to fully investigate the dynamics of adsorption processes on the surface of low–dimensional structures of III–V compounds [1–2].

2. Synthesis and study of nanowires

Vertically oriented GaAs, GaN and GaP NWs were synthesized on (111) silicon substrates by molecular beam epitaxy, typical parameters and growth conditions are presented in previous works [3–5]. The synthesized structures were studied by scanning electron microscopy, and transferred to an auxiliary substrate and studied by Raman scattering spectroscopy.

GaAs NWs have a length of about 25 μm and a cross section of 100–200 nm, and their Raman scattering spectra show modes that correspond to the zinc blende (ZB) GaAs crystal structure [6–7] GaN NWs about 6–8 μm long and 20–80 nm cross–section have sharp features in Raman spectra corresponding to the wurtzite structure [8].

The Raman spectrum of GaP NWs (about 25 μm long and 150–250 nm cross–section) is well consistent with the results of the work which examined high crystal quality ZB GaP [9].

3. Sensor fabrication and ammonia detection

The NWs were separated from the growth substrate by ultrasonication in isopropanol, and transferred to the surface of a sensor platform with gold interdigital contacts (contact pitch of 5 and 10 μm) with subsequent annealing for sensor fabrication. The Gold–NWs contacts formed are of the Schottky type, which proved by the voltage–current characterisation.

The impedance spectra were obtained in a comparative medium – distilled water and a target adsorbate – ammonia with concentrations of 10 and 100 ppm. Impedance measurement conditions: constant signal amplitude – 100mV, variable signal amplitude–20mV, frequency range: from 100 Hz to 500 kHz.

The GaAs NWs based sensor allowed us to qualitatively determine the presence of ammonia in distilled water by reducing the imaginary part of the impedance over the entire range of voltage frequencies relative to the sensor impedance spectrum in the presence of distilled water. However, no restoration of the original electrical performance was observed. We assume that this may be due to the defective nature of the adsorption centers on the NWs and the degradation of the GaAs crystal surface, which together determines the capacitive nature of the GaAs NWs sensor and makes a significant contribution to the reactive component of the impedance. The optimal frequency range for working with GaAs sensors is 200 Hz–8 kHz, where the greatest separation of the impedance spectra corresponding to water and ammonia are observed.

GaN and GaP NWs demonstrated high chemical stability to liquid medium. The first demonstrated the possibility of reproducible ammonia detection with the restoration of the electrical characteristics of the sensor and In the presence of ammonia, an increase in the imaginary part of the sensor impedance was observed with the real part almost unchanged over the entire frequency range under consideration. The second is suitable for quantitative detection of ammonia by reducing the imaginary and real part of the impedance during adsorption of ammonia, with the restoration of the original electrical characteristics in water. In this case, the entire considered range of measuring frequencies is suitable.

4. Conclusion

The equivalent electrical scheme of the sensors and signal normalization allowing for investigation of the changes in NWs conductivity are proposed. Normalization are consists in subtracting the contribution to the sensor impedance spectrum and allows one to evaluate the electrical properties of NWs and their correlation with adsorption properties.

We demonstrated an effective protocol for fabrication of III–V NWs based sensors and showed the optimal frequencies for working with sensors of this type for ammonia, which may be interesting in terms of characterization of conductivity nature and doping level of low–dimensional epitaxial nanostructures and sensoric applications.

References

[1] Journal of Applied Physics 96, 7574.
[2] Applied Nanoscience 2013, 3, 363–372.
[3] Cryst. Growth Des. 2020, 20, 1, 300–306.
[4] Technical Physics Letters, 2020, 46, 11,. 1080–1083.
[5] ACS Nano 2020, 14, 8, 10624–10632.
[6] JETP Letters 2014, 99, 396–399.
[7] PhysRevB. 2009, 80. 245325.
[8] Journal of Electronic Materials 2014, 43, 1379–1383.
[9] Appl. Phys. Lett 2014, 105, 193102.

Study of hardness and morphology of carbide coatings obtained on complex shaped steel items by electro-spark alloying

V Koshuro[1], **A Fomin**[1], **A Aman**[1,2], **S Palis**[3]

[1] Yuri Gagarin State Technical University of Saratov, Saratov 410054, Russia

[2] Otto Vollmann GmbH & Co. KG, Gevelsberg, Germany, 58285

[3] Otto-von-Guericke-Universität Magdeburg, Universitätsplatz 2, Magdeburg, Germany 39106

Corresponding author, e-mail: dimirion@mail.ru

Abstract. The work investigated the possibility of forming carbide coatings by electrospark alloying on steel products of complex shape. It has been established that electrospark alloying at an AC current of 1.0 to 4.5 A makes it possible to form coatings of hard carbide alloy VK6 and T15K6 characterized by hardness HRA 86.6 and 81.5 with the initial hardness of the steel product HRA 80.3.

1. Introduction

In most cases, protective coatings on steel products are formed from carbides, nitrides, borides, carbonitrides of a number of metals (Cr, W, Mo, V, Ti, Ta) and transition metal oxides (Zr, Ti, Al). At present, protective layers are formed on steels by CVD, PVD, ion-plasma spraying, etc. [1-2]. Nitride (TiN) coatings formed by CVD and PVD increase the corrosion resistance of the steel surface. In this case, the hardness of PVD coatings of the TiN system formed on steel substrates can reach 20 GPa, and the grain size can be 15-50 nm [3]. Layers of CrC /C, TiC and TiC/CrC/C systems increase the wear resistance of steel substrates [4]. At the same time, these layers are characterized by significant brittleness, small thickness and low values of adhesive strength, which sharply narrows the area of their rational use.

Despite the widespread use of CVD and PVD technologies, there remains a need for methods that allow the formation of wear-resistant layers characterized by high values of hardness, adhesive strength, low porosity, and a given surface morphology. The known method of electrospark alloying (ESA) allows surface alloying of metals and the formation of functional layers from conductive materials, including hard alloys [5]. Despite the knowledge of the ESA method, it remains necessary to study the features of the formation of high-strength coatings on products of complex shape.

2. Methodology

Steel products of complex shape with an initial hardness of HRA 80.3 were used as samples. Local spherical areas of the surface were hardened (Figure 1a). For the formation of coatings from hard materials of grades VK6 and T15K6 (ISO 513-75) at values of alternating current from 1.0 to 4.4 A, an "ARKOGRAF" electric spark marker was used. The morphology of the formed coatings was

investigated according to the well-known technique [6]. The measurement of the hardness of the formed carbide layers was carried out using a portable Rockwell hardness tester "TX PHR-2". The qualitative assessment of the adhesion of the applied layers was carried out on the HF1-HF6 scale according to Verein Deutscher Ingenieure Normen VDI 3198.

3. Results

During ESA, a heterogeneous coating was formed on selected curved areas (Figure 1b). Defects in the form of cracks, delamination and significant pores were not visualized.

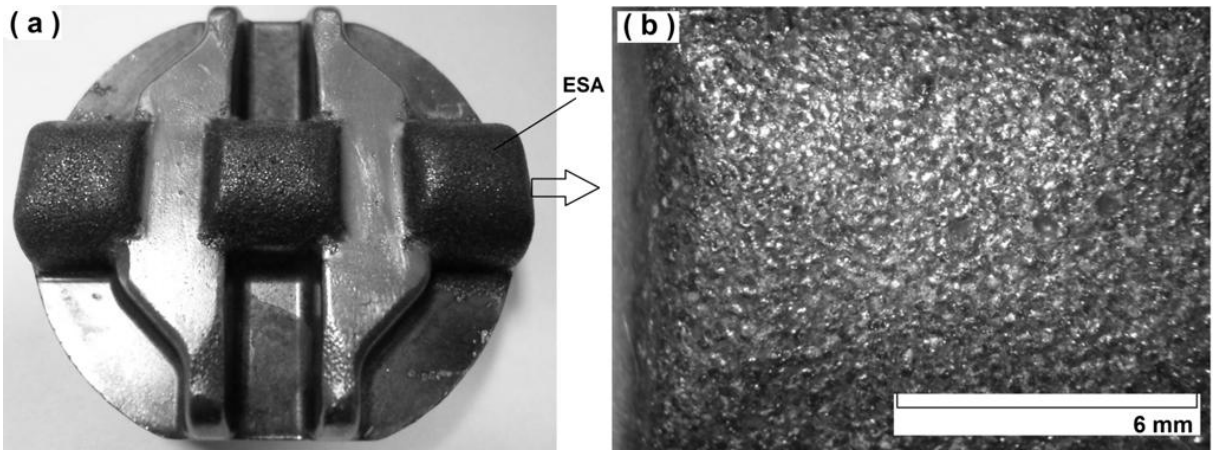

Figure 1. General view (a) of a steel sample with areas of ESA coating from T15K6 and the morphology of the formed coating (b)

Surface hardness increased from HRA 80.3 to 81.5 and 86.6 for T15K6 and VK6, respectively. The difference in hardness is justified by the different thicknesses of the layers being formed. After indentation, no cracks or delamination of the coating was found around the indentations, which corresponds to HF1 (VDI 3198) and is a high indicator of adhesive-cohesive strength.

4. Conclusions

As a result of the research, the possibility of forming carbide coatings on complex-profile steel surfaces has been established. Electrospark alloying makes it possible to obtain highly hard layers with high values of adhesive-cohesive strength.

Acknowledgments

The research was supported by the Ministry of Education and Science of the Russian Federation and German Academic Exchange Service (DAAD) in the framework of the program "Mikhail Lomonosov" (Project Executor Koshuro V.A.).

References

[1] Michalski J, Lunarska E, Wierzchon T and AlGhanem S 1998 *Surf Coat Tech* **72** 189.
[2] Helmersson U, Johansson B O, Sundgren J E, Hentzell H T G and Billgren P 1985 *J Vac Sci Technol A* **3** 308.
[3] Lukaszkowicz K and Dobrzański L A 2008 *J Mater Sci* **43** (10) 3400.
[4] Nilsson M and Olsson M 2011 *Wear* **273** (1) 55.
[5] LiQ H, Yue T M, Guo Z N and Lin X 2013 *Metall Mater Trans A* **44** (4) 1767.
[6] Fomina M, Koshuro V, Papshev V, Rodionov I, Fomin A 2018 *Data in Brief* **20** 1409.

Optimization of deep silicon plasma etching process for microstructures fabrication

V Kuzmenko[1,2], A Miakonkikh[1,2], K Rudenko[1,2]
[1]Valiev Institute of Physics and Technology of Russian Academy of Sciences, Moscow, Russia
[2]Moscow Institute of Physics and Technology, Dolgoprudny, Russia

kuzmenko.vo@phystech.edu

Abstract. The paper presents the study of cyclic process of deep anisotropic silicon plasma etching which is called Ox-Etch. This process has typical for cyclic etching process sidewall profile called scalloping. Opportunities for modification and optimization of process for specific application were investigated. Balance between etch rate and scalloping was established.

1. Introduction

Plenty of microstructures relevant for various applications are fabricated by deep silicon etching. Some devices of droplet microfluidics [1] can be based on thin trenches made in silicon. Array of holes in silicon can form two-dimensional photonic crystal, which can be applied for terahertz communication devices [2]. Another application is microstructures for 3D integrated capacitors using in dynamic random-access memory (DRAM) [3]. In order to increase capacitance and consequently density of the stored information, the area of the capacitor plates is increased, so usually capacitors are formed by conformal deposition of films on sidewalls of high aspect ratio structures in silicon. Manufacturing of all these high aspect ratio structures requires technology of deep anisotropic plasma etching of silicon. Different technologies of anisotropic silicon etching have their own features. One of these technologies is well-known Bosch process, in which anisotropy is achieved by protecting sidewalls of structure with fluorocarbon film. The idea of this process consists in the cyclic repetition of the steps of passivation of the surface with a polymer film in a fluorocarbon plasma and anisotropic etching with a DC bias in a fluorine-containing plasma. Structures etched in this process have typical sidewall profile with periodical notches called “scallops”.

Here an alternative approach of deep anisotropic silicon etching known as Oxidation-Etching (Ox-Etch approach) was studied. Earlier, it was proposed [4] and patented [5]. The idea is based on the replacement of polymer passivation by plasma oxidation of silicon. Silicon oxide 1–2 nm thick has sufficient plasma etch resistance for one etching cycle. The process studied in this work is a cyclical repetition of the following steps: 1) passivation in the O_2 plasma - the formation of a SiO_2 layer several nanometres thick on all open areas of silicon (oxidation step), 2) etching in SF_6 plasma - removal of passivation from the bottom with accelerated ions, and spontaneous isotropic etching (etching step). The method we are investigating has several advantages over the Bosch process. In the etching process, no hard-to-remove polymer film remains on the side walls, which facilitates subsequent technological operations. Furthermore, fluorocarbon gases used in Bosch process for passivation have significant global warming potential, which means that increased content of these

gases in atmosphere leads to an increase in the greenhouse effect. Passivation by O_2 plasma is more eco-friendly.

Also, it is quite well-known from the researchers of Bosch process that with increasing of aspect ratio etching process is different from it's start. The presence of such feature in the Ox-Etch process is also should be researched.

At present work approaches of modification and optimization of the oxidation-etching process are examined. In studied process DC bias is applied for a short time only for breakthrough passivation and then etching of exposed silicon regions is isotropic without bias. As DC bias break passivation layer predominantly on horizontal areas, sidewalls should be preserved from isotropic etching. Minimization of duration of DC bias should increase of selectivity in process.

2. Experimental

The experiment was carried out in the PlasmaLab 100 plasma etching tool (Oxford Instruments Plasma Technology) on silicon samples 2x2 cm with a SiO_2 mask 2 μm thick. Mask has round holes 12 μm and 16 μm width trenches. These structures are considered as a model for a variety of other structures in the fields of photonics, microfluidics, and other deep trench applications in microengineering.

Typical parameters of ICP discharge were as follows: pressure 10 mTorr, input power 1750 W, DC bias 40-80 Volts, although some parameters were varied.

Duration of both oxidation and etching steps were varied in order to research ability to tune etch rate and scalloping of the process. SEM pictures of microstructures were obtained after 50 cycles process. Increase of etching step duration increases etching rate and both scalloping and undercut. Increase of oxidation step decreases etch rate because of decrease in the proportion of etching in the cycle. This allow to find compromise between etch rate and undercut for specific application. Ability to control the undercut makes it possible to optimize the deep etching process.

3. Conclusion

In the work some new results are presented on the optimization of the previously proposed process of multistage plasma etching (Ox-Etch). The results obtained show the possibility of its application to create structures for plasmonics and microfluidics, as well as integrated high-capacity capacitors. Although the process has a number of disadvantages of the Bosch process, such as scalloping and the aspect dependence of etching, it also has a number of advantages - there is no need to use fluorocarbon gases (C_4F_8, C_3F_8, CHF_3), which have the property of forming fluorocarbon polymer films in plasma. The latter circumstance makes the process eco-friendly, and in addition excludes the formation of thick polymer films on the structures, and the need for regular conditioning of the reactor. Spectral measurements have shown that with long performance of the oxy-etch process (thousands of cycles), residues of fluorine-containing compounds are not observed in Ar plasma after a short conditioning cycle. At the same time, it is known that in the Bosch process, the formation of thick polymer films is so significant that mechanical cleaning of the reactor may be required on a regular basis.

Acknowledgments

The investigation was partially supported by Program no. 0066-2019-0004 of the Ministry of Science and Higher Education of Russia for Valiev Institute of Physics and Technology of RAS and partially funded by RFBR according to the research projects #20-07-00832.

References

[1] Yadavali S., Lee D. and Issadore D. 2019 *Sci. Rep.* **9** 12213
[2] Withayachumnankul W., Fujita M. and Nagatsuma T. 2018 *Adv. Optical Mater.* **6** 1800401
[3] Strambini L. et al. 2020 *Nano Energy* **68** 104281
[4] Miakonkikh A. V., Averkin S.N. and Rudenko K.V. 2019 *J. Phys.: Conf. Ser.* **1243** 012009
[5] Averkin S. N. et al. 2019 Patent RU 2691758 C1

Separation of III-N partially coalesced nanowire arrays from Si substrate

V V Lendyashova [1,2*], K P Kotlyar [1,3], R R Reznik [4], V O Gridchin [1,3], K Yu Shubina [1], T N Berezovskaya [1], E V Nikitina [1], I P Soshnikov [1,2,5], G E Cirlin [1,4,5]

[1] Alferov University, St. Petersburg, 194021, Russia
[2] Ioffe Institute, St. Petersburg 194021, Russia
[3] Saint-Petersburg State University, St.-Petersburg, 198504, Russia
[4] ITMO University, St. Petersburg 197101, Russia
[5] IAI RAS, St. Petersburg 198095, Russia

E-mail: * erilerican@gmail.com

Abstract . In modern optoelectronics, arrays or single nanowires (NWs) of III-N materials, in particular InGaN, separated from the original substrates are used to fabricate light-emitting diodes or single photon sources. This work describes a technology of separation super dense arrays or arrays of partially coalesced InGaN nanowires and single nanowires from a Si substrate by chemical etching in $HF:HNO_3$ solution, which allows preserving the optical properties of the structure for further use.

1. Introduction

Nowadays semiconductor nanowires (NWs) are promising for applications in nanophotonics and optoelectronics. One of the priorities is high-efficient light-emitting diodes (LEDs) based on III-N NWs [1]. Flexible LEDs based on the NWs arrays separated from the substrate, especially indium gallium nitride (InGaN) are of great interest. The single class of objects is partially coalesced arrays of nanowires – aggregate nanostructures – which are also used to create light-emitting devices [2] or act as a buffer layer for the growth of III-N layers on substrates with a large mismatch of lattice parameters [3]. For several applications, it is necessary to separate these structures from the original substrate, and the methods used for separately located NWs (mechanical separation, the formation of a composite material called?? polymer-NWs and its subsequent separation, etc.), in this case, do not lead to the desired result. In this regard, it is necessary to develop a technology of separating arrays or single NWs from the substrate (in particular, Si(111)) to further study the properties of synthesized NWs and to fabricate devices based on them.

2. Experiments and results

Arrays of partially coalesced NWs of indium gallium nitride (InGaN) on Si(111) substrate were synthesized by molecular beam epitaxy (MBE) at Riber Compact 12 MBE system as an example of III-N NWs. Initially, the InGaN NWs array was a structure with a total height of about 2 μm, consisting of partially coalesced in the mid-height zone spindle-shaped nanowires with a diameter from 80-100 at the tops and bases up to 200 nm (Figure 1a). The surface morphology of the samples

was studied with scanning electron microscopy (SEM) Zeiss Supra 25. The optical properties of the structure were exanimated by photoluminescence spectroscopy (Accent RPM Sigma machine) at each stage of separation.

The method of separation consists of wet chemical etching in $HF:HNO_3:H_2O$ $(1:1:3)$ solution at room temperature [4]. After placing the samples in a container with an acid solution etching was carried out in stages with results checked control of the results. It was observed that the separation of the structure primarily occurs around defects and along the edges of the sample, as shown in Figure 1b [5]. This feature is explained by the fact that in these sites it is easier for the etching solution to reach the NWs/Si interface. After separation, the NWs array, cleared of the residual etching solution, can be either immediately transferred to any type of substrate or placed in a cuvette for subsequent ultrasound treatment. Such an impact on the nanostructure allows the layer to be divided into small flaxes, single NWs, or parts of them (individual tops) depending on the morphology of the initial sample. Thereafter, it is possible to deposit parts of the NWs array or single NWs on the substrate (Figure 2).

The most interesting was the influence of etching and transfer of the array to another substrate on the optical properties of the structure. Photoluminescence spectra of the initial sample and InGaN NWs array transferred to glass did not show any significant changes in optical properties.

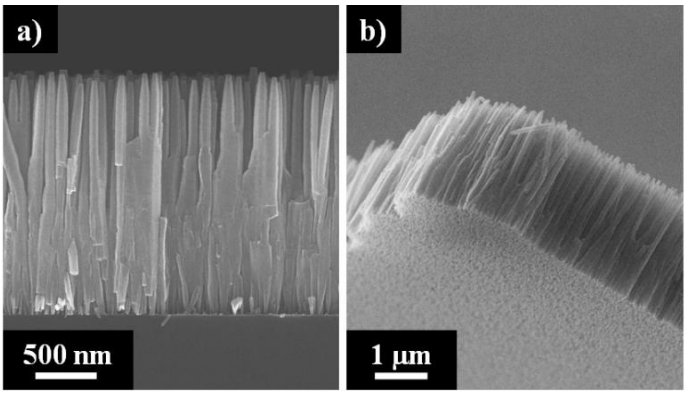

Figure 1(a,b). SEM images of (a) InGaN NWs array after MBE growth; (b) NWs array separated from the edge of the sample.

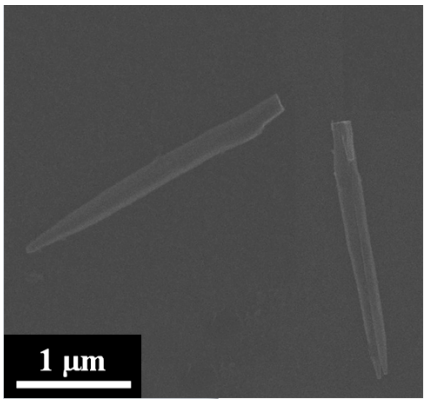

Figure 2. SEM image of single NWs after separation transferred on glass.

This work describes a new method of separation arrays of partially coalesced III-N NWs from Si(111) substrate by wet chemical etching in an $HF:HNO_3$ solution. It is shown that the proposed method allows preserving the optical properties of the structure during separation and transfer to other types of substrates, as well as separating single III-N NWs from the original substrate.

Acknowledgments
The samples were grown with the support of the Ministry of Science and Higher Education of the Russian Federation (state task №0791-2020-0003). SEM and Pl studies of the samples were supported by RFBR (grant 19-32-90156).

References
[1] Dubrovskii V G, Cirlin G E, Ustinov V M 2009 Semiconductors 43(12) 1539
[2] Kikuchi A, Kawai M, Tada M, Kushino K 2004 Jpn. J. Appl. Phys. 43 L1524
[3] Li S, Waag A 2012 J. Appl. Phys. 111 071101
[4] Karar N, Opila R, Beebe T Jr 2011 J. Electrochem. Soc. 158(6) D342-D350
[5] Kukushkin S A, Osipov A V, Red'kov A V 2017 Semiconductors 51(3) 414

Features of Electrophoretic Formation of Local Heat Sources Based on Nanosized Powder Al

E S Leonenko[1], L I Sorokina[1], E A Lebedev[1], R M Ryazanov[2]

[1] National Research University of Electronic Technology (MIET), 124498, Moscow, Zelenograd, Russia
[2] Scientific Manufacturing Complex "Technological Centre", 124498, Moscow, Zelenograd, Russia

E-mail: katejustkate86@gmail.com

Abstract: In this study the features of electrophoretic deposition (EPD) method to form nano-Al based energetic layers were investigated. The influence of solvents and additive components on the EPD process was analyzed, and the optimal composition of the suspension for the best deposition of layers based on nanoscale Al particles was acquired. The obtained layers can be used as an initiator of secondary reactions for on-chip energetic systems and a local heat source for joining surfaces by reactive bonding.

1. Introduction

Nowadays nanoscale energetic materials attract considerable research interest as a local heat source for low-temperature joining of thermosensitive elements. Another one of the fields where these materials can be used is as an initiator of secondary reactions for on-chip energetic systems. Usually thermite composite materials consist of fuel particles (Al) and oxidizer particles (metal oxides) [1, 2]. If using more active nanosized aluminum and initiate combustion in air, then an oxidizer is not needed - oxygen from the atmosphere will be used for the reaction. Electrophoretic deposition (EPD) is considered to be the most affordable method that has the ability to deposit thin layers locally [3]. Thus, goal of this study was to investigate how suspension composition affects its stability and how process modes affects the morphology of the layer surface.

2. Methodical

To carry out the experiments it is necessary to prepare suspensions. They consisted of solvent, main and additive components. For solvents isopropyl alcohol and acetone were used solely and in different ratios together. The main component of the suspension was Al nanopowder. Additive components as nickel (II) nitrate hexahydrate $N_2NiO_6 \cdot 6H_2O$ and hydroxypropylcellulose were used for suspension stabilization. The suspensions were dispersed in the ultrasonic bath.

The EPD process requires an electrophoretic cell. It includes two electrodes connected to a power source: first one – for deposition, second one – counter electrode; and a suspension immersed into a beaker. Layers were deposited at an electric field strength from 30 to 150 V/cm at different time limits. Surface morphology, thickness and stoichiometry of the obtained energetic materials were investigated using scanning electron microscopy (SEM) with an attachment for analysis of energy dispersive X-ray spectroscopy (EDS).

3. Results

First, the stability of suspension has been investigated. To stabilize it different solvents and additives were used. Based on the results, two compositions of suspensions showed better stability. The addition of nickel (II) nitrate hexahydrate into the suspension made of Al and isopropyl alcohol allows to increase the stability of the suspension. In another case the addition of acetone to the same suspension composition makes it possible to stabilize it.

Then the morphology of the obtained coats was examined with the scanning electron microscopy. Layers obtained from the suspension with acetone have uneven surface. The deposited layers turned out to be more porous, which negatively affected the adhesion of the formed layers, and some areas of the layer desorbed from the substrate during the process. Layers obtained from the suspension with addition of nickel (II) nitrate hexahydrate have much more even surface.

Afterwards the influence of different concentrations of $N_2NiO_6 \cdot 6H_2O$ to the velocity of the EPD process was studied. Analyzing the dependence of the process velocity on $N_2NiO_6 \cdot 6H_2O$ concentration suspension composition with 5 mg of the charger has higher velocity. Though it was decided to use the composition of the suspension with 10 mg of $N_2NiO_6 \cdot 6H_2O$, because the stability of the suspension was higher.

Based on the research results, the influence of solvents and additive components of suspension on the EPD process was analyzed, and the optimal composition of the suspension for deposition of layers based on nanosized Al particles was acquired. The obtained coats can be used as an initiator of secondary reactions for microelectromechanical systems (MEMS), and as a local heat source for reactive bonding of the surfaces.

4. Acknowledgments

This work was supported by the State assignment 2020-2022 (research project FSMR-2020-0018).

References

[1] Yin Y, Li X 2019 *Vacuum* **163** 216-223
[2] Sullivan K T, Zhu C, Tanaka D J, Kunz J D, Duoss E B, Gash A E 2013 *The Journal of Physical Chemistry* **117(6)** 1686-1693
[3] Besra L, Liu M 2006 *Progress in Materials Science* **52(1)** 1-61

Influence of active structure parameters on resonant frequency of acoustic transducer membranes

S V Malokhatko[1,2], E Yu Gusev[1], O A Ageev[1,2]

[1]Department of Nanotechnologies and Microsystems, Southern Federal University, Taganrog 347922, Russia
[2]Research and Education Center "Nanotechnologies", Southern Federal University, Taganrog 347922, Russia

e-mail: malohatko@sfedu.ru

Abstract. The paper presents the results of calculations of the resonant frequency of a multilayer square membrane for various combinations of active layer materials and metal electrodes. The dependences of the resonant frequency on the edge length, as well as on the thickness of the active layer of the piezoelectric and metal electrode for SiO_2/Ti/ZnO, SiO_2/Al/ZnO, SiO_2/Ti/PZT, SiO_2/Al/PZT structures are obtained. According to the calculations, the values of the resonant frequencies are in the ranges: 46.1–498.3 kHz for SiO_2/Ti/ZnO; 45.4–477.3 kHz for SiO_2/Al/ZnO; 39.4–411.4 kHz for SiO_2/Ti/PZT; 38.1–381 kHz for SiO_2/Al/PZT. It is shown that the resonant frequency can be increased by changing the geometric parameters of the membranes, however, the material and size of the piezoelectric layer make the greatest contribution. The results of analytical and numerical simulations of a particular case of a square SiO_2(1 μm)/Ti(1 μm)/ZnO(2 μm)/Ti(1 μm) membrane with a edge length of 600 μm are also compared. The results obtained can be used to optimize the design and manufacturing technology of ultrasonic transducer.

1. Introduction

Ultrasonic transducer have found application in various fields of industry and medicine [1, 2]. The key parameter when choosing an ultrasonic transducer for a specific application is the resonant frequency, the choice of which is a compromise between the resolution achieved at high frequencies and the attenuation, which is less common at lower frequencies [3]. The main element of the sensor is membrane (single layer/multilayer); sensor characteristics such as sensitivity, electromechanical coupling coefficient and frequency depend on it. A multilayer membrane includes an active layer of piezoelectric material located between metal electrodes. Studies of design solutions with different active layers (ZnO, PZT, AlN) and electrodes (Al, Mo, Ti, Pt, Au) are presented [1]. The values of ultrasound frequencies in such sensors start from 20 kHz. The actual objective is to choose the most optimal combination of materials in a multilayer structure and their thicknesses, for operation at frequencies above 20 kHz. The aim of the work is to theoretically study the influence of materials and geometry of the active piezoelectric layer (PZT, ZnO) and metal electrodes (Al, Ti) and the influence of their thicknesses on the values of resonant frequencies.

2. Theoretical details and results

The paper analyzes the piezoelectric materials and metal electrodes used in ultrasonic transducers. Based on the reference data on the properties of the materials, the most optimal combinations of the multilayer

structure were selected. A square-shaped membrane was chosen for calculations. The structure consisted of three layers: SiO_2, piezoelectric (ZnO, PZT) and electrode (Al, Ti). Since the structure is multilayer, the resonant frequency was calculated taking into account the parameters of each layer according to [4]. Calculations were carried out for 1) SiO_2/Ti/ZnO, 2) SiO_2/Al/ZnO, 3) SiO_2/Ti/PZT, 4) SiO_2/Al/PZT combinations. The SiO_2 thickness was assumed to fixed (1 μm), the thickness of the active (piezoelectric) layer varied in the range from 2 to 4 μm, and the electrodes from 1 to 2 μm, the edge length varied from 400 to 1000 μm. The dependences of the resonant frequency on the thickness of the piezoelectric material and metal, as well as on the edge length of of the square membrane, were obtained (Fig. 1).

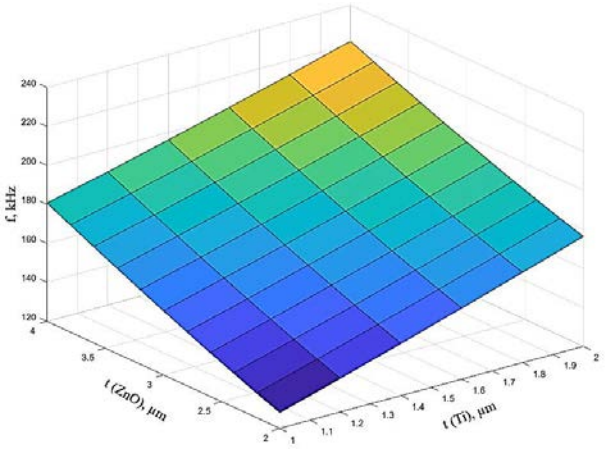

Figure 1. The dependence of the resonant frequency on the piezoelectric (ZnO) layer thickness and the electrode (Ti) thikness for 600 μm membrane edge length.

According to the obtained dependences, the the values of the resonant frequencies are in the ranges of 46.1–498.3 kHz for SiO_2/Ti/ZnO; 45.4 – 477.3 kHz for SiO_2/Al/ZnO; 39.4–411.4 kHz for SiO_2/Ti/PZT; 38.1–381 kHz for SiO_2/Al/PZT. To verify the results of analytical calculations, numerical simulation of the frequency characteristics of a multilayer membrane was performed for one of the particular cases: a square membrane of 600x600 μm SiO_2(1 μm)/Ti(1 μm)/ZnO(2 μm)/Ti(1 μm). The resonant frequency calculated numerically for such structure was 144 kHz, and the analytical frequency was 128 kHz. The difference is presumably due to the fact that the presence of the upper electrode was taken into account in the numerical model. The results obtained show that the resonant frequency decreases with increasing edge length and decreasing layer thicknesses, and that the choice of piezoelectric material makes a greater contribution to the change in the resonant frequency compared to the electrode material. The highest values of the resonant frequency were obtained for the SiO_2/Ti/ZnO combination, which makes it the most suitable for applications in devices operating at high frequencies. The results obtained can be used to optimize the design and technology of ultrasonic sensors.

Acknowledgment

The reported study was funded by RFBR, project number 20-37-90087. The work was done on the equipment of the Research and Education Centre «Nanotechnology» of Southern Federal University.

References

[1] Jung J, Lee W, Kang W, Shin E, Ryu J, Choi H 2017 *J. Micromech. Microeng.* **27** 113001
[2] Ageev O A, Konoplev B G 2019 *Nanotechnology in microelectronics* (Moscow: Nauka) 511
[3] Hoskins P R., Martin K , Thrush A 2010 *Diagnostic Ultrasound: Physics and Equipment* (Cambridge medicine. Cambridge University Press) 263
[4] Muralt P, Baborowski J, Barzegar A, Gentil S, Belgacem B, Petitgrand S, Bosseboeuf A, Setter N 2005 *IEEE Transactions on ultrasonics, ferroelectrics, and frequency control* **52** 2276

Influence of laser processing conditions on the depth and microhardness of layers formed on titanium

V Koshuro[1], E Osipova[1], O Markelova[1], M Fomina[1], A Fomin[1]
[1]Yuri Gagarin State Technical University of Saratov, Saratov 410054, Russia

Abstract. In this work, the depth and microhardness of layers formed on titanium during laser processing in graphite environment were investigated. The energy and duration of laser pulse varied from 0.76 to 10.17 J and from 0.5 to 3 ms, respectively. As a result of processing, the formation of layers characterized by depth of 8.3-800 μm and a microhardness of 9.68-28.01 GPa occurs. Regression models are constructed that describe the effect of laser processing conditions on the indicated characteristics of the layers. It was found that pulse energy had greatest influence on the depth and microhardness of hardened titanium.

1. Introduction

At present, cementation technologies are widely used to harden the titanium surface. The most well-known technologies, for example, induction carburizing, allow carburizing over entire surface of the product [1]. It is more rational to carry out local hardening by laser processing of titanium in graphite environment. As a result of carburizing, carried out using graphite powder and laser heating, carbide layer is formed from nonstoichiometric TiC, which makes it possible to increase the titanium hardness to $HV_{0.1}$ 1200 (11.8 GPa) [2]. Despite the existence of works on laser carburizing of titanium, the effect of laser processing conditions on thickness of hardened layers and their microhardness has not been sufficiently studied.

2. Methodology

Titanium plates 10×10×1 mm in size were used in the studies. The plates were preliminarily placed in the tooling and a bulk layer 100-300 μm thick from graphite powder with a dispersion of 10-35 μm was formed on their surface (Figure 1).

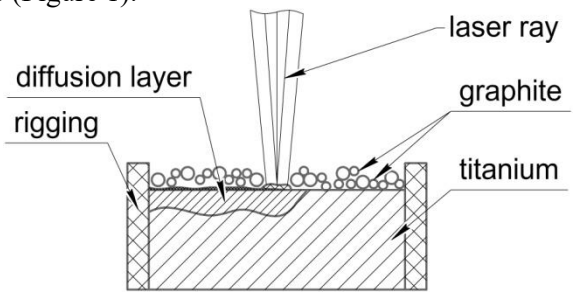

Figure 1. Laser treatment of titanium in a graphite environment

Laser treatment was carried out on an «LRS-50A» installation at an energy and duration of laser pulse from 0.76 to 10.17 J and from 0.5 to 3 ms, respectively. Laser radiation was focused into a spot 0.75 mm in diameter. The depth of structural changes was measured from the images of microsections

according to the well-known method [3]. Hardness of the coatings was evaluated by microindentation using «PMT-3M» (at the load of 0.98 N). The construction of regression models was carried out in the «DataFit 9» program.

3. Results

Laser treatment in a graphite medium made it possible to form a layered system on titanium, consisting of a thin coating, 0.5-6 μm thick, and diffusion layers 8.3-800 μm deep. The diffusion layers were characterized by the presence of finely dispersed dendritic structure. Pulse energy (E, J) had a pronounced effect on the thickness (h, μm) of diffusion layers (Figure 2a). The layers obtained at a duration (τ, ms) of 3 ms and average values of the pulse energy differed in the maximum microhardness (H, GPa) (Figure 2b).

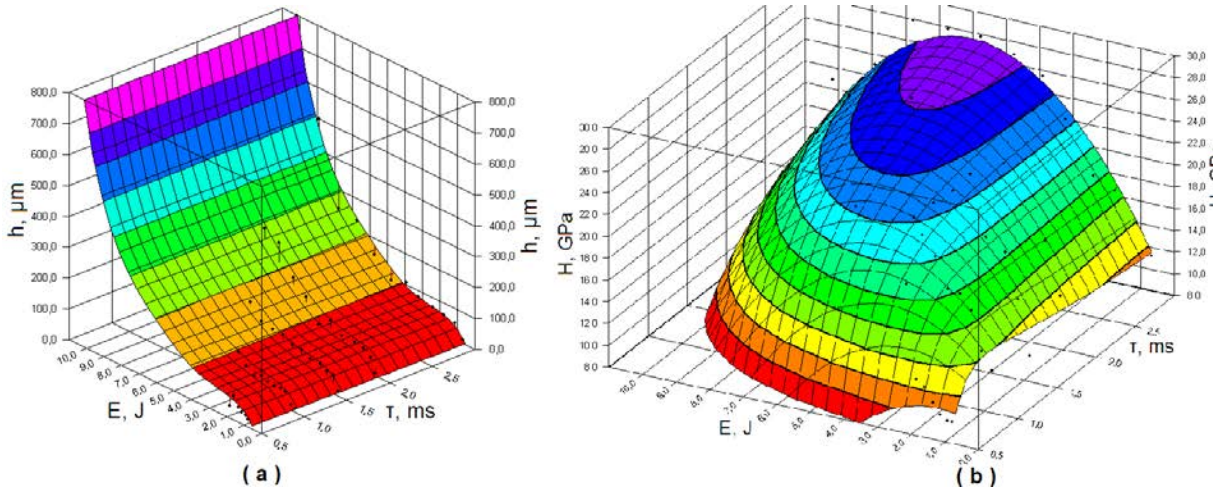

Figure 2(a, b). Influence of laser processing conditions (energy and duration of a laser pulse) on the depth **(a)** and microhardness **(b)** of layers formed on titanium

4. Conclusions

Laser treatment in a graphite medium made it possible to obtain a layered structure on titanium, consisting of coatings up to 6 μm thick and highly hard layers up to 800 μm deep. The significant thickness of the structures being formed allows surface finishing. The established dependences make it possible to choose the modes of laser treatment for the formation of structures with specified properties on titanium.

Acknowledgments

The research was supported by the scholarship of the President of the Russian Federation SP-2631.2019.1.

References

[1] Voyko A V, Fomina M A, Koshuro V A, Fomin A A, Rodionov I V, Atkin V S, Galushka V V, Zakharevich A M and Skaptsov A A 2018 *Proc. biomed. opt. imag.* **10716** 107161L

[2] Dai J J, Chen C Z, Li S Y, Zhuang L 2014 *Adv Mat Res* **936** 1086

[3] Fomina M, Koshuro V, Papshev V, Rodionov I, Fomin A 2018 *Data in Brief* **20** 1409

Modeling of the interaction of porphyrin molecules in a nonpolar solvent

V N Mironyuk[1], A J K Al-Alwani[1], N N Begletsova[1], A S Kolesnikova[1,2], M V Pozharov[3], A I Smirnova[4], N V Usol'tseva[4], E G Glukhovskoy[1]

[1] Education and Research Institute of Nanostructures and Biosystems, Saratov State University, Saratov, 410012, Russia
[2] Bogoliubov Laboratory of Theoretical Physics, Joint Institute for Nuclear Research, Dubna, Moscow Oblast, 141980, Russia
[3] Institute of Chemistry, Saratov State University, Saratov, 410012, Russia
[4] Nanomaterials Research Institute, Ivanovo State University, Ivanovo, 153025, Russia

E-mail: bestblogger@yandex.ru

Abstract. The paper presents the data of a theoretical study by the methods of molecular dynamics of the interaction of two molecules of derivatives of porphyrins of two types: 5,10,15,20-tetra(4-n-methyloxyphenyl)porphyrin (P) and asymmetric 5-(4-hydroxyphenyl)-10,15,20-tris (4-n-methyloxyphenyl)porphyrin (P-OH). We investigated three systems, each of which consisted of two identical substituted porphyrin molecules and chloroform molecules as a non-polar solvent. The effect of temperature on the geometry and energy of the system was investigated. It has been shown that asymmetrically-substituted molecules are not prone to the formation of aggregates, although the distance between two P-OH molecules was less than in the case of two P molecules.

1. Introduction and motivation

Obtaining highly ordered floating Langmuir monolayers on the water surface is an important task for the formation of nanocomposite structures of photosensors, solar cells, memory elements, electrical capacities, etc.

Such layers can be obtained when a surfactant (surfactant) in the form of a true solution in an organic solvent is applied to the water surface and at the same time (with a certain compression of the barriers) a true monolayer is formed (this is when the molecules uniformly occupy the entire area of the Langmuir bath between the barriers). This is typical for simple surfactant molecules. But this task is not trivial when complex molecules such as derivatives of porphyrin, phthalocyanine, proteins, etc. are present on the surface. Some authors, when trying to obtain a homogeneous and highly ordered monomolecular layer, come to the conclusion that it is impossible to obtain such a true monolayer [1]. Nevertheless, in our work, it was shown that the formation of low-defect monolayers by phthalocyanine derivatives can be achieved under certain conditions [2].

The laws of thermodynamics indicate that an increase in temperature can significantly affect the state of multicomponent systems. For example, the surface tension (σ) of water can vary in a very wide range - from 75 to 59 mN/m when the temperature changes from 0 to 100 °C. We have previously reported on the effect of temperature on phase transitions in floating (Langmuir) liquid crystal monolayers [3,4] and on the reorganization of Gibbs layers formed by metal nanoparticles stabilized by a surfactant shell from the subphase at the water/air interface [5].

The aim of this work was to theoretically study the effect of temperature on the features of the interaction of molecules of porphyrin derivatives, which are surrounded by chloroform molecules as a solvent.

2. Experimental details and results

The software of Hyperchem 8.0.8 was used for molecular modeling. The objects of study were symmetric 5,10,15,20-tetra(4-n-methyloxyphenyl)porphyrin (P) and asymmetric 5-(4-hydroxyphenyl)-10,15,20-tris (4-n-methyloxyphenyl)porphyrin (P-OH). Model systems consisted of two identical porphyrin molecules and chloroform molecules. Three systems were investigated [2,3]: I - with symmetrically substituted porphyrin molecules (P - P); II - with asymmetrically substituted and parallel porphyrin molecules (P-OH ↑↑ P-OH); III - with asymmetrically substituted and antiparallel porphyrin molecules(P-OH ↑↓ P-OH). The system I included 292 chloroform molecules, a non-polar solvent, systems II and III, 244 molecules each.

In all cases, modeling began with the same position of the porphyrin molecules, the planes of which were parallel to each other at a distance of 1.55 nm. Optimization of the original system was carried out by the molecular mechanics method MM+ with the Polak - Reiber calculation algorithm. The MM+ method takes into account the potential fields generated by all atoms of the calculated system and allow flexible modification of the calculation parameters depending on the specific problem. The distance between the porphyrin molecules was calculated as the distance between the centers of mass of the central porphyrin macrocycle of two molecules.

Modeling has shown that the distances between asymmetrically substituted porphyrin molecules of the system (P-OH ↑↑ P-OH and P-OH ↑↓ P-OH) are smaller than in the case of symmetrically substituted molecules (P - P). Contrary to expectations, the effect of temperature on the intermolecular distance was not monotonic, which would require additional research. The total energy of a system with a parallel arrangement of porphyrin molecules (P-OH ↑↑ P-OH) was lower than in the case of an antiparallel arrangement (P-OH ↑↓ P-OH).

The results obtained indicate that the molecules of symmetrically and asymmetrically substituted porphyrin form a true solution with chloroform. In addition, despite the fact that intermolecular interaction is still present, this influence is not critical and does not lead to the formation of aggregates.

Acknowledgments

The study was supported by a grant from the Russian Science Foundation (project No. 21-73-20057)

References

[1] Mildner J and Dynarowicz-Łątka P 2012 β-Carotene does not form a true Langmuir monolayer at the air/water interface *Colloids and Surfaces B: Biointerfaces* **90** 244–7

[2] Kazak A V, Marchenkova M A, Khorkov K S, Kochuev D A, Rogachev A V, Kholodkov I V, Usol'tseva N V, Savelyev M S and Yu. Tolbin A 2021 Ultrathin Langmuir–Schaefer films of slipped-cofacial J-type phthalocyanine dimer: supramolecular organization, UV/Vis/NIR study and nonlinear absorbance of femtosecond laser radiation *Applied Surface Science* 148993

[3] Begletsova N N, Mironyuk V N, Santer S, Smirnova A I, Usol'tseva N V and Glukhovskoy E G 2020 Effect of the composition and temperature of the subphase on the surface potential of the Langmuir monolayer of 8CB liquid crystal *J. Phys.: Conf. Ser.* **1697** 012112

[4] Chumakov A S, Al-Alwani A J, Gorbachev I A, Ermakov A V, Kletsov A A, Glukhovskoy E G, Kazak A V, Usol'tseva N V and Shtykov S N 2017 Temperature and mixing ratio effects in the formation of CdSe/CdS/ZnS quantum dots with 4′-n-octyl-4-p-cyanobiphenyl thin films *BioNanoSci.* **7** 666–71

[5] Begletsova N N, Baimagambetova L T, Mironyuk V N, Smirnova A I, Venig S B, Usol 'tseva N V and Glukhovskoy E G 2019 Formation of Gibbs and Langmuir floating layers based on copper nanoparticles: temperature and concentration effects *J. Phys.: Conf. Ser.* **1410** 012216

Optical and thermoelectric properties of carbon nanotubes with encapsulated fullerenes

Morozova E.V., Timkaeva D.A.

Ulyanovsk State University, Ulyanovsk, 432017, Russia

kat-valezhanina@yandex.ru

Abstract. We study optical and thermoelectric properties of carbon nanotubes (CNTs) with encapsulated C_{60} fullerene molecules. Using ab initio methods, we calculate the coefficients of absorption, optical conductivity, thermal conductivity, and thermoelectric figure of merit for metallic CNTs with fullerenes periodically located inside the nanotube at different distances from each other. As the distance between fullerenes decreases, the optical conductivity of CNT - C_{60} peapods at high frequencies is suppressed. The conductance of structures with fullerenes is less than the conductance of a clean tube and is approximately the same for the considered distances (12.3 and 19.7 Å) between fullerenes. The thermal conductivity of CNTs due to the encapsulation of fullerenes significantly (3-4 times) decreases for the considered CNT (8,8)-C_{60} systems.

1. Introduction

New hybrid systems based on carbon nanotubes (CNTs) and fullerenes connected by van der Waals interactions are sometimes called carbon peapods [1-3]. With insignificant variations in the CNT diameter, the fullerene geometry changes. Systems of nanopeapods are promising for applications in nanoelectronics [1-2]. Fullerenes arranged in an ordered manner inside essentially represent a set of quantum dots in a one-dimensional superlattice. By changing the concentration of fullerenes inside, types of fullerenes, it is possible to modulate the band structure of the CNT-fullerene system and control the electronic and phonon characteristics of nanopeapods.

In this work, using ab initio methods, we calculate the optical and thermoelectric properties of metallic CNTs with fullerenes periodically located inside the nanotube at different distances from each other.

2. Optical and thermoelectric properties

A metallic CNT (8,8) is considered. The distances between the C_{60} fullerenes in the nanopeapods were chosen equal to 12.3 and 19.7 Å, which corresponds to 5 and 8 longitudinal unit cell sizes (2.46 Å) of armchair CNTs. The C_{60} fullerene diameter is 7.1 Å, which is about 3 times the width of the armchair CNT unit cell. The smallest distance from the fullerene to the CNT wall is 1.875 Å.

The optimization of the considered CNT (8,8)-C_{60} systems was carried out using the DFT method implemented in QuantumATK (Synopsys). The cutoff energy of the electron wave functions is 500 eV. The criteria for reliable convergence for the total energy and force are eV and 0.01 eV/Å. To

describe the effects of electron exchange and correlation, we used the Purdue-Burke-Ernzerhof approximation generalized to the case of solids (GGA-PBEsol). To generate k points in the Brillouin zone for all nanotubes, the Monkhorst-Pack method with a grid was used.

The transfer coefficients were calculated using the nonequilibrium Green's function (NEGF) method, the DFT method, and nonequilibrium molecular dynamics. We used the standard model in which the central part of the tube is connected to semi-infinite left and right electrodes (see e.g. [3,4]). QuantumATK calculates the specified thermoelectric coefficients and Peltier coefficient according to linear response theory. The following relations are used

$$G_{\mathrm{e}} = \left.\frac{dI}{dV_{\mathrm{bias}}}\right|_{dT=0}, S = -\left.\frac{dV_{\mathrm{bias}}}{dT}\right|_{I=0}, \lambda_{\mathrm{e}} = \left.\frac{dI_Q}{dT}\right|_{I=0}, \Pi = \left.\frac{I_Q}{I}\right|_{dT=0} = SV_{\mathrm{bias}}.$$

Thermoelectric conductivity of materials is usually determined based on the value of the dimensionless figure of merit ZT, including the thermoelectric and electrical characteristics:

$$ZT = \frac{S^2 GT}{\lambda}$$

where S is the Seebeck coefficient, G is the electrical conductivity, equal to the sum of the electronic λ and phonon λ_{ph} thermal conductivity. The Seebeck coefficient is defined as the ratio of the voltage developed to the temperature gradient ($\Delta V / \Delta T$).

3. Conclusions

With a decrease in the distance between fullerenes, the optical conductivity of CNT-C_{60} at high frequencies is suppressed. The conductance of structures with fullerenes is slightly less than the conductance of a clean tube and is approximately the same for the considered distances (12.3 and 19.7 Å) between fullerenes. The thermal conductivity of CNTs significantly decreases due to the encapsulation of fullerenes. The Seeback coefficient *S* of CNTs significantly increases after the encapsulation of fullerene molecules, due to the strong interaction between the CNTs and the encapsulated C_{60} molecules. In this case, the obtained values for figure of merit are insufficient for thermoelectric applications of the considered systems.

Acknowledgments

This work is supported by the Ministry of Science and Higher Education of the Russian Federation (state program 0830-2020-0009*).*

References

[1] Okazaki T, Okubo S, Nakanishi T, Joung S K, Saito T, Otani M, Okada S, Bandow S and Iijima S 2008 *J. Am. Chem. Soc*. **130** pp 4122-4128

[2] Kodama T, Ohnishi M, Park W, Shiga T, Park J, Shimada T, Shinohara H, Shiomi J and Goodson K E 2017 *Nature mater*. **16** pp 892-897

[3] Kochaev A I, Meftakhutdinov R M, Sibatov R T and Timkaeva D A 2020 *Comput. Mater. Sci.* **186** p 109999

[4] Meftakhutdinov R M, Sibatov R T and Kochaev A I 2020 *J. Phys. Condens. Matter*. **32** p 345301

Analysis of frequency response sensor of MEMS gyroscope in vacuum chamber

I E Lysenko[1], **D V Naumenko**[1], **O A Ezhova**[1]
[1] Southern Federal University, Taganrog 347922, Russia

e-mail: dvnaumenko@sfedu.ru

Abstract. This article presents a study of the frequency response of a MEMS gyroscope in a vacuum chamber. On the basis of experimental studies by the method of laser Doppler vibrometry, the dependences of the amplitude of oscillations of the inertial mass in the vertical plane at various pressures are obtained. The bandwidth of the MEMS sensor is also obtained. These results were applied to a more accurate finite element simulation in ANSIS and refined electrostatic drive parameters and vibration amplitude along the drive axis were obtained.

1. Introduction

To increase the sensitivity of a MEMS gyroscope, a large oscillation amplitude of the inertial mass is required; therefore, most micromechanical gyroscopes operate in a vacuum [1]. The exception is gyroscopes operating at atmospheric pressure [2]. Investigation of the gyroscope operating modes in a vacuum provides a lot of information for subsequent tuning and debugging of the sensor).

2. Design of the MEMS gyro sensor

The investigated sensitive element of the micromechanical gyroscope is shown in Figure 1. The sensor consists of an inertial mass fixed on elastic suspensions. The electrostatic drive ensures the movement of the inertial mass along the axis of motion. The capacitance sensor picks up vibrations caused by the Coriolis force acting on the moving body. The sensor is made by volumetric technology on a SOI structure using reactive ion etching

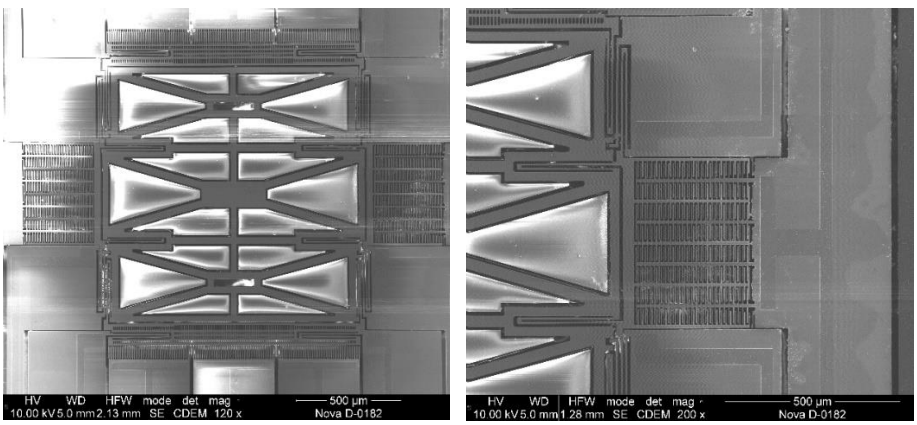

Figure 1. SEM image of the MEMS gyro

3. Experimental research

In the study of the samples, the technologies of scanning laser vibrometry using a microsystem analyzer Polytec MSA-500. Installation of a MEMS sensor for measurements is shown in the figure 2.

The sample (1) is placed in a vacuum chamber (2), the pressure of which is regulated by a vacuum pump (3). The microsystem analyzer (4) is matched with the generator (5) and makes measurements using embedded software. Post-processing of measurements is performed on a desktop computer (6).

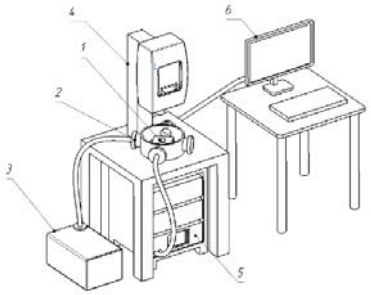

Figure 2. Scheme of the experimental stand

The study was carried out at three pressures of 5000Pa, 200Pa and 2Pa. Based on the measurement results, the dependence of the amplitude on the pressure was obtained, which is necessary for adjusting the device and determining the residual pressure after encapsulation.

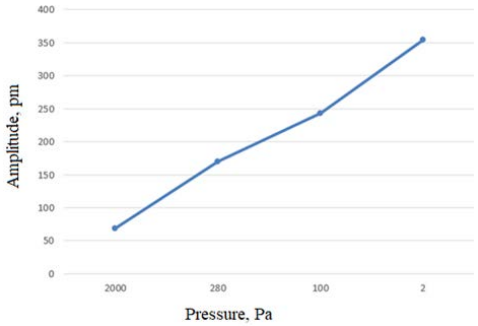

Figure 2. Experimental dependence of the amplitude on pressure.

4. Conclusion

As a result of the study, an experimental dependence of the amplitude of motion of an inert mass on pressure was obtained. Determination of the bandwidth of the device at various pressures and investigated the qualitative operation of the device at various pressures. The results obtained will be used to configure and debug the device, as well as to improve the accuracy of calculations by the finite element method.

Acknowledgments

This work was supported by RFBR research project No. 19-37-90136 “Development of the fundamental foundations for the construction of high-aspect torsion suspensions for inertial MEMS sensors”

References

[1] D Xia D., Yu C., Kong L., 2014, The Development of Micromachined Gyroscope Structure and Circuitry Technology, Sensors, Vol. 14, No. 1, pp. 1394riving Another reference

[2] Ding, Xukai Li, Hongsheng Ni, Yunfang Sang, Pengcheng. (2015). Analysis of Frequency Response and Scale-Factor of Tuning Fork Micro-Gyroscope Operating at Atmospheric Pressure. Sensors (Basel, Switzerland). 15. 2453-72. 10.3390/s150202453.

Spin-dependent transport through a helical Aharonov-Bohm interferometer

R.A. Niyazov[1,2], D.N. Aristov[2,1] and V.Yu. Kachorovskii[3]

[1]St. Petersburg State University, 7/9 Universitetskaya nab., 199034 St. Petersburg, Russia
[2]NRC "Kurchatov Institute", Petersburg Nuclear Physics Institute, Gatchina 188300, Russia
[3]A. F. Ioffe Physico-Technical Institute, 194021 St. Petersburg, Russia

r.niyazov@spbu.ru

Abstract. We discuss spin-dependent transport via tunnelling Aharonov-Bohm interferometer formed by helical edge states tunnel-coupled to metallic leads. We focus on experimentally relevant high-temperature case as compared to the level spacing and obtain the full 4×4 matrix of transmission coefficients, conductance and spin polarization in the presence of magnetic impurities. We describe this tunnelling interferometer in terms of ensemble of flux-tunable qubits which can effectively operate at high temperature and can be used for quantum calculations. The obtained results have high prospects in quantum computing.

1. Introduction

Interference has crucial role both in fundamental and applied aspects of modern physics. It widely used in optical and electronic systems. One of the simplest realizations of quantum electronic interferometer is a ring-geometry setup, with a single ballistic quantum channels tunnel-coupled to metallic leads. In such a device conductance oscillates with the magnetic field due to the Aharonov-Bohm effect. The shape and amplitude of the oscillations depend essentially on the strength of the tunneling coupling and on the relation between temperature, T, and level spacing, Δ. For $T \ll \Delta$ and weak tunneling coupling there are narrow resonant peaks in the dependence of conductance, G, on the magnetic flux Φ. The positions of the peaks depend on the electron Fermi energy and on the strength of the electron-electron interaction. Remarkably, the interference effects are not entirely suppressed with increasing the temperature, and the resonant behavior of $G(\Phi)$ survives for the case $T \gg \Delta$. Specifically, the high-temperature conductance of the noninteracting ring weakly coupled to the contacts exhibits sharp antiresonances at the dimensionless flux $\phi = \Phi/\Phi_0 = 1/2 + n$, where $\Phi_0 = hc/e$ is the flux quantum and n is an arbitrary integer number [1].

A promising opportunity for a technological breakthrough in this direction is associated with the discovery of topological insulators [2], which are materials insulating in the bulk, but exhibiting conducting channels at the surface or at the boundaries. These states are one-dimensional helical channels where the electron spin projection is connected with its velocity, e.g., electrons traveling in one direction are characterized by spin "up", while electrons moving in the opposite direction are characterized by spin "down". Remarkably, the electron transport via helical edge states (HES) is ideal, in the sense that electrons do not experience backscattering from conventional non-magnetic impurities,

similarly to what occurs in edge states of Quantum Hall Effect systems, but without invoking high magnetic fields.

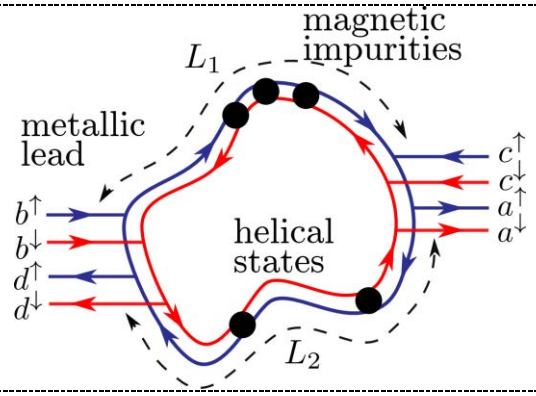

Figure 1. Helical Aharonov-Bohm interferometer with the magnetic impurities.

2. Model

The HES of two-dimensional topological insulator are tunnel-coupled to metallic nonmagnetic point contacts (see Fig. 1). We model metallic contacts by single-channel spinful wires, so that electrons are injected into the HES through so-called tunnel Y junctions. We assume that the electrons in the metallic leads are not polarized. Since we consider nonmagnetic leads, the different spin projections do not mix at the contacts. In the same time HES itself contains classical magnetic impurities with large magnetic moments.

3. Results and Discussion

Introducing transfer matrix of the interferometer as a whole one can compute conductance and the spin polarization of the setup in high-temperature regime [3]. Here, we going further and obtain full S-matrix. It includes both transmission and reflection processes. Such S-matrix allows to describe the setup as two qubits gate in terms of generic unitary Hadamard operator [4] that opens a wide avenue for high-temperature quantum computing.

Acknowledgments

The work of R.N. was funded by RFBR, project number 19-32-60077. The work of D.A. and V.K. was funded by the Russian Science Foundation, Grant No. 20-12-00147.

References

[1] A. P. Dmitriev, I. V. Gornyi, V. Y. Kachorovskii, and D. G. Polyakov, Phys. Rev. Lett. 105, 036402 (2010).

[2] M. Z. Hasan and C. L. Kane, Rev. Mod. Phys. 82, 3045 (2010).

[3] R. A. Niyazov, D. N. Aristov, and V. Y. Kachorovskii, npj Comput. Mater. 6, 174 (2020).

[4] P. Földi, B. Molnár, M. G. Benedict, and F. M. Peeters, Phys. Rev. B 71, 033309 (2005).

Researching of the structure and mechanical properties of gas-thermal coatings after induction heat treatment

E Osipova[1], **O Markelova**[1], **V Koshuro**[1], **A Fomin**[1]
[1] Yuri Gagarin State Technical University of Saratov, Saratov 410054, Russia

Abstract. This article discusses the process of induction-thermal modification of titanium coatings formed by plasma spraying. The influence of the inductor current on the temperature of the processed samples has been experimentally established. According to the research results, it was found that during thermal modification, the structure and mechanical properties of titanium coatings changed. It was found that with an increase in the heating temperature from 750 to 1200 °C, the porosity increased from 56±2 to 61±1 %, the layer thickness decreased from 320±30 to 114±15 μm. It was also found that heat treatment led to a change in the shape of the nanoscale elements of the coating. Due to the change in the structure of the coating material during oxidation, the microhardness increased from 1035–1532 to 1825–1883 $HV_{0.98}$.

1. Introduction

Restorative medicine constructions are often made from titanium-based alloys [1]. To increase the rate of osseointegration, the surface of a titanium implant is subjected to modification (texturing) or biocompatible coatings are formed by different methods. The technology of electroplasma spraying (EPS) is widely used. The sprayed coatings are characterized by uneven elemental-phase composition, the presence of structural defects and residual stresses in the sprayed material. To improve the functional properties of plasma coatings, induction heat treatment (IHT) is used, which makes it possible to form nanostructured metal oxide layers on titanium, which increase the osteoconductive properties of the implant surface. [2].

The purpose of this work was to study the effect of the inductor current, and, consequently, the temperature of the IHT on the structure and hardness of plasma sprayed titanium coatings.

2. Methodology

Samples for research were titanium disks with a diameter of 15 mm and a thickness of 0.5 mm, preliminarily subjected to abrasive blasting and cleaning in a surfactant solution. The coating was formed by electroplasma spraying of PTS grade titanium powder with a dispersion of 100–150 μm using "UPN-28" equipment. The following spraying modes were used: plasma torch arc current –350 A (± 1%); spraying distance – 150±10 mm; transporting gas consumption – 10±5 l/min; plasma-forming gas consumption – 25±5 l/min. IHT of the samples was carried out on the "VCh-15" installation at a constant exposure of 300 s and different values of the inductor current: I = 3.5–8.0 kA, providing a change in the temperature of the sample from 750 to 1200 °C. The analysis of the coating structure was carried out by a scanning electron microscopic method (SEM) using a "MIRA 2 LMU"

microscope. The size of structural elements, porosity of the formed layers were determined using the program for analyzing the geometric parameters of micro-objects "Metallograph". Microhardness analysis was carried out on a "PMT-3" hardness tester with a load on the Vickers indenter equal to 0.98 N.

3. Results

After plasma spraying, the porosity of the coating was 56±2 %. On the surface, individual particles of a rounded shape with a size of up to 20 μm were noticeable. Thermal modification in the low temperature range led to an increase in porosity up to 61±1 %. The number of spherical particles less than 5 μm in size decreased, while the number of larger particles of 10–50 μm in size remained practically unchanged. At a temperature of 900–950 °C, the porosity was 55±2 %. The structure of the surface of the modified coating was dominated by particles with a size of 30–40 μm. Temperature 1150–1200 °C did not lead to a significant change in porosity, which remained equal to 56±1 %. The shape of individual structural elements of the coating after IHT changed from correct to vermicular and prismatic.

Microindentation showed that the resulting porous structure had a hardness of 1035–1532 $HV_{0.98}$ (Figure 1). After low-temperature modification, the microhardness reached 1825 $HV_{0.98}$. Thermal modification in the medium and high temperature ranges led to the stabilization of microhardness at the level of 1599 $HV_{0.98}$ and 1883 $HV_{0.98}$, respectively.

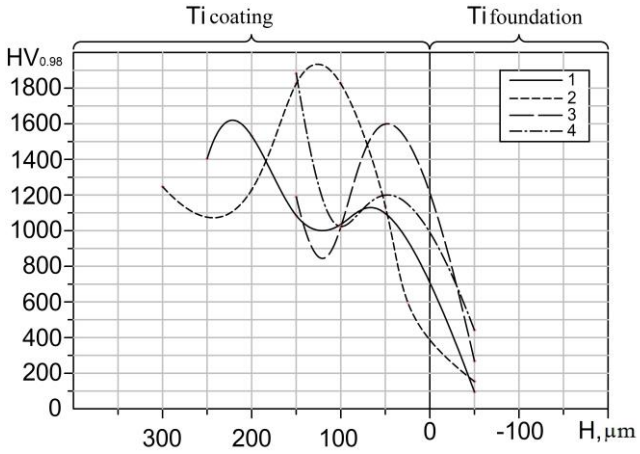

Figure 1. The distribution of the coating`s microhardness over the sample`s depth:
1 – EPS coating; 2 – T = 750–800 °C; 3 – T = 900–950 °C; 4 – T = 1150–1200 °C

4.Conclusions

Thus, it was shown that the IHT process allows changing the surface structures and microhardness of the coating due to the thermal action. The nature of the changes depends on the magnitude of the inductor current and the temperature of the modification process.

Acknowledgments

The article was prepared in the course of scientific research under the grant of the President of the Russian Federation No. MD-965.2021.4.

References

[1] Pohler O.E.M. 2000 *Injury* **31** D7.
[2] Fomin A., Dorozhkin S., Fomina M., Koshuro V., Rodionov I., Zakharevich A., Petrova N., Skaptsov A. 2016 *Ceram Int* **42(9)** 10838.

Improving the physical and mechanical properties of tool steel by induction chemical-thermal treatment

P Palkanov[1], **V Koshuro**[1], **A Fomin**[1]
[1]Yuri Gagarin State Technical University of Saratov, Saratov 410054, Russia

Abstract. The study results of the structure and microhardness of the surface layer of high-speed tool steel after induction chemical-thermal treatment in a gaseous nitrogen-containing medium at a temperature of 900–1100 °C were presented. Due to the strengthening treatment of products a gradient diffusion nitride layer with a thickness of about 200 μm and a surface microhardness of 1950±70 $HV_{1,98}$ was formed.

1. Introduction

In modern industry, various types of working media are used for nitriding. The most common of them is a gas mixture of ammonia and propane (1:1). The nitriding process in this environment is performed in shaft or vacuum retort furnaces in the temperature range from 520 to 570 °C for 60–90 hrs. As a result of processing, a strengthened diffusion layer with a thickness of 150±50 μm and a microhardness of 900–1100 HV is obtained [1]. Recently, the method of ion-plasma nitriding is also often applied, which is performed in special installations with a nitrogen-containing rarefied medium consisting of nitrogen or ammonia at temperatures from 300 to 590 °C with a cycle duration of about 24 hrs. Ionic nitriding allows obtaining a nitrided layer with the thickness of 300±50 μm and a microhardness of 1000–1300 HV [2].

An alternative heating method for chemical-thermal treatment (CTT) can be induction heating, which reduces the process time [3]. Based on the mentioned above, the most promising way of heating products during the nitriding process can be induction heating [4,5]. The purpose of this work is to study the effect of the operating current of the inductor on the physical and mechanical properties of products treated in a nitrogen gas environment.

2. Methodology

Nitriding was performed by installing the fabricated samples into a chamber for induction chemical-thermal treatment (ICTT). The ICTT process was carried out in a temperature range of 900–1000 °C for 10 min at a pressure of 0.2±0.05 MPa. The heating rate and temperature were controlled by varying the operating current of the inductor from 300 to 360 A.

3. Results

When studying the microstructure of nitrided samples, the uniformity of the modified nitride layer was observed, the thickness of which reached 200 μm (Figure 1). Along with nitriding, hardening of the underlying layer was conducted.

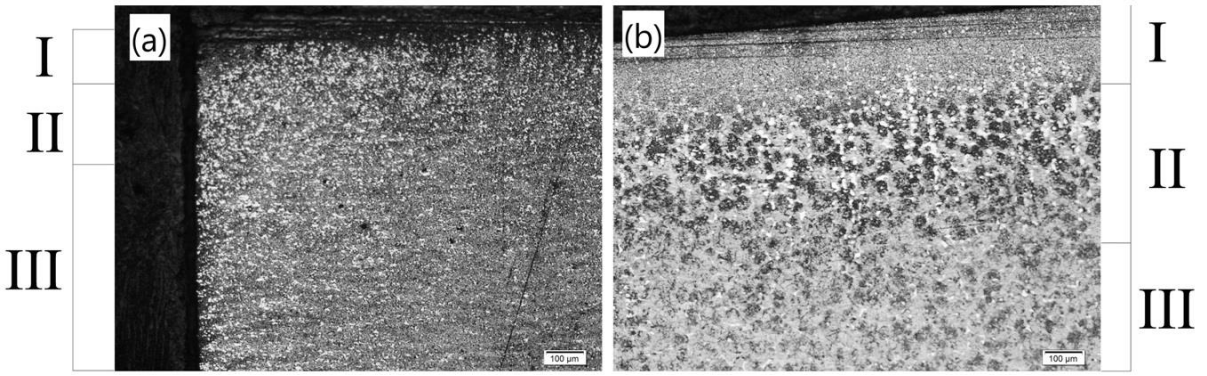

Figure 1. Layered structure of the samples containing the strengthened layer (I), the diffusion layer (II) and the substrate metal (III) produced at an operating current of 300 A (**a**); at an operating current of 320 A (**b**).

Hardness of the samples in the initial state was 256±9 $HV_{1,98}$. The maximum microhardness of the surface of the nitrided layers reached 1928–1950 $HV_{1.98}$. At a current of 300–320 A, layers were formed with a uniformly decreased microhardness over the cross section equalling 150 μm. The depth from 30 to 250 μm was characterized by high hardness (1694–1281 $HV_{1.98}$), which was associated with the formation of finely dispersed strengthening phases.

4. Conclusions

Thus, the resulting layers on metal products were characterized by the required combination of high microhardness and a large depth of the strengthened layer, which can be effectively used under conditions of friction and dynamic loads. A nitrided layer with a thickness of 160–200 μm and a high microhardness of 1928–1950 $HV_{1.98}$ was formed on the surface of high-speed R6M5 steel by the ICTT method.

Acknowledgments

The research was supported by the “U.M.N.I.K.” program (Project Executor Palkanov P.A., 2021).

References

[1] Wang B, Sun S, Guo M, Jin G, Zhou Z and Fu W 2015 *Surf Coat Technol* **279** 60
[2] Rocha A, Strohaecker T and Hirsch T 2003 *Surf Coat Technol* **165** 176
[3] Fomin A, Voyko A, Fomina M, Mokrousov S and Koshuro V 2020 *Compos Struct* **245** 112393
[4] Takesue S, Kikuchi S, Misaka Y, Morita T and Komotori J 2020 *Surf Coat Technol* **399** 126160
[5] Fomin A, Fedoseev M, Palkanov P, Voyko A, Fomina M, Koshuro V, Zakharevich A, Kalganova S and Rodionov I 2018 *Proc SPIE* **10716** 107161N

Robotic ensemble platform for emulation of friction-assisted phase formation in active matter

V A Porvatov[1,2], A D Rozenblit[3], G Yu Gritsenko[4], D A Petrova[2], E I Kretov[5], D S Filonov[1], A Souslov[6], and N A Olekhno[3*]

[1]Moscow Institute of Physics and Technology, 141701 Moscow, Russia
[2]University of Science and Technology "MISIS", 119991 Moscow, Russia
[3]ITMO University, 197101 Saint Petersburg, Russia
[4]Lomonosov Moscow State University, 119991 Moscow, Russia
[5]Max Delbrück Center for Molecular Medicine in the Helmholtz Association, 13125 Berlin, Germany
[6]University of Bath, Bath, UK

E-mail: *olekhnon@gmail.com

Abstract. Robotic swarms attain growing popularity as a platform for experimental studies of non-equilibrium phenomena in ensembles of actively moving particles. In the present work, we develop and optimize a setup based on self-rotating bristle-bots which is capable of emulating different friction between individual active particles. This allows us for the first time to study how characteristic phases of active matter depend on friction, considering jammed, liquid and gaseous states of robotic system.

1. Introduction

Active matter dynamics recently emerged as a novel branch of physics considering mechanical phenomena in ensembles of particles that convert their internal energy into mechanical work, resulting in non-equilibrium physics. Examples of such systems include various micro- and nanoscale setups, ranging from bacterial colonies [1] and liquid crystals with molecular motors [2] to self-propelled colloidal particles [3, 4]. However, the complexity of conducting microscale experiments led to a rapid development of swarm robotics platform [5] as a mean of their emulation offering an unprecedented degree of control over the system parameters.

In the present work, we expand active matter studies in robotic ensembles and develop a setup of high novelty. The proposed platform allows to study not only the packing density of robots, but also such a crucial for small setups characteristic as side friction between robots.

2. Experimental setup

In order to clearly distinguish the formation of condensed phases in a robotic swarm related to phase transitions rather then to the interaction with boundary, we focus on self-rotating robots. We realize experimentally the ensemble of 80 self-rotating bristle-bots vibrating at frequencies 60 Hz, figure 1(a). The vibration of electric motor is converted to the translation movement by circular-shaped layer of elastic legs at bottom of each bristle-bot, causing individual bots to rotate. Each robot is 50 mm in diameter and consists of the 3d-printed body made of PLA plastic, vibration motor, rechargeable 3.7V battery, and a control circuit. The circuit allows turning the robots on and off by infrared remote

control. The robots are placed inside circular boundaries of different diameters to adjust the packing density. To change the friction between individual bristle-bots, a set of different side surfaces is fabricated, which are interchanged manually.

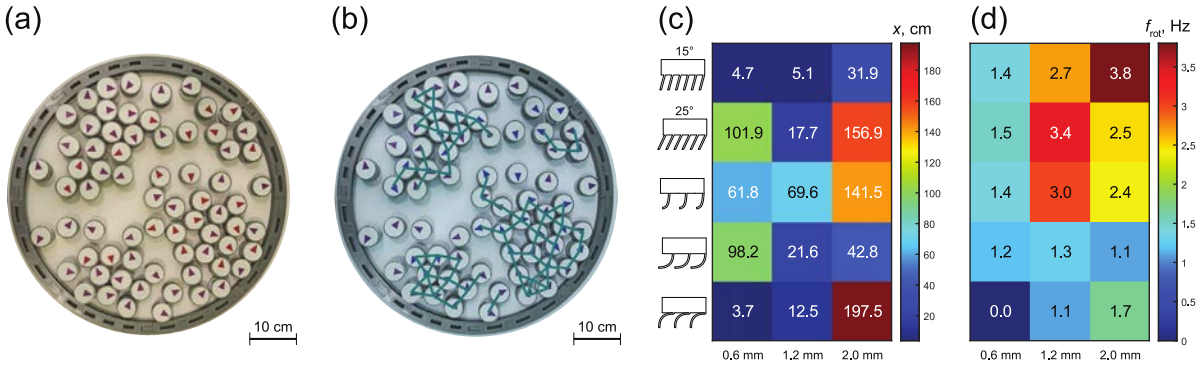

Figure 1. (a) Experimental setup. (b) Extracted robots' positions and clusters of touching robots. (c, d) Optimization maps of bot legs design showing the distance travelled by the robot x(c) and self-rotation frequency f (d) for different shapes and thicknesses of elastic bristles.

The motion of the system is captured with a camera and then analyzed with the help of OpenCV library in order to simultaneously track the markers placed on top of every bristle-bot, allowing to capture a detailed kinematics of the system, figure 1(b).

3. Bristle-bot design optimization

As seen from figure 1(c,d), the shape of bristle bots' legs significantly affects the movement pattern. To this end, we carried out an optimization procedure, considering five different shapes of flexible bristles (including straight-line bristles with angles of of $\alpha = 15^o$ and $\alpha = 20^o$ to the normal, arc bristles with radii of $r = 2.2$ mm and $r = 5.5$ mm, and inverse arcs with $r = 5.5$ mm along with three different bristle thicknesses h. The results demonstrate that a large self-rotation frequency together with a low translation velocity is observed for the straight bristles with $\alpha = 15^o$ and $h = 1.2$ mm.

4. Conclusion

We have developed, optimized, and experimentally realized the active matter setup consisting of self-rotating bristle-bots. The implemented setup allows studying the effects of particle interactions on phase transitions in active matter, largely extending the results of recent paper [5]. First experimental studies of the setup reveal pronounced and non-monotonous dependence of the characteristic phases in robotic ensemble on the friction between individual robots.

Acknowledgments

The experimental part of the work was supported by the Russian Foundation for Basic Research (GrantNo. 20-19-00491).

References

[1] Mathijssen A J T M, Guzm\'{a}n-Lastra F, Kaiser A, and L\"{o}wen H 2018 *Phys. Rev. Lett.*
[2] Duclos G, et al. 2020 *Science* **367** 1120-1124
[3] Bricard A, Caussin J-B, Desreumaux N, Dauchot O, and Bartolo D 2013 *Nature* **503** 95-98
[4] Ginot F, Theurkauff I, Detcheverry F, Ybert C, Cottin-Bizonne C 2018 *Nat. Commun.* **9** 696
[5] Wang G, et al. 2021 *Phys. Rev. Lett.* **126**, 108002

Fabrication of probe tips via the FIB method for nanodiagnostics of the surface of solids by atomic force microscopy

D J Rodriguez, H A Ballouk, A V Kotosonova, O I Osotova, A S Kolomiytsev

Southern Federal University, Institute of Nanotechnologies, Electronics and Equipment Engineering, Taganrog, 347922, Russia

E-mail: priviet122@gmail.com

Abstract. In this work, we carried out an investigation of commercial atomic force microscope (AFM) probes for contact and semi-contact modes, which were modified by focused ion beam (FIB). This method was used to modify the original tip shape of silicon AFM probes, by ion-etching and ion-enhance gas deposition. we show a better performance of the FIB-modified probes in contrast with the non-modified commercial probes. These results were obtained after using both probes in semi-contact mode in a calibration grating sample.

1. Introduction

Atomic force microscopy (AFM) is a powerful tool for studying topography and other physical and chemical properties of the surface of solids with nanometer spatial resolution. Standard AFM probes are manufactured using classical microelectronic technologies and have a limited range of geometric parameters, which often leads to undesirable image distortions [1]. In order to obtain adequate measurements of the geometric parameters of structures at nanoscale, it is necessary to manufacture probes with a special tip shape, for example, with an increased aspect ratio or a reduced tip radius in comparison with standard probes. One of the methods that allow the formation of sharp probes in a wide range of geometric parameters is the local ion-stimulated deposition of materials from the gas phase using a focused ion beam (FIB) [2]. The aim of this work is to produce AFM probes via the FIB method in addition to the study of the influence of the geometric parameters of the probes on the accuracy of the measurements of periodical structures at the nanoscale via the AFM method.

2. Experimental

In this work, experimental studies were carried out using a scanning electron-ion microscope Nova NanoLab 600 (FEI, Netherlands), equipped with a Ga+ liquid metal ion source (LMIS) FIB a system of focused ion beams. The tip of the probes was formed on the basis of the beams of standard AFM cantilevers HA_HR (NT-MDT Spectrum Instruments, Russia), whose own probes were previously removed by ion-beam etching. The new probes were formed by ion-stimulated carbon deposition, when a volatile compound C10H8 was fed into the zone of impact of the ion beam.

To study the influence of the probe shape on the accuracy of measuring the surface topology of nanoscale structures, cantilevers with two types of probes were made: cylindrical with a high aspect

ratio and conical stepped. The formation of a probe with a high aspect ratio of the tip was carried out by carbon deposition via FIB with a current of 50 pA, an accelerating voltage of 30 keV, and an ion beam exposure time at a point of – 1 microsecond. The height of the resulting tip was 4.75 microns with a diameter of 675 nm. The step probe was deposited in the form of a structure of four disks with a height of 1.5; 2; 3 and 1 microns and diameters of 4.5; 1.8; 0.7 and 0.35 nm, respectively. The ion current during deposition was 0.5 nA.

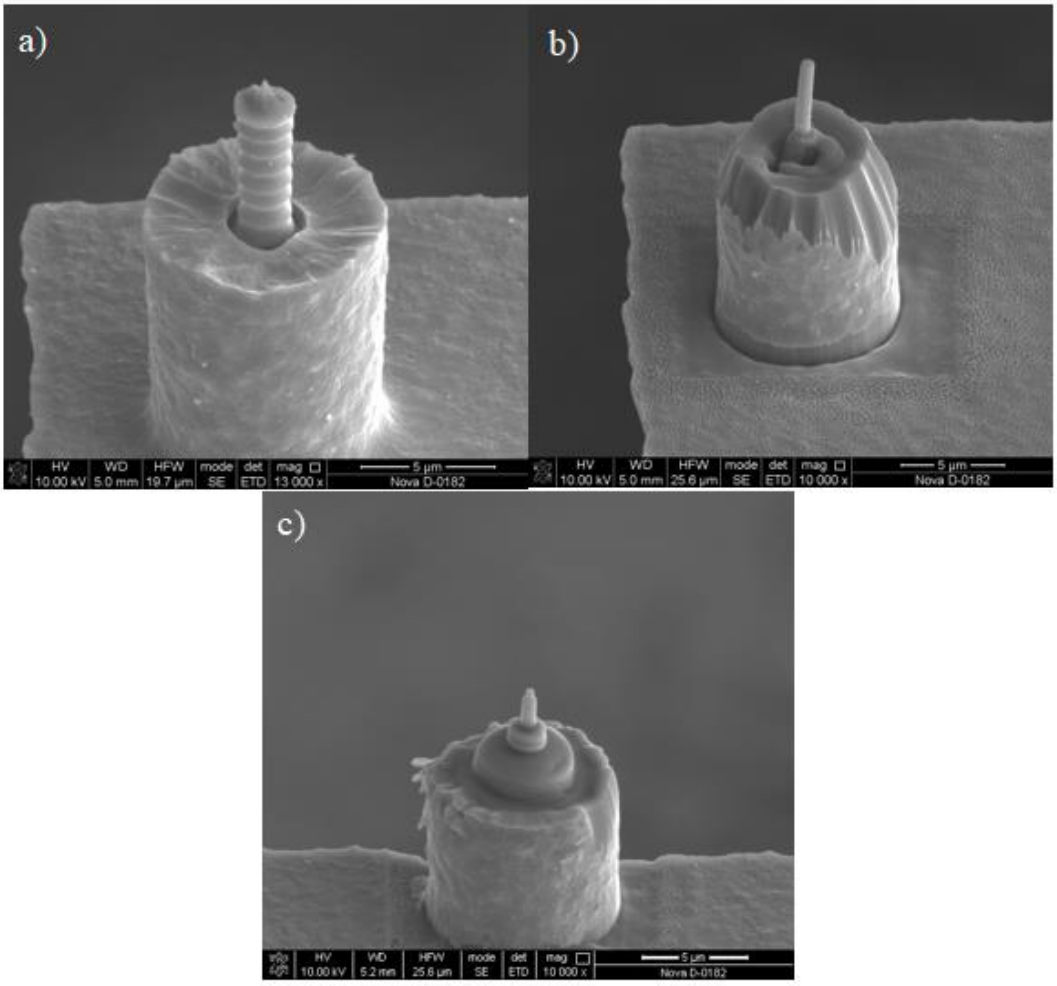

Figure 1.- SEM images of: **(a)** Commercial silicon AFM probe; **(b)** Cylindrical probe and **(c)** Conical stepped probe.

To assess the influence of the shape of the obtained probes on the measurement accuracy in comparison with standard cantilevers, the surface of the TGZ3 calibration grating (NT-MDT Spectrum Instruments, Russia) was studied using the obtained cantilevers in the semi-contact AFM mode. To compare the results of the study, such a scan was also performed using the NSG10 cantilever (NT-MDT Spectrum Instruments, Russia).

3. Results and discussion

To assess the accuracy of the relief results, the obtained surface profilograms were compared with the reference grid profile. The methodology for evaluating the measurement accuracy was based on finding the ratio of the sum of the areas of the plots that have a deviation from the reference and the area of the reference structure. The deviation calculated by this method was: 26.46% for the NSG10

cantilever, 12.8% for the high-aspect probe, and 18.08% for the step probe. The angle of inclination of the wall of the vertical grid element was approximately 40°, 15° and 25° for the left walls and 60°, 20° and 40° for the right. According to the obtained data, it can be concluded that both manufactured probes introduced less distortion into the image than the standard AFM probe, which allowed to increase the measurement accuracy by 1.46 times for the step probe and by 2.07 times for the high-aspect probe.

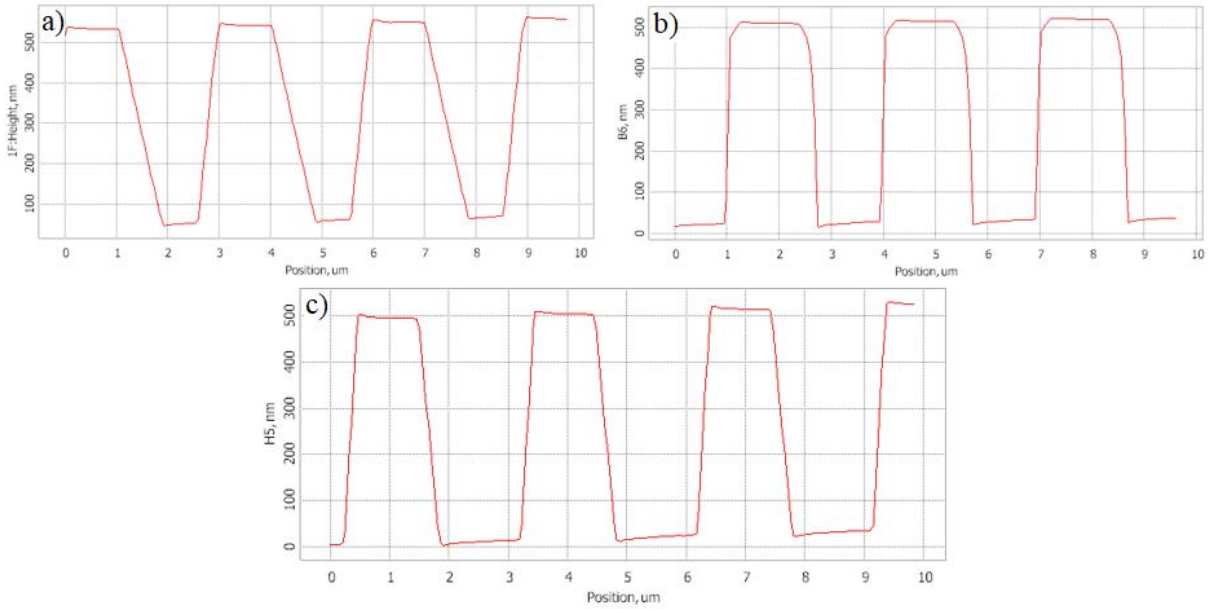

Figure 2. - AFM graphic TGZ3 calibration grating of: **(a)** Commercial silicon AFM probe; **(b)** Cylindrical probe and **(c)** conical stepped probe.

The performed studies have shown that the use of the FIB method makes it possible to form probes with high speed, accuracy and reproducibility, the parameters of which differ significantly from the parameters of standard probes, which can significantly increase the accuracy of the study of the surface relief. The results of this work can be useful in the study of micro-nanostructures and can also be used for further development of the technology for manufacturing and modifying probes by the FIB method.

Acknowledgements

The studies were carried out with the financial support of the Ministry of Science and Higher Education of the Russian Federation within the framework of a state task in the field of scientific activity No. [0852-2020-0015].

References

[1] De Felicis D., Mughal M., Bemporad E. A method to improve the quality of 2.5 dimensional micro-and nanostructures produced by focused ion beam machining. Micron. 2017. 101. P. 8–15.

[2] Yu. E. Vysokikh, T.V. Mikhailova et.al. Carbon tip aperture cantilevers: Fabrication & features in near-field magneto-optical imaging, Journal of Magnetism and Magnetic Materials 529 (2021) 167837.

Carbon nanotubes sorting due to commensurate molecular wrapping

D.S. Roshal[1], O.V. Konevtsova[1], V.P. Dmitriev[1, 2], S.B. Rochal[1]

[1]Faculty of Physics, Southern Federal University, Rostov-on-Don, 344090 Russia
[2]Swiss-Norwegian Beamlines at ESRF, Grenoble, 38043 France

e-mail: rochal.d@yandex.ru

Abstract: Single-walled carbon nanotubes (SWCNTs) can be sorted in their structural parameters by using organic molecules and polymers. Here we consider the molecules of flavin group and 2,4-dichlorophenoxyacetic acid, that demonstrate a profound affinity for only specific nanotubes and form dense coatings on them. We show for the first time that successful formation of the considered coatings depends on the ability of molecules to wrap the SWCNT in a commensurate way. Commensurability provides a decrease in the free energy of the resulting bilayer system and makes the coating much more stable. We reveal selection rules that relate the nanotube chiral vector with geometric characteristics of the adhering molecules. The proposed theory unambiguously explains known experimental results on the formation of spiral wrappings of SWCNTs by flavin group molecules and points out to other organic molecules and polymers suitable for effective SWCNT sorting.

1. Introduction

Many possible practical applications of SWCNTs often require the use of nanotubes with certain physical properties and, as a consequence, a certain chiral vector. At present, all such applications are hindered by the extreme complexity of synthesizing SWCNTs with controlled chirality. One of the directions for solving this problem is the search for such molecules that are deposited on strictly defined SWCNTs and, due to this, make it possible to "catch" such tubes from solution.

The aim of this work is to model and study the principles of structural organization of the coating of SWCNTs with 2,4-D molecules, flavin mononucleotide (FMN) and other similar molecules, as well as to predict what other molecules can facilitate sorting of nanotubes with different chirality vectors.

2. Molecules of 2,4-dichlorophenoxyacetic acid (2,4-D molecules)

A system of SWCNTs and adsorbed molecules is modeled. Its free energy can be written as the sum of energies describing the interactions of individual molecules and the coupling of the molecules and nanotube's atoms:

$$E = \varepsilon_1 \sum_{i>j}^{N_m} \left[\left(\frac{\sigma}{|\boldsymbol{r}_i - \boldsymbol{r}_j|} \right)^{12} - 2 \left(\frac{\sigma}{|\boldsymbol{r}_i - \boldsymbol{r}_j|} \right)^{6} \right] + \varepsilon_2 \sum_{j}^{N_a} \sum_{i}^{N_m} \left[\left(\frac{\rho}{|\boldsymbol{r}_i - \boldsymbol{R}_j|} \right)^{12} - 2 \left(\frac{\rho}{|\boldsymbol{r}_i - \boldsymbol{R}_j|} \right)^{6} \right] \quad (1)$$

where $\boldsymbol{r}_i$ & $\boldsymbol{R}_j$ localize the effective centers of the molecules and the nanotube atoms, respectively; σ is the distance minimizing the pair interaction between the molecules, ρ is the equilibrium distance between the molecule and the carbon atom, ε_1 & ε_2 are the depth of potential wells, N_a & N_m are the numbers of nanotube atoms and organic molecules. Using modeling and symmetry analysis, we demonstrate that functionalizing molecules can form regular periodic superstructures on the surface of

selected SWCNTs, commensurate with the nanotube lattice. A set of criteria was found that predict energetically favorable molecular structures using the example of 2,4-D molecules on the surface of SWCNTs (6, 5) [1].

3. FNM molecules

It is shown [1] that FMN is adsorbed only on SWCNTs (8,6) due to the appearance of commensurability between the nanotube lattice and the functionalizing coating. In particular, it is found that the double-helical coating wraps the tube along the (-2,7) direction. Using geometric analysis, it is shown that along the same direction FNM spirals wrap the tube (6,7) modified with mercury, as well as the spirals of the FMN analogue, FC-12, wrap tube (6,5).

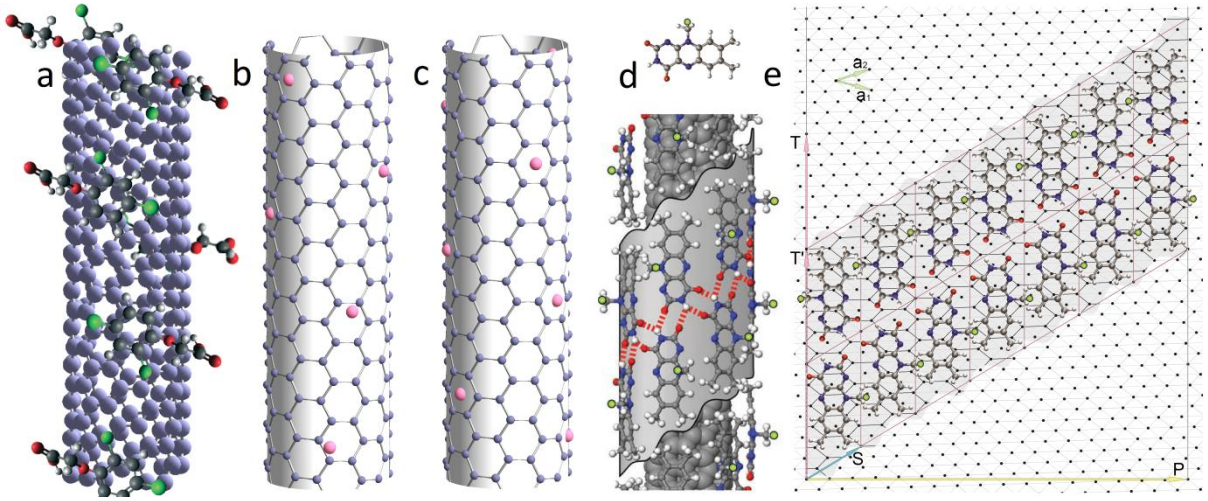

Figure 1 (a-e). Commensurability of SWCNT (6,5) and its coating with **(a-c)** 2,4-D or **(d-e)** FC-12 molecules. **(a, d)** is modified from [2,3]; **(b, c)** model structures obtained by free energy (1) minimization. In **(c)**, in contrast to **(b)**, energy (1) is at the global minimum and a geometrically ideal coating of SWCNTs (6,5) with a multiplied hexagonal order appears. **(e)** Proposed net of the coating **(d)**. FC-12 molecules are positioned within parallelograms, shown as bold purple lines. Each turn of the helix, formed from FC-12 molecules on a tube (6,5), consists of exactly 7 molecules, the 8th molecule is located above the first.

The established geometric principles may also be applicable for predicting the results of sorting of SWCNTs by other molecules, for example, by 1-pyrenebutyric acid, poly (9,9-dioctylfluorene-2,7-diyl), or various FMN analogs. The proposed ideas can be used to modify the molecular dynamics approaches describing the assembly of various coatings and trigger a new wave of studies of the various molecules deposition on SWCNTs. The considered geometric methods can find applications in other areas of physics [4].

Acknowledgments

S.R., O.K. and D.R. acknowledge financial support from the Russian Foundation for Basic Research (Grant № 18-29-19043 mk).

References

[1] Konevtsova O V, Roshal D S, Dmitriev V P, Rochal S B 2020 *Nanoscale* **12** 15725.
[2] Ju S-Y, Kopcha W P, Papadimitrakopoulos F 2009 *Science* **323** 1319
[3] Rocha J-D R, Rogers R E, Dichiarac A B, Capassea R C 2017 *Environ. Sci.: Water Res. Technol.* **3** 203
[4] Konevtsova O V, Roshal D S, Bozic A L, Podgornik R, Rochal S B 2019 *Soft Matter* **15** 7663

In situ Investigation of Individual Filament Growth in Conducting Bridge Memristor by Contact Scanning Capacitance Microscopy

M A Ryabova, D A Antonov, A V Kruglov, I N Antonov, D O Filatov and O N Gorshkov

Lobachevskii University of Nizhnii Novgorod, 603950 Nizhnii Novgorod, Russia

rmargo01@mail.ru

Abstract. We report on the first time application of Contact Scanning Capacitance Microscopy (CSCM) to trace the growth of an individual Ni filament in a $ZrO_2(Y)$ film on a Ni sublayer (together with a conductive Atomic Force Microscope probe composing a nanometer-sized virtual memristor). An increasing of the filament length in the course of electro-forming results in an increasing of the capacitance between the probe and the sample, which can be detected by CSCM technique. This way, the filament growth can be monitored in real time *in situ*.

1. Introduction

In recent years, resistive switching (RS) effect in thin dielectric films has attracted much attention due to its potential application in next-generation non-volatile computer memory (Resistive Random Access Memory, RRAM) devices – memristors [1]. The RS is a reversible switching of resistance of a thin insulator of a capacitor-like stack under a voltage applied to the plates. In most cases, the RS mechanism is understood in terms of forming and rapture of conductive filaments (CFs) formed inside the insulator under the electric field between the plates. In so-called conducting bridge (CB) RRAM, the CFs consist of metal atoms (e.g. Au, Ag, Cu, etc.) injected into the insulator (SiOx, etc.) [2].

To date, such methods as Cross-Sectional Transmission Electron Microscopy and Scanning Tunneling Microscopy [3] as well as Conductive Atomic Force Microscopy (CAFM) have been applied to study the growth/rapture of the CFs *in situ*. In the present work, we applied Contact Scanning Capacitance Microscopy (CSCM) [5] to trace the growth of an individual Ni CF in a $ZrO_2(Y)$/Ni film for the first time.

2. Experiment and results

The $ZrO_2(Y)$ film (~12% mol. Y_2O_3) with thickness $d \approx 10$ nm was deposited by magnetron sputtering onto a Si substrate with a pre-deposited 10-nm thick Ni sublayer. The experiment was carried out with NT-MDT® Solver Pro™ AFM in the contact mode using NT-MDT® HA-HR DCP AFM probes with conducting diamond-like coated tips. The probe was brought into a contact with the ZrO2(Y) film surface, and a sawtooth voltage (amplitude 6V, period 6s) was applied between the CAFM probe and the Ni sublayer. The forming of the Ni CF inside the $ZrO_2(Y)$ film started at a negative bias applied to the CAFM probe with respect to the sample due to an electrochemical (anodic) oxidation of the Ni

sublayer surface at the Ni/ZrO_2(Y) interface, drift of Ni^{++} ions in the electric field between the probe and the Ni sublayer, and reduction of the Ni^{++} ions at the growing filament tip (figure 1a) [6].

Figure 1b shows kinetics of the capacitance between the CAFM probe and the sample $C_{CF}(t)$ (t being the time) measured in the course of the forming process using an add-on for CSCM.

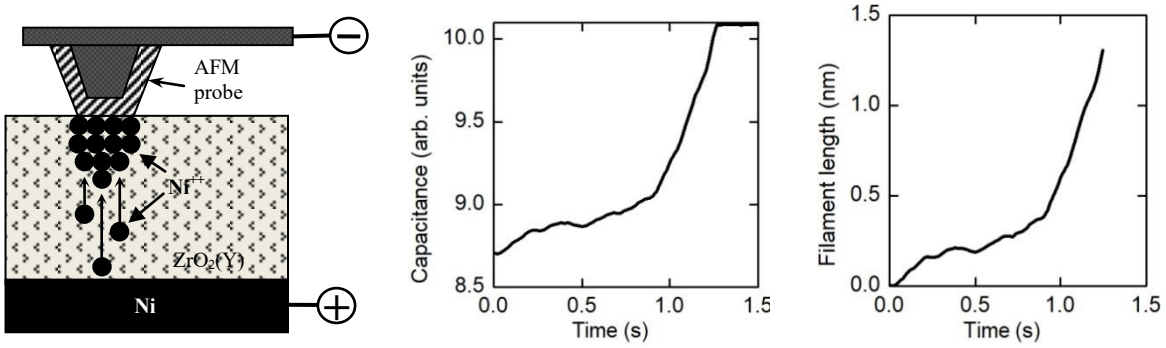

(a) (b) (c)

Figure 1 (a, b, c). Schematic representation of the filament forming process in the ZrO_2(Y) film on the Ni sublayer under the biased CAFM probe (a); kinetics of the capacitance $C_{CF}(t)$ (b) and of the CF length l_{CF} (c) extracted from the $C_{CF}(t)$ dependence

The increasing of C_{CF} was attributed to the increasing of the CF length l_{CF} in the course of forming. A dependence of C_{CF} on l_{CF} can be expressed in the flat capacitor approximation as

$$C_{CF} = \frac{\varepsilon\varepsilon_0 S}{d - l_{CF}}, \quad (1)$$

where S is the effective filament cross-section area, ε is the dielectric permittivity of the insulator material, and ε_0 is the electric constant. As $l_{CF} \to d$, $C_{CF} \to \infty$. In the experiment, the overload of the CSCM add-on lock-in amplifier took place at $t \approx 1.25$s (figure 1b).

Figure 1c shows a dependence $l_{CF}(t)$ calculated from the one $C_{CF}(t)$ according to (1). Once $l_{CF}(t)$ was obtained, one can calculate many other characteristics of the filament growth process, e.g. the filament growth rate as a function of the electric field strength in the gap between the CF tip and the conductive substrate, etc.

3. Conclusion

Concluding, in the present study we have demonstrated experimentally a capability of CSCM technique to trace the growth of the CF in the virtual memristors composed of the CAFM probe contact to the functional dielectric film on the conductive substrate and, moreover, to measure the time dependence of the CF dimensions, at least, semi-quantitatively. In this scope, the CSCM technique worked out in the present study seems to be very promising for application in future studies of the CF dynamics during the forming and RS processes in various material systems.

Acknowledgments

The present work was support Russian Foundation for Basic Research (20-02-00830).

References

[1] Amiri P K (Ed.) 2020 *Emerging Memory and Computing Devices in the Era of Intelligent Machines* (MDPI AG).
[2] Lee S H, Zhu X and Lu W D 2020 *Nano Research* **13** 1228
[3] Yang Y, Takahashi Y, Tsurumaki-Fukuchi A et al. 2017 *J Electroceram* **39** 73
[4] Williams C C, Hough W P and Rishton S A 1989 *Appl Phys Lett* **55** 203
[5] Lubben M and Valov I 2019 *Adv Electron Mater* 1800933

Study of ripple formation on Si surface under Ga ion beam bombardment

M A Smirnova, A S Ivanov, V I Bachurin and A B Churilov

P.G. Demidov Yaroslavl State University

e-mail: masha_19957@mail.ru

Abstract: The process of microrelief formation on Si (100) surface under 30 keV Ga^+ ion beam bombardment with doses $2 \cdot 10^{17}$ - $4 \cdot 10^{18}$ ion/cm^2 at incident angles θ = 0 - 50˚ were studied. It was found that wave liked structures form on the surface at θ = 25˚ - 35˚ and doses $6 \cdot 10^{17}$ - $2 \cdot 10^{18}$ ion/cm^2. The nice ripple formed at θ = 30±2˚ incident angles and irradiation dose 10^{18} ion/cm^2.

1. Introduction

The formation of micro- and nanostructures on the surface of semiconductor materials by ion bombardment has recently attracted interest. In particular, a large number of works is devoted to the formation of periodic wavelike structures on a nanometer scale called ripples. The review [1] presents the main results, devoted to the experimental and theoretical study of the formation of such structures on the surface of various materials irradiated with ions of inert and chemically active gases. The main regularities of the parameters of the forming structures were experimentally established. Thus, ion bombardment may have different effects on the surface, depending on many factors such as incident ion energy, type of ions, angle of incidence, sputtered substrate temperature and material composition and etc. There are differences between using inert and chemically active ion beams in the process of ripple formation. The irradiation dose, which the ripple formation begins with, is one of the distinguishing features. In case of using chemically active ions this dose is orders of magnitude less than in case of using inert ions. This article presents the results of the experimental study of formation of a microrelief on a Si surface irradiated with a 30 keV Ga^+ ion beam. This type of ions is neutral in relation to Si, since the implanted ions don't form chemical compounds with silicon atoms but they are present in the surface layer in the form of precipitates [2]. This behavior of embedded ions differs from classical rare-gas atoms. At the moment, there is a small number of works [3, 4] devoted to the formation of the microrelief on the Si surface by gallium ion beams. Although, focused Ga+ ion beams are a widespread experimental tool in the formation of nanostructures on various surfaces, under different irradiation conditions (angle of incidence, irradiation dose, etc.).

2. Experimental results

The irradiation experiments of Si (100) with a 30 keV Ga^+ ion beam were carried out on a Quanta 3D 200i. Beams with a diameter of 4 μm and 300 nm were used at various irradiation parameters (percentage of overlap, delay time, scanning mode). Two series of experiments were carried out. In the first one the angles of incidence of the ion beam were Θ = 25°, 30°, 35°, 40°, irradiation doses were D = $2 \cdot 10^{17}$, $4 \cdot 10^{17}$, $6 \cdot 10^{17}$, $8 \cdot 10^{17}$, 10^{18}, $2 \cdot 10^{18}$, $4 \cdot 10^{18}$ ion/cm^2. In the second - the angles of incidence of

the ion beam were Θ = 0°, 20°, 30°, 40°, 50° irradiation doses were D = 10^{18} ion/cm^2. The surface topography was explored in situ by using a Quanta 3D 200i facility and ex situ by Supra 40 electron microscope in detail.

It was found that at irradiation doses and angles of incidence more than 40° the formation of a relief on the surface does not occur. At angles of incidence of the ion beam less than 25° and irradiation doses exceeding $4\cdot10^{17}$ ion/cm^2, a granular structure is formed on the surface and it becomes reticulated (characteristic size about 100 nm) with the irradiation dose increasing. At angles of incidence in the range from Θ = 25° to 35° and irradiation doses higher than $4\cdot10^{17}$ ion/cm^2, a wavy relief appears. Ripple formation was observed at angle of incidence Θ = 25°. Figure 1 demonstrates micrographs of a Si surface irradiated with a Ga^+ ion beam at an incidence angle 30°.

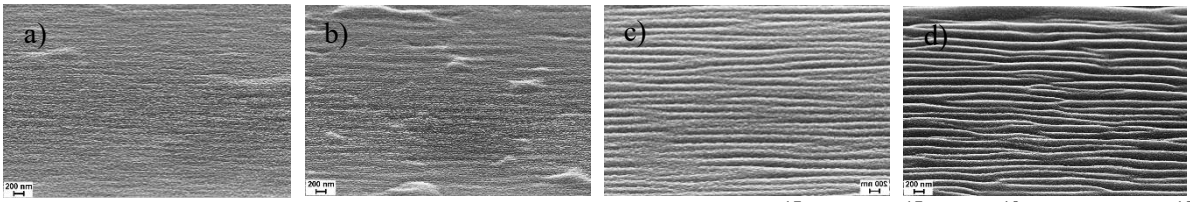

Figure 1. Micrographs of the Si surface. Irradiation doses: a) $4\cdot10^{17}$, b) $6\cdot10^{17}$, c) 10^{18}, and d) $2\cdot10^{18}$ ion/cm^2.

Figure 1 shows that at the generation of ripples (D = $4\cdot10^{17}$, $6\cdot10^{17}$ ion/cm^2) bright hills (hilloks) are observed on the surface. Those hilloks are Ga drops. It was determinated by the analysis of the irradiated surface by the SIMS method on the Cameca IMS 4f. At irradiation doses higher than $2\cdot10^{18}$ ion/cm^2, there is an intersection of waves and the destruction of wave-like structure.

3. Conclusions

As noted above, behavior of Ga ions in the near-surface layer significantly differs from embedded ions of inert gases, for example, Ar. The implanted Ga atoms form precipitates near the surface [2], which are located at the depth of the ions projective range, as shown in [5]. Apparently, the emergence of such irregularities on the surface in the form of Ga drops is the reason of ripple formation. This ripples are formed at Si surface at irradiation doses by two orders of magnitude less than at inert gas ion bombardment (Ar, Xe) with close energies. The absence of relief at angles of incidence of the ion beam more than 35° is due to a sharp drop in the Ga content in the near-surface layer [5]. The sputtering yield almost does not change [5] at angles of incidence less than 25°. The necessary condition for the appearance of a wavy relief on the surface under ion irradiation is not met [1].

Acknowledgments

This study was performed with financial support from the Ministry of Education and Science of the Russian Federation within the framework of the state assignment of the P.G. Demidov Yaroslavl State University of topic no. 0856-2020-0006 and using equipment of the facilities sharing centre “Micro- and Nanostructures Diagnostics”.

References

[1] Munoz-Garcia J, Vazquez L, Castro M, Gago R, Redono-Cubero A, Moreno-Barrado A and Cuerno R 2014 *Mater. Sci. & Eng.* R **86** 1
[2] Frey L, Lehrer C and Ryssel H 2003 *Appl. Phys.* A **76** 1017
[3] Habenicht S, Lieb K P, Koch J and Wieck A D 2002 *Phys. Rev* B **65** 115327
[4] Qian H X and Znou W 2012 *Mater. Letters* **77** 1
[5] Bachurin V I, Zhuravlev I V, Pukhov D E, Rudy A S, Simakin S G, Smirnova M A, Churilov A B 2020 *J. Surf. Invest.* **14** 784

Properties of Plasma Enhanced Atomic Layer Deposited Ruthenium Thin Films from $Ru(EtCp)_2$

E A Smirnova[1] , A V Miakonkikh[1] , A E Rogozhin[1] , K V Rudenko[1]

[1]Valiev Institute of Physics and Technology of Russian Academy of Sciences, Moscow 117218, Russia

smirnova@ftian.ru

Abstract. Ruthenium thin films were deposited by plasma enhanced atomic layer deposition using bis(ethylcyclopentadienyl)ruthenium(II) or $Ru(EtCp)_2$ and oxygen plasma. The growth characteristics have been studied on silicon substrate with different interfaces in a wide temperature range. On Si and SiO_2, a nucleation delay period has been observed, which can be substantially redused by the use of a tantalum nitride underlayer of ~ 0.3 nm. The surface analysis shows that the substrate's temperature strongly affects the composition of the film from ruthenium oxide at low temperatures to pure ruthenium film at higher temperatures.

1. Introduction

Atomic-layer deposition (ALD) of ruthenium films has recently become an actual and popular problem due to the prospects for its application in metallization systems of integral systems [1-5]. The interest in ruthenium is partly due to its high technological properties of the noble metal at a relatively low cost, which makes it possible to use it in the mass production of integrated circuits. Ultrathin continuous films without any voids are needed when Ru is used as a diffusion barrier for Cu interconnects. The application of Ru as a conducting interconnection material requires Ru with low resistivity and low impurity contents. Plasma-enhanced ALD (PEALD) is one of the most attractive methods for producing films with these characteristics, given its inherent ability to easily transition to three-dimensional structures.

A typical ALD process consists of the alternating dosing of precursor and coreactant gas that interact with a substrate through self-limiting surface reactions. In this work, we examine the growth and nucleation of Ru thin films deposited using bis(ethylcyclopentadienyl)ruthenium(II) precursor in PEALD process that includes an oxygen plasma pulse. In particular, we look at how the substrate temperature influences the growth and nucleation of the film and how it can be used to manipulate the material properties.

It was shown earlier [6] that one of the main problems of film growth is also delamination, which is apparently associated with mechanical stresses in the film. This becomes especially critical for films with a thickness of more than 50 nm.

The research of the resistance of Ru-based films obtained in the optimal mode is presented in the previous work [7].

2. Experiment

ALD processes were performed in commercial FlexAl system (Oxford Instruments Plasma Technology) with a base pressure of 10^{-6} Torr, using a 13.56 MHz ICP remote plasma source.

$Ru(EtCp)_2$ was contained in a bubbler, preheated to 70°C and delivered to the reactor by argon flow gas at a flow rate of 150 sccm. The manifold lines were heated to 100 °C and the reactor walls to 120 °C to prevent the condensation of the precursor. The recipe for Ru ALD consisted of a 2 s $Ru(EtCp)_2$ dosing, 1 s pumping, 4 s Ar purge, 2 s step of oxygen pressure stabilization in the chamber, 1 s O_2 plasma ignition and exposure (O_2 pressure of 0.065 Torr), and 4 s Ar purge.

Depending on the thickness of the films, adequate ex situ methods were used to measure the growth rate: for films with a thickness of less than 10 nm, a spectroscopic ellipsometry (Woollam M-2000X) was used, and for thicker films, a cross-section scanning electron microscopy (Carl Zeiss Ultra-55). Stress analysis of samples was carried out using a Zygo New View 5000 interference microscope.

3. Results and Discussion

We examine the range of growth temperature of 200–400 °C and it turned out that the substrate temperature plays a critical role in determining whether Ru or RuO_2 is deposited. It was noticed that at 375 °C an abrupt change in surface reaction mechanisms takes place, leading to the changing in film composition and structure from polycrystalline RuO_2 at low temperatures to pure Ru film at higher temperatures.

For this, the deflections of single-crystal silicon wafers with a thickness of 380 μm were measured with films deposited on them. The measurement was carried out in a field of 5 mm x 5 mm; the vertical measurement accuracy was about 1 nm. The obtained distributions were highly approximated by a spherical profile, and the mechanical stress in the film was calculated using the Stoney formula. The application of this approach will allow optimizing the stresses in the films by varying the deposition modes and plasma treatment, which will make it possible to obtain films of metallic ruthenium with better quality.

Mechanical stress data are consistent with the roughness of the films. The mechanism of relaxation of the ruthenium film on a single-crystal silicon surface is associated with the formation of blisters. Stress values of 2.8–4.6 GPa (on Si) were measured.

Acknowledgments

The investigation was partially supported by Program no. 0066-2019-0004 of the Ministry of Science and Higher Education of Russia for Valiev Institute of Physics and Technology of RAS and partially funded by RFBR, according to the research project № 18-29-27029

References

[1] Rungthiwa Methaapanon, Scott M. Geyer, Han-Bo-Ram Lee and Stacey F. Bent, *J. Mater. Chem.*, 2012, **22**, 25154

[2] Sonali N. Chopra, Martijn F. J. Vos, Marcel A. Verheijen, John G. Ekerdt, Wilhelmus M. M. Kessels, and Adriaan J. M. Mackus, *J. Vac. Sci. Technol*., 2020, A **38**, 062402

[3] Popovici, M.; Groven, B.; Marcoen, K.; Phung, Q. M.; Dutta, S.; Swerts, J.; Meersschaut, J.; Van Den Berg, J. A., Franquet, A., Moussa, A., et al. *Chem. Mater*. 2017, **29**, 4654−4666

[4] Müller R, Ghazaryan L, Schenk P, Wolleb S, Beladiya V, Otto F, Kaiser N, Tünnermann A, Fritz T, Szeghalmi A, *Coatings*. 2018, 8(**11**):413

[5] Dutta, S., Kundu, S., Gupta, A., Jamieson, G., Granados, J.F.G., Bömmels, J., Wilson, C.J., et al. *IEEE Electron. Device Lett*. 2017, **38**, 949–951.

[6] E A Smirnova et al 2020 *J. Phys.: Conf. Ser.* **1695** 012045

[7] Rogozhin, A., Miakonkikh, A., Smirnova, E., Lomov, A., Simakin, S., Rudenko, K. *Coatings* 2021, **11**, 117

The electron transmission properties in a system of two chained orthogonal rings

M O Smolkina[1], **I Yu Popov**[1], **A M Vorobiev**[1]
[1]Faculty of Control Systems and Robotics, ITMO University, St. Petersburg, 197101, Russia

Abstract. The electron transmission properties in a model of two chained orthogonal quantum rings in a magnetic field with one input and one output wires were studied by using quantum waveguide theory. The model was obtained for three-dimensional space. It also was shown that perfect transmission can be governed by a change in the construction orientation in the respect to the field.

1. Introduction

One of the basic questions in the field is as follows: How can one control the electron transport in a nanosystem? The most natural way is related to using of external electric or magnetic field. There are a number of works describing systems composed of quantum rings and the manipulation with the value of magnetic field to control the electron transmission in nanostructures [1-3]. In our work, we suggest a construction composed of two chained orthogonal rings (i.e., the graph is not plane) which allows one to control the electron transmission due to the direction of the magnetic field or, in other words, due to the construction orientation in respect to the field.

2. Theoretical model

We propose a possible model of a quantum device consisting of two rings. One ring is in the ZOY plane and the other is in the XOY plane. These two rings are orthogonal to each other and have a junction point. The device also has an input wire, which is connected to the first (left) ring. The second (right) ring is equipped with an output wire. This construction can rotate around the Y axis, while the magnetic field vector is directed along the Z axis and does not change its direction. For rings a one-dimensional approximation is considered, and the scattering problem is taken as a base.

The functions in the incoming and outgoing leads, denoted by: $\psi_I(x_I), \psi_{II}(x_{II})$ can be written as

$$\psi_I(x_I) = e^{ikx_I} + C_1 e^{-ikx_I}, \psi_{II}(x_{II}) = C_{10} e^{ikx_I}, \tag{1}$$

for upper and lower arms of two similar rings:

$$\begin{aligned} \psi_{L_{up}}(\gamma) &= C_2 e^{ikR_L\gamma} + C_3 e^{-ikR_L\gamma}, \\ \psi_{L_{low}}(\gamma) &= C_4 e^{ikR_L\gamma} + C_5 e^{-ikR_L\gamma}, \\ \psi_{R_{up}}(\gamma) &= C_6 e^{ikR_R\gamma} + C_7 e^{-ikR_R\gamma}, \\ \psi_{R_{low}}(\gamma) &= C_8 e^{ikR_R\gamma} + C_9 e^{-ikR_R\gamma}, \end{aligned} \tag{2}$$

where $R_L(R_R)$ is the radius of the left (right) ring, γ is the angle between junctions of the rings and wires, k is a wave number.

The magnetic Kirchhoff conditions are as follows:

$$\begin{cases} e^{(-1)^{\mu} i\Phi_e(\gamma_e)}\psi_e(\gamma_e) = \psi_{e'}(\gamma_e)e^{(-1)^{\mu} i\Phi_{e'}(\gamma_e)} \\ \sum_e (-1)^{[e]}\partial\psi_e(\gamma_e)e^{(-1)^{\mu} i\Phi_e(\gamma_e)} = 0, \end{cases} \quad (3)$$

where $[e]=0$ for the output edge and $[e]=1$ for the input edge, γ_e is an angle between junctions of the rings and wires. Since the orientations of the edges in some points will not coincide with the parameters on the ring, we will take into account the negative sign in front of Φ_e, so μ equals 0 or 1, depending on the orientation. Besides

$$\Phi_e = \begin{cases} 0, \\ \int_{\gamma_e} a(\tau)d\tau, \end{cases} \quad (4)$$

where 0 is in the beginning of the edge, $\int_{\gamma_e} a(\tau)d\tau$ in the end of the edge.

As mentioned earlier, the magnetic field is assumed to be directed along the Z axis, therefore $\Phi_1(\gamma) = \frac{1}{2}BR_L{}^2\gamma\cos(\alpha), \Phi_2(\gamma) = \frac{1}{2}BR_R{}^2\gamma\sin(\alpha)$, where $\Phi_1(\gamma)$ belongs to the ring in the ZOY plane and $\Phi_2(\gamma)$ belongs to the ring in the XOY plane, α is a rotation angle around the Y axis.

Using the magnetic Kirchhoff conditions and the expressions for leads, edges and for $\Phi_1(\gamma), \Phi_2(\gamma)$ and employing the Gaussian elimination method, we can obtain all the unknown coefficients $C_1, C_2, \ldots C_{10}$. Finally, the reflection coefficient can be written as $\mathrm{R}_{ref} = C_1 \cdot C_1^*$, the transmission coefficient: $T = C_{10} \cdot C_{10}{}^*$.

3. Numerical results

We have done a numerical study to illustrate some essential characteristics of the electron transport in the proposed device. The value of transmission coefficient T varies in the range from 0 to 1 when changing the wave number, the rotation angle, the radii of the rings and the angles between junction points. If the value of transmission coefficient approaches 1, we can say that the wave passes in this output wire, otherwise, when approaching 0, the wave in the wire does not pass. We have found such values of the parameters: the rotation angle, radii of the rings, wave number k, angles between junctions of the rings and wires, when the transmission coefficient T is close to 1.

Acknowledgements

The reported study was funded by RFBR, project number 19-31-90164.

References

[1] Pavlov B S and Popov I Yu and Geyler V A and Pershenko O S 2000 Possible construction of quantum multiplexer *Europhys. Lett.* **52** (2) pp 196-202

[2] Geyler V A and Popov I Yu 2001 Quantum interference rectifier *Physica E: Low-dimensional Systems and Nanostructures* **9** (4) pp 631-634

[3] Dehghana E and Khoshnouda D S and Naeimi A S 2018 Logical spin-filtering in a triangular network of quanum nanorings with a Rashba spin-orbit interaction *Physica B* **529** pp 21-26

Al-CuO_x multilayer nanostructures: formation features and thermal properties of new type of local heat source

A I Novoseltsev[1], L I Sorokina[1], A V Sysa[2], R M Ryazanov[2], E A Lebedev[1,2]

[1] National Research University of Electronic Technology – MIET, 124498, Moscow, Zelenograd, Russia
[2] Scientific-Manufacturing Complex "Technological Centre", 124498, Moscow, Zelenograd, Russia

larasork@gmail.com

Abstract. In this work, multilayer nanostructured thermite materials are considered - a new type of local heat sources. Aluminum and copper oxide were chosen as components of the thermite mixture. The formation of multilayer structures was carried out on the surface of the substrate by the method of magnetron sputtering. The features of the deposition process, as well as the energy properties of the formed, have been investigated. The results obtained confirm the prospects of using this class of materials as local heat sources.

1. Introduction

Technological progress in micro- and nanoelectronics requires the solution of new problems associated with the technology of surface joining. Reaction bonding or soldering using thin layers of energetic materials, acting as local heat sources, already now make it possible to effectively solve a number of technological problems. Energy materials manufactured in the form of multilayer structures consist of two or more components and are able to maintain in their volume a self-propagating exothermic reaction in the wave combustion mode after initial initiation. The reaction front temperature can significantly exceed 1000 °C and reaches this value in milliseconds. For soldering, a layer of energetic material is placed between the solder layers, and initiation occurs with an electric spark or low-power laser. The heat released during the reaction melts the solder, which wets the surfaces to be joined and, after solidification, forms a reliable joint. Depending on the physical state of the surfaces to be joined, all joining processes can be divided into three groups - solid bonding [1], solder bonding [2] and fusion bonding [3]. In the latter case, melting of the surfaces to be joined is necessary, which, as a rule, is associated with significant heating of the object, which can lead to the loss of its unique properties. And this is precisely the main problem of micro- and nano-assemblies - how to limit and accurately dose the heating, and how to limit the heated volume or how to localize it? Energetic nanoscale multilayer foils for bonding surfaces have been developed and partially commercialized in the last decade. Due to their high reactivity and intense heat release, these functional foils can act as heat sources for joining thermosensitive materials and micro- and nano-sized components [4].

2. Experimental details

Multilayer structures with different thicknesses of individual layers were formed by alternate sputtering of Al and CuO_x targets by magnetron sputtering. Studies of the formed materials using energy-dispersive X-ray spectroscopy and stylus profilometry made it possible to reveal the dependences of the deposition

rate and composition of copper oxide layers on the partial pressure of oxygen in the process of target sputtering. Thermal effects were measured by differential scanning calorimetry, and the propagation velocity of the wave combustion front was carried out using high-speed video camera.

3. Results

Figure 1 shows a cross-section photo of multilayer structure before and after combustion. After combustion the reagents melt and drops are formed from the reaction products – Al_2O_3 and Cu.

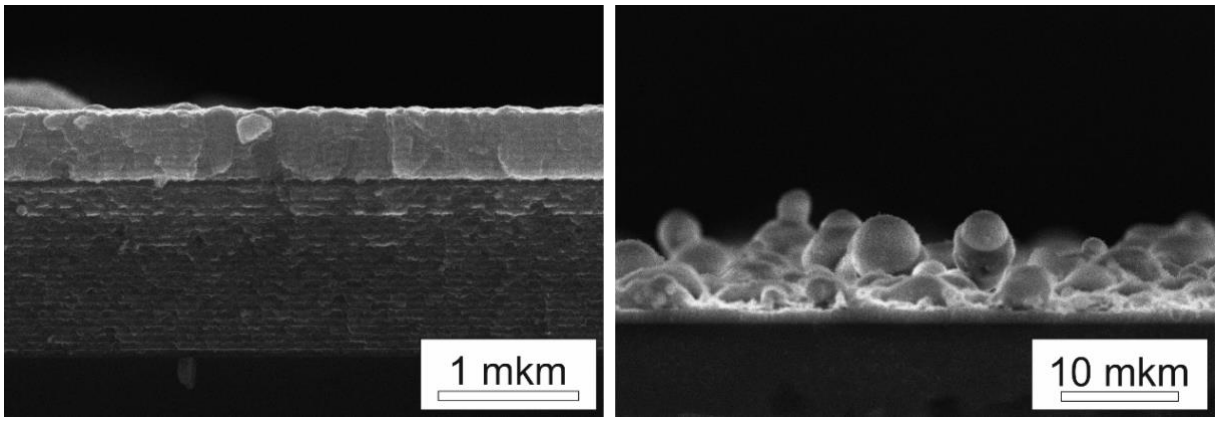

Figure 1. SEM images of cross-sections of multilayer Al-CuO_x structures before (left) and after (right) combustion.

Figure 2 shows a storyboard of the initiation and combustion of a multilayer Al-CuO_x structure. It is clearly seen, that wave combustion propagates uniformly from the point of initiation in all directions. The wave propagation speed was 6,6 m/s.

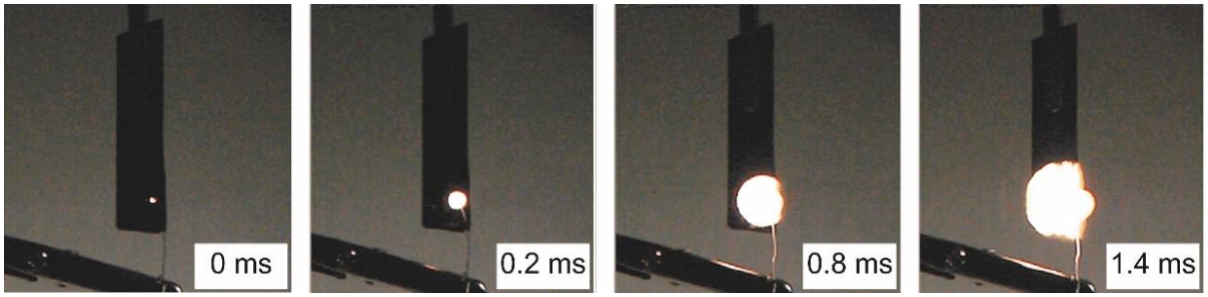

Figure 2. Storyboard of the combustion process of Al-CuO_x.

The experimental results obtained made it possible to optimize not only the formation process multilayer structures, but also its energetic properties.

Acknowledgments

This work was supported by the State assignment 2020-2022 № FSMR-2020-0018

References

[1] Lu Y, Huang J Y, Wang C, Sun S and Lou J 2010 *Nature Nanotechnology* **5(3)** 218
[2] Do J-W, Chang N N, Estrada D, Lian F, Cha H and Duan X J 2015 *ACS Nano* 15 **9(5)** 4806
[3] Hu A, Peng P, Alarifi H, Zhang X Y, Guo J Y and Zhou Y 2012 *J. of Laser App.* **24(4)** 042001
[4] Simões S, Viana F, Ramos A S, Vieira M T and Vieira M F 2014 *Micr. and Microanal.* **21(1)** 132

Processing of electron diffraction data on a transmission electron microscope

S V Vasilev [1], I S Fattakhov[2]
[1]Valievinstitute of physics and technology of RAS, Yaroslavl Branch, Universitetskaya 21, Yaroslavl, 150007, Russia
[2] Department of Nanotechnology in Electronics, P.G. Demidov Yaroslavl State University,Sovetskaya Street 14, Yaroslavl, 150003, Russia

E-mail: 33ychenikan@mail.ru

Abstract. Modern physics has many ways of analyzing substance and its surface. One of the most effective methods is transmission electron microscopy. In this work, carbon coating on cemented steel was analyzed by method of electron diffraction.

1. Introduction

This paper presents the results of studies of electron diffraction of carbon coating on cemented steel, which should be determined as part of the analysis. In Figure 1 we present electron diffraction and logarithmic patterns for this sample.

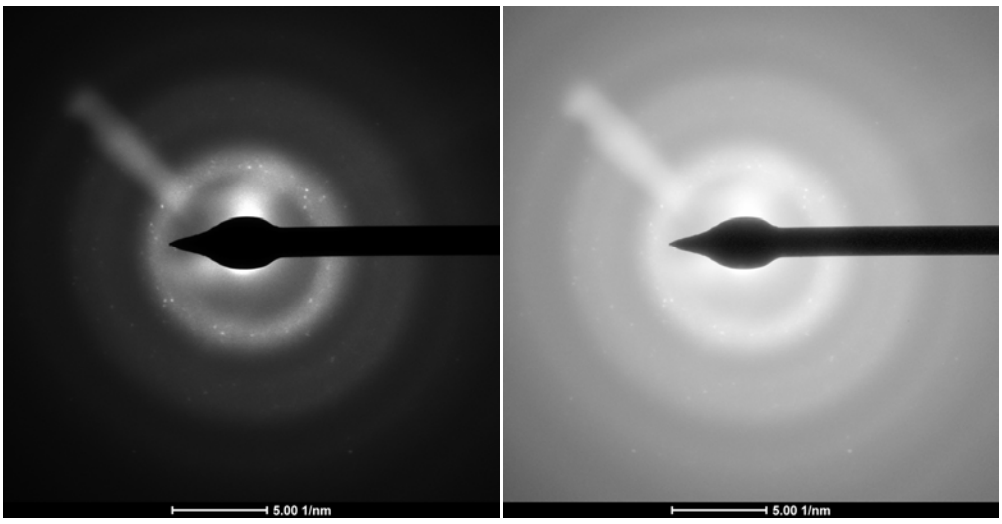

A B

Figure 1. Electron diffraction images: A) original pattern, B) logarithmic pattern

2. Results

We found 4 reflexes and their interplanar spacing:2,213 Å ;1,354 Å;1,129 Å;0,816 Å. Using database ICDD PDF2020 and [1] we determined study compound and Miller indexes. The results obtained are shown in table 1.

Table 1. Obtaining data from the analysis of the electronogram

Experimental data values of interplanar distances, Å	Values of interplanar distances for the Fe4C standard (03-065-5723), Å	Miller indexes for the benchmark
2,213±0,044	2,2389	(1 1 1)
1,354±0,027	1,3710	(2 2 0)
1,129±0,023	1,1194	(2 2 2)
0,816±0,016	0,8267	(3 3 2)

The survey was carried out on the equipment of the center for collective use of scientific equipment diagnostics of micro-and nanostructures.

To sum up, we determined the substance and the type of its crystal lattice is Fe_4C with a face-centered crystal lattice.

References

[1] Weinstein B K 1956 Structural electronography; Academy of Sciences of the USSR (Institute of Crystallography - Moscow: Academy of Sciences of the USSR) ed by Z G Pinsker p 342

Investigation of the dielectric fatigue of active dielectrics on the example of lead titanate films $PbTiO_3$

A V Fimin, E A Pecherskaya, A V Pecherskiy, V S Aleksandrov, A V Volik, A E Shepeleva

Department of Information and measuring equipment and metrology, Penza State University, Penza 440026, Russia

e.a.pecher@gmail.com

Abstract. The phenomenon of dielectric fatigue of active dielectrics, which consists in a decrease in the residual polarization depending on the number of switching cycles, is researched. A model of the dependence of the residual polarization of ferroelectric materials on the number of switching cycles is proposed. The model is based on piecewise - linear approximation of the results of measurements of the hysteresis loops of thin films $PbTiO_3$ at a temperature T = 470 (°C), the electric field strength E = 100 (kV/cm). The developed model was used in the development of a technique for studying dielectric fatigue, depending on different modes of material switching.

1. Introduction

The class of active dielectrics is widely used in various functional electronics products, such as small-sized capacitors, non-volatile memory chips, and others, since in the ferroelectric phase, at certain values of the external electric field strength, these materials have high values of anisotropic relative permittivity. The influence of an external electric field of polarization contributes to the switching of superminiature domains - memory cells, into which information is recorded at this moment. Therefore, an important qualitative characteristic of ferroelectric films is the number of polarization switching cycles (more than 10^{10} times) [1]. From a metrological point of view, the task is to develop the following methods:

- methods for measuring hysteresis loops of polarization dependences on the electric field strength P(E), determining characteristic parameters;
- methods of studying the dynamics of changes in the characteristic parameters of the hysteresis loop (that is, their temporal instability) depending on time; depending on the number of switching cycles.

The physical mechanisms of thin ferroelectric films fatigue have been studied, for example, in [2 - 4].

2. Modeling of the mechanism of dielectric fatigue of films $PbTiO_3$

According to the achieved measurement method, the cumulative hysteresis loops $P(E)$ are measured with the help of an automated installation during the interval switching of the polarization cycle N, on the basis of which the dependence of the residual polarization range on the total volume of the polarization switching cycles is formed [5]. The graph of the dependence of the residual polarization on the number of switching cycles of the polarization $P_r(\lg N)$ for thin films of lead titanate $PbTiO_3$ at a temperature of T = 470 (°C), the electric field strength E = 100 (kV / cm) is shown in Figure 1.

The dependence $P_r(\lg N)$ is approximated by three straight lines in accordance with the following expressions:

$$P_r = \begin{cases} c, \text{if } 0 < N \le N_1, \\ a + b \cdot \lg N, \text{if } N_1 < N \le N_2, \\ e + v \cdot \lg N, \text{if } N_2 < N \le N_3, \end{cases} \quad (1)$$

where the values of the coefficients (*c, a, b, e, v*) in the approximating equations of the straight lines, as well as the intervals themselves, bounded by the values N_1, N_2, are selected in accordance with the least squares method.

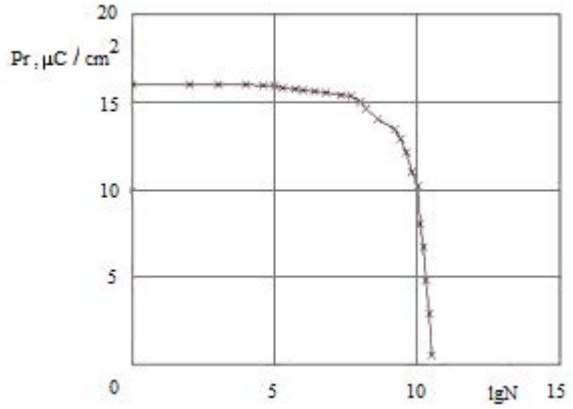

Figure 1 – Dependence of the residual polarization on the number of switches

The described above method for modeling the dependences $P_r(\lg N)$ of active dielectrics was used to develop a technique for studying dielectric fatigue in three modes of material switching (continuous polarization switching mode, polarization switching mode with alternating long waiting times, and a mode with an uneven polarization switching frequency).

3. Conclusion

The studied model allows us to present in more depth the design of sensitive elements formed by lead titanate films or similar active dielectrics from the composition of various functional electronics products. This method allows us to take into account the degradation of the material, which is expressed in the stability of reliable measurement results and an increase in the service life of the sensor as a whole.

Acknowledgements

The reported study was funded by RFBR according to the research project № 20-38-90151.

References

[1] Delimova L A, Gushchina E V, Yuferev V S 2016 Peculiarities of Electrical Characteristics of Ferroelectric Memory Elements Based on PZT-Films *Russ Phys J* 58 pp 1301–1305

[2] Sidorkin A S, Nesterenko L P and Pakhomov A Y 2012 Influence of fatigue processes on the switching currents in lead titanate and lead zirconate-titanate films *Phys. Solid State* 54 pp 1008–1010

[3] Nguyen H T, Sidorkin A S, Milovidova S D 2020 Dielectric properties of ferroelectric nanocomposites of nanocrystalline cellulose and sodium nitrite *Appl Nanoscience* 10 499–506

[4] Darinskii B, Sidorkin A, Sigov A and Popravko N 2018 Influence of Depolarizing Fields and Screening Effects on Phase Transitions in Ferroelectric *Composites Materials*, 11 p 85

[5] Pecherskaya E A, Artamonov D V, Kondrashin V I, Golubkov P E, Karpanin O V, Zinchenko T O 2017 Software - Hardware Complex for Measurement and Control of Ferroelectrics Parameters *IOP Conference Series: Materials Science and Engineering*, 225 (1), 012254

Induction-thermal action effect on the surface area of titanium products

M Fomina[1]A, Shchelkunov[1] , A Shumilin[1]

[1]Yuri Gagarin State Technical University of Saratov, Saratov 410054, Russia

e-mail: fominamaspb@mail.ru

Abstract. The changes in the surface area of titanium samples occurring during induction heat treatment (IHT) were studied. The dependence of the surface area of titanium samples on the exposure temperature was revealed. When a titanium sample was heated to a temperature of 1000 ºC in the air at an exposure time of 60 s, there was a 45-fold area increase.

1. Introduction

Increasing the surface of titanium parts is used in the manufacture of dental implants. Sandblasting and plasma spraying of porous coatings are conventional methods for preparing the surface of implants [1,2]. The developed surface morphology facilitates integration with the surrounding biological tissues [1]. Oxidation of titanium parts is a simple way to obtain a morphologically heterogeneous surface oxide layer [3]. The works on the synthesis of anatase powders with a high specific surface area are also known [4,5]. However, the production of an adhesive strong coating with a controlled surface area is of practical interest.

2. Methodology

The samples for the study were made of VT1-00 commercially pure titanium and had the shape of a cylinder with a diameter of 5 mm and length of 5 mm. Thermal oxidation was carried out using "VCh-15A" induction equipment. The IHT comprised several stages: accelerated heating, high-temperature exposure and cooling in a quiet mode (on a ceramic plate). The IHT temperature varied in the range of 800–1000 °C with a fixed duration of 60 s. The "Surface Area & Pore Size Analyzer System Quantachrome Nova 2000e" complex was used to measure the surface area. Sample preparation was characterized by the following parameters: outgas time 2 hrs; outgas temp +200 ºC; analysis gas – nitrogen. The surface area was measured using the BET (Single Point Surface Area) method at a pressure ratio of P/P_0 = 0.3.

3. Results

The surface areas of geometrically identical samples grew with increasing IHT temperature (Figure 1). When heated to a temperature of 850 ºC and above, the surface layers of titanium were actively saturated with oxygen. This led to the appearance of an oxide layer and changes in the morphology of the samples. The areas of two titanium cylindrical samples were measured simultaneously for each heating mode. The measured value of the surface area of the samples (without heat treatment) was at the sensitivity limit of the device.

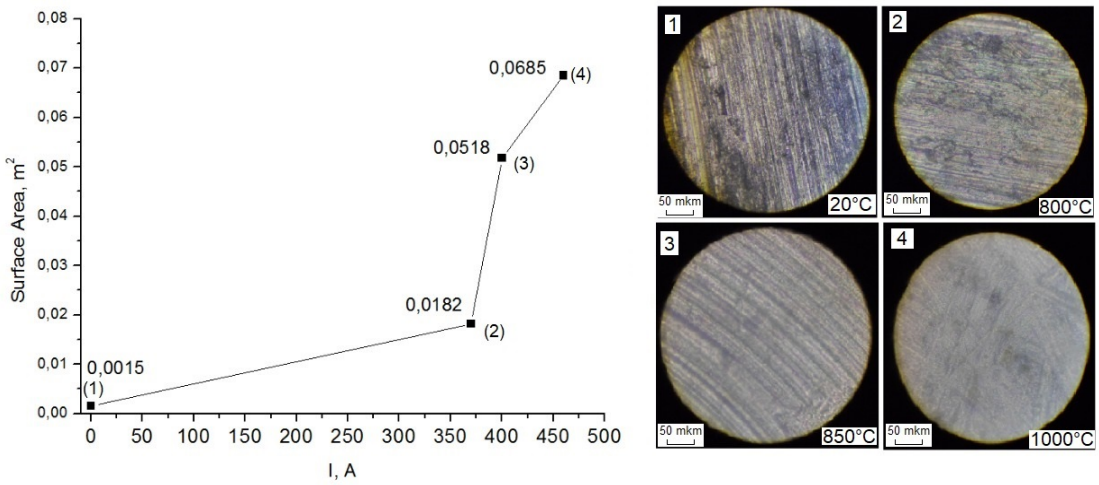

Figure 1. Dependence of the surface area on the inductor current and photomicrographs showing the sample morphology after IHT.

The increase in surface area was explained by the formation of a morphologically non-homogeneous oxide layer [3]. The layer thickness depended on the heating temperature and the exposure time at a given temperature. At the temperatures of 770–800, 850–880 and 1000–1030 ºC, there was a 12-, 35- and 45-fold area increase, respectively. Thus, the real area of the oxidized sample was 45 times larger than that of the cylinder, the surface of which was formed only by machining (turning).

4. Conclusion

The possibility of changing the functional surface area of titanium products by controlled heating and growth of the oxide coating was shown. IHT in the air at a temperature of about 1000–1030 ºC allowed a 45-fold increase in the surface area of the titanium sample compared to the initial value, which, combined with high mechanical strength (hardness, wear resistance), will provide a higher quality of titanium products.

Acknowledgments

The research was supported by the Russian Science Foundation (project No. 18-79-10040).

References

[1] Velasco-Ortega E, Alfonso-Rodríguez C A, Monsalve-Guil L, España-López A, JiménezGuerra A, Garzón I, Alaminos M and Gil F J 2016 *Mater Sci Eng C* **64** 1

[2] Zhang W, Gu J, Zhang, Cheng, Xie Y and Zheng X 2019 *Surf Coat Technol* **358** 511

[3] Fomin A, Egorov I and Shchelkunov A 2018 *Proc SPIE* **10716** 107161O

[4] Zhang Z, Brown S, Goodall J B M, Weng X, Thompson K, Gong K, Kellici S, Clark R J H, Evans J R G and Darr J A 2009 *J Alloys Compd* **476** 451

[5] Li J, Wan W, Zhou H, Lia J and Xu D 2011 *Chem Commun* **47** 3439

Work function tailoring in gallium phosphide nanowires

V Sharov[1,2], P Alekseev[2], V Fedorov[1], I Mukhin[1,3]

[1]Alferov University, St. Petersburg, 194021, Russia
[2]Ioffe Institute, St. Petersburg 194021, Russia
[3]ITMO University, St. Petersburg 197101, Russia

vl_sharov@mail.ru

Abstract. In this work we investigate effects of the crystal phase, twinning defects and shell formation on the work function distribution over the surface of axially heterostructured GaP/GaPAs/GaP nanowires via frequency-modulated Kelvin probe force microscopy. The study revealed that the work function of pure zinc blende and wurtzite GaP is 4.34 eV and 4.20 eV respectively. The work function is found to be sensitive to the flat defects. Formation of a sub-monolayer thick GaPAs shell results in drastic increase of the work function (up to 4.75 eV). Thus, in this work we introduce several techniques for manipulating GaP nanowire work function.

1. Introduction

Semiconductor nanowires (NWs) are prospective for next-generation nano-optoelectronics [1]. In particular, GaP NWs demonstrate effective wave-guiding properties and broadband nonlinear frequency conversion, and find applications in green to amber optical range optoelectronic devices [2]. Electronic properties of semiconductor surfaces and interfaces are governed by a work function value. The ability to control the work function is relevant for fabrication of ohmic contacts in nanowire-based devices [3-5]. Despite the well-known effects of the phase polytypism in III-V NWs, the influence of the crystal phase on its electronic properties remains ambiguous. Here, the local work function of axially heterostructured GaP/GaPAs nanowires is investigated via Kelvin probe force microscopy.

2. Results and discussion

The studied NWs were grown by self-catalytic molecular beam epitaxy. The NWs possessed mixed wurtzite/zinc blende (WZ/ZB) crystal structure that was studied via transmission electron microscopy and micro-Raman mapping. ZB parts exhibited rotation twinning along the growth direction which is typical for the self-catalytic growth while WZ regions were defect-free. Also, the NWs were partly covered with sub-monolayer GaPAs shell. Spatial distribution of the local work function over the NW surface was investigated via frequency-modulated Kelvin probe force microscopy. The study revealed significant work function variation depending on NW crystal structure and the presence of As-containing shell. Thus, the work function of pure (110) ZB GaP and pure (11-20) WZ GaP was found to be 4.34 and 4.20 eV respectively. The sub-monolayer shell was found to shift the work function up to 4.75 eV.

The impact of twinning defects in ZB GaP on the work function was taken into account via one-dimensional Schrodinger-Poisson calculations. The twins can be considered as wurtzite bilayers. In this case, the work function of twinned ZB GaP lies between that of pure ZB and pure WZ. The introduced model is in agreement with the experimental results. Thus, the possibility to vary the work function of

GaP NWs over 0.55 eV is shown. Also, the ability to distinguish different crystal phases of the same material by means of Kelvin probe microscopy is shown for the first time. Another section of your paper

3. Conclusion

Here we introduce different ways for the work function tailoring in gallium phosphide nanowires. The ability to tune the work function and electron affinity can be useful for the ohmic contacts formation in GaP NW-based devices.

Acknowledgments

The work was supported by the ministry of science and higher education of the Russian Federation (0791-2020-0005).

References

[1] Barrigón E et al. 2019 *Chem. Rev.* **119.15** 9170-9220
[2] Fedorov V et al. 2020 *ACS nano* **14.8** 10624-10632.
[3] Speckbacher M et al. 2016 *Nano lett.* **16.8** 5135-5142.
[4] Standing A et al. 2015 *Nature comm.* **6.1** 1-7.
[5] Alekseev P et al. 2019 *Nano lett.* **19.7** 4463-4469.

Study of the hardness distribution after induction heat treatment of titanium over the surface and the cross-section

A Shchelkunov[1], I Egorov[1], A Fomin[1]

[1]Yuri Gagarin State Technical University of Saratov, Saratov 410054, Russia

E-mail: shelkynov.a_94@mail.ru

Abstract. In this work, the mechanical properties (microhardness) of a titanium disk after induction heat treatment (IHT) were studied. The influence of the processing parameters (inductor current and temperature) on the distribution of microhardness over the cross-section of the experimental samples was established.

1. Introduction

Currently, there is a growing demand for the use of titanium and its alloys in various industries, as well as in the field of biomedicine [1]. For this reason there is a need in studying the ways to modify its structure. The problem of using commercially pure titanium in medicine is associated with low values of tribological characteristics [2,3]. One of the options for increasing physical and mechanical parameters, in particular hardness, and reducing the friction coefficient is the formation of oxide-ceramic structures by chemical-thermal treatment [4,5].

2. Methodology

The samples to be studied were prepared from commercially pure titanium (VT1-00) and had cylindrical shapes (diameter 14 mm, thickness 2 mm). Prior to the induction heat treatment (IHT), the surface of the samples was processed by stepwise grinding by abrasive paper (P400 – P2500) until the surface roughness Ra = 0.16–0.32 μm was obtained. Another stage preceding IHT included the washing of the samples in ethanol.

IHT of titanium disks was performed using "HF-15A" setup. The treatment comprised three stages: intense heating, exposure and free cooling in the open air. The main processing parameters were the inductor current, temperature and processing duration. The temperature range corresponded to T = 900–1500 °C (±50 °C) with a duration t = 1–3, 60, 120, 300 s. The inductor current value ranged from 2.5 to 3.5 kA.

The microhardness over the surface and the cross-section of the sample was measured using "PMT-3" hardness tester (GOST 9450-76). The load on the indenter was 0.19 N. A microsection was made to measure the microhardness over the cross-section of the sample. The beginning of the measurement (from the surface of active saturation with air oxygen) was performed stepwise (50, 150 200, 300, 400, 500, 750, 1000 μm).

The temperature during IHT was controlled by thermal imaging analysis and colorimetric method (using a heat color scale). The operating current was measured using "UNI-T UT205" current clamp.

3. Results

The samples subjected to IHT were divided into three groups: low temperature (900–1100 °C), medium temperature (1150–1250 °C), and high temperature ones (1300–1500 °C). The surface microhardness in the low-temperature samples varied from 5–8 GPa to 8–11 GPa. The cross-sectional data were lower than those obtained on the surface and equaled from 7.6 to 2.6 GPa. For the medium temperature mode, the surface microhardness varied from 8–9 GPa to 16 GPa. At high temperature IHT (T = 1200±50 °C and t = 300 s), areas with a hardness of up to 20 GPa were found. In the study of the microhardness over the cross section, the values varied from 10.6 to 2.6 GPa. High temperature data were obtained for the surface measurements in the range of 8–14 GPa with the solid inclusions of 15–18 GPa. For the third group of samples, the regularity of reduced microhardness was retained and corresponded to the range of 4.5–13.6 GPa.

4. Conclusion

Thus, the average value of microhardness for the low temperature IHT group of samples (depth within 200–250 μm) was 14–18 % higher relative to deep layers (from 300 to 1000 μm), for the medium temperature group – 13–15 %, and for the high temperature group – 15– 22 %. The presence of a highly hard coating (up to 10–20 GPa) and a hard near-surface layer can increase the tribological characteristics of titanium products, which will expand the area of their effective use in the manufacture of medical products.

Acknowledgments

The reported study was funded by RFBR, project number No. 20-33-90053.

References

[1] Sarma J, Kumar R, Sahoo A K and Panda A 2020 *Mater Today Proc* **23** 561
[2] Senthilselvan J, Monisha K, Gunaseelan M, Yamini S, Kumar S Arun, Kanimozhi K, Manonmani J, Shariffc S M and Padmanabham G 2020 *Mater Charact* **160** 110118
[3] Dolgun E, Zemlyakov E, Shalnova S, Gushchina M and Promahov V 2020 *Mater Today* **30** 688
[4] Maytorena-Sánchez A, Hernández-Torres J, López-Huerta F, Hernández-Campos M A, Zamora-Peredo L, Pacio-Castillo M, Serrano-De la Rosa L E and García-González L 2021 *Mater Lett* **282** 128679
[5] Fomin A, Egorov I, Shchelkunov A, Fomina M, Koshuro V and Rodionov I 2018 *Compos Struct* **206** 467

Study of Langmuir monolayers and Langmuir-Schaefer films based on symmetrical *meso*-aryl-substituted porphyrin derivative

V N Mironyuk[1], A J K Al-Alwani[1], N N Begletsova[1], M V Pozharov[2], A I Smirnova[3], N V Usol'tseva[3], E G Glukhovskoy[1]

[1] Education and Research Institute of Nanostructures and Biosystems, Saratov State University, Saratov, 410012, Russia
[2] Institute of Chemistry, Saratov State University, Saratov, 410012, Russia
[3] Nanomaterials Research Institute, Ivanovo State University, Ivanovo, 153025, Russia

E-mail: bestblogger@yandex.ru

Abstract In this work, an experimental study of the features of the formation of meso-aryl-substituted porphyrin Langmuir monolayers was carried out. We analyzed the main mechanical parameters of monolayers, which were calculated from compression isotherms for close-packed states, as well as for the values of surface pressures at which monolayers were transferred onto solid substrates. Monolayers were transferred onto the surface of monocrystalline (silicon oxide wafer) at surface pressures of 8, 25, and 60 mN/m, and their morphology was investigated by atomic force microscopy (AFM) in the semicontact mode. Analysis of AFM images revealed the expected coarsening of molecular aggregates with an increase in the transfer pressure, and also that the maximum ordering of aggregates of porphyrin molecules is formed at a surface transfer pressure of 25 mN/m.

1. Introduction and motivation

Thin films of porphyrin derivatives are a promising material for creating thin film photovoltaic devices [1]. In this regard, an important technological problem is to control the production of ordered monomolecular layers. The Langmuir-Blodgett (LB) technology is well suited for this task, a particular case of which is the Langmuir-Schaeffer (LS) technology.

The properties of porphyrin strongly depend on the inclusion of metals inside the porphyrin ring, the presence of peripheral substituents type, which increases the number of compounds with unique properties. The molecule of the studied symmetrically substituted porphyrin has 4 hexadecyloxyphenyl substituents at the *meso*-positions of the macrocycle [2]. This substitution gives reason to expect that the amphiphilic properties of these molecules will be maximally expressed, the molecules will be easily ordered on the water surface, and their monolayer will be the most technologically advanced.

LB technology makes it possible to obtain monolayer and multilayer films of various organic molecules (such as DNA, polymers, macroheterocyclic compounds [3]), as well as films based on nanoparticles in an organic matrix [4]. By controlling the surface tension and surface potential, it is possible to achieve the required condensation of molecules and nanoobjects on the surface of water or a solid substrate.

The aim of the work is: 1 - to obtain floating (Langmuir) monolayers based on symmetrically substituted porphyrin and 2 - to study the influence of the conditions of their formation and transfer (the amount of solution introduced to the surface of the subphase, the degree of compression of monolayers) on the morphology of thin films transferred to a solid substrate by the method Langmuir-Schaefer.

2. Experiment, results and discussion

Isotherms of porphyrin monolayers were formed by using KSV NIMA LB Trough 2002 KN (medium-sized bath with a compression ratio of approximately 1:9). Deionized water at a temperature of 24 ℃ was used as an aqueous subphase. The studies used a solution of symmetrically substituted porphyrin in chloroform with a concentration of 10^{-4} M. Different volumes of porphyrin solution were placed on the water surface - 50, 100, 150 μL. The time of complete evaporation of the solvent was 10 min, after which the monolayer was compressed by two barriers at a constant rate of 13 mm/min (symmetric compression mode). Compression isotherms showed an implicit dependence on the volume of the solution applied to the surface of the subphase. The parameters of a monolayer in a densely packed state were determined. The maximum compression pressure was 66 mN/m. The calculated specific area per molecule immediately after the spread (before compression) of the porphyrin solution was about 5.3; 3.9; 2.6 nm^2 for 50, 100, 150 μL, respectively. The state of close packing for 50 μl was not achieved, and for 100 and 150 μl of the solution the specific area were 0.45 and 0.57 nm^2, respectively.

The transfer of monolayer was carried out on solid substrate of monocrystalline silicon. The natural oxide of the silicon surface was not removed, but it was pretreated with ethanol and chloroform. Monolayers were transferred by the Langmuir-Schaeffer method (horizontal lift) at surface pressures of 8; 25; and 60 mN/m. The surface relief of the samples was studied using a SOLVER NANO (AFM NT-MDT) in the semicontact mode. The resulting images were processed using the Gwyddion Version 2.58 data visualization and analysis software.

Typical dimensions for nanoobjects were 100-150 nm in plan and up to 10 nm in height for films obtained at a pressure of 8 mN/m, and with a planar size of 450-500 nm and a height of up to 20 nm for films obtained at a pressure of 60 mN/m, that is the height and lateral dimensions of the objects increased with increasing transfer pressure. Statistical processing of AFM images also showed the expected coarsening of molecular aggregates and film roughness with an increase in the surface transfer pressure to 60 mN/m.

Acknowledgments

The study was supported by a grant from the Russian Science Foundation (project No. 21-73-20057)

References

[1] Zeng K, Tong Z, Ma L, Zhu W-H, Wu W and Xie Y 2020 Molecular engineering strategies for fabricating efficient porphyrin-based dye-sensitized solar cells *Energy Environ. Sci.* **13** 1617–57

[2] Begletsova N N, Mironyuk V N, Ezhov A V, Smirnova A I, Usol'tseva N V and Glukhovskoy E G 2020 Features of formation of Langmuir monolayers of porphyrin derivatives on the surface of aqueous solutions of copper nanoparticles *J. Phys.: Conf. Ser.* **1697** 012118

[3] Kazak A V, Marchenkova M A, Smirnova A I, Seregin A Yu, Rogachev A V, Klechkovskaya V V, Arkharova N A, Warias J E, Murphy B M, Tereschenko E Yu, Usol'tseva N V and Kovalchuk M V 2020 Floating layers and thin films of mesogenic mix-substituted phthalocyanine holmium complex *Thin Solid Films* **704** 137952

[4] Kim V P, Ermakov A V, Glukhovskoy E G, Rakhnyanskaya A A, Gulyaev Yu V, Cherepenin V A, Taranov I V, Kormakova P A, Potapenkov K V, Usmanov N N, Saletsky A M, Koksharov Yu A and Khomutov G B 2014 Planar nanosystems on the basis of complexes formed by amphiphilic polyamine, magnetite nanoparticles, and DNA molecules *Nanotechnol Russia* **9** 280–7

The influence of a pentagonally structured Pd-coating on the low-temperature hydrogen permeability of palladium-based membranes

I. Petriev[1,2], P. Pushankina[1], I. Lucenko[1], Y. Glazkova[1], T. Malkov[1]

[1]Department of Physics, Kuban State University, Krasnodar, 350040, Russia
[2]Laboratory of problems of stable isotope spreading in living systems, Southern Scientific Centre of the RAS, Rostov-on-Don, 344000, Russia

petriev_iliya@mail.ru

Abstract. Methods of modifying the surface of Pd-23%Ag alloy films have been developed in order to increase the rate of hydrogen permeability and to produce palladium-containing nanoparticle and nanoflower type coatings. Modification of the membrane surface makes it possible to measure the permeability in the temperature range up to 100°C. Membranes modified with nanoflower type pentagonally branched crystallites show a flux density of hydrogen of up to 0.39 mmol s^{-1} m^{-2} at a pressure of 0.3 MP in the low temperature range (<100°C). The flux density of hydrogen for membranes modified by such coatings is 2.1 times higher than the flux of hydrogen through membranes modified by the classical palladium black method.

1. Introduction

Palladium-based membranes are used to generate high-purity hydrogen. One of the ways to modify the membrane surface is to develop a nanostructured layer using powdered chemisorbing hydrogen substances [1]. The aim of this study was to obtain resistant to long-term use palladium-containing films, modified with a pentagonally structured coating of the "nanoflower" type, capable of transfering hydrogen at low temperatures. This will reduce energy costs in the process of producing high-purity hydrogen, as well as use the developed membranes to develop a hydrogen electrode of an oxygen-hydrogen fuel cell operating at low (0-100°C) temperatures.

2. Results and discussion

In this study two methods of surface modification have been developed: the classical method of palladium black "nanoparticles" and a novel author method "nanoflowers". Modified films surface microphotographs, obtained by scanning electron microscope JEOL JSM-7500F, are shown in Figure 1.

Pentagonally structured palladium nanocrystallites were obtained by the electrochemical method from a growth solution containing a surfactant tetrabutylammonium bromide. A necessary condition for obtaining such structures was a current density reduced than the classical palladium black method.
Thin (10 μm) palladium-silver films were modified on both sides with the developed coatings. After that, these films were used as membranes in studies of hydrogen permeability. The values of the hydrogen flux for membranes modified by the "nanoflower" method are approximately 2.1 times

higher than the values for membranes obtained by the classical palladium black method that can be seen from Figure 2.

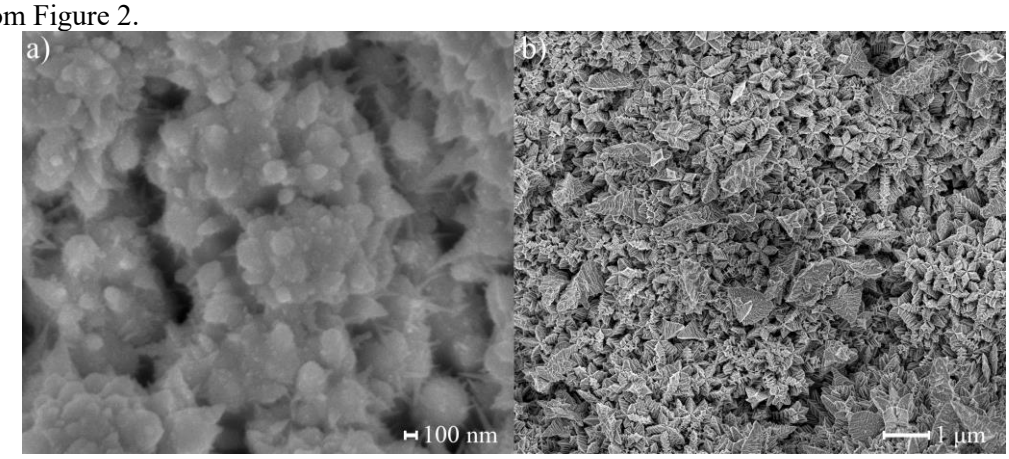

Figure 1. Microphotographs of the Pd-Ag films surface with modifying coatings obtained by methods: (a) "nanoparticles" and (b) "nanoflowers".

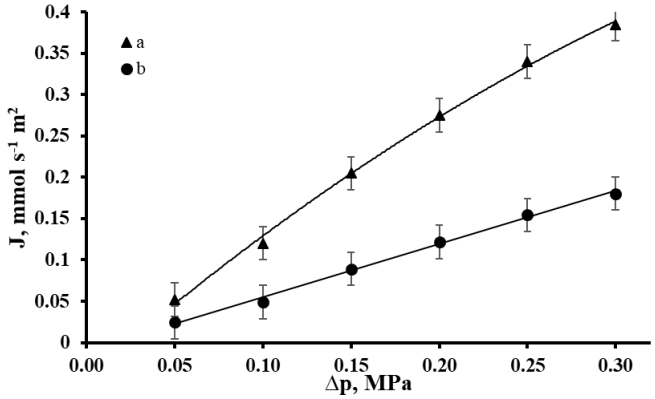

Figure 2. Dependence of the flux on the hydrogen gauge pressure on the inlet side of membranes modified by methods (a) "nanoflowers" and (b) "nanoparticles".

The membrane surface coatings formation with fundamentally new "nanoflowers" structure increases the surface adsorption activity, which affects the material catalytic activity with respect to reactions involving hydrogen, as in [2]. It is supposed that this is the reason for the decrease of the hydrogen molecules dissociation and recombination energy barrier on the membrane surface, which leads to the increased rate of the hydrogen permeation through the Pd-23% Ag alloy membrane. The obtained experimental data allow to say that the membrane surface adsorption activity enhance is due to an extensive way of increasing in the development, specific area of the coating as well as an intensive way of creating a given modifying coating structural organization.

Acknowledgments

The research was funded by RFBR and administration of Krasnodar Territory, project number № 20-42-235001 and Ministry of Science and Higher Education state assignment of Kuban state university № FZEN-2020-0022.

References

[1] W. Vielstich, Brennstoffelemente. Moderne Verfahren zur elektrochemischen Energlegewfnming. Weinheim: Verlag Chemie (1965).

[2] Lytkina A.A., Orekhova N.V., Ermilova M.M. et. al.// Int. J. Hydrogen Energy. 2019. V. 44. № 26. P. 13310.